



**HAL**  
open science

# Magnetic flux distorsion in two-phase liquid metal flow

Mithlesh Kumar

► **To cite this version:**

Mithlesh Kumar. Magnetic flux distorsion in two-phase liquid metal flow. Fluids mechanics [physics.class-ph]. Institut National Polytechnique de Toulouse - INPT, 2016. English. NNT: 2016INPT0021 . tel-04238673

**HAL Id: tel-04238673**

**<https://theses.hal.science/tel-04238673v1>**

Submitted on 12 Oct 2023

**HAL** is a multi-disciplinary open access archive for the deposit and dissemination of scientific research documents, whether they are published or not. The documents may come from teaching and research institutions in France or abroad, or from public or private research centers.

L'archive ouverte pluridisciplinaire **HAL**, est destinée au dépôt et à la diffusion de documents scientifiques de niveau recherche, publiés ou non, émanant des établissements d'enseignement et de recherche français ou étrangers, des laboratoires publics ou privés.



Université  
de Toulouse

# THÈSE

En vue de l'obtention du

## DOCTORAT DE L'UNIVERSITÉ DE TOULOUSE

Délivré par :

Institut National Polytechnique de Toulouse (INP Toulouse)

Discipline ou spécialité :

Dynamique des fluides

---

Présentée et soutenue par :

M. MITHLESH KUMAR

le mercredi 23 mars 2016

Titre :

MAGNETIC FLUX DISTORTION IN TWO-PHASE LIQUID METAL FLOW

---

Ecole doctorale :

Mécanique, Energétique, Génie civil, Procédés (MEGeP)

Unité de recherche :

Institut de Mécanique des Fluides de Toulouse (I.M.F.T.)

Directeur(s) de Thèse :

M. PHILIPPE TORDJEMAN

M. WLADIMIR BERGEZ

Rapporteurs :

M. GERARD VINSARD, INP DE NANCY

M. LAURENT DAVOUST, INP DE GRENOBLE

Membre(s) du jury :

M. CHRISTOPHE AIRIAU, UNIVERSITE TOULOUSE 3, Président

M. PHILIPPE TORDJEMAN, INP TOULOUSE, Membre

M. THOMAS GUNDRUM, HZDR, Membre

M. WLADIMIR BERGEZ, INP TOULOUSE, Membre



# Acknowledgments

The work presented in this thesis, is a collaboration between Commissariat à l'énergie atomique et aux énergies alternatives (CEA), Cadarache, France and Institut de Mécanique des Fluides de Toulouse (IMFT), Toulouse, France. There are a number of researchers and technicians associated from both research facilities who have actively participated in this work.

I would first like to thank my PhD supervisor Philippe Tordjeman and co-supervisor Wladimir Bergez at IMFT, for their able guidance and motivation over the course of this work. I am grateful to the technical support of Gregory Ehses and Herve Ayroles in designing my experiments at IMFT Toulouse. Its my duty to acknowledge the work of our interns, Emeryk Ablonet for his experiments with hole-type voids and Marie Poulain for her experiments on ECFM in 5-coils configuration at IMFT. I wish them best of luck. Thanks are also due to Matthieu Cavaro at CEA Cadarache, whose investigations regarding gas presence in SFR forms the starting point for the work presented in this thesis. Besides, I would like to thank Kevin Paumel at CEA, for fruitful discussions on various results and his insightful queries from which I have greatly benefited. Its my duty to thank my funding agency CEA Cadarache, and in particular Jean-Philippe Jeannot, Olivier Gastaldi and Christian Latgé. I further acknowledge the help of secretaries at both IMFT and CEA who have helped me over the years with administrative formalities.

I am grateful for the warm welcome at CEA Cadarache and friendly working environment at IMFT Toulouse. I would like to thank all my colleagues whose scientific aptitude encourages to think in the right direction.



# Abstract

A Generation IV Sodium cooled Fast Reactor (SFR) is being researched and developed at CEA, Cadarache France under the project named ASTRID. Monitoring gas presence in SFR is important with respect to its safe operation. In accordance with the principles of diversity, techniques based on different measurement principles have been proposed. This thesis concerns the detection and characterization of void using magnetic flux perturbation principle. An Eddy Current Flow Meter (ECFM) device is used for this purpose. From the technological point of view, the objective is to evaluate the feasibility of ECFM as a flow and/or void monitoring/characterizing device; and to determine which parameters are of interest and what are the precision of these measurements; and whether it is possible to measure the flow rate and void fraction simultaneously with the same ECFM device. From the physics point of view, the ECFM system involves the magnetic flux perturbation due to voids in the presence of Faraday induction and Lorentz force effects. Therefore ECFM integrated signal contains informations about the void, Faraday induction and Lorentz force effects based perturbation in magnetic flux and their couplings. Our objective is to understand the nature and extent of these couplings.

Specific experiments have been developed to study the effects of flow velocity, void fraction and magnetic flux pulsations on the response of an ECFM. It consists in modeling the two-phase flow by a moving aluminium rod (plug flow) with holes and grooves to simulate voids. Flow velocity range of variation was  $0 \leq U \leq 1$  m/s, void fraction  $0 \leq \alpha \leq 6.9\%$  and pulsation  $1500 < \omega < 12000$  rad/s (for this range of pulsations the electromagnetic skin depth is of order but smaller than the aluminium rod radius). An ellipse fitting method was proposed to analyze the output signal of the secondary coils. The results show that ECFM is sensitive to void fractions between 0.3 % and 6.9%. Furthermore, the response to void fraction is insensitive to the mean velocity of the two-phase medium. A second approach based on demodulation analyses of the secondary coils output signal has been developed. We have proposed a theoretical model based on a first order expansion of magnetic flux in  $U$  and  $\alpha$ . With this model it was possible to interpret the experimental results in terms of contributions of  $U$  and  $\alpha$ . Despite the strong coupling between Faraday induction and Lorentz force effects, the results show that the contributions of  $U$  and  $\alpha$  can be well separated at low magnetic Reynolds number ( $Re_m < 0.12$ ) and low  $\alpha$  values ( $\alpha < 6.9\%$ ). A very important result is that the contribution of  $\alpha$  on magnetic flux is insensitive to variations of velocity in this range

of  $Re_m$ . Moreover, different geometries of void have been studied: grooves and holes. It was observed that the geometry of void do not change the variation of magnetic flux with  $\alpha$ . This second approach revealed to be more sensitive to void fraction variations than ellipse fitting method. Finally, preliminary experiments with liquid metal galinstan with glass beads were done, which showed sensitivity of ECFM signal with velocity and void. In conclusion, this work has shown that ECFM can measure simultaneously void and velocity in the range of parameters studied, in particular  $0.06\% < \alpha < 6.9\%$ .

# Résumé

Cette thèse se situe dans le cadre du projet ASTRID du CEA qui concerne l'étude et le développement de la génération IV de réacteurs nucléaires à Neutrons Rapides refroidis par Sodium liquide (RNR Na). La surveillance de la présence de gaz dans un RNR est importante pour son fonctionnement en toute sécurité. Conformément au principe de diversité, des techniques basées sur différents principes de mesure ont été proposés. Cette thèse porte sur la détection et la caractérisation de présence de bulles de gaz en utilisant le principe de perturbation du flux magnétique. Un débitmètre à distorsion de flux (DDF) est utilisé à cet effet. Du point de vue technologique, l'objectif est d'évaluer la faisabilité de l'utilisation d'un DDF en vue de la surveillance et la caractérisation du taux de vide dans le Sodium liquide, ainsi que de déterminer quels sont les paramètres d'intérêt et quelle est la précision de ces mesures; enfin, s'il est possible de mesurer le débit et le taux de vide simultanément avec un DDF. Du point de vue de la physique, le DDF mesure la perturbation du flux magnétique due aux courants de Foucault induits par l'hydrodynamique d'un écoulement de liquide conducteur. En présence de vide dans le conducteur, une nouvelle source de perturbation apparaît du fait de la modification, par le taux de vide, de la distribution du champ magnétique. En effet, la présence de vide agit sur les distributions locales de courants électriques dues au couplage des phénomènes d'induction et de forces de Lorentz. Notre objectif est de comprendre la nature de ces couplages et de proposer une méthode qui permette de caractériser la présence de vide à partir du signal de sortie du DDF, de mesurer le taux de vide et d'étudier la sensibilité de cette mesure aux variations des paramètres de l'écoulement et du champ électromagnétique (vitesse et pulsation, en particulier).

Dans ce travail, des expériences spécifiques ont été développées pour étudier les effets de la vitesse, du taux de vide et de la pulsation du flux magnétique sur la réponse d'un DDF. Ces expériences modélisent un écoulement diphasique idéal (écoulement piston) consistant en une barre mobile d'aluminium (écoulement piston) contenant des trous et des cannelures pour simuler le taux de vide. Dans ces expériences la vitesse, le taux de vide et la pulsation sont parfaitement contrôlé et leur domaine de variations sont les suivants :  $0 \leq U \leq 1$  m/s pour la vitesse,  $0 \leq \alpha \leq 6.9\%$  pour le taux de vide et  $1500 < \omega < 12000$  rad/s pour la pulsation (dans cette gamme de pulsations, on notera que la profondeur de pénétration du champ électromagnétique est de l'ordre de, mais plus petit que, le rayon du barreau d'aluminium). Une méthode d'ellipse-fitting appliqué au signal de sortie du DDF a été utilisée pour caractériser l'effet du taux de vide. Les



résultats montrent que le DDF est sensible pour des fractions volumique de vide entre 0.3 % and 6.9% . En outre, la réponse aux variations de taux de vide est insensible à la vitesse du barreau. Cette technique est peu adaptée aux mesures des faibles taux de vide ( $< 0.1\%$ ). Une deuxième approche a été développée, sur la base de l'analyse du signal démodulé du DDF. Cette analyse s'appuie sur un modèle théorique du flux magnétique obtenu par un développement au 1er ordre par rapport à  $U$  et  $\alpha$ . Ce modèle permet d'interpréter les résultats expérimentaux en termes de contributions de  $U$  et  $\alpha$  au flux magnétique. Malgré le couplage fort entre l'induction Faraday et les forces de Lorentz, les résultats montrent que les contributions de  $U$  et  $\alpha$  peuvent être séparées correctement pour des petites valeurs du nombre de Reynolds magnétique ( $Re_m < 0.12$ ), et de faible taux de vide ( $\alpha < 6.9\%$ ). Un résultat très important est que la contribution de  $\alpha$  sur le flux magnétique est insensible aux variations de vitesse dans cette gamme de  $Re_m$ . De plus, l'effet de la géométrie du vide a été étudié pour deux configurations : cannelures et trous. Il a été observé que la géométrie du vide n'a pas d'effet sur les variations du flux magnétique avec  $\alpha$ . Cette seconde approche est plus sensible aux variations de fraction volumique du vide que la méthode de l'ellipse-fitting. Enfin, des expériences préliminaires avec un liquide métallique (Galinstan) contenant des perles de verre, ont été faites et ont montré une bonne sensibilité du signal du DDF avec la vitesse et le taux de vide. En conclusion, ce travail a montré qu'il est possible de mesurer simultanément un taux de vide et un débit pour la gamme de variations des paramètres étudiés, en particulier  $0.06\% < \alpha < 6.9\%$ .

# Contents

<b>Introduction</b>	<b>3</b>
<b>1 Context and objectives</b>	<b>5</b>
1.1 Fourth generation Sodium cooled fast reactors . . . . .	5
1.2 Gas presence in sodium . . . . .	6
1.3 Industrial strategy . . . . .	8
1.4 Fundamental equations . . . . .	10
1.4.1 Properties of liquid sodium . . . . .	10
1.4.2 Basics of electromagnetic fields . . . . .	11
1.4.3 Basics of fluid motion . . . . .	13
1.4.4 The Hartmann problem . . . . .	14
1.5 Electromagnetic techniques . . . . .	18
1.5.1 Induced voltage technique . . . . .	18
1.5.2 Induced field technique . . . . .	19
1.6 Scope of the thesis . . . . .	20
<b>2 Literature Review</b>	<b>23</b>
2.1 ECFM in single phase flows . . . . .	23
2.2 ECFM in two-phase flows . . . . .	32
2.3 Single fluid with equivalent properties . . . . .	39
2.3.1 Dependence of induced emf on electrical conductivity . . . . .	40
2.3.2 Effective electrical conductivity of two-phase media . . . . .	40
2.4 General two-phase medium . . . . .	46
2.4.1 Models without induction effects . . . . .	47
2.4.2 Models at high pulsations . . . . .	52
2.5 Conclusions and unanswered questions . . . . .	60
<b>3 Theoretical analyses of ECFM</b>	<b>63</b>
3.1 Single phase flow . . . . .	64
3.2 Two-phase flow . . . . .	74
3.2.1 Small Faraday and small Lorentz force effects . . . . .	75
3.2.2 Significant Faraday induction and small Lorentz force effects . . . . .	79
3.3 Lissajous ellipse fitting approach . . . . .	80

3.4	Conclusions . . . . .	82
<b>4</b>	<b>Experiments in model two-phase liquid metal flow</b>	<b>85</b>
4.1	Experimental set up . . . . .	85
4.1.1	Two-phase medium . . . . .	87
4.1.2	Uniaxial displacement controller . . . . .	90
4.1.3	Excitation and acquisition . . . . .	91
4.1.4	ECFM assembly . . . . .	95
4.2	Difference signal approach . . . . .	96
4.2.1	Methodology . . . . .	96
4.2.2	Results . . . . .	101
4.2.3	Discussions . . . . .	112
4.3	Lissajous ellipse fitting approach . . . . .	117
4.3.1	Methodology . . . . .	117
4.3.2	Results . . . . .	118
4.3.3	Discussions . . . . .	131
4.4	Conclusions . . . . .	131
<b>5</b>	<b>Experiments with liquid Galinstan</b>	<b>135</b>
5.1	Experimental set up . . . . .	137
5.2	Method and Results . . . . .	141
5.3	Conclusions . . . . .	147
	<b>Conclusions and Perspectives</b>	<b>149</b>
	<b>Appendices</b>	<b>153</b>
<b>A</b>	<b>Publication: Thermo-magnetic behaviour of AFM-MFM cantilevers</b>	<b>153</b>
<b>B</b>	<b>Publication: Void effects on eddy current distortion in two-phase liquid metal</b>	<b>163</b>
<b>C</b>	<b>Review of two-phase MHD</b>	<b>167</b>
<b>D</b>	<b>Theoretical expansion in Lissajous ellipse fitting approach</b>	<b>173</b>
	<b>Bibliography</b>	<b>177</b>

# List of Figures

1.1	Schematic of a pool type fast neutron reactor. . . . .	6
1.2	Design improvements to minimize gas presence in normal and incident conditions in SFR . . . . .	9
1.3	Geometry of the Hartmann problem . . . . .	14
1.4	Boundary conditions in Hartmann problem . . . . .	15
1.5	Velocity profiles for various $Ha$ . . . . .	16
1.6	The schematic diagram of an induced voltage flowmeter. . . . .	19
1.7	A flow-through type ECFM. . . . .	20
2.1	Three coils ECFM . . . . .	25
2.2	Three coils ECFM sensitivity to flow . . . . .	26
2.3	A 5-coils ECFM. . . . .	27
2.4	A similar 3-coils ECFM system . . . . .	27
2.5	ECFM flow signal vs $\omega$ . . . . .	29
2.6	ECFM flow signal magnitude and phase vs $\omega$ . . . . .	30
2.7	ECFM flow signal sensitivity to flow vs temperature . . . . .	31
2.8	ECFM flow signal sensitivity to flow vs temperature at critical frequency . . . . .	31
2.9	ECFM possible locations in an SFR . . . . .	32
2.10	Oscilloscope trace of ECFM signal in presence of gas . . . . .	33
2.11	Response of ECFM to large gas bubble . . . . .	33
2.12	ECFM sensitivity to $\alpha$ , for continuous gas vs single bubbles case . . . . .	34
2.13	Saturation of ECFM sensitivity to $\alpha$ . . . . .	35
2.14	An experimental set up for liquid metal two-phase flow studies with ECFM . . . . .	36
2.15	The schema of phase sensitive ECFM signal treatment [43]. . . . .	36
2.16	Optimum phases for flow and void related fluctuations [43]. . . . .	37
2.17	Quadrature phase signal vs $\alpha$ . . . . .	37
2.18	CIFT technique . . . . .	39
2.19	Induced potential in ECFM secondary coils vs $\sigma$ . . . . .	40
2.20	Network model for electrical conductivity . . . . .	41
2.21	Description of the Maxwell medium . . . . .	42
2.22	Electrical conductivity of two-phase medium in Maxwell's model . . . . .	43
2.23	Comparison of $\mathcal{O}(\alpha)$ and $\mathcal{O}(\alpha^2)$ models for electrical conductivity . . . . .	44
2.24	Comparison of various models for equivalent electrical conductivity of two-phase medium . . . . .	45

2.25	Induced emf in ECFM with $\alpha$ using Maxwell's model . . . . .	46
2.26	The two types of eddy currents. . . . .	48
2.27	Electromagnetic flowmeter signal in two-phase flows . . . . .	48
2.28	Electromagnetic flowmeter sensitivity to $\alpha$ . . . . .	49
2.29	Treatment of Faraday induction eddy currents in Electromagnetic flowmeters . . . . .	50
2.30	A classic normalized impedance plane curve. . . . .	52
2.31	An infinite cylinder with flaw enclosed by a single turn coil . . . . .	54
2.32	Sensitivity of an external coil to sub-surface void . . . . .	55
2.33	Sensitivity of an external coil to void on the surface . . . . .	57
2.34	Small vs large skin depth compared to void size . . . . .	58
2.35	Laplace vs Born limit for surface cracks . . . . .	58
2.36	The eddy current distribution around voids . . . . .	59
3.1	Distribution of radial magnetic fields inside ECFM . . . . .	66
3.2	Geometry for calculation of eddy currents distribution at first order. . . . .	67
3.3	The distribution of the magnetic fields and current densities inside 5-coils ECFM . . . . .	70
3.4	Scema for numerical simulations in COMSOL <sup>®</sup> . . . . .	71
3.5	Flow sensitivity vs flow-channel radius . . . . .	72
3.6	Flow sensitivity vs length of primary and secondary coils . . . . .	72
3.7	Flow sensitivity vs length of secondary coils keeping length of primary coil as constant . . . . .	73
3.8	Flow signal vs $U$ . . . . .	73
3.9	Flow signal vs $\omega$ . . . . .	74
3.10	Biot Savart's law. . . . .	76
3.11	Typical Lissajous curve of secondary coil signals . . . . .	81
3.12	Phase difference of emf in two secondary coils vs $U$ . . . . .	82
4.1	Block diagram of the experimental set up for three coils ECFM. . . . .	86
4.2	Schematic of the experimental set up for three coils ECFM. . . . .	87
4.3	Picture of groove-type aluminium rods . . . . .	88
4.4	Schema for void fraction calculations for groove-type rods . . . . .	88
4.5	Picture of hole-type rods . . . . .	89
4.6	Schema for void fraction calculations for hole-type rods . . . . .	89
4.7	Schematic of a uniaxial displacement controller . . . . .	90
4.8	Test of velocity and positions of ECFM on uni-axial displacement controller . . . . .	91
4.9	Test of stability of applied AC current . . . . .	92
4.10	Description of oscilloscope used in the experiments . . . . .	93
4.11	Functional description of a Lockin amlifier . . . . .	93
4.12	Schematic of demodulation using a Lockin amplifier . . . . .	94
4.13	Picture of Lockin amplifier used in experiments . . . . .	94
4.14	ECFM fabricated for experiments at IMFT. . . . .	95
4.15	Experimental setup which models two-phase flow for studies with ECFM. . . . .	96

4.16	Typical demodulated voltage difference of the two secondary coils . . . . .	98
4.17	FFT spectral density of $  \Delta V  ^2$ signal . . . . .	99
4.18	Induced emf for non-periodic distribution of grooves . . . . .	100
4.19	$\Delta V$ vs $t(s)$ for $\alpha = 0\%$ . . . . .	101
4.20	Results analyzed with the first theoretical approach . . . . .	102
4.21	$\phi_0$ vs $\omega$ for groove-type voids . . . . .	103
4.22	$\phi_0$ vs $\omega$ for hole-type voids . . . . .	104
4.23	$Re_m\phi_u$ vs $\omega$ for groove-type voids . . . . .	104
4.24	$Re_m\phi_u$ vs $\omega$ for hole-type voids . . . . .	105
4.25	$Re_m\phi_u$ vs $U$ for groove-type voids . . . . .	105
4.26	$Re_m\phi_u$ vs $U$ for hole-type voids . . . . .	106
4.27	$\psi_\alpha$ vs $\omega$ for groove-type voids . . . . .	106
4.28	$\psi_\alpha$ vs $\omega$ for hole-type voids . . . . .	107
4.29	$\psi_\alpha$ vs $U$ for groove-type voids . . . . .	107
4.30	$\psi_\alpha$ vs $U$ for hole-type voids . . . . .	108
4.31	$  \psi_\alpha  $ vs $\alpha$ . . . . .	108
4.32	$\omega_\alpha$ vs $U$ and $\omega$ . . . . .	109
4.33	The magnitude of first harmonic in spectral density of $  \Delta V  ^2$ vs $Re_m$ for groove-type voids . . . . .	110
4.34	The magnitude of first harmonic in spectral density of $  \Delta V  ^2$ vs $Re_m$ for hole-type voids . . . . .	110
4.35	The magnitude of second harmonic in spectral density of $  \Delta V  ^2$ vs $Re_m$ for groove-type voids . . . . .	111
4.36	The magnitude of second harmonic in spectral density of $  \Delta V  ^2$ vs $Re_m$ for hole-type voids . . . . .	111
4.37	Numerical simulation for $\vec{B}_0$ . . . . .	114
4.38	Dynamics of $A_1$ and $A_2$ . . . . .	116
4.39	$\Delta V$ time signal . . . . .	118
4.40	$\Delta V$ FFT spectrum density . . . . .	119
4.41	$\Delta V$ (V) vs $U$ . . . . .	120
4.42	A typical Liassajous curve obtained by $V_1(t)$ vs $V_2(t)$ fitted by ellipse fitting algorithm . . . . .	121
4.43	$\Delta\beta$ vs $I$ . . . . .	122
4.44	$\Delta V$ and $\beta$ time signal for single void . . . . .	122
4.45	$\Delta V$ and $\beta$ time signal for $\alpha = 6.9\%$ . . . . .	123
4.46	$\Delta V$ and $\beta$ time signal for $\alpha = 0.3\%$ . . . . .	124
4.47	$\Delta V$ and $\beta$ time signal for $\alpha = 0\%$ . . . . .	125
4.48	Effect of assymetry in secondary coils on $\delta\beta$ . . . . .	125
4.49	$\beta$ spectral density . . . . .	126
4.50	$\Delta\beta$ vs $\omega$ . . . . .	126
4.51	$\Delta\beta$ vs $U$ . . . . .	127
4.52	Schematic of 5-coils ECFM experiments. . . . .	128
4.53	Typical $\beta(t)$ time signal for 5-coils ECFM . . . . .	129

4.54	Comparison of histograms of $\beta(t)$ at two different $U$ . . . . .	130
5.1	Picture of experimental bench for Galinstan experiments . . . . .	138
5.2	Picture of Galinstan reservoir . . . . .	139
5.3	View of individual threads with glass beads. . . . .	139
5.4	Schematic of the experimental set up. . . . .	140
5.5	Spatial distribution of beads . . . . .	140
5.6	$\Delta V$ time signal for $\alpha = 0\%$ . . . . .	142
5.7	$\text{Re}_m \phi_u$ vs $U$ for $\alpha = 0\%$ . . . . .	143
5.8	$\Delta V$ time signal for beads confined to one cross-section plane . . . . .	144
5.9	$\Delta V$ vs $t$ for $\alpha = 0\%$ and $\alpha = 0.1\%$ . . . . .	144
5.10	FFT spectrum density of $\Delta V$ for $\alpha = 0\%$ and $\alpha = 0.1\%$ . . . . .	145
5.11	$\Delta V$ vs $t$ for $\alpha = 1.4\%$ . . . . .	146
5.12	FFT spectral density of $\Delta V$ for $\alpha = 1.4\%$ . . . . .	147

# List of Tables

- 4.1 Dimensions of groove-type rods . . . . . 87
- 4.2 Dimensions of hole-type rods . . . . . 89
  
- 5.1 Table of comparison of physical properties of liquid metal. . . . . 136
- 5.2 Values of parameters defining beads distribution in Galinstan . . . . . 141





# Nomenclature

## Greek symbols

$\alpha$	Void volume fraction
$\beta$	Tilt angle
$\Delta\beta$	Magnitude of perturbations in tilt angle
$\delta$	Skin-depth of magnetic flux
$\epsilon_0$	Electrical permittivity of free space
$\eta$	Dynamic viscosity
$\lambda_\alpha$	Separation between voids
$\mu_0$	Magnetic permeability of free space
$\nu$	Frequency of AC current in primary coil of ECFM
$\phi$	Magnetic flux
$\phi_0$	Magnetic flux in static medium
$\text{Re}_m\phi_u$	Magnitude of perturbation in magnetic flux due to Lorentz force effects
$\psi_\alpha$	Magnitude of perturbation in magnetic flux due to void effects
$\sigma$	Electrical conductivity
$\sigma_\alpha$	Electrical conductivity of two-phase medium
$\rho$	Density
$\tau$	Characteristic time scale
$\chi$	Compressibility
$\omega$	Pulsation of AC current in primary coil of ECFM

## Latin Symbols

$A, \vec{A}$	Magnetic vector potential
--------------	---------------------------

$B, \vec{B}$	Magnetic flux density
$B_0, \vec{B}_0$	Externally imposed magnetic flux density
$B_r, \vec{B}_r$	Radial component of magnetic flux density
$B_z, \vec{B}_z$	Axial component of magnetic flux density
$c$	Celerity
$d_g$	depth of a groove
$d_h$	diameter of a hole
$D$	Flow channel diameter
$e$	Euler's number
$E, \vec{E}$	Electric field
$F, \vec{F}$	Lorentz force
Ha	Hartmann number
$I, I_0$	Current in the primary coil
$J, \vec{J}$	Electrical current density
$J_t, \vec{J}_t$	Eddy currents density due to Faraday induction effects
$J_f, \vec{J}_f$	Eddy currents density due to Lorentz Force effects
$J^e, \vec{J}^e$	Electrical current density in primary coil
$L$	Characteristic length scale
$l_g$	Length of a groove
$l_h$	Depth of a hole
$L_p, L, s$	Length of primary and secondary coil respectively
$N_p, N_s$	Number of turns in primary and secondary coils
$^{239}Pu$	Plutonium-239 isotope
$Q$	Flow rate
$R$	Flow channel radius
Re	Reynolds number
$Re_m$	Magnetic Reynolds number
$S$	Enclosed surface area
$t$	time

$u, \vec{u}, U, \vec{U}$	Velocity
$^{238}\text{U}$	Uranium-238 isotope
$V$	Induced emf
$V_u$	Flow induced emf
$\Delta V$	Difference of induced emfs in two secondary coils
$Z$	Coil impedance

### Other symbols

$\parallel$	Component in-phase with the current in primary coil
$\perp$	Component in quadrature-phase ( $\pi/2$ out of phase) with the current in primary coil
$\ Q\ $	Norm of a quantity $Q$
$\langle Q_1 Q_2\rangle$	Scalar products of quantities $Q_1$ and $Q_2$
$[Q_1, Q_2]$	Vector with magnitudes $Q_1$ and $Q_2$ respectively in two directions

### Derivatives

$\frac{\partial}{\partial t}$	Partial derivative with respect to time
$\frac{\partial}{\partial x_i}$	Partial derivative with respect to coordinate $x_i$
$\frac{d}{dx_i}, \frac{d}{dx_i}$	Proper derivative with respect to coordinate $x_i$
$\frac{D}{Dt}, \frac{D}{Dt}$	Material derivative or total derivative



# Abbreviations

AC	Alternating Current
ASN	Autorité de Sureté Nucléaire
ASTRID	Advanced Sodium Technological Reactor for Industrial Demonstration
ALNICO	Aluminium Nickel Cobalt alloy
CEA	Commissariat à l'énergie atomique et aux énergies alternatives
CIFT	Contactless Inductive Flow Tomography
DTN	Département de Technologie Nucléaire
ECFM	Eddy Current Flow Meter
EM	Electro-Magnetic
emf, <i>emf</i>	Electro-Motive Force
FFT	Fast Fourier Transform
GaInSn	Gallium Indium tin eutectic alloy commonly known as Galinstan
GFR	Gas-cooled Fast Reactor
GIF	Generation IV International Forum
IMFT	Institut Mécanique des Fluides de Toulouse
LIET	Laboratoire d'instrumentation et d'essai technologique
MHD	Magneto-Hydro Dynamics
MIT	Mutual Inductance Tomography
MSR	Molten Salt Reactor
Na	Chemical symbol of sodium
PEEK	Polyether Ether Ketone
SCWR	Super-Critical Water-cooled Reactor

SFR	Sodium Fast Reactor
SP	Single-phase flow
TP	Two-phase flow
VHTR	Very High-Temperature gas cooled Reactor

# Introduction

Sodium cooled Fast Reactors (SFR) are one of the promising reactor concepts among other Generation IV nuclear reactor technologies. France is developing a prototype Generation IV SFR called ASTRID (Advanced Sodium Technological Reactor for Industrial Demonstration). Generation IV nuclear reactors are characterized by their improved safety among some other unique features. France has gained feedback of experience from operation of three previous French SFRs, Rapsodie, Phénix and Superphénix. The demonstration of safe operation in the presence of gas in sodium has been identified as one of the requirements for ASTRID. Gases in sodium come from the Argon cover gas, nuclear reactions etc. This gas presence in sodium modifies its acoustic celerity, thus hindering acoustic/ultrasonic based under-sodium monitoring and control. Hypothetical situation of gas pocket formation and a subsequent release of a large gas bubble, has the potential of introducing neutronic and thermal hydraulic perturbations in reactor core. To study these effects, we require reliable detection and characterization of gas in sodium. But sodium being opaque, renders many commonly used techniques for gas detection in two-phase flows unusable. Two physical principles have been proposed in this regard: acoustic techniques and electromagnetic techniques. This thesis concerns the later.

Techniques based on magnetic flux distortion, commonly known as Eddy Current Flow Meter (ECFM) is known to SFR flow monitoring applications. In ECFM, external coil(s) creates AC magnetic flux in the medium. The motion of liquid metal (through/over ECFM) creates distortion in this external flux owing to Lorentz force effects. This distortion is sensed by secondary search coil(s). In two-phase liquid metal flow, additional distortion in magnetic flux comes from the presence of voids/bubbles in the medium.

From the physics point of view, our objective is to understand the Lorentz force effects due to flow velocity  $U$ , Faraday induction effects due to pulsation of magnetic flux  $\omega$  and void effects due to void volume fraction  $\alpha$ . This also includes an understanding of coupling between these three and their subsequent effect on magnetic flux distortion in two-phase liquid metal flow.

From technological point of view, our objective is to first determine whether ECFM is sensitive to the presence of voids in two-phase liquid metal flows. Then we evaluate whether it is possible to characterize  $\alpha$  and  $U$  simultaneously with one ECFM. And subsequently define limits of detection of  $\alpha$  and  $U$ .



This thesis is organized as follows: We begin by setting the context, define objectives and scope of this thesis in chapter 1. Chapter 2 is concerned with the literature review of ECFM in single-phase and two-phase flows. We notice a lack of literature on theoretical description of ECFM in two-phase flows. However, electromagnetic fields and magnetic flux distortion due to voids, have been studied in very low and high pulsation ranges in other fields. From the description of Maxwell nearly two centuries ago, to electromagnetic flowmeters and change in impedance studies in electromagnetic evaluation of materials, we find various models which have been subsequently divided into two categories: models without induction effects and models at high pulsations. We also find experiments and numerical simulations that describe the dynamics of bubbles in two-phase MHD. However, this later was neglected in this study. In chapter 3, we theoretically analyze an ECFM, which is subsequently fabricated for two-phase flow experiments with ECFM. Next, three approaches are proposed to characterize  $U$  and  $\alpha$  effects in liquid metal two-phase flows. A model two-phase flow experimental setup is developed in chapter 4. Here, liquid metal is replaced by aluminium rods. Grooves and holes over these rods simulate voids. ECFM translates over the aluminium rod at a given constant velocity. This is equivalent to a plug flow. This experimental setup is ideal for characterizing  $U$ ,  $\omega$  and  $\alpha$  effects using the proposed theoretical approaches. Here, we can control well  $U$ ,  $\alpha$  and void distributions. Even if the Faraday induction, Lorentz force and void effects are intimately coupled, we were able to separate  $U$  and  $\alpha$  effects. The results further demonstrate the feasibility of void and flow characterization simultaneously for low magnetic Reynolds number and low void volume fractions. The experimental results were explained with the help of simple scaling relations based on Maxwell's equations. Results with aluminium rods have been proposed to be validated in experiments with liquid Galinstan containing glass beads. Chapter 5, provides some preliminary results for this later. Finally, we provide conclusions and review some perspectives, both from scientific and industrial point of views.

The work presented in this thesis forms the basis of four journal papers: Thermomagnetic behavior of AFM-MFM cantilevers (published in Measurement science and technology), Void effects on eddy current distortion in two-phase liquid metal (published in Review of scientific instruments), Towards quantitative void fraction measurement with an eddy current flowmeter for fourth generation sodium cooled fast reactors (accepted for publication in Transactions on nuclear science), Magnetic flux distortion in two-phase liquid metal flow (submitted to journal of applied physics). In addition it contributes to one conference paper: Quantitative void fraction measurements with an eddy current flowmeter for generation IV Sodium cooled Fast Reactor (in ANIMMA 2015 Conference record IEEE).

We reproduce the first two papers at the end of this manuscript in appendix A and appendix B respectively. The first paper models the behavior of AFM cantilevers in an external magnetic field. This is a first step. The ultimate objective is to study the distribution of eddy currents at one bubble surface under Faraday induction and Lorentz force effects. The second paper summarizes  $U$  and  $\alpha$  effects on ECFM emf in two-phase flows.

Appendix C provides literature review of bubble dynamics in two-phase MHD flows. Appendix D gives theoretical development for Lissajous curve fitting approach. In appendix E, we give time plot and FFT spectra analyzed for difference emf in ECFM. Appendix E is considerably big and thus it is provided as a supplementary.



# Chapter 1

## Context and objectives

The natural fossil fuel based resources are fast dwindling due to increasing population and a rapid increase in per capita energy consumption related to rising standards of living. Therefore, in view of the impending fossil fuel based energy crisis other avenues of energy resources are being explored. Wind energy, solar energy and hydro-based energy are some of the solutions being used in present. Nuclear fission based reactors are also being considered as viable options for quasi-long term usage [1]. A nuclear reactor has a high energy density compared to conventional fossil fuel based power plants. Fission of one atom gives 100,000,000 times more energy than burning one atom of carbon in a fossil fuel.

To evaluate the role of nuclear fission based reactors in the current energy mix, a consortium called Generation IV International Forum (GIF) was formed in the year 2000. The objective was to evaluate the current status of nuclear reactor technology and suggest future strategy for generation IV nuclear reactors. After reviewing about one hundred different reactor concepts, GIF announced the selection of six reactor technologies that offer the potential for meeting Generation IV goals: Very High-Temperature gas cooled Reactor (VHTR), Gas-cooled Fast Reactor (GFR), Sodium-cooled Fast Reactor (SFR), Lead-cooled Fast Reactor (LFR), Molten Salt Reactor (MSR), and Super-Critical Water-cooled Reactor (SCWR). Among these six reactor technologies Sodium cooled Fast Reactor (SFR) is being led and developed at CEA, Cadarache France. This project is named ASTRID which stands for Advanced Sodium Technological Reactor for Industrial Demonstration.

### 1.1 Fourth generation Sodium cooled fast reactors

A fast nuclear reactor is based on fission reaction by high energy (fast) neutrons inside its core (see figure 1.1). Fast neutrons unlike the thermal (low energy) neutrons have the ability to burn higher actinides, and also convert non-fissile  $^{238}\text{U}$  to fissile  $^{239}\text{Pu}$ . The use of fast neutron also eliminates the need for moderator used in thermal reactors, decreasing substantially the volume of the reactor core. The smaller size of core is beneficial for cost considerations because it requires less coolant and structural material. The

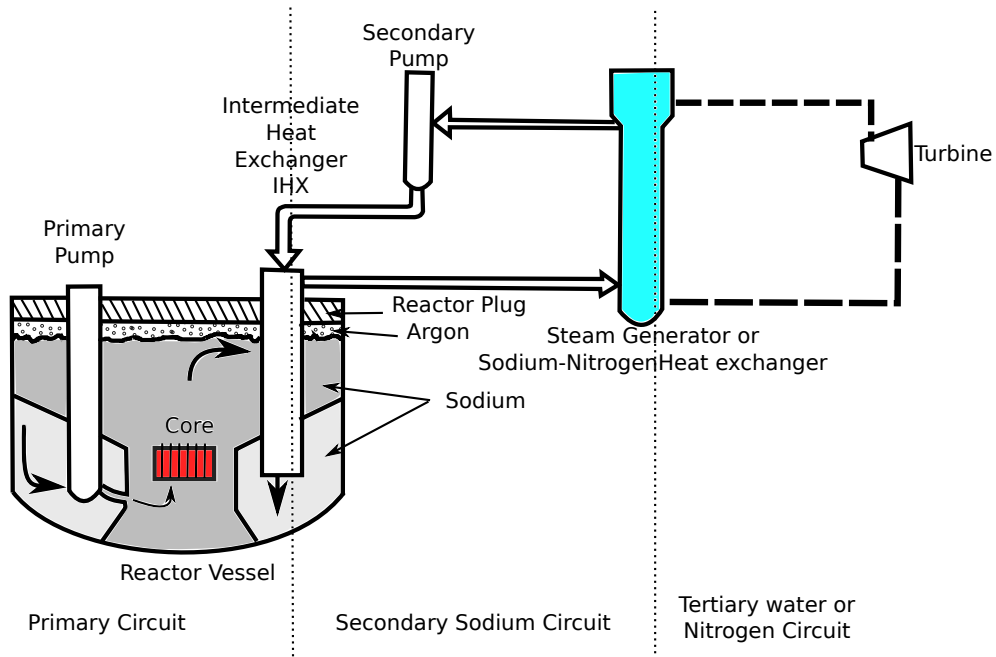


Figure 1.1: Schematic of a pool type fast neutron reactor.

smaller core is also a requirement for efficient breeding in the  $^{238}\text{U}$  blanket surrounding the core [2]. The use of a compact core increases energy densities generated in a fast nuclear reactor core. One of the solutions in these situations is the use of liquid metals as core coolants for their highly efficient heat transfer properties. Today, liquid sodium is the best available liquid metal coolant for this purpose due to the following reasons: 1) relatively low melting temperature ( $98\text{ }^\circ\text{C}$ ), 2) low neutron capture cross-section, 3) minimal activation under irradiation, 4) good flow and heat transfer properties and 5) good compatibility with fuel and structural materials. Fast nuclear reactors which use liquid sodium as core coolant are called Sodium-cooled Fast Reactors (SFR).

Figure 1.1 shows the working principle of a pool type SFR. Fuel pins containing fissile, fertile and shielding materials are bundled together in sub-assemblies. These sub-assemblies are arranged in a specified geometrical configuration and constitute the core. The primary pumps force the ambient reactor coolant to pass through the core which removes heat. The hot coolant is cooled in the intermediate heat exchanger which feeds the secondary circuit. The secondary circuit in turn transfers the heat to the steam generator (or Sodium-Nitrogen heat exchanger), which supplies steam (or Nitrogen) to the turbine. The rotation of the turbine blades produces electricity.

## 1.2 Gas presence in sodium

Liquid sodium coolant is present in primary and secondary circuits of the SFR (see figure 1.1). In each of these circuits there are several possible mechanisms by which gas can

enter the sodium. One of the main sources responsible for the continuous formation of free gas in the primary sodium of SFRs is gas dissolution. This occurs in some areas of the reactor having reached saturation equilibrium which is governed by Henry's law. This dissolution phenomenon, particularly at the sodium/cover gas interface, results in a nucleation phenomenon in areas supersaturated in dissolved gas. This supersaturation occurs in areas where the sodium cools (i.e. at the heat exchanger outlets) and/or when the hydrostatic pressure decreases. Nucleation increases as a function of surface roughness of in-pool components. Studies conducted in Superphénix demonstrate that nucleation is responsible for most of the gas in primary sodium during nuclear reactor operation at nominal power. The size of the gas bubbles due to nucleation is approximately  $10\ \mu\text{m}$  [3]. Gas entrainment is another source of bubble presence in sodium. The upper free surface of the primary liquid sodium is in contact with argon cover gas in the plenum. The purpose of the cover gas is to accommodate sodium thermal expansions and its separation from oxygen present in atmospheric air. When the free surface of sodium is agitated (vorticity, shear, etc.), vortexes and/or waves of differing strengths are formed. These entrain the argon cover gas which in turn travels in form of bubbles via primary pump through the core. Nuclear reactions with sodium, impurities in sodium, with  $\text{B}_4\text{C}$  in control rods and with fissile fuel in fuel pins also produce gaseous products. The gases produced in fuel pins can enter sodium in case of cladding failure. A cladding failure event occurred in Phénix plant in May 1979. It led to the release of fission gas (xenon-135 among others). A cladding failure incident also occurred in Clementine fast nuclear reactor in United States in 1952. A local sodium boiling accident may also result in the presence of non conducting vapors in sodium. Auxiliary circuits (e.g. sodium purification system) involving any sources of gas would also contribute to the presence of gas in the primary sodium. In case of a leak in the steam generator (or sodium-nitrogen heat exchanger), hydrogen (or nitrogen) gas is expected to be present in the secondary sodium loop. Indirect estimations made for Pénix and Superphénix reactors show that the void fraction in the primary sodium is  $10^{-4}$  to  $10^{-6}$  while bubble radii is in the range  $10\ \mu\text{m}$  to  $100\ \mu\text{m}$  [4][5].

The presence of gas bubbles in liquid sodium significantly modifies its acoustic properties. Yet the opacity of sodium means that acoustic measuring methods must be used to ensure continuous monitoring. The disruptions due to gas presence can disable the time of flight measurement techniques, passive acoustic monitoring and all acoustic or ultrasonic systems. A substantial amount of gas void fraction in the primary pool (several percentages) can lead to loss of core cooling capabilities of the heat exchangers. Smaller bubbles may coalesce to make a bigger bubble, which while passing through the core might introduce neutronic or thermo-hydraulic perturbations. The neutronic perturbations then translates to reactivity fluctuations which leads to local power excursions. The neutronic perturbations, above a certain threshold, can induce a reactor shutdown through automated feed back mechanisms. This will incur significant costs on the operator. The gas passing through the core ultimately ends up in the cover gas plenum. An accumulation of these radioactive gases in the gas plenum overtime increases the background noise in the radiation detectors situated in the gas plenum. This seriously

degrades the signal to noise ratio of the detector measurements. It would be necessary to monitor the gas presence in the primary sodium at all times in this regard. The presence of hydrogen (or nitrogen) in secondary sodium will serve as an indicator of micro-leak in the steam generator. An early and fast detection of this event can minimize the damages to this heat exchanger. The direct measurements of the gas presence is also necessary to validate the numerical codes (for example, VIBUL code) which predict the gas behavior and its consequences. This is integral to safe operation of a nuclear reactor. Although it had been overlooked during the Phénix and Superphénix design phases, recognition of the continuous presence of primary sodium was the subject of specific requests from the French nuclear safety authority in 1994 and 1995 to the operator of Superphénix. In particular, the operator was asked to "examine (...) the possibility of assessing more precisely (...) the value (of the) en-gassing rate, either by improving the measurement methods already used, or by defining other measurement methods" [6, 7]. Extensive test campaigns thus started in the Superphénix reactor but the shutdown of Superphénix in 1998 prevented the operator from fully answering these requests. In view of this request, it is imperative to develop methods for characterizing the presence of gas in sodium in the context of designing the ASTRID experimental reactor.

For a more detailed discussion of causes and consequences of the bubble presence in SFRs the reader is referred to other resources [4].

### 1.3 Industrial strategy

Finding a solution to the problem of gas presence in liquid sodium, as discussed in the previous section, is essential to the ASTRID project. Studies on potential sources of gas presence in SFR were launched which led to the suggestions for elimination of these sources by design [5]. Some of these additional systems are shown in figure 1.2. Some other sources of en-gassing, for example, entrainment and dissolution of gas at sodium-Argon interface in cover gas plenum still remains a challenge. Therefore we conclude that decreasing the gas content in sodium is possible, however its presence will remain an unavoidable problem. In this case, it is necessary to continuously monitor and control the gas presence in liquid sodium.

Most of the techniques that are generally used in two-phase void fraction measurements are not usable in liquid sodium in SFR. For example, optical visualization techniques cannot be used since liquid metals are opaque. Neutron, Gamma and X ray densitometry techniques work on the basis of difference in macroscopic attenuation cross-sections for liquid metal and gas phases. The application of these techniques requires shielding from the background radiations which is not possible inside the nuclear reactor vessel.

The high contrast in density between liquid metal and gas bubbles forms the basis for acoustic techniques for gas detection [4]. The speed of sound (celerity) ( $c$ ) in a medium depends upon its density ( $\rho$ ) and its compressibility ( $\chi$ ) :  $c = \sqrt{\frac{1}{\rho\chi}}$ .  $\rho$  and  $\chi$  of liquid metal and gas phases are very different. Therefore the net effective  $c$  in two-phase medium is a function of the gas void volume fraction. This is the working principle of

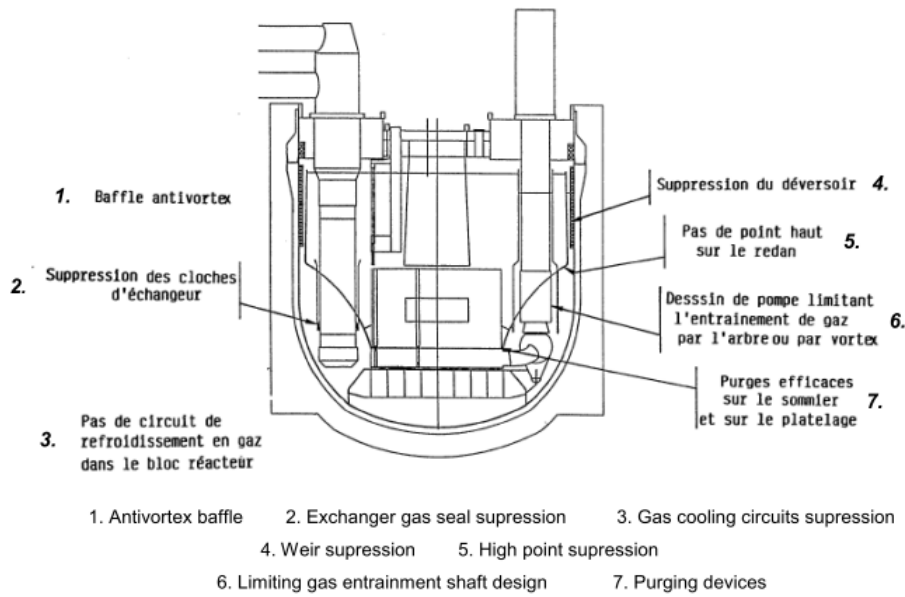


Figure 1.2: The proposed design improvements to minimize gas presence in normal and incident conditions in SFR [5].

**low frequency acoustic velocity measurement** technique. One transducer produces sound waves which pass through the two-phase medium and is received by the sensing transducer. The speed of this sound wave decreases as a function of void fraction. The first corresponding model in this regard was proposed by Wood [8]. This technique is highly sensitive and reliable to bubbles of sizes less than  $100\ \mu\text{m}$ . Indeed, the frequency of the wave has to be lower than the resonance frequencies of the bubbles which are inversely proportional to their sizes. Piezoelectric transducer technology used today cannot produce waves below  $10\ \text{kHz}$  and hence the maximum bubble size that can be measured reliably is  $200\ \mu\text{m}$ . Another acoustic technique which is under consideration is **non-linear acoustic mixing of frequencies**. Imaging frequency  $\omega_i$  is mixed with the pump frequency  $\omega_p$  ( $\omega_i \ll \omega_p$ ) to produce a frequency modulated wave in acoustically non-linear medium (two-phase medium). The pump frequency is chosen in the range of resonance frequencies for bubbles which is related to the radius of the bubbles. Characteristic frequencies that appear in frequency spectrum give the information on bubble sizes. The whole spectrum of bubble sizes are scanned by changing  $\omega_p$ . There are some issues concerning the determination of exact void fraction using this technique [9]. Further R&D on this technique is in progress for its implementation in industrial conditions of liquid sodium, with acoustic transducers compatible with this medium, under the operating conditions of a nuclear reactor.

Electromagnetic techniques use high contrast in electrical conductivity between liquid metal and gas to characterize the two phase flow. Electromagnetic techniques along with the acoustic techniques provide redundancy and diversity in measuring techniques.



There are several other reasons for the need to develop devices based on electromagnetic techniques. The device output signal is naturally electrical, eliminating the need for transducers to convert the signal to electrical. In addition to saving costs on additional hardware it also decreases the response time of the device. This is very useful for alarm based critical systems. Electromagnetic devices have firm mechanical construction and do not involve any moving parts. According to Yada, this advantage prevents the flow channel blockage which might happen in case a moving part breaks from the device assembly and flows away with the ambient liquid sodium [10]. Unlike acoustic techniques, they have (in principle) no upper limit regarding bubble sizes and void fractions. The lower limit is still a subject of research. To introduce the working principles of these techniques we feel the need to present some basic equations in Magneto-Hydro Dynamics (MHD). This is presented in the next section. The discussion of the electromagnetic techniques and devices appears in section 1.5.

## 1.4 Fundamental equations

The implementation of electromagnetic techniques in liquid metal flows requires the understanding of the coupling between the electromagnetic fields and the motion of the medium. This involves the mass and momentum conservation laws for the working fluid under the influence of a net electromagnetic field and the Maxwell's equations which govern the behavior of electromagnetic fields. Along with these equations, we need several constitutive relations to formulate a well defined problem for our system. The choice of equations and terms in it, depends on physical properties of the medium. Therefore, we begin this section by listing the physical properties of liquid sodium at SFR core exit. We would then discuss flow and electromagnetic fields in subsequent sub-sections.

### 1.4.1 Properties of liquid sodium

Liquid sodium is lighter and less viscous than water. Its density is  $\rho = 830 \text{ kg m}^{-3}$  and its dynamic viscosity is  $\eta = 0.0002 \text{ Pa s}$  at  $500^\circ\text{C}$  [11, 12]. The speed of sound in sodium is  $2450 \text{ m s}^{-1}$  compared to  $340 \text{ m s}^{-1}$  in air. Liquid sodium has excellent heat transfer properties. Its specific heat capacity is  $c_p = 1.334 \text{ kJ kg}^{-1} \text{ K}^{-1}$  and  $c_v = 1.170 \text{ kJ kg}^{-1} \text{ K}^{-1}$  and its thermal conductivity is  $80 \text{ W m}^{-1} \text{ K}^{-1}$ . The thermal conductivity of water at room temperature is  $0.6 \text{ W m}^{-1} \text{ K}^{-1}$ . Liquid sodium melting temperature is  $97.7^\circ\text{C}$  while it boils at  $883^\circ\text{C}$ . Surface tension of sodium is  $187 \text{ mN m}^{-1}$ .

Liquid sodium being metallic has a very high electrical conductivity,  $\sigma = 3.7 \times 10^6 \text{ S m}^{-1}$ . The same for the gases present in liquid sodium is  $\sigma \approx 0$ . Sodium is weakly paramagnetic. Its mass magnetic susceptibility is  $\chi_g = 0.6 \times 10^{-6} \text{ g cm}^{-3}$  which is  $\chi_m = 5 \times 10^{-8}$  in dimensionless units [13, 14]. The magnetic permeability of sodium, therefore, can be taken as that of vacuum,  $\mu_0 = 4\pi \times 10^{-7} \text{ H m}^{-1}$ . Its electrical susceptibility is also very low and the value of electrical permittivity can be taken as that of vacuum,  $\epsilon_0 = 8.85 \times 10^{-12} \text{ F m}^{-1}$ .

Liquid sodium ignites when in contact with air at 320 °C, it is therefore imperative to protect sodium free surface by inert gas. It also undergoes highly exothermic reactions with water and some other halogenated hydrocarbons. It is corrosive to many metals. Although refractory materials are compatible with high temperature sodium they often develop cracks. Pipes and ducts become coated with conducting condensate. Therefore, to extract electrical signals the use of induction based techniques are preferred [15].

### 1.4.2 Basics of electromagnetic fields

Due to high electrical conductivity and zero polarizability of liquid sodium, accumulation of charges inside its volume is not possible. A finite electric field  $\vec{E}$  due to accumulation of charges will quickly homogenize this charge distribution on time scale,  $\tau = \epsilon_0/\sigma \approx 10^{-18}$  s. So the Gauss's law which relates distribution of electric charges to the resulting electric field inside liquid sodium will be

$$\nabla \cdot \vec{E} = 0 \quad (1.1)$$

The distribution of free charges on the interface separating electrically conducting and non-conducting media may however be non-zero. The tangential component  $E_t \hat{\mathbf{t}}$  of  $\vec{E}$  just outside the conducting medium is zero because any finite  $E_t \hat{\mathbf{t}}$  on the surface will redistribute the charges to make  $E_t \hat{\mathbf{t}} = 0$ . But the normal  $E_n \hat{\mathbf{n}}$  can be non-zero depending on the net surface charge density,  $\sigma_c$ .

$$E_t^1 = E_t^2 \quad \text{and} \quad E_n^1 = E_n^2 + \frac{\sigma_c}{\epsilon_0}$$

Where, 1 and 2 denote electrically conducting and non-conducting media respectively. These charges on the interface however do not appear on their own and need some external source of free charge. Therefore in an actual liquid sodium-gas two-phase flow both  $E_t \hat{\mathbf{t}}$  and  $E_n \hat{\mathbf{n}}$  are continuous at the interface.

A circulating  $\vec{E}$  is produced in response to time varying magnetic field  $\vec{B}$  in the electrically conducting medium. This is Faraday's law.

$$\nabla \times \vec{E} = -\frac{\partial \vec{B}}{\partial t} \quad (1.2)$$

The Faraday's law in integral form has two alternative forms

$$\oint_C \vec{E} \cdot d\vec{l} = -\frac{d}{dt} \int_S \vec{B} \cdot d\vec{S} \quad \text{and} \quad \oint_{C_i} \vec{E} \cdot d\vec{l} = -\int_{S_i} \frac{\partial \vec{B}}{\partial t} \cdot d\vec{S}$$

In the first equation,  $\vec{E}$  and  $\vec{B}$  fields are measured in the rest frame of current loop  $C$  enclosing an area  $S$ . In the second form,  $\vec{E}$  and  $\vec{B}$  fields are measured in the laboratory frame of reference.

The magnetic fields  $\vec{B}$  differ from the electric fields  $\vec{E}$ , here separate magnetic charges (monopoles) do not exist. So there is no source and sink for magnetic lines of forces. This gives us Gauss's law for  $\vec{B}$ .

$$\nabla \cdot \vec{B} = 0 \quad (1.3)$$

The circulation of  $\vec{B}$  along a closed path is equal to the amount of normal current passing through it. The total current is equal to the sum of electric and dielectric currents. This is Ampère-Maxwell's law,

$$\nabla \times \vec{B} = \mu_0 \vec{J} + \mu_0 \epsilon_0 \frac{\partial \vec{E}}{\partial t}$$

The displacement current in the equation above (last term on r.h.s.) can be neglected if the dielectric relaxation number,  $K_r = \omega \epsilon / \sigma \ll 1$  ( $\omega$  is the angular frequency of variation of  $\vec{E}$  and  $\vec{B}$  fields). This is known as quasi-static approximation. In liquid sodium, for  $\omega = 6280 \text{ rad s}^{-1}$  corresponding to frequency  $\nu = 1000 \text{ Hz}$ ,  $K_r \sim 10^{-15}$ . Therefore it is safe to use the following form of Ampère-Maxwell's law in our study,

$$\nabla \times \vec{B} = \mu_0 \vec{J} \quad (1.4)$$

As discussed above, from Faraday's law the motion of electrically conducting medium under time varying magnetic field induces two kinds of emf's: 1) transformer emf associated exclusively to the variation of magnetic fields in time ( $-\frac{\partial \vec{B}}{\partial t}$ ), 2) motional emf associated with the Lorentz force on free charges in the medium. These two emf's will induce eddy currents and are given by the generalized ohm's law as

$$\vec{J} = \sigma (\vec{E} + \vec{u} \times \vec{B}) \quad (1.5)$$

We define  $J_t = \sigma \vec{E}$  as transformer induced eddy current and  $J_f = \sigma \vec{u} \times \vec{B}$  as the flow induced eddy current. We can combine all the equations governing the behavior of electromagnetic fields as described above. This gives us the magnetic induction equation,

$$\frac{\partial \vec{B}}{\partial t} = \lambda \nabla^2 \vec{B} + \nabla \times (\vec{u} \times \vec{B}) \quad (1.6)$$

Here  $\lambda = 1/\mu_0 \sigma$  is the diffusivity of magnetic fields in the medium. The magnetic induction equation is analogous to the transport equation for vorticity  $\vec{\omega} = \nabla \times \vec{u}$ . The extent to which diffusion of vorticity prevails over convection of vorticity in fluid is governed by the Reynolds number  $\text{Re}$  (to be defined later). By analogy we have magnetic Reynolds number  $\text{Re}_m$  defined as the ratio of diffusive to the convective time scales.

$$\text{Re}_m = \frac{\tau_d}{\tau_c} = \frac{L^2 \mu \sigma}{L/U} = UL\mu\sigma \quad (1.7)$$

where,  $L$  is a characteristic length. For a perfect conductor ( $\sigma = \infty$ )  $\text{Re}_m = \infty$ , the diffusion is very slow with respect to convection ( $\tau_d \gg \tau_c$ ). In this case changes in  $\vec{B}$  is governed only by convection. Amount of magnetic flux linked to any conducting loop in the fluid remains constant. This is the famous frozen in field concept (frozen flux theorem of Alfvén) where magnetic lines of forces move with the fluid and a perturbation in  $\vec{u}$  brings equivalent perturbation in  $\vec{B}$  and vice versa. In real conductors, diffusion of flux happens through ohmic dissipation.

The normal electrical current on the fluid-gas interface is zero assuming gas does not conduct electricity ( $\sigma_g = 0$ ).

$$J_n^1 = 0 = J_n^2$$

The net normal magnetic field on the gas bubble surface is again continuous because  $\vec{B}$  is divergence free.

$$B_n^1 = B_n^2$$

The tangential components of the magnetic fields however are discontinuous if a surface current  $J_s \hat{\mathbf{t}}$  exists on the interface

$$B_t^1 = B_t^2 + \mu_0 J_s$$

### 1.4.3 Basics of fluid motion

The fluid motion is governed by the familiar Navier's stokes equation. The statement for an incompressible Newtonian fluid motion is

$$\rho \frac{D\vec{u}}{Dt} = -\nabla p + \nabla \cdot \bar{\bar{\tau}} + \vec{f}$$

where  $\rho$  is the fluid density.  $D/Dt$  is the material derivative defined as

$$\frac{D}{Dt} = \frac{\partial}{\partial t} + \vec{u} \cdot \nabla$$

$\bar{\bar{\tau}}$  is the viscous stress tensor term and  $\vec{f}$  is other volumetric force terms.

$$\tau_{ij} = \eta \left( \frac{\partial u_i}{\partial x_j} + \frac{\partial u_j}{\partial x_i} \right)$$

where  $\eta$  is the dynamic viscosity of the fluid. The law of conservation of mass, also called the continuity equation, is

$$\frac{\partial \rho}{\partial t} + \nabla \cdot \rho \vec{u} = 0$$

For an incompressible fluid, we obtain

$$\nabla \cdot \vec{u} = 0$$

The boundary condition on  $\vec{u}$  is  $\vec{u} = 0$  at any solid surface. This is called no slip condition. The equation for fluid motion in the presence of electromagnetic fields and without other volumic forces is

$$\rho_0 \frac{D\vec{u}}{Dt} = -\nabla p + \eta \nabla^2 \vec{u} + J \times \vec{B} \tag{1.8}$$

The last term on R.H.S. of equation (1.8), is the so called Lorentz force term. This term opposes the relative movement of the fluid and the magnetic field.

There are four most common dimensionless groups in MHD literature. Magnetic Reynolds number  $Re_m$  has already been defined. Reynolds number  $Re$  is the ratio of viscous diffusion time scale to convection time scale of fluid momentum.

$$Re = \frac{\rho_0 L^2 / \eta}{L/U} = \frac{\rho_0 U L}{\eta} \quad (1.9)$$

The Hartman number is square root of the ratio of viscous diffusion time scale to the time scale of Lorentz force effects.

$$Ha = \sqrt{\frac{\rho_0 L^2 / \eta}{\rho_0 / \sigma B^2}} = BL \sqrt{\frac{\sigma}{\eta}} \quad (1.10)$$

The magnetic interaction number is the ratio of convection time scale to the time scale of Lorentz force effects.

$$N = \frac{L/U}{\rho_0 / \sigma B^2} = \frac{\sigma B^2 L}{\rho_0 U} \quad (1.11)$$

Note that  $N = Ha^2 / Re$ .

#### 1.4.4 The Hartmann problem

The nature of coupling between fluid motion and the applied external magnetic fields can be better understood by studying the Hartman problem. It is a well known problem in MHD. We present here the standard solutions. The explanation for the derivation can be found in this reference [16]. Non-dimensional forms of equations (1.6) and (1.8) are used in this problem. Consequently all the quantities in this section are non-dimensionalised. The motion of electrically conducting fluid ( $u_y \hat{y}$ ) happens between two infinite parallel plates.

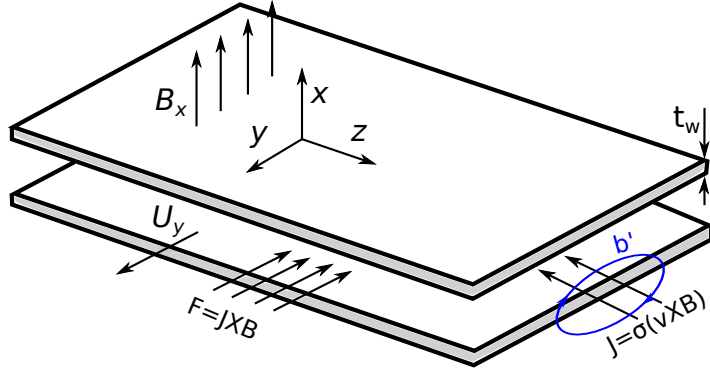


Figure 1.3: The geometry of the Hartmann Problem.

A steady uniform external magnetic field  $B_0 \hat{x}$  is applied perpendicular to fluid motion. This will induce eddy currents in the medium governed by the non-dimensionalised form of the induction equation (1.6). The no slip condition at boundary walls give  $u(\pm 1) = 0$ . The tangential magnetic field at the boundary depends on the

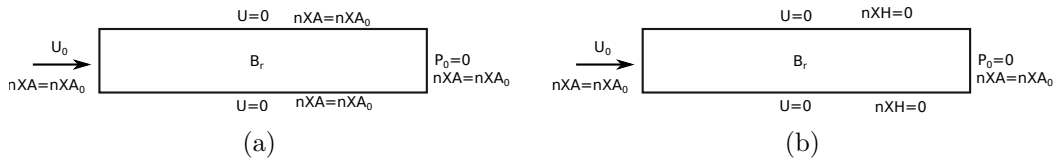


Figure 1.4: The boundary conditions used in the numerical simulation of Hartman Problem, (a)  $c \rightarrow 0$  (b)  $c \rightarrow \infty$  at parallel plates. Here  $\vec{A}$  is magnetic vector potential defined as  $\vec{B} = \nabla \times \vec{A}$ .  $P_0$  is outlet pressure,  $U_0$  is inlet velocity,  $B_r$  is an applied constant and uniform magnetic flux density perpendicular to flow and  $H$  is the magnetic field.

wall conductance ratio defined as  $c = \sigma_w t_w / \sigma L$ ; where,  $\sigma_w$  is electrical conductivity of the wall and  $t_w$  is the wall thickness (see ref. [17]). The tangential magnetic field is continuous at the fluid-wall interface for  $c \rightarrow \infty$ , while it vanishes when  $c \rightarrow 0$  at the wall. This is because the normal current density  $J_n$  is continuous at the interface when  $c \rightarrow \infty$  and is zero when  $c \rightarrow 0$ . The solutions to the above defined system is

$$u(x) = u_c \left[ 1 - \frac{\cosh(\text{Ha}x)}{\cosh(\text{Ha})} \right] \quad (1.12)$$

$$b(x) = -\frac{x}{\text{Ha}} + u_c \frac{\sinh(\text{Ha}x)}{\cosh(\text{Ha})} \quad (1.13)$$

$$u_c = \frac{1}{\text{Ha}} \frac{c + 1}{c\text{Ha} + \tanh(\text{Ha})} \quad (1.14)$$

We anticipate the need to use a numerical solver as a tool to understand interactions in more complicated geometries. So the Hartman problem was also studied using COMSOL<sup>®</sup>. It is a finite element based solver which allows multi-physics coupling. For our case, we use a 2D geometry. The magnetic induction equation is modeled by “AC DC” physics while the Navier stokes equation was introduced using “Single Phase Flow (spf)” module. The constant external magnetic field was modeled by the “Remnant magnetic flux” ( $B_r$  in figure 1.4). Magnetic potential corresponding to external magnetic field is applied at all four walls in  $c \rightarrow 0$  case, while “perfect magnetic conductor” condition was used at the two parallel plate walls in  $c \rightarrow \infty$  case.

Figure 1.5 shows the coupled effect of motion and externally applied magnetic field. We notice a decrease in fluid flow rate as the Hartman number is increased. If the flow rate was kept constant, for example by a pump, one would expect a similar distortion in  $\vec{u}$  profile while the area under this curve remains constant. This distortion in flow profile comes from the interaction of the flow induced currents with the total magnetic field in the medium. The flow induced eddy currents  $\vec{J}_f$  are induced in response to the motion of free charges in the medium across the magnetic field.  $\vec{J}_f$  is maximum in the middle of the two plates because the velocity in the core is maximum,  $\vec{J}_f = \vec{u} \times \vec{B}$ . Due to the dense current densities in the core of the flow, the Lorentz force opposing fluid motion across  $B_0$  is also maximum in the middle and therefore the net action of  $\vec{B}$  through Ha on  $\vec{U}$  profile is to flatten it in the core. This effect is similar to turbulence where an

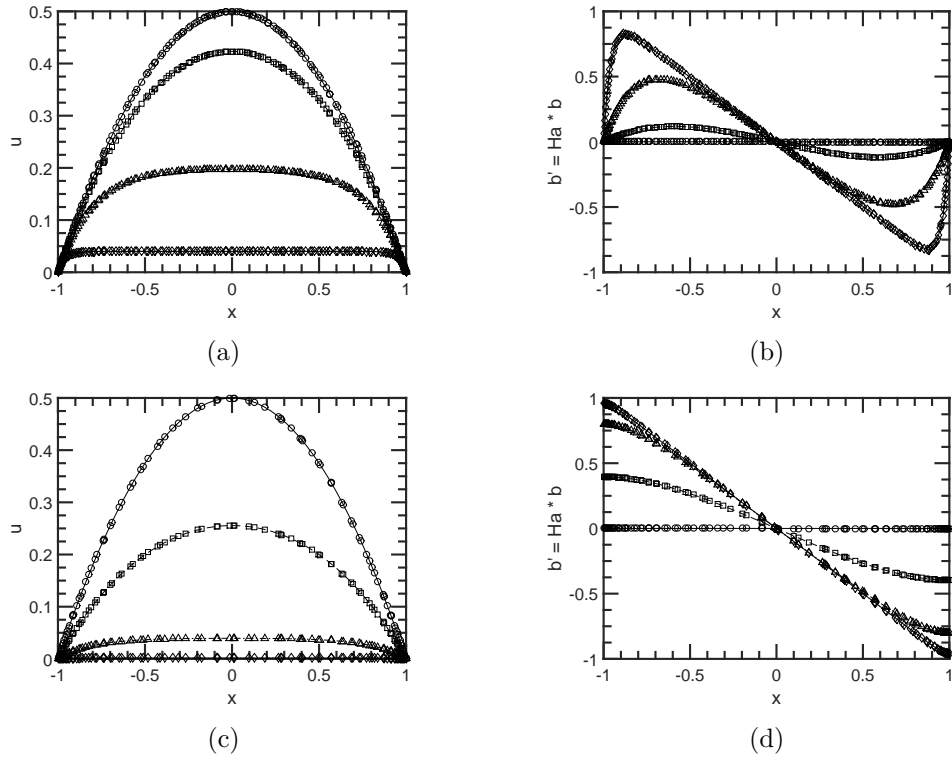


Figure 1.5: The distortion in (a) velocity profile ( $c \rightarrow 0$ ), (b) the induced magnetic field ( $c \rightarrow 0$ ), (c) velocity profile ( $c \rightarrow \infty$ ), (d) the induced magnetic field ( $c \rightarrow \infty$ ), for  $Ha = 0$  ( $\circ$  COMSOL<sup>TM</sup>, — Analytical);  $Ha = 1.5$  ( $\square$  COMSOL<sup>TM</sup>, -- Analytical);  $Ha = 5$  ( $\triangle$  COMSOL<sup>TM</sup>, - · - Analytical);  $Ha = 25$  ( $\diamond$  COMSOL<sup>TM</sup>, ... Analytical).

increase in Reynolds number  $Re$  tends to decrease the thickness of the boundary layer and the flow profile tends to flatten in the core. The induced eddy currents  $\vec{J}_f$  has its own magnetic field  $b'$ , whose magnitude depends upon  $Re_m$ . Notice a change in sign of this induced magnetic flux in the core. This is because the circulation of  $b'$  is equal to  $\mathbf{J}_f$  (see figure 1.3).

The distortion in  $\vec{u}$  profile due to Lorentz force is more severe in  $c \rightarrow \infty$  case than  $c \rightarrow 0$  case (compare figure 1.5a and 1.5c). If the volumetric flow rate is not fixed, we expect a more rapid decrease in volumetric flow rate in response to increasing  $Ha$ . The current density  $\vec{J}_f$  in  $c \rightarrow \infty$  case is non-zero at the wall because of conducting nature of the wall which provides electrically conducting path for current. Therefore, the corresponding Lorentz forces extend till the wall thus increasing the net Lorentz force on fluid. This is also evident in the plots for  $b'$ . For the later case, this tangential magnetic field is non zero at the wall due to a non zero normal current density.

For the case of vanishing and diverging magnetic fields,  $Ha \rightarrow 0$  and  $Ha \rightarrow \infty$  respectively, equation 1.12-1.14 can be approximated by expansion of hyperbolic functions. For  $Ha \rightarrow 0$ , we obtain

$$u(x) = \frac{1}{2}(1 - x^2)$$

This is the parabolic flow profile, characteristic of a Poiseuille flow. The core velocity in this case is  $u_c \sim Ha^{-1}$ . For  $Ha \rightarrow \infty$ , the hyperbolic functions are expanded in terms of exponential functions. The final expression is

$$u(x) = u_c \{1 - \exp [Ha (|x| - 1)]\}$$

In this case, exponential boundary layer is formed at the plate wall. This is called the Hartman layer. The thickness of the Hartmann boundary layer is  $\delta_{Ha} \sim \mathcal{O}(Ha^{-1})$ . The corresponding core velocity is  $u_c \sim Ha^{-2}$ .

Figures 1.5a-1.5d also show a good agreement between the results of numerical simulation and the analytical solution.

To see the effect of a time varying magnetic field, we will treat a simple case when there is no fluid motion. Taking the case of insulating parallel plates (as in the Hartman problem), let us assume  $\vec{u} = 0$  and  $B(t) = B_0 \exp(-i\omega t)$ . The time varying magnetic fields will induce transformer induced eddy currents  $\vec{J}_t$  in the medium in accordance with the Faraday's law and Maxwell Ampère's law. The magnetic induction equation in this situation is,

$$\frac{d^2 B}{dx^2} = i\mu_0\sigma\omega B$$

The solution to this equation is  $B(x) = B_0 \exp(-x/\delta) \exp(-i\omega t) \exp(-ix/\delta)$ . The magnetic field propagates with exponentially diminishing amplitude inside the medium. The  $x$  value at which  $B_0$  decreases by factor  $e$  ( $\approx 2.71828$ ) is called the skin depth or the penetration depth of magnetic fields. It is defined as

$$\delta = \sqrt{\frac{2}{\mu_0\sigma\omega}} \quad (1.15)$$



In practical situation of interest, the motion of electrically conducting medium will take place in the presence of time varying magnetic fields. In these situations, we would expect both the  $\vec{J}_f$  and  $\vec{J}_t$  to contribute. Their relative strength would depend upon flow velocity  $\vec{u}$  and frequency of variation of magnetic fields  $\nu$ . Our work concerns the the perturbation in magnetic flux in two-phase medium. Therefore objective will be to understand the behavior of these eddy currents around non-conducting heterogeneities.

For the conditions around ECFM at nuclear reactor core outlet, the characteristic value of length scale is  $L = 2.6 \times 10^{-2}$  m, characteristic velocity is  $1 \text{ m s}^{-1}$  and fluid electrical conductivity is  $\sigma = 3 \times 10^6 \text{ S m}^{-1}$ . The values of non-dimensional numbers are  $\text{Re} = 10^5$ ,  $\text{Re}_m = 0.12$  and  $\text{Ha} = 0 - 10$ . The high value of  $\text{Re}$  suggests that the flow will be highly turbulent with very small boundary layer. In addition,  $\text{Ha}$  would have the effect of further decreasing this boundary layer. It would be safe to assume a flat uniform profile in this situation.  $\text{Re}_m \ll 1$ , which means that the total magnetic flux density,  $B \approx B_0$ . The penetration depth of magnetic fields in liquid sodium at magnetic field variation frequency of  $\nu = 1000 \text{ Hz}$  is  $\delta \approx 9 \text{ mm}$ .

## 1.5 Electromagnetic techniques

Electromagnetic techniques have seen a long journey since Faraday first tried to measure the flow of river Thames in 1882. These techniques work on the distortion of externally applied magnetic fields by moving electrically conducting medium in motion. This is governed by the induction equation (equation (1.6)). These external  $\vec{B}$  fields are generally weak so as to minimize the effect on fluid motion (see equation 1.8). On the basis of the form of the applied external  $\vec{B}$  and on the basis of method of detection of the perturbation on  $\vec{B}$ , the electromagnetic techniques are divided into two broad disciplines:

### 1.5.1 Induced voltage technique

In the induced voltage technique, the electrically conducting liquid flows through the flow channel in the presence of transverse magnetic field  $\vec{B}$ . If  $\vec{B}$  is produced using permanent magnets it is called the permanent magnet flowmeter. If  $\vec{B}$  is produced using electromagnetic coils it is called the electromagnetic flowmeter.  $\vec{B}$  fields are either static or slowly varying. The interaction of flow velocity  $\vec{U}$  with  $\vec{B}$  induces a potential difference across the electrodes (see figure 1.6) and drives current  $\vec{J}$  in accordance with the ohm's law (equation (1.5)). Interaction of  $\vec{J}$  and  $\vec{B}$  will produce volumetric force  $\vec{F}$  as shown in the Navier Stokes equation (1.8). The influence of  $\vec{F}$  on  $\vec{U}$  is minimal at low  $\text{Ha}$ .

The behavior of this type of device in two-phase liquid metal flows is known in literature [18]. No other electromagnetic device can compete with it in terms of precision for single phase flow measurement applications [19]. However there are certain drawbacks regarding the implementation of this technique in SFR. This technique is inherently invasive because electrodes need to be in contact with the flow. Contact with the liquid

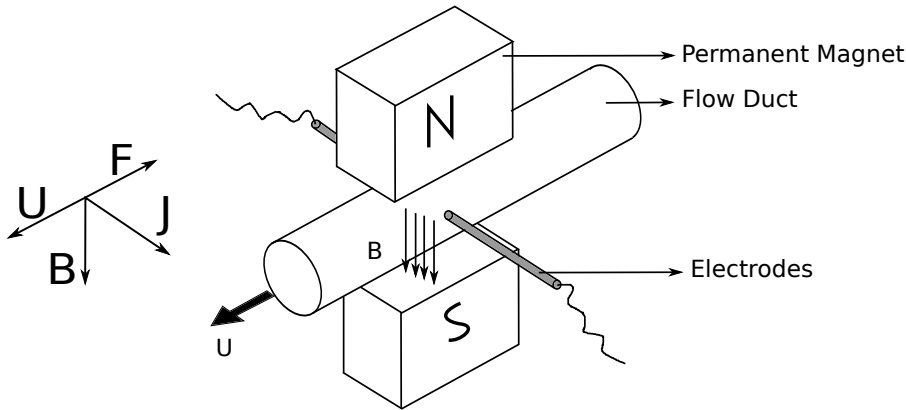


Figure 1.6: The schematic diagram of an induced voltage flowmeter.

metal creates a temperature dependent electrochemical potential at the interface of two dissimilar metals which is a source of significant noise. If permanent magnets are to be used to generate  $\vec{B}$ , we need specially fabricated magnets such as ALNICO V or ALNICO VIII to sustain high temperature and nuclear radiation environments. Also the magnets will be activated due to the presence of Cobalt in the magnets, this creates a problem of device handling. Saddle coil EM flowmeters have been used in prototype fast reactors but they are long in length and their application is restrictive [19]. Indeed, both permanent magnetic flowmeters and EM flowmeters are known to be bigger in size and might not satisfy geometrical constraints of desired application. Since electrical conductivity of liquid sodium is very high, significant amount of flow induced eddy currents will be short-circuited in the flow, decreasing the sensitivity of these flowmeters to  $U$  and void.

### 1.5.2 Induced field technique

Induced field techniques (Eddy Current Flow Meter (ECFM)) are based on the distortion of externally imposed magnetic flux in electrically conducting medium by  $U$  and void. An AC current through primary coil  $P$  creates magnetic flux in the medium and also through the secondary coil/s  $S$  (see figure 1.7). The interaction of this imposed flux with the two-phase medium induces eddy currents  $J_\theta$  that creates an extra magnetic field which changes emf in the secondary coil/s. This emf contains informations on flow  $U$ . The flow of electrically conducting liquid may be through the core of the coils ( flow-through type ECFM) or outside the coils (probe type ECFM). Any number of exciting and sensing coils can be used depending on the application.

ECFM has many advantages over other electromagnetic techniques. An ECFM requires weak magnetic fields, thereby saving magnet power [19]. It uses AC current to excite the primary coil, so the response time of this device is faster than the electromagnetic flowmeter. Therefore, it can report the transients fairly quickly to allow sufficient reaction time for feed back loops. It is known to produce large AC signals which is an

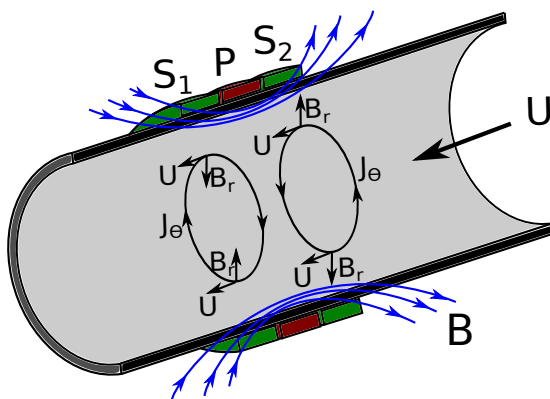


Figure 1.7: A flow-through type ECFM.

advantage in high noise environments. ECFM is non invasive, thus there is no need to contact liquid sodium. It does not use magnets and the material for its construction are relatively easily and cheaply available. It has been known to operate at high temperatures and gives temperature independent signals [20]. It is light in weight and usually very small in size. Diameters as small as 5 mm and length as small as 1 cm have been reported in the literature [21]. It also offers relatively easy handling and can be placed in very limited spaces such as at the exit of the primary pump.

## 1.6 Scope of the thesis

The presence of gas in primary as well as secondary sodium loops is an important safety problem. We have found that its monitoring is necessary. Flux distortion technique is one of the suitable candidates for gas bubble detection in liquid Sodium. It is non-intrusive and can survive harsh conditions characteristic of a nuclear reactor primary loop. Moreover, its application is not only limited to the nuclear reactor, it can be used with any electrically conducting liquid for flow monitoring. The potential of this kind of technique for detection and characterization of electrically non-conducting heterogeneities in the conducting medium needs to be studied.

On the technological side, our main concern is to determine the feasibility of ECFM as a flow and/or void monitoring/characterizing device to address the issue of SFR safety. This is to be achieved by understanding its output signal in single and two-phase flows. We would like to know whether flow measurements and void characterization is possible to achieve simultaneously with one ECFM. What is the precision of such measurements. Which parameters should be recorded and how? What are the possible improvements in method of signal acquisition that can be accomplished with ECFM system? These questions will be answered through a theoretical model for ECFM in two-phase flows. This model will be validated by experiments.

From the physics point of view, the ECFM system involves the two-phase fluid motion in the presence of time varying electromagnetic fields. The ECFM signal, therefore,

contains informations about the eddy currents, the flow rate and the void fraction. What are the elementary mechanisms that are responsible for the flow and void fraction effects on ECFM integral signal? Are these mechanisms coupled? Can we, on the basis of a model and a measurement technique, decouple them? These questions are equivalent to characterizing and understanding the eddy currents perturbations by flow and void fraction effects.

The bibliography on this subject is given in chapter 2. The first part of this bibliography concerns the evaluation of existing theoretical models and experimental results on ECFM in single and two-phase flows. The mechanisms for the effects of void on the externally applied magnetic flux is discussed in the second part.



## Chapter 2

# Literature Review

Both the Navier Stokes equation (1.8) governing fluid motion and the induction equation (1.6) describing electromagnetic fields are non-linear and coupled. In the presence of the second phase (bubbles/slugs/inclusions/gas/void) this situation becomes even more complicated. Even the dynamic effects on bubble motion under given electromagnetic fields in itself is complicated to treat theoretically and to the author's knowledge most of the literature that exists on this topic is experimental and numerical simulations. A review of these effects is given in the appendix to underscore the effects that were not considered in this PhD.

In this chapter we will mostly limit ourselves to scaling relations and some approximate expressions for the ECFM behavior in single and two-phase flows. Section 2.1 concerns the literature review of ECFM in single phase flows. In section 2.2, a literature survey on ECFM in two-phase flows is given. It is to be expected that the presence of bubbles in electrically conducting liquid changes the integrated magnetic flux via change in electrical conductivity. In a homogeneous mixture of conducting and non-conducting media, the change in this integrated flux is time independent. On the other hand, for a heterogeneous medium, the perturbation in integrated magnetic flux is expected to depend on the mean bubble separation and lengths of coils. This would manifest itself as fluctuations in integrated flux. A research on homogeneous models is given in section 2.3 while the literature on the heterogeneous models is given in the section 2.4. The last section 2.5 is reserved for conclusions and summary. A bibliographic study on two-phase ECFM tells us that no analytical study and theoretical formulation exists for ECFM system in two-phase flows. To fill this gap we use the results from other fields of study, namely, electromagnetic flowmeters in two-phase flows and the non-destructive techniques for flaw detection.

### 2.1 ECFM in single phase flows

In an Eddy Current Flow Meter, the motion of liquid metal produces a distortion in the external time varying magnetic field which is governed by the induction equation (1.6). This distortion in external field is linear with the flow rate to first order in  $Re_m$  (low

$\text{Re}_m$ ). The detection of this distortion forms the working principle of an ECFM [19].

We take the case of flow in a cylindrical pipe. The external magnetic flux is imposed by a co-axial coil enclosing this pipe and carrying AC current density of magnitude  $J_0(r, z)$  and pulsation  $\omega$  (see figure 2.1). Due to axial symmetry, the problem is set up in terms of magnetic vector potential  $\vec{A}$ , where  $\vec{A}$  is given by  $\vec{B} = \nabla \times \vec{A}$ . In this case, we only need to solve for  $A_\theta$  since all the induced eddy currents will be azimuthal. In cylindrical coordinates, the magnetic induction equation (1.6) in terms of  $\vec{A}_\theta$  becomes,

$$\left(\nabla^2 + k_0^2\right) A_\theta(r, z) = -\mu_0 J_0(r, z) + \mu_0 \sigma v(r) \frac{\partial A_\theta(r, z)}{\partial z} \quad (2.1)$$

where,  $k_0^2 = i\omega\mu_0\sigma$  and  $v(r)$  is the velocity of flowing liquid. In general, this equation is coupled with the Navier Stoke's equation (equation (1.8)) through  $v(r)$ . Usually,  $v(r)$  is assumed to be known and of the form  $v(r) = U(1 - (r/R)^n)$  [22]. Here,  $R$  is the flow channel radius. This assumption is possible as the Hartman number  $\text{Ha}$  is usually small because of weak magnetic flux and small characteristic length scale in ECFM. Under this assumption, we do not have to solve for the Navier Stoke's equation (equation (1.8)). The analytical solution to equation (2.1), can be obtained by assuming  $v(r) = U$  (plug flow) and the continuity of tangential electric and magnetic fields at the boundaries. The final expression can be obtained in terms of eigenvalue expansion of modified Bessel functions [23]. The analytical solution compares well with experimental results up to  $\omega = 4700 \text{ rad s}^{-1}$ . Approximate solutions have also been developed by Wiegand *et al.* using electromagnetic reciprocity. The solutions are in terms of the Bessel functions [24]. Numerical computation has also been done using finite difference discretization [22, 25], finite element discretization [20, 26] and innovative current ring theory of Baker [25]. In the later case, due to axial symmetry of the ECFM system, the whole geometry is divided into current rings. Their mutual interactions are modeled using lumped circuit element theory and a system of linear equations is solved iteratively. The Green's function approach has also been used [27]. The solution  $A^0(r, z)$  to equation 2.1 corresponds to  $v(r) = 0$ . Then a finite velocity  $v(r) = U$  is added as a small perturbation assuming small  $\text{Re}_m$ . We obtain solution of the form:  $A(r, z) = A^0(r, z) + A^u(r, z)$ . The extra velocity dependent emf in any encircling coil due to the flow is given as

$$V_u = i\omega a^2 r r_0 \mu_0^2 I \sigma U \int_{-\infty}^{\infty} dk k \sin(kd) K_1(kr) K_1(kr_0) \times \frac{I_1(k_1 R)^2 - I_0(k_1 R) I_2(k_1 R)}{[ka I_1(k_1 R) K_0(kR) + k_1 R I_0(k_1 R) K_1(kR)]^2} \quad (2.2)$$

where,  $k_1^2 = k^2 - k_0^2$ ,  $d$  is the distance between the primary and secondary coil,  $r_0$  and  $r$  are the radii of primary and secondary coils respectively and  $R$  is the radius of the flow channel. The behavior of ECFM system would now depend on its configuration: number of coils and design of coils (length, radius, number of turns etc) among some other parameters. And for this purpose, we will now analyze different kinds of ECFM and their properties.

The first ECFM device was patented by Lehde and Lang in 1948 [28]. It consisted of one secondary coil  $S$  with two primary coils  $P_1$  and  $P_2$  placed coaxially at either ends of this secondary coil as shown in figure 2.1a. The primary coils are identical in design and carry equal and opposite currents. The net axial magnetic flux through the secondary coil is therefore zero in the absence of motion in this well balanced configuration. The induced emf in the secondary coil is expected to be zero in this case. The radial component of magnetic field, however is in same direction from both the coils. These radial magnetic fields interact with the flowing electrically conducting medium and produce eddy currents (called flow induced eddy currents) inside the medium. This results in a net magnetic flux through the secondary coil. Assuming that  $P_1$  creates  $V_u$  (given by equation (2.2)) in  $S$  and  $P_2$  creates  $V_u$  in  $S$ , the net flow induced potential in  $S$  will be  $2V_u$ .

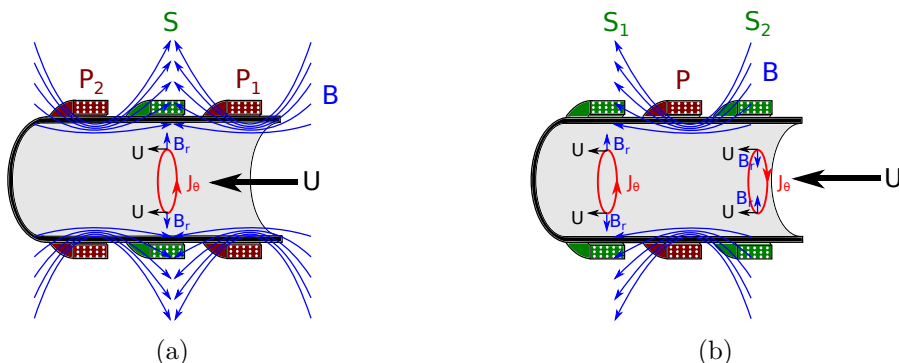


Figure 2.1: (a) 3-coils ECFM system proposed by Lehde *et al.* [28], (b) better 3-coils ECFM system suggested by Shercliff [19].

Shercliff has suggested an improved three coil ECFM assembly shown in figure 2.1b. Taking analogy from a differential transformer, let us call this a differential configuration. It has a primary coil in the middle and two secondary coils are placed coaxially with this primary coil on either side. These two secondary coils are identical in design. The axial magnetic field on either side of the primary coil are in the same direction. Therefore, in the absence of motion equal emfs are induced in the two secondary coils and if we take a difference of emf it is zero. The radial magnetic fields however are in the opposite directions at either extremities of the primary coil. They interact with the medium to produce equal and opposite flow induced eddy currents at the two secondary coils which results in emf  $V_u$  in  $S_1$  and  $-V_u$  in  $S_2$  (or vice versa depending on current in  $P$ ). The difference emf therefore is again  $2V_u$  at small  $Re_m$ .

The second configuration (figure 2.1b) is better than the first configuration (figure 2.1a). Let us assume that there is a source of electromagnetic noise (stray magnetic field) at some distance from the ECFM, which induces a parasitic emf  $\epsilon$  in the first configuration. The total potential in  $S$  will be  $2V_u + \epsilon$ . In the second configuration, it is  $V_u + \epsilon$  in  $S_1$  and  $-V_u + \epsilon$  in  $S_2$ . The difference emf in the second configuration will be  $V_u + \epsilon - (-V_u + \epsilon) = 2V_u$ . Therefore, the signal to noise ratio of the second configuration is better than the first configuration. However, we note that the sensitivity of the two



arrangements to flow are the same ( $2V_u$ ). This was confirmed by the experimental results of Brewer *et al.* [21].

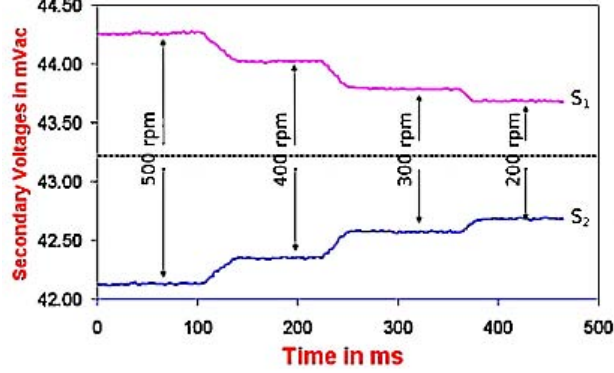


Figure 2.2: Induced emf in the two secondary coils for 3-coils ECFM in differential configuration placed at primary pump outlet in an SFR [29].

Figure 2.2 shows a typical output signal for a 3-coils ECFM in differential configuration placed at primary pump outlet in an SFR. The pump outlet flow rate is given in terms of rotations per minute : rpm. Notice that the voltage in coil  $S_2$  increases by the same amount as it decreases by in  $S_1$  in response to a finite flow. The less evident effect is however a non-zero potential between  $S_1$  and  $S_2$  at zero flowrate (not shown in figure 2.2). This is because in the practical situations the two secondary coils are not exactly balanced. To increase the stability of the device the two secondary coils must be exactly balanced because unbalanced secondary coils would have different coupling to the primary coil and would behave asymmetrically to the surrounding electrically conducting structure, other materials and flowing liquid metal:  $2V_u + \Delta\epsilon(\sigma(T), \mu(T), \dots)$  [30]. Here  $T$  is the ambient temperature. Since it is not practical to obtain exactly identical coils, a series resistor is used to balance the emf in no flow condition. It has been suggested to use the current from the primary coil to achieve this voltage balance [21].

An increase in sensitivity to flow has been observed for a 5-coils device (see figure 2.3) as compared to a 3-coils ECFM of figure 2.1b [22]. But the signal to noise ratio remains the same because inherent noise rejection capability of 3-coils ECFM of figure 2.1b is lost in a 5-coils ECFM. A 5-coils ECFM consists of three primary coils: one at the middle and two at the extreme ends along the coil axis. Two secondary coils are placed in such a way as to separate adjacent primary coils from each other. The primary coils at the extreme ends carry currents in opposite direction ( $180^\circ$  out of phase) compared to the current in the  $P_1$  coil. The axial magnetic fields at the secondary coil cancel out in the absence of the flow. The dense radial magnetic fields interact with the electrically conducting medium to produce same emf in the two secondary coils. The total sum of the two emfs is theoretically  $4V_u + 2\epsilon$  at low magnetic Reynolds number  $Re_m$  and in the presence of the noise sources.

Other kinds of ECFM have also been reported. The description of a single coil

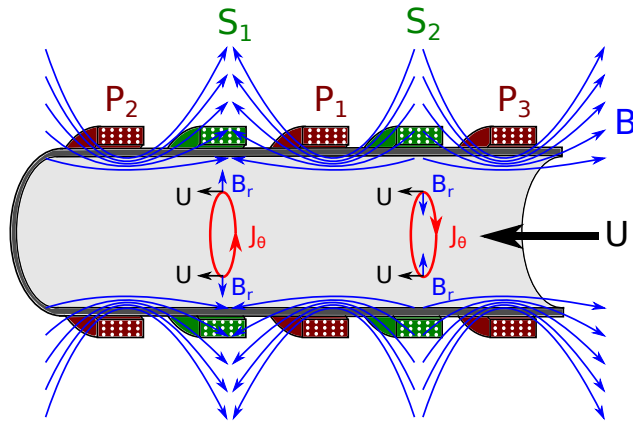


Figure 2.3: A 5-coils ECFM.

ECFM [31], two coils ECFM [31] and four coil ECFM [28] can be found in literature. Each of them have their own advantages and disadvantages. An innovative 3-coils ECFM was proposed by Shercliff and is the topic of current research. As shown in figure 2.4, external magnetic field is produced by a central coil. Since the magnetic field weakens at the edges, eddy currents are set up in opposite directions in the two search coils. The difference of induced emf at low  $Re_m$  is proportional to the flow rate. A similar configuration was also patented by Lehde *et al.*, but it consisted of four coils and required to split the flow channel [28].

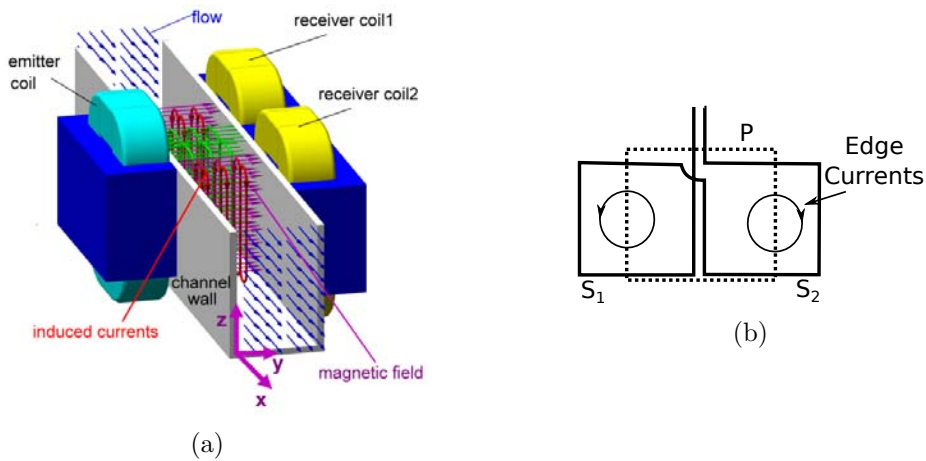


Figure 2.4: A similar 3-coils ECFM system (a) Schematic [32], (b) it's working principle [19].

An ECFM can be placed outside (flow-through type ECFM) or inside (probe type ECFM) the flow channel. Wiegand contends that a flow-through type flowmeter device offers better fluid-coil coupling [24]. Furthermore, ECFM can be in contact with the

liquid metal (wet type) or separated from it by the use of a thimble (dry type). Costello *et al.* found the sensitivity to flow of wet configuration to be 62% larger than that of dry configuration [33]. In addition to this a magnetic shield can also improve immunity of ECFM system to external spurious signals. This should increase the signal to noise ratio [20]. The symmetrical flow channel around ECFM assembly also maximizes the signal to noise ratio [21, 25].

There are two ways to interpret the ECFM output signal : difference of rms magnitudes and phases of induced emf in two secondary coils [34, 35]. Priede *et al.* have found that ECFM device based on phase rather than on the rms voltage output is more sensitive and robust. For a two secondary-one primary ECFM system, the difference of phase in the two secondary coils can be written as [34]

$$\Phi_u = \arctan \left[ \frac{\bar{\omega}\pi^{-1}\text{Re}_m K K_\sigma}{K_\sigma^2 + \bar{\omega}^2 (1 + \pi^{-1}\text{Re}_m K)} \right] \quad (2.3)$$

where,  $\bar{\omega} = \omega\tau$  is dimensionless pulsation of current in primary coil,  $\tau = LR^{-1}$  is the fluid-coils system time scale,  $\text{Re}_m$  is magnetic Reynolds number and  $K$  and  $K_\sigma$  are calibration constants. In this expression, we notice that  $\Phi_u$  is linear in  $\text{Re}_m$  when  $\text{Re}_m \rightarrow 0$ . It was reported that non-linearity is severe after  $\text{Re}_m = 0.3$ . The functional dependence of  $\Phi_u$  on pulsation is similar to  $f(x) = x/(1+x^2)$  for vanishing  $\text{Re}_m$ , which predicts an initial increase in  $\Phi_u$  followed by a rapid decrease after attaining a maximum value. So, the sensitivity of the phase detection based flow sensor to  $U$  changes with the frequency and this sensitivity would decrease after a critical frequency  $\nu_{cp}$ . Similarly, the sensitivity based on  $V_{u,rms}$  signal also decreases with the device operating frequency after a critical frequency  $\nu_{cr}$ . But this critical frequency  $\nu_{cr}$  is smaller than  $\nu_{cp}$ . The accuracy of the measure based on phase is  $\pm 1.5\%$  while that on rms magnitude of the difference signal is  $\pm 10\%$  [34].

The effect of changing flow regime on  $V_u$  does not change the calibration with respect to the mean velocity, although the effects of boundary layer is prominent at low skin depths. The non-linearity increases with increasing  $U$  due to increase in Lorentz force. Wiegand studied the effects of changing flow regimes on the ECFM flow signal and found a power law kind of relationship.

$$V_u = K\text{Re}^n U \quad (2.4)$$

Here,  $\text{Re}$  is in the range  $4 \times 10^3 < \text{Re} < 4 \times 10^6$ .  $n$  ( $< 0.028$ ) was found to be very small for this range of  $\text{Re}$ , which means that the voltage output to flow velocity relationship is almost linear. The weak non linearity would increase with the flow velocity. He also tested the in-phase (signal with 0 rad phase with current in primary coil) and quadrature-phase (signal with  $\pm\pi/2$  rad phase with current in primary coil) components of the flow signal and found that the in-phase component was order of magnitude larger than the quadrature signal. Figure 2.5 shows the in-phase, quadrature and total flow signals. Notice that after a certain frequency, the in-phase signal decreases while after this frequency the quadrature signal first decreases and then increases. From the physics

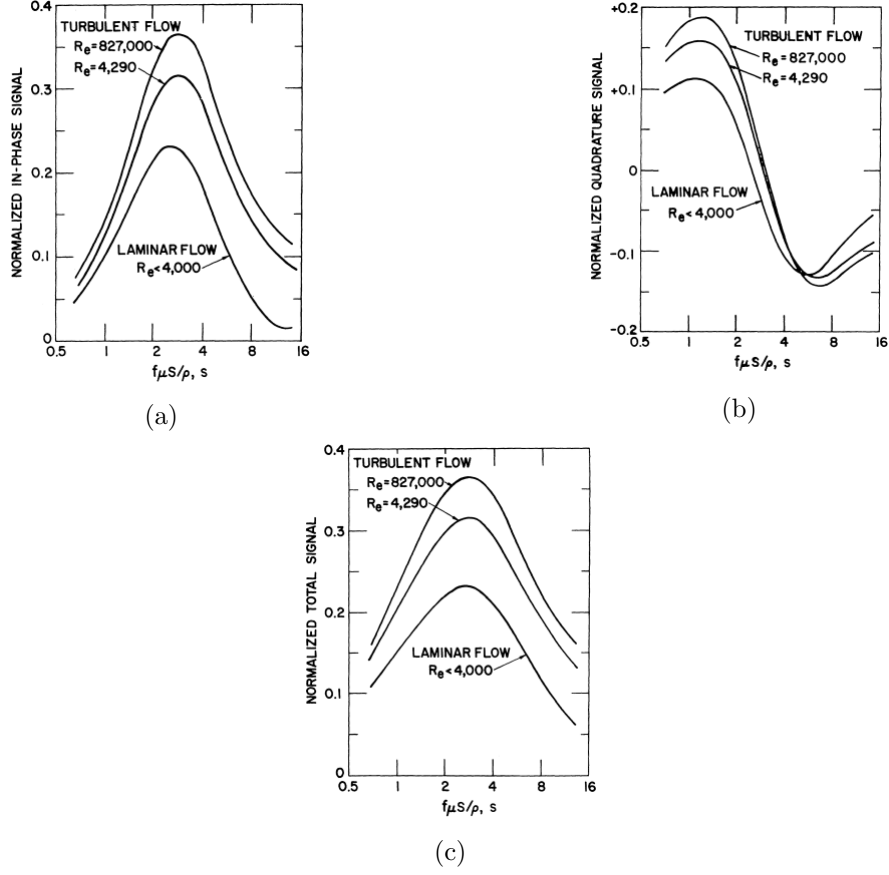


Figure 2.5: The ECFM flow signal (a) In-phase, (b) Quadrature, (c) Total.[24]

point of view, initial increase comes from increasing strength and rate of oscillations of induced eddy currents till the skin depth is equal to the flow channel radius (see equation (15) in this reference [22]). Thereafter, a decrease in the flow signal with frequency comes from the decrease in the penetration depth and less contribution from the flow. This later can be better understood by plotting the expression in equation (2.2). The plot parameters in figure 2.6 are: radius of the primary coil  $r_0 = 4.5$  mm, radii of the secondary coils  $r = 4.1$  mm, radius of the flow channel  $a = 1.25$  mm, flow velocity  $U = 3 \text{ m s}^{-1}$ , conducting liquid resistivity  $\rho = 130 \mu\Omega \text{ cm}$  and current the primary coil  $I_0 = 1$  A. The skin depth can be calculated as:  $\delta = 0.57/\sqrt{\nu}$  m. The skin depth at  $\nu = 1$  MHz is  $\delta = 0.57$  mm. This is approximately half of the flow channel radius.  $V_u$  first increases till  $\delta \sim r_0$ , then thereafter it keeps decreasing. On the other hand, the phase of  $V_u$  keeps on decreasing. After, the peak frequency the phase decreases very sharply initially till it reaches an almost constant value. This means that the ratio of quadrature to in-phase component amplitudes will saturate at some frequency. The tendency of amplitude of  $V_u$  can be approximated as follows: : Let us assume that  $\delta$  is the penetration depth,  $I_0$  is the current in the primary coil,  $C$  is some proportionality constant,  $R$  is flow channel

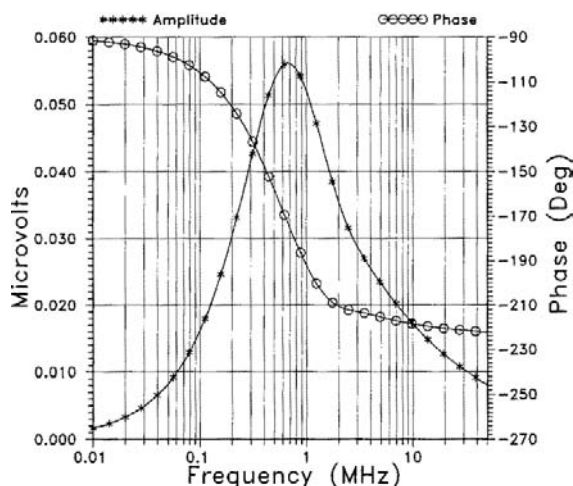


Figure 2.6: A plot of equation (2.2) with  $\nu$ . [27]

radius and  $d\mathbf{l}$  is a current element for circular flow induced eddy currents close to the surface of the rod. In this case if we assume that the radial magnetic fields decay exponentially ( $B_r = B_0 \exp\left(\frac{-(R-r)}{\delta}\right) = CI_0 \exp\left(\frac{-(R-r)}{\delta}\right)$ ) as we move from the surface to the core of the conductor, we get an expression for emf induced due to fluid motion as,

$$\begin{aligned}
 V_u &\sim \oint (\mathbf{v} \times \mathbf{B}) \cdot d\mathbf{l} = U\delta \frac{CI_0}{\delta} \int_{R-\delta}^R r \exp\left(\frac{-(R-r)}{\delta}\right) dr \\
 &= UC I_0 \delta (0.6R - 0.2\delta) \sim k \left[ \left(\frac{\delta}{R}\right) - 0.3 \left(\frac{\delta}{R}\right)^2 \right] \quad (2.5)
 \end{aligned}$$

In expression (2.5), we see a similar exponentially decreasing trend for the ECFM total signal as is shown in figure 2.5c after dimensionless frequency 3. At small penetration depths, the effects of the fluid momentum boundary layer will also be more pronounced [36]. Baker has observed a 20% reduction in  $V_u$  by decreasing the mean velocity in the boundary layer by 5%. Spurious signals such as flow reversal might be observed in this case. Equation (2.5) also predicts a linear relation between current in primary coil and the ECFM signal.

The increasing external temperature would decrease the sensitivity of the induced emf to flow for two reasons: 1) it decreases the electrical conductivity of the ambient liquid metal, 2) it increases the resistivity of the primary coil which limits the current for a given externally applied voltage [30]. In this case, it has also been suggested to use the ratio  $V_2 - V_1 / V_2 + V_1$  rather than the difference voltage. Here,  $V_1$  and  $V_2$  are induced voltages in secondary coils  $S_1$  and  $S_2$  respectively, of an ECFM in 3-coils differential configuration. Ara *et al.* have found that there exists a critical frequency  $\nu_c$  at which this ratio becomes independent of temperature fluctuations. Dohi *et al.* have found the value of this critical frequency to be 500 Hz in their experiments [37]. The existence of  $\nu_c$  was confirmed by Sharma *et al.* (see figure 2.7 and 2.8) [20]. The common practice is to

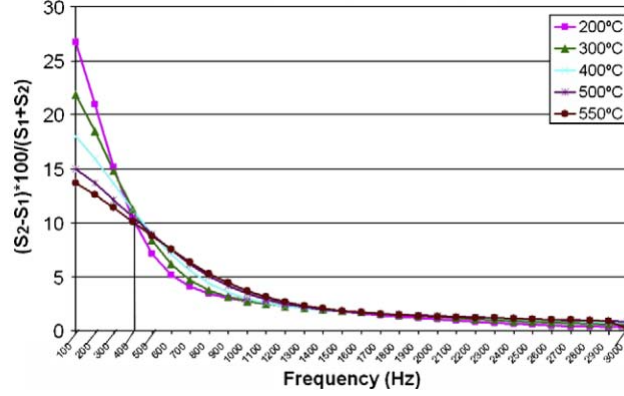


Figure 2.7:  $(V_2 - V_1) \times 100 / (V_2 + V_1)$  vs  $\nu$  (Hz) at different temperatures [20].

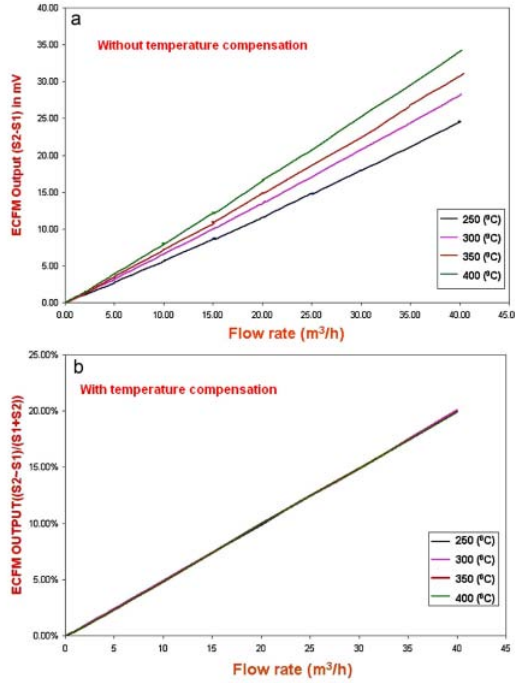


Figure 2.8: (a)  $V_2 - V_1$  and (b)  $(V_2 - V_1) \times 100 / (V_2 + V_1)$ , vs  $U$  at critical frequency  $\nu_c$  and at different temperatures [29].

chose the frequency slightly different from but very close to  $\nu_c$  due to some other factors. In general  $\nu_c$  changes with the coil diameter and the size of the flow cross-section. The physical mechanism responsible for  $\nu_c$  is not known.

A typical use of ECFM is in a Sodium cooled Fast nuclear Reactor (SFR). The device is expected to work within design specifications for up to 700 °C for safety reasons [25]. The velocities as high as  $5 \text{ m s}^{-1}$  may be encountered [21]. This means that the device

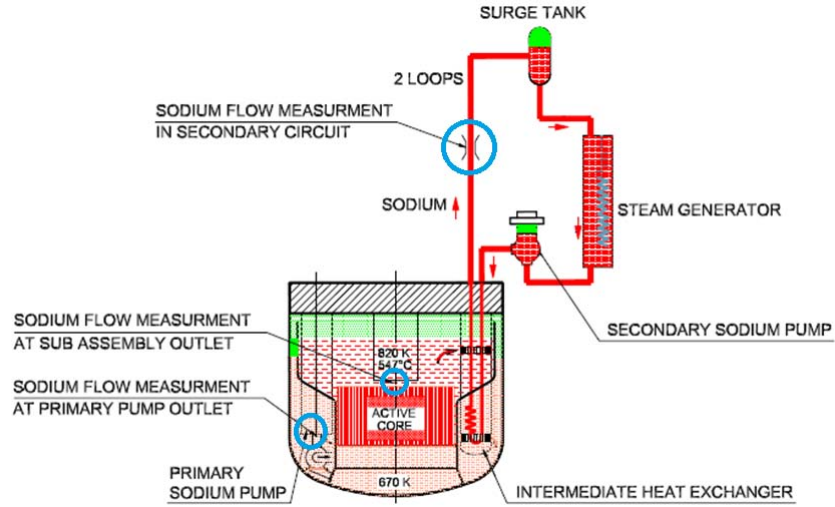


Figure 2.9: ECFM possible locations in an SFR, marked in blue circles.[20]

must be linear within the range,  $U = 0 - 5$  m/s. Figure 2.9 shows the possible locations where ECFM can be installed [20]. Since liquid sodium ignites spontaneously in contact with air or water, it is not used in ordinary lab experiments with ECFM. Instead, plain aluminium solid rod has been used in lab experiments to validate theoretical modeling and to optimize the flow sensor [21, 23]. The aluminium is translated at a given velocity back and forth using hydraulic power. In this case, the aluminium rod simulates a plug flow which is a characteristic of high Reynolds number flows typical to the use of liquid metals in fast nuclear reactors.

## 2.2 ECFM in two-phase flows

Only observations without clear explanations exist for ECFM response in two-phase flows. The same is reported in this section. Experimental observations show that the difference of *emf* induced between the two ECFM secondary coils is sensitive to the passage of gas in gas-liquid metal two-phase flows [38, 39]. Figure 2.10 shows the oscilloscope trace of the modulations in ECFM signal corresponding to a gas injection in core component test loop at Argonne national lab [39]. The argon gas was injected at a rate of 100 cc/s for 5 s using a hand held syringe. The sodium velocities are  $3.7 \text{ m s}^{-1}$  and  $2.5 \text{ m s}^{-1}$  respectively. Excitation current in the primary coil was  $I = 500 \text{ mA}$  at frequency  $\nu = 1000 \text{ Hz}$ . Sodium temperature was  $T = 593 \text{ }^\circ\text{C}$ . Even for no-gas case, we see very small but non-zero fluctuations on ECFM signal. This should be primarily due to turbulent flow fluctuations. When gas is injected in the flow, we note an increase in the amplitude of fluctuations. These fluctuations increase with increase in relative gas flow rate. Unfortunately, since we do not know about the flow channel radius, it is not possible to comment upon the volumic fraction of gas tested in these experiments.

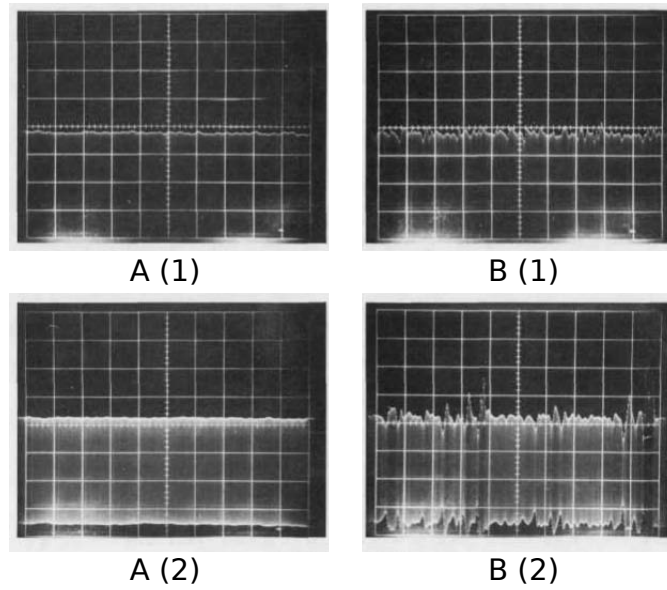


Figure 2.10: Oscilloscope trace of  $emf$  in ECFM for (A) no gas and (B) gas cases at sodium velocities (1)  $3.7 \text{ m s}^{-1}$  and (2)  $2.5 \text{ m s}^{-1}$  [39].

Numerical simulations in a 2D axis-symmetric geometry with a ring type bubble has also been reported [25]. Figure 2.11 shows the response of an ECFM probe to

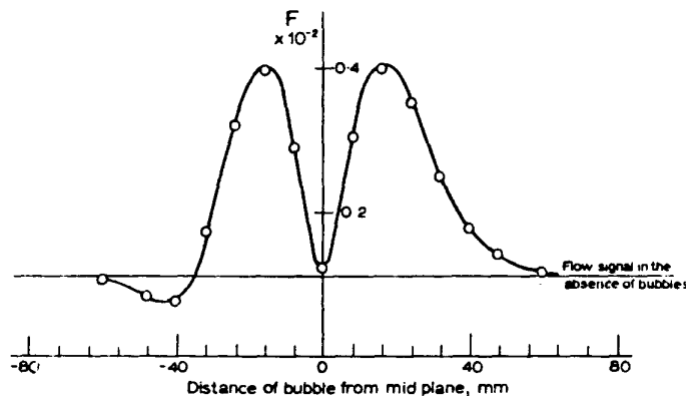


Figure 2.11: The response of ECFM to the passage of a large single bubble [25].

the passage of a large single bubble. This bubble completely blocks the annular space between probe-type ECFM and flow channel inner wall. Notice that this response is similar to the passage of a current dipole through an electromagnetic probe [40].

Hess *et al.* have worked with ECFM for gas void fractions in the range of  $\alpha = 0.3\% - 10\%$ . Based on their experimental results they divided the ECFM void signal into two groups [41]:



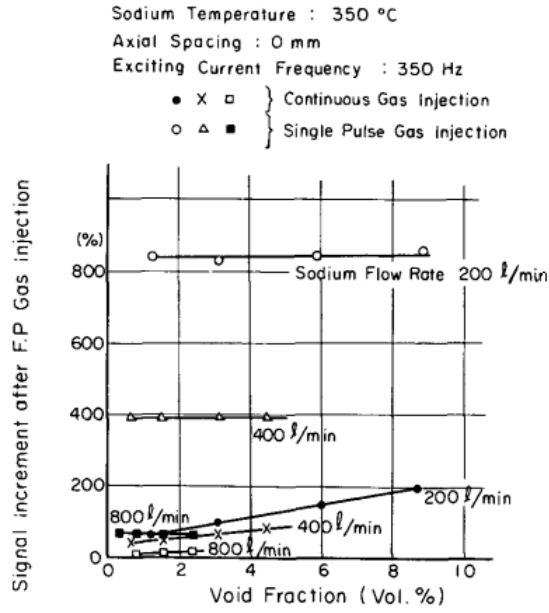


Figure 2.12: ECFM output vs  $\alpha$ . The signal for continuous gas injection is smaller than for single bubbles.[42]

- **Noise amplitude mode (NAM)**: this mode corresponds to the response of the ECFM signal to the passage of continuous gas (annular flow etc.) or the passage of very small bubbles uniformly dispersed in continuous phase. A DC shift of ECFM signal is observed.
- **Noise frequency mode (NFM)**: this mode corresponds to the passage of larger distinct bubbles. Modulations (signal peaks) are observed in the ECFM signal.

Sensitivity of the ECFM is greater for NFM mode than for the continuous passage of gas [42]. For the NFM case the time between the subsequent pulses corresponded to the bubble translation time through ECFM which is related to the bubble velocity. This means that the void signal is the result of the disruption in geometrical and electromagnetic symmetry along the length of ECFM. The sensitivity to  $\alpha$  increased with increasing frequency. Mochizuki *et al.* also found that the signal sensitivity to void decreased with the flowrate (see figure 2.12) [42]. The inverse dependence with the flowrate might be the result of void crushing and subsequent uniformity in bubble distribution at high flowrate [43].

Ogino *et al.* have found that the ECFM device output signal increases by a maximum of 500% in response to the passage of the second phase [44]. They did their experiments for void fraction in the range  $\alpha = 0\% - 6\%$ . Furthermore, the signal to noise characteristics changed significantly from gaussian with the passage of the gas. They have reported that the void signal tends to saturate after  $\alpha = 3.5\%$  (see figure 2.13).

Nakamoto *et al.* have considered the effect of coupling between the flow signal and

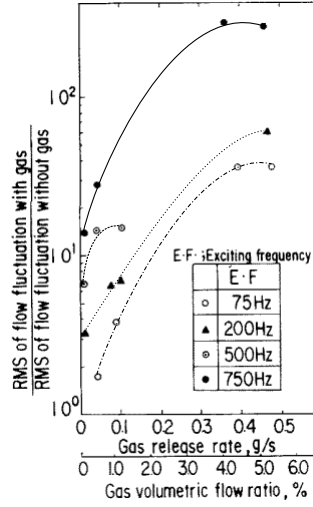


Figure 2.13: ECFM output signal saturates after  $\alpha = 4.0\%$  [44].

the void signal[43]. Their experimental set up consisted of a subassembly outlet mock up in a test tank, 2.5 m in height and 1.1 m in internal diameter, as shown in figure 2.14. Liquid sodium was used as the coolant. An auxiliary gas injection circuit was added to the test section. The gas was preheated to the same temperature as that of the liquid sodium and subsequently injected in the sodium flow through a pin of 1 mm in diameter. This pin was placed upside down in order to ensure zero gas velocity at the time of injection. ECFM device was fixed at the top of the central sub-assembly. The experiments were performed at flow velocity near  $U = 0.83$  m/s and for void fractions  $\alpha = 0 - 2\%$ . The void fraction was defined as follows

$$\alpha(\%) = \frac{\text{gas flow rate}}{\text{sodium flow rate} + \text{gas flow rate}} \times 100 \quad (2.6)$$

This is the definition used for void fraction in other two-phase void measurement experiments also. Here, we assume the bubbles to be extremely small and this definition will not be valid if the slip ratio between gas voids and ambient liquid flow is significant.

Nakamoto *et al.* realized that the signal output based on rms value is sensitive to flow disturbances and hence have a poor signal to noise ratio for void detection. They made the hypothesis that the flow and flow fluctuations signal in ECFM should be in-phase with the exciting current in the primary coil. Therefore, it is possible by the help of a phase sensitive measurement to obtain void signal which is presumed to have a different phase than that of flow fluctuations signal. This principle is depicted in figure 2.15. In single phase flow, the difference of emf in two secondary coils of a 3-coils ECFM is  $E_f$ . It is related to flow rate. The turbulent flow fluctuations induce parasitic signal  $e_f$ . This is mediated by the Lorentz force term in magnetic induction equation.  $E_f$  exhibits the same characteristics as we saw in previous section. The flow signal amplitude tends to increase initially with increasing frequency and starts decreasing after attaining a

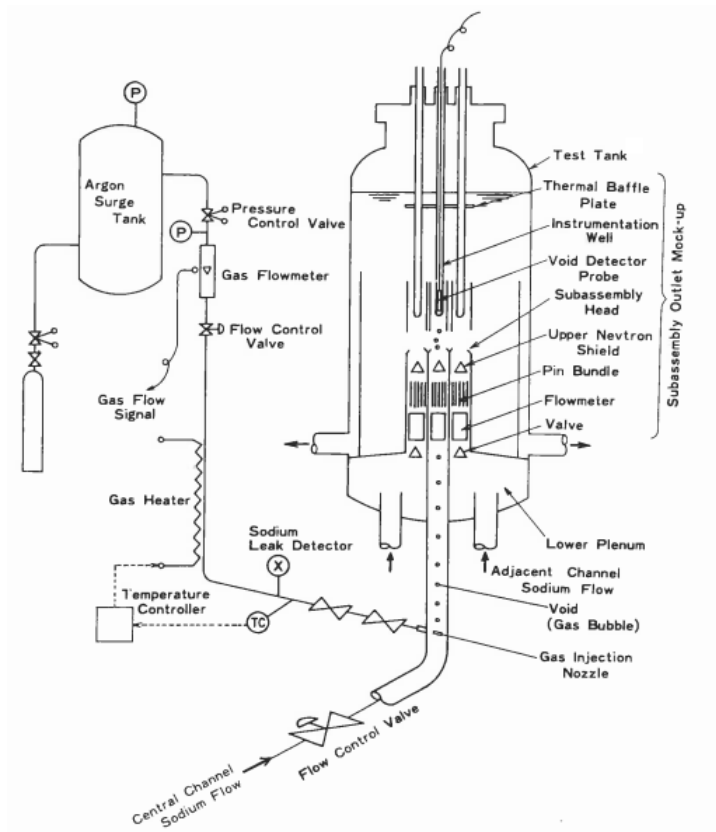


Figure 2.14: The experimental set up of Nakamoto *et al.* [43].

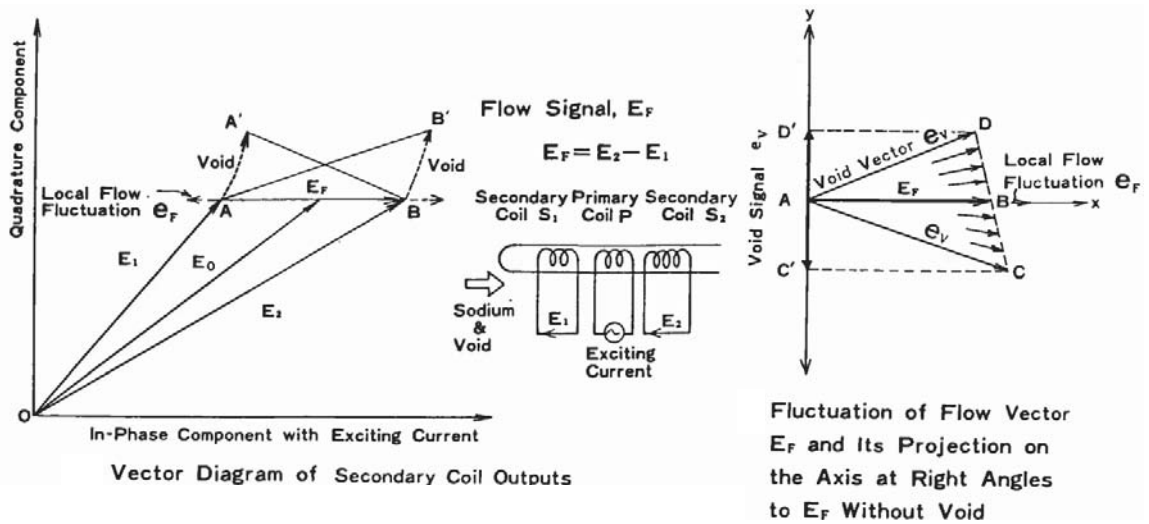


Figure 2.15: The schema of phase sensitive ECFM signal treatment [43].

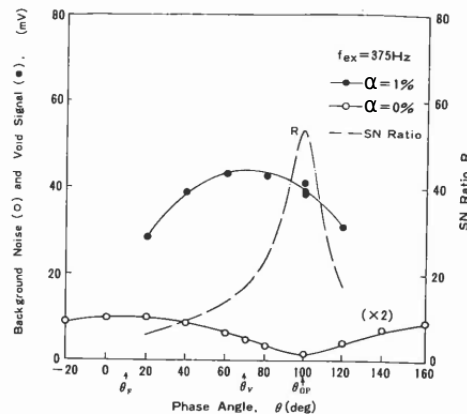


Figure 2.16: Optimum phases for flow and void related fluctuations [43].

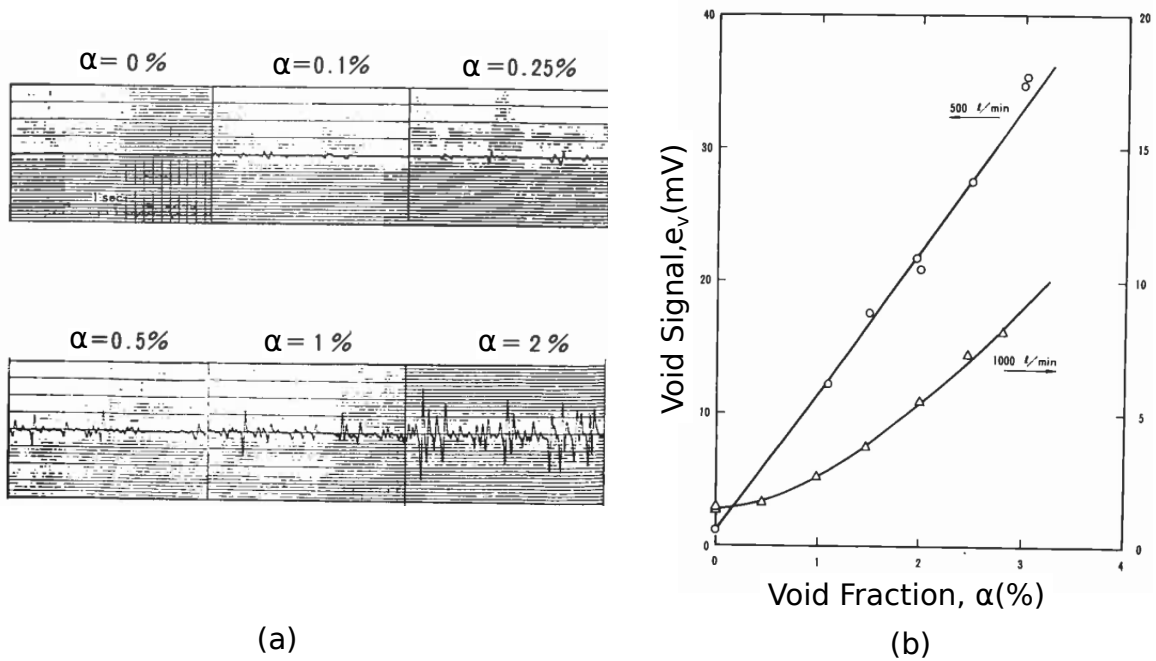


Figure 2.17: (a) Quadrature-phase ECFM signal ( $e_v$ ) at different values of  $\alpha$  (%), (b) standard deviation of quadrature-phase ( $e_v$ ) fluctuations vs  $\alpha$  (%) [43].

maximum. The passage of voids (bubbles) induce  $e_v$ . The rms of  $e_v$  is recorded as the void signal.

To calibrate the sensitivity of difference  $emf$  to flow fluctuations and  $\alpha$  an experiment was performed at a constant frequency for  $\alpha = 0\%$  and  $\alpha = 1\%$  respectively. The phase of the measured difference signal with respect to the phase of the AC current in the primary coil is varied to determine the optimum phase at which the magnitudes of  $e_f$

and  $e_v$  are maximum respectively. For  $\alpha = 0\%$  case, the rms of fluctuations in difference signal quantifies magnitude of turbulent flow fluctuations which (as shown in figure 2.16) seems to be maximum at a phase difference  $0^\circ$ . For  $\alpha = 1\%$  case, the rms of fluctuations in difference signal quantifies both the magnitude of turbulent flow fluctuations and fluctuations due to the passage of voids. It is maximum at a phase difference  $70^\circ$ . This justifies Nakamoto *et al.* hypothesis that the flow and void fluctuations are nearly in quadrature to each other ( $90^\circ$ , but here it is  $70^\circ$ ). Fluctuations in  $e_v$  increase with increasing frequency of the primary coil excitation current. In figure 2.17(a), we see that the magnitude of fluctuations in  $e_v$  also keeps on increasing as a function of the void fraction  $\alpha(\%)$ . Sensitivity to void was found to decrease with the flowrate (see figure 2.17(b)). To explain this result Nakamoto *et al.* provided two possible reasons: (1) the two-phase medium is completely homogeneous due to phenomenon of crushing of void and subsequent uniformity in bubble distribution at high flowrate; (2) Nakamoto *et al.* used a band pass filter of width 13 Hz which suppressed the void modulation signal at high flowrate. The coupling between flowrate and the void fraction appears to be superficial. Furthermore, these explanations are rather speculative in nature. It is in this regard that some clarifications are required and further studies need to be performed.

Flux distortion techniques are also used in some other similar systems. For example, Mutual Inductance Tomography (MIT) [45] and Contactless Inductive Flow Tomography (CIFT) [46] have been proposed to monitor flow profiles of melt in metallurgy applications. In both the techniques, the coils are excited by given current sequentially and induced voltage is detected in respective opposite coils (see figure 2.18a). The frequency of excitation is kept low to ensure proper coupling between opposing coils. Terzija *et al.* have used the CIFT technique to monitor the effect of argon gas injection when liquid metal eutectic alloy GaInSn (galinstan) is allowed to pass through a nozzle into a reservoir. This system simulates the situation when melt is poured into die (cast) in metallurgy. The experimental results are given for excitation of coil 3 and detection using coil 7 (see figure 2.18a). The voltage in coil 7 is zero in the absence of flowing melt through the sensor. When the melt-argon gas mixture flows through the sensor, it changes the induced signal in coil 7. This distortion in magnetic flux comes from induced eddy currents in the two-phase melt. For fixed volume of melt and higher gas flow rates (high  $\alpha$ ), they have observed a shift of mean value of ‘established’ voltage towards the value without melt-argon mixture (value in air). This comes from decrease in average electrical conductivity of the melt-argon mixture at higher  $\alpha$ . They also observed large fluctuations over this mean signal. This fluctuating component of the signal also increased in magnitude with  $\alpha$ . For the case of low gas flow rates, they attribute the existence of the peaks in the induced signal to the passage of bubbles (see figure 2.18c) [47]. These kind of studies are still nascent and demonstrate the feasibility of flux distortion based techniques in two-phase flow applications. As conclusion the authors have suggested future work to better understand the modulations of the signal.

In this section, we have have found that there are two effects observed for ECFM in two-phase flows: (1) the mean DC shift in the signal amplitude corresponding to passage

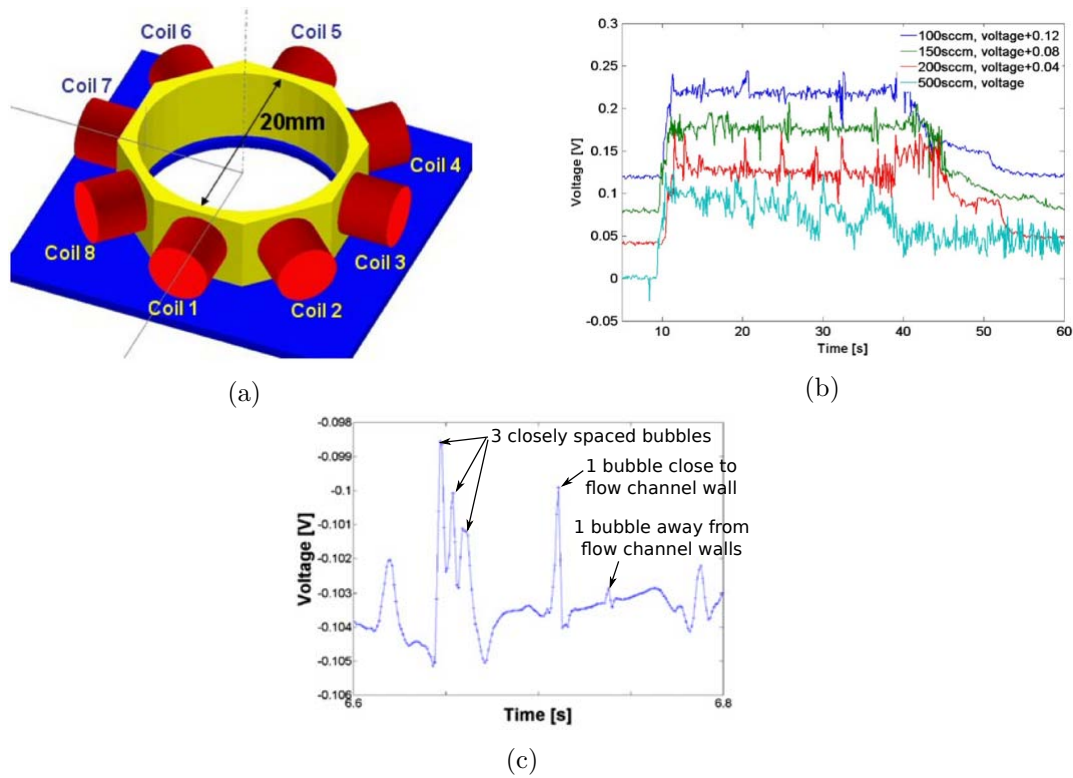


Figure 2.18: (a) An 8 coil sensor for MIT or CIFT *et al.* [46], (b) Two phase results for melt-argon flow (c) The zoom of oscillations at low gas flow rates [47].

of continuous gas or a homogeneous mixture of very small gas bubbles through ECFM, (2) oscillations/modulations over this mean amplitude corresponding to the passage of large single bubbles. The mechanisms behind these two effects are not known. The literature survey in the next section will help us build tools for their understanding.

## 2.3 Single fluid with equivalent properties

If the gas bubbles were very small and homogeneously dispersed in liquid sodium, we can treat the two-phase medium as a single continuous medium with equivalent values of physical properties that characterizes this mixture. By ‘homogeneously’, we mean that the mean separation between the bubbles is very small with respect to flow channel diameter. Then, the average void effect comes from alteration of the average electrical conductivity in two-phase flows. If we know the dependence of the ECFM signal on the electrical conductivity and the dependence of the electrical conductivity on the void fraction, we can correlate the effect of void fraction on the induced emf in ECFM secondary coils.

### 2.3.1 Dependence of induced emf on electrical conductivity

For the no flow case, the induced emf in the ECFM secondary coils, depends upon the electrical conductivity of the enclosed medium through the analytical expression of Dodds *et al.* [48]. For the case of finite motion between the ECFM coils and the medium (plug flow), the analytical expression of Hirayama *et al.* [23] can be used. These expressions can also be used to determine the distribution of eddy currents in the medium in the single phase flow. These integral expressions are eigenvalue expansions in terms of modified Bessel functions and involve computers to evaluate the induced emf. Other than this, there is no explicit expression or graph that shows effect of electrical conductivity on the induced emf in ECFM secondary coils to the best of author's knowledge. An easier way to see the effect of electrical conductivity on the induced emf is a finite element simulation that has been used recently for ECFM in single phase flows [20]. The detailed description of the same is given in the next chapter. Here, we show the results only, for 3-coils ECFM in differential configuration.

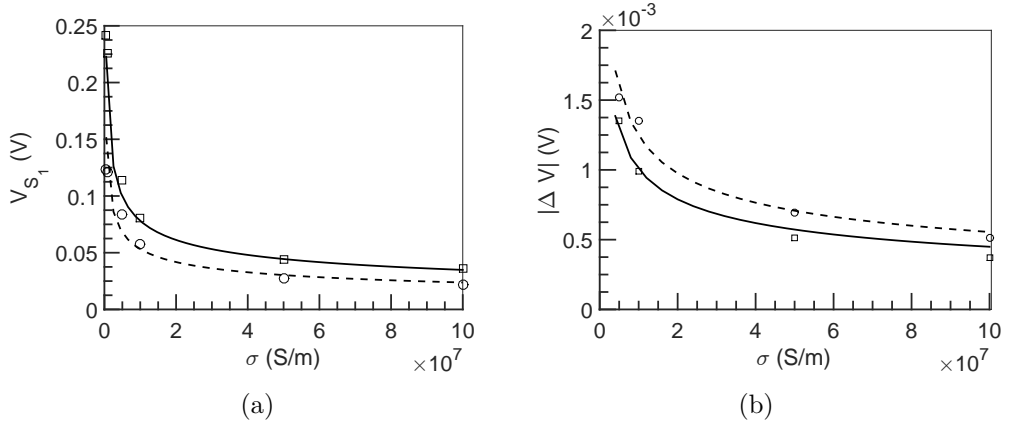


Figure 2.19: (a) Induced emf in  $S_1$ , (b) Difference of induced emf in  $S_1$  and  $S_2$  vs  $\sigma$ , for  $U = 1 \text{ m/s}$  at  $\omega = 3142 \text{ rad s}^{-1}$  ( $\circ$ ) and  $\omega = 6284 \text{ rad s}^{-1}$  ( $\square$ ).

As shown in figure 2.19a, the induced emf in secondary coil  $S_1$  follows a power law in  $\sigma$ :  $V \sim \sigma^{-0.35}$ . The behavior of the induced emf in  $S_2$  is same. Also, this only corresponds to the case of small penetration depth  $\delta < R$ . Same trend is obtained for the balance of emf in the two secondary coils at  $U = 1 \text{ m/s}$  as shown in figure 2.19b.

### 2.3.2 Effective electrical conductivity of two-phase media

In this section, we discuss the mean effective electrical conductivity ( $\sigma_\alpha$ ) of a two-phase medium as a function of volume fraction  $\alpha$  of the dispersed phase. The electrical conductivity of the continuous phase is  $\sigma$ , while the electrical conductivity of the dispersed phase is taken as zero. Since the movement of electrical current is mathematically analogous to the quantities related to other transport phenomena [49], the results obtained in this section will also hold for quantities such as magnetic permeability, electrical permit-

tivity, heat conductivity and viscosity. Although the contrast in the value of transport parameters for two-phases might not be as large as for electrical conductivity ( $\sigma$  vs zero). These results are obtained in the absence of any induction effects and involve expansion of static electrical potential for two-phase media.

The simplest possible models are series and parallel models. Since the medium offers resistance to the flux (for example, current density or heat flux), the media can be modeled as some arrangement of resistors in an electrical circuit. In Parallel model, the medium is assumed to consist of layers of medium 1 (continuous phase) and medium 2



Figure 2.20: Equivalent medium as a network of electrical resistors (a) Parallel model (b) Series model.

(dispersed phase) arranged alternatively perpendicular to the flow of current flux (see figure 2.20a). The equivalent model in terms of resistors is a combination of resistors in series. In series model, the medium is assumed to consist of layers of medium 1 and medium 2 parallel to the flow of current flux (see figure 2.20b). The equivalent model in terms of resistors is a combination of resistors in parallel. If  $\alpha$  is the void fraction of medium 2 in medium 1, the equivalent electrical conductivity ( $\sigma_\alpha$ ) of the two-phase medium for parallel model case is

$$\sigma_\alpha = (1 - \alpha)\sigma_1 + \alpha\sigma_2 = \sigma(1 - \alpha) \quad (2.7)$$

For the case of series model, the same is given by

$$\frac{1}{\sigma_\alpha} = \frac{1 - \alpha}{\sigma_1} + \frac{\alpha}{\sigma_2} = 0 \quad (2.8)$$

As is evident from equations (2.7) and (2.8), the series and parallel models offer lower and upper bounds respectively on the transport properties of equivalent medium. This fact was also noticed by Wiener and some other researchers [50, 51]. Series and parallel models are called Voigt and Reuss models in case of elastic modulus [52, 53]. The so called Network models [54] represent the microstructure of the equivalent media as a distribution of resistors linked to each other in series and parallel. To represent each micro domain by a resistor and their complicated network involves calculations using parallel and series laws of electrical network theory. This can be very expensive and thus the Network model is only used in some specific cases [55]. Even though series



and parallel models are very simple in nature, they have found applications in many processes. For example, for air-water two-phase flows Lafferty & Hammitt found a good agreement of experimental data with equation 2.7 [56]. The parallel model was also used for the case of two-phase MHD power generators in a slightly modified way,  $\sigma_\alpha = \sigma(1 - 1.1\alpha)$  [57].

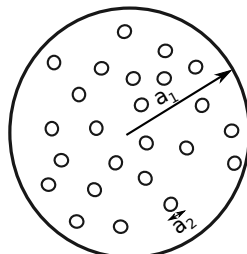


Figure 2.21: Maxwell's medium: spheres of radii  $a_2$  are dispersed in continuous medium of radius  $a_1$ .

**Maxwell's model :** Maxwell's model assumes a dilute suspension of very small spheres inside a bigger sphere. As shown in figure 2.21,  $n$  spheres (medium 2), each of radius  $a_2$ , are distributed randomly inside a spherical medium of radius  $a_1$  (medium 1). The mean separation between all these spheres is  $\lambda$ . We assume :

- $a_2 \ll \lambda \ll a_1$ .
- No Faraday induction effects,  $\omega \rightarrow 0$ .
- No Lorentz force effects,  $U \rightarrow 0$ .
- Very low void volume fraction,  $\alpha = \frac{na_2^3}{a_1^3} \ll 1$ .

Under these assumptions Laplace equation for electrical potential ( $V$ ) is solved to calculate the distribution of electrical currents in the medium.

$$\nabla^2 V = 0 \tag{2.9}$$

Following boundary conditions are used on the void surface:

- Potential is continuous:  $V_1 = V_2$
- The normal component of electrical current density is constant:  $\vec{J}_{n,1} = \vec{J}_{n,2} \implies 1/k_1 \partial V_1 / \partial n = 1/k_2 \partial V_2 / \partial n$

where,  $k_1$  and  $k_2$  are specific resistances of medium 1 and medium 2 respectively. The total electrostatic potential due to this mixture is obtained by linear superposition of the potentials of each of these small spheres. The mutual interference between the spheres is neglected. The separation between the spheres are so great that the alteration in the

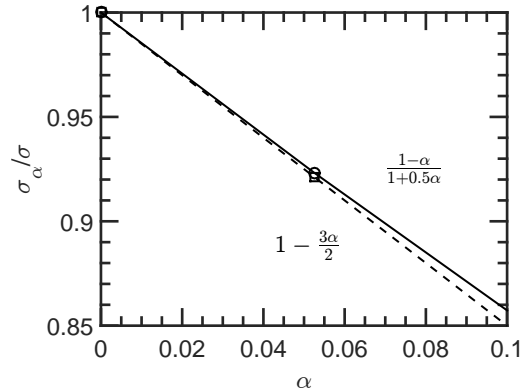


Figure 2.22:  $\sigma_\alpha/\sigma$  vs  $\alpha$  for Maxwell's model.

path of electrical currents around one sphere does not influence the current around any other sphere.

In this case, Maxwell has shown that, the equivalent specific resistance  $K$  of the compound medium is given by [58],

$$K = \frac{2k_2 + k_1 + \alpha(k_2 - k_1)}{2k_1 + k_1 - 2\alpha(k_2 - k_1)} k_1 \quad (2.10)$$

If the spheres of medium 2 were non-conducting ( $k_2 \rightarrow \infty$ ), equation (2.10) reduces to

$$K = \frac{1 + 0.5\alpha}{1 - \alpha} k_1$$

Therefore the electrical conductivity  $\sigma_\alpha$  of the compound medium consisting of non conducting spheres distributed inside a medium of electrical conductivity  $\sigma$  is related to its the void fraction by the following expression,

$$\sigma_\alpha = \sigma \frac{1 - \alpha}{1 + 0.5\alpha} \quad (2.11)$$

Expanding the result of Maxwell (equation (2.11)) in Taylor series gives ( $\alpha \ll 1$ )

$$\sigma_\alpha = \sigma \left[ (1 - \alpha) \left( 1 + \frac{\alpha}{2} \right)^{-1} \right] = \sigma \left[ 1 - \frac{3\alpha}{2} + 3 \left( \frac{\alpha}{2} \right)^2 - 3 \left( \frac{\alpha}{2} \right)^3 + \dots \right] \approx \sigma \left( 1 - \frac{3\alpha}{2} \right) \quad (2.12)$$

Note that these equations are valid for small  $\alpha$ , since we have derived this expression on the assumption that the separation between the spheres is large. Indeed, as shown in figure 2.22, we see that the first two terms work well for  $\alpha < 10\%$ . Hamilton-Crosser model [59] is a generalization of Maxwell's model to account for non-spherical shape of particles of the dispersed phase.

$$\sigma_\alpha = \sigma_1 \frac{\sigma_2 + (n-1)\sigma_1 - \alpha(n-1)(\sigma_1 - \sigma_2)}{\sigma_2 + (n-1)\sigma_1 + \alpha(\sigma_1 - \sigma_2)} = \sigma \left( 1 - \frac{3\alpha}{2} \right)_{n=3} \quad (2.13)$$

Where  $n$  is the shape factor of the particles of the dispersed phase.  $n = 3$  corresponds to the case of spherical particles dispersed in continuous phase. Note that for  $n = 3$ , the equation (2.13) gives the same result as that obtained with Maxwell's model.  $n = 6$  corresponds to the case when dispersed particles are cylindrical. Maxwell's model has also been used to calculate other transport properties in two-phase media [50, 60–66].

Maxwell's theory of effective electrical conductivity is order  $\mathcal{O}(\alpha)$ . A correction up to  $\mathcal{O}(\alpha^2)$  to equation (2.11) can be obtained by allowing for interactions between pairs of spheres. The void fraction  $\alpha$  is the fraction of volume of second medium present in a unit volume of the first medium. Therefore, the probability of one sphere within distance  $a$  ( $a$  is the radius of the non conducting sphere) is  $\mathcal{O}(\alpha)$  and the probability of two spheres within distance  $a$  will be  $\mathcal{O}(\alpha^2)$ . This means to allow for an order  $\mathcal{O}(\alpha^2)$  correction we only need to consider interaction between pairs of spheres. This problem has been solved by taking analogy with the heat conduction. The electrical conductivity in our case at  $\mathcal{O}(\alpha^2)$  is [67]

$$\sigma_\alpha = \sigma \left[ 1 - 3 \left( \frac{\alpha}{2} \right) + 3 \left( \frac{\alpha}{2} \right)^2 \left\{ 1 - \frac{1}{2^3} + \frac{1}{2^4} - \frac{1}{2^8} + \dots \right\} \right] \quad (2.14)$$

Numerical evaluation of the series in equation (2.14) converges for over 100 terms. The solution is

$$\sigma_\alpha = \sigma \left[ 1 - 3 \left( \frac{\alpha}{2} \right) + 3 \left( \frac{\alpha}{2} \right)^2 \times 0.784 \right] \quad (2.15)$$

The comparison of  $\mathcal{O}(\alpha)$  and  $\mathcal{O}(\alpha^2)$  models are shown in figure 2.23. These two models

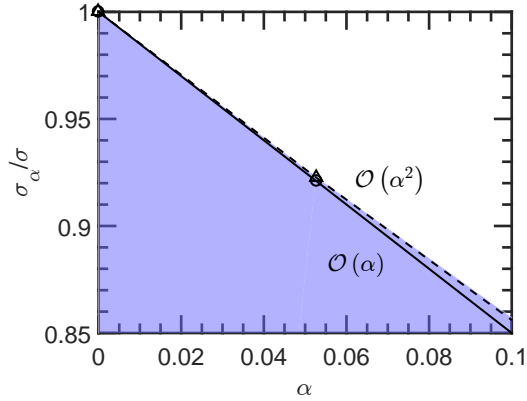


Figure 2.23:  $\sigma_\alpha/\sigma$  vs  $\alpha$ : A Comparison of  $\mathcal{O}(\alpha)$  (—) and  $\mathcal{O}(\alpha^2)$  (---) models and lower and upper bounds of Hashin *et al.* shown as the shaded area.

give the same value of  $\sigma_\alpha$  for  $\alpha < 10\%$ . Physically, it means that the electrical current around one non-conducting sphere does not interact with electrical currents around any other non-conducting spheres for  $\alpha < 10\%$ .

Hashin and Shtrikman [49] have obtained upper and lower bounds on  $\sigma_\alpha$  by considering a ‘composite spheres’ medium (Note: Voigt and Reuss bounds are wider and can be found in an appropriate reference [68]. For the sake of brevity we show here the theory which provides narrowest possible bounds).

$$0 \leq \frac{\sigma_\alpha}{\sigma} \leq \frac{1 - \alpha}{1 + 0.5\alpha} \quad (2.16)$$

The equivalent medium is assumed to be composed of composite spheres. A composite sphere is a sphere of first medium ( $\sigma$ ); inside this sphere we place spheres of varying sizes of the other medium ( $\sigma = 0$ ).

We notice that the expression for the upper bound in equation (2.16) is same as the one obtained by Maxwell (equation (2.11)) for the case of electrical conductivity of a medium containing non-interacting spheres. This means that the electrical conductivity is highest for the case where the non-conducting spheres do not interact, while decreases as they start interacting with more and more neighbors. For this interaction between the spheres to increase,  $\alpha$  must increase, which decreases  $\sigma_\alpha$  at the same time.

Both the models,  $\mathcal{O}(\alpha)$  and  $\mathcal{O}(\alpha^2)$  do not work at large  $\alpha$ . The former gives negative electrical conductivity while the later gives a non-zero intercept at  $\alpha = 100\%$ . At higher  $\alpha$ , we speculate the interaction of the electrical current around a given sphere with many other spheres, even separated at large distances compared to the diameter of the sphere. Analytical solutions in these situations are not possible. Even the numerical schemes which treat the system as boundary value problem are only accurate to first order  $\mathcal{O}(\alpha)$  [69, 70]. To extend the formulation to higher orders by allowing for the long range interactions between spheres leads to coefficients in terms of divergent integrals. The spatial correlation functions between these spheres are ambiguous and the resulting power series converges very slowly as  $\alpha$  increases [67]. To tackle this situation researchers have

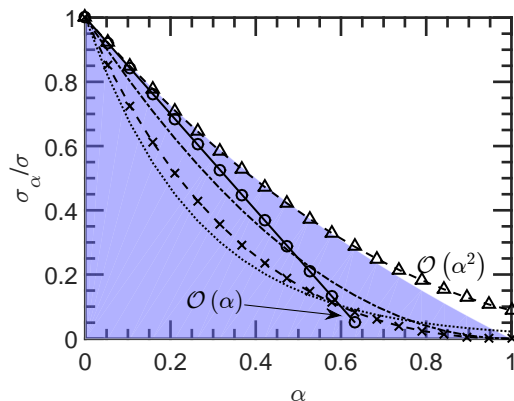


Figure 2.24:  $\sigma_\alpha/\sigma$  vs  $\alpha$ : A Comparison of  $\mathcal{O}(\alpha)$  and  $\mathcal{O}(\alpha^2)$  models with empirical relations of Petrick and Lee [ $\cdots$  : equation (2.17) and  $\times$  : equation (2.18)] and Archie’s power law ( $-\cdot-$ ). The shaded area shows the lower and upper bounds of Hashin *et al.*

used empirical relations or approximate theoretical models. For example, an empirical

relation of the following form was proposed by Petrick and Lee [71],

$$\sigma_\alpha = \sigma \exp(-3.8\alpha) \quad (2.17)$$

The theoretical model was validated with the experimental results of NaK – N<sub>2</sub> two-phase flow and an excellent agreement was found for the full range of  $\alpha$  (0 – 100%). Petrick and Lee have also suggested the following relation for NaK-N<sub>2</sub> two-phase flow in MHD generator [71].

$$\sigma_\alpha = \sigma \frac{(1 - \alpha)^2}{1 + \alpha}, \quad 0 \leq \alpha \leq 0.70 \quad (2.18)$$

Archie's law models the effective transport properties of brine saturated rocks. Applied to our case it predicts

$$\sigma_\alpha = \sigma(1 - \alpha)^2 \quad (2.19)$$

To conclude, we see the effect of change in emf in ECFM secondary coils as a function of void fraction. We restrict the argument to  $0 < \alpha < 10\%$ . For this case the interaction between the neighboring bubbles can be neglected and therefore we will use the Maxwell's model (2.11). We will also use the empirical relation of Petrick and Lee for NaK–N<sub>2</sub> two-phase flows (2.18). In both the cases, we find that the increase in the induced

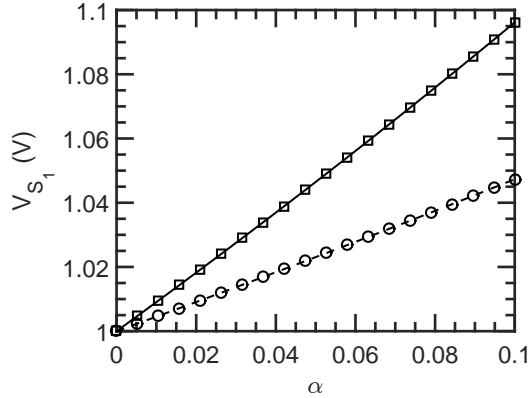


Figure 2.25:  $V_{S_1}$  vs  $\alpha$ : Comparison of induced signal in  $S_1$  based on Maxwell's model (○ : equation (2.11)) with the one based on the empirical relation of Petrick and Lee (□ : equation (2.18)).

potential is linear with  $\alpha$ . Maxwell's model predicts a 5% increase in the induced signal, while the model of Petrick and Lee predicts a 10% increase, corresponding to an increase of void fraction from 0 to 10%.

## 2.4 General two-phase medium

This section presents the effects of large single bubbles/inclusions on the externally imposed magnetic fields. This will help us understand the emf fluctuations (modulations)

in ECFM signal. In subsection 2.4.1, we analyze models for distortion in eddy currents due to  $\alpha$  and  $U$  at very low pulsations  $\omega < 100 \text{ rad s}^{-1}$ . These models assume decoupling between Faraday induction and Lorentz force effects. In subsection 2.4.2, we provide literature survey of models describing distortion in eddy currents due to  $\alpha$  at very high pulsations ( $10^4 < \omega < 10^7 \text{ radian/s}$ ). The Lorentz force effects are neglected in these models.

### 2.4.1 Models without induction effects

Consider a system as shown in figure 1.6. Instead of permanent magnets, we use electromagnets, which produce AC magnetic field of high intensity but low pulsation ( $\omega < 100 \text{ rad s}^{-1}$ ). Two-phase medium flows in a circular cylinder, under this slowly varying external magnetic field. The distortion due to  $U$  and  $\alpha$  is measured with the help of two electrodes.

The physical laws governing this problem are given in section 1.4.2. The influence of flow on the potential difference at the electrodes in single phase flow can be calculated as

$$\nabla^2 V = \vec{B} \cdot \nabla \times \vec{U} \quad (2.20)$$

where,  $\Delta V$  is the induced potential difference at the electrodes and  $U$  is the mean flow velocity. The direction of the electric field ( $\vec{E}_f$ ) and hence electrical current density ( $\vec{J}_f$ ) calculated from the Poisson's equation 2.20 is towards the electrodes. Therefore measuring this current serves as a flowmeter. We call this signal as flow induced emf.

The time varying nature of externally imposed magnetic field also induces rotational electric fields ( $\vec{E}_t$ ), which orient perpendicular to the electrodes in single phase flow. Hence, the corresponding current density ( $\vec{J}_t$ ) does not flow towards electrodes and does not contribute in single phase flow [72]. We call the corresponding emf as transformer induced emf. In this case it is zero.

A pictorial depiction of the two types of eddy currents,  $\vec{J}_f$  (given by  $\vec{J}_f = \sigma(\vec{U} \times \vec{B})$ ) and  $\vec{J}_t$  (given by  $\nabla \times (\vec{J}_t/\sigma) = -\partial\vec{B}/\partial t$ ) is shown in figure 2.26.

Cha *et al.* have performed two-phase flow experiments with electromagnetic flowmeters, using water-nitrogen and later with sodium-nitrogen as two-phase medium [18, 73]. In the absence of bubbles or slugs,  $\vec{E}_t$  is essentially normal to the electrodes and hence have no influence on the induced potential difference. In this case, the total potential difference can be calculated from equation 2.20. Since, the pulsations are in the range:  $20 < \omega < 100 \text{ rad s}^{-1}$ , the flow induced emf is out of phase with the transformer induced emf by  $\pi/2$  (the two signals are mutually orthogonal) because the flow induced emf is proportional to magnetic flux density but the transformer induced emf is proportional to its first derivative [18].

Now, let us take the case of a large slug passing through the electromagnetic flowmeter in water-air two-phase flow [18, 73]. The reference voltage  $V_{ref}$  is obtained on a  $1 \Omega$  resistor in series with the coil excitation current in electromagnet. As shown in figure 2.27, at **A**, there is no air slug and rotational electric field is orthogonal to the normal  $\hat{n}$  to electrode faces. Hence there is no component of transformer induced eddy currents

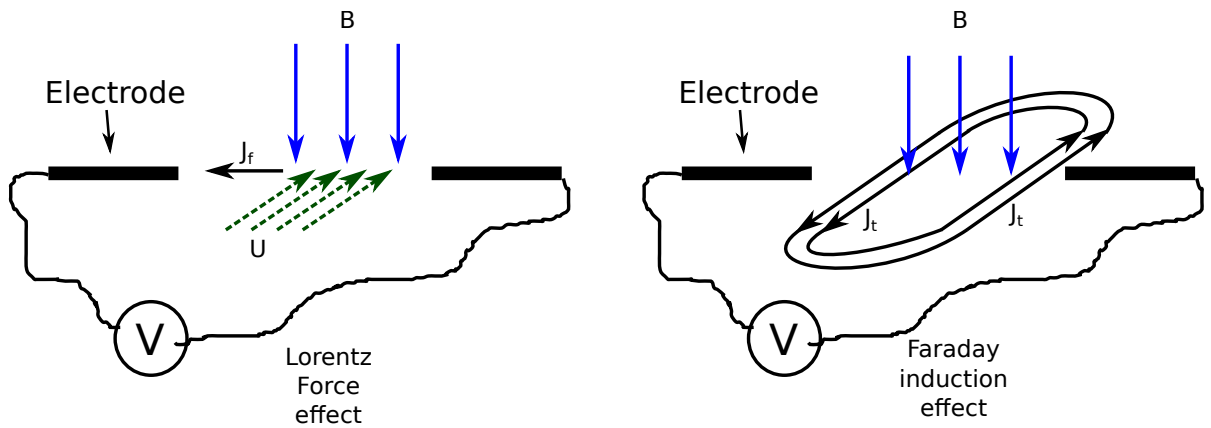


Figure 2.26: The two types of eddy currents.

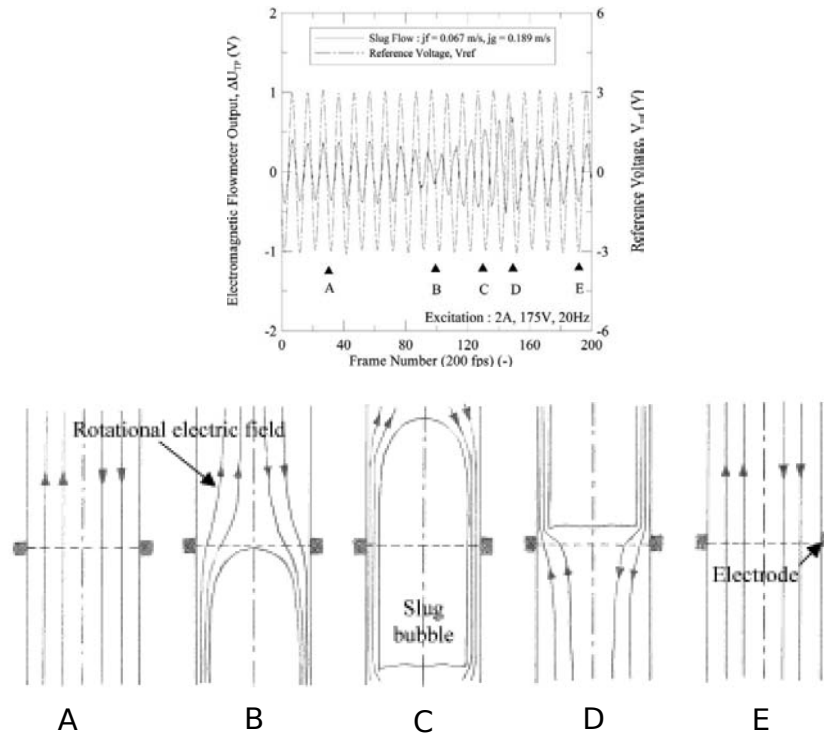


Figure 2.27: Electromagnetic flowmeter signal response to a large slug in water-air flow [18, 73].

going into electrodes. The potential difference at the electrodes comes from the flow induced eddy currents. This component is in-phase with  $V_{ref}$ . At **B**, there is a finite component of  $\vec{E}_t$  going towards the electrode faces and hence finite transformer induced electrical current goes into electrodes. In this case, transformer induced emf contributes and we notice a phase difference of  $\pi/2$  between this emf and  $V_{ref}$ . Physically, the bubble

changes the direction of  $\vec{E}_t$  lines towards electrodes. At **C**,  $\vec{E}_t$  is again parallel to the electrode faces and hence no transformer emf contributes. However, the inverted liquid mean velocity around the nose till the tail of the slug introduces a  $\pi$  phase difference between induced emf and  $V_{ref}$ . This was confirmed by the use of high speed CCD camera. At **D**, the component of  $\vec{E}_t$  towards the wall is inverted as compared to the case **B**, and hence it introduces a phase  $3\pi/2$ . Case **E** is same as case **A**.

The two-phase potential in air-water and sodium-nitrogen two-phase flow is obtained as follows: the single phase potential is

$$\Delta V_{SP} = 2BUb = \frac{2BQ_l}{\pi b} \quad (2.21)$$

where, where,  $SP$  denotes single-phase,  $b$  is the flow channel radius,  $Q_l$  is liquid flowrate and  $B$  is the magnetic flux orthogonal to mean flow velocity  $U$ . In two-phase flow the liquid flowrate  $Q_l$  and the gas flowrate  $Q_g$  are related to the total flow rate as  $Q = Q_l + Q_g$ . The void fraction is calculated as  $\alpha = Q_g/Q$ . The two-phase emf at electrodes become

$$\Delta V_{TP} = \frac{2BQ}{\pi b} = \frac{2BQ_l}{\pi b(1-\alpha)} = \frac{\Delta V_{SP}}{(1-\alpha)} \quad (2.22)$$

where,  $TP$  stands for two-phase. The increase in potential in two-phase comes from acceleration of local fluid velocity if liquid flowrate is fixed. As shown in figure 2.28, the

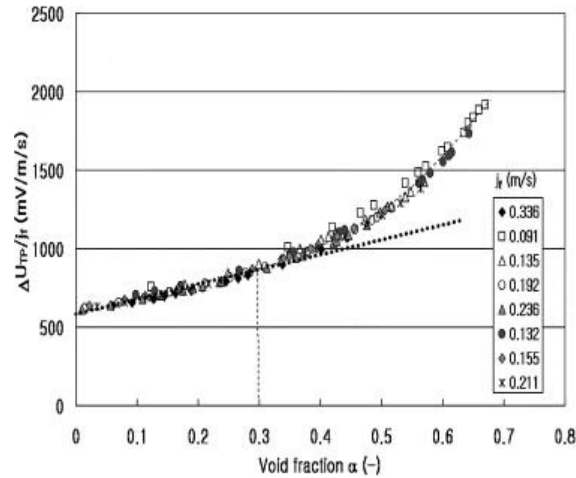


Figure 2.28: Electromagnetic flowmeter two-phase potential vs  $\alpha$  in sodium-nitrogen flow [18].

two-phase potential normalized by the sodium superficial velocity is a linear function of  $\alpha$  up to  $\alpha \lesssim 30\%$ . The information on the nitrogen bubbles can be obtained from shift in phase of the two-phase potential. Which can be used to find out the liquid flowrate.

The sensitivity (calibration) of the potential at the electrodes to mean velocity  $U$  depends on the distribution of velocity field  $u(r, \theta)$  inside the flow-channel. The question arises whether this sensitivity would change in the presence of second phase. To answer



this question, Wyatt considered three cases: (1) isotropic-uniformly dispersed second phase, (2) annular flow: gas in the core while the continuous phase in the annular region, and (3) annular flow: gas in the annular region and continuous phase in the core [74]. In all these cases he found the sensitivity to be independent of  $\alpha$ . This confirmed the results of an earlier investigation by Bernier *et al.* [75]. Wyatt also found that these results are not strictly true for non-uniform isotropic, uniform non-isotropic, non-uniform non-isotropic suspensions of dispersed phase. This is because of different sensitivity of the flowmeter to different points in the cross-section.

To correlate quantitatively the transformer induced signal with the bubble size, Krafft *et al.* modeled the influence of bubble on rotational electric field  $\vec{E}_t$ . Here, the flow induced potential was modeled similar to as shown above. The flow and transformer induced potentials were separated using a trapezoidal excitation. The flow signal is sensed in sync with the flat part of trapezoidal waveform, is corrected for the sign change in magnetic field and then averaged over one cycle. This flow signal is linear with the mean velocity of the conducting phase. The transformer signal was sensed in sync with the rising and falling regions of trapezoidal waveform. Given a time varying magnetic field, the electric field was calculated using the Faraday's law. The induced eddy currents were then determined from Ohm's law. A current dipole replaced the bubble and satisfied the boundary condition that the normal current on the bubble surface is zero. The strength of this dipole was calculated from the strength of the eddy currents at the location of the bubble in its absence. The bubbles were assumed to be spherical and of very small size as compared to flow-channel diameter. The modulation in the transformer signal due to bubble was given by  $\Delta V \sim (c/b)^3 \sim \alpha$ , where  $c$  is the bubble radius,  $b$  is the flow channel radius and  $\alpha$  is the local void fraction. For

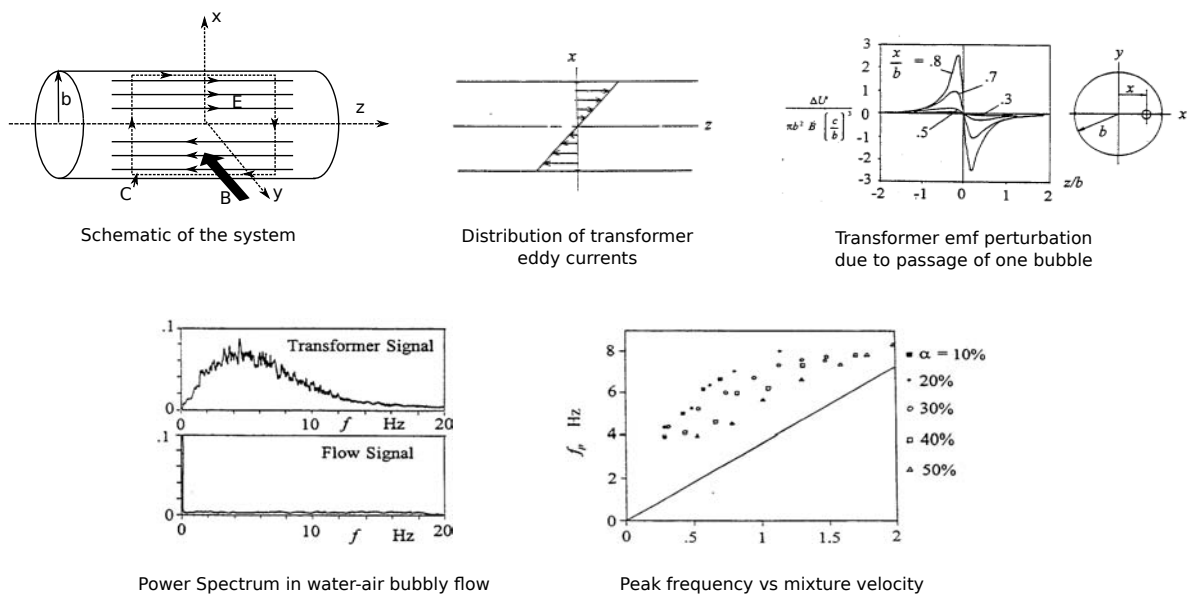


Figure 2.29: Schematic of the system and results of Krafft *et al* [40].

the passage of well separated bubbles in experiments with water-air two-phase flows, the time difference between peak maximum and minimum in the modulated transformer emf depended on the bubble velocity. For a dispersed bubbly flow, the dominant frequency in the power spectrum of the transformer emf corresponded to the bubble velocity and characteristic length scale of the system (see figure 2.29). The transformer signal due to the bubbles randomly distributed in time is modeled by a Poisson process as,

$$V(t) = \sum_{i=-\infty}^{\infty} A_i V'(t - t_i); \quad V'(t) = -A_i t e^{-\lambda|t|} \quad (2.23)$$

where,  $A$  is amplitude (function of bubble size and position) and  $1/\lambda = L/2v$  is the time period of oscillation in induced potential at electrodes due to one void,  $v$  is the bubble velocity and  $L$  is wavelength of oscillation in induced potential. In the given system,  $L = 50$  mm. The power spectrum is obtained as,

$$W(\omega) \equiv \lim_{T \rightarrow \infty} \frac{1}{T} \left| \int_{-T/2}^{T/2} V(t) e^{-i\omega t} dt \right|^2 = \mu A_{rms}^2 \frac{(2\lambda\omega)^2}{(\lambda^2 + \omega^2)^4} \quad (2.24)$$

This spectra peaks at

$$f_p = \frac{\omega}{2\pi} = \frac{\lambda}{2\pi\sqrt{3}} = \frac{v_m/L}{2\pi\sqrt{3}} = 3.68v_m \quad (2.25)$$

Assuming no-slip between the two phases, the mixture velocity  $v_m$  is same as the mean velocity  $U$  of the conducting phase. This is plotted as a solid line in power spectra plot in figure 2.29. Measured values of  $f_p$  are all above this line. This indicates that a finite slip does exist between the two phases.

**Discussions and interpretations** Poisson's equation is solved to obtain static potential measured by two electrodes in single-phase flow, which is related to induced potential in two-phase flows as  $\Delta V_{TP} = \Delta V_{SP}/(1 - \alpha)$ . Since the electromagnetic (em) flowmeters work under low pulsations, it is possible to separate flow induced potential from the bubble induced potential. There are two ways to do it: (1) by doing a phase sensitive measurement, (2) Using trapezoidal excitation in electromagnets, the average signal in sync with the flat portion of trapezoidal excitation is the flow signal while the one obtained in sync with the rising and falling portions of the trapezoidal waveform is transformer signal (bubble signal). The bubble passage time is related to the mean bubble velocity and the length scale of em flowmeter. For randomly distributed bubbles, their arrival at the electromagnetic flowmeter can be modeled as a Poisson process. The peak in the power spectrum of transformer emf in bubbly flows seems to be a linear function of  $U$ . The effect of slip ratio between the two phases seems to be significant.

However, the results of electromagnetic flowmeters might not be readily applicable to the case of ECFM in two-phase liquid metal which is based on sensing the distortion of flux through the distortion in induced eddy currents. Since, the frequencies used in ECFM is relatively high, we would have to solve for the induced magnetic fields using

the magnetic induction equation (1.6). The flow induced and bubble induced emf should be decoupled at small  $\omega$ , but at large pulsations, the flow and bubble induced emfs might not be decoupled.

### 2.4.2 Models at high pulsations

Here, we discuss the impedance change of an air-coil, excited by high pulsation ( $\omega$ ) AC currents, when it is brought closer to electrically conducting medium containing voids/heterogeneities. The Lorentz force effects are neglected. The objective is to understand  $\omega$  and  $\alpha$  effects on externally imposed magnetic flux.

The impedance of the exciting coil changes when it is brought close to the electrically conducting medium [76]. The real part of this change is related to resistive losses in the medium (power dissipation due to eddy currents in medium) while the imaginary part comes from the opposing magnetic fields of the induced eddy currents (Faraday induction effect).

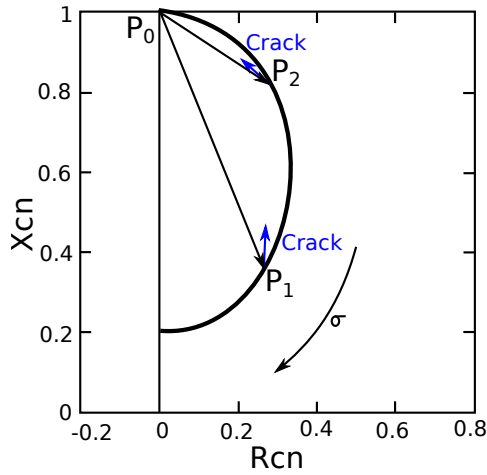


Figure 2.30: A classic normalized impedance plane curve.

Let us say that the reactance and resistance of the exciting coil in absence of electrically conducting medium is  $X_0$  and  $R_0$  respectively (point  $P_0$  in figure 2.30) Its complex impedance will be  $Z_0 = R_0 + jX_0$ . This impedance becomes  $Z_c = R_c + jX_c$  in the presence of the conducting medium. The normalized impedance changes will be  $R_{cn} = (R_c - R_0)/X_0$  and  $X_{cn} = X_c/X_0$ . Point  $P_0$  changes to point  $P_1$  and  $P_2$  when coils are close to conducting media characterized by electrical conductivity  $\sigma_1$  and  $\sigma_2$  respectively;  $\sigma_1 > \sigma_2$  [77]. The reason for this change is resistive dissipation in the medium and the opposing magnetic flux of the induced eddy currents in the medium. Notice that the resistive dissipation of the eddy currents first increases and then decreases with increasing  $\sigma$ . The reactance on the other hand keeps on decreasing till all the eddy currents are excluded from the volume of the conducting medium (super conductor). At this  $\sigma$  value, the only resistive dissipation that occurs is in the exciting coil as if it was

in the air. The total magnetic flux (external and induced) through the coil is minimal at this  $\sigma$  and thus the relative reactance is also very small. This confirms the fact that the influence of the two-phase media on in-phase and quadrature-phase signals in ECFM will be governed via skin depth  $\delta$ .

For the void effect calculations, the change in impedance  $\Delta Z$  is calculated by the difference in electromagnetic power given by the Poynting vector in the two cases: with and without the void. The use of Lorentz reciprocity theorem then reduces this problem to calculating a volume integral around the void/crack [78]. The theoretical analysis of the void interaction with the external coil depends on whether it is located at the surface or buried inside the medium.

### Void inside the medium

For the case of small voids buried inside the conducting material, the results of theoretical hydrodynamics can be used [79]. The small void is modeled as a dipole (barrier to electrical current flow), whose strength is calculated from the condition that the normal component of eddy current is zero at the void surface.

In large skin depth limit, the impedance change due to a small electrically non-conducting sphere not close to the surface was calculated by Burrows as [80]

$$\Delta Z = \frac{3}{2}\sigma\omega^2 v \left( \frac{\vec{A}_{defect}}{I_0} \right)^2 \quad (2.26)$$

where,  $\sigma$  is the electrical conductivity of the continuous medium,  $v$  is the volume of the void,  $A_{defect}$  is the magnetic vector potential at the void and  $I_0$  is the current in the exciting coil. Note that the vector potential is directly proportional to the induced eddy currents as  $\vec{J} = \sigma\vec{E} = -i\omega\sigma\vec{A}$ . The presence of a heterogeneity obstructs the path of the eddy currents, thus changing the local reactance and the resistance. The eddy current dissipation has been found to decrease while the inductive part increases with the presence of the flaw. This means that both in-phase and quadrature-phase ECFM signal will change in response to the bubbles in two-phase medium. The change in in-phase signal being governed by a increase/decrease in resistive losses while an increase in quadrature-phase signal being governed by a decrease in opposing magnetic fluxes.

Consider the case of an infinite conducting cylinder containing a flaw of arbitrary shape and size placed inside a single turn coil as shown in figure 2.31 [81]. The problem of determining the distributions of  $\vec{E}$  and  $\vec{H}$  fields is set in terms of a diffusion equation for magnetic vector potential  $\vec{A}$ :  $\nabla^2\vec{A} + k^2\vec{A} = -\mu J_0$ ; where  $k^2 = -i\omega\mu\sigma$  and  $J_0$  is the amplitude of sinusoidal current density in the external exciting coil.  $k = 0$  everywhere except in region I, while  $J_0 = 0$  everywhere except at the external coil. The approximate expression for the magnetic vector potential inside the conducting medium without the void is

$$A_\phi^I = \frac{\mu_0 I a}{\pi} \frac{I_1(\sqrt{i}\kappa r)}{\sqrt{i}\kappa b I_0(\sqrt{i}\kappa b)} \int_0^\infty \frac{K_1(\lambda a)}{K_1(\lambda b)} \cos(\lambda z) d\lambda \quad (2.27)$$

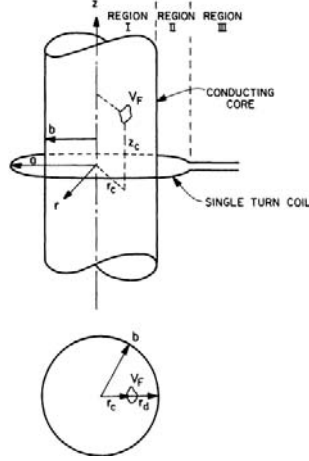


Figure 2.31: An infinite cylinder with flaw enclosed by a single turn coil [81].

where,  $I_1$  and  $K_1$  are the modified Bessel functions of order one and  $\lambda$  is the eigenvalue. Using Burrows expression (equation (2.26)), the impedance change due to small flaw can now be calculated as

$$\Delta Z \approx \frac{\sigma V_f \omega^2 \mu_0^2}{\pi^2} \left[ \frac{\sqrt{i} I_1(\sqrt{i} \kappa r)}{\kappa b I_0(\sqrt{i} \kappa r)} \right]^2 \times \left[ a \int_0^\infty \frac{K_1(\lambda a)}{K_1(\lambda b)} \cos(\lambda z) d\lambda \right]^2 \Bigg|_{r_c, z_c} = \frac{\sigma V_f \omega^2 \mu_0^2}{\pi^2} F_d F_a \quad (2.28)$$

The value of the terms in the first square bracket  $F_d$  depend on the depth of the flaw and affect both the magnitude and phase of  $\Delta Z$ . The value of the terms in the second square bracket  $F_a$  depend on axial location of the flaw with respect to the excitation coil. This term only contributes to the magnitude of  $\Delta Z$ . For flaw depths of the same order of the skin depth, the depth dependent portion of equation (2.28) (the depth factor) is given in the simplified form as

$$F_d = \frac{1}{2} \left( \frac{\delta}{b} \right)^2 \frac{b}{r_c} e^{-2r_d/\delta} e^{-j2(r_d/\delta - \pi/4)} \quad (2.29)$$

The axial location dependent term is approximated as

$$F_a = \left[ \frac{B}{B^2 + (\beta z')^2} \right]^2 \quad (2.30)$$

where,  $\beta = a/b$ ,  $z' = z_c/a$  and  $B = 0.815\beta - 0.794$ . As shown in figure 2.32, the in-phase component of the impedance change denoted as  $\text{real}(F_d)$ , first increases and then decreases as the void moves from the inner core to the outer surface ( $r_d/\delta \rightarrow 0$ ). This means that the resistive losses due to void depends on the radial location of the void in the medium. Furthermore, for larger radius (smaller  $\delta/b$ ) cylinders, the effect will decrease. This is because the eddy current "density" changes with the cylinder radius for given external magnetic flux. The effect of the presence of void inside the cylinder is

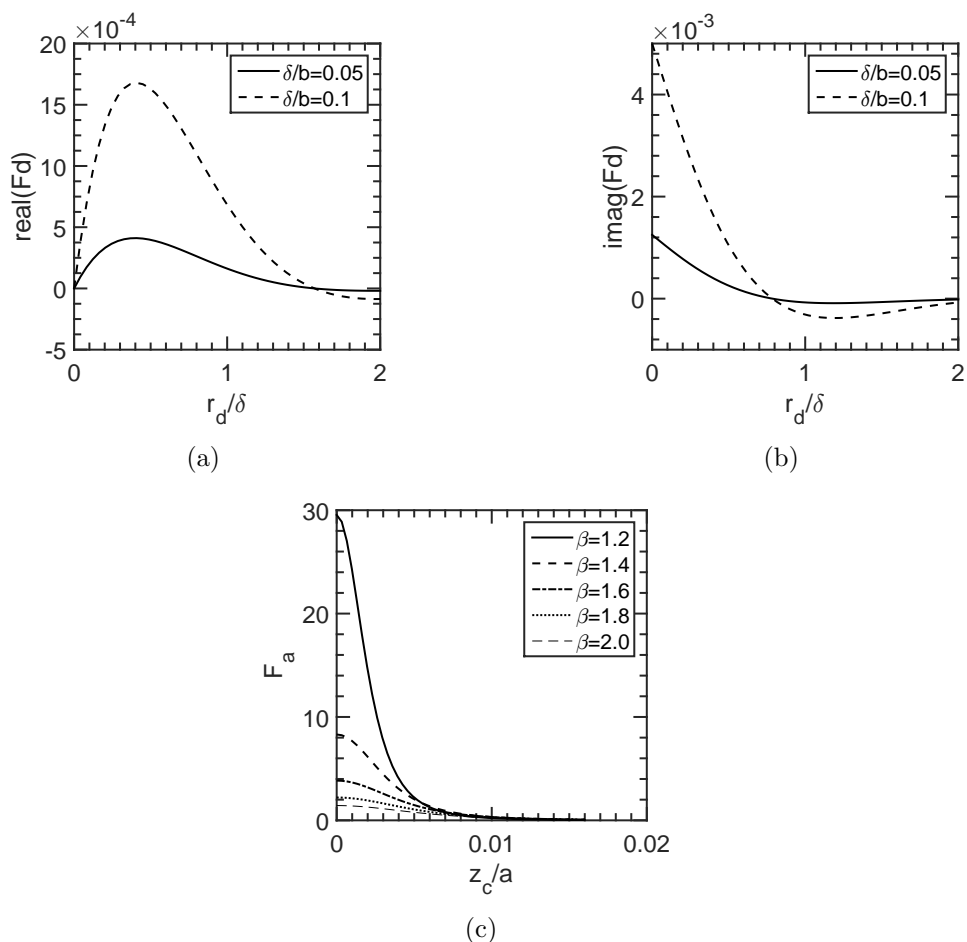


Figure 2.32: The results for the radial and axial movement of void positions: (a) In-phase  $F_d$  with normalized distance from cylinder outer surface, (b) Quadrature-phase  $F_d$  with normalized distance from cylinder outer surface and (c)  $F_a$  with normalized distance from the coil center along the axial direction;  $\delta = 2.6$  mm.

to allow more and more external magnetic flux to penetrate and hence the void increases the quadrature phase emf (denoted as  $\text{imag}(F_d)$ ) of the exciting coil towards its value in air (without conducting cylinder). This is true when the void is located near the surface and as it moves towards the outer surface ( $r_d/\delta \rightarrow 0$ ) this effect further increases. The presence of the void in the core on cylinder axis and near it is however opposite. In this case, the void pushes the induced current densities in the core towards the outer wall, thus decreasing the amount of external flux that penetrates the medium. The zero crossing point in  $\text{imag}(F_d)$  can be used to find out the radial location of the void. One can adjust the frequency in the exciting coil in such a way so as to make  $\text{imag}(F_d) = 0$ . At this frequency the radial location of the void is given by  $r_d = \pi/16\sigma\mu\nu$ . Also worth noticing is the fact that the imaginary component of  $\Delta Z$  is much larger in magnitude

than the real component. As mentioned earlier, the axial factor only influences the real part of  $\Delta Z$ . As the void approaches the coil along the coil axis, this axial factor increases and is maximum when the void is inside the coil. This fact can be utilized to determine the axial location of a void. Keeping the coil size as constant, as we decrease the cylinder radius (increase  $\beta$ ) the axial factor decreases. This is because the amount of magnetic flux passing thorough the cylinder is less and therefore the amount of induced eddy currents is less which results in weaker void effects.

In this sub-section, we saw the influence of small void buried inside the medium on the exciting coil impedance. In the following sub-section we see the effects when this void is located at the surface.

### Void at the surface

Spal *et. al.* have studied theoretically, the effect of a thin crack of depth  $d$  and of infinite extent in axial direction on an infinite electrically conducting rod of radius  $a$  as shown in figure 2.33 [82]. This cylinder is placed inside an infinite solenoid which is excited by harmonic current of type  $e^{i\omega t}$ . The results can be summarized as follows: If skin depth is large, the in-phase impedance decreases with  $d/a$  because the crack tends to inhibit the current flow and reduce the dissipation. This is analogous to dissipation in laminated cores of transformers. If skin depth is small, the in-phase signal increases with  $d/a$  and the crack tends to enhance the dissipation. This is because the crack increases the surface area thus increasing the loss. Also note that the solutions are same for  $a/\delta = 0.5$  and 0.2 which means that the effect of small skin depth starts at  $\delta \sim 2a$ . At  $\delta = 0.5a$ , the in-phase signal exhibits a non-monotonic behavior with  $d/a$ . The absolute value of the in-phase signal shows saturation characteristic with  $d/a$ . The quadrature-phase impedance increases monotonically with increasing  $d/a$  at all  $a/\delta$  and exhibits same saturation characteristics as the in-phase signal. The physical reason for this increase in quadrature component is that the crack allows more magnetic flux to enter the core and increases the inductance. Parallel argument can be made on the basis of figure 2.33 (b). Notice that for a constant  $d/a$ , as the skin depth decreases (frequency increases), the real part of the induced potential first increases and then decreases. On the other hand, the imaginary part continuously decreases. In the small skin depth limit the quadrature signal is found to increase as  $(d/a)^2$  with flaw dimensions. Therefore, if  $(d/a) \sim \mathcal{O}(1)$ , the void fraction is given by  $\alpha \sim d^2/a^2$  and the quadrature signal will be  $V_{\alpha,\perp} \sim \alpha$ .

In general, for the open surface cracks, there are three cases depending upon the ratio of the dimension of heterogeneity  $a$  and the skin depth  $\delta$ .

**Large skin depth compared to flaw dimensions (small  $a/\delta$ )** : Since the motion dependent source for eddy currents is neglected in these cases, any field quantity  $\vec{F}$  such as current density, magnetic field or electric field ( $\vec{F} = \vec{J}, \vec{B}$  or  $\vec{E}$ ) will be governed by the diffusion equation given by

$$\nabla^2 \vec{F} = i\omega\mu_0\sigma\vec{F} \quad (2.31)$$

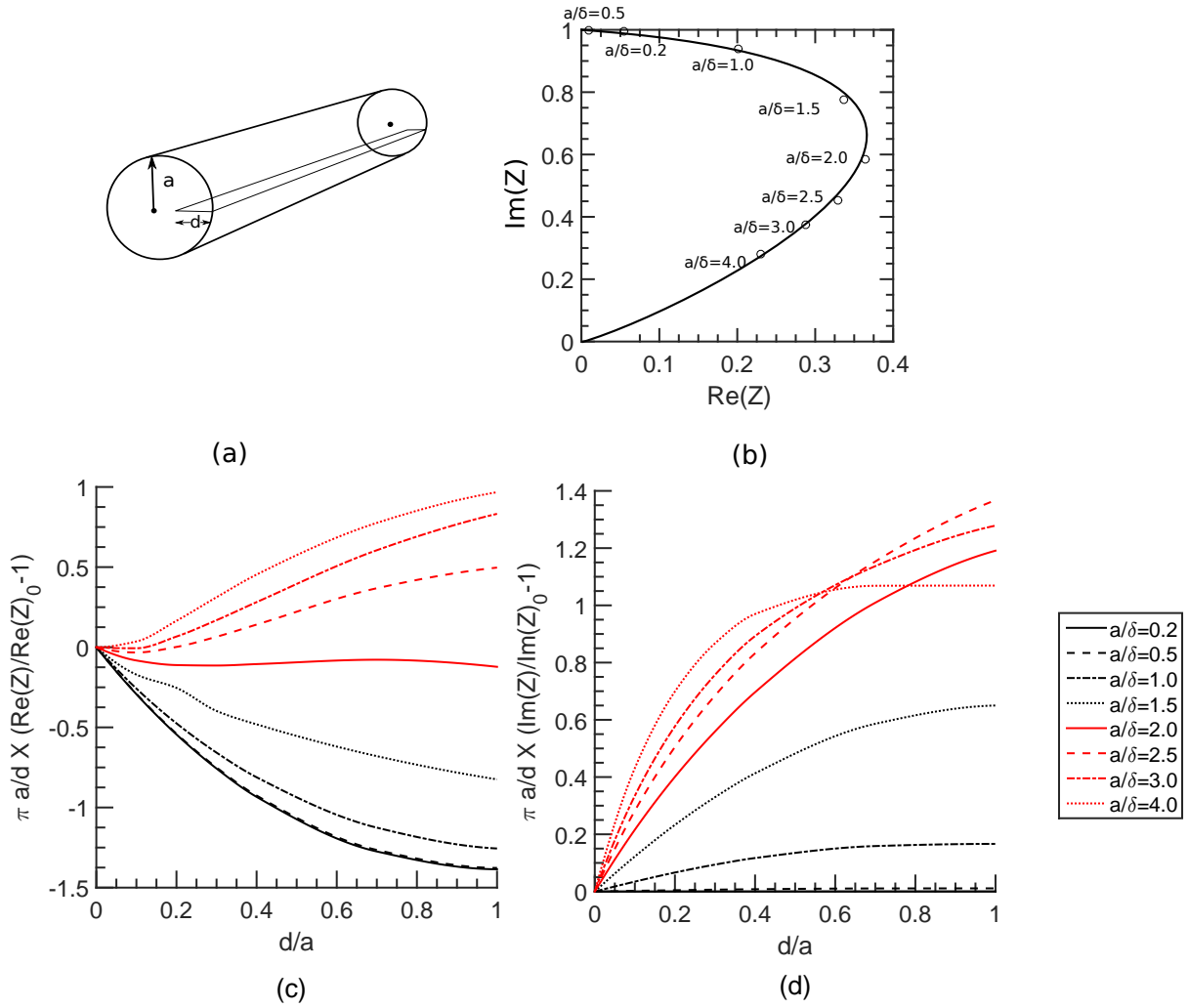


Figure 2.33: (a) An infinite conducting rod with an infinite crack placed inside a coaxial infinite length solenoid, (b)  $\text{Im}(Z)$  vs  $\text{Re}(Z)$  for  $d/a = 0.4$ , (c) non-dimensional in-phase potential, (d) non-dimensional quadrature-phase potential as a function of crack dimension.

Note that we are only concerned with small frequencies so that the dielectric currents are neglected. The term on the L.H.S. in the equation above is much larger than the term on R.H.S. which is proportional to  $\delta^{-2}$ . Therefore we can assume the right hand side to be zero (quasi-static approximation). The results from theoretical hydrodynamics for incompressible fluids can be used in this case [83]. For the case of interaction with a spherical void, solutions for flow past a rigid sphere can be used. The influence of this spherical defect on the exciting coil emf via perturbations in the eddy currents is given by the expression of Burrows (see equation 2.26).



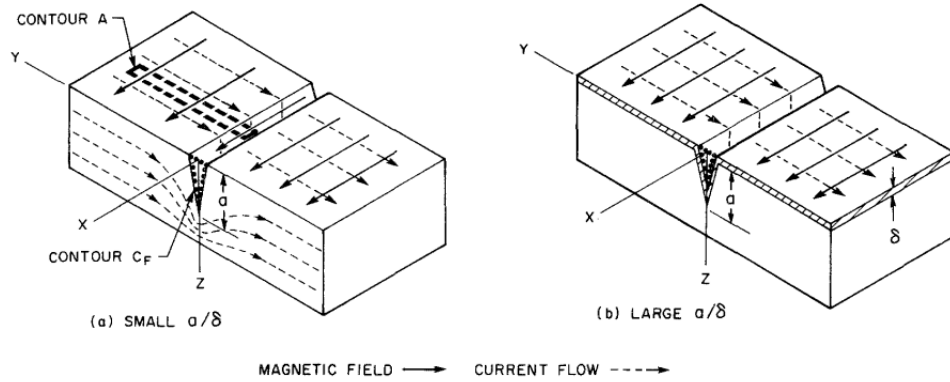


Figure 2.34: The distribution of magnetic fields and eddy currents for (a) Small  $a/\delta$ , (b) Large  $a/\delta$  [83].

**Small skin depth compared to flaw dimensions (large  $a/\delta$ )** : In this case the unperturbed magnetic fields are limited to the surface within  $\delta$  (see figure 2.34(b)). If the heterogeneity is also at the surface as in figure 2.34(b), then it is known that the eddy currents density is uniform at the two faces of the cone but non uniform at the tip and the lips. This non-uniformity extends over a distance  $\delta$ .

The thin skin theory has two extreme asymptotic limits: One described by Laplace model and the other by Born model [84]. For the geometry shown in figure 2.35, thin skin

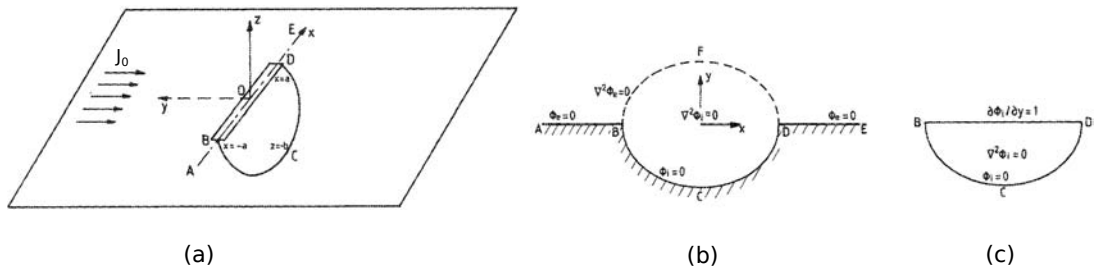


Figure 2.35: (a) A 2D elliptical surface breaking crack and a uniform incident current, (b) The electric potential in Laplace limit valid for ferromagnetic conductors, (c) The electric potential in Born limit valid for non-ferromagnetic conductors. The equations were written in non-dimensional form [84].

theory makes the hypothesis that the magnetic and electric fields at the heterogeneity vary on scale  $\mathcal{O}(l)$  in  $X$  and  $Y$  directions. In  $Z$  direction it varies on  $\mathcal{O}(l)$  and  $\mathcal{O}(\delta)$  outside and inside the conducting medium respectively. Note that for a semi-elliptical crack shown in figure 2.35,  $a$  and  $b$  are of the same order  $l$ . For the case without crack, the equations outside and inside the metal will differ. The electromagnetic fields in  $X$  and  $Y$  directions have the same behavior but along  $Z$  direction inside the metal it would follow an exponential law. Since the eddy current exists only inside the metal, the equations outside differ from the inside only by the Faraday's law. If magnetic field

$\vec{H} = \nabla\psi$ , then ( $k = i\omega\mu\sigma$ , and  $|kl| \gg 1$ )

$$\frac{\partial^2\psi}{\partial x^2} + \frac{\partial^2\psi}{\partial y^2} + \frac{\partial^2\psi}{\partial z^2} = 0 \quad \text{outside metal} \quad (2.32)$$

$$\frac{\partial^2\psi}{\partial x^2} + \frac{\partial^2\psi}{\partial y^2} + \frac{k\mu_0}{\mu} \frac{\partial\psi}{\partial z} = 0 \quad \text{inside metal} \quad (2.33)$$

The eddy currents inside the metal are obtained using equation (2.33):  $J_x = \sigma E_x \simeq -k(\partial\psi/\partial y)_{z=0}e^{kz}$ ,  $J_y \simeq \sigma E_y = -k(\partial\psi/\partial x)_{z=0}e^{kz}$  and  $J_z \simeq \sigma E_z = 0$ . Let  $m = \frac{k\mu_0}{\mu}$ . For  $m \rightarrow 0$ , equation (2.33) at  $z = 0$  inside the metal becomes,  $\frac{\partial^2\psi}{\partial x^2} + \frac{\partial^2\psi}{\partial y^2} = 0$ . This case is valid for ferromagnetic materials. This is called the Laplace model of thin skin theory. For  $m \rightarrow \infty$ , equation (2.33) at  $z = 0$  inside the metal becomes,  $\frac{\partial\psi}{\partial z} = 0$ . This case is valid for non-magnetic materials. This is called the Born model of thin skin theory. In effect the eddy currents tend to become denser at the crack tips and sparse at the corners as shown in figure 2.36 [85].

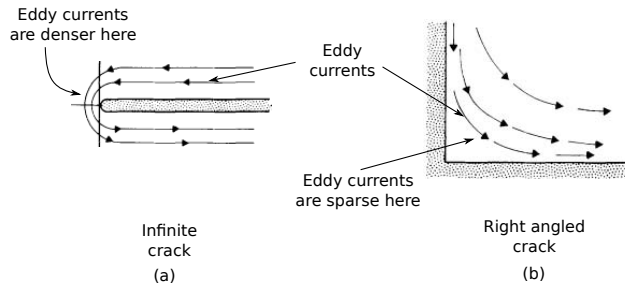


Figure 2.36: The eddy current distribution at (a) A crack tip, (b) A right angled corner [85].

**Discussions and interpretations** In this section, we assume high pulsations ( $10^4 < \omega < 10^6 \text{ rad s}^{-1}$ ) and neglect the Lorentz force effects. We find that in the absence of heterogeneities, the in-phase impedance of an external coil carrying AC current placed in the vicinity of an electrically conducting medium, first increases and then decreases as we increase the electrical conductivity of the conducting medium. This is explained in terms of resistive dissipation in the medium as a function of the skin depth. The quadrature-phase impedance keeps on decreasing till it reaches a very small value at which point no-magnetic flux penetrates the medium.

For a very small void inside a conducting cylinder, the effect of the presence of void on the exciting coil impedance depends upon the radial and axial position of the void. While the radial position of the void influences both the real and imaginary parts of this impedance change, the axial position only influence the in-phase part.

For the case of an infinite cylinder inside an infinite length solenoid, the effect of an infinite crack on its surface along the axial direction, depends on the skin depth. The effect of void size on the in-phase impedance is non-monotonic (resistive losses have

a non-monotonic behavior), while the effect on the quadrature-phase signal is always monotonic (inductance keeps on decreasing with void fraction). In general, the calculation of impedance change, when void is located on the surface depends on the skin depth. When skin depth  $\delta$  is large with respect to the crack dimensions  $a$  ( $a/\delta \ll 1$ ), the results of theoretical hydrodynamics can be used. The heterogeneity is modeled as a small dipole. The strength of this dipole is calculated by the condition that the normal eddy current at the surface of this heterogeneity is zero. For the limiting case of small skin depths ( $a/\delta \ll 1$ ), thin skin theory exists. For the case of non-ferromagnetic metal, Born approximation is valid.

For ECFM in two-phase case, if we neglect the effects of flow induced eddy currents, the change in the in-phase signal in the two secondary coils should be expected to be governed by the resistive dissipation in the two-phase media. Furthermore, the in-phase signal might be expected to be non-monotonic with bubble size. The increase in void fraction will increase the magnetic flux penetrating the medium and hence the quadrature component of the induced ECFM secondary signal will increase monotonically with  $\alpha$  at any value of  $\delta$ . If the skin depth is large with respect to flow channel radius, we can use the results from theoretical hydrodynamics to model small bubbles. The results of Burrows can be used directly 2.26. When the skin depth is small or  $\mathcal{O}(a/\delta \sim 1)$ , the analysis more complicated.

## 2.5 Conclusions and unanswered questions

For an ECFM in single phase flows, there is one component of flow signal in-phase with the current in the primary, while the other component is  $\pi/2$  out of phase (quadrature phase). The influence of the flow on in-phase signal is found to be more as compared to the quadrature-phase. So, there are two quantities of interest in an ECFM signal: r.m.s. difference voltage and the phase of this signal voltage. There exists a frequency  $\nu_c$  at which temperature induced errors in the signal  $V_2 - V_1/V_2 + V_1$  vanishes. The physical mechanism behind this phenomenon is not known. In lab experiments with ECFM, it is common to use aluminium as a model of electrically conducting liquid. This simulates a plug flow situation.

The two-phase experiments with the ECFM indicates two major features in ECFM signal: the shift (relatively very small) in average signal and modulations/oscillations over this mean. The amplitude of these oscillations increase with the void fraction. The results also suggest coupling between the flow induced signals and the void induced signals. But due to relatively small literature, it is difficult to arrive at definitive conclusions. Some more studies are needed to better understand flow-void coupling. We did not find any comprehensive theoretical model for ECFM in two-phase flows.

For very small bubbles dispersed homogeneously in conducting medium, Maxwell model can be used to calculate equivalent electrical conductivity of the two-phase medium at small  $\alpha$ . This model assumes the absence of Faraday induction and Lorentz force effects. The emf in each secondary coil of ECFM and their difference depend on this two-phase electrical conductivity as  $V \sim \sigma_\alpha^{-0.3}$ . Using the Maxwell's model for  $\sigma_\alpha$ , we

find a linear relation of  $V$  with  $\alpha$ . This predicts a change of 5% in this emf, when  $\alpha$  changes by 10%.

The literature concerning electromagnetic flowmeters, suggest the possibility of decoupling of flow induced emf from the bubble induced emf by analyzing the in-phase and quadrature phase potentials. The theoretical models for the same assume small pulsation  $\omega < 100 \text{ rad s}^{-1}$ .

If we neglect the contributions of motion induced eddy currents, the literature on induction at high frequencies but no Lorentz force can be used. The results indicate that the interaction of external coil with the medium happens via the modification in the resistive losses and the magnetic flux of the induced eddy currents. The presence of void influences the resistive losses in a non-monotonic manner while it always allows more external magnetic flux to enter the medium. The influence of  $\alpha$  on the ECFM emf should be similar. The quadrature-signal is supposed to be influenced more than the in-phase signal in the presence of bubbles for ECFM in two-phase flows.

In all these cases, the motion to void coupling in presence of AC electromagnetic fields was not studied, which needs to be understood.



## Chapter 3

# Theoretical analyses of ECFM

The objective of this chapter is to analyze theoretically the magnetic flux in ECFM in single and two-phase flows. In single-phase flows, the distribution of magnetic fields and eddy currents is studied as a function of coil lengths and radii. ECFM sensitivity to mean flow velocity  $U$  is also studied as a function of coils radii, lengths and pulsation  $\omega$  of current in the primary coil using numerical simulation. This helps us to design an ECFM for experiments. In two-phase flow, the objective is to propose theoretical approaches which help us to interpret the experimental results, in terms of  $U$ ,  $\alpha$  (the void volume fraction) and  $\omega$  effects on ECFM signals.

The theoretical models that already exist in the literature, to analyze ECFM device in single phase flows, were given in the previous chapter (chapter 2). On the other hand, we found that only experimental observations exists for ECFM in two-phase flows. There are theories that describe Faraday induction and Lorentz force effects in either very low frequency range or very high frequency range. But these are not valid for the frequencies of interest in concerned application (SFR).

For single phase flow described in section 3.1, we have taken a much simpler but approximative approach. First, we consider a 5-coils ECFM in the absence of electrically conducting medium. This allows us to calculate the distribution of externally imposed magnetic field. Then, we consider an electrically conducting medium in motion at a constant velocity  $U$  (plug flow) through the 5-coils ECFM. We calculate the first order eddy currents from the externally imposed magnetic fields. Assumption here is to neglect the magnetic fields of induced eddy currents. This is true for very small frequencies and very small  $Re_m \ll 1$ . This is similar to the theory of Baker [25]. Finally, on the basis of a numerical simulation in COMSOL<sup>TM</sup> for a 3-coils ECFM, we take into account of magnetic fields of induced eddy currents. This model allows to study pulsation dependence of flow signal in ECFM in addition to study of effects of coil parameters (coils length, coils radii etc.) on ECFM signal.

Section 3.2 enlists three theoretical models for ECFM in two-phase flows. The first model given in subsection 3.2.1, is the response of induced emf in ECFM secondary coils when the pulsation of the primary coil current is small and  $Re_m \ll 1$ . This means a very weak Faraday induction and small Lorentz force effects. The next subsection 3.2.2

presents a first order perturbation model for magnetic flux in the other regime, *i.e.*, when frequency is high but  $\text{Re}_m \ll 1$ . This means significant Faraday induction but weak Lorentz force effects. Use of the Lissajous curves of secondary coil signals gives us another method which allows us to characterize void fraction  $\alpha$ . The last section 3.3 describes the mathematical basis for this approach. We find in this last case that the parameter of interest which characterizes void fraction  $\alpha$ , is complicated to analyze mathematically, but easy to use experimentally. All the theoretical models have been developed for  $\text{Re}_m \ll 1$ . We do not consider the case  $\text{Re}_m \gtrsim 1$ . This is because for ECFM in SFR  $\text{Re}_m < 0.1$  [25].

### 3.1 Single phase flow

The objective in this section is to calculate the distribution of magnetic fields and eddy currents in the electrically conducting single-phase medium under ECFM, and to evaluate theoretically, the  $U$  sensitivity of ECFM as functions of coils length, radii and pulsation of exciting current in primary coil(s). This section is organized as follows:

We begin by a simple theoretical model of ECFM and calculate distribution of magnetic fields in the absence of electrically conducting medium.

Next, in the presence of electrically conducting medium, the first order eddy currents are calculated using Faraday's law, Ampere's law, Lorentz force law and Ohm's law. Here, the magnetic fields that result from induced eddy currents have been neglected. This simple model gives us a qualitative idea of eddy currents distribution (at first order) inside electrically conducting medium

Finally, we evaluate ECFM sensitivity to  $U$  using a numerical simulation in COMSOL<sup>®</sup>. This simulation takes into account the magnetic fields of induced eddy currents. This kind of numerical simulation was briefly discussed in the previous chapter and was also used in chapter 1 to study the Hartmann problem.

**Magnetic fields distribution of primary coils** We take an ECFM in 5-coils configuration and assume the absence of electrically conducting medium. A volumetric current density element  $\vec{J}_0$  produces magnetic field in accordance with the Biot-savart's law,

$$\vec{B}_0(\vec{r}) = \frac{\mu_0}{4\pi} \int_C \frac{\vec{J}_0 \times \vec{r} dV}{r^3}. \quad (3.1)$$

This equation can be used to obtain fields generated by primary coils. Equation (3.1) can be used to solve for the magnetic fields of a single turn current carrying coil of infinitesimal thickness and infinitesimal length. The resulting relation can be found in standard literature [86, 87]. The magnetic vector potential  $\vec{A}_0$  is defined as  $\vec{B}_0 = \nabla \times \vec{A}_0$ . The analytical expression in terms of  $\vec{A}_0$ , for a current carrying coil of finite thickness and finite length, can be obtained by integrating the corresponding relation for infinitesimal

thickness and infinitesimal length coil. We obtain the following relation for the former:

$$A_{0,\theta} = \frac{\mu_0}{4\pi} \frac{I}{L_p} \sqrt{\frac{R}{r}} \left[ \zeta k \left( \frac{k^2 + h^2 - h^2 k^2}{h^2 k^2} K(k^2) - \frac{1}{k^2} E(k^2) + \frac{h^2 - 1}{h^2} \Pi(h^2, k^2) \right) \right]_{\zeta_-}^{\zeta_+}. \quad (3.2)$$

Magnetic vector potential orients itself along azimuthal direction since the current in the primary coil is azimuthally oriented. Magnetic flux density can be obtained by differentiating equation (3.2). The radial component of  $\vec{B}_0$  is:

$$B_{0,r} = \frac{\mu_0}{4\pi} \frac{I}{L_p} \sqrt{\frac{R}{r}} \left[ \left( \frac{k^2 - 2}{k} K(k^2) + \frac{2}{k} E(k^2) \right) \right]_{\zeta_-}^{\zeta_+}. \quad (3.3)$$

The axial component of  $B_0$  is:

$$B_{0,z} = -\frac{\mu_0}{4\pi} \frac{I}{2L_p} \sqrt{\frac{1}{Rr}} \left[ \zeta k \left( K(k^2) + \frac{R-r}{R+r} \Pi(h^2, k^2) \right) \right]_{\zeta_-}^{\zeta_+} \quad (3.4)$$

$$h^2 = \frac{4Rr}{(R+r)^2}, \quad k^2 = \frac{4Rr}{(R+r)^2 + \zeta^2}$$

$$\zeta_{\pm} = z \mp \frac{L_p}{2},$$

where,  $R$  and  $L_p$  are the radius and the length of the primary coil respectively,  $r$  and  $z$  are the radial and axial coordinates respectively,  $I$  is the current magnitude in the primary coil and  $E$ ,  $K$  and  $\Pi$  are complete elliptic integral of first, second and third kind respectively.

The ECFM assembly is a combination of coils placed axially on a common axis. As an example, we show here the magnetic fields of a 5-coil ECFM (see figure 3.1). In a 5-coils ECFM, there are three primary coils, where each alternative primary coil is separated by a secondary coil (as shown in figure 2.3). The radii of all the coils (primary and secondary) is  $R$ , while  $L_p$  and  $L_s$  are length of the primary and the secondary coils respectively. The two primary coils on the extremity, create magnetic fields in opposition to the central primary coil. The total magnetic field can be calculated by superposition of magnetic fields created by each primary coil.

Figure 3.1 shows the contour plot for the distribution of radial magnetic flux density  $B_{0,r}$  inside secondary coil  $S_1$  of a 5-coils ECFM. We recall that the electrically conducting single-phase medium is absent in this model. The interest in the radial magnetic field arises from the need to understand the sensitivity distribution of flow signal inside flow channel [19]. Due to low magnetic fields on axis as compared to the flow channel wall, a small perturbation inside the core will produce very small effect on flow signal as compared to the flow signal response to a perturbation near flow channel wall. This was pointed out by Shercliff and other researchers for electromagnetic flowmeters [19]. For electromagnetic flowmeters, concepts of weight function and weight vector have been defined which map the sensitivity of electromagnetic flowmeter to various points inside



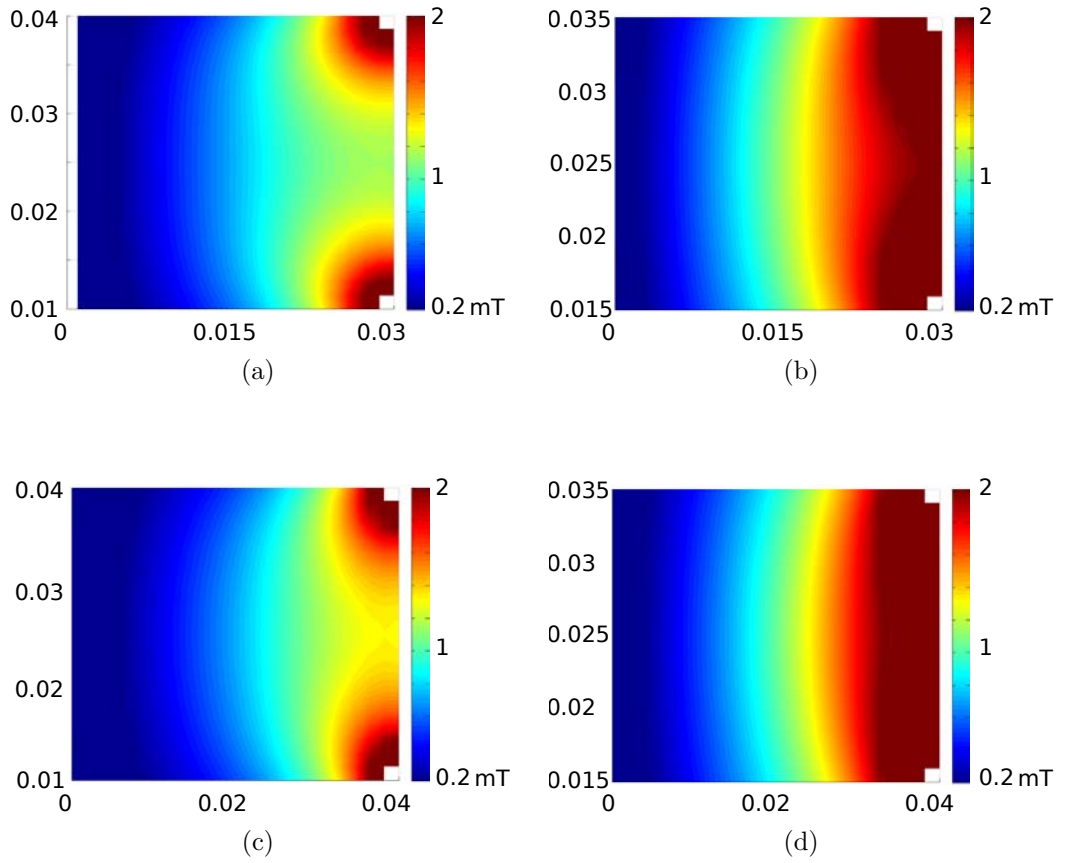
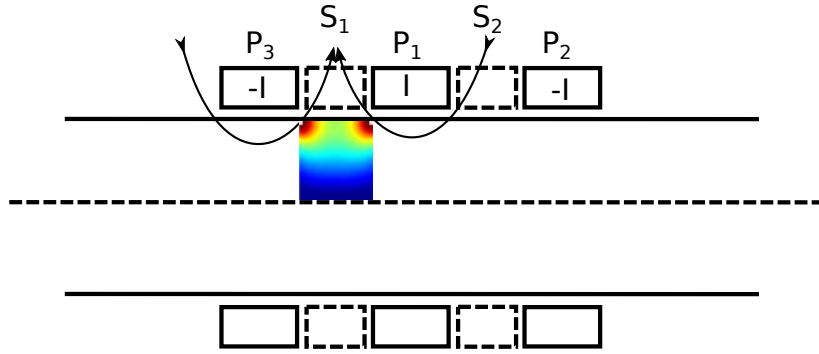


Figure 3.1:  $B_r$  (mT) within the secondary coil (isovalues) for (a)  $R = 3$  cm,  $L_p = 2$  cm,  $L_s = 3$  cm, (b)  $R = 3$  cm,  $L_p = 3$  cm,  $L_s = 2$  cm, (c)  $R = 4$  cm,  $L_p = 2$  cm,  $L_s = 3$  cm, (d)  $R = 4$  cm,  $L_p = 3$  cm,  $L_s = 2$  cm.

the flow volume. In figure 3.1, the distribution of the magnetic fields changes as a function of  $L_s$ ,  $L_p$  and  $R$ . We observe that the radial fields are concentrated at either ends of each primary coil. The use of two primary coils carrying equal and opposite currents increases the density of radial fields inside a secondary coils. This is evidenced when we decrease  $L_s$  from figures 3.1a and 3.1c compared to figures 3.1b and 3.1d. Since the radial fields decrease in magnitude from periphery towards the flow channel core, an increase in concentration of  $B_{0,r}$  is observed when we decrease  $R$ . This is seen in figures 3.1c and 3.1d compared to figures 3.1a and 3.1b. An increase in the length of the primary coils decreases current density and thus the decreases the strength of the magnetic fields. We observe relatively weaker magnetic field strength in figures 3.1b and 3.1d compared to figures 3.1a and 3.1c. Unfortunately, this effect is masked by increase in field concentration due to decrease in  $L_s$ .

**Eddy currents distribution in single-phase electrically conducting medium in motion** We introduce a single-phase electrically conducting medium in motion with velocity  $U$  in the axial direction (plug flow) under combined AC field  $\vec{B}_0(t) = B_0 \cos \omega t$  created by coils  $P_1$ ,  $P_2$  and  $P_3$ . To obtain total radial and axial magnetic fields, we superpose the fields created by  $P_1$ ,  $P_2$  and  $P_3$  using equations (3.3) and (3.4). We limit our calculation to first order, *i.e.*, we do not consider the effect of magnetic fields created by induced eddy currents on externally imposed AC magnetic field. In the conducting medium, under external AC magnetic field, eddy currents can be calculated using the ohm's law as,

$$\vec{J} = \sigma(\vec{E} + \vec{U} \times \vec{B}_0), \quad (3.5)$$

where,  $\sigma$  is the electrical conductivity of the medium.

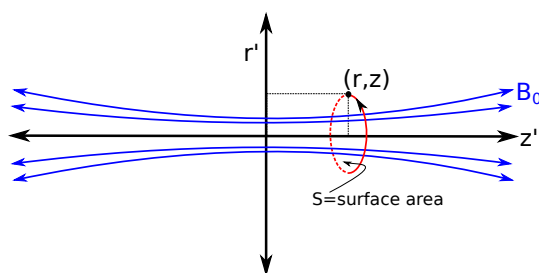


Figure 3.2: Geometry for calculation of eddy currents distribution at first order.

In equation (3.5),  $\vec{E}$  comes from time varying nature of magnetic flux. Electric field at point  $(r, z)$  (see figure 3.2) in the medium is equal to the time rate of change of axial

magnetic field given by the Maxwell-Faraday law as:

$$\begin{aligned}\nabla \times \vec{E} &= -\frac{\partial \vec{B}_0}{\partial t}, \\ \int_s \nabla \times \vec{E} \cdot d\vec{S} &= -j\omega \int_s \vec{B}_0 \cdot d\vec{S}, \\ \Rightarrow E_\theta(r, z) &= \frac{-j\omega \int_0^r r' B_{0,z}(r', z) dr'}{r}.\end{aligned}\quad (3.6)$$

It is easy to verify that the electric fields and hence the eddy currents are oriented along azimuthal ( $\theta$ ) direction. The transformer induced eddy currents density at first order become,

$$J_t(r, z) = \sigma E_\theta(r, z) = \frac{-j\omega\sigma \int_0^r r' B_{0,z}(r', z) dr'}{r}.\quad (3.7)$$

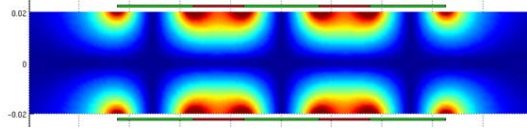
The term  $\vec{U} \times \vec{B}_0$  in equation (3.5) comes from the interaction of moving medium with the applied external radial magnetic fields ( $B_{0,r}$ ) governed by the Lorentz force law. At low  $Re_m$ , flow induced eddy currents density can be obtained as:

$$J_f(r, z) = \sigma U B_{0,r}(r, z),\quad (3.8)$$

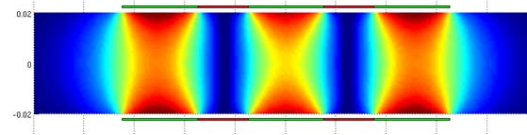
where,  $U$  is given uniform velocity along axial direction. Notice that the total eddy current  $\vec{J} = \vec{J}_f + \vec{J}_t$  is complex (from equations (3.7) and (3.8)). The complex notation, as we recall, represents the fact that these quantities are out of phase in time by a specified amount. For example,  $J_t$  lags behind  $J_f$  by  $t = \pi/2/\omega = 0.25$  ms at pulsation  $\omega = 6284$  Hz. Figure 3.3 shows the distribution of the applied external fields and the induced current densities in the medium to first order. The radii of the coils and the flow cross-section were  $R = 2$  cm each, the length of the primary coils is  $L_p = 3$  cm and the same for secondary coils is  $L_s = 2$  cm. The electrical conductivity is  $5 \times 10^5$  S m<sup>-1</sup>, value representative of sodium. The pulsation of current excitation is 3142 rad s<sup>-1</sup>. Number of turns in the primary and secondary coils is respectively,  $N_p = 150$  and  $N_s = 100$ . Even with this simple modeling we notice several features of an ECFM 5-coils system. First of all the induced magnetic flux density decreases from the periphery of the flow cross-section to the core of the flow. Its radial component is concentrated at the junction of primary and secondary coil (figure 3.3a). As a consequence, the flow induced eddy currents are also localized close to each end of the primary coil (see figure 3.3d). The direction of these eddy currents, however, is different at the two ends (clockwise vs counter-clockwise around cylinder axis). For a 3-coils ECFM, these eddy currents increase/decrease the magnetic flux through the two secondary coils and the difference of induced emf in the two coils is proportional to flow rate at low  $Re_m$ . As we infer from the results, the advantage of a 5-coils system is that it increases the concentration of radial magnetic fields and thus increases sensitivity of ECFM to flow. On the other hand, a 3-coils ECFM is smaller and relatively simpler to analyze. Another advantage, which was not presented in the results, is that an ECFM in a 3-coils configuration operates in difference mode (difference pf emf in two secondary coils). Thus if the two secondary coils are exactly identical and placed symmetrically at either end of a primary coil, they

automatically cancel out noise from external sources. In view of these advantages, we chose to analyze ECFM in 3-coils configuration in the next section.

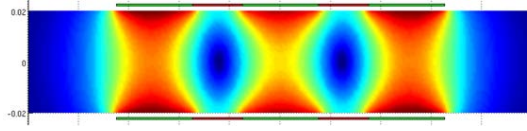
The axial magnetic flux  $B_z$ , is concentrated mostly inside the primary coils (see figure 3.3b). The corresponding effect on transformer induced eddy currents is shown in figure 3.3e. The distribution of rms current density, as shown in figure 3.3f, is inhomogeneous in radial direction. The bubbles in the flow will perturb the eddy currents which is sensed by the secondary coils. Since the strength of eddy currents close to the wall is strongest, the same bubbles passing through the periphery of flow cross-section will produce higher perturbation in ECFM secondary signal than the one passing through the core. This will be even more severe in the presence of skin effect. Skin effect is the phenomenon in which the magnetic flux of induced eddy currents in the medium will tend to exclude from the medium the externally imposed time varying magnetic flux. This effect tends to limit the penetration depth of the magnetic fields in the medium. We did not consider this effect in our first order model.



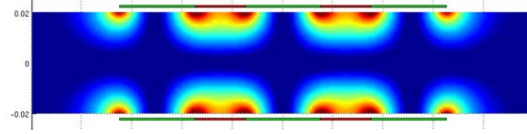
(a) The distribution of radial magnetic field (imposed) in the electrically conducting liquid (iso-value). The color scale is in Tesla. The magnitude of radial magnetic field varies from 0.1 to 1 mT.



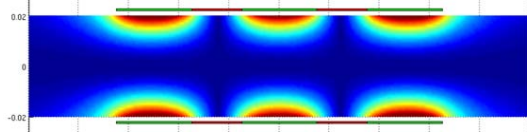
(b) The distribution of axial magnetic field (imposed) in the electrically conducting liquid (iso-value). The color scale is in Tesla. The magnitude of axial magnetic field varies from 0.5 to 2.2 mT.



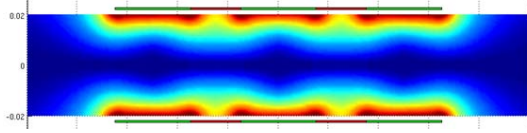
(c) The distribution of norm of magnetic field (imposed) in the electrically conducting liquid (iso-value). The color scale is in Tesla. The magnitude of total magnetic field varies from 0.1 to 2.2 mT.



(d) The distribution of flow-induced current density  $\vec{J}_f$  in the electrically conducting liquid (iso-value). The color scale is in  $\text{A}/\text{m}^2$ . The magnitude of flow-induced current density varies from 500 to 5000  $\text{A}/\text{m}^2$ .



(e) The distribution of current density induced in the electrically conducting liquid due to changing magnetic fields in the medium (iso-value). The color scale is in  $\text{A}/\text{m}^2$ . The magnitude of current density varies from 500 to 5000  $\text{A}/\text{m}^2$ .



(f) The distribution of total (RMS) current density in the electrically conducting liquid (iso-value). The color scale is in  $\text{A}/\text{m}^2$ . The magnitude of total current density varies from 1000 to 6000  $\text{A}/\text{m}^2$ .

Figure 3.3: The distribution of the magnetic fields and current densities for the selected 5-coils ECFM,  $L_p = 30$  mm,  $L_s = 20$  mm,  $R = 20$  mm. Shown in red: Secondary coil, in green: Primary coils.

**Numerical simulation in COMSOL<sup>®</sup>** To include skin effect one has to solve the induction equation (1.6). A Finite Element Simulation of the problem was realized using COMSOL<sup>®</sup> simulation software with Magnetic Fields physics in Frequency domain. The geometry is shown in figure 3.4. The equation solved is the advection - diffusion of the magnetic vector potential  $\mathbf{A}$ :

$$\nabla^2 \mathbf{A} - \mu\sigma(\mathbf{U} \times (\nabla \times \mathbf{A})) + j\omega\sigma \mathbf{A} = \mu_0 \mathbf{J}^e. \quad (3.9)$$

$\mathbf{J}^e$  represents the externally applied current density and it is non-zero only in the domain which represents the primary coil. Due to symmetry about the flow channel axis, the applied current density  $\mathbf{J}^e$  is azimuthal, the problem is 2D axisymmetric and we need to solve for only one component of the magnetic vector potential:

$$\mathbf{A} = A(r, z) \hat{\mathbf{e}}_\theta. \quad (3.10)$$

Magnetic insulation condition is used at the edges of the computational domain. It consists in prescribing all the components of magnetic vector potential as zero on these edges. Grid size independence was verified by using three different mesh size settings: finer, extra fine and extremely fine respectively. Minimum mesh size varies at edges, boundaries and interfaces (upto  $10^{-2}$  mm). With the help of this numerical simulation,

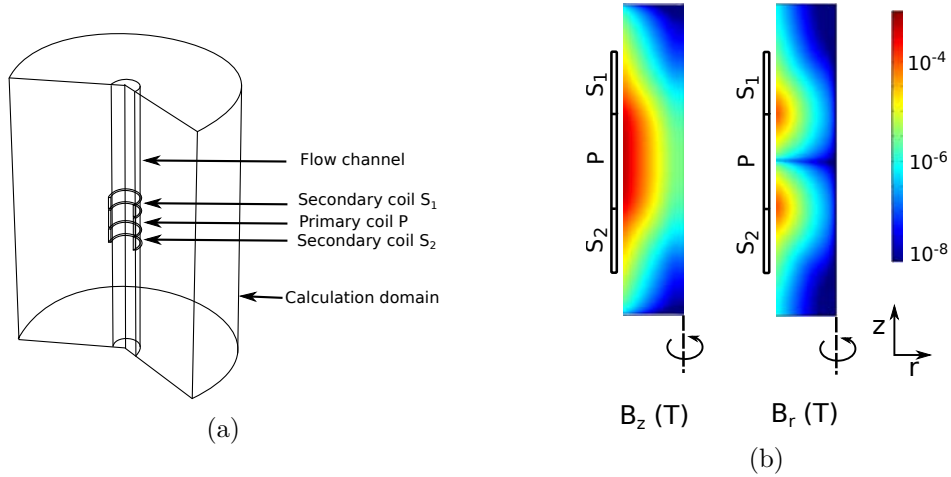


Figure 3.4: (a) The geometry of the numerical simulation. (b) Distribution of axial and radial magnetic flux density inside the flow channel on logarithmic color scale at  $I = 250$  mA,  $\omega = 6284 \text{ rad s}^{-1}$  and  $U = 0$  m/s.

it is possible to study the effect of various coil parameters. In all the results shown henceforth in this section, the AC current in the primary coil is  $I = 1$  A. The electrical conductivity of the medium is taken as  $\sigma = 3.77 \times 10^7 \text{ S m}^{-1}$ , representative of Aluminium. Magnetic permeability is  $\mu_0 = 4\pi \times 10^{-7} \text{ H m}^{-1}$ .

Figure 3.5 shows the effect of changing the radius of flow channel  $R_f$  at velocity  $U = 1 \text{ m s}^{-1}$ , primary current pulsation  $\omega = 3142, 12566 \text{ rad s}^{-1}$ . It is assumed that

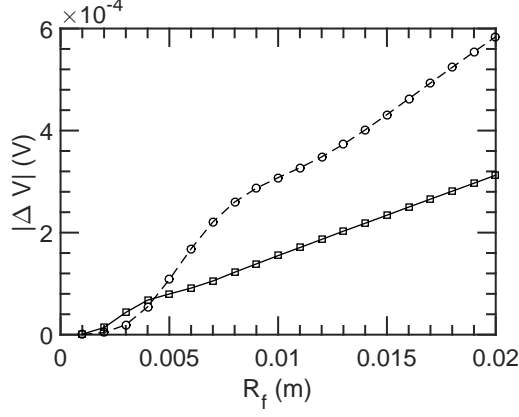


Figure 3.5:  $|\Delta V|$  vs  $R$  at  $U = 1 \text{ m s}^{-1}$ ,  $\omega = 3142$  ( $\circ$ ),  $12566$  ( $\square$ )  $\text{rad s}^{-1}$ .

$R_p = R_f + 0.75 \text{ mm} = R_s$ ; where  $R_p$  and  $R_s$  are the radii of primary and secondary coils respectively. Length of the primary and secondary coils are coil  $L_p = 30 \text{ mm}$  and  $L_s = 20 \text{ mm}$  respectively. The number of turns in primary coil ( $N_p$ ) and secondary coil ( $N_s$ ) are  $N_p = 70$  and  $N_s = 50$  respectively. We denote the difference of induced emfs in secondary coil  $S_2$  and  $S_1$  as  $|\Delta V|$ .

We notice an almost linearly increasing trend in difference voltage  $|\Delta V|$  with increasing  $R_f$ . This is consistent with equation (2.5). Furthermore, we observe that the slope of  $|\Delta V|$  vs  $R_f$  curve is steeper between  $R_f = \delta$  and  $2\delta$  for both values of  $\omega$ .  $\delta = 3.7$  and  $2.6 \text{ mm}$  respectively for  $\omega = 3142$  and  $6248 \text{ rad s}^{-1}$ .  $|\Delta V|$  decreases with  $\omega$ . We conclude that increasing  $R_f$  will increase sensitivity to  $U$ .

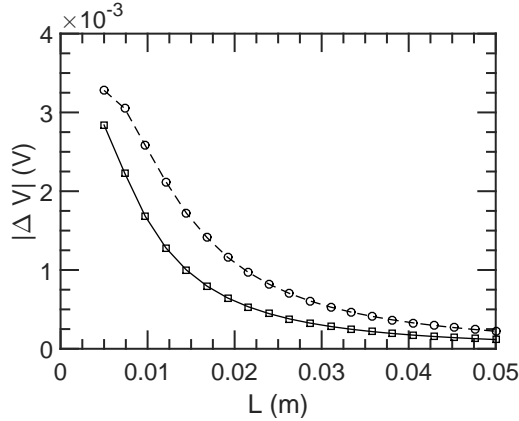


Figure 3.6:  $|\Delta V|$  vs  $L$  at  $U = 1 \text{ m s}^{-1}$ ,  $\omega = 3142$  ( $\circ$ ),  $12566$  ( $\square$ )  $\text{rad s}^{-1}$ .

Figure 3.6 shows the effect of changing the length of the three coils simultaneously, keeping the number of turns of wires in each coils as constant:  $N_p = 70$ ,  $N_s = 50$ .  $U = 1 \text{ m s}^{-1}$ , primary current pulsation  $\omega = 3142, 12566 \text{ rad s}^{-1}$  and  $R_f = 19.25 \text{ mm}$ ,  $R_p = R_s = 20 \text{ mm}$ . We assume that  $L = L_p = L_s$ . We notice a power law  $|\Delta V| \sim L^{-1}$

with increasing  $L$ . This is consistent with the classic result for total magnetic flux inside a solenoid, which is linear in number of turns per unit length. Again  $|\Delta V|$  decreases with  $\omega$ . We conclude that increasing  $L$  without increasing  $N_p$  and  $N_s$  would result in a decrease in sensitivity to  $U$ .

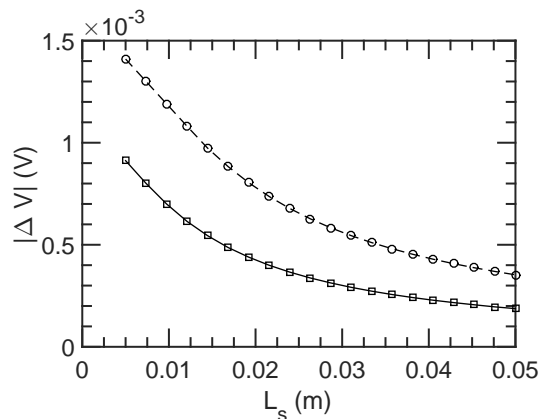


Figure 3.7:  $|\Delta V|$  vs  $L_s$  at  $U = 1 \text{ m s}^{-1}$ ,  $\omega = 3142$  ( $\circ$ ),  $12566$  ( $\square$ )  $\text{rad s}^{-1}$ .

Figure 3.7 shows the effect of changing  $L_s$ , keeping  $L_p$  constant and  $N_p = 70$ ,  $N_s = 50$ .  $U = 1 \text{ m s}^{-1}$ , primary current pulsation  $\omega = 3142, 12566 \text{ rad s}^{-1}$  and  $R_f = 19.25 \text{ mm}$ ,  $R_p = R_s = 20 \text{ mm}$ . We notice again a power law  $|\Delta V| \sim L^{-1}$  with increasing  $L_s$ . This can be again explained in terms of number density of turns. We conclude that increasing  $L_s$  without increasing  $N_s$  would result in a decrease in sensitivity to  $U$ .

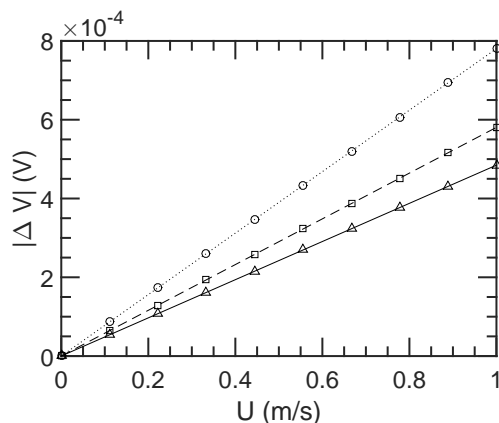


Figure 3.8:  $|\Delta V|$  vs  $U$  at  $\omega = 3142$  ( $\circ$ ),  $6283$  ( $\square$ ) and  $9425 \text{ rad s}^{-1}$  ( $\triangle$ ).

Figure 3.8 shows the effect of changing  $U$  at  $L_p = 30 \text{ mm}$ ,  $L_s = 20 \text{ mm}$ ,  $N_p = 70$ ,  $N_s = 50$ .  $U = 1 \text{ m s}^{-1}$ ,  $\omega = 3142, 6283$  and  $9425 \text{ rad s}^{-1}$  and  $R_f = 19.25 \text{ mm}$ ,  $R_p = R_s = 20 \text{ mm}$ .

$|\Delta V| \sim U^1$  with increasing  $U$ . This linearity is consistent with the literature. We also note that  $|\Delta V|$  sensitivity to  $U$  decreases with  $\omega$ .



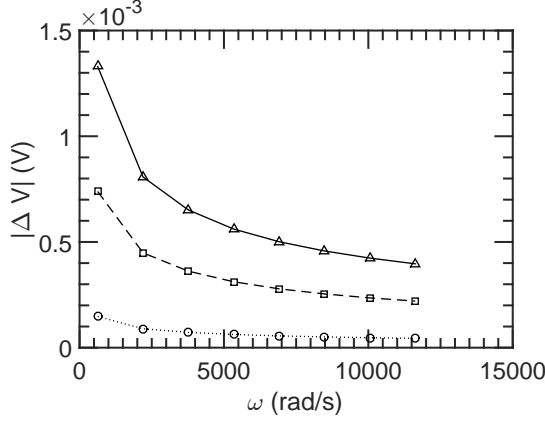


Figure 3.9:  $|\Delta V|$  vs  $\omega$  at  $U = 0.1$  ( $\circ$ ),  $0.5$  ( $\square$ ) and  $0.9$  ( $\triangle$ )  $\text{m s}^{-1}$ .

Figure 3.9 shows the effect of changing  $\omega$  at  $L_p = 30$  mm,  $L_s = 20$  mm,  $N_p = 70$ ,  $N_s = 50$ .  $U = 0.1, 0.5$  and  $0.9 \text{ m s}^{-1}$  and  $R_f = 19.25$  mm,  $R_p = R_s = 20$  mm.

$|\Delta V|$  follows a power law in  $\omega$  :  $|\Delta V| \sim \omega^{-0.5} \sim \delta$ . This is consistent with equation (2.5). The increase in pulsation, decreases the penetration depth  $\delta$  of the magnetic fields. Less  $\delta$  means a decrease in flow flux coupling.

## 3.2 Two-phase flow

In the previous section, we analyzed ECFM in single phase flows. We find that, the external excitation current in the primary coil creates eddy currents in the medium. These eddy currents are governed by Faraday induction and Lorentz force law. The total magnetic flux in a 3-coils ECFM in the presence of current in the primary and the eddy currents may now be written as,

$$\phi = \int \vec{B} \cdot d\vec{s}.$$

In two-phase flow, the eddy currents are affected by the presence of void. Therefore, we expect distortion in the total magnetic flux  $\phi$ , due to velocity  $U$  (governed by Lorentz force law), pulsation  $\omega$  (governed by Faraday induction law) and the voids (given by void volume fraction,  $\alpha$ ). Their effect on  $\phi$  and other electromagnetic field quantities are coupled.

From the literature review presented in the previous chapter, we find different approaches to model the  $\alpha$  and velocity effects on the magnetic flux. The model of Maxwell is valid for a dilute suspension of small spheres in a continuous medium. Besides small void fraction assumption, there are no Faraday induction and Lorentz force effects in Maxwell's model. The equivalent electrical conductivity of this static two-phase medium at small  $\alpha$ , is then calculated based on multipolar expansion of the electrical potential of small spheres diluted in the continuous medium.

Theoretical models at high frequencies are based on the Lorentz reciprocity theorem. We obtain integral expressions for void effect in terms of magnetic vector potential. These expressions are expanded to arrive at analytical relations for change in impedance corresponding to the presence of void. We found in the previous chapter, the calculations for the perturbation in impedance due to a single small defect in a conducting medium. This was given by the expression of Burrows, equation (2.26). Using very small skin depth assumption, it was possible to calculate the impedance change for the AC field produced by a single turn coil in cylindrical conducting medium containing small spherical void. Calculations for some other geometries were also shown. These results are only valid for small skin depths and do not allow to predict the perturbation in magnetic flux due to distribution of voids in the core of a conducting flow.

Models without induction effects, generally come from works on electromagnetic flowmeters. For single phase conducting flow in a circular cylinder at constant or very slowly varying magnetic fields (*i.e.*  $\omega \leq 100 \text{ rad s}^{-1}$ ), the electrical potential is given by a Poisson equation:  $\nabla^2 V = \nabla \cdot (\vec{U} \times \vec{B})$ . For the two-phase flows, the solution of this equation, for axisymmetric distribution of velocity and voids (homogeneous bubbly or annular flow) can be solved. The expression for electrical potential difference, in two-phase flows, between two electrodes is  $V \sim 1/(1 - \alpha)$ . We also found that  $\alpha$  is generally defined as the relative flow rate of gas and not as the real volumic fraction, which is difficult to measure experimentally in liquid metal.

The objective of this section is to propose theoretical models which help to interpret the distortion in  $\phi$  due to velocity  $U$ , void fraction  $\alpha$  and pulsation  $\omega$  in experiments with a 3-coils ECFM. In subsection 3.2.1, we present a model valid for large penetration depths,  $\delta \gg D$  and magnetic Reynolds number  $\text{Re}_m \ll 1$ .  $D$  is the flow channel diameter, and  $\text{Re}_m$  is defined as,  $\text{Re}_m = \sigma \mu_0 U \delta$ . In subsection 3.2.2, we propose a magnetic flux perturbation model valid for  $\delta \ll D$ .

### 3.2.1 Small Faraday and small Lorentz force effects

$$(\delta \gg D, \text{Re}_m \ll 1)$$

In this case it is possible to decouple the Faraday and the Lorentz term. The current in the primary coil  $I = I_0 \cos \omega t$  produces magnetic field  $B_0(t) = B_0 \cos \omega t$  in the medium in accordance with the Biot-Savart's law (see figure 3.10).

$$B_0(t) = \frac{\mu_0}{4\pi} \oint \frac{I_0(t) d\vec{l} \times \vec{r}}{|\vec{r}|^3}.$$

We denote the corresponding direct flux as  $A$ , given by

$$A \cos \omega t = \int_S B_0 dS \cos \omega t. \quad (3.11)$$

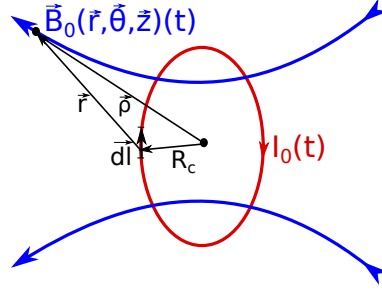


Figure 3.10: Biot Savart's law.

**Only Faraday induction, no Lorentz force effects** We assume  $U = 0$ . In this case, the time varying direct magnetic field creates an electric field given by

$$\nabla \times \vec{E}_1 = -\frac{\partial \vec{B}_0(t)}{\partial t}. \quad (3.12)$$

which in turn generates Faraday induction eddy currents,

$$\vec{J}_t = \sigma \vec{E}_1. \quad (3.13)$$

These eddy currents produce their own magnetic fields given by,

$$\nabla \times \vec{B}_1 = \mu \vec{J}_t. \quad (3.14)$$

Let us non-dimensionalise the first order fields in terms of zero-order fields.

$$\vec{B}^* = \frac{\vec{B}}{B_0}, \quad r^* = \frac{r}{D}, \quad t^* = t\omega, \quad \vec{E}^* = \frac{\vec{E}}{E_0}, \quad \vec{J}^* = \frac{D^2}{I_0} \vec{J}, \quad \vec{U}^* = \frac{\vec{U}}{U},$$

where,  $I_0$  is the magnitude of current in the primary coil and is taken as the characteristic current,  $\tau = 1/\omega$  is the pulsation of current in primary coil and is taken as the characteristic time scale,  $D$  is the diameter of flow channel and is taken as the characteristic length scale and  $\vec{U}$  is the flow velocity. The characteristic velocity  $U$  is equal to uniform flow velocity of two phase medium. It can now be readily deduced that

$$B_1 \sim \mu\sigma\omega D^2 B_0 \sim \left(\frac{D}{\delta}\right)^2 B_0.$$

In a similar way,  $B_1$  will again induce Faraday induction eddy which would create second order magnetic field  $B'_1$ , which would subsequently create  $B''_1$  and so on. The net magnetic field in the presence of only Faraday induction effects (absence of Lorentz force effects) can be written as

$$B = B_0 + B_1 + B'_1 + B''_1 + \dots = B_0 \left[ 1 + \left(\frac{D}{\delta}\right)^2 + \left(\frac{D}{\delta}\right)^4 + \dots \right]. \quad (3.15)$$

If  $D \ll \delta$ , we can truncate the series in above equation to the first perturbation term ( $B_1$ ). Using  $B_1(t) = B_1 \sin \omega t$ , the corresponding magnetic flux is obtained as

$$a\omega \sin \omega t = \int_S B_1 dS \sin \omega t,$$

where,  $a\omega$  is magnetic flux of Faraday induction induced eddy currents.

**No Faraday induction, only Lorentz force effects** Now let us assume that Faraday induction is absent and we calculate the effects of Lorentz force under externally imposed magnetic field  $B_0 \cos \omega t$ . The contribution of the flow induced eddy current is

$$\vec{J}_f = \sigma \vec{U} \times \vec{B}_0.$$

These flow induced eddy currents produce their own magnetic fields given by

$$\nabla \times \vec{B}_2 = \mu \vec{J}_f.$$

It can again be deduced that

$$B_2 \sim \mu D \sigma U B_0 = \text{Re}_m B_0.$$

As before,  $B_2$  will again induce flow induced eddy currents which would create second order magnetic field  $B_2'$ , which would subsequently create  $B_2''$  and so on. The net magnetic field in the presence of only Lorentz force effects (absence of Faraday induction effects) can be written as

$$B = B_0 + B_2 + B_2' + B_2'' + \dots = B_0 \left[ 1 + \text{Re}_m + \text{Re}_m^2 + \dots \right]. \quad (3.16)$$

If  $\text{Re}_m \ll 1$ , we can truncate the series in above equation to the first perturbation term ( $B_2$ ). Using  $B_2(t) = B_2 \cos \omega t$ , the corresponding magnetic flux is obtained as

$$Ub \cos \omega t = \int_S B_2 dS \cos \omega t,$$

where,  $Ub$  is the magnetic flux of flow induced eddy currents.

**Presence of both Faraday induction and Lorentz force effects** In this case, we combine the two cases treated above. The total difference flux through the two secondary coils can be written as,

$$\phi(t) = (A_1 - A_2) \cos \omega t + U(b_1 + b_2) \cos \omega t - \omega(a_2 - a_1) \sin \omega t. \quad (3.17)$$

In case of periodic distribution of the dispersed phase, the terms can be expanded in Fourier series:

$$\begin{aligned} a_i(t) &= a_i + \delta a_i \cos(\omega_\alpha t + \theta) + \dots, \\ b_i(t) &= b_i + \delta b_i \cos(\omega_\alpha t + \theta) + \dots \end{aligned}$$

where,  $\theta$  is an arbitrary phase.  $S_1$  encounters void before  $S_2$ , and therefore  $\theta$  is different for the two secondary coils. The amplitudes  $\delta a_i$  and  $\delta b_i$  depend on the void volume fraction as :  $\delta a_i = \delta a_i(\alpha)$  and  $\delta b_i = \delta b_i(\alpha)$  respectively, and  $\omega_\alpha$  is the void characteristic pulsation which can be calculated from spatial periodicity of the voids  $\lambda_\alpha$  as,

$$\omega_\alpha = U k_\alpha, \quad k_\alpha = 2\pi/\lambda_\alpha, \quad (3.18)$$

where,  $k_\alpha$  is the characteristic wave number of the dispersed phase.

Assuming that the two secondary coils are identically coupled to the primary coil and the media, the in-phase ( $\cos \omega t$ ) component, quadrature phase ( $\sin \omega t$ ) component and the norm of the induced difference flux in the two secondary coils become,

$$\text{Quadrature-phase flux,} \quad \phi_\perp = 2\omega\delta a \sin(\Delta\theta/2) \sin(\omega_\alpha t), \quad (3.19)$$

$$\text{In-phase flux,} \quad \phi_\parallel = 2Ub + 2U\delta b \cos(\Delta\theta/2) \cos(\omega_\alpha t). \quad (3.20)$$

$$\text{Norm of flux,} \quad \|\phi\|^2 = C_1 + C_2 \cos\left(\omega_\alpha t - \frac{\pi L}{\lambda_\alpha}\right) + C_3 \cos\left(2\omega_\alpha t - \frac{2\pi L}{\lambda_\alpha}\right) + \dots, \quad (3.21)$$

where,

$$\begin{aligned} \Delta\theta &= Lk_\alpha, \\ C_1 &= 4U^2b^2 + \dots, \\ C_2 &= 8U^2b\delta b \cos\frac{\Delta\theta}{2}, \\ C_3 &= -2\omega^2\delta a^2 \sin^2\left(\frac{\Delta\theta}{2}\right). \end{aligned}$$

We find that the in-phase component of the difference flux is sensitive to the motion ( $U$ ), while the quadrature component comes from Faraday induced flux in the medium and is insensitive to  $U$ . Both in-phase and quadrature components are sensitive to  $\alpha$ . The first harmonic  $C_2$  of the norm  $\|\Delta\phi\|^2$  is the coupled term and depends on both  $U$  and  $\alpha$ . The second harmonic  $C_3$  is independent of  $U$  and only depends upon  $\alpha$ . The constant term  $C_1$  in equation (3.21) depends linearly on  $U^2$  and is independent of  $\alpha$  to first order.

The expansion developed in this section is only valid for  $D/\delta \ll 1$  and  $\text{Re}_m \ll 1$ . The Faraday induction effects are assumed to be completely decoupled from the Lorentz force effects. The Faraday induced fluxes are developed in  $(D/\delta)^2$  and this series will diverge for  $D/\delta \gtrsim 1$ , as we see in equation (3.15). The motion induced flux is developed in  $\text{Re}_m$  and as such it will diverge for  $\text{Re}_m \geq 1$ , as we given by equation (3.16) . Furthermore, we have restricted the expansion for perturbation due to  $\alpha$  to first harmonic. In the next section, we derive expressions for perturbation in magnetic flux when Faraday induction effects are significant and are coupled to Lorentz force effects.

### 3.2.2 Significant Faraday induction and small Lorentz force effects

$$(\delta \lesssim D, \text{Re}_m \ll 1)$$

For  $D/\delta \gtrsim 1$  it is no longer possible to decouple the induced fluxes from the applied external flux. In this case we propose a flux perturbation model which takes into account of the induced perturbation due to  $\alpha$  and  $U$ . However it is no longer possible to distinguish between the applied external flux and the induced flux in the medium. At low  $\text{Re}_m$  (diffusion dominates advection in magnetic flux transport equation), the amplitude of the net flux crossing coils  $S_1$  and  $S_2$  is given at first order by:

$$\phi = \int \vec{B} \cdot d\vec{s} = \phi_0 + \text{Re}_m \phi_u + \phi_\alpha(t), \quad (3.22)$$

where  $\phi_0$  is the average flux in the absence of motion due to Faraday effects,  $\text{Re}_m \phi_u$  is the average flux due to Lorentz force effects, and  $\phi_\alpha$  is the perturbation of the total flux due to the dispersed phase and is related to the distortion of the induced eddy currents. All the fluxes are spatially averaged over the length of the secondary coils.  $\phi_0$  is defined as the time average when  $U$  vanishes

$$\phi_0 = \lim_{U \rightarrow 0} \left[ \frac{U}{L} \int_0^{L/U} \phi dt \right], \quad (3.23)$$

where,  $L$  is a length large enough for the integral to be independent of  $L$ . In this condition, the fluid properties become continuous. Ideally,  $\phi_0 = 0$  for well balanced  $S_1$  and  $S_2$  without motion and without void.

In case of periodic distribution of the dispersed phase, this term can be expanded in Fourier series:

$$\phi_\alpha(t) = \psi_\alpha \cos(\omega_\alpha t + \theta) + \dots, \quad (3.24)$$

where the amplitude  $\psi_\alpha$  depends on the volume fraction  $\alpha$ . In this analysis  $\omega_\alpha \ll \omega$ . The in-phase and quadrature phase fluxes are given by,

$$\phi_{||} = \phi_{0,||} + \text{Re}_m \phi_{u,||} + \psi_{\alpha,||} \cos(\omega_\alpha t + \theta), \quad (3.25)$$

$$\phi_{\perp} = \phi_{0,\perp} + \text{Re}_m \phi_{u,\perp} + \psi_{\alpha,\perp} \cos(\omega_\alpha t + \theta). \quad (3.26)$$

$\Delta V$  is obtained by time derivation of  $\phi$ . The induced difference voltages are,

$$\Delta V_{\perp} = -\omega \phi_{||} = -\omega [\phi_{0,||} + \text{Re}_m \phi_{u,||} + \psi_{\alpha,||} \cos(\omega_\alpha t + \theta)], \quad (3.27)$$

$$\Delta V_{||} = -\omega \phi_{\perp} = -\omega [\phi_{0,\perp} + \text{Re}_m \phi_{u,\perp} + \psi_{\alpha,\perp} \cos(\omega_\alpha t + \theta)]. \quad (3.28)$$

The square of the modulus of induced difference voltage is  $||\Delta V||^2 = \Delta V_{||}^2 + \Delta V_{\perp}^2$ . Considering the first terms in  $O(\text{Re}_m)$  ( $\text{Re}_m \ll 1$ ),

$$||\Delta V||^2 \approx \omega^2 \left\{ \langle \phi_0 | \phi_0 \rangle + \frac{\langle \psi_\alpha | \psi_\alpha \rangle}{2} + 2 \langle \phi_0 | \psi_\alpha \rangle \cos(\omega_\alpha t + \theta) + \frac{\langle \psi_\alpha | \psi_\alpha \rangle}{2} \cos(2\omega_\alpha t + 2\theta) \right. \\ \left. + 2 \text{Re}_m [\langle \phi_0 | \phi_u \rangle + \langle \phi_u | \psi_\alpha \rangle \cos(\omega_\alpha t + \theta)] \right\}. \quad (3.29)$$

In this formula,  $\phi_i$  is defined as a vector,  $\phi_i = [\phi_{i,\parallel}, \phi_{i,\perp}]$ .  $\langle \phi_i | \phi_j \rangle$  represents the scalar product between the two vectors  $i$  and  $j$ .

In equation (3.25)-(3.28),  $\phi_{0,\parallel}$  and  $\phi_{0,\perp}$  are the in-phase and quadrature components of the mean flux through the secondary coils in the absence of motion.  $\phi_{0,\parallel}$  is primarily composed of the axial magnetic field created by the primary coil  $P$  while  $\phi_{0,\perp}$  primarily comes from the Faraday induced eddy currents. However, in this case ( $\delta < D$ ) there is no clear decoupling of the external fields from the induced flux; both in-phase and quadrature components of total flux contain their contributions.

In equation (3.25)-(3.28),  $\text{Re}_m \phi_{u,\parallel}$  and  $\text{Re}_m \phi_{u,\perp}$  represent the DC shift in mean flux  $\phi_{0,\parallel}$  and  $\phi_{0,\perp}$  respectively and are caused by the interaction of motion ( $U$ ) with the radial magnetic flux density  $B_r$ . Again, the shape and magnitude of in-phase and quadrature components of  $B_r$ , depend on both externally applied magnetic fields and the induced fields. It controls the magnitude of  $\text{Re}_m \phi_{u,\parallel}$  and  $\text{Re}_m \phi_{u,\perp}$ .

$\psi_{\alpha,\parallel}$  and  $\psi_{\alpha,\perp}$  are the amplitude of the void induced perturbations and will be studied with the help of spectral density of total flux.

In equation (3.24),  $||\Delta V||^2$  is expressed as a function of the dominant term in Fourier expansion. The last term in  $\text{Re}_m$  corresponds to the magnetic flux component perturbed by the motion. We note that  $\langle \phi_0 | \phi_0 \rangle$  and  $\langle \psi_\alpha | \psi_\alpha \rangle$  appear at zero order. The terms  $\langle \phi_0 | \psi_\alpha \rangle$ ,  $\langle \phi_0 | \phi_u \rangle$  and  $\langle \phi_u | \psi_\alpha \rangle$  represent the coupling effects of Faraday induction, Lorentz force and dispersed phase. The term  $\langle \phi_u | \phi_u \rangle$ , which appears at second order in  $\text{Re}_m$  has been neglected.

From the experiments and based on this model, the contributions of the dispersed phase and of the velocity on the net magnetic flux can be measured by Fourier analysis of the  $||\Delta V||^2$  signal. The amplitude of  $\omega_\alpha$  term at zero velocity  $\langle \phi_0 | \psi_\alpha \rangle$  gives the perturbation due to  $\alpha$  effects. The second  $\omega_\alpha$  term, which depends on  $\text{Re}_m \langle \phi_u | \psi_\alpha \rangle$  exhibits the coupling effects between the velocity and the void fraction on the induced eddy currents. At last, the amplitude of  $2\omega_\alpha$  term  $\langle \psi_\alpha | \psi_\alpha \rangle$  characterizes the influence of the dispersed phase and is independent of the Lorentz force effects.

### 3.3 Lissajous ellipse fitting approach

Ellipse fitting algorithms are popular in the fields of digital signal processing and image analyses [88][89]. When two signals  $V_1(t)$  and  $V_2(t)$  are out of phase and satisfy certain conditions, their Lissajous curve is an ellipse (Fig. 3.11). Let the induced voltages in secondary coils  $S_1$  and  $S_2$  be  $V_1$  and  $V_2$  respectively:

$$V_1(t) = |V_1| \cos(\omega t + \theta_1) + C_1, \quad (3.30)$$

$$V_2(t) = |V_2| \cos(\omega t + \theta_2) + C_2. \quad (3.31)$$

The algebraic manipulation of these will give,

$$\left( \frac{|V_1| - C_1}{|V_1|} \right)^2 + \left( \frac{|V_2| - C_2}{|V_2|} \right)^2 - 2 \frac{(|V_1| - C_1)(|V_2| - C_2)}{|V_1||V_2|} \cos(\Delta\theta) - \sin^2(\Delta\theta) = 0. \quad (3.32)$$

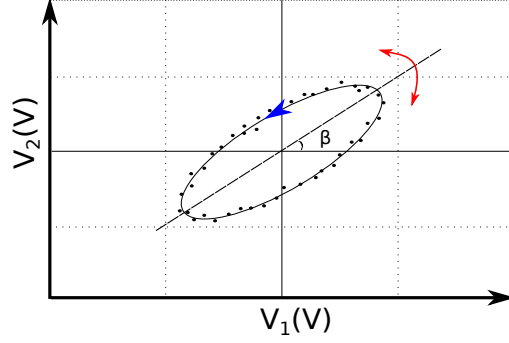


Figure 3.11: Typical Lissajous curve of signals  $V_1(t)$  and  $V_2(t)$ .

This can be written as,

$$F(V_1, V_2) = aV_1^2 + 2bV_1V_2 + cV_2^2 + 2dV_1 + 2fV_2 + g = 0. \quad (3.33)$$

The values of various coefficients are

$$\begin{cases} a = |V_2|^2, \\ b = -|V_1||V_2| \cos(\Delta\theta), \\ c = |V_1|^2, \\ d = -|V_2|^2 C_1 + |V_1||V_2| C_2 \cos(\Delta\theta), \\ f = -|V_1|^2 C_2 + |V_1||V_2| C_1 \cos(\Delta\theta). \end{cases} \quad (3.34)$$

Equation (3.33) yields an ellipse for condition,  $b^2 - 4ac < 0$ . Using the values of coefficients, this would mean  $|V_1|, |V_2| \neq 0$  and  $\Delta\theta \neq n\pi, n = 0, 1, 2, \dots$ . The phase difference is given by:

$$\cos(\Delta\theta) = -\frac{\text{sgn}(a)b}{\sqrt{ac}}. \quad (3.35)$$

The angle of inclination of this ellipse with respect to  $V_1(t)$  is called the tilt angle and it is given by

$$\beta = \begin{cases} 0, & \text{for } b = 0 \text{ and } a < c, \\ \frac{1}{2}\pi, & \text{for } b = 0 \text{ and } a > c, \\ \frac{1}{2} \cot^{-1} \frac{a-c}{2b}, & \text{for } b \neq 0 \text{ and } a < c, \\ \frac{\pi}{2} + \frac{1}{2} \cot^{-1} \frac{a-c}{2b}, & \text{for } b \neq 0 \text{ and } a > c. \end{cases} \quad (3.36)$$

$|V_1|, |V_2|$  and  $\theta$  are functions of velocity  $U$  and void fraction  $\alpha$  of the two phase medium under study. The presence of voids will modify eddy currents, which subsequently affects  $|V_1|, |V_2|$  and  $\theta$ . This allows one to use ellipse fitting as a tool to analyze the impedance of the medium under investigation. In this way, various ellipse parameters could be used to characterize the two phase flows. In this thesis, we use tilt angle  $\beta$  to quantify  $\alpha$ . An equivalent formula for  $\beta$  is:

$$\beta = \left| \frac{1}{2} \arctan \left( \frac{-2 \cos(\Delta\theta) |V_1| |V_2|}{|V_1|^2 - |V_2|^2} \right) \right|. \quad (3.37)$$



At low magnetic Reynolds number  $Re_m$ ,  $\Delta\theta$  is linear with  $U$ , but very close to  $0^\circ$  or  $180^\circ$  [32, 34]. The numerical simulation in COMSOL<sup>®</sup> described earlier, shows that for  $0 \leq Re_m \leq 0.12$ ,  $0 \leq \Delta\theta(\text{rad}) \leq 0.025$  and consequently  $0.9997 \leq \cos \Delta\theta \leq 1$  (see figure 3.12). Therefore, in the absence of voids the ellipse approaches a straight line inclined

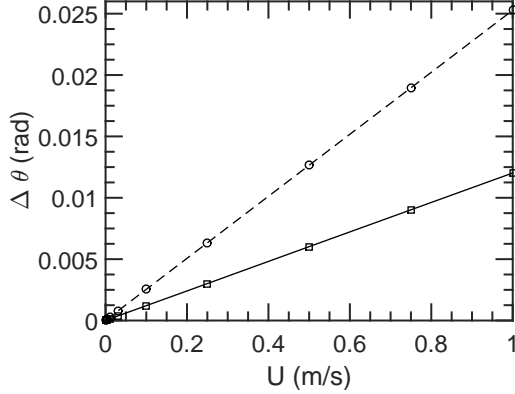


Figure 3.12:  $\Delta\theta$  vs  $U$  at  $\omega = 3142$  (○) and  $6248$  (□)  $\text{rad s}^{-1}$ .

near  $45^\circ$ . When a void is under  $S_1$ ,  $|V_1|$  becomes much larger than  $|V_2|$  and  $V_1(t)$  has a slightly different phase than  $V_2(t)$ . We get a prominent tilted ellipse. The tilt fluctuates about  $45^\circ$  when voids pass through the flow cross-section. We can relate the fluctuation in the tilt angle to characterize the void presence. From the time signal of  $\beta$  we calculate the amplitude of oscillation  $\Delta\beta$  by FFT algorithm.

Further decomposition of equation (3.36) in terms of expansion for induced voltages as obtained in previous sections is possible. But this leads to intractably large expressions which defeats the purpose of the decomposition: term by term understanding with respect to Lorentz force and Faraday induction effects. Nevertheless, this decomposition is provided in the appendix.

### 3.4 Conclusions

From theoretical point of view, there are various ways to model ECFM in single phase flows. In literature, researchers choose not to solve the Navier stokes equation and the magnetic induction equation is solved assuming a given velocity magnitude and profile. In this chapter, we did Finite element simulations of the same problem. These simulations show that the flow sensitive difference voltage  $|\Delta V|$ , increases with the primary and secondary coil radii. This is attributed to increase in surface area for the flux to penetrate.  $|\Delta V|$  decreases with the length of primary and secondary coils, when total number of turns is kept constant. This is due to a decrease in number density of coil turns.  $|\Delta V|$  is linear in  $U$ .  $|\Delta V|$  sensitivity to  $U$  decreases with increasing  $\omega$ . The difference of phase between the two secondary coils is also linear in  $U$ .

To model  $U$ ,  $\alpha$  and  $\omega$  effects in ECFM, three approaches were proposed. In all the cases,  $\text{Re}_m \ll 1$ .

The first model assumes no coupling between Faraday induction and Lorentz force effects, which we find is possible under assumptions:  $D \ll \delta$  and  $\text{Re}_m \ll 1$ . Here we obtain the magnetic fields by expansion in terms of  $(D/\delta)^2$  and  $\text{Re}_m$ . Based on the assumption  $D \ll \delta$  and  $\text{Re}_m \ll 1$ , we calculated expression for total flux through the ECFM for the special case of periodic distribution of dispersed phase. We find that the in-phase component of magnetic flux is linearly proportional to  $U$  and  $\alpha$ , while the quadrature phase component only depends on  $\alpha$ . The norm of the magnetic flux perturbation is a sum of a constant term and first two harmonics. The constant term is proportional to  $U^2$ , the first harmonic is proportional to  $U^2$  and  $\alpha$  and the second harmonic is proportional to  $\alpha$ . We conclude that this theoretical model, valid for  $D \ll \delta$  and  $\text{Re}_m \ll 1$ , predicts  $U$  and  $\alpha$  effects on different components of norm of magnetic flux. Therefore, we require FFT spectral analyses in order to separate flow and void signals. We also note that this model does not lead to an explicit expression in  $\alpha$ .

The second model was proposed for the cases when  $\delta \ll D$  and  $\text{Re}_m \ll 1$ , *i.e.*, Faraday induction effects are significant and cannot be separated from the Lorentz force effects. We expand the net magnetic flux in terms of perturbation by  $U$  and  $\alpha$ . This expansion is valid at low  $\text{Re}_m$  ( $\text{Re}_m \ll 1$ ). In the presence of periodic distribution of dispersed phase, we find that both the in-phase and quadrature phase component of magnetic flux depend on  $U$  and  $\alpha$  through  $\text{Re}_m \phi_u$  and  $\psi_\alpha$  terms. The first harmonic of norm of magnetic flux, is coupled term in  $U$  and  $\alpha$ . On the other hand, this theoretical model predicts that the second harmonic only depends on  $\psi_\alpha$  to first order in  $\text{Re}_m$ . We conclude that FFT spectral analyses of the norm of magnetic flux will allow us to characterize  $U$  and  $\alpha$  effects in this regime with the help of the proposed theory. This can also be achieved with phase sensitive analyses and direct measurement of amplitudes of perturbations on in-phase and quadrature phase raw signals. In this model, we find explicit expressions in  $U$  and  $\alpha$ .

We have also proposed a purely experimental methodology called the Lissajous ellipse fitting approach to characterize  $\alpha$ . The basic idea is to make Lissajous curve with signals in the two secondary coils. This makes an ellipse in the presence of voids. We fit an ellipse and use the fluctuations in the orientation of this ellipse to measure  $\alpha$ . The mathematical basis for the same was given. The advantage of this method is its simplicity. No phase sensitive measurements is required. In this method, we do not have explicit expressions in  $U$  and  $\alpha$ .

All these models would be confronted in chapter 4 with experiments.



## Chapter 4

# Experiments in model two-phase liquid metal flow

In this chapter, we present experimental results regarding two phase medium under AC magnetic fields. The ultimate objective is to understand the void and velocity induced perturbations in magnetic flux in the presence of Faraday induction and Lorentz force effects.

This chapter is organized as follows: section 4.1 explains the experimental setup and its construction. We use a model experimental set up in which a plug flow is simulated by static aluminium rods over which we translate ECFM with a given velocity  $U$  m/s. Grooves and holes have been machined on these rods to simulate voids. Their geometrical void fraction is denoted as  $\alpha$ .

Two approaches were tested in this thesis. The first approach is **the difference signal approach** and is given in section 4.2. In this approach, the ECFM is used in three-coils configuration. Primary coil is excited by an AC current. The difference of emf between the two secondary coils is measured. The objective is to record  $U$ ,  $\alpha$  and  $\omega$  effects on this difference. This approach is more intuitive and allows easy interpretation of Faraday induction and Lorentz force effects.

Thereafter, in section 4.3 we see the experiments and analyses for the **Lissajous ellipse fitting approach**. ECFM has been used in both three-coils and five-coils configurations. The signals from the two secondary coils make a Lissajous curve as recorded by an oscilloscope. This is subsequently analyzed using ellipse fitting algorithms. We measure  $U$ ,  $\alpha$  and  $\omega$  effects on the orientation of fitted ellipse. This approach is relatively simpler to implement experimentally.

In the last section 4.4, we summarize some important inferences from these experiments.

### 4.1 Experimental set up

A general overview of the experimental setup is presented as a block diagram shown in figure 4.1. Specific blocks in this diagram are explained in subsequent subsections.

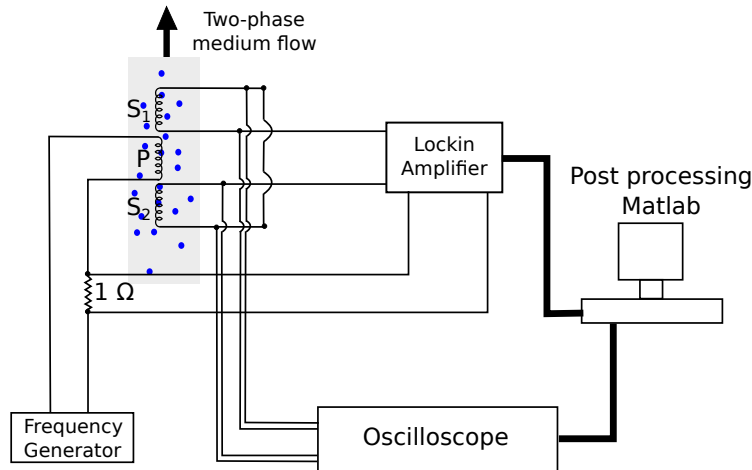


Figure 4.1: Block diagram of the experimental set up for three coils ECFM.

A frequency generator excites the primary coil  $P$  in the 3-coils ECFM assembly. The resulting magnetic flux created by the primary coil is sensed by secondary coils  $S_1$  and  $S_2$ . The flow of two phase medium through ECFM assembly will perturb the magnetic flux. The magnetic flux is monitored and analyzed with the help of oscilloscope and Lockin amplifier.

These instruments record the emf in coils  $S_1$ ,  $S_2$  and the difference of the induced emf between these two coils. The signals so recorded is post processed using MATLAB<sup>®</sup> in a PC.

There are several issues with a two-phase liquid metal loop. The fact that the liquid metal is opaque hinders the use of common optical tools such as CCD camera. Therefore it is difficult to know the real time size and distribution of bubbles. The control of the flow profile is also difficult. In addition, turbulent flow fluctuations would appear as unwanted noise in the perturbation flux being sensed by the secondary coils. Temperature and pressure controls are also required. The most difficult part of a general liquid metal two-phase flow loop is the controlled gas injection technique. Corrosion of the materials is also an issue. Liquid metals, such as Sodium, also need precaution in handling and maintenance and require shielding from air and moisture. Some other liquid metals such as mercury are poisonous.

In view of several technical challenges associated with a liquid metal loop it seemed prudent to avoid the same in the first attempt. An equivalent system was proposed which mimics a two-phase liquid metal flow. This experimental setup is shown in figure 4.2 with ECFM in a three-coils configuration. Here the two-phase medium is simulated by aluminium rods. Grooves and holes are machined on their outer surface to simulate voids (bubbles). The aluminium rod is fixed at its two extreme ends on two poles. To simulate the relative motion, the ECFM assembly is fixed to a uniaxial translator. This device translates ECFM assembly over aluminium rod at a given constant velocity. This simulates a plug flow. The role of frequency generator is to drive AC current through

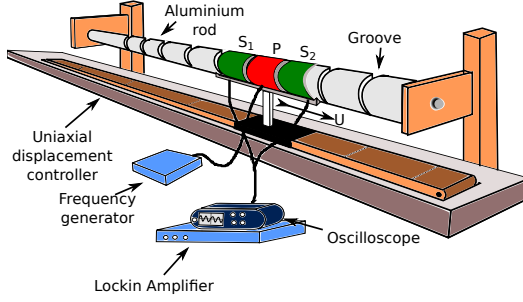


Figure 4.2: Schematic of the experimental set up for three coils ECFM.

the primary coil, while oscilloscope and Lockin amplifier record the emf in coils  $S_1$ ,  $S_2$  and the difference of the induced emf between these two coils, as well as the current in the primary coil.

#### 4.1.1 Two-phase medium

The two-phase medium is simulated by various aluminium rods. To simulate voids, we machine holes and grooves on its outer surface.

The dimensions for “groove-type” rods are given in table 4.1. Seven types of groove-type aluminium cylinders have been used. They are shown in figure 4.3.  $L_r$  and  $R$  are length and radius respectively of each rod (refer to figure 4.4).  $l_g$  and  $d_g$  are the length and depth of grooves.  $\lambda_\alpha$  is the wavelength that indicates spatial periodicity of the grooves. The geometrical void fraction  $\alpha$  is calculated for each rod as follows.

Since the grooves are distributed periodically, it would be sufficient to calculate the geometrical void fraction for one cell of axial length  $\lambda_\alpha$ . In this case, we would divide the volume occupied by one groove to the volume of a cylindrical rod of length  $\lambda_\alpha$  and radius  $R$ .

$$\alpha = \frac{[\pi R^2 - \pi (R - d_g)^2] l_g}{\pi R^2 \lambda_\alpha} = \frac{2Rd_g l_g - d_g^2 l_g}{R^2 \lambda_\alpha} \quad (4.1)$$

Table 4.1: Dimensions of groove-type rods in mm.

S/N	$L_r$	$R$	$d_g$	$l_g$	$\lambda_\alpha$	$\alpha$
a	300	19.25	—	—	—	0%
b	300	19.25	4.25	2.80	—	1 groove
c	300	19.25	0.38	1.40	18.00	0.3%
d	800	19.00	1.80	2.00	18.00	2.0%
e	800	19.00	3.20	2.60	18.00	4.5%
f	300	19.25	4.23	3.00	16.85	6.9%
g	300	19.25	4.25	3.00	—	—

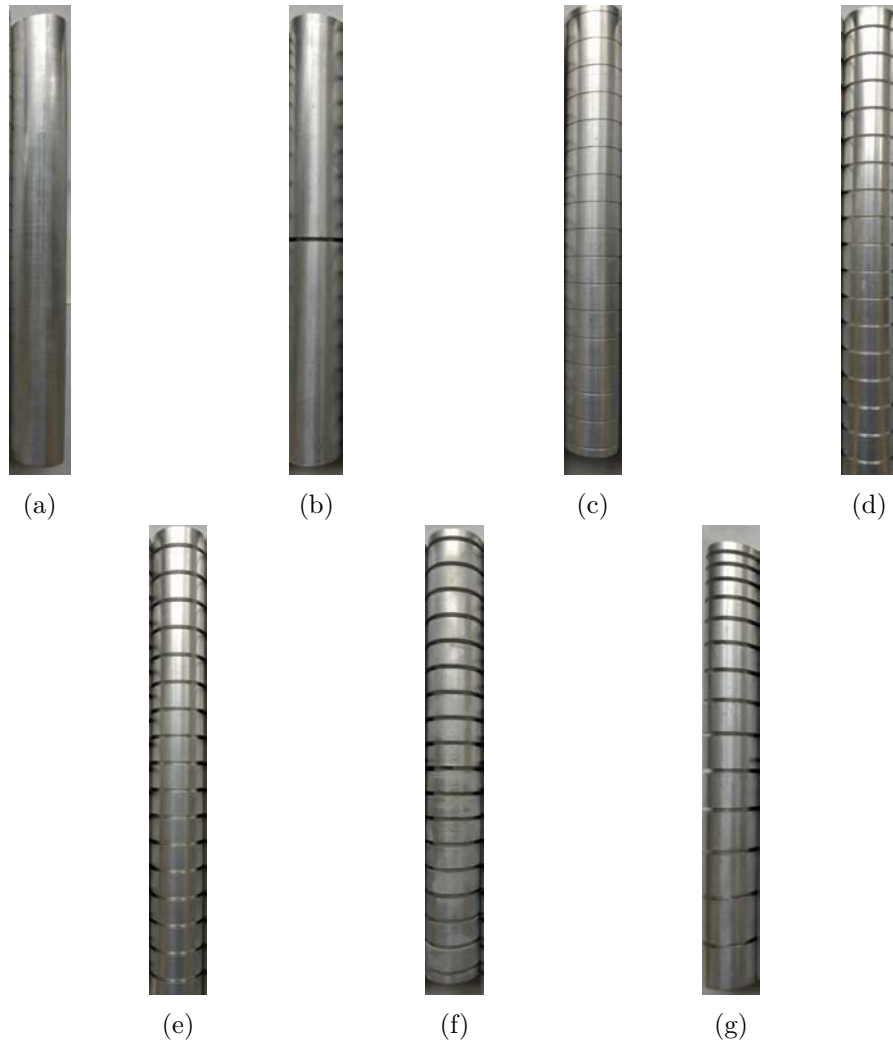


Figure 4.3: The Groove-type aluminium rods. (a)  $\alpha = 0\%$ , (b) one void, (c)  $\alpha = 0.3\%$ , (d)  $\alpha = 2.0\%$ , (e)  $\alpha = 4.5\%$ , (f)  $\alpha = 6.9\%$ , (g) Variable separated.

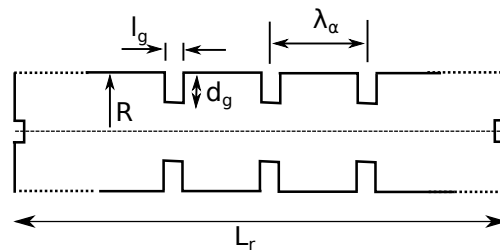


Figure 4.4: Geometrical quantities arising in formula (4.1) for a groove type rod.

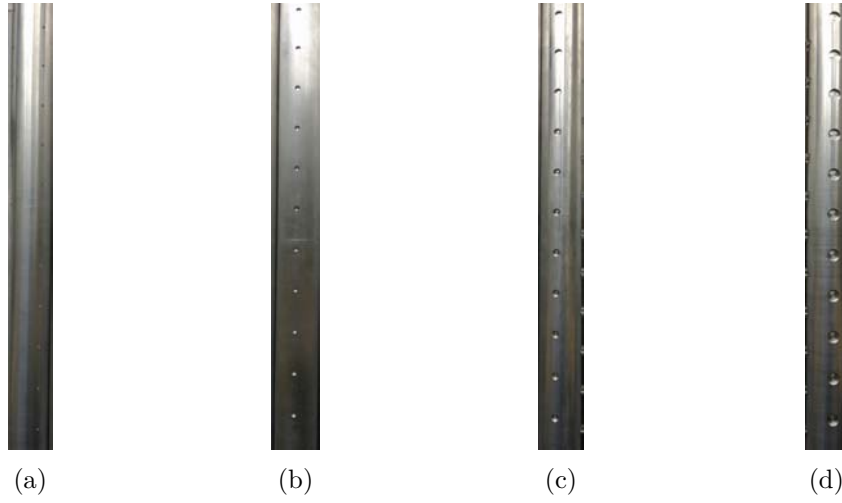


Figure 4.5: The hole-type aluminium rods. (a)  $\alpha = 0.06\%$ , (b)  $\alpha = 0.22\%$  (c)  $\alpha = 0.54\%$ , (d)  $\alpha = 1.62\%$ .

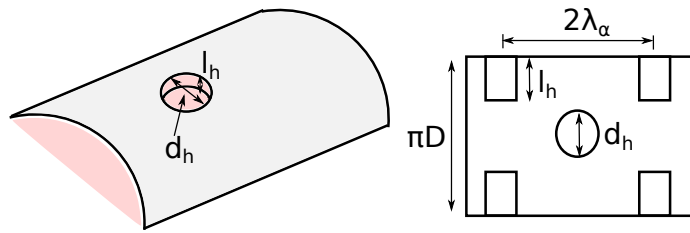


Figure 4.6: Bore hole on cylinder outer surface and geometrical quantities appearing in equation (4.2).

Table 4.2: Dimensions of hole-type rods in mm.

S/N	$L_r$	$R$	$d_h$	$l_h$	$\lambda_\alpha$	$\alpha$
a	800	19.25	2.00	2.00	17.45	0.06%
b	800	19.25	3.90	2.00	17.45	0.22
c	800	19.25	6.04	2.00	17.45	0.54%
d	800	19.25	10.23	2.00	17.45	1.62%

Different hole-type rods were used in the experiments and are shown in figure 4.5. The holes are cylindrical bore-type dug on cylinder outer surface as shown in figure 4.6. Therefore each hole is defined by its height  $l_h$  and its diameter  $d_h$ . Each cross-section of aluminium cylinder contains two holes placed diametrically opposite on rod outer surface. The next cross-section would also contain two holes but rotated azimuthally by  $90^\circ$ . This pattern repeats itself. The dimensions of the four hole-type rods are given in table 4.2.



In this configuration, the geometrical void fraction can be calculated as

$$\alpha = \frac{2\pi(d_h/2)^2 l_h}{\lambda_\alpha \pi (D/2)^2} = \frac{2d_h^2 l_h}{\lambda_\alpha D^2} \quad (4.2)$$

#### 4.1.2 Uniaxial displacement controller

Uniaxial displacement controller (UDC) is a device that translates a load in a given direction at a given constant velocity. Two kinds of UDC were tested for stability in velocity. The one chosen for the experiments is Movopart MV 100 shown in figure 4.7.

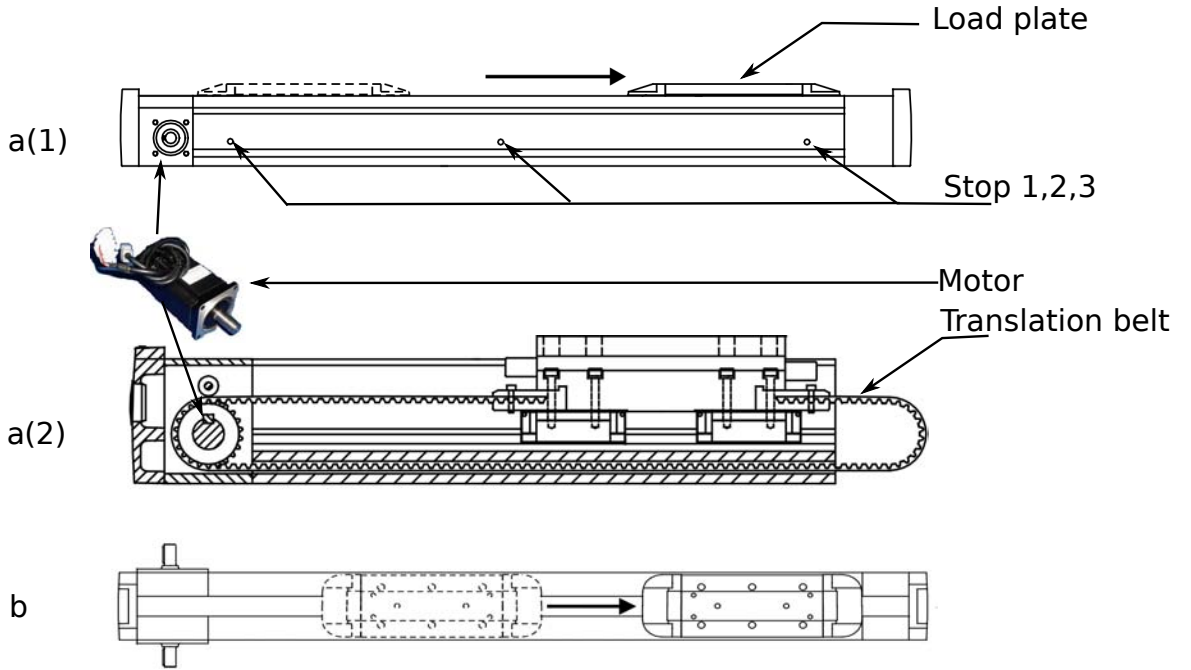


Figure 4.7: Schematic of a uniaxial displacement controller. (a) side view, (b) top view.

It is a rod-less actuator. A belt connected to a Servostar MAC23 motor is used to create uniaxial motion. A plate is connected to this belt. Load ( $\lesssim 10$  kg) can be screwed to this plate. It can attain a maximum velocity of  $5 \text{ m s}^{-1}$ . Stop 1,2,3 are three markers which can be used to fix start and stop positions. This can also be programmed. In the later case Stop 1,2,3 can be used as emergency stoppages at two extreme ends. There are two choices for acceleration/deceleration phases: trapezoidal and exponential. For the trapezoidal case, the acceleration is constant and it takes significant amount of time and distance to reach  $U \text{ m s}^{-1}$  from  $0 \text{ m s}^{-1}$ . For the exponential case, the acceleration is exponential whose exponent can be adjusted using a set of parameters in Servostar motor. There is a trade off between the rapid acceleration/deceleration phases and the stability of  $U$ . Figure 4.8 compares stability vs acceleration time for two chosen set of parameters in PID controller for UDC motor. The X-axis is arbitrary. The Y-axis shows

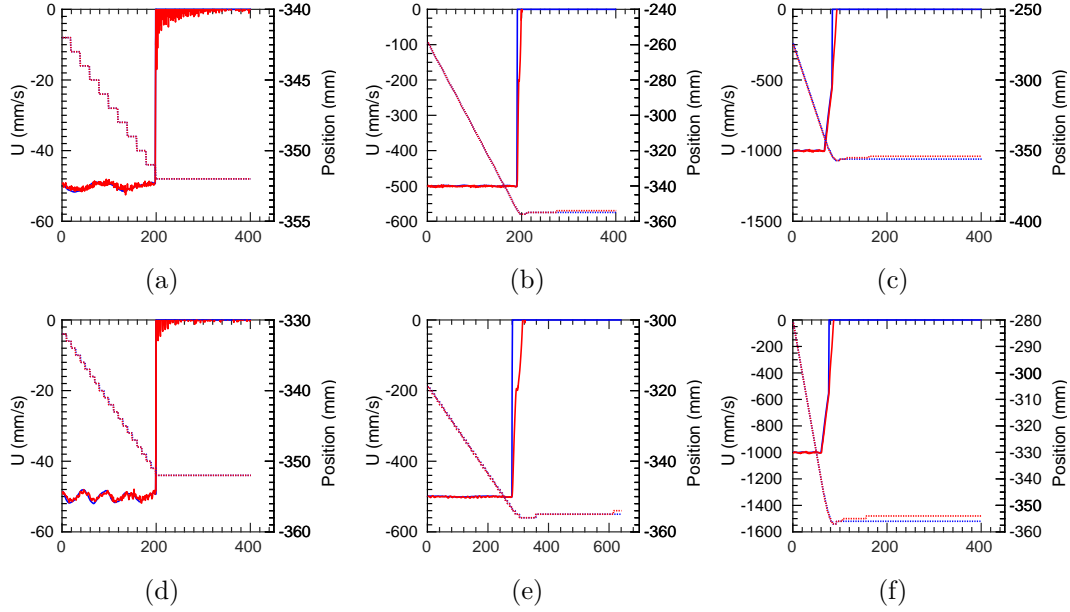


Figure 4.8: Velocity profile (—) and Position coordinates ( $\dots$ ) when ECFM is in motion, for two sets of parameter settings for UDC. Set 1: (a,b,c), Set 2: (d,e,f). Expected values: ( $\text{---}, \dots$ ), Real values: ( $\text{---}, \dots$ ).

the expected (blue) vs real (red) velocity  $U(t)$  and positions  $P(t)$ .  $U(t)$  rises rapidly and attains a constant value  $U_c$ . The position  $P(t)$  follows the law:  $P(t) = Ut$ . For high  $U_c$ ,  $U(t)$  is very stable as expected. At low  $U_c$ , we observe oscillations in  $U(t)$ . This can introduce error in  $U$  upto a maximum of 5%.

### 4.1.3 Excitation and acquisition

The excitation in the primary coil should be achieved through a frequency generator. We would like to fix the phase and magnitude of AC current in primary coil. In this way, we fix the phase and magnitude of externally applied magnetic flux due to primary coil. To achieve this, the ideal choice will be a stable AC current generator. A frequency generator which produces an AC voltage was used. As shown in figure 4.1, the current generated by the frequency generator is measured across an  $1\ \Omega$  resistor by a Lockin amplifier which samples the in-phase ( $\cos \omega t$ ) and quadrature phase ( $\sin \omega t$ ) components. This is explained in detail later. In figure 4.9, we observe current in the circuit for a given pulsation  $\omega$  and a fixed current magnitude in frequency generator. ECFM is translated back and forth 6 times (3 times each back and forth) with  $U = 1\ \text{m s}^{-1}$  on aluminium rod with  $\alpha = 6.9\%$ . We notice that the in-phase current  $I_{\parallel}$  is stable and the maximum error is 0.05%. The quadrature phase current  $I_{\perp}$  can be neglected in comparison to  $I_{\parallel}$ . The norm of the current,  $I = \sqrt{I_{\parallel}^2 + I_{\perp}^2}$  also remains constant within 0.05%. We conclude that the change in impedance of the medium does not affect the amplitude and phase

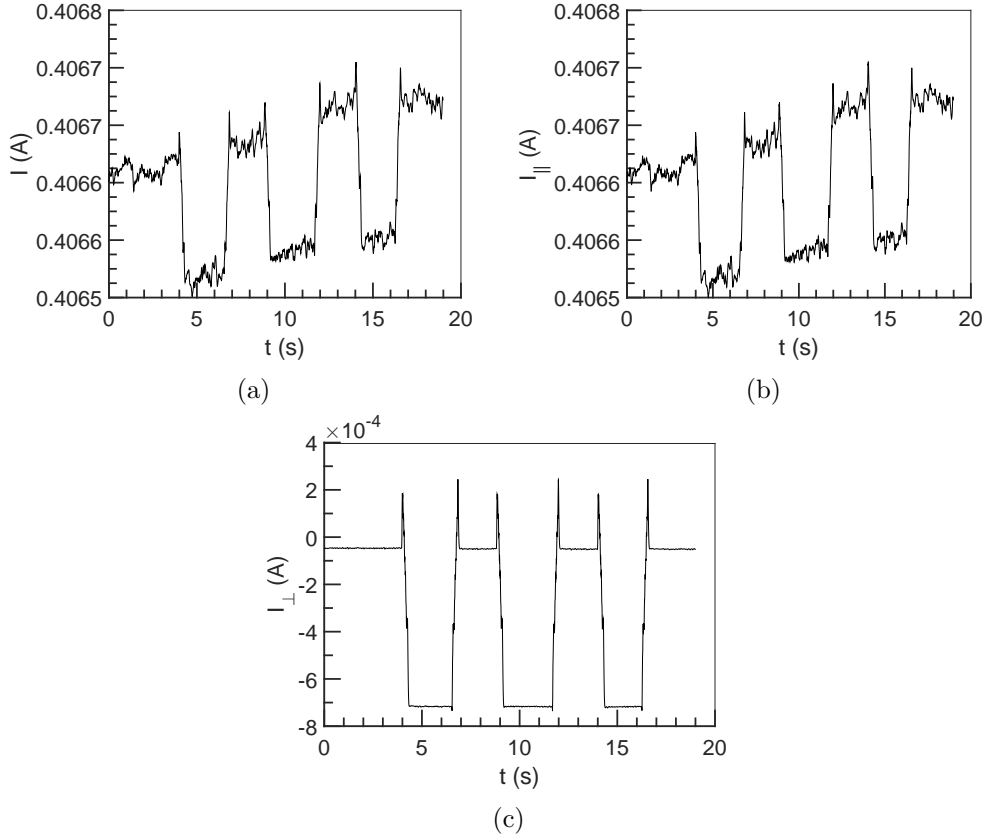


Figure 4.9: Applied AC current, (a)  $I(A)$ , (b)  $I_{||}(A)$ , (c)  $I_{\perp}(A)$  for  $U = 1 \text{ ms}^{-1}$  and  $\alpha = 6.9\%$ .

of imposed current and the imposed external magnetic flux.

To observe the magnetic flux perturbation in two-phase flow, we sense the induced potential in the two secondary coils using a digital oscilloscope and a Lockin amplifier.

The oscilloscope used was MDO3104 by Tektronix (MDO stands for Mixed Domain Oscilloscope). The advantage of this oscilloscope is that it comes with an in-built spectrum analyzer which helps to visualize signal spectrum in real time. The input low-pass filter bandwidth can be adjusted so as to reject very high frequency noise. Sampling rate  $F_s$  is chosen high enough to respect Nyquist-Shannon sampling theorem.  $F_s$  is calculated by the following formula

$$F_s = \frac{R_l}{T} \quad (4.3)$$

where,  $R_l$  is the record length (total number of samples) and  $T$  is the total time of record. The resolution in time may be as low as 2 ns (resolution in time is inverse of the maximum sampling rate). The maximum amplitude resolution is  $1 \times 10^{-4} \text{ V}$ . We will



Figure 4.10: Digital oscilloscope MDO 3104 from Tektronix.

see below that the time and amplitude resolution of a digital oscilloscope is inferior to that of a Lockin amplifier.

To separate the effects of velocity and void fraction, the idea was to look at the in-phase and quadrature components. This is achieved by using a Lockin Amplifier which samples the in-phase and quadrature components of distorted flux with respect to the imposed current in the primary coil. Lockin amplifiers are high performance demodulators and are capable of operating under conditions of very low signal-to-noise ratio. The principle of signal acquisition using Lockin amplifier is shown in figure 4.11 and 4.12. The phase sensitive detector of Lockin amplifier mixes the input signal with a

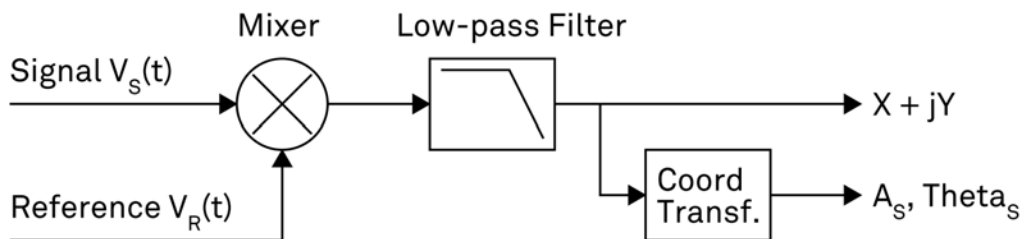


Figure 4.11: Principle of signal acquisition using a Lockin Amplifier.

reference signal before passing the mixture through a low pass filter. The output signal has a very high signal to noise ratio and in some cases can measure signals in the  $nV$  range. To sample in-phase and quadrature components of input signal, Lockin amplifier uses two phase-sensitive detectors in parallel. One of the phase sensitive detectors uses the reference signal while the other shifts the reference signal by  $90^\circ$  before the mixing stage. Let us assume that  $V_R$  is the reference signal given by,  $V_R = \sqrt{2} \exp(-j\omega t)$ , where  $\omega$  is the demodulation frequency. In our case  $\omega$  is the pulsation of AC current in the primary coil. At the demodulation stage, the acquired signal through the secondary

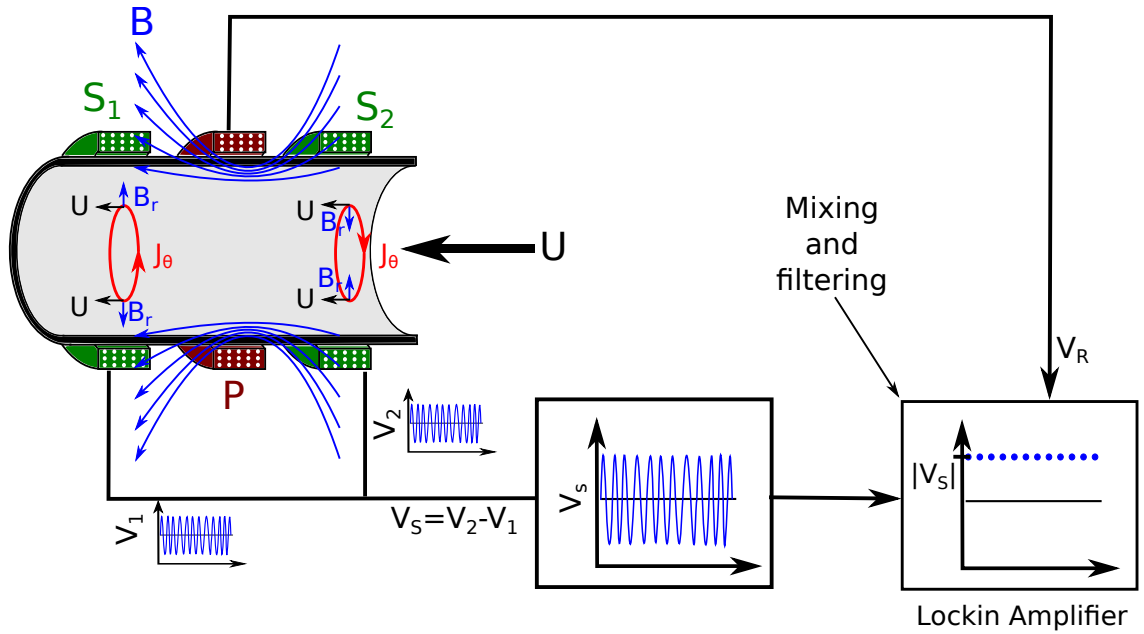


Figure 4.12: Schematic of demodulation using a Lockin amplifier.



Figure 4.13: Lockin amplifier HF2LI MF by Zurich instruments used in the experiments.

sensor coils  $V_S = A_S \cos(\omega_s t + \theta_s)$  is multiplied with  $V_R$  and integrated (filtered) to achieve a demodulation (conversion to DC).

$$V_S * V_R = V_s * \sqrt{2} \exp(-j\omega t) = \frac{A_s}{\sqrt{2}} \exp j[(\omega - \omega_s)t + \theta_S] + \frac{A_s}{\sqrt{2}} \exp -j[(\omega + \omega_s)t + \theta_S]$$

The subsequent low-pass filtering yields

$$X + jY = \langle V_S * V_R \rangle = F(\omega - \omega_s) \frac{A_s}{\sqrt{2}} \exp j[(\omega - \omega_s)t + \theta_S]$$

$F(\omega - \omega_s)$  is the filter response. Ideally, we would like to obtain  $F(\omega - \omega_s) = 1$  within the allowed bandwidth  $\Delta\omega = \omega - \omega_s$  and  $F(\omega - \omega_s) = 0$  outside the selected bandwidth  $\Delta\omega$ . Therefore filter bandwidth selection is of utmost importance. In our experiments, the Lockin amplifier used 24 dB/oct low-pass filter. In the absence of perturbation in magnetic flux due to void and external sources of noise, we would expect  $\omega_s = \omega$  and hence a DC output voltage  $X + jY = \frac{A_s}{\sqrt{2}} \exp j\theta_S$  is to be expected. The Lockin amplifier used in our experiments was HF2LI MF from Zurich instruments. It shares its advantages with other Lockin amplifiers. In addition, its Multi-Frequency (MF) feature allows to perform experiments at several pulsation values ( $\omega$ ) in one single run. However, this functionality was not used in our experiments. Lockin amplifier shown in figure 4.13 is interfaced with a PC with the help of a proprietary software.

#### 4.1.4 ECFM assembly

After analyzing theoretically several possible configurations (varying lengths and radii of coils), ECFM assembly shown in figure 4.14 was fabricated at IMFT for liquid metal two-phase flow studies. The wire material is copper and the hollow bobbin structure is made of PVC. The ECFM is of flow-through type with 5 coils. The coils  $P_1$ ,  $P_2$  and  $P_3$  are intended to be the primary coils. The coils  $S_1$  and  $S_2$  are intended to be the secondary coils. The same ECFM assembly can be used in 3 coils configuration. In this case the two ends of  $P_2$  and  $P_3$  are left open (open-circuited) and hence do not play any role.

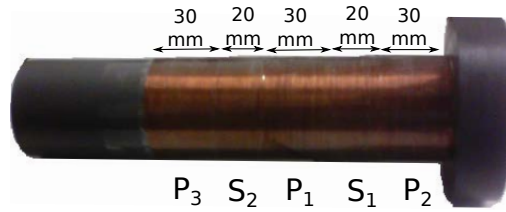


Figure 4.14: ECFM fabricated for experiments at IMFT.

The dimensions of the device are: length of primary coils  $L_p = 30$  mm, length of secondary coils  $L_s = 20$  mm, inner diameter of plastic pipe  $D_i = 40$  mm, outer diameter of plastic pipe  $D_o = 44$  mm, number of turns of copper wire, in primary coils  $N_p = 70$ , in secondary coils  $N_s = 50$  mm, wire thickness  $d_w = 0.4$  mm.

Figure 4.15 shows the experimental bench on which the two phase experiments were performed. We notice that the primary coil is given an excitation through a preamplifier

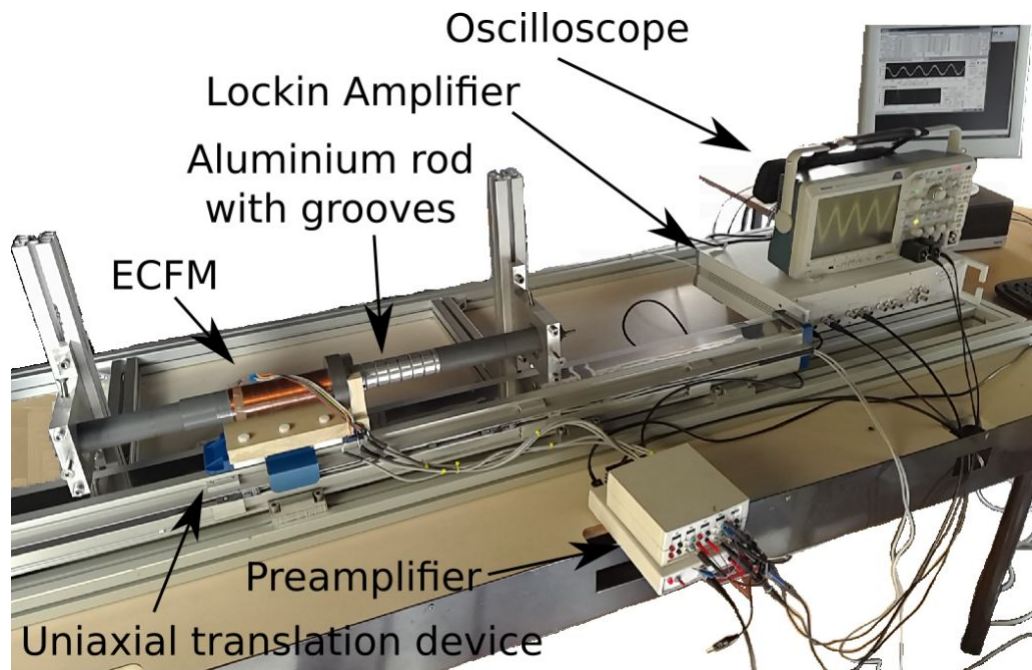


Figure 4.15: Experimental setup which models two-phase flow for studies with ECFM.

which in turn is connected to an in-built frequency generator of a Lockin amplifier. The output signals sensed by the secondary coils is fed to the digital oscilloscope and Lockin amplifier via a connector box. The signals acquired by the Lockin amplifier is registered in a PC. On the other hand, the signals of the secondary coils are registered on an external USB in the oscilloscope. ECFM is screwed to UDC load plate. The motor of the UDC is not in the picture. The regulation and control of UDC is again done using PC. The aluminium rod is held in its place by two pole structures erected on each extremity.

## 4.2 Difference signal approach

### 4.2.1 Methodology

The experimental set-up for this experiment was as described in the previous section. All the rods were used in the experiments. Their specifications can be found in table 4.1 and 4.2. The ECFM was used in a 3 coil configuration:  $P$ ,  $S_1$  and  $S_2$ ; where  $P$  was used for excitation and  $S_1$  and  $S_2$  are used for sensing the integrated magnetic flux. The excitation and acquisition was achieved using the Lockin amplifier to obtain phase-sensitive measurements. The oscilloscope was not used except for some specific cases in

order to validate the consistency of the measurements. The data was saved on a PC during the course of experiments and later analyzed using Matlab.

The experiments were realized at room temperature for which the electrical conductivity of aluminium is  $\sigma = 3.77 \times 10^7 \text{ S m}^{-1}$ . The aluminium is slightly paramagnetic with relative permeability of  $\mu_r = 1.000\,022$ . Therefore magnetic permeability in aluminium can be taken as  $\mu_r = 4\pi \times 10^{-7} \text{ H m}^{-1}$ . The range of pulsations used was  $\omega = 1571$  to  $12\,566 \text{ rad s}^{-1}$ . The corresponding skin-depth of magnetic flux is between  $\delta = 5.2 \text{ mm}$  and  $1.8 \text{ mm}$ . As mentioned previously the current in the circuit is determined indirectly with the help on  $1 \Omega$  resistor in series. The range of magnitude of AC current used was between  $I = 200$  and  $400 \text{ mA}$ . We verified that this magnitude remains stable within  $0.05\%$  during the course of experiments (see figure 4.9). The phase of  $I$  was taken as reference for each experiments. The secondary coils emf was measured in the Lockin amplifier with respect to this phase. Therefore, it is possible to record either magnitude  $\|\Delta V\|$  and phase  $\theta$  or in-phase  $\Delta V_{\parallel}$  and quadrature phase  $\Delta V_{\perp}$  components of the difference emf signals. We chose to record the later. In any case one can be obtained from the other as follows:  $\|\Delta V\| = \sqrt{\Delta V_{\parallel}^2 + \Delta V_{\perp}^2}$  and  $\theta = \arctan(\Delta V_{\perp}/\Delta V_{\parallel})$ . All the experimental results are given for a normalized intensity amplitude of  $1 \text{ A}$ .

For each measurement, a specific rod was mounted and fixed on the two extreme poles of experimental bench (see figure 4.15). ECFM was translated back and forth over this rod several times. Experiments with this system is very reproducible because the system is highly deterministic. Since ECFM is being used in a difference mode, the contribution of external noises is also minimized. In any case the sources of external noises were verified to be insignificant at these pulsation values.

For the range of pulsation used in these experiments,  $\delta < D$ . Therefore, the magnetic flux perturbation theory developed in section 3.2.2 was used to analyze and interpret the acquired data.

Figure 4.16a shows a typical demodulated in-phase difference emf  $\Delta V_{\parallel}$ . This kind of plot is also obtained for  $\Delta V_{\perp}$  and  $\|\Delta V\|$  signals. For the specific case in figure 4.16,  $\alpha = 0.3\%$  at  $\omega = 4712 \text{ rad/s}$  and  $U = 0.1 \text{ m/s}$  for figure 4.16a and 4.16c;  $U = e - 3 \text{ m/s}$  for figure 4.16b. The average magnetic flux  $\phi_{0,\perp}$  in the two-phase media is determined by integrating magnetic flux for a sufficiently large time at  $U \rightarrow 0$ . This was discussed in the previous chapter. Experimentally,  $\phi_0$  is measured as the average value of the signal over several grooves when there is very slow motion, typically  $U = 10^{-3} \text{ m/s}$ . This is shown in figure 4.16b. In this case, the Lorentz force can be neglected. In motion at constant  $U$ , the average value of the signal is shifted with a value proportional to  $\text{Re}_m$ . In presence of periodic voids ( $\alpha \neq 0\%$ ), this signal oscillates around this value. The amplitude of this oscillation gives  $\psi_\alpha$ .

To determine  $\psi_\alpha$ , the FFT spectrum density of the perturbations have to be obtained. The FFT spectrum of the time signal shown in figure 4.16 is displayed in figure 4.16c. We notice a prominent peak at  $\omega_\alpha$  whose magnitude gives  $\psi_\alpha$ . The subsequent harmonics were neglected in the flux perturbation expansion theory (equations 3.24-3.29). In the spectrum, the peak at  $2\omega_\alpha$  is negligible when compared to peak at  $\omega_\alpha$ . This result justifies the expansion till first harmonic in the Fourier series of the void fraction perturbation



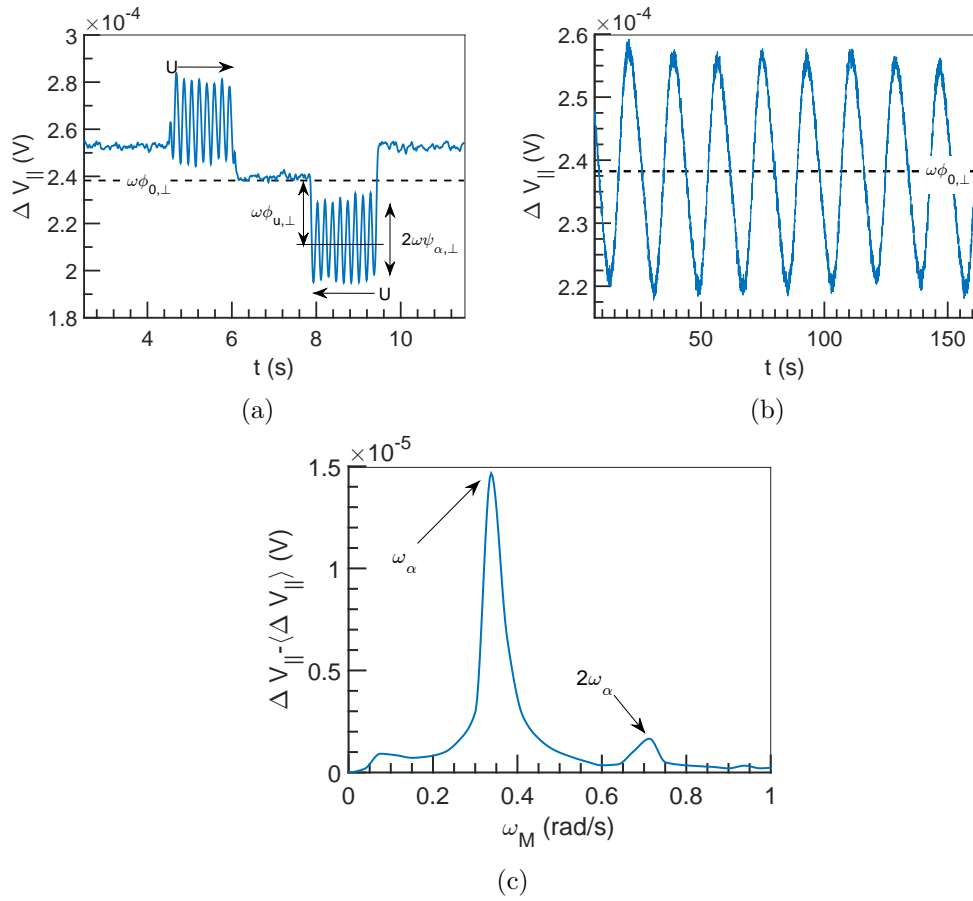


Figure 4.16: Typical demodulated voltage difference of the two secondary coils,  $\Delta V_{||}$  measured vs time for  $\alpha = 0.3\%$  at  $\omega = 4712$  rad/s and (a)  $U = 0.1$  m s $^{-1}$ , (b)  $U = 10^{-3}$  m s $^{-1}$ , (c) Corresponding FFT spectral density of fluctuations of  $\Delta V_{||}$  vs the modulating pulsation  $\omega_M$  (at  $U = 10^{-3}$  m s $^{-1}$ ).

(equations 3.25, 3.26).

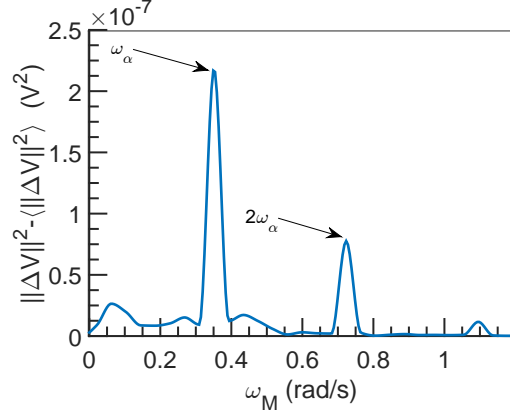


Figure 4.17: FFT spectral density of fluctuations of  $\|\Delta V\|^2$  vs the modulating pulsation  $\omega_M$  for  $\alpha = 6.9\%$  and  $U = 0.001$  m/s at 6283 rad/s.

The interpretation of  $\|\Delta V\|^2$  signal is slightly different according to the theory. An example of the FFT spectrum of the fluctuations of  $\|\Delta V\|^2$  signal is displayed in figure 4.17. This was obtained for  $\alpha = 6.9\%$  and  $U = 0.001$  m/s at 6283 rad/s. We notice two first prominent harmonic peaks in  $\omega_\alpha$ . The amplitude of the peak at  $3\omega_\alpha$  gives the first residue of equation (3.29). The amplitude of the first peak is  $\omega^2 A_1 = \omega^2 [2\langle\phi_0|\psi_\alpha\rangle + 2\text{Re}_m\langle\phi_u|\psi_\alpha\rangle]$  and the amplitude of the second peak is  $\omega^2 A_2 = \omega^2 \frac{\langle\psi_\alpha|\psi_\alpha\rangle}{2}$ . So the second peak in FFT of  $\|\Delta V\|^2$  can be used to calculate  $\sqrt{2A_2} = \langle\psi_\alpha|\psi_\alpha\rangle$ . The first peaks in FFT of  $\Delta V_{\parallel}$  and  $\Delta V_{\perp}$  are used to calculate  $\psi_{\alpha,\parallel}$  and  $\psi_{\alpha,\perp}$ . Then we obtain,  $\langle\psi_\alpha|\psi_\alpha\rangle = \psi_{\alpha,\parallel}^2 + \psi_{\alpha,\perp}^2$ . We have verified that the value of  $\langle\psi_\alpha|\psi_\alpha\rangle$  calculated from the two methods is the same.

In summary, the experimental results were treated by two approaches: first, the in-phase and quadrature phase components of  $\phi_0$ ,  $\phi_u$  and  $\phi_\alpha$  are directly measured from  $\Delta V(t)$ ; second,  $A_1$ ,  $A_2$  and  $\omega_\alpha$  were measured from the FFT of  $\|\Delta V\|^2$ .

We have checked that the two approaches are still valid for non-periodic void distribution as long as  $\omega_\alpha$  can be measured. This can be seen in figure 4.18 obtained for  $\omega = 6248$  rad/s and  $U = 10^{-2}$  m s $^{-1}$ . The dimensions for this rod is given in table 4.1. We observe in figure 4.18, that the intensity of the two first harmonic peaks decreases and the width increases, when the spatial distribution of the grooves widens. The mean separation  $\langle\lambda_\alpha\rangle$  between the grooves is 13 mm. However, considering that the first groove cannot be sensed by secondary coil, due to ECFM making a transition from support rod to the aluminium rod, the calculations using rest of the grooves gives  $\langle\lambda_\alpha\rangle = 11$  mm. At  $U = 10^{-2}$  m s $^{-1}$ , this gives  $\omega_\alpha = 2.59$  rad s $^{-1}$ . From the FFT spectrum density of  $\|\Delta V\|^2$  shown in figure 4.18c, we obtain  $\omega_\alpha = 2.59 \pm 0.35$  rad s $^{-1}$  and  $\omega_\alpha = 5.17 \pm 0.35$  rad s $^{-1}$ . This is the same as the theoretical  $\omega_\alpha$  within precision of measurement.

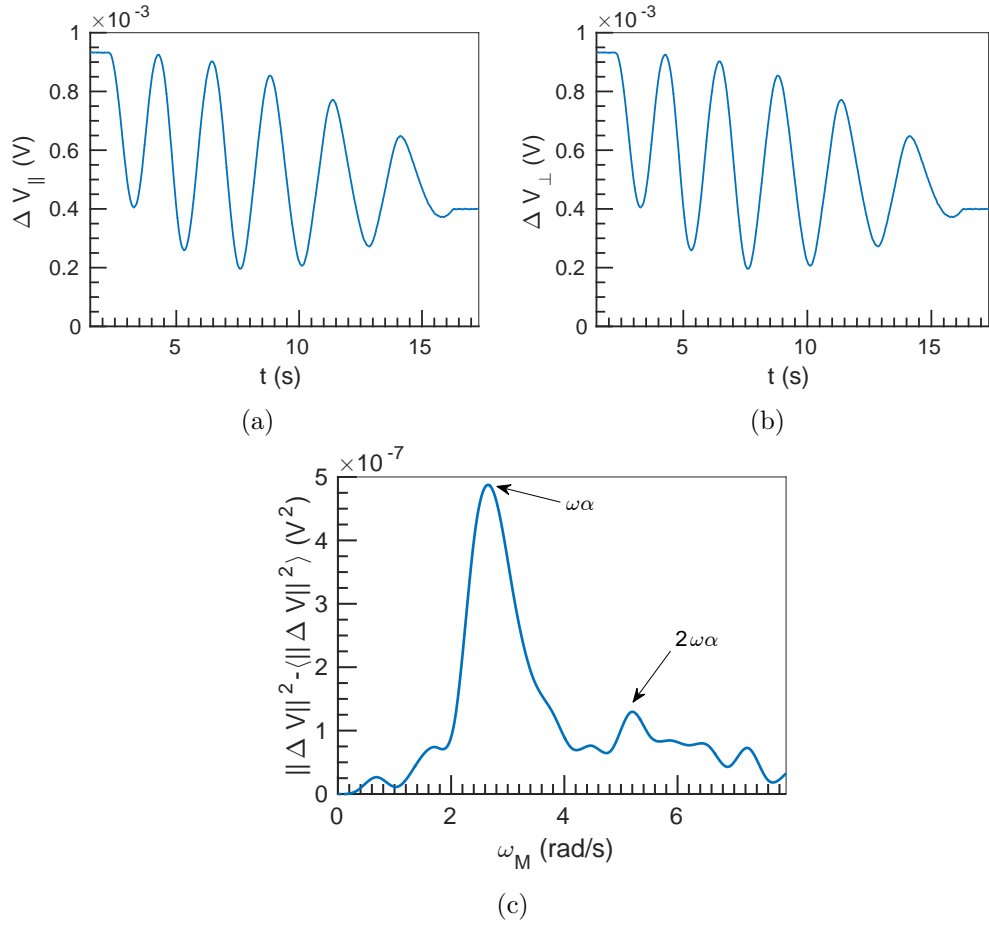


Figure 4.18: (a)  $\Delta V_{\parallel}$ , (b)  $\Delta V_{\perp}$  vs  $t(s)$  and  $\|\Delta V\|^2 - \langle \|\Delta V\|^2 \rangle$  vs  $\omega_M$  for rod with non-periodic void distribution at  $\omega = 6248$  rad/s and  $U = 10^{-2}$  m s<sup>-1</sup>.

## 4.2.2 Results

Since  $\delta < D$ , the results should be interpreted with the help of theory developed in section 3.2.2. Nevertheless, we wanted to test whether the theory which assumes small Faraday induction effects can still predict reasonably well some of the experimental effects. Therefore, we begin this section by interpretations of the experimental results in terms of the former theory.

### Interpretation based on Small Faraday induction theory

In section 3.2.1, under the assumption of small Faraday induction effects, we were able to split the terms which depend on  $\alpha$  and  $U$ . More precisely we predict that the effect of  $\alpha$  is on both the in-phase and quadrature phase components of difference flux. On the other hand, we predict that the effect of  $U$  is only on the in-phase flux. In our experiments, we were able to confirm the former but the later was found to be wrong, *i.e.*, contrary to expectations, the effect of  $U$  is on both the in-phase and quadrature phase signals. This is shown in figure 4.19. We see that both the components of the demodulated difference emf between the two secondary coils are sensitive to  $U$ .

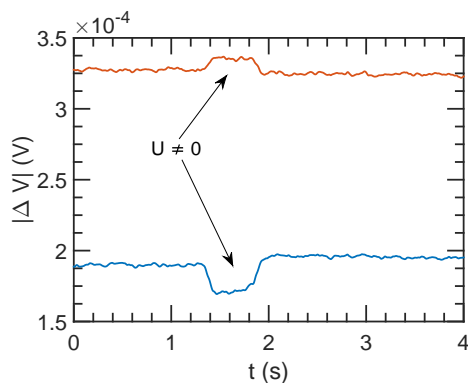


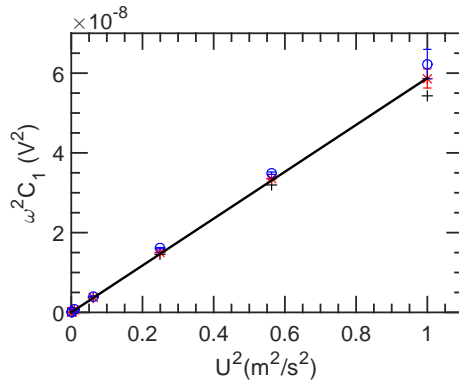
Figure 4.19:  $\Delta V_{||}$  (—) and  $\Delta V_{\perp}$  (—) for  $\alpha = 0\%$  at  $U = 0.1 \text{ m s}^{-1}$  and  $\omega = 3124 \text{ rad s}^{-1}$ .

The coefficients obtained in equation (3.21) also give the  $U$  and  $\alpha$  effects with the help of FFT spectrum.

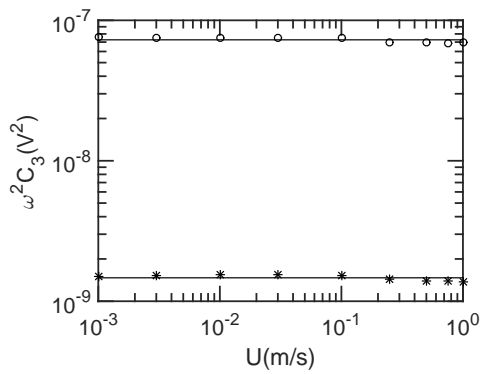
Since  $C_1 = 4U^2b^2 + \dots$ , we expect  $C_1$  to be linear in  $U^2$  upto the first term. This is shown in figure 4.20a. The other remarkable result is the validity of  $\alpha$  independence predicted by this expansion.

$\omega^2 C_3$  is plotted in figure 4.20b. Since  $C_3 = -2\omega^2 \delta a^2 \sin^2(\frac{\Delta\theta}{2})$ , we expect  $C_3$  to be linear in  $\alpha^2$  and independent of  $U$ . This later is also confirmed in figure 4.20b.

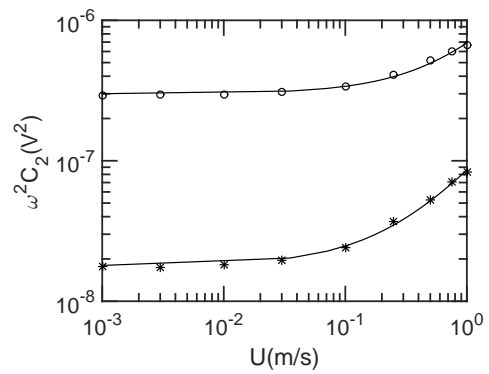
$\omega^2 C_2 = 8U^2 b \delta b \cos(\Delta\theta/2)$  vs  $U$  is plotted in figure 4.20c. A linear fitting of  $\omega^2 C_2$  vs  $U$  suggests  $C_2 \sim m \times U + \text{constant}$ . This is difficult to explain with this model. From the result for  $C_1$  we find that  $b$  is independent of  $U$  and  $\alpha$ . But the proposed model does not give functional dependence of  $\delta b$  on  $U$ . This shows the limitation of the theoretical model presented in section 3.2.1.



(a)



(b)



(c)

Figure 4.20: (a)  $\omega^2 C_1$  (V<sup>2</sup>) vs  $U^2$  (m<sup>2</sup> s<sup>-2</sup>), (b)  $\omega^2 C_3$  (V<sup>2</sup>) vs  $U$  (m s<sup>-1</sup>) and (c)  $\omega^2 C_2$  (V<sup>2</sup>) vs  $U$  (m s<sup>-1</sup>) for  $\alpha = 0\%$  (+),  $0.3\%$  (\*) and  $6.9\%$  (o) at  $\omega = 6248$  rad s<sup>-1</sup> and  $I = 400$  mA.

Failure of the small Faraday induction theory in predicting some experimental results, show that the assumption of small Faraday induction is no more valid. The existence of both in-phase and quadrature phase emf signals for  $\alpha = 0\%$  hints towards strong Faraday induction effects. In the next section, we test the theory presented in section 3.2.2 which takes into account of significant Faraday induction effects.

### Interpretation based on Significant Faraday induction theory

The failure of low induction based theory, in explaining the Lorentz force effects on both phases of difference emf and the linearity of first harmonic of  $||\Delta V||^2$  with  $U$  demonstrates its limitations. So we would now interpret the experimental results with the help of theory developed in 3.2.2, which is based on the assumption of strong Faraday induction effects.

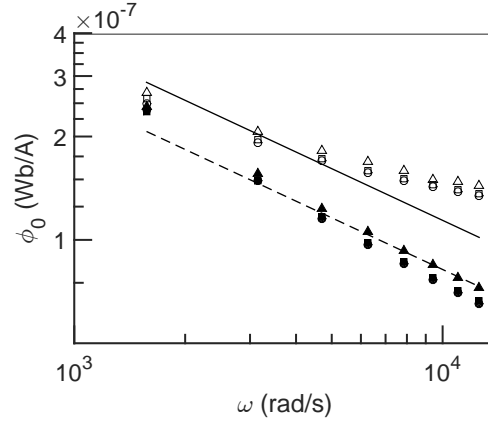


Figure 4.21:  $\phi_0$  vs  $\omega$  at  $U = 0.001 \text{ m s}^{-1}$  for  $\alpha = 0\%$  ( $\circ$ ,  $\bullet$ ),  $0.3\%$  ( $\square$ ,  $\blacksquare$ ),  $6.9\%$  ( $\triangle$ ,  $\blacktriangle$ ); where  $\phi_{0,\parallel}$  : unfilled symbols and  $\phi_{0,\perp}$  : filled symbols. Lines represent the power law in  $\omega^{-1/2}$ . Rod type: Grooves.

Figure 4.21 compares  $\phi_{0,\parallel}(\omega)$  and  $\phi_{0,\perp}(\omega)$  for  $\alpha = 0\%$ ,  $\alpha = 0.3\%$  and  $\alpha = 6.9\%$ . A similar plot for hole-type rods is shown in figure 4.22 for  $\alpha = 0.06\%$ ,  $\alpha = 0.22\%$ ,  $\alpha = 0.54\%$  and  $\alpha = 1.62\%$ . We observe that  $\phi_{0,\parallel}$  and  $\phi_{0,\perp}$  are weakly dependent on  $\alpha$ . Furthermore, the results show that  $\phi_{0,\parallel} > \phi_{0,\perp}$ , whatever  $\omega$ . The frequency dependence of  $\phi_{0,\perp}$  obeys to an approximate power law,  $\omega^{-1/2}$ . We observe that the deviation to this power law is larger at high pulsations. For  $\phi_{0,\parallel}$ , if the power law  $\omega^{-1/2}$  seems to be valid at low pulsations, the deviations are very large at higher pulsations.

As an example, figure 4.23 shows the pulsation dependence of  $\text{Re}_m \phi_{u,\parallel}$  and  $\text{Re}_m \phi_{u,\perp}$  at a constant velocity  $U = 1 \text{ m s}^{-1}$  for groove-type rods. A similar plot is shown in figure 4.24 for hole-type rods. We note that  $\text{Re}_m \phi_{u,\parallel} < \text{Re}_m \phi_{u,\perp}$ . These two fluxes exhibit two different power laws with pulsation,  $\text{Re}_m \phi_{u,\parallel} \sim \omega^{-1}$  and  $\text{Re}_m \phi_{u,\perp} \sim \omega^{-3/2}$ . The effect of  $\alpha$  on  $\phi_u$  can be neglected. We also notice a difference in magnitude between hole-type and groove-type rods. This suggests a geometrical dependence of  $\phi_u$  to voids.

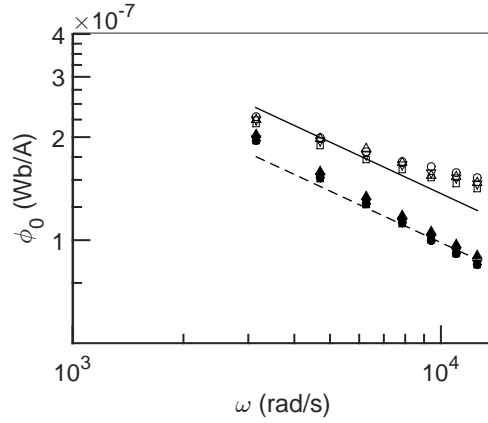


Figure 4.22:  $\phi_0$  vs  $\omega$  at  $U = 0.001 \text{ m s}^{-1}$  for  $\alpha = 0.06\%$  ( $\circ$ ,  $\bullet$ ),  $0.22\%$  ( $\square$ ,  $\blacksquare$ ),  $0.54\%$  ( $\nabla$ ,  $\blacktriangledown$ ),  $1.62\%$  ( $\triangle$ ,  $\blacktriangle$ ); where  $\phi_{0,\parallel}$ : unfilled symbols and  $\phi_{0,\perp}$ : filled symbols. Lines represent the power law in  $\omega^{-1/2}$ . Rod type: holes.

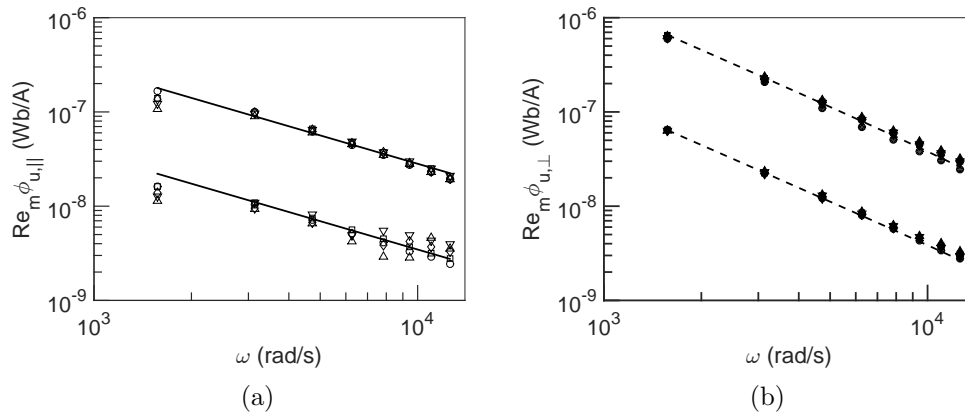


Figure 4.23:  $\text{Re}_m \phi_u$  vs  $\omega$  at  $U = 0.1$  and  $1 \text{ m s}^{-1}$  for  $\alpha = 0\%$  ( $\bullet$ ),  $0.3\%$  ( $\blacksquare$ ),  $2.0\%$  ( $\blacklozenge$ ),  $4.5\%$  ( $\blacktriangledown$ ),  $6.9\%$  ( $\blacktriangle$ ); (a)  $\text{Re}_m \phi_{u,\parallel}$ : unfilled symbols and (b)  $\text{Re}_m \phi_{u,\perp}$ : filled symbols. (—) represents  $\omega^{-1}$  and (---) represents  $\omega^{-3/2}$ . Rod type: grooves.

However, a more plausible reason is a possible difference in rod to coil alignment in the two experimental set ups.

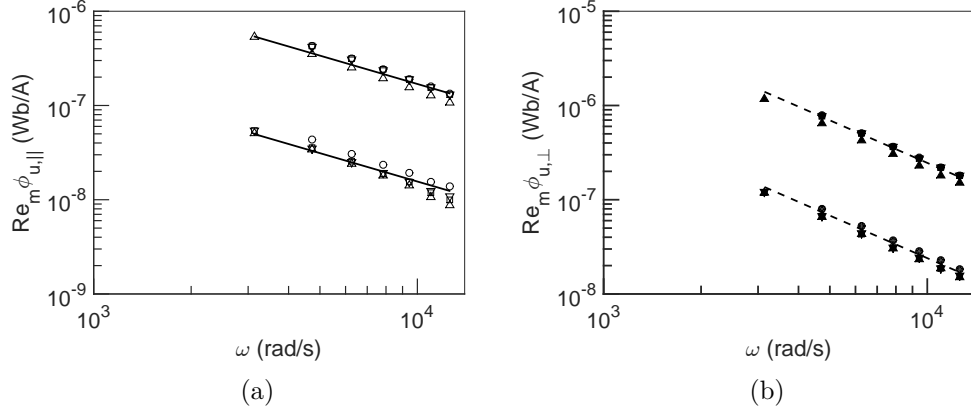


Figure 4.24:  $\text{Re}_m \phi_u$  vs  $\omega$  at  $U = 0.1$  and  $1 \text{ m s}^{-1}$  for  $\alpha = 0.06\%$  ( $\circ, \bullet$ ),  $0.22\%$  ( $\square, \blacksquare$ ),  $0.54\%$  ( $\nabla, \blacktriangledown$ ),  $1.62\%$  ( $\triangle, \blacktriangle$ ); (a)  $\text{Re}_m \phi_{u,\parallel}$  : unfilled symbols and (b)  $\text{Re}_m \phi_{u,\perp}$  : filled symbols. (—) represents  $\omega^{-1}$  and (---) represents  $\omega^{-3/2}$ . Rod type: holes.

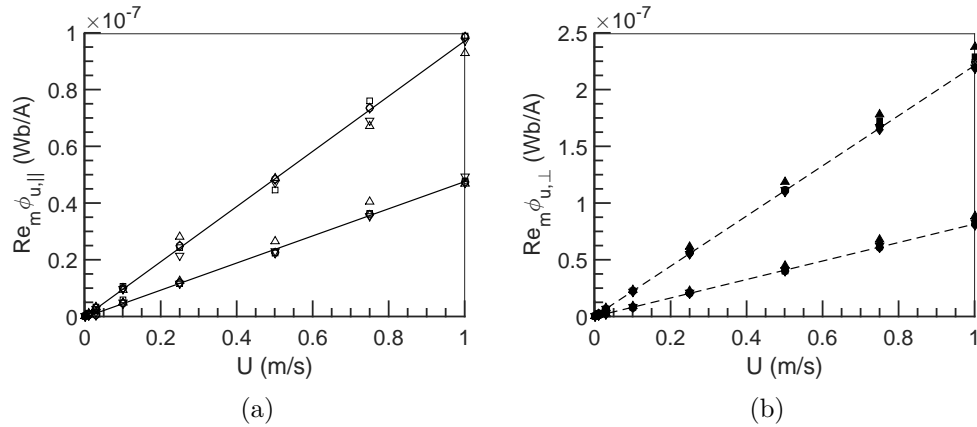


Figure 4.25:  $\text{Re}_m \phi_u$  vs  $U$  at  $\omega = 3142$  and  $6284 \text{ rad s}^{-1}$  for  $\alpha = 0.0\%$  ( $\bullet$ ),  $0.3\%$  ( $\blacksquare$ ),  $2.0\%$  ( $\blacklozenge$ ),  $4.5\%$  ( $\blacktriangledown$ ),  $6.9\%$  ( $\blacktriangle$ ); (a)  $\text{Re}_m \phi_{u,\parallel}$  : unfilled symbols and (b)  $\text{Re}_m \phi_{u,\perp}$  : filled symbols. Rod type: grooves.

The linearity of the two components of  $\text{Re}_m \phi_u$  with velocity at constant pulsations  $\omega = 3142$  and  $6284 \text{ rad s}^{-1}$  is verified in figure 4.25 for groove-type rods. For the hole-type rods, a similar plot is shown in figure 4.26 at constant pulsations  $\omega = 4713$  and  $6284 \text{ rad s}^{-1}$ . This result has also been confirmed for other pulsations in the considered range of this study. We verified that the slope  $\text{Re}_m \phi_{u,\parallel}(U)$  and  $\text{Re}_m \phi_{u,\perp}(U)$  are independent of  $\alpha$ .



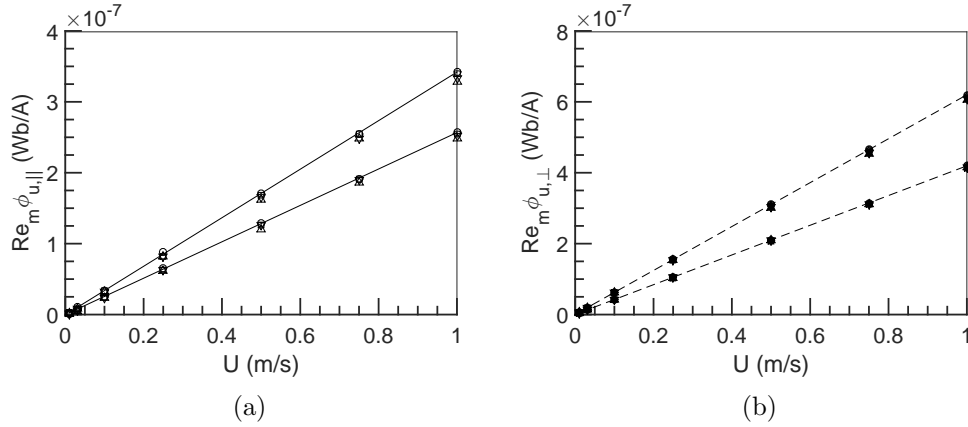


Figure 4.26:  $\text{Re}_m \phi_u$  vs  $U$  at  $\omega = 4713$  and  $6284 \text{ rad s}^{-1}$  for  $\alpha = 0.06\%$  ( $\circ, \bullet$ ),  $0.22\%$  ( $\square, \blacksquare$ ),  $0.54\%$  ( $\nabla, \blacktriangledown$ ),  $1.62\%$  ( $\triangle, \blacktriangle$ ); (a)  $\text{Re}_m \phi_{u,\parallel}$  : unfilled symbols and (b)  $\text{Re}_m \phi_{u,\perp}$  : filled symbols. Rod type: holes.

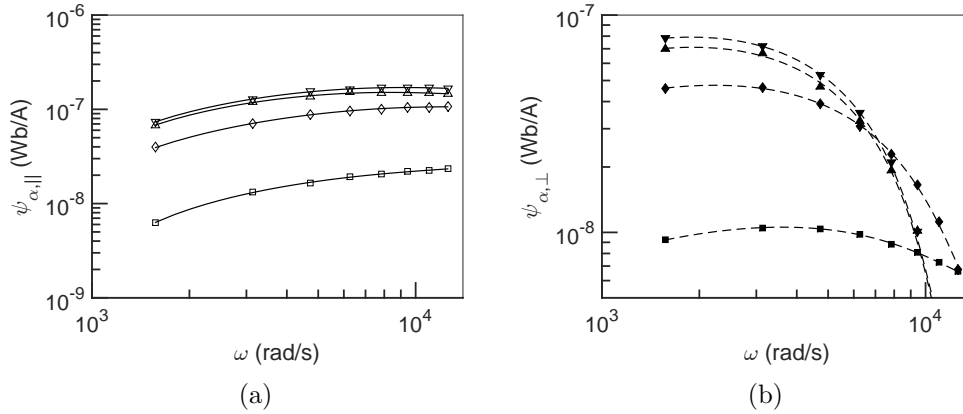


Figure 4.27: (a)  $\psi_{\alpha,\parallel}$  and (b)  $\psi_{\alpha,\perp}$  vs  $\omega$  at  $U = 1 \text{ m s}^{-1}$  for  $\alpha = 0.0\%$  ( $\bullet$ ),  $0.3\%$  ( $\blacksquare$ ),  $2.0\%$  ( $\blacklozenge$ ),  $4.5\%$  ( $\blacktriangledown$ ),  $6.9\%$  ( $\blacktriangle$ ). Rod type: grooves.

The study of the pulsation dependence of  $\psi_\alpha$  for different  $\alpha$  values at constant velocity, have shown a non-power law behavior for the two components  $\psi_{\alpha,\parallel}$  and  $\psi_{\alpha,\perp}$ . Figure 4.27a and 4.27b display  $\psi_\alpha$  vs  $\omega$  at  $U = 1 \text{ m s}^{-1}$  for groove type rods. A similar plot is also shown for hole-type rods in figure 4.28a and 4.28b.

First, we observe that  $\psi_\alpha(\omega)$  curves are function of  $\alpha$ . The variations with pulsation of the two components at constant  $\alpha$  are really different. All the curves for  $\psi_{\alpha,\perp}(\omega)$  collapse to a vertical asymptote at about  $12\,600 \text{ rad s}^{-1}$ . Consequently,  $\psi_{\alpha,\perp}$  tends to zero beyond this critical pulsation. On the other hand,  $\psi_{\alpha,\parallel}(\omega)$  at a constant  $\alpha$  increases with the pulsation and reaches a plateau value at high pulsation. Hence for  $\omega > 7000 \text{ rad s}^{-1}$ ,

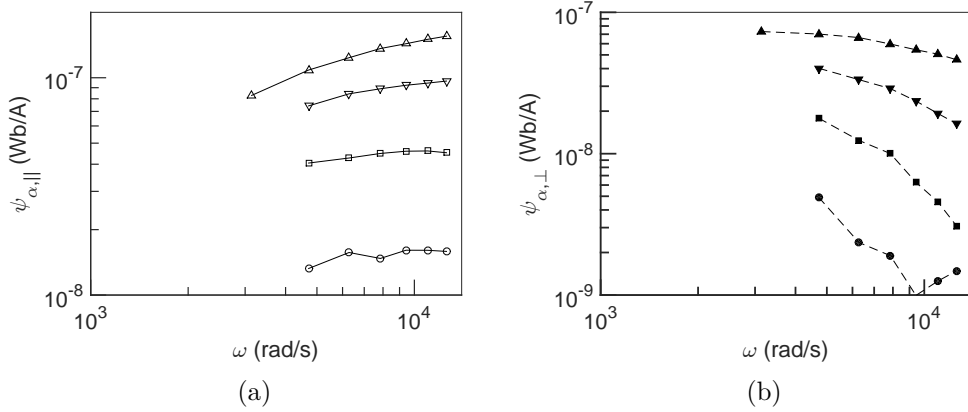


Figure 4.28: (a)  $\psi_{\alpha,||}$  and (b)  $\psi_{\alpha,\perp}$  vs  $\omega$  at  $U = 1 \text{ m s}^{-1}$  for  $\alpha = 0.06\%$  ( $\circ$ ,  $\bullet$ ),  $0.22\%$  ( $\square$ ,  $\blacksquare$ ),  $0.54\%$  ( $\nabla$ ,  $\blacktriangledown$ ),  $1.62\%$  ( $\triangle$ ,  $\blacktriangle$ ). Rod type: holes.

$\psi_{\alpha,||}$  is independent of  $\omega$ . The two  $\psi_\alpha$  components are on the same order of magnitude at low pulsations and differ by more than one decade at high pulsation. This behavior is really different than those of  $\phi_0$  and  $\text{Re}_m \phi_u$ .

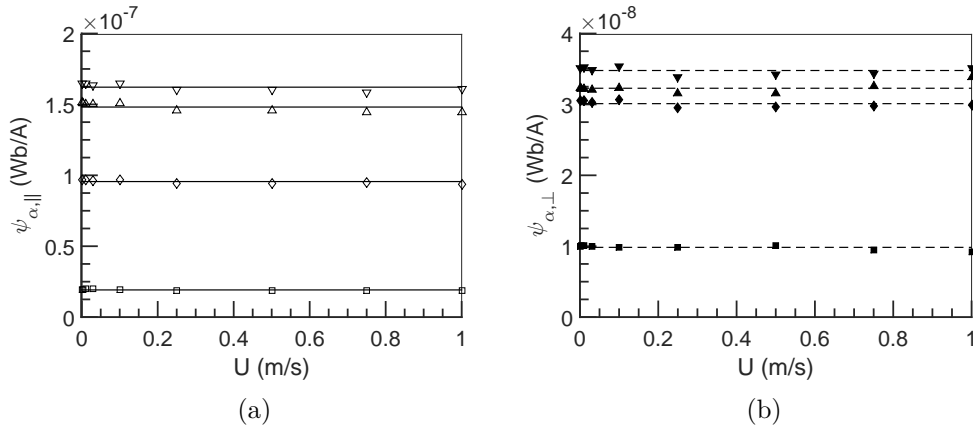


Figure 4.29: (a)  $\psi_{\alpha,||}$  and (b)  $\psi_{\alpha,\perp}$  vs  $U$  at  $\omega = 6248 \text{ rad s}^{-1}$  for  $\alpha = 0.0\%$  ( $\circ$ ),  $0.3\%$  ( $\square$ ),  $2.0\%$  ( $\diamond$ ),  $4.5\%$  ( $\nabla$ ),  $6.9\%$  ( $\triangle$ ). Rod type: grooves.

The velocity dependence of  $\psi_\alpha$  are presented in figures 4.29a and 4.29b for groove-type rods and in figures 4.30a and 4.30b for hole-type rods. For both components of  $\psi_\alpha$ , we observe the remarkable result that  $\psi_\alpha$  is independent of  $U$ .

Combining the results obtained with holes and grooves geometries, the plot of  $|\psi_\alpha(\alpha)|$  at a constant  $U$  and  $\omega$  is given in Fig 4.31. We observe that the results obtained with both geometries are consistent. This is remarkable because it appears that  $\langle \psi_\alpha | \psi_\alpha \rangle$  depends only on  $\alpha$  values and not on the geometry of the voids. The experiments show that  $\psi_\alpha \sim \alpha$  for  $\alpha < 4\%$  and saturates for higher values in the range of  $\alpha$  studied. This

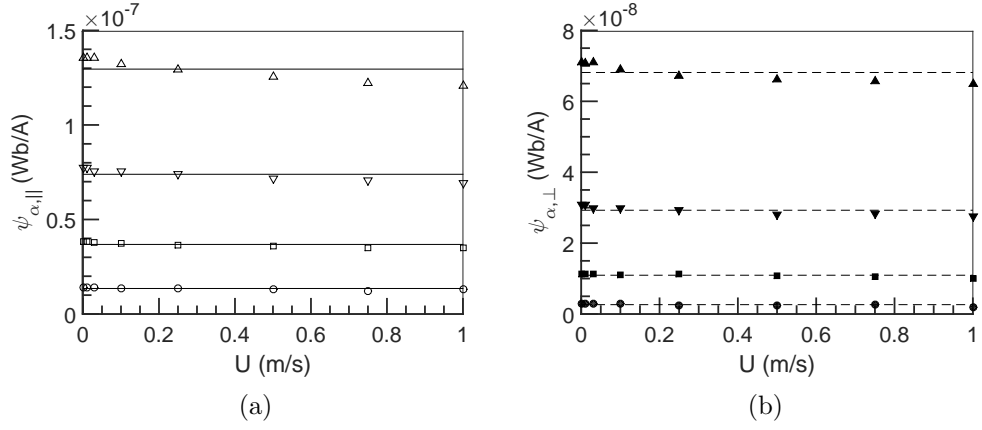


Figure 4.30: (a)  $\psi_{\alpha,||}$  and (b)  $\psi_{\alpha,\perp}$  vs  $U$  at  $\omega = 6248 \text{ rad s}^{-1}$  for  $\alpha = 0.06\%$  ( $\circ, \bullet$ ),  $0.22\%$  ( $\square, \blacksquare$ ),  $0.54\%$  ( $\nabla, \blacktriangledown$ ),  $1.62\%$  ( $\triangle, \blacktriangle$ ). Rod type: holes.

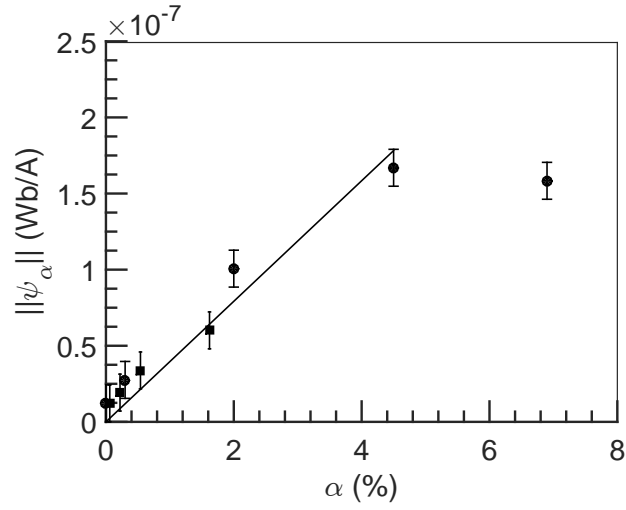


Figure 4.31:  $\|\psi_\alpha\| = \langle \psi_\alpha | \psi_\alpha \rangle^{1/2}$  vs  $\alpha$  at  $\omega = 6280 \text{ rad s}^{-1}$ .  $\bullet$  : grooves,  $\blacksquare$  : holes.

result is in agreement with literature where the authors obtained a similar curve for the fluctuations of emf signal.[44]

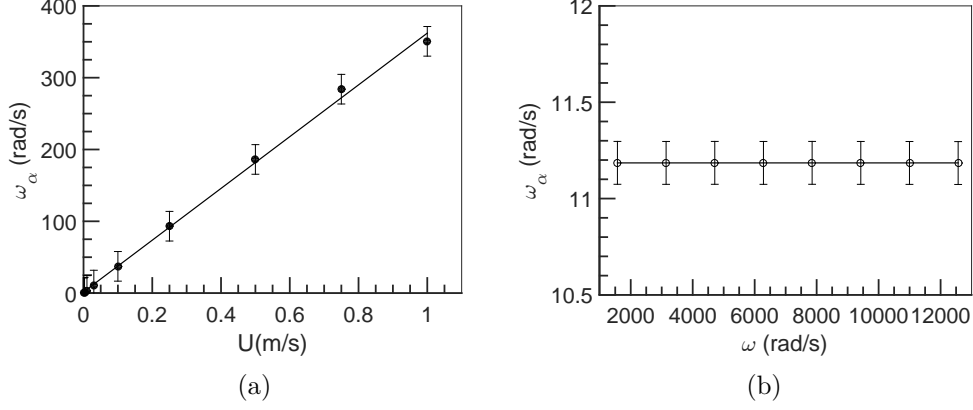


Figure 4.32: (a)  $\omega_\alpha$  vs  $U$  at  $\omega = 6280 \text{ rad s}^{-1}$ , (b)  $\omega_\alpha$  vs  $\omega$  at  $U = 3 \times 10^{-2} \text{ m s}^{-1}$  for  $\alpha = 6.9\%$ .

In order to study the coupling between the Lorentz force and the Faraday effects, we analyze the Fourier transform of  $||\Delta V||^2$ . For all cases, we measured  $\omega_\alpha$  and we verified that  $\omega_\alpha = k_\alpha U$  at a constant pulsation, in agreement with our model (figure 4.32). Furthermore, we check that  $\omega_\alpha$  is independent of  $\omega$  at constant  $U$ .

In figure 4.33 for groove-type rod and figure 4.34 for hole-type rod,  $A_1$  is plotted with different  $\alpha$  at  $\omega = 6283 \text{ rad s}^{-1}$ . As predicted, we observe that  $A_1$  is a linear function of the velocity. The intercept with the vertical axis gives  $\langle \phi_0 | \psi_\alpha \rangle$  which increases linearly with  $\alpha$  at low  $\alpha$ . The slope is  $\langle \phi_u | \psi_\alpha \rangle$ . We note that the coupling between  $U$  and  $\alpha$  increases with  $\alpha$  and saturates as observed previously for  $\psi_\alpha$ . This last effect has been confirmed by Fourier analysis and figures 4.35 and 4.36 show the independence of  $\langle \psi_\alpha | \psi_\alpha \rangle$  with velocity. For all the experiments the values of fluxes obtained by direct processing and by Fourier transform are similar.

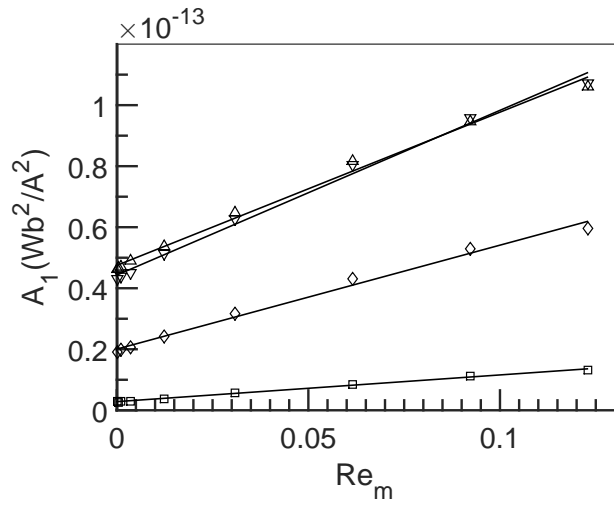


Figure 4.33:  $A_1(\text{Wb}^2 \text{A}^{-2}) = 2\langle\phi_0|\psi_\alpha\rangle + 2\text{Re}_m\langle\phi_u|\psi_\alpha\rangle$  vs  $\text{Re}_m$  for  $\alpha = 0.0\%$ (●),  $0.3\%$ (■),  $2.0\%$ (◆),  $4.5\%$ (▼),  $6.9\%$ (▲),  $\omega = 6280 \text{ rad s}^{-1}$ . Rod type: grooves.

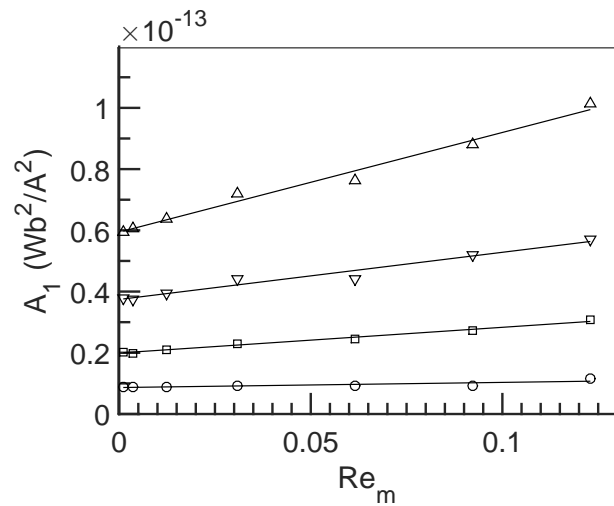


Figure 4.34:  $A_1(\text{Wb}^2 \text{A}^{-2}) = 2\langle\phi_0|\psi_\alpha\rangle + 2\text{Re}_m\langle\phi_u|\psi_\alpha\rangle$  vs  $\text{Re}_m$  for  $\alpha = 0.06\%$ (○, ●),  $0.22\%$ (□, ■),  $0.54\%$ (▽, ▼),  $1.62\%$ (△, ▲),  $\omega = 6280 \text{ rad s}^{-1}$ . Rod type: holes.

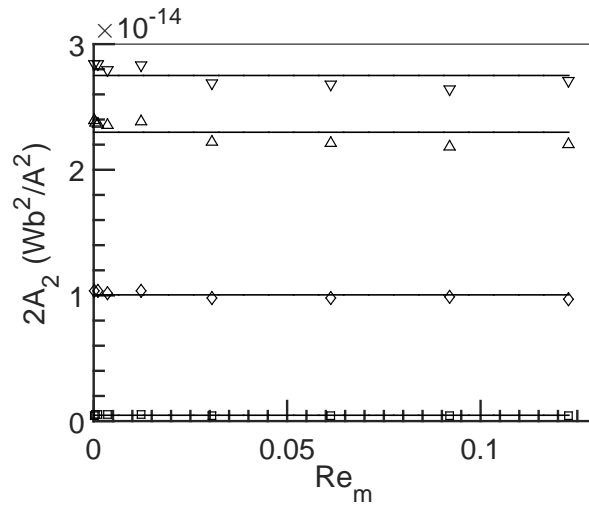


Figure 4.35:  $2A_2(\text{Wb}^2 \text{A}^{-2}) = \langle \psi_\alpha | \psi_\alpha \rangle$  vs  $\text{Re}_m$  for  $\alpha = 0.0\%$  (●),  $0.3\%$  (■),  $2.0\%$  (◆),  $4.5\%$  (▼),  $6.9\%$  (▲),  $\omega = 6280 \text{ rad s}^{-1}$ . Rod type: grooves.

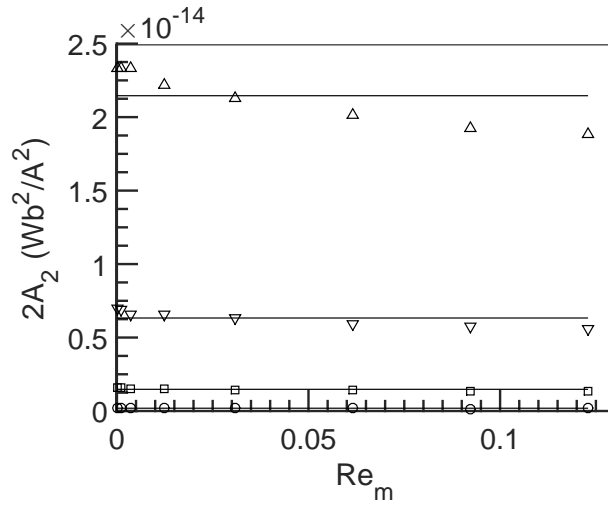


Figure 4.36:  $2A_2(\text{Wb}^2 \text{A}^{-2}) = \langle \psi_\alpha | \psi_\alpha \rangle$  vs  $\text{Re}_m$  for  $\alpha = 0.06\%$  (○, ●),  $0.22\%$  (□, ■),  $0.54\%$  (▼, ▼),  $1.62\%$  (△, ▲),  $\omega = 6280 \text{ rad s}^{-1}$ . Rod type: holes.

### 4.2.3 Discussions

The objective of this section is to discuss the experimental results presented in the previous section, with the help of scaling laws based on Maxwell's equations.

The analyses of all the results given in the previous section, show clearly the validity of the magnetic flux perturbation approach presented in section 3.2.2. This approach takes into account of the coupling between Faraday induction and the Lorentz force effects when Faraday induction effects are significant. This model was used to characterize  $U$  and  $\alpha$  effects in all the experimental results given in the previous section. It is remarkable that the theory which was developed on assumptions of  $\text{Re}_m \rightarrow 0$  and  $\alpha \rightarrow 0$  is also valid for finite  $\text{Re}_m$  and  $\alpha$ . Also, the sensitivity is good enough to get  $\alpha$  of order 0.06%. The experimental results were obtained for two void geometries: grooves and holes. The property that the void induced perturbation in magnetic flux is independent of the void geometry, confirms the validity and robustness of the model at first order.

All the experimental FFT spectra for in-phase and quadrature phase signals are characterized by first harmonic peak which justifies the development till first harmonic for  $\psi_\alpha$ .

In the model, the choice of the characteristic length is determining. When  $\delta < D$ , the natural characteristic length is  $\delta$ . For example, for the electric field  $E$ , the application of the Stoke's circulation theorem in flow cross-section inside ECFM, gives

$$\begin{aligned}
 \nabla \times \vec{E} &= -\frac{\partial \vec{B}}{\partial t}, \\
 \int_S \nabla \times \vec{E} \cdot d\vec{s} &= -\int_S \frac{\partial \vec{B} \cdot \vec{s}}{\partial t}, \\
 \int_C \nabla \times \vec{E} \cdot d\vec{l} &= -\int_S \frac{\partial \vec{B} \cdot \vec{s}}{\partial t}, \\
 E\pi D &\sim \omega\pi D\delta B, \\
 \frac{E}{\delta} &\sim \omega B.
 \end{aligned} \tag{4.4}$$

This relation suggests that the correct length scale is  $\delta$  rather than  $D$ . The same characteristic length also occurs in the diffusion equation for  $\vec{B}$ . Indeed, considering the magnetic induction equation (1.6), we obtain

$$\begin{aligned}
 \frac{\partial B}{\partial t} &= \frac{1}{\mu_0\sigma} \nabla^2 B \\
 \omega\mu_0\sigma B &= \frac{1}{L^2} B \implies L^2 \sim \frac{1}{\omega\mu_0\sigma} \implies L \sim \delta
 \end{aligned}$$

**Scaling relations for first order magnetic fields in absence of motion** Assume a static single-phase medium. The AC current  $I(t)$  in the ECFM primary coil produces zero order magnetic field in this medium by Biot Savart's law.

$$B_{0,\parallel} = \frac{\mu_0}{4\pi} \int \frac{Idl}{|r|^2} \quad (4.5)$$

The corresponding zero order electric field in the medium is:

$$\begin{aligned} \nabla \times E_0 &= \frac{-\partial B_{0,\parallel}}{\partial t} \\ E_{0,\perp} &\sim -\omega\delta B_{0,\parallel} \end{aligned}$$

Note the phase change in  $E$ . This electric field drives eddy currents as

$$J_{0,\perp} = -\sigma E_{0,\perp} \sim -\sigma\omega\delta B_{0,\parallel}$$

Which in turn would create the magnetic field at first order as

$$\begin{aligned} \nabla \times B'_{0,\perp} &= \mu_0 J_{0,\perp} \sim -\mu_0\sigma\omega\delta B_{0,\parallel} \\ B'_{0,\perp} &\sim -\mu_0\sigma\omega\delta^2 B_{0,\parallel} \implies B'_{0,\perp} \sim B_{0,\parallel} \end{aligned} \quad (4.6)$$

This means that the total magnetic flux for no motion and no void case, where only Faraday induction plays a role, is given at first order by

$$B_0^{Total} \sim B_{0,\parallel} + B'_{0,\perp} \quad (4.7)$$

Since  $B'_{0,\perp} \sim B_{0,\parallel}$ , the order of magnitude of the first order magnetic fields created by the zero order Faraday induction eddy currents is same. This also means that the corresponding in-phase and quadrature phase fluxes will be of same order of magnitude. These results were validated experimentally.  $\phi_{0,\parallel}$  is of the same order of magnitude as  $\phi_{0,\perp}$  in figures 4.21 and 4.22.

The total flux at first order for no motion case is given by

$$\phi_0^{Total} = \int B_0^{Total} dS \sim \pi\delta D B_0^{Total} \implies \phi_0^{Total} \sim \delta = \omega^{-1/2} \quad (4.8)$$

Here, the effective surface for the integration of the flux at first order was taken as  $\pi D\delta$ . Equation (4.8) is valid on the assumption that the average magnetic field in  $\delta$  is on a same order at all frequencies. This was verified with the help of a numerical simulation in COMSOL<sup>®</sup> (see figure 4.37). Equation (4.8) explains the tendency found in figures 4.21 and 4.22 that  $\phi_0 \sim \omega^{-1/2}$ . It also explains why we found  $\phi_{0,\parallel}/\phi_{0,\perp} \sim \mathcal{O}(1)$  in the experiments.



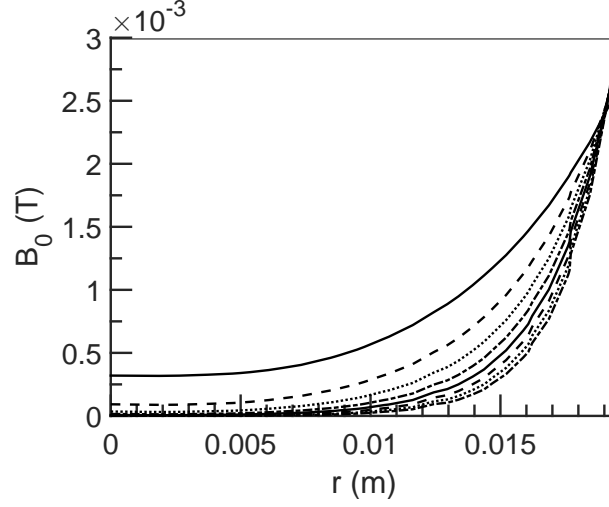


Figure 4.37: Numerical simulation for  $\vec{B}_0$ , for  $\omega$  in the range  $\omega = 1571$  to  $12\,566$   $\text{rad s}^{-1}$ ,  $\alpha = 0\%$  at  $U = 0$  m/s. The radius of the flow cross-section is  $R = 19.25$  mm.

**Scaling relations for first order magnetic fields in presence of motion** Assume again a single-phase medium in motion with mean velocity  $U$  (plug flow). The direct magnetic field and the magnetic field of Faraday induction induced eddy currents have been analyzed. Now, we analyze the magnetic fields of eddy currents due to Lorentz force effects. For the Lorentz force induced eddy currents, we follow a similar procedure. In the presence of the external magnetic field given by equation (4.5), the Lorentz force induced eddy currents are induced as,

$$J_{u,\parallel} \sim \sigma U B_{0,\parallel}$$

These eddy currents produce their own magnetic field as

$$\begin{aligned} \nabla \times B_{u,\parallel} &= \mu_0 J_{u,\parallel} \sim -\mu_0 \sigma U B_{0,\parallel} \\ B_{u,\parallel} &\sim -\mu_0 \sigma U \delta B_{0,\parallel} \implies B_{u,\parallel} \sim \delta \end{aligned}$$

The corresponding magnetic flux is

$$\text{Re}_m \phi_{u,\parallel} = \int B_{u,\parallel} dS \sim \pi \delta D B_{u,\parallel} \sim -\pi \delta D \mu_0 \sigma U \delta B_{0,\parallel} \implies \text{Re}_m \phi_{u,\parallel} \sim \delta^2 = \omega^{-1} \quad (4.9)$$

This explains the experimental trend found in figure 4.23a and 4.24a that  $\text{Re}_m \phi_{u,\parallel} \sim \omega^{-1}$ . Equation (4.9) also confirms the linearity of  $\text{Re}_m \phi_{u,\parallel}$  with  $U$  found in figures 4.25a and 4.26a. We also find that  $B_{u,\parallel}/B_{0,\parallel} \sim \text{Re}_m$ .

Since,  $B'_{0,\perp}$  and  $B_{0,\parallel}$  in equation (4.7) are of the same order in magnitude,  $B'_{0,\perp}$  will also produce Lorentz force induced eddy currents of comparable magnitude. In this case

we would have,

$$J_{u,\perp} \sim \sigma U B'_{0,\perp}$$

These eddy currents produce their own magnetic field as

$$\begin{aligned} \nabla \times B_{u,\perp} &= \mu_0 J_{u,\perp} \sim -\mu_0 \sigma U B_{0,\perp} \\ B_{u,\perp} &\sim -\mu_0 \sigma U \delta B'_{0,\perp} \implies B_{u,\perp} \sim \delta \end{aligned}$$

The corresponding magnetic flux is

$$\text{Re}_m \phi_{u,\perp} = \int B_{u,\perp} dS = \pi \delta D B_{u,\perp} \sim -\pi \delta D \mu_0 \sigma U \delta B'_{0,\perp} \implies \text{Re}_m \phi_{u,\perp} \sim \delta^2 = \omega^{-1} \quad (4.10)$$

Firstly, we confirm the linearity of  $\text{Re}_m \phi_u$  with  $U$  as found in figures 4.25b and 4.26b. But equation (4.10) fails to explain the experimental trend found in figure 4.23b and 4.24b that  $\text{Re}_m \phi_{u,\parallel} \sim \omega^{-3/2}$ . To this end we suspect the contribution of other terms in series expansion for Lorentz force and Faraday induction induced magnetic fields. The ratio of equation 4.9 and 4.10 is  $B_{0,\parallel}/B'_{0,\perp}$ , which is  $\mathcal{O}(1)$ . Therefore, we find that  $\phi_{u,\parallel}/\phi_{u,\perp} \sim \mathcal{O}(1)$ , *i.e.*,  $\text{Re}_m \phi_{u,\parallel}$  and  $\text{Re}_m \phi_{u,\perp}$  are of same order of magnitudes. This is confirmed by the experimental result presented in figures 4.23 – 4.26. These results point out a strong coupling between Faraday induction and Lorentz force effects.

The analyses based on Maxwell's equations at first order, predict well the ratio of in-phase and quadrature-phase components in terms of orders of magnitudes. But this analysis cannot predict the exact ratio of the two components.

**Scaling relations for first order magnetic fields in presence of void** Assume a static two-phase medium containing voids. For small  $\alpha$  values, the effective electrical conductivity of the two-phase medium can be obtained by a Taylor's expansion,  $\sigma = \sigma_0 + \sigma' \alpha + \sigma'' \alpha^2 + \dots \approx \sigma_0 + \sigma' \alpha$ . Since the two-phase medium is static, we use the results derived for Faraday induction eddy currents. Taylor expansion for  $\sigma$  and equation (4.6) gives,  $\psi_\alpha \sim \alpha$ . This linearity was observed experimentally in figure 4.31, for  $\alpha \lesssim 4\%$ . For groove depth smaller than  $\delta$  and for small  $\alpha$  values

$$\alpha = \frac{\pi D d_g l_g}{\pi D \delta \lambda_\alpha} \sim \frac{1}{\delta} \quad (4.11)$$

This means that  $\alpha$  scales as  $1/\delta$ . From equation (4.8), we know that  $\psi_\alpha \sim \delta$ . Combining the two relations we obtain,  $\psi_\alpha \sim \alpha \delta \sim (1/\delta) \delta = \delta^0 \sim \omega^0$ . This relation yields to a pulsation independence of  $\psi_\alpha$ . This was derived on the assumption of  $\delta > d_g$ , *i.e.*  $\psi_\alpha \sim \omega^0$  relation is confirmed experimentally in figures 4.27 and 4.28 at small pulsations. This does not explain the vertical asymptote for  $\psi_{\alpha,\perp}$  at high pulsations.

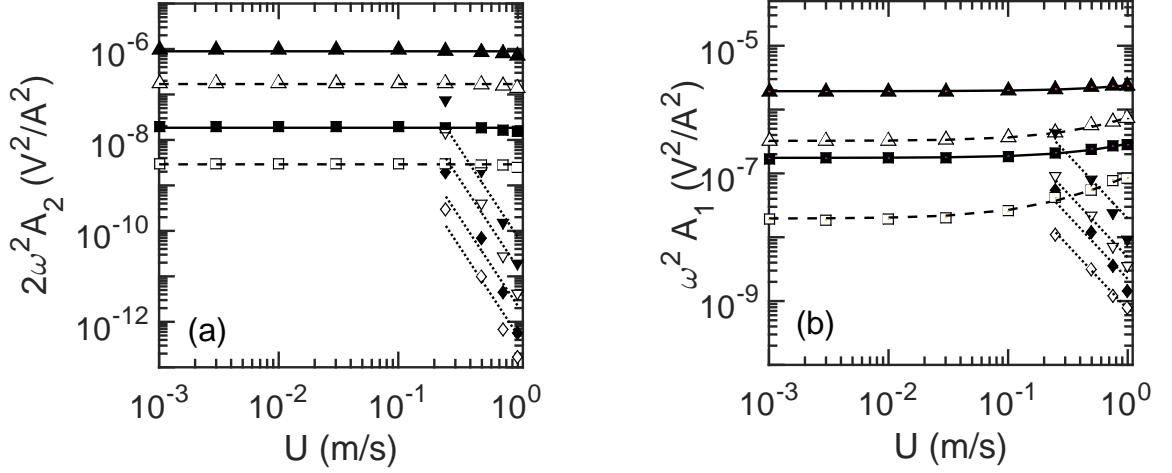


Figure 4.38: Amplitude of the second (a) and first (b) peaks of the spectral density of  $\|\Delta V\|^2$  vs velocity at 3142 rad/s (unfilled markers) and 6283 rad/s (filled markers):  $\alpha = 0.3\%$  ( $\square, \blacksquare$ ) and ( $\diamond, \blacklozenge$ ) with low pass filter 24 dB/oct;  $\alpha = 6.9\%$  ( $\triangle, \blacktriangle$ ) and ( $\nabla, \blacktriangledown$ ) with low pass filter 24 dB/oct.

At last we verify, the consistency of  $\psi_\alpha$  dynamics on  $A_1$  and  $A_2$ . We used a low pass filter at a cut off frequency  $\omega_c = 42.7$  rad/s. This filter is characterized by an attenuation of 24 dB/oct in signal intensity. Since  $\omega_\alpha \sim U$ , the corresponding critical velocity is around  $U_c \sim 10^{-1}$  m/s. After  $U_c$ , the  $A_1$  and  $A_2$  values are supposed to decrease in  $1/U^2$  and  $1/U^4$ , respectively. Figure 4.38 show that the experimental data verify the expected dynamics.

The scaling laws presented so far do not explain some effects find in the experiments.  $\phi_{0,\parallel}$  deviates from  $\omega^{-1/2}$  trend at high pulsations. This is because of strong Faraday induction and subsequent perturbation of imposed  $\phi_{0,\parallel}$  by higher order eddy currents.  $\phi_{u,\perp}$  does not follow  $\omega^{-1}$  law as derived here, instead it varies with pulsation as  $\omega^{-3/2}$ . This would happen when the magnetic fields of both Faraday induction induced eddy currents and Lorentz force induced eddy currents are significant. And clearly, the characteristic length of the magnetic flux and that of the flow are not sufficiently separated ( $\delta \lesssim D$ ). The coupling effects between  $\alpha$  and  $U$  effects are strong as evidenced by  $A_1$  plots in figures 4.33 and 4.34. We recall that  $\omega^2 A_1$  is the first harmonic in the FFT spectrum of squared norm of the difference emf signal between  $S_1$  and  $S_2$ . Even if the coupling effects are strong, we were able to separate  $U$  and  $\alpha$  effects because  $\phi_u$  is independent of  $\alpha$  and  $\psi_\alpha$  is independent of  $U$  at first order. This is valid only for small  $\text{Re}_m$  and  $\alpha$  values. We find in figures 4.25 and 4.26, that the DC shift in the demodulated difference emf signal is linear in  $U$  and independent of  $\alpha$ , providing the flowmeter aspect of ECFM for two-phase liquid metal flow applications. On the other hand, in figures 4.29, 4.30, 4.35 and 4.36, we observe  $U$  independence of  $\alpha$  modulation in the ECFM signal. In addition, the linear trend of this signal with  $\alpha$  in figure 4.31 ensures the void volume

fraction measurement in two-phase liquid metal flow applications with flux distortion techniques. Experimentally, we have verified these results in the range  $0 < \text{Re}_m < 0.12$  and  $0.06\% < \alpha \leq 6.9\%$ .

### 4.3 Lissajous ellipse fitting approach

#### 4.3.1 Methodology

The experimental set-up for these experiments were slightly different than the one used for the results in previous section. Only four aluminium rods were used,  $\alpha = 0\%$ ,  $0.3\%$ ,  $6.9\%$  and a rod with a single groove. All the rods were of groove-type. Their specifications can be found in table 4.1. The ECFM was used in a 3 coil configuration:  $P$ ,  $S_1$  and  $S_2$ ; where  $P$  was used for excitation and  $S_1$  and  $S_2$  are used for sensing the induced emf. The excitation was done using an external frequency generator, while induced emf in secondary coil was measured in a digital oscilloscope. The data was saved on a USB flash drive during the course of experiments and later analyzed using Matlab on a PC.

The experiments were realized at room temperature. The range of pulsations used was  $\omega = 1571$  to  $30\,159 \text{ rad s}^{-1}$ . The corresponding skin-depth of magnetic flux is between  $\delta = 5.2 \text{ mm}$  and  $\delta = 1.2 \text{ mm}$ . In variance with the previous approach, the current in the circuit is determined using an ammeter in series. The magnitude of AC current used was  $I = 250 \text{ mA}$ . We verified that this magnitude remains stable during the course of experiments.

For each measurement, a specific rod was mounted and fixed on the two extreme poles of experimental bench (see figure 4.15). At either sides of these, PVC supports were screwed in order to extend the ECFM translation length. ECFM was translated back and forth over this rod several times with  $U$  in the range  $0.001 \text{ m s}^{-1}$  to  $1 \text{ m s}^{-1}$ .

After acquisition, the data corresponding to induced emf in  $S_1$  and  $S_2$  is analyzed in Matlab. The description of the algorithm is as follows: data of a specific small time window is loaded and perform a least square fitting of equation (3.33). Thereafter, relevant coefficients are obtained using set of equations (3.34). The angle of inclination of this ellipse is calculated from set of equations (3.36).  $\beta(t)$  FFT spectrum density gives us signature of  $\alpha$ . This approach has an advantage that the Lissajous curves can also be directly monitored on the oscilloscope. So it is relatively simpler approach.

We recall that if the induced voltages in the two secondary coils  $S_1$  and  $S_2$  are,  $V_1 = |V_1| \sin(\omega t - \theta_1)$  and  $V_2 = |V_2| \sin(\omega t - \theta_2)$  respectively, then the tilt angle of the fitted ellipse is given by:

$$\beta = \left| \frac{1}{2} \arctan \left( \frac{-2 \cos(\Delta\theta) |V_1| |V_2|}{|V_1|^2 - |V_2|^2} \right) \right|$$

where,  $\Delta\theta = \theta_1 - \theta_2$ .  $\Delta\theta$  is the extra phase introduced by the void in one coil with respect to the other. Physically, it is governed by perturbations of Faraday and motion induced

eddy currents which have different phases. At low magnetic Reynolds number  $Re_m$ ,  $\Delta\theta$  is linear with  $U$ , but very close to  $0^\circ$  or  $180^\circ$  [32, 34]. The numerical simulation described in the next section shows that for  $0 \leq Re_m \leq 0.12$ ,  $0 \leq \Delta\theta(\text{rad}) \leq 0.025$  and consequently  $0.9997 \leq \cos \Delta\theta \leq 1$ . Therefore, in the absence of voids the ellipse approaches a straight line inclined near  $45^\circ$ . When a void is under  $S_1$ ,  $|V_1|$  becomes much larger than  $|V_2|$  and  $V_1(t)$  has a slightly different phase than  $V_2(t)$ . We get a prominent tilted ellipse. The tilt fluctuates about  $45^\circ$  when voids pass through the flow cross-section. We can relate the fluctuation in the tilt angle to characterize the void presence. From the time signal of  $\beta$ , we calculate the amplitude of oscillation  $\Delta\beta$  by FFT algorithm.  $\Delta\beta$  depends on void volume fraction  $\alpha$ .

To simultaneously validate the results, Finite Element Simulations of the problem was realized using COMSOL<sup>®</sup> simulation software with Magnetic Fields physics in Frequency domain. The equation solved is the advection - diffusion of  $\mathbf{A}$ , the magnetic vector potential (see equation (3.9)).  $\mathbf{J}^e$  represents the externally applied current density and it is non-zero only in the domain which represents the primary coil. Since the grooves do not break the path of eddy currents and the externally applied current density  $\mathbf{J}^e$  is azimuthal, the problem is 2D axisymmetric and we need to solve for only one component of the magnetic vector potential.

Magnetic insulation condition is used at the edges of the computational domain. It consists in prescribing all the components of magnetic vector potential as zero on these edges. Grid size independence was verified by using three different mesh size settings: finer, extra fine and extremely fine respectively. Minimum mesh size varies at edges, boundaries and interfaces (up to  $10^{-2}$  mm).

### 4.3.2 Results

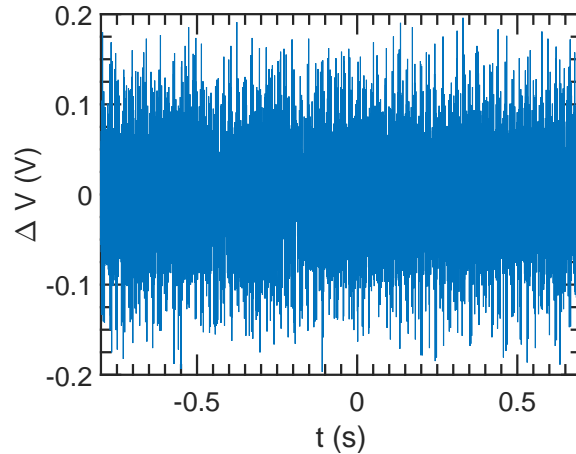


Figure 4.39: Typical  $\Delta V = V_1 - V_2$  signal vs time for  $\alpha = 0\%$  at  $\omega = 6284 \text{ rad s}^{-1}$  and  $U = 0.1 \text{ m s}^{-1}$ .

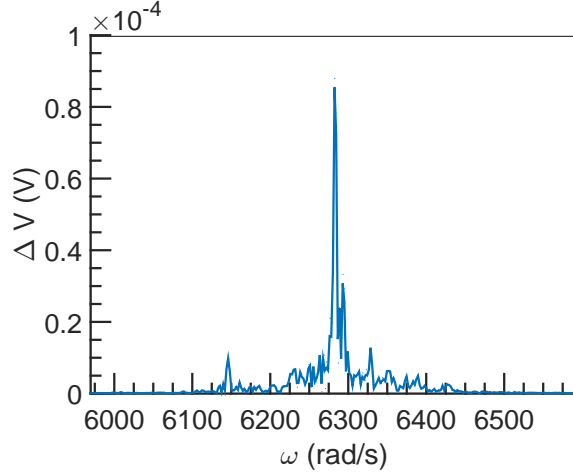


Figure 4.40: FFT spectral density of  $\Delta V$  ( $= V_1 - V_2$ ) signal for  $\alpha = 0\%$  at  $\omega = 6284 \text{ rad s}^{-1}$  and  $U = 0.1 \text{ m s}^{-1}$ .

In figure 4.39, a typical difference signal  $\Delta V = V_1 - V_2$  as recorded in the oscilloscope, is shown vs time for  $\alpha = 0\%$  at  $\omega = 6284 \text{ rad s}^{-1}$  and  $U = 0.1 \text{ m s}^{-1}$ . This signal is filtered using a digital Butterworth band-pass filter. Figure 4.40 shows FFT of  $\Delta V$  after filtering. The amplitude  $|\Delta V|$  of  $\Delta V$  signal can be obtained from the peak at corresponding pulsation of the current excitation. In case of figure 4.40, we notice a peak at  $\omega = 6284 \text{ rad s}^{-1}$ . Expected linearity of the amplitude of  $\Delta V$  (V) with  $U$  (m/s) is verified in figure 4.41 for the plain rod. Measured sensitivity is around  $0.07 \text{ mV/ms}^{-1}$ . The linear fitting shows a finite value equal to  $0.074 \text{ mV}$  at  $U = 0 \text{ m/s}$ , which corresponds to unbalanced secondary coils. This is also the order of magnitude of the voltages induced in individual secondary coils. Notice that the contribution of flow induced term is one order smaller even at highest  $U$ :  $0.007/0.074 \sim 0.1$ . This is because  $\text{Re}_m \sim 0.1$  in our experiments.

Figure 4.42 displays an example of a typical Liassajous curve obtained by  $V_1(t)$  vs  $V_2(t)$  for  $\alpha = 6.9\%$  (figure 4.42a),  $\alpha = 0.3\%$  (figure 4.42b) and  $\alpha = 0\%$  (figure 4.42c) at  $\omega = 6284 \text{ rad s}^{-1}$  and  $U = 0.1 \text{ m s}^{-1}$ . As explained earlier, this ellipse is fitted by ellipse fitting algorithm based on equation (3.33). Thereafter, relevant coefficients are obtained using set of equations (3.34). The angle of inclination of this ellipse is calculated from set of equations (3.36).  $\beta(t)$  FFT spectrum density gives us signature of  $\alpha$ .

Since the secondary signal voltages  $V_1$  and  $V_2$  are linear function of the primary coil excitation current,  $I$ , it is to be expected from equation (3.37) that  $\Delta\beta$  is independent of  $I$ . This is confirmed by figure 4.43 which shows that the change in primary coil excitation current magnitude,  $I$  has no effect on the amplitude of the  $\beta$  signal within the range of experimental uncertainty.

Figures 4.44-4.47 show the response of the ECFM signal to the presence of grooves. In all these cases, primary coil  $P$  is excited by current  $I = 250 \text{ mA}$  at pulsation  $\omega = 6284 \text{ rad s}^{-1}$ . For the same control parameters ( $I, U, \omega$ ), the only difference between

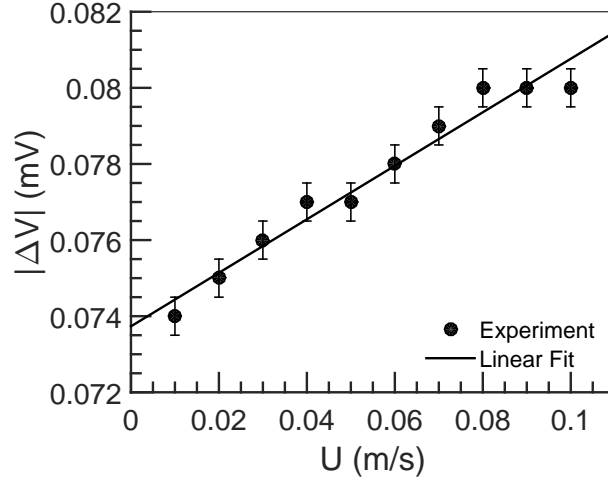


Figure 4.41: Amplitude of  $\Delta V$  (V) vs  $U$  (m/s) ( $\alpha = 0\%$  and  $\omega = 6284 \text{ rad s}^{-1}$ ).

experiments and numerical simulation is the symmetry of ECFM assembly. While in simulations we have a perfectly symmetric system, in practice we cannot manufacture a perfectly balanced ECFM assembly which is also evident from figure 4.41. In the case of perfectly symmetric system, the intercept at  $U = 0 \text{ m/s}$  is expected to be  $0 \text{ V}$  but figure 4.41 shows a value  $0.074 \text{ mV}$ . figure 4.48 shows the effect of asymmetry in ECFM assembly on the  $\beta$  signal amplitude,  $\Delta\beta$ . Keeping the number of turns in each secondary coil  $S_1$  and  $S_2$  as constant, their lengths were altered as  $L_s - kL_s$  and  $L_s + kL_s$  respectively in the numerical simulations. In such a case, factor of asymmetry,  $k$  can refer to compactness of winding in secondary coils. We observe that  $\Delta\beta$  is maximum for a perfectly symmetrical system ( $k = 0$ ) while it decreases as a function of asymmetry. In practice, ECFM assembly is never perfectly symmetric. The ratio of  $\Delta\beta$  obtained from numerical simulation and experiments at same parameter values give us an idea about the degree of asymmetry in the experimental ECFM assembly. There are many reasons for asymmetry besides compactness. The profile of  $\Delta\beta$  with asymmetry should be expected to vary according to the type of asymmetry (for example: compactness, lift off, distance from primary coil etc.). It is advisable to calibrate the device for this factor after fabrication. Consequently, the numerical results have been rescaled by factor 0.6 and a small static  $\beta$  was removed from experimental data in Figs. 4.44-4.47 for comparison with the numerical results. We also note that figure 4.48 does not explain such a large rescaling factor (0.6).

In figure 4.44, we see the signal obtained for a one groove rod. We observe the perturbation in both  $\Delta V$  as ECFM assembly translates over the groove at  $U = 0.1 \text{ m/s}$ , and its corresponding signature on the tilt angle signal,  $\beta(t)$ . We notice that  $\beta(t)$  without groove is close to  $45^\circ$  and that the variation due to the grooves has a maximum amplitude of  $1.5^\circ$  which is easily detectable. The first peak corresponds to the passage

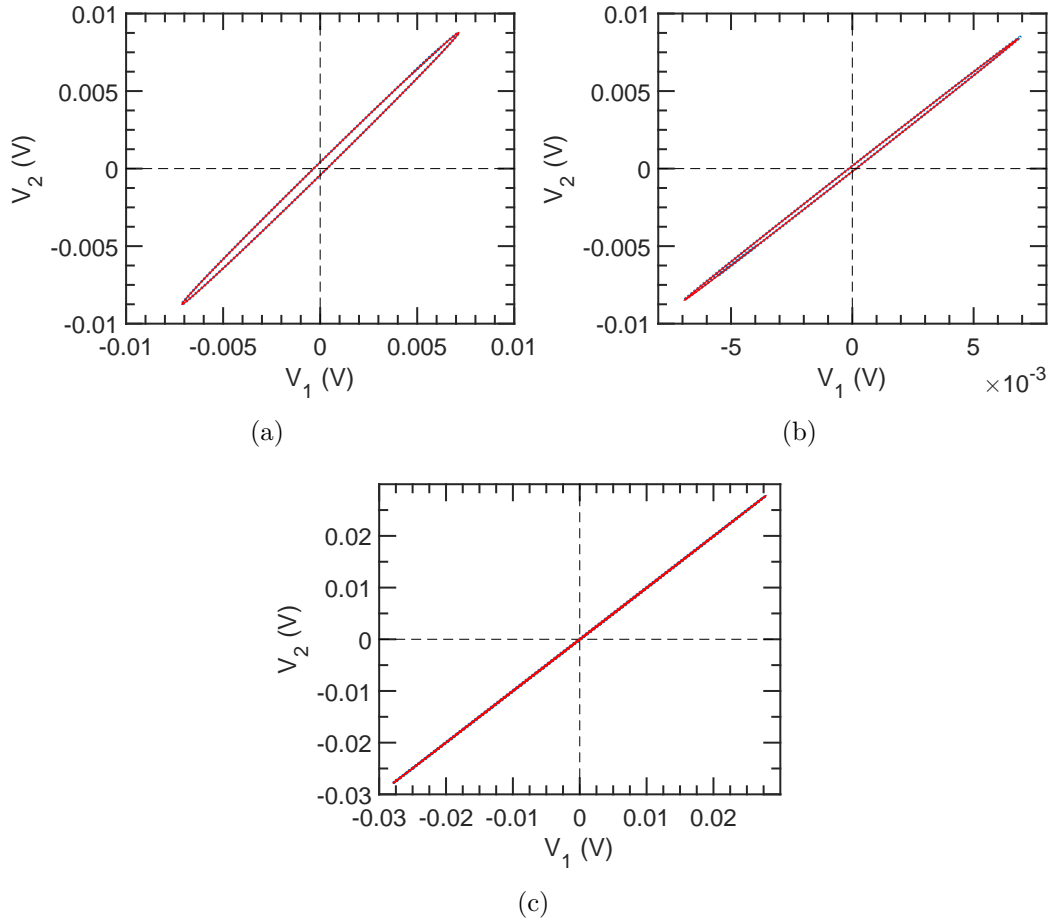


Figure 4.42: An example of a typical Liassajous curve obtained by  $V_1(t)$  vs  $V_2(t)$  fitted by ellipse fitting algorithm, for (a)  $\alpha = 6.9\%$ , (b)  $\alpha = 0.3\%$  and  $\alpha = 0\%$  at  $\omega = 6284 \text{ rad s}^{-1}$  and  $U = 0.1 \text{ m s}^{-1}$ .

of the groove inside  $S_1$  and second peak to that inside  $S_2$ . The distance between the two peaks is 0.3 s, which at  $U = 0.1 \text{ m/s}$  gives a length scale,  $L = 3 \text{ cm}$  which is the separation between the two secondary coils.

The effects of void fraction on  $\beta$  signal can be observed by comparing figure 4.45-4.47. The standard deviations for the three  $\beta(t)$  curves are 0.044 for 0%, 0.062 for 0.3% and 0.276 for 6.9%. It shows that at 0.3% we are close to the limit of detection. FFT gives the amplitude of oscillation of  $\beta$  signal,  $\Delta\beta$  with a reasonable accuracy (figure 4.49). Furthermore, peak to peak distance is equal to the spatial frequency of grooves. This gives information on distribution of the dispersed phase through Fourier analysis.

Figure 4.44-4.47 also demonstrate an excellent agreement between the experimental results and the numerical simulations for  $\beta$  signal.

Figure 4.50 shows the effect of pulsation on  $\Delta\beta$ . When the pulsation increases,  $\Delta\beta$



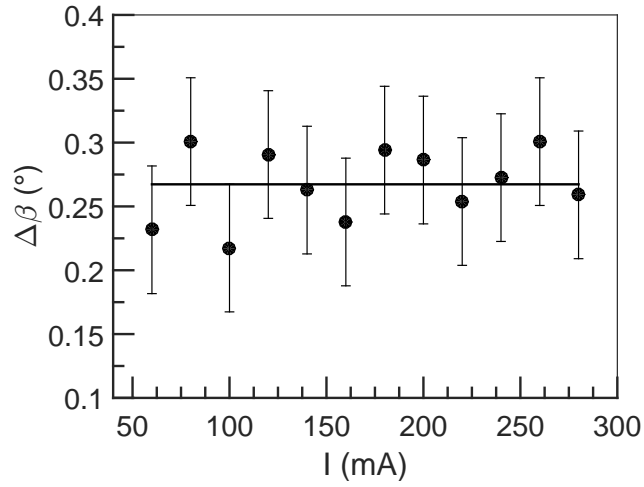
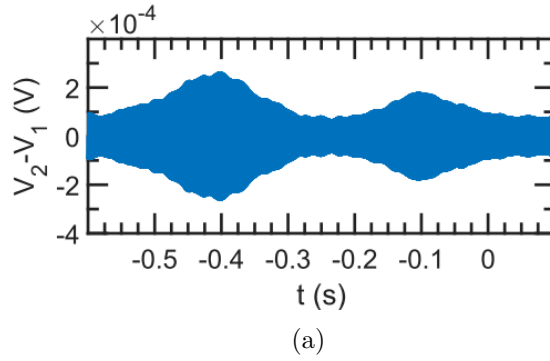
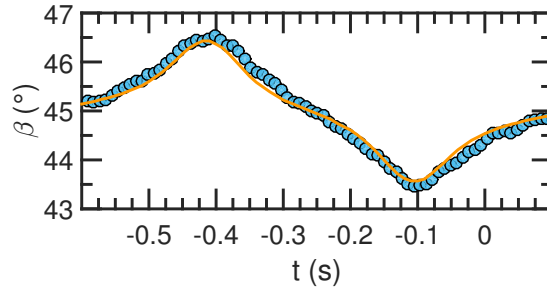


Figure 4.43:  $\Delta\beta$  (°) vs  $I$  (mA),  $U = 0.1$  m/s,  $\omega = 6284$  rad s<sup>-1</sup>,  $\alpha = 6.9\%$



(a)



(b)

Figure 4.44: Rod with one groove  $U = 0.1$  m/s and  $\omega = 6284$  rad s<sup>-1</sup>. a)  $\Delta V$  vs time. b)  $\beta$  vs  $t(s)$ . (• : experimental data; — : numerical simulation)

tends towards saturation. This happens because at low pulsations the magnetic field can penetrate upto the core of the rod. As we increase the pulsation, the magnetic flux is excluded from the core leading to an exponential decrease in the skin depth.

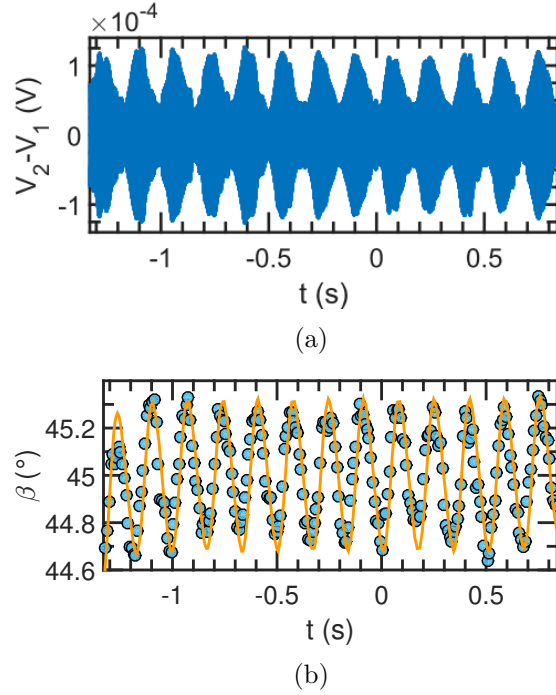
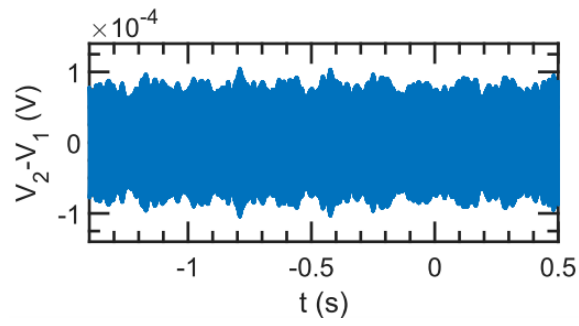


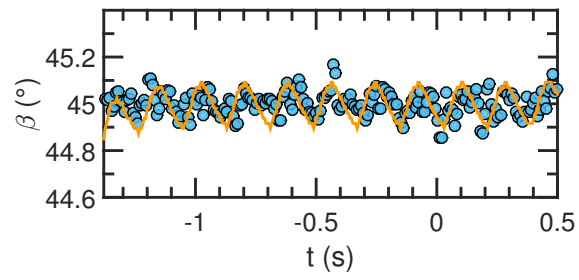
Figure 4.45:  $\alpha = 6.9\%$ ,  $U = 0.1$  m/s and  $\omega = 6284$  rad s $^{-1}$ . a)  $\Delta V$  vs time. b)  $\beta$  vs  $t(s)$ . ( $\bullet$  : experimental data; — : numerical simulation)

We have shown at the beginning of this section, that the contribution of flow induced potential is one order smaller than average induced potentials in each secondary coils. Theoretically,  $\beta(U)$  for  $Re_m \leq 0.12$  is,  $\beta(U) \leq \left| \frac{1}{2} \arctan(-20) \right| \implies \Delta\beta(U) = \beta(0) - \beta(1) \leq 45.0^\circ - 43.5^\circ = 1.5^\circ$ . Flow fluctuations of the order of 1 m/s should change  $\Delta\beta$  up to a maximum  $1.5^\circ$ . But in our experiments, there are no flow fluctuations and therefore  $\Delta\beta$  should be independent of  $U$ . This is confirmed in figure 4.51, where  $\Delta\beta$  is independent of the velocity. This result suggests that in steady flows,  $\Delta\beta$  depends only on  $\alpha$ , however the period of  $\beta$  oscillations depends on the velocity. Moreover, this implies that the effects of void fraction are mainly through Faraday induction rather than the Lorentz force.

The effect of homogenization defined by mean groove separation length  $\lambda = 0.5(d_1 + d_2)$  has not been studied. The change in  $\lambda_\alpha$  affects the groove frequency in FFT spectrum of  $\beta(t)$ .  $\Delta\beta = 0$  for continuous gas. It is expected that  $\Delta\beta$  will start to decrease when the axial length of the annular slugs approach the length of the primary coil in dimension. This will typically happen around  $\alpha \geq 30\%$  [18].

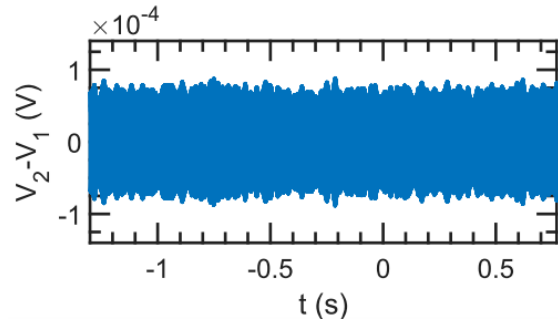


(a)

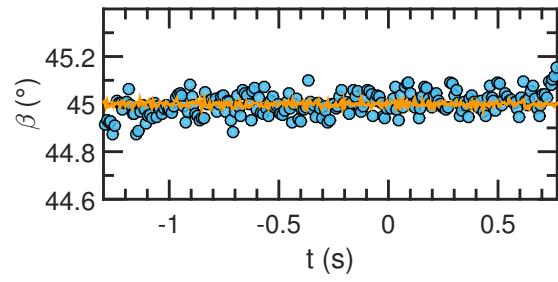


(b)

Figure 4.46:  $\alpha = 0.3\%$ ,  $U = 0.1$  m/s and  $\omega = 6284$  rad s $^{-1}$ . a)  $\Delta V$  vs time. b)  $\beta$  vs  $t(s)$ . (• : experimental data; — : numerical simulation)



(a)



(b)

Figure 4.47:  $\alpha = 0\%$ ,  $U = 0.1 \text{ m/s}$  and  $\omega = 6284 \text{ rad s}^{-1}$ . a)  $\Delta V$  vs time. b)  $\beta$  vs  $t(s)$ . (• : experimental data; — : numerical simulation)

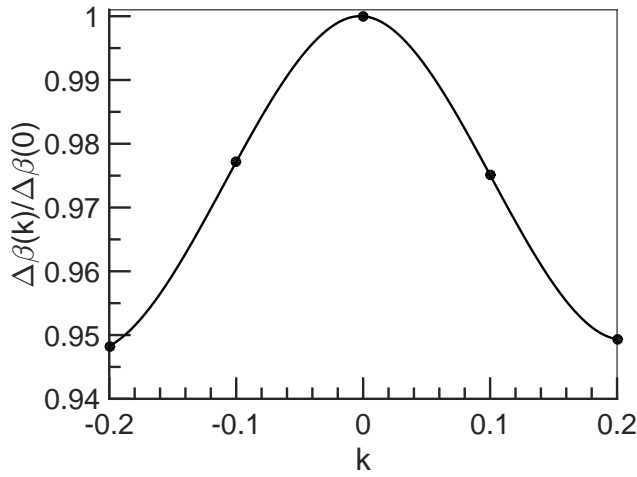


Figure 4.48:  $\Delta\beta(k)$  is maximum for a perfectly symmetric system ( $k = 0$ ) and it decreases as a function of asymmetry ( $k \neq 0$ ). COMSOL simulation for  $\alpha = 6.9\%$  at  $U = 0.01 \text{ m/s}$ ,  $I = 200 \text{ mA}$  and  $\omega = 6284 \text{ rad s}^{-1}$ .

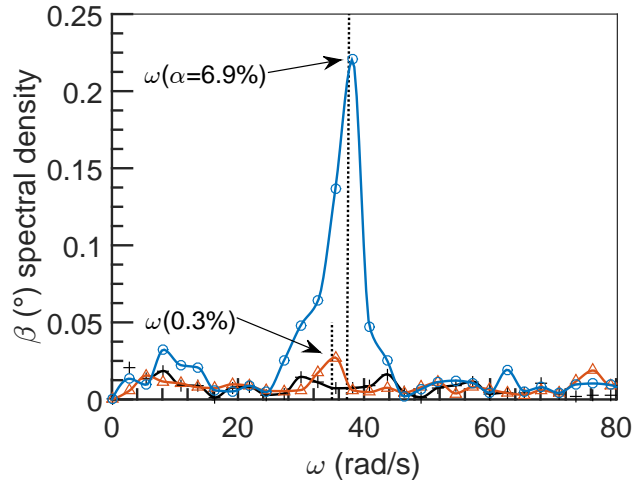


Figure 4.49:  $\beta$  spectral density for +,  $\triangle$  and  $\circ$  for  $\alpha = 0.0, 0.3$  and  $6.9\%$  respectively at  $U = 0.1$  m/s and  $\omega = 6284$  rad s $^{-1}$ .

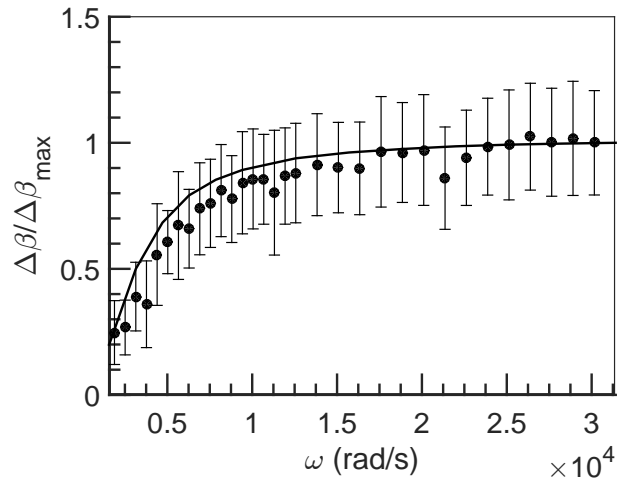


Figure 4.50: Normalised amplitude  $\Delta\beta$  as a function of pulsation for  $\alpha = 6.9\%$ ,  $U = 0.1$  m/s and  $I = 200$  mA. ( $\bullet$ : experimental data;  $—$ : numerical simulation;  $\Delta\beta_{max} = \Delta\beta(\omega = 6284$  rad s $^{-1}$ )

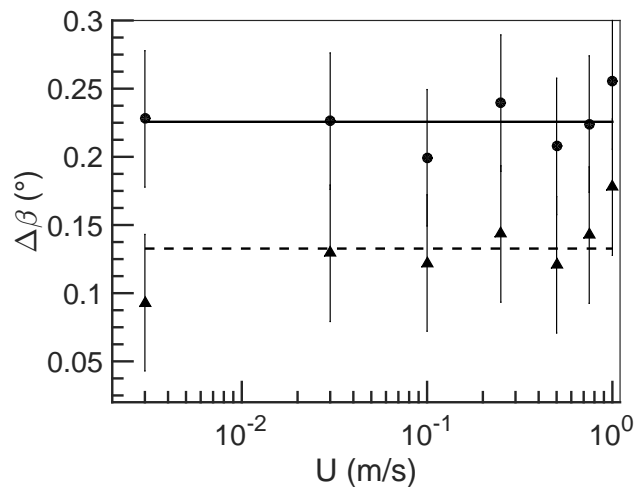


Figure 4.51:  $\Delta\beta$  vs  $U$  for  $\alpha = 6.9\%$ ,  $I = 200 \text{ mA}$ ,  $\omega = 6284 \text{ rad s}^{-1}$  ( $\bullet$ ) and  $\omega = 3142 \text{ rad s}^{-1}$  ( $\blacktriangle$ )

**Lissajous curve fitting with 5 coil ECFM** Experiments with this approach were also performed for ECFM in 5-coils configuration. We recall, that in 5-coils configuration, there are three primary coils, the central primary coil is excited in series opposition to the primary coils at extreme ends (see figure 5.8).

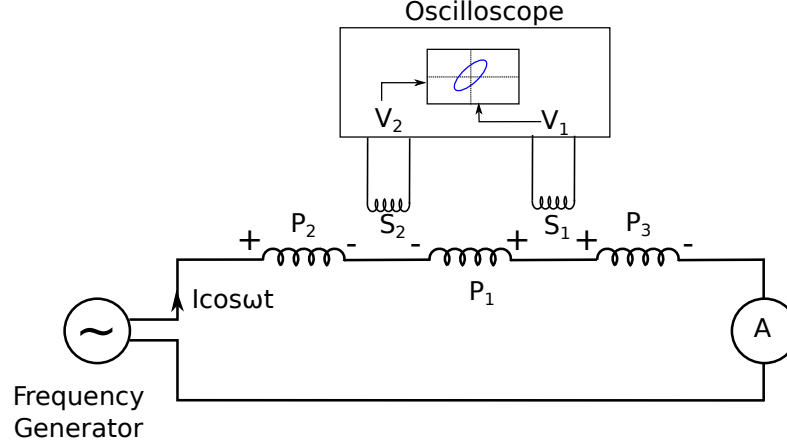


Figure 4.52: Schematic of 5-coils ECFM experiments.

We define an ideal case as: when the three primary coils are exactly identical to each other, the two secondary coils are exactly identical to each other and the placement of these coils is symmetrical with respect to  $P_1$ . In the ideal case, and when  $\alpha = 0\%$ , the emf in  $S_1$  and  $S_2$  are 0 V and 0 V respectively when  $U = 0$  m/s. But it is  $V_u$  and  $-V_u$  when  $U \neq 0$ . In accordance with equation (5.8), when a void is under  $S_1$ ,  $V_1$  is large compared to  $V_2$ . Therefore, we observe larger oscillations as compared to the case of 3-coils ECFM.

In figure 4.53, we show  $\beta(t)$  time signal for  $\alpha = 0\%$  (see figure 4.53a), 1 groove (see figure 4.53b),  $\alpha = 0.3\%$  (see figure 4.53c),  $\alpha = 6.9\%$  (see figure 4.53d), variable separation of grooves (see figure 4.53e) at  $U = 0.1$  m/s and  $\omega = 6284$  rad s $^{-1}$  for ECFM in 5-coils configuration. We notice that increasing the perturbations in  $\beta$  increases with increasing  $\alpha$  value. For the case of variable separations of groove, we see that the amplitude of perturbation decreases as the separation between the grooves decrease.

In figure 4.54, we see a qualitative comparison of  $\beta(t)$  signal at two different velocities for  $\alpha = 0.3\%$ . We conclude that  $\Delta\beta$  is independent of the mean velocity.

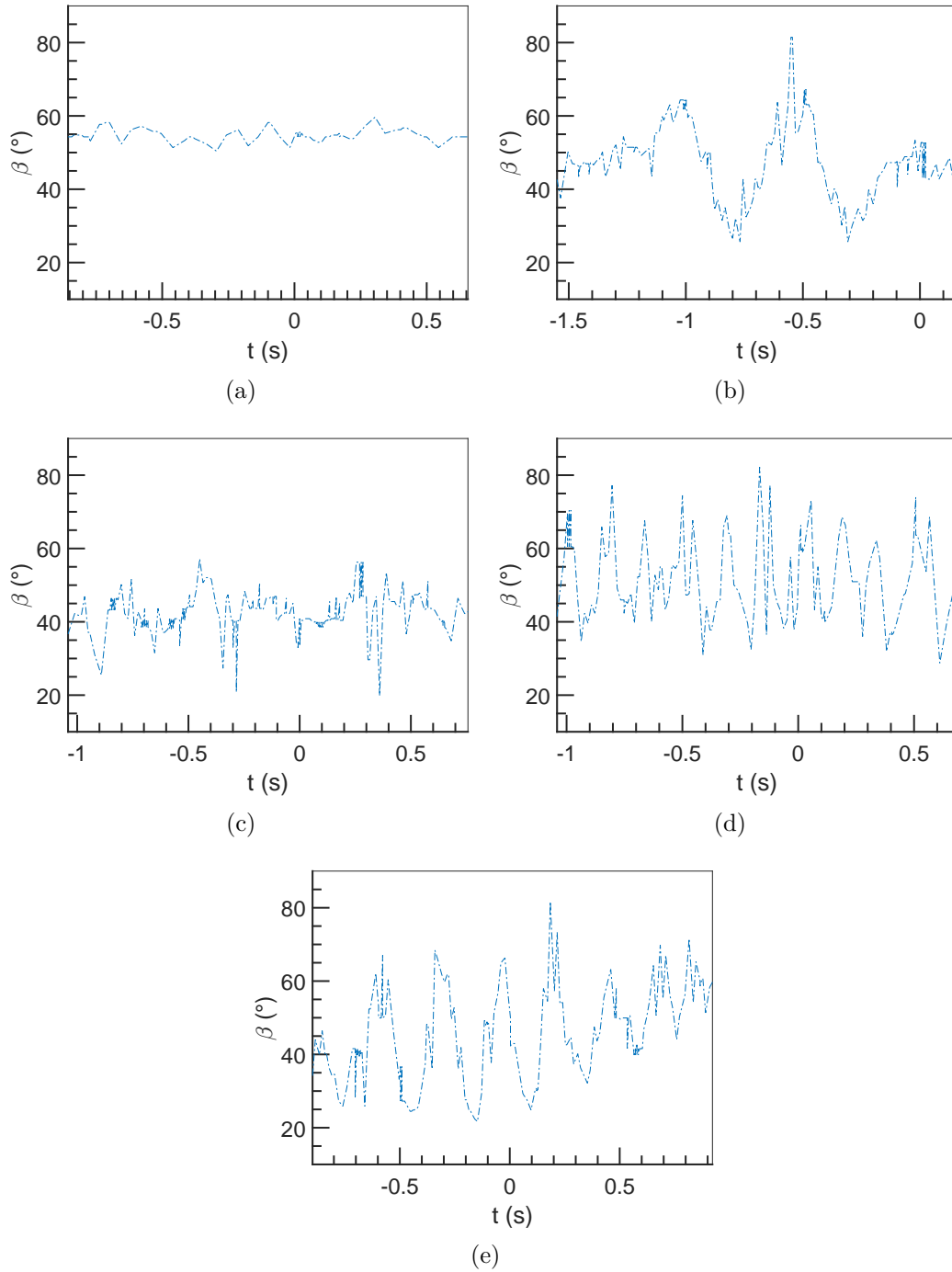


Figure 4.53: Typical  $\beta(t)$  time signal for (a)  $\alpha = 0\%$ , (b) 1 groove, (c)  $\alpha = 0.3\%$ , (d)  $\alpha = 6.9\%$ , (e) Random separation of grooves at  $U = 0.1$  m/s and  $\omega = 6284$  rad s $^{-1}$  for ECFM in 5-coils configuration.



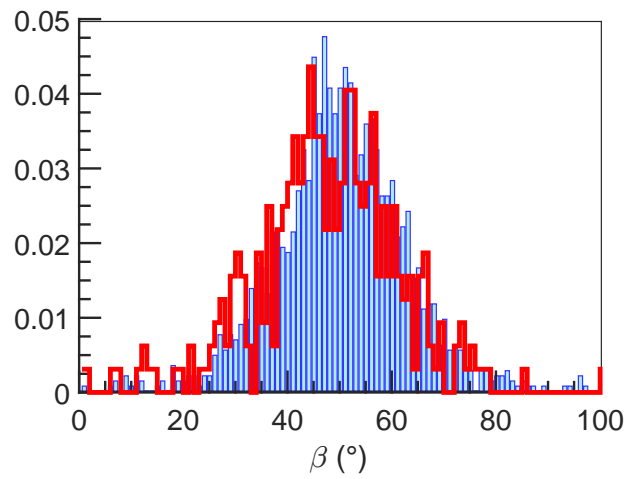


Figure 4.54: Comparison of histograms of  $\beta(t)$  at (a)  $U = 0.02 \text{ m s}^{-1}$  ( $\blacksquare$ ) and (b)  $U = 0.1 \text{ m s}^{-1}$  ( $\blacksquare$ ), and  $\omega = 6284 \text{ rad s}^{-1}$  for  $\alpha = 0.3\%$ .

### 4.3.3 Discussions

An experimental method has been introduced to study potentiality of a flow-through type ECFM to measure void fraction for liquid metal two-phase flows. Periodic grooves on solid aluminium cylinder was used as a model of liquid metal two-phase flow. The model experimental set up used in this paper allows us to control well the experimental parameters such as void volume, location, velocity etc. We use the technique of ellipse fit and correlate the fluctuations in tilt of this ellipse with the void fraction. The same problem was also modeled numerically in COMSOL<sup>®</sup> simulation software. The results show a good agreement between the experiments and the numerical simulations. The main results for 3-coils ECFM are :

- $\beta$  signal for the single groove case demonstrate the detection capability of ECFM for large grooves. By comparing the  $\beta$  signal for various rods, we find that it is sensitive to  $\alpha$ .  $\Delta\beta \propto \alpha^n$   $n \approx 0.7$ , is the trend of variation of  $\Delta\beta$  with the void fraction.  $\beta$  signal for  $\alpha = 0.3\%$  is noisy. This is approximately the lower limit of void fraction that can reliably be detected using this method.
- $\Delta\beta$  increases with pulsation and reaches an asymptotic value. This is related to its dependence on penetration depth of the magnetic fields in the medium.  $\Delta\beta$  is independent of the primary coil excitation current. The experiments conducted at various velocity values show that for the normal reactor conditions ( $U \sim 1$  m/s),  $\Delta\beta$  does not change with  $U$  assuming a steady flow. This is important for reliable measurements of void fraction.

The results for 5-coils configuration are similar to that of 3-coils configuration. But the perturbation amplitude response ( $\Delta\beta$ ) to void is significantly larger than the 3-coils configuration.

In this study we find that ECFM signals analyzed with the technique of ellipse fit is simple and promising. Compared to acoustic methods, the upper limit on detectable  $\alpha$  is much larger. The signals are not only fast and large but are also decoupled from the mean flow velocity. Further studies are needed to confirm these results for a general liquid metal two-phase flow in an SFR [73]. In particular, the results presented here do not account for possible randomness in  $\alpha$  distribution and velocity fluctuations.

## 4.4 Conclusions

This chapter presents, experimental results for the magnetic flux distortion in two-phase liquid metal flow excited by an AC magnetic field. We designed a specific experimental setup with a moving ECFM. The two-phase liquid metal was modeled by aluminium rods along which ECFM translates at constant velocity. Two methods were presented. The difference signal method provides more intuitive understanding regarding Faraday induction and Lorentz force effects. But relative complexity in signal acquisition and treatment is higher as compared to the Lissajous ellipse fitting method. On the other

hand, the perturbations in the  $\beta$  signal due to  $\alpha$  is relatively difficult to interpret in terms of physical processes such as induction.

The voids were simulated by machining holes and grooves on the rods. In all the experiments,  $\alpha$  varies between 0 and 6.9%. The coil lengths are larger but comparable to  $\lambda_\alpha$ . We have studied the effects of pulsation of exciting electrical current ( $1.5 \times 10^3 \leq \omega \leq 12.5 \times 10^3 \text{ rad s}^{-1}$ ), of the flow velocity ( $0 \leq U \leq 1 \text{ m s}^{-1}$ ) and of the void volume fraction on the magnetic flux distortion. In this configuration, the relative motion of aluminium simulates a plug flow. In all the experiments, the magnetic flux was demodulated with a Lockin amplifier in order to characterize its in-phase and quadrature-phase components.

For the difference signal approach, two theoretical models were presented. The first method assumes the penetration depth of magnetic fields to be much larger than the flow cross-section diameter. It successfully predicts linearity of  $C_1$  (DC component of  $||\Delta V||^2$  signal) with  $U^2$  in addition to its  $\alpha$  independence. Furthermore, it predicts  $C_3$  (second harmonic) to be linear in  $\alpha^2$  which was validated by experimental results. We found two shortcomings with this theory. It predicts the existence of only  $\Delta V_\perp$  and not  $\Delta V_\parallel$ , in absence of voids. But experimentally, we found that both  $\Delta V_\perp$  and  $\Delta V_\parallel$  exist. This theory also predicts that the first harmonic of  $||\Delta V||^2$  signal is quadratic in  $U$ :  $C_2 \sim U^2$ . Experimentally, we found that  $C_2 \sim U^1$ . This could not be explained since this theory does not give the functional dependence of  $\delta b$  on  $U$ .

The results show clearly that the distortion in magnetic flux results from a strong coupling between Faraday induction and Lorentz force effects. To explain the discrepancies in the previous theoretical model, we took into account of this coupling in our second model. It was no longer possible to separate Faraday induction and Lorentz force effects. The magnetic flux was rather decomposed into terms in  $\text{Re}_m$  and  $\alpha$  on the assumption that  $\text{Re}_m \ll 1$  and  $\alpha \ll 1$ . In this new perturbative model, the total magnetic flux is given by :  $\phi \approx \phi_0 + \text{Re}_m \phi_u + \phi_\alpha$ .

The study of the pulsation dependence of the magnetic flux points out that  $\phi_{0,\parallel}$  and  $\text{Re}_m \phi_{u,\perp}$  are dependent of a strong coupling between Faraday induction and Lorentz force effects. On the other side,  $\phi_{0,\perp}$  and  $\text{Re}_m \phi_{u,\parallel}$  seem to depend mainly on Faraday induction for the first and on Lorentz force for the second. Indeed, the scaling laws  $\phi_{0,\perp} \sim \omega^{-1/2}$  and  $\text{Re}_m \phi_{u,\parallel} \sim \omega^{-1}$  can be deduced directly from Maxwell-Faraday and Maxwell-Ampere equations, respectively. An important result is that  $\text{Re}_m \phi_u$  is linear in  $U$  and independent of  $\alpha$ .  $\psi_\alpha$  is independent of  $U$  and linear in  $\alpha$ . This experimental result can be justified theoretically because  $\text{Re}_m$  and  $\alpha$  are small. It has been validated for both the void geometries: grooves and holes.

For practical applications, the Fourier analysis of the demodulated voltage difference between the two secondary coils  $||\Delta V||$ , allows to measure the velocity and the void fraction. Indeed, the first peak of  $||\Delta V||^2$  FFT increases linearly with  $U$ . Hence, the second peak is proportional to  $\alpha^2$ . This approach can be used after calibration. From a practical point of view, the Fourier analysis of  $||\Delta V||^2$  is sufficient to measure simultaneously the velocity and the void fraction of a conducting liquid in large number of applications. In these experiments, we found that amplitude of perturbation in magnetic

flux due to voids is linear in  $\psi_\alpha$  for  $\alpha$  below 4%, and saturates thereafter. This result already exists in literature and was mentioned in figure 2.13 in chapter 3.

At this stage, the coupling between Faraday induction and the Lorentz force effects is not well understood. A theoretical model should be developed to calculate the eddy current distortions due to the flow and the void at the local scale and their contributions on the magnetic flux at the flow scale.

For the Lissajous ellipse fitting approach, we conclude that amplitude of fluctuations in orientation of fitted ellipse on Lissajous curve made by induced emfs in two secondary coils, increases with  $\alpha$ . Due to low magnetic Reynolds number in liquid metal applications, Lissajous ellipse fitting approach should give  $U$  independent  $\beta$  signal. The lower limit of  $\alpha$  at which this approach is still sensitive seems to be  $\alpha = 0.3\%$ . The agreement between the experimental and the numerical results indicate that we can develop a benchmark on which several other designs under various external conditions can be tested numerically.

We presented three approaches: difference signal approach with small Faraday induction effects, difference signal approach with significant Faraday induction effects and the Lissajous ellipse fitting approach. The objective was to understand the  $\alpha$  effect on induced emf in ECFM. The results demonstrate that the last approach is simpler and more practical. Two inconveniences being, it is difficult to develop a theoretical model for this approach and poor signal quality at  $\alpha = 0.3\%$ . The use of 5-coils ECFM has the potential of improving the sensitivity of  $\Delta\beta$  on  $\alpha$ . The difference signal theory at small Faraday induction effects is only valid for large penetration depths. The theory predicts that the perturbation in magnetic flux due to Lorentz Force effects is only on  $\Delta V_\perp$ . Hence with the help of a phase sensitive detector such as a Lockin amplifier, it is possible to monitor flow and  $\alpha$  simultaneously, using only one ECFM device. Complementary to this theory is magnetic flux perturbation model at small magnetic flux penetrations. This model predicts that FFT spectral density of  $||\Delta V||^2$  is sufficient to provide measure of  $U$  and  $\alpha$ . Unlike the other two approaches, this last approach gives expressions explicit in  $U$  and  $\alpha$ .

These results show that ECFM is sensitive to voids in two-phase flows. It is also possible to characterize  $U$  and  $\alpha$  simultaneously, with a single ECFM device. In the next chapter, we present development of liquid galinstan experimental set-up and some preliminary results.



## Chapter 5

# Experiments with liquid Galinstan

The results in the previous chapter were obtained for model experimental set up, *i.e.*, aluminium rods with grooves or holes with spatial periodicity. Before extending these results to an actual liquid sodium flow, we first consider performing the same set of experiments with the liquid Galinstan. Liquid Galinstan is a commercially available liquid metal eutectic alloy of Gallium (Ga), Indium (In), and Tin (Sn). The composition of Ga, In, and Sn differs depending on the vendor. A typical composition is 67 wt% Ga, 20.5 wt% In and 12.5 wt% Sn, though it varies between 62 wt% to 95 wt% Ga, 5 wt% to 22 wt% In, 0 wt% to 16 wt% Sn [90]. Galinstan is liquid at room temperature [91]. It's typical properties are listed in the table 5.1. Low toxicity of Galinstan as compared to Mercury and its low reactivity as compared to sodium and sodium potassium alloys makes it the preferred choice for liquid metal experiments in research facilities.

As seen in table 5.1, Galinstan is six times heavier than water. In our context, this exerts a significant load on the structure of experimental bench. It's electrical conductivity is comparable to that of liquid sodium, but ten times smaller than the Aluminium rods. Consequently, the magnetic Reynolds number calculated for Galinstan as compared to Aluminium is also low. Liquid Galinstan is opaque and hence common optical methods such as CCD camera can not be used. Therefore it is a difficult task to know and control the size and spatial distribution of gas bubbles in a liquid Galinstan loop.

The objective of this chapter is to perform preliminary experiments in order to valid experiments with Aluminium rods. In these investigations, two phase-medium is modeled by fixing small glass beads at fixed positions inside ceramic tubes filled with Galinstan. We use the magnetic flux perturbation approach to analyze the results. This chapter is organized as follows: section 5.1 presents the experimental setup. Section 5.2 details the experimental results. Section 5.3, concludes and gives a short outlook for further experiments (suggestions).

Table 5.1: Table of comparison of physical properties of liquid metal.

Property	Liquid Sodium[11][12][14]	Aluminium	Galinstan[90]
Composition	Na	Al	Ga(67%), In(20.5%), Sn(12.5%)
Density	$830 \text{ kg m}^{-3}$	$2700 \text{ kg m}^{-3}$	$6360 \text{ kg m}^{-3}$
Melting point	$97.2 \text{ }^\circ\text{C}$	—	$10.5 \text{ }^\circ\text{C}$
Electrical conductivity	$3.6 \times 10^6 \text{ S m}^{-1}$ at $500 \text{ }^\circ\text{C}$	$3.77 \times 10^7 \text{ S m}^{-1}$ at $20 \text{ }^\circ\text{C}$	$3.1 \times 10^6 \text{ S m}^{-1}$ at $20 \text{ }^\circ\text{C}$
Viscosity	$2.2 \times 10^{-4} \text{ Pa s}$ at $500 \text{ }^\circ\text{C}$	—	$2.98 \times 10^{-7} \text{ Pa s}$ at $20 \text{ }^\circ\text{C}$
Surface tension	$0.158 \text{ N m}^{-1}$ at $500 \text{ }^\circ\text{C}$	—	$0.533 \text{ N m}^{-1}$ at $20 \text{ }^\circ\text{C}$
Skin depth, $\delta$	12 mm ( $3142 \text{ rad s}^{-1}$ ), 8.4 mm ( $6284 \text{ rad s}^{-1}$ )	3.7 mm ( $3142 \text{ rad s}^{-1}$ ), 2.6 mm ( $6284 \text{ rad s}^{-1}$ )	13 mm ( $3142 \text{ rad s}^{-1}$ ), 9 mm ( $6284 \text{ rad s}^{-1}$ )
Magnetic Reynolds number, $\text{Re}_m(1 \text{ m/s}, 3142 \text{ rad s}^{-1})$	0.05	0.17	0.05
Magnetic property	Paramagnetic ( $\chi \sim 10^{-7}$ )	Paramagnetic ( $\chi \sim 10^{-5}$ )	Paramagnetic

## 5.1 Experimental set up

The two-phase experiments with liquid Galinstan are similar to the ones with the Aluminium rods presented in the previous chapter. In the functional block diagram shown in figure 4.1, the only part which changes is the two-phase medium. The excitation and acquisition is achieved in the same way. An internal frequency generator of a Lockin amplifier excites the primary coil and the difference emf between  $S_1$  and  $S_2$  is recorded in the Lockin amplifier. The signal so recorded is post processed using MATLAB<sup>®</sup>.

As shown in figures 5.4 and 5.1, the ECFM is fixed on a uniaxial translator which displaces it at a given constant velocity  $U$ . Hollow ceramic cylindrical tubes (2 mm thickness) made of Macor were bought from Final advanced solution<sup>®</sup>. Macor is the trademark for a machineable glass-ceramic. Macor has a density of  $2520 \text{ kg m}^{-3}$ , a Young's modulus of 66.9 GPa at 25 °C. These ceramic tubes are filled with liquid Galinstan as shown in figures 5.1 and 5.2. The internal and external diameters of all the ceramic tubes used were  $D = 34 \text{ mm}$  and  $D_o = 38 \text{ mm}$  respectively. One end of this cylinder is sealed with a plug made of PEEK (Polyether ether ketone) and the other end is sealed with a cap made of same material. This is achieved with the help of a Silicon glue: MS polymer (also called Modified Silane adhesive and Silyl Modified polymers). The voids are simulated by glass beads of given diameters (refer to table 5.2). These glass beads are pasted with the help of another glue on  $N$  threads as shown in figure 5.3.  $N$  is the number of threads used in each configuration. The glue used for this purpose is a cyanoacrylate adhesive bought from Whitec. The threads are uni-filament fishing line from Pure fishing<sup>™</sup> and are of diameter  $35 \mu\text{m}$ . The threads are fixed at the two ends with a tip of glue. Radially, these threads are 12 mm away from the axis (5 mm from the ceramic valve) (figure 5.1).

Several configurations of void volume fraction ( $\alpha$ ), beads size ( $d$ ) and spatial distribution ( $\lambda_\alpha$ ) have been prepared. Here  $\lambda_\alpha$  is the axial separation between beads on one thread. Since beads are placed periodically along the axis, it is possible to calculate a characteristic modulation pulsation at ECFM velocity  $U$  as  $\omega_\alpha = 2\pi U/\lambda_\alpha$ . For a uniform distribution, there exists a geometrical relation between  $\alpha$ ,  $d$ ,  $\lambda_\alpha$  and the number  $N$  which writes:

$$\alpha = \frac{N \frac{\pi d^3}{6}}{\frac{\pi D^2 \lambda_\alpha}{4}} = \frac{2Nd^3}{3D^2\lambda_\alpha} \quad (5.1)$$

Table 5.2, enlists the parameter values for several different configurations. Since maximum  $d$  is 5 mm and threads are 5 mm inside ceramic wall, the inner end of the glass beads are on an average 7.5 mm inside the ceramic wall. This is approximately equal to  $\delta = 7.4 \text{ mm}$  at pulsation  $\omega = 9420 \text{ rad s}^{-1}$ . Even if the beads were 10 mm away from ceramic wall, the beads will be approximately within one  $\delta$  at pulsation  $\omega = 6284 \text{ rad s}^{-1}$  ( $\delta = 9 \text{ mm}$ ).

Liquid Galinstan is stored in a stainless steel reservoir under nitrogen pressure. The reservoir was cleaned with acetone and air was removed by vacuum pump. Several



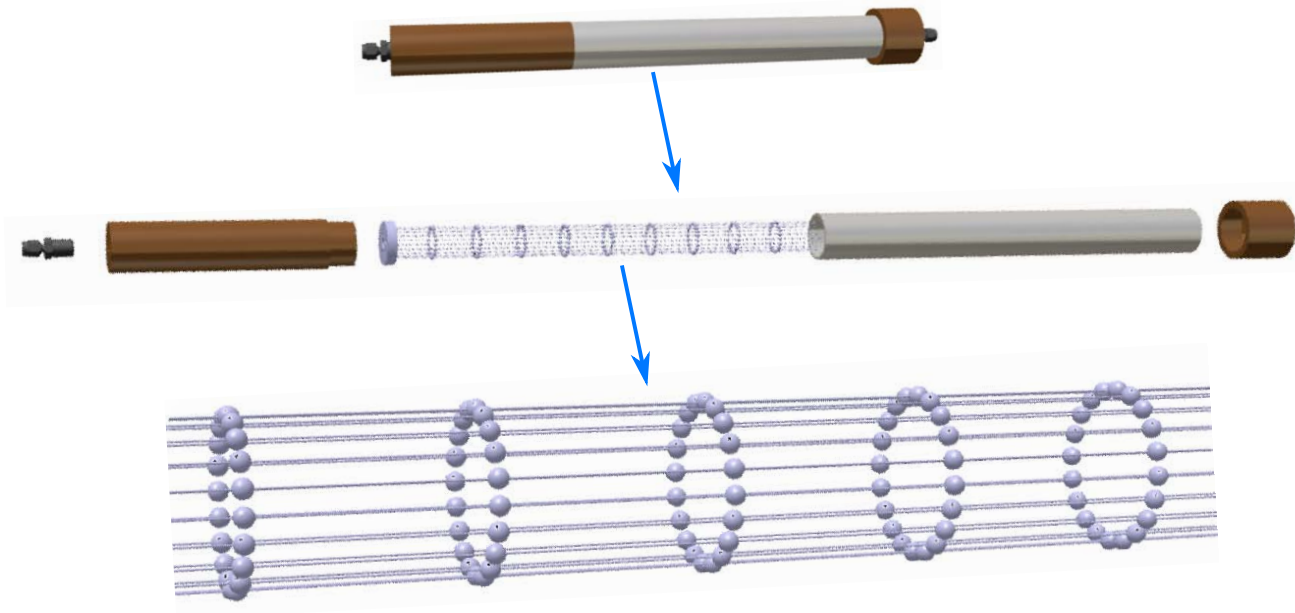


Figure 5.1: Experimental bench with view of the ceramic tube containing Galinstan, Peek ends, and spatial distribution of beads and threads.

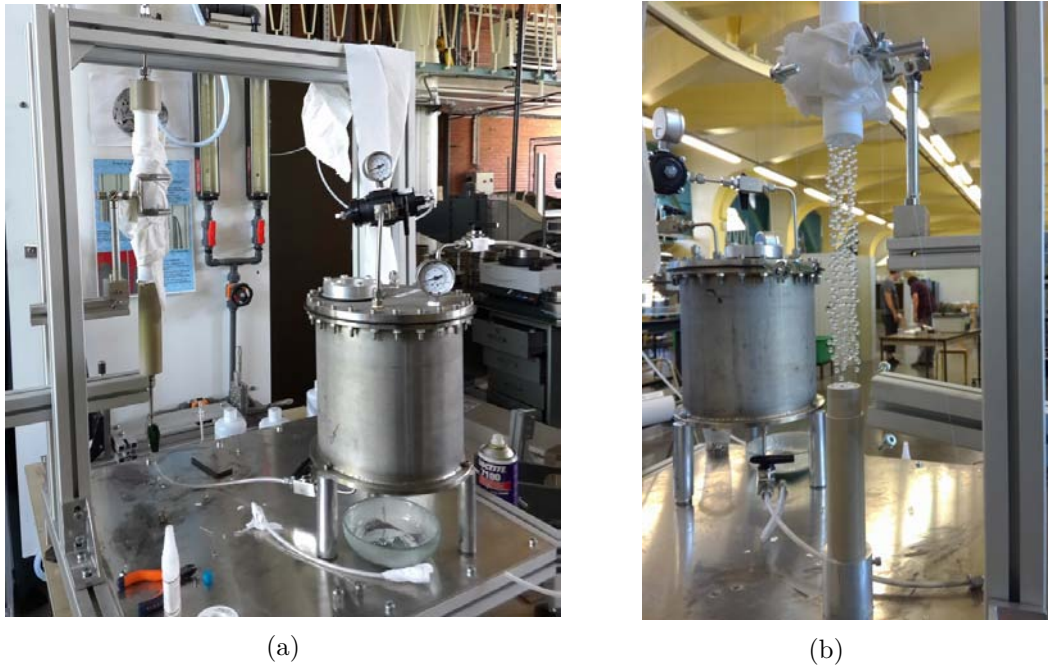


Figure 5.2: Galinstan reservoir. (a) Filling operation of Galinstan inside the ceramic tube (vertical) under Nitrogen pressure, (b) Network of glass beads glued to threads.

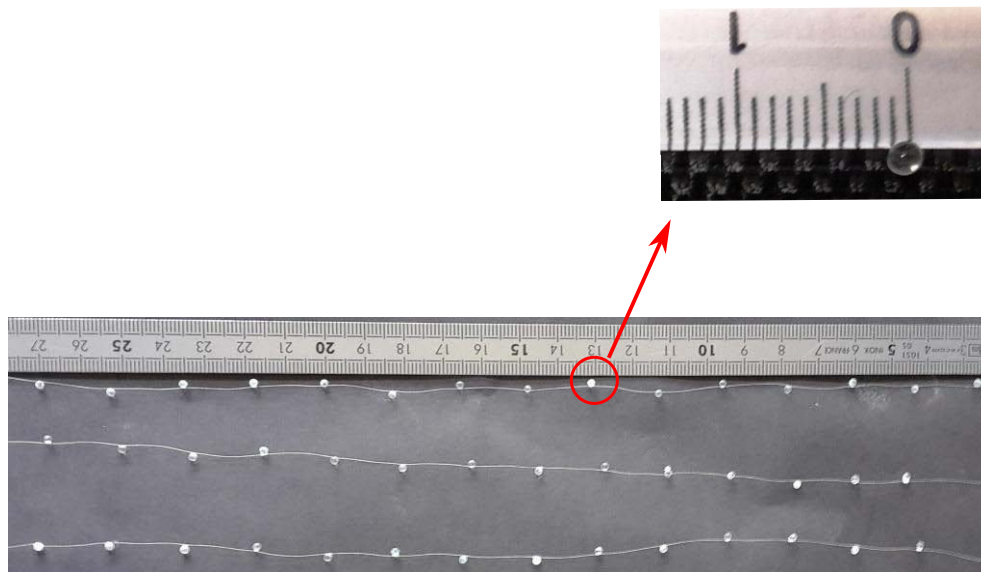


Figure 5.3: View of individual threads with glass beads.

cycles of nitrogen injection and ejection were performed. Thereafter, a pressure below 1 atm is created inside this reservoir. Liquid Galinstan comes in plastic bottles and is

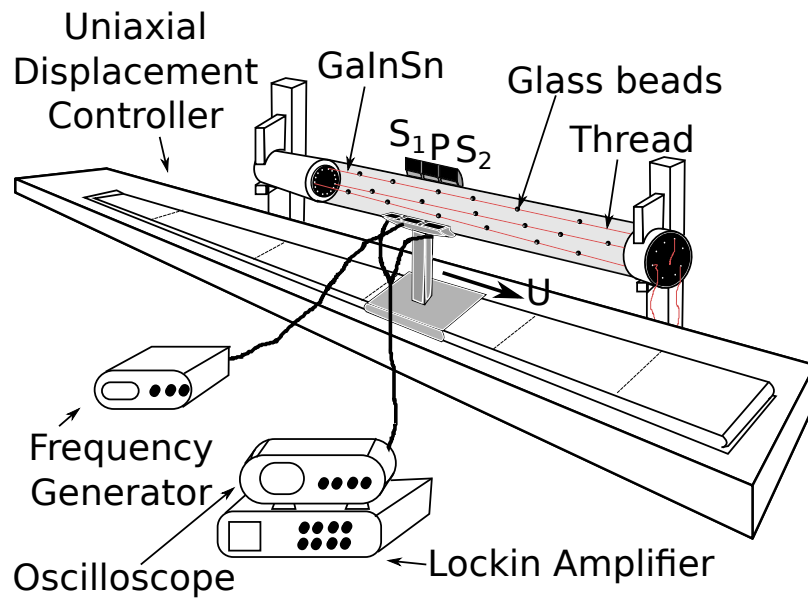


Figure 5.4: Schematic of the experimental set up.

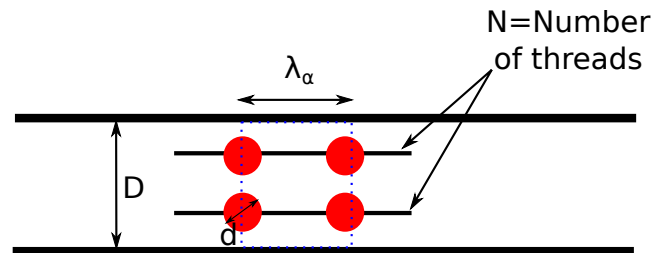


Figure 5.5: Spatial distribution of beads and configuration parameters (here  $N = 2$ ).

sucked in reservoir under this high negative pressure. After this the reservoir is sealed and subsequently pressurized under nitrogen to prevent Galinstan oxidation. The high nitrogen pressure is also used to push Galinstan inside the ceramic tubes against gravity (again in bottom to top configuration) as shown in figure 5.2. The rate at which we fill these ceramic tubes can be controlled by controlling the nitrogen pressure and valve opening.

Table 5.2: Values of parameters defining beads distribution in Galinstan for different configurations – see equation (5.1) and figure 5.5.  $N$  is the number of threads,  $d$  is diameter of the bead,  $\lambda_\alpha$  is the separation between subsequent beads and  $\alpha(\%)$  is geometrical void volume fraction.

S. no.	N	$d(\text{mm})$	$\lambda_\alpha(\text{mm})$	$\alpha(\%)$
a	3	2	17.7	0.1%
b	8	5	7.4	10%
c	3	5	23.3	1.4%
d	3	5	—	beads in 1 cross-section plane
e	0	—	—	0%

## 5.2 Method and Results

The experiments were realized at room temperature for which the physical properties of Galinstan is given in table 5.1. The range of pulsations for AC current in primary coil was  $\omega = 1571$  to  $12\,566 \text{ rad s}^{-1}$ . The corresponding skin-depth of magnetic flux is between  $\delta = 19 \text{ mm}$  and  $\delta = 7 \text{ mm}$ . The current in the circuit is determined indirectly with the help on  $1 \Omega$  resistor in series. The range of magnitude of AC current used was between  $I = 200$  and  $400 \text{ mA}$ . We verified that this magnitude remains stable during the course of experiments. The phase of  $I$  was fixed for each experiments. The secondary coil emf was measured in the Lockin amplifier with respect to this phase. All the experimental results are given for a normalized intensity amplitude of  $1 \text{ A}$ .

For each measurement, a ceramic tube with liquid Galinstan and a specific beads distribution, was mounted and fixed on the two extreme poles of experimental bench (see figure 5.1). ECFM was translated back and forth over this tube several times. The magnetic flux perturbation approach developed in section 3.2.2 was used to analyze and interpret the acquired data.

This section starts with experiments on a ceramic tube containing no beads, *i.e.*,  $\alpha = 0\%$ . The specifications for this configuration is given in table 5.2 under S. no. (e). The objective here is to test  $U$  effect on magnetic flux distortion in Galinstan, with the help of magnetic flux perturbation theory. This would confirm flowmeter function and sensitivity of ECFM. Then to verify whether ECFM is sensitive to the presence of voids inside (read: not only on surface) the medium, experiments are performed on ceramic tube containing beads in one cross-section plane. The specifications for this configuration is given in table 5.2 under S. no. (d). In this configuration, we would expect one oscillation (modulation) in ECFM difference emf when it passes over this cross-section plane. Next, we present experiments with ceramic tube with  $\alpha = 0.1\%$ . The specifications for this configuration is given in table 5.2 under S. no. (a). The objective here is to test  $\alpha$  sensitivity of ECFM in the presence of a distribution of beads. In the end, we test the influence of homogenization in distribution of beads. The ceramic tube for this experiment is S. no. (c) in table 5.2, with  $\alpha = 1.4\%$ .

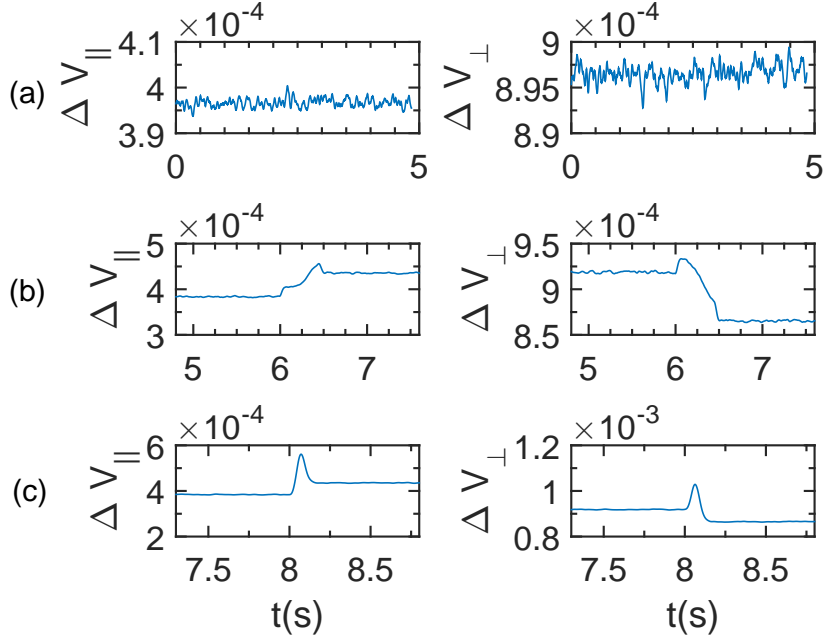


Figure 5.6: Time signal for  $\alpha = 0\%$  at  $\omega = 3142 \text{ rad s}^{-1}$  and  $U =$  (a)  $0 \text{ m s}^{-1}$ , (b)  $0.1 \text{ m s}^{-1}$ , (c)  $1 \text{ m s}^{-1}$ .

Figure 5.6 displays the raw time plots for ceramic tube with  $\alpha = 0\%$  for three different values of velocities  $U = 0$ ,  $U = 0.1$  and  $U = 1 \text{ m s}^{-1}$ . We have observed for the experiments with the Aluminium rods that the motion of ECFM will introduce a DC shift in the time signal of  $\Delta V$ . Since the acceleration (-deceleration) is  $a = 25 \text{ m s}^{-2}$ , the time signal should increase instantaneously, thereafter should be constant, followed by a sudden decrease to the level which corresponds to the electromagnetic conditions on the other side of the ceramic tube.

The value of maximum on the time plot as compared to DC level for  $U = 0 \text{ m/s}$  gives  $\text{Re}_m \phi_u$ . Figure 5.7 displays  $\text{Re}_m \phi_u$  vs  $U$  at  $\omega = 3142$  and  $\omega = 6284$ . As predicted by the results with the Aluminium rod, we find  $\text{Re}_m \phi_{u,\parallel} < \text{Re}_m \phi_{u,\perp}$ . Also as we increase the pulsation, the sensitivity of magnetic flux perturbation to  $U$  decreases. This is demonstrated by decrease in slopes with increasing  $\omega$ . The deviation from linearity is an indication of finite motion of liquid Galinstan when ECFM is in motion. We suspect that increase in  $U$  increases the the Lorentz force on liquid Galinstan, which induces flow of Galinstan and subsequently decreases the relative velocity between ECFM and Galinstan. We can estimate the maximum Hartmann number for this case with following parameters: pulsation  $\omega = 3142 \text{ rad s}^{-1}$  ( $\delta = 12.8 \text{ mm}$ ), dynamic viscosity and electrical conductivity of Galinstan  $\eta = 2.98 \times 10^{-7} \text{ Pa s}$  and  $\sigma = 3.1 \times 10^6 \text{ S m}^{-1}$  respectively and magnetic field  $B_0 = \mu NI/L = 1.2 \text{ mT}$  ( $\mu = 4\pi \times 10^{-7} \text{ H m}^{-1}$  is magnetic permeability of free space,  $N(= 70)$ ,  $I(= 0.4 \text{ A})$  and  $L(= 70 \text{ mm})$  are the number of turns, current

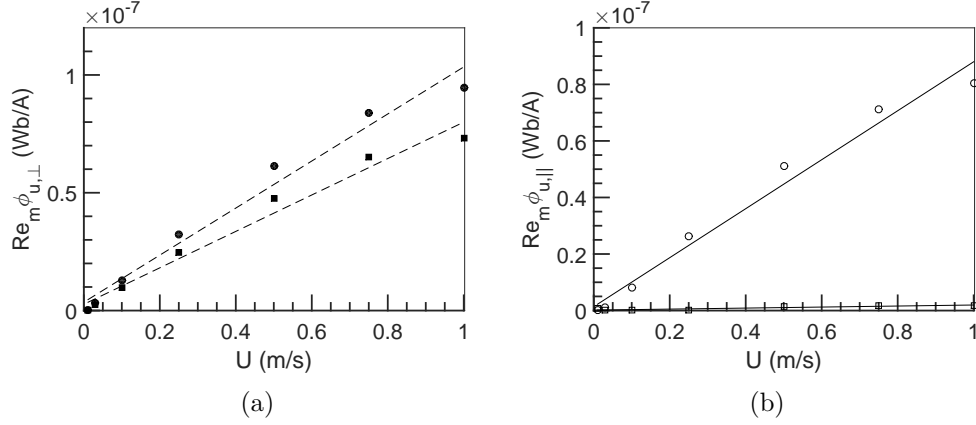


Figure 5.7: (a)  $\text{Re}_m \phi_{u,||}$  (filled markers), (b)  $\text{Re}_m \phi_{u,\perp}$  (unfilled markers) vs  $U$  at  $\omega = 3142$  (○, ●) and  $6284 \text{ rad s}^{-1}$  (□, ■) for  $\alpha = 0\%$ .

and length of primary coil).

$$\text{Ha} = B_0 \delta \sqrt{\frac{\sigma}{\eta}} = 50$$

As discussed in chapter 1, at this value of  $\text{Ha}$ , the Lorentz force is significant and tends to flatten the radial velocity profile. An order of magnitude for induced velocity  $U_g$  towards ECFM in Galinstan can be estimated as

$$\frac{\rho U_g^2}{\delta} = \sigma U B_0^2$$

$$U_g = \sqrt{\frac{\delta U \sigma B^2}{\rho}} = 0.026 \text{ m s}^{-1}$$

where,  $U = 1 \text{ m s}^{-1}$  is the velocity of ECFM and  $\rho = 6360 \text{ kg m}^{-3}$  is the density of Galinstan. Here, we have assumed  $U$  to be relative velocity between static Galinstan and ECFM. The Lorentz force at two ends of the primary coil would add to create Galinstan velocity of  $2 \times U_g \approx 0.05 \text{ m s}^{-1}$ . This is two orders of magnitude smaller than  $U$ . The comparison of slopes in figure 4.25 and 5.7 also shows that ECFM sensitivity to  $U$  is same for Aluminium and Galinstan.

Figure 5.8 shows the difference emf between the two secondary coils in ECFM, which translates over ceramic tube with  $\alpha = 0\%$  (configuration S. no. (d) in table 5.2). In this configuration, three threads are used. We glue one bead on each thread at the same axial location (in one cross-section plane). The ECFM was translated at  $U = 10^{-2} \text{ m s}^{-1}$ . The pulsation in the primary coil is  $\omega = 3142 \text{ rad s}^{-1}$ . The beads are fixed 90 mm away from the PEEK plug. In figure 5.8, the two oscillations, one in the beginning and the other at the end, correspond to ECFM forward and backward motion respectively over the axial location containing beads. The presence of prominent oscillation in time signal demonstrates that the ECFM is sensitive to the presence of glass beads embedded inside Galinstan. This proves that ECFM is not only sensitive to voids at the surface but also

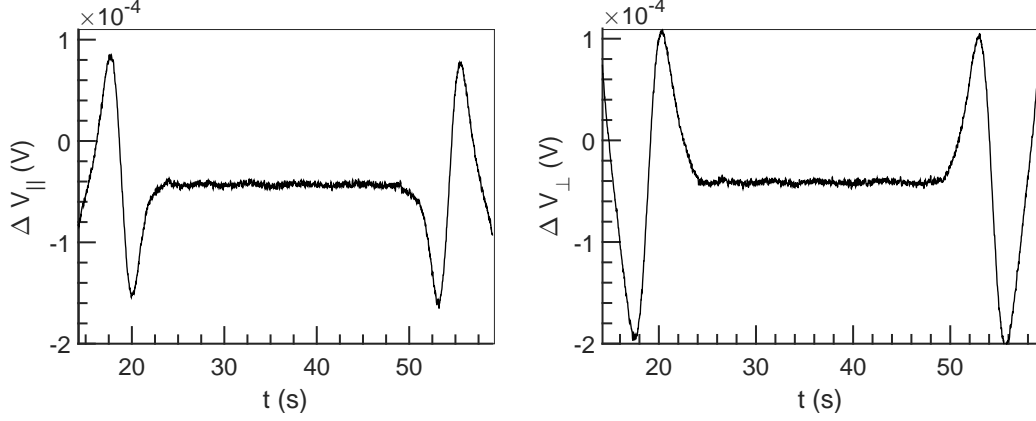


Figure 5.8: (a)  $\Delta V_{||}$  and (b)  $\Delta V_{\perp}$  vs  $t$  for beads in only one cross-section plane (S. no. (d) in table 5.2) at  $U = 10^{-2} \text{ m s}^{-1}$  and  $\omega = 3142 \text{ rad s}^{-1}$ .

to the ones inside electrically conducting medium. We also notice that the quadrature signal ( $\Delta V_{\perp}$ ) is larger than the in-phase signal ( $\Delta V_{||}$ ). This is consistent with the results for Aluminium rods.

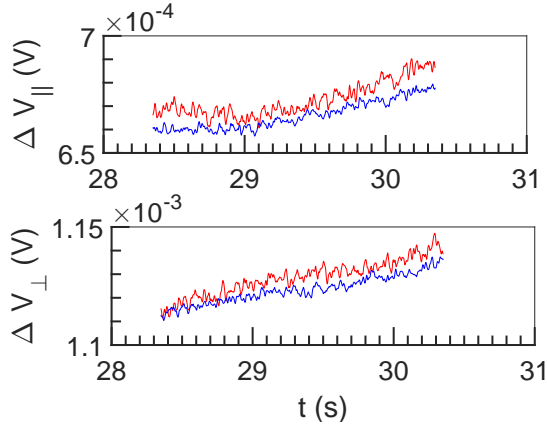


Figure 5.9:  $\Delta V(V)$  vs  $t(s)$  for  $\alpha = 0\%$  (—) and  $\alpha = 0.1\%$  (—) at  $\omega = 6248 \text{ rad s}^{-1}$  and  $U = 10^{-2} \text{ m s}^{-1}$ .

Figure 5.9 shows the time plot of  $\Delta V$  at  $U = 10^{-2} \text{ m s}^{-1}$  and  $\omega = 6248 \text{ rad s}^{-1}$  for  $\alpha = 0\%$  (blue) and  $\alpha = 0.1\%$  (red) respectively. We notice an insignificant DC shift in the time signal for  $\alpha = 0.1\%$  as compared to  $\alpha = 0\%$ . On the other hand, the expected void induced oscillations are not obvious from these graphs. FFT spectral density of these time signals are displayed in figure 5.10. It shows that difference emf signal is noisier for  $\alpha = 0.1\%$  as compared to  $\alpha = 0\%$ . Extremely low values of  $\Delta V$  fluctuations amplitude and the absence of a distinguishable characteristic peak at  $\omega_{\alpha} = 3.5 \text{ rad s}^{-1}$  with  $\alpha = 0.1\%$  can be a result of low  $\alpha$  value or the result of homogenization in the bead distribution.

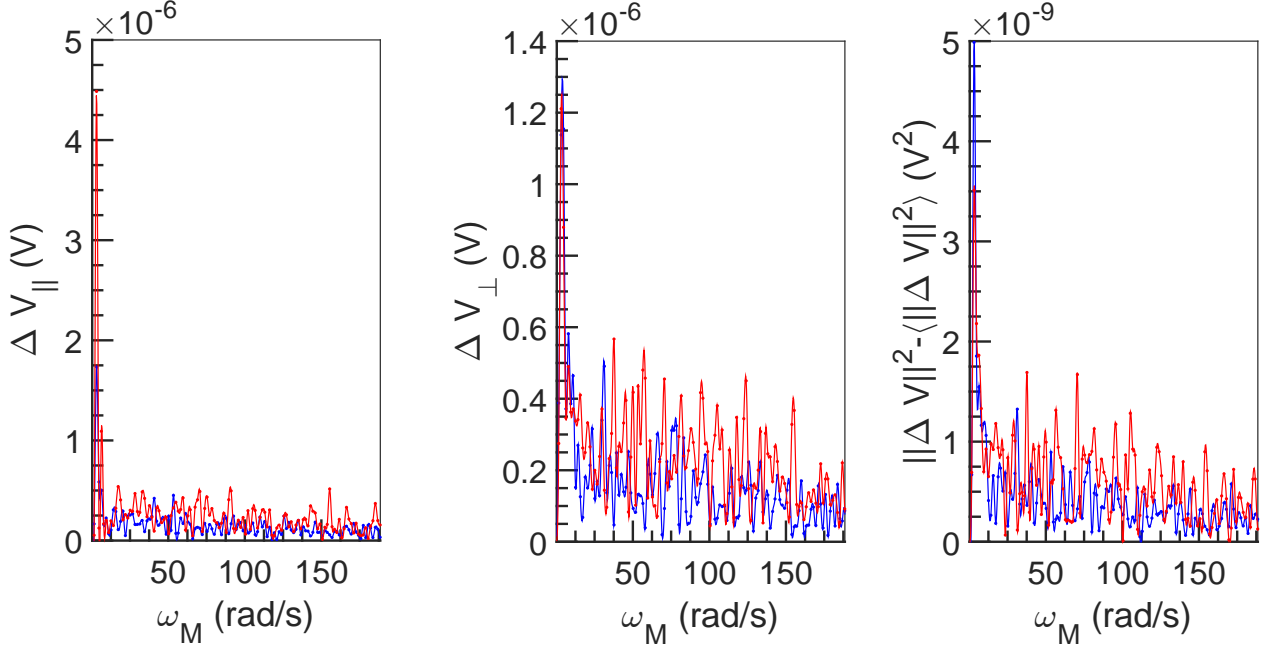


Figure 5.10: FFT spectrum density of  $\Delta V(V)$  for  $\alpha = 0\%$  (—) and  $\alpha = 0.1\%$  (—) at  $\omega = 6248 \text{ rad s}^{-1}$  and  $U = 10^{-2} \text{ m s}^{-1}$ .

To verify whether low  $\alpha$  value plays a role, we conducted experiments with  $\alpha = 10\%$ , but the results were similar. So, we conclude that the low sensitivity to voids is the result of homogenization. Even though we maintain periodicity of beads on each thread, we failed to control the position of the first bead, which was random. Subsequently position of all the beads on one thread as compared to the beads on other threads is random. This resulted in homogenization of beads.

To overcome this, a test configuration was designed with specifications as given in table 5.2 (S. no. (c)). This time, the position of the first bead was same for all three threads. Therefore, the glass beads were placed (approximately) periodically in axial direction. Figure 5.11 shows the time plot obtained for this tube. The first oscillation on extreme left and the last oscillation on extreme right in this figure, corresponds to the transition of the ECFM from the PEEK plug on to the ceramic tube. The subsequent oscillations contain signature of void induced perturbations. We see that the number of oscillations are around 3 or 4. This is insufficient for statistically good FFT spectral density.

We plot FFT spectral density of  $\Delta V_{||}$ ,  $\Delta V_{\perp}$  and  $||\Delta V||^2$  in figure 5.12. We take the same raw time signal as shown in figure 5.11. The theoretical value of characteristic modulation pulsation is  $\omega_{\alpha} = 27 \text{ rad s}^{-1}$ . From figure 5.12, we obtain  $\omega_{\alpha} = 28 \pm 4 \text{ rad s}^{-1}$  for  $\Delta V_{||}$ ,  $\omega_{\alpha} = 22 \pm 4 \text{ rad s}^{-1}$  for  $\Delta V_{\perp}$  and  $\omega_{\alpha} = 22 \pm 4 \text{ rad s}^{-1}$  for  $||\Delta V||^2$ .  $0.5\langle\psi_{\alpha}|\psi_{\alpha}\rangle$  calculated from  $\Delta V_{||}$  and  $\Delta V_{\perp}$  is  $2.4 \times 10^{-9} \text{ V}$  compared to  $6.8 \times 10^{-9} \text{ V}$  as obtained



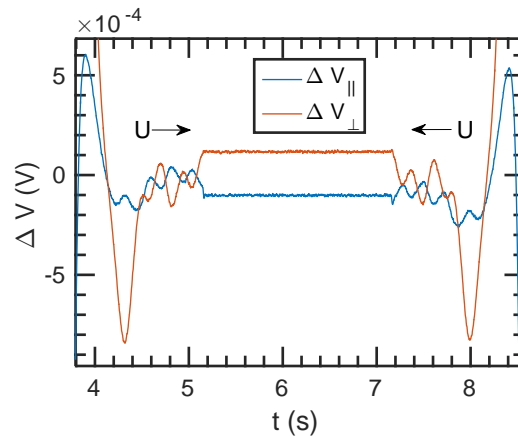
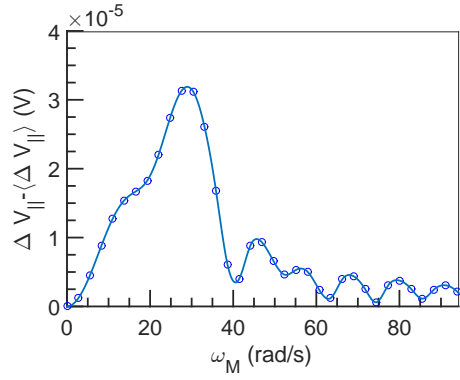
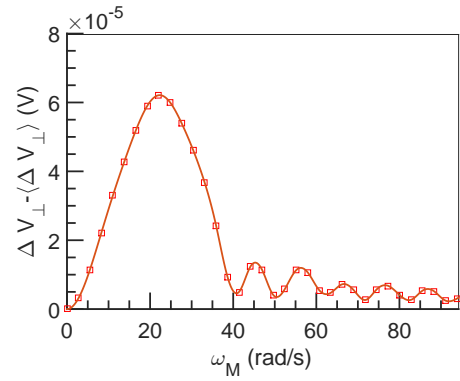


Figure 5.11:  $\Delta V_{||}$  (—) and  $\Delta V_{\perp}$  (—) vs  $t(s)$  for  $\alpha = 1.4\%$  at  $\omega = 9425 \text{ rad s}^{-1}$  and  $U = 0.1 \text{ m s}^{-1}$ .

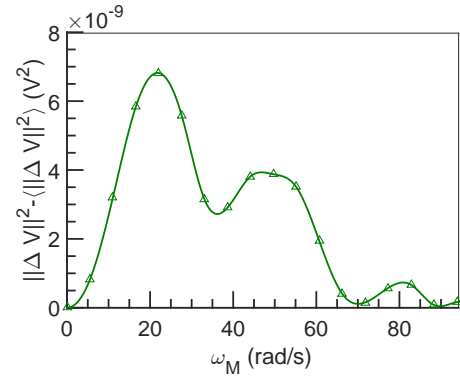
from the second peak for  $||\Delta V||^2$ . So the values we obtain for  $\psi_{\alpha}$  by two methods, are comparable in order of magnitude but not identical. This indicates that the magnetic flux perturbation theory might be applicable to experiments with liquid Galinstan.



(a)



(b)



(c)

Figure 5.12: (a)  $\Delta V_{||} - \langle \Delta V_{||} \rangle$ , (b)  $\Delta V_{\perp} - \langle \Delta V_{\perp} \rangle$  and (c)  $\|\Delta V\|^2 - \langle \|\Delta V\|^2 \rangle$  vs  $\omega_M$  at  $U = 0.1 \text{ m s}^{-1}$  for  $\alpha = 1.4\%$ .

### 5.3 Conclusions

We have developed specific experiments: hollow ceramic tubes filled with liquid Galinstan containing a network of glass beads. This allows us to control well the size and

position of the void.

In figure 5.6, we find that ECFM is sensitive to  $U$ . We analyze this signal with the help of magnetic flux perturbation approach. As shown in figure 5.7,  $\text{Re}_m \phi_u$  vs  $U$  plot is linear. This confirms the velocimetry function of the ECFM in liquid Galinstan.

The experiments with Galinstan tubes containing glass beads in one tube cross-section plane, demonstrates that ECFM signal is not only sensitive to voids at the surface, which we saw in the previous chapter, but also to the voids inside the medium within one skin depth. The same could not be replicated with  $\alpha = 0.1\%$ . Subsequently, we proposed that the homogenization was responsible for the later. A test rod with  $\alpha = 1.4\%$  was designed and tested. But this time we ensured the periodicity of  $\alpha$  distribution in axial direction. The raw time signal for this tube shows void induced perturbations. The similarity of  $\psi_\alpha$  value calculated from in-phase and quadrature phase signal components of  $\Delta V$ , and that calculated from  $||\Delta V||^2$ , confirms the relevance of magnetic flux perturbation theory even for liquid Galinstan.

Finally, we conclude that to obtain meaningful results from these kind of experiments we need to increase the axial length of ceramic tubes. Subsequently, we should use vertical set-up in place of presently used horizontal set-up. This is to ensure mechanical integrity, *i.e.*, avoid bending of tubes.

# Conclusions

Our objective was to analyze an electromagnetic technique to address the issue of gas detection and characterization in two-phase liquid metal flows. Although the concerned application is Sodium cooled Fast Reactor, the results can also be extended to other industrial and natural processes involving two-phase liquid metal flows. On the technological side, our objective was to test the feasibility, limits, and procedures for  $U$  and  $\alpha$  detection and characterization in two-phase liquid metal flows with ECFM. Since, this involves motion of liquid metal in presence of electromagnetic fields and voids, many physical processes and their couplings play a role from physics point of view. Our role was to investigate the effect of pulsation  $\omega$  which affects through Faraday induction, velocity  $U$  governed by Lorentz force effects and  $\alpha$  which distorts local eddy currents at local scales and magnetic flux at  $\phi$ -integrated scale.

Literature review given in chapter 2, provides the direction for subsequent chapters in this manuscript. The results in literature for ECFM in single phase flows suggest that induced emfs in ECFM is linear in  $U$  at small  $Re_m$ . The effect of  $U$  is more on in-phase emf signal in ECFM than on the quadrature-phase emf. The experiments with ECFM in two-phase liquid metal flows suggest that ECFM is sensitive to void presence in liquid metal. Significant modulations/oscillations on ECFM emf are signatures of bubbles passing through ECFM. The amplitude of these oscillations are found to be linear in  $\alpha$  for  $\alpha \lesssim 4.5\%$ . The effect of void induced modulations is more on the quadrature phase emf compared to in-phase emf. We find lack of a comprehensive model to characterize ECFM signals in two-phase liquid metal flow experiments. Maxwell's model treats the case of a homogeneously distributed spheres in electrically conducting medium in the absence of Faraday induction and Lorentz force effects and for very small  $\alpha$ . This model predicts a linear relation between the equivalent electrical conductivity and  $\alpha$  of this kind of two-phase medium. There are models which take into account of Lorentz force effects at low pulsations  $\omega < 100 \text{ rad s}^{-1}$ . These model predict decoupling of  $U$  and  $\alpha$  effects on induced potentials. The models at high pulsations neglect Lorentz force effects. They predict the change in both in-phase and quadrature phase emfs.

We analyzed theoretically, an ECFM in chapter 3. A finite element simulation in COMSOL<sup>®</sup> helps us to study the distribution in magnetic fields and subsequently design an ECFM for experiments. We propose the theory for three approaches to characterize ECFM signals in two-phase flows. In the first approach, we model the difference emf between two secondary coils. We assume decoupling between Faraday induction and

Lorentz force effects. This is possible when  $\delta \gg D$  and  $\text{Re}_m \ll 1$ . The theoretical expression for in-phase emf depends on  $U$  and  $\alpha$ , while the quadrature phase emf is independent of  $U$  but dependent on  $\alpha$ . In the special case of periodic distribution of voids, the squared norm of difference flux can be expanded in terms of harmonics. The constant term  $C_1$  is a function of  $\alpha$ , the first harmonic  $C_2$  is linear in  $U^2$  and depend on  $\alpha$ , while the second harmonic  $C_3$  is depends on  $\alpha$  but is independent of  $U$ . We do not have an explicit expression in  $\alpha$  in this approach. The second approach also models the net difference flux between the two secondary coils. However, this time we assume  $\delta \lesssim D$  and  $\text{Re}_m \ll 1$ . Here, Faraday induction effects are significant and cannot be separated from the Lorentz force effects. Subsequently, we propose magnetic flux decomposition in terms of  $\text{Re}_m$  and  $\alpha$ , assuming  $\text{Re}_m \ll 1$  and  $\alpha \ll 1$ . The total flux is written as  $\phi_0 + \text{Re}_m \phi_u + \phi_\alpha$ . This model predicts that both in-phase and quadrature phase difference fluxes depend on  $U$  and  $\alpha$ . Moreover, Fourier decomposition of squared norm of difference flux predicts that the first harmonic is a coupled term between  $U$  and  $\alpha$ . The second harmonic depends explicitly on  $\alpha$  and independent of  $U$ . Mathematical basis for a Lissajous ellipse fitting approach was also presented in this chapter. However, this last does not give explicit expressions in  $U$  and  $\alpha$ .

These theoretical models were confronted with experiments with ECFM in an experimental setup which models two-phase liquid metal flow (chapter 4). Aluminium rods represent electrically conducting medium while grooves and holes machined on its outer surface simulate voids. The motion of ECFM over rod, simulates plug flow. This experimental setup easily allows to control the velocity, void size and void locations. The pulsation in the range  $1.5 \times 10^3 \leq \omega \leq 12.5 \times 10^3 \text{ rad s}^{-1}$ , velocity in  $0 \leq U \leq 1 \text{ m s}^{-1}$  and void fractions in range  $0.06\% \leq \alpha \leq 6.9\%$  was studied. From the experimental results, we were able to confirm that  $C_1 \sim U^2$  and is independent of  $\alpha$ , and  $C_3 \sim \alpha^2$  exactly as predicted by the first theory. But we also found that  $C_2 \sim \alpha$ , instead of  $C_2 \sim \alpha^2$  as predicted by the theory. Also both the in-phase and quadrature phase emfs were perturbed by  $U$ . This clearly comes from strong Faraday induction effects.

Then we analyzed the experimental results with magnetic flux perturbation theory. As predicted by the theory we obtain each component of the flux:  $\phi_0$ ,  $\text{Re}_m \phi_u$  and  $\psi_\alpha$  in the time signal. We find that  $\text{Re}_m \phi_u$  is linear in  $U$  and independent of  $\alpha$ , while  $\psi_\alpha$  is independent of  $U$  and linear in  $\alpha$  for  $\alpha \lesssim 4.5\%$ . These results are valid even though the corresponding theory assumed  $\alpha \ll 1$  and  $\text{Re}_m \ll 1$ . We also found that the in-phase emf is more sensitive to  $U$  than the quadrature phase emf, while the quadrature-phase emf is more sensitive to  $\alpha$  than in-phase emf. This is in agreement with the literature. The pulsation dependence studies show,  $\phi_{0,\perp} \sim \omega^{-1/2}$  and  $\phi_{u,\parallel} \sim \omega^{-1}$ . These results were explained with a simple analysis based on Maxwell's equations. On the other hand, we found that  $\phi_{0,\parallel}$  deviates strongly from  $\omega^{-1/2}$  at large pulsations, and  $\phi_{u,\perp} \sim \omega^{-3/2}$ . This points towards strong Faraday induction effects. We also find a strong coupling between  $\alpha$  and  $U$  effects, as given by term  $A_1$  in FFT spectrum density of squared norm of difference emf signal. In the Lissajous ellipse fitting approach, we find that the sensitivity of 5-coils ECFM to void is more than the 3-coils ECFM. The amplitude of fluctuations in the orientation of ellipse increases as a function of  $\alpha$ , but it is independent of  $U$ . This

was explained in terms of small  $\text{Re}_m$ . We find that the lower limit of detection with this approach is approximately 0.3% compared to 0.06% for the magnetic flux perturbation approach. An advantage of this last approach is its simplicity.

To confirm the results obtained for the model two-phase flow, experimental setup with liquid Galinstan has been developed and shown in chapter 5. The glass beads inside ceramic cylinders filled with liquid Galinstan simulate voids. For  $\alpha = 0\%$ , the experimental results are similar to the ones obtained for plain aluminium rod.  $\text{Re}_m\phi_u$  is linear in  $U$ ,  $\text{Re}_m\phi_{u,\parallel} < \text{Re}_m\phi_{u,\perp}$  and  $\text{Re}_m\phi_u$  decreases with  $\omega$ . The experiment with bead confined to one cross-section plane, confirms the sensitivity of ECFM to void buried inside electrically conducting medium (but within  $\delta$ ). We were also able to confirm that  $\psi_{\alpha,\parallel} > \psi_{\alpha,\perp}$ . The results of experiments with  $\alpha = 1.4\%$  shows the sensitivity of ECFM to a distribution of voids. However, same could not be replicated with  $\alpha = 0.1\%$ , due to small size of beads and homogenization in their positioning.

As future perspectives, we suggest to increase the axial length of the ceramic tubes in Galinstan experiments. And to repeat two-phase experiments with other void fractions. Other than this, we find the necessity to develop numerical simulations to explain void effects at local (void) scale. This helps to visualize electromagnetic fields at local scale when void effects, Faraday induction effects and Lorentz force effects are coupled.



## Appendix A

# Publication: Thermo-magnetic behaviour of AFM-MFM cantilevers



# Thermo-magnetic behaviour of AFM–MFM cantilevers

M Kumar<sup>1,2</sup>, R Arinero<sup>1,3</sup>, W Bergez<sup>1</sup> and Ph Tordjeman<sup>1</sup>

<sup>1</sup> Université de Toulouse, INPT-CNRS, Institut de Mécanique des Fluides de Toulouse,

2 allée du Pr Camille Soula, 31400 Toulouse, France

<sup>2</sup> CEA Cadarache, 13115 Saint-Paul-lez-Durance

<sup>3</sup> Univ. Montpellier, IES, UMR 5214, F-34000, Montpellier, France

E-mail: [philippe.tordjeman@imft.fr](mailto:philippe.tordjeman@imft.fr)

Received 17 February 2015, revised 28 April 2015

Accepted for publication 14 May 2015

Published 25 June 2015



## Abstract

Atomic force microscopy (AFM) experiments were performed to study the behaviour of AFM cantilevers under an external magnetic field  $B$  and temperature field produced by a coil with an iron core. Four cantilever types were studied. Forces were measured for different  $B$  values and at various coil-to-cantilever separation distances. The results were analysed on the basis of a phenomenological model. This model contains the contribution of two terms, one monopole–monopole interaction at short distance, and one apparent paramagnetic interaction in  $\nabla B^2$  at large distance, which represents the temperature effects. We observe a good agreement between the model and the experimental data.

Keywords: magnetic force microscopy (MFM), AFM, cantilever, coating, dc magnetic field.

(Some figures may appear in colour only in the online journal)

## 1. Introduction

The behaviour of AFM cantilevers under a magnetic field is primarily known through a well-established technique called magnetic force microscopy (MFM) [1, 2]. If the tip approaches the sample surface to within a distance of typically 10–500 nm, magnetic interaction of the tip with the stray field emanating from the sample becomes detectable. It is thus possible to explore magnetic domains with sub-micrometer spatial resolutions. MFM has been used to study the properties of materials for magnetic recording media [3–5], to optimize the recording modes of magnetic heads [6], to investigate the structure and properties of nanoparticles, alloys and nanocomposites [7] and thin films [8], and in the development of methods for magnetic recording with ultrahigh density [9]. MFM uses magnetized probes. In the dynamic mode, the resonance frequency or phase shifts are proportional to magnetic force gradients [3]. In order to quantify the observed effects, it has been common to use monopole and dipole approximations to describe the MFM tip–sample interactions [10]. Metal rings carrying electrical current with inner diameters between 1 and 5  $\mu\text{m}$  were used to calibrate the MFM tip's effective magnetic charge and effective magnetic moment along the

tip axis [11–13]. Quantitative MFM has been strictly limited to magnetic interactions at very short range under a very low magnetic field. This standard approach is convenient for many applications but it is not adapted to study quantitatively the local magnetic properties of condensed phases under an external magnetic field. To this end, it is important to separate the influence of the external magnetic field from the influence of the sample on the MFM probe.

Such studies are important to understand, for example, the orientation of magnetic domains (in bulk or thin films) under a dc or ac external field, or the magnetic instability of ferrofluids (peak patterning) where local response is closely related to the global excitation [14]. These studies require one to characterize the response of AFM cantilevers under an external magnetic field in the absence of samples.

In this paper, we investigate the force experienced by different cantilevers due to the combined effects of a magnetic field and a temperature field, both produced by a dc current in a millimetric coil. This work shows that the cantilevers experience repulsion or attraction far from the coil and only attraction at short distance. The force depends mainly on the coating material as well as on the bulk material of the cantilevers. We point out that effects of temperature dominate the

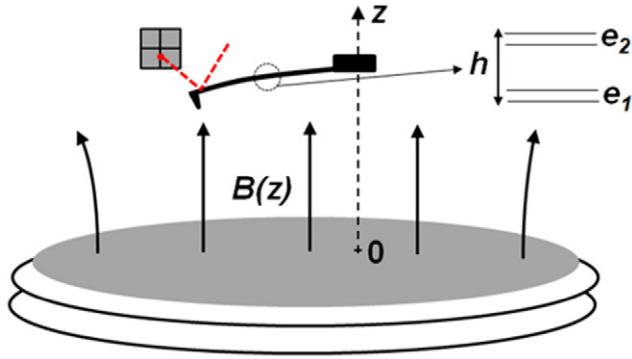


**Figure 1.** Schematic representation of the experimental set-up. An AFM probe is placed in an external magnetic field produced by a large coil with iron core. For a three-layer cantilever of total thickness  $h$ ,  $e_1$  is the thickness of the coating on the tip side and  $e_2$  on the reflector side.

interaction force at large distance while magnetic effects dominate at short distance. A phenomenological equivalent magnetic model that takes into account the thermal effects can be used to predict the behaviour of cantilevers at the two scales. The paper is organized as follows: in section 2 we describe the materials and methods. The experimental results are presented in section 3 and are discussed in section 4.

## 2. Materials and methods

Different commercial AFM cantilevers were placed in the vicinity of a coil of  $N_C$  turns ( $N_C = 40$ ), with a core of iron, carrying a dc current  $I_C$ , as described in figure 1.  $z$  is the distance between the top surface of the iron core and the position of the fixed end of the cantilever.  $z$  is measured by the vertical piezo-transducer of the AFM.

The magnetic field produced by the coil as a function of the distance  $z$  is given by:

$$B(z) = \mu_0 \frac{N_C I_C}{2h_C} \left( \frac{z}{\sqrt{R_C^2 + z^2}} - \frac{z + h_C}{\sqrt{R_C^2 + (z + h_C)^2}} \right), \quad (1)$$

where  $h_C$  and  $R_C$  are respectively the height and the radius of the coil ( $h_C \approx 4.5$  mm and  $R_C \approx 4$  mm).

The relation between  $B$  and  $I_C$  is linear as presented in figure 2. For typical values of  $I_C$  ranging from 0 to 3 A, the field is constant in time and varies from 0 to 12 mT. The field calibration has been realized by means of a Hall effect Gaussmeter (GM07 from Hirst Magnetic Instruments Ltd) positioned in contact with the core at its centre. We have also measured a remanent magnetic field of 0.4 mT in the centre of the iron core when the current is switched off. In parallel, the temperature  $T$  of the iron core increases in  $I_C^2$  by Joule heating (figure 2). Consequently, in our experiments, the production of a magnetic field is systematically associated to a thermal field.

AFM experiments were performed with the Agilent™ 5500 in order to measure the force applied to cantilevers of different types when a dc current of various intensity is passing through the coil. For each cantilever, we determined the sensitivity

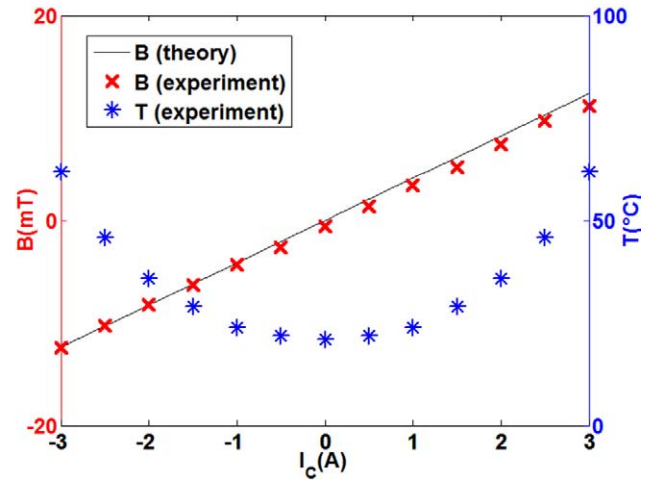


**Figure 2.** Iron core temperature and magnetic field measured by a Hall effect Gaussmeter in contact with the iron core and comparison with the theoretical values for  $z = 100$   $\mu$ m.

( $\text{nm V}^{-1}$ ) by measuring the curve of voltage deflection versus vertical displacement when the tip comes in contact with the iron core or aluminium plate (contact mode). No lateral deflection was observed in our experiments. Moreover, we checked that the stiffness calibrated by the thermal tuning method is in agreement with the value given by the manufacturers. Hence, it is straightforward to obtain the force applied to the cantilever in presence of a magnetic and thermal field from the stiffness and the sensitivity. The cantilevers are shown in figure 3. MFMR probes from Nanoworld™ are designed for MFM. They are made from highly doped monolithic silicon and their average stiffness  $k$  is equal to  $2.8 \text{ N m}^{-1}$ . On the tip-side of the cantilever, a coating of approximately 40 nm thick cobalt alloy is deposited. On the reflector side, a 30 nm thick aluminum coating enhances the reflectance and prevents light from interfering within the cantilever. MESP from Bruker™ are also MFM probes where both tip and reflector sides are coated with a 50 nm thick CoCr layer. The cantilever stiffness is  $k \approx 3 \text{ N m}^{-1}$ . Hydra 6V from AppNano™ are V-shaped soft cantilevers ( $k \approx 0.08 \text{ N m}^{-1}$ ) made of  $\text{Si}_3\text{N}_4$ . The tip is made of silicon and the reflector side is gold coated. Finally, we also used  $3.7 \text{ N m}^{-1}$  stiff, non-coated Si cantilevers (Fort from AppNano™). No further information was available on the composition and fabrication of coatings.

The experiments were realized with cantilevers taken from two or three different batches of the same type. Due to the fabrication process, cantilevers of the same batch have slightly different geometrical and material properties. For this reason, each measurement was repeated ten times with different cantilevers. The force values reported on the curves in this paper correspond to the average of these measurements given with a maximum standard deviation of 15%. The accuracy of the distance controlled by the piezo-transducer and of the magnetic field is  $\pm 1$   $\mu$ m and  $\pm 10^{-2}$  mT, respectively.

To separate the effects of the magnetic field with those of the thermal field, we designed a small aluminium plate ( $1 \times 1 \text{ cm}^2$ ) heated by a straight Cu wire. No magnetic field

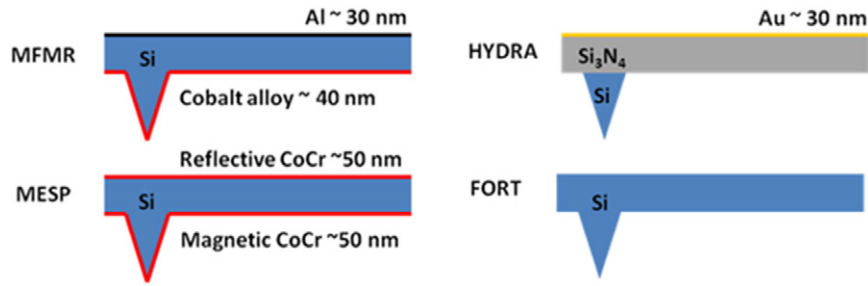


Figure 3. Commercial AFM cantilevers used in the experiments.

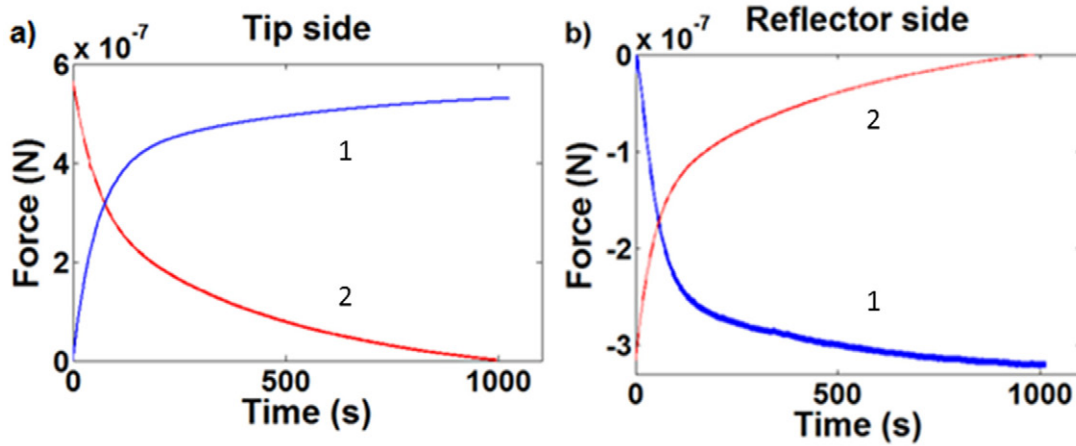


Figure 4. Typical transient regimes observed at  $z = 100 \mu\text{m}$  for MFMR cantilevers when the magnetic field ( $B = 10\text{mT}$ ) is turned on (curve 1) and then turned off (curve 2). (a) tip side configuration and (b) reflector side configuration.

was produced and the temperature could be varied from room temperature up to  $\sim 40^\circ\text{C}$ .

### 3. Experimental results

#### 3.1. Effects of the magnetic and thermal fields

We consider, as a first example, the response at long probe-to-surface distance ( $z = 100 \mu\text{m}$ ) of an MFMR cantilever in a standard configuration, i.e. with the tip directed towards the surface. We refer this configuration as ‘tip side’. In the presence of a dc magnetic field ( $B = 10\text{mT}$  and  $T = 46^\circ\text{C}$ ), the force versus time curve exhibits both short and long characteristic times,  $\tau_1$  and  $\tau_2$  respectively (figure 4(a)). The force is positive, which means repulsion, and reaches relatively high values around  $600\text{nN}$ . After  $1000\text{s}$ , the current is switched off.

We observe a decay that is characterized by a slightly different rate of variation. When the MFMR cantilever is turned upside down (backside directed towards the surface, ‘reflector side’ configuration), the force becomes attractive and its time variation shows the same characteristic times (figure 4(b)). We point out that the same transient regimes occur for both configurations, when the field is turned on and off. However, the magnitude of the force differs in the reflector side and tip side cases by a factor 2. The main result is that the force applied on the cantilever depends on the orientation of the cantilever. Applying a dc potential between the cantilever and the iron core, we also verified that the interaction force is not due to static electrical charges.

In terms of reproducibility, field-on or field-off repeated measurements showed a similar tendency with different MFMR cantilevers coming from the same batch. The values of  $\tau_1$  and  $\tau_2$  vary between  $45\text{--}55\text{s}$  and  $400\text{--}500\text{s}$ , respectively. These two times are larger by some orders of magnitude than characteristic spin relaxation times. In consequence, the transient effects do not seem to be linked to magnetism.

We have verified that  $\tau_1$  does not match the time constant of the equivalent RL circuit. The inductance and the resistance of the coil are  $L = \frac{\mu_0 N^2 \pi R^2}{hc}$  and  $R = \frac{\rho_w L_w}{S_w}$ , where  $\rho_w = 17 \times 10^{-9} \Omega\text{m}$ ,  $L_w = 0.1\text{m}$  and  $S_w \approx 10^{-9}\text{m}^2$  are the resistivity, the length and the section area of the wire, respectively. The electrical time constant  $\tau = L/R$  is equal to a few  $\mu\text{s}$ , which is much lower than  $\tau_1$ . This time seems to be related to the convective effects due to direct heating of ambient air by the coil (the magnitude of the air velocity is of the order of  $\sqrt{g\beta\Delta T l}$ , where  $\beta$  is the thermal expansion coefficient,  $\Delta T$  the temperature difference between coil and ambient air and  $l$  is the height of the coil). Furthermore, the second time constant  $\tau_2$  corresponds to the thermal diffusion characteristic time corresponding to temperature equilibrium of the system:  $\tau_2 = \frac{C_p}{2hS}$ , where  $h$  is the natural convection coefficient corresponding to heat transfer between the iron core and air ( $h \approx 18\text{W K m}^{-2}$  estimated from [15]),  $S$  is the area of the iron core ( $S = 6.3 \times 10^{-5}\text{m}^2$ ) and  $C_p$  its heat capacity ( $C_p = 1.1\text{JK}^{-1}$ ).

The variations of force with the magnetic field for the four cantilever types are presented in figure 5. For each value of

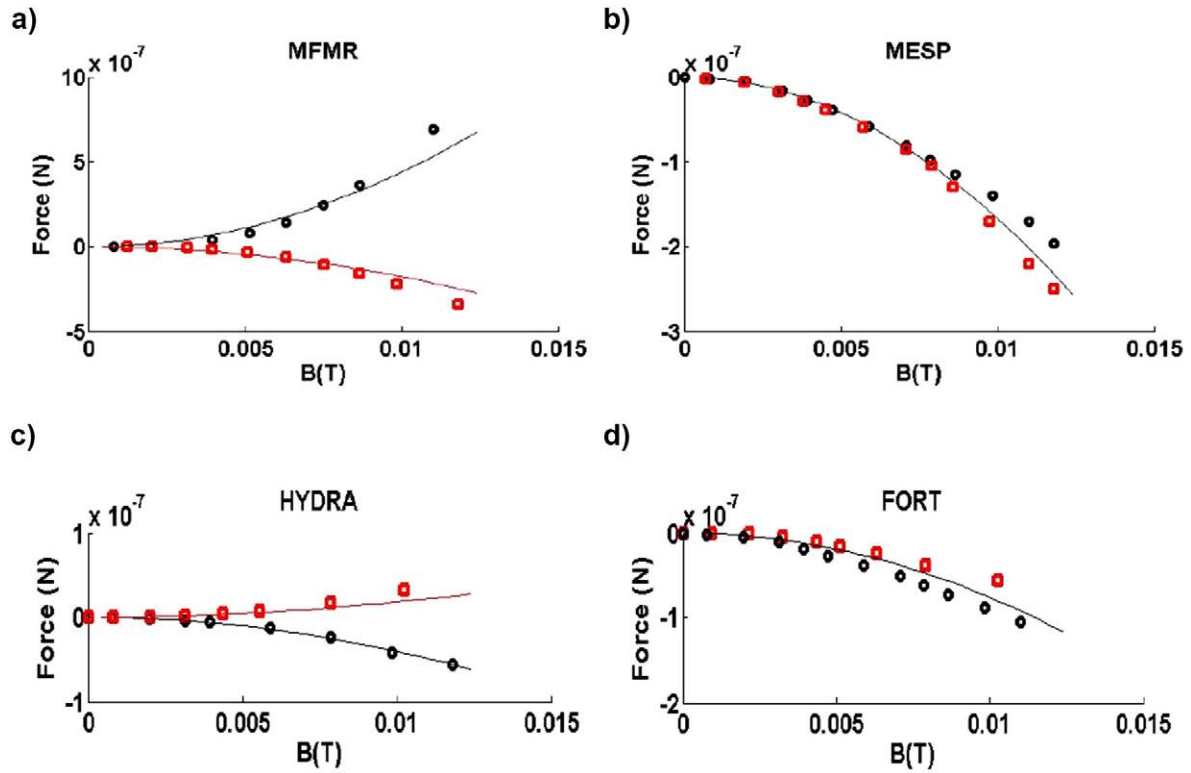


**Figure 5.** Force versus magnetic field at  $z = 100 \mu\text{m}$ . Experimental data: (○) tip side configuration; (□) reflector side configuration. MFMR (a), MESP (b), HYDRA (c) and FORT (d). Solid lines: comparison with the model (equations (8) and (9)).

magnetic field, a delay of 10 min is observed before the force is measured at  $z = 100 \mu\text{m}$ . All the results show that the interaction force varies as a function of  $B^2$ . In the case of MFMR (figure 5(a)), we clearly distinguish strong repulsive and attractive behaviours on tip and reflector side, respectively.

The dependence of the interaction force on the magnetic field is represented in figures 5(b)–(d) for MESP, HYDRA and FORT cantilevers, respectively. MESP cantilevers have the same coating on the tip and reflector sides and show the same attractive behaviour on both sides. HYDRA cantilevers are attracted on the tip side which is uncoated and repulsed on the reflector side which is gold coated. Finally, FORT cantilevers, which are uncoated, are attracted on both sides. We note however a deviation between the results for the two orientations due to differences in the geometrical and material properties of the two sides. The forces are of the same order for MFMR, MESP and FORT cantilevers. On the other hand, the forces measured with HYDRA cantilevers are one order of magnitude lower. The attractive and repulsive behaviours are summarized in table 1.

### 3.2. Cantilever–coil distance effects

In this section, we present the variation of force as a function of distance for different dc magnetic fields. The results for the MFMR cantilevers are presented in figure 6. For each value of the magnetic field, the force exhibits two different behaviours for short range and long range distances: at short distance, the force is attractive whatever the orientation of the cantilever and scales as  $-1/z^2$ . The dependence is not measurable below

a few  $\mu\text{m}$  because the cantilever deflection is too large. At long distance, the force reaches an asymptotic value. It is repulsive for tip side cases and attractive for reflector side cases. The asymptotic value varies with the magnitude of  $B$ , as shown in figure 5(a).

The MESP probes display similar behaviour as MFMR, i.e. a  $-1/z^2$  force dependence at short distance and an asymptotic force at long distance, which is now attractive for both tip side and reflector side orientations. These results are in agreement with figure 5(b).



HYDRA cantilevers (figure 8) show the same short distance trend as the other cantilever types. The asymptotic force values are coherent with figure 5(c). It was difficult to measure forces above 5 mT in the tip side configuration because of the low cantilever stiffness, which implies very large deflections. For example, considering  $k \sim 0.08 \text{ N m}^{-1}$  and a sensitivity factor  $\chi \sim 100 \text{ nm V}^{-1}$  between the signal of the photodetector and the deflection, the limit of 10V of the photodetector is exceeded at forces above 80 nN. Experimental results with FORT cantilevers are represented in figure 9. Tip and reflector side responses present a similar attractive behaviour within the experimental uncertainties.

## 4. Discussion

### 4.1. Long range force model

In order to analyse the effects of large variations of temperature, we studied the long range response of the cantilevers using the aluminium plate heated by the Joule effect without

**Table 1.** Long distance (at  $z = 100 \mu\text{m}$ ) attractive (A) or repulsive (R) response of the four cantilever types for tip side and reflector side configurations. Apparent magnetic coefficients were obtained by fitting the experimental data.

Probe reference			Apparent magnetic coefficients
MFMR	R	A	$\Gamma_1 \cong -2.93 \times 10^8$ $\Gamma_2 \cong 3.91 \times 10^8$ $\Gamma_{\text{bulk}} \cong 186$
MESP	A	A	$\Gamma_1 = \Gamma_2 \cong 2.84 \times 10^4$ $\Gamma_{\text{bulk}} \cong 186$
HYDRA	A	R	$\Gamma_1 = 0$ $\Gamma_2 \cong -1.66 \times 10^8$ $\Gamma_{\text{bulk}} \cong 8.31 \times 10^6$
FORT	A	A	$\Gamma_1 = 0$ $\Gamma_2 = 0$ $\Gamma_{\text{bulk}} \cong 186$

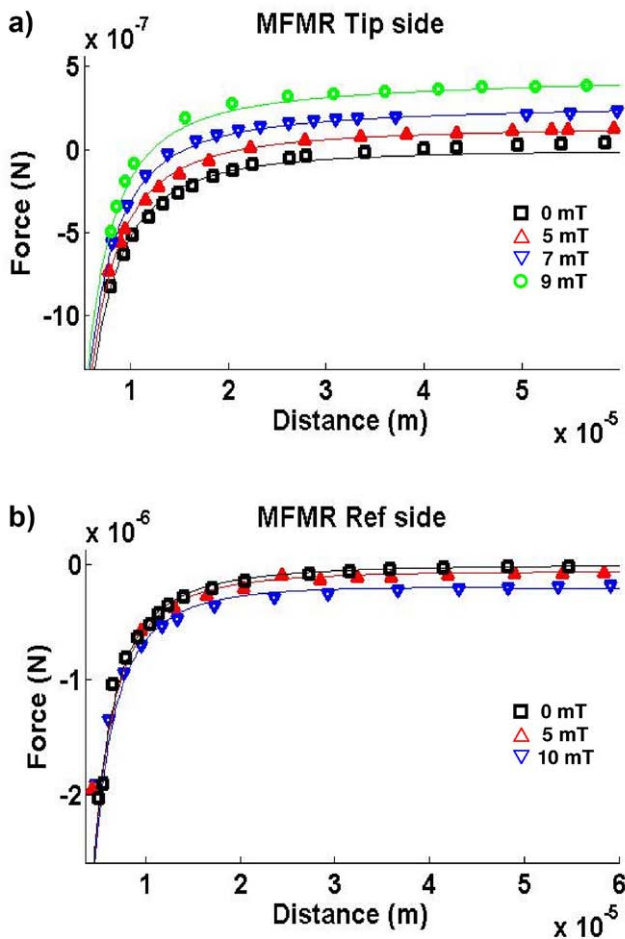


**Figure 6.** Magnetic force versus distance for MFMR probes, measured at different  $B$  values. (a) tip side configuration; (b) reflector side configuration. Solid lines: comparison with the model (equations (8)–(10)).

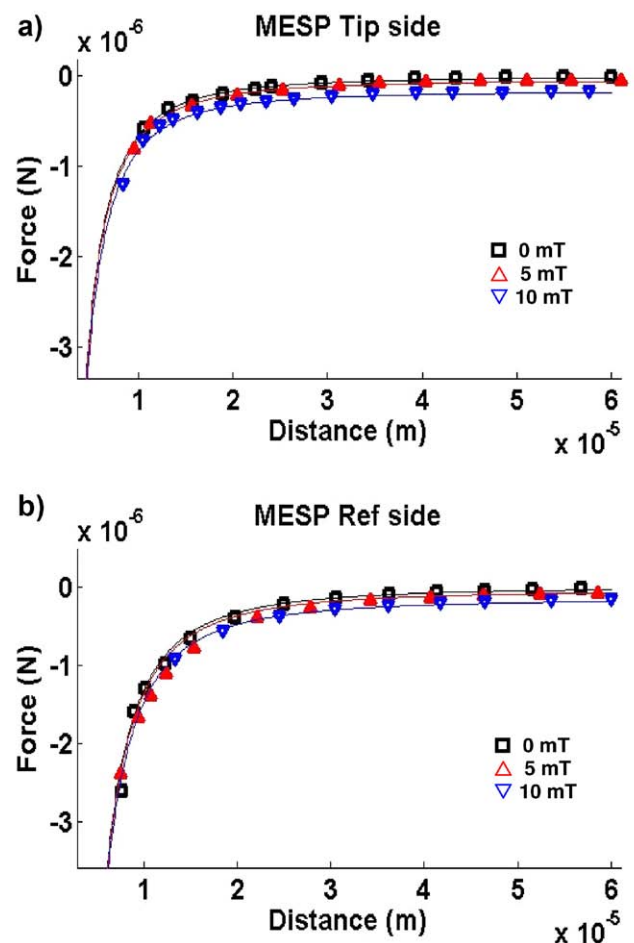


**Figure 7.** Magnetic force versus distance for MESP probes, measured at different  $B$  values. (a) tip side configuration; (b) reflector side configuration. Solid lines: comparison with the model (equations (8)–(10)).

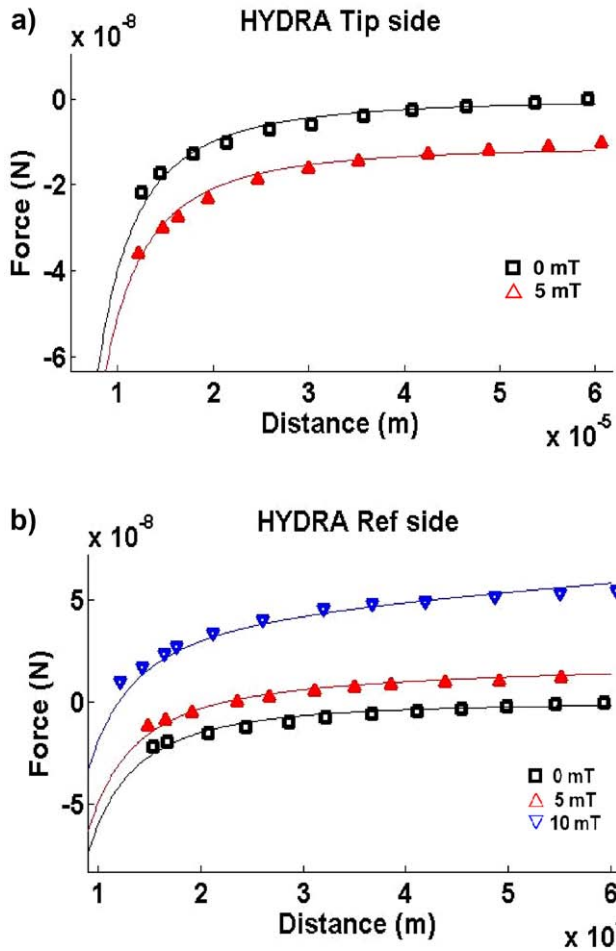


**Figure 8.** Magnetic force versus distance for HYDRA probes, measured at different  $B$  values. (a) tip side configuration; (b) reflector side configuration. Solid lines: comparison with the model (equations (8)–(10)).

a magnetic field. For all the cantilevers, we observed that the long range asymptotic forces ( $z > 100 \mu\text{m}$ ) are of the same order of magnitude than those measured with the electrical coil. In particular, we found exactly the same attractive and repulsive responses when the orientations of the cantilevers were reversed. Hence, in the magnetic experiments, the thermoelastic properties seem to control the long range behaviour by the temperature gradient effect and, for multilayer cantilevers, by the difference in the coefficients of thermal expansion.

In the framework of linear elasticity, the radius of curvature of the bent multilayer cantilever is given by:

$$R = \frac{\int E(z)z^2 dz}{\int E(z)\epsilon(z)z dz}, \quad (2)$$

where  $E(z)$  is Young's modulus at the position  $z$  in the cantilever and  $\epsilon(z)$  is the thermal deformation of the cantilever at  $z$ , which is proportional to the thermal expansion coefficients of the layers and their temperature variations [16]. When  $R \ll L$ , where  $L$  is the length of the cantilever, the deflection is  $\delta \approx \frac{L^2}{2R}$  and the bending force is  $F = k\delta$ .

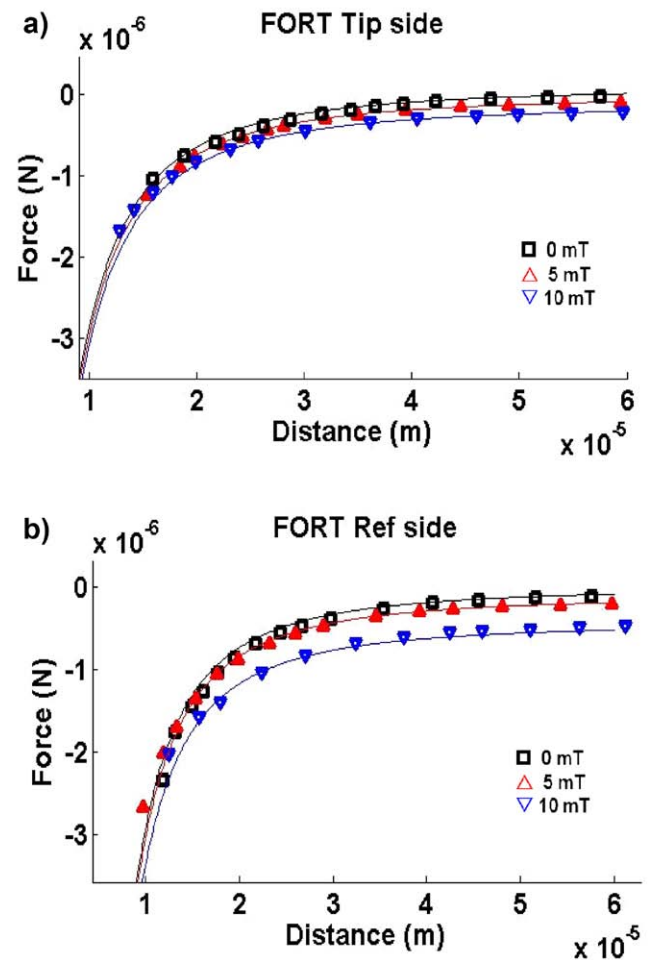


**Figure 9.** Magnetic force versus distance for FORT probes, measured at different  $B$  values. (a) tip side configuration; (b) reflector side configuration. Solid lines: comparison with the model (equations (8)–(10)).

Equation (2) also takes into account the effects of the temperature gradient in the cantilever. In case of a uniform temperature and a bimorph cantilever, equation (2) is similar to equation (4) in [17]. Modelling the cantilever bending requires precise values of the thicknesses and the thermoelastic film properties of the layers, and the geometry of the cantilever. With values of these parameters given in the literature, we obtain a good qualitative agreement with the experimental response of the cantilever: first, the maximum deflection scales as  $I_C^2$  and second, we find the same attractive and repulsive behaviour in tip and reflector side configurations (figure 5). However, the magnitudes of the forces are difficult to predict precisely due to the uncertainties in the physical data and the presence of the internal stresses.

We propose a simple phenomenological model based on the force balance of a multilayer cantilever that takes into account the main experimental observations at long range, i.e. the force is a square function of the electrical current and then of  $B^2$ , and the specific behaviour of each cantilever in the tip and reflector side configurations. This model was also developed because it is easier to control the magnetic field via the electrical current (Biot–Savart law) than the temperature field

due to its highly non-linear behaviour. Moreover, the thermal properties of the multilayer cantilever are not always well established.

In the model, we consider that the cantilever is characterized by its length  $L$ , width  $w$  and thickness  $h$ , and is clamped at one extremity.  $e_1$  and  $e_2$  are the thickness of the coating layers on tip and reflector sides, respectively ( $e_1, e_2 \ll h$ ). Considering a cantilever substrate with thin film layers, equation (2) can be approximated by the differential equation governing the cantilever deflection  $y$  along the  $x$ -axis:

$$\frac{d^2y}{dx^2} = \frac{M(x)}{EI}, \quad (3)$$

where  $E$  and  $I$  are Young's modulus and the moment of inertia of the bulk substrate, and  $M$  the total bending moment.  $M$  and

$I$  are respectively given by  $M(x) = \left(\frac{\rho}{2}\right)(x-L)^2$ , where  $\rho$  is the force per unit length and  $I = \frac{wh^3}{12}$ . In the case of V-shaped cantilevers (HYDRA), this last expression must be multiplied by 2. From the conditions at the clamped end,  $y(0) = 0$  and  $dy(0)/dx = 0$ , we obtain the general expression of the deflection:

$$y(x) = \frac{\rho x^2}{24EI}(4xL - L^2 - x^2). \quad (4)$$

The deflection is measured at the laser spot,  $x = 0.95L$ . We postulate that the effects of orientation are due to the multilayer structure of the cantilevers as shown in figure 1 and  $\rho$  is a function of  $B^2$ . The force per unit length experienced by the cantilever is given by  $\rho = \rho_1 + \rho_{\text{bulk}} + \rho_2$ , where  $\rho_1$  and  $\rho_2$  are the forces per unit length in the coating layers, and  $\rho_{\text{bulk}}$  is that experienced in the bulk substrate. By analogy with paramagnetism, we assume that the forces on the cantilever are:

$$\rho_1 = \frac{we_1\Gamma_1}{2\mu_0} \frac{dB^2}{dz} \Big|_{z_1}, \quad (5)$$

$$\rho_2 = \frac{we_2\Gamma_2}{2\mu_0} \frac{dB^2}{dz} \Big|_{z_2}, \quad (6)$$

$$\rho_{\text{bulk}} = \frac{w\Gamma_{\text{bulk}}}{2\mu_0} \int_{z_1}^{z_2} \frac{dB^2}{dz} dz, \quad (7)$$

where  $\Gamma_1$ ,  $\Gamma_2$  and  $\Gamma_{\text{bulk}}$  are 'apparent magnetic coefficients' of tip side, reflector side and bulk layers respectively, and  $\mu_0$  is the vacuum magnetic permeability.  $z_1$  and  $z_2$  are the vertical positions of the coating layers defined as  $z_1 = z$  and  $z_2 = z + h$  for the tip side configuration and  $z_1 = z + h$  and  $z_2 = z$  for the reflector side configuration (figure 1).

At a constant tip-to-surface distance  $z$ , we deduce from equation (1) that  $\frac{dB^2}{dz}$  and  $\frac{d^2B^2}{dz^2}$  are proportional to  $I^2$  and therefore to  $B^2$ , in such a way that  $\rho = KB^2$ . By fitting the experimental curves presented in figure 5, it is then possible to estimate  $K$  for both tip and reflector side configurations. From

the Taylor series expansions of  $\rho_1$  and  $\rho_2$  at  $z + h/2$ , we obtain for the tip side configuration:

$$\rho = \frac{w}{2\mu_0} \frac{dB^2}{dz} \Big|_{z+\frac{h}{2}} (e_1\Gamma_1 + e_2\Gamma_2 + h\Gamma_{\text{bulk}}) + \frac{wh}{2\mu_0} \frac{d^2B^2}{dz^2} \Big|_{z+\frac{h}{2}} (e_2\Gamma_2 - e_1\Gamma_1) + O(h^2), \quad (8)$$

In the same way, the force per unit length for the reflector side configuration is:

$$\rho = \frac{w}{2\mu_0} \frac{dB^2}{dz} \Big|_{z+\frac{h}{2}} (e_1\Gamma_1 + e_2\Gamma_2 + h\Gamma_{\text{bulk}}) + \frac{wh}{2\mu_0} \frac{d^2B^2}{dz^2} \Big|_{z+\frac{h}{2}} (e_1\Gamma_1 - e_2\Gamma_2) + O(h^2). \quad (9)$$

The case of uncoated FORT cantilevers (see figure 5(d)), for which  $e_1 = 0$  and  $e_2 = 0$ , has been used to determine  $\Gamma_{\text{bulk}} \cong 186$  in silicon based cantilevers (MFMR and MESP). From this value it is possible to determine  $\Gamma_1$  and  $\Gamma_2$  coefficients for MFMR and MESP by fitting the experimental data (figure 5) with the linear system (8) and (9). In the case of HYDRA probes,  $e_1 = 0$  in equations (8) and (9). All the apparent magnetic  $\Gamma$  coefficients were calculated from the fit of the averaged experimental data by standard linear regression and are reported in table 1.

We point out that the  $\Gamma$  coefficients obtained in this phenomenological model have no link with the standard magnetic susceptibilities and show sensitivity to the total thermal field. For example, the magnetic properties of the silicon material found in the literature [18] give an interaction force much lower in magnitude than what we have observed.

In figure 5, the experimental data are fitted by the model (equations (8) and (9)). We find a good agreement for the  $B^2$  dependence of the interaction force for all the cantilevers with a unique value of  $\Gamma_{\text{bulk}}$  for a Si substrate.

#### 4.2. Full range force model

The variation of the interaction force with the distance displays two regimes, at short and long distance. At long distance, the  $z$  dependence is derived from the applied magnetic field (equations (1) and (5)–(7)). At short distance, the interaction force curves for different applied field converge to a unique one. Without any current, the cantilever is submitted to the remanent magnetic field of the iron core. When there is no magnetic field and no magnetization but heating (experiments with the aluminium plate), the force is of smaller magnitude and exhibits only capillary effects at short distance. In the limit of short distance and in the presence of a magnetic field, the force–distance relation scales as  $-1/z^2$  for all the cantilevers (figures 6–9) and can be modelled by monopole–monopole interaction. In such an approximation, the force is expressed as:

**Table 2.** Product of magnetic monopoles ( $g_m^{\text{probe}} g_m^{\text{surface}}$  in  $\text{A}^2 \text{m}^2$ ) obtained by fitting the experimental data for the four cantilever types for tip side and reflector side configurations.

Probe reference	Tip side	Reflector side
MFMR	$1 \times 10^{-10}$	$2 \times 10^{-10}$
MESP	$2.5 \times 10^{-10}$	$2.5 \times 10^{-10}$
HYDRA	$3 \times 10^{-10}$	$4.5 \times 10^{-10}$
FORT	$4.5 \times 10^{-10}$	$5.5 \times 10^{-10}$

$$F_{\text{monopoles}} = -\frac{\mu_0 g_m^{\text{probe}} g_m^{\text{surface}}}{4\pi z^2}, \quad (10)$$

where  $g_m^{\text{probe}}$  is the equivalent monopole associated with the probe and  $g_m^{\text{surface}}$  that associated with the sample surface. The monopole model can be understood as an effect of local magnetic field that can be decomposed in a multipolar expansion, in which the first monopole–monopole term dominates. In our experiments, the local force characterizes the magnetization of the iron surface. In other situations, this force could be measured to characterize the magnetization of a medium by an external field (such as, for instance, a ferrofluid).

From the experiments, we cannot determine the  $g_m$  coefficients in equation (10) separately. Only the product of magnetic monopole intensities  $g_m^{\text{probe}} g_m^{\text{surface}}$  can be estimated. These values are obtained by fitting the raw data and are summarized in table 2. We note that the order of magnitude of all the monopole products is  $\sim 10^{-10} \text{A}^2 \text{m}^2$ , which could be used to estimate the short distance interaction force for this iron core.

In order to determine the full range interaction force undergone by the cantilevers, equations (8)–(10) can be combined. Figures 6–9 show the comparison between this full range model and the experimental data, for which the  $\Gamma$  coefficients are identical to those calculated from figure 5. While the multilayer model predicts the correct behaviour of the cantilever, the question remains of how the chemical composition and the process of fabrication affect the thermal and magnetic properties of cantilevers. At long range, in addition to temperature, other physical effects can contribute to the bending of the cantilevers, such as magnetostriction [19–21].

Based on this study, we can propose a method to develop MFM experiments to investigate the magnetic response of a given sample to a dc or ac external magnetic field. In order to obtain a good lateral resolution, the MFM tip has to be close to the sample surface (less than 50 nm). In this case, the force on the cantilever is dominated by monopole–monopole interaction. First, we have to find a cantilever characterized by a low  $g_m^{\text{probe}}$  value and a repulsive behaviour in the tip side configuration (as MFMR) in order to increase the range of the measured force by the photodiode. Second, the cantilever stiffness must be large to limit the cantilever deflection in the presence of a large interaction force.

## 5. Conclusion

The study of the near-field behaviour of samples by AFM under an external magnetic field requires knowledge of the cantilever response in similar conditions. Therefore, we have characterized in this paper the response of the AFM cantilevers to an external dc magnetic field. A coil with an iron core was used to produce the external magnetic field. The force exerted on the cantilever was measured by its deflection. The results for four types of cantilevers have been presented and discussed. We have measured both the effects of  $B$  and temperature. At long distance, we observed that the temperature effects dominate while the magnetic effects dominate at short distance. We have proposed a phenomenological model based on two contributions: a monopole–monopole interaction at short distance and a multilayer interaction at long distance characterized by a generalized paramagnetic force proportional to  $\nabla B^2$  modelling the temperature effects. Based on this work, it is possible to define the cantilever properties that are adapted for the study of the mechanisms at the nanoscale occurring in magnetic samples under external magnetic fields.

## Acknowledgments

We would like to thank Hervé Ayroles of ‘Signaux et Images’ team at IMFT Toulouse for his technical assistance, and Cédric Charvillat of CIRIMAT laboratory for AFM technical support. This work has been financially supported by CEA Cadarache and CNRS.

## References

- [1] Martin Y and Wickramasinghe H K 1987 Magnetic imaging by force microscopy with 1000 Å resolution *Appl. Phys. Lett.* **50** 1455
- [2] Sáenz J J, García N, Grütter P, Meyer E, Heinzelmann H, Wiesendanger R, Rosenthaler L, Hidber H R and Güntherodt H J 1987 Observation of magnetic forces by the atomic force microscope *J. Appl. Phys.* **62** 4293
- [3] Prins M W J, Groeneveld R H M, Abraham D L, Schad R, van Kempen H and van Kesteren H W 1996 Scanning tunneling microscope for magneto-optical imaging *J. Vac. Sci. Technol. B* **14** 1206
- [4] Manalis S, Babcock K, Massie J, Elings V and Dugas M 1995 Submicron studies of recording media using thin-film magnetic scanning probes *Appl. Phys. Lett.* **66** 2585
- [5] Philips G N and Suzuki T 1997 Quantitative analysis of written bit transitions in 5 Gbit/in<sup>2</sup> media by magnetic force microscopy *J. Magn. Magn. Mater.* **175** 115
- [6] Proksch R, Schmidt J, Austvold S and Skidmore G 1997 Direct observation of the high frequency write response of recording heads using the magnetic force microscope *J. Appl. Phys.* **81** 4522
- [7] Gibbs M R J, Al-Khafaji M A, Rainforth W M, Davies H A, Babcock K, Chapman J N and Heyderman L 1995 A comparison of domain images obtained for nanophase alloys by magnetic force microscopy and high resolution Lorentz electron microscopy *J. IEEE Trans. Magn.* **31** 3349



- [8] Hehn M, Cherifi-Khodjaoui K, Ounadjela K, Bucher J P and Arabski J 1997 Engineering magnetic responses in hcp cobalt thin films *J. Magn. Magn. Mater.* **165** 520
- [9] Homma T, Kurokawa Y, Nakamura T, Osaka T and Otsuka I 1996 Magnetic force microscopy analysis of the micromagnetization mode of double-layered perpendicular magnetic recording media *J. Vac. Sci. Technol. B* **14** 1184
- [10] Hartmann U 1999 Magnetic force microscopy *Annu. Rev. Mater. Res.* **29** 53
- [11] Lohau J, Kirsch S, Carl A, Dumpich G and Wassermann E F 1999 Quantitative determination of effective dipole and monopole moments of magnetic force microscopy tips *J. Appl. Phys.* **86** 3410
- [12] Kong L and Chou S Y 1997 Quantification of magnetic force microscopy using a micronscale current ring *J. Appl. Phys.* **81** 5026
- [13] Arie T, Yoshida N, Akita S and Nakayama Y 2001 Quantitative analysis of the magnetic properties of a carbon nanotube probe in magnetic force microscopy *J. Phys. D: Appl. Phys.* **34** L43-5
- [14] Chang C H, Tan C W, Miao J, Barbastathis G 2009 Self-assembled ferrofluid lithography: patterning micro and nanostructures by controlling magnetic nanoparticles *Nanotechnology* **20** 495301
- [15] Rohsenow W M, Hartnett J P and Cho Y I 1998 *Handbook of Heat Transfer* 3rd edn (New York: McGraw-Hill) p 4.16
- [16] Honda T, Arai K I and Yamaguchi M 1994 Fabrication of magnetostrictive actuators using rare-earth (Tb,Sm)Fe thin films *J. Appl. Phys.* **75** 6994
- [17] Timoshenko S 1925 Analysis of bi-metal thermostats *J. Opt. Soc. Am.* **11** 233
- [18] Haynes W M (ed) 2014 *Handbook of Chemistry and Physics* 94th edn (Internet Version) (Boca Raton, FL/London: CRC Press/Taylor and Francis)
- [19] Guerrero V H and Wetherhold R C 2003 Magnetostrictive bending of cantilever beams and plates *J. Appl. Phys.* **94** 6659
- [20] du Trémolet de Lacheisserie E and Peuzin J C 1994 Magnetostriction and internal stresses in thin films: the cantilever method revisited *J. Magn. Magn. Mater.* **136** 189
- [21] McCorkle P 1923 Magnetostriction and magnetoelectric effects in iron, nickel and cobalt *Phys. Rev.* **22** 271

## Appendix B

**Publication: Void effects on eddy current distortion in two-phase liquid metal**

## Note: Void effects on eddy current distortion in two-phase liquid metal

M. Kumar,<sup>1,2</sup> Ph. Tordjeman,<sup>1,a)</sup> W. Bergez,<sup>1</sup> and M. Cavaro<sup>2</sup>

<sup>1</sup>Université de Toulouse, Institut de Mécanique des Fluides de Toulouse, Allée du Professeur Camille Soula, 31400 Toulouse, France

<sup>2</sup>CEA, Cadarache, DEN/DTN/STCP/LIET, Building 202, 13108 St Paul Lez Durance, France

(Received 17 July 2015; accepted 29 September 2015; published online 9 October 2015)

A model based on the first order perturbation expansion of magnetic flux in a two-phase liquid metal flow has been developed for low magnetic Reynolds number  $Re_m$ . This model takes into account the distortion of the induced eddy currents due to the presence of void in the conducting medium. Specific experiments with an eddy current flow meter have been realized for two periodic void distributions. The results have shown, in agreement with the model, that the effects of velocity and void on the emf modulation are decoupled. The magnitude of the void fraction and the void spatial frequency can be determined from the spectral density of the demodulated emf. © 2015 AIP Publishing LLC. [<http://dx.doi.org/10.1063/1.4932990>]

Characterization of void fraction in two-phase liquid metal is a challenging issue in many applications. The measurement of void fraction in liquid metal is a notoriously difficult problem because these materials are opaque, aggressive, often very hot, and inaccessible. For example, the presence of bubbles in the primary loop of a sodium cooled fast nuclear reactor modifies the neutronic and heat transfer properties of flow, which is a cause of concern from the safety point of view.<sup>1</sup> In metallurgy, bubbles and non metallic impurities decrease the efficiency of heating by induction and change dramatically the mechanical properties of the manufactured products.<sup>2</sup> On the other hand, bubbles manifest also in natural magnetohydrodynamics flows, as observed in geophysics earth's outer core or in interstellar medium.<sup>3</sup> In recent years, we have seen a renewed interest in techniques based on Faraday induction<sup>4,5</sup> and Lorentz force<sup>6</sup> for flow measurements.<sup>7</sup> From a theoretical point of view, the distortion of the induced eddy currents by the presence of void is an open problem.<sup>8</sup> In this paper, we propose a perturbative theory that allows us to develop a methodology to characterize the void fraction using a standard sensor.<sup>9,10</sup>

We consider a moving two phase liquid metal with a void fraction  $\alpha$  and a characteristic velocity  $U$ . The medium is assumed to flow through a primary coil  $P$ , which is excited by an AC current  $I = I_0 \cos \omega t$ . The perturbation of the induced magnetic flux due to the Faraday and Lorentz force effects is measured by two secondary coils ( $S_1$  and  $S_2$ ) placed coaxially on either sides of the primary coil. This corresponds to a standard configuration in flow measurement with the advantage to minimize external noise and, in our case, to amplify the distortion due to void fraction. The model consists to calculate the void fraction contribution to the emf difference between the two secondary coils  $\Delta V$ . In this problem, the magnetic Reynolds number  $Re_m$  is defined by the penetration depth of the magnetic field in the medium as the characteristic length ( $\delta = \sqrt{\frac{2}{\sigma \mu_0 \omega}}$ ):  $Re_m = \sigma \mu_0 U \delta$ , where  $\sigma$  is the electrical conductivity of the medium and  $\mu_0$  is

the magnetic permeability of vacuum. At low  $Re_m$  (diffusion dominates advection in magnetic flux transport equation), the amplitude of the net flux crossing coils  $S_1$  and  $S_2$  is given at first order by

$$\phi = \int \vec{B} \cdot d\vec{s} = \phi_0 + Re_m \phi_u + \phi_\alpha(t), \quad (1)$$

where  $\phi_0$  is the average flux in the absence of motion due to Faraday effects,  $\phi_u$  is the average flux due to Lorentz force effects, and  $\phi_\alpha$  is the perturbation of the total flux due to the dispersed phase. This last term has its origin in the perturbation of the eddy currents in presence of the non-conducting dispersed phase and is related to the induction effects to first order. In case of periodic distribution of the dispersed phase, this term can be expanded in Fourier series,

$$\phi_\alpha(t) = \psi_\alpha \cos(\omega_\alpha t + \theta) + \dots, \quad (2)$$

where the amplitude  $\psi_\alpha$  depends on the volume fraction  $\alpha$  and  $\omega_\alpha$  characterizes the spatial distribution ( $\omega_\alpha = U k_\alpha$ , where  $k_\alpha$  is the spatial frequency of dispersed phase). In this analysis,  $\omega_\alpha \ll \omega$ . One notes that  $\phi_0 = 0$  for ideally well balanced  $S_1$  and  $S_2$ . Magnetic field in the medium results from the coupling between the Maxwell-Faraday and the Maxwell-Ampere equations, considering that the eddy currents in the conducting media in motion are  $\vec{J} = \sigma(\vec{E} + \vec{U} \times \vec{B})$ . Consequently, the magnetic field in the medium has two contributions, one in phase and one in quadrature with  $I$  ( $\vec{B}(t) = \vec{B}_\parallel \cos \omega t + \vec{B}_\perp \sin \omega t$ ), which leads to a total flux also with both components.  $\Delta V$  is given by differentiating with time the flux between  $S_1$  and  $S_2$ :  $\Delta V^2 = \Delta V_\parallel^2 + \Delta V_\perp^2$ . Considering the first terms in  $O(Re_m)$  ( $Re_m \ll 1$ ),

$$\begin{aligned} \Delta V^2 \approx \omega^2 \left\{ \langle \phi_0 | \phi_0 \rangle + \frac{\langle \psi_\alpha | \psi_\alpha \rangle}{2} + 2 \langle \phi_0 | \psi_\alpha \rangle \cos(\omega_\alpha t + \theta) \right. \\ \left. + \frac{\langle \psi_\alpha | \psi_\alpha \rangle}{2} \cos(2\omega_\alpha t + 2\theta) \right. \\ \left. + 2 Re_m [\langle \phi_0 | \phi_u \rangle + \langle \phi_u | \psi_\alpha \rangle \cos(\omega_\alpha t + \theta)] \right\}. \quad (3) \end{aligned}$$

In this formula,  $\phi_i$  is defined as a vector,  $\phi_i = [\phi_{i,\parallel}, \phi_{i,\perp}]$ .  $\langle \phi_i | \phi_j \rangle$  represents the scalar product between the two vectors

<sup>a)</sup>Electronic mail: philippe.tordjeman@imft.fr

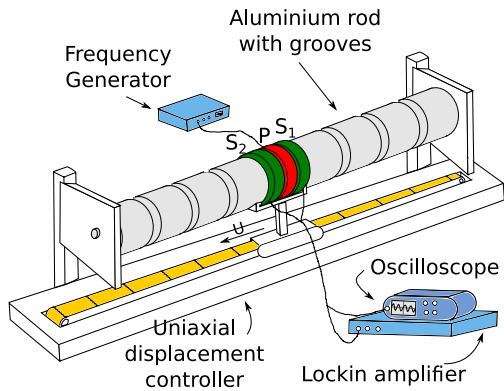


FIG. 1. Design of the experimental set up.  $P$ ,  $S_1$ , and  $S_2$  are, respectively, the primary and the two secondary coils.

$i$  and  $j$ . In RHS of Equation (3), the four first terms correspond to the dominant components in Fourier expansion of  $\Delta V^2$  and the last terms are the perturbations induced by motion. In Equation (3), only the amplitudes of  $\phi_0$  and  $\psi_\alpha$  appear at zero order, and  $\langle \phi_u | \phi_u \rangle$  being a second order term in  $\text{Re}_m$  does not appear. The terms  $\langle \phi_0 | \psi_\alpha \rangle$ ,  $\langle \phi_0 | \phi_u \rangle$ , and  $\langle \phi_u | \psi_\alpha \rangle$  represent the coupling effects of Faraday induction, Lorentz force, and dispersed phase. The Fourier analysis of the  $\Delta V^2$  signal allows to determine these components and particularly the term  $\langle \psi_\alpha | \psi_\alpha \rangle$ , which is expected to characterize the influence of the dispersed phase.

We have developed specific experiments to validate this theoretical approach. A moving Eddy Current Flow Meter (ECFM)<sup>11</sup> assembly was designed (Fig. 1). It consists of three coils ( $P$ ,  $S_1$ , and  $S_2$ ) of diameter 40 mm each and length 30 mm for  $P$  and 20 mm for  $S_1$  and  $S_2$ , with copper winding of 70 turns for  $P$  and 50 for  $S_1$  and  $S_2$ . ECFM is fixed on a uniaxial displacement controller, which can move at velocity,  $U = 10^{-3} - 1$  m/s. The conducting fluid is modeled by an aluminium rod along which the ECFM moves (see Fig. 1). Three aluminium rods (of diameter 38.5 mm) were used in the experiments: a plain rod which represents single phase liquid metal ( $\alpha = 0\%$ ) and two rods with grooves ( $\alpha = 0.3\%$  and  $\alpha = 6.9\%$ ), which represent two-phase liquids. The grooves were machined at the rod surface with a period of 18.00 mm and 16.85 mm, a depth 0.38 mm and 4.23 mm, and a width 1.4 mm and 3.00 mm, respectively. The advantage of this system is that the geometric void fraction  $\alpha$  is exactly known and there are no problems of liquid metal circulation. The experiment was realized at room temperature for which the electrical conductivity of the aluminium rod is  $\sigma = 3.8 \times 10^7$  S/m. We use a lockin amplifier (HF2LI-MF, Zurich Instruments) to excite the primary coil at 3142 rad/s ( $\delta \approx 3.7$  mm) and 6283 rad/s ( $\delta \approx 2.6$  mm). The amplitude of current intensity for all the experiments is in the range of 200–400 mA. All the experimental results are given for a normalized intensity amplitude of 1 A. Moreover, we have checked that the current remains constant within 0.1% during an experiment. The voltage induced in  $S_1$  and  $S_2$  is measured by the lockin amplifier. In the experiments, the phase of the primary current is taken as reference.  $\Delta V$  is demodulated with the lockin amplifier in order to determine the components in phase and in quadrature. For each measurement, the ECFM

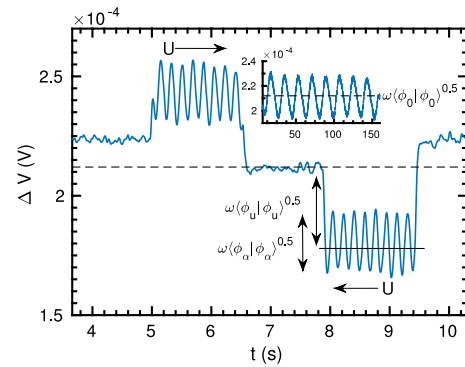


FIG. 2. Typical demodulated voltage difference of the two secondary coils,  $\Delta V$  measured vs time for  $\alpha = 0.3\%$  at  $\omega = 3142$  rad/s and  $U = 0.1$  m/s (inlay:  $U = 0.001$  m/s).

was translated back and forth several times. Experiments with this system are very reproducible because the system is highly deterministic. Finally, we have verified that the electromagnetic background noise is not significant at these frequencies.

Fig. 2 displays a typical demodulated  $\Delta V$  signal. This kind of signal can be obtained for in phase and quadrature components and also for the norm.  $\phi_0$  is defined as the average value of the signal when there is very slow motion, typically  $U = 10^{-3}$  m/s (inlay of Fig. 2). In this case, the Lorentz force can be neglected. In motion at constant  $U$ , the average value of the signal is translated with a mean amplitude proportional to  $\text{Re}_m \phi_u$ . In presence of grooves ( $\alpha \neq 0\%$ ), this signal oscillates around this value. The amplitude of this oscillation gives  $\psi_\alpha$ . Fig. 3 shows an example of the FFT spectrum of the difference between  $\Delta V$  signal and its temporal average value for  $\alpha = 6.9\%$  at  $U = 0.1$  m/s and 6283 rad/s. We observe the first three harmonic peaks in  $\omega_\alpha$ . From the FFT spectral density, we obtained  $\omega_\alpha = 0.35 \pm 0.05$  rad/s. This value is in agreement with that calculated from the geometry of grooves:  $\omega_\alpha = 0.37$  rad/s. For  $\alpha = 0.3\%$ , we measured  $\omega_\alpha = 0.35 \pm 0.04$  for a theoretical value  $\omega_\alpha = 0.35$ . All the spectra obtained from the experiments validate the expansion at first order in  $\text{Re}_m$  of the magnetic flux and also the Fourier series of the void fraction perturbation on eddy current equations (1) and (2). The amplitude of the peak at  $3\omega_\alpha$  gives the first residue of Equation (3).

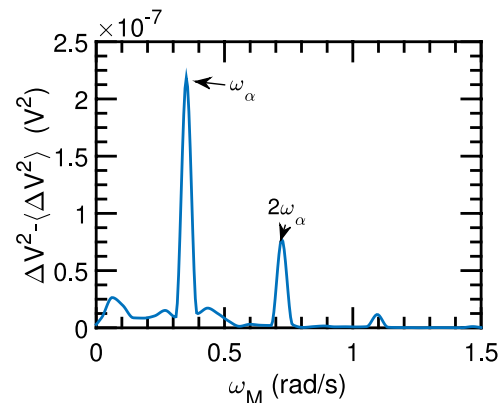


FIG. 3. FFT spectral density of  $\|\Delta V^2\|$  vs the modulating pulsation  $\omega_M$  for  $\alpha = 6.9\%$  and  $U = 0.001$  m/s at 6283 rad/s.

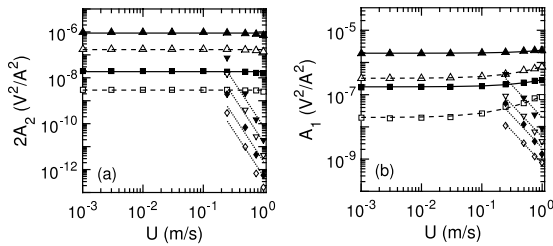


FIG. 4. Amplitude of the second (a) and first (b) peaks of the spectral density of  $\|\Delta V\|^2$  vs velocity at 3142 rad/s (unfilled markers) and 6283 rad/s (filled markers):  $\alpha = 0.3\%$  ( $\square$ ,  $\blacksquare$ ) and ( $\diamond$ ,  $\blacklozenge$ ) with low pass filter 24 dB/oct;  $\alpha = 6.9\%$  ( $\triangle$ ,  $\blacktriangle$ ) and ( $\nabla$ ,  $\blacktriangledown$ ) with low pass filter 24 dB/oct.

According to this equation, the amplitude of the first peak is  $A_1 = \omega^2 [\langle \phi_0 | \psi_\alpha \rangle + 2\text{Re}_m \langle \phi_u | \psi_\alpha \rangle]$  and the amplitude of the second peak is  $A_2 = \omega^2 \frac{\langle \psi_\alpha | \psi_\alpha \rangle}{2}$ . We have checked that the value of  $\sqrt{2A_2}/\omega$  is equal to the norm of  $\psi_\alpha$ , which has been obtained from the direct FFT of  $\phi_\alpha$  signal.

Fig. 4(a) compares  $2A_2$  vs velocity for  $\alpha = 0.3\%$  and  $\alpha = 6.9\%$  and for both frequencies, 3142 and 6283 rad/s. These experiments showed that  $A_2$  is independent of the velocity whatever the frequency and the void fraction. On the other hand, the magnitude of  $A_2$  depends on the void fraction and the frequency. The experimental data show that  $\sqrt{A_2}/\omega$  is a constant (within 12% error). Furthermore the experiments point out that the  $\alpha$  dependence of  $A_2$  is given by  $\psi_\alpha \sim \alpha^n$ ,  $n < 1$ . In the limit of the accuracy, we found  $n \approx 0.6$  for both frequencies. Comparison with the plain rod shows that  $A_2$  is very sensitive to the presence of void fraction even at low value of  $\alpha$  ( $\alpha = 0.3\%$ ).

For groove depth smaller than  $\delta$ , the effective void fraction is  $\alpha_\delta \sim \alpha/\delta$ , and if  $\alpha$  is small enough,  $\psi_\alpha \sim \alpha$  ( $n = 1$ ). In this case, we found from the Maxwell's equations that  $\psi_\alpha \sim \omega^0$ , in agreement with experiments. The experimental value  $n \approx 0.6$  corresponds to the case where groove depth is larger than  $\delta$  and  $\alpha_\delta > \alpha$ .

The amplitude of  $A_1$  vs velocity is shown in Fig. 4(b) for  $\alpha = 0.3\%$  and  $\alpha = 6.9\%$  at both angular frequencies 3142 rad/s and 6283 rad/s. We recall that  $A_1$  characterizes the coupling effects of the void fraction on Faraday induction and on the Lorentz force. In our first order expansion model,  $A_1$  is linear with  $\psi_\alpha$ . Fig. 4(b) points out that the value of  $A_1$  increases with  $\alpha$ , following the same power law relation  $\psi_\alpha \sim \alpha^{0.6}$ . For the two frequencies, we observe that  $A_1$  is linear with velocity, coming from the coupling term  $2\omega^2 \text{Re}_m \langle \phi_u | \psi_\alpha \rangle$ .

Due to the order of magnitude of  $\langle \phi_0 | \psi_\alpha \rangle$  compared to  $2\text{Re}_m \langle \phi_u | \psi_\alpha \rangle$ , the velocity effects on  $A_1$  is more visible at low values of  $A_1$  in log-log representation. Finally, the exact concordance between  $A_1$  and  $A_2$  validates the perturbation model given by Equation (3).

To further investigate the consistency of  $\psi_\alpha$  dynamics on  $A_1$  and  $A_2$ , we used a low pass filter at a cutoff frequency  $\nu_c = 6.8$  Hz. This filter is characterized by an attenuation of 24 dB/oct in signal intensity. Since  $\omega_\alpha \sim U$ , the corresponding critical velocity is around  $U_c \sim 10^{-1}$  m/s. After  $U_c$ , the  $A_1$  and  $A_2$  values are supposed to decrease in  $1/U^2$  and  $1/U^4$ , respectively. Fig. 4 show that the experimental data verify the expected dynamics.

In this work, we have calculated the effects of the void fraction of a two-phase liquid metal flow on the induced magnetic flux. We have shown that for a periodic void distribution, the amplitude of the emf difference is modulated at a frequency  $\omega_\alpha$  characteristic of the distribution and with an amplitude which is a function of  $\alpha$ . We have shown the interest to analyze the FFT signal of demodulated emf difference in order to determine the void fraction. This is possible because the effects of velocity and void are decoupled. The experiments with a standard ECFM validates the perturbation approach used in the model. For more realistic non-periodic void distributions, this approach can still be used to analyze the void effects on emf signal as long as  $\omega_\alpha$  can be measured.

The authors acknowledge Hervé Ayroles and Grégory Ehses at IMFT Toulouse for their technical assistance. This work has been financially supported by CEA, Cadarache.

<sup>1</sup>A. Judd, *J. Phys. D: Appl. Phys.* **2**, 261 (1969).

<sup>2</sup>M. Lalpoor, D. Eskin, and L. Katgerman, *Mater. Sci. Eng.: A* **497**, 186 (2008).

<sup>3</sup>N. Gehrels and W. Chen, *Nature* **361**(6414), 706-707 (1993).

<sup>4</sup>P. Sharma, S. S. Kumar, B. Nashine, R. Veerasamy, B. Krishnakumar, P. Kalyanasundaram, and G. Vaidyanathan, *Ann. Nucl. Energy* **37**, 332 (2010).

<sup>5</sup>F. Stefani, T. Gundrum, and G. Gerbeth, *Phys. Rev. E* **70**, 056306 (2004).

<sup>6</sup>A. Thess, E. Votyakov, and Y. Kolesnikov, *Phys. Rev. Lett.* **96**, 164501 (2006).

<sup>7</sup>J. Priede, D. Buchenau, and G. Gerbeth, *Meas. Sci. Technol.* **22**(5), 055402 (2011).

<sup>8</sup>J. C. Maxwell, *A Treatise on Electricity and Magnetism* (Clarendon Press, 1881), Vol. 1.

<sup>9</sup>C. C. Feng, W. Deeds, and C. V. Dodd, *J. Appl. Phys.* **46**, 2935 (1975).

<sup>10</sup>K. Nakamoto, S. Tamura, K. Ishii, H. Kuwahara, N. Ohyamaand, and T. Muramatsu, *Nucl. Eng. Des.* **82**, 393 (1984).

<sup>11</sup>H. Lehde and W. T. Lang, U.S. patent 2,435,043 (27 January 1948).

# Appendix C

## Review of two-phase MHD

The objective of this appendix is to present a literature review of two-phase MHD. This review helped us to define the goals of this PhD and to understand the limits of our study.

The presence of electromagnetic fields influence the motion of electrically conducting fluid through Lorentz force. This motion of fluid under electromagnetic field induces electrical currents which distort the applied electromagnetic fields. In this appendix, we review the coupled dynamics of two-phase media and electromagnetic fields. There is a considerable amount of literature in this field due to rising interest in the liquid metal-gas two-phase flows over last few decades. This is mainly due to some specific requirements in energy industry and metallurgy. A reliable knowledge of fluid flow-electromagnetic fields coupling is required in this context. For the application in Sodium cooled Fast nuclear reactor, we are concerned with bubble sizes of less than 0.2 mm. We define two non-dimensional numbers,

$$Eo = \frac{g\Delta\rho d_b^2}{\sigma}, \quad Mo = \frac{g\eta^4\Delta\rho}{\rho^2\sigma^3}$$

Where, Eotvos number  $Eo$  is the ratio of surface tension forces to the body forces in bubble and  $Mo$  is the Morton number.  $d_b, \rho, \sigma, \eta$  and  $g$  are diameter of the bubble, density, surface tension, dynamic viscosity of the fluid and acceleration due to gravity, respectively. For sodium at 500 °C,  $Eo \approx 0.05$  and  $Mo \approx 4 \times 10^{-14}$  for bubble of diameter 1 mm. The ratio of bubble horizontal to vertical diameter gives an estimate of bubbles shape[92]

$$\bar{E} = \frac{1}{1 + 0.163Eo^{0.757}} \approx 0.98, \quad Eo < 40, \quad Mo \leq 10^{-6} \quad (C.1)$$

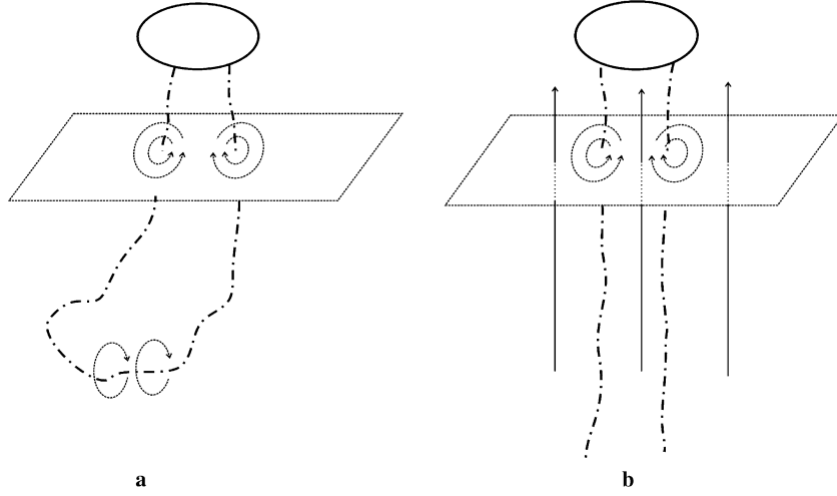
Notice that the horizontal and vertical diameters are almost equal. Therefore, we conclude that the bubbles in our case are spherical and can be treated as spheres.

The discussions in the following subsections are arranged as follows: we start by discussing the MHD boundary conditions on rigid spherical bubble surface; then we take the case of a 2D obstacle as an example to familiarize the reader with flow of current

density around bubbles under some assumptions; and lastly we review the existing theories and experimental results which explain the fluid-electromagnetic fields coupling in their respective ranges of non-dimensional numbers.

The case of a rising bubble motion in the presence of magnetic fields is the simplest configuration. Even in the absence of magnetic field Schwerdtfeger has showed that the terminal velocity of argon gas bubbles in mercury is smaller than that in water[93]. The presence of a magnetic field perpendicular to bubble motion decreases the bubble speed. This suggests the action of Lorentz forces will affect the bubble motion in liquid metal-gas flows under electromagnetic fields. Mori *et al.* investigated single bubble motion in the presence of a horizontal DC magnetic field[94]. For small bubbles, the terminal velocity  $u_t$  increased with increasing  $\mathbf{B}$  upto 1 mT. Beyond 1.5 mT,  $u_t$  decreased with increasing  $\mathbf{B}$ . For larger bubbles, increase in  $\mathbf{B}$  decreased  $u_t$ . With this experiment they confirmed two mechanisms governing bubble speeds in liquid metal subjected to  $\mathbf{B}$  fields[95]. Firstly, the drag on a moving bubble/sphere/ellipsoid/disc increases with the increase in magnetic field. Secondly, the bubble wake structure is modified significantly by a vertical magnetic field. The bubble zig zag motion or spiral motion then tends towards a rectilinear ascent. When former effect dominates  $u_t$  decreases, while it increases when later effect dominates. Fröhlich *et al.* confirm the same with their experimental study utilizing Ultrasound Transit Time (UTT) technique (see [96] for explanation of UTT), for argon gas bubble motion in liquid Galinstan[95]. For small argon gas injection flow rate, the bubbles are small. Therefore, the bubble rising velocity in case of  $\mathbf{B} = 0$  is larger than that in case of  $\mathbf{B} \neq 0$ . On the other hand, for higher argon gas flow rates (large bubbles) reverse trend is true. The consistency of results was also verified by changing the diameter of nozzle used for argon gas injection, whereby an increase in nozzle diameter resulted in a decrease in bubble rise velocity. For argon gas bubbles in sodium chloride aqueous solution ( $\sigma \approx 10^3 \text{ S m}^{-1}$ ), a 3% drop in the bubble velocity was observed corresponding to an increase in perpendicular magnetic field from 0 T to 7 T[97]. In the context of our study, the magnetic fields are of the order of 1 mT. Thus any change in the bubble velocity for these values of magnetic fields will be insignificant. Therefore the bubble velocities can be taken as that of the ambient fluid.

The rising bubbles also exhibit oscillatory motion which is attributed to the their wake structure. This wake structure depends on shape and size of the bubble[98]. Two unstable modes with same frequencies but shifted in phase by  $\pi/2$  have been reported. The first mode causes a planar zig zag trajectory of the bubble, while the second mode gives a spiral trajectory to the ascending bubble[99]. A strong magnetic field parallel to the bubble motion causes an enlargement of the eddies in the wake[100]. The application of magnetic field diminishes the velocity components perpendicular to the magnetic field via Lorentz force. This makes the bubble path more rectilinear. This interaction is more easily seen with an intuitive depiction in figure ???. One can notice the modification of the wake structure via interaction of the vortices with the applied external magnetic field. This proposed mechanism was later validated by the numerical and experimental results for argon gas bubble motion in liquid Galinstan[95]. Zhang *et al.* have studied the motion of rising single argon gas bubble in a static column of Galinstan under DC



(a) Wake behind the rising bubble in stagnant liquid column influences bubble motion,  
(b) This wake is modified by  $\mathbf{B}$  in such a way that the bubble motion becomes more rectilinear[100].

magnetic field[100]. The bubble oscillation frequency changed non-monotonically with the bubble size. The bubble terminal velocity  $u_t$  was also found to depend on the bubble diameter, however, it did not match the theoretical expression of Mendelson which is

$$u_t = \sqrt{\frac{2\sigma}{\rho_l d_e} + \frac{g d_e}{2}} \quad (\text{C.2})$$

where  $d_e$  is the bubble diameter,  $\sigma$  is the surface tension,  $g$  is the acceleration due to gravity and  $\rho_l$  is the density of liquid. Oscillations in  $u_t$  were similar in cases  $\mathbf{B} = 0$  and  $\mathbf{B} \neq 0$ , but the mean  $u_t$  increased with  $\mathbf{B}$ . Also the amplitude of bubble oscillation decreased with an increase in  $\mathbf{B}$ . The drag coefficients on the bubble were found to increase with the strength of this magnetic field for smaller bubbles ( $d < 4$  mm) and decrease with increasing magnetic field for larger bubbles ( $d < 5.4$  mm). In earlier studies on solid sphere motion in liquid metal, the drag coefficient was found to increase monotonically with  $\mathbf{B}$ [101, 102]. This means that the bubble deformation plays an important role in determining drag on large bubbles. The horizontal and vertical velocity components in the wake are also significantly damped by  $\mathbf{B}$ . However its effect on horizontal and vertical velocities is different.

Shin *et al.* have reported the elongation of single bubble along the direction of externally applied uniform magnetic field in a uniaxial straining flow [103]. The shape of a bubble was found to be a function of three parameters: the Reynolds number



Re, the Weber number<sup>1</sup>  $W$  and the magnetic interaction parameter<sup>2</sup>  $N$ . For a given Re, the critical Weber number  $W_c$  at which the bubble breaks into two decreases as  $N$  increases. Below  $W_c$ , bubbles do not break no matter how large is  $N$ . However, the bubble deformation increases monotonously with  $N$ . This is called the stable region. Lower the value of Re, lower is  $W_c$ .

The dynamics of dispersed two-phase MHD flow is more complicated than the case of a single bubble motion. The turbulent structure of continuous medium will influence the distribution of the dispersed phase. The velocity fluctuations which contribute to turbulent intensity have three contributions: the shear layers in the mean flow, the irregular movement of the gas inclusions, and the turbulent wakes of the gas bubbles. Therefore it is to be expected that the turbulence intensity will be more in the case of two-phase flows than the single phase fluid motion. This turbulence intensity typically increases as the square root of bubble void fraction for rising bubbles case and for void fractions less than 6.5% [104]. The turbulence velocity fluctuations increases with increasing magnetic flux density[105]. Therefore, it is to be expected that the flow induced fluctuations in ECFM will increase in turbulent two-phase flows. Furthermore, the turbulence in two-phase flows is enhanced in the plane perpendicular to the magnetic field. Therefore, the three dimensional turbulence structure is converted to quasi two dimensional one[106] after some large value of Hartman number  $Ha$ .

With regards to the phase distribution, it has been found that the presence of magnetic field introduces significant amount of anisotropy in the direction perpendicular to it, independent of the sign of the magnetic field. This result suggests a favorable movement of bubbles along a specific axis. Indeed, bubble dispersion in a direction parallel to magnetic field has been reported to reduce as the magnetic field strength was increased[107], the corresponding Hartman number is  $Ha \sim 10^2 - 10^3$ . This anisotropy is the result of a preferred direction of alignment of vortices. The bubble dispersion again becomes isotropic at some critical high value of  $Ha$ . This is attributed to the pinch effect[108]. Here the MHD pressure in the cross-section(difference of magnetic pressure of externally imposed and induced magnetic fields), which is maximum in the core of the flow, pushes the bubbles towards the wall. If the magnetic fields are applied in the same direction as fluid-gas motion, the isotropy in bubble dispersion is retained. This is again due to the alignment of vorticity in a direction parallel to the magnetic field. To better understand the coupling of electromagnetic field with two-phase flow, the problem of momentum transfer from dispersed gas bubbles to the surrounding liquid metal flow has also been studied[109]. The bubble slip ratio defined as  $S = v_{bubble}/v_{liquid}$ , was found to decrease exponentially with the increasing strength of transverse magnetic field  $B$ . On the other hand,  $S$  decreased exponentially initially, but started to increase after  $B = 0.2$  T, for the case of longitudinal magnetic field. The drag coefficients increase as a function of  $B$ . These experiments were reported at  $Re \sim 30000$ . For the case of  $Re \sim 10^5$ , the slip

---

<sup>1</sup>Weber number  $W$  is defined as the ratio of fluids inertial to its surface tension:  $W = \rho U^2 L / \sigma$ ; where  $\rho$  and  $\sigma$  are the fluid density and surface tension and  $U$  and  $L$  are characteristic velocity and length scales respectively.

<sup>2</sup>Interaction parameter  $N$  is defined as the ratio of inertial to electromagnetic forces:  $N = Ha^2 / Re$

ratio increased with increasing  $B$ . In our case we are interested in the later ( $Re \sim 10^5$ ). At this  $Re$ , for  $B = 0$  we have  $S = 5 - 7$  depending on the void fraction. This means the velocity of the bubbles cannot be taken same as that of the ambient liquid. Also the imposition of magnetic field will slightly alter their speeds. However,  $B$  in our case is in mT, so the influence of  $B$  on  $S$  can be neglected.

Serizawa *et al.* have reported experimental results of NaK-nitrogen two-phase flow in the presence of strong magnetic fields. Phenomenon of bubble break up and coalescence have been observed in the presence of magnetic fields [110]. For bubbly flows an increase in magnetic field will increase bubble coalescence while long gas slugs tend to break up at increasing rate as the strength of magnetic field is increased. In case of no magnetic field, the distribution of the gas bubbles was symmetric about the cylinder axis. In the presence of magnetic field anisotropy in bubble distribution was observed in the direction perpendicular to  $\mathbf{B}$ . For bubbly flows, an increase in  $\mathbf{B}$  enhanced the bubble coalescence, the elongated bubbles accumulated preferentially near the wall and  $u_t$  decreased. For slug flows, the slugs break up with increasing  $\mathbf{B}$ ,  $u_t$  decreases and the reverse flow of liquid during the passage of the slugs decreased with increasing  $\mathbf{B}$ . For annular flow, the increase in  $\mathbf{B}$  increased the thickness of liquid film thickness on the wall. Regarding the distribution of void in flow cross-section, Saito *et al.* have also found a general behavior of bubbles to accumulate at the walls rather than at the center[57]. Their experiments concerned with the NaK-N<sub>2</sub> two-phase flows in MHD power generators. They have explained the movement of void towards wall in terms of pinch effect. The M.HD pressure drop did not change much with increasing  $\mathbf{B}$ . They also found that the gas-liquid slip ratio has a very weak dependence on  $\mathbf{B}$ , while it changes primarily as a function of the ratio of liquid to gas flow rates (*i.e.*  $\alpha$ ).

There have been some studies in the presence of time varying magnetic fields too. Zhang *et al.* have used traveling magnetic field (TMF) on a bubble plume in a cylindrical column of Galinstan[111]. The injection of argon gas bubbles through single orifice at the center of the cylinder pushes the fluid upwards at the centerline of the cylinder. Upward/downward TMF sets up co-current/counter-current flows with respect to original bubble plume driven flow. This can be utilized as a powerful tool to control the global flow and to enhance the mixing. The mean velocity (upwards/downwards) at a radial position close to cylinder periphery increased with increasing magnetic field while the fluctuating component of velocity also grows continuously with the strength of  $\mathbf{B}$ . The horizontal liquid velocities at free surface depends upon bubble rise velocity, concentration and distribution. This can also be used to improve surface properties of final products in casting processes. Vogt *et al.* have recently used Rotating Magnetic Field (RMF) for the same purpose[112]. An RMF, as opposed to a static magnetic field, is a magnetic field which rotates its polarities in space in azimuthal direction around the centerline of the cylinder or pipe containing the flow. Four characteristic zones were observed, representing four different flow patterns[112]. Taylor number (Ta) is the ratio of centrifugal or so-called inertial forces due to rotation of a fluid about an axis to viscous forces. For extremely low Taylor number and high gas flow rates pure bubble driven flow was observed. At very high Taylor numbers pure RMF driven flow was observed. Two

intermediate flow regimes represented situations in which bubble plumes rise on one side while convection sets up on the other side. Rakoczy *et al.* have done the same for a Rotating Magnetic Field (RMF)[113]. Sauter mean diameter is defined as follows:

$$d_{32} = \frac{\sum_{i=1}^N N_i d_i^3}{\sum_{i=1}^N N_i d_i^2} \quad (\text{C.3})$$

Physically, the Sauter mean diameter,  $d_{32}$  is the diameter of an equivalent sphere that has the same volume to surface area ratio as those of bubbles. The results of Rakoczy *et al.* show that Ha has significant effect on  $d_{32}$ . For  $0.006 < \text{Ha} < 0.12$ , the ratio  $D^* = [d_{32}]_{\text{Ha} \neq 0} / [d_{32}]_{\text{Ha} = 0}$  for air bubbles in NaCl brine decreased with increasing gas flow rate and Ha. On the contrary, for the cases of air bubbles in tap water and air bubbles in synthetic waste water,  $D^*$  increased with Ha. The tendency with the gas flow rate was same.

There are some other similar studies. In all these studies the bubble motion is idealized: the details such as bubble wake structure and its modification in the presence of  $\mathbf{B}$  or the bubble slip ratio are neglected or assumed to be insignificant. The focus is to obtain an average *e.m.f.* corresponding to a given  $\alpha$ .

The discussions in this appendix helps us to conclude that MHD turbulent two-phase flows are relatively difficult to analyze due to the existence of the several coupled physical mechanisms and non-linearities in their mathematical descriptions. Therefore, it would be instructive to use model experimental set-up in which different parameters could be decoupled. For the first time, it would be advisable to assume a given flow velocity and flow profile and absence of flow induced fluctuations. In addition, the experimental set-up should be built in such a way that the void locations, and size are fixed. This is done to avoid the coupled dynamics associated with bubbles in two-phase MHD flow.

## Appendix D

# Theoretical expansion in Lissajous ellipse fitting approach

The objective in this appendix is to develop a theory which helps us characterize the experimental  $\beta$  signals in terms of  $U$ ,  $\alpha$  and  $\omega$ . We assume small pulsation  $\omega$ , such that,  $\delta \gg D$  and  $\text{Re}_m \ll 1$ . In this case, it is possible to decouple the Faraday induction and the Lorentz force effects. The theory developed in subsection 3.2.1 of chapter 3 will be used here.

Given following two signals

$$V_1(t) = D_1 \cos(\omega t + \phi_1) + C_1 \quad (\text{D.1})$$

$$V_2(t) = D_2 \cos(\omega t + \phi_2) + C_2 \quad (\text{D.2})$$

The algebraic manipulation of these will give,

$$\left(\frac{V_1 - C_1}{D_1}\right)^2 + \left(\frac{V_2 - C_2}{D_2}\right)^2 - 2\frac{(V_1 - C_1)(V_2 - C_2)}{D_1 D_2} \cos(\Delta\phi) - \sin^2(\Delta\phi) = 0 \quad (\text{D.3})$$

This can be written as,

$$F(V_1, V_2) = aV_1^2 + 2bV_1V_2 + cV_2^2 + 2dV_1 + 2fV_2 + g = 0 \quad (\text{D.4})$$

The values of various coefficients are

$$\begin{cases} a = D_2^2 \\ b = -D_1 D_2 \cos(\Delta\phi) \\ c = D_1^2 \\ d = -D_2^2 C_1 + D_1 D_2 C_2 \cos(\Delta\phi) \\ f = -D_1^2 C_2 + D_1 D_2 C_1 \cos(\Delta\phi) \end{cases} \quad (\text{D.5})$$

The phase difference is given by

$$\cos(\Delta\phi) = -\frac{\text{sgn}(a)b}{\sqrt{ac}} \quad (\text{D.6})$$

The tilt angle is given by

$$\beta = \begin{cases} 0, & \text{for } b = 0 \text{ and } a < c \\ \frac{1}{2}\pi, & \text{for } b = 0 \text{ and } a > c \\ \frac{1}{2} \cot^{-1} \frac{a-c}{2b}, & \text{for } b \neq 0 \text{ and } a < c \\ \frac{\pi}{2} + \frac{1}{2} \cot^{-1} \frac{a-c}{2b}, & \text{for } b \neq 0 \text{ and } a > c \end{cases} \quad (\text{D.7})$$

Our signals are given by,

$$\frac{V_1}{N_s \omega} = V_1^{new} = (A_1 + b_1 v) \sin(\omega t) - \omega a_1 \cos(\omega t) \quad (\text{D.8})$$

$$\frac{V_2}{N_s \omega} = V_2^{new} = (A_2 - b_2 v) \sin(\omega t) - \omega a_2 \cos(\omega t) \quad (\text{D.9})$$

Notice from (D.5), (D.6) and (D.7), that the factor  $N_s \omega$  will cancel out in all the equations of interest. So from here on we would develop  $V_1^{new}$  and  $V_2^{new}$ . Also we would call  $V_1^{new}$  and  $V_2^{new}$  as  $V_1$  and  $V_2$  respectively.

Let

$$\sin(\phi_1) = \frac{-(A_1 + b_1 v)}{D_1}, \cos(\phi_1) = \frac{-\omega a_1}{D_1} \quad (\text{D.10})$$

$$\sin(\phi_2) = \frac{-(A_2 - b_2 v)}{D_1}, \cos(\phi_2) = \frac{-\omega a_2}{D_1} \quad (\text{D.11})$$

Putting equation (D.10) and equation (D.11) in equation (D.8) and equation (D.9), we get

$$V_1 = -D_1 \sin(\phi_1) \sin(\omega t) + D_1 \cos(\phi_1) \cos(\omega t) \quad (\text{D.12})$$

$$V_2 = -D_2 \sin(\phi_2) \sin(\omega t) + D_2 \cos(\phi_2) \cos(\omega t) \quad (\text{D.13})$$

This can be further simplified to,

$$V_1 = D_1 \cos(\omega t + \phi_1) \quad (\text{D.14})$$

$$V_2 = D_2 \cos(\omega t + \phi_2) \quad (\text{D.15})$$

These eqns are similar to equation (D.1) and equation (D.2). Using equation (D.7), we can write the expression for the tilt angle as,

$$\beta = \frac{1}{2} \cot^{-1} \frac{a-c}{2b} \quad (\text{D.16})$$

First we would like to simplify the factor,  $\frac{a-c}{2b}$  as follows (using set of eqns. D.5):

$$\frac{a-c}{2b} = \frac{D_1^2 - D_2^2}{2D_1 D_2 \cos(\Delta\phi)} \quad (\text{D.17})$$

Using equation (D.10) and eqn. D.11, we get

$$D_1 = \sqrt{(A_1 + b_1 v)^2 + \omega^2 a_1^2}, \quad \tan(\phi_1) = \frac{(A_1 + b_1 v)}{\omega a_1} \quad (\text{D.18})$$

$$D_2 = \sqrt{(A_2 - b_2v)^2 + \omega^2 a_2^2} \quad , \quad \tan(\phi_2) = \frac{(A_2 - b_2v)}{\omega a_2} \quad (\text{D.19})$$

We have

$$D_1^2 - D_2^2 = (A_1 + b_1v)^2 + \omega^2 a_1^2 - (A_2 - b_2v)^2 - \omega^2 a_2^2 \quad (\text{D.20})$$

$$= (A_1 + b_1v)^2 - (A_2 - b_2v)^2 + \omega^2 a_1^2 - \omega^2 a_2^2 \quad (\text{D.21})$$

$$= [(A_1 - A_2) + (b_1 + b_2)v] [(A_1 + A_2) + (b_1 - b_2)v] - \omega^2 (a_1 - a_2)(a_1 + a_2) \quad (\text{D.22})$$

In the presence of grooves, the coefficients of contribution from various factors change as follows,

$$a_1 = a_1^0 + \delta a_1 \cos(\omega_g t + \theta_1) \quad (\text{D.23})$$

$$a_2 = a_2^0 + \delta a_2 \cos\left(\omega_g \left(t - \frac{L_p + L_s}{v}\right) + \theta_1\right) \quad (\text{D.24})$$

where,

$$\omega_g = 2\pi f_g = \frac{2\pi v}{d_1 + d_2} \quad (\text{D.25})$$

$f_g$  is the groove frequency,  $L_p$  is the length of the primary coil,  $L_s$  is the length of the secondary coil,  $d_1$  is the width of the groove and  $d_2$  is the separation of the grooves.

$$a_2 = a_2^0 + \delta a_2 \cos(\omega_g t + \theta_2) \quad (\text{D.26})$$

where,

$$\theta_2 = \theta_1 - 2\pi \frac{L_p + L_s}{d_1 + d_2} \quad (\text{D.27})$$

and,

$$\theta_{avg} = \frac{\theta_1 + \theta_2}{2}, \quad \Delta\theta = \theta_2 - \theta_1 = -2\pi \frac{L_p + L_s}{d_1 + d_2} \quad (\text{D.28})$$

Similarly,

$$b_1 = b_1^0 + \delta b_1 \cos(\omega_g t + \theta_1) \quad (\text{D.29})$$

$$b_2 = b_2^0 + \delta b_2 \cos(\omega_g t + \theta_2) \quad (\text{D.30})$$

Assume that the two secondary coils are identical. This would make  $b_1^0 \approx b_2^0$ ,  $\delta b_1 \approx \delta b_2$ ,  $a_1^0 \approx a_2^0$  and  $\delta a_1 \approx \delta a_2$ . Also assume that  $A_1 \approx A_2$ . Equation (D.22) becomes

$$\begin{aligned} D_1^2 - D_2^2 = & 4v \left[ b^0 + \delta b \cos\left(\frac{\Delta\theta}{2}\right) \cos(\omega_g t + \theta_{avg}) \right] \left[ A - v\delta b \sin\left(\frac{\Delta\theta}{2}\right) \sin(\omega_g t + \theta_{avg}) \right] \\ & + 4\omega^2 \delta a \sin\left(\frac{\Delta\theta}{2}\right) \sin(\omega_g t + \theta_{avg}) \left[ a^0 + \delta a \sin\left(\frac{\Delta\theta}{2}\right) \cos(\omega_g t + \theta_{avg}) \right] \end{aligned} \quad (\text{D.31})$$

Now, we would like to evaluate  $D_1 D_2$ . From equations (D.18) and (D.19), we have

$$D_1 D_2 = \sqrt{[(A_1 + b_1v)^2 + \omega^2 a_1^2] [(A_2 - b_2v)^2 + \omega^2 a_2^2]} \quad (\text{D.32})$$

$$D_1^2 = (A_1 + b_1 v)^2 + \omega^2 a_1^2 = (A^2 + 2Ab^0 v + (b^{02} - \delta b^2)v^2 + (a^{02} - \delta a^2)\omega^2) + 2(\delta b^2 v^2 + \delta a^2 \omega^2) \cos(2\omega_g t + 2\theta_1) + 2(A\delta b v + b^0 \delta b v^2 + a^0 \delta a \omega^2) \cos(\omega_g t + \theta_1) \quad (\text{D.33})$$

Similarly

$$D_2^2 = (A_2 - b_2 v)^2 + \omega^2 a_2^2 = (A^2 - 2Ab^0 v + (b^{02} - \delta b^2)v^2 + (a^{02} - \delta a^2)\omega^2) + 2(\delta b^2 v^2 + \delta a^2 \omega^2) \cos(2\omega_g t + 2\theta_2) + 2(-A\delta b v + b^0 \delta b v^2 + a^0 \delta a \omega^2) \cos(\omega_g t + \theta_2) \quad (\text{D.34})$$

Let

$$K_1 = (A^2 + 2Ab^0 v + (b^{02} - \delta b^2)v^2 + (a^{02} - \delta a^2)\omega^2) \quad (\text{D.35})$$

$$K_2 = 2(\delta b^2 v^2 + \delta a^2 \omega^2) \quad (\text{D.36})$$

$$K_3 = 2(A\delta b v + b^0 \delta b v^2 + a^0 \delta a \omega^2) \quad (\text{D.37})$$

$$K_4 = (A^2 - 2Ab^0 v + (b^{02} - \delta b^2)v^2 + (a^{02} - \delta a^2)\omega^2) \quad (\text{D.38})$$

$$K_5 = 2(-A\delta b v + b^0 \delta b v^2 + a^0 \delta a \omega^2) \quad (\text{D.39})$$

These equations give,

$$D_1 D_2 = \sqrt{[K_1 + K_2 \cos(2\omega_g t + 2\theta_1) + K_3 \cos(\omega_g t + \theta_1)] [K_4 + K_2 \cos(2\omega_g t + 2\theta_2) + K_5 \cos(\omega_g t + \theta_2)]} \quad (\text{D.40})$$

From equation (D.18) and (D.19) we can obtain the phase difference as follows,

$$\Delta\phi = \tan^{-1} \left( \frac{A_1 + b_1 v}{\omega a_1} \right) - \tan^{-1} \left( \frac{A_2 - b_2 v}{\omega a_2} \right) \quad (\text{D.41})$$

$$= \frac{\left( \frac{A_1 + b_1 v}{\omega a_1} \right) - \left( \frac{A_2 - b_2 v}{\omega a_2} \right)}{1 + \left( \frac{A_1 + b_1 v}{\omega a_1} \right) \left( \frac{A_2 - b_2 v}{\omega a_2} \right)} \quad (\text{D.42})$$

$$\frac{\Delta\phi}{\omega} = \frac{(a_2 - a_1)A + (b_1 a_2 + b_2 a_1)v}{a_1 a_2 \omega^2 + (A_1 a_2 + b_1 a_2 v)(A_2 a_1 - b_2 a_1 v)} \quad (\text{D.43})$$

$$\frac{\Delta\phi}{\omega} = \frac{(a_2 - a_1)A + (b_1 a_2 + b_2 a_1)v}{a_1 a_2 [(A^2 + \omega^2) - Av(b_1 + b_2) - b_1 b_2 v^2]} \quad (\text{D.44})$$

$$= \frac{-2\delta a A \sin(\frac{\Delta\theta}{2}) \sin(2\omega_g t + \theta_{avg}) + (2a^0 b^0 + \delta a \delta b \cos(\Delta\theta) + 2 \cos(\frac{\Delta\theta}{2}))}{(a^0 \delta b b^0 \delta a) \cos(2\omega_g t + \theta_{avg}) + \delta a \delta b \cos(2\omega_g t + 2\theta_{avg})} v$$

$$= \frac{(a_0^2 + \frac{\delta a^2}{2} \cos(\Delta\theta) + 2a_0 \delta a \cos(\frac{\Delta\theta}{2}) \cos(2\omega_g t + \theta_{avg}) \frac{\delta a^2}{2} \cos(2\omega_g t + 2\theta_{avg})) [(A^2 + \omega^2) - Av(2b^0 + 2\delta b \cos(\frac{\Delta\theta}{2}) \cos(2\omega_g t + \theta_{avg})) - ((b_0^2 + \frac{\delta b^2}{2} \cos(\Delta\theta) + 2b_0 \delta b \cos(\frac{\Delta\theta}{2}) \cos(2\omega_g t + \theta_{avg}) + \frac{\delta b^2}{2} \cos(2\omega_g t + 2\theta_{avg})) v^2]}{(\text{D.45})}$$

We can combine equation (D.16), equation (D.17), equation (D.31), equation (D.40) and equation (D.45), to obtain the expression for tilt angle.

We find in the last equation that expansion in terms of  $U$  and  $\omega$  leads to intractable relation for  $\beta$ . Therefore, it is better to determine experimental correlations for  $\beta$  signal for  $U$ ,  $\omega$  and  $\alpha$  effects.

# Bibliography

- [1] M. Ichimiya, T. Mizuno, and S. Kotake, “A next generation sodium-cooled fast reactor concept and its r&d program,” *Nuclear Engineering and Technology*, vol. 39, no. 3, p. 171, 2007.
- [2] A. E. Waltar and A. B. Reynolds, *Fast breeder reactors*. Pergamon Press, 1981.
- [3] L. Rahmani, “Mesure de l’engagement dans le circuit primaire de superphénix par visée ultrasonique,” tech. rep., EDF - E L R SF/94 952 A, 1994.
- [4] M. Cavaro, *Apport de l’acoustique non linéaire à la caractérisation de l’engagement du sodium liquide: application aux réacteurs nucléaires de quatrième génération*. PhD thesis, Aix Marseille 2, 2010.
- [5] M. Cavaro, “The gas presence in primary sodium of french sfrs,” tech. rep., CEA/DEN/CAD/DTN/STPA/LIET, 2013.
- [6] ASN, “Lettre dsin 764/94 du 22/12/94,” tech. rep., ASN, 1994.
- [7] ASN, “Lettre dsin 303/95 du 25/07/95,” tech. rep., ASN, 1995.
- [8] A. B. Wood, *A textbook of sound*. G. Bell and sons, 1964.
- [9] M. Cavaro, C. Payan, J. Moysan, and F. Baqué, “Microbubble cloud characterization by nonlinear frequency mixing,” *The Journal of the Acoustical Society of America*, vol. 129, no. 5, pp. EL179–EL183, 2011.
- [10] H. Yada, “Fuji electromagnetic flowmeters for liquid sodium,” *Fuji Electric Journal*, vol. 43, no. 24, p. 194, 1970.
- [11] J. Fink and L. Leibowitz, “Thermodynamic and transport properties of sodium liquid and vapor,” tech. rep., Argonne National Lab., IL (United States), 1995.
- [12] V. Sobolev, “Database of thermophysical properties of liquid metal coolants for gen-iv,” *SCK-CEN, Scientific Report BLG-1069*, 2010.
- [13] N. H. Nachtrieb, “Magnetic susceptibility of some liquid metals, molten salts, and their solutions,” *The Journal of Physical Chemistry*, vol. 66, no. 6, pp. 1163–1167, 1962.



- [14] R. Bowers, “Magnetic susceptibility of sodium metal,” *Physical Review*, vol. 100, no. 4, p. 1141, 1955.
- [15] D. Hayes, “Instrumentation for liquid sodium in nuclear reactors,” *Journal of Physics E: Scientific Instruments*, vol. 7, no. 2, p. 69, 1974.
- [16] U. Müller and L. Bühler, *Magneto-fluid dynamics in channels and containers*. Springer Science & Business Media, 2013.
- [17] J. Shercliff, “The flow of conducting fluids in circular pipes under transverse magnetic fields,” *Journal of Fluid Mechanics*, vol. 1, no. 06, pp. 644–666, 1956.
- [18] J.-E. Cha, Y.-C. Ahn, K.-W. Seo, H. Y. Nam, J. H. Choi, and M. H. Kim, “The performance of electromagnetic flowmeters in a liquid metal two-phase flow,” *Journal of nuclear science and technology*, vol. 40, no. 10, pp. 744–753, 2003.
- [19] J. A. Shercliff, *The theory of electromagnetic flow-measurement*. CUP Archive, 1987.
- [20] P. Sharma, S. S. Kumar, B. Nashine, R. Veerasamy, B. Krishnakumar, P. Kalyanasundaram, and G. Vaidyanathan, “Development, computer simulation and performance testing in sodium of an eddy current flowmeter,” *Annals of Nuclear Energy*, vol. 37, no. 3, pp. 332–338, 2010.
- [21] J. Brewer, R. A. Jaross, and R. L. Brown, “Eddy-current probe-type sodium flowsensor for ftf reactor fuel channel flow monitoring,” *Nuclear Science, IEEE Transactions on*, vol. 18, no. 1, pp. 372–377, 1971.
- [22] C.-C. Feng, W. Deeds, and C. Dodd, “Analysis of eddy-current flowmeters,” *Journal of Applied Physics*, vol. 46, no. 7, pp. 2935–2940, 1975.
- [23] M. Hirayama, “Theoretical model of an eddy-current flowsensor,” *IEEE Transactions on Nuclear Science*, vol. 3, no. 24, pp. 2021–2030, 1977.
- [24] D. E. Wiegand, “Summary of an analysis of the eddy-current flowmeter,” *Nuclear Science, IEEE Transactions on*, vol. 15, no. 1, pp. 28–36, 1968.
- [25] R. C. Baker, “Electromagnetic flowmeters for fast reactors,” *progress in Nuclear Energy*, vol. 1, no. 1, pp. 41–61, 1977.
- [26] N. Vidal, G. Aguirre-Zamalloa, J. Barandiaran, A. Garcia-Arribas, and J. Gutierrez, “Fem analysis of an eddy current water flow meter,” *Journal of Magnetism and Magnetic Materials*, vol. 304, no. 2, pp. e838–e840, 2006.
- [27] A. H. Kahn and L. C. Phillips, “Development in the theory and analysis of eddy current sensing of velocity in liquid metals,” *Research in Nondestructive Evaluation*, vol. 4, no. 4, pp. 237–248, 1992.

- [28] L. Henry and W. T. Lang, “Device for measuring rate of fluid flow,” Jan. 27 1948. US Patent 2,435,043.
- [29] S. Sureshkumar, M. Sabih, S. Narmadha, N. Ravichandran, R. Dhanasekharan, C. Meikandamurthy, G. Padmakumar, R. Vijayashree, V. Prakash, and K. Rajan, “Utilization of eddy current flow meter for sodium flow measurement in fbrs,” *Nuclear Engineering and Design*, vol. 265, pp. 1223–1231, 2013.
- [30] B. Fontaine, “Compte-rendu d’essai ultime n<sup>o</sup> 7 - interaction dac- fertile comportement hydraulique du dac,” tech. rep., CEA, 2009.
- [31] H. Libby and J. Jensen, *Feasibility study of probe-type liquid metal flowmeters for FTR subassemblies*. Jan 1969.
- [32] J. Priede, D. Buchenau, and G. Gerbeth, “Contactless electromagnetic phase-shift flowmeter for liquid metals,” *Measurement Science and Technology*, vol. 22, no. 5, p. 055402, 2011.
- [33] T. Costello, R. Laubham, W. Miller, and C. Smith, “Fftf probe-type eddy-current flowmeter: wet versus dry performance evaluation in sodium,” *Nuclear Technology*, vol. 19, no. 3, pp. 174–180, 1973.
- [34] D. Buchenau, S. Eckert, G. Gerbeth, R. Stieglitz, and M. Dierckx, “Measurement technique developments for lbe flows,” *Journal of Nuclear Materials*, vol. 415, no. 3, pp. 396–403, 2011.
- [35] G. Popper, D. Wiegand, M. Glass, *et al.*, *Summary Review of Flowmeters Suitable for Measuring Sodium Flow at Temperatures Up to 1200 F in the Fast Flux Test Facility (FFTF)*. Argonne National Laboratory, 1967.
- [36] R. Hans, J. Knaak, and H. Weiss, “Flow measurement in main sodium pipes,” 1979.
- [37] A. Dohi, M. Oda, and S. Iida, “Development of an in-core flow meter for the lmfbr,” 1976.
- [38] S. Poinot, “Examen de la reponse de la pompe bauphix et de son ddf a une injection de gaz dans le circuit d’essais,” tech. rep., CEA, Cadarache., 1990.
- [39] C. Scheibelhut, “Instrumentation and control activities at argonne. annual report for period ending june 30, 1971.,” tech. rep., comp.; Argonne National Lab., III., 1971.
- [40] R. Krafft, J. Hemp, and M. Sanderson, “Investigation into the use of the electromagnetic flowmeter for two-phase flow measurements,” in *Advances in Sensors for Fluid Flow Measurement, IEE Colloquium on*, pp. 5–1, IET, 1996.
- [41] B. Hess and E. Ruppert, “Instrumentation for core and coolant monitoring in liquid-metal fast breeder reactors (lmfbr),” 1975.

- [42] K. Mochizuki, M. Matsumiya, T. Hoshi, K. Ogushi, and S. Hayakawa, “An in-core flow meter for a fuel failure detection and location system for the lmfbr,” in *Nuclear power plant control and instrumentation 1973*, 1973.
- [43] K. Nakamoto, S. Tamura, K. Ishii, H. Kuwahara, N. Ohyama, and T. Muramatsu, “Application of an eddy-current type flowmeter to void detection at the lmfbr core exit,” *Nuclear engineering and design*, vol. 82, no. 2, pp. 393–404, 1984.
- [44] T. Ogino, H. Inujima, and K. Haga, “Feasibility study of lmfbr local core anomaly detection by use of temperature and flow fluctuations,” *Journal of Nuclear Science and Technology*, vol. 21, no. 3, pp. 172–186, 1984.
- [45] X. Ma, A. Peyton, S. Higson, and P. Drake, “Development of multiple frequency electromagnetic induction systems for steel flow visualization,” *Measurement Science and Technology*, vol. 19, no. 9, p. 094008, 2008.
- [46] N. Terzija, W. Yin, G. Gerbeth, F. Stefani, K. Timmel, T. Wondrak, and A. Peyton, “Electromagnetic inspection of a two-phase flow of gainsn and argon,” *Flow Measurement and Instrumentation*, vol. 22, no. 1, pp. 10–16, 2011.
- [47] N. Terzija, W. Yin, G. Gerbeth, F. Stefani, K. Timmel, T. Wondrak, and A. Peyton, “Use of electromagnetic induction tomography for monitoring liquid metal/gas flow regimes on a model of an industrial steel caster,” *Measurement Science and Technology*, vol. 22, no. 1, p. 015501, 2011.
- [48] C. Dodd and W. Deeds, “Analytical solutions to eddy-current probe-coil problems,” *Journal of applied physics*, vol. 39, no. 6, pp. 2829–2838, 1968.
- [49] Z. Hashin and S. Shtrikman, “A variational approach to the theory of the effective magnetic permeability of multiphase materials,” *Journal of applied Physics*, vol. 33, no. 10, pp. 3125–3131, 1962.
- [50] C. Böttcher, O. Van Belle, P. Bordewijk, A. Rip, and D. D. Yue, “Theory of electric polarization,” *Journal of The Electrochemical Society*, vol. 121, no. 6, pp. 211C–211C, 1974.
- [51] R. W. Zimmerman, “Thermal conductivity of fluid-saturated rocks,” *Journal of Petroleum Science and Engineering*, vol. 3, no. 3, pp. 219–227, 1989.
- [52] W. Kreher and W. Pompe, *Internal stresses in heterogeneous solids*, vol. 9. Akademie Verlag, 1989.
- [53] C. Wong and R. S. Bollampally, “Thermal conductivity, elastic modulus, and coefficient of thermal expansion of polymer composites filled with ceramic particles for electronic packaging,” *Journal of Applied Polymer Science*, vol. 74, no. 14, pp. 3396–3403, 1999.

- [54] A. Bouguerra, “Prediction of effective thermal conductivity of moist wood concrete,” *Journal of Physics D: Applied Physics*, vol. 32, no. 12, p. 1407, 1999.
- [55] J. Chen, B. Yu, P. Xu, and Y. Li, “Fractal-like tree networks increasing the permeability,” *Physical Review E*, vol. 75, no. 5, p. 056301, 2007.
- [56] J. Lafferty and F. G. Hammitt, “A conductivity probe for measuring local void fractions in two-phase flow,” *Nuclear Technology*, vol. 3, no. 5, pp. 317–323, 1967.
- [57] M. Saito, S. Inoue, and Y. Fujii-e, “Gas-liquid slip ratio and mhd pressure drop in two-phase liquid metal flow in strong magnetic field,” *Journal of Nuclear Science and Technology*, vol. 15, no. 7, pp. 476–489, 1978.
- [58] J. C. Maxwell, *A treatise on electricity and magnetism*, vol. 1. Clarendon press, 1881.
- [59] R. Hamilton and O. Crosser, “Thermal conductivity of heterogeneous two-component systems,” *Industrial & Engineering chemistry fundamentals*, vol. 1, no. 3, pp. 187–191, 1962.
- [60] T. C. Choy, *Effective medium theory: principles and applications*. No. 102, Oxford University Press, 1999.
- [61] L. Gao and J. Gu, “Effective dielectric constant of a two-component material with shape distribution,” *Journal of Physics D: Applied Physics*, vol. 35, no. 3, p. 267, 2002.
- [62] D. McLachlan, “An equation for the conductivity of binary mixtures with anisotropic grain structures,” *Journal of Physics C: Solid State Physics*, vol. 20, no. 7, p. 865, 1987.
- [63] A. Eucken, “Allgemeine gesetzmäßigkeiten für das wärmeleitvermögen verschiedener stoffarten und aggregatzustände,” *Forschung auf dem Gebiet des Ingenieurwesens A*, vol. 11, no. 1, pp. 6–20, 1940.
- [64] V. D. Bruggeman, “Berechnung verschiedener physikalischer konstanten von heterogenen substanzen. i. dielektrizitätskonstanten und leitfähigkeiten der mischkörper aus isotropen substanzen,” *Annalen der physik*, vol. 416, no. 8, pp. 636–664, 1935.
- [65] V. D. Bruggeman, “Berechnung verschiedener physikalischer konstanten von heterogenen substanzen. i. dielektrizitätskonstanten und leitfähigkeiten der mischkörper aus isotropen substanzen,” *Annalen der physik*, vol. 416, no. 8, pp. 665–679, 1935.
- [66] R. Landauer, “The electrical resistance of binary metallic mixtures,” *Journal of Applied Physics*, vol. 23, no. 7, pp. 779–784, 1952.

- [67] D. J. Jeffrey, “Conduction through a random suspension of spheres,” in *Proceedings of the Royal Society of London A: Mathematical, Physical and Engineering Sciences*, vol. 335, pp. 355–367, The Royal Society, 1973.
- [68] E. Kröner, “Bounds for effective elastic moduli of disordered materials,” *Journal of the Mechanics and Physics of Solids*, vol. 25, no. 2, pp. 137–155, 1977.
- [69] J. Hetherington and M. Thorpe, “The conductivity of a sheet containing inclusions with sharp corners,” in *Proceedings of the Royal Society of London A: Mathematical, Physical and Engineering Sciences*, vol. 438, pp. 591–604, The Royal Society, 1992.
- [70] M. Wang and N. Pan, “Predictions of effective physical properties of complex multiphase materials,” *Materials Science and Engineering: R: Reports*, vol. 63, no. 1, pp. 1–30, 2008.
- [71] M. Petrick and K. Lee, “Performance characteristics of a liquid metal mhd generator,” tech. rep., Argonne National Lab., Ill., 1964.
- [72] J. Hemp, “Theory of eddy currents in electromagnetic flowmeters,” *Journal of Physics D: Applied Physics*, vol. 24, no. 3, p. 244, 1991.
- [73] J.-E. Cha, Y.-C. Ahn, K.-W. Seo, H.-Y. Nam, J.-H. Choi, and M.-H. Kim, “An experimental study on the characteristics of electromagnetic flowmeters in the liquid metal two-phase flow,” *Flow Measurement and Instrumentation*, vol. 14, no. 4, pp. 201–209, 2003.
- [74] D. Wyatt, “Electromagnetic flowmeter sensitivity with two-phase flow,” *International journal of multiphase flow*, vol. 12, no. 6, pp. 1009–1017, 1986.
- [75] R. Bernier and C. Brennen, “Use of the electromagnetic flowmeter in a two-phase flow,” *International Journal of Multiphase Flow*, vol. 9, no. 3, pp. 251–257, 1983.
- [76] W. Lord and R. Palanisamy, “Development of theoretical models for nondestructive testing eddy-current phenomena,” *Eddy-Current Characterization of Materials and Structures*, no. 722, p. 1, 1981.
- [77] J. García-Martín, J. Gómez-Gil, and E. Vázquez-Sánchez, “Non-destructive techniques based on eddy current testing,” *Sensors*, vol. 11, no. 3, pp. 2525–2565, 2011.
- [78] J. R. Bowler, “Eddy-current interaction with an ideal crack. i. the forward problem,” *Journal of Applied Physics*, vol. 75, no. 12, pp. 8128–8137, 1994.
- [79] B. Auld and J. Moulder, “Review of advances in quantitative eddy current nondestructive evaluation,” *Journal of Nondestructive evaluation*, vol. 18, no. 1, pp. 3–36, 1999.

- [80] C. V. Dodd, "Solutions to electromagnetic induction problems.," tech. rep., Oak Ridge National Lab., Tenn., 1967.
- [81] A. J. Zaman, S. Long, C. G. Gardner, W. F. Richards, *et al.*, "The change in impedance of a single-turn coil due to a flaw in a coaxial conducting cylinder," *Instrumentation and Measurement, IEEE Transactions on*, vol. 33, no. 1, pp. 5–10, 1984.
- [82] R. Spal and A. Kahn, "Eddy currents in a conducting cylinder with a crack," *Journal of Applied Physics*, vol. 50, no. 10, pp. 6135–6138, 1979.
- [83] B. Auld, F. Muennemann, and D. Winslow, "Eddy current probe response to open and closed surface flaws," *Journal of Nondestructive Evaluation*, vol. 2, no. 1, pp. 1–21, 1981.
- [84] A. Lewis, D. Michael, M. C. Lugg, and R. Collins, "Thin-skin electromagnetic fields around surface-breaking cracks in metals," *Journal of applied physics*, vol. 64, no. 8, pp. 3777–3784, 1988.
- [85] A. Kahn, R. Spal, and A. Feldman, "Eddy-current losses due to a surface crack in conducting material," *Journal of Applied Physics*, vol. 48, no. 11, pp. 4454–4459, 1977.
- [86] W. R. Smythe and W. R. Smythe, *Static and dynamic electricity*, vol. 3. McGraw-Hill New York, 1950.
- [87] E. Durand, *Magnétostatique*. Masson et Cie, 1968.
- [88] P. M. Ramos, F. M. Janeiro, M. Tlemçani, and A. C. Serra, "Recent developments on impedance measurements with dsp-based ellipse-fitting algorithms," *Instrumentation and Measurement, IEEE Transactions on*, vol. 58, no. 5, pp. 1680–1689, 2009.
- [89] A. Fitzgibbon, M. Pilu, and R. B. Fisher, "Direct least square fitting of ellipses," *Pattern Analysis and Machine Intelligence, IEEE Transactions on*, vol. 21, no. 5, pp. 476–480, 1999.
- [90] N. Morley, J. Burris, L. Cadwallader, and M. Nornberg, "Gainsn usage in the research laboratory," *Review of Scientific Instruments*, vol. 79, no. 5, p. 056107, 2008.
- [91] S. Prokhorenko, "Structure and viscosity of gallium, indium, and tin in the vicinity of the crystallization temperature," *Materials Science*, vol. 41, no. 2, pp. 271–274, 2005.
- [92] R. Clift, J. R. Grace, and M. E. Weber, *Bubbles, drops, and particles*. Courier Corporation, 2005.

- [93] K. Schwerdtfeger, “Velocity of rise of argon bubbles in mercury,” *Chemical Engineering Science*, vol. 23, no. 8, pp. 937–938, 1968.
- [94] Y. Mori, K. Hijikata, and I. Kuriyama, “Experimental study of bubble motion in mercury with and without a magnetic field,” *Journal of Heat Transfer*, vol. 99, no. 3, pp. 404–410, 1977.
- [95] J. Fröhlich, S. Schwarz, S. Heitkam, C. Santarelli, C. Zhang, T. Vogt, S. Boden, A. Andruszkiewicz, K. Eckert, S. Odenbach, *et al.*, “Influence of magnetic fields on the behavior of bubbles in liquid metals,” *The European Physical Journal Special Topics*, vol. 220, no. 1, pp. 167–183, 2013.
- [96] A. Andruszkiewicz, K. Eckert, S. Eckert, and S. Odenbach, “Gas bubble detection in liquid metals by means of the ultrasound transit-time-technique,” *The European Physical Journal Special Topics*, vol. 220, no. 1, pp. 53–62, 2013.
- [97] K. Iwai, J. Akiyama, M. G. Sung, I. Furuhashi, and S. Asai, “Application of a strong magnetic field on materials fabrication and experimental simulation,” *Science and Technology of Advanced Materials*, vol. 7, no. 4, pp. 365–368, 2006.
- [98] P. Ern, F. Risso, D. Fabre, and J. Magnaudet, “Wake-induced oscillatory paths of bodies freely rising or falling in fluids,” *Annual Review of Fluid Mechanics*, vol. 44, pp. 97–121, 2012.
- [99] K. Ellingsen and F. Risso, “On the rise of an ellipsoidal bubble in water: oscillatory paths and liquid-induced velocity,” *Journal of Fluid Mechanics*, vol. 440, pp. 235–268, 2001.
- [100] C. Zhang, S. Eckert, and G. Gerbeth, “Experimental study of single bubble motion in a liquid metal column exposed to a dc magnetic field,” *International Journal of Multiphase Flow*, vol. 31, no. 7, pp. 824–842, 2005.
- [101] T. Maxworthy, “Experimental studies in magneto-fluid dynamics: pressure distribution measurements around a sphere,” *Journal of Fluid Mechanics*, vol. 31, no. 04, pp. 801–814, 1968.
- [102] G. Yonas, “Measurements of drag in a conducting fluid with an aligned field and large interaction parameter,” *Journal of Fluid Mechanics*, vol. 30, no. 04, pp. 813–821, 1967.
- [103] S. Shin and I. Kang, “Effects of magnetic field on the shape of a bubble in a uniaxial straining flow,” *International journal of multiphase flow*, vol. 28, no. 1, pp. 105–125, 2002.
- [104] P. S. Lykoudis, S. T. Revankar, and D. B. Black, “Suppression of bubble-induced turbulence in the presence of a magnetic field,” *Progress in turbulence research*, pp. 121–129, 1994.

- [105] G. Fabris, P. Dunn, and E. Pierson, “Local measurements in two-phase liquid-metal mhd,” tech. rep., Argonne National Lab., Ill.(USA), 1978.
- [106] J. Sommeria and R. Moreau, “Why, how, and when, mhd turbulence becomes two-dimensional,” *Journal of Fluid Mechanics*, vol. 118, pp. 507–518, 1982.
- [107] S. Eckert, G. Gerbeth, and O. Lielausis, “The behaviour of gas bubbles in a turbulent liquid metal magnetohydrodynamic flow: Part i: Dispersion in quasi-two-dimensional magnetohydrodynamic turbulence,” *International journal of multiphase flow*, vol. 26, no. 1, pp. 45–66, 2000.
- [108] R. J. Moreau, *Magnetohydrodynamics*, vol. 3. Springer Science & Business Media, 1990.
- [109] S. Eckert, G. Gerbeth, and O. Lielausis, “The behaviour of gas bubbles in a turbulent liquid metal magnetohydrodynamic flow: Part ii: Magnetic field influence on the slip ratio,” *International journal of multiphase flow*, vol. 26, no. 1, pp. 67–82, 2000.
- [110] A. Serizawa, T. Ida, O. Takahashi, and I. Michiyoshi, “Mhd effect on nak-nitrogen two-phase flow and heat transfer in a vertical round tube,” *International Journal of Multiphase Flow*, vol. 16, no. 5, pp. 761–788, 1990.
- [111] C. Zhang, S. Eckert, and G. Gerbeth, “The impact of a vertically travelling magnetic field on the flow in a cylindrical liquid metal bubble plume,” *Metallurgical and Materials Transactions B*, vol. 40, no. 5, pp. 700–711, 2009.
- [112] T. Vogt, A. Andruszkiewicz, S. Eckert, K. Eckert, S. Odenbach, and G. Gerbeth, “Mixing enhancement in gas-stirred melts by rotating magnetic fields,” *Metallurgical and Materials Transactions B*, vol. 43, no. 6, pp. 1454–1464, 2012.
- [113] R. Rakoczy and S. Masiuk, “Experimental study of bubble size distribution in a liquid column exposed to a rotating magnetic field,” *Chemical Engineering and Processing: Process Intensification*, vol. 48, no. 7, pp. 1229–1240, 2009.





# Introduction

This document is an appendix to the submitted manuscript titled: Magnetic flux distortion in two-phase liquid metal flow. We have provided in this appendix, the difference emf time signals recorded in the Lockin amplifier and corresponding FFT spectra, at various values of  $U$ ,  $\omega$  and  $\alpha$ . Even though each experiment was repeated six times, we only show the first two measurements in each case. All the time plots and FFT spectrum densities presented here, have been used in the submitted manuscript.

## Notations

$\alpha$	Void volume fraction
$\omega$	Pulsation of AC current in primary coil of ECFM
$U$	Velocity of ECFM
$\Delta V$	Difference emf between secondary coils $S_1$ and $S_2$
$I$	Current in primary coil
$\Delta V_{\parallel}$	Component of difference emf in-phase with $I$
$\Delta V_{\perp}$	Component of difference emf quadrature ( $\pi/2$ out of phase) with $I$
$I_{\parallel}$	Component of measured current in primary coil circuit, in-phase with $I$
$\ \Delta V\ ^2$	Squared norm of difference emf
$\langle \ \Delta V\ ^2 \rangle$	Mean of squared norm of difference emf



# Contents

<b>1</b>	<b>For <math>\alpha = 0\%</math></b>	<b>7</b>
<b>2</b>	<b>For <math>\alpha = 0.3\%</math></b>	<b>49</b>
<b>3</b>	<b>For <math>\alpha = 6.9\%</math></b>	<b>93</b>
<b>4</b>	<b>For <math>\alpha = 2.0\%</math></b>	<b>137</b>
<b>5</b>	<b>For <math>\alpha = 4.5\%</math></b>	<b>171</b>
<b>6</b>	<b>For <math>\alpha = 0.06\%</math></b>	<b>205</b>
<b>7</b>	<b>For <math>\alpha = 0.22\%</math></b>	<b>241</b>
<b>8</b>	<b>For <math>\alpha = 0.54\%</math></b>	<b>277</b>
<b>9</b>	<b>For <math>\alpha = 1.62\%</math></b>	<b>313</b>



# Chapter 1

**For**  $\alpha = 0\%$

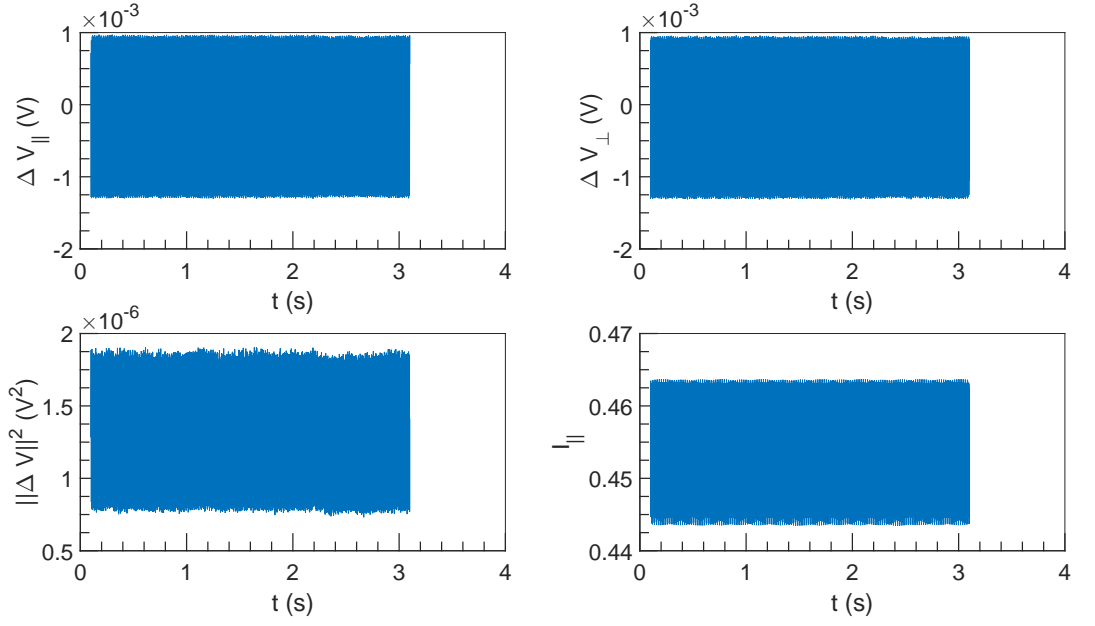


Figure 1.1:  $\Delta V$  and  $I$  vs  $t$  at  $U = 0 \text{ ms}^{-1}$ ,  $\omega = 1571 \text{ rad s}^{-1}$  and  $\alpha = 0\%$ .

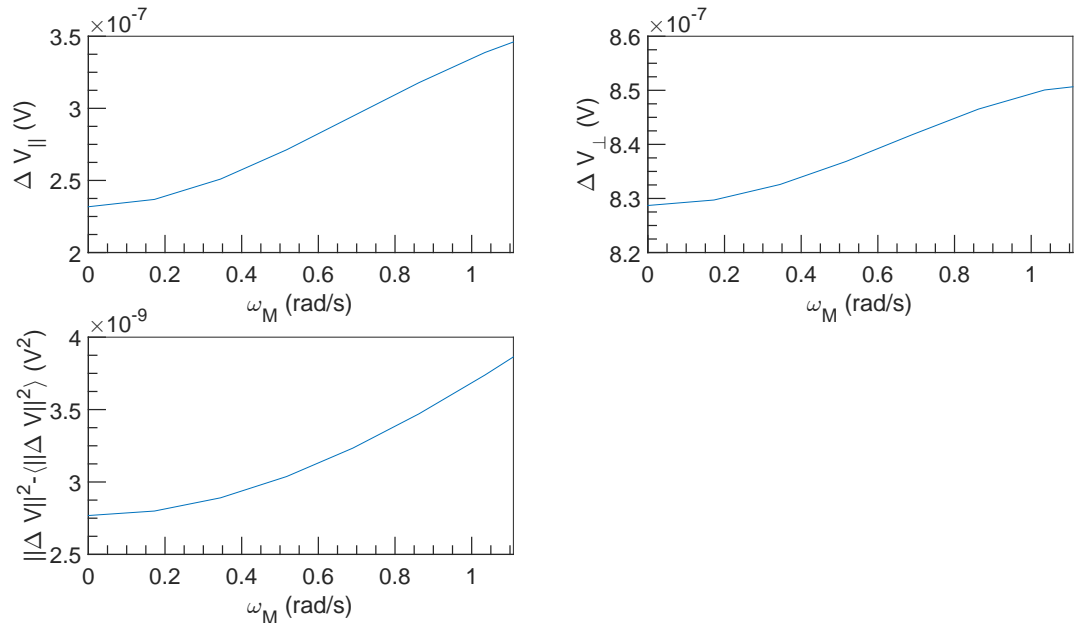


Figure 1.2: FFT spectral density of  $\Delta V$  vs  $\omega_M$  at  $U = 0 \text{ ms}^{-1}$ ,  $\omega = 1571 \text{ rad s}^{-1}$  and  $\alpha = 0\%$ .

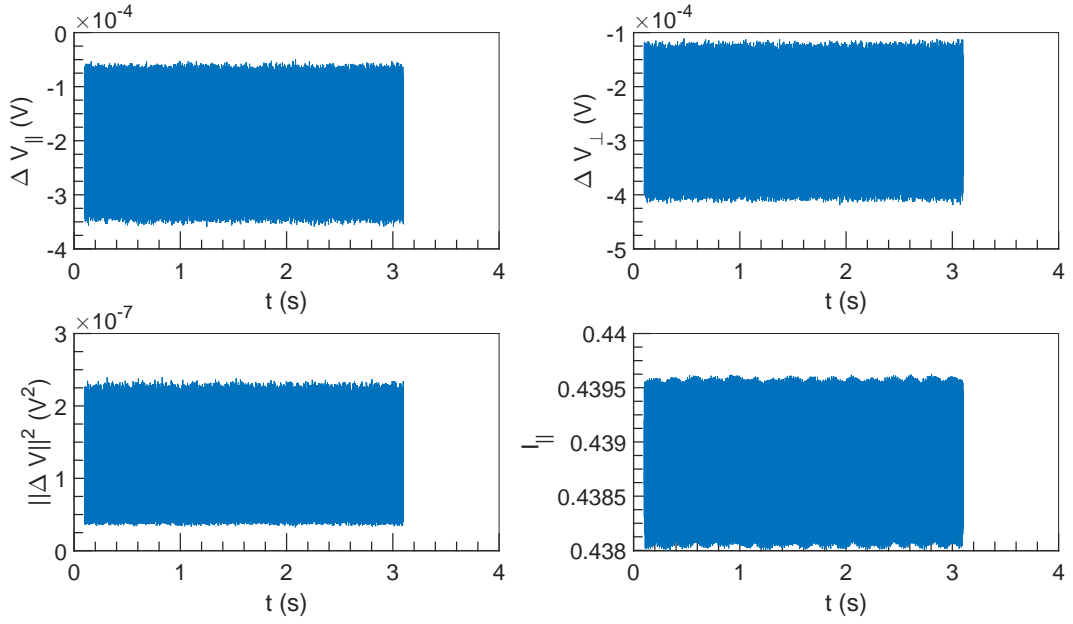


Figure 1.3:  $\Delta V$  and  $I$  vs  $t$  at  $U = 0 \text{ m s}^{-1}$ ,  $\omega = 3142 \text{ rad s}^{-1}$  and  $\alpha = 0\%$ .

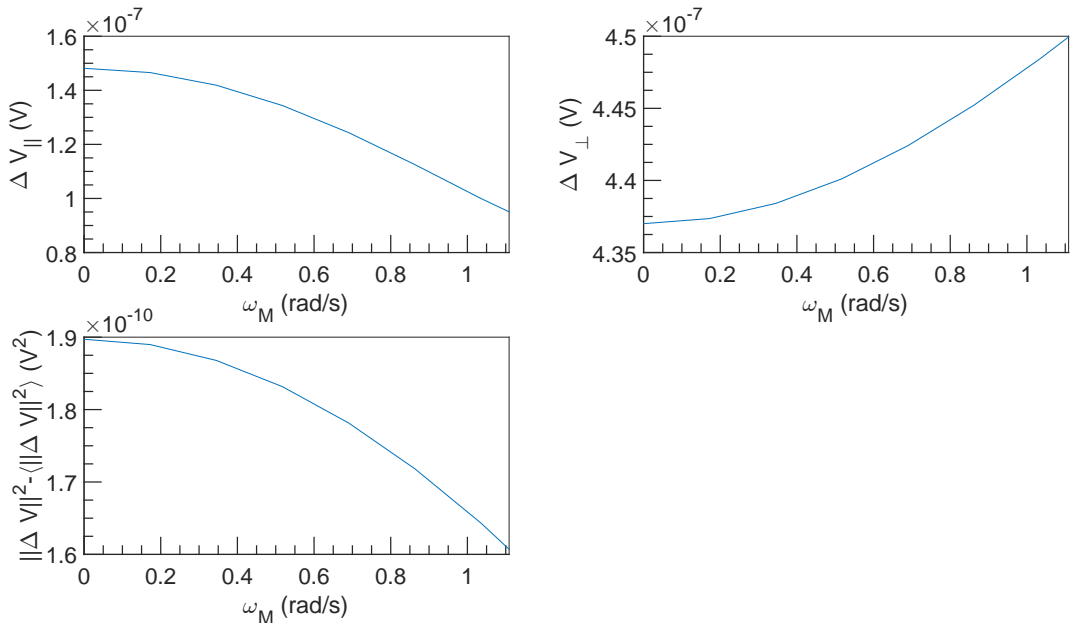


Figure 1.4: FFT spectral density of  $\Delta V$  vs  $\omega_M$  at  $U = 0 \text{ m s}^{-1}$ ,  $\omega = 3142 \text{ rad s}^{-1}$  and  $\alpha = 0\%$ .



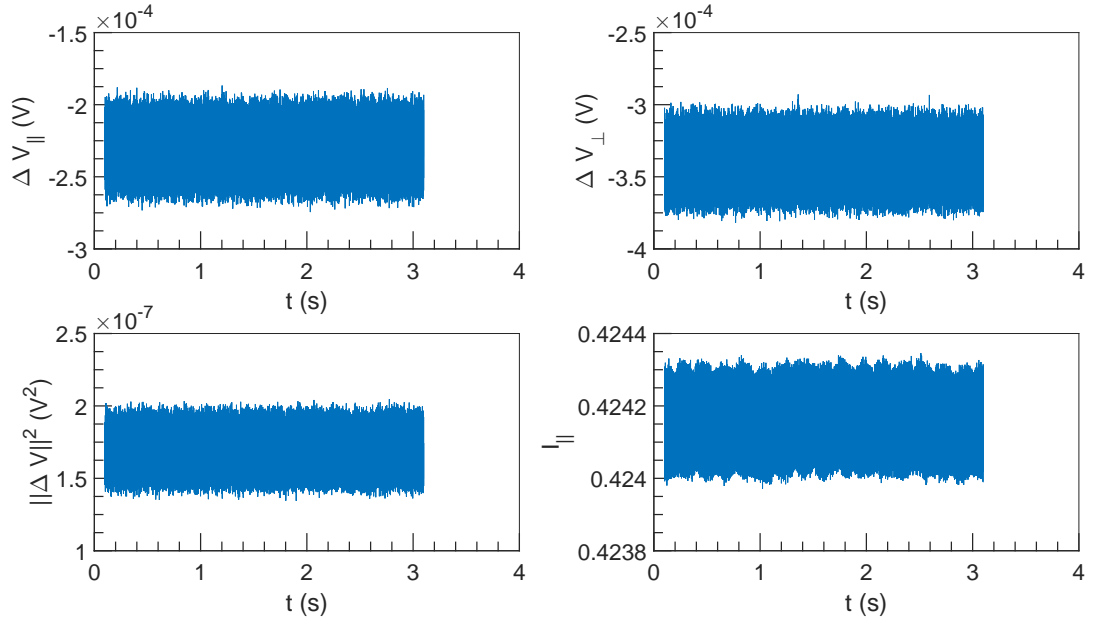


Figure 1.5:  $\Delta V$  and  $I$  vs  $t$  at  $U = 0 \text{ m s}^{-1}$ ,  $\omega = 4712 \text{ rad s}^{-1}$  and  $\alpha = 0\%$ .

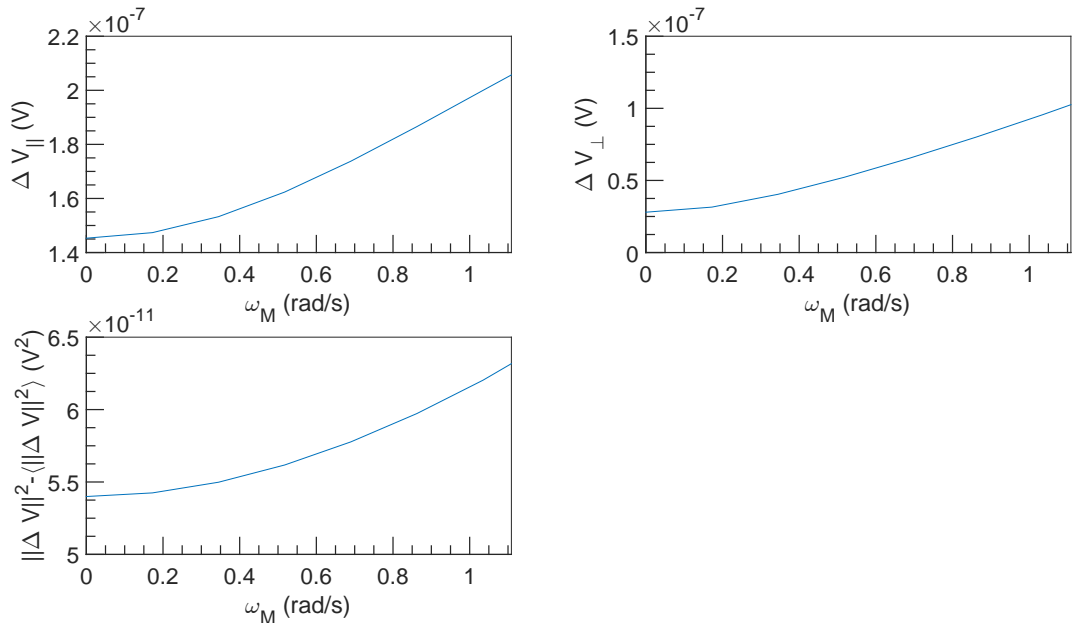


Figure 1.6: FFT spectral density of  $\Delta V$  vs  $\omega_M$  at  $U = 0 \text{ m s}^{-1}$ ,  $\omega = 4712 \text{ rad s}^{-1}$  and  $\alpha = 0\%$ .

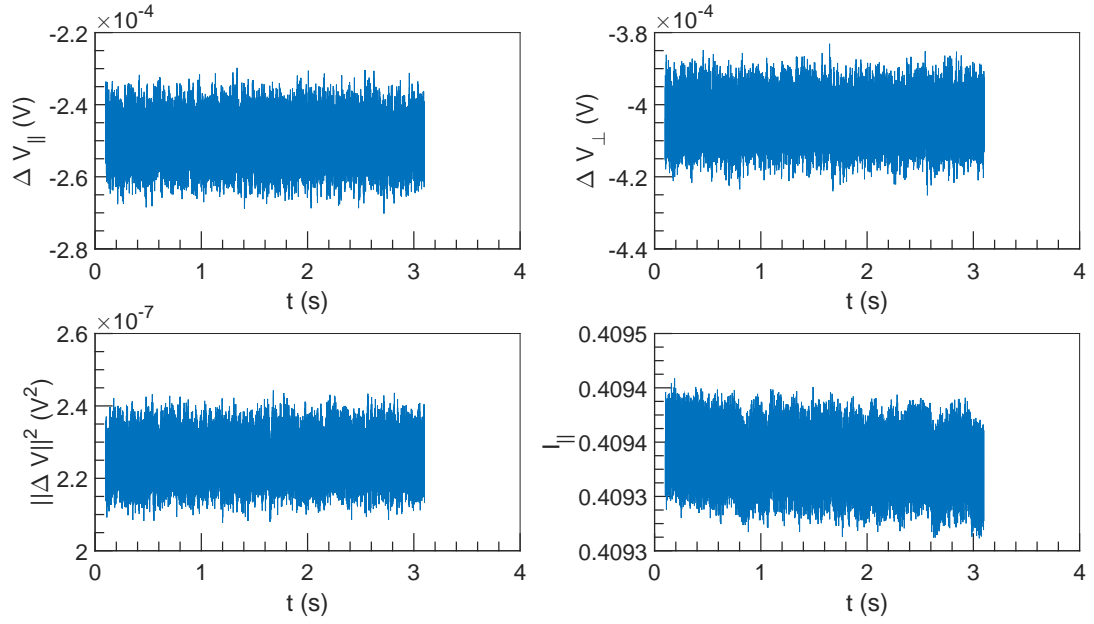


Figure 1.7:  $\Delta V$  and  $I$  vs  $t$  at  $U = 0 \text{ m s}^{-1}$ ,  $\omega = 6283 \text{ rad s}^{-1}$  and  $\alpha = 0\%$ .

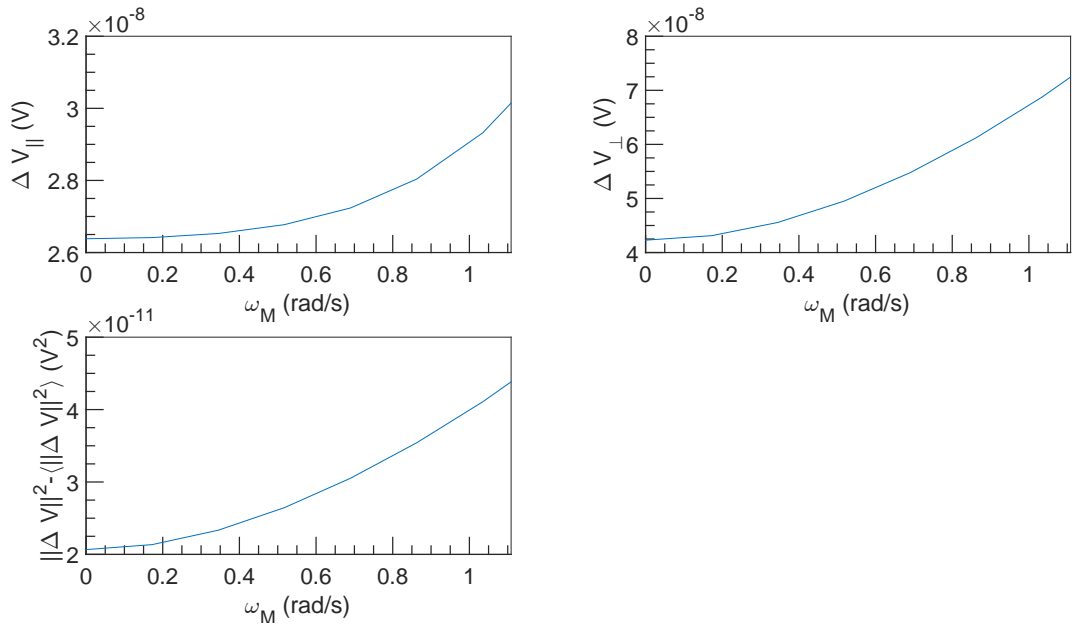


Figure 1.8: FFT spectral density of  $\Delta V$  vs  $\omega_M$  at  $U = 0 \text{ m s}^{-1}$ ,  $\omega = 6283 \text{ rad s}^{-1}$  and  $\alpha = 0\%$ .

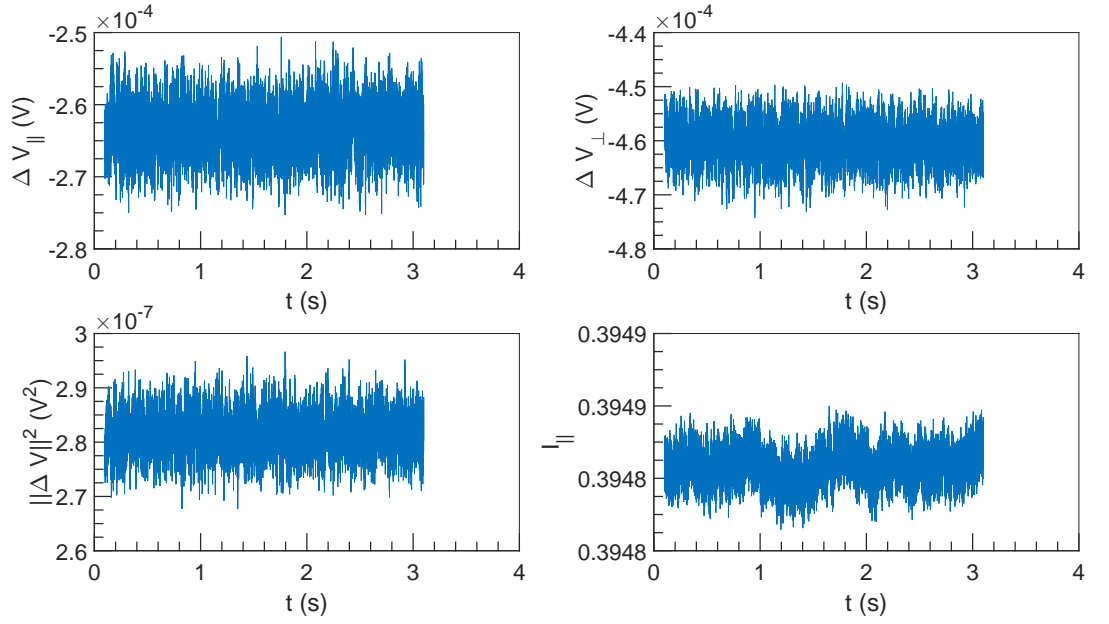


Figure 1.9:  $\Delta V$  and  $I$  vs  $t$  at  $U = 0 \text{ ms}^{-1}$ ,  $\omega = 7854 \text{ rad s}^{-1}$  and  $\alpha = 0\%$ .

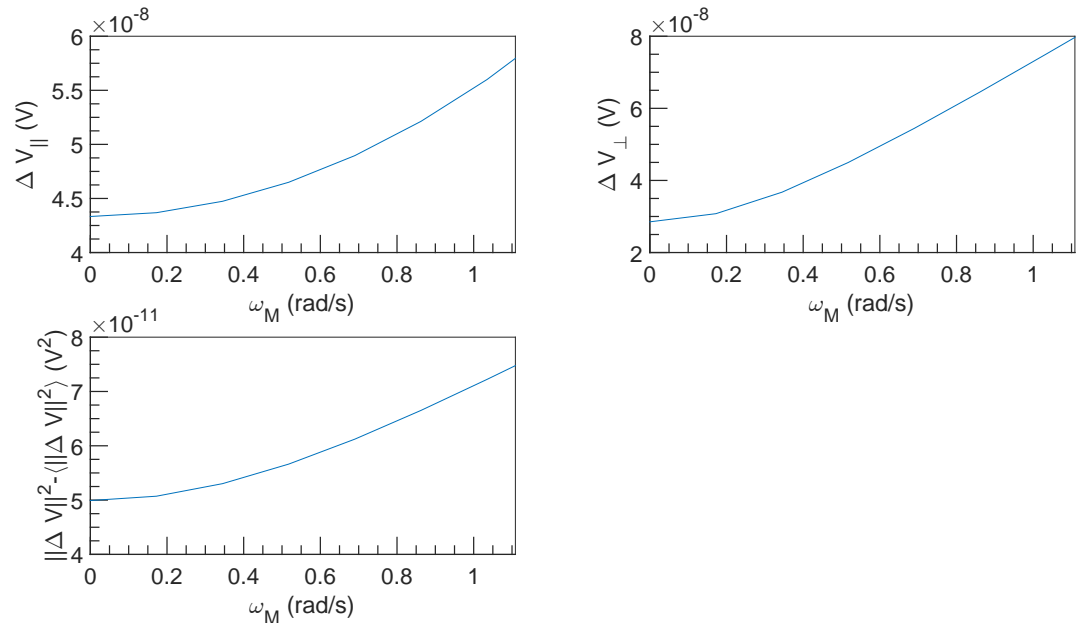


Figure 1.10: FFT spectral density of  $\Delta V$  vs  $\omega_M$  at  $U = 0 \text{ ms}^{-1}$ ,  $\omega = 7854 \text{ rad s}^{-1}$  and  $\alpha = 0\%$ .

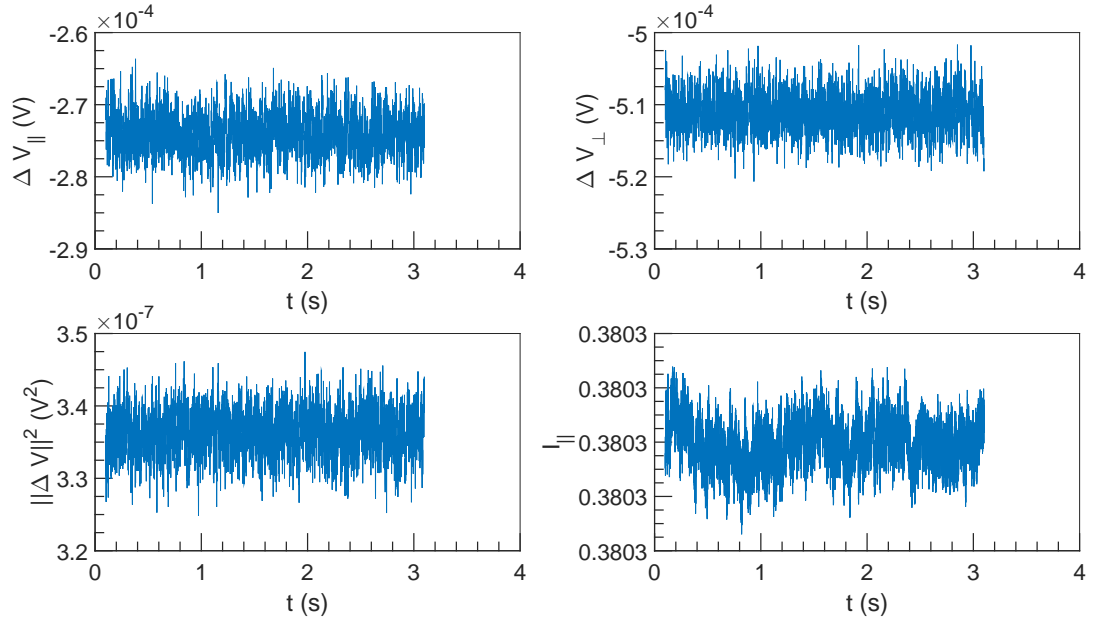


Figure 1.11:  $\Delta V$  and  $I$  vs  $t$  at  $U = 0 \text{ m s}^{-1}$ ,  $\omega = 9425 \text{ rad s}^{-1}$  and  $\alpha = 0\%$ .

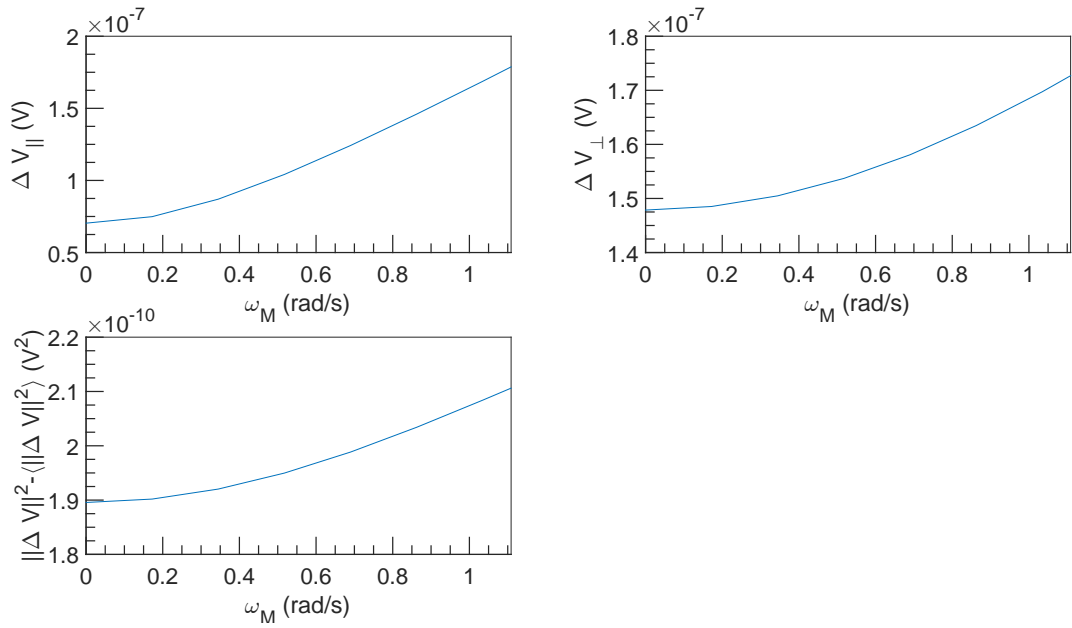


Figure 1.12: FFT spectral density of  $\Delta V$  vs  $\omega_M$  at  $U = 0 \text{ m s}^{-1}$ ,  $\omega = 9425 \text{ rad s}^{-1}$  and  $\alpha = 0\%$ .

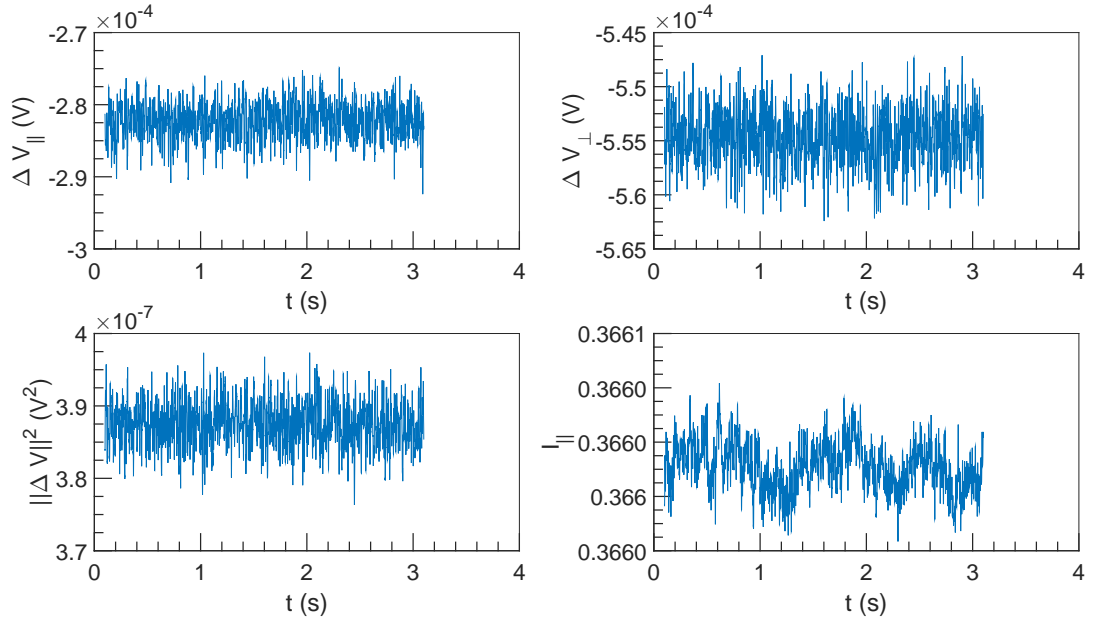


Figure 1.13:  $\Delta V$  and  $I$  vs  $t$  at  $U = 0 \text{ m s}^{-1}$ ,  $\omega = 10996 \text{ rad s}^{-1}$  and  $\alpha = 0\%$ .

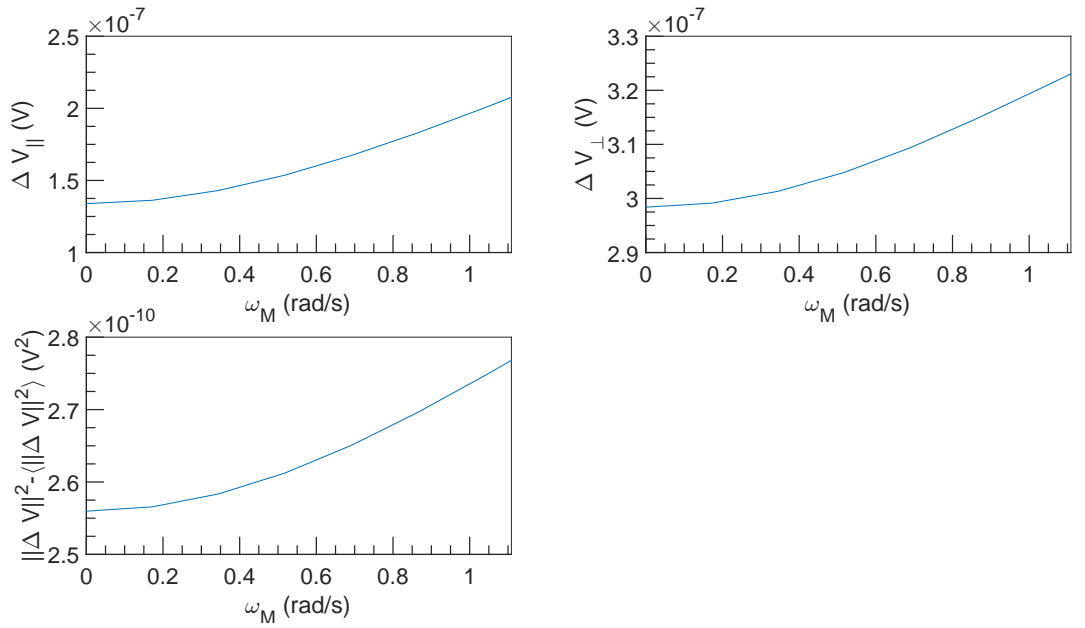


Figure 1.14: FFT spectral density of  $\Delta V$  vs  $\omega_M$  at  $U = 0 \text{ m s}^{-1}$ ,  $\omega = 10996 \text{ rad s}^{-1}$  and  $\alpha = 0\%$ .

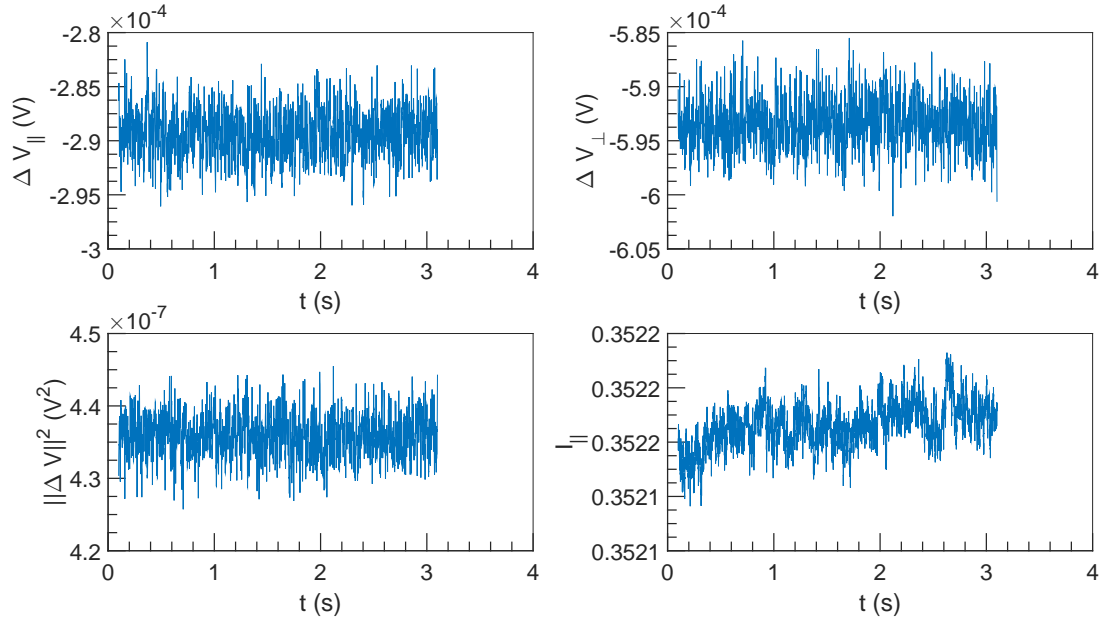


Figure 1.15:  $\Delta V$  and  $I$  vs  $t$  at  $U = 0 \text{ m s}^{-1}$ ,  $\omega = 12566 \text{ rad s}^{-1}$  and  $\alpha = 0\%$ .

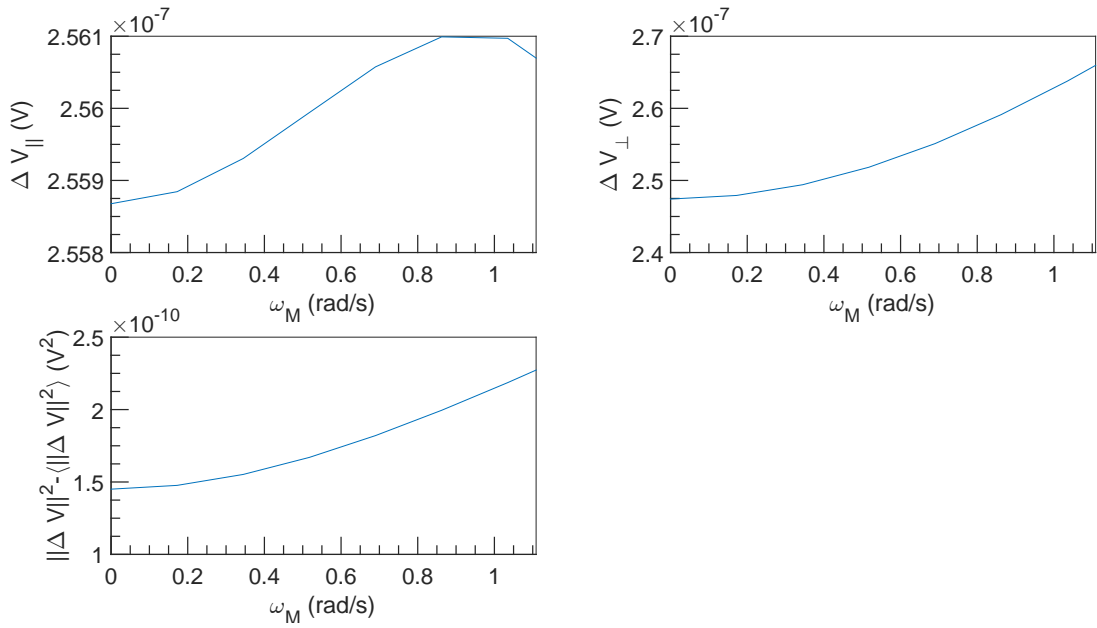


Figure 1.16: FFT spectral density of  $\Delta V$  vs  $\omega_M$  at  $U = 0 \text{ m s}^{-1}$ ,  $\omega = 12566 \text{ rad s}^{-1}$  and  $\alpha = 0\%$ .

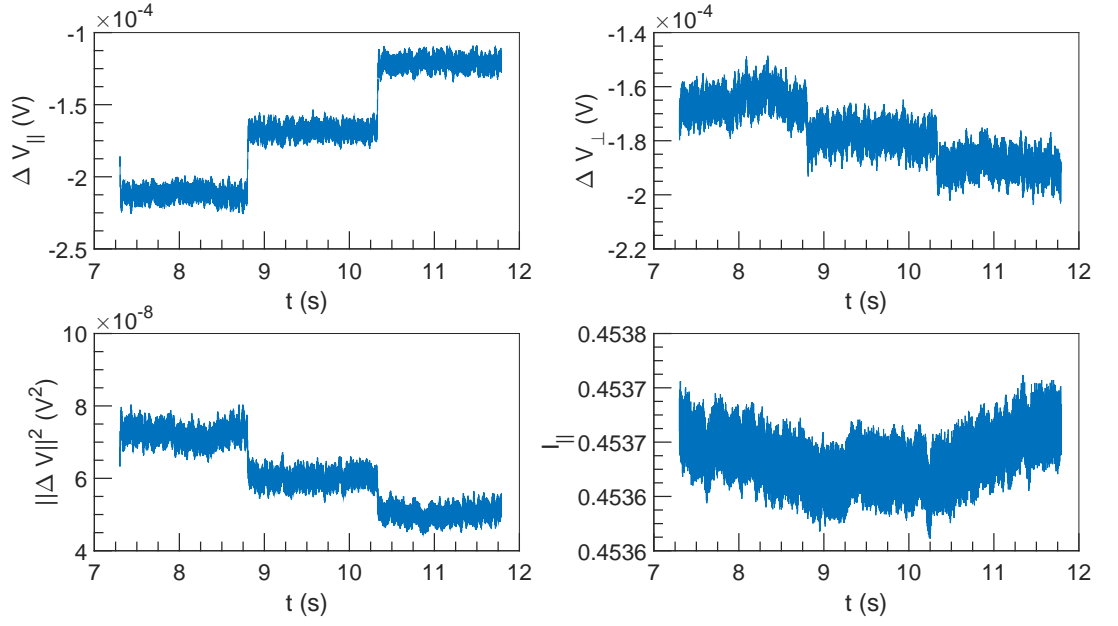


Figure 1.17:  $\Delta V$  and  $I$  vs  $t$  at  $U = 0.1 \text{ m s}^{-1}$ ,  $\omega = 1571 \text{ rad s}^{-1}$  and  $\alpha = 0\%$ .

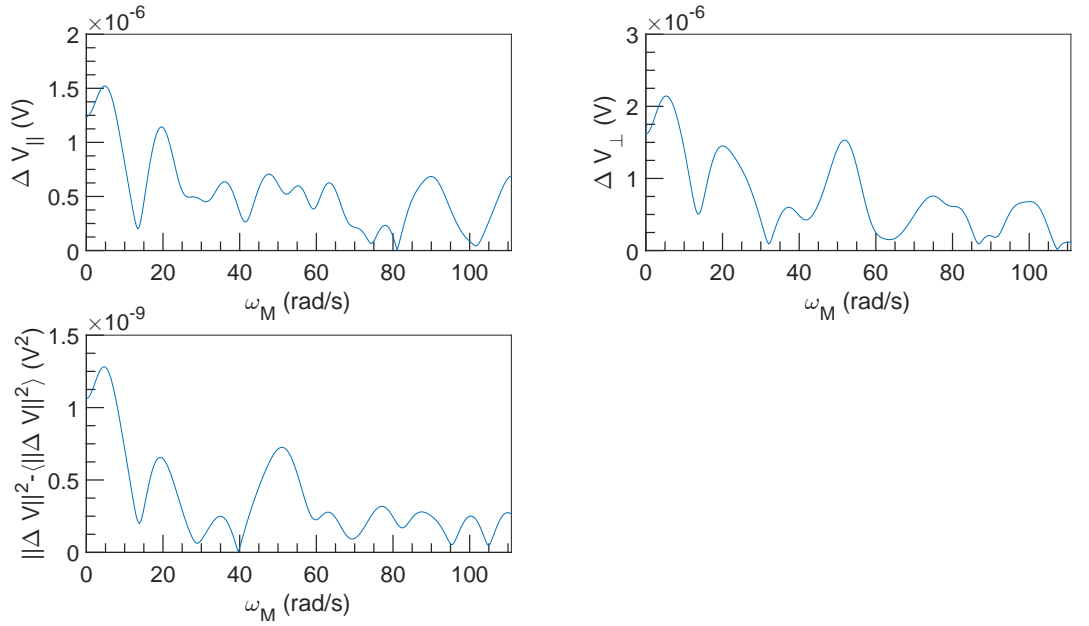


Figure 1.18: FFT spectral density of  $\Delta V$  vs  $\omega_M$  at  $U = 0.1 \text{ m s}^{-1}$ ,  $\omega = 1571 \text{ rad s}^{-1}$  and  $\alpha = 0\%$ .

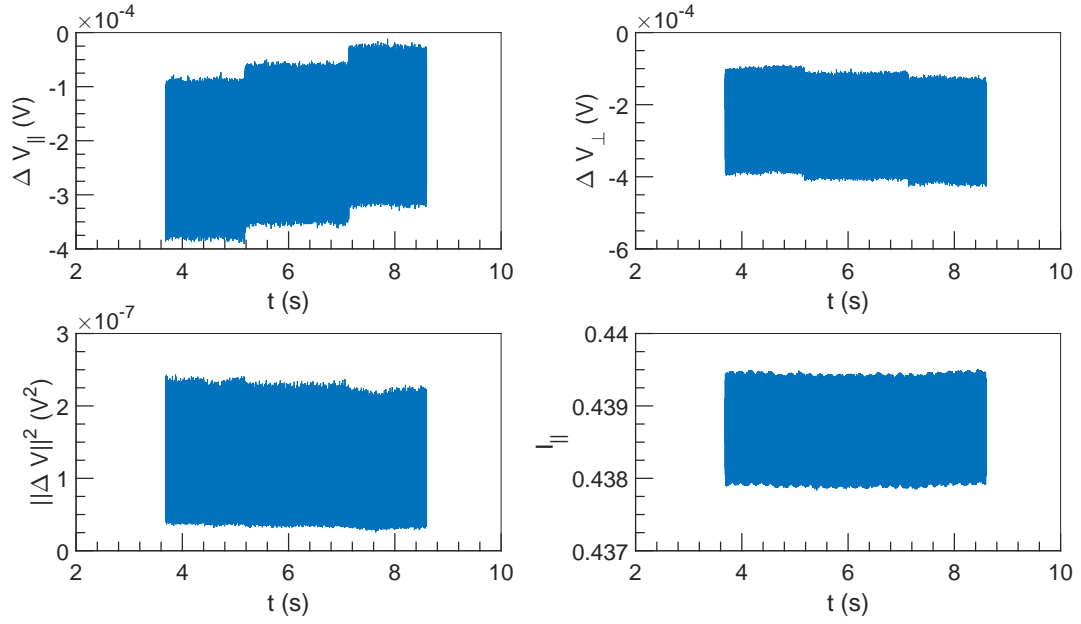


Figure 1.19:  $\Delta V$  and  $I$  vs  $t$  at  $U = 0.1 \text{ m s}^{-1}$ ,  $\omega = 3142 \text{ rad s}^{-1}$  and  $\alpha = 0\%$ .

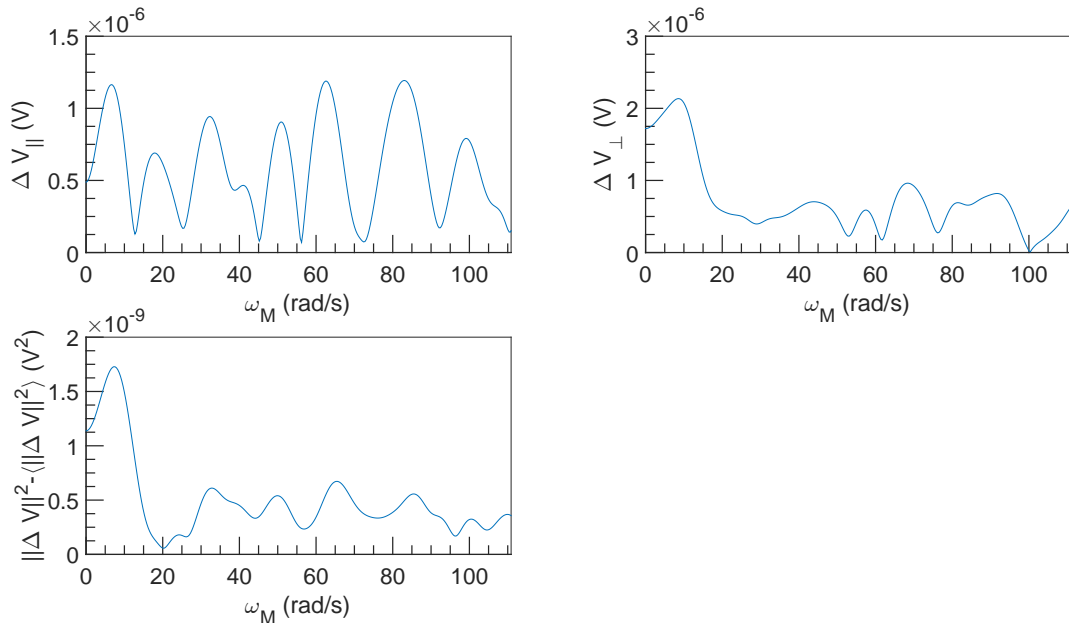


Figure 1.20: FFT spectral density of  $\Delta V$  vs  $\omega_M$  at  $U = 0.1 \text{ m s}^{-1}$ ,  $\omega = 3142 \text{ rad s}^{-1}$  and  $\alpha = 0\%$ .



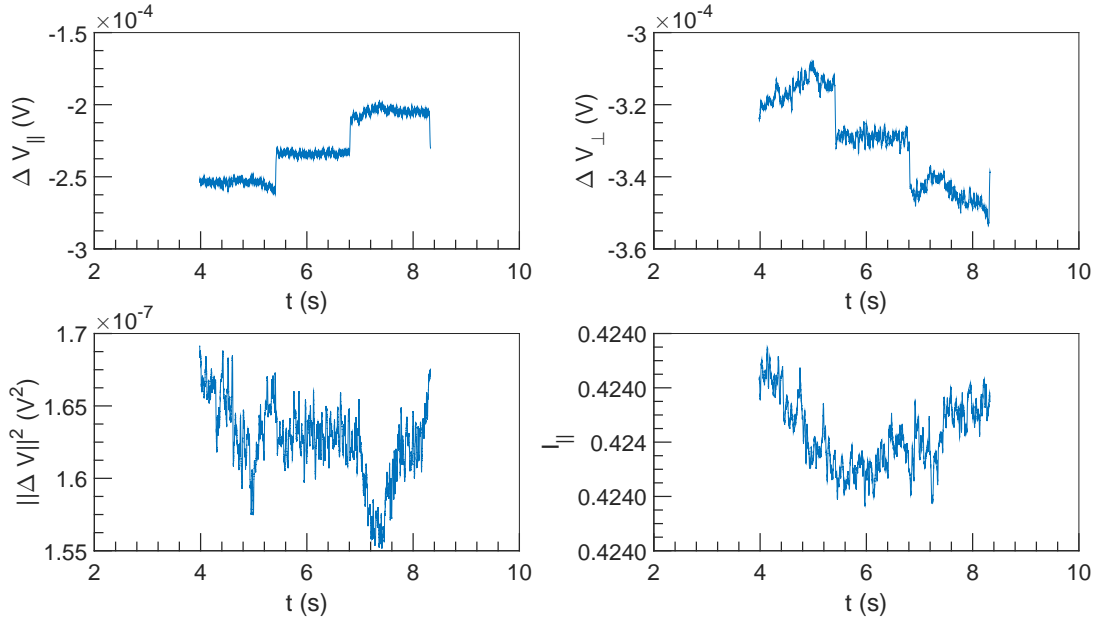


Figure 1.21:  $\Delta V$  and  $I$  vs  $t$  at  $U = 0.1 \text{ m s}^{-1}$ ,  $\omega = 4712 \text{ rad s}^{-1}$  and  $\alpha = 0\%$ .

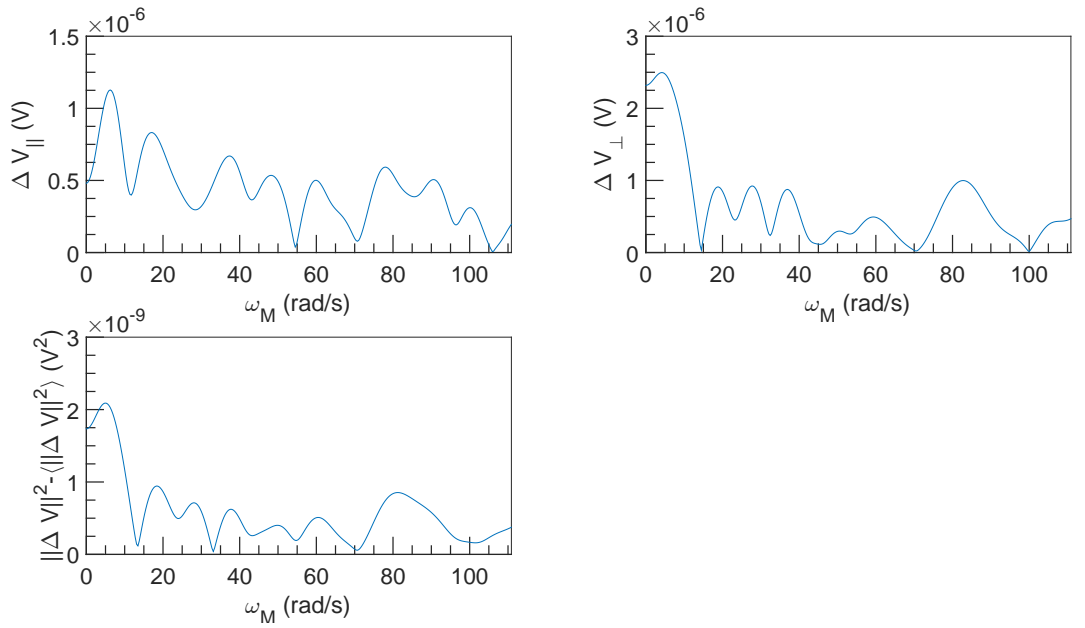


Figure 1.22: FFT spectral density of  $\Delta V$  vs  $\omega_M$  at  $U = 0.1 \text{ m s}^{-1}$ ,  $\omega = 4712 \text{ rad s}^{-1}$  and  $\alpha = 0\%$ .

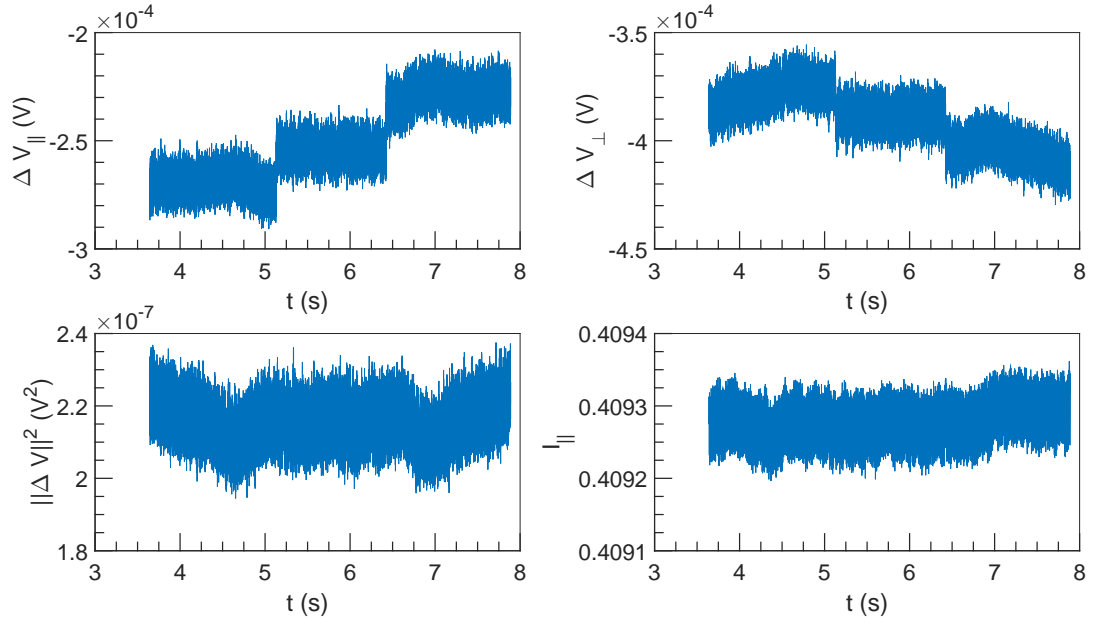


Figure 1.23:  $\Delta V$  and  $I$  vs  $t$  at  $U = 0.1 \text{ m s}^{-1}$ ,  $\omega = 6283 \text{ rad s}^{-1}$  and  $\alpha = 0\%$ .

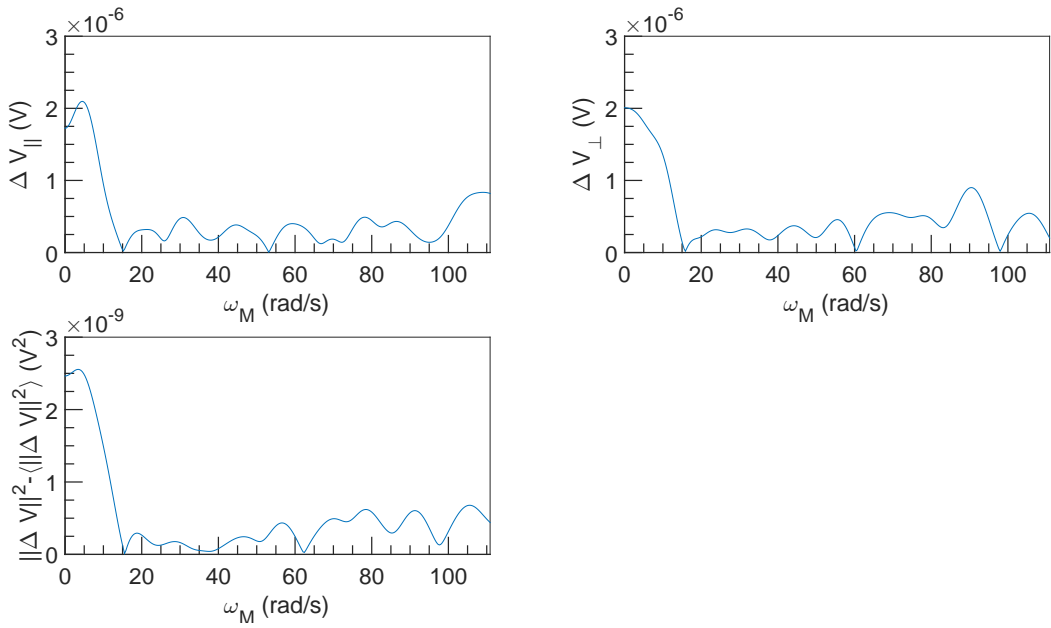


Figure 1.24: FFT spectral density of  $\Delta V$  vs  $\omega_M$  at  $U = 0.1 \text{ m s}^{-1}$ ,  $\omega = 6283 \text{ rad s}^{-1}$  and  $\alpha = 0\%$ .

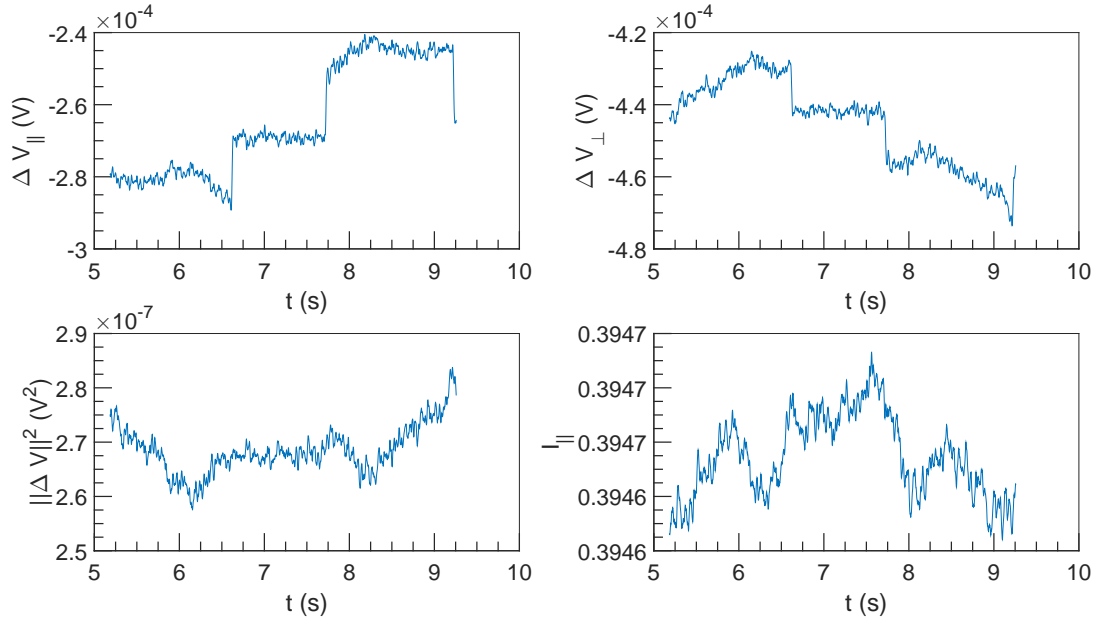


Figure 1.25:  $\Delta V$  and  $I$  vs  $t$  at  $U = 0.1 \text{ m s}^{-1}$ ,  $\omega = 7854 \text{ rad s}^{-1}$  and  $\alpha = 0\%$ .

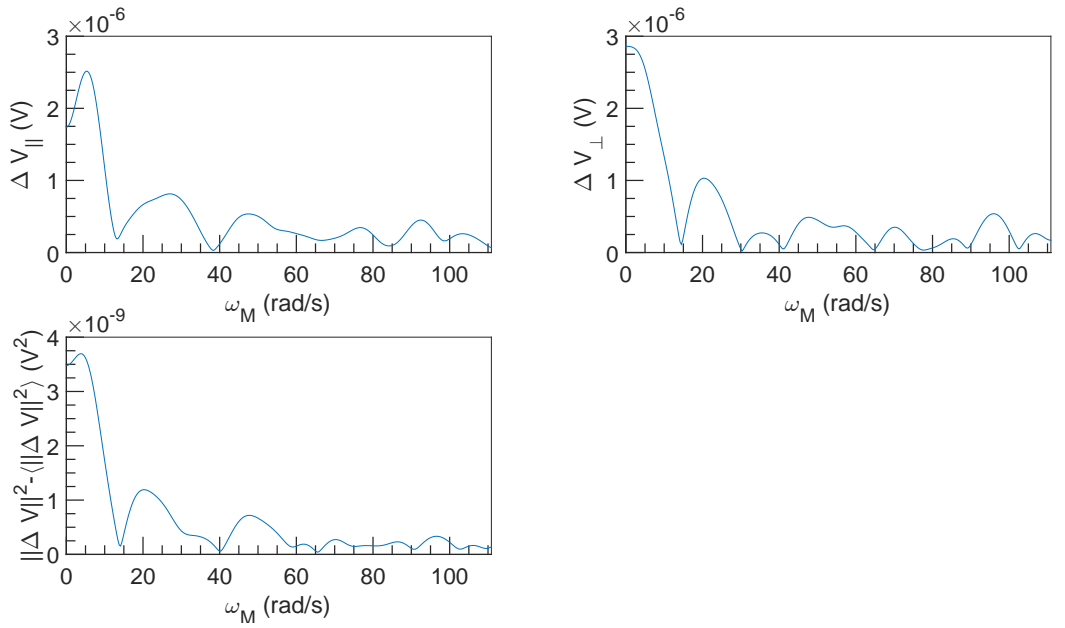


Figure 1.26: FFT spectral density of  $\Delta V$  vs  $\omega_M$  at  $U = 0.1 \text{ m s}^{-1}$ ,  $\omega = 7854 \text{ rad s}^{-1}$  and  $\alpha = 0\%$ .

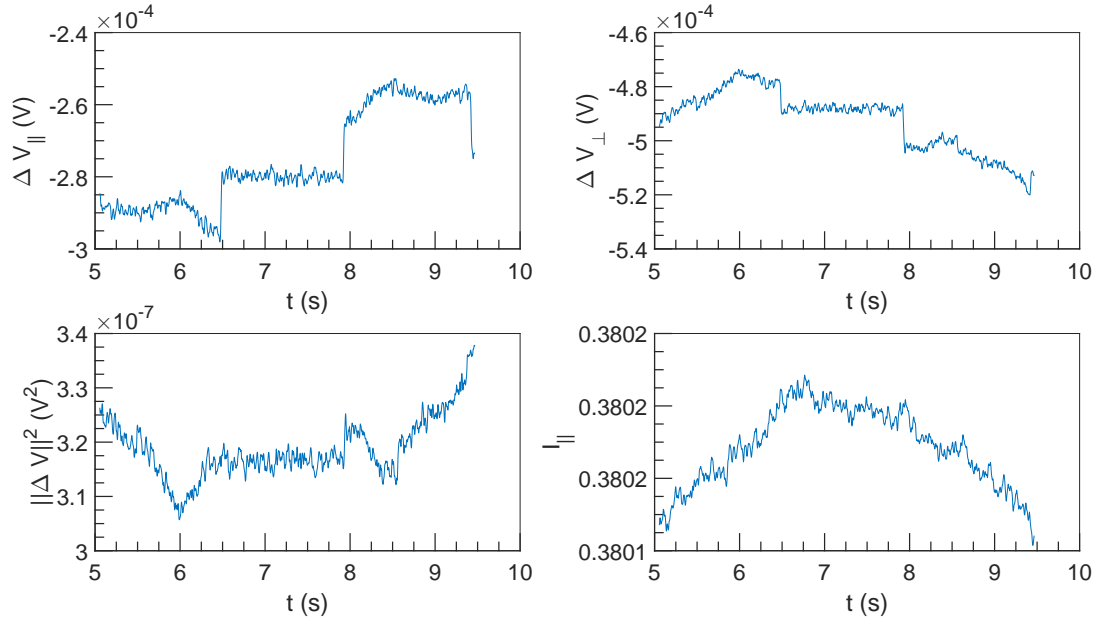


Figure 1.27:  $\Delta V$  and  $I$  vs  $t$  at  $U = 0.1 \text{ m s}^{-1}$ ,  $\omega = 9425 \text{ rad s}^{-1}$  and  $\alpha = 0\%$ .

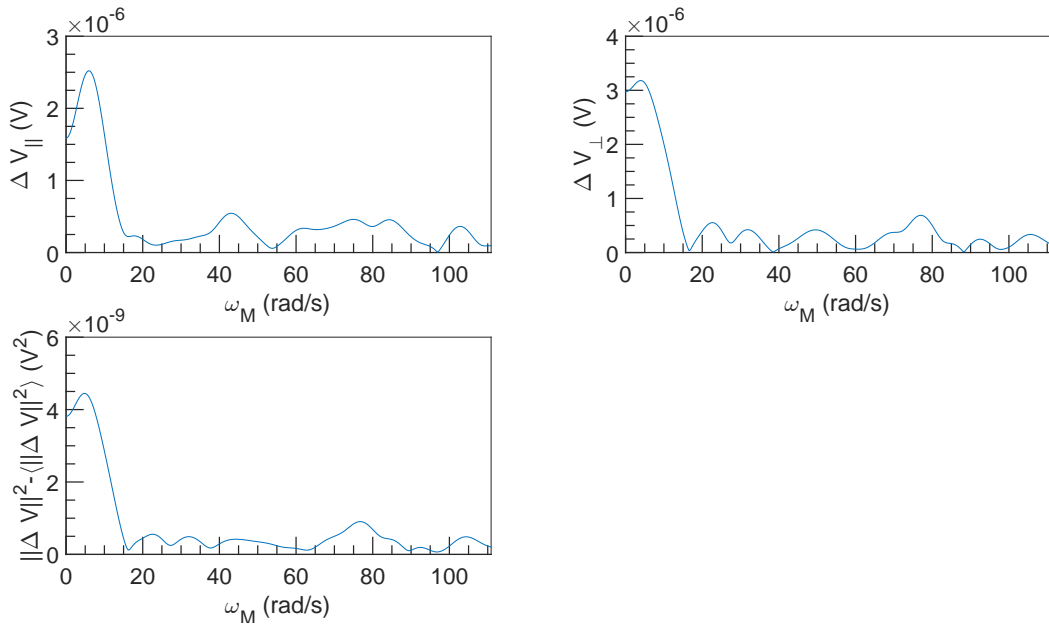


Figure 1.28: FFT spectral density of  $\Delta V$  vs  $\omega_M$  at  $U = 0.1 \text{ m s}^{-1}$ ,  $\omega = 9425 \text{ rad s}^{-1}$  and  $\alpha = 0\%$ .

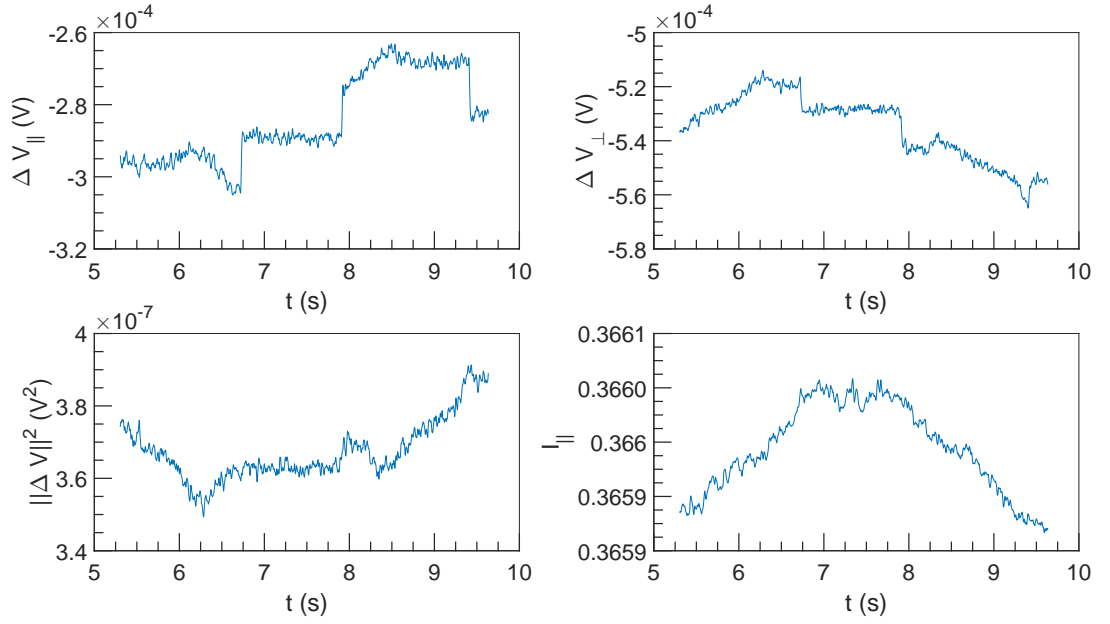


Figure 1.29:  $\Delta V$  and  $I$  vs  $t$  at  $U = 0.1 \text{ ms}^{-1}$ ,  $\omega = 10996 \text{ rad s}^{-1}$  and  $\alpha = 0\%$ .

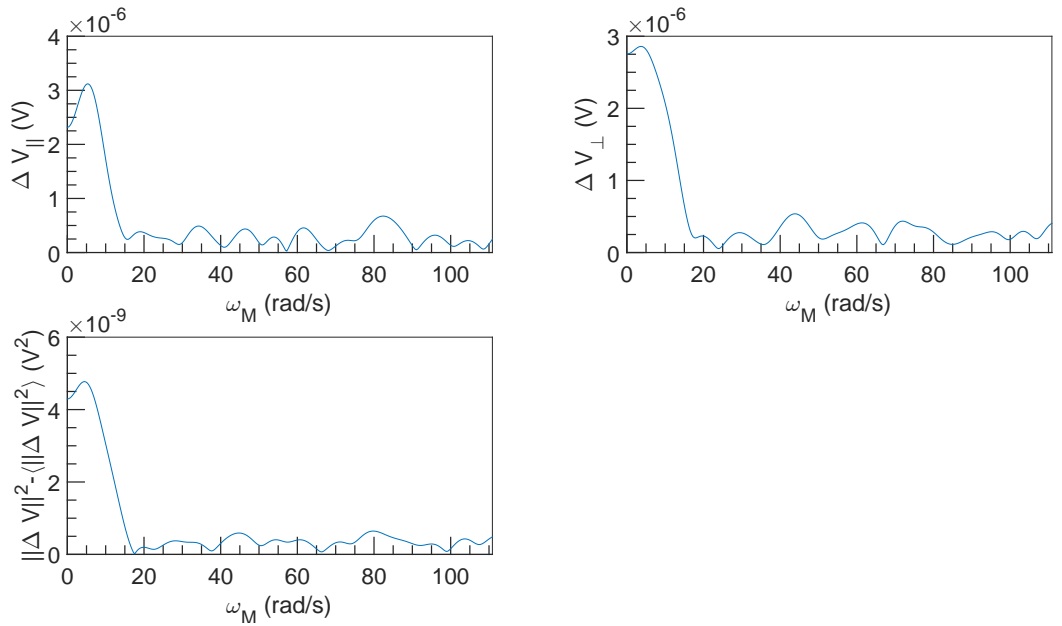


Figure 1.30: FFT spectral density of  $\Delta V$  vs  $\omega_M$  at  $U = 0.1 \text{ ms}^{-1}$ ,  $\omega = 10996 \text{ rad s}^{-1}$  and  $\alpha = 0\%$ .

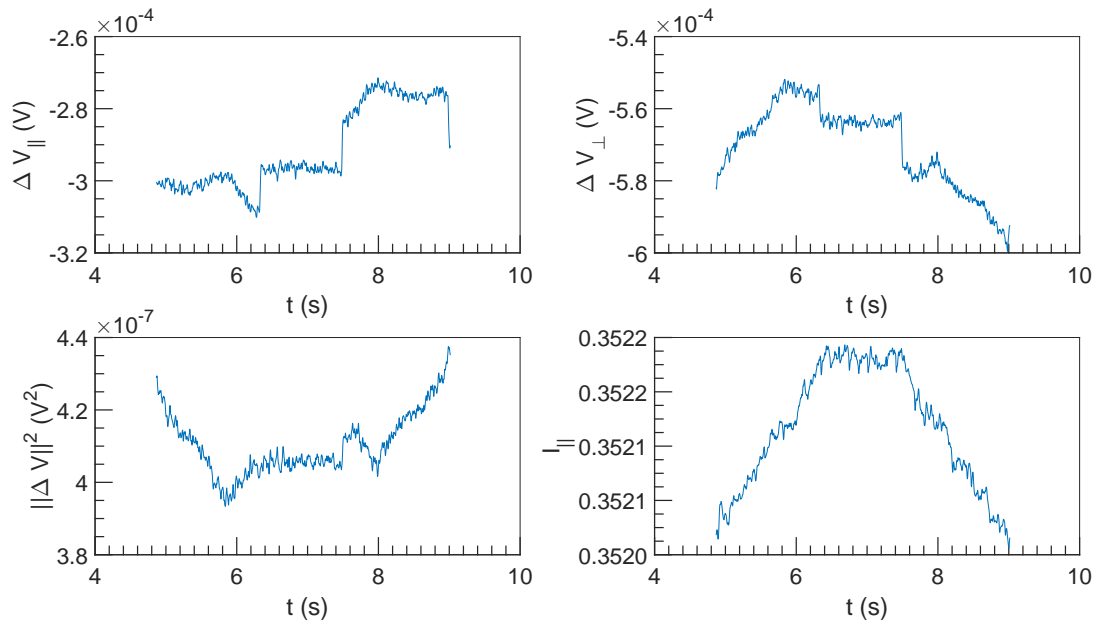


Figure 1.31:  $\Delta V$  and  $I$  vs  $t$  at  $U = 0.1 \text{ ms}^{-1}$ ,  $\omega = 12566 \text{ rad s}^{-1}$  and  $\alpha = 0\%$ .

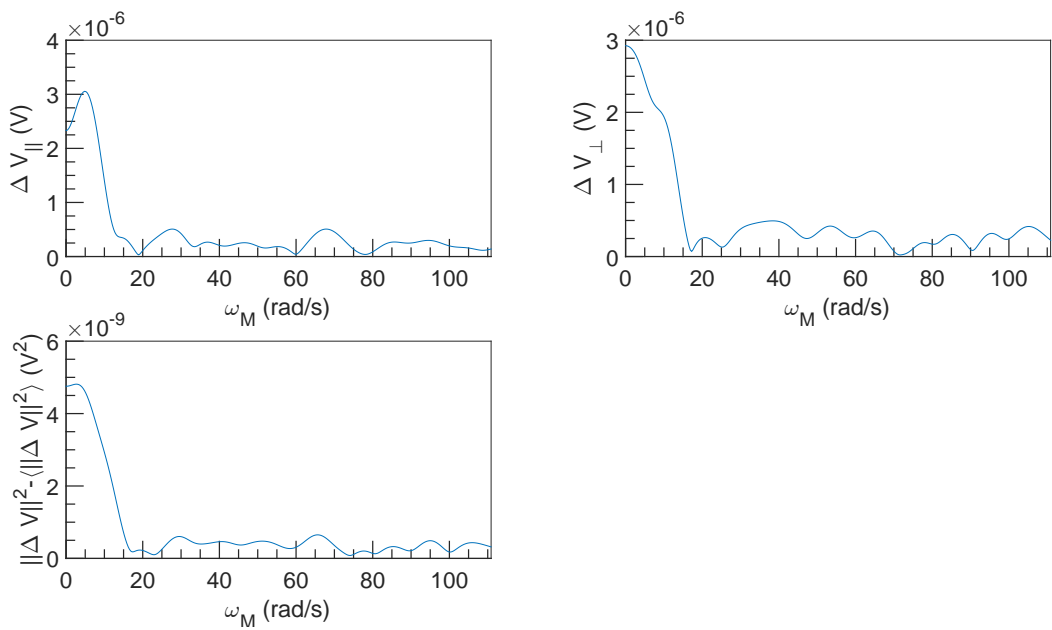


Figure 1.32: FFT spectral density of  $\Delta V$  vs  $\omega_M$  at  $U = 0.1 \text{ ms}^{-1}$ ,  $\omega = 12566 \text{ rad s}^{-1}$  and  $\alpha = 0\%$ .

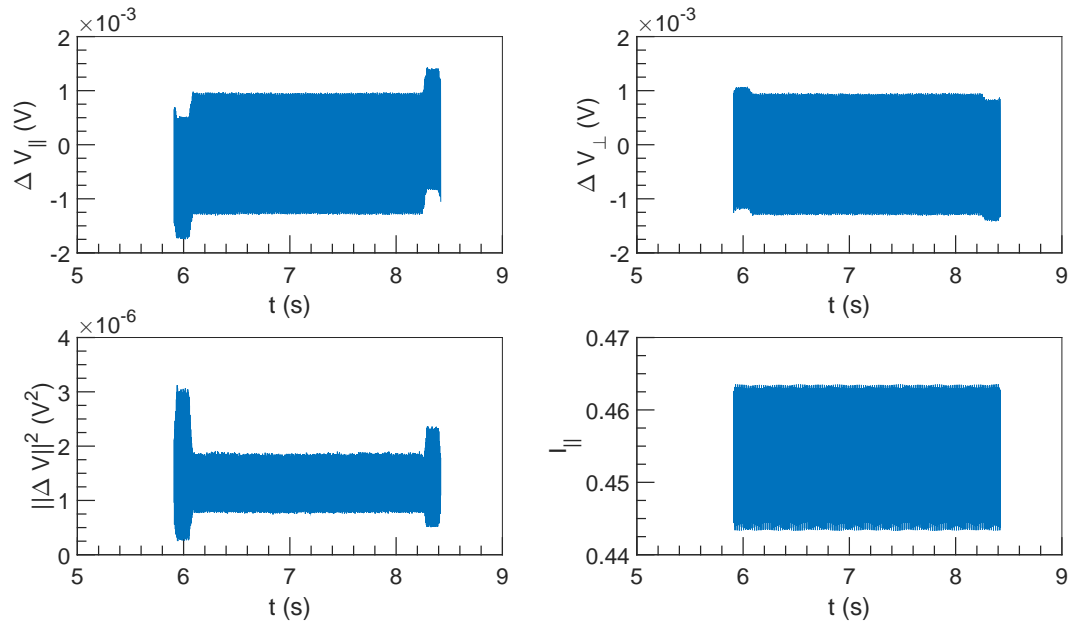


Figure 1.33:  $\Delta V$  and  $I$  vs  $t$  at  $U = 1 \text{ m s}^{-1}$ ,  $\omega = 1571 \text{ rad s}^{-1}$  and  $\alpha = 0\%$ .

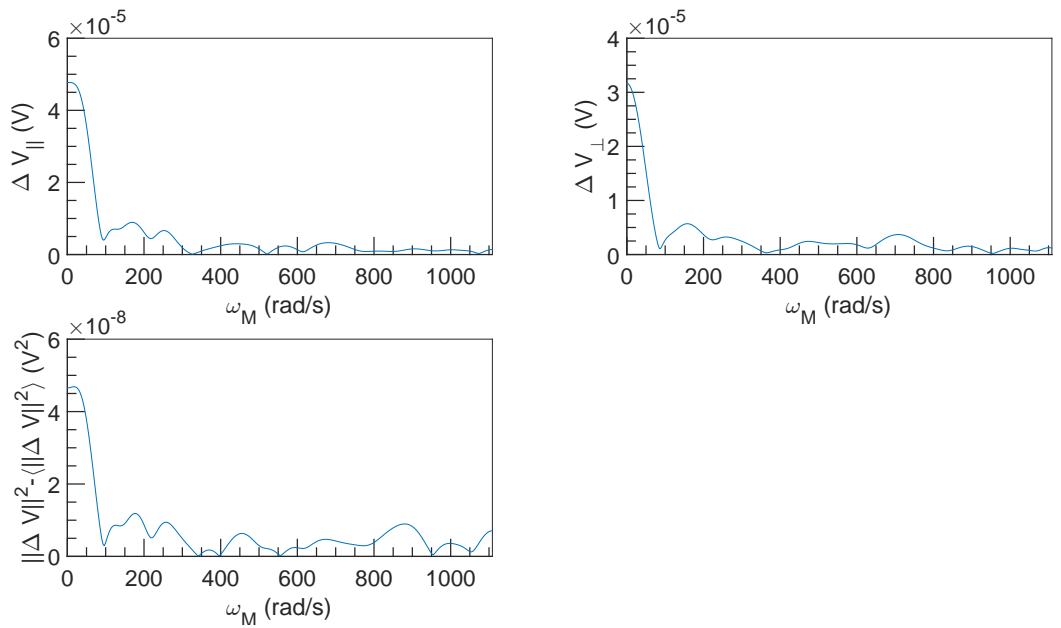


Figure 1.34: FFT spectral density of  $\Delta V$  vs  $\omega_M$  at  $U = 1 \text{ m s}^{-1}$ ,  $\omega = 1571 \text{ rad s}^{-1}$  and  $\alpha = 0\%$ .

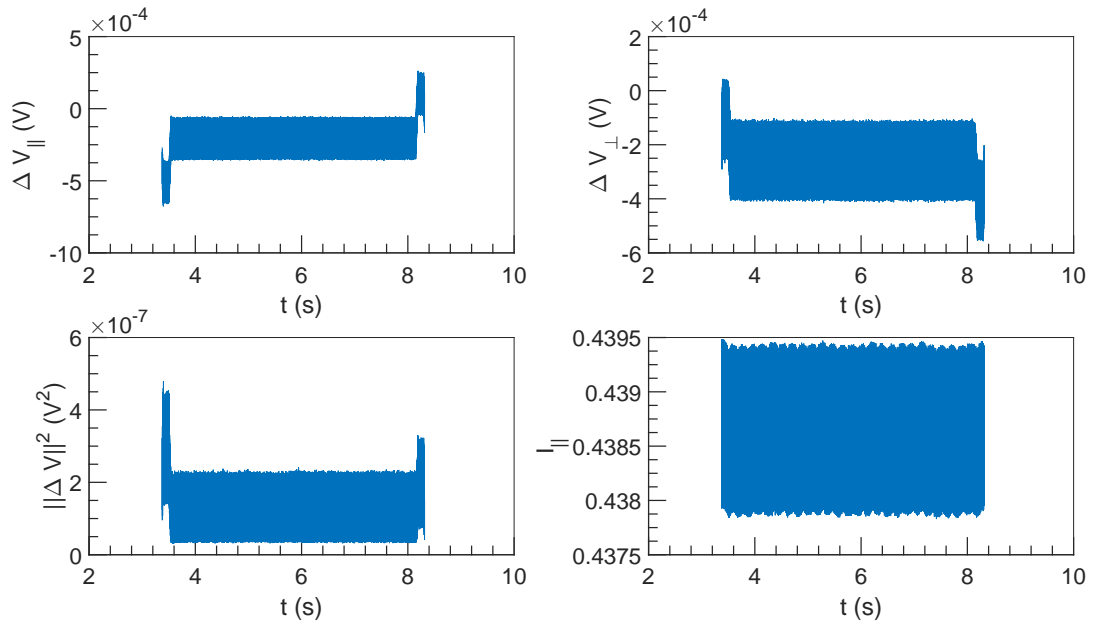


Figure 1.35:  $\Delta V$  and  $I$  vs  $t$  at  $U = 1 \text{ m s}^{-1}$ ,  $\omega = 3142 \text{ rad s}^{-1}$  and  $\alpha = 0\%$ .

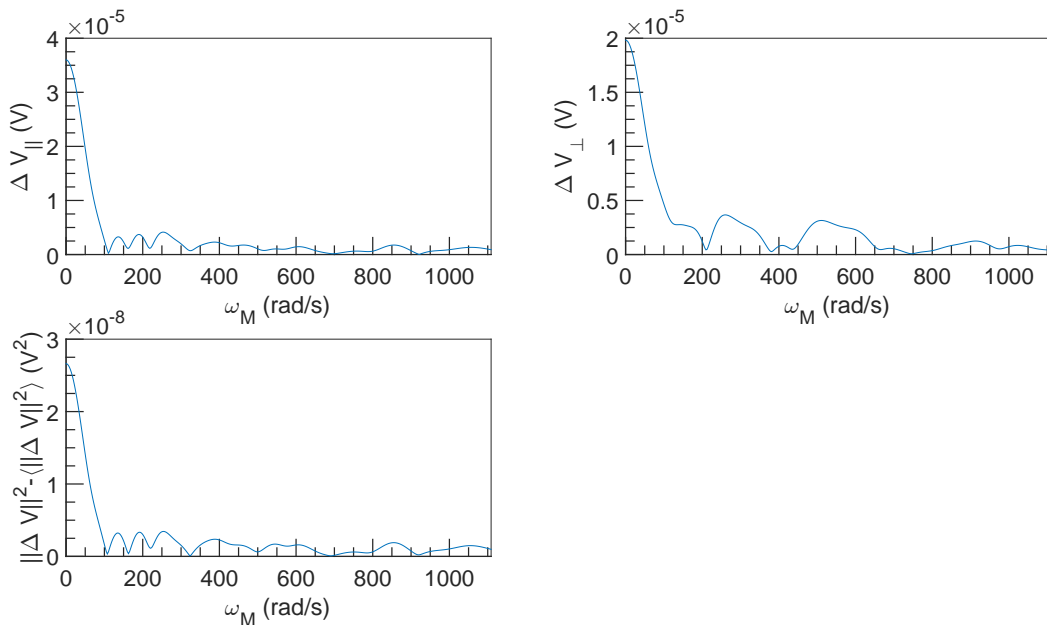


Figure 1.36: FFT spectral density of  $\Delta V$  vs  $\omega_M$  at  $U = 1 \text{ m s}^{-1}$ ,  $\omega = 3142 \text{ rad s}^{-1}$  and  $\alpha = 0\%$ .



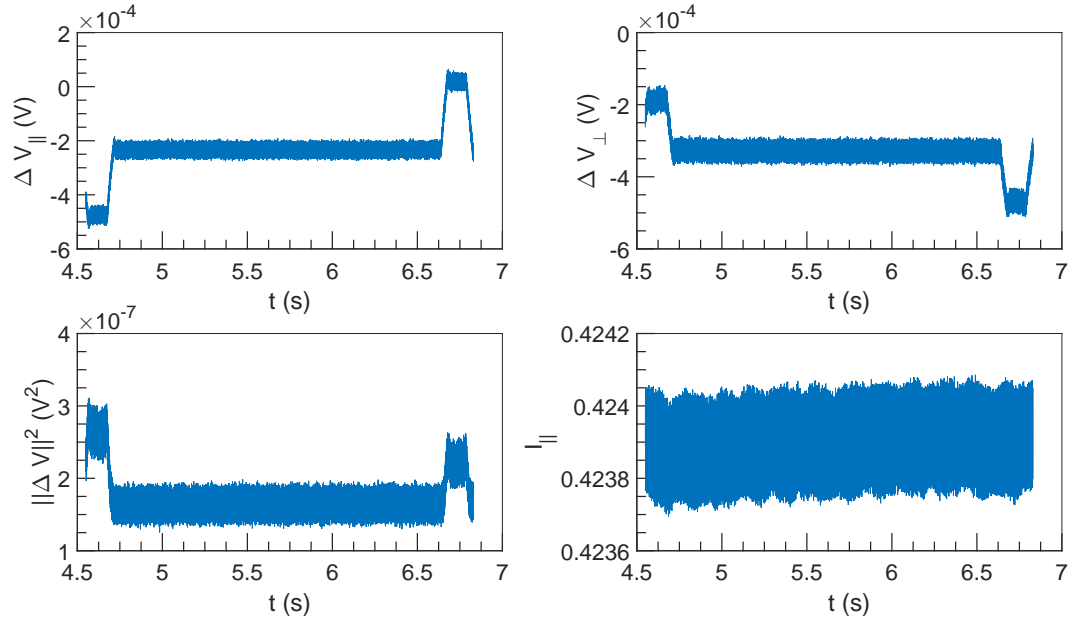


Figure 1.37:  $\Delta V$  and  $I$  vs  $t$  at  $U = 1 \text{ m s}^{-1}$ ,  $\omega = 4712 \text{ rad s}^{-1}$  and  $\alpha = 0\%$ .

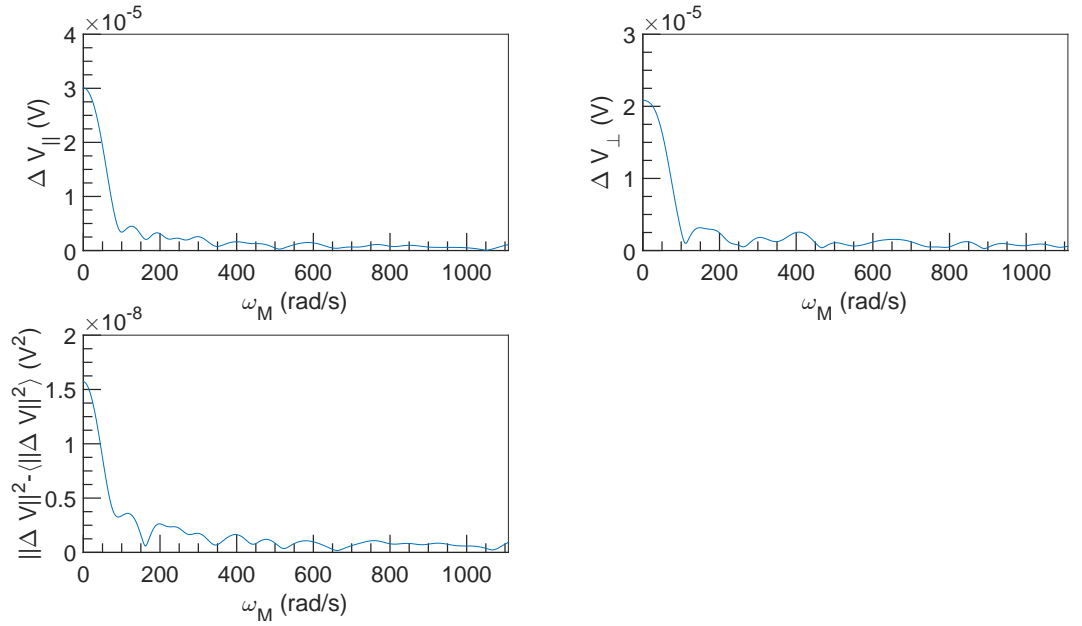


Figure 1.38: FFT spectral density of  $\Delta V$  vs  $\omega_M$  at  $U = 1 \text{ m s}^{-1}$ ,  $\omega = 4712 \text{ rad s}^{-1}$  and  $\alpha = 0\%$ .

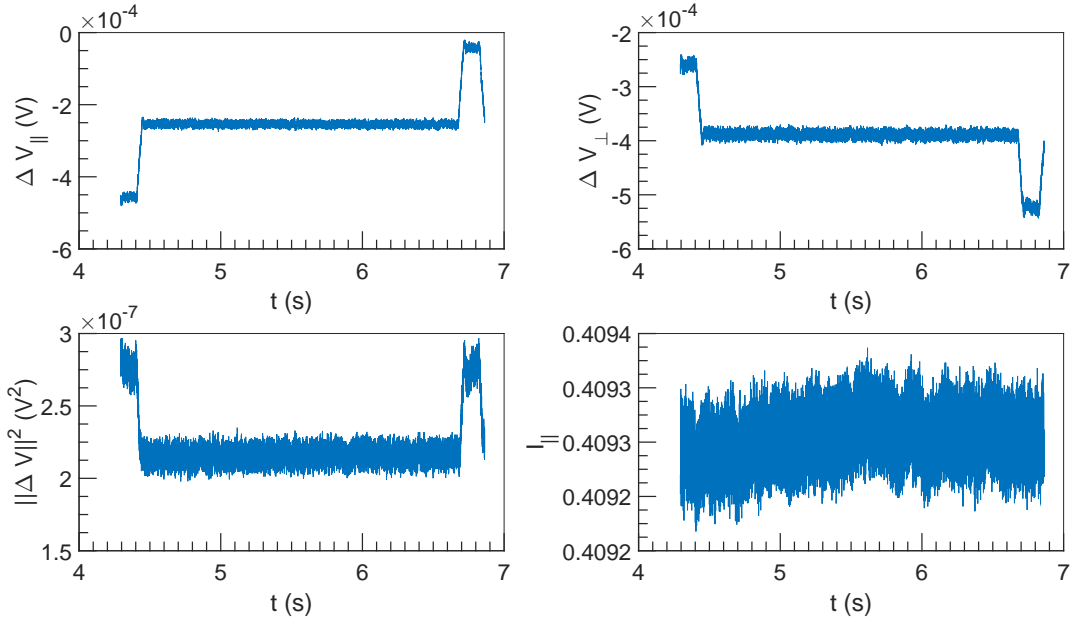


Figure 1.39:  $\Delta V$  and  $I$  vs  $t$  at  $U = 1 \text{ m s}^{-1}$ ,  $\omega = 6283 \text{ rad s}^{-1}$  and  $\alpha = 0\%$ .

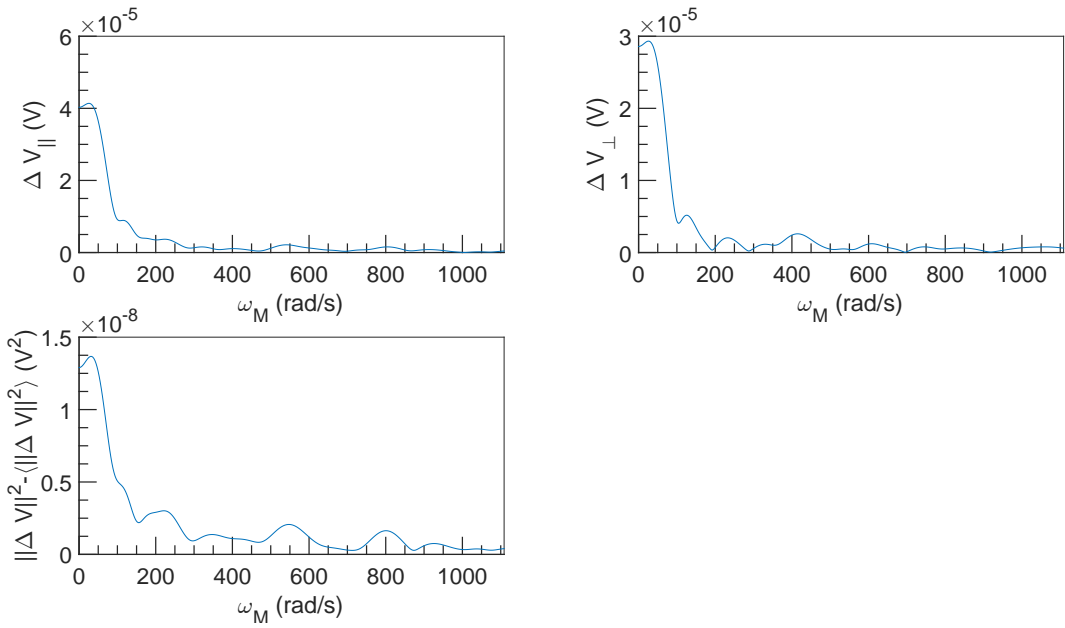


Figure 1.40: FFT spectral density of  $\Delta V$  vs  $\omega_M$  at  $U = 1 \text{ m s}^{-1}$ ,  $\omega = 6283 \text{ rad s}^{-1}$  and  $\alpha = 0\%$ .

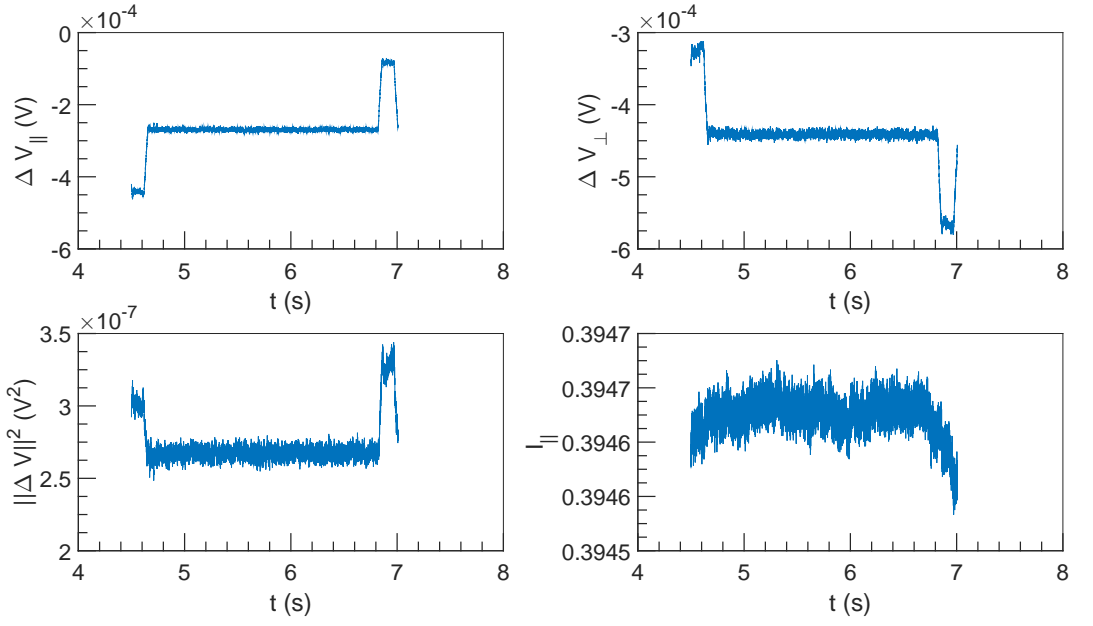


Figure 1.41:  $\Delta V$  and  $I$  vs  $t$  at  $U = 1 \text{ m s}^{-1}$ ,  $\omega = 7854 \text{ rad s}^{-1}$  and  $\alpha = 0\%$ .

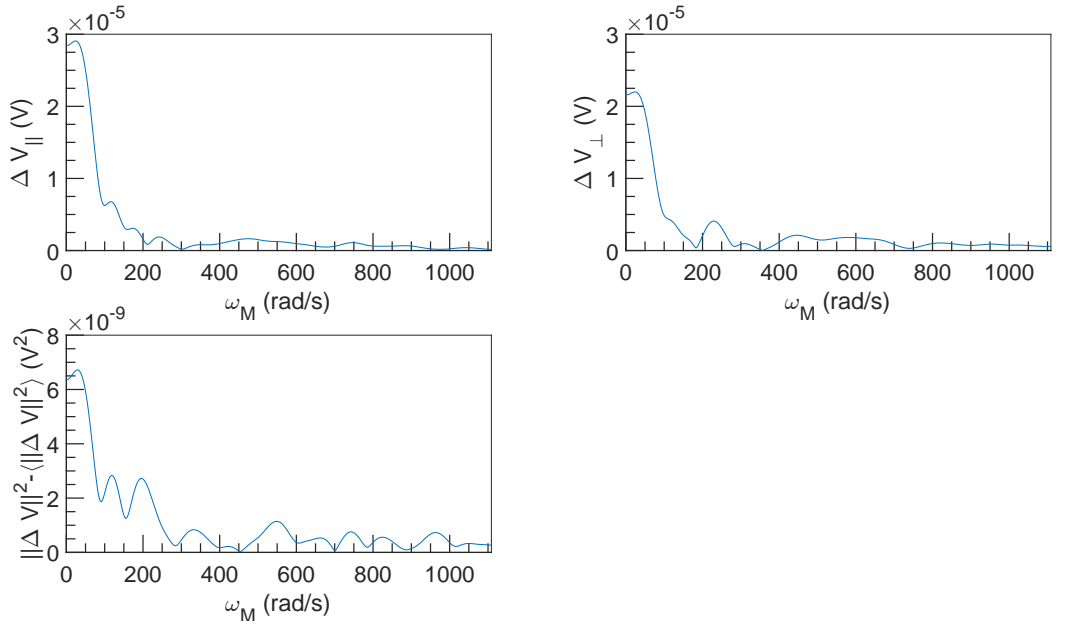


Figure 1.42: FFT spectral density of  $\Delta V$  vs  $\omega_M$  at  $U = 1 \text{ m s}^{-1}$ ,  $\omega = 7854 \text{ rad s}^{-1}$  and  $\alpha = 0\%$ .

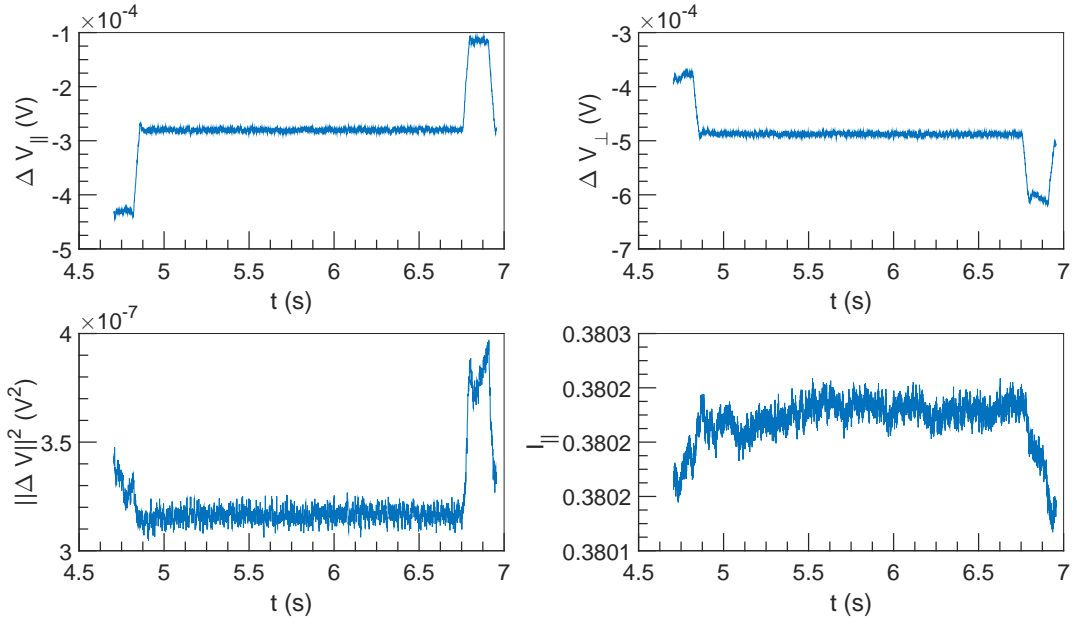


Figure 1.43:  $\Delta V$  and  $I$  vs  $t$  at  $U = 1 \text{ m s}^{-1}$ ,  $\omega = 9425 \text{ rad s}^{-1}$  and  $\alpha = 0\%$ .

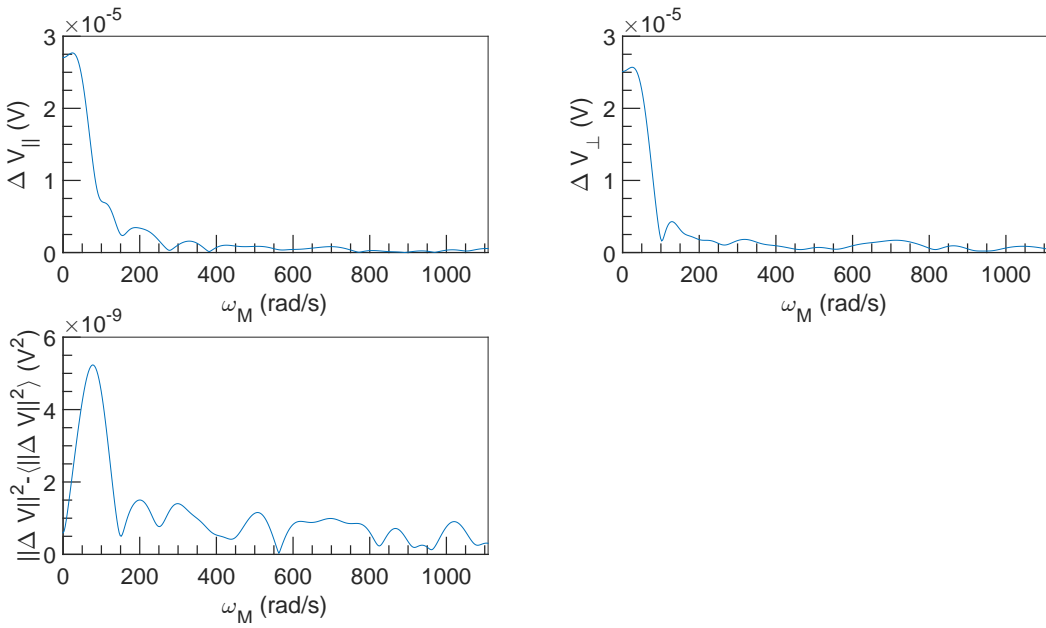


Figure 1.44: FFT spectral density of  $\Delta V$  vs  $\omega_M$  at  $U = 1 \text{ m s}^{-1}$ ,  $\omega = 9425 \text{ rad s}^{-1}$  and  $\alpha = 0\%$ .

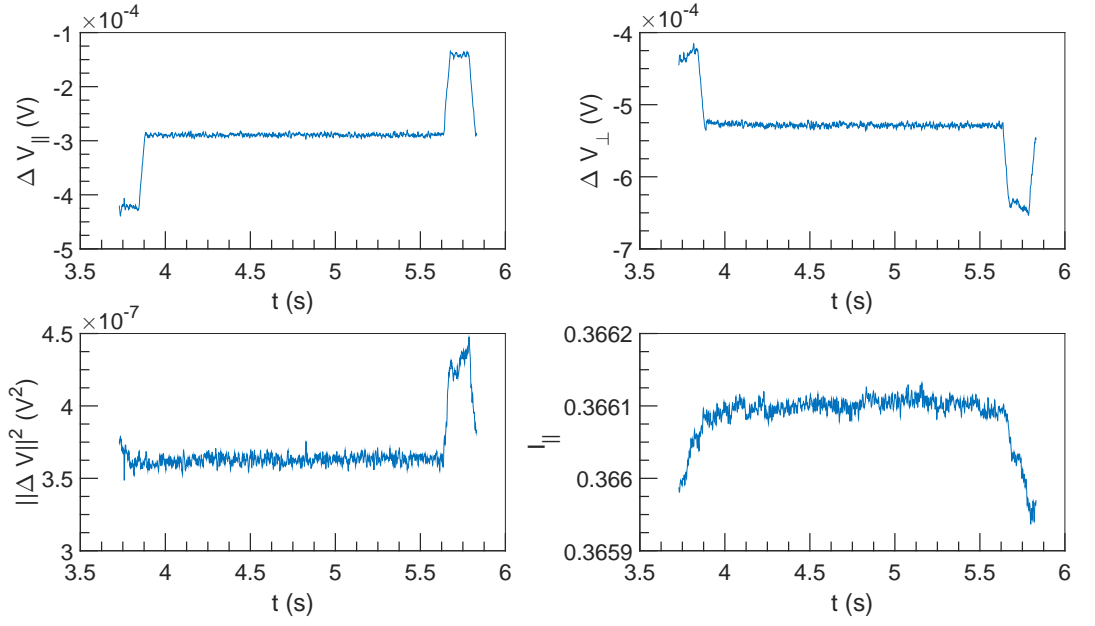


Figure 1.45:  $\Delta V$  and  $I$  vs  $t$  at  $U = 1 \text{ m s}^{-1}$ ,  $\omega = 10996 \text{ rad s}^{-1}$  and  $\alpha = 0\%$ .

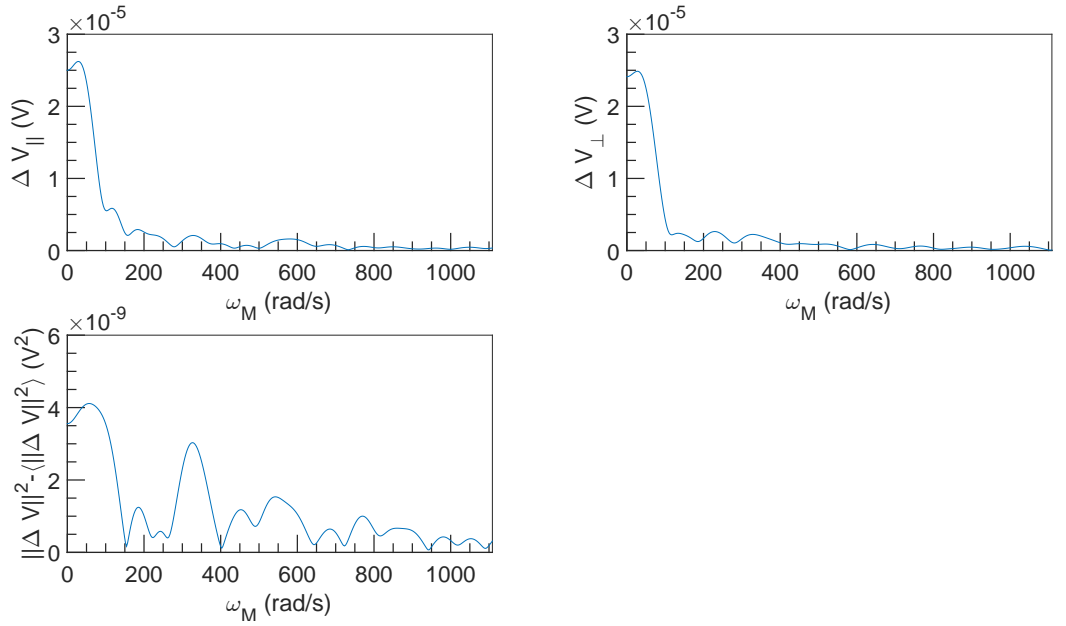


Figure 1.46: FFT spectral density of  $\Delta V$  vs  $\omega_M$  at  $U = 1 \text{ m s}^{-1}$ ,  $\omega = 10996 \text{ rad s}^{-1}$  and  $\alpha = 0\%$ .

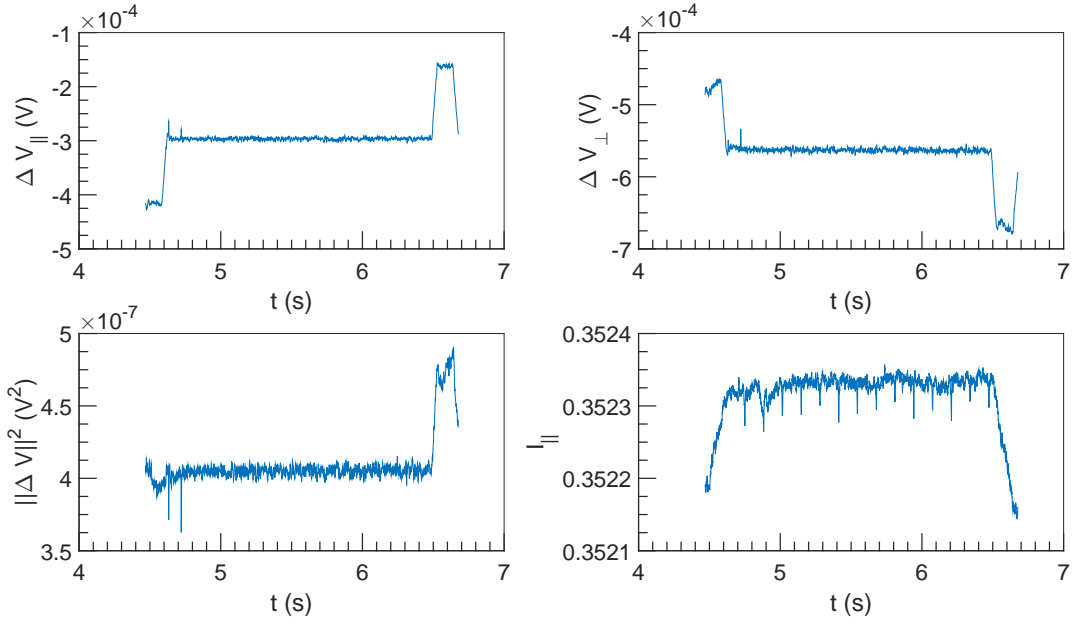


Figure 1.47:  $\Delta V$  and  $I$  vs  $t$  at  $U = 1 \text{ m s}^{-1}$ ,  $\omega = 12566 \text{ rad s}^{-1}$  and  $\alpha = 0\%$ .

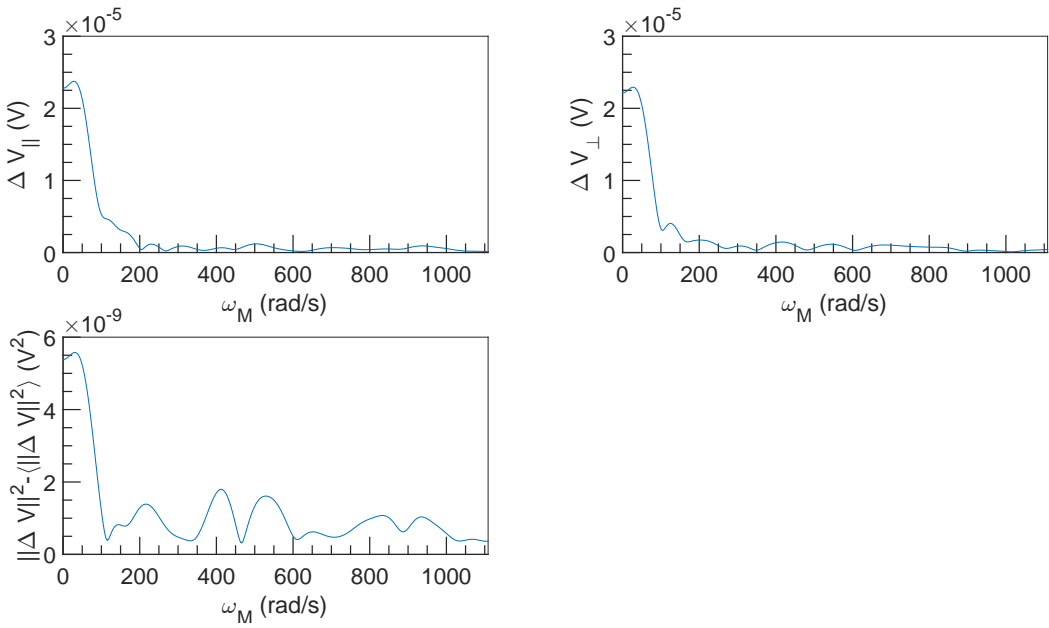


Figure 1.48: FFT spectral density of  $\Delta V$  vs  $\omega_M$  at  $U = 1 \text{ m s}^{-1}$ ,  $\omega = 12566 \text{ rad s}^{-1}$  and  $\alpha = 0\%$ .

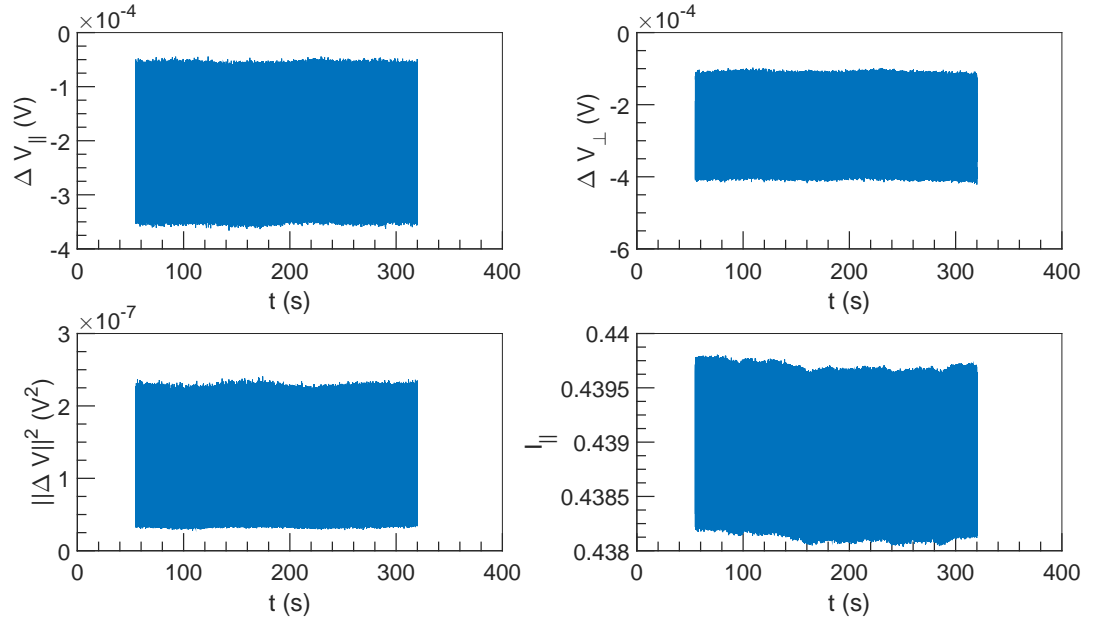


Figure 1.49:  $\Delta V$  and  $I$  vs  $t$  at  $U = 10^{-3} \text{ m s}^{-1}$ ,  $\omega = 3142 \text{ rad s}^{-1}$  and  $\alpha = 0\%$ .

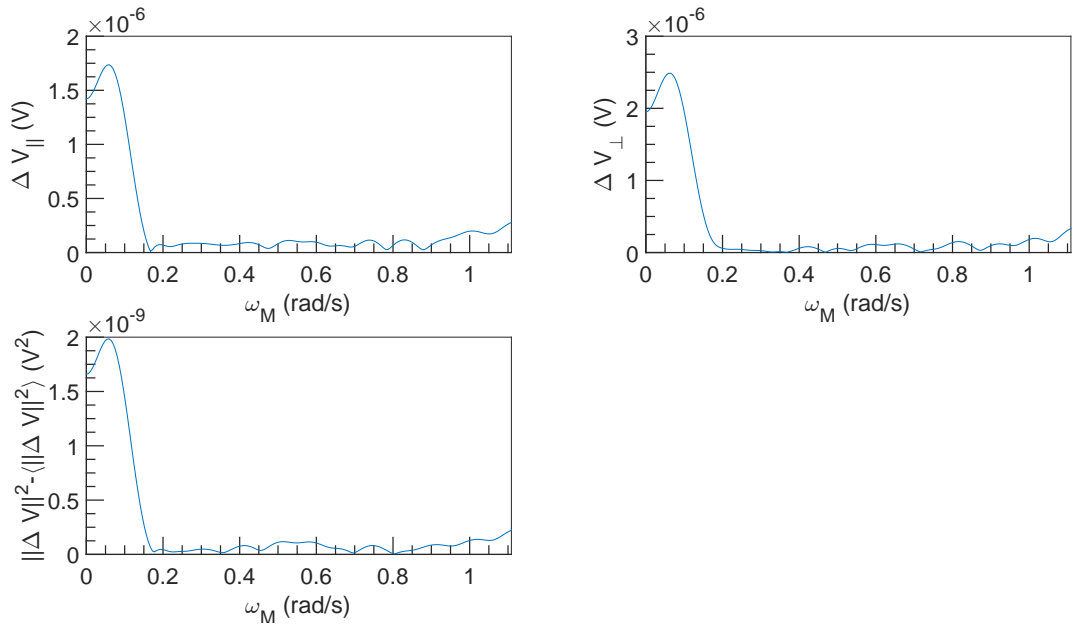


Figure 1.50: FFT spectral density of  $\Delta V$  vs  $\omega_M$  at  $U = 10^{-3} \text{ m s}^{-1}$ ,  $\omega = 3142 \text{ rad s}^{-1}$  and  $\alpha = 0\%$ .

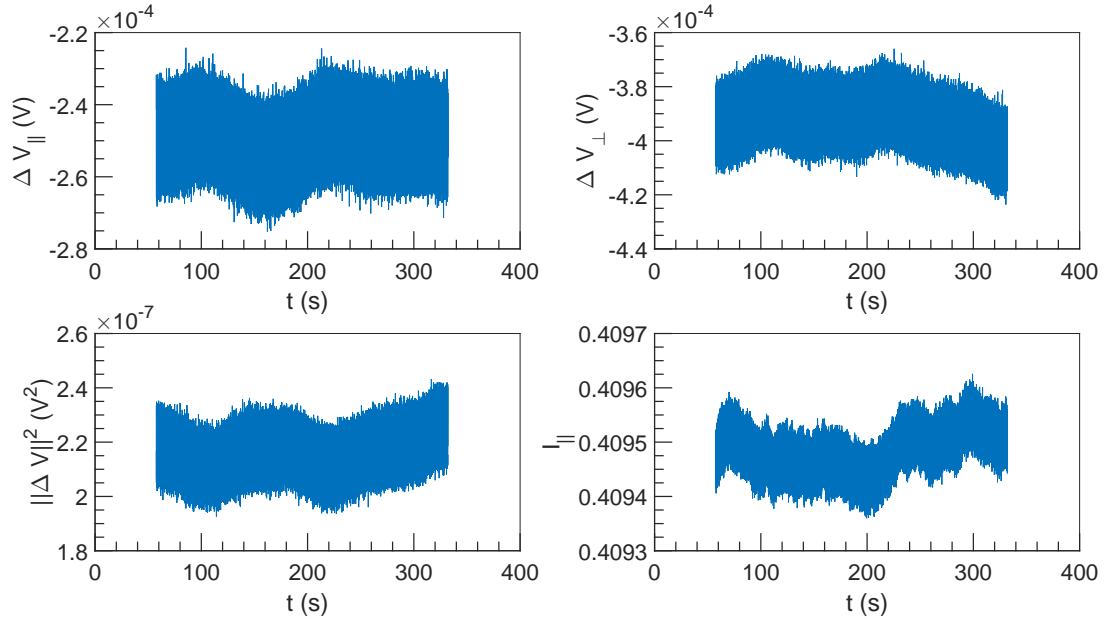


Figure 1.51:  $\Delta V$  and  $I$  vs  $t$  at  $U = 10^{-3} \text{ m s}^{-1}$ ,  $\omega = 6283 \text{ rad s}^{-1}$  and  $\alpha = 0\%$ .

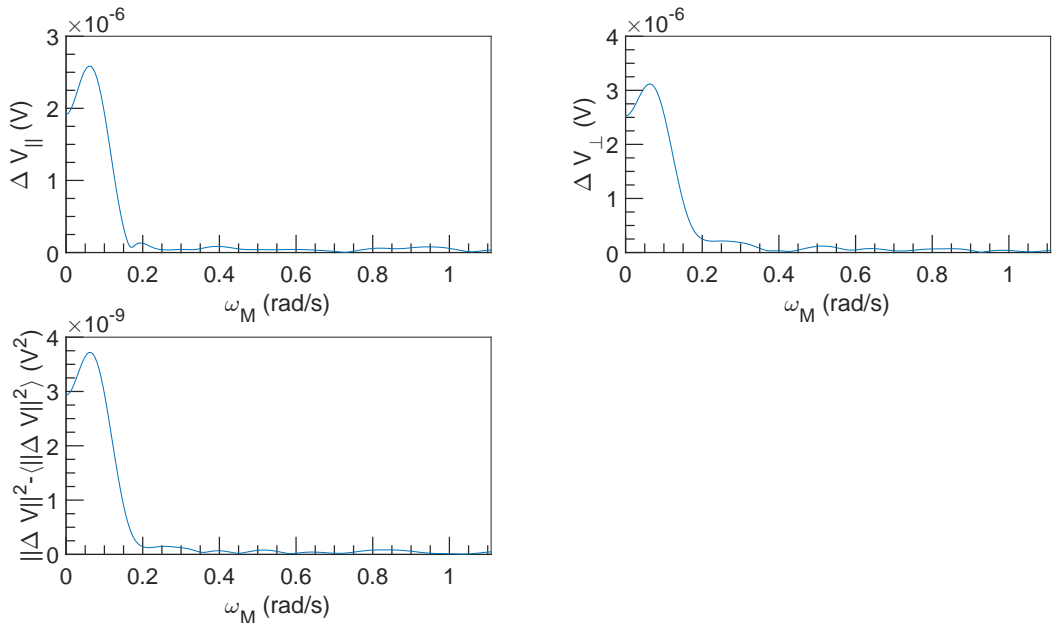


Figure 1.52: FFT spectral density of  $\Delta V$  vs  $\omega_M$  at  $U = 10^{-3} \text{ m s}^{-1}$ ,  $\omega = 6283 \text{ rad s}^{-1}$  and  $\alpha = 0\%$ .



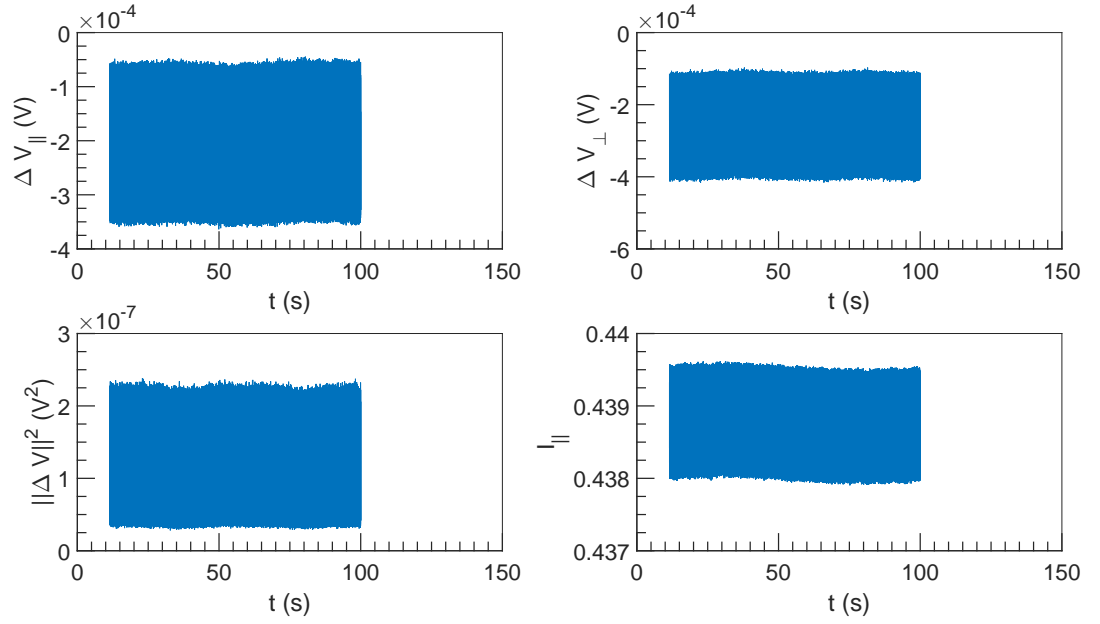


Figure 1.53:  $\Delta V$  and  $I$  vs  $t$  at  $U = 3 \times 10^{-3} \text{ m s}^{-1}$ ,  $\omega = 3142 \text{ rad s}^{-1}$  and  $\alpha = 0\%$ .

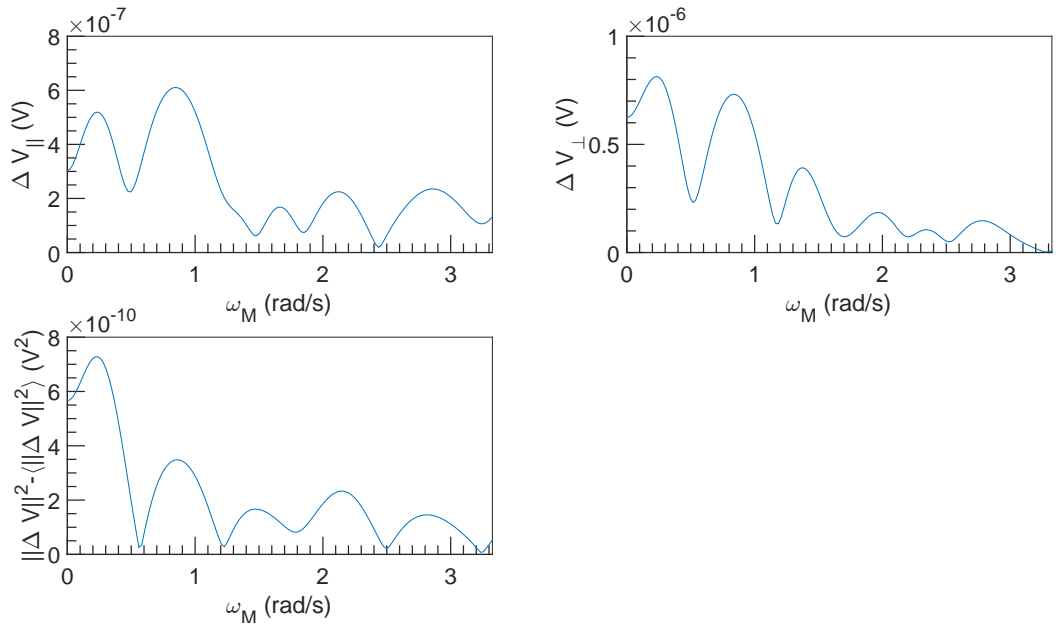


Figure 1.54: FFT spectral density of  $\Delta V$  vs  $\omega_M$  at  $U = 3 \times 10^{-3} \text{ m s}^{-1}$ ,  $\omega = 3142 \text{ rad s}^{-1}$  and  $\alpha = 0\%$ .

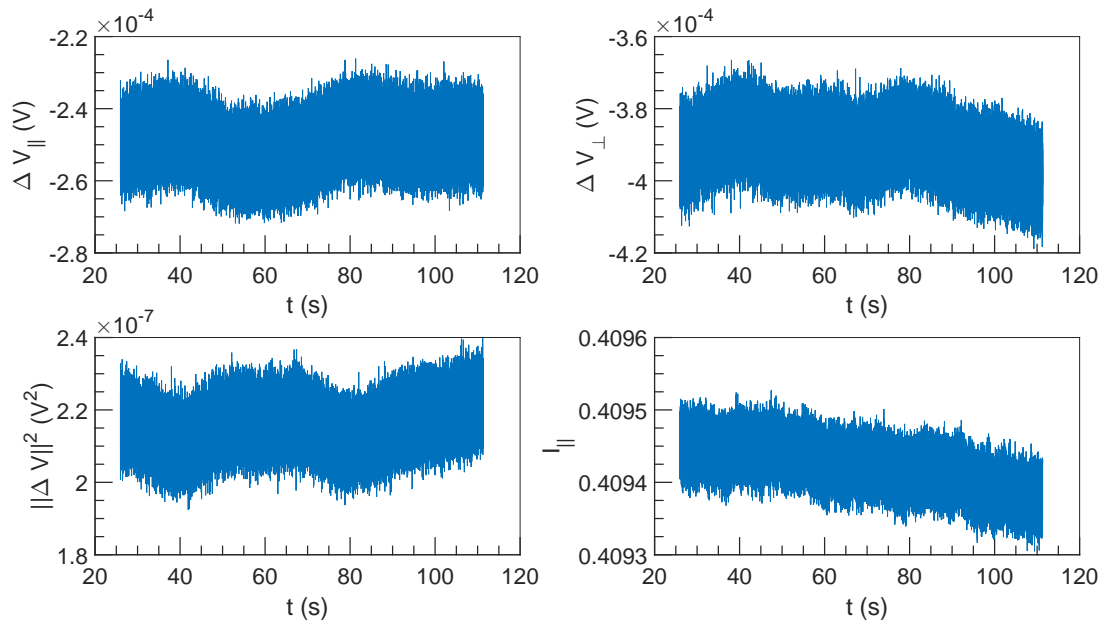


Figure 1.55:  $\Delta V$  and  $I$  vs  $t$  at  $U = 3 \times 10^{-3} \text{ m s}^{-1}$ ,  $\omega = 6283 \text{ rad s}^{-1}$  and  $\alpha = 0\%$ .

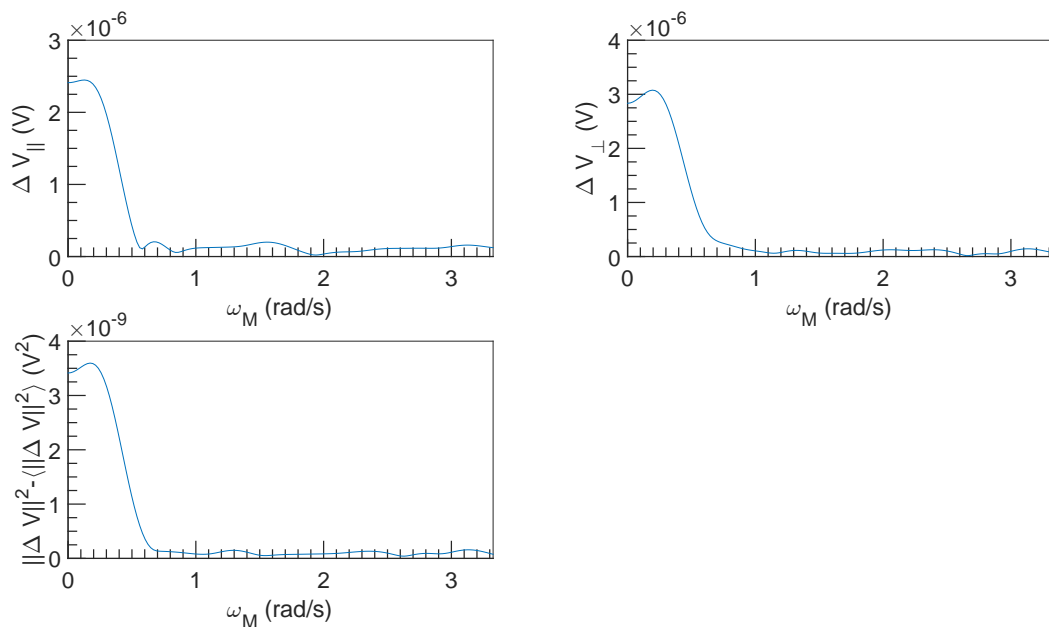


Figure 1.56: FFT spectral density of  $\Delta V$  vs  $\omega_M$  at  $U = 3 \times 10^{-3} \text{ m s}^{-1}$ ,  $\omega = 6283 \text{ rad s}^{-1}$  and  $\alpha = 0\%$ .

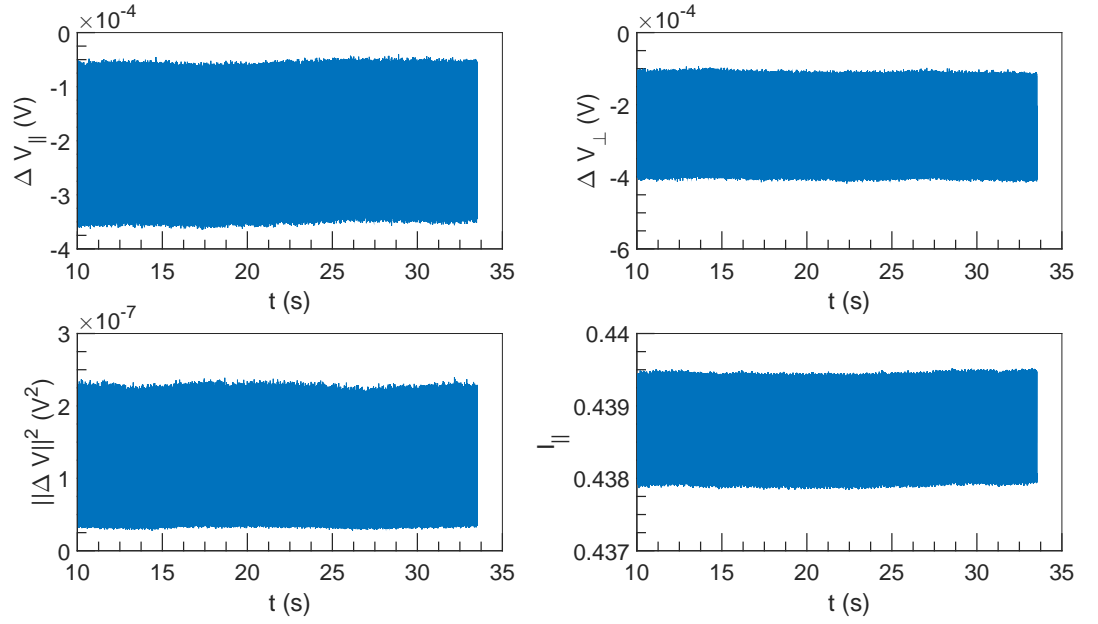


Figure 1.57:  $\Delta V$  and  $I$  vs  $t$  at  $U = 10^{-2} \text{ m s}^{-1}$ ,  $\omega = 3142 \text{ rad s}^{-1}$  and  $\alpha = 0\%$ .

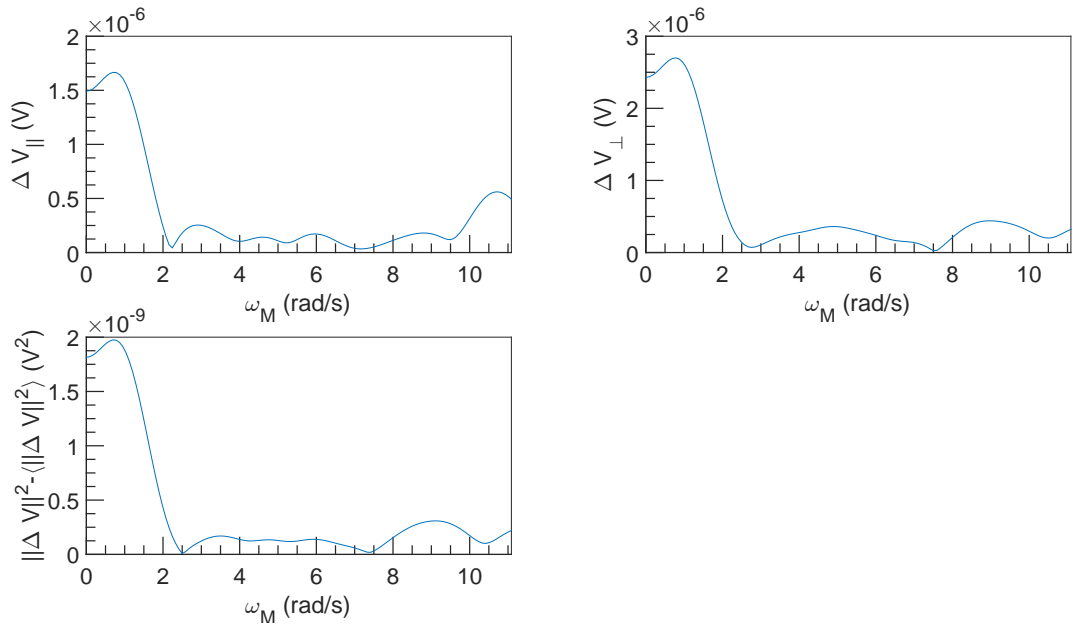


Figure 1.58: FFT spectral density of  $\Delta V$  vs  $\omega_M$  at  $U = 10^{-2} \text{ m s}^{-1}$ ,  $\omega = 3142 \text{ rad s}^{-1}$  and  $\alpha = 0\%$ .

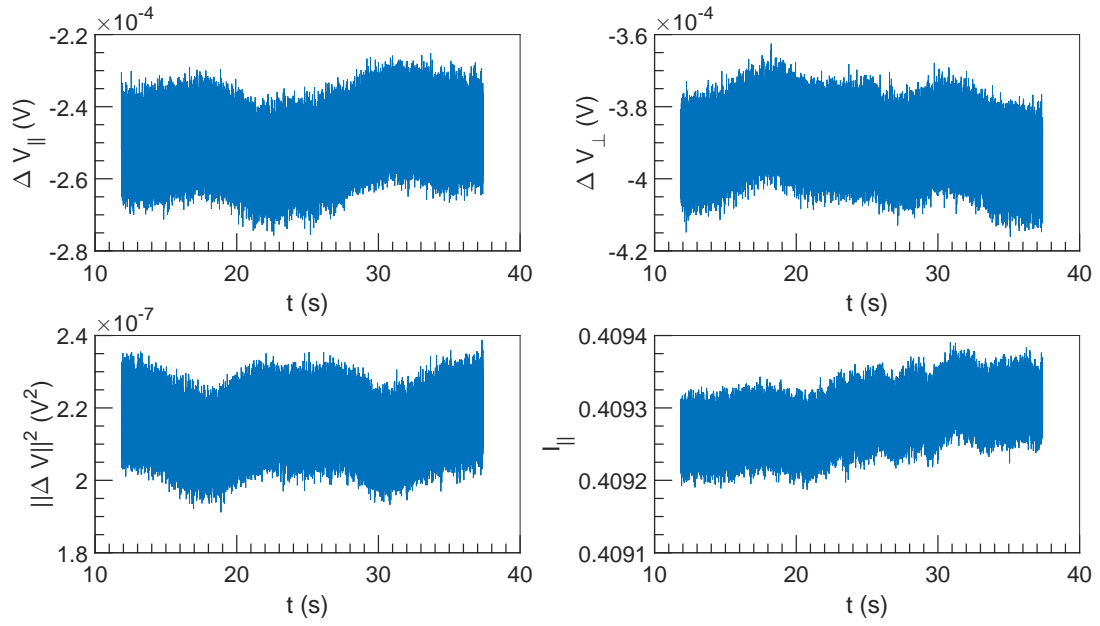


Figure 1.59:  $\Delta V$  and  $I$  vs  $t$  at  $U = 10^{-2} \text{ m s}^{-1}$ ,  $\omega = 6283 \text{ rad s}^{-1}$  and  $\alpha = 0\%$ .

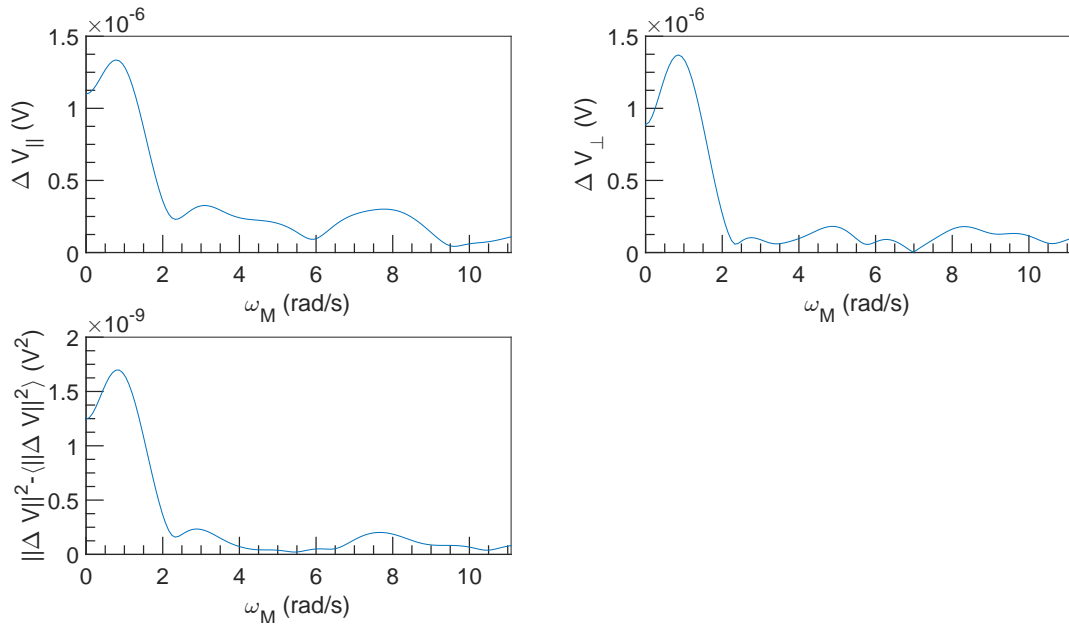


Figure 1.60: FFT spectral density of  $\Delta V$  vs  $\omega_M$  at  $U = 10^{-2} \text{ m s}^{-1}$ ,  $\omega = 6283 \text{ rad s}^{-1}$  and  $\alpha = 0\%$ .

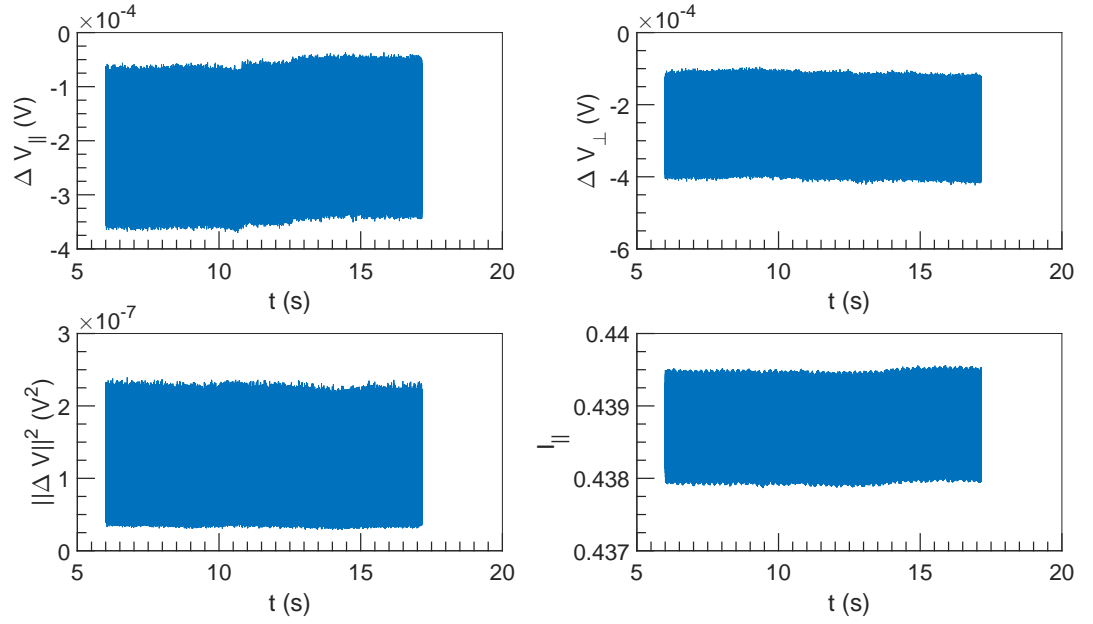


Figure 1.61:  $\Delta V$  and  $I$  vs  $t$  at  $U = 3 \times 10^{-2} \text{ m s}^{-1}$ ,  $\omega = 3142 \text{ rad s}^{-1}$  and  $\alpha = 0\%$ .

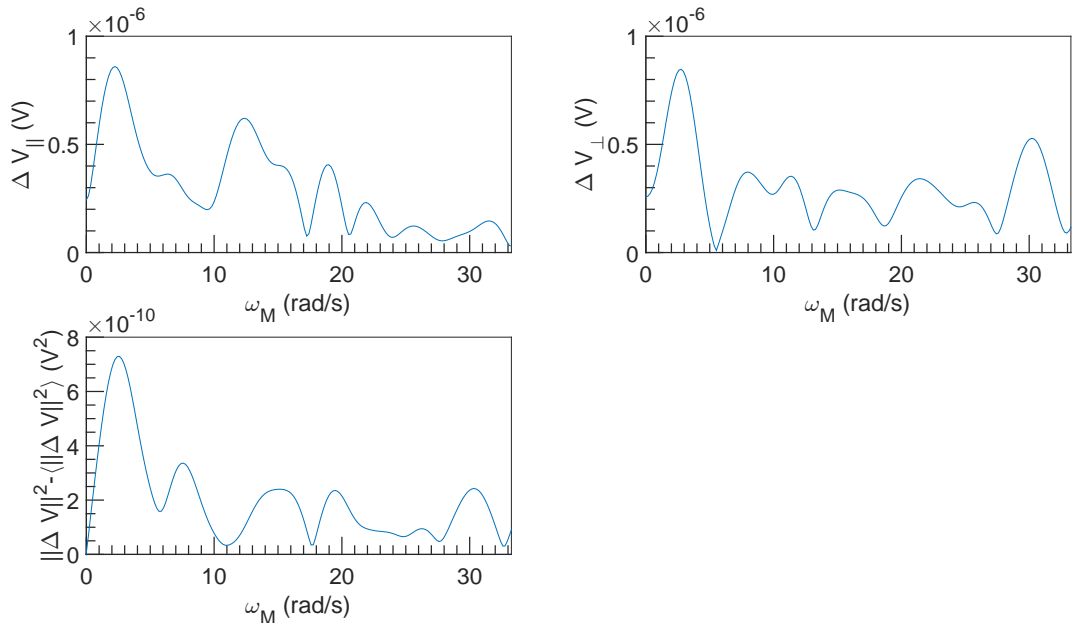


Figure 1.62: FFT spectral density of  $\Delta V$  vs  $\omega_M$  at  $U = 3 \times 10^{-2} \text{ m s}^{-1}$ ,  $\omega = 3142 \text{ rad s}^{-1}$  and  $\alpha = 0\%$ .

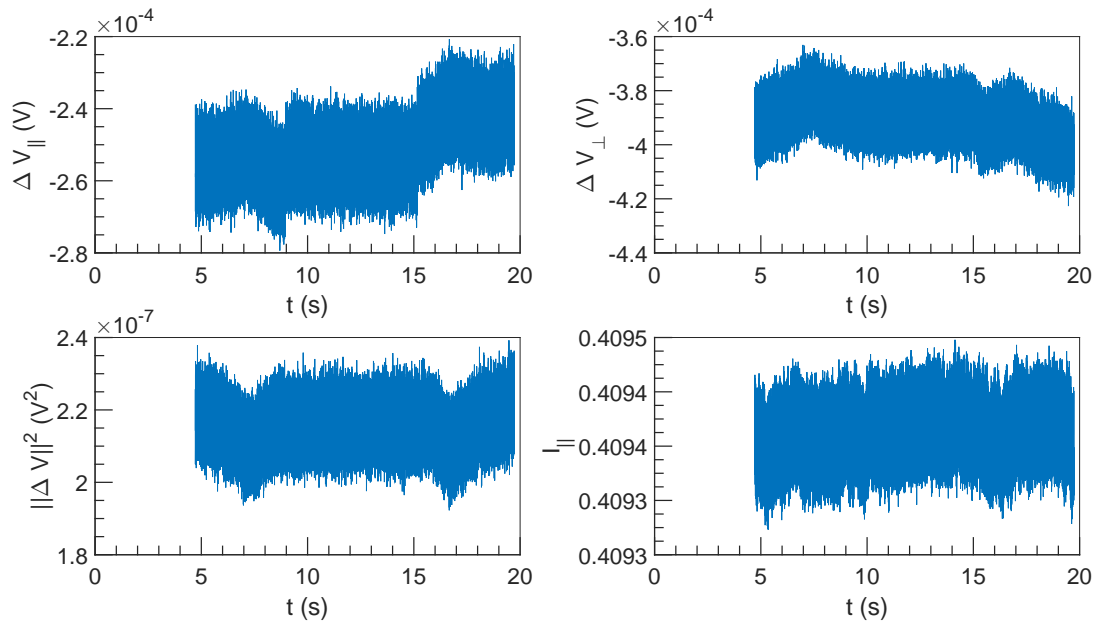


Figure 1.63:  $\Delta V$  and  $I$  vs  $t$  at  $U = 3 \times 10^{-2} \text{ m s}^{-1}$ ,  $\omega = 6283 \text{ rad s}^{-1}$  and  $\alpha = 0\%$ .

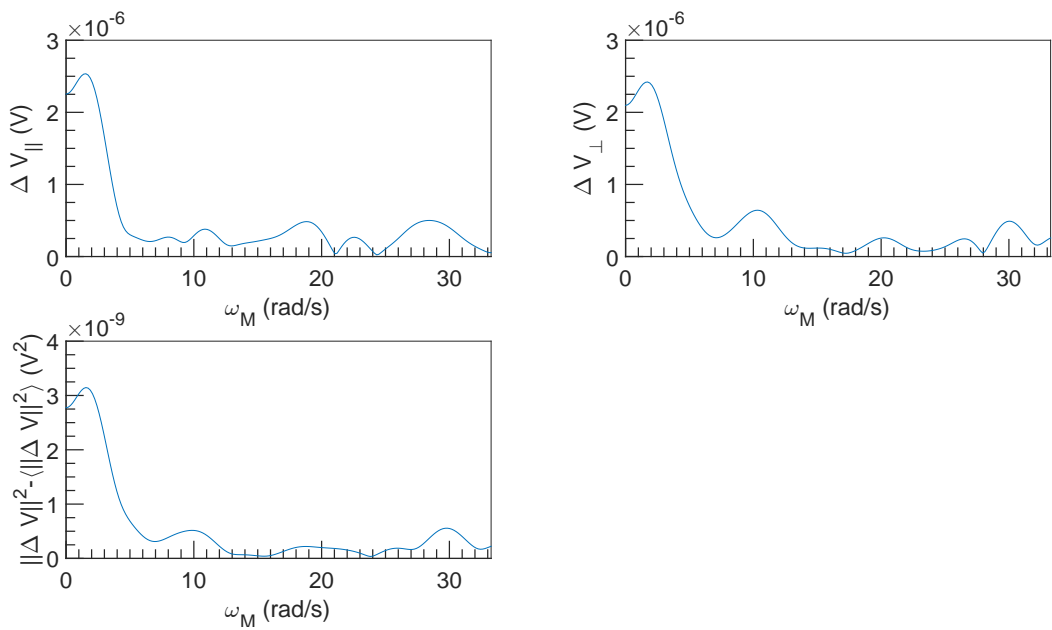


Figure 1.64: FFT spectral density of  $\Delta V$  vs  $\omega_M$  at  $U = 3 \times 10^{-2} \text{ m s}^{-1}$ ,  $\omega = 6283 \text{ rad s}^{-1}$  and  $\alpha = 0\%$ .

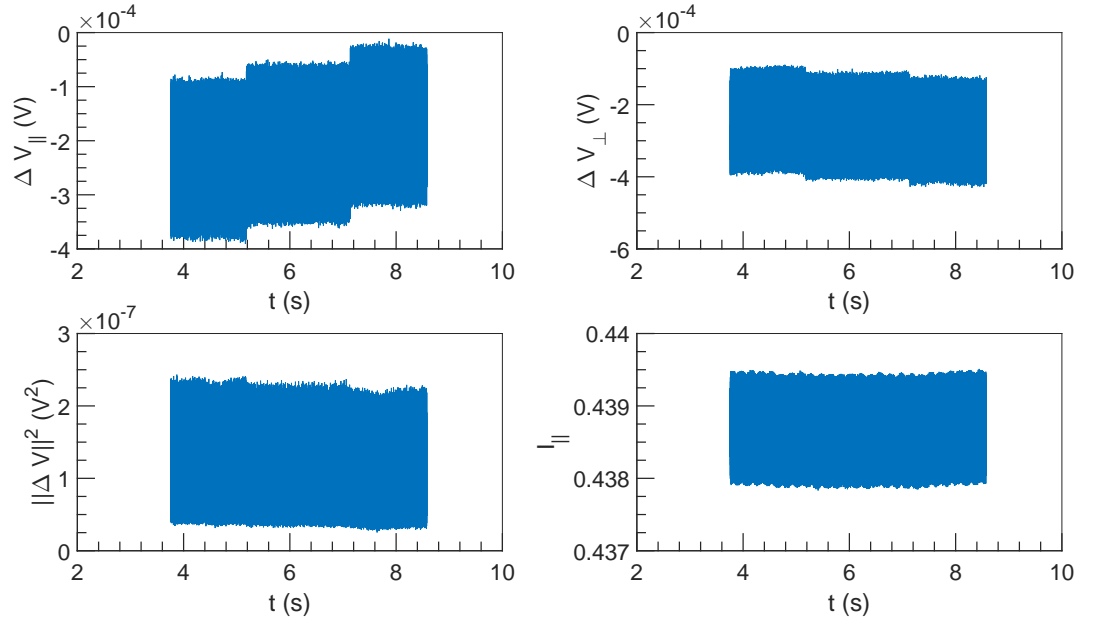


Figure 1.65:  $\Delta V$  and  $I$  vs  $t$  at  $U = 0.1 \text{ m s}^{-1}$ ,  $\omega = 3142 \text{ rad s}^{-1}$  and  $\alpha = 0\%$ .

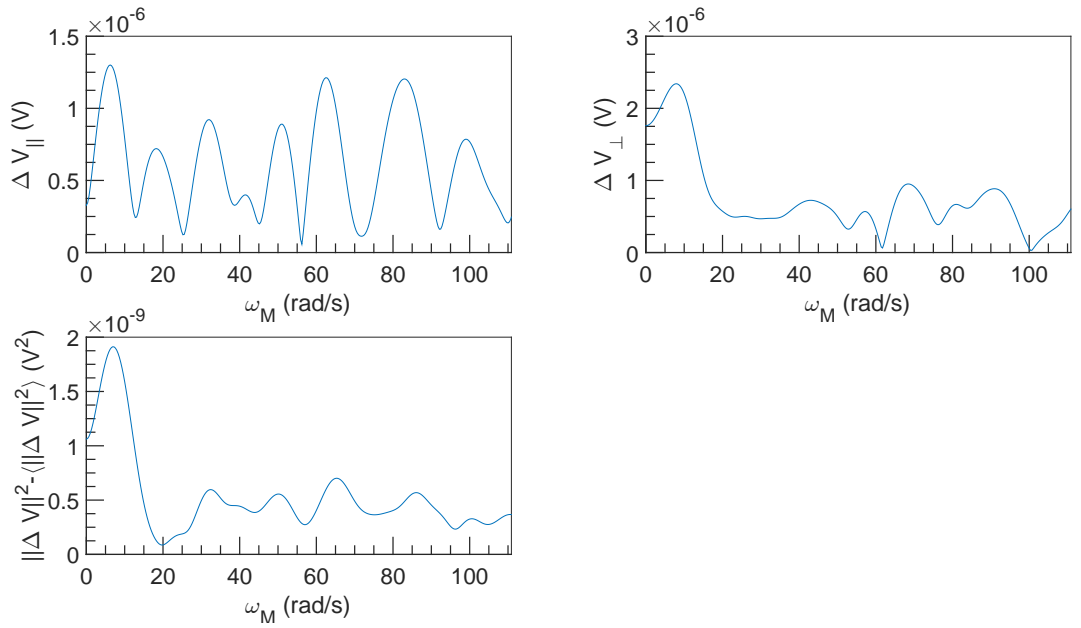


Figure 1.66: FFT spectral density of  $\Delta V$  vs  $\omega_M$  at  $U = 0.1 \text{ m s}^{-1}$ ,  $\omega = 3142 \text{ rad s}^{-1}$  and  $\alpha = 0\%$ .

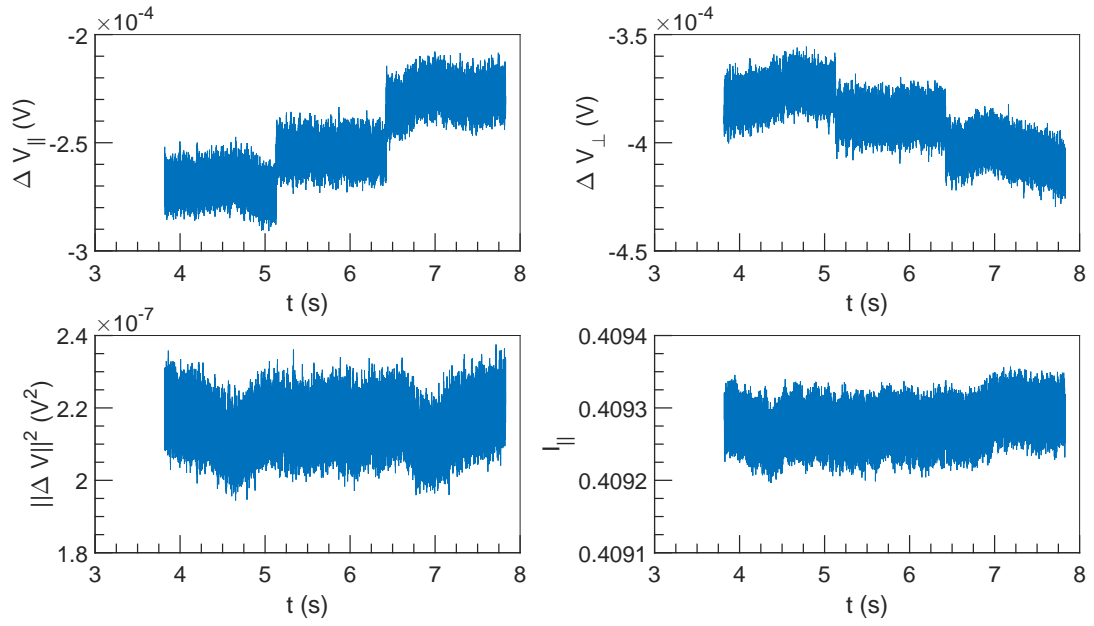


Figure 1.67:  $\Delta V$  and  $I$  vs  $t$  at  $U = 0.1 \text{ m s}^{-1}$ ,  $\omega = 6283 \text{ rad s}^{-1}$  and  $\alpha = 0\%$ .

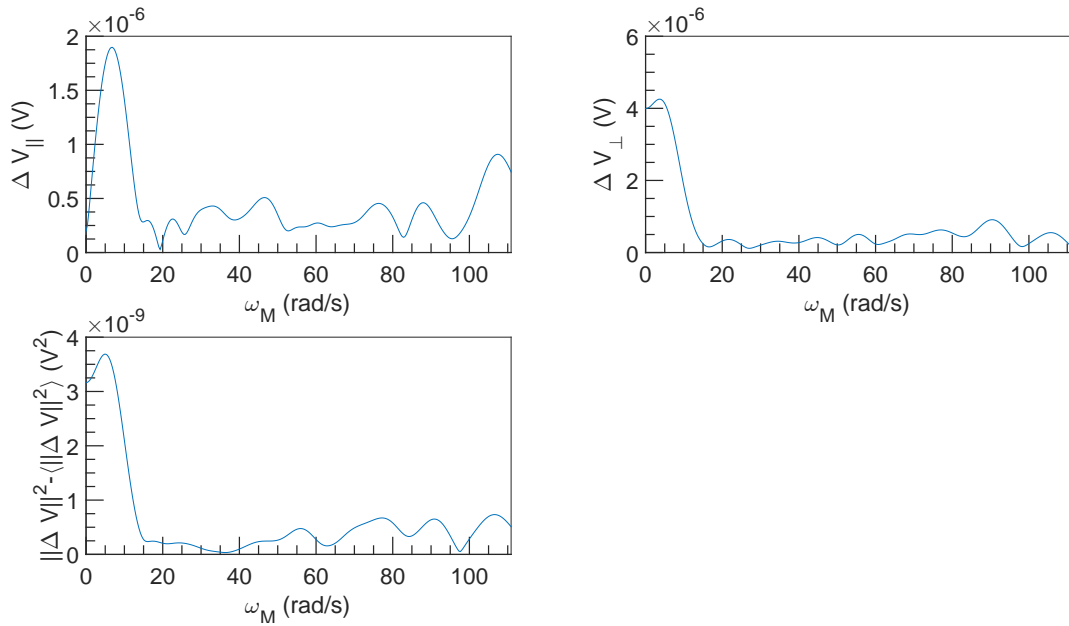


Figure 1.68: FFT spectral density of  $\Delta V$  vs  $\omega_M$  at  $U = 0.1 \text{ m s}^{-1}$ ,  $\omega = 6283 \text{ rad s}^{-1}$  and  $\alpha = 0\%$ .



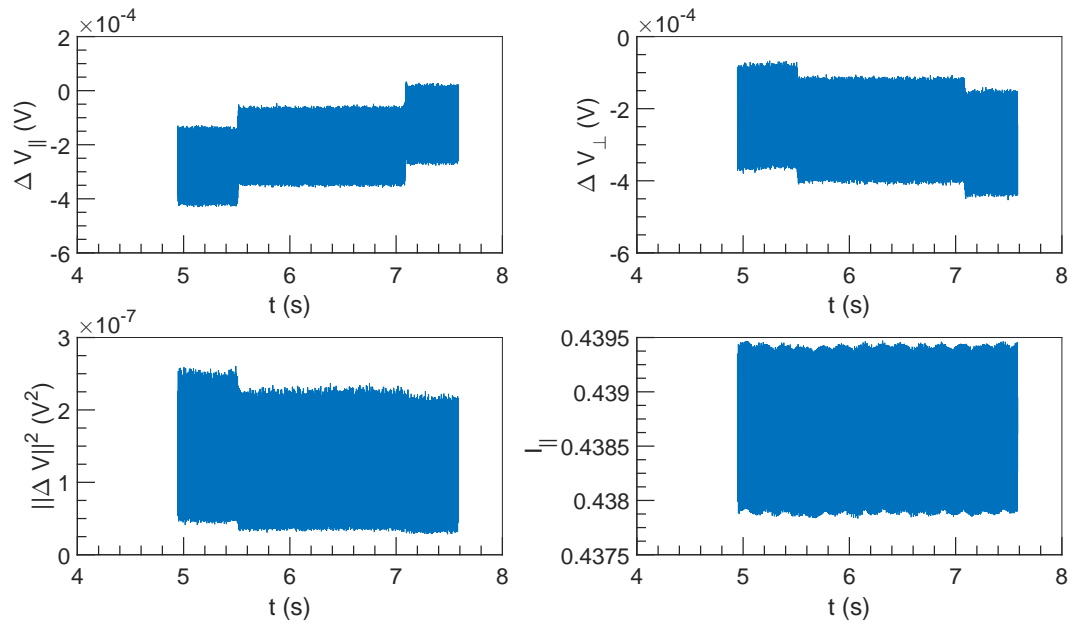


Figure 1.69:  $\Delta V$  and  $I$  vs  $t$  at  $U = 0.25 \text{ ms}^{-1}$ ,  $\omega = 3142 \text{ rad s}^{-1}$  and  $\alpha = 0\%$ .

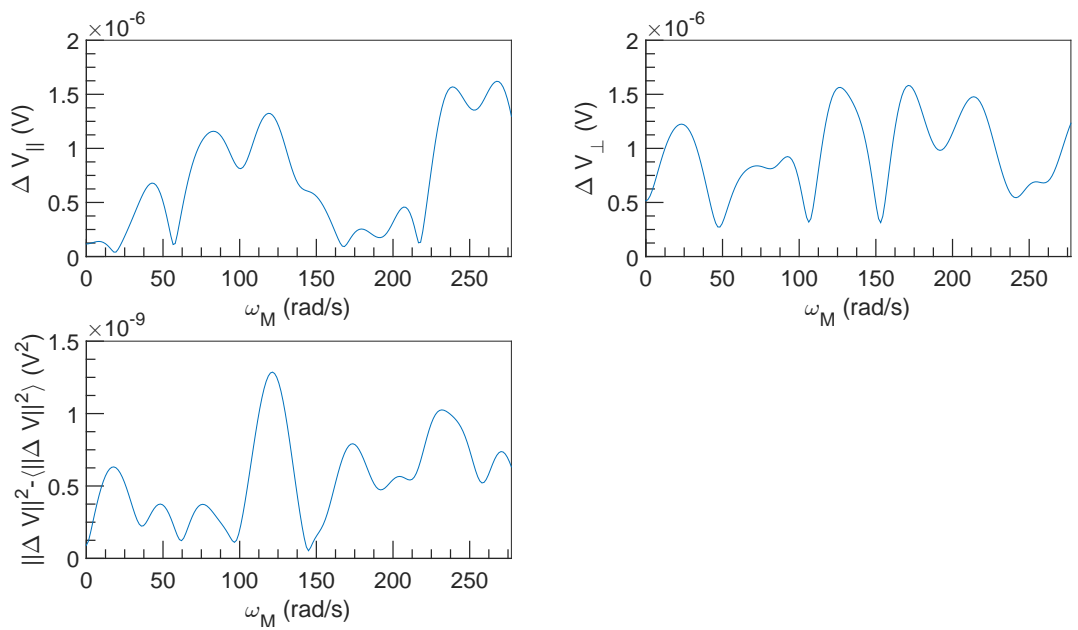


Figure 1.70: FFT spectral density of  $\Delta V$  vs  $\omega_M$  at  $U = 0.25 \text{ ms}^{-1}$ ,  $\omega = 3142 \text{ rad s}^{-1}$  and  $\alpha = 0\%$ .

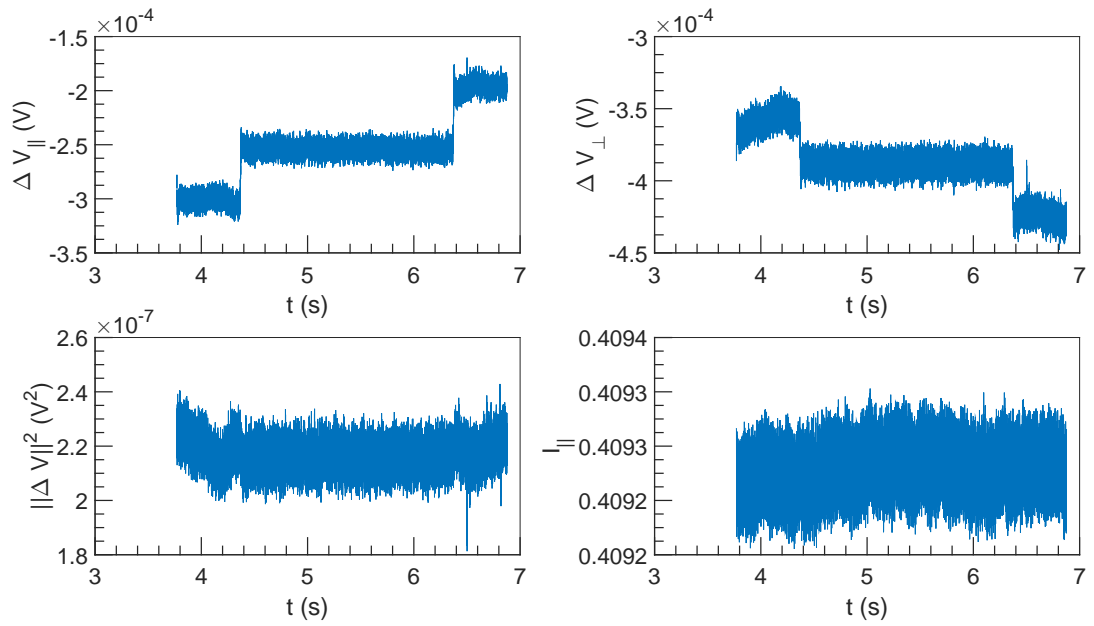


Figure 1.71:  $\Delta V$  and  $I$  vs  $t$  at  $U = 0.25 \text{ ms}^{-1}$ ,  $\omega = 6283 \text{ rad s}^{-1}$  and  $\alpha = 0\%$ .

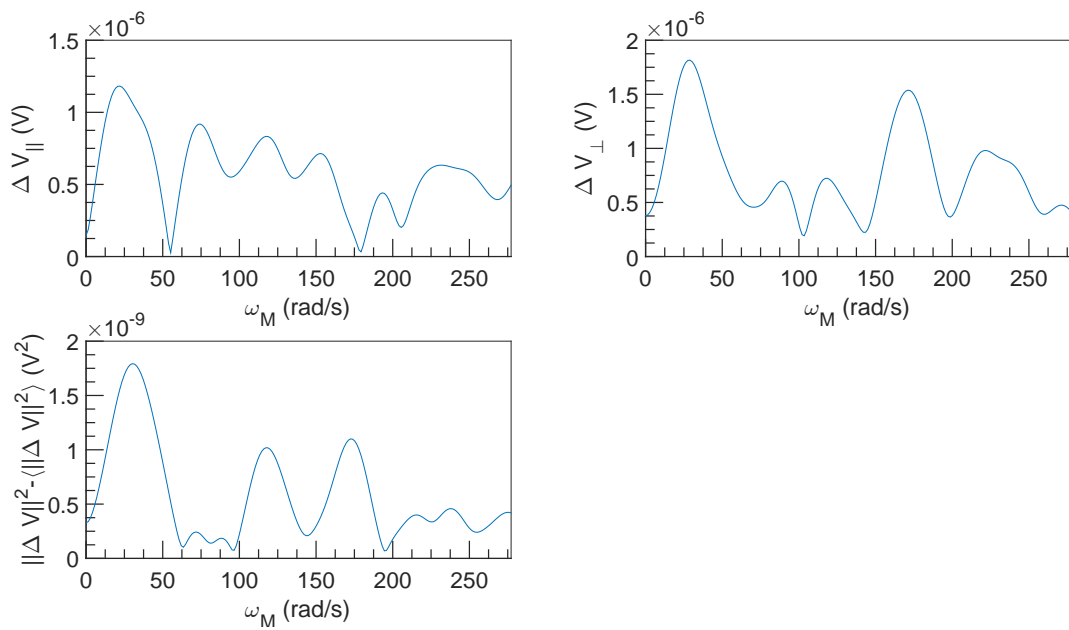


Figure 1.72: FFT spectral density of  $\Delta V$  vs  $\omega_M$  at  $U = 0.25 \text{ ms}^{-1}$ ,  $\omega = 6283 \text{ rad s}^{-1}$  and  $\alpha = 0\%$ .

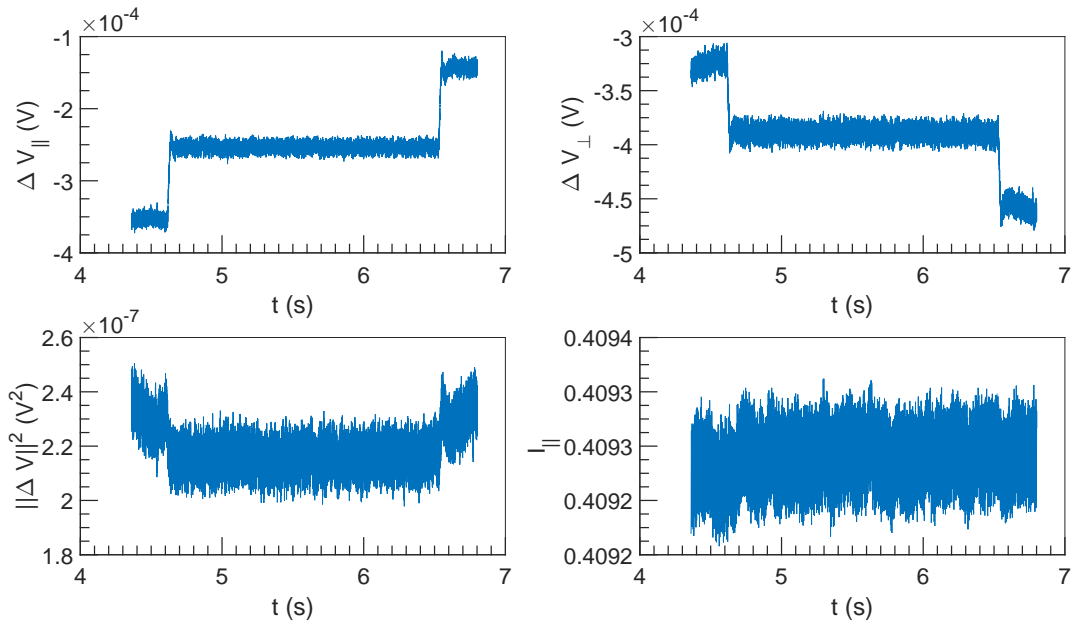


Figure 1.73:  $\Delta V$  and  $I$  vs  $t$  at  $U = 0.5 \text{ m s}^{-1}$ ,  $\omega = 6283 \text{ rad s}^{-1}$  and  $\alpha = 0\%$ .

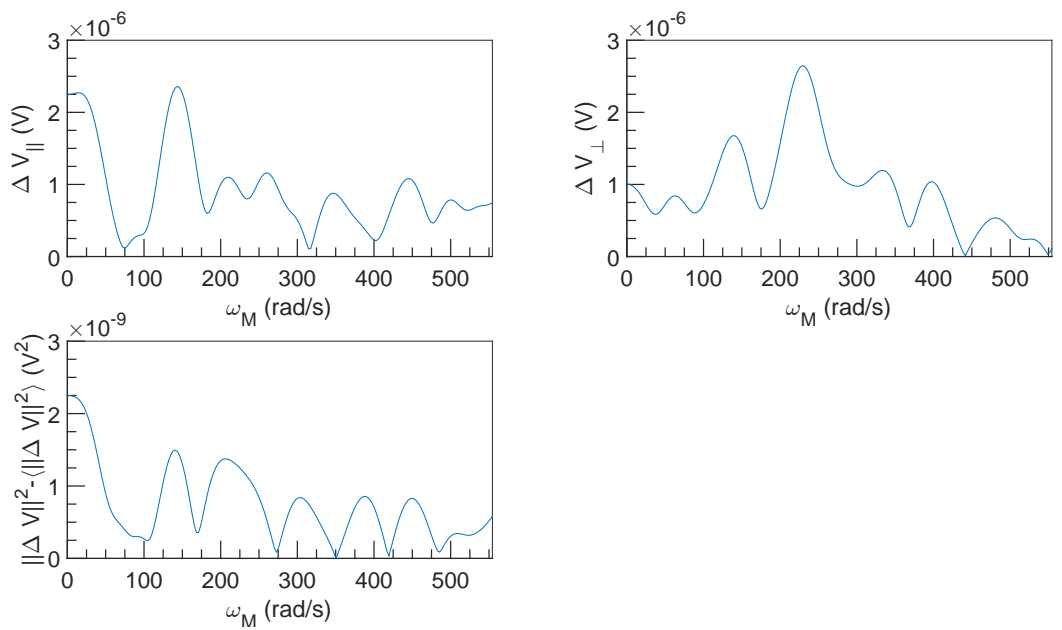


Figure 1.74: FFT spectral density of  $\Delta V$  vs  $\omega_M$  at  $U = 0.5 \text{ m s}^{-1}$ ,  $\omega = 6283 \text{ rad s}^{-1}$  and  $\alpha = 0\%$ .

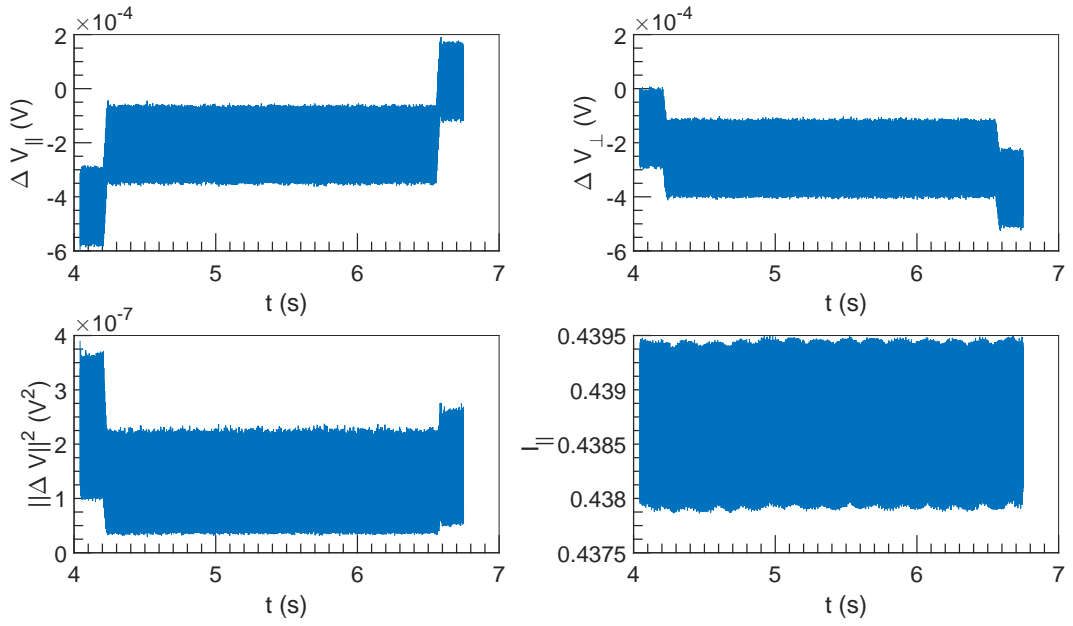


Figure 1.75:  $\Delta V$  and  $I$  vs  $t$  at  $U = 0.75 \text{ ms}^{-1}$ ,  $\omega = 3142 \text{ rad s}^{-1}$  and  $\alpha = 0\%$ .

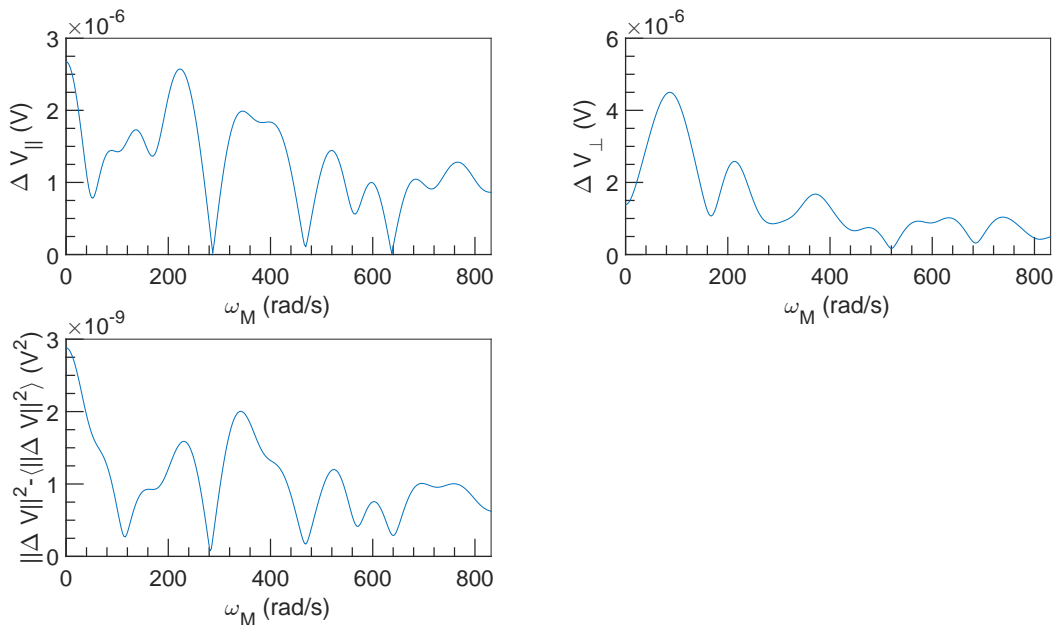


Figure 1.76: FFT spectral density of  $\Delta V$  vs  $\omega_M$  at  $U = 0.75 \text{ ms}^{-1}$ ,  $\omega = 3142 \text{ rad s}^{-1}$  and  $\alpha = 0\%$ .

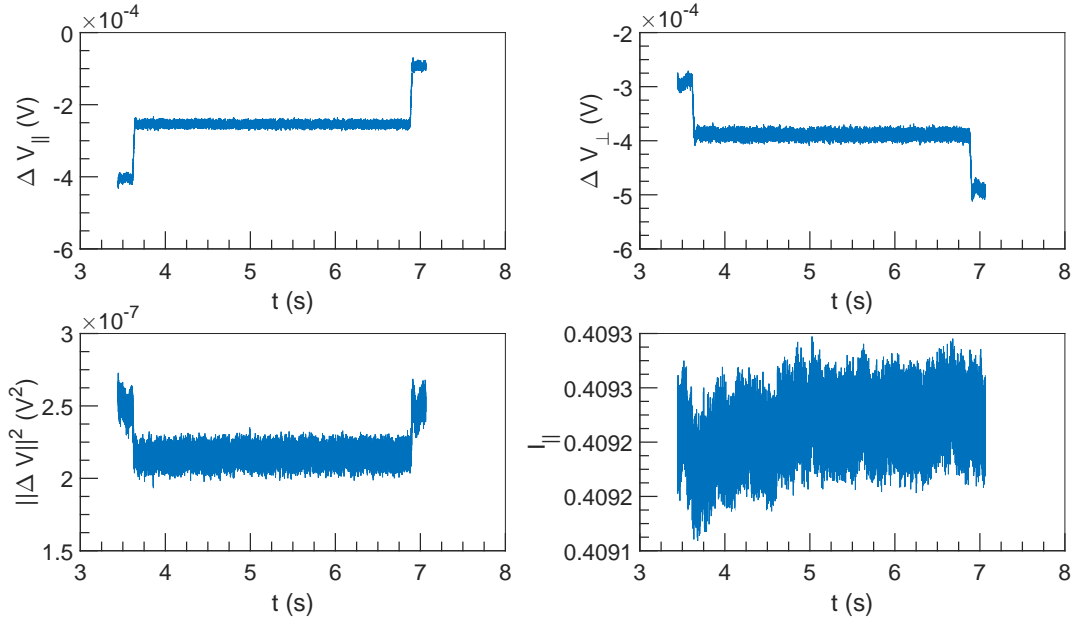


Figure 1.77:  $\Delta V$  and  $I$  vs  $t$  at  $U = 0.75 \text{ ms}^{-1}$ ,  $\omega = 6283 \text{ rad s}^{-1}$  and  $\alpha = 0\%$ .

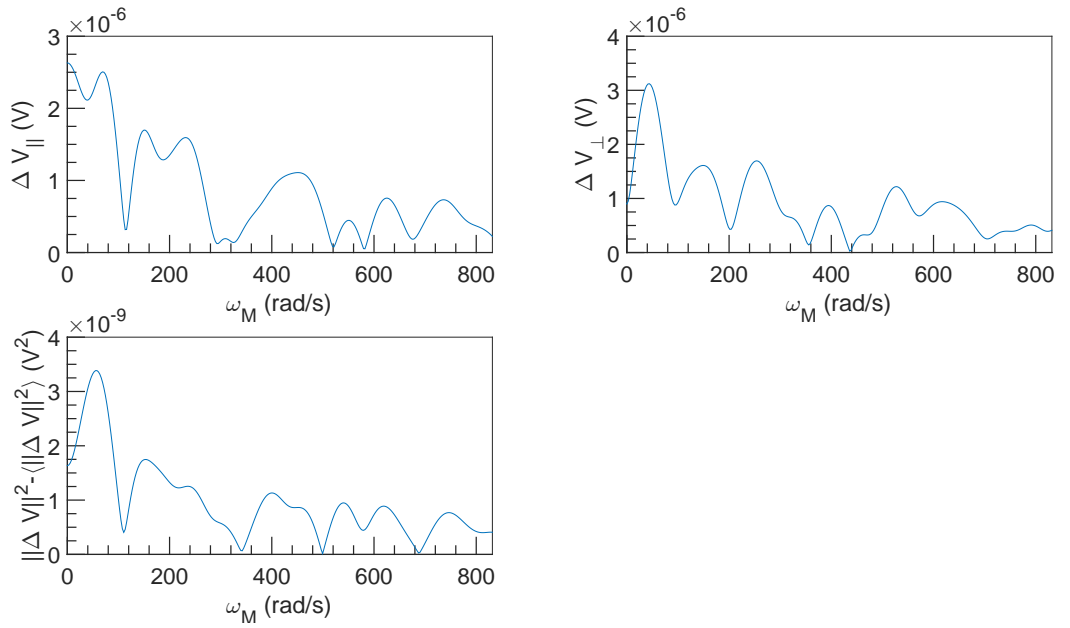


Figure 1.78: FFT spectral density of  $\Delta V$  vs  $\omega_M$  at  $U = 0.75 \text{ ms}^{-1}$ ,  $\omega = 6283 \text{ rad s}^{-1}$  and  $\alpha = 0\%$ .

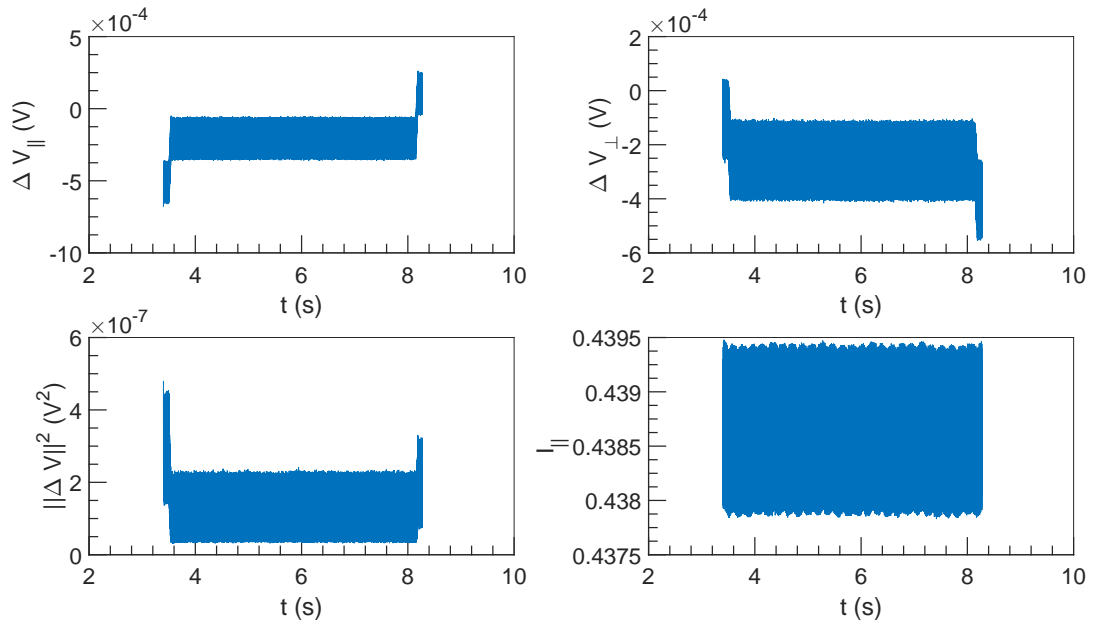


Figure 1.79:  $\Delta V$  and  $I$  vs  $t$  at  $U = 1 \text{ m s}^{-1}$ ,  $\omega = 3142 \text{ rad s}^{-1}$  and  $\alpha = 0\%$ .

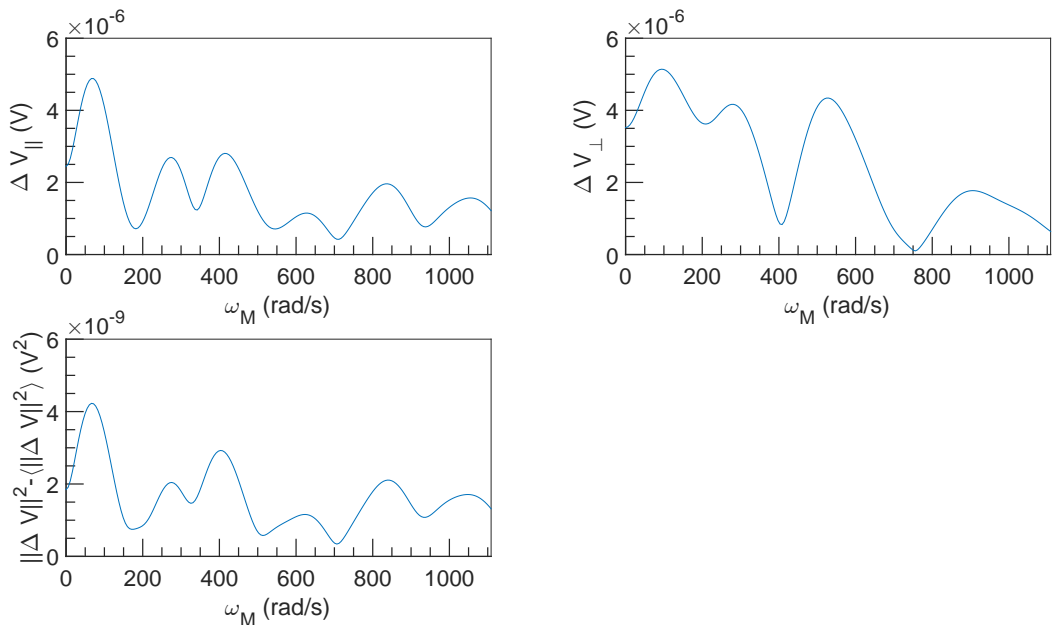


Figure 1.80: FFT spectral density of  $\Delta V$  vs  $\omega_M$  at  $U = 1 \text{ m s}^{-1}$ ,  $\omega = 3142 \text{ rad s}^{-1}$  and  $\alpha = 0\%$ .

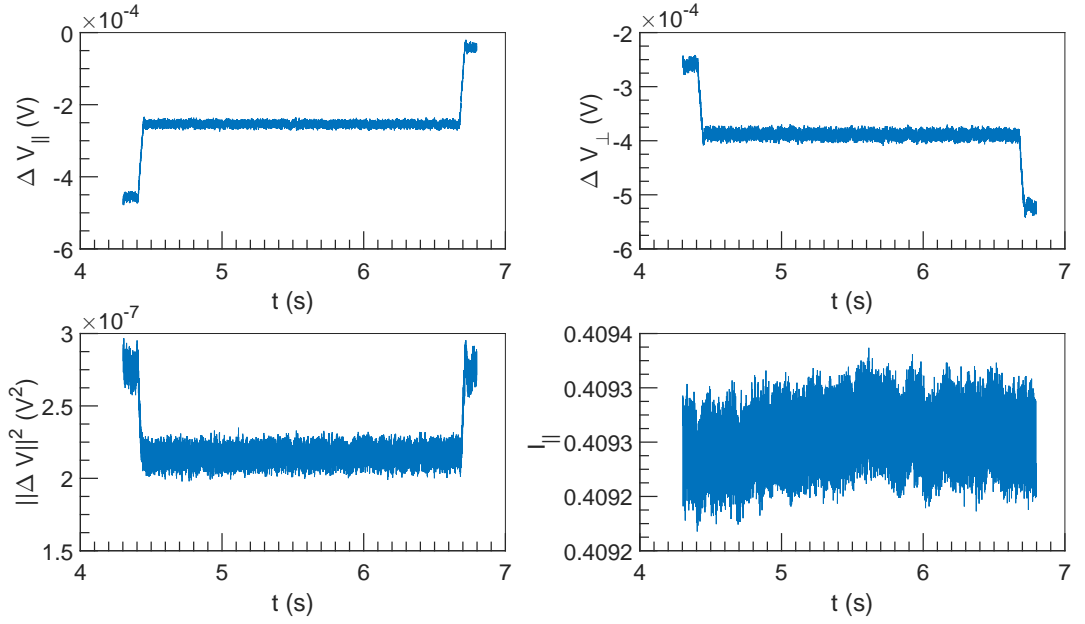


Figure 1.81:  $\Delta V$  and  $I$  vs  $t$  at  $U = 1 \text{ m s}^{-1}$ ,  $\omega = 6283 \text{ rad s}^{-1}$  and  $\alpha = 0\%$ .

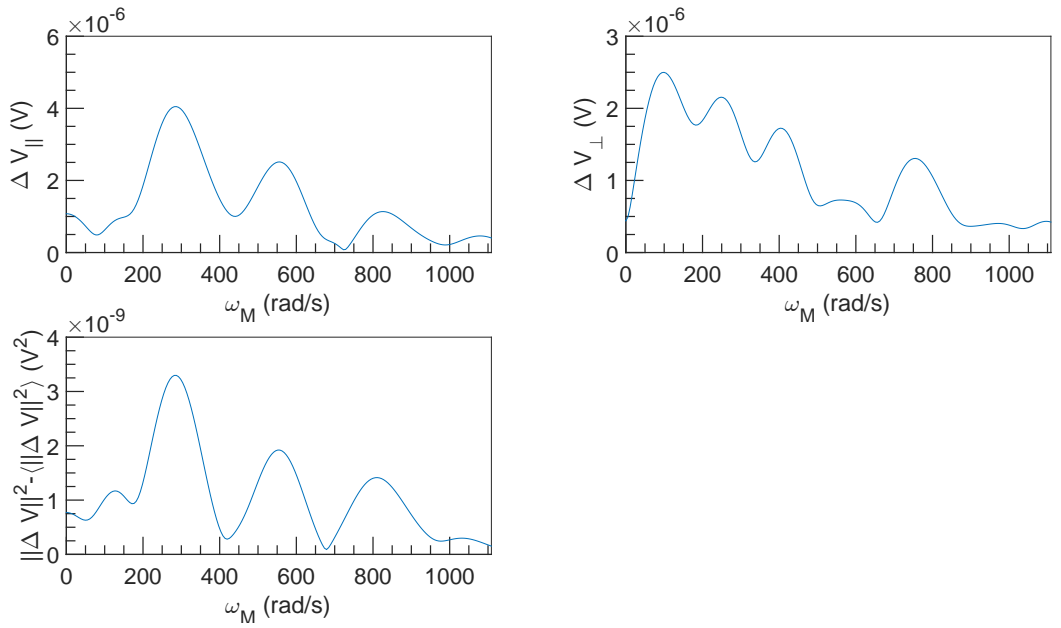


Figure 1.82: FFT spectral density of  $\Delta V$  vs  $\omega_M$  at  $U = 1 \text{ m s}^{-1}$ ,  $\omega = 6283 \text{ rad s}^{-1}$  and  $\alpha = 0\%$ .

## Chapter 2

**For**  $\alpha = 0.3\%$



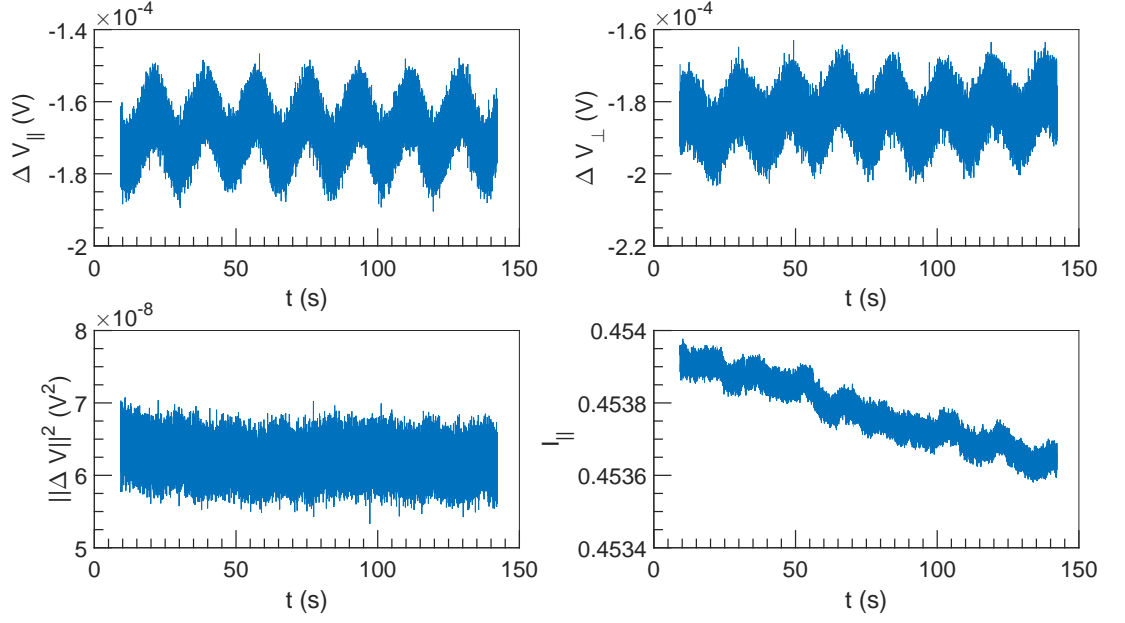


Figure 2.1:  $\Delta V$  and  $I$  vs  $t$  at  $U = 10^{-3} \text{ m s}^{-1}$ ,  $\omega = 1571 \text{ rad s}^{-1}$  and  $\alpha = 0.3\%$ .

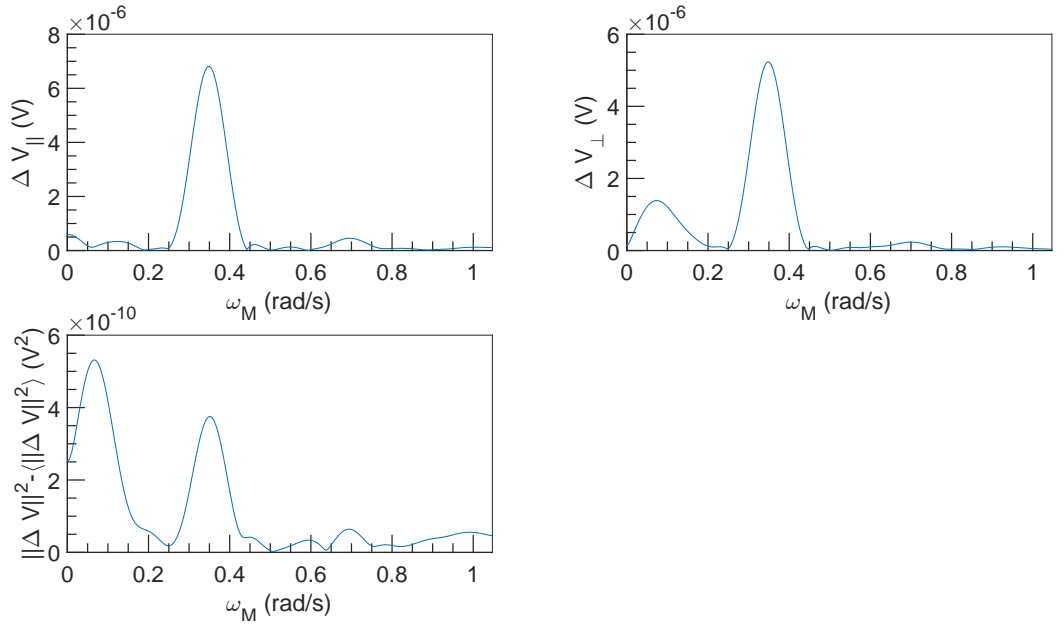


Figure 2.2: FFT spectral density of  $\Delta V$  vs  $\omega_M$  at  $U = 10^{-3} \text{ m s}^{-1}$ ,  $\omega = 1571 \text{ rad s}^{-1}$  and  $\alpha = 0.3\%$ .

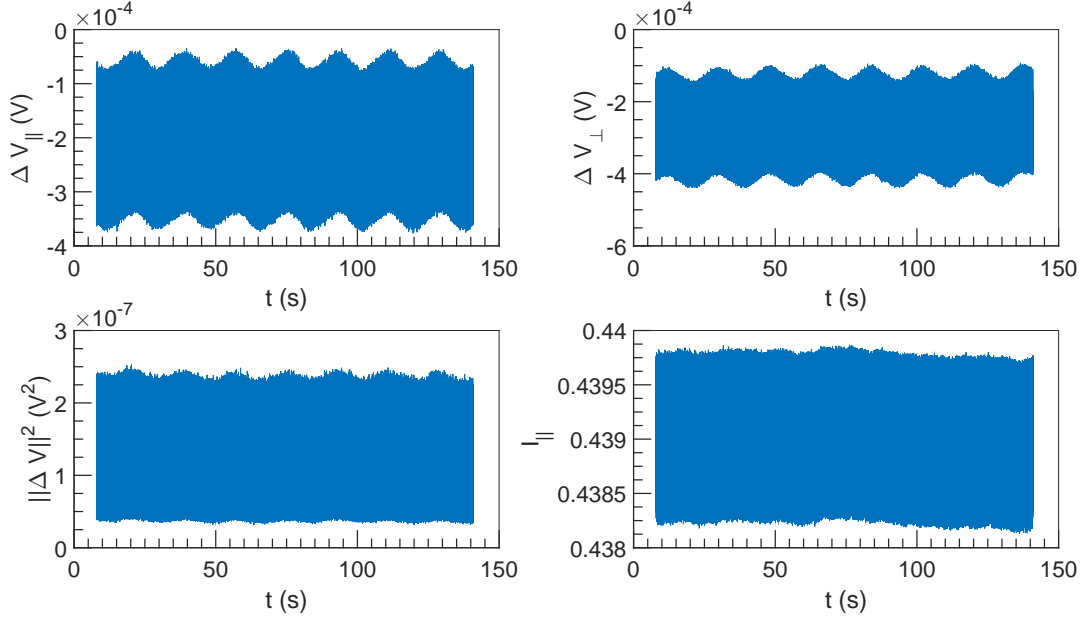


Figure 2.3:  $\Delta V$  and  $I$  vs  $t$  at  $U = 10^{-3} \text{ m s}^{-1}$ ,  $\omega = 3142 \text{ rad s}^{-1}$  and  $\alpha = 0.3\%$ .

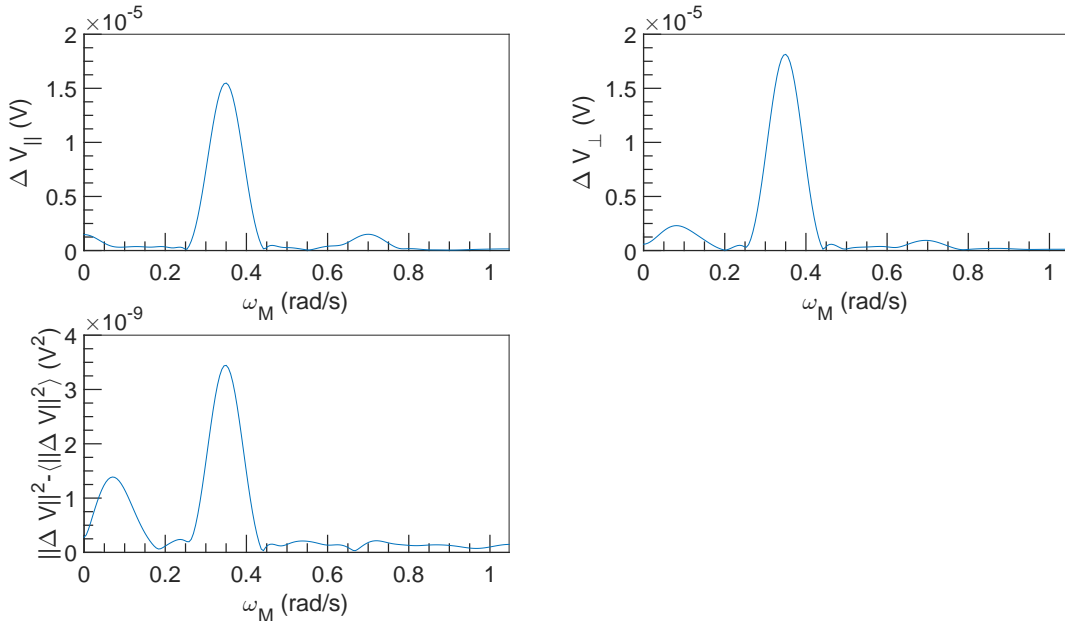


Figure 2.4: FFT spectral density of  $\Delta V$  vs  $\omega_M$  at  $U = 10^{-3} \text{ m s}^{-1}$ ,  $\omega = 3142 \text{ rad s}^{-1}$  and  $\alpha = 0.3\%$ .

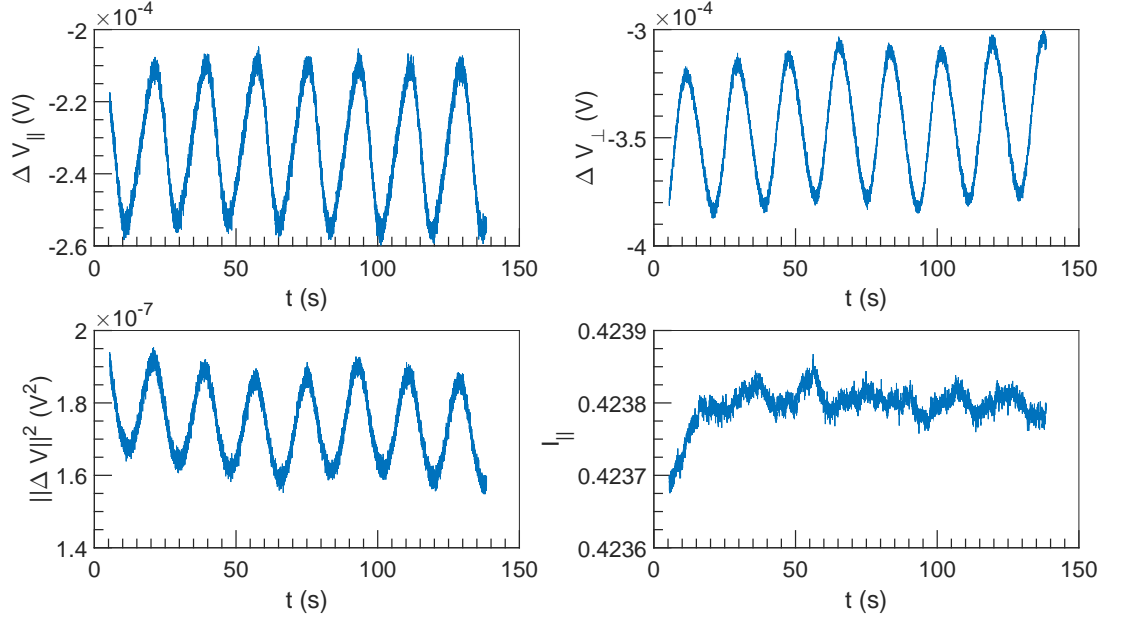


Figure 2.5:  $\Delta V$  and  $I$  vs  $t$  at  $U = 10^{-3} \text{ m s}^{-1}$ ,  $\omega = 4712 \text{ rad s}^{-1}$  and  $\alpha = 0.3\%$ .

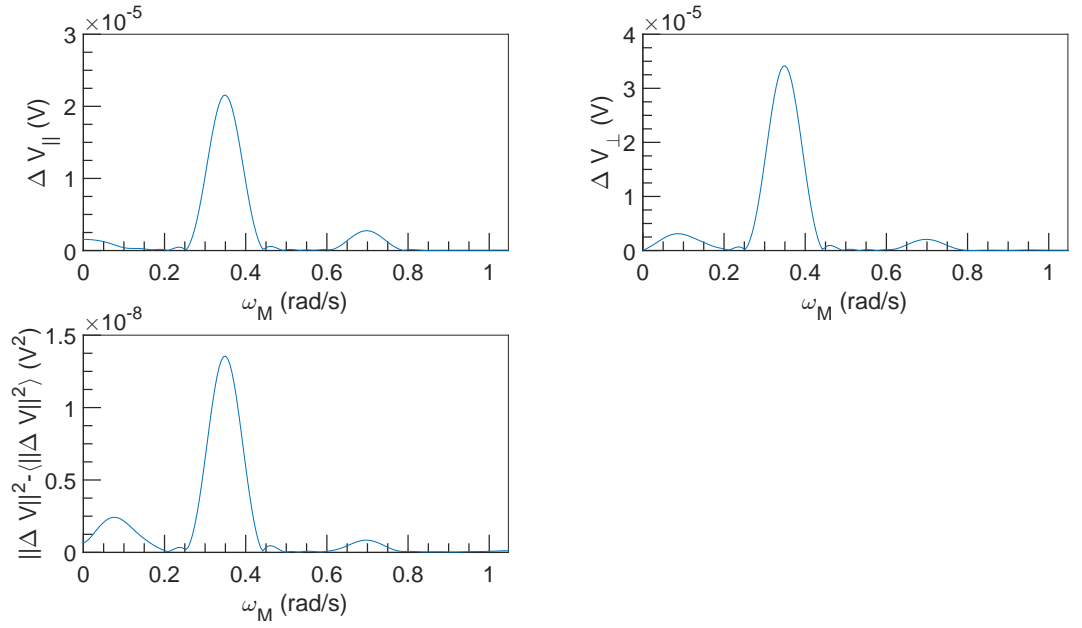


Figure 2.6: FFT spectral density of  $\Delta V$  vs  $\omega_M$  at  $U = 10^{-3} \text{ m s}^{-1}$ ,  $\omega = 4712 \text{ rad s}^{-1}$  and  $\alpha = 0.3\%$ .

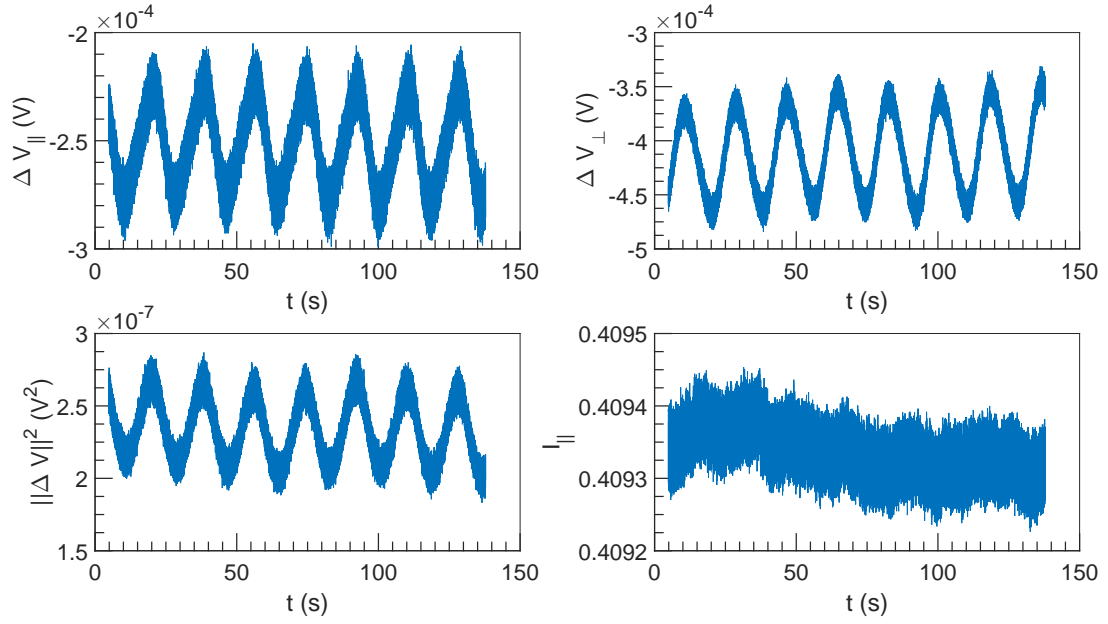


Figure 2.7:  $\Delta V$  and  $I$  vs  $t$  at  $U = 10^{-3} \text{ m s}^{-1}$ ,  $\omega = 6283 \text{ rad s}^{-1}$  and  $\alpha = 0.3\%$ .

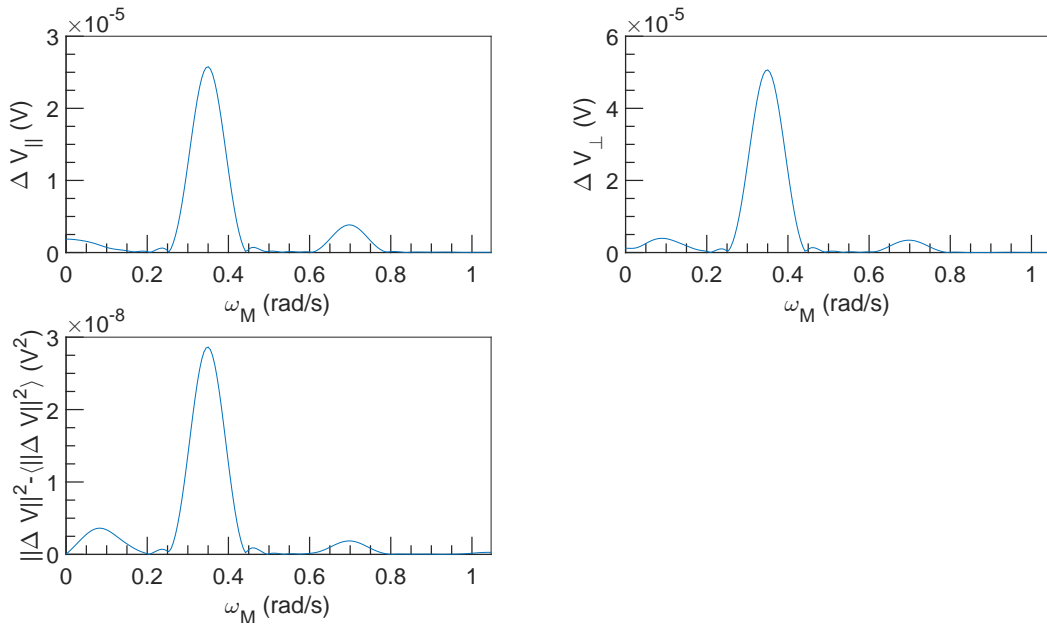


Figure 2.8: FFT spectral density of  $\Delta V$  vs  $\omega_M$  at  $U = 10^{-3} \text{ m s}^{-1}$ ,  $\omega = 6283 \text{ rad s}^{-1}$  and  $\alpha = 0.3\%$ .

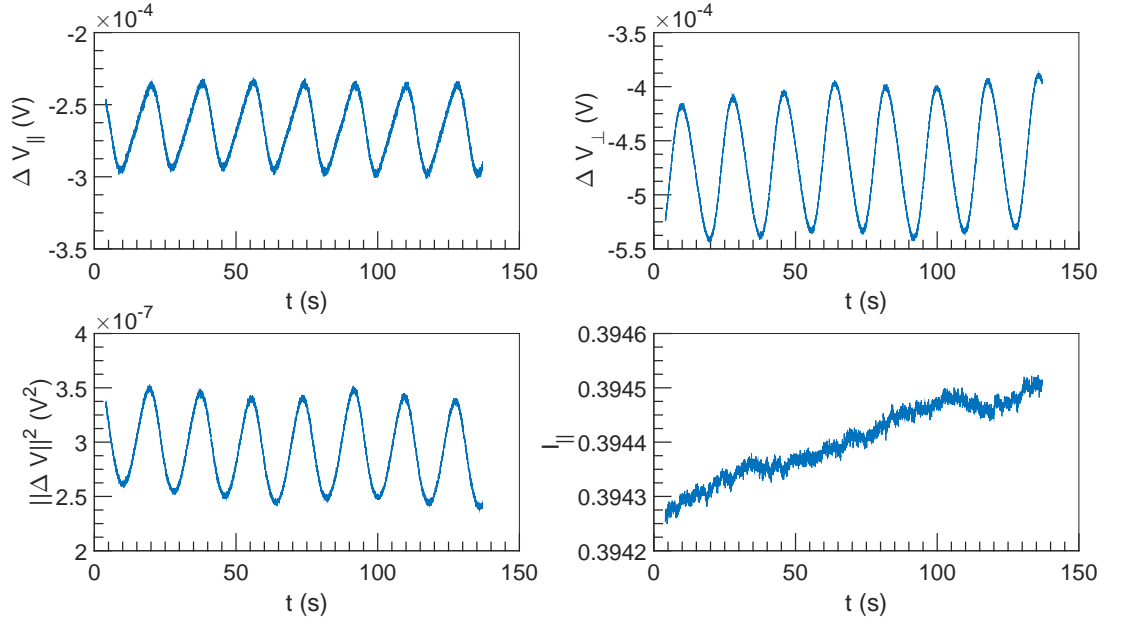


Figure 2.9:  $\Delta V$  and  $I$  vs  $t$  at  $U = 10^{-3} \text{ m s}^{-1}$ ,  $\omega = 7854 \text{ rad s}^{-1}$  and  $\alpha = 0.3\%$ .

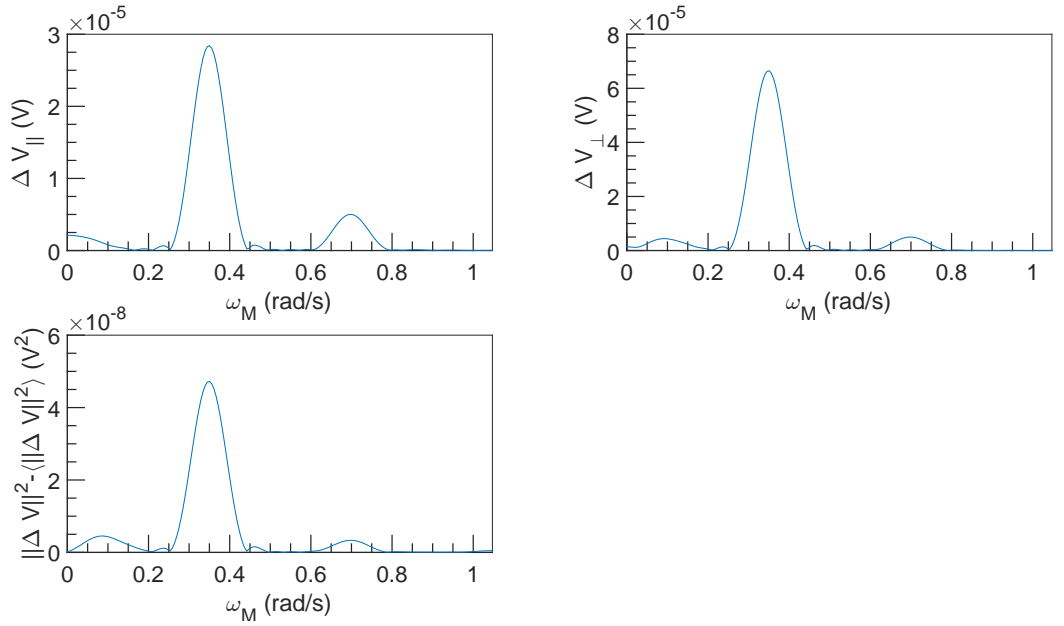


Figure 2.10: FFT spectral density of  $\Delta V$  vs  $\omega_M$  at  $U = 10^{-3} \text{ m s}^{-1}$ ,  $\omega = 7854 \text{ rad s}^{-1}$  and  $\alpha = 0.3\%$ .

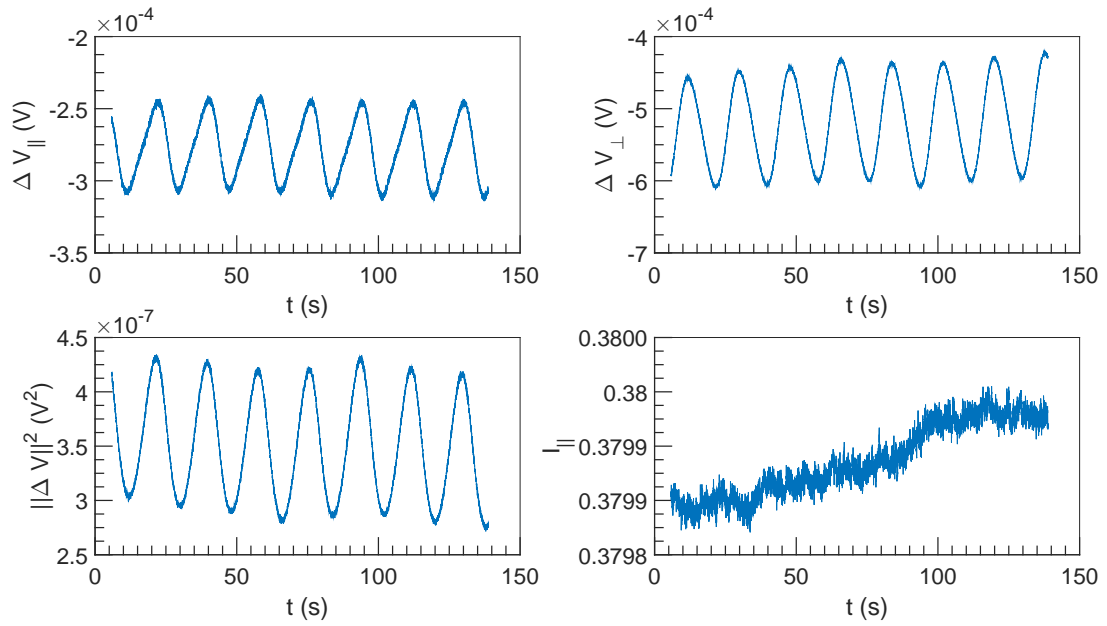


Figure 2.11:  $\Delta V$  and  $I$  vs  $t$  at  $U = 10^{-3} \text{ m s}^{-1}$ ,  $\omega = 9425 \text{ rad s}^{-1}$  and  $\alpha = 0.3\%$ .

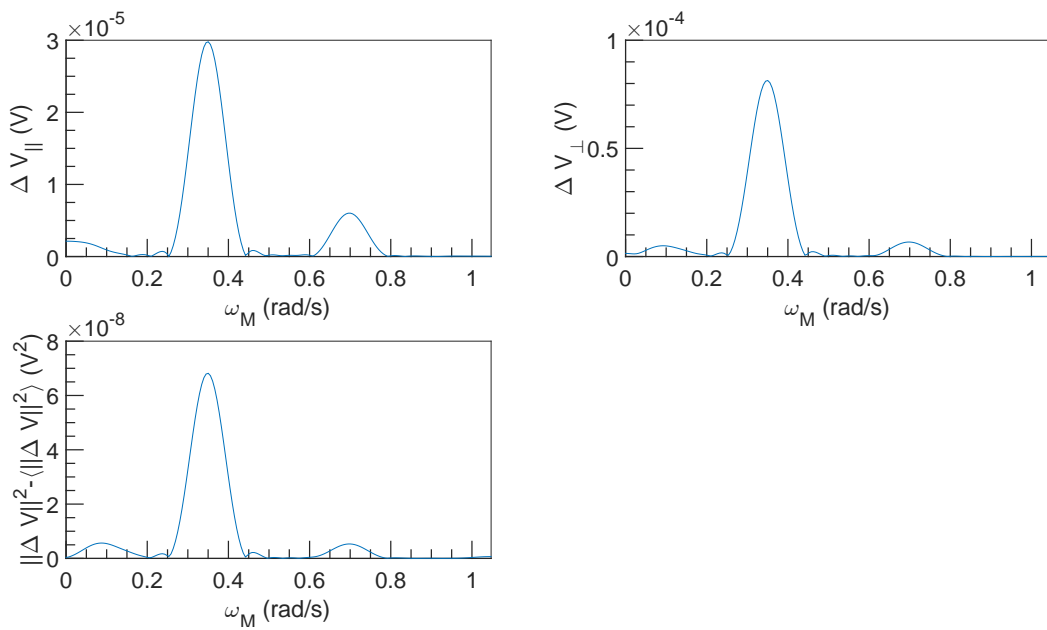


Figure 2.12: FFT spectral density of  $\Delta V$  vs  $\omega_M$  at  $U = 10^{-3} \text{ m s}^{-1}$ ,  $\omega = 9425 \text{ rad s}^{-1}$  and  $\alpha = 0.3\%$ .

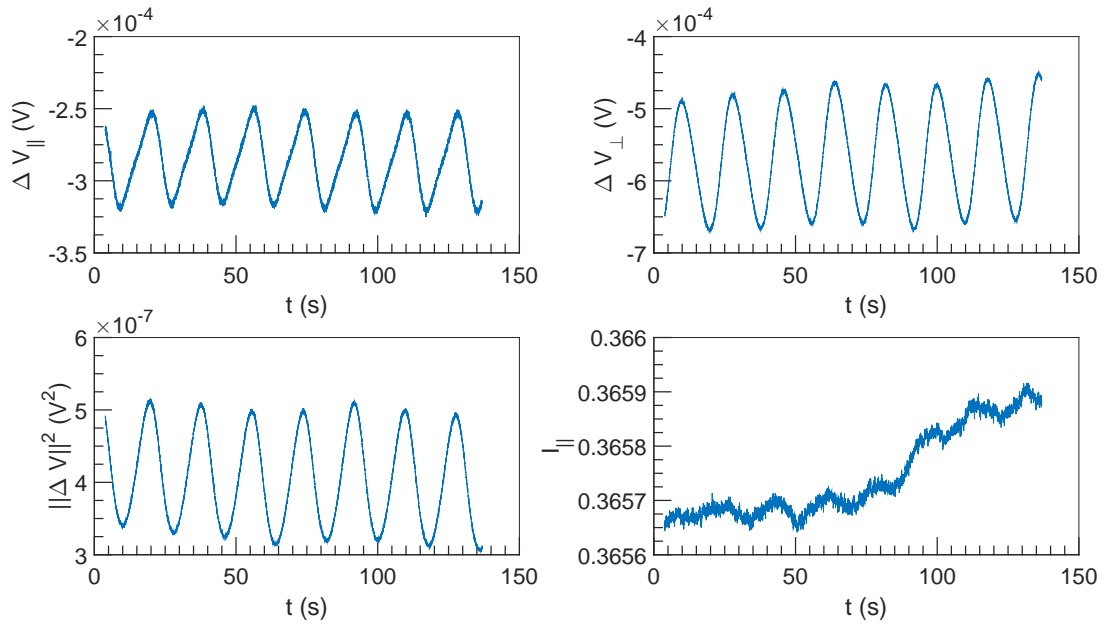


Figure 2.13:  $\Delta V$  and  $I$  vs  $t$  at  $U = 10^{-3} \text{ m s}^{-1}$ ,  $\omega = 10\,996 \text{ rad s}^{-1}$  and  $\alpha = 0.3\%$ .

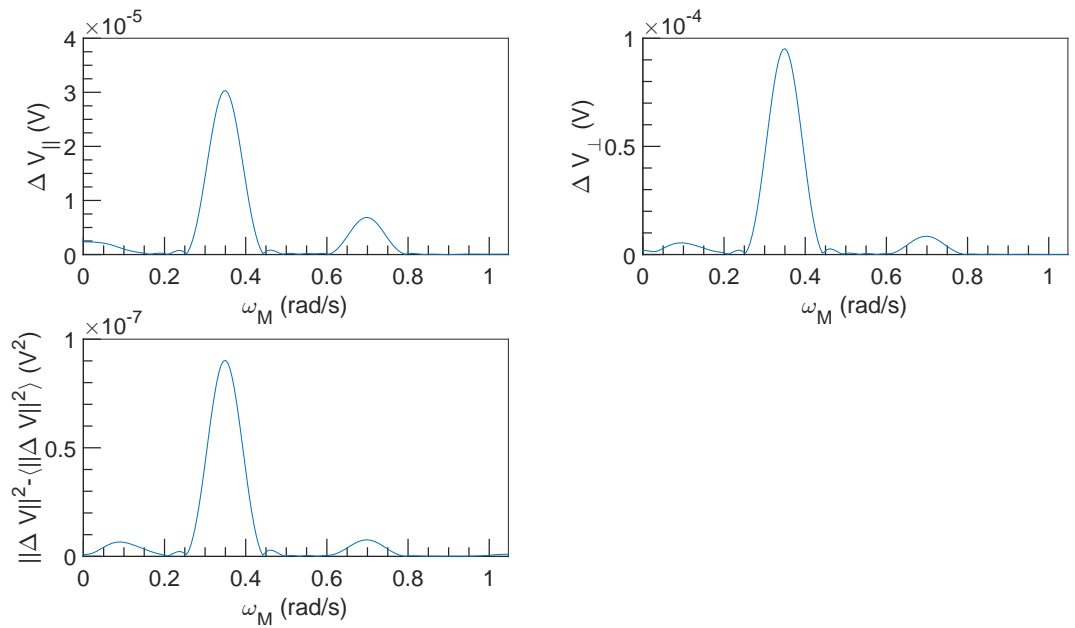


Figure 2.14: FFT spectral density of  $\Delta V$  vs  $\omega_M$  at  $U = 10^{-3} \text{ m s}^{-1}$ ,  $\omega = 10\,996 \text{ rad s}^{-1}$  and  $\alpha = 0.3\%$ .

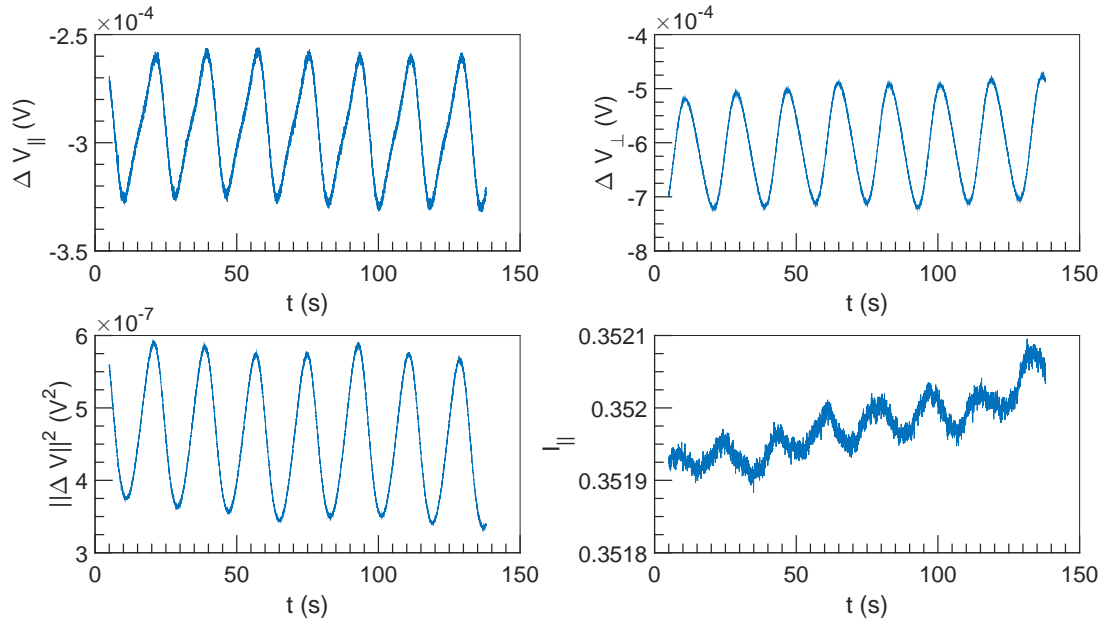


Figure 2.15:  $\Delta V$  and  $I$  vs  $t$  at  $U = 10^{-3} \text{ m s}^{-1}$ ,  $\omega = 12566 \text{ rad s}^{-1}$  and  $\alpha = 0.3\%$ .

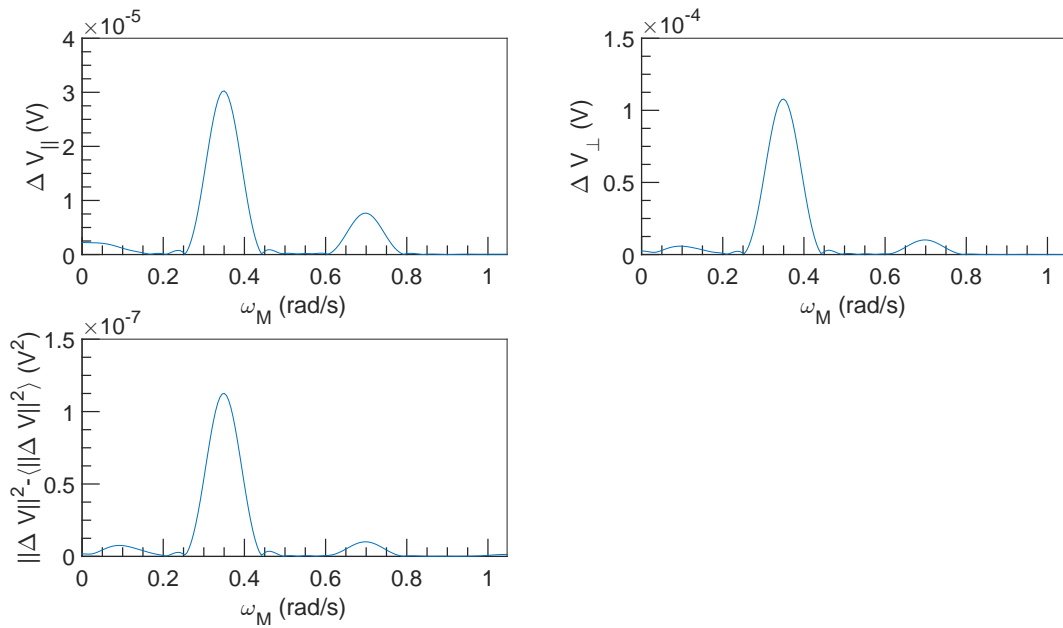


Figure 2.16: FFT spectral density of  $\Delta V$  vs  $\omega_M$  at  $U = 10^{-3} \text{ m s}^{-1}$ ,  $\omega = 12566 \text{ rad s}^{-1}$  and  $\alpha = 0.3\%$ .



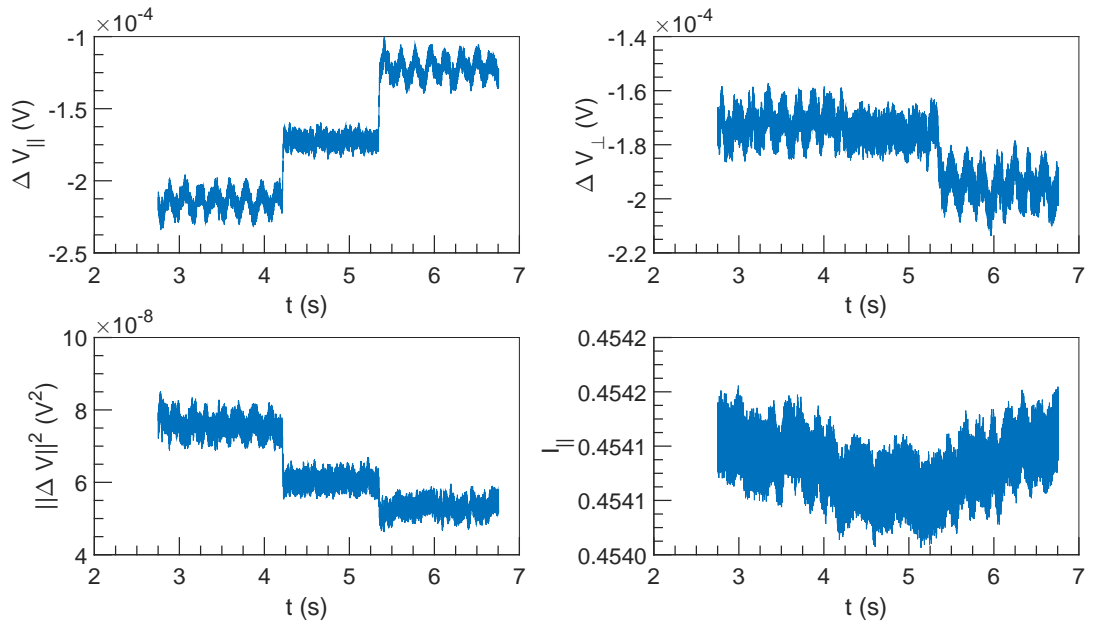


Figure 2.17:  $\Delta V$  and  $I$  vs  $t$  at  $U = 0.1 \text{ m s}^{-1}$ ,  $\omega = 1571 \text{ rad s}^{-1}$  and  $\alpha = 0.3 \%$ .

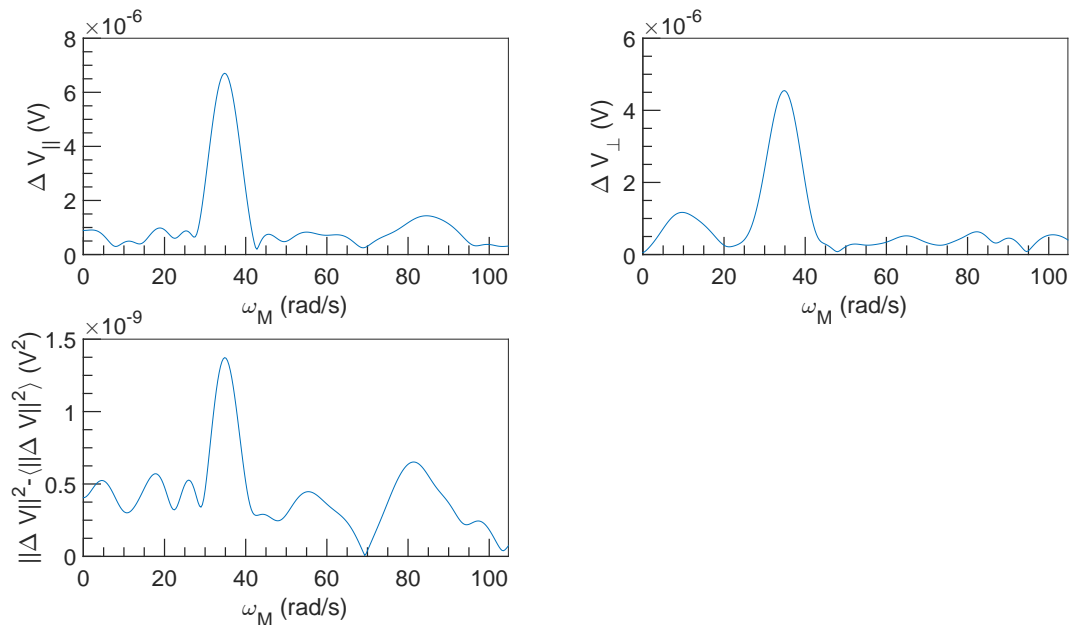


Figure 2.18: FFT spectral density of  $\Delta V$  vs  $\omega_M$  at  $U = 0.1 \text{ m s}^{-1}$ ,  $\omega = 1571 \text{ rad s}^{-1}$  and  $\alpha = 0.3 \%$ .

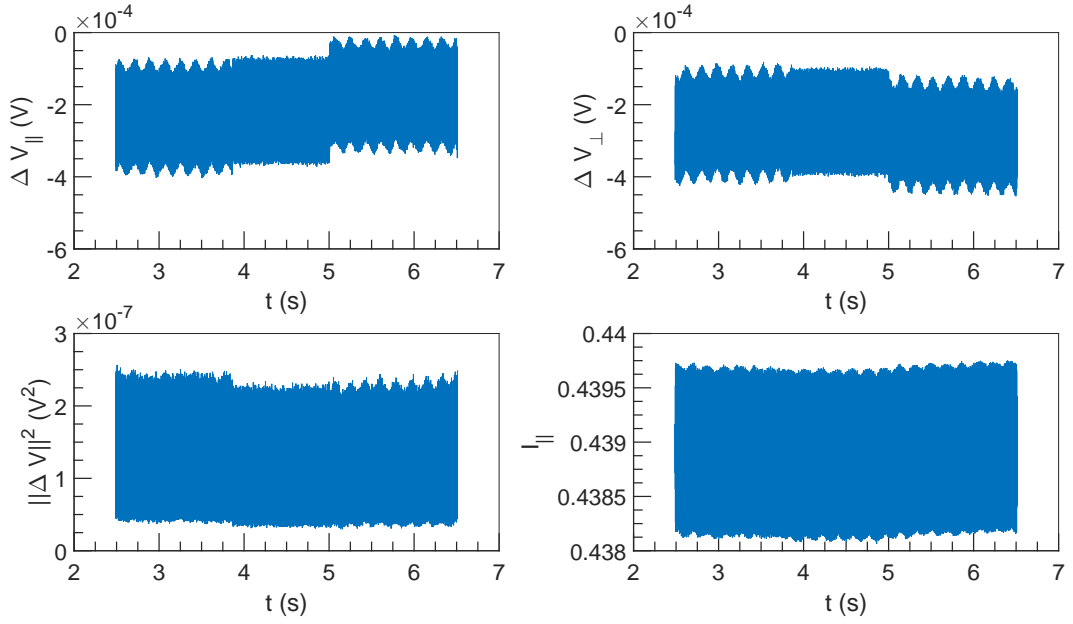


Figure 2.19:  $\Delta V$  and  $I$  vs  $t$  at  $U = 0.1 \text{ m s}^{-1}$ ,  $\omega = 3142 \text{ rad s}^{-1}$  and  $\alpha = 0.3 \%$ .

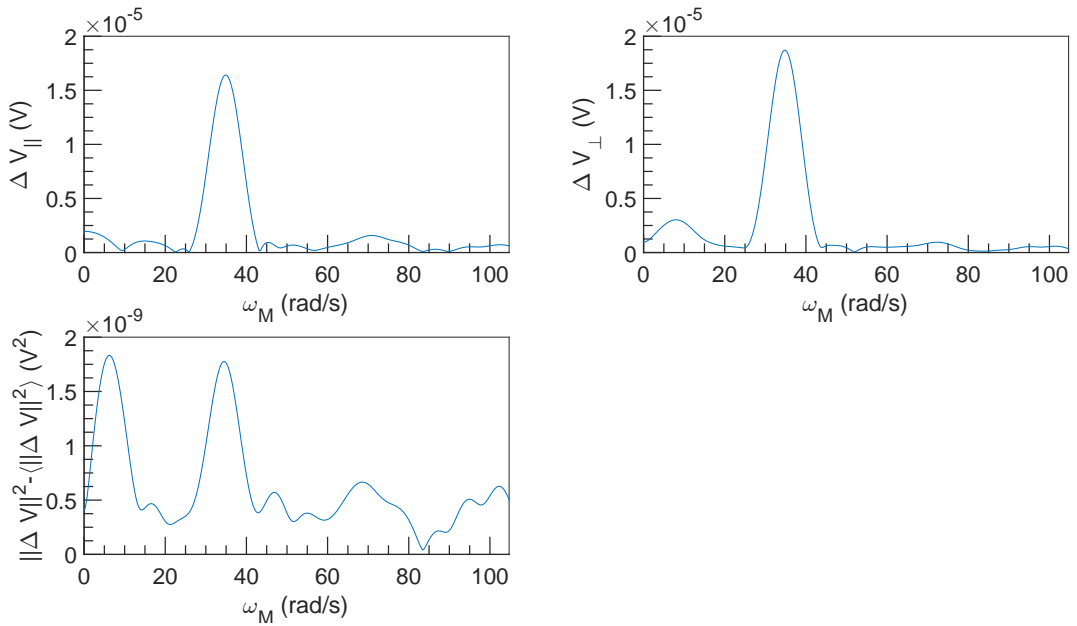


Figure 2.20: FFT spectral density of  $\Delta V$  vs  $\omega_M$  at  $U = 0.1 \text{ m s}^{-1}$ ,  $\omega = 3142 \text{ rad s}^{-1}$  and  $\alpha = 0.3 \%$ .

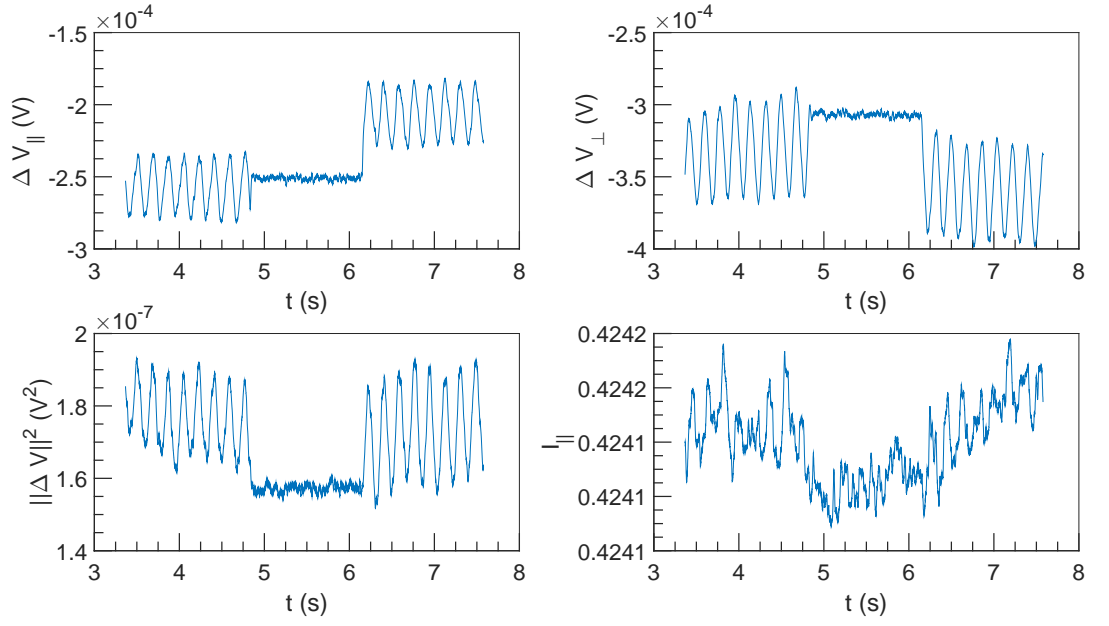


Figure 2.21:  $\Delta V$  and  $I$  vs  $t$  at  $U = 0.1 \text{ m s}^{-1}$ ,  $\omega = 4712 \text{ rad s}^{-1}$  and  $\alpha = 0.3 \%$ .

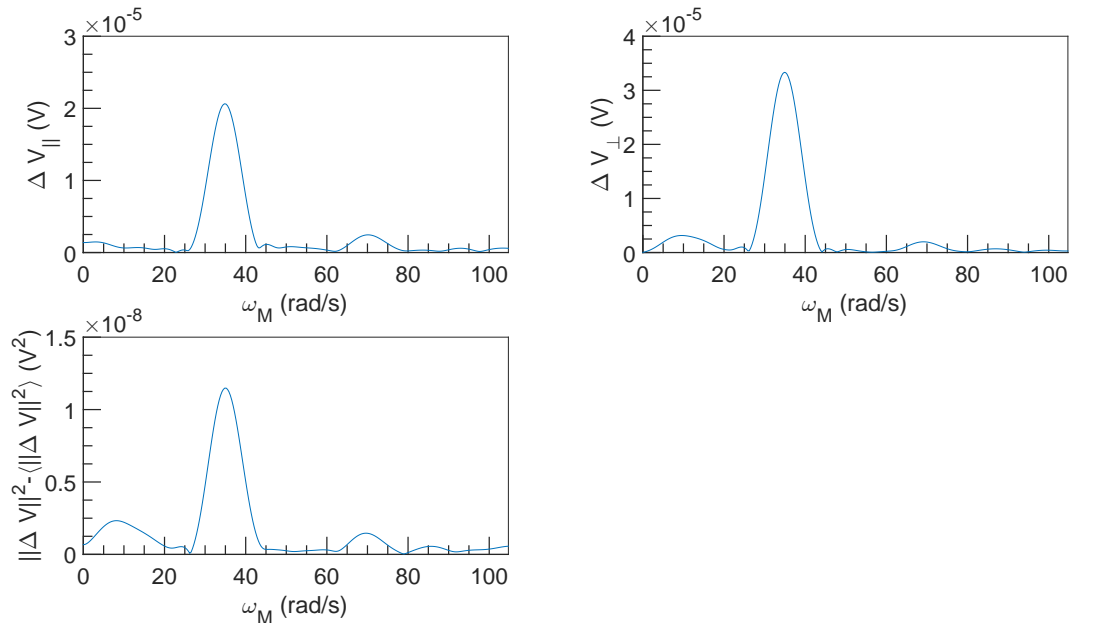


Figure 2.22: FFT spectral density of  $\Delta V$  vs  $\omega_M$  at  $U = 0.1 \text{ m s}^{-1}$ ,  $\omega = 4712 \text{ rad s}^{-1}$  and  $\alpha = 0.3 \%$ .

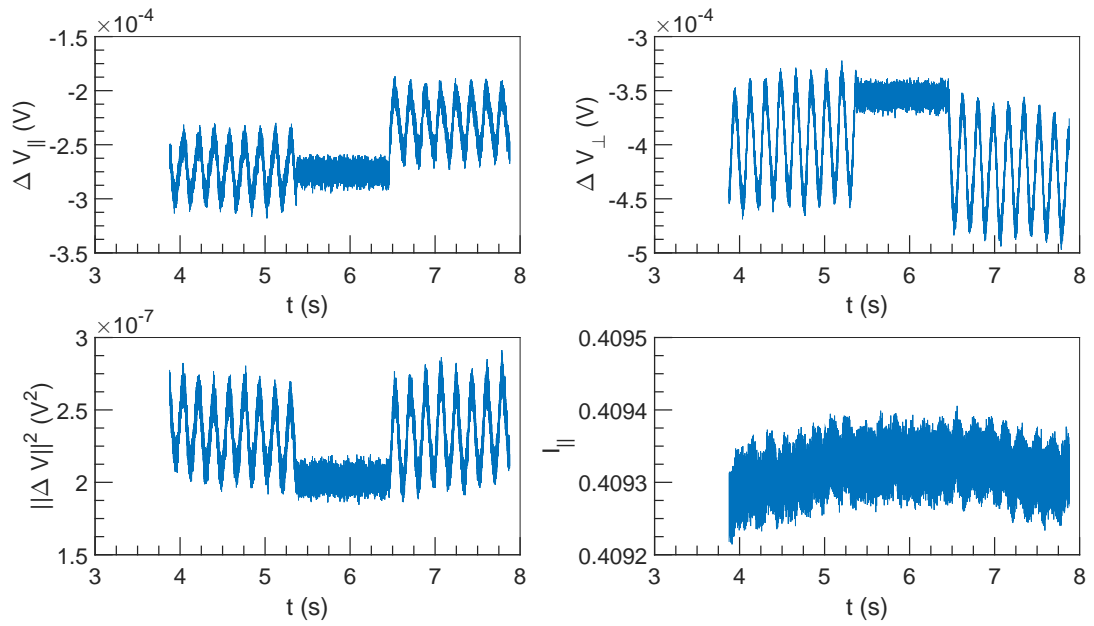


Figure 2.23:  $\Delta V$  and  $I$  vs  $t$  at  $U = 0.1 \text{ m s}^{-1}$ ,  $\omega = 6283 \text{ rad s}^{-1}$  and  $\alpha = 0.3 \%$ .

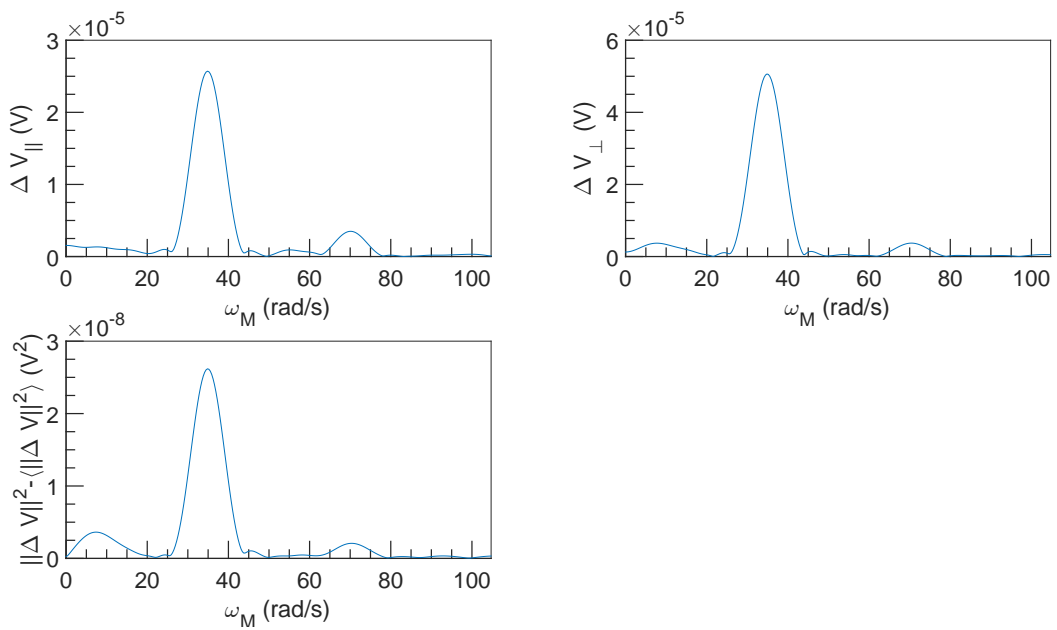


Figure 2.24: FFT spectral density of  $\Delta V$  vs  $\omega_M$  at  $U = 0.1 \text{ m s}^{-1}$ ,  $\omega = 6283 \text{ rad s}^{-1}$  and  $\alpha = 0.3 \%$ .

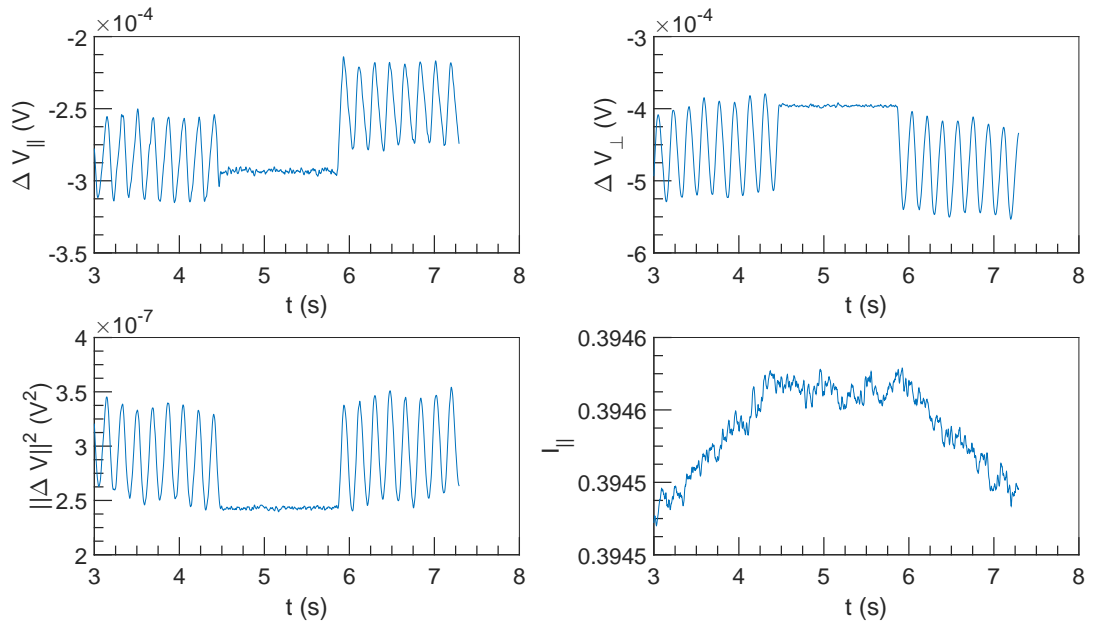


Figure 2.25:  $\Delta V$  and  $I$  vs  $t$  at  $U = 0.1 \text{ m s}^{-1}$ ,  $\omega = 7854 \text{ rad s}^{-1}$  and  $\alpha = 0.3 \%$ .

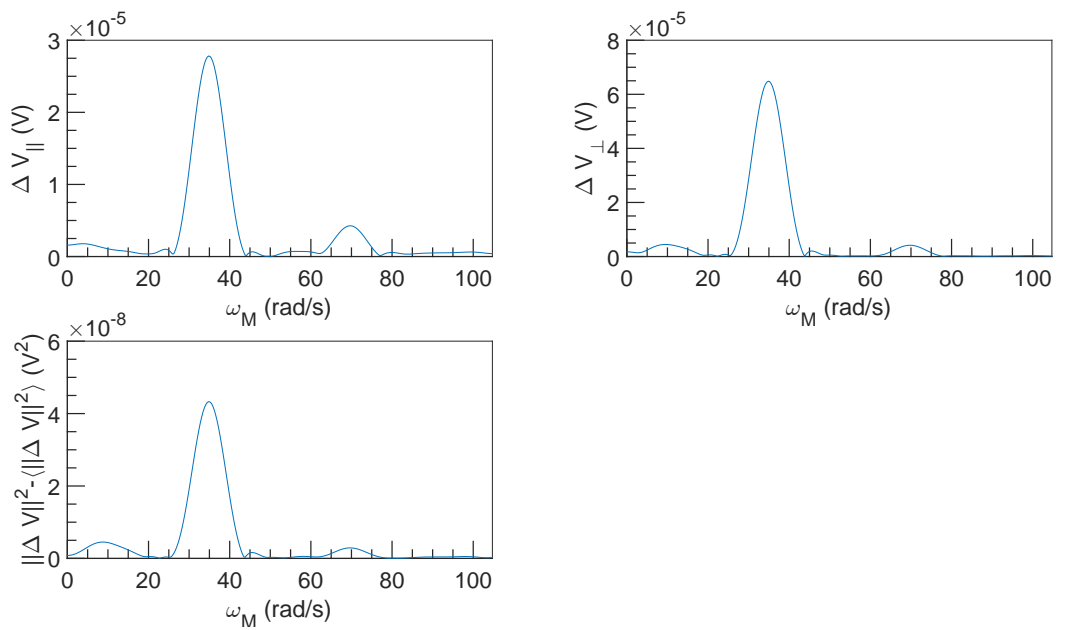


Figure 2.26: FFT spectral density of  $\Delta V$  vs  $\omega_M$  at  $U = 0.1 \text{ m s}^{-1}$ ,  $\omega = 7854 \text{ rad s}^{-1}$  and  $\alpha = 0.3 \%$ .

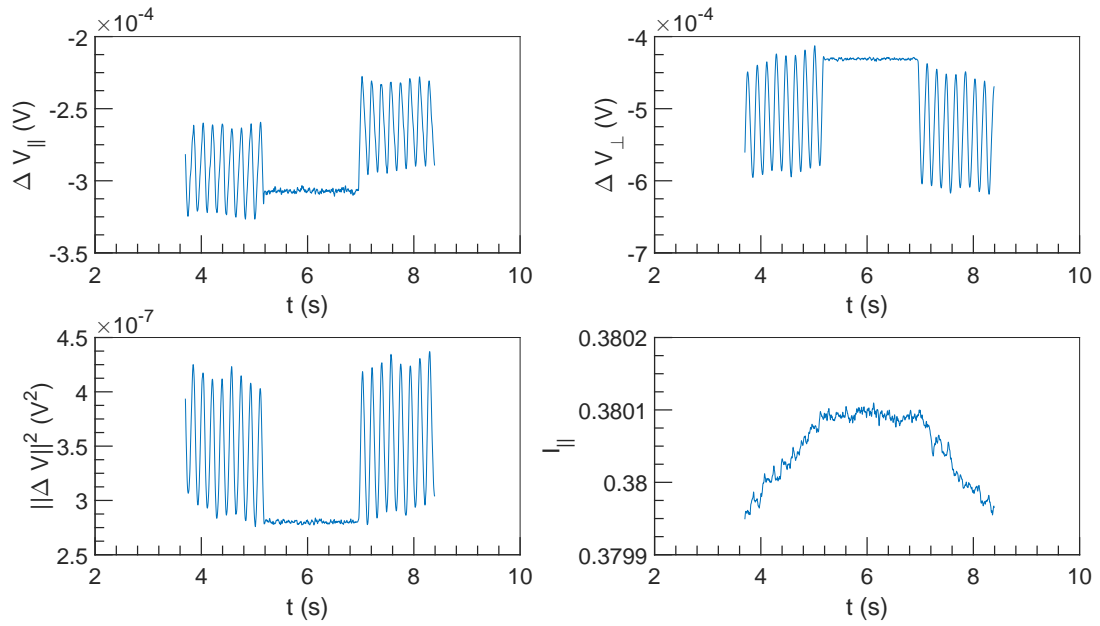


Figure 2.27:  $\Delta V$  and  $I$  vs  $t$  at  $U = 0.1 \text{ m s}^{-1}$ ,  $\omega = 9425 \text{ rad s}^{-1}$  and  $\alpha = 0.3 \%$ .

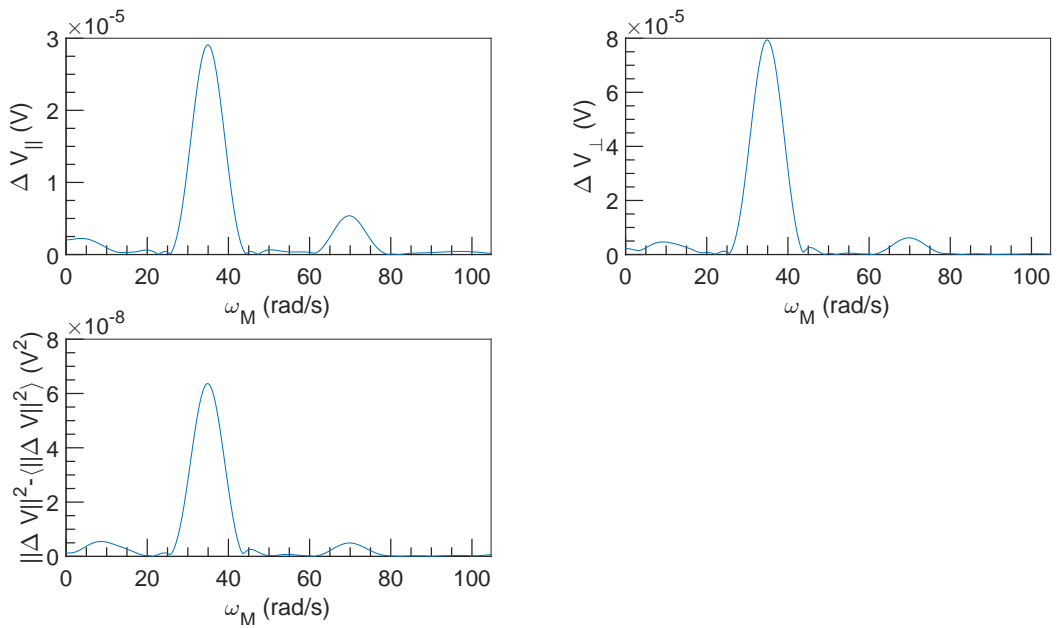


Figure 2.28: FFT spectral density of  $\Delta V$  vs  $\omega_M$  at  $U = 0.1 \text{ m s}^{-1}$ ,  $\omega = 9425 \text{ rad s}^{-1}$  and  $\alpha = 0.3 \%$ .

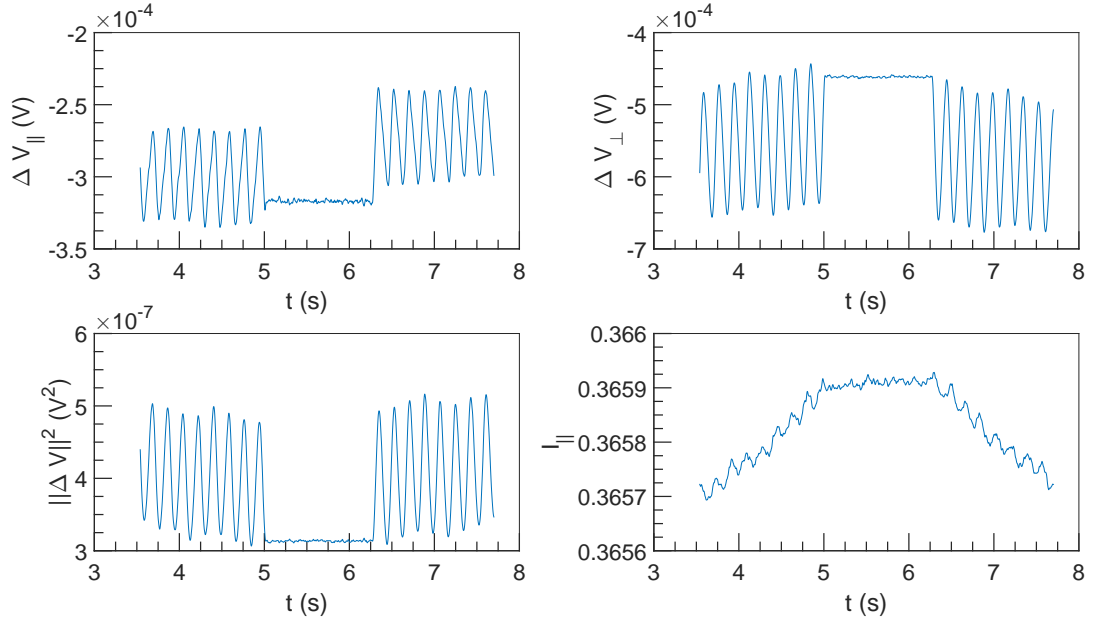


Figure 2.29:  $\Delta V$  and  $I$  vs  $t$  at  $U = 0.1 \text{ m s}^{-1}$ ,  $\omega = 10996 \text{ rad s}^{-1}$  and  $\alpha = 0.3\%$ .

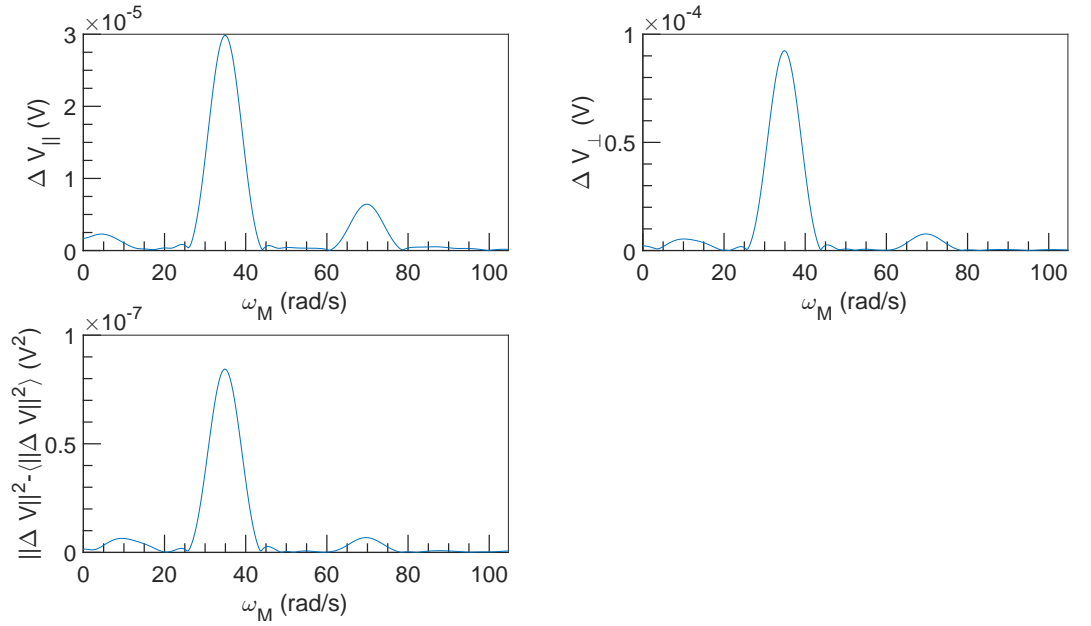


Figure 2.30: FFT spectral density of  $\Delta V$  vs  $\omega_M$  at  $U = 0.1 \text{ m s}^{-1}$ ,  $\omega = 10996 \text{ rad s}^{-1}$  and  $\alpha = 0.3\%$ .

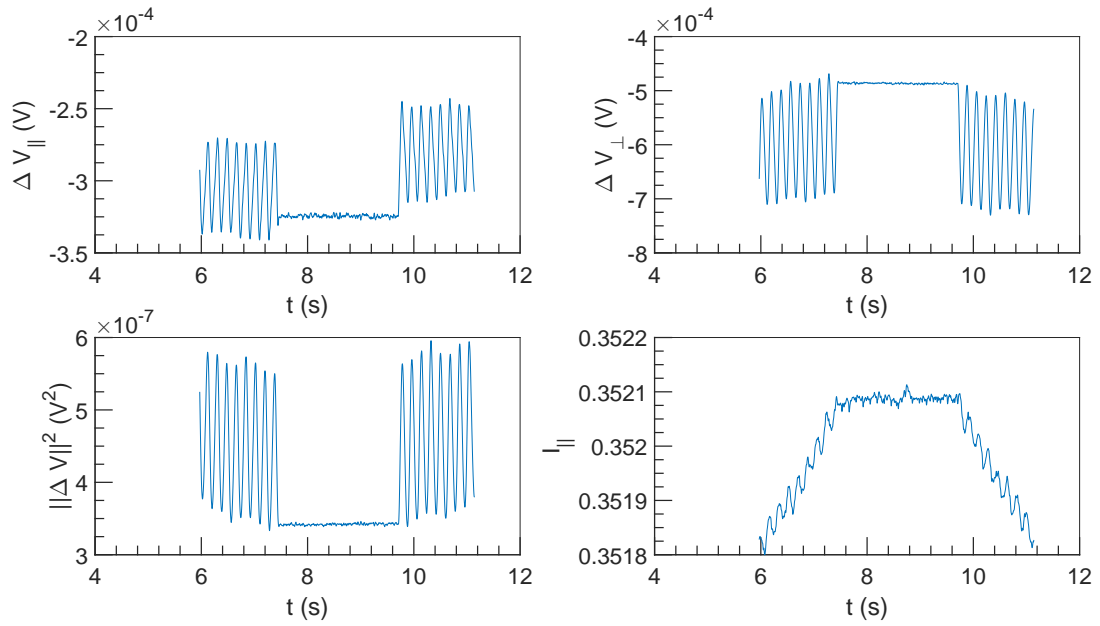


Figure 2.31:  $\Delta V$  and  $I$  vs  $t$  at  $U = 0.1 \text{ m s}^{-1}$ ,  $\omega = 12566 \text{ rad s}^{-1}$  and  $\alpha = 0.3\%$ .

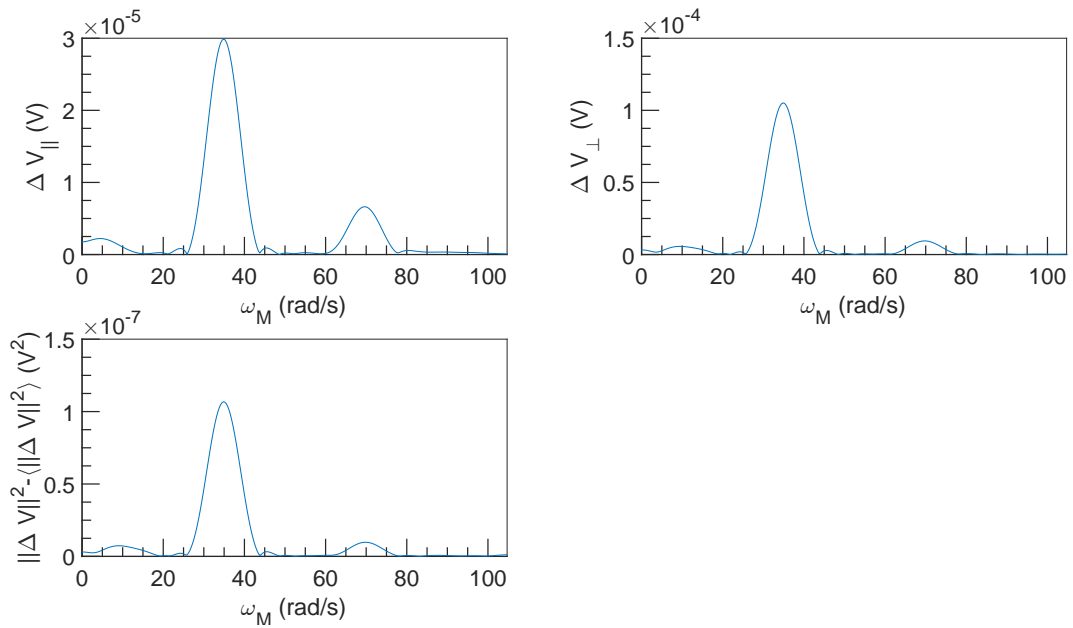


Figure 2.32: FFT spectral density of  $\Delta V$  vs  $\omega_M$  at  $U = 0.1 \text{ m s}^{-1}$ ,  $\omega = 12566 \text{ rad s}^{-1}$  and  $\alpha = 0.3\%$ .



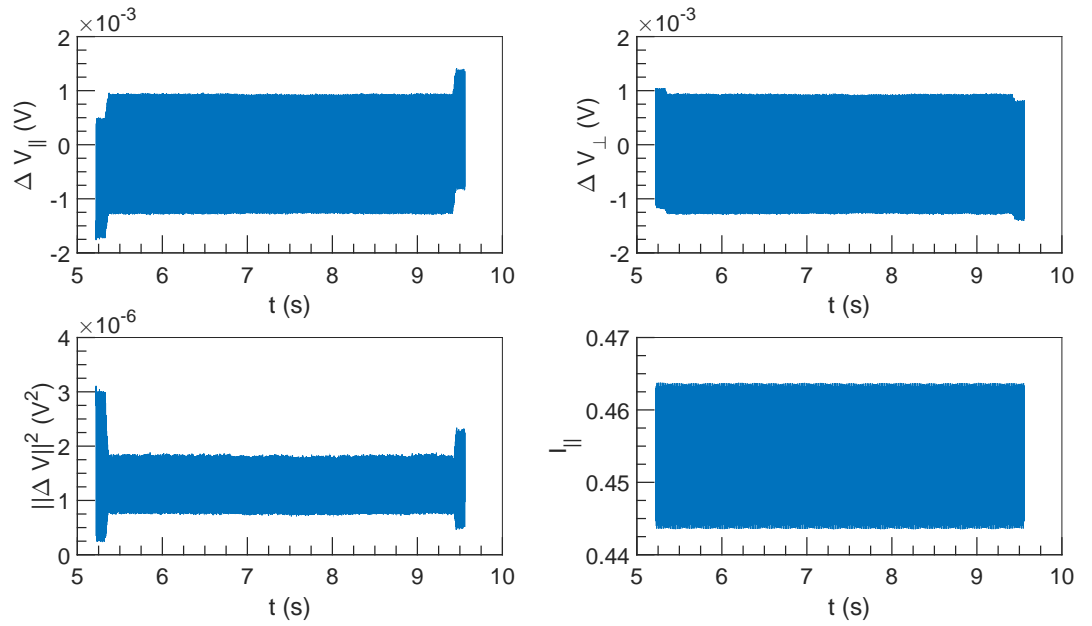


Figure 2.33:  $\Delta V$  and  $I$  vs  $t$  at  $U = 1 \text{ m s}^{-1}$ ,  $\omega = 1571 \text{ rad s}^{-1}$  and  $\alpha = 0.3\%$ .

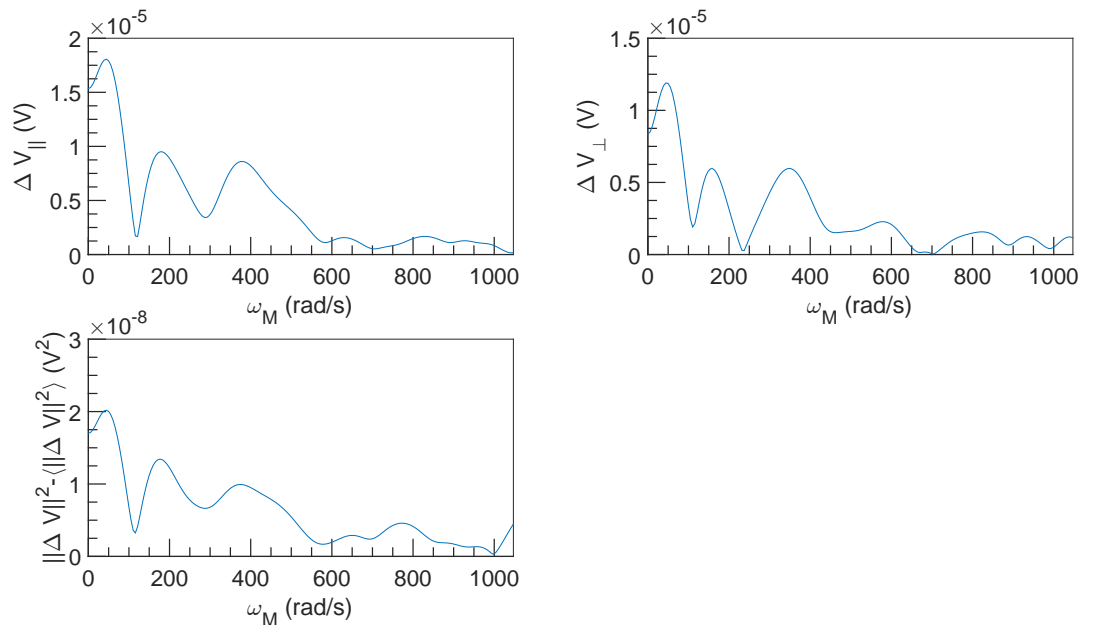


Figure 2.34: FFT spectral density of  $\Delta V$  vs  $\omega_M$  at  $U = 1 \text{ m s}^{-1}$ ,  $\omega = 1571 \text{ rad s}^{-1}$  and  $\alpha = 0.3\%$ .

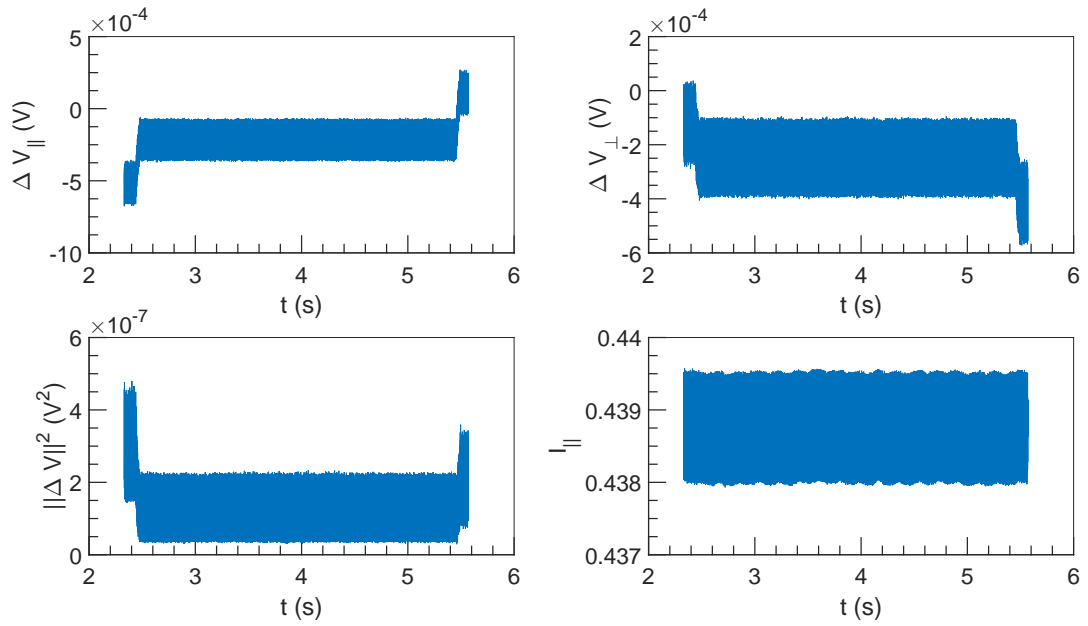


Figure 2.35:  $\Delta V$  and  $I$  vs  $t$  at  $U = 1 \text{ m s}^{-1}$ ,  $\omega = 3142 \text{ rad s}^{-1}$  and  $\alpha = 0.3\%$ .

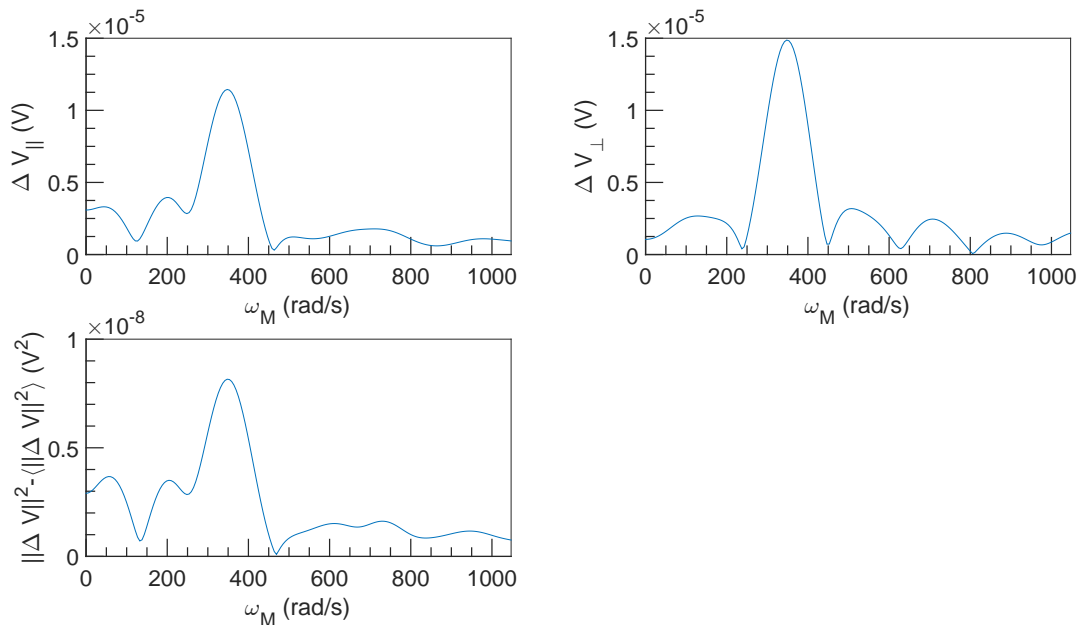


Figure 2.36: FFT spectral density of  $\Delta V$  vs  $\omega_M$  at  $U = 1 \text{ m s}^{-1}$ ,  $\omega = 3142 \text{ rad s}^{-1}$  and  $\alpha = 0.3\%$ .

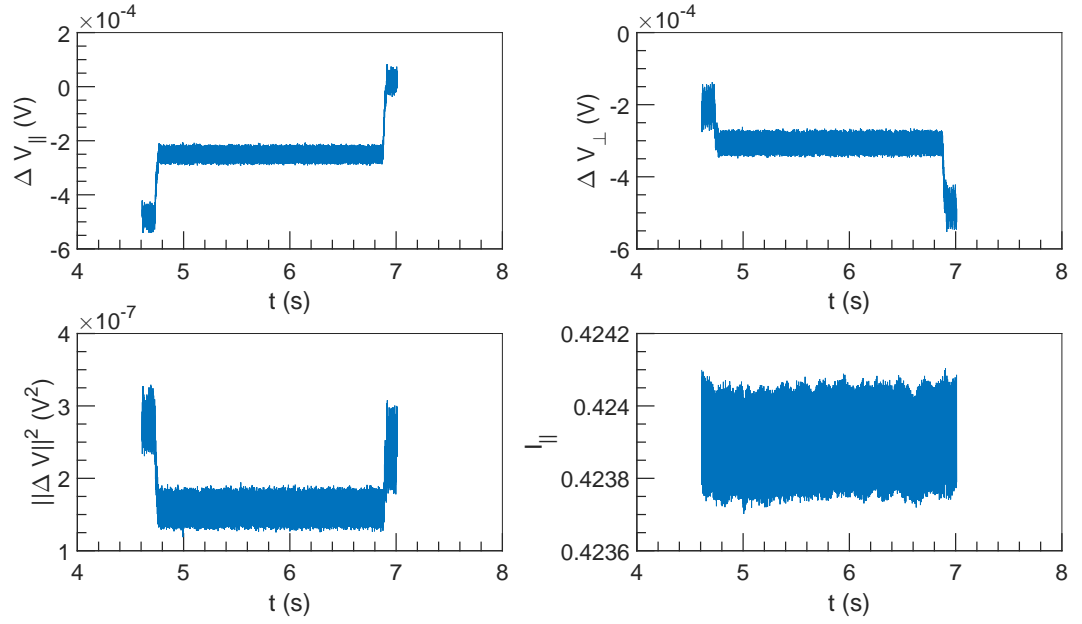


Figure 2.37:  $\Delta V$  and  $I$  vs  $t$  at  $U = 1 \text{ m s}^{-1}$ ,  $\omega = 4712 \text{ rad s}^{-1}$  and  $\alpha = 0.3 \%$ .

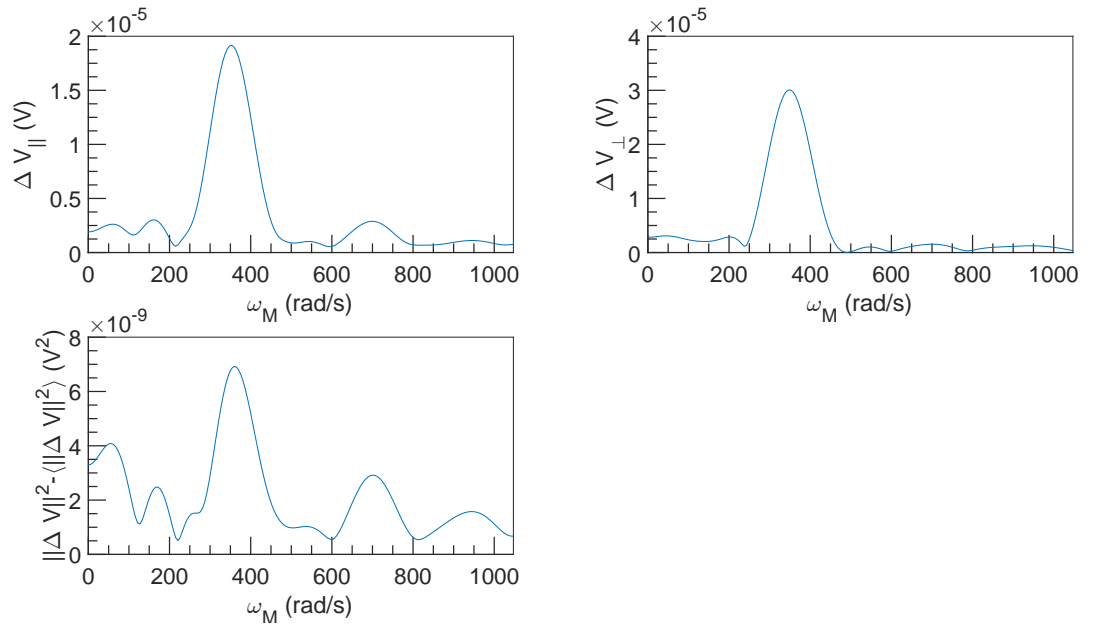


Figure 2.38: FFT spectral density of  $\Delta V$  vs  $\omega_M$  at  $U = 1 \text{ m s}^{-1}$ ,  $\omega = 4712 \text{ rad s}^{-1}$  and  $\alpha = 0.3 \%$ .

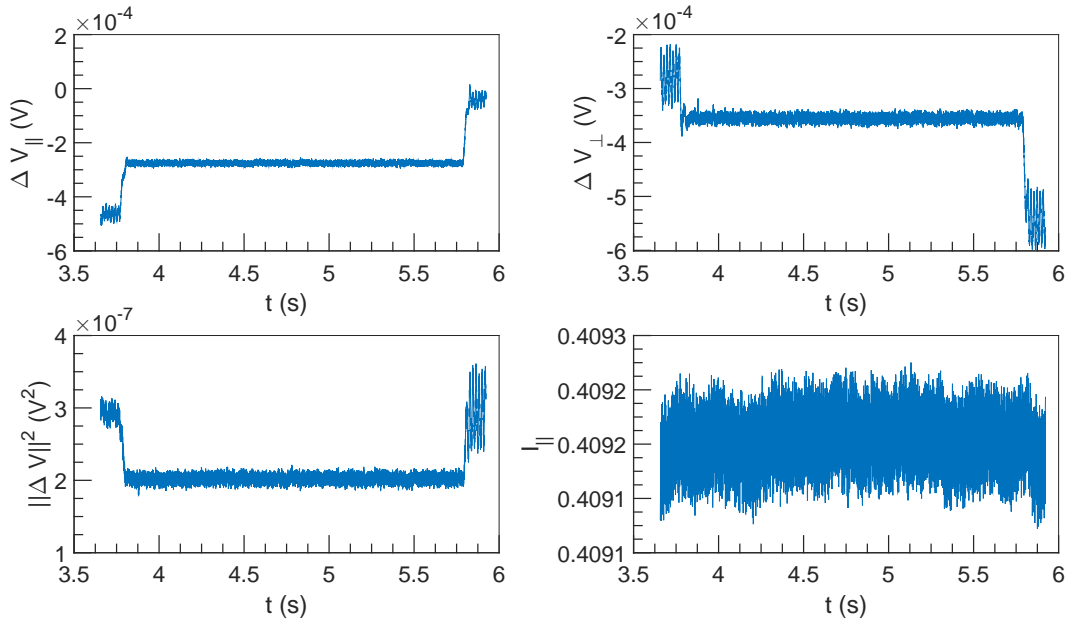


Figure 2.39:  $\Delta V$  and  $I$  vs  $t$  at  $U = 1 \text{ m s}^{-1}$ ,  $\omega = 6283 \text{ rad s}^{-1}$  and  $\alpha = 0.3\%$ .

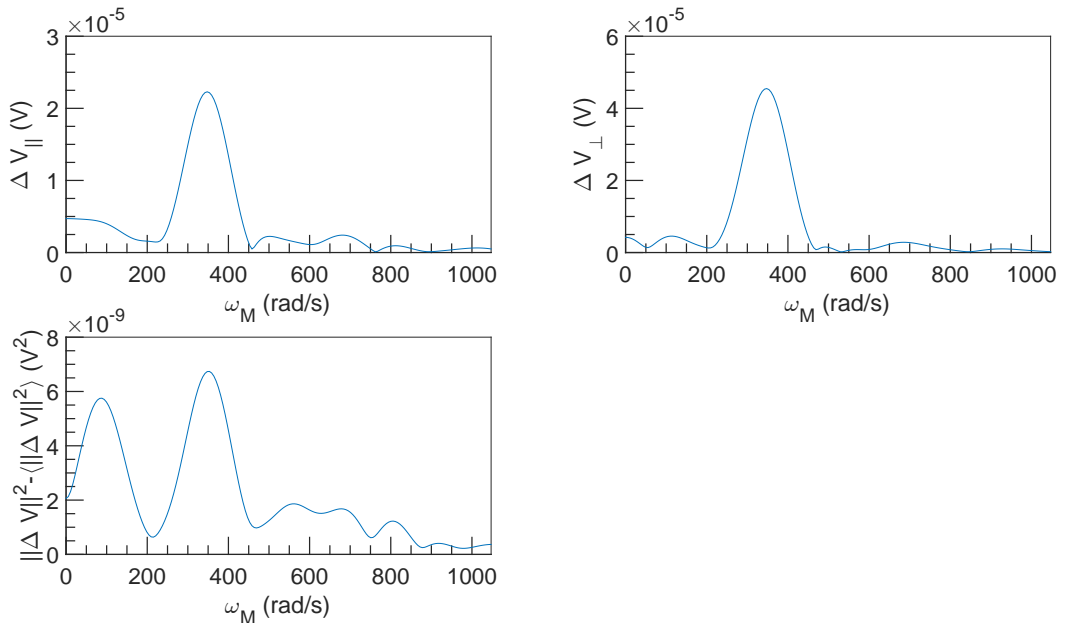


Figure 2.40: FFT spectral density of  $\Delta V$  vs  $\omega_M$  at  $U = 1 \text{ m s}^{-1}$ ,  $\omega = 6283 \text{ rad s}^{-1}$  and  $\alpha = 0.3\%$ .

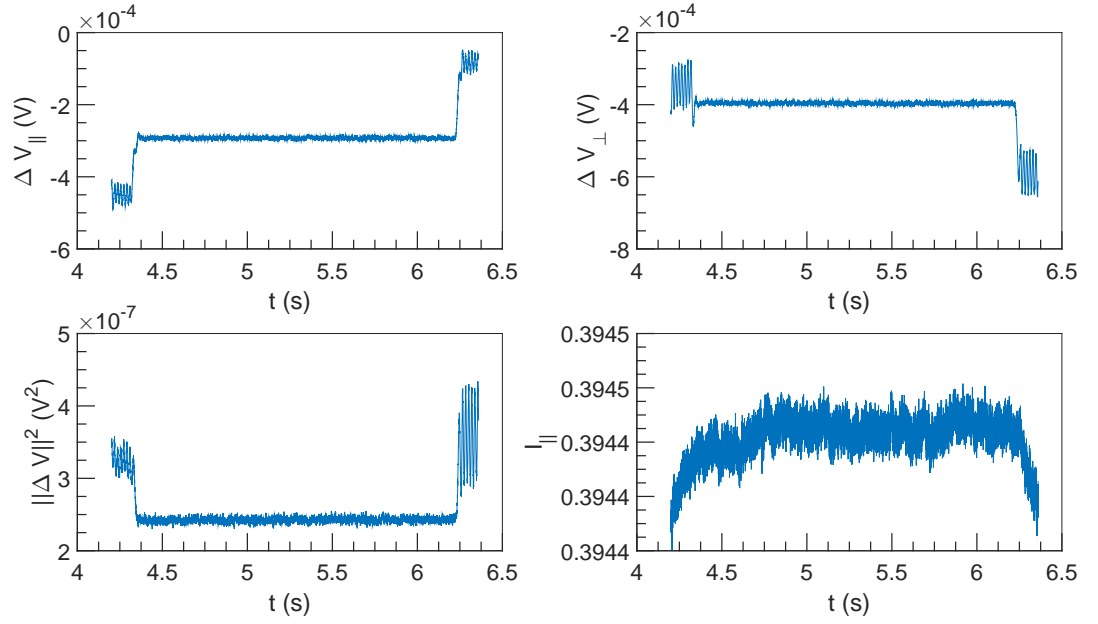


Figure 2.41:  $\Delta V$  and  $I$  vs  $t$  at  $U = 1 \text{ ms}^{-1}$ ,  $\omega = 7854 \text{ rad s}^{-1}$  and  $\alpha = 0.3\%$ .

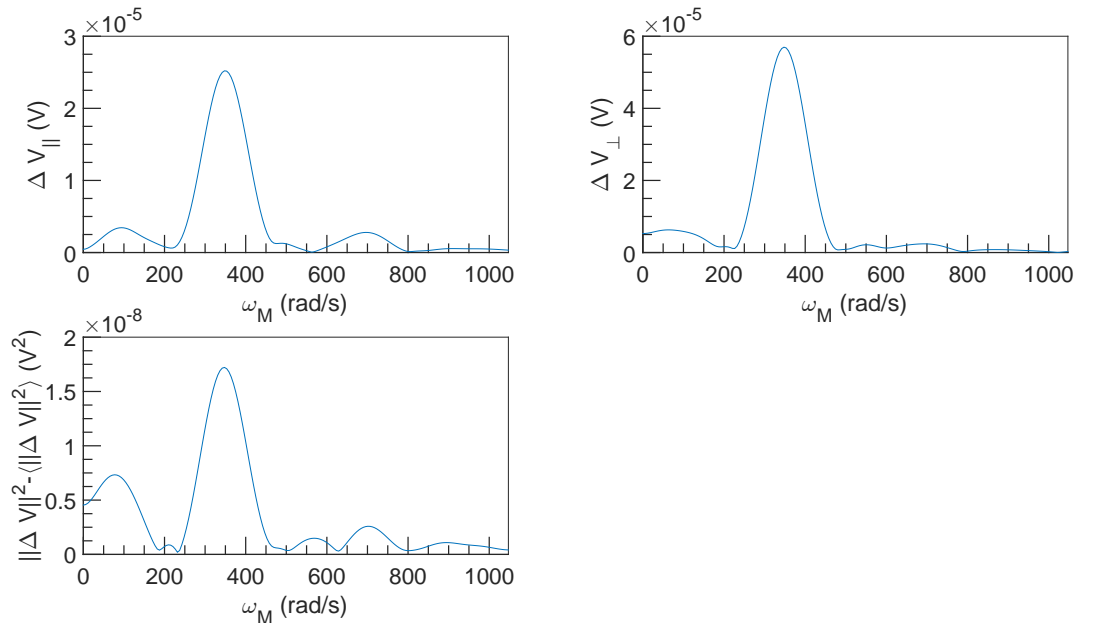


Figure 2.42: FFT spectral density of  $\Delta V$  vs  $\omega_M$  at  $U = 1 \text{ ms}^{-1}$ ,  $\omega = 7854 \text{ rad s}^{-1}$  and  $\alpha = 0.3\%$ .

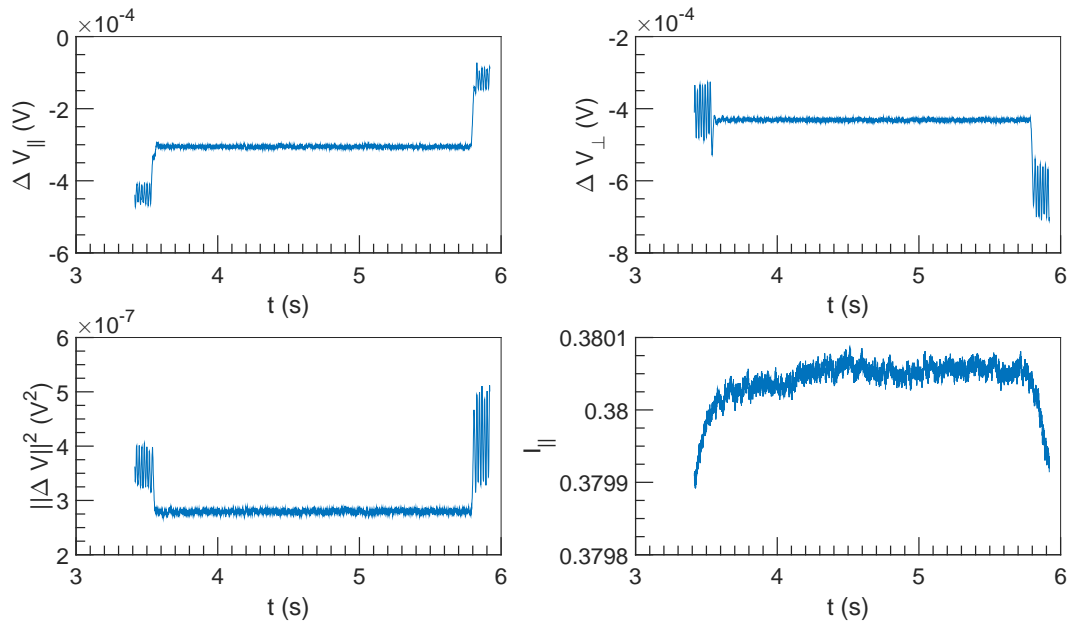


Figure 2.43:  $\Delta V$  and  $I$  vs  $t$  at  $U = 1 \text{ m s}^{-1}$ ,  $\omega = 9425 \text{ rad s}^{-1}$  and  $\alpha = 0.3 \%$ .

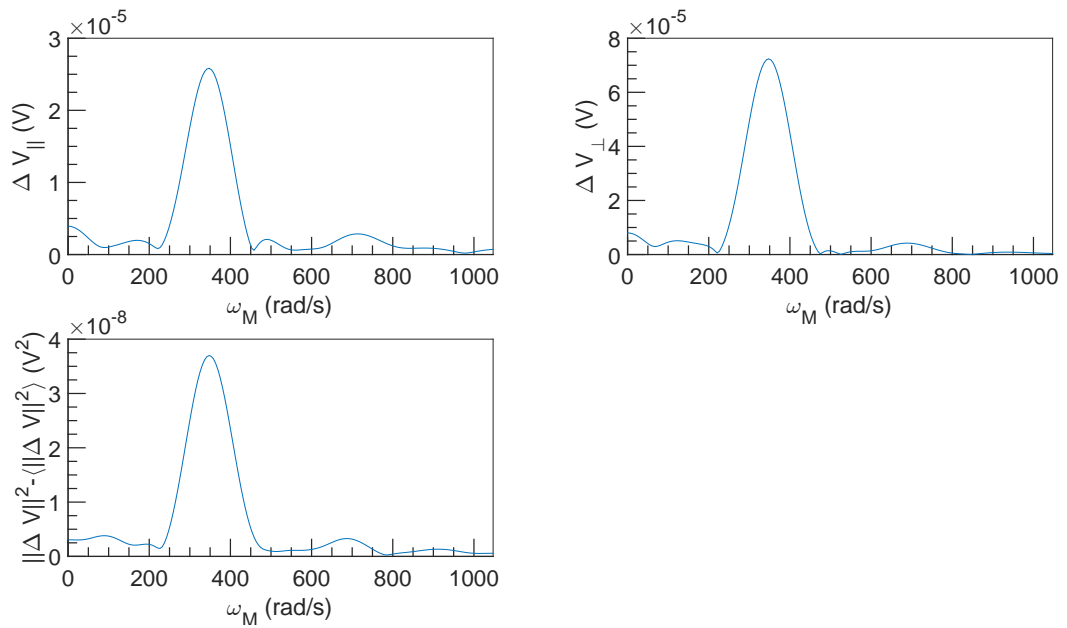


Figure 2.44: FFT spectral density of  $\Delta V$  vs  $\omega_M$  at  $U = 1 \text{ m s}^{-1}$ ,  $\omega = 9425 \text{ rad s}^{-1}$  and  $\alpha = 0.3 \%$ .

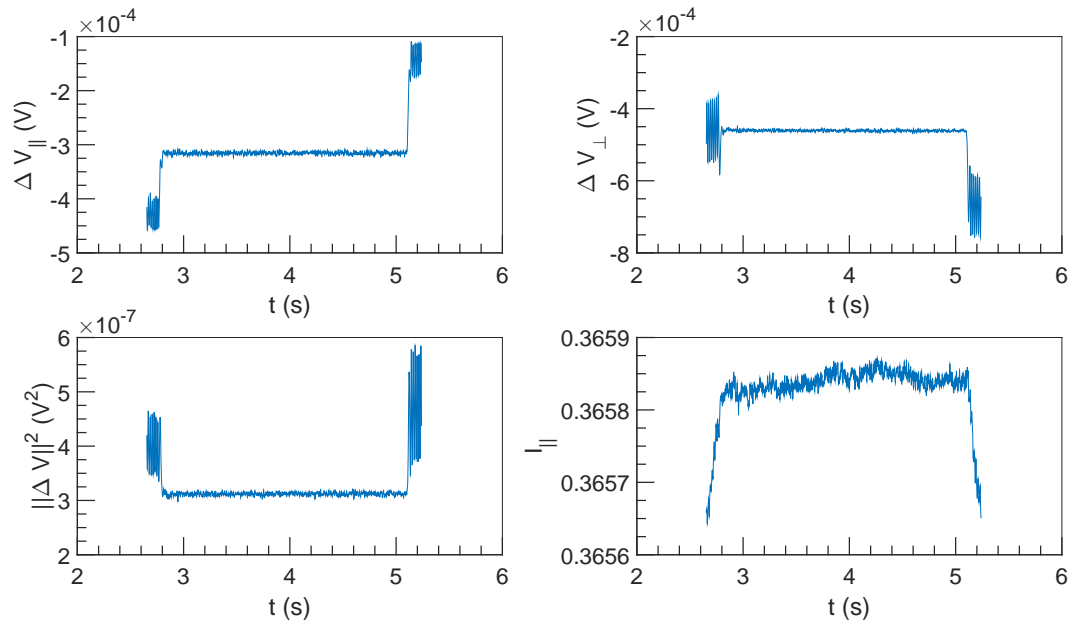


Figure 2.45:  $\Delta V$  and  $I$  vs  $t$  at  $U = 1 \text{ m s}^{-1}$ ,  $\omega = 10\,996 \text{ rad s}^{-1}$  and  $\alpha = 0.3\%$ .

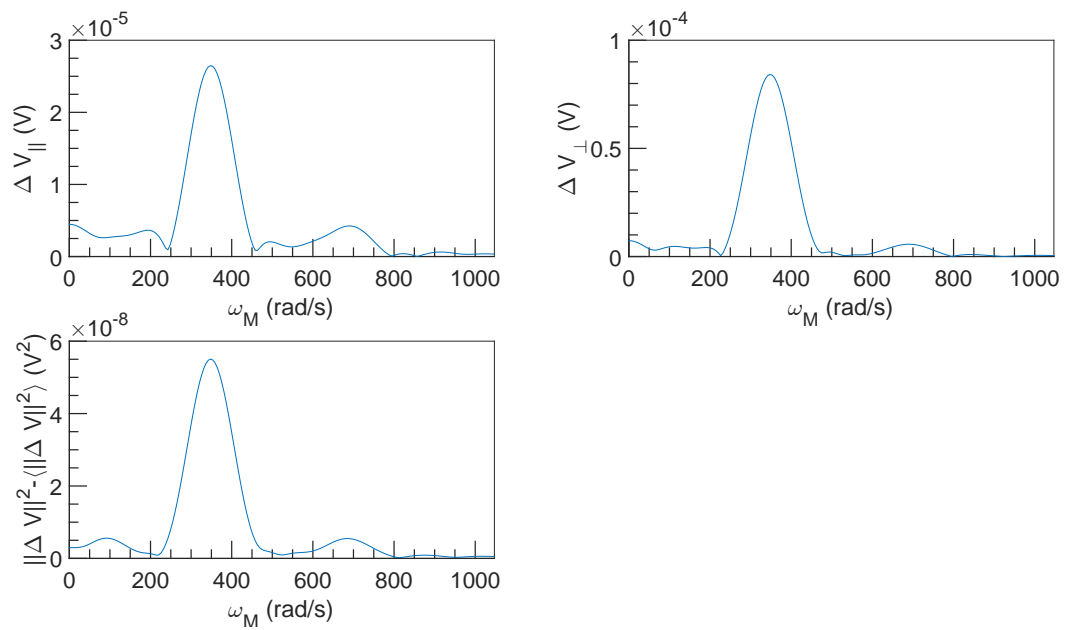


Figure 2.46: FFT spectral density of  $\Delta V$  vs  $\omega_M$  at  $U = 1 \text{ m s}^{-1}$ ,  $\omega = 10\,996 \text{ rad s}^{-1}$  and  $\alpha = 0.3\%$ .

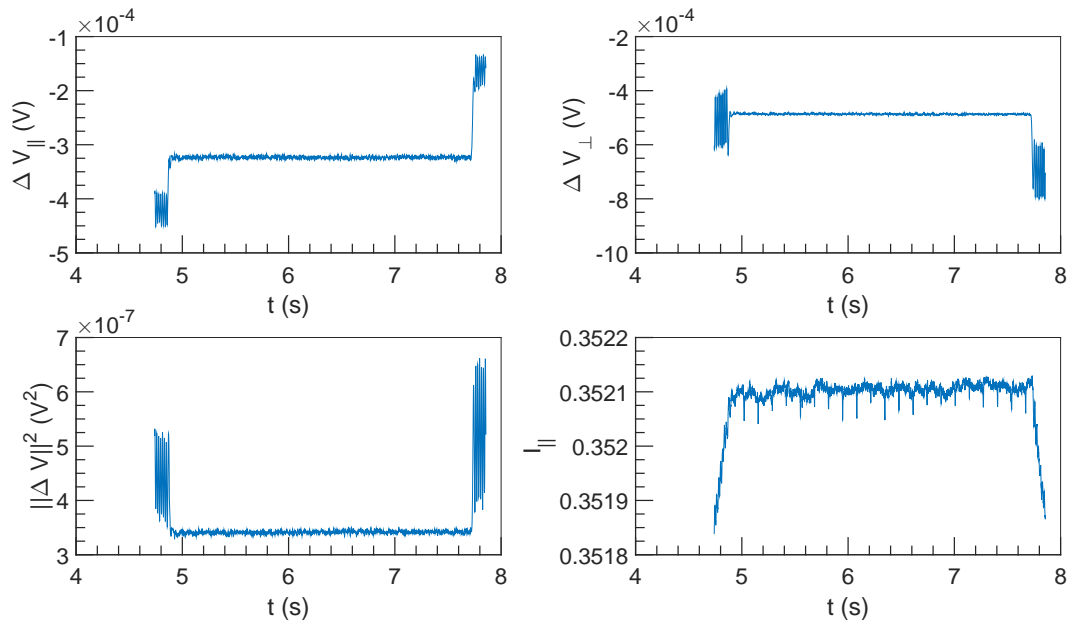


Figure 2.47:  $\Delta V$  and  $I$  vs  $t$  at  $U = 1 \text{ m s}^{-1}$ ,  $\omega = 12\,566 \text{ rad s}^{-1}$  and  $\alpha = 0.3\%$ .

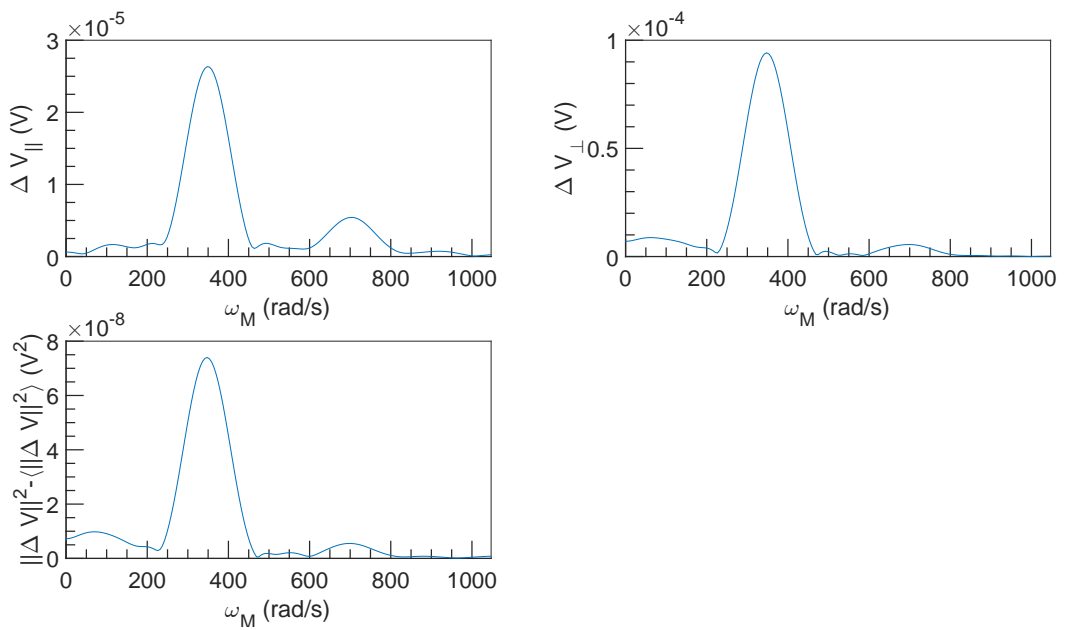


Figure 2.48: FFT spectral density of  $\Delta V$  vs  $\omega_M$  at  $U = 1 \text{ m s}^{-1}$ ,  $\omega = 12\,566 \text{ rad s}^{-1}$  and  $\alpha = 0.3\%$ .



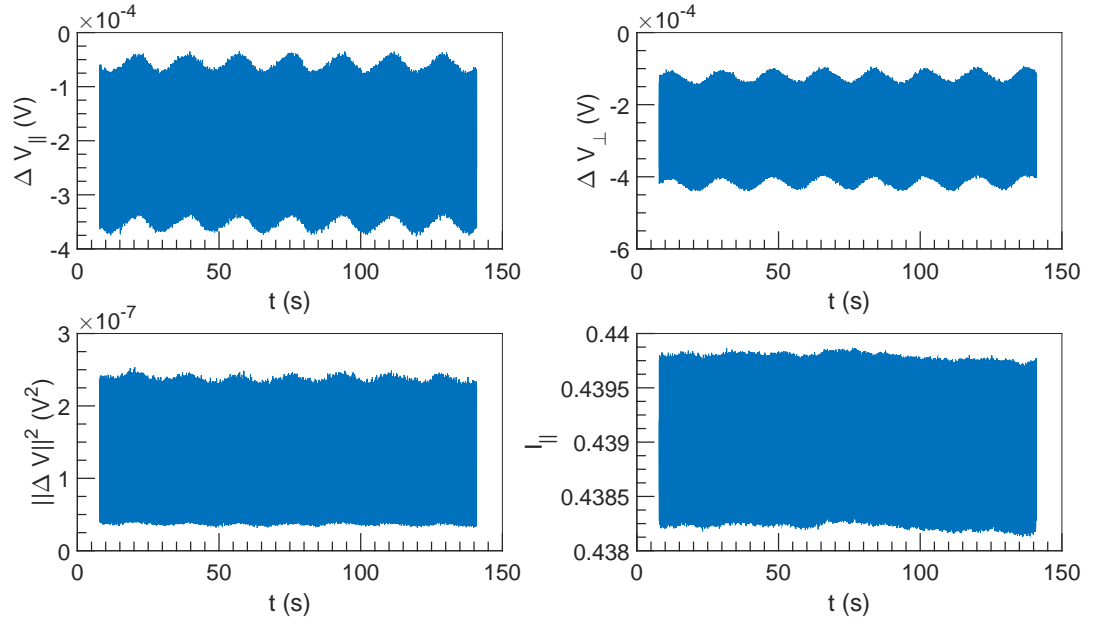


Figure 2.49:  $\Delta V$  and  $I$  vs  $t$  at  $U = 10^{-3} \text{ m s}^{-1}$ ,  $\omega = 3142 \text{ rad s}^{-1}$  and  $\alpha = 0.3\%$ .

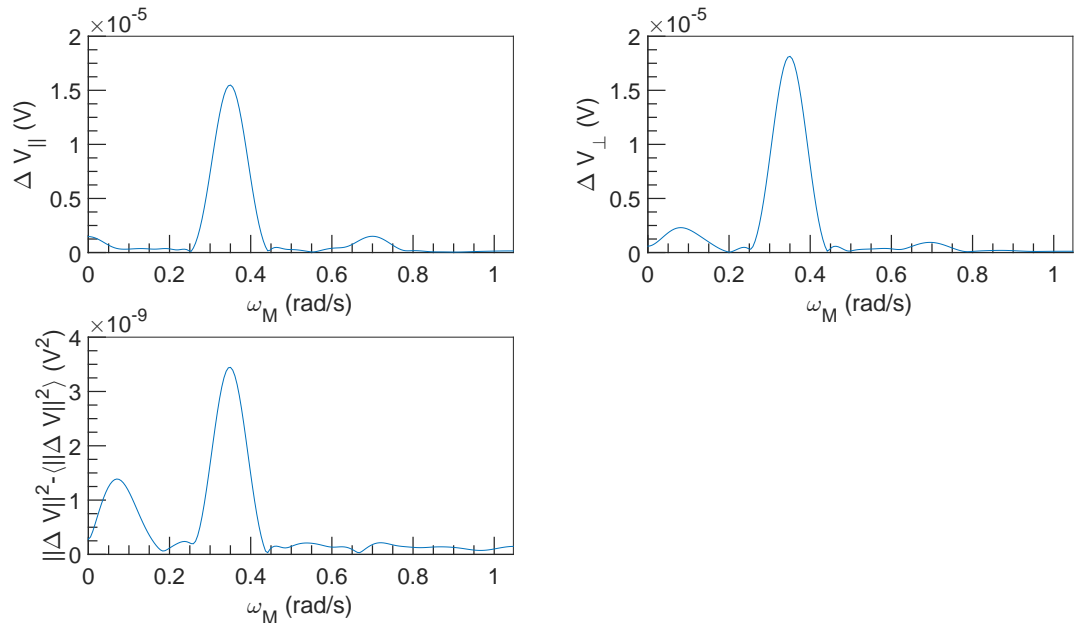


Figure 2.50: FFT spectral density of  $\Delta V$  vs  $\omega_M$  at  $U = 10^{-3} \text{ m s}^{-1}$ ,  $\omega = 3142 \text{ rad s}^{-1}$  and  $\alpha = 0.3\%$ .

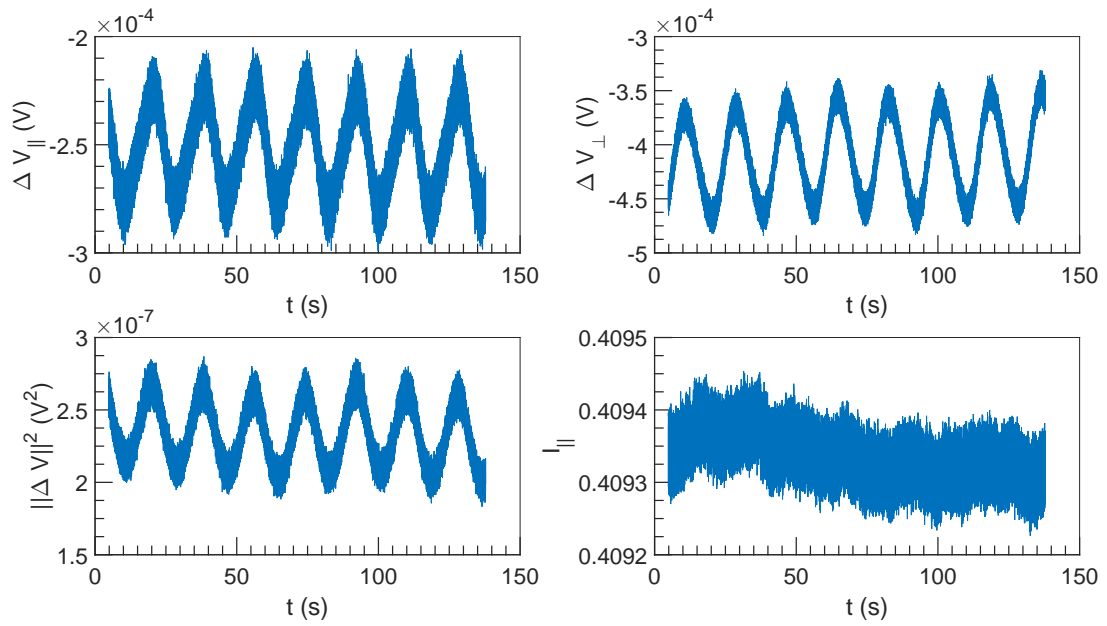


Figure 2.51:  $\Delta V$  and  $I$  vs  $t$  at  $U = 10^{-3} \text{ m s}^{-1}$ ,  $\omega = 6283 \text{ rad s}^{-1}$  and  $\alpha = 0.3\%$ .

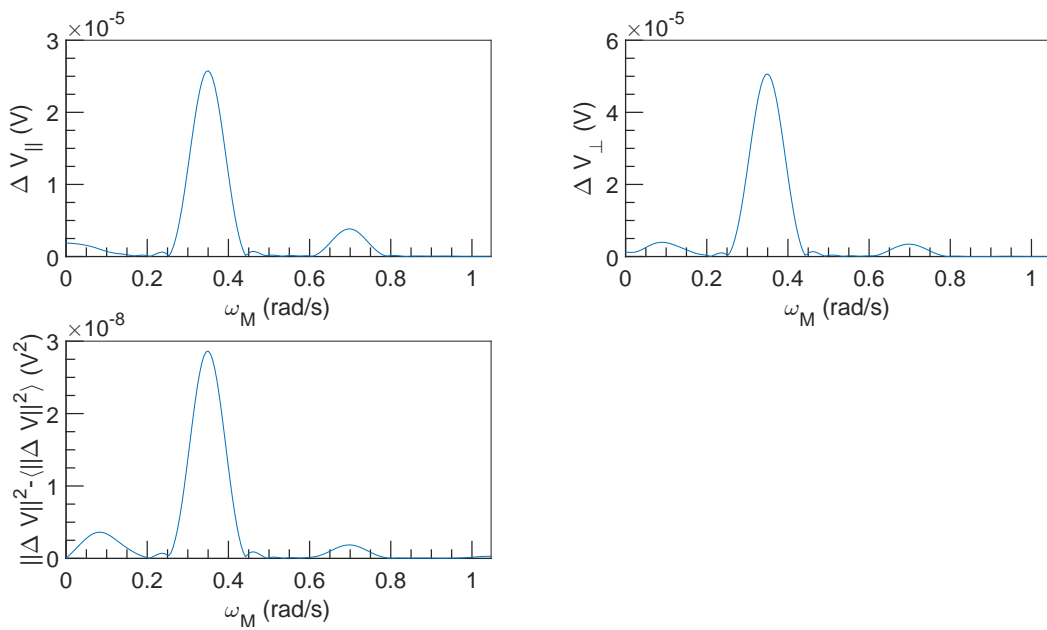


Figure 2.52: FFT spectral density of  $\Delta V$  vs  $\omega_M$  at  $U = 10^{-3} \text{ m s}^{-1}$ ,  $\omega = 6283 \text{ rad s}^{-1}$  and  $\alpha = 0.3\%$ .

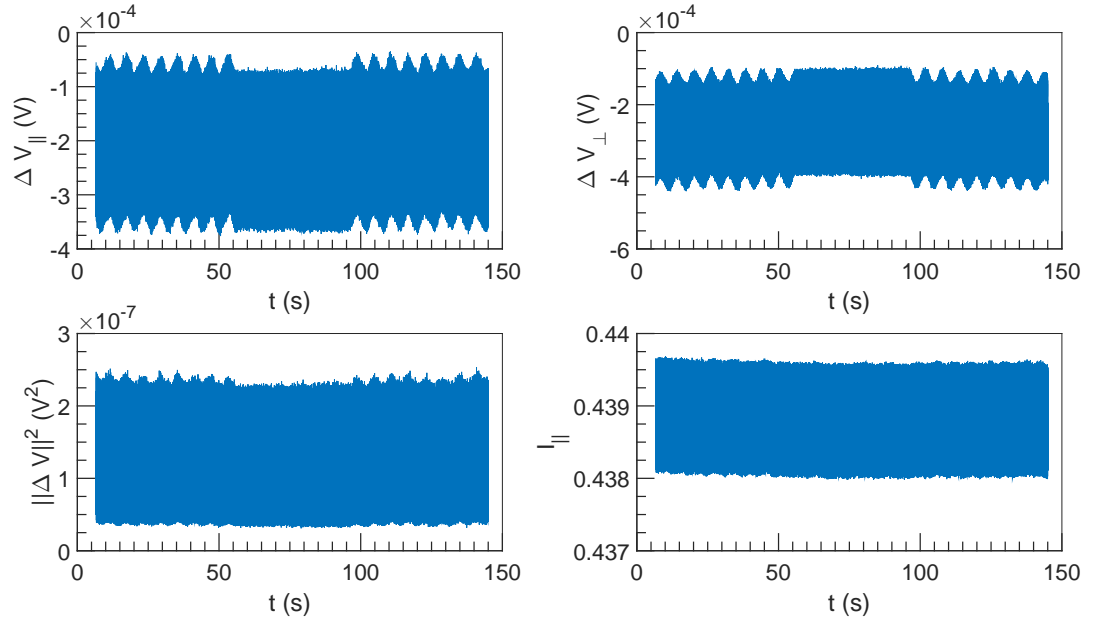


Figure 2.53:  $\Delta V$  and  $I$  vs  $t$  at  $U = 3 \times 10^{-3} \text{ m s}^{-1}$ ,  $\omega = 3142 \text{ rad s}^{-1}$  and  $\alpha = 0.3\%$ .

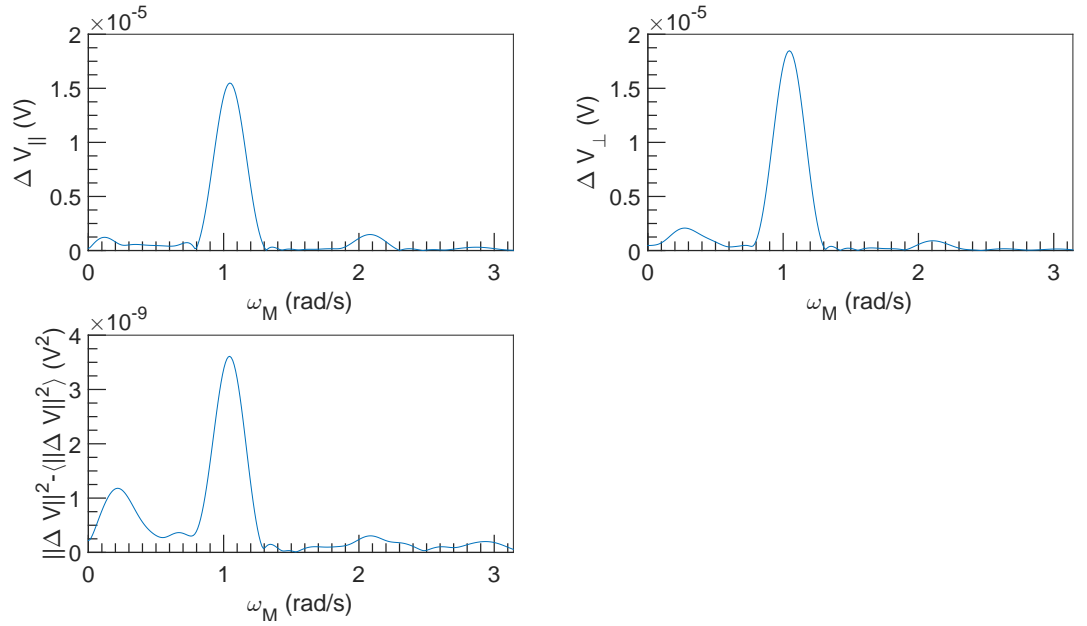


Figure 2.54: FFT spectral density of  $\Delta V$  vs  $\omega_M$  at  $U = 3 \times 10^{-3} \text{ m s}^{-1}$ ,  $\omega = 3142 \text{ rad s}^{-1}$  and  $\alpha = 0.3\%$ .

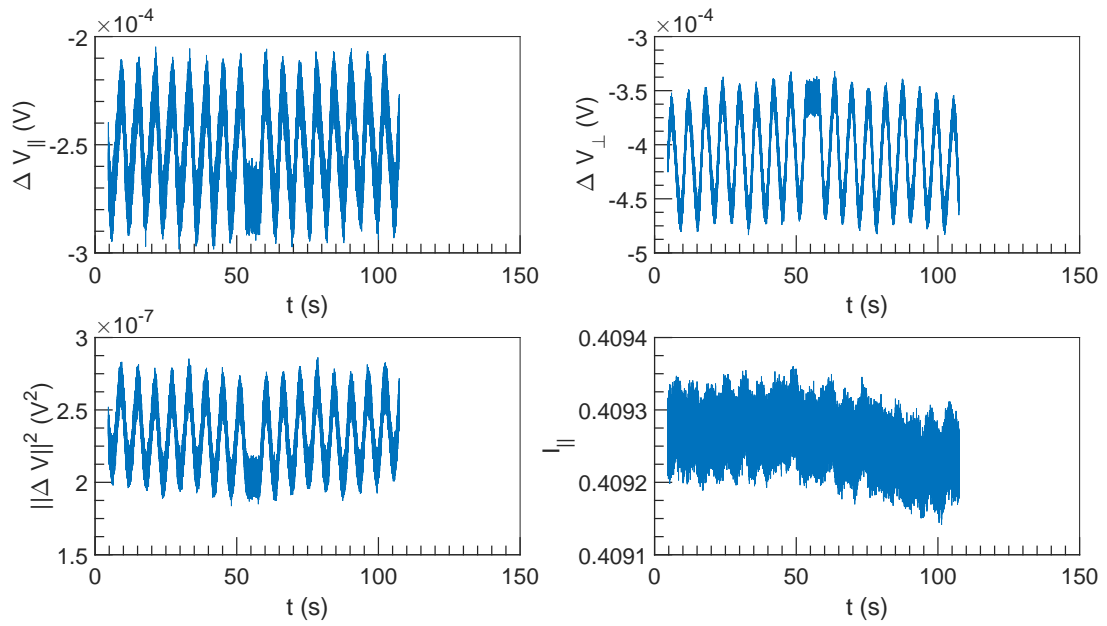


Figure 2.55:  $\Delta V$  and  $I$  vs  $t$  at  $U = 3 \times 10^{-3} \text{ m s}^{-1}$ ,  $\omega = 6283 \text{ rad s}^{-1}$  and  $\alpha = 0.3\%$ .

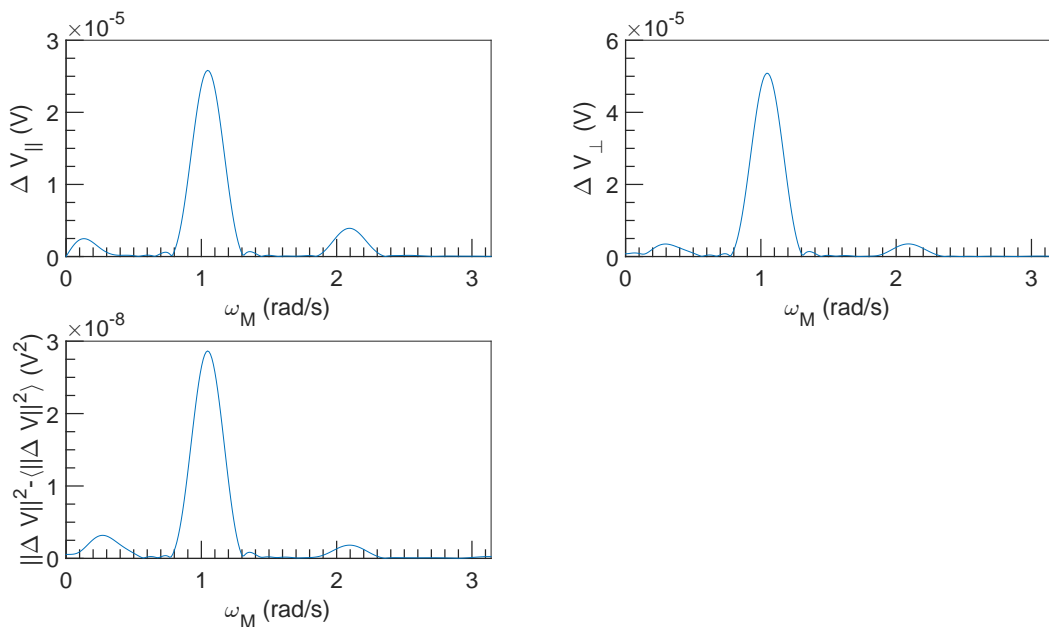


Figure 2.56: FFT spectral density of  $\Delta V$  vs  $\omega_M$  at  $U = 3 \times 10^{-3} \text{ m s}^{-1}$ ,  $\omega = 6283 \text{ rad s}^{-1}$  and  $\alpha = 0.3\%$ .

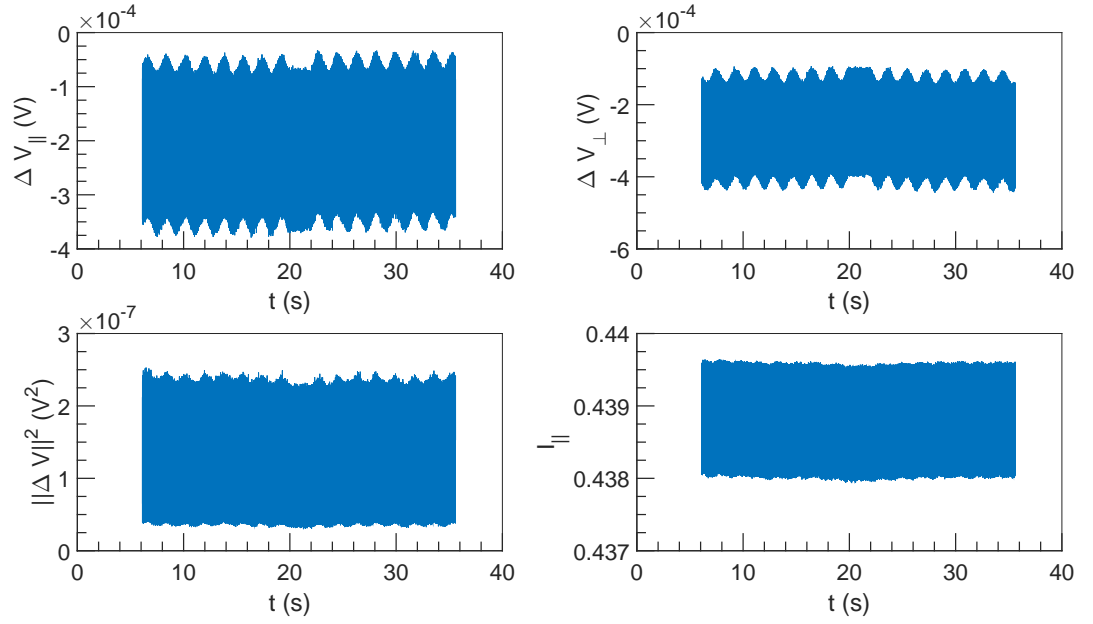


Figure 2.57:  $\Delta V$  and  $I$  vs  $t$  at  $U = 10^{-2} \text{ m s}^{-1}$ ,  $\omega = 3142 \text{ rad s}^{-1}$  and  $\alpha = 0.3\%$ .

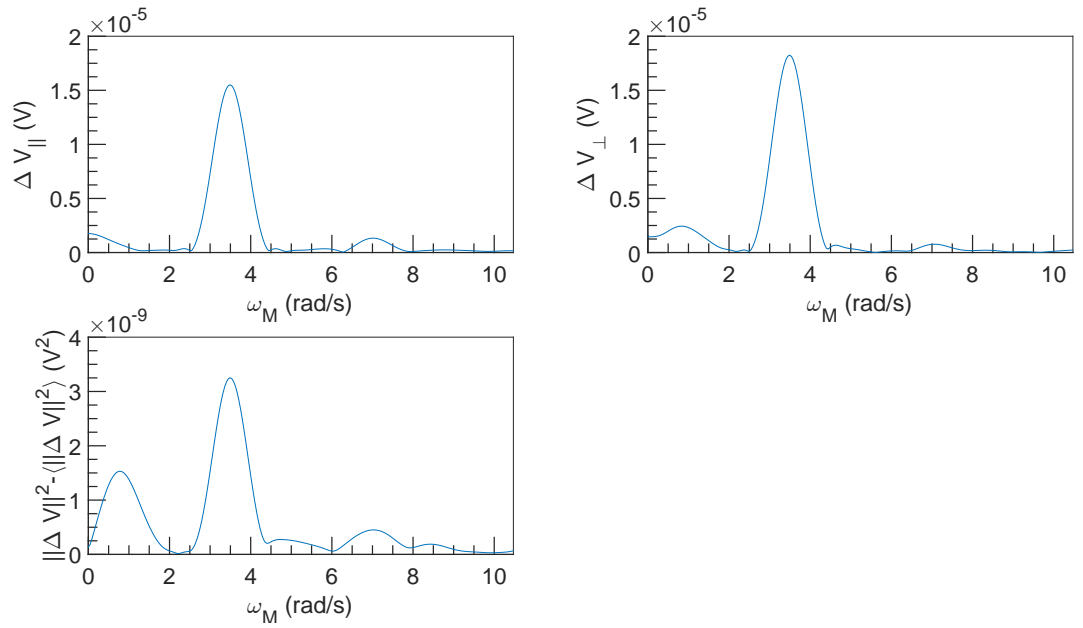


Figure 2.58: FFT spectral density of  $\Delta V$  vs  $\omega_M$  at  $U = 10^{-2} \text{ m s}^{-1}$ ,  $\omega = 3142 \text{ rad s}^{-1}$  and  $\alpha = 0.3\%$ .

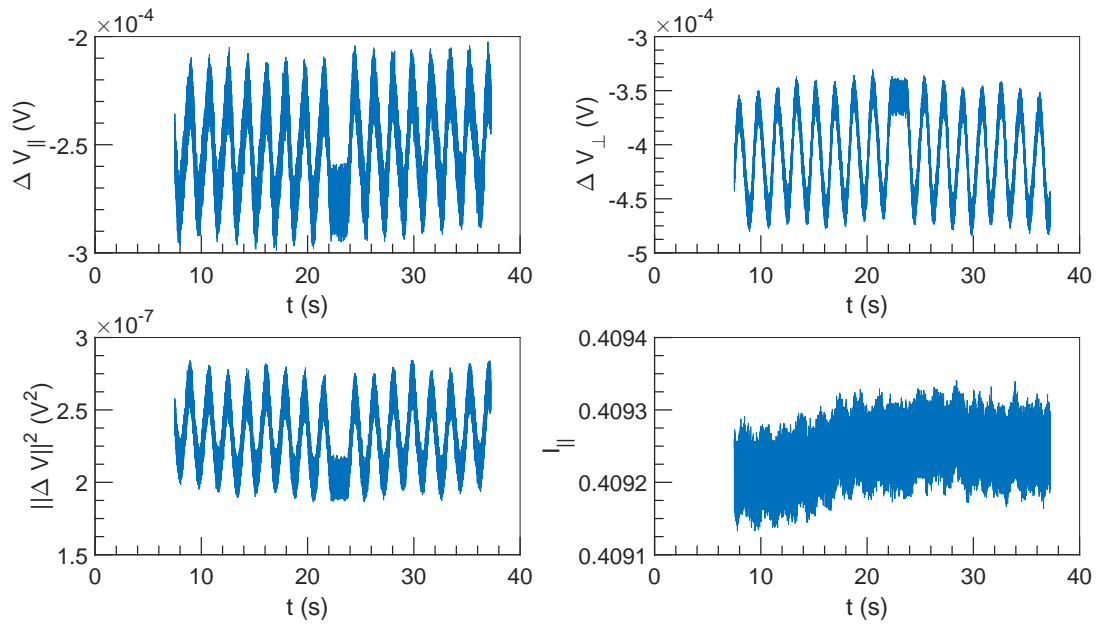


Figure 2.59:  $\Delta V$  and  $I$  vs  $t$  at  $U = 10^{-2} \text{ m s}^{-1}$ ,  $\omega = 6283 \text{ rad s}^{-1}$  and  $\alpha = 0.3\%$ .

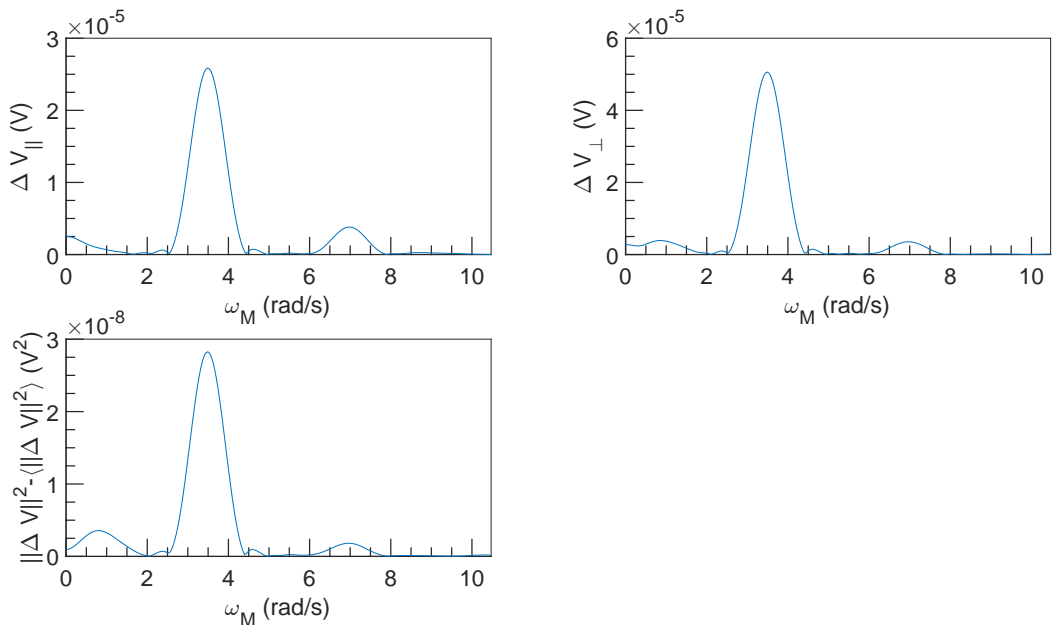


Figure 2.60: FFT spectral density of  $\Delta V$  vs  $\omega_M$  at  $U = 10^{-2} \text{ m s}^{-1}$ ,  $\omega = 6283 \text{ rad s}^{-1}$  and  $\alpha = 0.3\%$ .

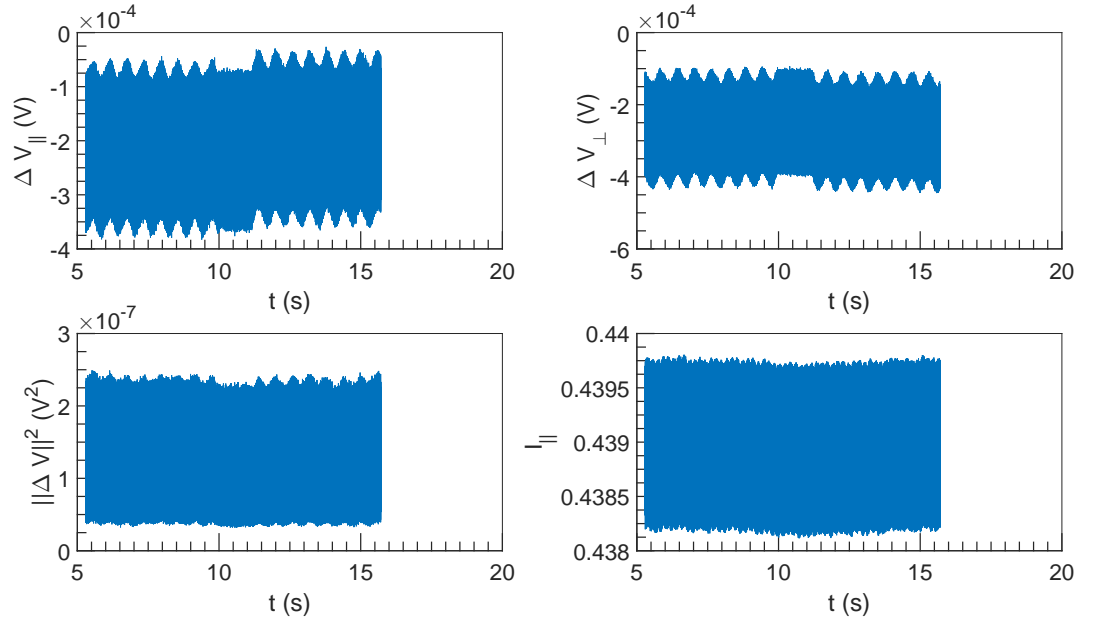


Figure 2.61:  $\Delta V$  and  $I$  vs  $t$  at  $U = 3 \times 10^{-2} \text{ m s}^{-1}$ ,  $\omega = 3142 \text{ rad s}^{-1}$  and  $\alpha = 0.3\%$ .

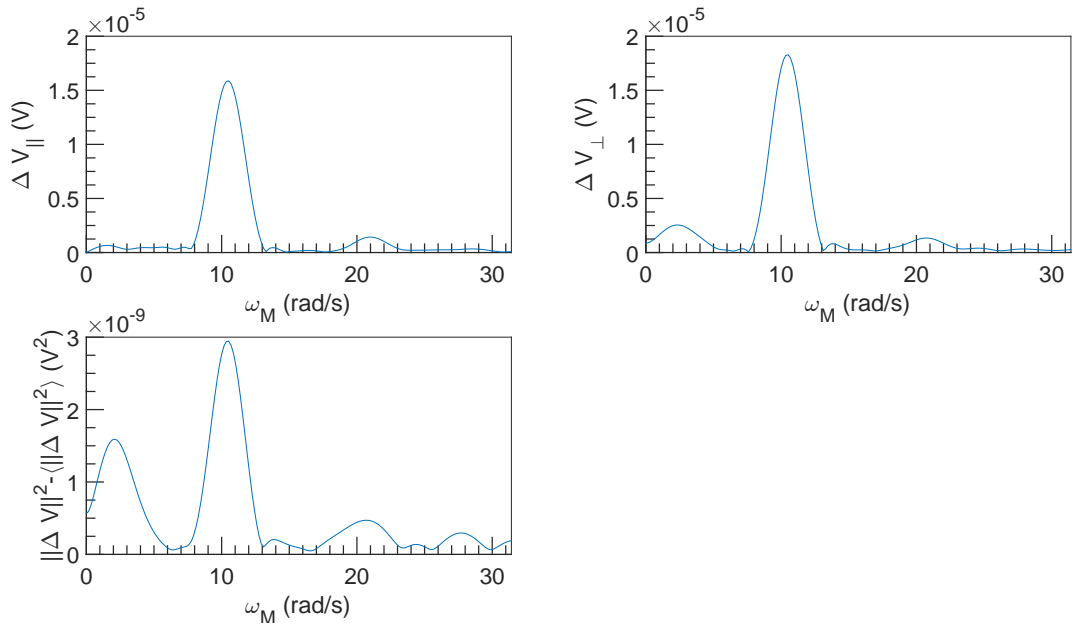


Figure 2.62: FFT spectral density of  $\Delta V$  vs  $\omega_M$  at  $U = 3 \times 10^{-2} \text{ m s}^{-1}$ ,  $\omega = 3142 \text{ rad s}^{-1}$  and  $\alpha = 0.3\%$ .

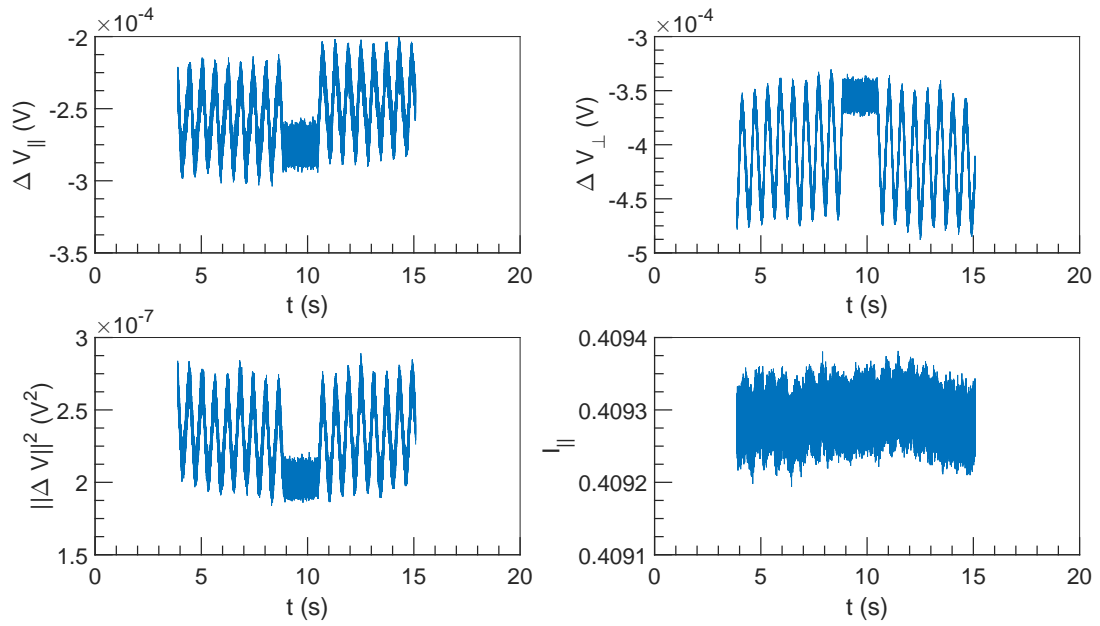


Figure 2.63:  $\Delta V$  and  $I$  vs  $t$  at  $U = 3 \times 10^{-2} \text{ m s}^{-1}$ ,  $\omega = 6283 \text{ rad s}^{-1}$  and  $\alpha = 0.3\%$ .

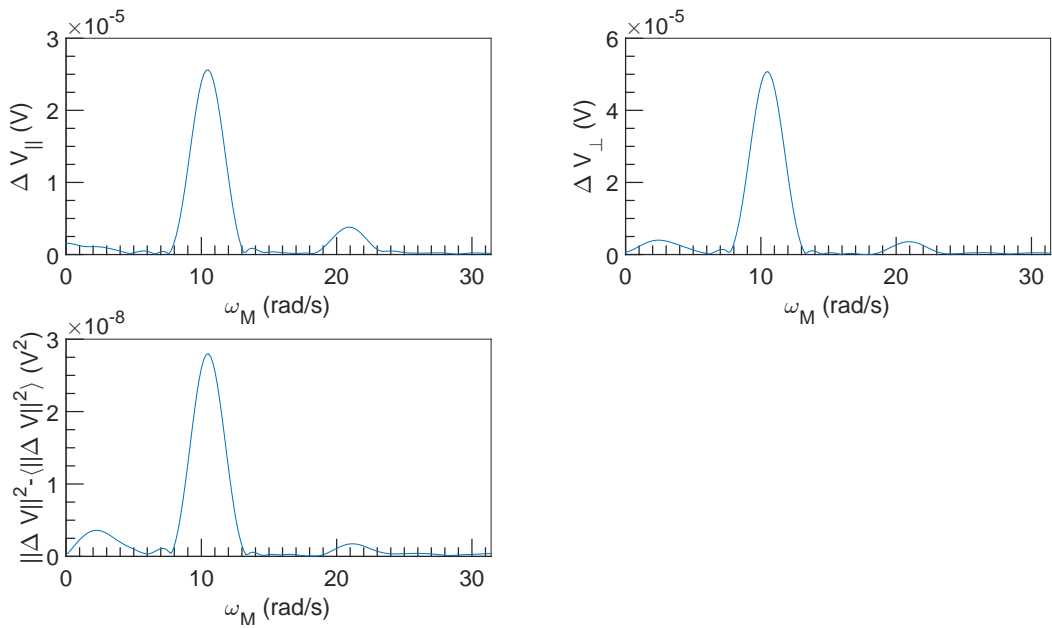


Figure 2.64: FFT spectral density of  $\Delta V$  vs  $\omega_M$  at  $U = 3 \times 10^{-2} \text{ m s}^{-1}$ ,  $\omega = 6283 \text{ rad s}^{-1}$  and  $\alpha = 0.3\%$ .



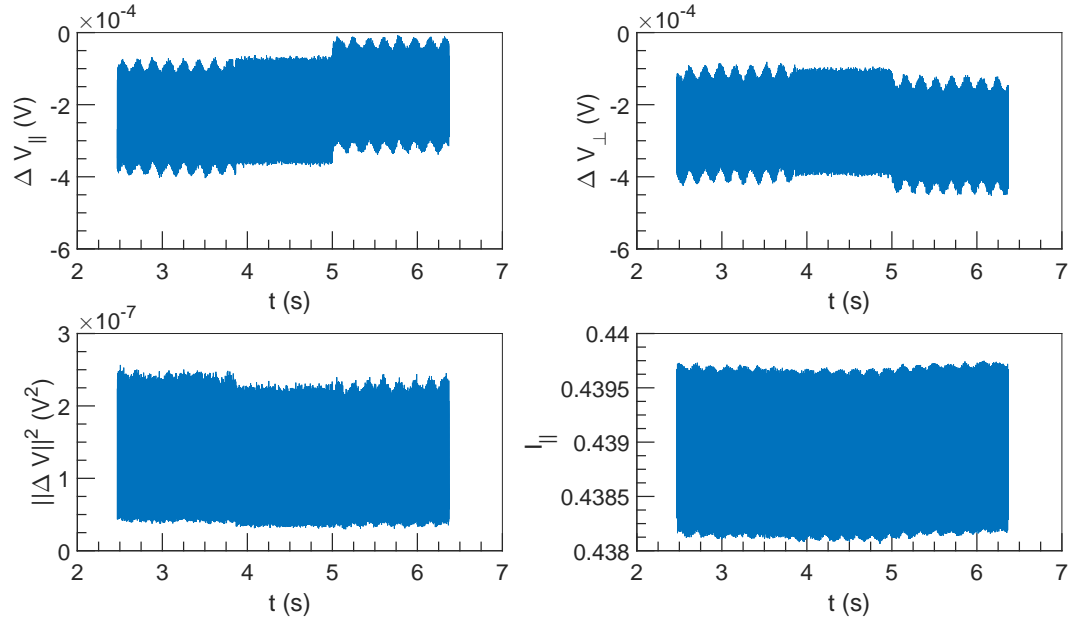


Figure 2.65:  $\Delta V$  and  $I$  vs  $t$  at  $U = 0.1 \text{ m s}^{-1}$ ,  $\omega = 3142 \text{ rad s}^{-1}$  and  $\alpha = 0.3 \%$ .

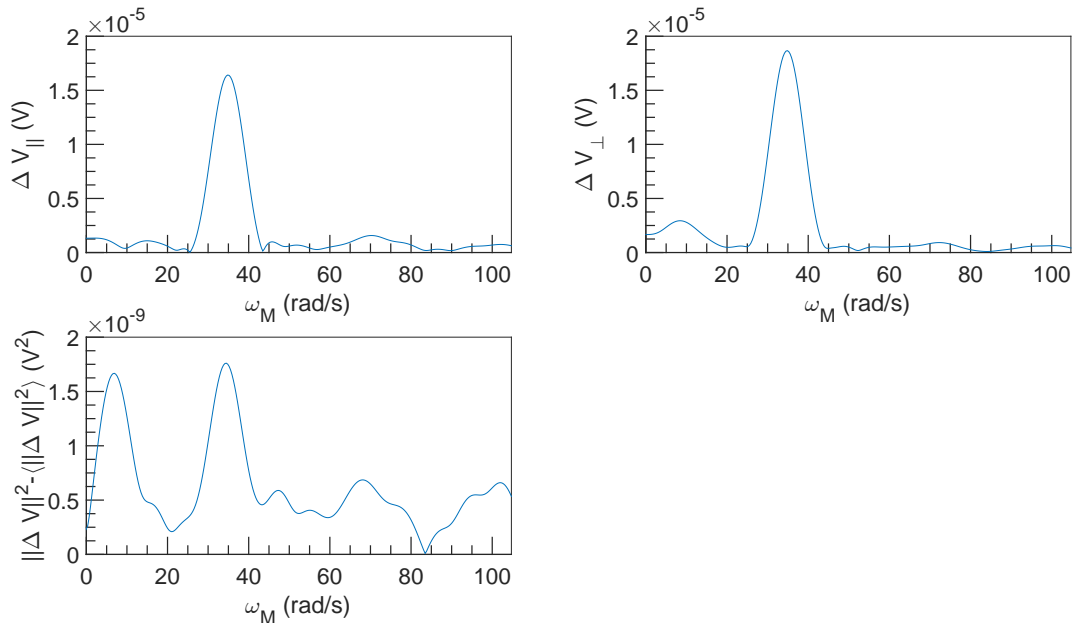


Figure 2.66: FFT spectral density of  $\Delta V$  vs  $\omega_M$  at  $U = 0.1 \text{ m s}^{-1}$ ,  $\omega = 3142 \text{ rad s}^{-1}$  and  $\alpha = 0.3 \%$ .

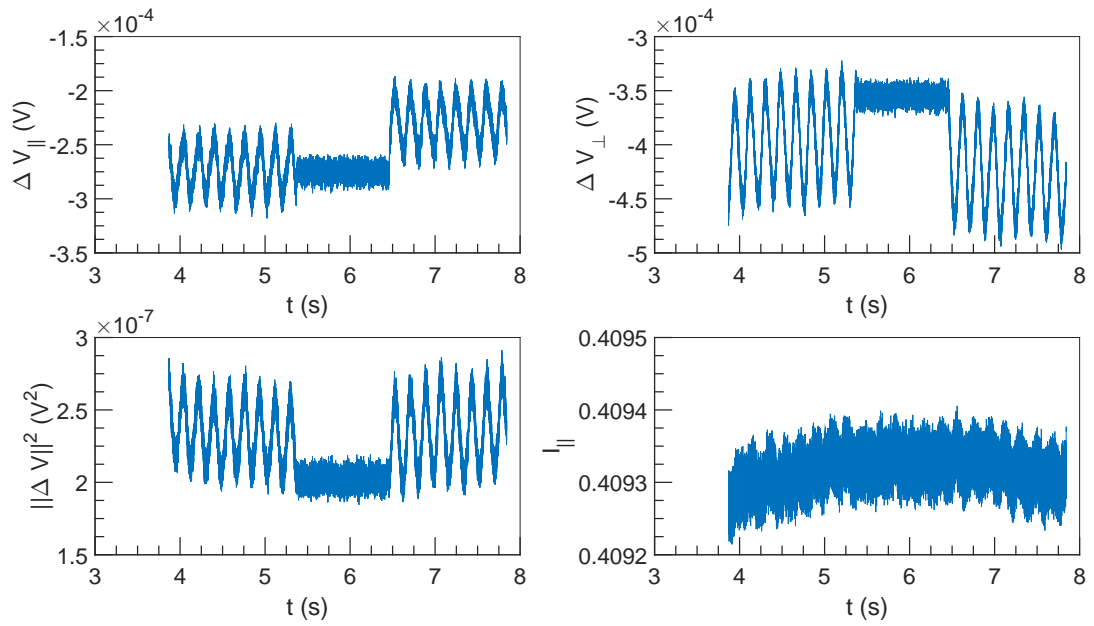


Figure 2.67:  $\Delta V$  and  $I$  vs  $t$  at  $U = 0.1 \text{ m s}^{-1}$ ,  $\omega = 6283 \text{ rad s}^{-1}$  and  $\alpha = 0.3 \%$ .

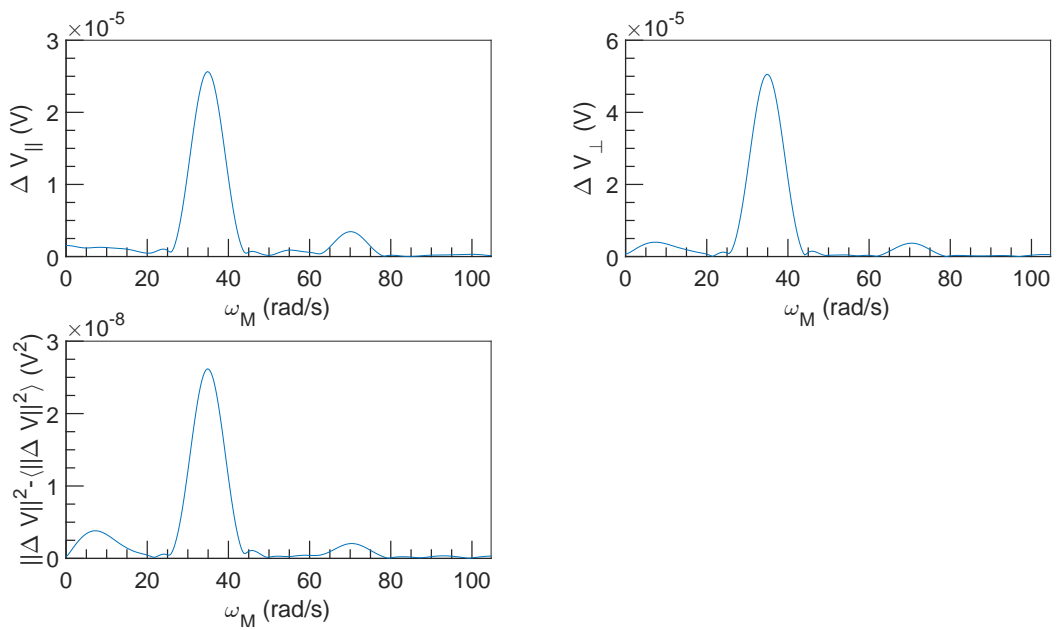


Figure 2.68: FFT spectral density of  $\Delta V$  vs  $\omega_M$  at  $U = 0.1 \text{ m s}^{-1}$ ,  $\omega = 6283 \text{ rad s}^{-1}$  and  $\alpha = 0.3 \%$ .

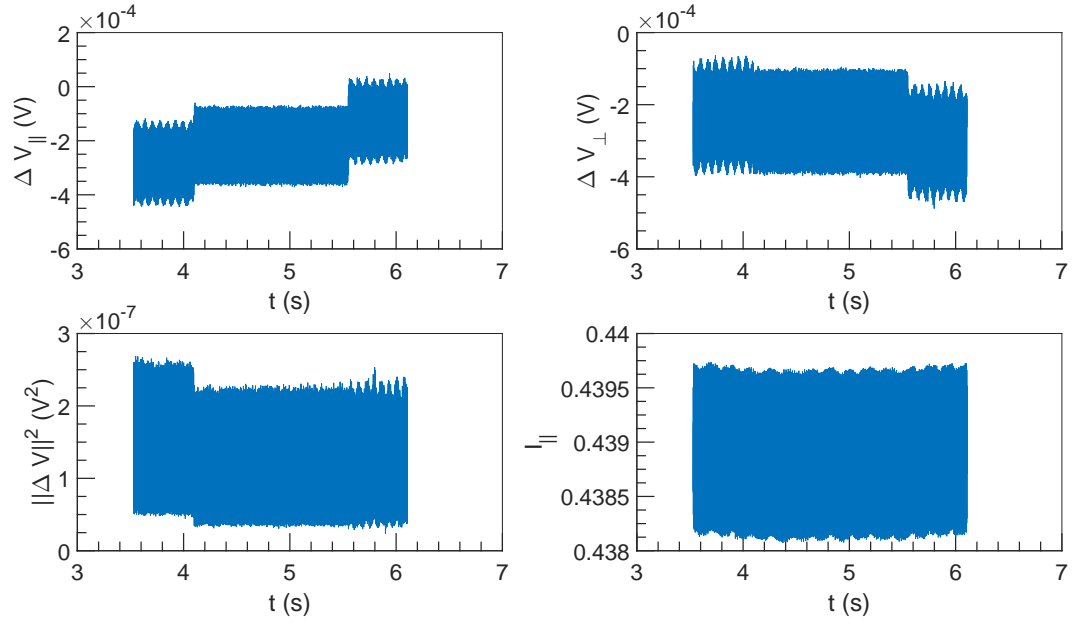


Figure 2.69:  $\Delta V$  and  $I$  vs  $t$  at  $U = 0.25 \text{ ms}^{-1}$ ,  $\omega = 3142 \text{ rad s}^{-1}$  and  $\alpha = 0.3\%$ .

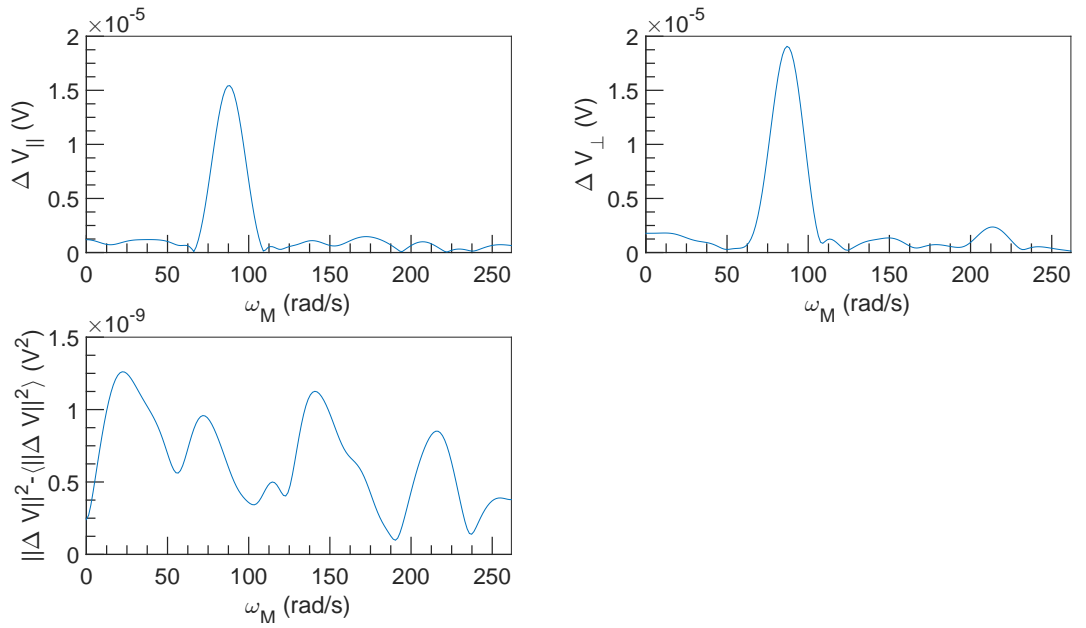


Figure 2.70: FFT spectral density of  $\Delta V$  vs  $\omega_M$  at  $U = 0.25 \text{ ms}^{-1}$ ,  $\omega = 3142 \text{ rad s}^{-1}$  and  $\alpha = 0.3\%$ .

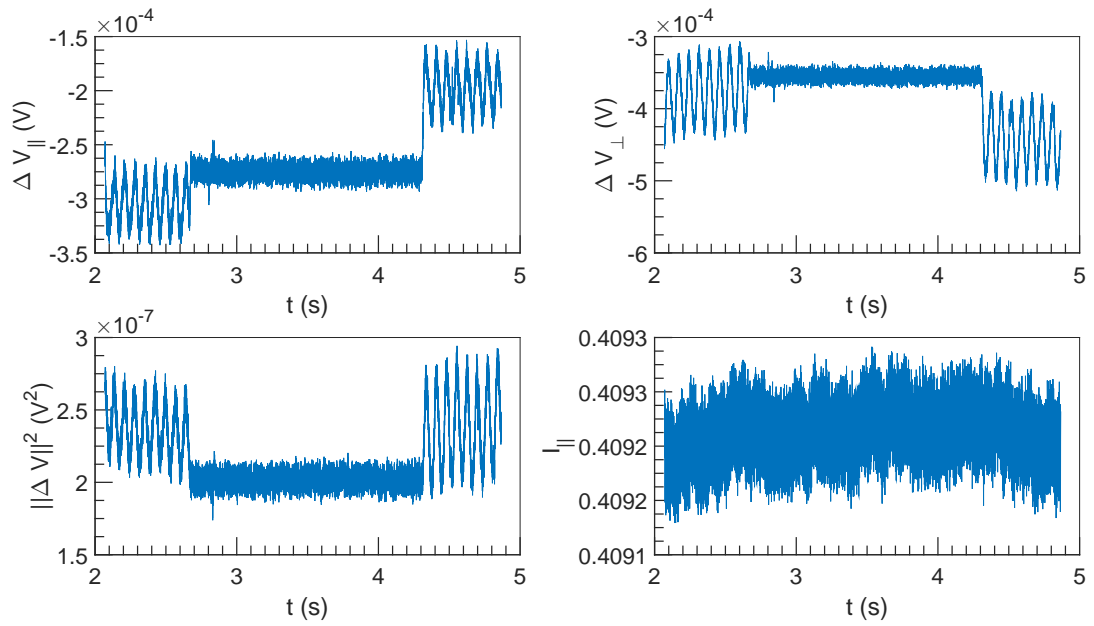


Figure 2.71:  $\Delta V$  and  $I$  vs  $t$  at  $U = 0.25 \text{ m s}^{-1}$ ,  $\omega = 6283 \text{ rad s}^{-1}$  and  $\alpha = 0.3\%$ .

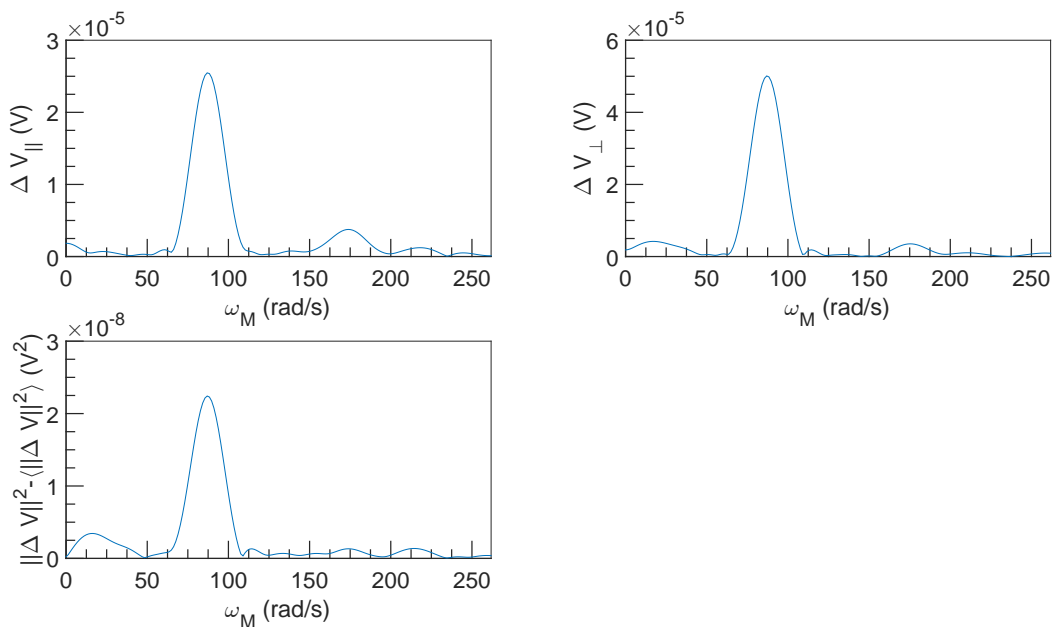


Figure 2.72: FFT spectral density of  $\Delta V$  vs  $\omega_M$  at  $U = 0.25 \text{ m s}^{-1}$ ,  $\omega = 6283 \text{ rad s}^{-1}$  and  $\alpha = 0.3\%$ .

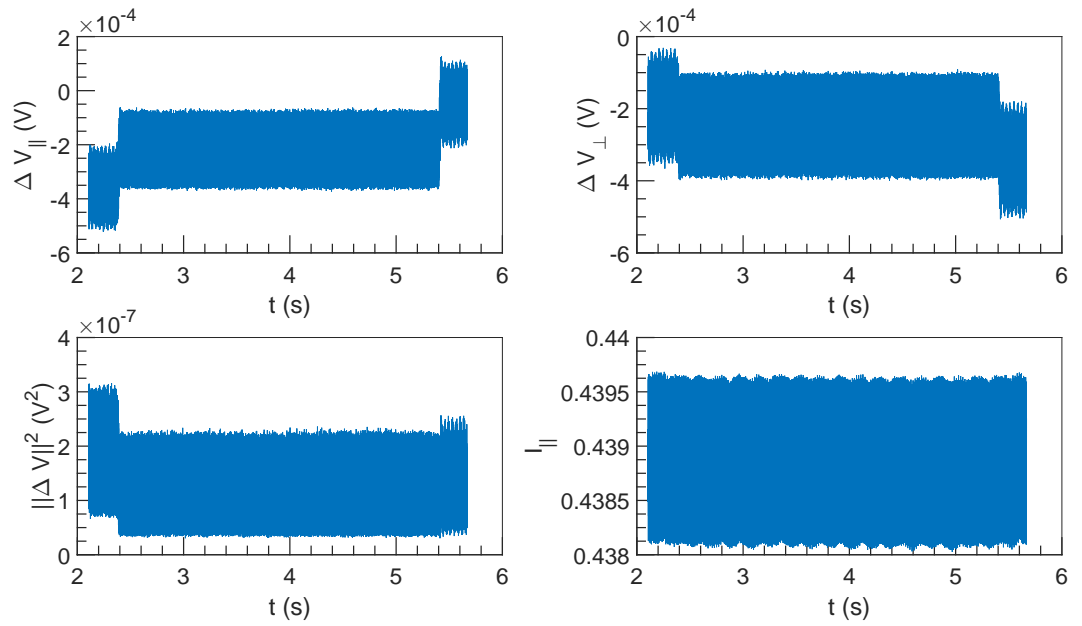


Figure 2.73:  $\Delta V$  and  $I$  vs  $t$  at  $U = 0.5 \text{ m s}^{-1}$ ,  $\omega = 3142 \text{ rad s}^{-1}$  and  $\alpha = 0.3 \%$ .

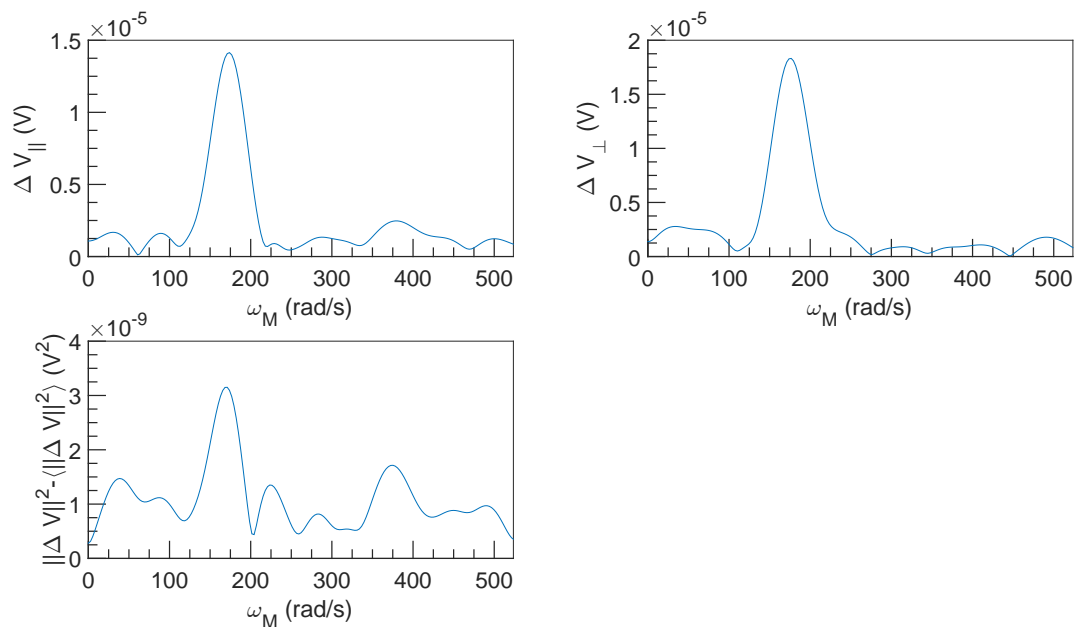


Figure 2.74: FFT spectral density of  $\Delta V$  vs  $\omega_M$  at  $U = 0.5 \text{ m s}^{-1}$ ,  $\omega = 3142 \text{ rad s}^{-1}$  and  $\alpha = 0.3 \%$ .

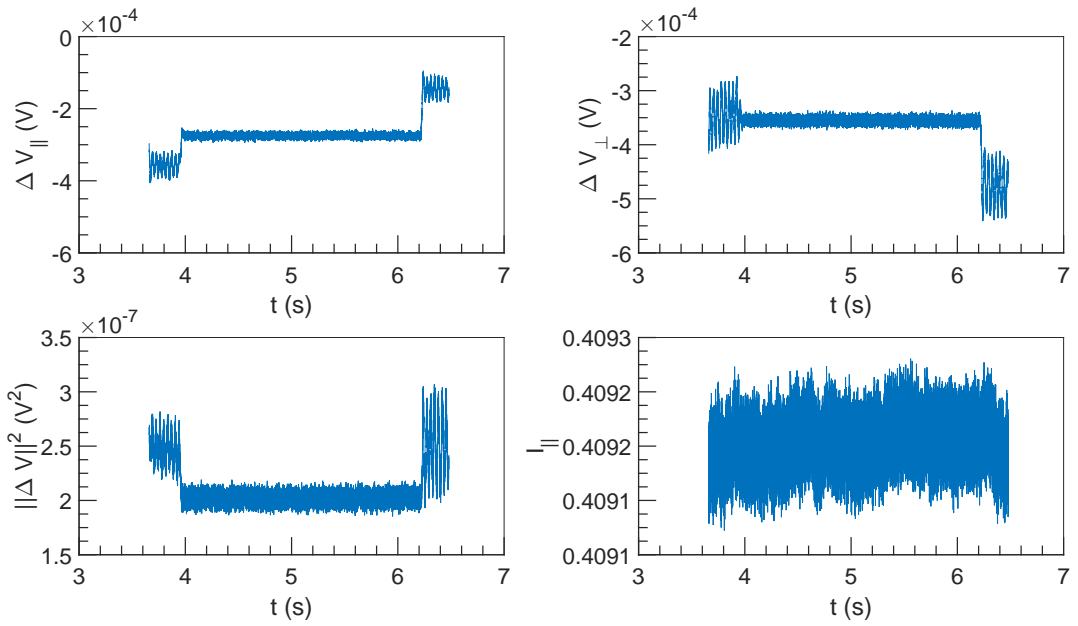


Figure 2.75:  $\Delta V$  and  $I$  vs  $t$  at  $U = 0.5 \text{ m s}^{-1}$ ,  $\omega = 6283 \text{ rad s}^{-1}$  and  $\alpha = 0.3 \%$ .

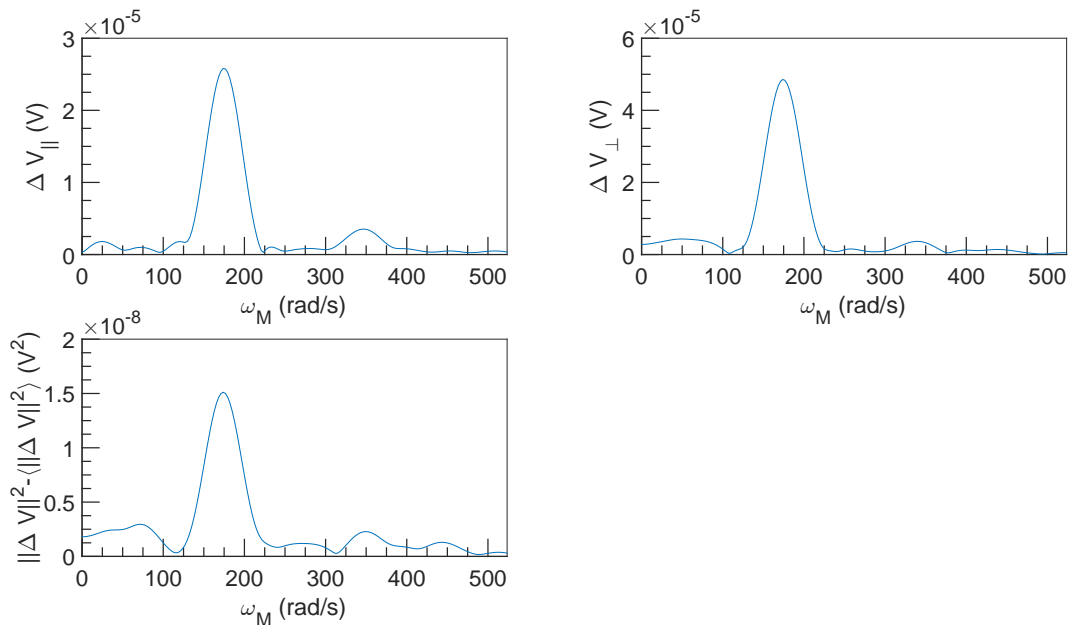


Figure 2.76: FFT spectral density of  $\Delta V$  vs  $\omega_M$  at  $U = 0.5 \text{ m s}^{-1}$ ,  $\omega = 6283 \text{ rad s}^{-1}$  and  $\alpha = 0.3 \%$ .

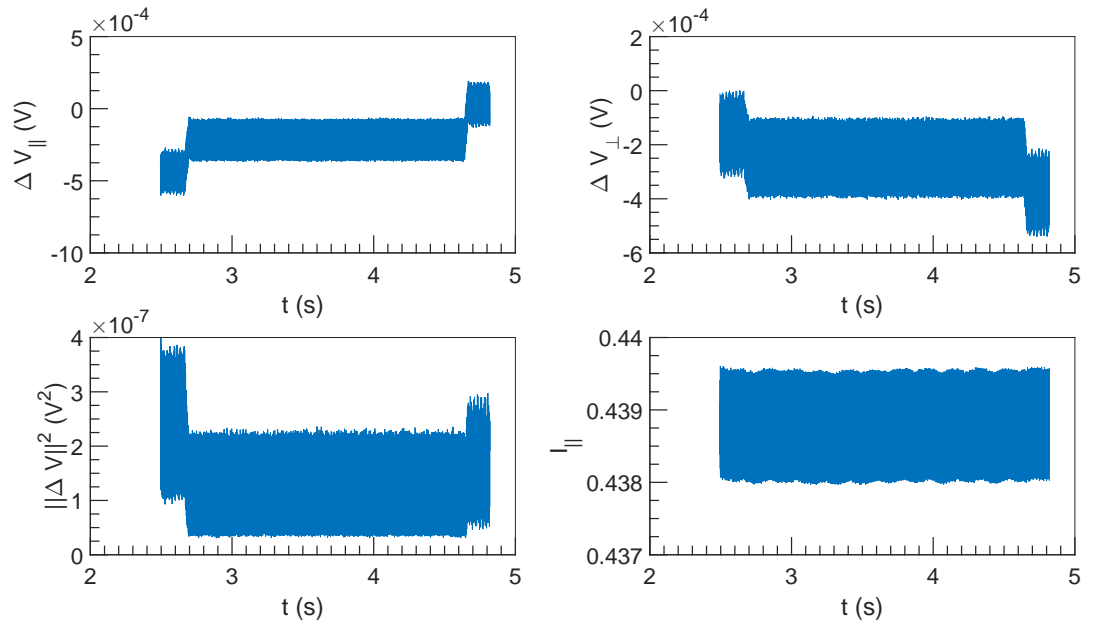


Figure 2.77:  $\Delta V$  and  $I$  vs  $t$  at  $U = 0.75 \text{ ms}^{-1}$ ,  $\omega = 3142 \text{ rad s}^{-1}$  and  $\alpha = 0.3\%$ .

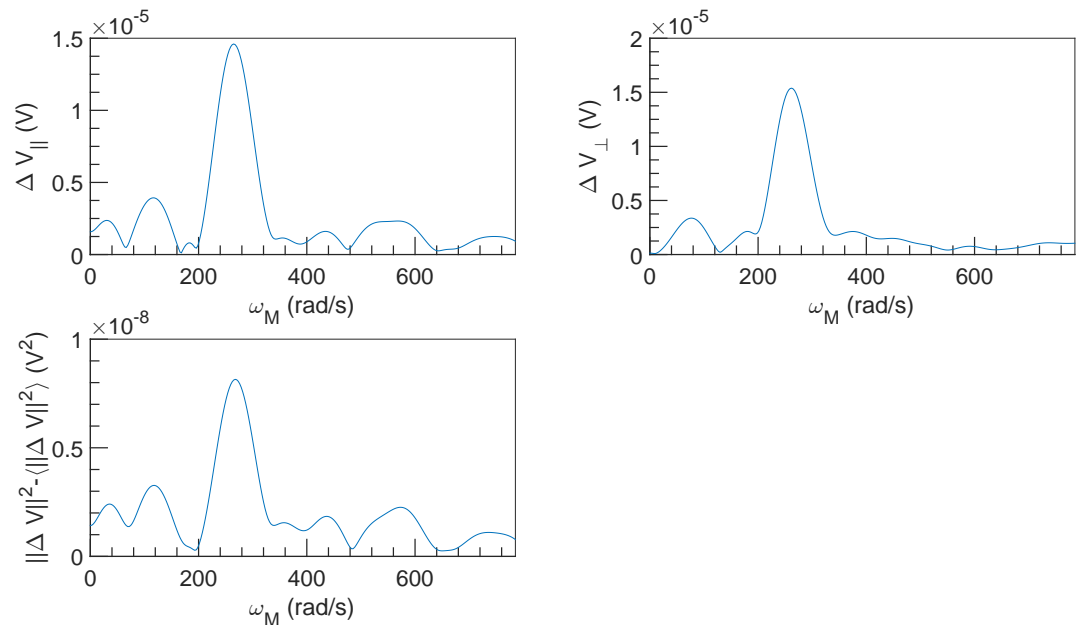


Figure 2.78: FFT spectral density of  $\Delta V$  vs  $\omega_M$  at  $U = 0.75 \text{ ms}^{-1}$ ,  $\omega = 3142 \text{ rad s}^{-1}$  and  $\alpha = 0.3\%$ .

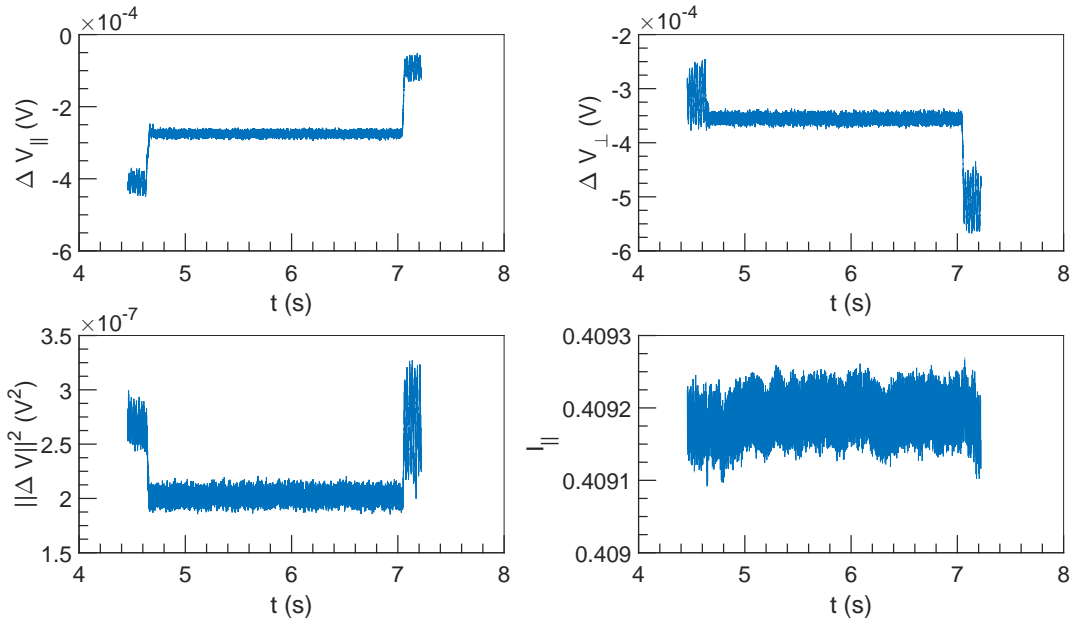


Figure 2.79:  $\Delta V$  and  $I$  vs  $t$  at  $U = 0.75 \text{ m s}^{-1}$ ,  $\omega = 6283 \text{ rad s}^{-1}$  and  $\alpha = 0.3\%$ .

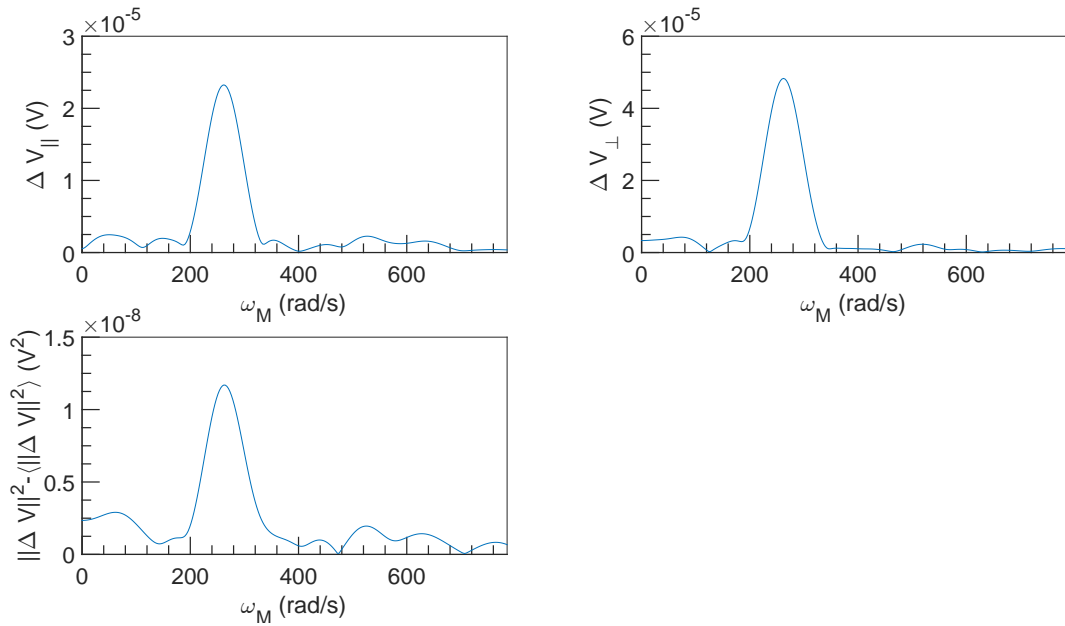


Figure 2.80: FFT spectral density of  $\Delta V$  vs  $\omega_M$  at  $U = 0.75 \text{ m s}^{-1}$ ,  $\omega = 6283 \text{ rad s}^{-1}$  and  $\alpha = 0.3\%$ .



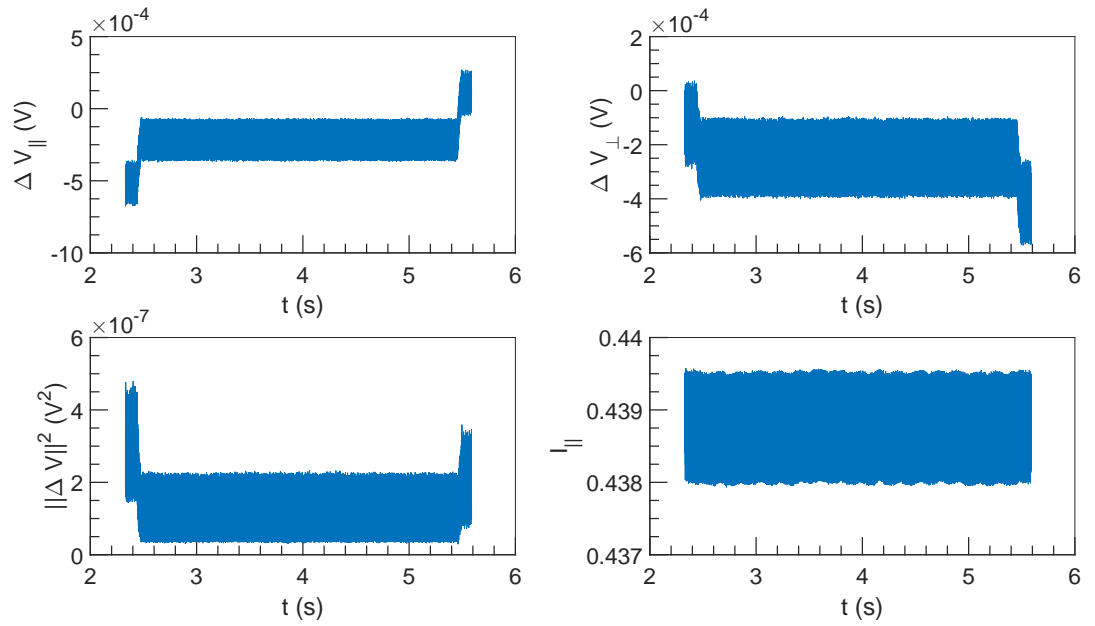


Figure 2.81:  $\Delta V$  and  $I$  vs  $t$  at  $U = 1 \text{ m s}^{-1}$ ,  $\omega = 3142 \text{ rad s}^{-1}$  and  $\alpha = 0.3\%$ .

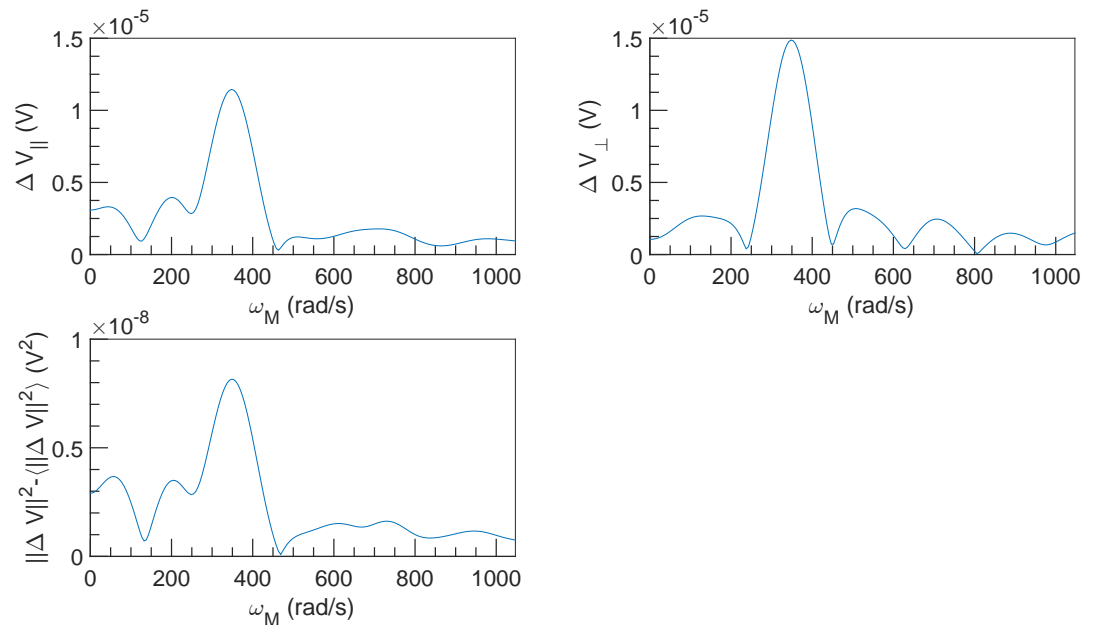


Figure 2.82: FFT spectral density of  $\Delta V$  vs  $\omega_M$  at  $U = 1 \text{ m s}^{-1}$ ,  $\omega = 3142 \text{ rad s}^{-1}$  and  $\alpha = 0.3\%$ .

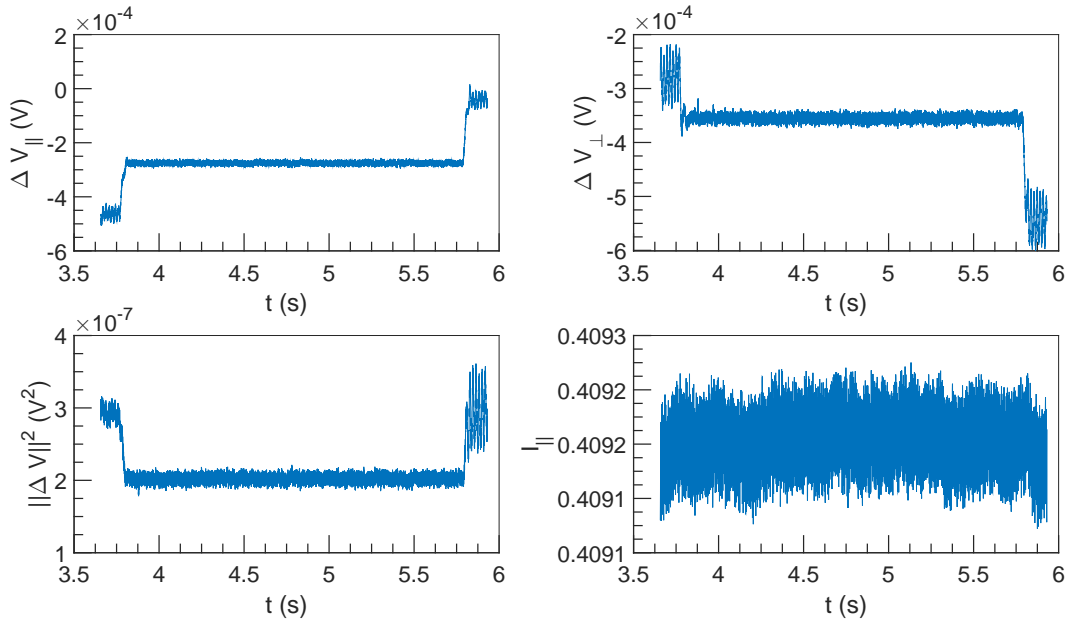


Figure 2.83:  $\Delta V$  and  $I$  vs  $t$  at  $U = 1 \text{ ms}^{-1}$ ,  $\omega = 6283 \text{ rad s}^{-1}$  and  $\alpha = 0.3\%$ .

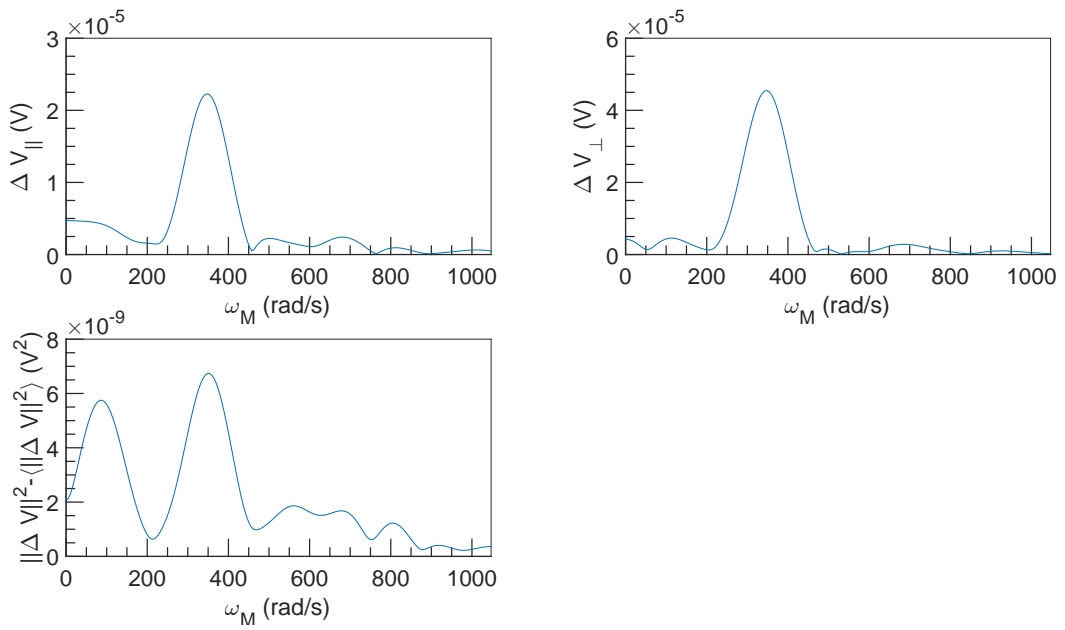


Figure 2.84: FFT spectral density of  $\Delta V$  vs  $\omega_M$  at  $U = 1 \text{ ms}^{-1}$ ,  $\omega = 6283 \text{ rad s}^{-1}$  and  $\alpha = 0.3\%$ .

## Chapter 3

For  $\alpha = 6.9\%$

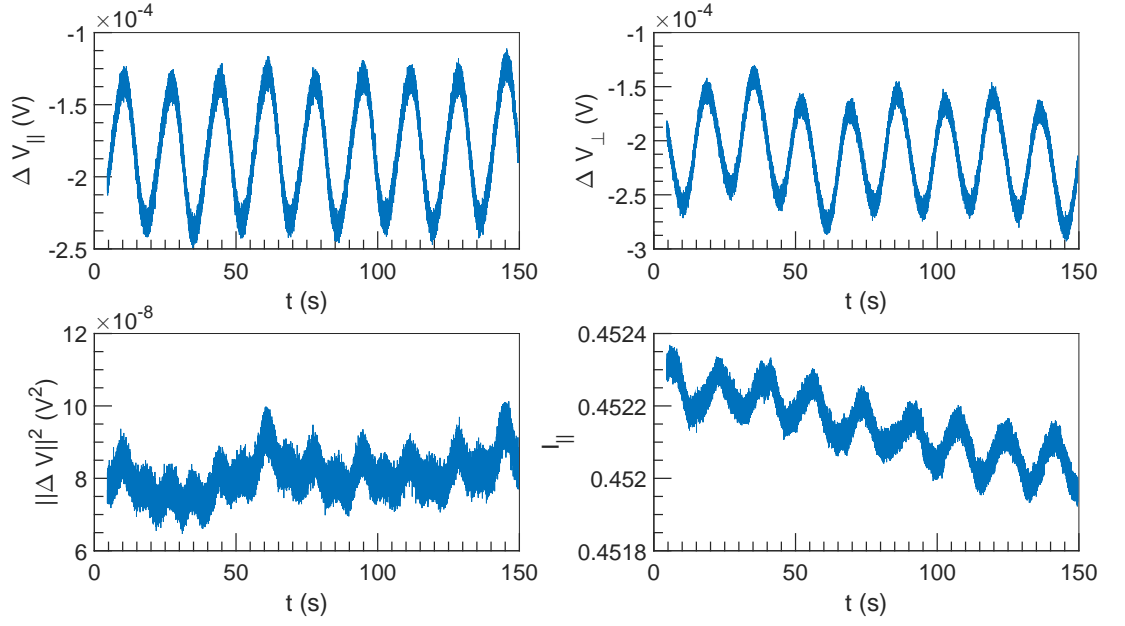


Figure 3.1:  $\Delta V$  and  $I$  vs  $t$  at  $U = 10^{-3} \text{ m s}^{-1}$ ,  $\omega = 1571 \text{ rad s}^{-1}$  and  $\alpha = 6.9\%$ .

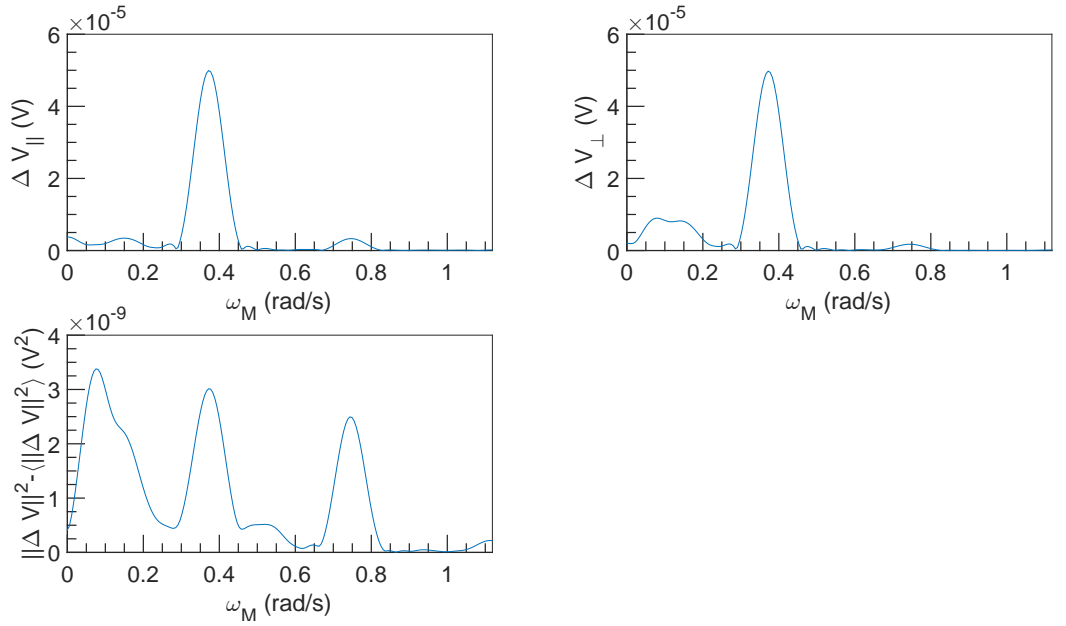


Figure 3.2: FFT spectral density of  $\Delta V$  vs  $\omega_M$  at  $U = 10^{-3} \text{ m s}^{-1}$ ,  $\omega = 1571 \text{ rad s}^{-1}$  and  $\alpha = 6.9\%$ .

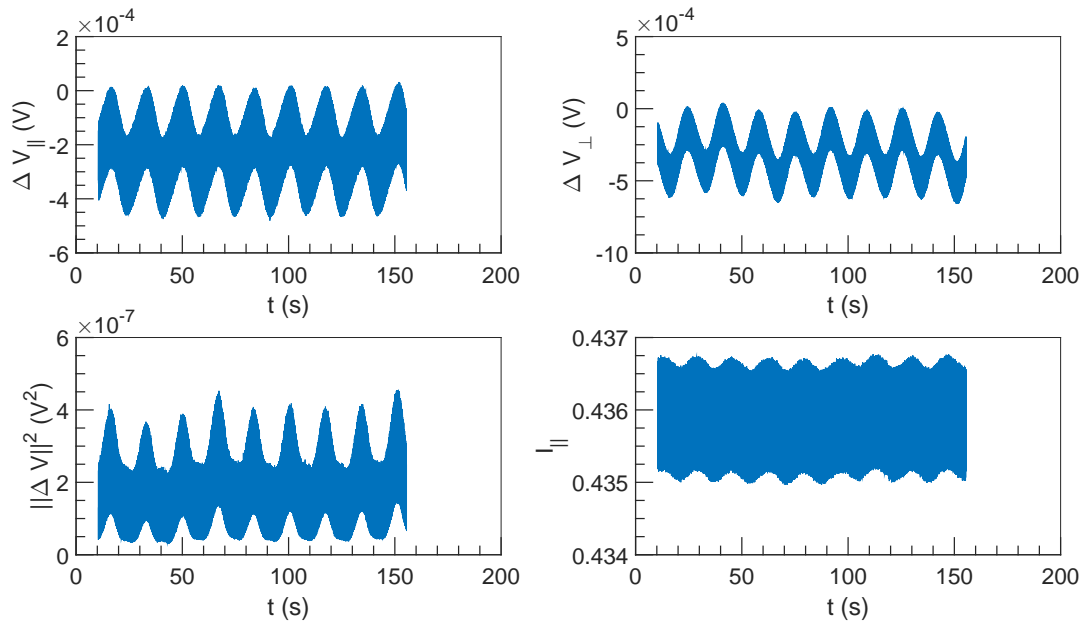


Figure 3.3:  $\Delta V$  and  $I$  vs  $t$  at  $U = 10^{-3} \text{ m s}^{-1}$ ,  $\omega = 3142 \text{ rad s}^{-1}$  and  $\alpha = 6.9\%$ .

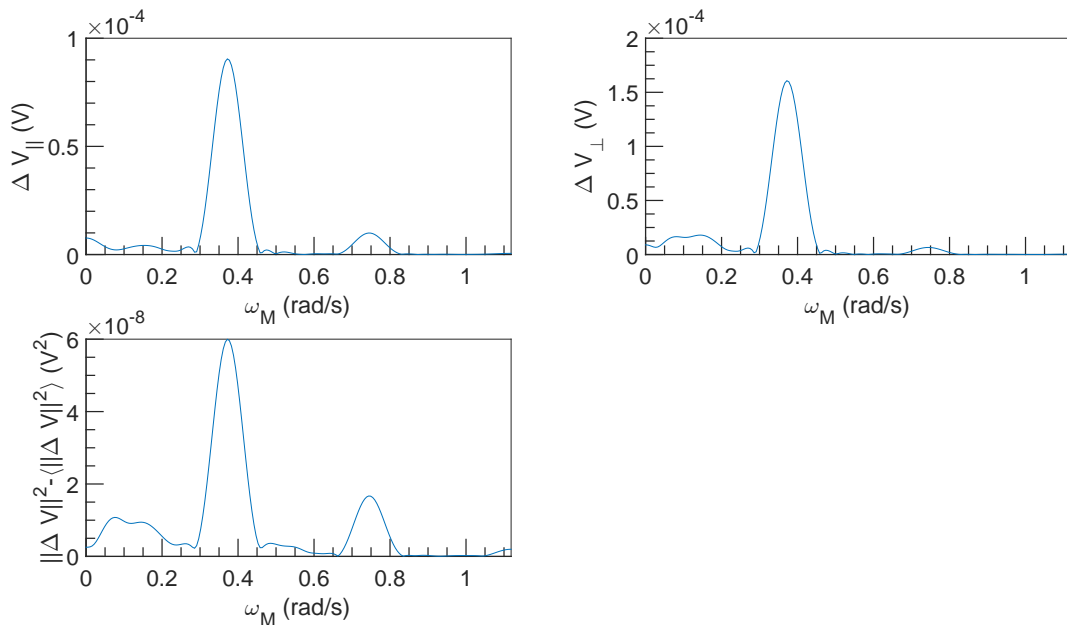


Figure 3.4: FFT spectral density of  $\Delta V$  vs  $\omega_M$  at  $U = 10^{-3} \text{ m s}^{-1}$ ,  $\omega = 3142 \text{ rad s}^{-1}$  and  $\alpha = 6.9\%$ .

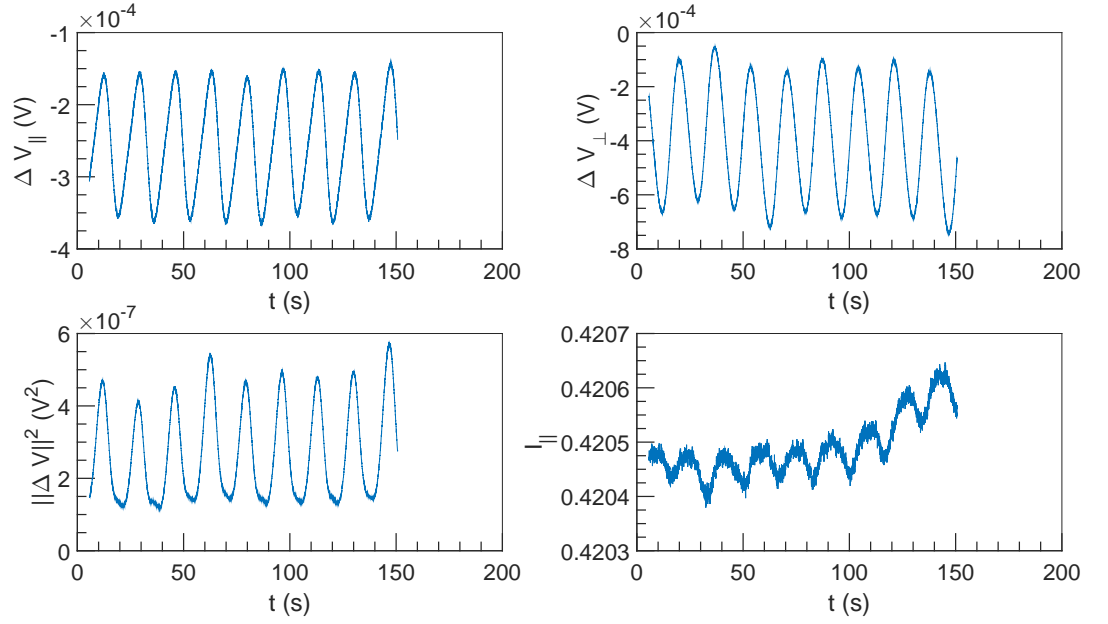


Figure 3.5:  $\Delta V$  and  $I$  vs  $t$  at  $U = 10^{-3} \text{ m s}^{-1}$ ,  $\omega = 4712 \text{ rad s}^{-1}$  and  $\alpha = 6.9\%$ .

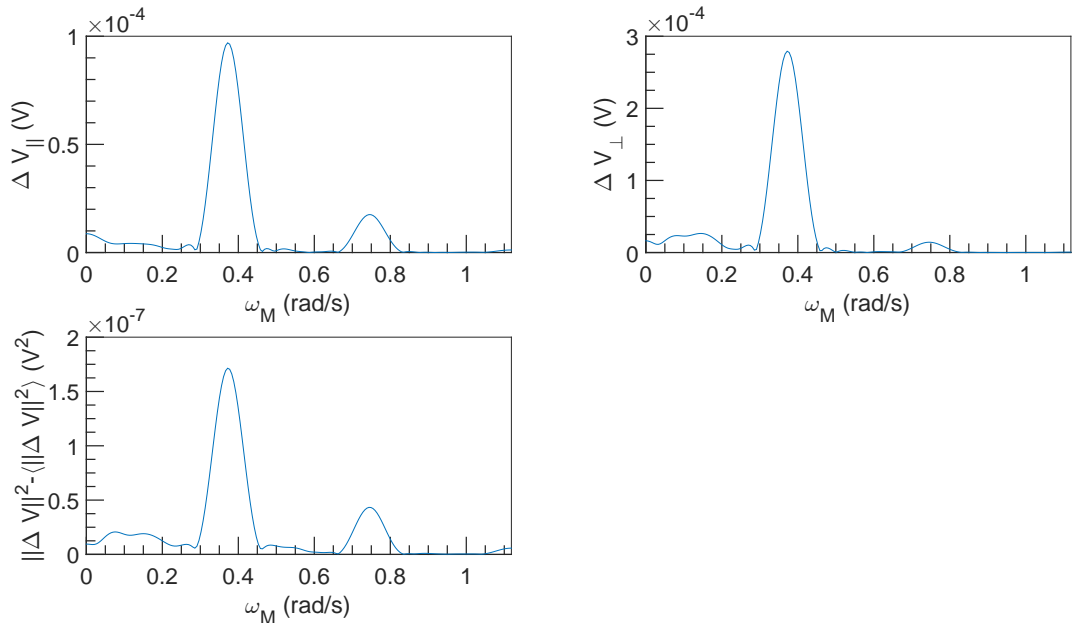


Figure 3.6: FFT spectral density of  $\Delta V$  vs  $\omega_M$  at  $U = 10^{-3} \text{ m s}^{-1}$ ,  $\omega = 4712 \text{ rad s}^{-1}$  and  $\alpha = 6.9\%$ .

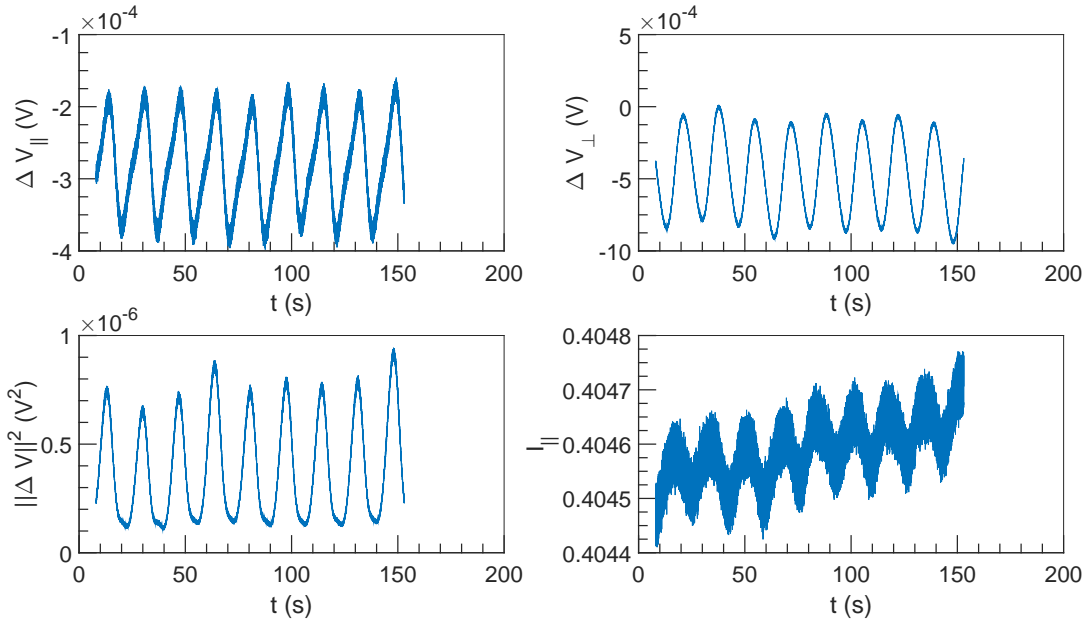


Figure 3.7:  $\Delta V$  and  $I$  vs  $t$  at  $U = 10^{-3} \text{ m s}^{-1}$ ,  $\omega = 6283 \text{ rad s}^{-1}$  and  $\alpha = 6.9\%$ .

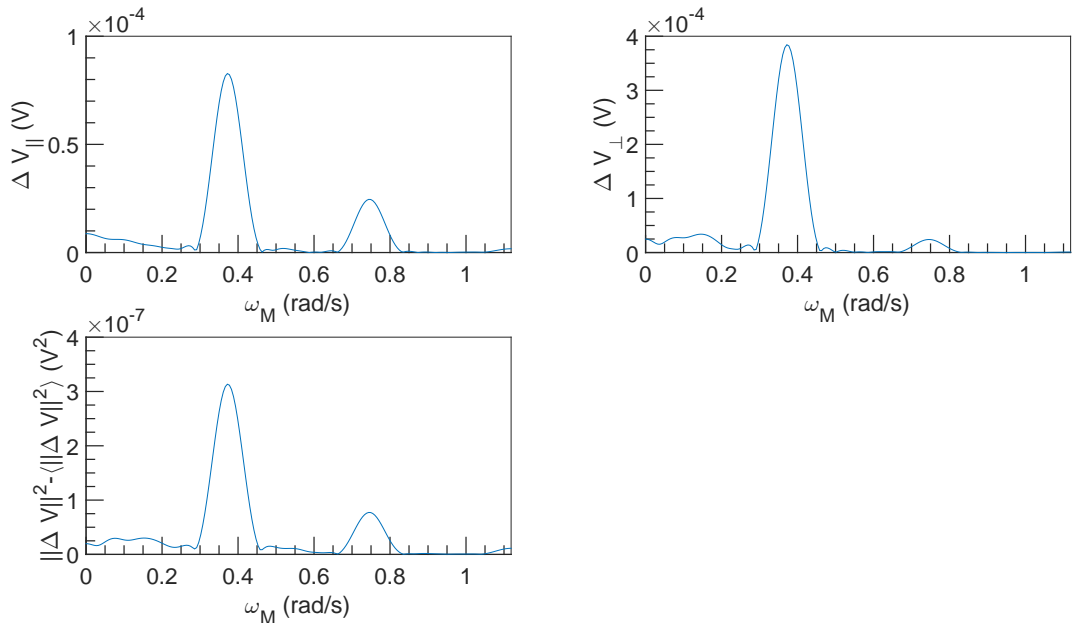


Figure 3.8: FFT spectral density of  $\Delta V$  vs  $\omega_M$  at  $U = 10^{-3} \text{ m s}^{-1}$ ,  $\omega = 6283 \text{ rad s}^{-1}$  and  $\alpha = 6.9\%$ .

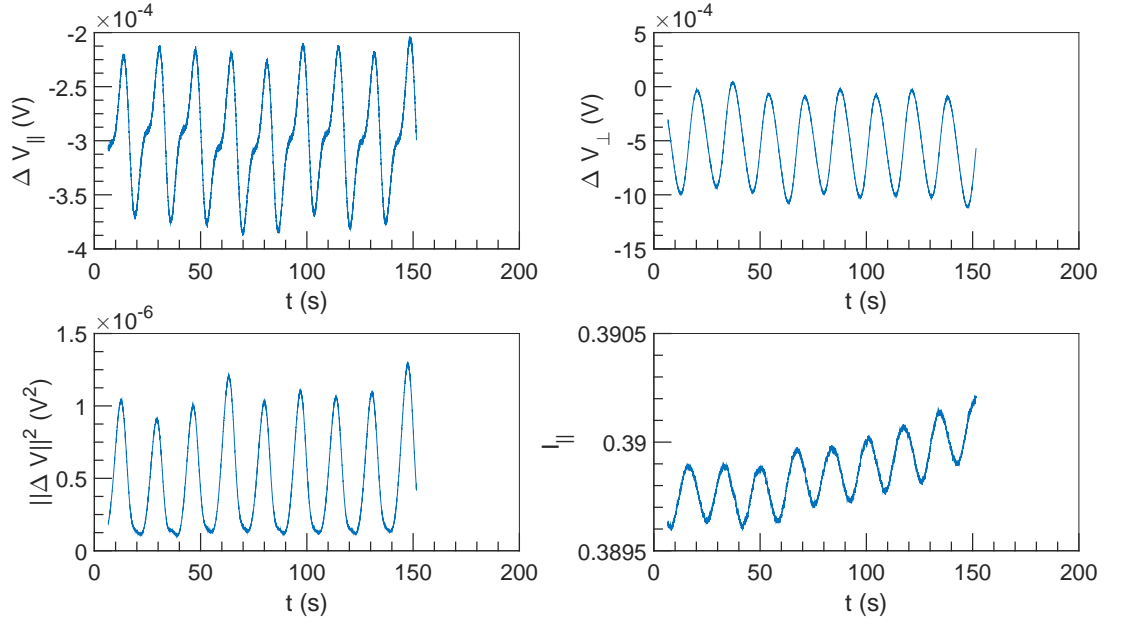


Figure 3.9:  $\Delta V$  and  $I$  vs  $t$  at  $U = 10^{-3} \text{ m s}^{-1}$ ,  $\omega = 7854 \text{ rad s}^{-1}$  and  $\alpha = 6.9\%$ .

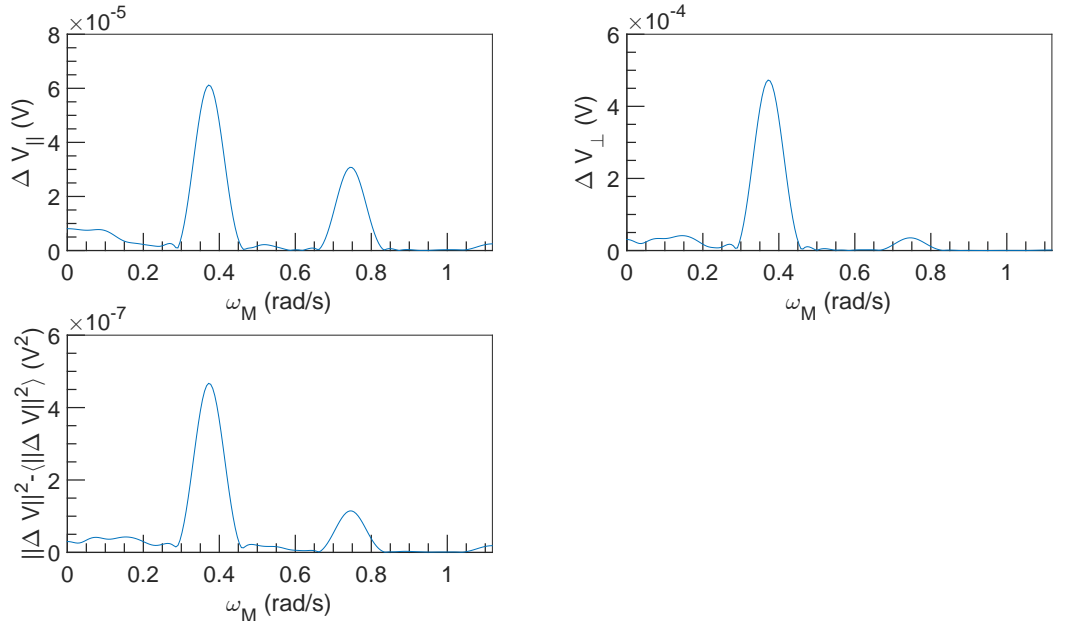


Figure 3.10: FFT spectral density of  $\Delta V$  vs  $\omega_M$  at  $U = 10^{-3} \text{ m s}^{-1}$ ,  $\omega = 7854 \text{ rad s}^{-1}$  and  $\alpha = 6.9\%$ .



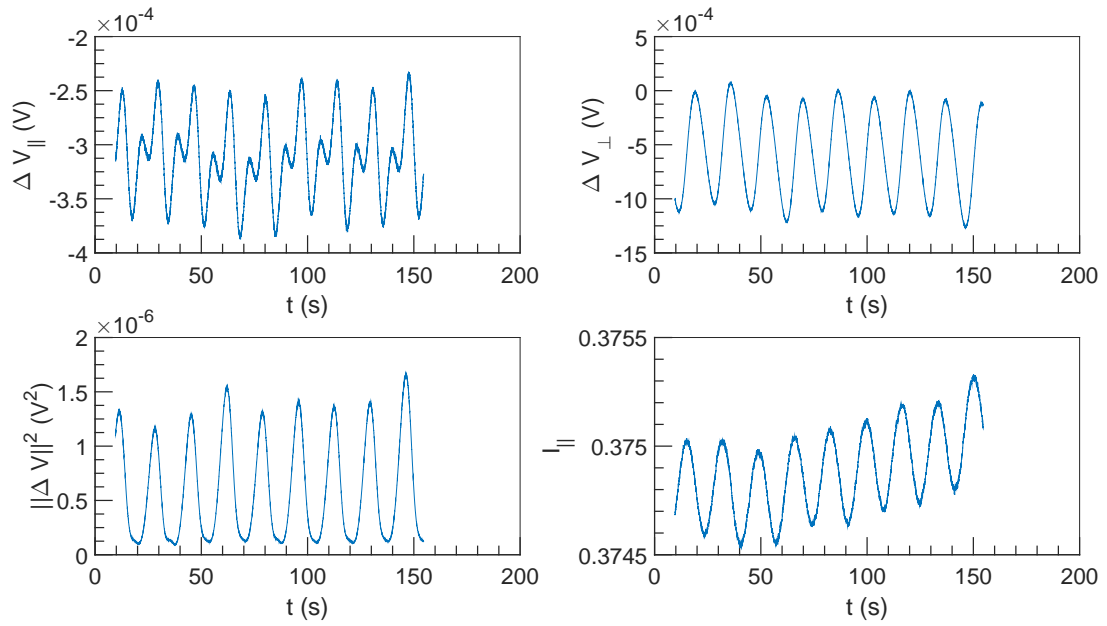


Figure 3.11:  $\Delta V$  and  $I$  vs  $t$  at  $U = 10^{-3} \text{ m s}^{-1}$ ,  $\omega = 9425 \text{ rad s}^{-1}$  and  $\alpha = 6.9\%$ .

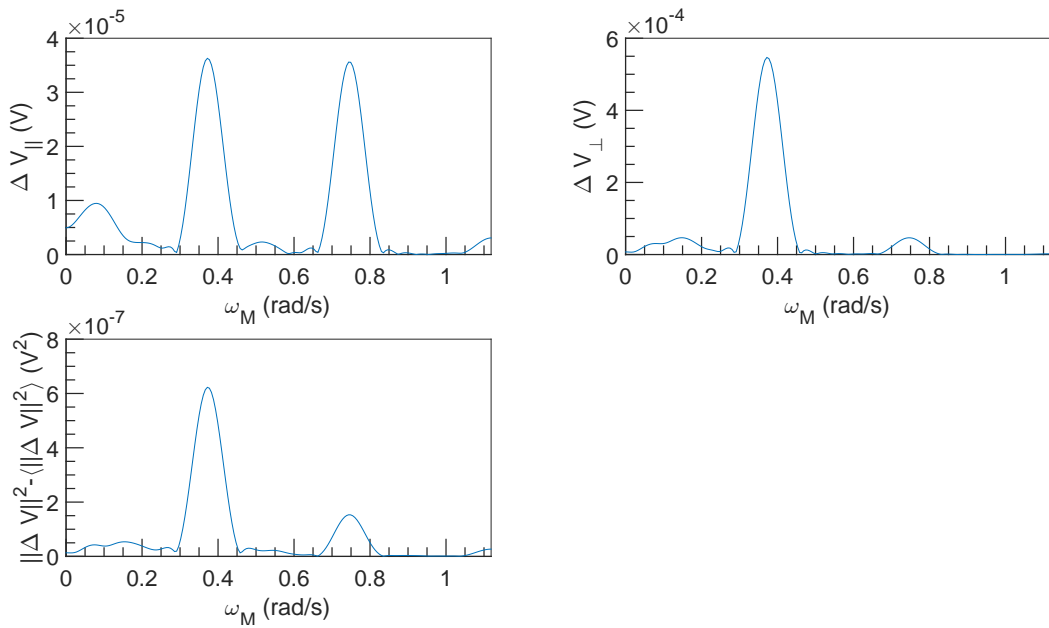


Figure 3.12: FFT spectral density of  $\Delta V$  vs  $\omega_M$  at  $U = 10^{-3} \text{ m s}^{-1}$ ,  $\omega = 9425 \text{ rad s}^{-1}$  and  $\alpha = 6.9\%$ .

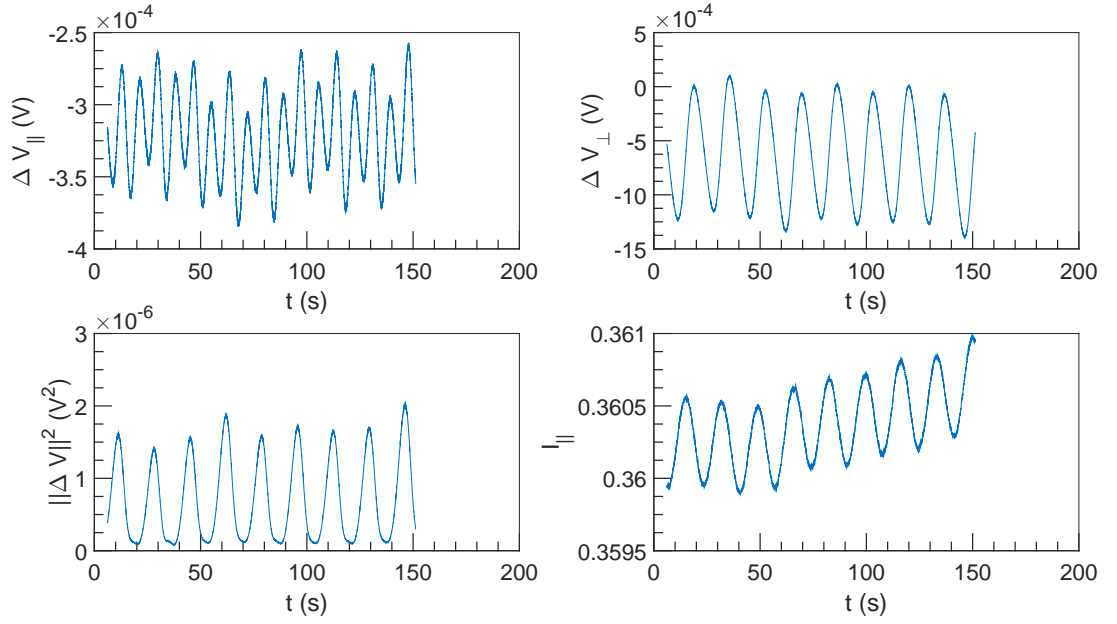


Figure 3.13:  $\Delta V$  and  $I$  vs  $t$  at  $U = 10^{-3} \text{ m s}^{-1}$ ,  $\omega = 10\,996 \text{ rad s}^{-1}$  and  $\alpha = 6.9\%$ .

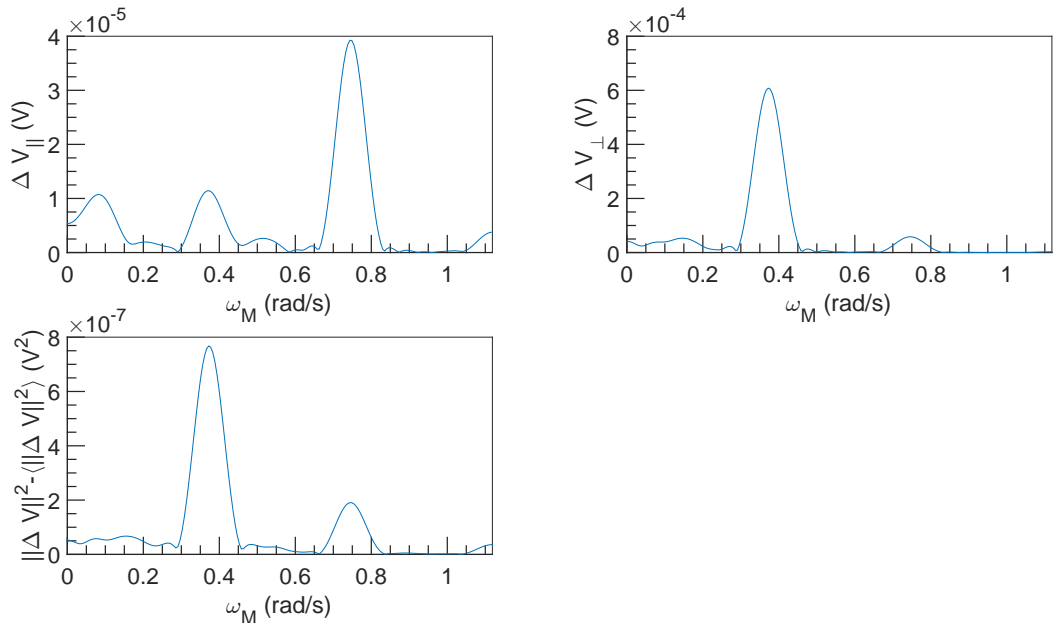


Figure 3.14: FFT spectral density of  $\Delta V$  vs  $\omega_M$  at  $U = 10^{-3} \text{ m s}^{-1}$ ,  $\omega = 10\,996 \text{ rad s}^{-1}$  and  $\alpha = 6.9\%$ .

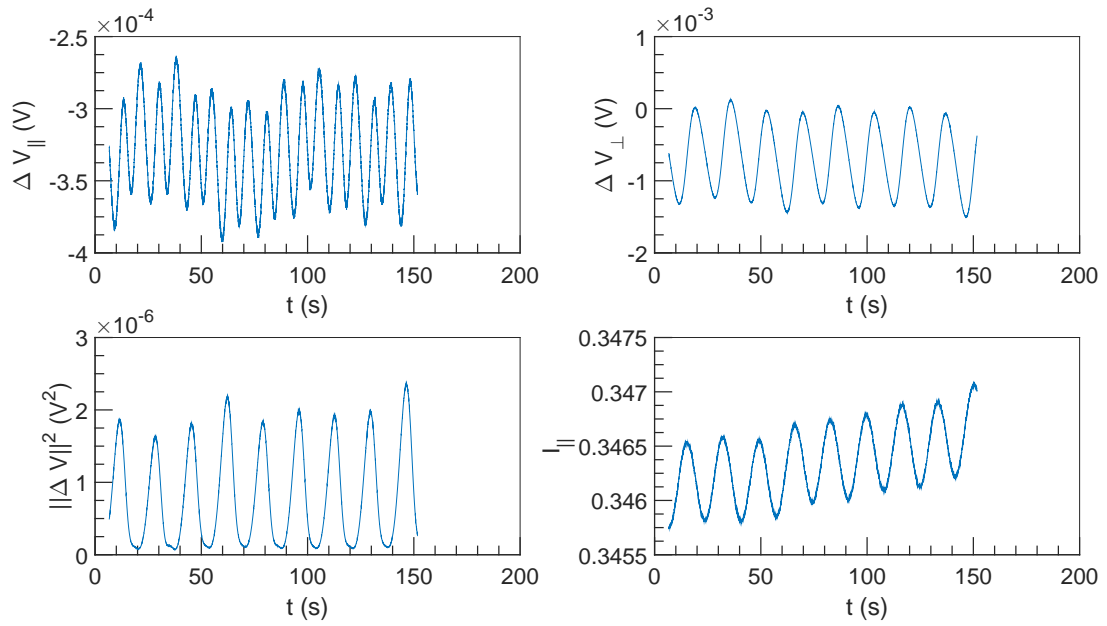


Figure 3.15:  $\Delta V$  and  $I$  vs  $t$  at  $U = 10^{-3} \text{ m s}^{-1}$ ,  $\omega = 12566 \text{ rad s}^{-1}$  and  $\alpha = 6.9\%$ .

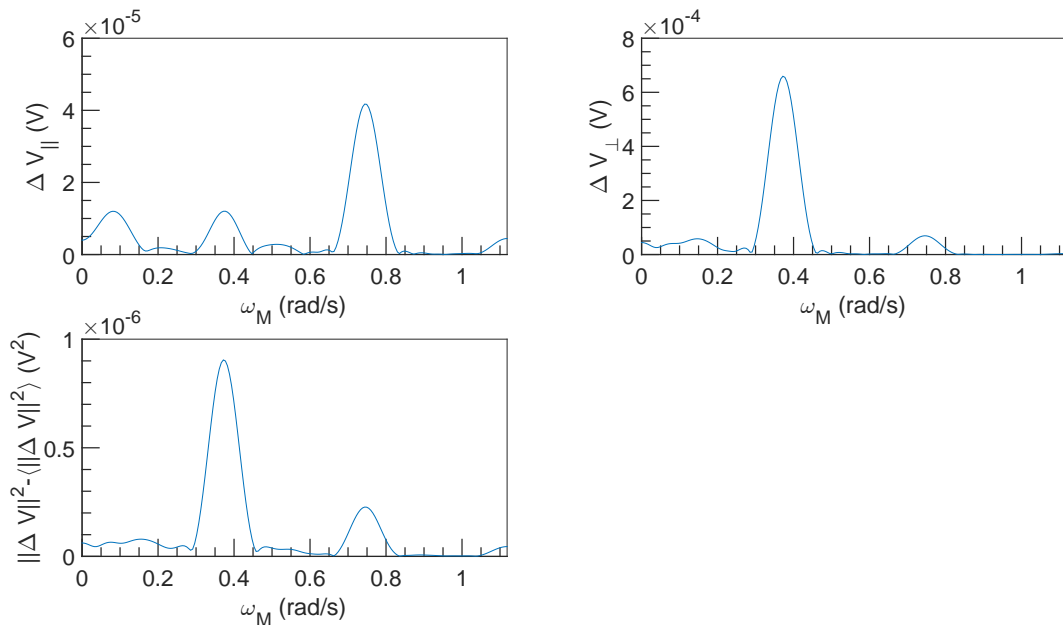


Figure 3.16: FFT spectral density of  $\Delta V$  vs  $\omega_M$  at  $U = 10^{-3} \text{ m s}^{-1}$ ,  $\omega = 12566 \text{ rad s}^{-1}$  and  $\alpha = 6.9\%$ .

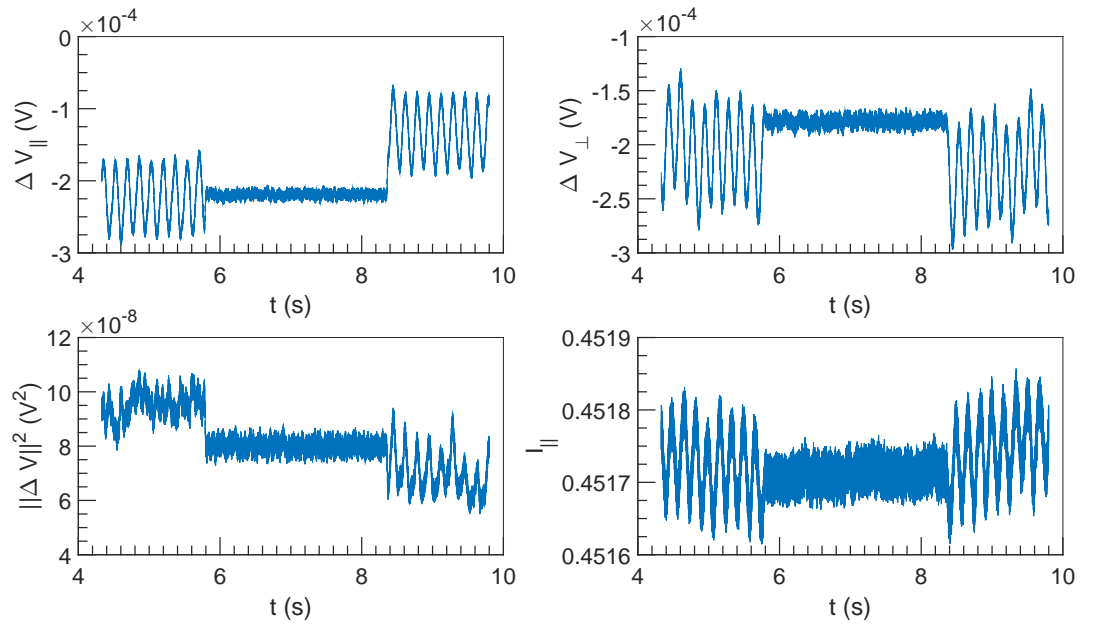


Figure 3.17:  $\Delta V$  and  $I$  vs  $t$  at  $U = 0.1 \text{ m s}^{-1}$ ,  $\omega = 1571 \text{ rad s}^{-1}$  and  $\alpha = 6.9\%$ .

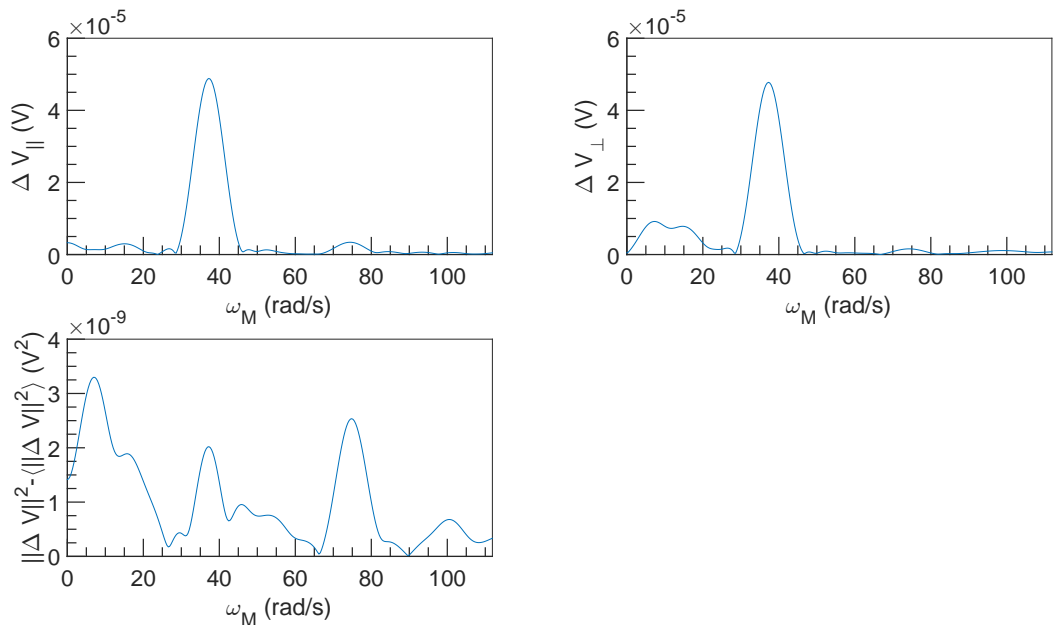


Figure 3.18: FFT spectral density of  $\Delta V$  vs  $\omega_M$  at  $U = 0.1 \text{ m s}^{-1}$ ,  $\omega = 1571 \text{ rad s}^{-1}$  and  $\alpha = 6.9\%$ .

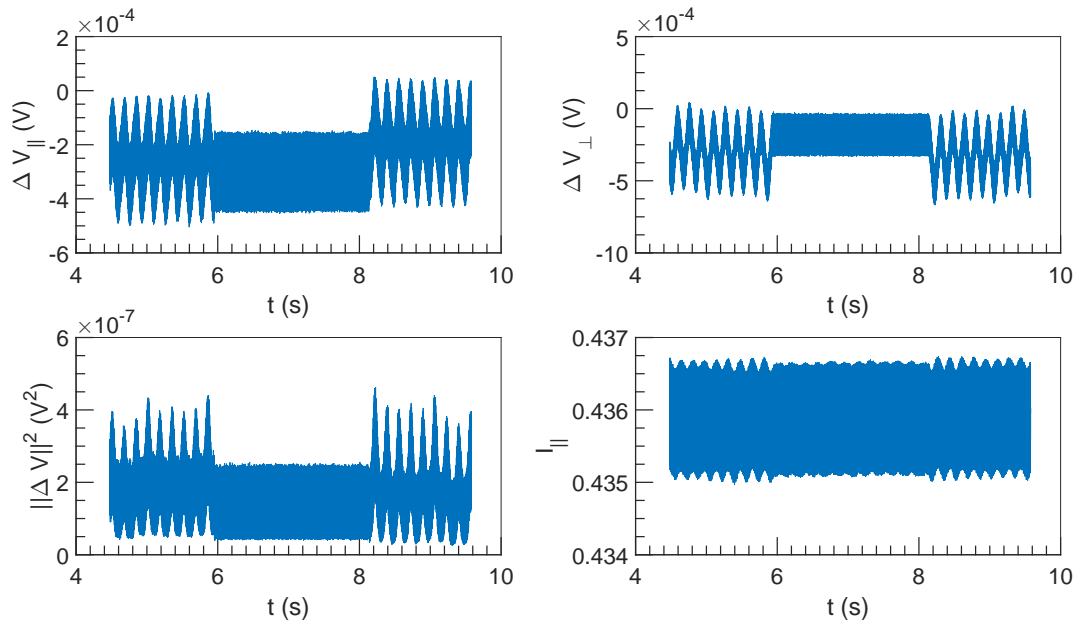


Figure 3.19:  $\Delta V$  and  $I$  vs  $t$  at  $U = 0.1 \text{ m s}^{-1}$ ,  $\omega = 3142 \text{ rad s}^{-1}$  and  $\alpha = 6.9\%$ .

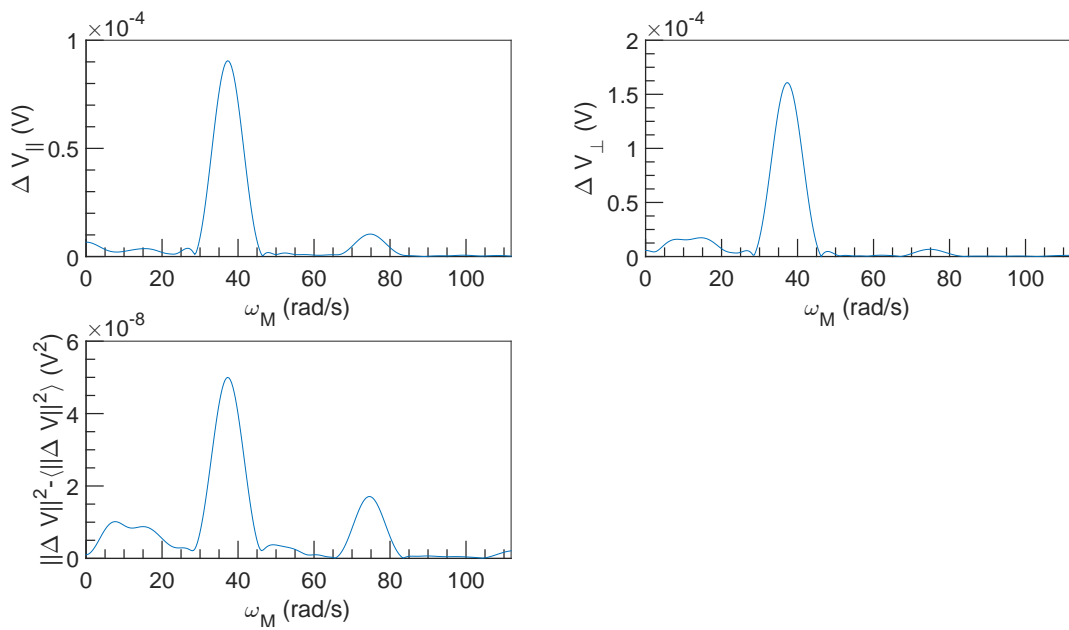


Figure 3.20: FFT spectral density of  $\Delta V$  vs  $\omega_M$  at  $U = 0.1 \text{ m s}^{-1}$ ,  $\omega = 3142 \text{ rad s}^{-1}$  and  $\alpha = 6.9\%$ .

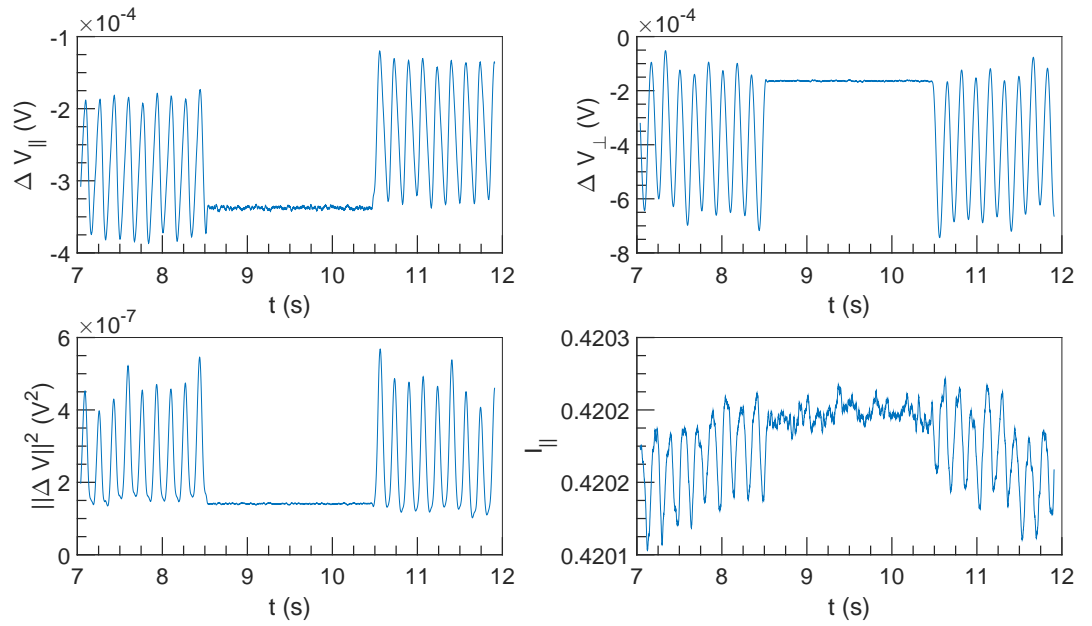


Figure 3.21:  $\Delta V$  and  $I$  vs  $t$  at  $U = 0.1 \text{ m s}^{-1}$ ,  $\omega = 4712 \text{ rad s}^{-1}$  and  $\alpha = 6.9\%$ .

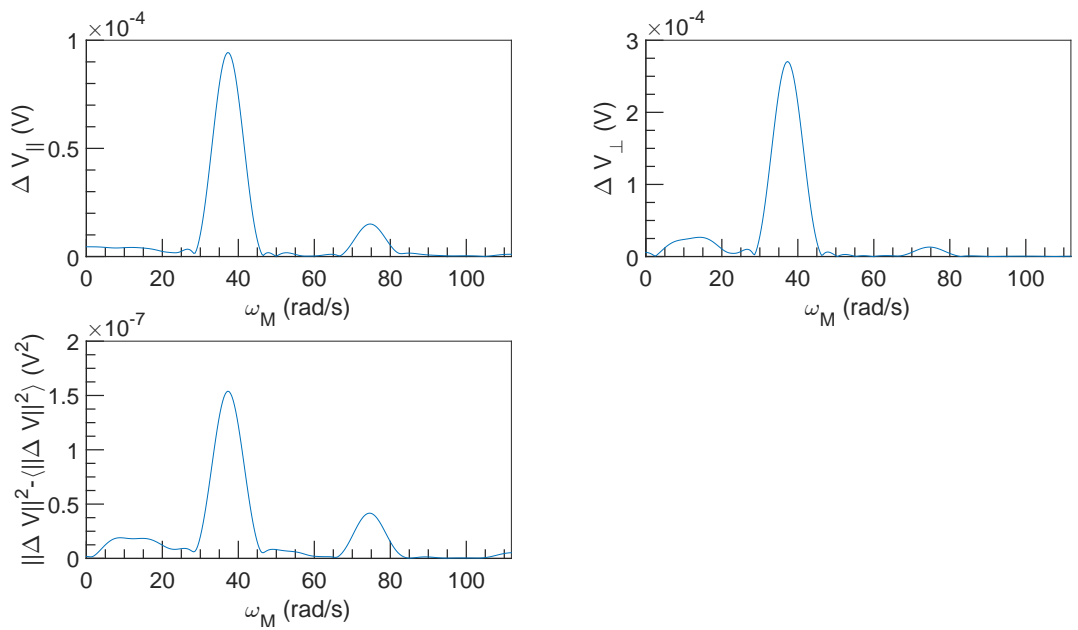


Figure 3.22: FFT spectral density of  $\Delta V$  vs  $\omega_M$  at  $U = 0.1 \text{ m s}^{-1}$ ,  $\omega = 4712 \text{ rad s}^{-1}$  and  $\alpha = 6.9\%$ .

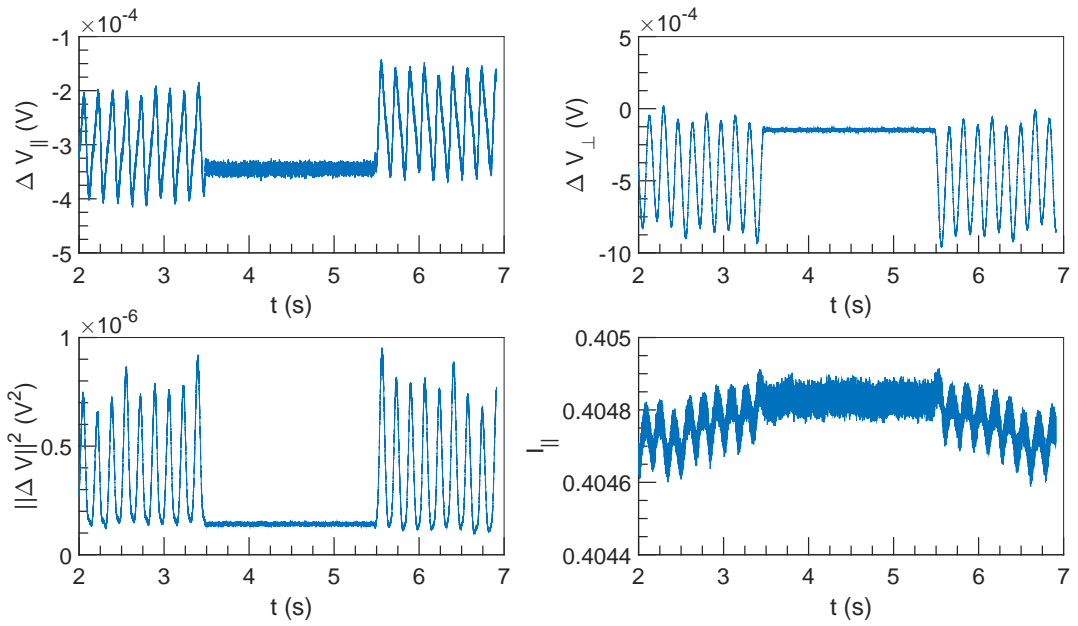


Figure 3.23:  $\Delta V$  and  $I$  vs  $t$  at  $U = 0.1 \text{ m s}^{-1}$ ,  $\omega = 6283 \text{ rad s}^{-1}$  and  $\alpha = 6.9\%$ .

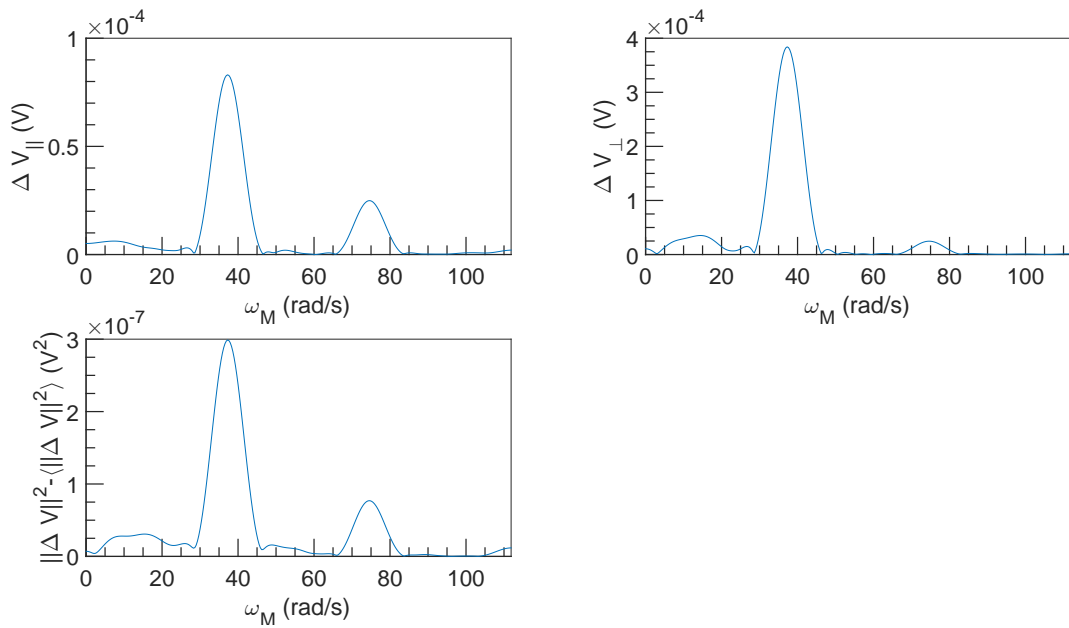


Figure 3.24: FFT spectral density of  $\Delta V$  vs  $\omega_M$  at  $U = 0.1 \text{ m s}^{-1}$ ,  $\omega = 6283 \text{ rad s}^{-1}$  and  $\alpha = 6.9\%$ .

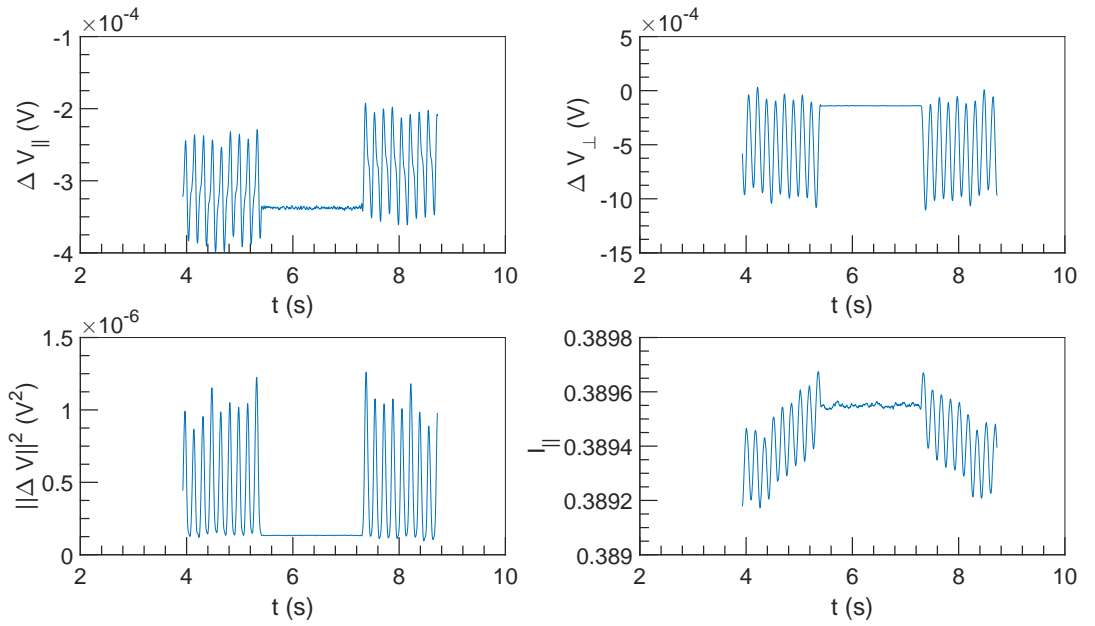


Figure 3.25:  $\Delta V$  and  $I$  vs  $t$  at  $U = 0.1 \text{ m s}^{-1}$ ,  $\omega = 7854 \text{ rad s}^{-1}$  and  $\alpha = 6.9\%$ .

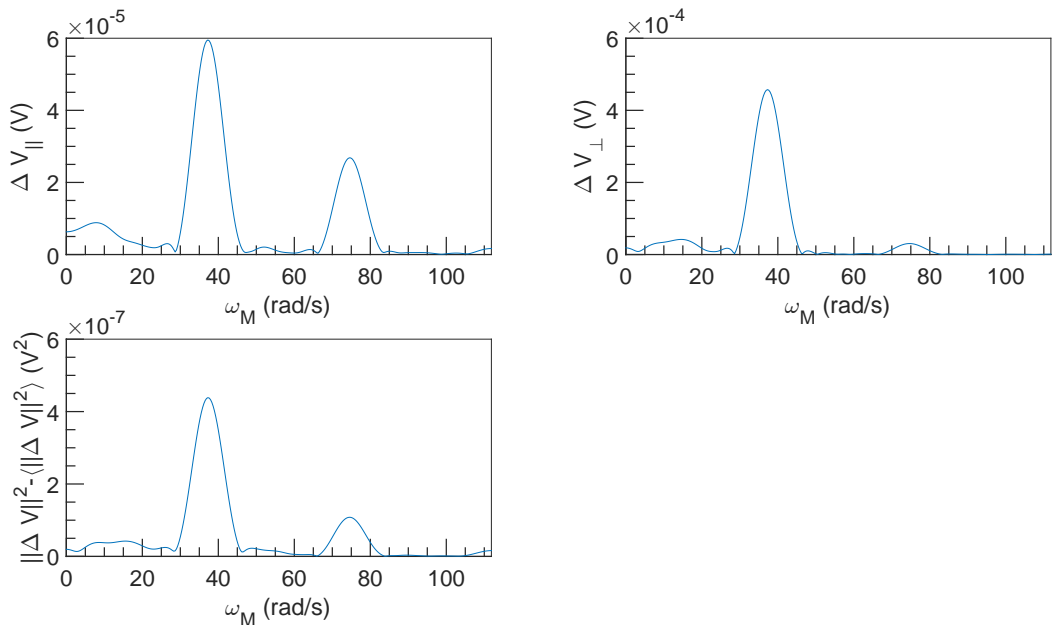


Figure 3.26: FFT spectral density of  $\Delta V$  vs  $\omega_M$  at  $U = 0.1 \text{ m s}^{-1}$ ,  $\omega = 7854 \text{ rad s}^{-1}$  and  $\alpha = 6.9\%$ .



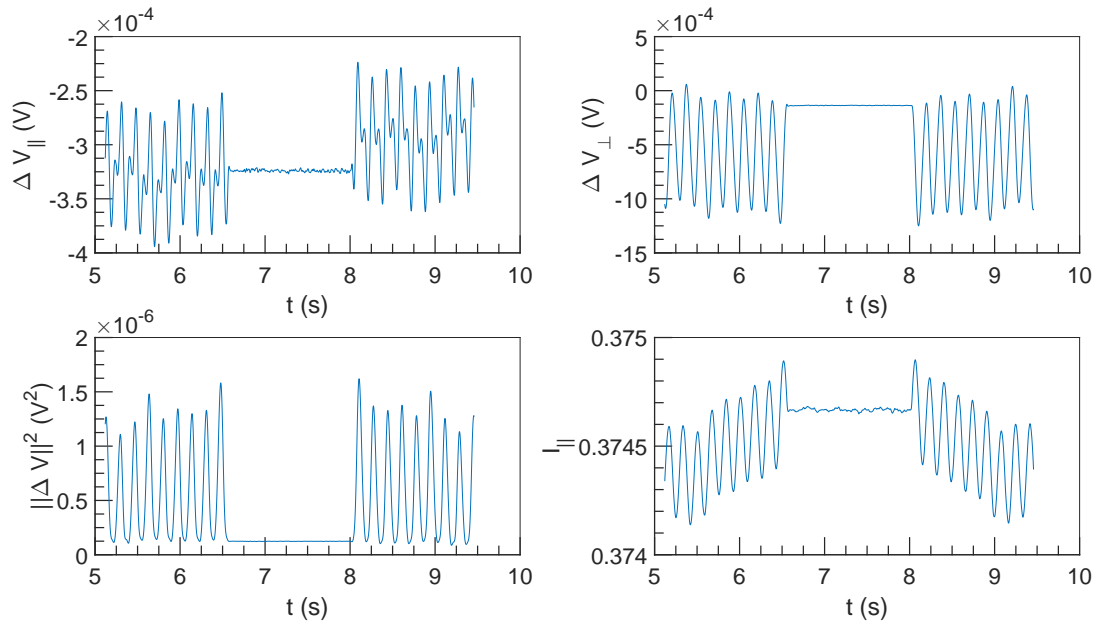


Figure 3.27:  $\Delta V$  and  $I$  vs  $t$  at  $U = 0.1 \text{ m s}^{-1}$ ,  $\omega = 9425 \text{ rad s}^{-1}$  and  $\alpha = 6.9\%$ .

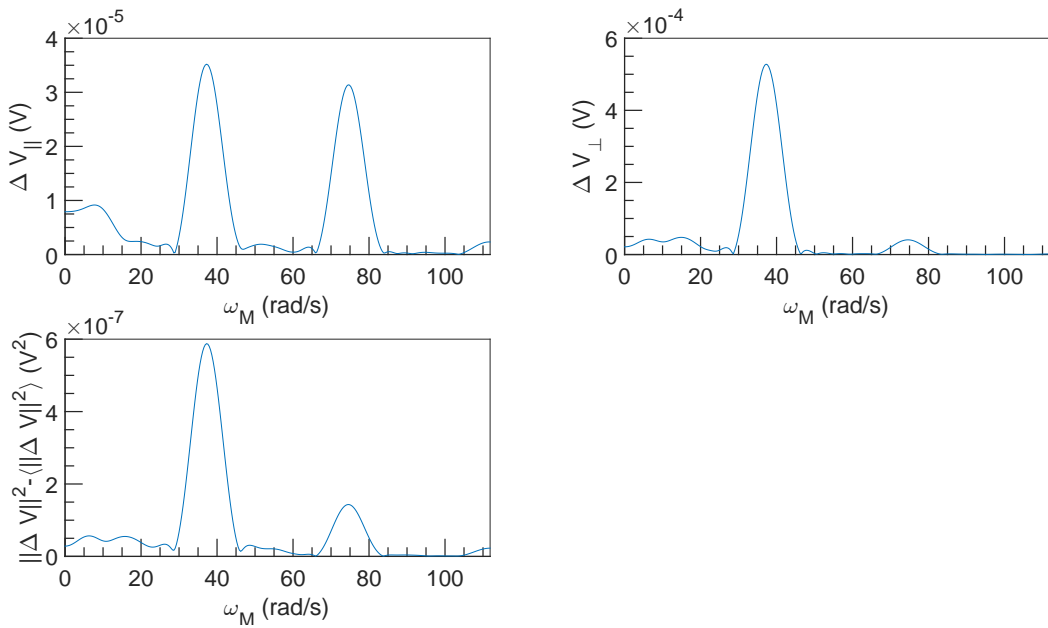


Figure 3.28: FFT spectral density of  $\Delta V$  vs  $\omega_M$  at  $U = 0.1 \text{ m s}^{-1}$ ,  $\omega = 9425 \text{ rad s}^{-1}$  and  $\alpha = 6.9\%$ .

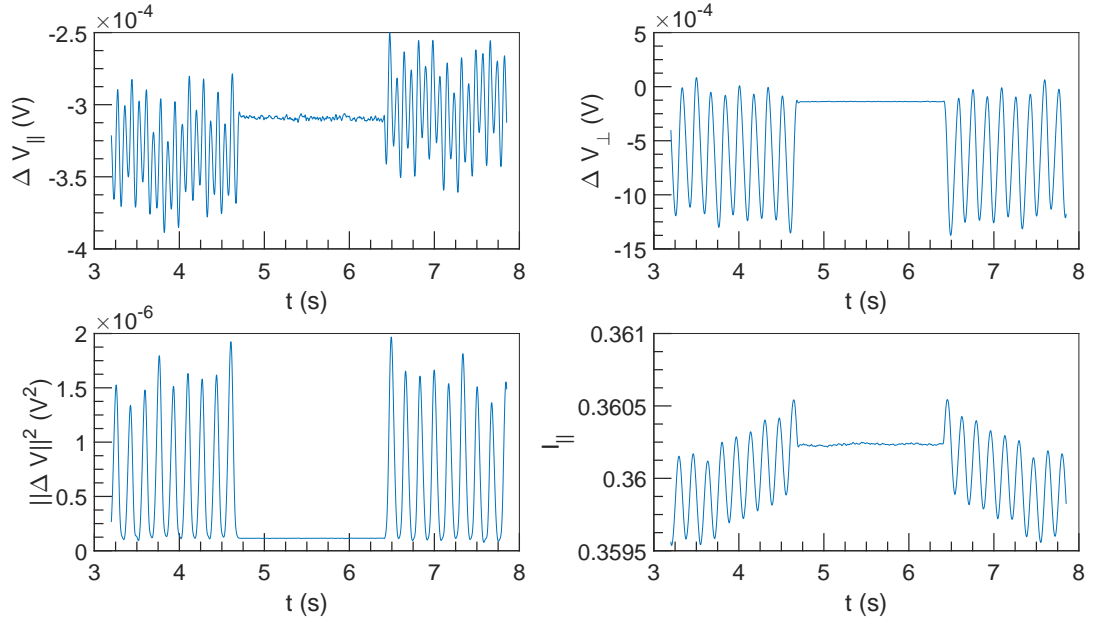


Figure 3.29:  $\Delta V$  and  $I$  vs  $t$  at  $U = 0.1 \text{ m s}^{-1}$ ,  $\omega = 10996 \text{ rad s}^{-1}$  and  $\alpha = 6.9\%$ .

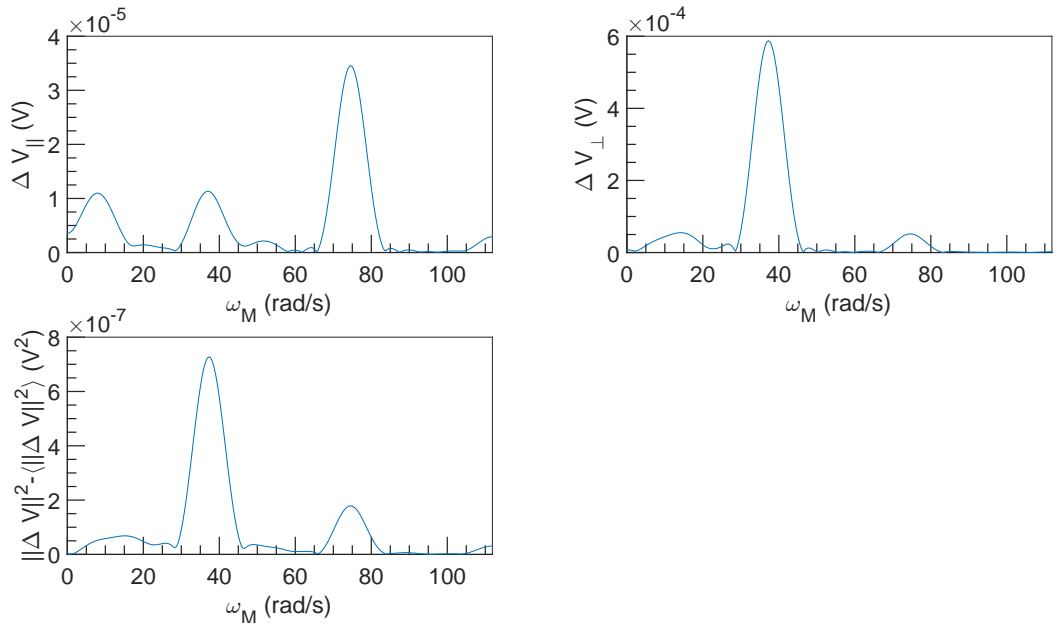


Figure 3.30: FFT spectral density of  $\Delta V$  vs  $\omega_M$  at  $U = 0.1 \text{ m s}^{-1}$ ,  $\omega = 10996 \text{ rad s}^{-1}$  and  $\alpha = 6.9\%$ .

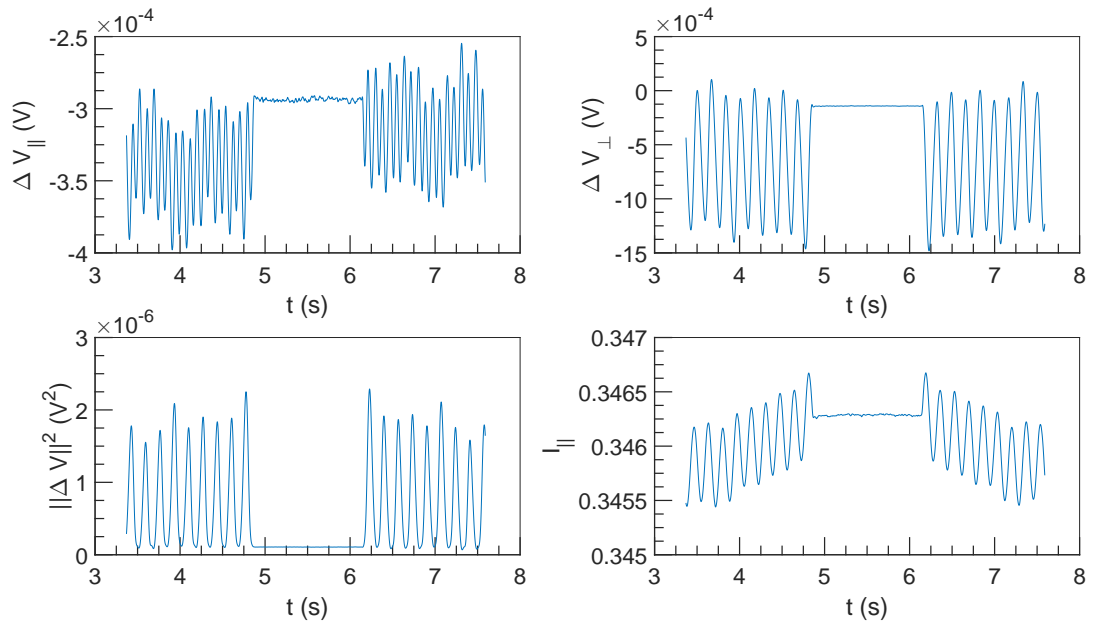


Figure 3.31:  $\Delta V$  and  $I$  vs  $t$  at  $U = 0.1 \text{ m s}^{-1}$ ,  $\omega = 12566 \text{ rad s}^{-1}$  and  $\alpha = 6.9\%$ .

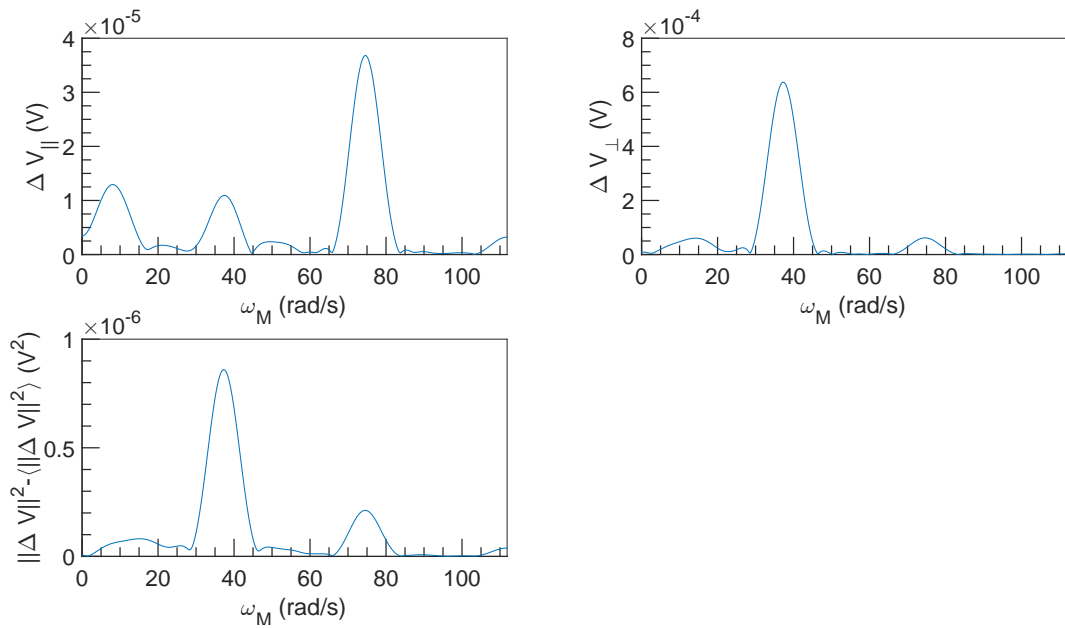


Figure 3.32: FFT spectral density of  $\Delta V$  vs  $\omega_M$  at  $U = 0.1 \text{ m s}^{-1}$ ,  $\omega = 12566 \text{ rad s}^{-1}$  and  $\alpha = 6.9\%$ .

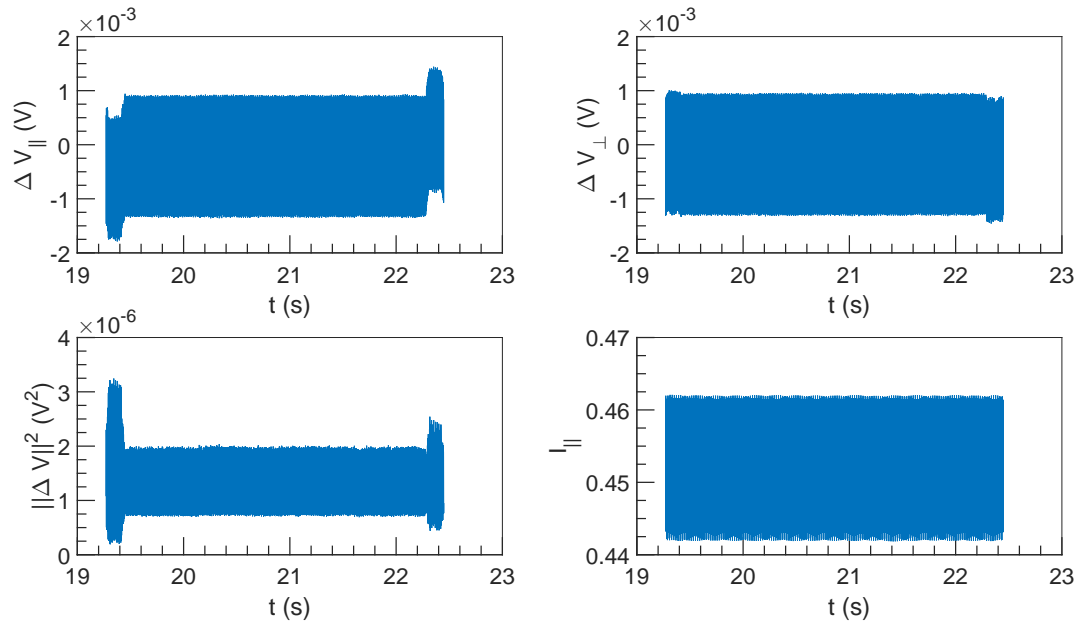


Figure 3.33:  $\Delta V$  and  $I$  vs  $t$  at  $U = 1 \text{ m s}^{-1}$ ,  $\omega = 1571 \text{ rad s}^{-1}$  and  $\alpha = 6.9\%$ .

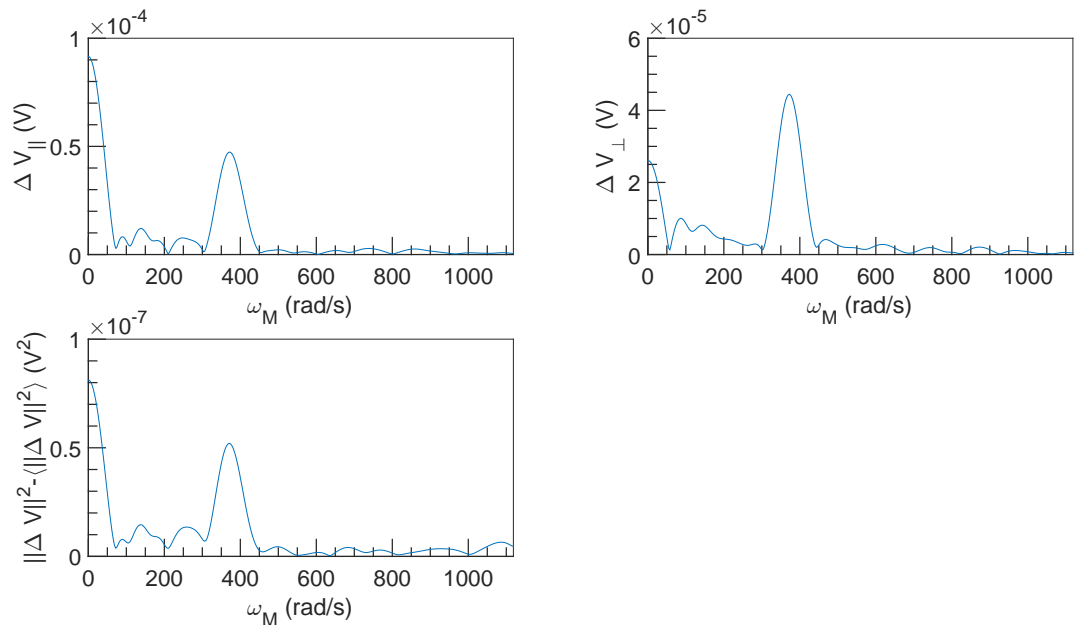


Figure 3.34: FFT spectral density of  $\Delta V$  vs  $\omega_M$  at  $U = 1 \text{ m s}^{-1}$ ,  $\omega = 1571 \text{ rad s}^{-1}$  and  $\alpha = 6.9\%$ .

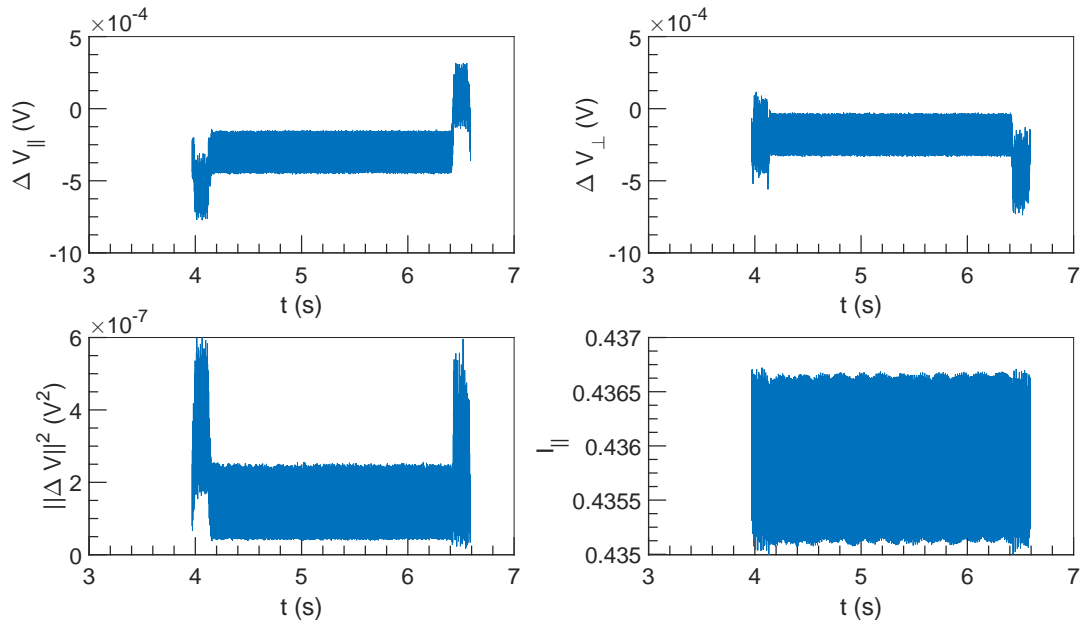


Figure 3.35:  $\Delta V$  and  $I$  vs  $t$  at  $U = 1 \text{ m s}^{-1}$ ,  $\omega = 3142 \text{ rad s}^{-1}$  and  $\alpha = 6.9\%$ .

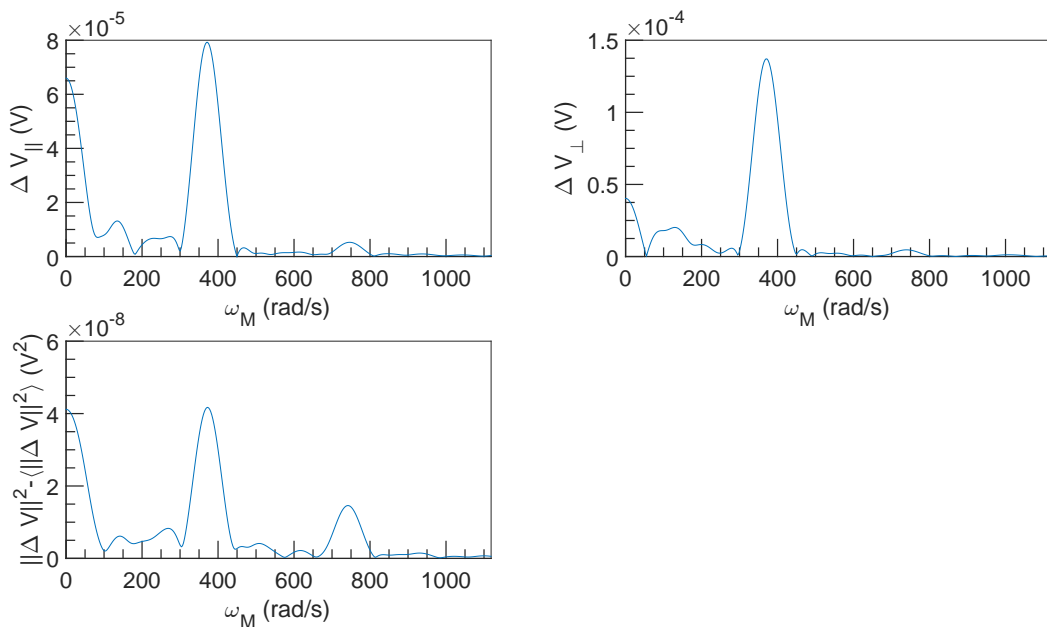


Figure 3.36: FFT spectral density of  $\Delta V$  vs  $\omega_M$  at  $U = 1 \text{ m s}^{-1}$ ,  $\omega = 3142 \text{ rad s}^{-1}$  and  $\alpha = 6.9\%$ .

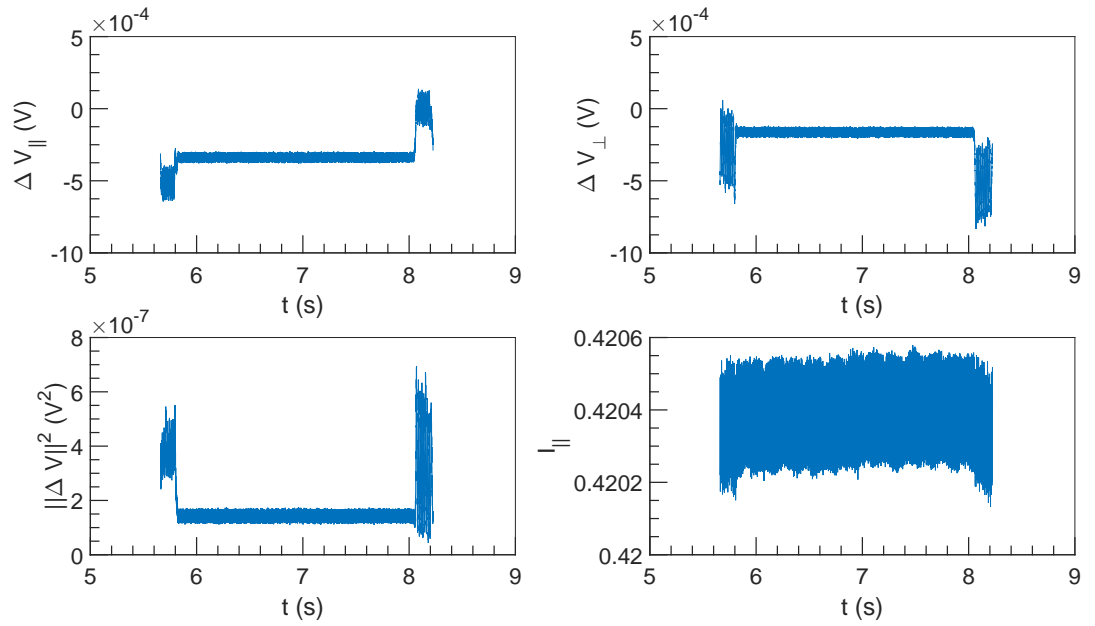


Figure 3.37:  $\Delta V$  and  $I$  vs  $t$  at  $U = 1 \text{ m s}^{-1}$ ,  $\omega = 4712 \text{ rad s}^{-1}$  and  $\alpha = 6.9\%$ .

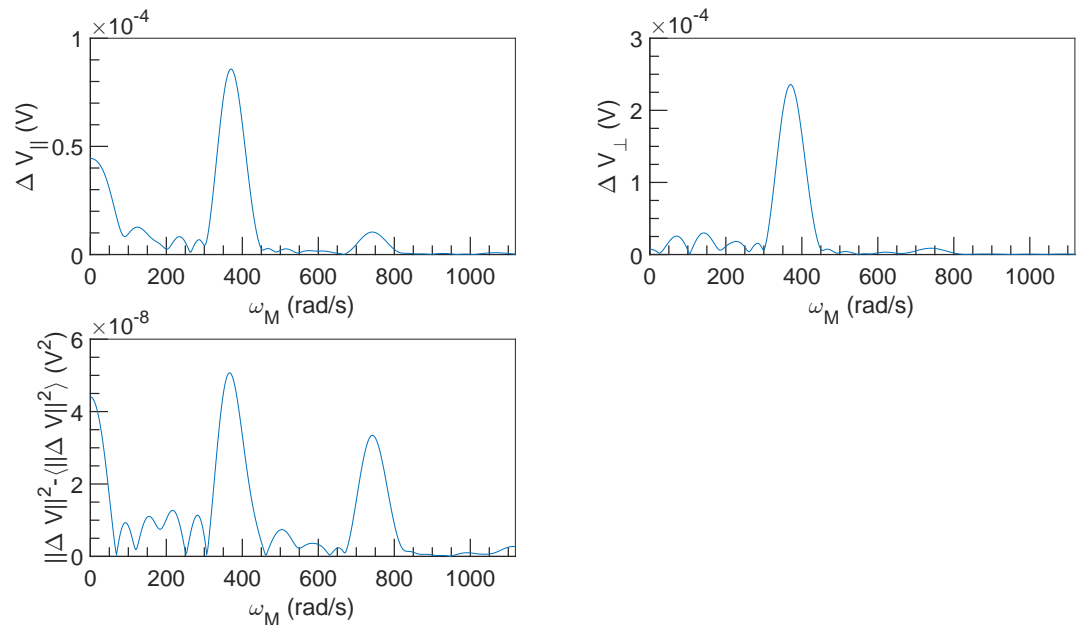


Figure 3.38: FFT spectral density of  $\Delta V$  vs  $\omega_M$  at  $U = 1 \text{ m s}^{-1}$ ,  $\omega = 4712 \text{ rad s}^{-1}$  and  $\alpha = 6.9\%$ .

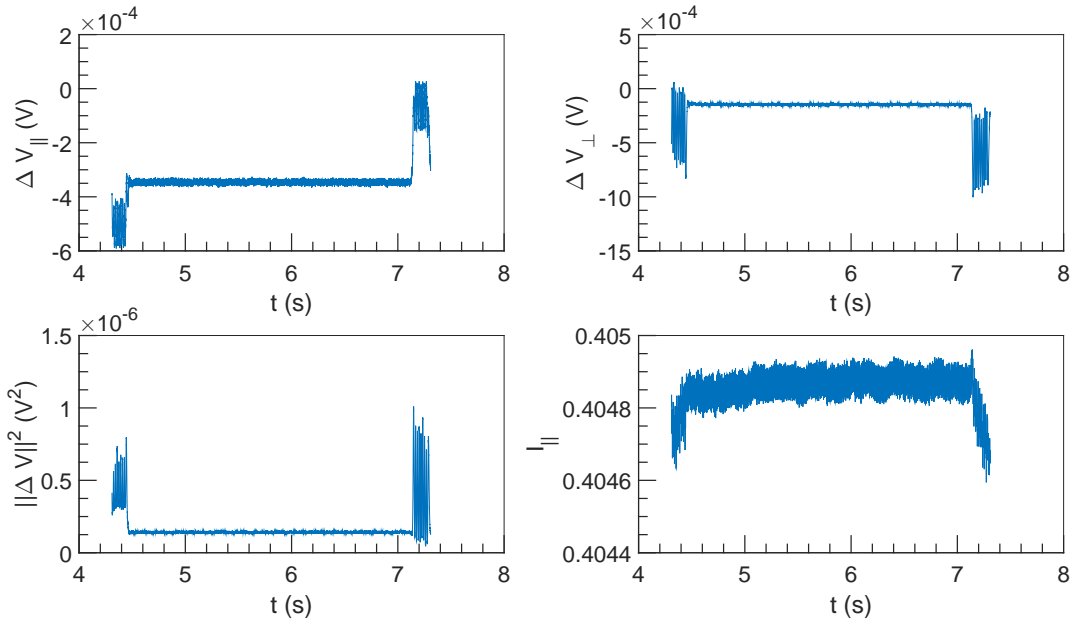


Figure 3.39:  $\Delta V$  and  $I$  vs  $t$  at  $U = 1 \text{ m s}^{-1}$ ,  $\omega = 6283 \text{ rad s}^{-1}$  and  $\alpha = 6.9\%$ .

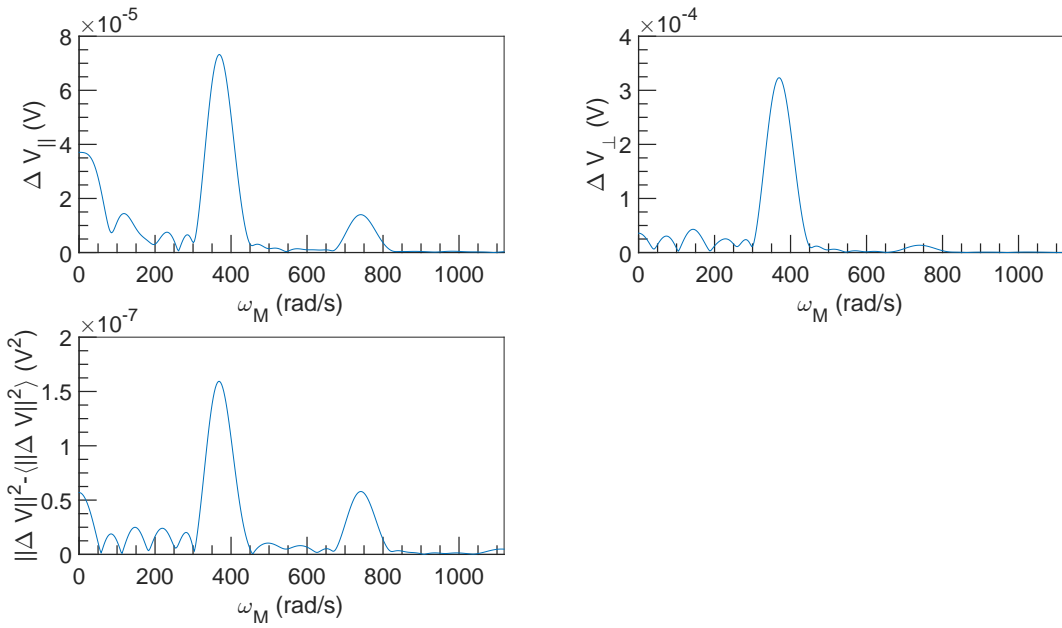


Figure 3.40: FFT spectral density of  $\Delta V$  vs  $\omega_M$  at  $U = 1 \text{ m s}^{-1}$ ,  $\omega = 6283 \text{ rad s}^{-1}$  and  $\alpha = 6.9\%$ .

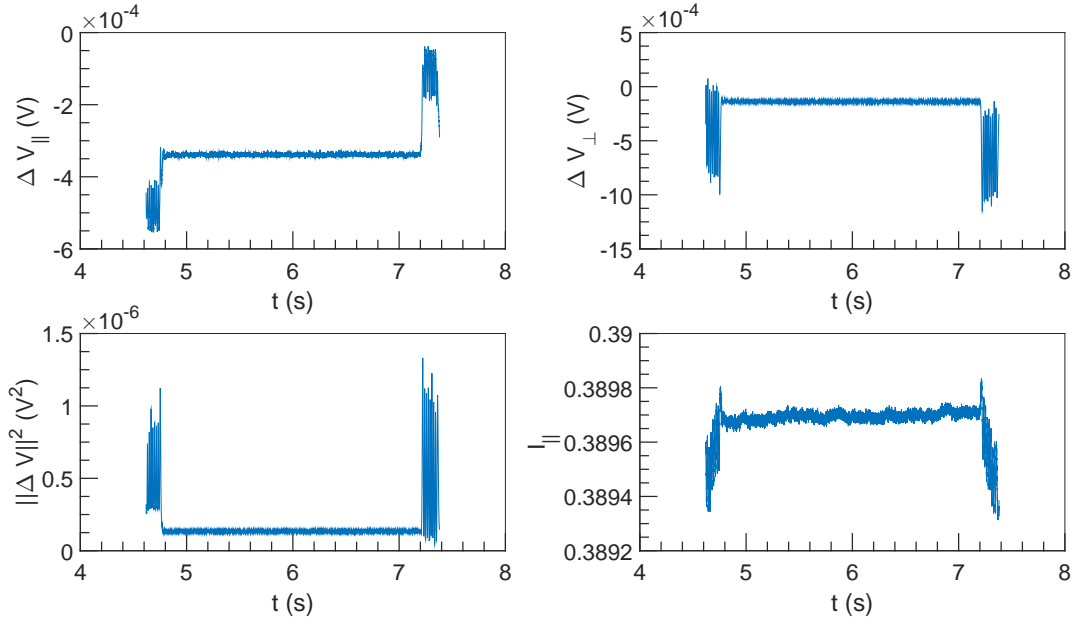


Figure 3.41:  $\Delta V$  and  $I$  vs  $t$  at  $U = 1 \text{ m s}^{-1}$ ,  $\omega = 7854 \text{ rad s}^{-1}$  and  $\alpha = 6.9\%$ .

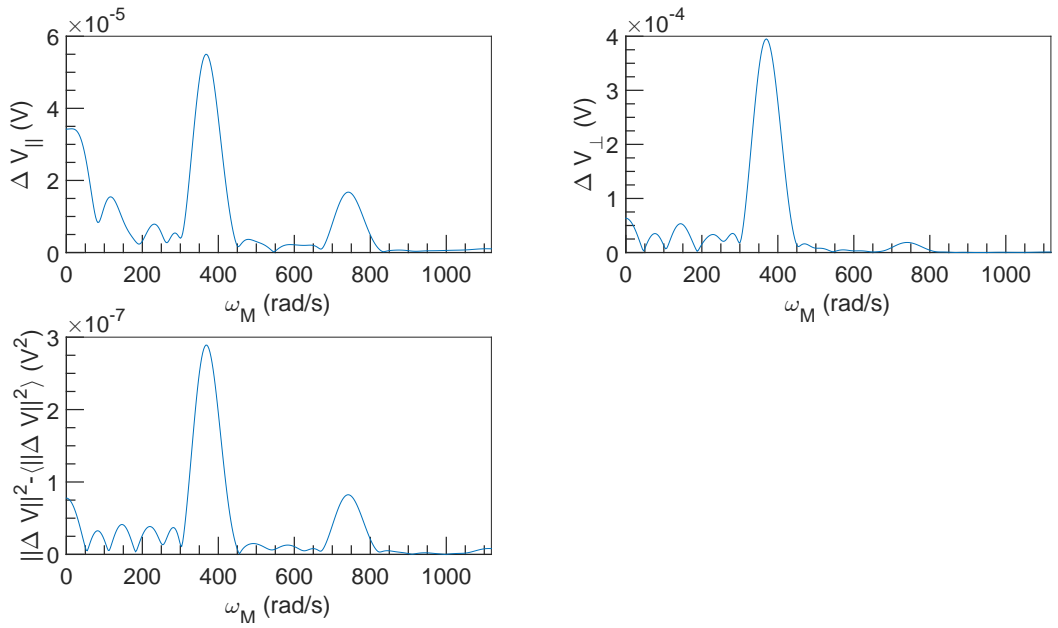


Figure 3.42: FFT spectral density of  $\Delta V$  vs  $\omega_M$  at  $U = 1 \text{ m s}^{-1}$ ,  $\omega = 7854 \text{ rad s}^{-1}$  and  $\alpha = 6.9\%$ .



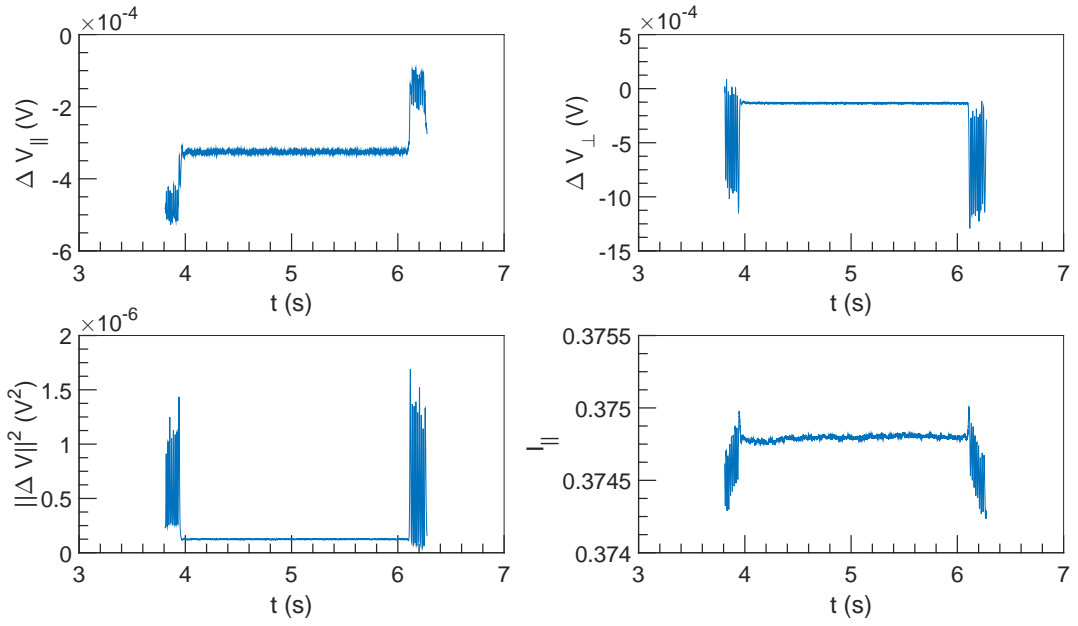


Figure 3.43:  $\Delta V$  and  $I$  vs  $t$  at  $U = 1 \text{ m s}^{-1}$ ,  $\omega = 9425 \text{ rad s}^{-1}$  and  $\alpha = 6.9\%$ .

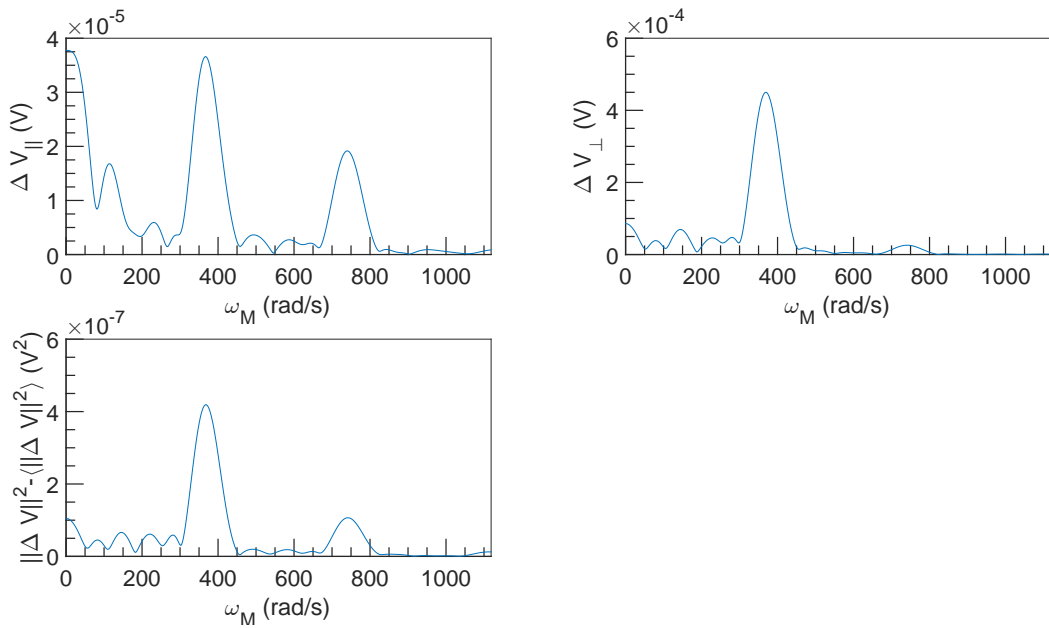


Figure 3.44: FFT spectral density of  $\Delta V$  vs  $\omega_M$  at  $U = 1 \text{ m s}^{-1}$ ,  $\omega = 9425 \text{ rad s}^{-1}$  and  $\alpha = 6.9\%$ .

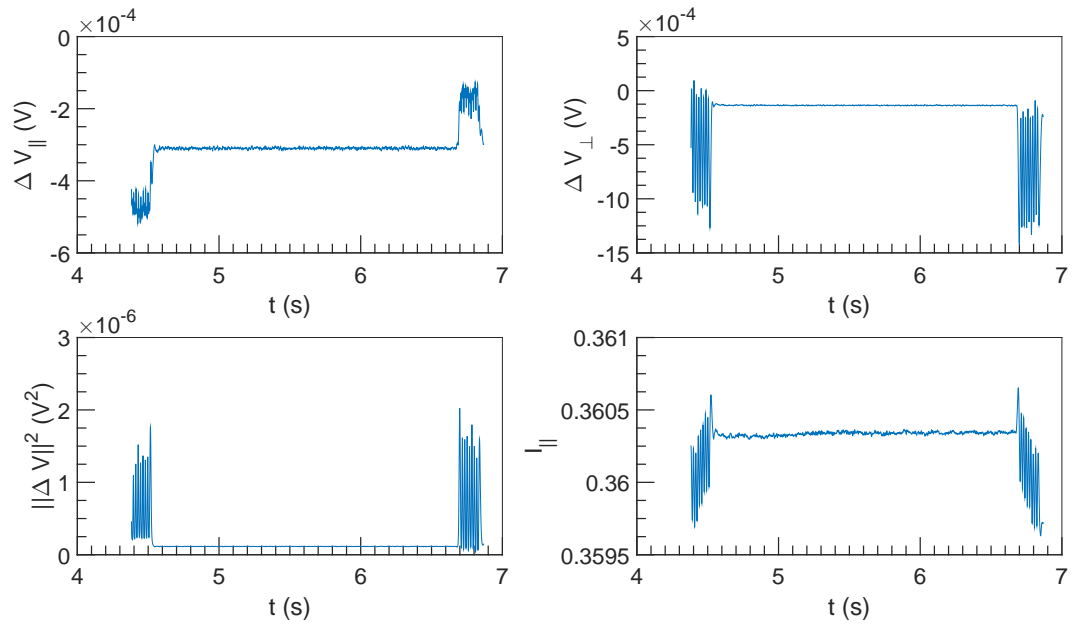


Figure 3.45:  $\Delta V$  and  $I$  vs  $t$  at  $U = 1 \text{ m s}^{-1}$ ,  $\omega = 10\,996 \text{ rad s}^{-1}$  and  $\alpha = 6.9\%$ .

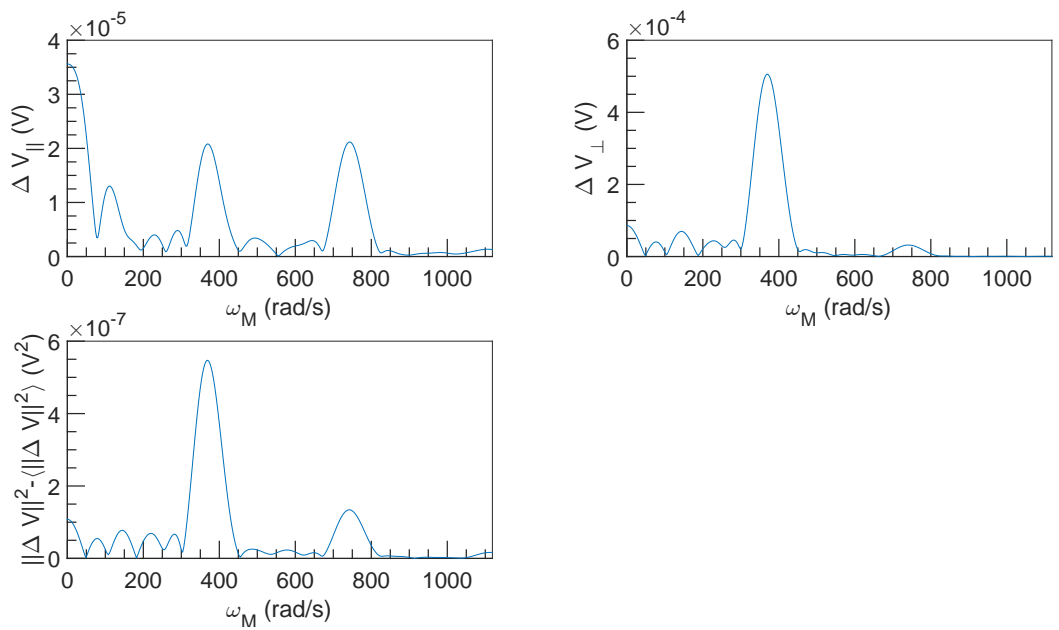


Figure 3.46: FFT spectral density of  $\Delta V$  vs  $\omega_M$  at  $U = 1 \text{ m s}^{-1}$ ,  $\omega = 10\,996 \text{ rad s}^{-1}$  and  $\alpha = 6.9\%$ .

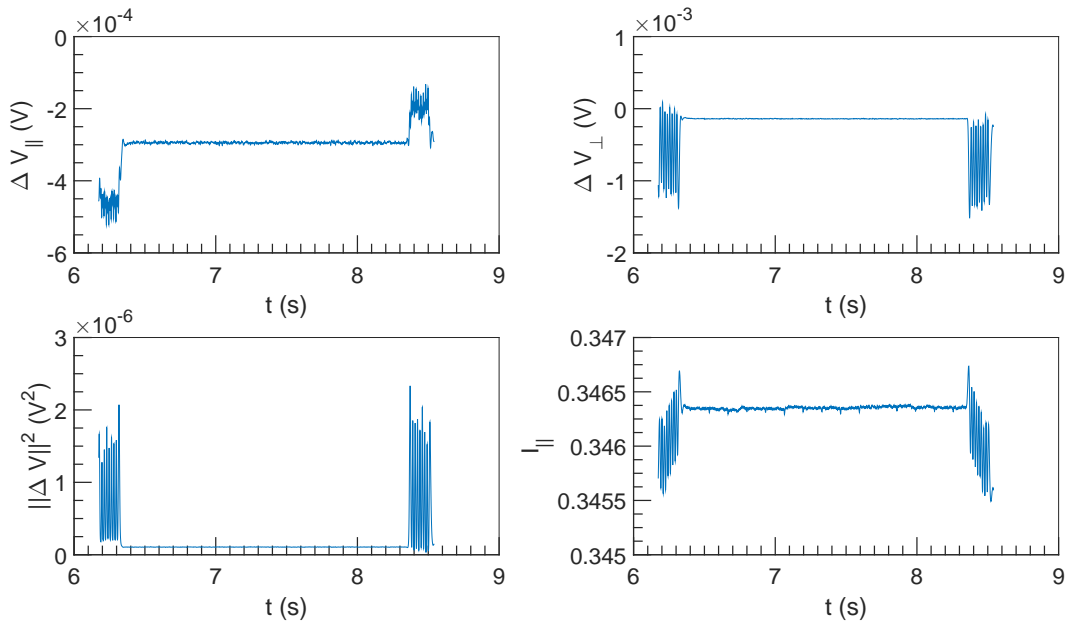


Figure 3.47:  $\Delta V$  and  $I$  vs  $t$  at  $U = 1 \text{ m s}^{-1}$ ,  $\omega = 12\,566 \text{ rad s}^{-1}$  and  $\alpha = 6.9\%$ .

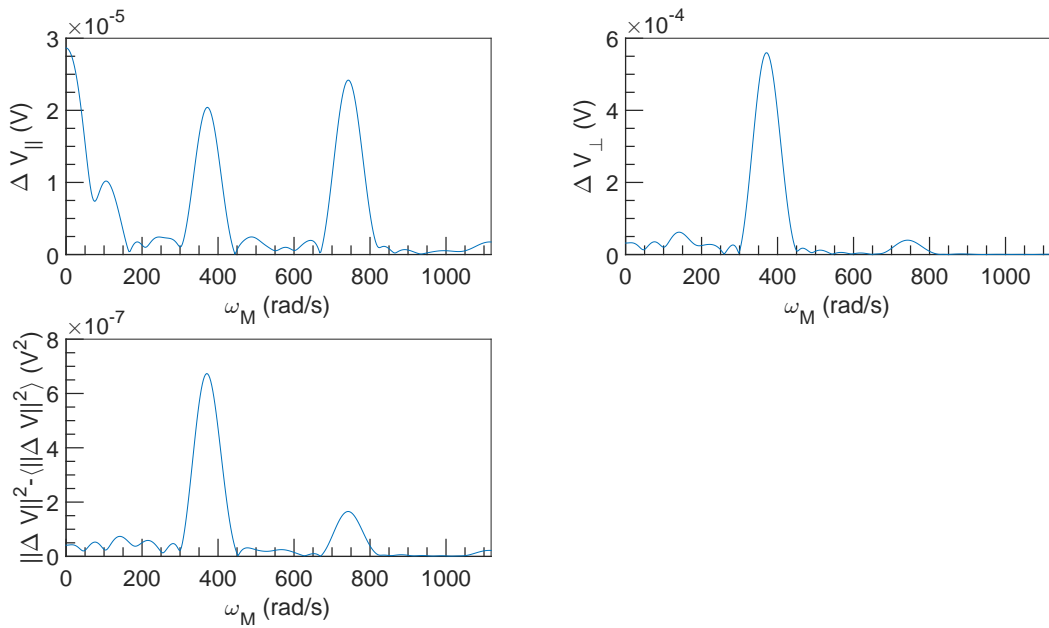


Figure 3.48: FFT spectral density of  $\Delta V$  vs  $\omega_M$  at  $U = 1 \text{ m s}^{-1}$ ,  $\omega = 12\,566 \text{ rad s}^{-1}$  and  $\alpha = 6.9\%$ .

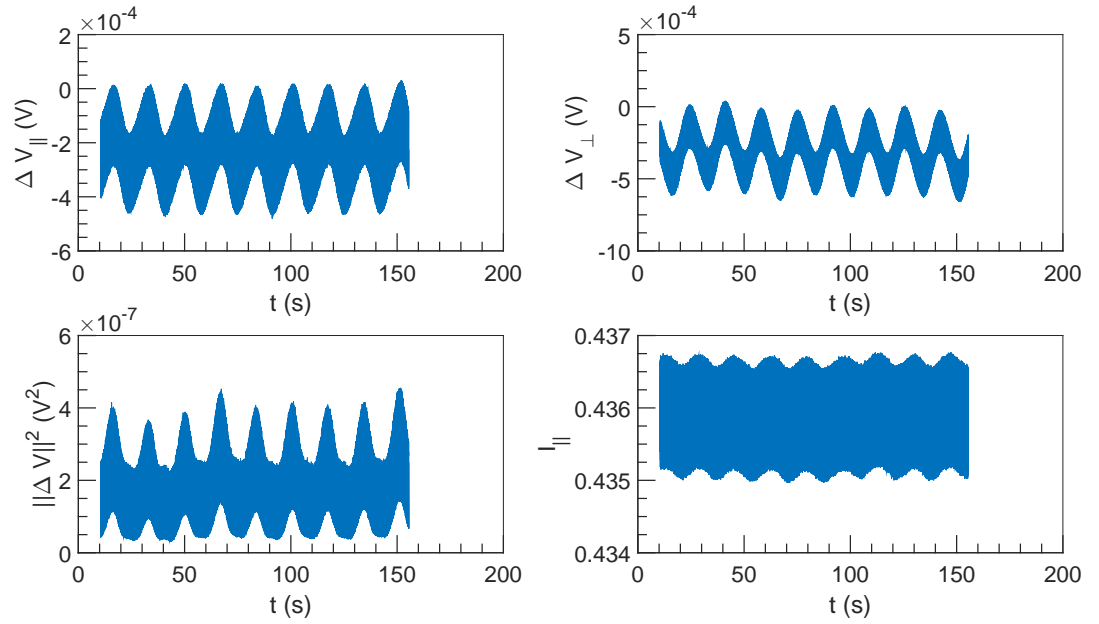


Figure 3.49:  $\Delta V$  and  $I$  vs  $t$  at  $U = 10^{-3} \text{ m s}^{-1}$ ,  $\omega = 3142 \text{ rad s}^{-1}$  and  $\alpha = 6.9\%$ .

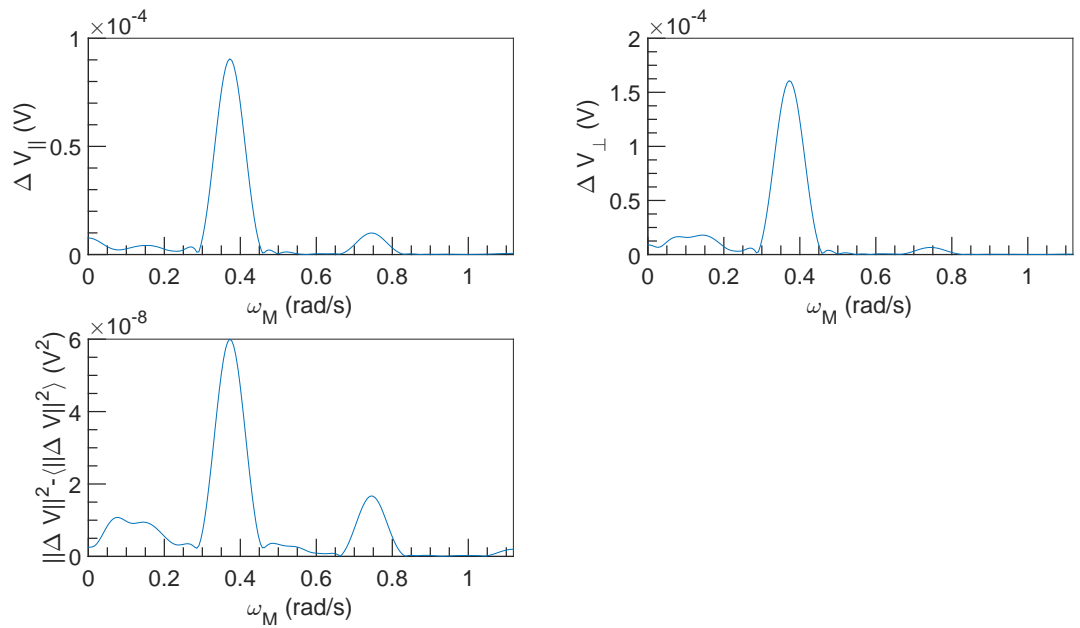


Figure 3.50: FFT spectral density of  $\Delta V$  vs  $\omega_M$  at  $U = 10^{-3} \text{ m s}^{-1}$ ,  $\omega = 3142 \text{ rad s}^{-1}$  and  $\alpha = 6.9\%$ .

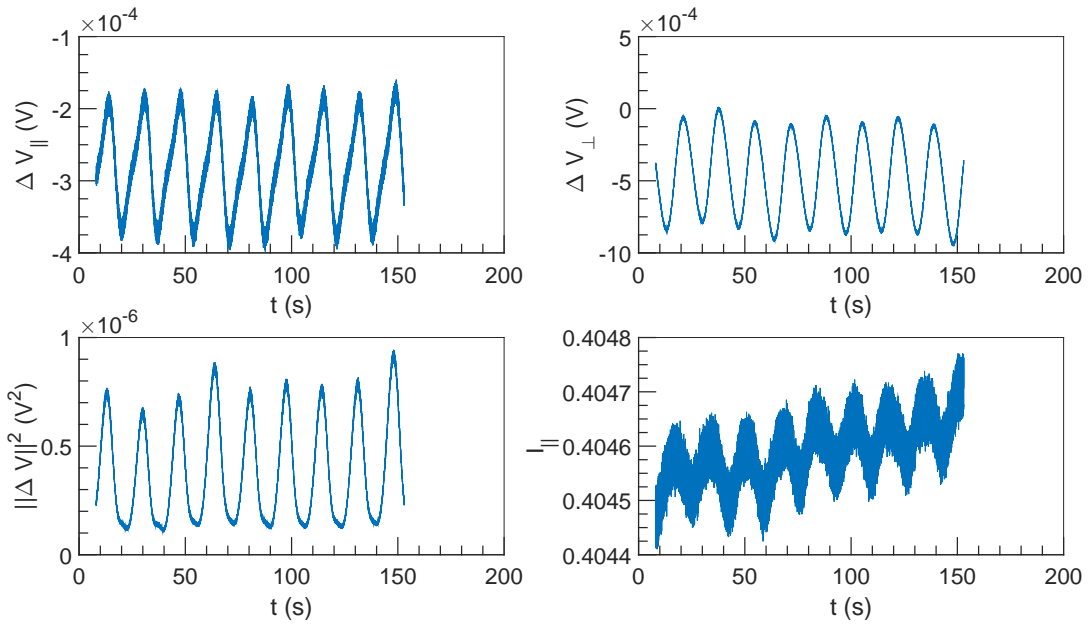


Figure 3.51:  $\Delta V$  and  $I$  vs  $t$  at  $U = 10^{-3} \text{ m s}^{-1}$ ,  $\omega = 6283 \text{ rad s}^{-1}$  and  $\alpha = 6.9\%$ .

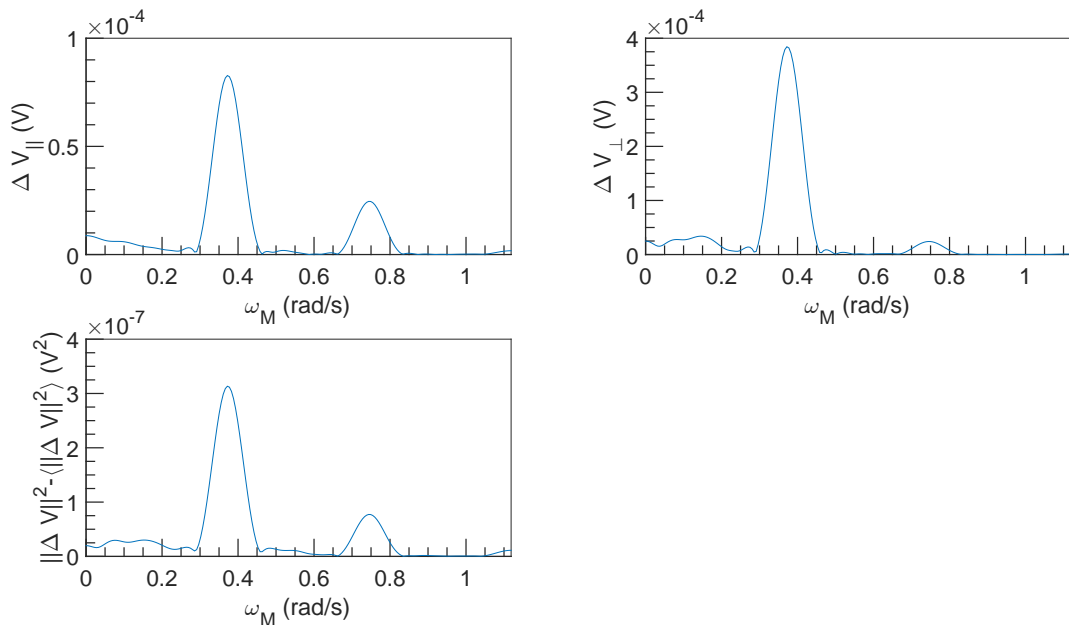


Figure 3.52: FFT spectral density of  $\Delta V$  vs  $\omega_M$  at  $U = 10^{-3} \text{ m s}^{-1}$ ,  $\omega = 6283 \text{ rad s}^{-1}$  and  $\alpha = 6.9\%$ .

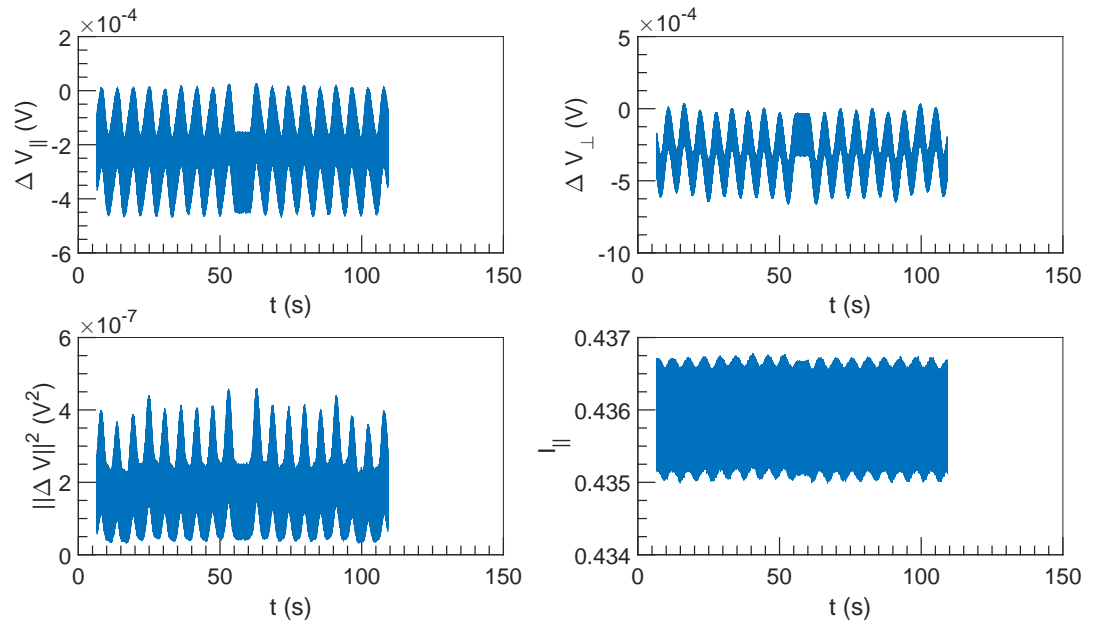


Figure 3.53:  $\Delta V$  and  $I$  vs  $t$  at  $U = 3 \times 10^{-3} \text{ m s}^{-1}$ ,  $\omega = 3142 \text{ rad s}^{-1}$  and  $\alpha = 6.9\%$ .

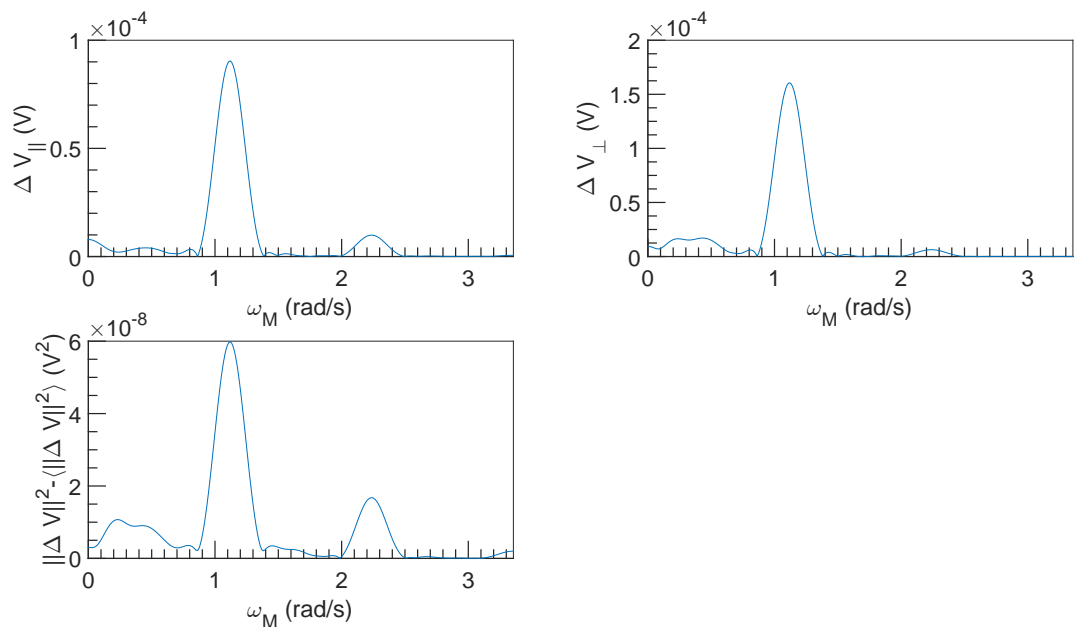


Figure 3.54: FFT spectral density of  $\Delta V$  vs  $\omega_M$  at  $U = 3 \times 10^{-3} \text{ m s}^{-1}$ ,  $\omega = 3142 \text{ rad s}^{-1}$  and  $\alpha = 6.9\%$ .

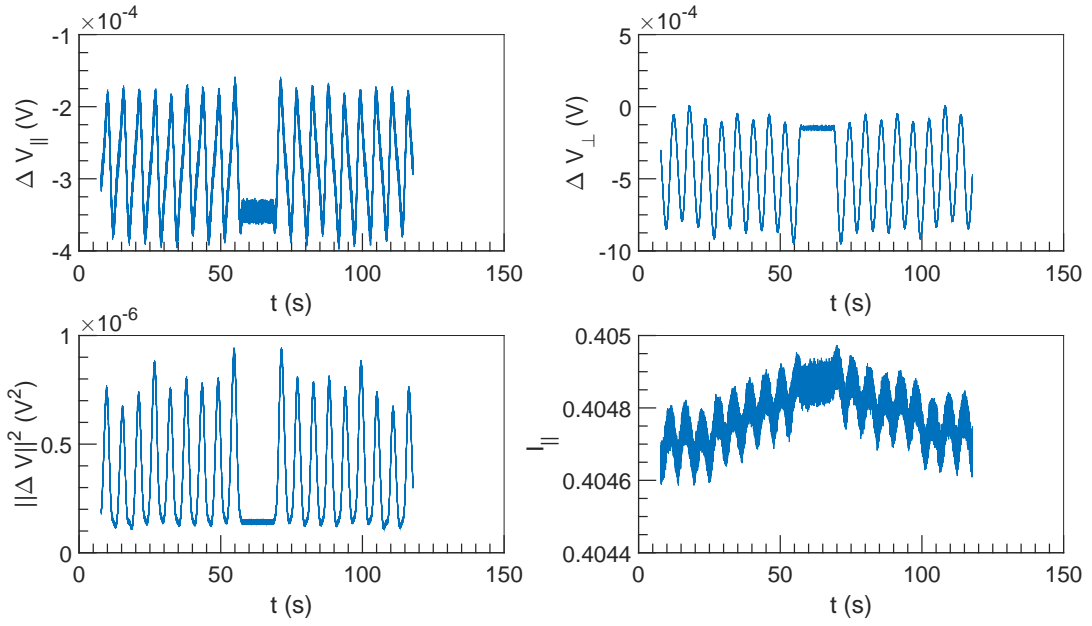


Figure 3.55:  $\Delta V$  and  $I$  vs  $t$  at  $U = 3 \times 10^{-3} \text{ m s}^{-1}$ ,  $\omega = 6283 \text{ rad s}^{-1}$  and  $\alpha = 6.9\%$ .

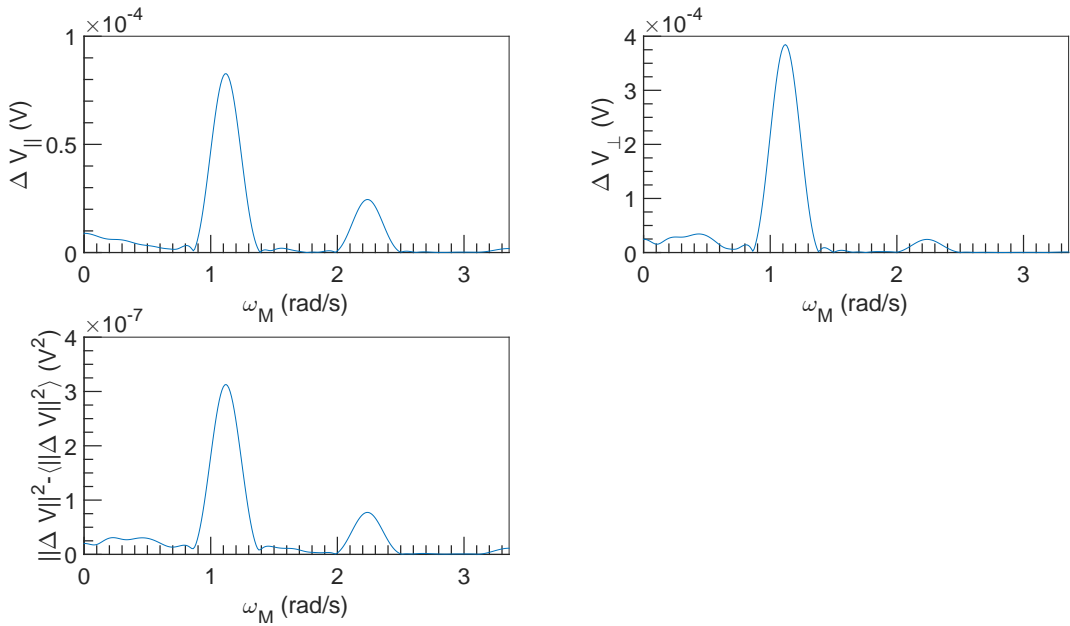


Figure 3.56: FFT spectral density of  $\Delta V$  vs  $\omega_M$  at  $U = 3 \times 10^{-3} \text{ m s}^{-1}$ ,  $\omega = 6283 \text{ rad s}^{-1}$  and  $\alpha = 6.9\%$ .

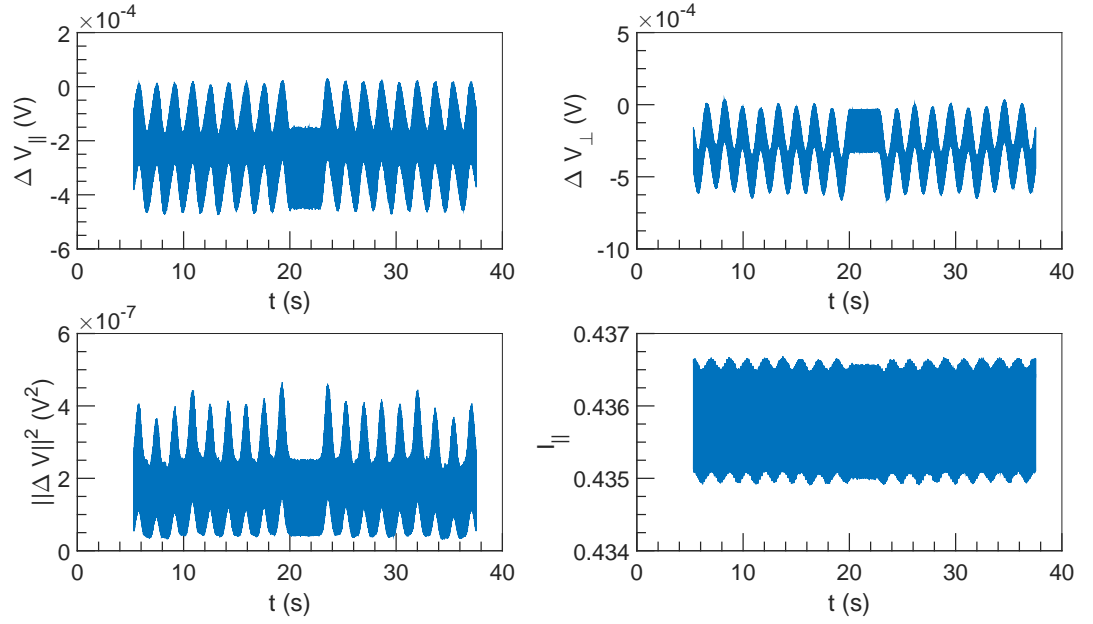


Figure 3.57:  $\Delta V$  and  $I$  vs  $t$  at  $U = 10^{-2} \text{ m s}^{-1}$ ,  $\omega = 3142 \text{ rad s}^{-1}$  and  $\alpha = 6.9\%$ .

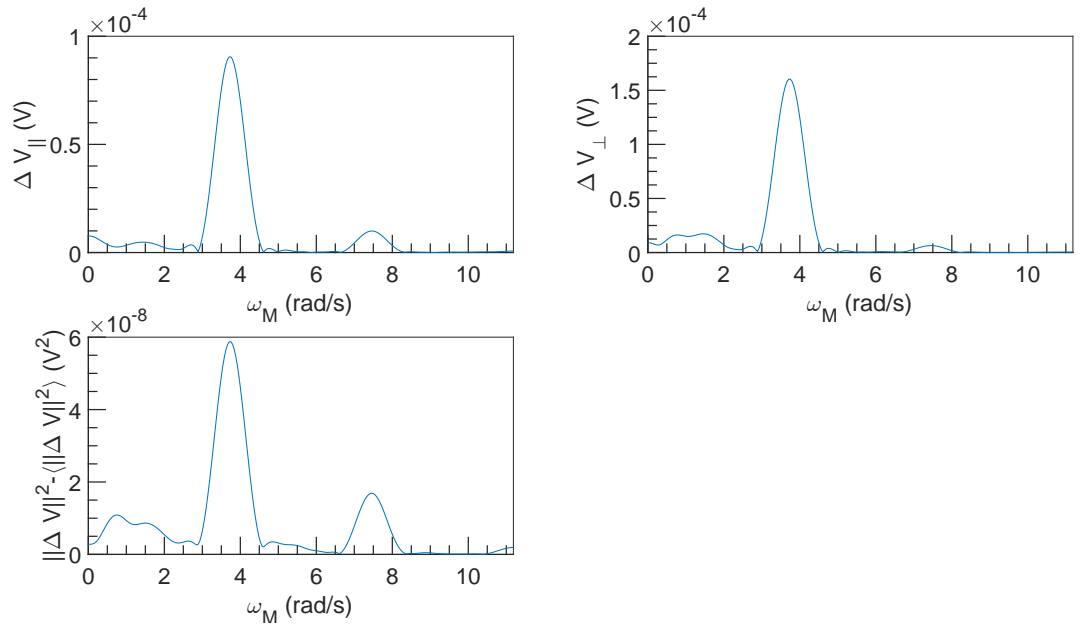


Figure 3.58: FFT spectral density of  $\Delta V$  vs  $\omega_M$  at  $U = 10^{-2} \text{ m s}^{-1}$ ,  $\omega = 3142 \text{ rad s}^{-1}$  and  $\alpha = 6.9\%$ .



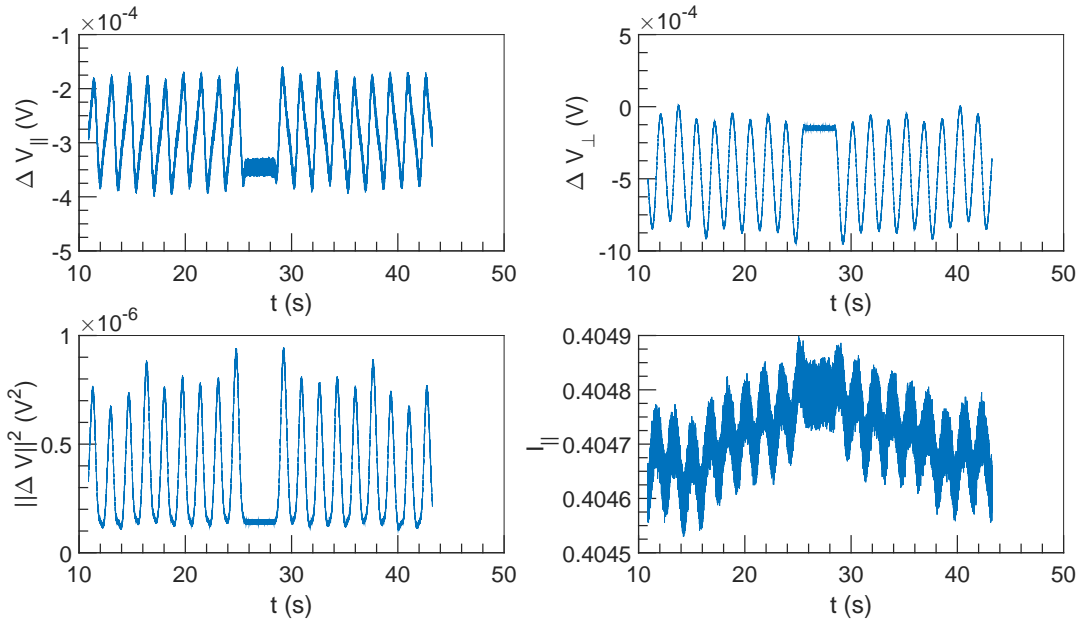


Figure 3.59:  $\Delta V$  and  $I$  vs  $t$  at  $U = 10^{-2} \text{ m s}^{-1}$ ,  $\omega = 6283 \text{ rad s}^{-1}$  and  $\alpha = 6.9\%$ .

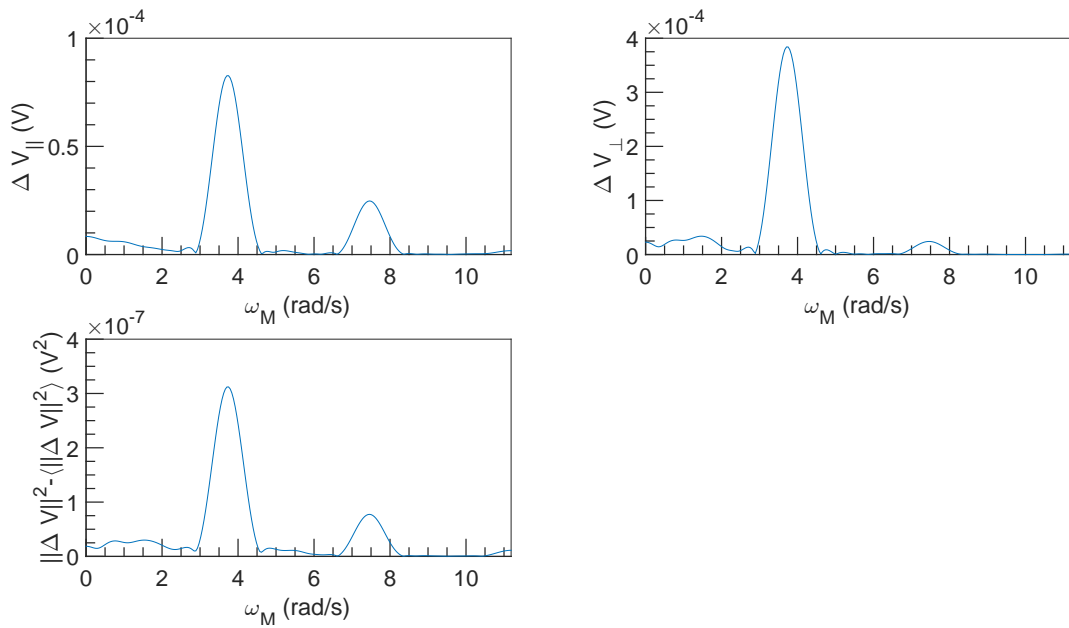


Figure 3.60: FFT spectral density of  $\Delta V$  vs  $\omega_M$  at  $U = 10^{-2} \text{ m s}^{-1}$ ,  $\omega = 6283 \text{ rad s}^{-1}$  and  $\alpha = 6.9\%$ .

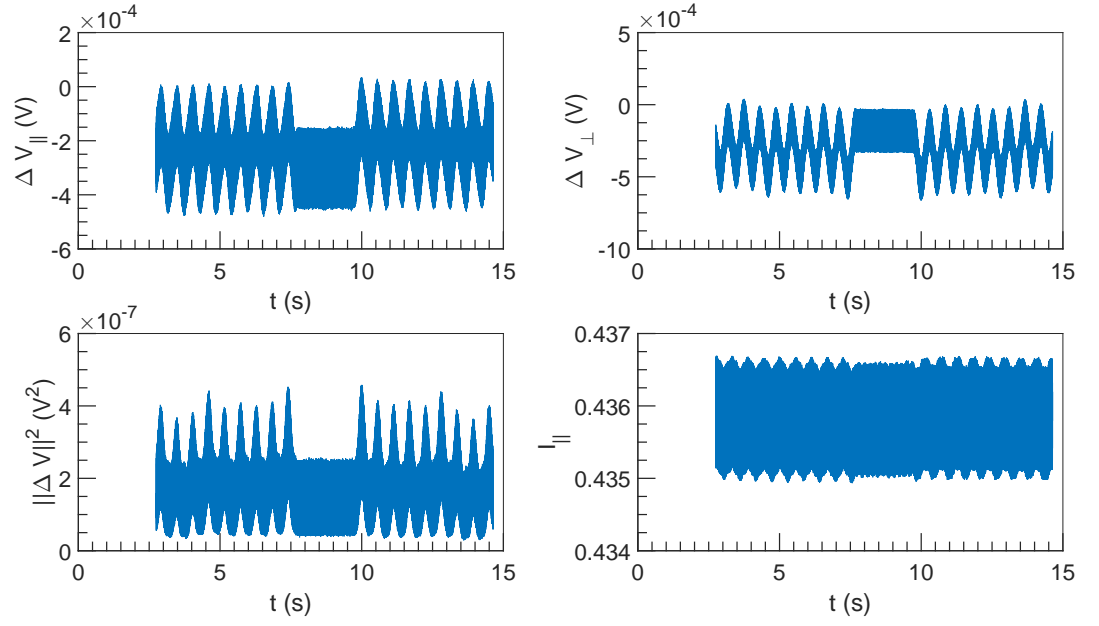


Figure 3.61:  $\Delta V$  and  $I$  vs  $t$  at  $U = 3 \times 10^{-2} \text{ m s}^{-1}$ ,  $\omega = 3142 \text{ rad s}^{-1}$  and  $\alpha = 6.9\%$ .

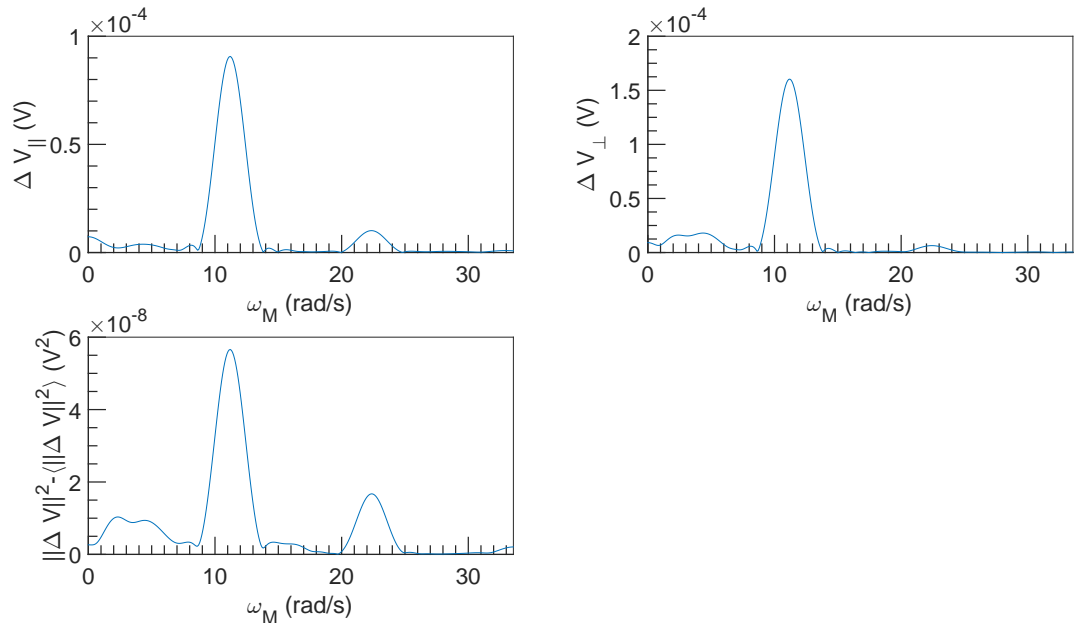


Figure 3.62: FFT spectral density of  $\Delta V$  vs  $\omega_M$  at  $U = 3 \times 10^{-2} \text{ m s}^{-1}$ ,  $\omega = 3142 \text{ rad s}^{-1}$  and  $\alpha = 6.9\%$ .

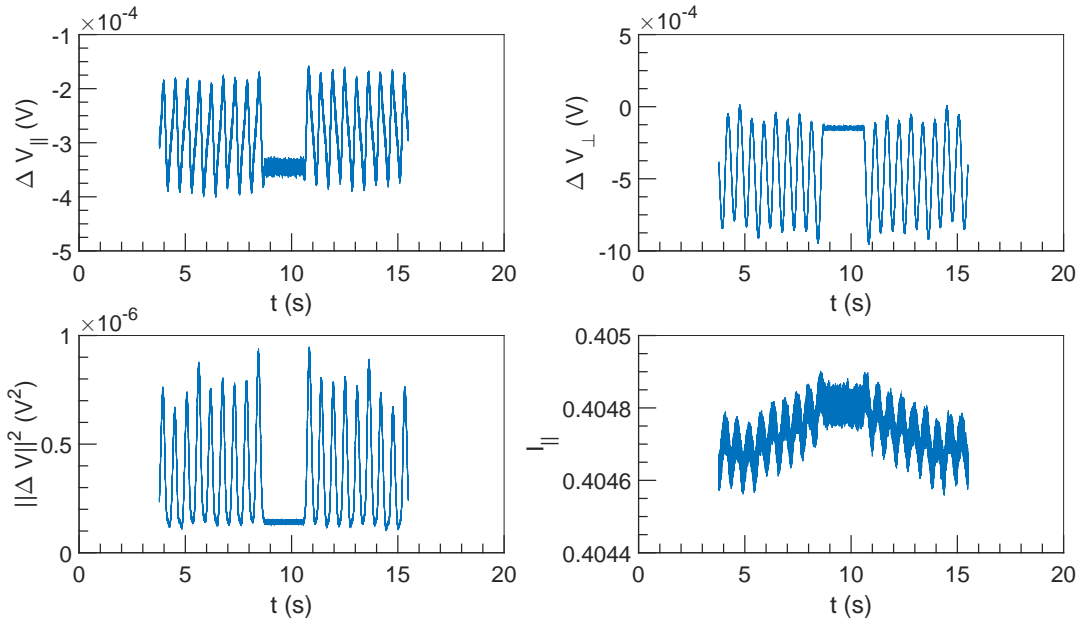


Figure 3.63:  $\Delta V$  and  $I$  vs  $t$  at  $U = 3 \times 10^{-2} \text{ m s}^{-1}$ ,  $\omega = 6283 \text{ rad s}^{-1}$  and  $\alpha = 6.9\%$ .

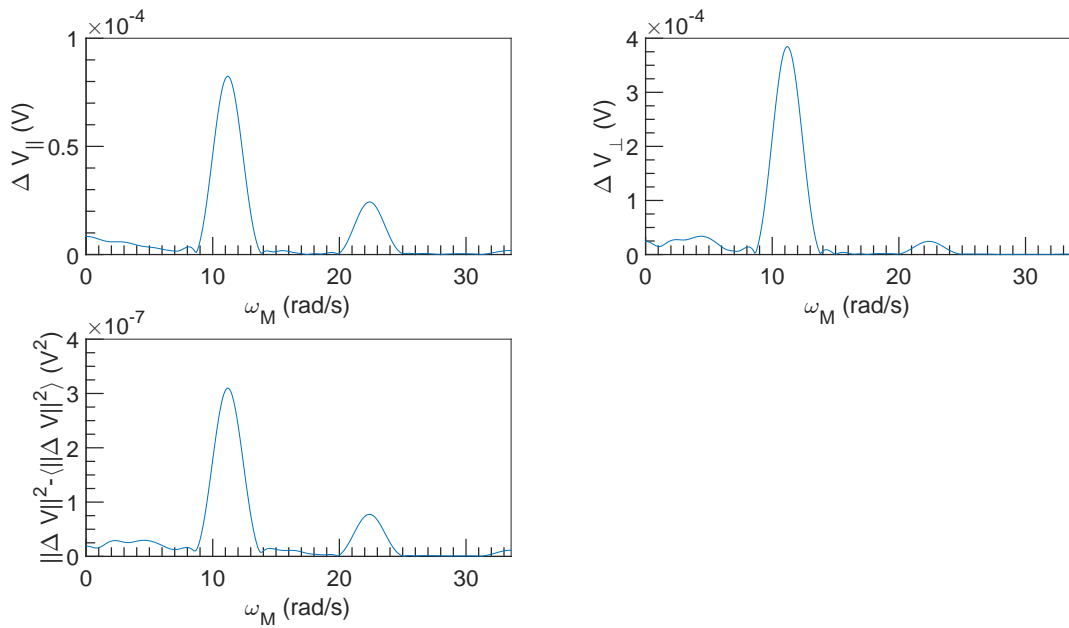


Figure 3.64: FFT spectral density of  $\Delta V$  vs  $\omega_M$  at  $U = 3 \times 10^{-2} \text{ m s}^{-1}$ ,  $\omega = 6283 \text{ rad s}^{-1}$  and  $\alpha = 6.9\%$ .

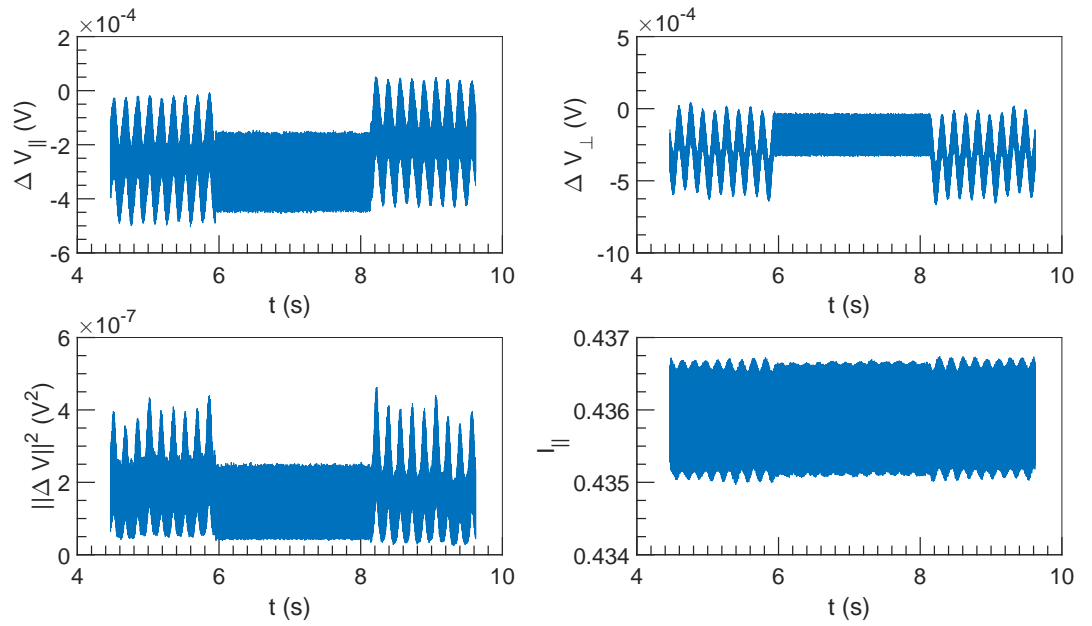


Figure 3.65:  $\Delta V$  and  $I$  vs  $t$  at  $U = 0.1 \text{ m s}^{-1}$ ,  $\omega = 3142 \text{ rad s}^{-1}$  and  $\alpha = 6.9\%$ .

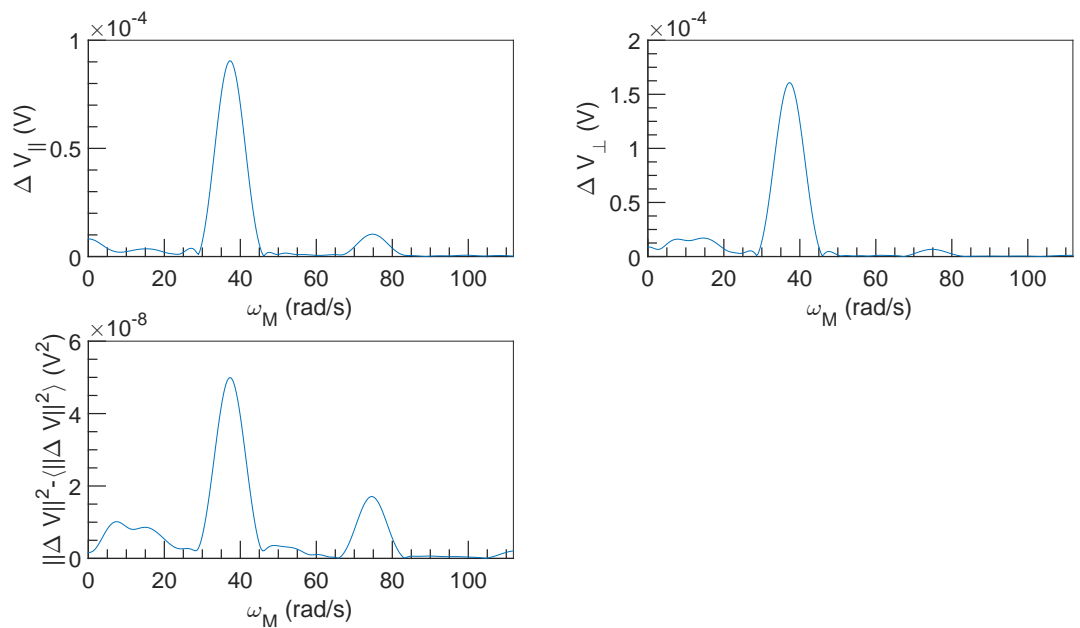


Figure 3.66: FFT spectral density of  $\Delta V$  vs  $\omega_M$  at  $U = 0.1 \text{ m s}^{-1}$ ,  $\omega = 3142 \text{ rad s}^{-1}$  and  $\alpha = 6.9\%$ .

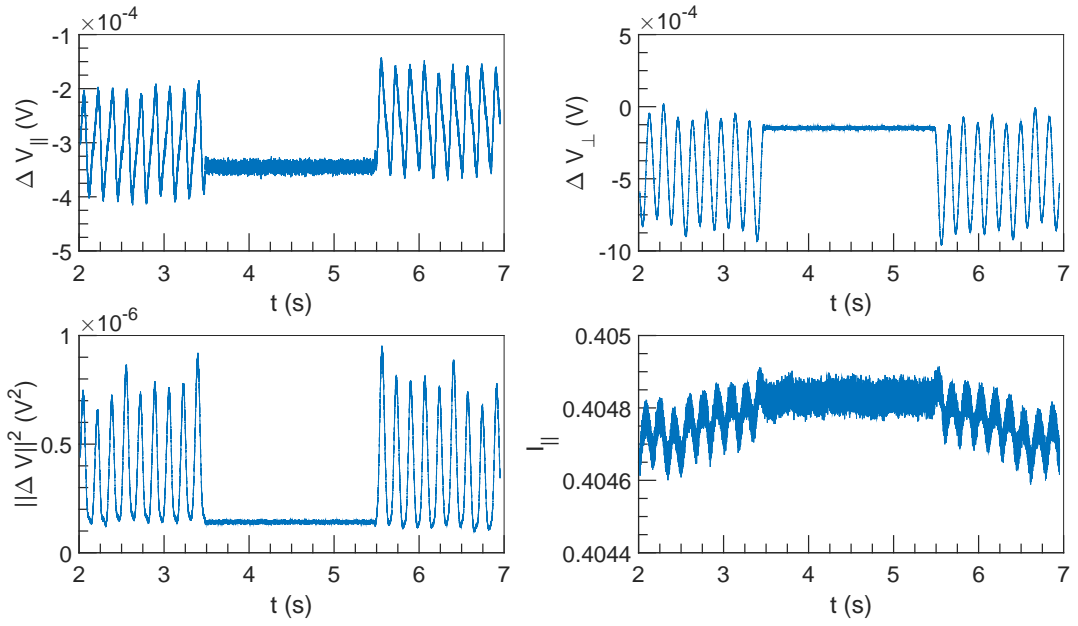


Figure 3.67:  $\Delta V$  and  $I$  vs  $t$  at  $U = 0.1 \text{ m s}^{-1}$ ,  $\omega = 6283 \text{ rad s}^{-1}$  and  $\alpha = 6.9\%$ .

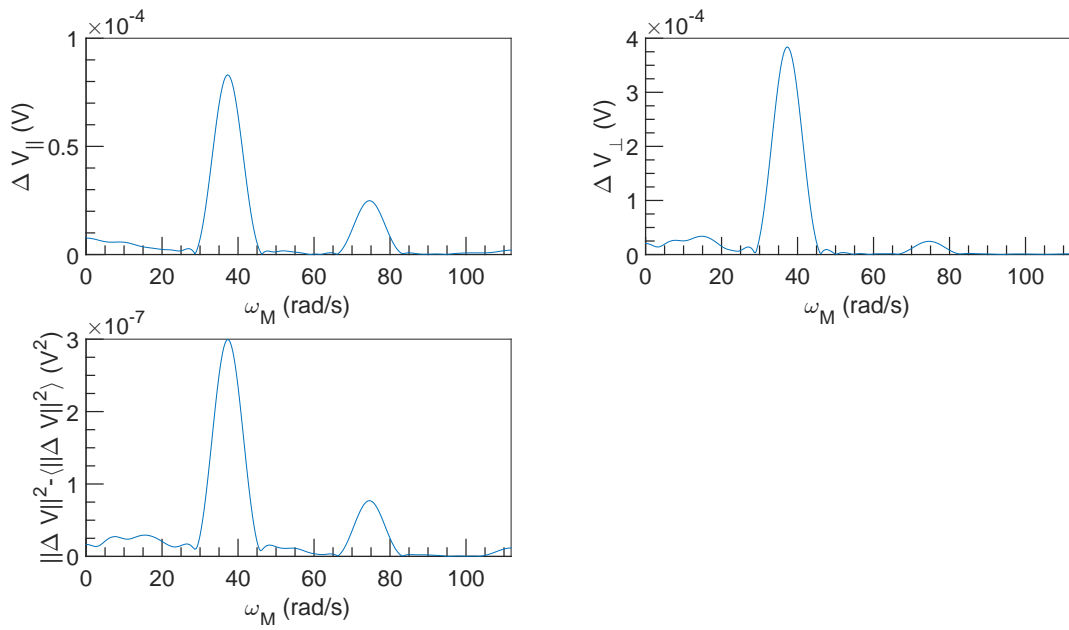


Figure 3.68: FFT spectral density of  $\Delta V$  vs  $\omega_M$  at  $U = 0.1 \text{ m s}^{-1}$ ,  $\omega = 6283 \text{ rad s}^{-1}$  and  $\alpha = 6.9\%$ .

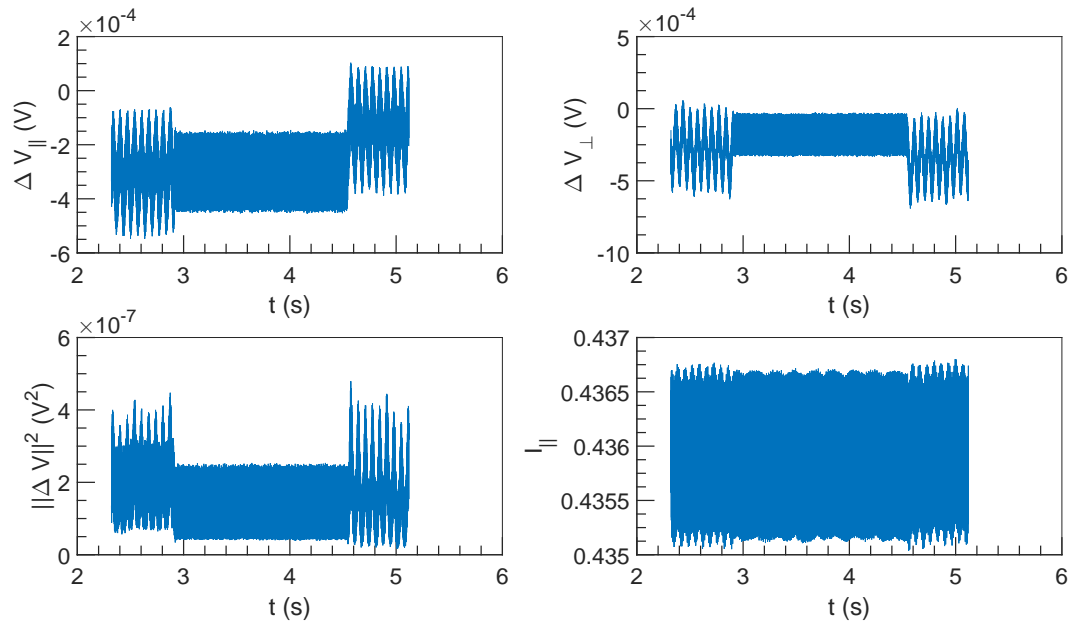


Figure 3.69:  $\Delta V$  and  $I$  vs  $t$  at  $U = 0.25 \text{ ms}^{-1}$ ,  $\omega = 3142 \text{ rad s}^{-1}$  and  $\alpha = 6.9\%$ .

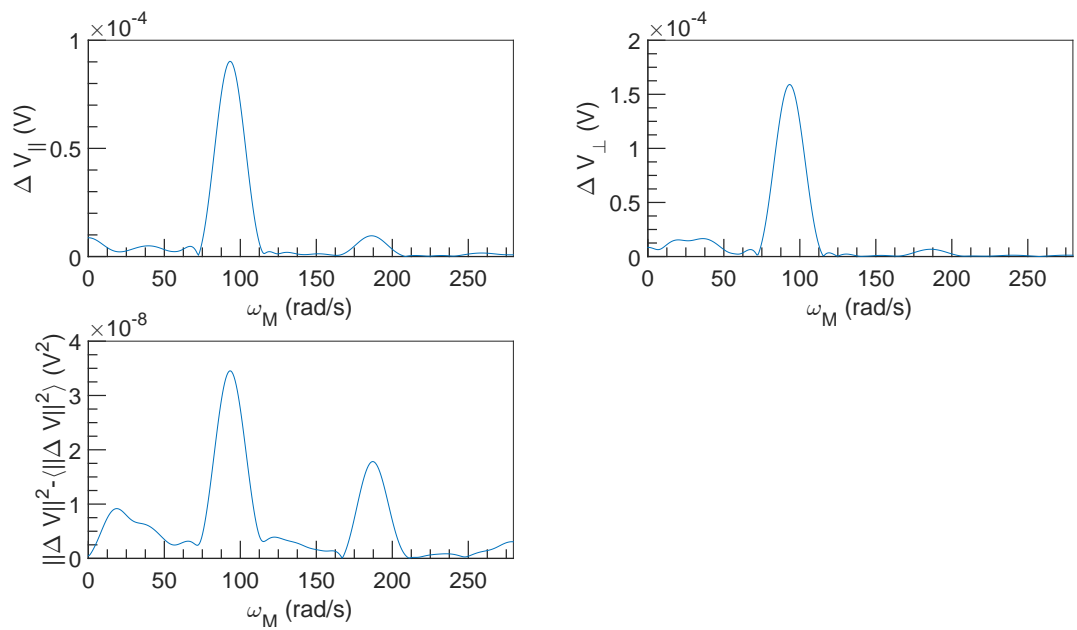


Figure 3.70: FFT spectral density of  $\Delta V$  vs  $\omega_M$  at  $U = 0.25 \text{ ms}^{-1}$ ,  $\omega = 3142 \text{ rad s}^{-1}$  and  $\alpha = 6.9\%$ .

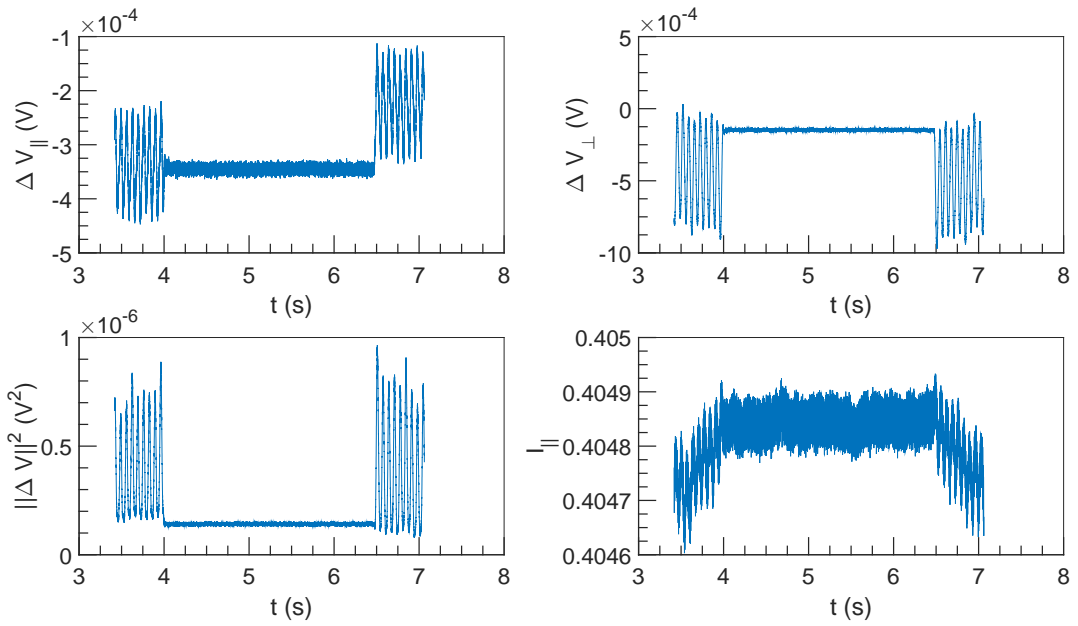


Figure 3.71:  $\Delta V$  and  $I$  vs  $t$  at  $U = 0.25 \text{ m s}^{-1}$ ,  $\omega = 6283 \text{ rad s}^{-1}$  and  $\alpha = 6.9\%$ .

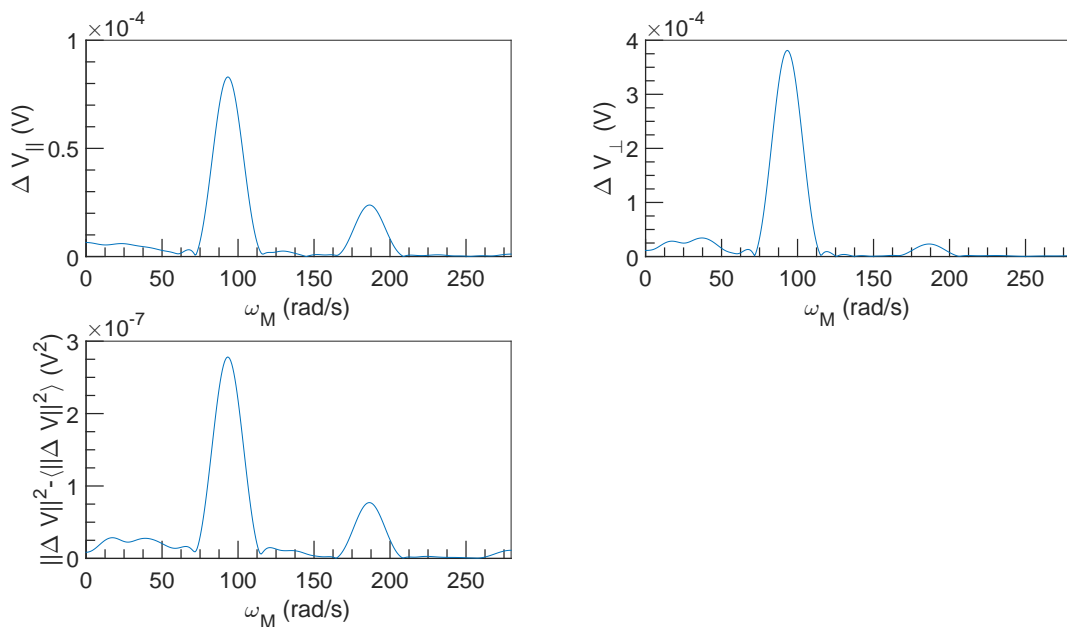


Figure 3.72: FFT spectral density of  $\Delta V$  vs  $\omega_M$  at  $U = 0.25 \text{ m s}^{-1}$ ,  $\omega = 6283 \text{ rad s}^{-1}$  and  $\alpha = 6.9\%$ .

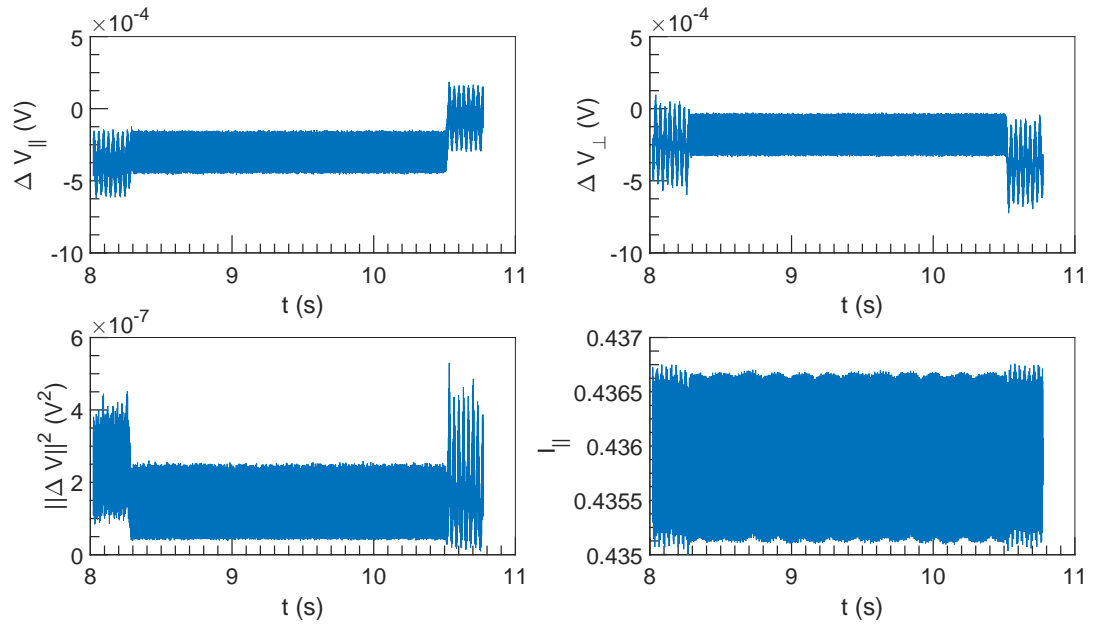


Figure 3.73:  $\Delta V$  and  $I$  vs  $t$  at  $U = 0.5 \text{ m s}^{-1}$ ,  $\omega = 3142 \text{ rad s}^{-1}$  and  $\alpha = 6.9\%$ .

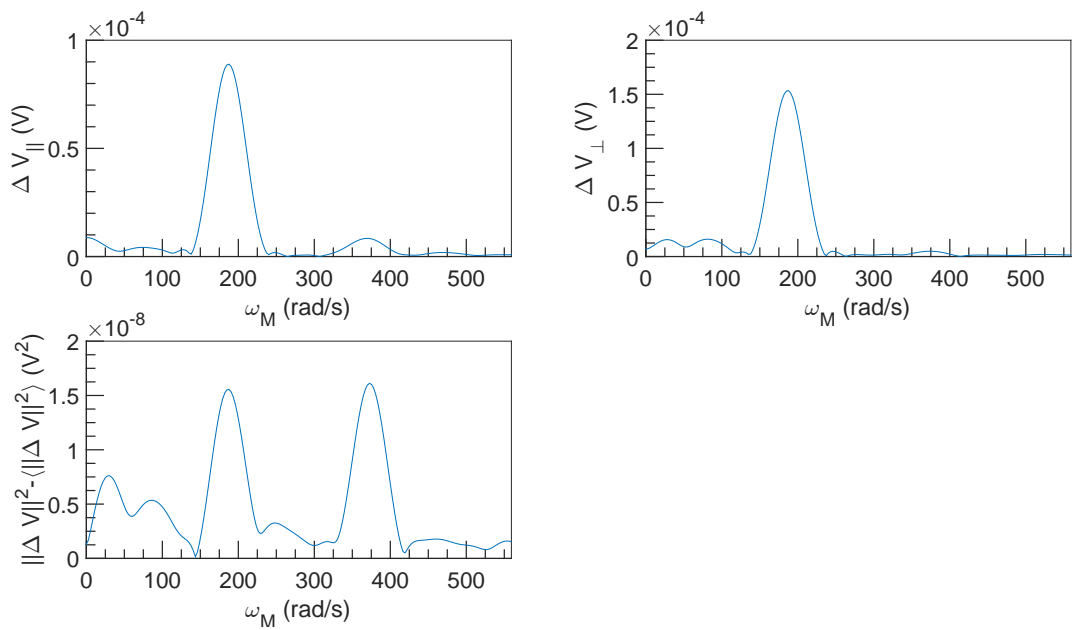


Figure 3.74: FFT spectral density of  $\Delta V$  vs  $\omega_M$  at  $U = 0.5 \text{ m s}^{-1}$ ,  $\omega = 3142 \text{ rad s}^{-1}$  and  $\alpha = 6.9\%$ .



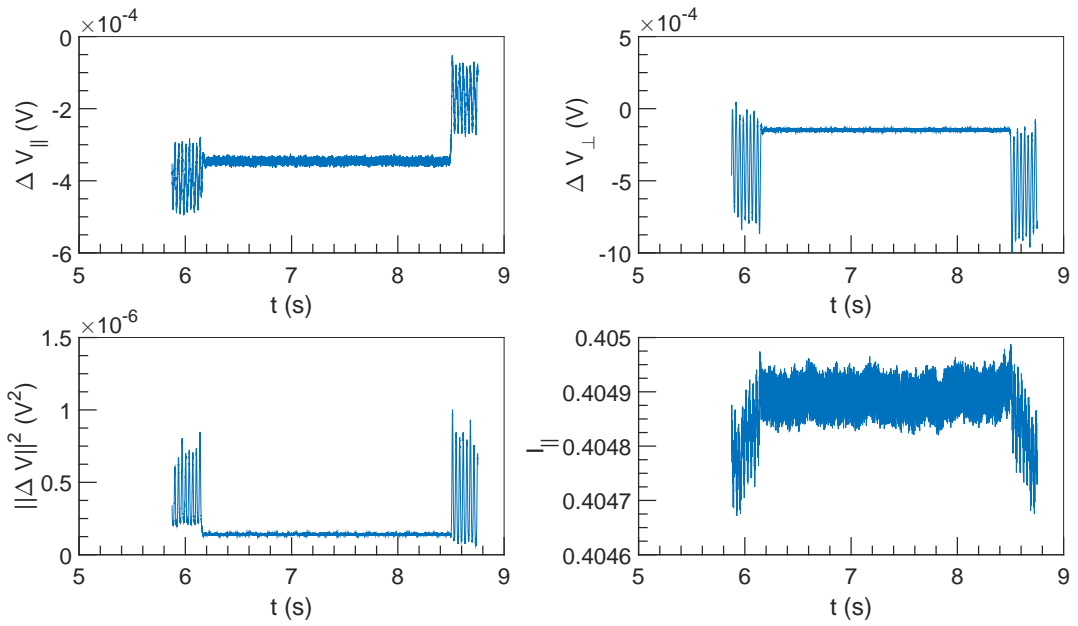


Figure 3.75:  $\Delta V$  and  $I$  vs  $t$  at  $U = 0.5 \text{ m s}^{-1}$ ,  $\omega = 6283 \text{ rad s}^{-1}$  and  $\alpha = 6.9\%$ .

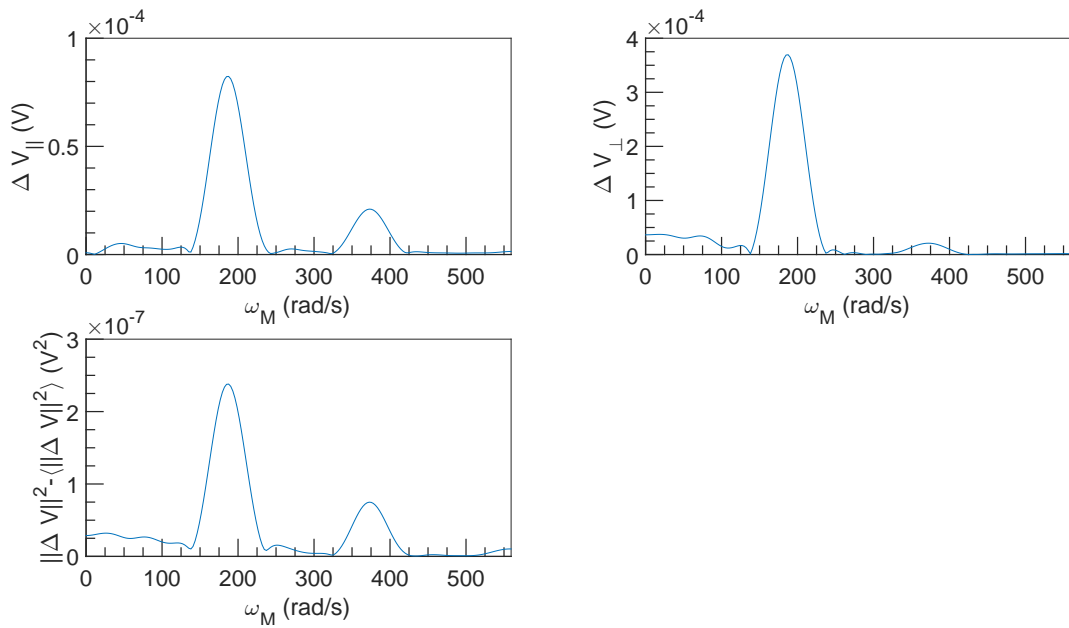


Figure 3.76: FFT spectral density of  $\Delta V$  vs  $\omega_M$  at  $U = 0.5 \text{ m s}^{-1}$ ,  $\omega = 6283 \text{ rad s}^{-1}$  and  $\alpha = 6.9\%$ .

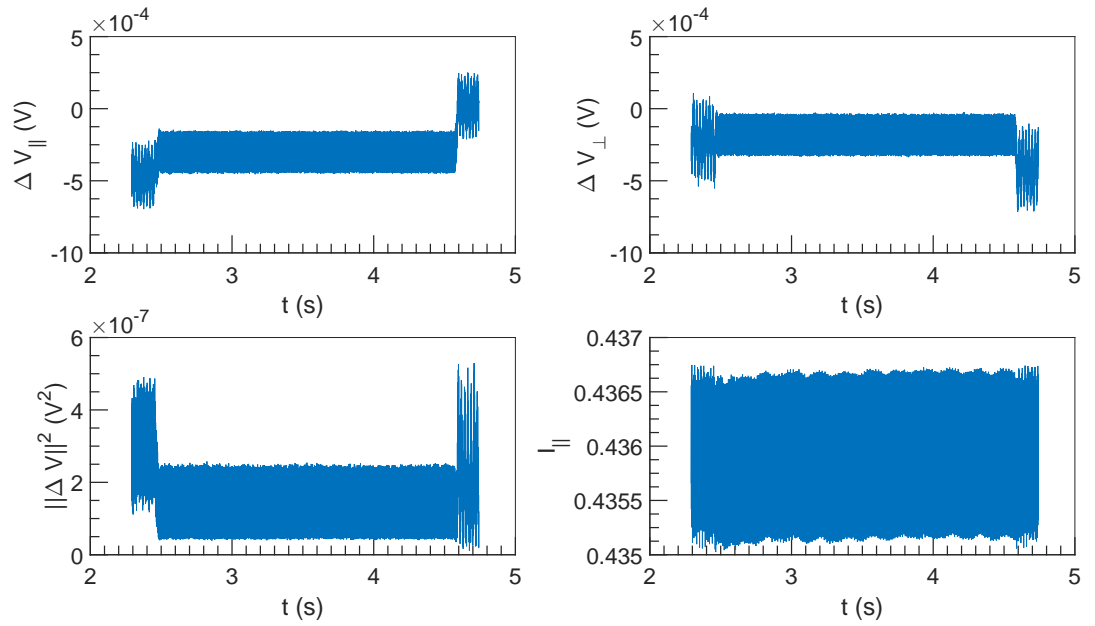


Figure 3.77:  $\Delta V$  and  $I$  vs  $t$  at  $U = 0.75 \text{ ms}^{-1}$ ,  $\omega = 3142 \text{ rad s}^{-1}$  and  $\alpha = 6.9\%$ .

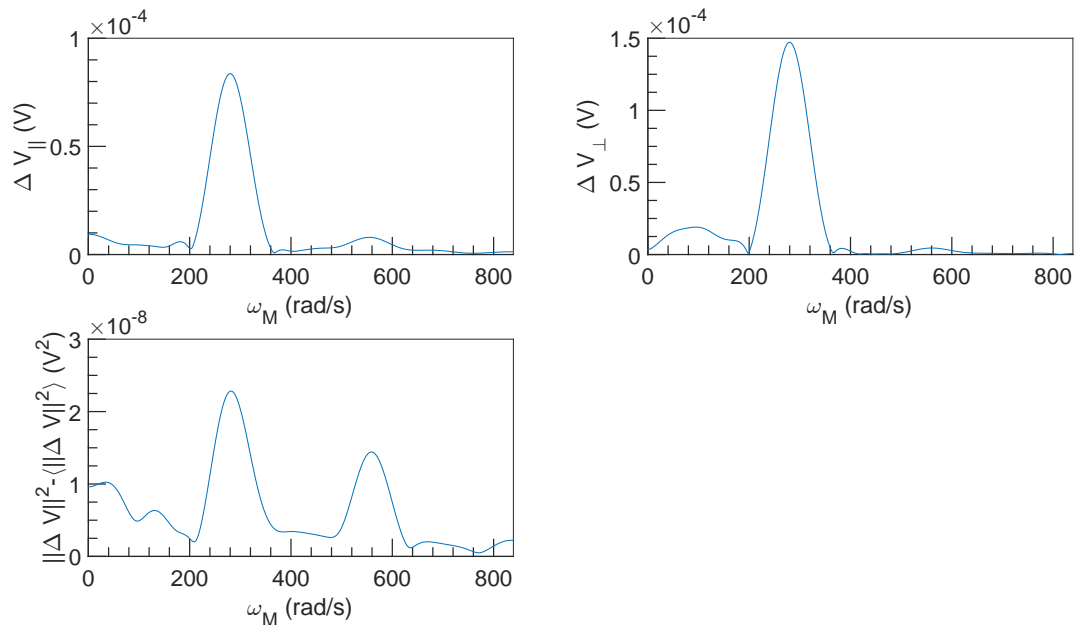


Figure 3.78: FFT spectral density of  $\Delta V$  vs  $\omega_M$  at  $U = 0.75 \text{ ms}^{-1}$ ,  $\omega = 3142 \text{ rad s}^{-1}$  and  $\alpha = 6.9\%$ .

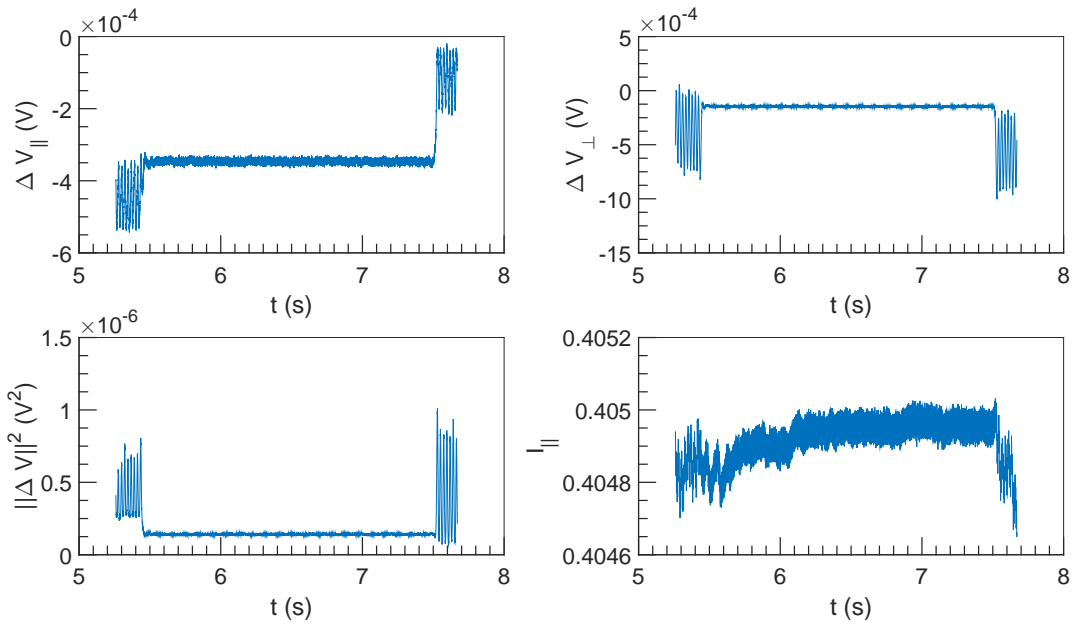


Figure 3.79:  $\Delta V$  and  $I$  vs  $t$  at  $U = 0.75 \text{ ms}^{-1}$ ,  $\omega = 6283 \text{ rad s}^{-1}$  and  $\alpha = 6.9\%$ .

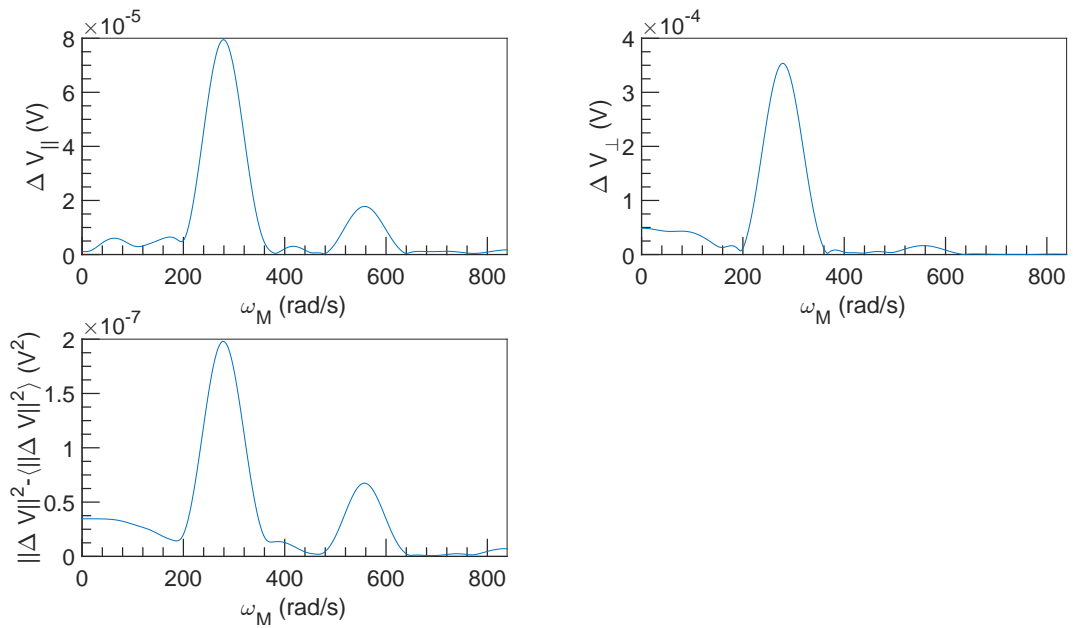


Figure 3.80: FFT spectral density of  $\Delta V$  vs  $\omega_M$  at  $U = 0.75 \text{ ms}^{-1}$ ,  $\omega = 6283 \text{ rad s}^{-1}$  and  $\alpha = 6.9\%$ .

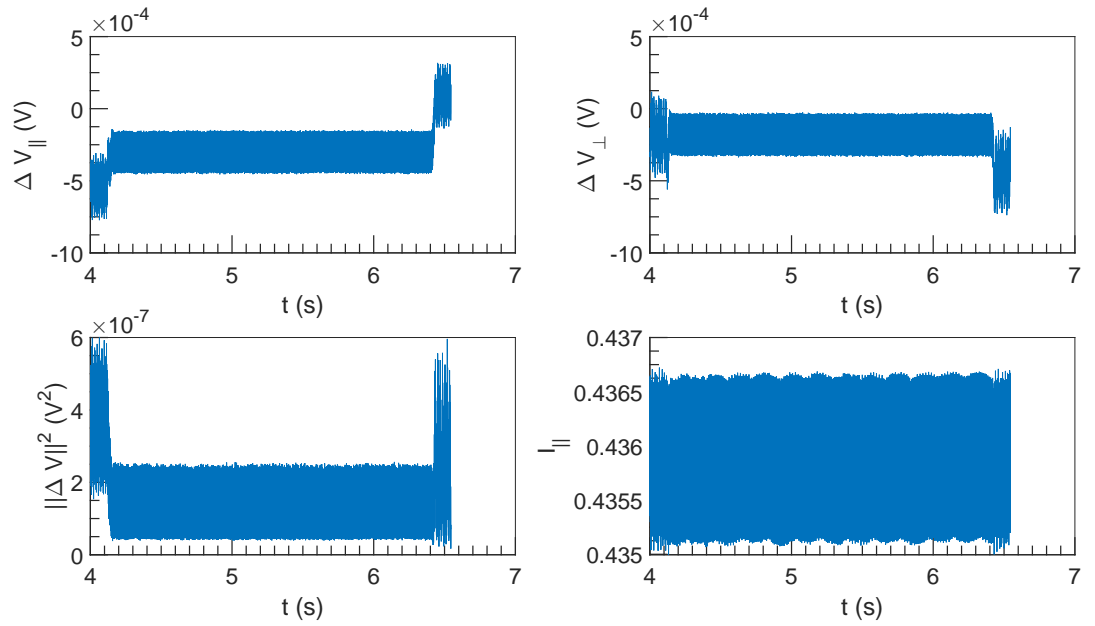


Figure 3.81:  $\Delta V$  and  $I$  vs  $t$  at  $U = 1 \text{ m s}^{-1}$ ,  $\omega = 3142 \text{ rad s}^{-1}$  and  $\alpha = 6.9\%$ .

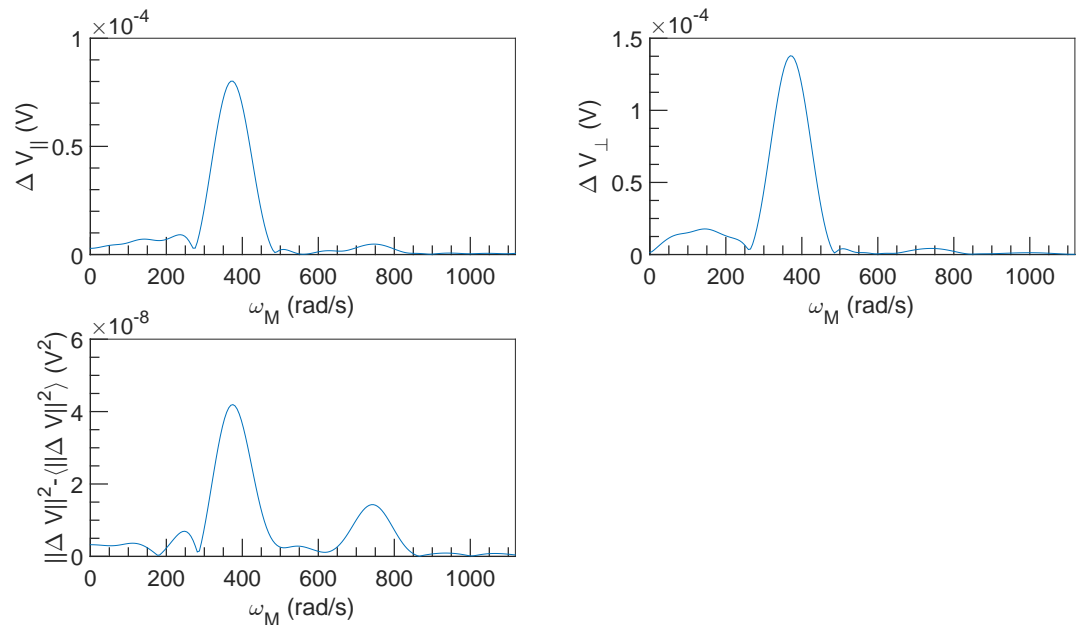


Figure 3.82: FFT spectral density of  $\Delta V$  vs  $\omega_M$  at  $U = 1 \text{ m s}^{-1}$ ,  $\omega = 3142 \text{ rad s}^{-1}$  and  $\alpha = 6.9\%$ .

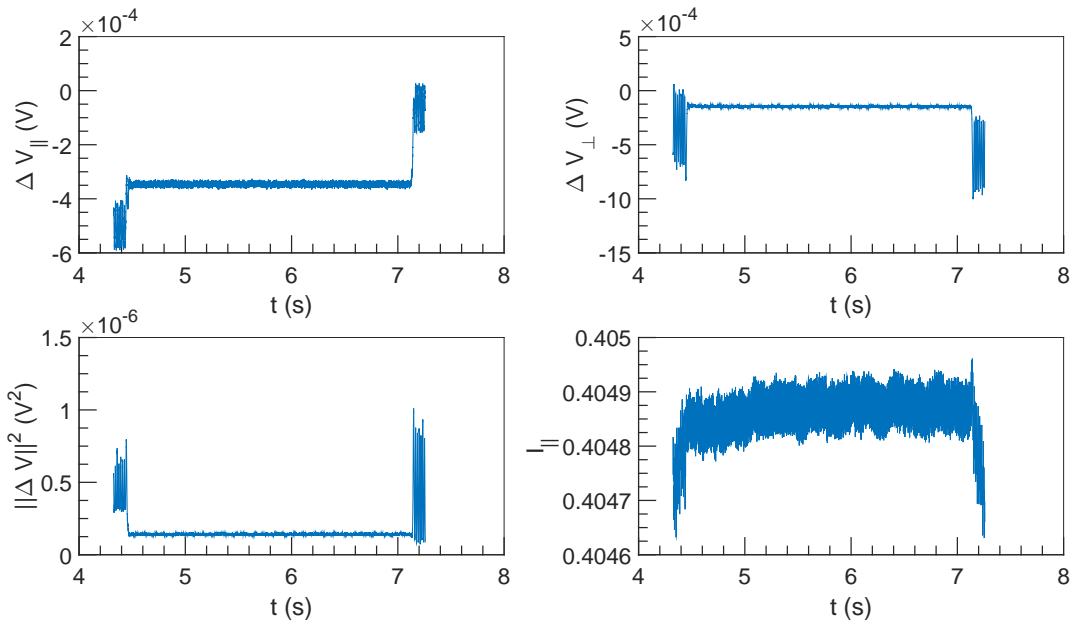


Figure 3.83:  $\Delta V$  and  $I$  vs  $t$  at  $U = 1 \text{ m s}^{-1}$ ,  $\omega = 6283 \text{ rad s}^{-1}$  and  $\alpha = 6.9\%$ .

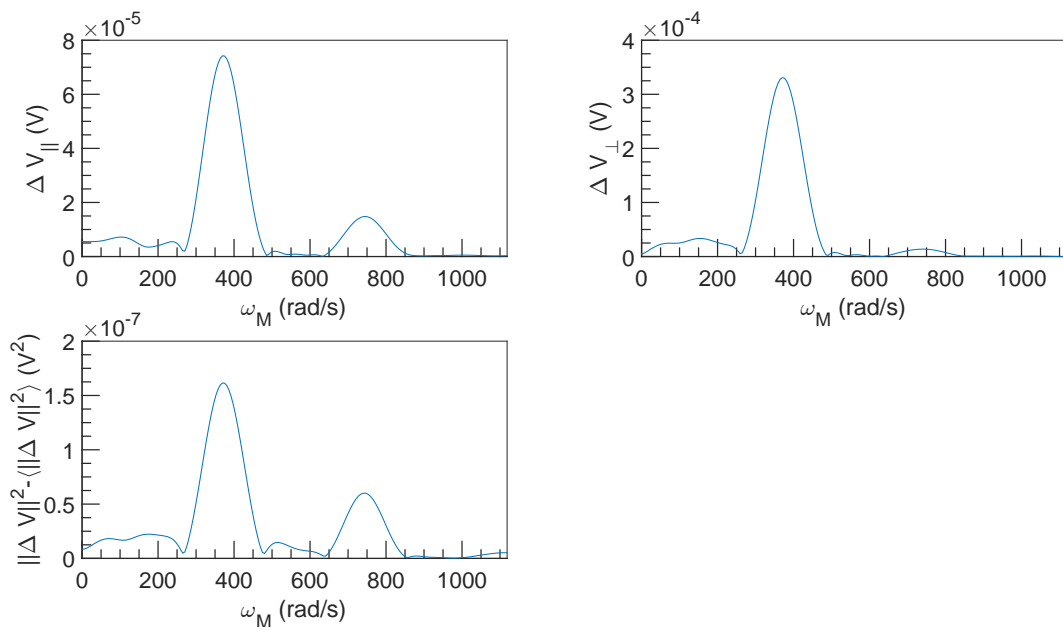


Figure 3.84: FFT spectral density of  $\Delta V$  vs  $\omega_M$  at  $U = 1 \text{ m s}^{-1}$ ,  $\omega = 6283 \text{ rad s}^{-1}$  and  $\alpha = 6.9\%$ .

## Chapter 4

**For**  $\alpha = 2.0\%$

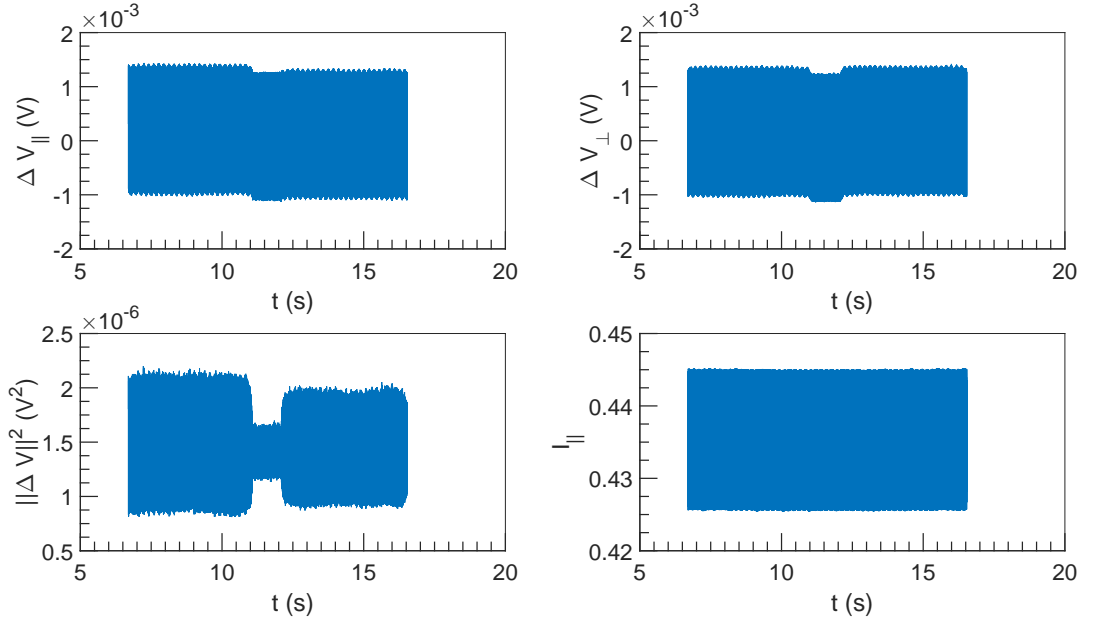


Figure 4.1:  $\Delta V$  and  $I$  vs  $t$  at  $U = 0.1 \text{ m s}^{-1}$ ,  $\omega = 1571 \text{ rad s}^{-1}$  and  $\alpha = 2.0\%$ .

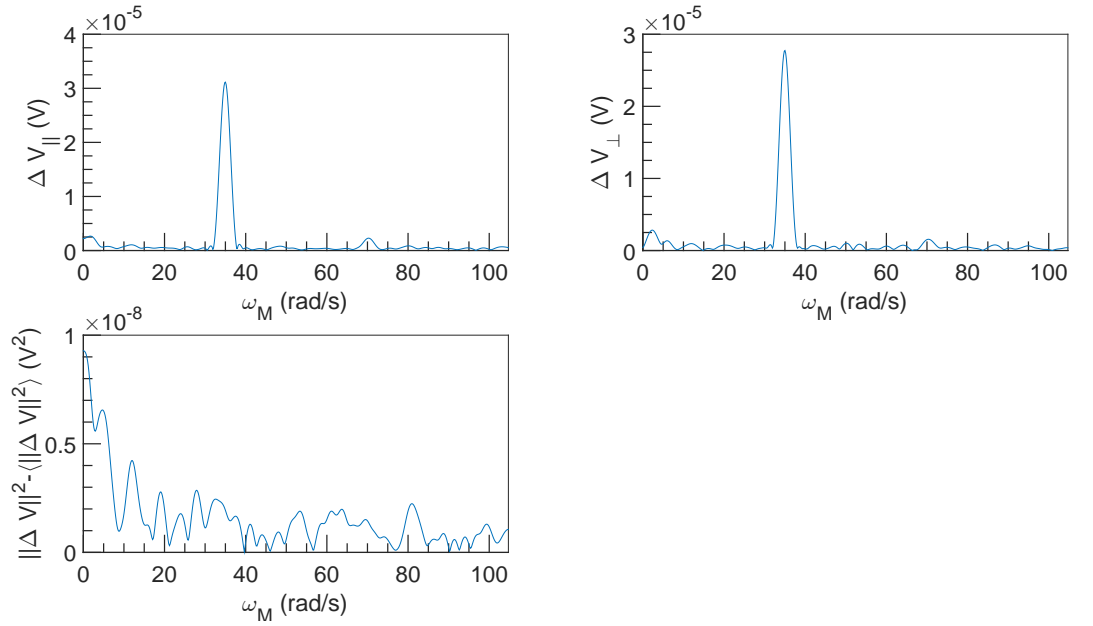


Figure 4.2: FFT spectral density of  $\Delta V$  vs  $\omega_M$  at  $U = 0.1 \text{ m s}^{-1}$ ,  $\omega = 1571 \text{ rad s}^{-1}$  and  $\alpha = 2.0\%$ .

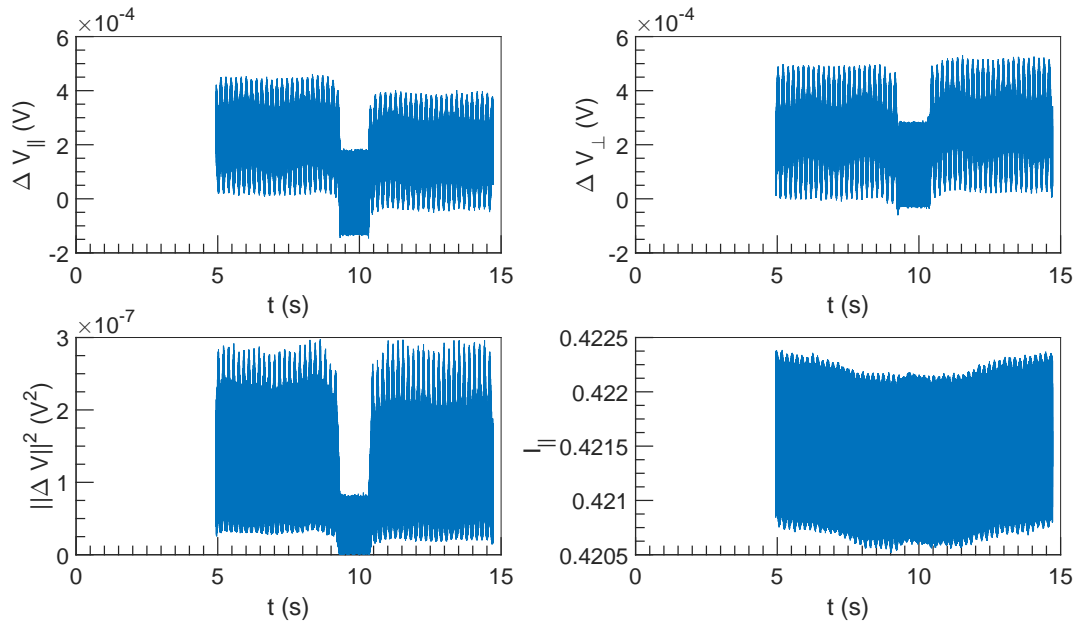


Figure 4.3:  $\Delta V$  and  $I$  vs  $t$  at  $U = 0.1 \text{ m s}^{-1}$ ,  $\omega = 3142 \text{ rad s}^{-1}$  and  $\alpha = 2.0\%$ .

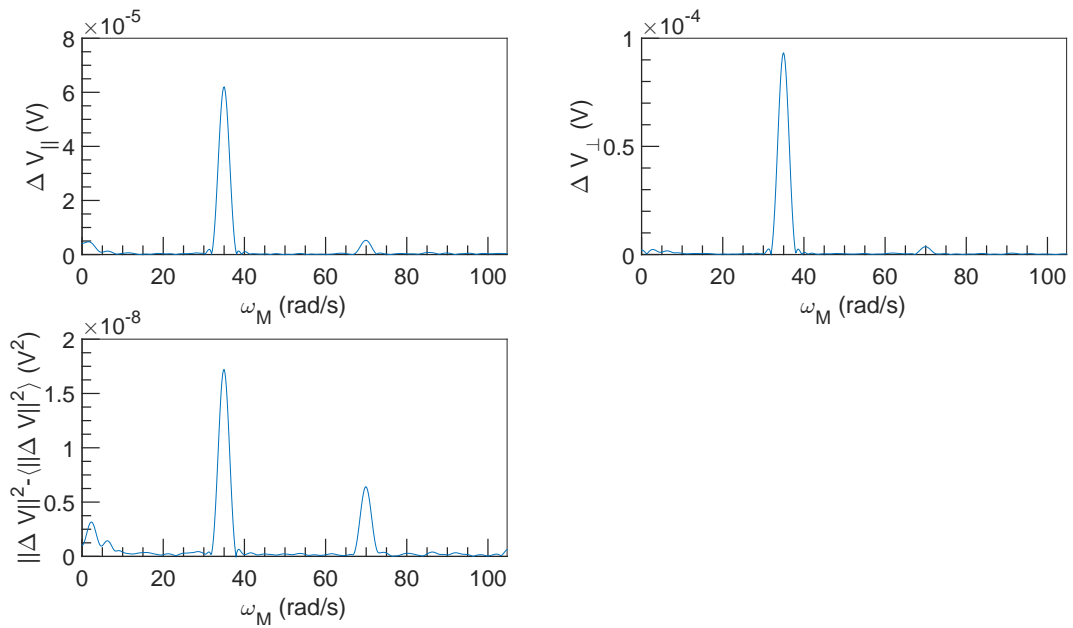


Figure 4.4: FFT spectral density of  $\Delta V$  vs  $\omega_M$  at  $U = 0.1 \text{ m s}^{-1}$ ,  $\omega = 3142 \text{ rad s}^{-1}$  and  $\alpha = 2.0\%$ .



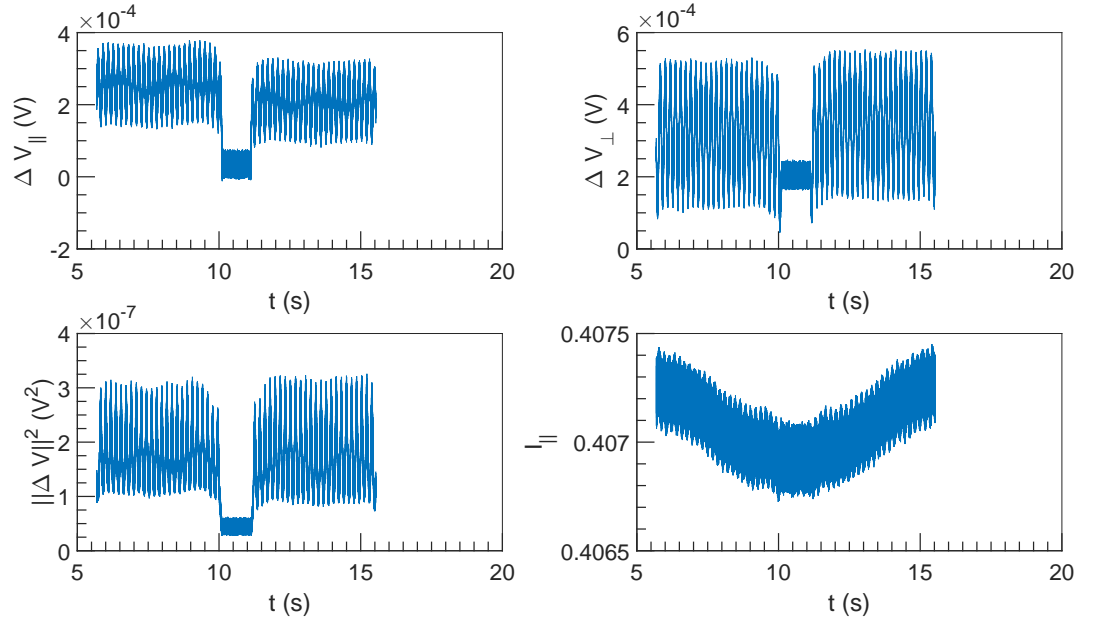


Figure 4.5:  $\Delta V$  and  $I$  vs  $t$  at  $U = 0.1 \text{ m s}^{-1}$ ,  $\omega = 4712 \text{ rad s}^{-1}$  and  $\alpha = 2.0\%$ .

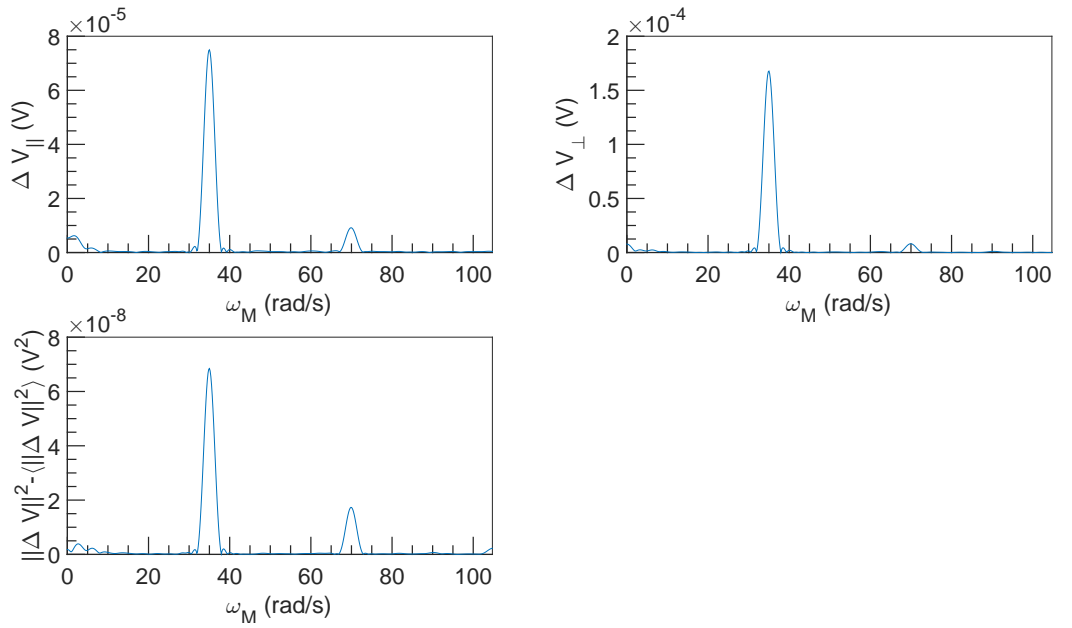


Figure 4.6: FFT spectral density of  $\Delta V$  vs  $\omega_M$  at  $U = 0.1 \text{ m s}^{-1}$ ,  $\omega = 4712 \text{ rad s}^{-1}$  and  $\alpha = 2.0\%$ .

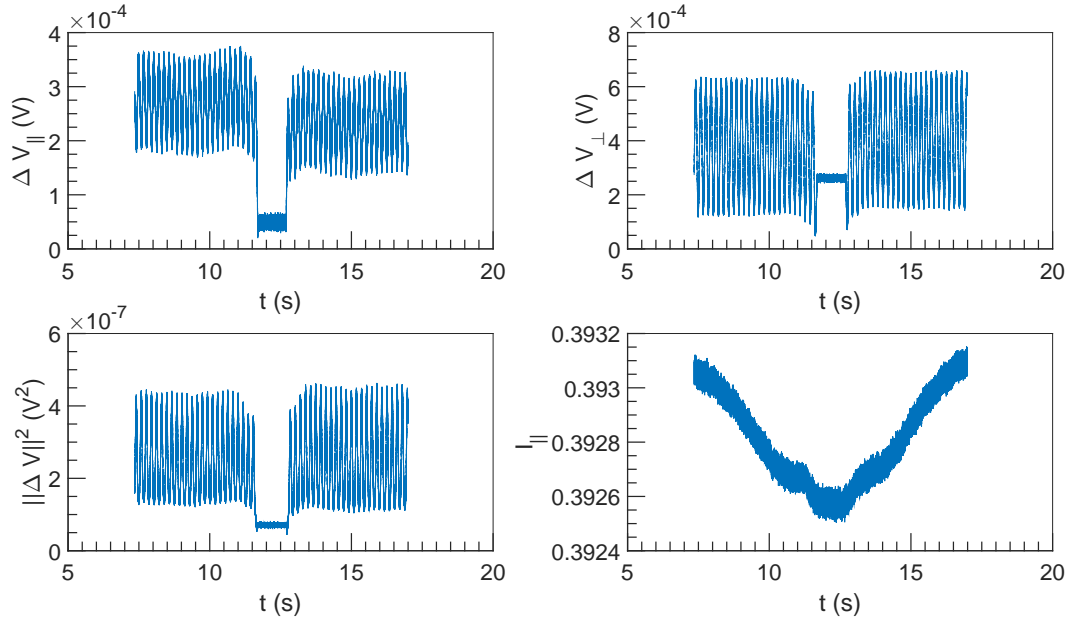


Figure 4.7:  $\Delta V$  and  $I$  vs  $t$  at  $U = 0.1 \text{ m s}^{-1}$ ,  $\omega = 6283 \text{ rad s}^{-1}$  and  $\alpha = 2.0\%$ .

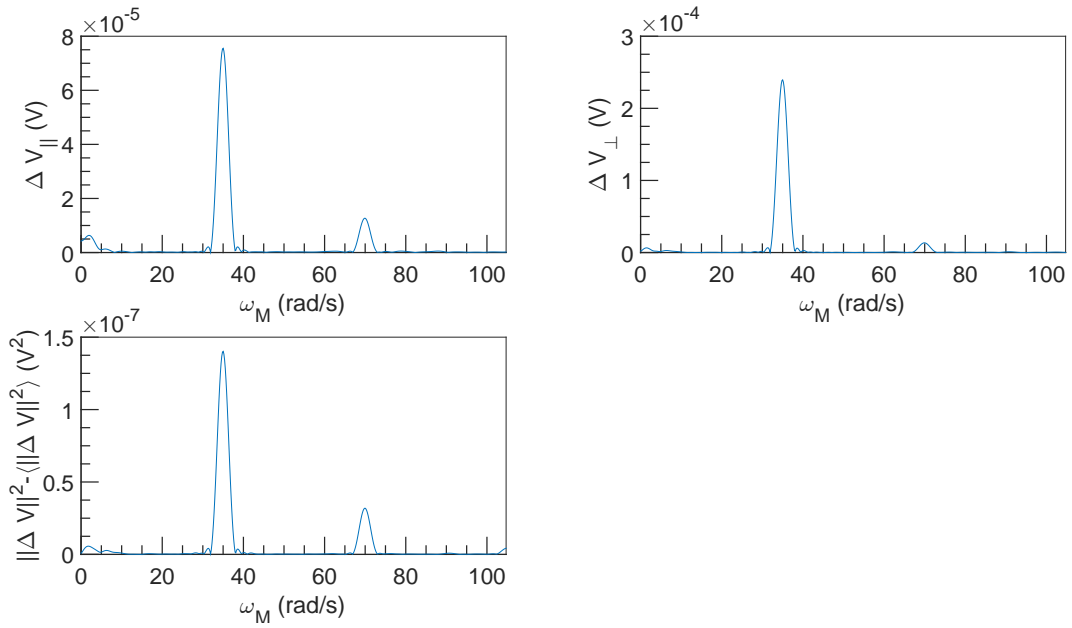


Figure 4.8: FFT spectral density of  $\Delta V$  vs  $\omega_M$  at  $U = 0.1 \text{ m s}^{-1}$ ,  $\omega = 6283 \text{ rad s}^{-1}$  and  $\alpha = 2.0\%$ .

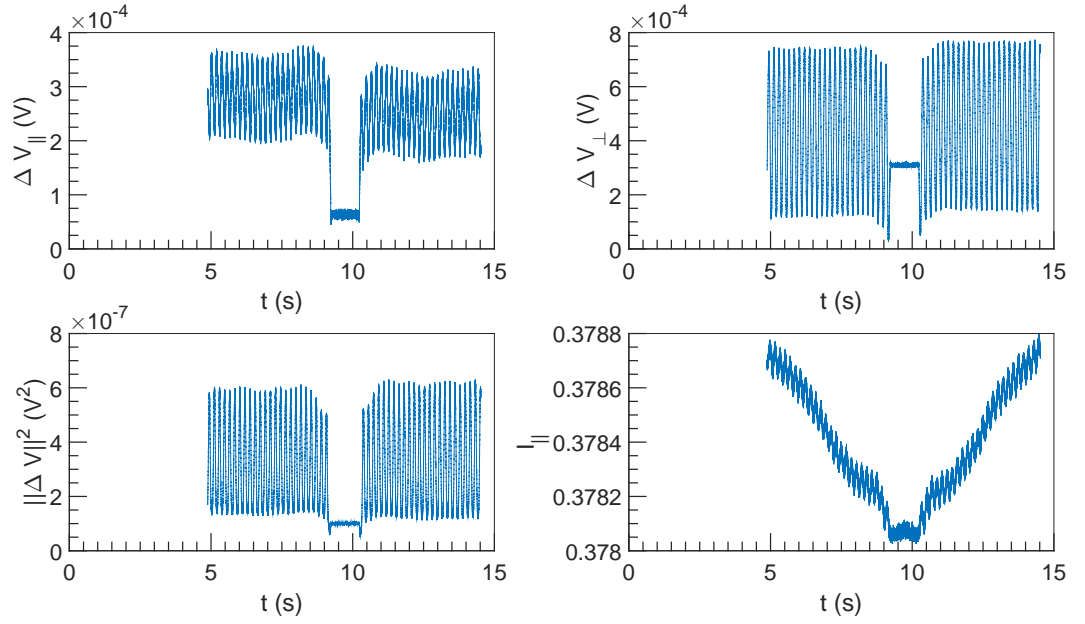


Figure 4.9:  $\Delta V$  and  $I$  vs  $t$  at  $U = 0.1 \text{ m s}^{-1}$ ,  $\omega = 7854 \text{ rad s}^{-1}$  and  $\alpha = 2.0\%$ .

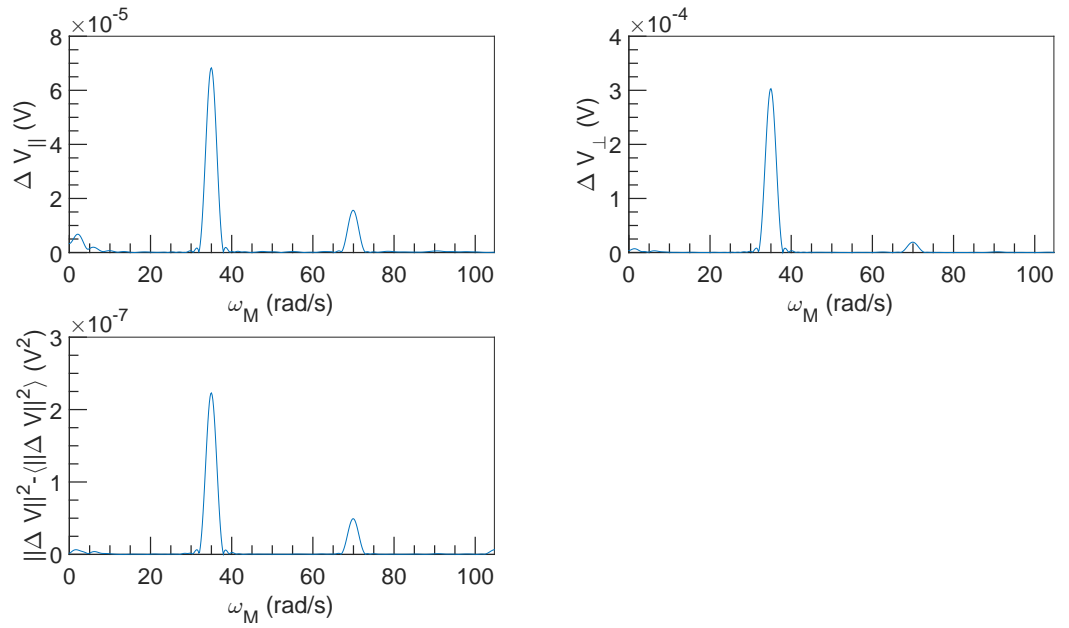


Figure 4.10: FFT spectral density of  $\Delta V$  vs  $\omega_M$  at  $U = 0.1 \text{ m s}^{-1}$ ,  $\omega = 7854 \text{ rad s}^{-1}$  and  $\alpha = 2.0\%$ .

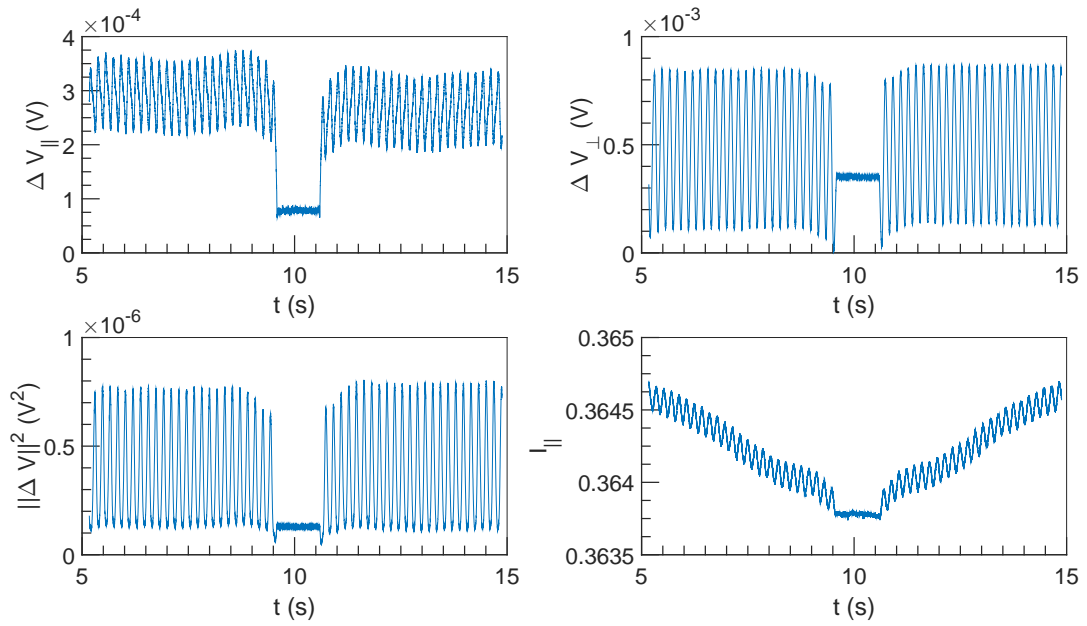


Figure 4.11:  $\Delta V$  and  $I$  vs  $t$  at  $U = 0.1 \text{ m s}^{-1}$ ,  $\omega = 9425 \text{ rad s}^{-1}$  and  $\alpha = 2.0 \%$ .

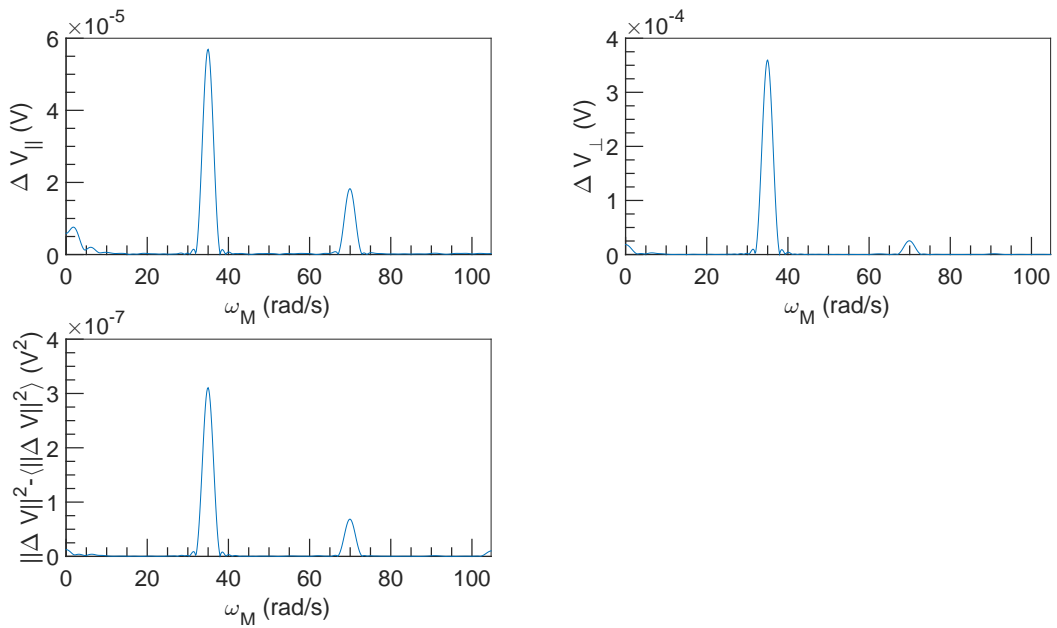


Figure 4.12: FFT spectral density of  $\Delta V$  vs  $\omega_M$  at  $U = 0.1 \text{ m s}^{-1}$ ,  $\omega = 9425 \text{ rad s}^{-1}$  and  $\alpha = 2.0 \%$ .

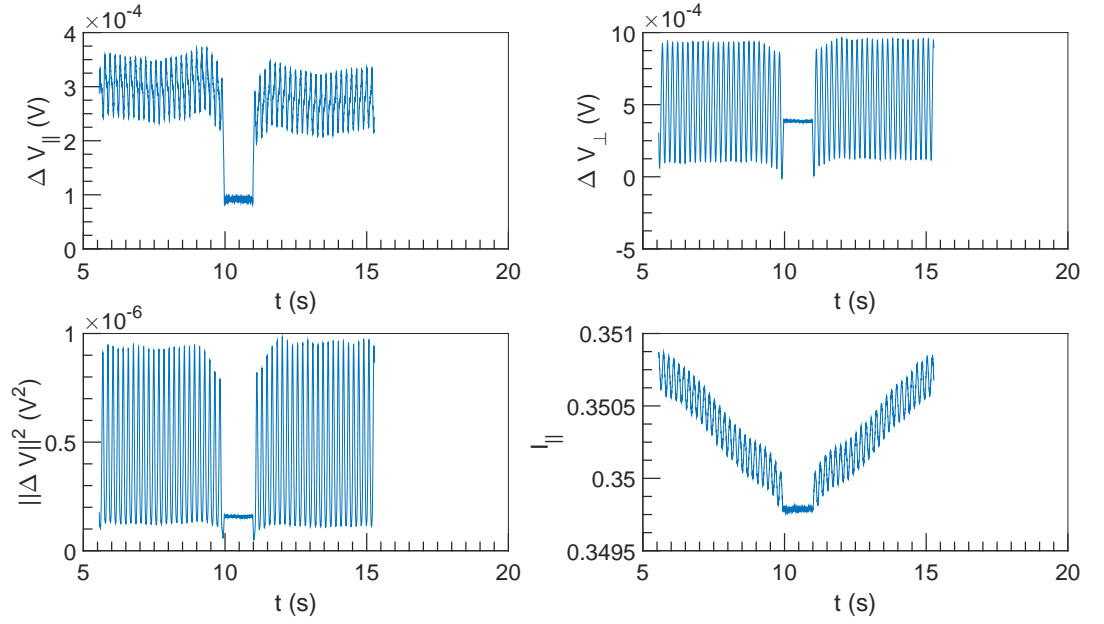


Figure 4.13:  $\Delta V$  and  $I$  vs  $t$  at  $U = 0.1 \text{ m s}^{-1}$ ,  $\omega = 10996 \text{ rad s}^{-1}$  and  $\alpha = 2.0\%$ .

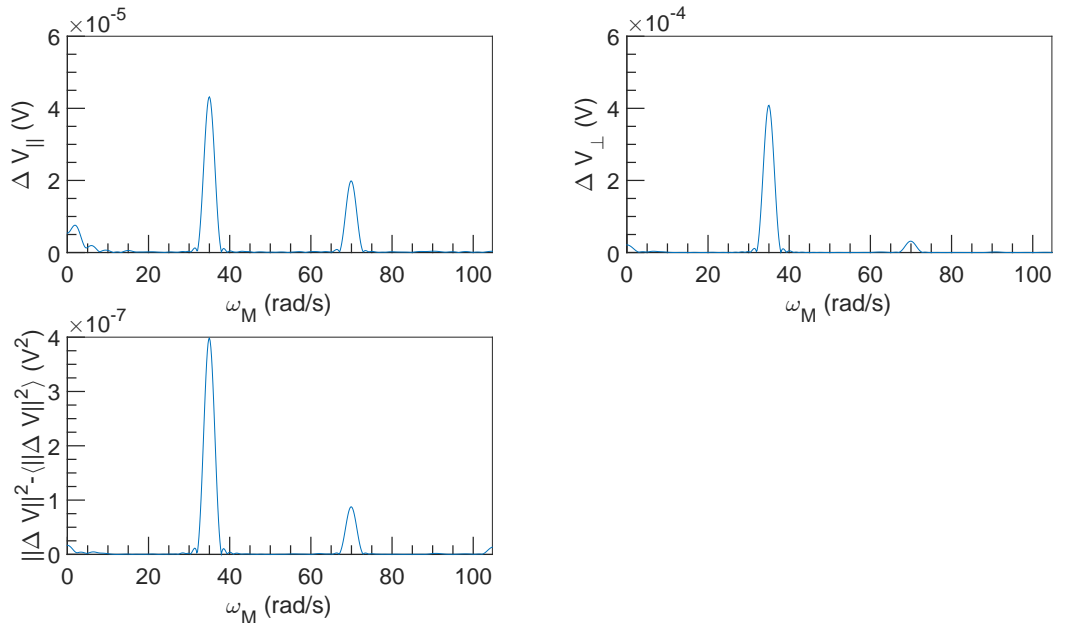


Figure 4.14: FFT spectral density of  $\Delta V$  vs  $\omega_M$  at  $U = 0.1 \text{ m s}^{-1}$ ,  $\omega = 10996 \text{ rad s}^{-1}$  and  $\alpha = 2.0\%$ .

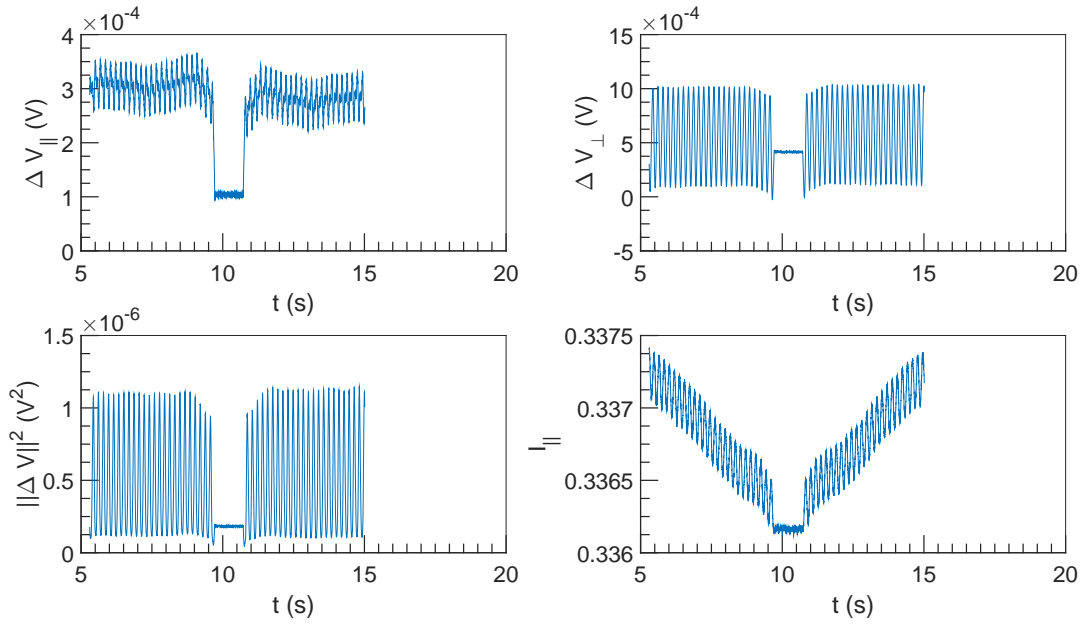


Figure 4.15:  $\Delta V$  and  $I$  vs  $t$  at  $U = 0.1 \text{ m s}^{-1}$ ,  $\omega = 12566 \text{ rad s}^{-1}$  and  $\alpha = 2.0\%$ .

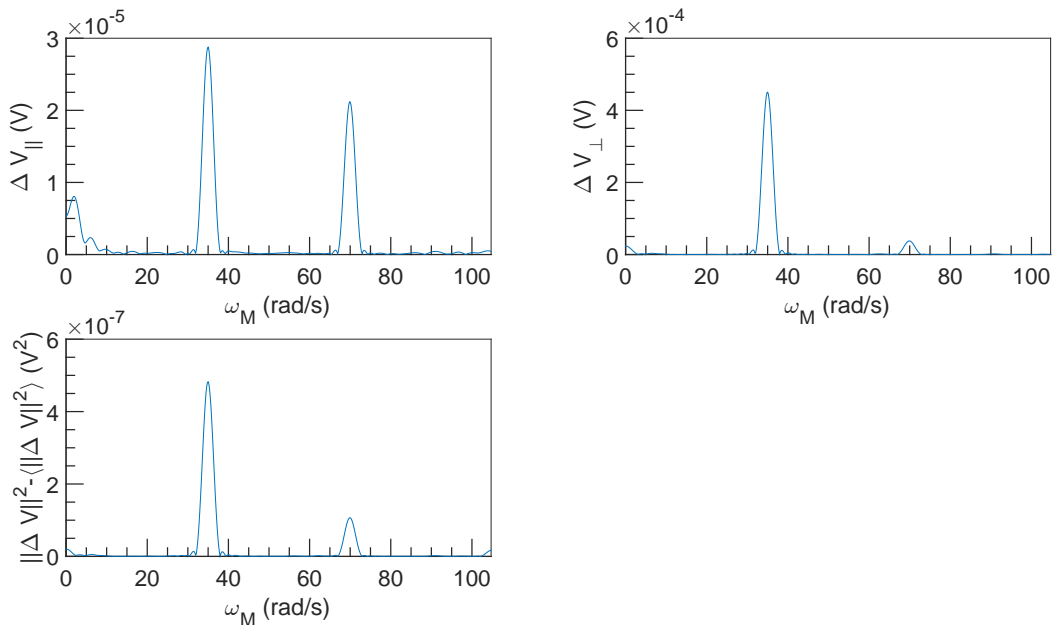


Figure 4.16: FFT spectral density of  $\Delta V$  vs  $\omega_M$  at  $U = 0.1 \text{ m s}^{-1}$ ,  $\omega = 12566 \text{ rad s}^{-1}$  and  $\alpha = 2.0\%$ .

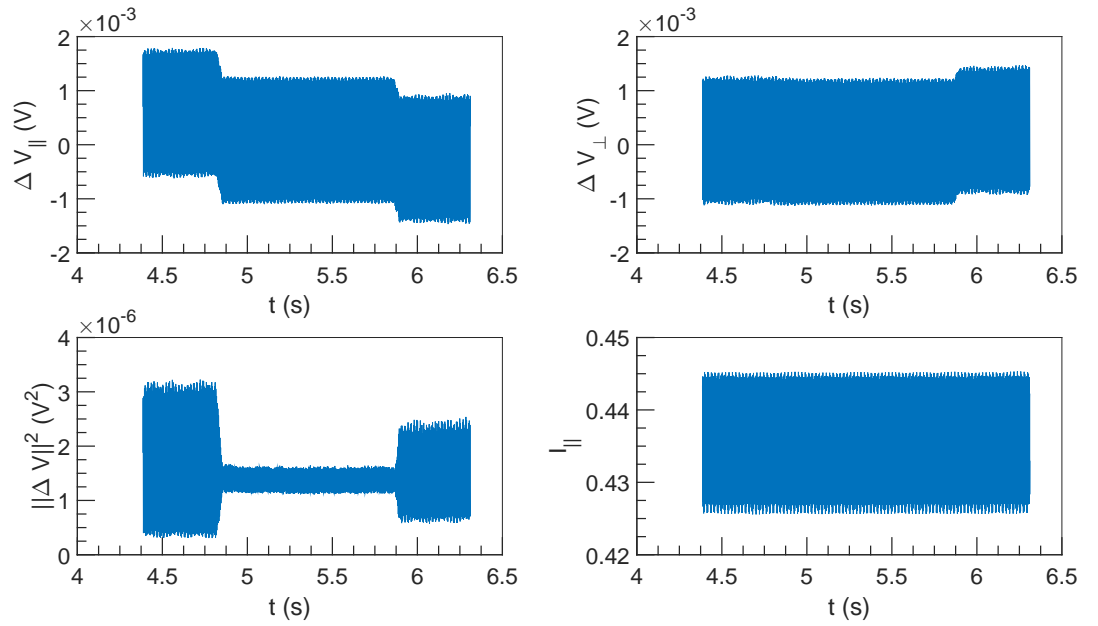


Figure 4.17:  $\Delta V$  and  $I$  vs  $t$  at  $U = 1 \text{ m s}^{-1}$ ,  $\omega = 1571 \text{ rad s}^{-1}$  and  $\alpha = 2.0\%$ .

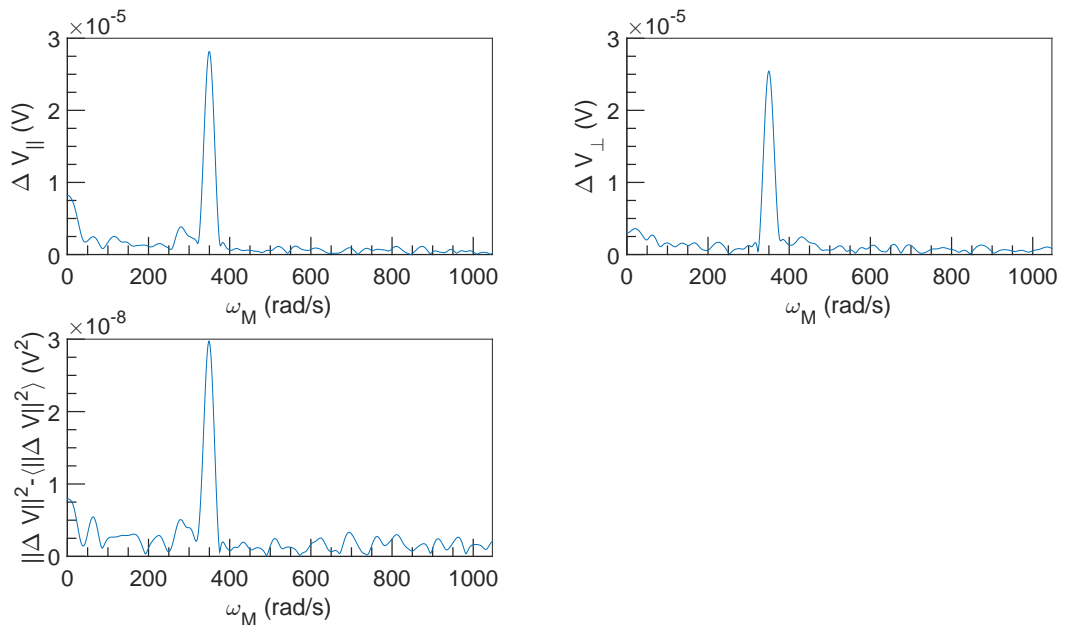


Figure 4.18: FFT spectral density of  $\Delta V$  vs  $\omega_M$  at  $U = 1 \text{ m s}^{-1}$ ,  $\omega = 1571 \text{ rad s}^{-1}$  and  $\alpha = 2.0\%$ .

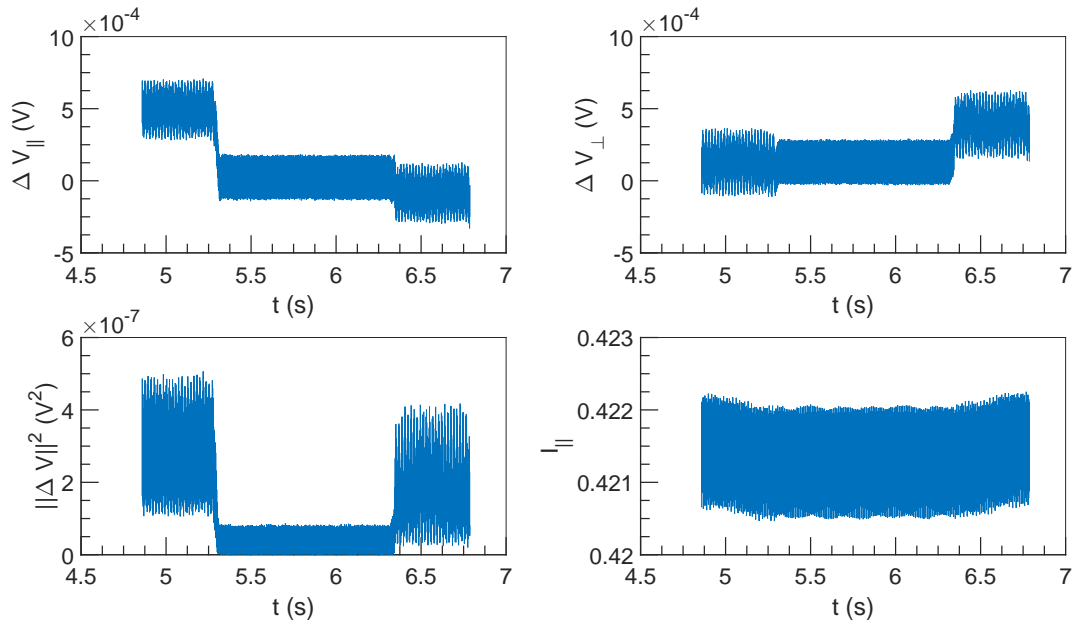


Figure 4.19:  $\Delta V$  and  $I$  vs  $t$  at  $U = 1 \text{ ms}^{-1}$ ,  $\omega = 3142 \text{ rad s}^{-1}$  and  $\alpha = 2.0\%$ .

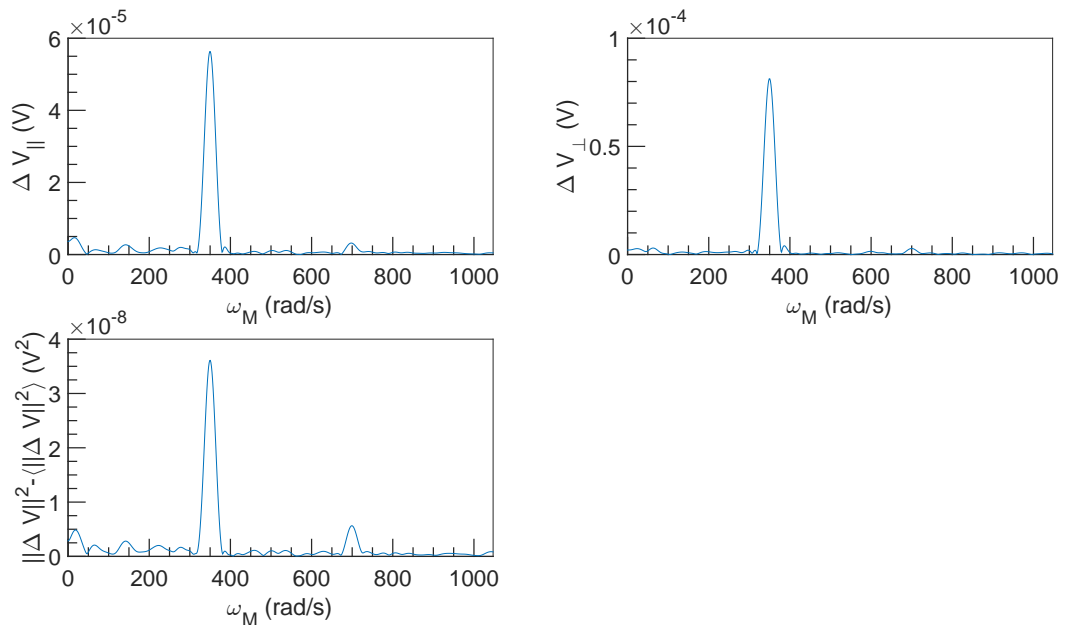


Figure 4.20: FFT spectral density of  $\Delta V$  vs  $\omega_M$  at  $U = 1 \text{ ms}^{-1}$ ,  $\omega = 3142 \text{ rad s}^{-1}$  and  $\alpha = 2.0\%$ .



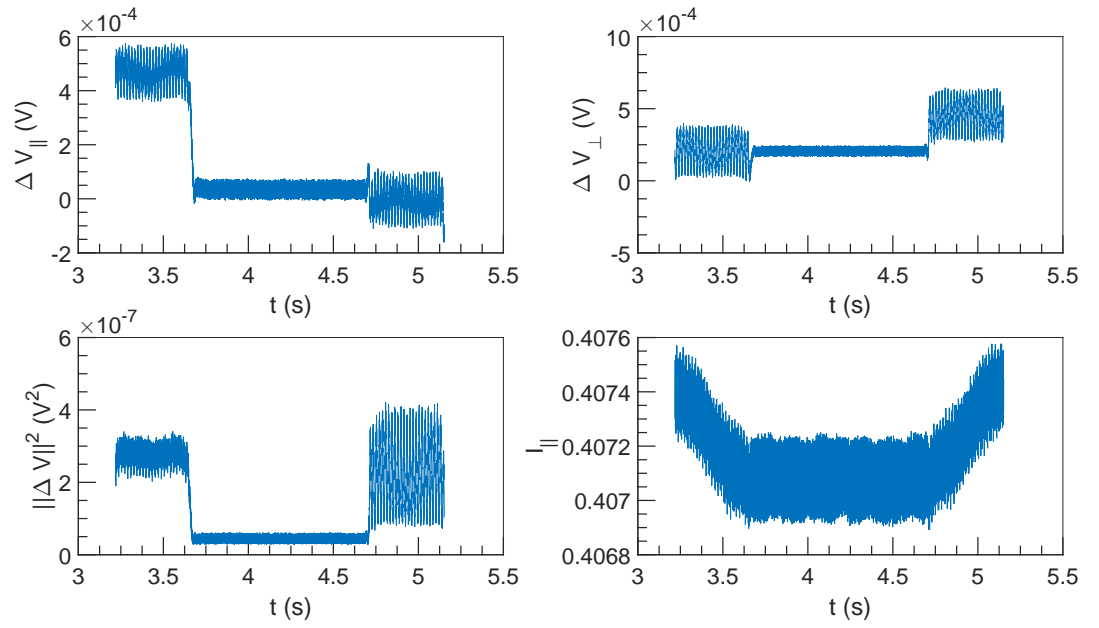


Figure 4.21:  $\Delta V$  and  $I$  vs  $t$  at  $U = 1 \text{ m s}^{-1}$ ,  $\omega = 4712 \text{ rad s}^{-1}$  and  $\alpha = 2.0\%$ .

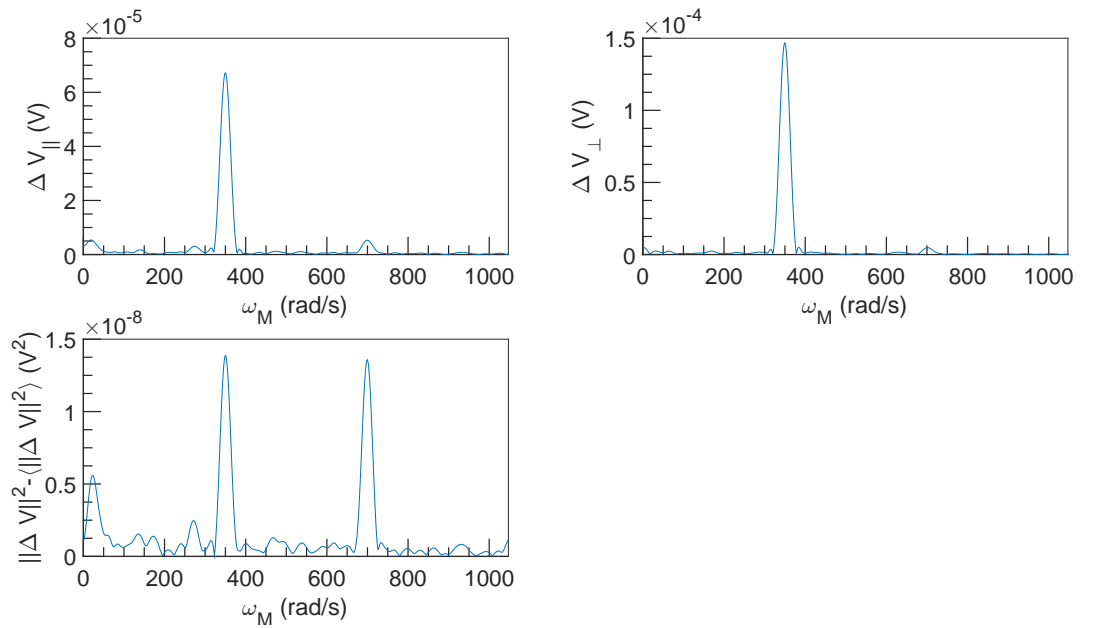


Figure 4.22: FFT spectral density of  $\Delta V$  vs  $\omega_M$  at  $U = 1 \text{ m s}^{-1}$ ,  $\omega = 4712 \text{ rad s}^{-1}$  and  $\alpha = 2.0\%$ .

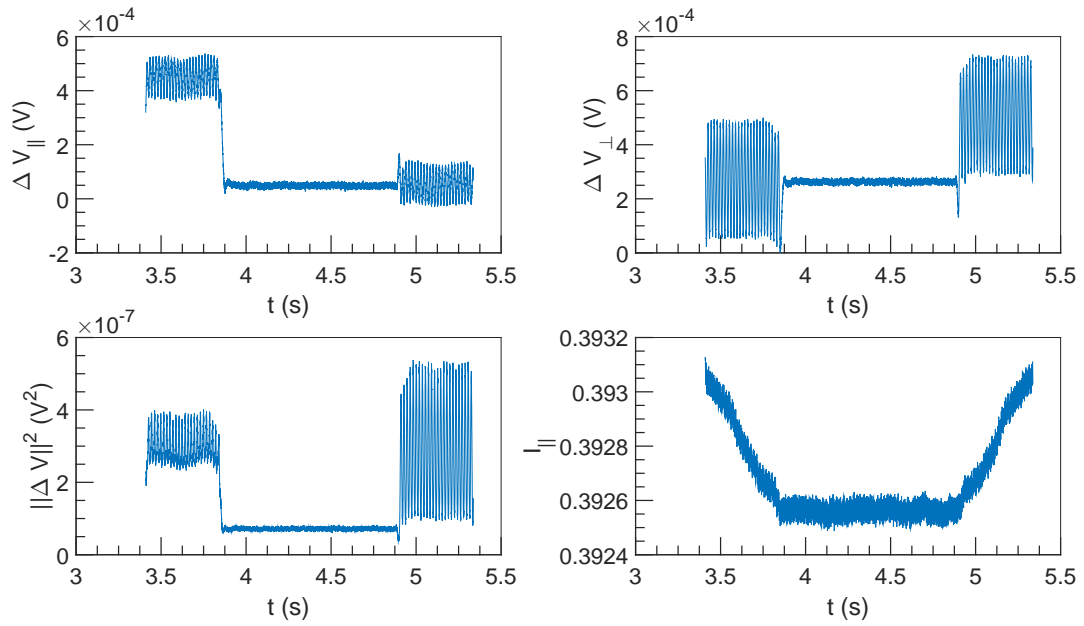


Figure 4.23:  $\Delta V$  and  $I$  vs  $t$  at  $U = 1 \text{ ms}^{-1}$ ,  $\omega = 6283 \text{ rad s}^{-1}$  and  $\alpha = 2.0\%$ .

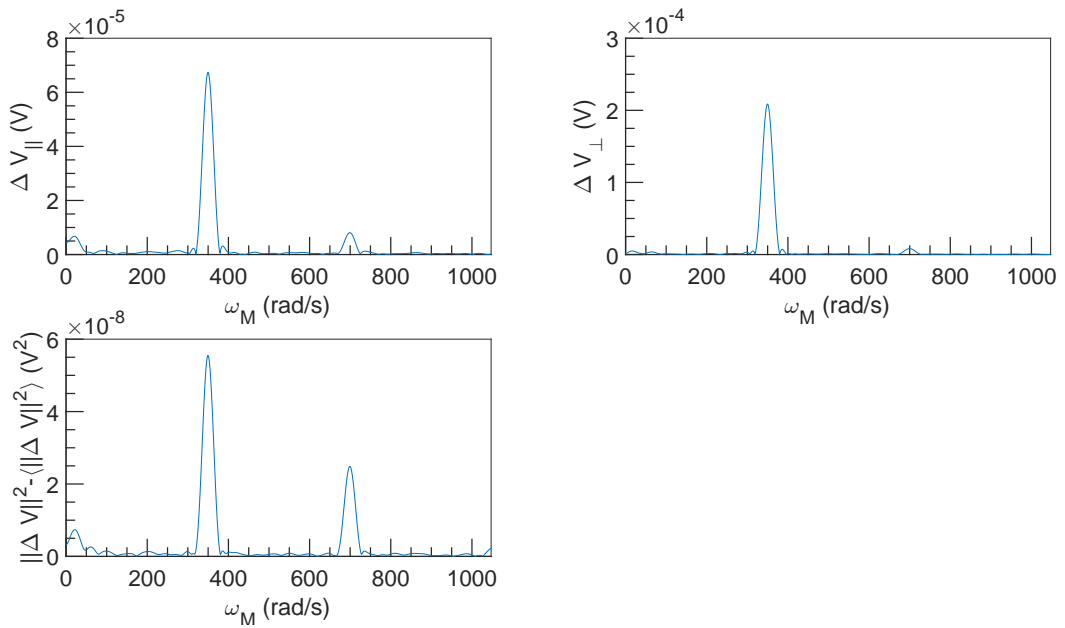


Figure 4.24: FFT spectral density of  $\Delta V$  vs  $\omega_M$  at  $U = 1 \text{ ms}^{-1}$ ,  $\omega = 6283 \text{ rad s}^{-1}$  and  $\alpha = 2.0\%$ .

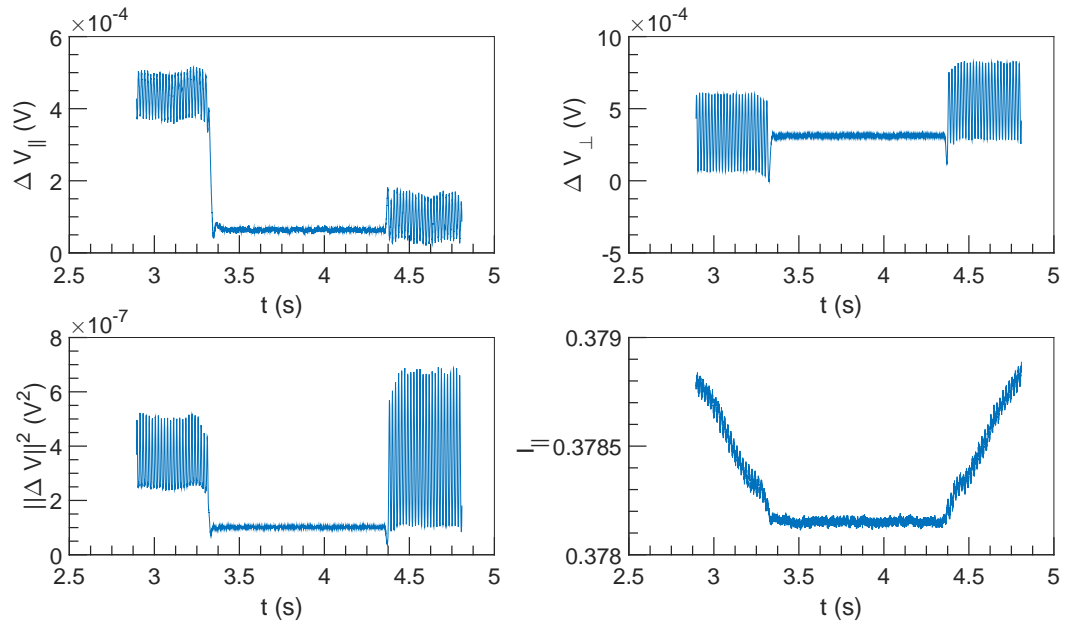


Figure 4.25:  $\Delta V$  and  $I$  vs  $t$  at  $U = 1 \text{ m s}^{-1}$ ,  $\omega = 7854 \text{ rad s}^{-1}$  and  $\alpha = 2.0 \%$ .

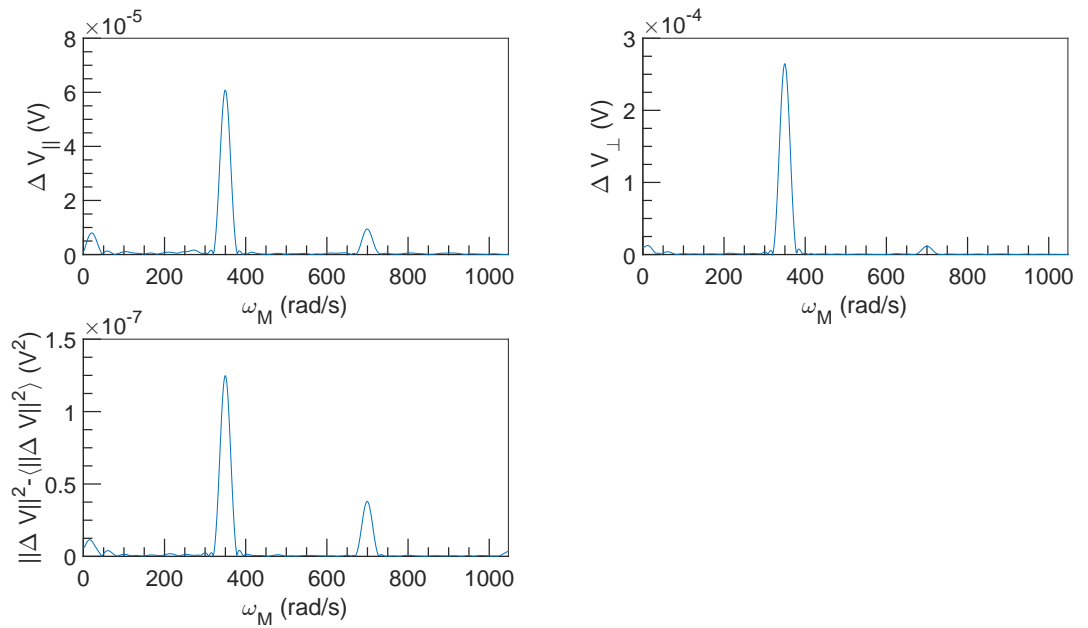


Figure 4.26: FFT spectral density of  $\Delta V$  vs  $\omega_M$  at  $U = 1 \text{ m s}^{-1}$ ,  $\omega = 7854 \text{ rad s}^{-1}$  and  $\alpha = 2.0 \%$ .

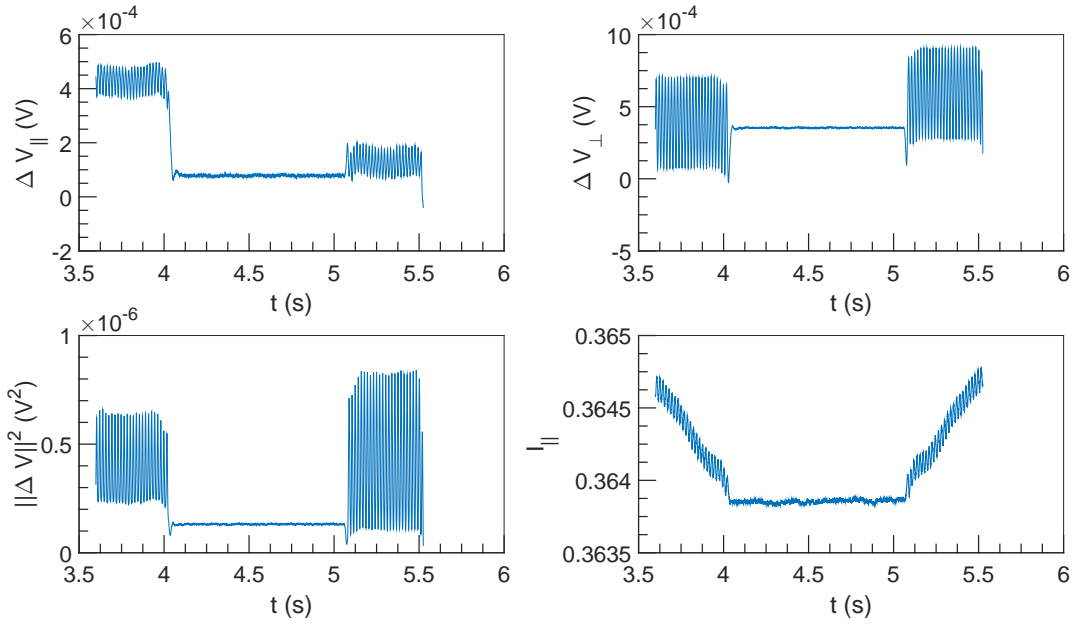


Figure 4.27:  $\Delta V$  and  $I$  vs  $t$  at  $U = 1 \text{ m s}^{-1}$ ,  $\omega = 9425 \text{ rad s}^{-1}$  and  $\alpha = 2.0\%$ .

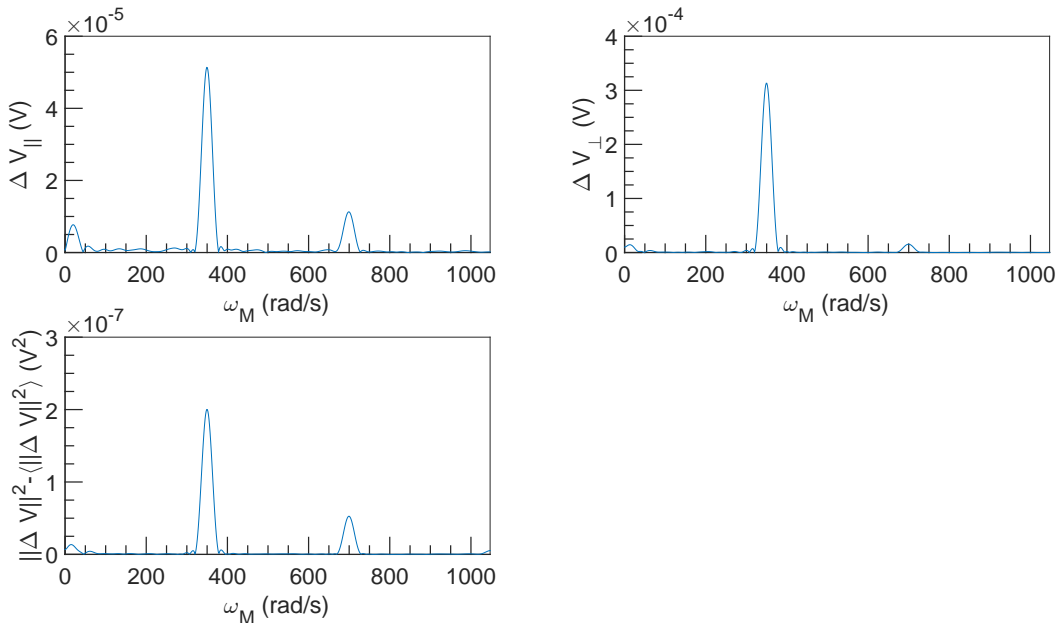


Figure 4.28: FFT spectral density of  $\Delta V$  vs  $\omega_M$  at  $U = 1 \text{ m s}^{-1}$ ,  $\omega = 9425 \text{ rad s}^{-1}$  and  $\alpha = 2.0\%$ .

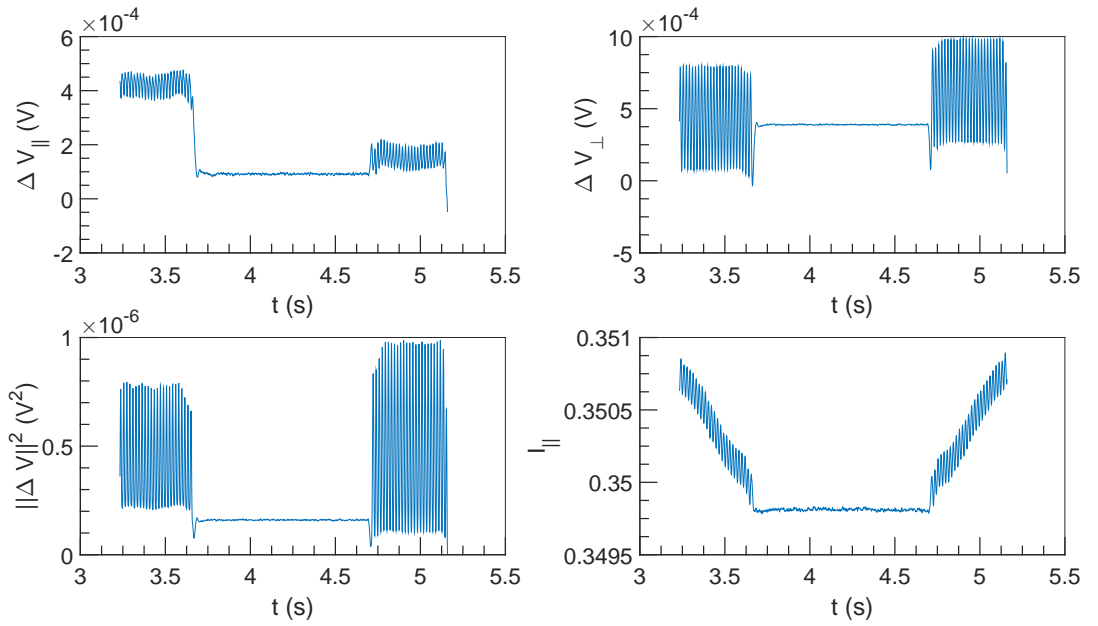


Figure 4.29:  $\Delta V$  and  $I$  vs  $t$  at  $U = 1 \text{ m s}^{-1}$ ,  $\omega = 10\,996 \text{ rad s}^{-1}$  and  $\alpha = 2.0\%$ .

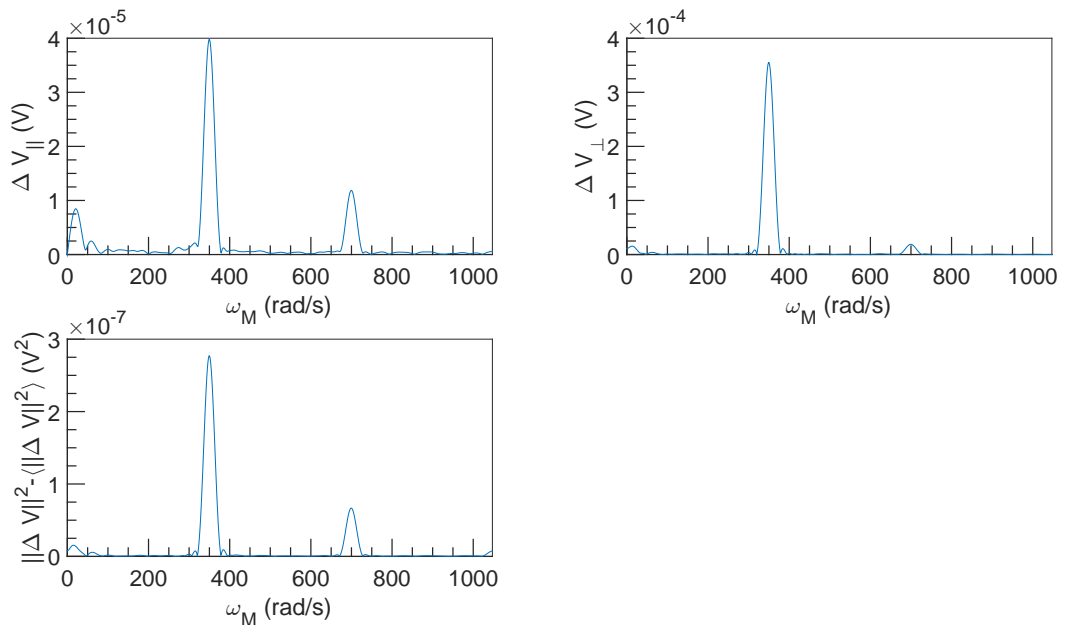


Figure 4.30: FFT spectral density of  $\Delta V$  vs  $\omega_M$  at  $U = 1 \text{ m s}^{-1}$ ,  $\omega = 10\,996 \text{ rad s}^{-1}$  and  $\alpha = 2.0\%$ .

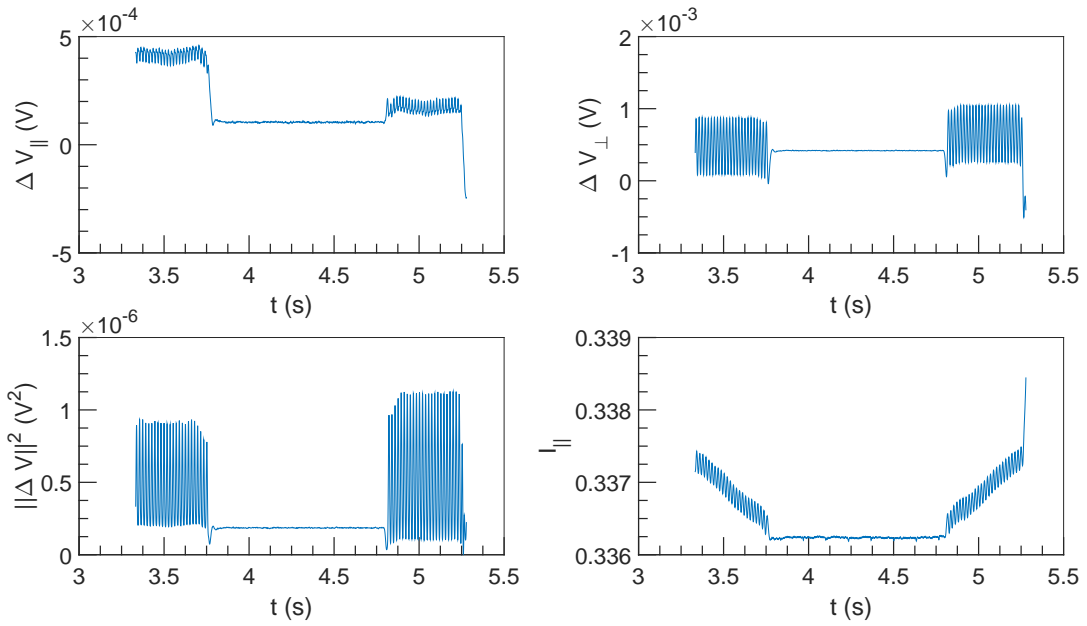


Figure 4.31:  $\Delta V$  and  $I$  vs  $t$  at  $U = 1 \text{ m s}^{-1}$ ,  $\omega = 12566 \text{ rad s}^{-1}$  and  $\alpha = 2.0\%$ .

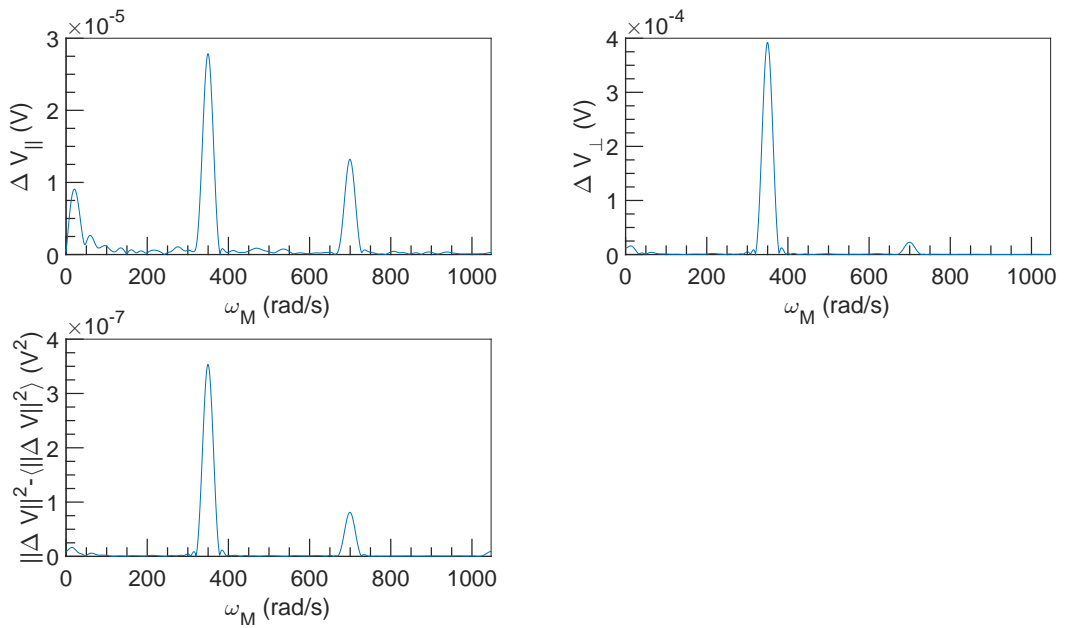


Figure 4.32: FFT spectral density of  $\Delta V$  vs  $\omega_M$  at  $U = 1 \text{ m s}^{-1}$ ,  $\omega = 12566 \text{ rad s}^{-1}$  and  $\alpha = 2.0\%$ .

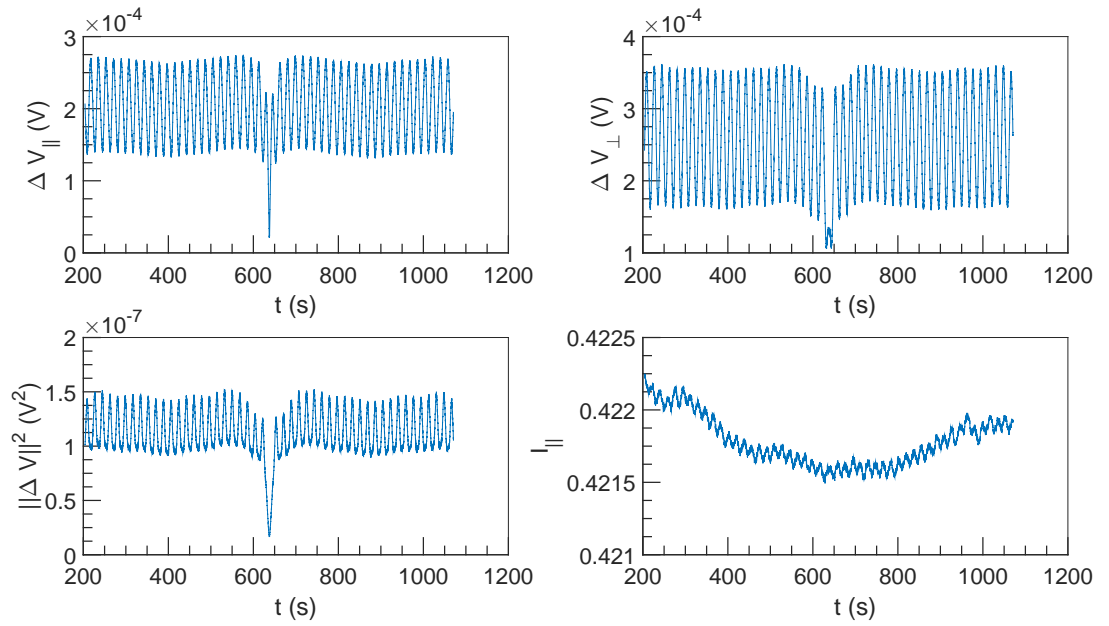


Figure 4.33:  $\Delta V$  and  $I$  vs  $t$  at  $U = 10^{-3} \text{ m s}^{-1}$ ,  $\omega = 3142 \text{ rad s}^{-1}$  and  $\alpha = 2.0\%$ .

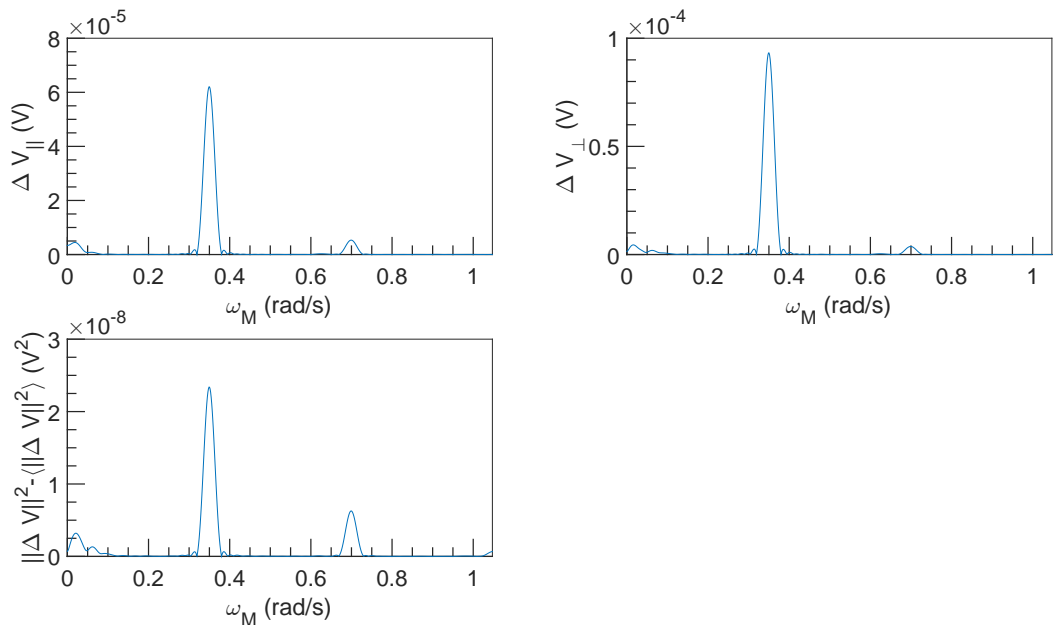


Figure 4.34: FFT spectral density of  $\Delta V$  vs  $\omega_M$  at  $U = 10^{-3} \text{ m s}^{-1}$ ,  $\omega = 3142 \text{ rad s}^{-1}$  and  $\alpha = 2.0\%$ .

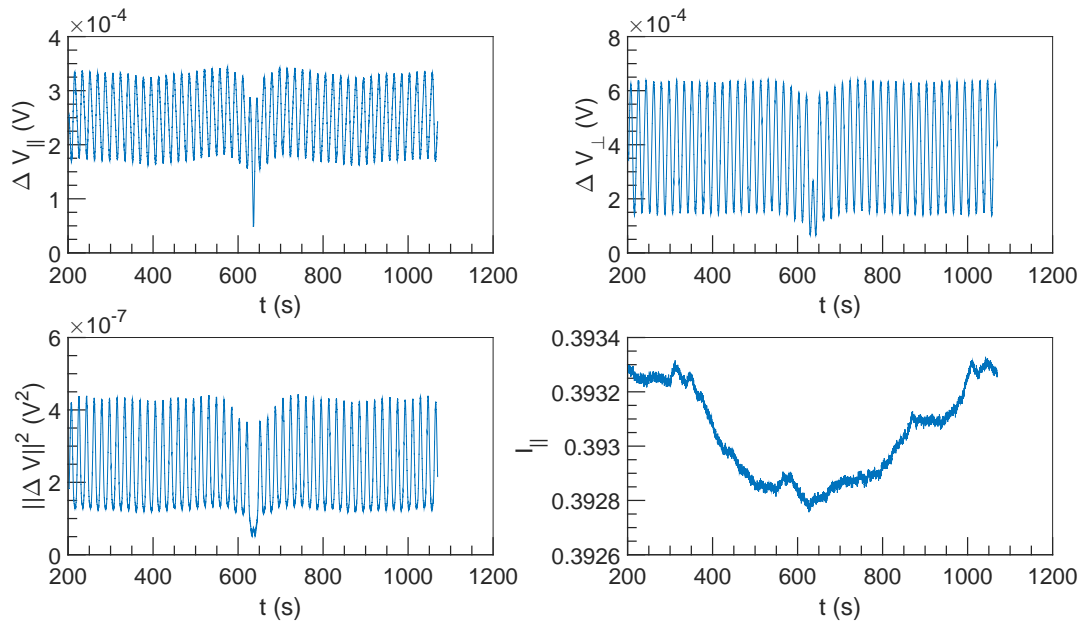


Figure 4.35:  $\Delta V$  and  $I$  vs  $t$  at  $U = 10^{-3} \text{ m s}^{-1}$ ,  $\omega = 6283 \text{ rad s}^{-1}$  and  $\alpha = 2.0\%$ .

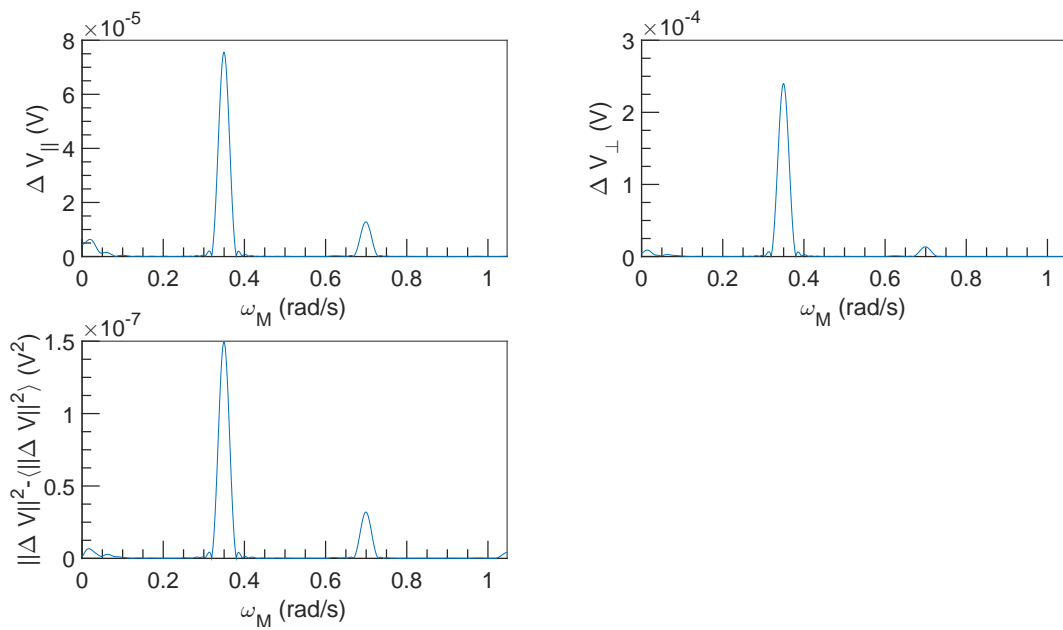


Figure 4.36: FFT spectral density of  $\Delta V$  vs  $\omega_M$  at  $U = 10^{-3} \text{ m s}^{-1}$ ,  $\omega = 6283 \text{ rad s}^{-1}$  and  $\alpha = 2.0\%$ .



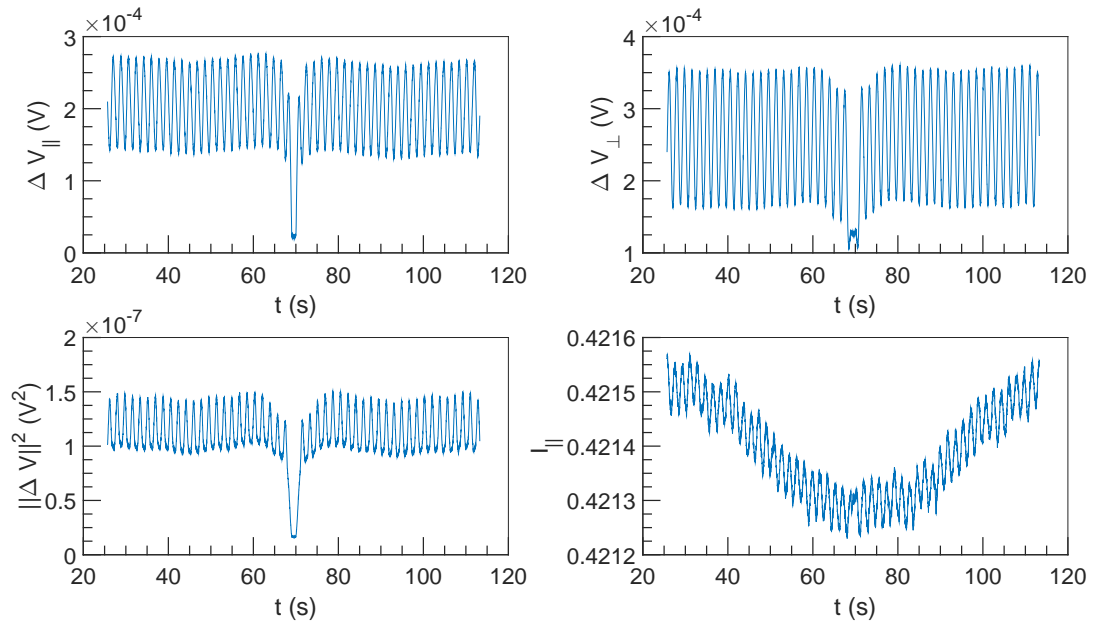


Figure 4.37:  $\Delta V$  and  $I$  vs  $t$  at  $U = 10^{-2} \text{ m s}^{-1}$ ,  $\omega = 3142 \text{ rad s}^{-1}$  and  $\alpha = 2.0\%$ .

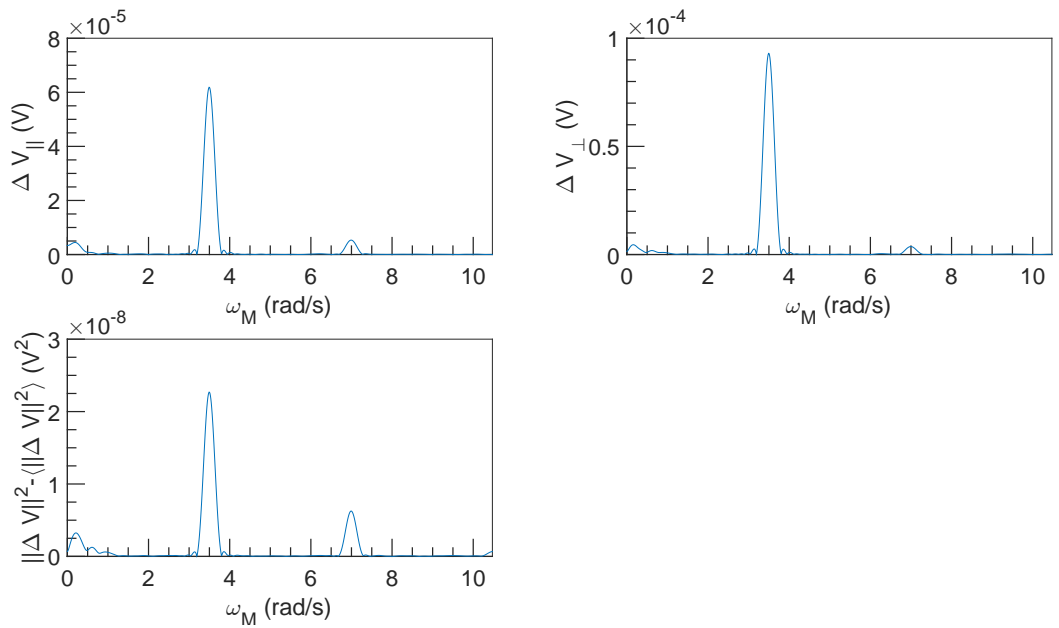


Figure 4.38: FFT spectral density of  $\Delta V$  vs  $\omega_M$  at  $U = 10^{-2} \text{ m s}^{-1}$ ,  $\omega = 3142 \text{ rad s}^{-1}$  and  $\alpha = 2.0\%$ .

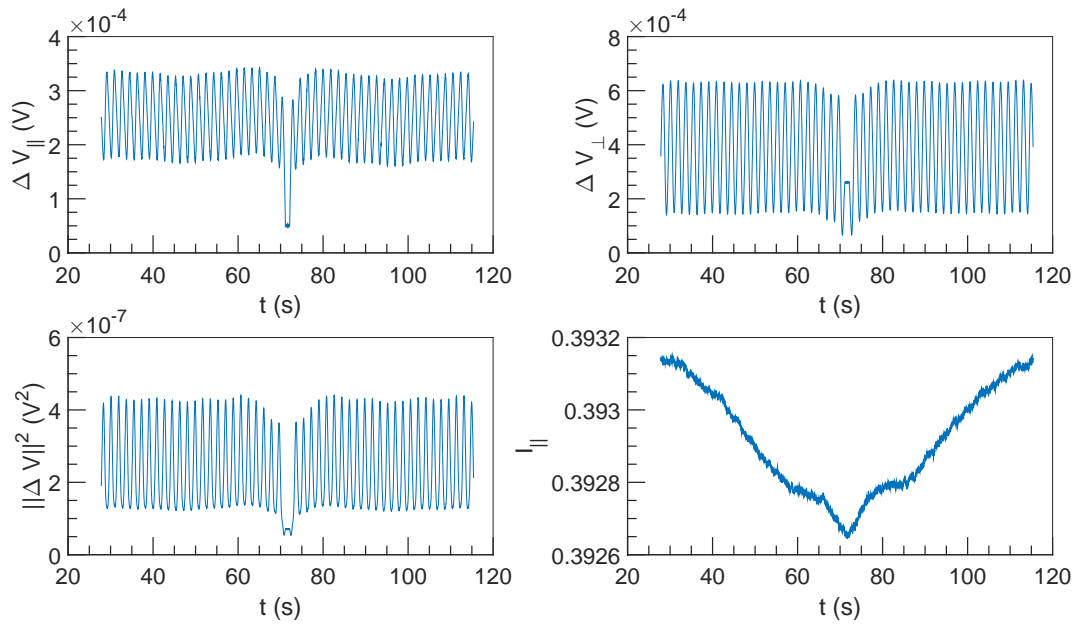


Figure 4.39:  $\Delta V$  and  $I$  vs  $t$  at  $U = 10^{-2} \text{ m s}^{-1}$ ,  $\omega = 6283 \text{ rad s}^{-1}$  and  $\alpha = 2.0\%$ .

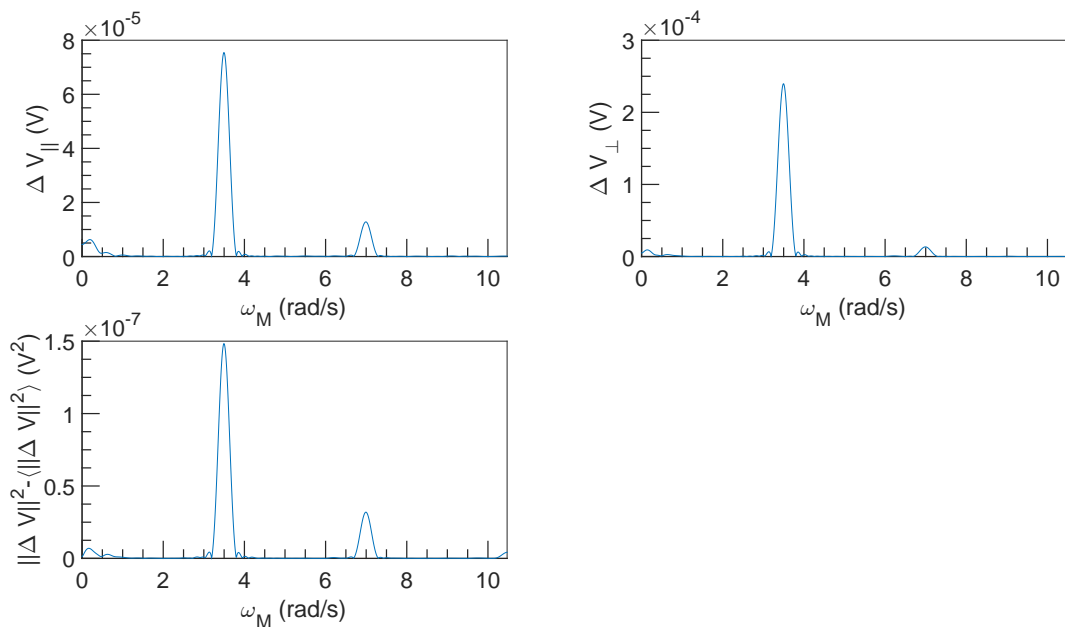


Figure 4.40: FFT spectral density of  $\Delta V$  vs  $\omega_M$  at  $U = 10^{-2} \text{ m s}^{-1}$ ,  $\omega = 6283 \text{ rad s}^{-1}$  and  $\alpha = 2.0\%$ .

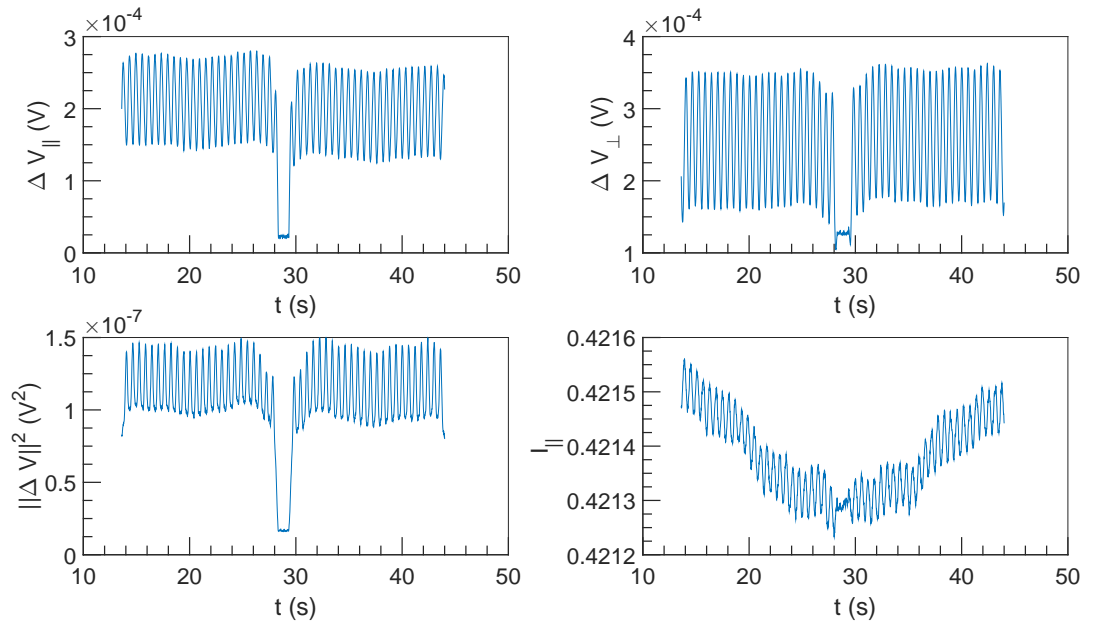


Figure 4.41:  $\Delta V$  and  $I$  vs  $t$  at  $U = 3 \times 10^{-2} \text{ m s}^{-1}$ ,  $\omega = 3142 \text{ rad s}^{-1}$  and  $\alpha = 2.0\%$ .

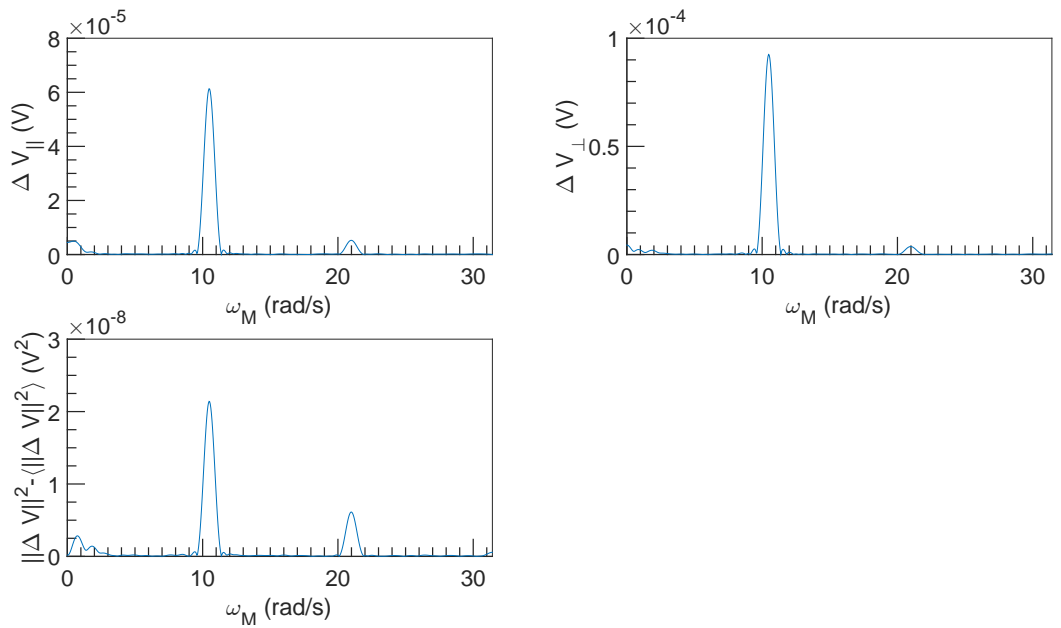


Figure 4.42: FFT spectral density of  $\Delta V$  vs  $\omega_M$  at  $U = 3 \times 10^{-2} \text{ m s}^{-1}$ ,  $\omega = 3142 \text{ rad s}^{-1}$  and  $\alpha = 2.0\%$ .

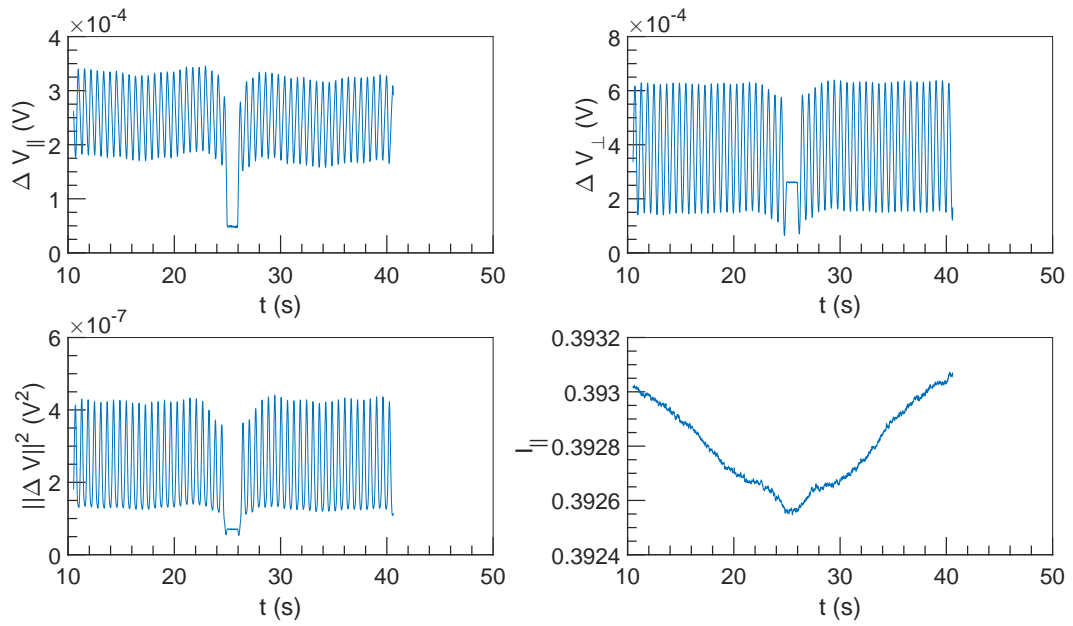


Figure 4.43:  $\Delta V$  and  $I$  vs  $t$  at  $U = 3 \times 10^{-2} \text{ m s}^{-1}$ ,  $\omega = 6283 \text{ rad s}^{-1}$  and  $\alpha = 2.0\%$ .

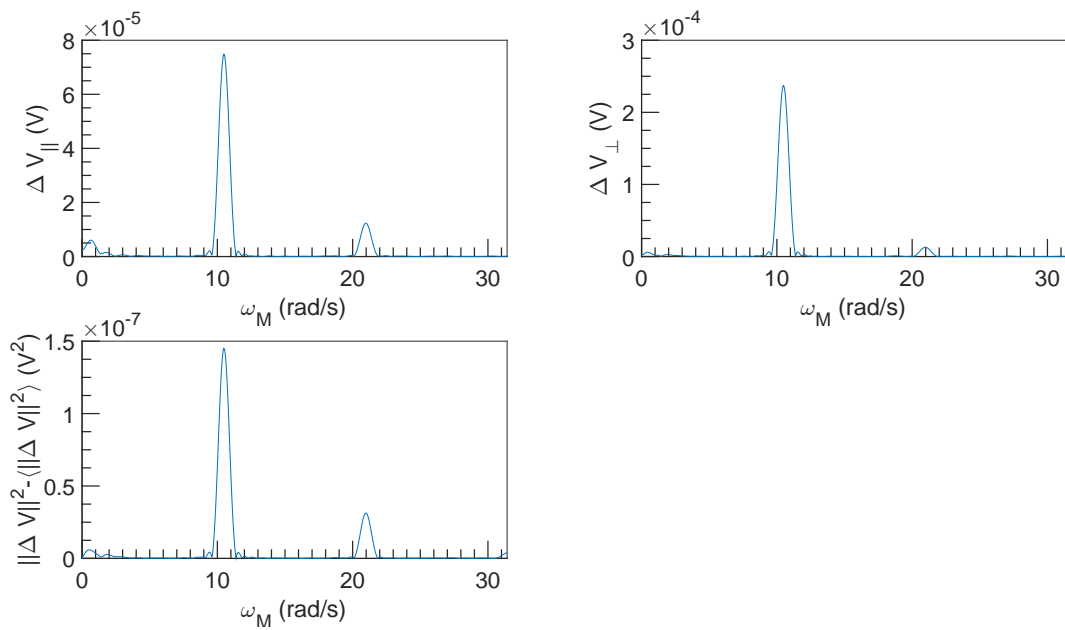


Figure 4.44: FFT spectral density of  $\Delta V$  vs  $\omega_M$  at  $U = 3 \times 10^{-2} \text{ m s}^{-1}$ ,  $\omega = 6283 \text{ rad s}^{-1}$  and  $\alpha = 2.0\%$ .

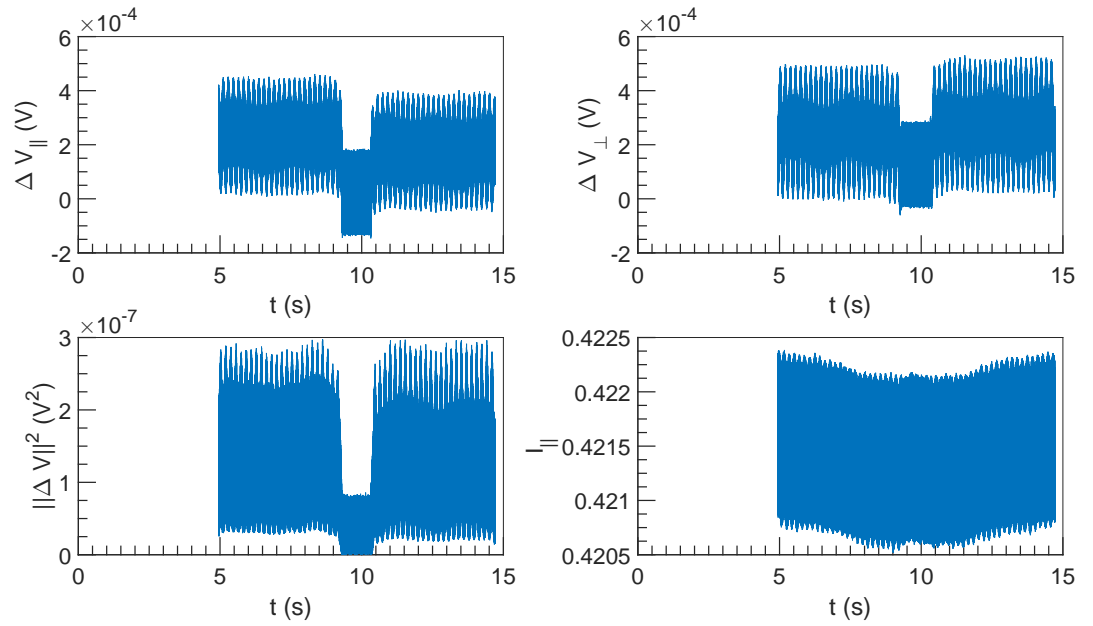


Figure 4.45:  $\Delta V$  and  $I$  vs  $t$  at  $U = 0.1 \text{ m s}^{-1}$ ,  $\omega = 3142 \text{ rad s}^{-1}$  and  $\alpha = 2.0\%$ .

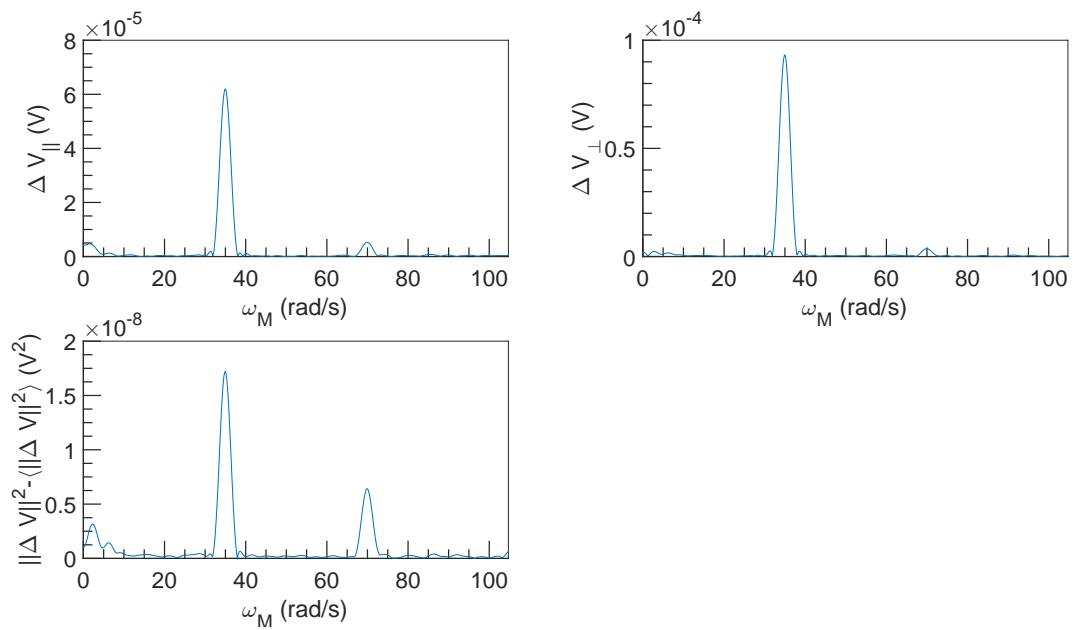


Figure 4.46: FFT spectral density of  $\Delta V$  vs  $\omega_M$  at  $U = 0.1 \text{ m s}^{-1}$ ,  $\omega = 3142 \text{ rad s}^{-1}$  and  $\alpha = 2.0\%$ .

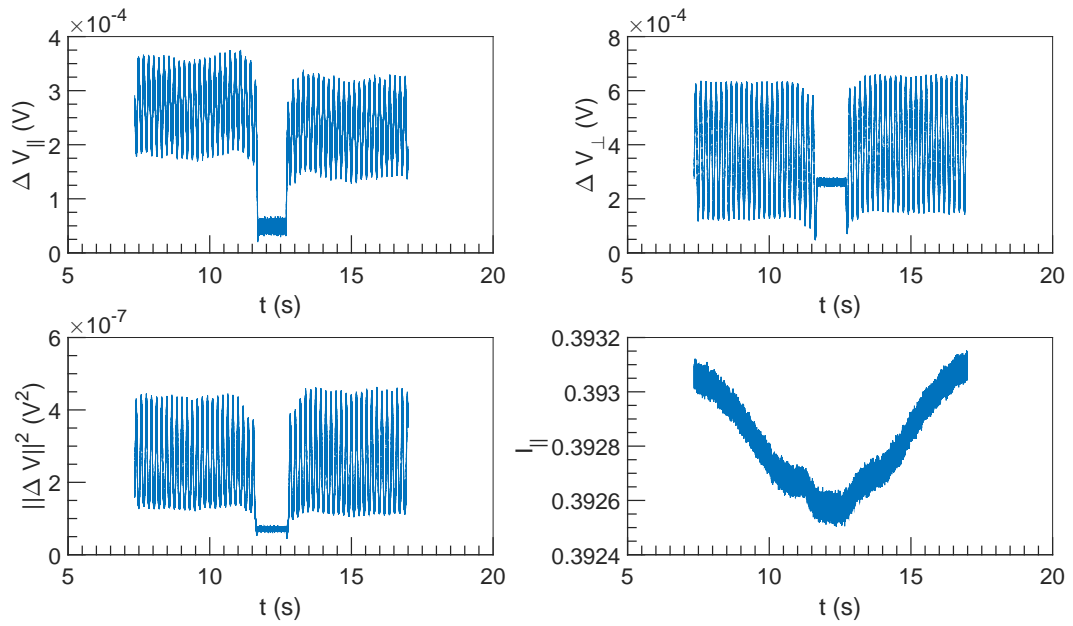


Figure 4.47:  $\Delta V$  and  $I$  vs  $t$  at  $U = 0.1 \text{ m s}^{-1}$ ,  $\omega = 6283 \text{ rad s}^{-1}$  and  $\alpha = 2.0 \%$ .

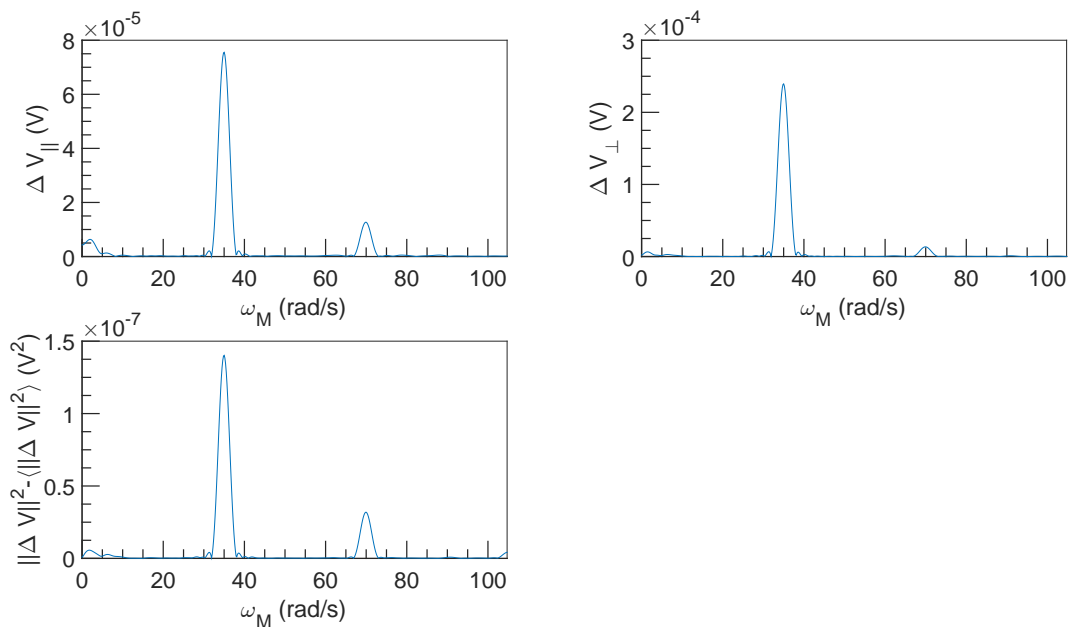


Figure 4.48: FFT spectral density of  $\Delta V$  vs  $\omega_M$  at  $U = 0.1 \text{ m s}^{-1}$ ,  $\omega = 6283 \text{ rad s}^{-1}$  and  $\alpha = 2.0 \%$ .

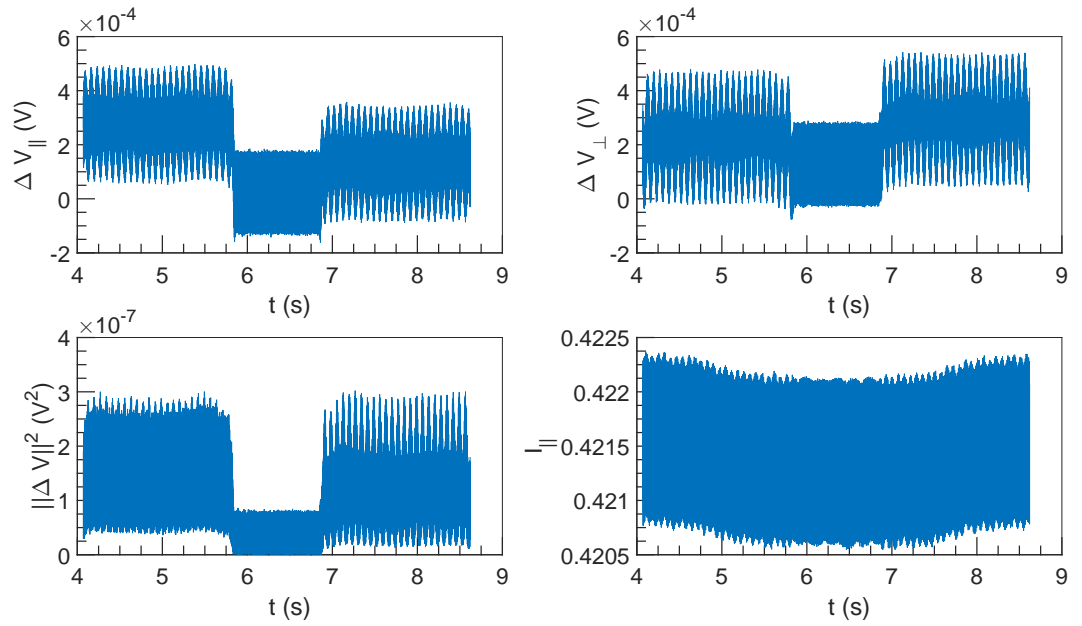


Figure 4.49:  $\Delta V$  and  $I$  vs  $t$  at  $U = 0.25 \text{ ms}^{-1}$ ,  $\omega = 3142 \text{ rad s}^{-1}$  and  $\alpha = 2.0\%$ .

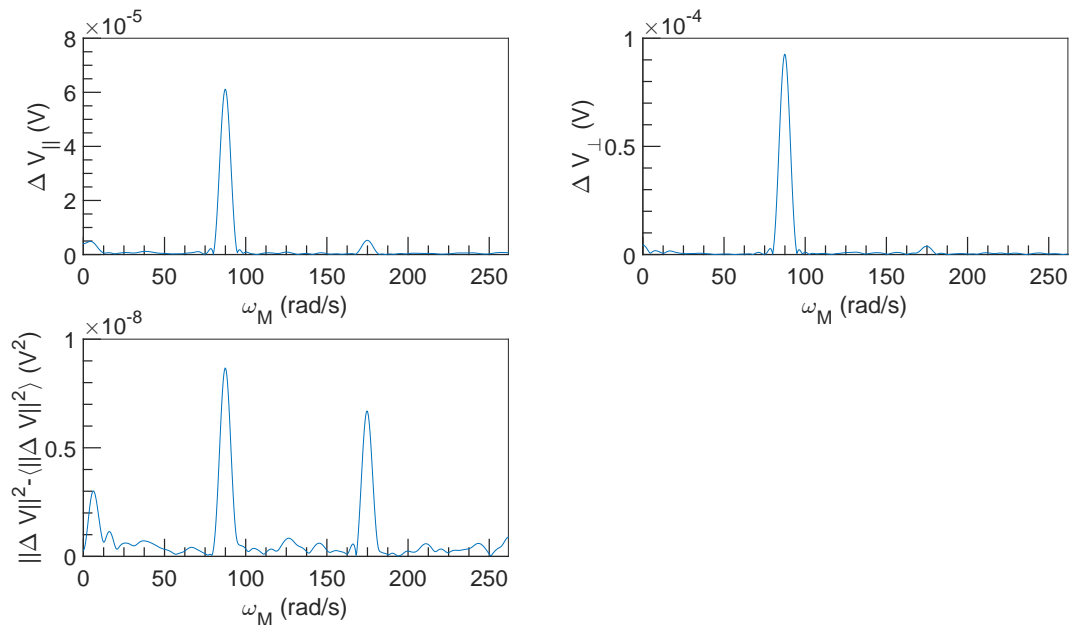


Figure 4.50: FFT spectral density of  $\Delta V$  vs  $\omega_M$  at  $U = 0.25 \text{ ms}^{-1}$ ,  $\omega = 3142 \text{ rad s}^{-1}$  and  $\alpha = 2.0\%$ .

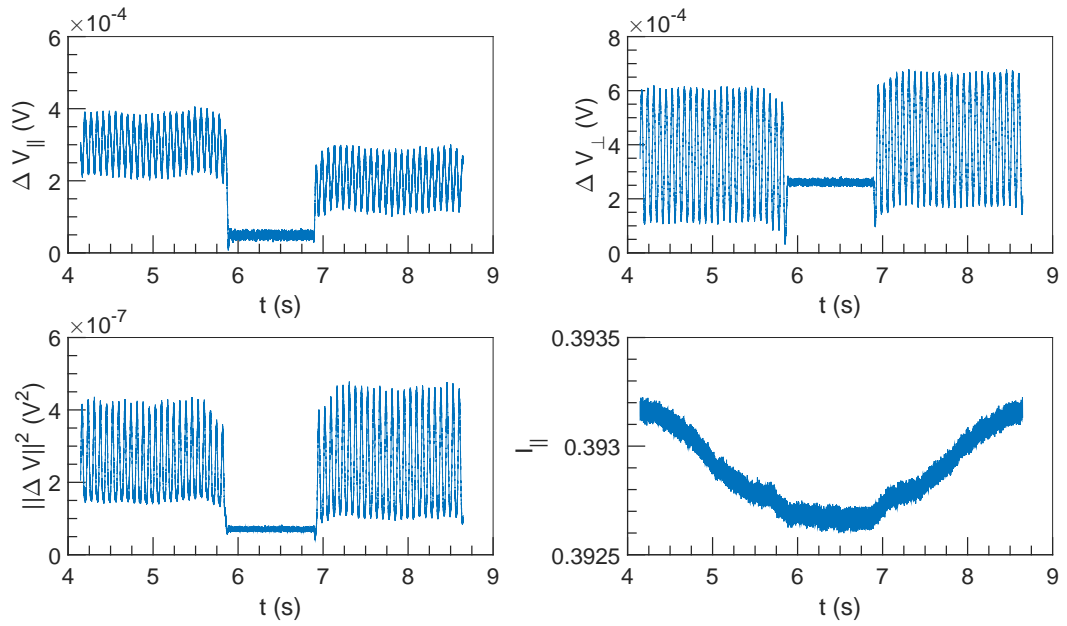


Figure 4.51:  $\Delta V$  and  $I$  vs  $t$  at  $U = 0.25 \text{ m s}^{-1}$ ,  $\omega = 6283 \text{ rad s}^{-1}$  and  $\alpha = 2.0 \%$ .

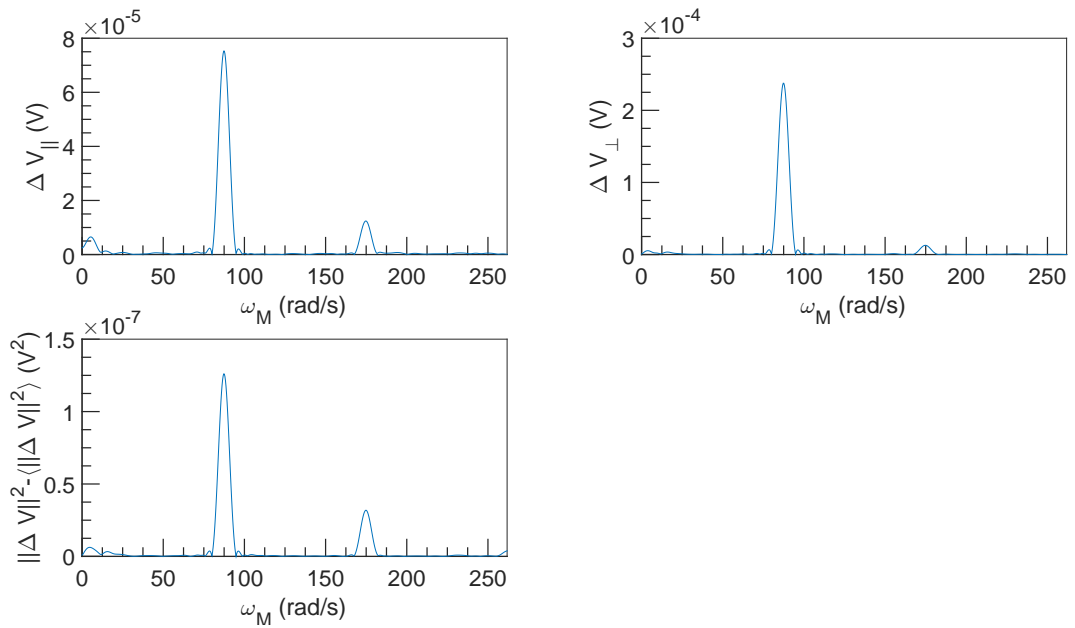


Figure 4.52: FFT spectral density of  $\Delta V$  vs  $\omega_M$  at  $U = 0.25 \text{ m s}^{-1}$ ,  $\omega = 6283 \text{ rad s}^{-1}$  and  $\alpha = 2.0 \%$ .



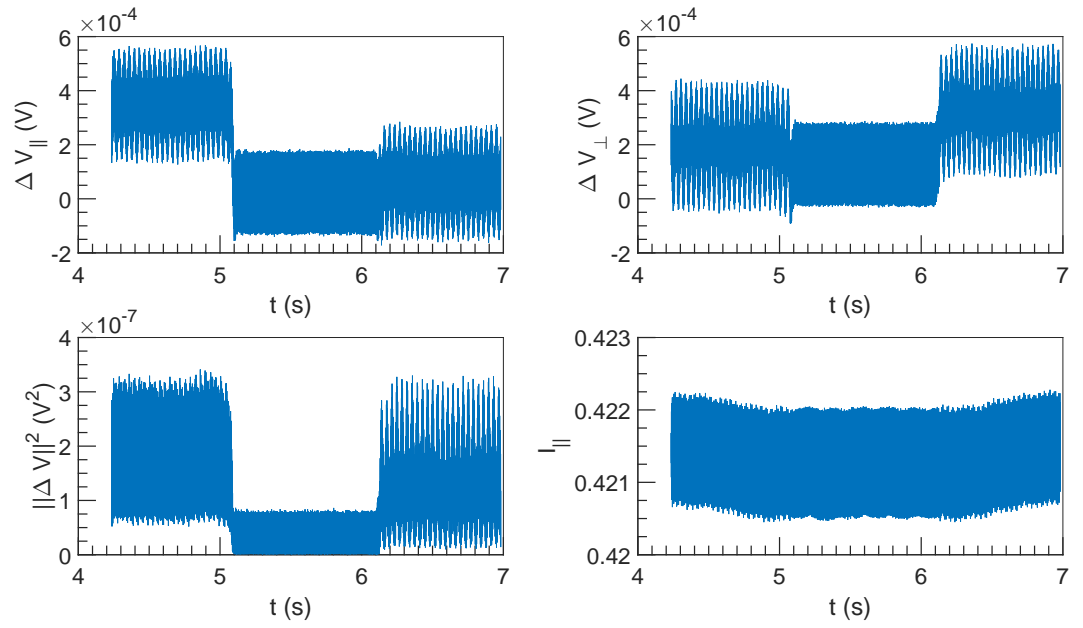


Figure 4.53:  $\Delta V$  and  $I$  vs  $t$  at  $U = 0.5 \text{ m s}^{-1}$ ,  $\omega = 3142 \text{ rad s}^{-1}$  and  $\alpha = 2.0 \%$ .

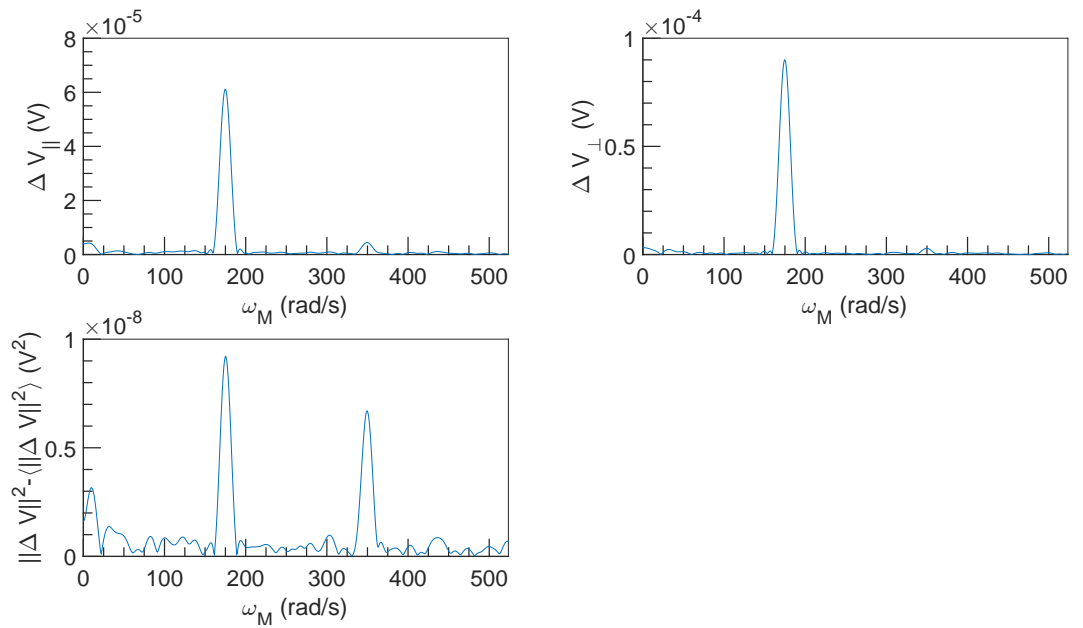


Figure 4.54: FFT spectral density of  $\Delta V$  vs  $\omega_M$  at  $U = 0.5 \text{ m s}^{-1}$ ,  $\omega = 3142 \text{ rad s}^{-1}$  and  $\alpha = 2.0 \%$ .

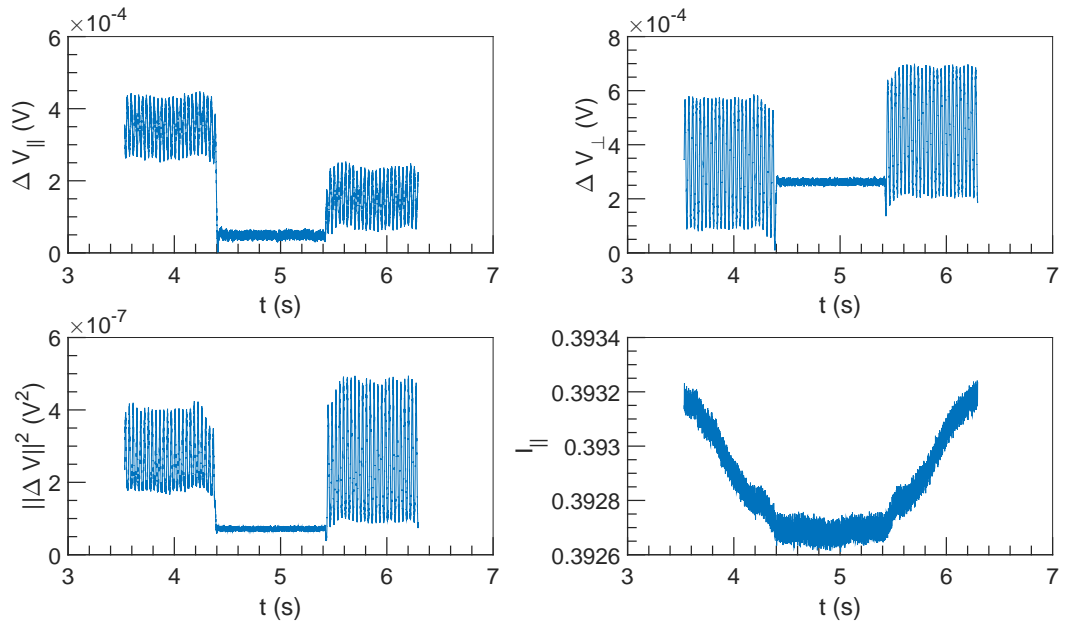


Figure 4.55:  $\Delta V$  and  $I$  vs  $t$  at  $U = 0.5 \text{ m s}^{-1}$ ,  $\omega = 6283 \text{ rad s}^{-1}$  and  $\alpha = 2.0 \%$ .

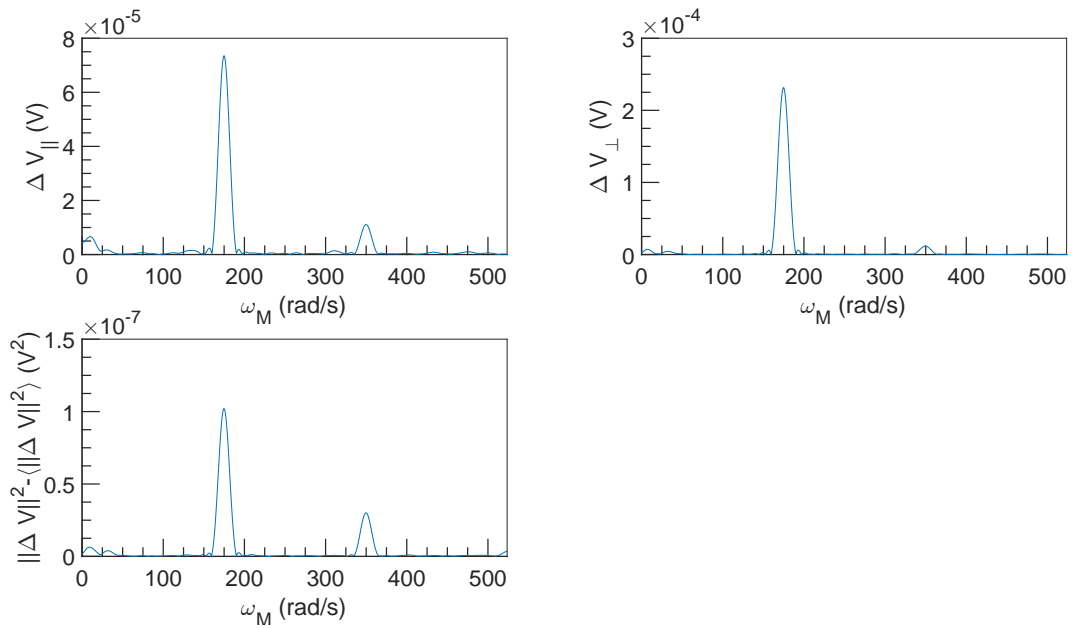


Figure 4.56: FFT spectral density of  $\Delta V$  vs  $\omega_M$  at  $U = 0.5 \text{ m s}^{-1}$ ,  $\omega = 6283 \text{ rad s}^{-1}$  and  $\alpha = 2.0 \%$ .

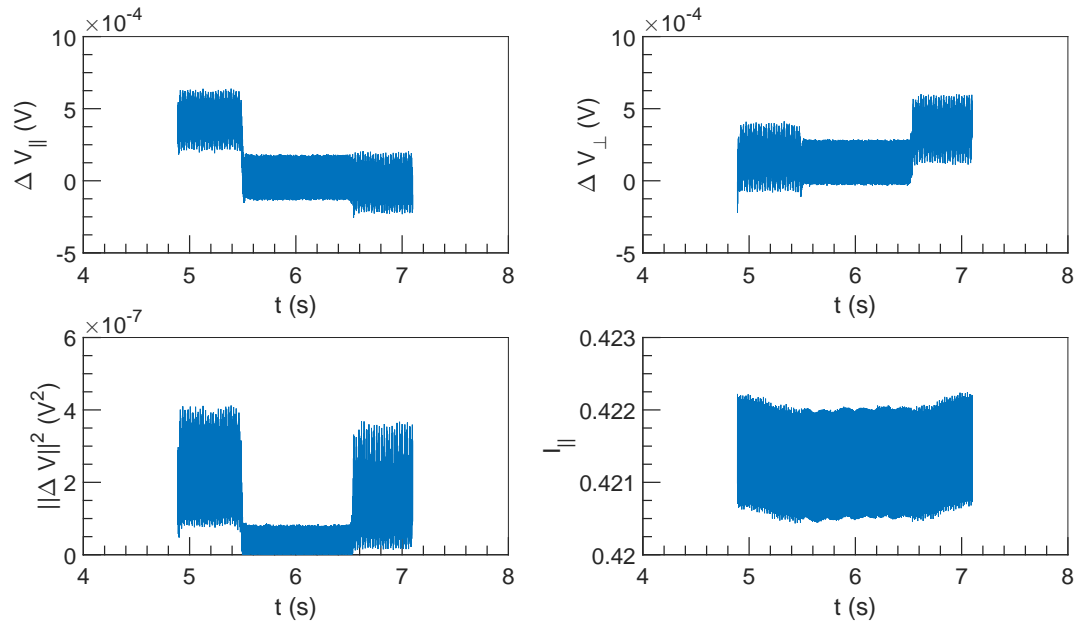


Figure 4.57:  $\Delta V$  and  $I$  vs  $t$  at  $U = 0.75 \text{ ms}^{-1}$ ,  $\omega = 3142 \text{ rad s}^{-1}$  and  $\alpha = 2.0\%$ .

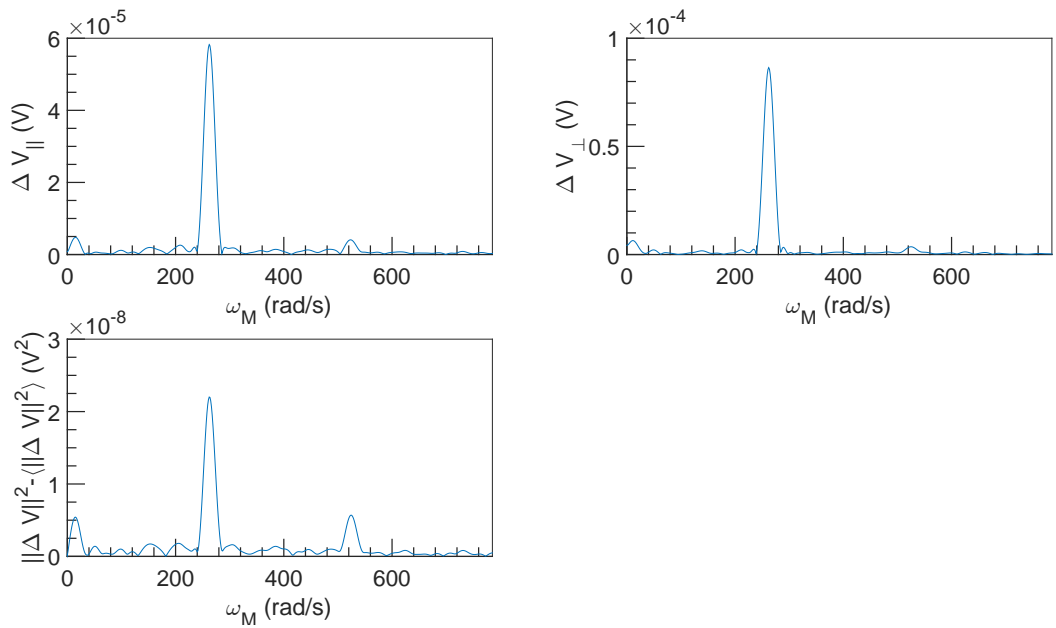


Figure 4.58: FFT spectral density of  $\Delta V$  vs  $\omega_M$  at  $U = 0.75 \text{ ms}^{-1}$ ,  $\omega = 3142 \text{ rad s}^{-1}$  and  $\alpha = 2.0\%$ .

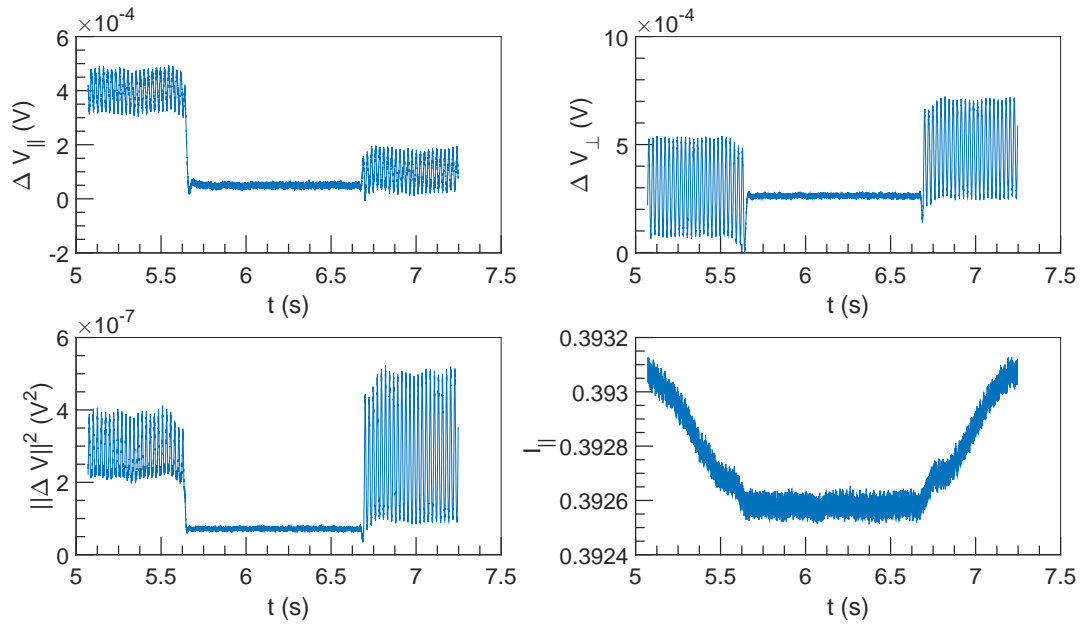


Figure 4.59:  $\Delta V$  and  $I$  vs  $t$  at  $U = 0.75 \text{ ms}^{-1}$ ,  $\omega = 6283 \text{ rad s}^{-1}$  and  $\alpha = 2.0\%$ .

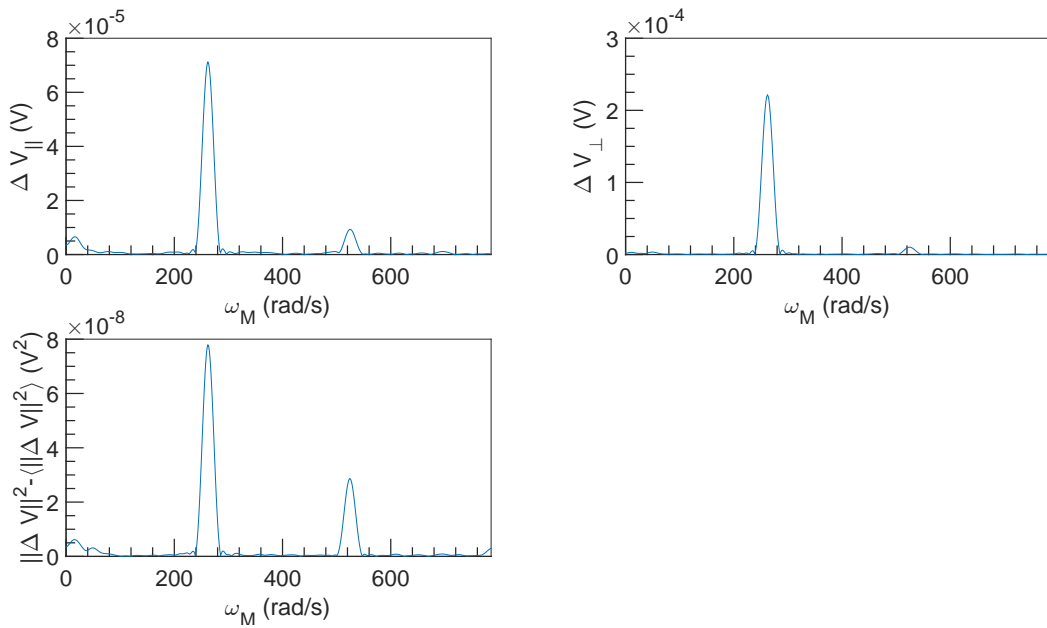


Figure 4.60: FFT spectral density of  $\Delta V$  vs  $\omega_M$  at  $U = 0.75 \text{ ms}^{-1}$ ,  $\omega = 6283 \text{ rad s}^{-1}$  and  $\alpha = 2.0\%$ .

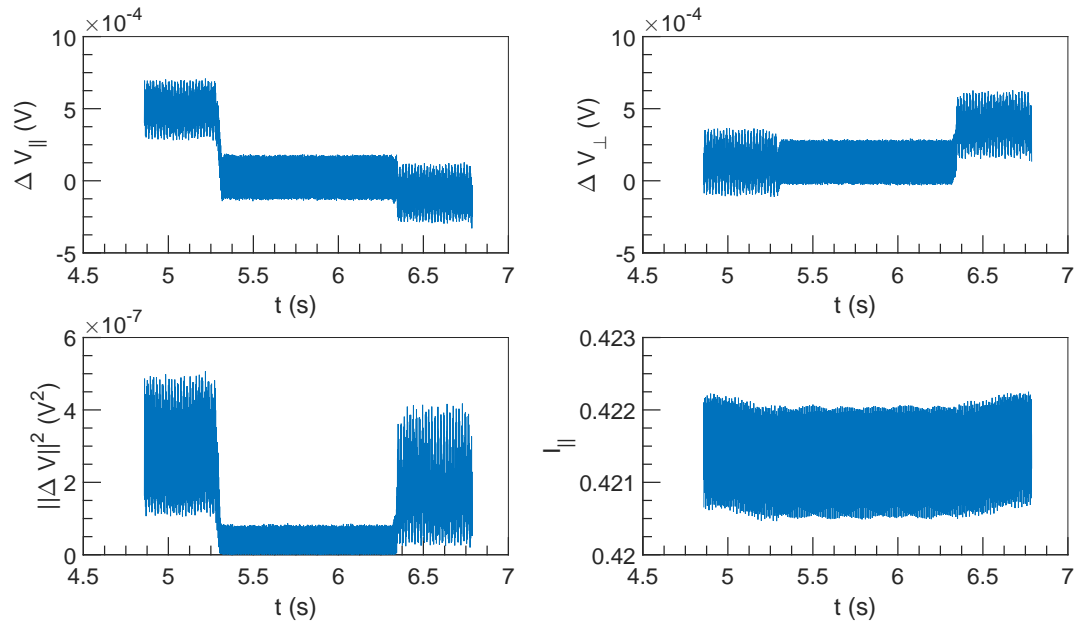


Figure 4.61:  $\Delta V$  and  $I$  vs  $t$  at  $U = 1 \text{ ms}^{-1}$ ,  $\omega = 3142 \text{ rad s}^{-1}$  and  $\alpha = 2.0\%$ .

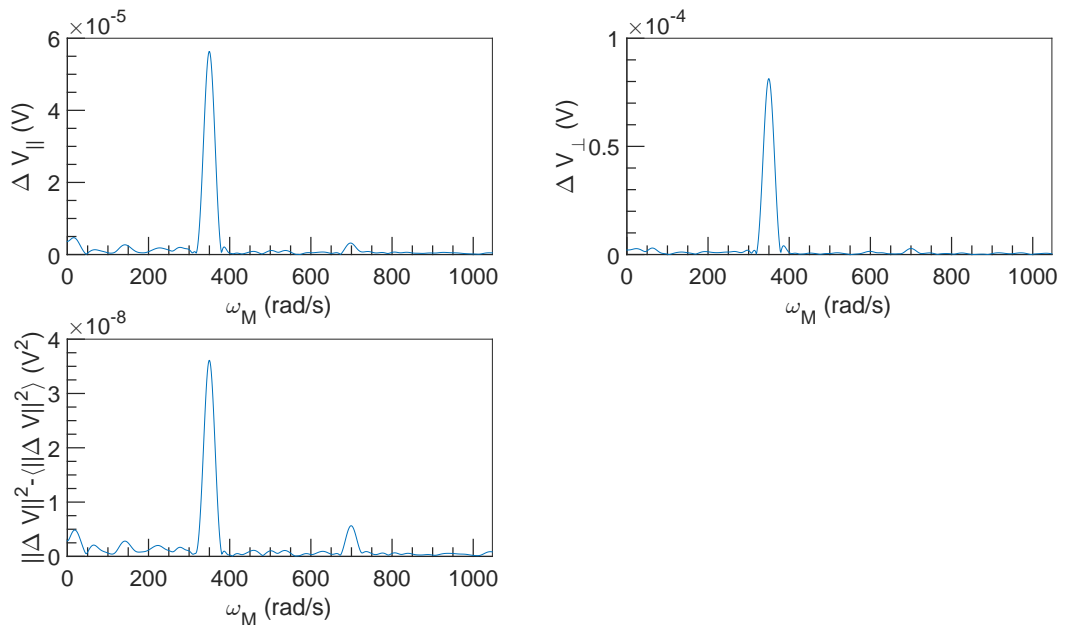


Figure 4.62: FFT spectral density of  $\Delta V$  vs  $\omega_M$  at  $U = 1 \text{ ms}^{-1}$ ,  $\omega = 3142 \text{ rad s}^{-1}$  and  $\alpha = 2.0\%$ .

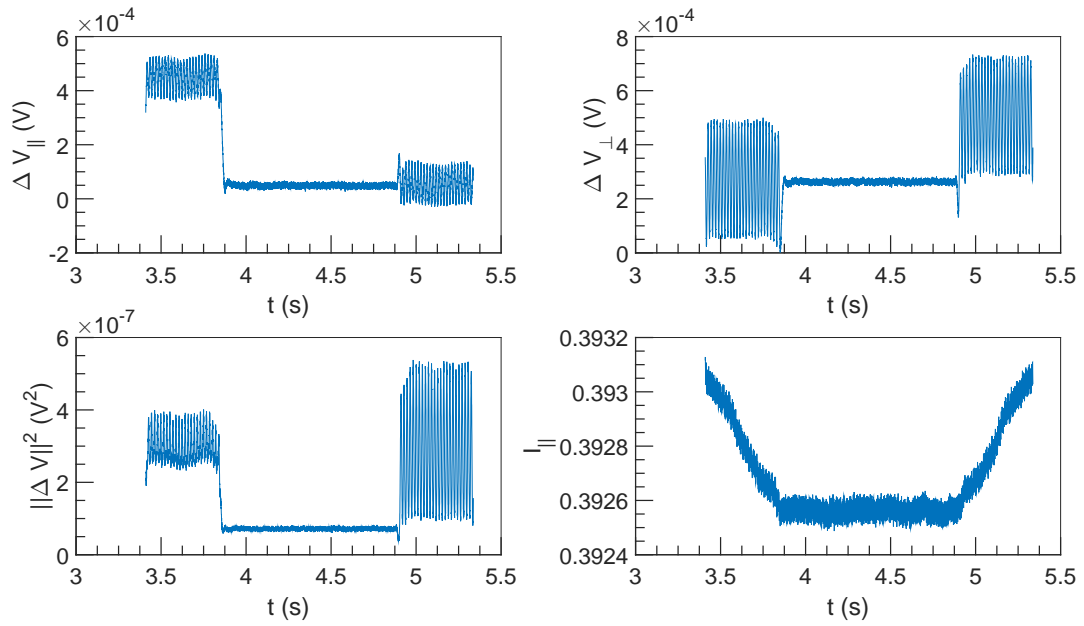


Figure 4.63:  $\Delta V$  and  $I$  vs  $t$  at  $U = 1 \text{ ms}^{-1}$ ,  $\omega = 6283 \text{ rad s}^{-1}$  and  $\alpha = 2.0\%$ .

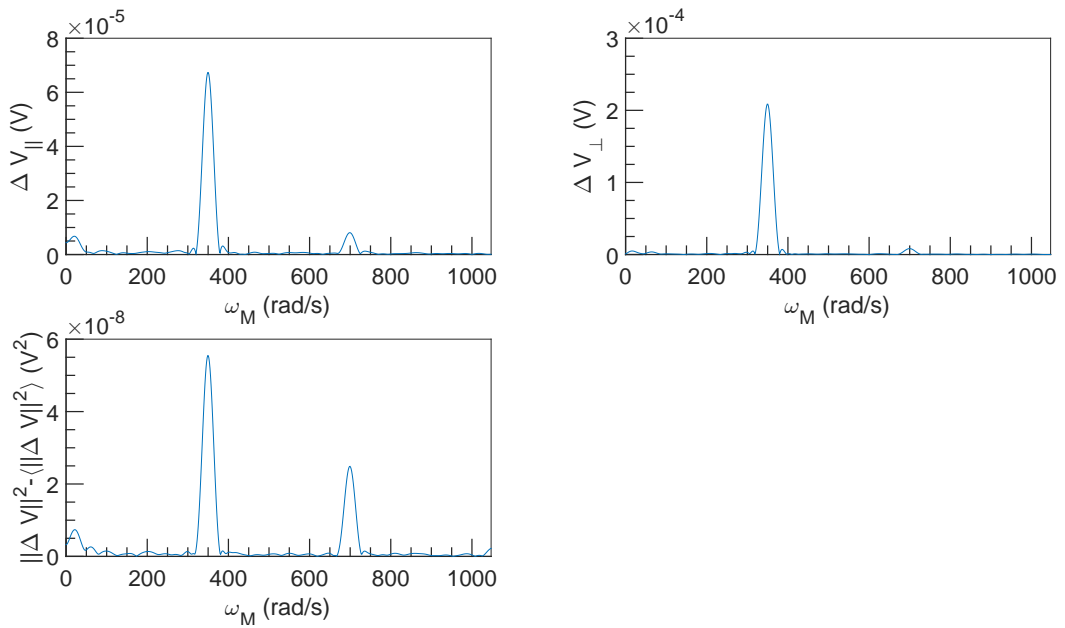


Figure 4.64: FFT spectral density of  $\Delta V$  vs  $\omega_M$  at  $U = 1 \text{ ms}^{-1}$ ,  $\omega = 6283 \text{ rad s}^{-1}$  and  $\alpha = 2.0\%$ .

## Chapter 5

**For**  $\alpha = 4.5\%$

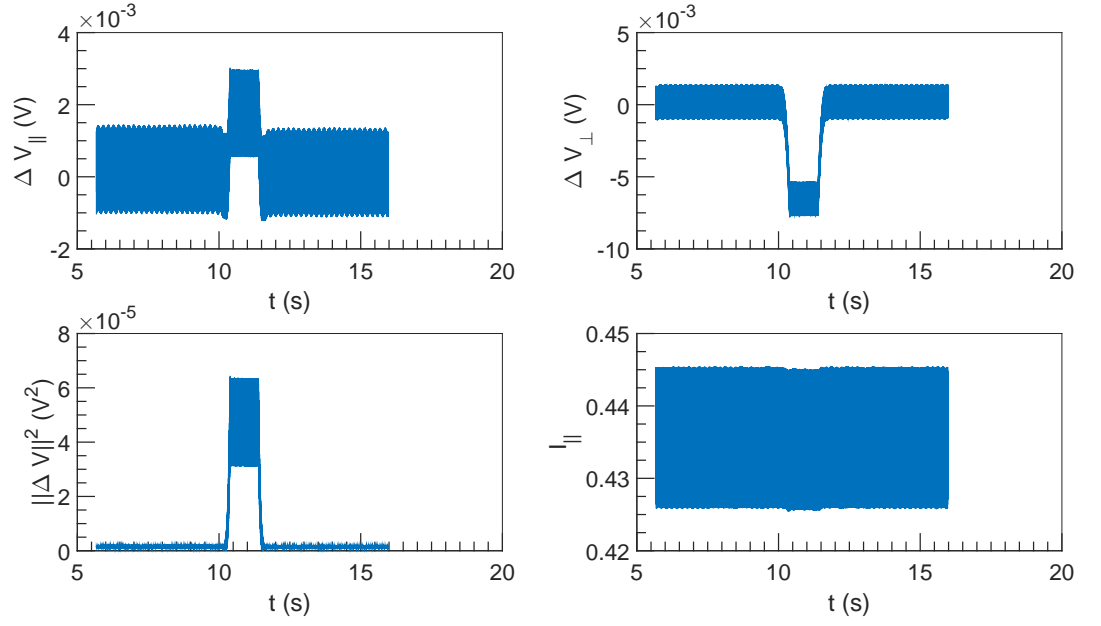


Figure 5.1:  $\Delta V$  and  $I$  vs  $t$  at  $U = 0.1 \text{ m s}^{-1}$ ,  $\omega = 1571 \text{ rad s}^{-1}$  and  $\alpha = 4.5\%$ .

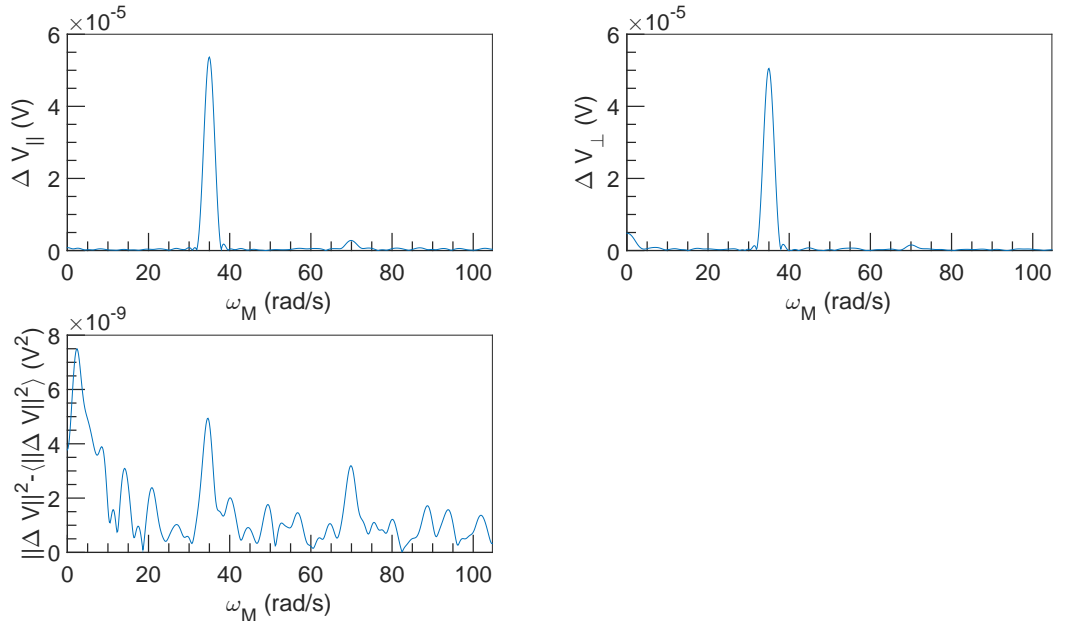


Figure 5.2: FFT spectral density of  $\Delta V$  vs  $\omega_M$  at  $U = 0.1 \text{ m s}^{-1}$ ,  $\omega = 1571 \text{ rad s}^{-1}$  and  $\alpha = 4.5\%$ .



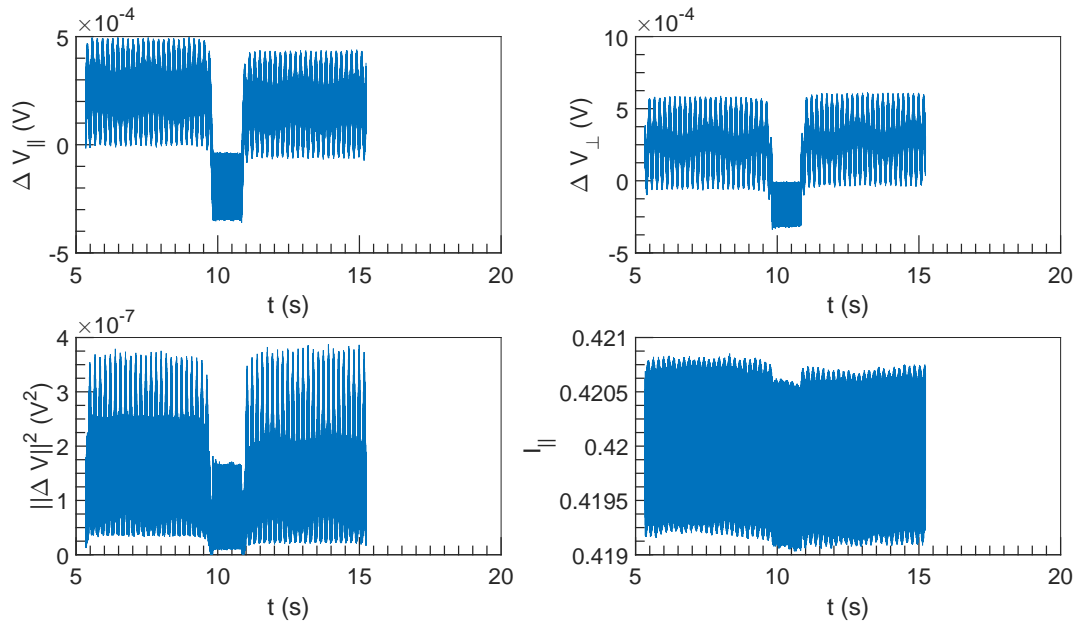


Figure 5.3:  $\Delta V$  and  $I$  vs  $t$  at  $U = 0.1 \text{ m s}^{-1}$ ,  $\omega = 3142 \text{ rad s}^{-1}$  and  $\alpha = 4.5\%$ .

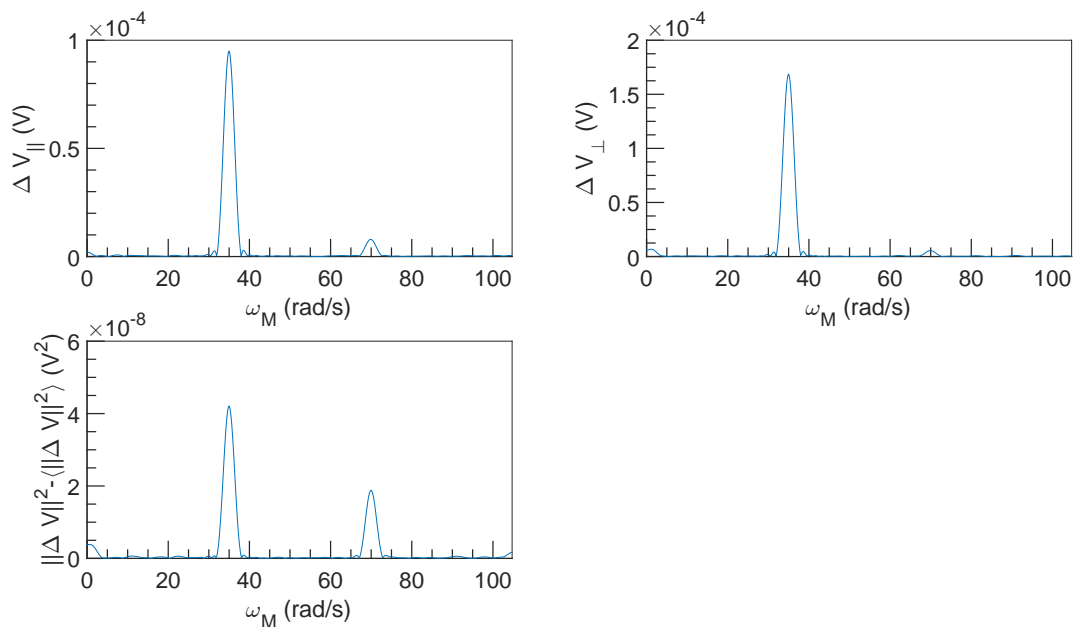


Figure 5.4: FFT spectral density of  $\Delta V$  vs  $\omega_M$  at  $U = 0.1 \text{ m s}^{-1}$ ,  $\omega = 3142 \text{ rad s}^{-1}$  and  $\alpha = 4.5\%$ .

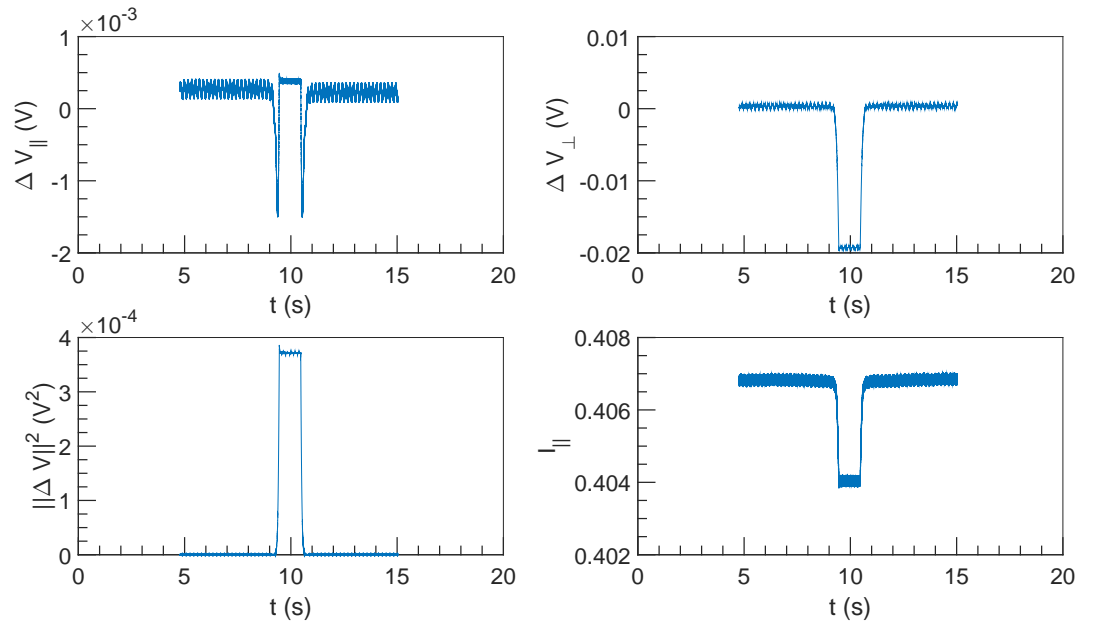


Figure 5.5:  $\Delta V$  and  $I$  vs  $t$  at  $U = 0.1 \text{ m s}^{-1}$ ,  $\omega = 4712 \text{ rad s}^{-1}$  and  $\alpha = 4.5\%$ .

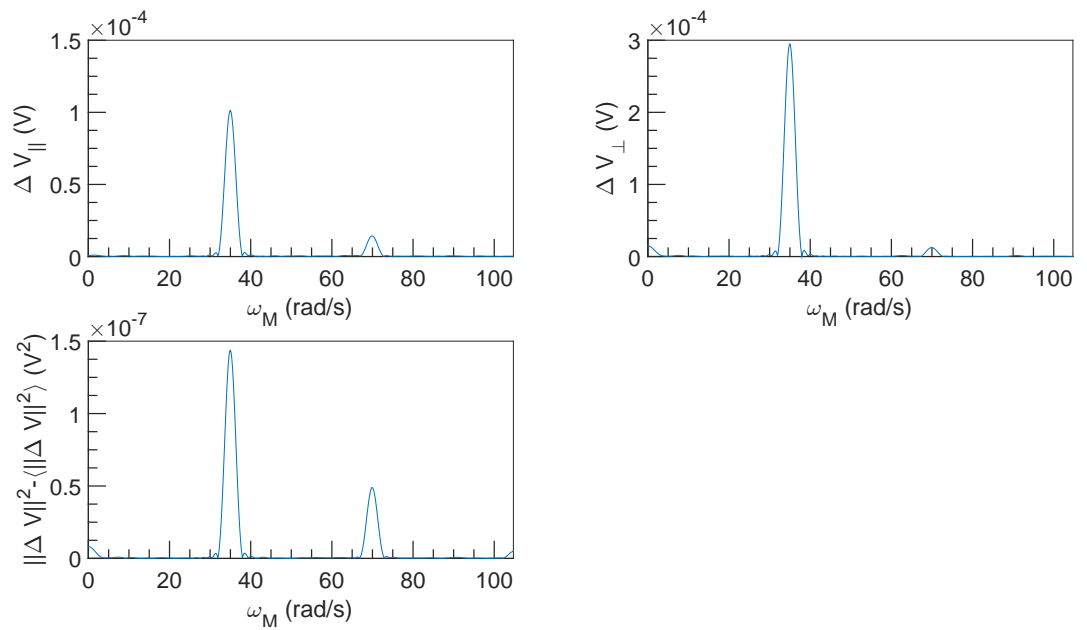


Figure 5.6: FFT spectral density of  $\Delta V$  vs  $\omega_M$  at  $U = 0.1 \text{ m s}^{-1}$ ,  $\omega = 4712 \text{ rad s}^{-1}$  and  $\alpha = 4.5\%$ .

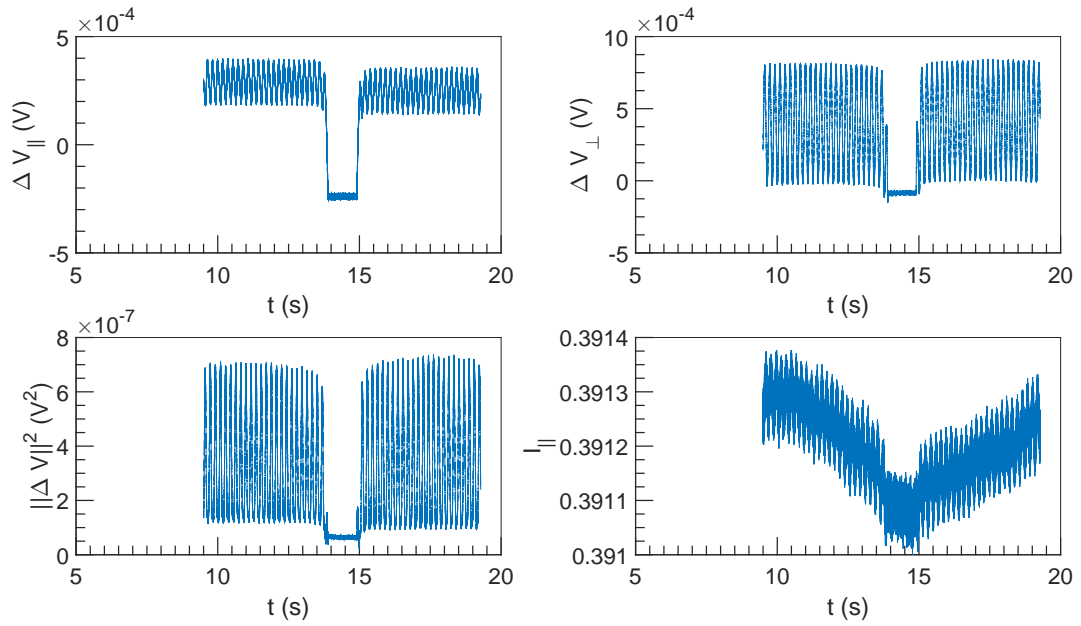


Figure 5.7:  $\Delta V$  and  $I$  vs  $t$  at  $U = 0.1 \text{ m s}^{-1}$ ,  $\omega = 6283 \text{ rad s}^{-1}$  and  $\alpha = 4.5\%$ .

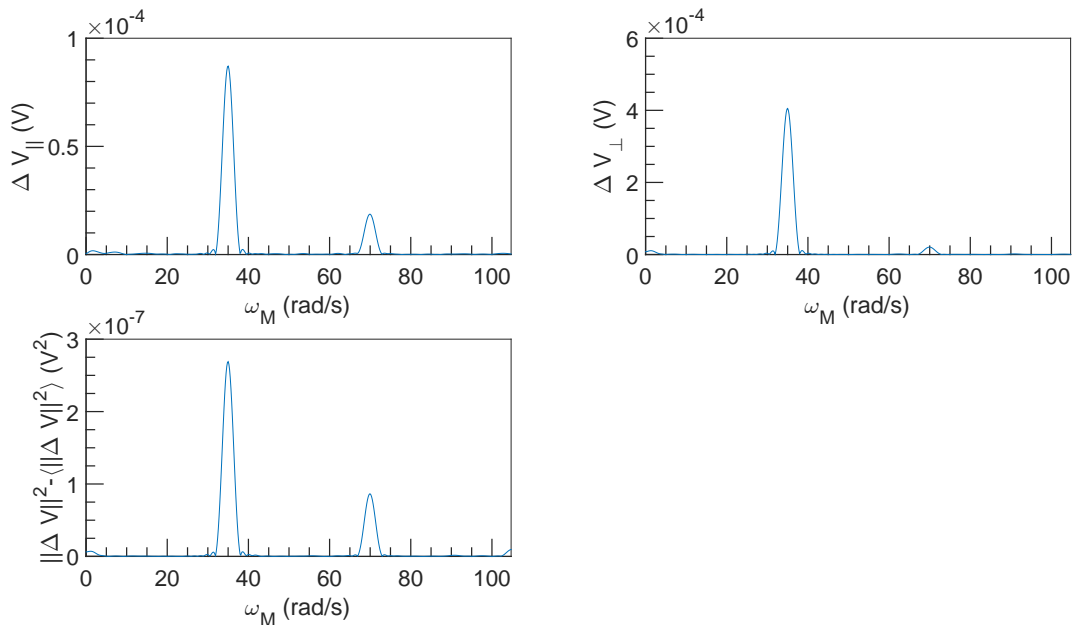


Figure 5.8: FFT spectral density of  $\Delta V$  vs  $\omega_M$  at  $U = 0.1 \text{ m s}^{-1}$ ,  $\omega = 6283 \text{ rad s}^{-1}$  and  $\alpha = 4.5\%$ .

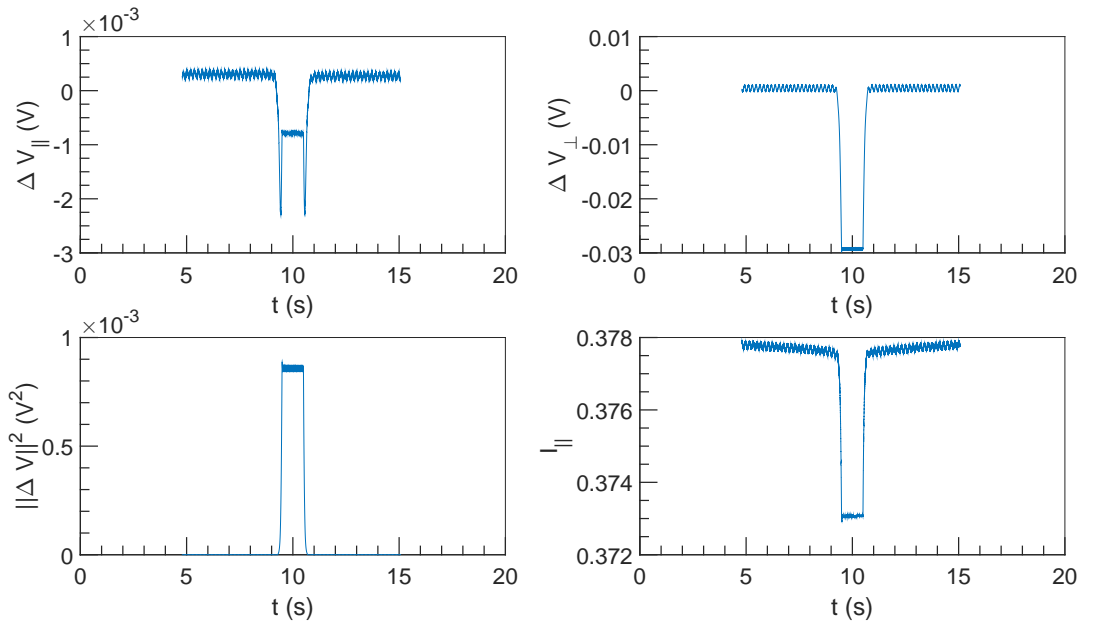


Figure 5.9:  $\Delta V$  and  $I$  vs  $t$  at  $U = 0.1 \text{ m s}^{-1}$ ,  $\omega = 7854 \text{ rad s}^{-1}$  and  $\alpha = 4.5\%$ .

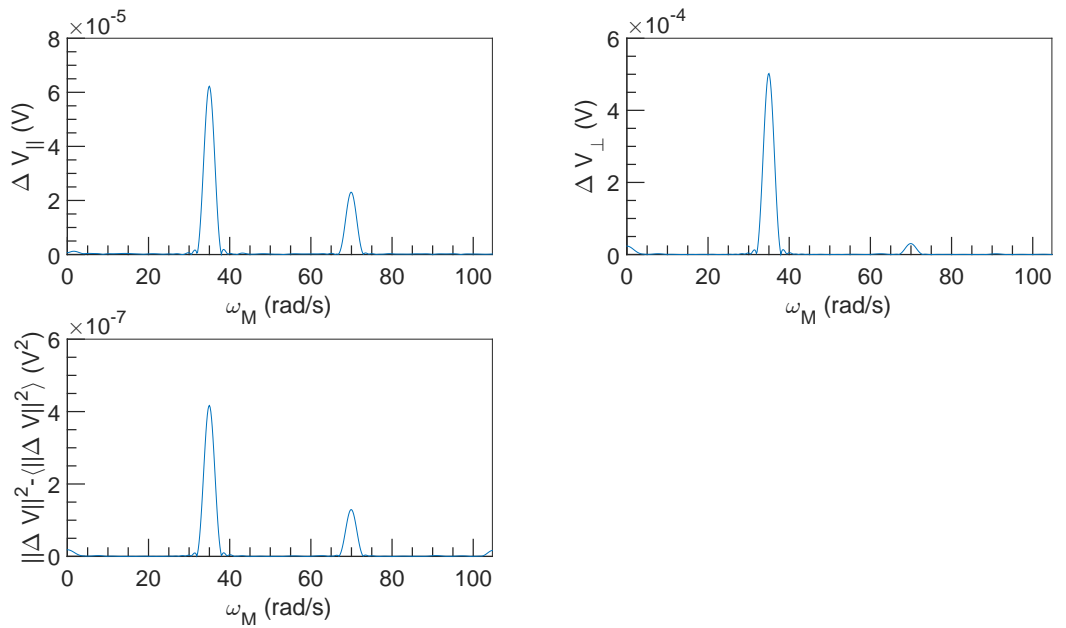


Figure 5.10: FFT spectral density of  $\Delta V$  vs  $\omega_M$  at  $U = 0.1 \text{ m s}^{-1}$ ,  $\omega = 7854 \text{ rad s}^{-1}$  and  $\alpha = 4.5\%$ .

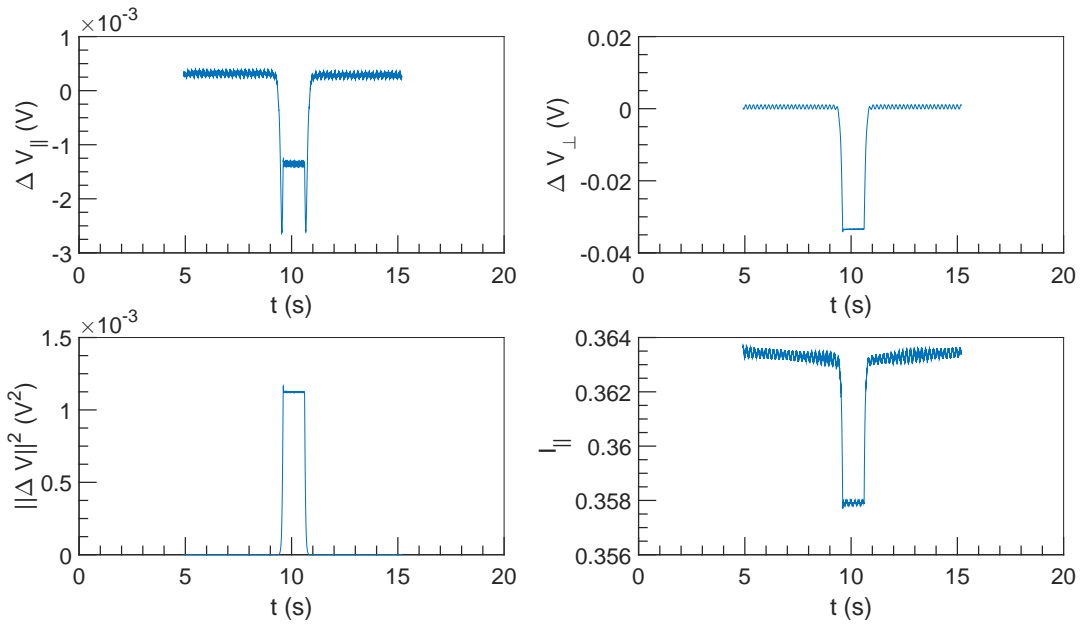


Figure 5.11:  $\Delta V$  and  $I$  vs  $t$  at  $U = 0.1 \text{ m s}^{-1}$ ,  $\omega = 9425 \text{ rad s}^{-1}$  and  $\alpha = 4.5 \%$ .

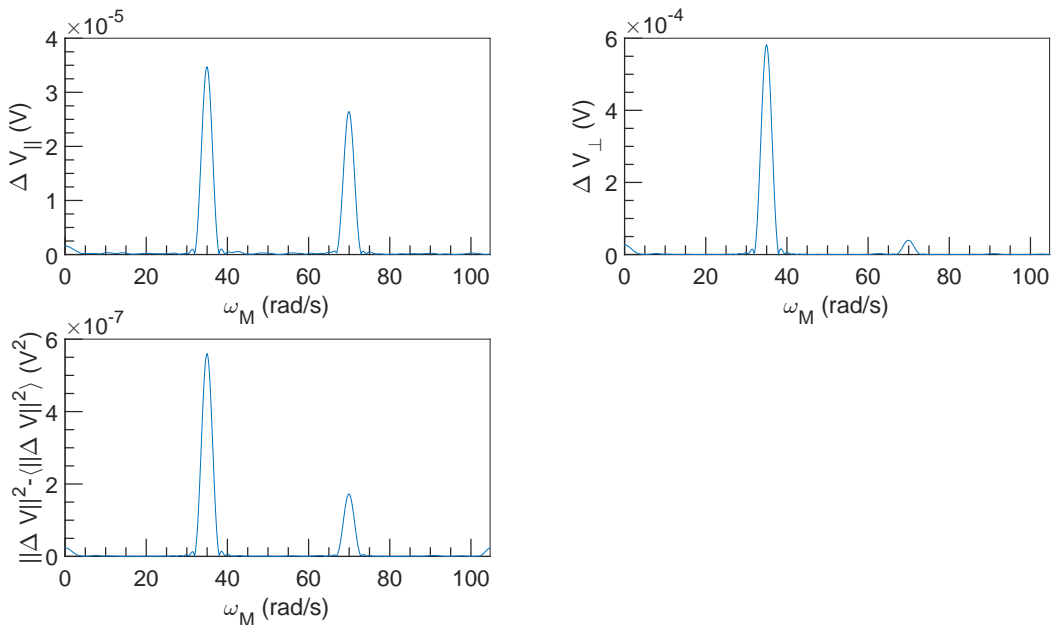


Figure 5.12: FFT spectral density of  $\Delta V$  vs  $\omega_M$  at  $U = 0.1 \text{ m s}^{-1}$ ,  $\omega = 9425 \text{ rad s}^{-1}$  and  $\alpha = 4.5 \%$ .

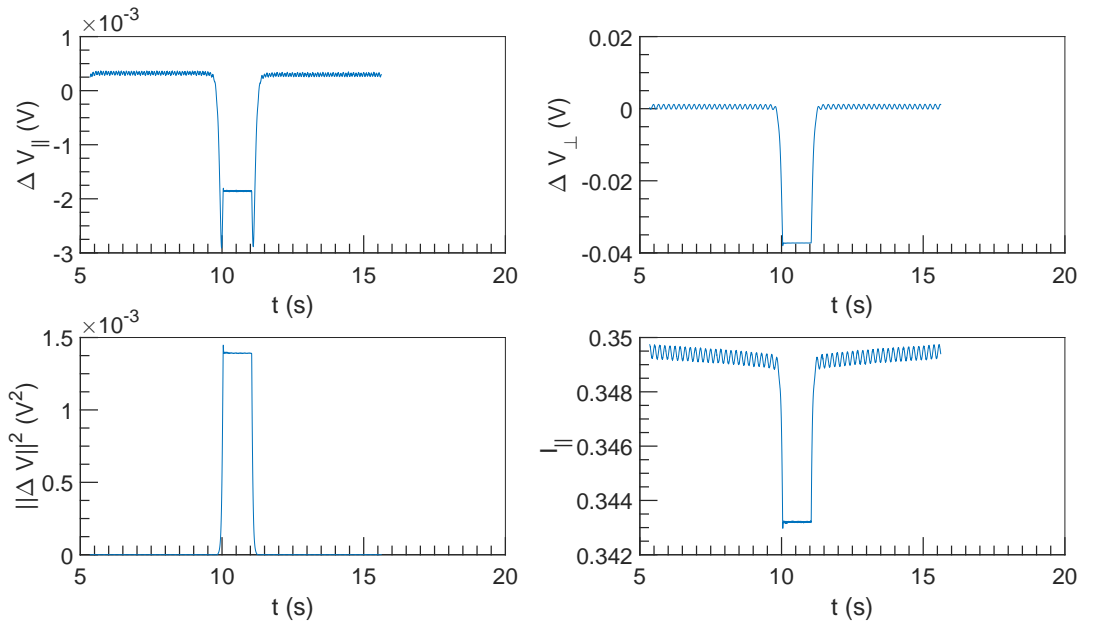


Figure 5.13:  $\Delta V$  and  $I$  vs  $t$  at  $U = 0.1 \text{ m s}^{-1}$ ,  $\omega = 10996 \text{ rad s}^{-1}$  and  $\alpha = 4.5\%$ .

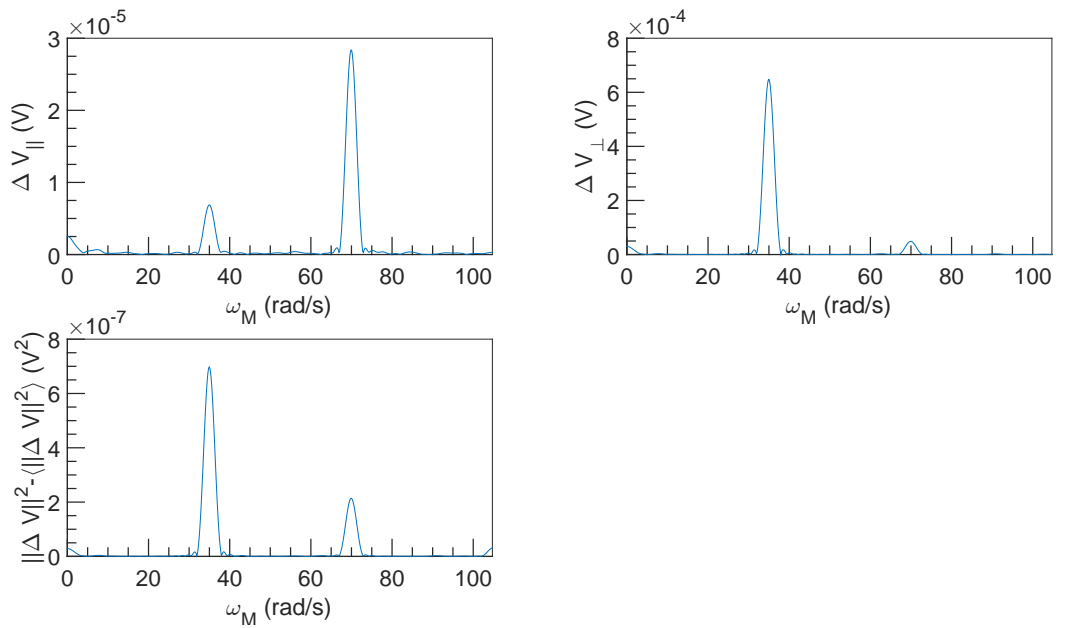


Figure 5.14: FFT spectral density of  $\Delta V$  vs  $\omega_M$  at  $U = 0.1 \text{ m s}^{-1}$ ,  $\omega = 10996 \text{ rad s}^{-1}$  and  $\alpha = 4.5\%$ .

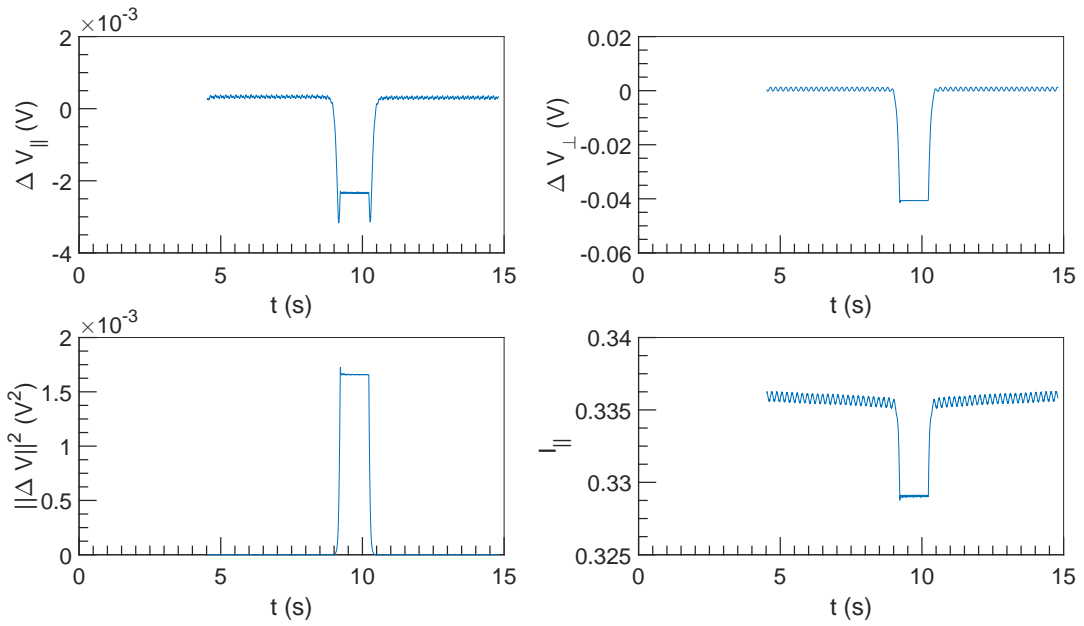


Figure 5.15:  $\Delta V$  and  $I$  vs  $t$  at  $U = 0.1 \text{ m s}^{-1}$ ,  $\omega = 12566 \text{ rad s}^{-1}$  and  $\alpha = 4.5\%$ .

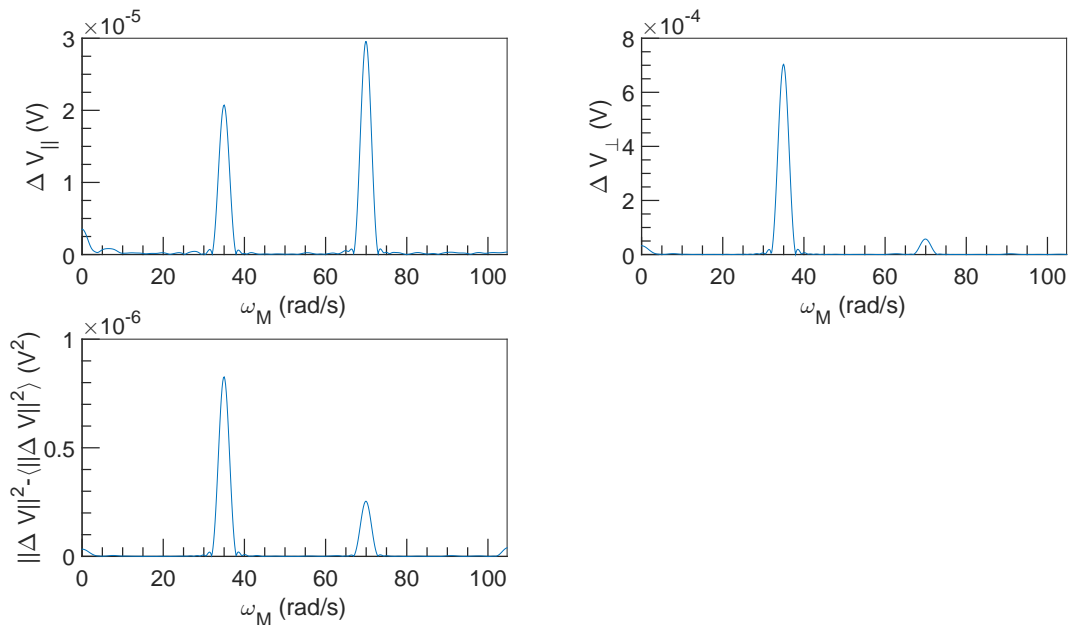


Figure 5.16: FFT spectral density of  $\Delta V$  vs  $\omega_M$  at  $U = 0.1 \text{ m s}^{-1}$ ,  $\omega = 12566 \text{ rad s}^{-1}$  and  $\alpha = 4.5\%$ .

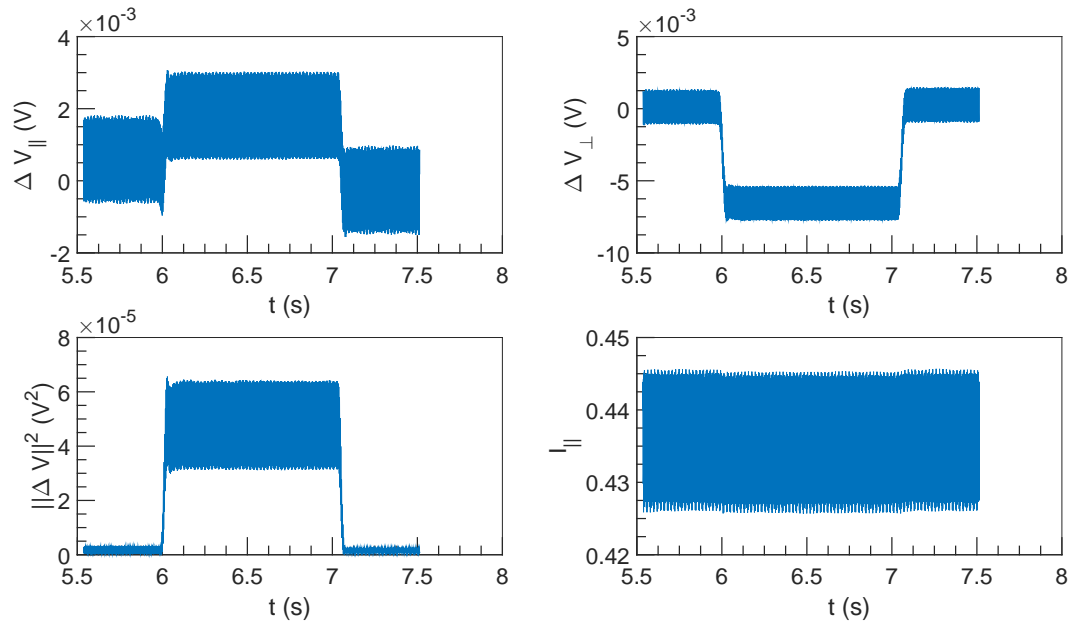


Figure 5.17:  $\Delta V$  and  $I$  vs  $t$  at  $U = 1 \text{ m s}^{-1}$ ,  $\omega = 1571 \text{ rad s}^{-1}$  and  $\alpha = 4.5\%$ .

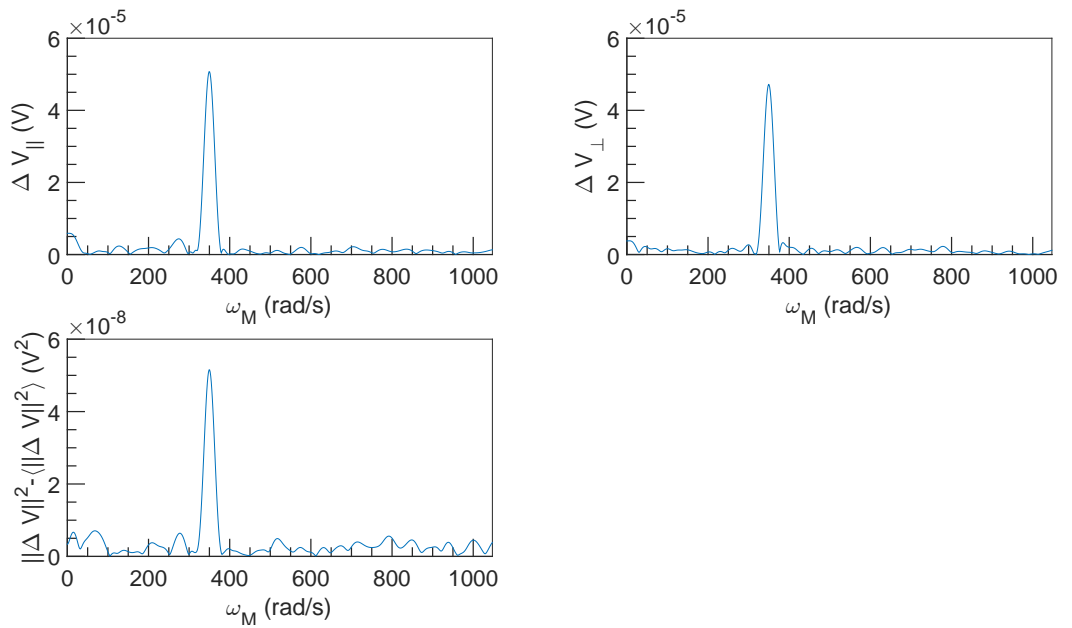


Figure 5.18: FFT spectral density of  $\Delta V$  vs  $\omega_M$  at  $U = 1 \text{ m s}^{-1}$ ,  $\omega = 1571 \text{ rad s}^{-1}$  and  $\alpha = 4.5\%$ .



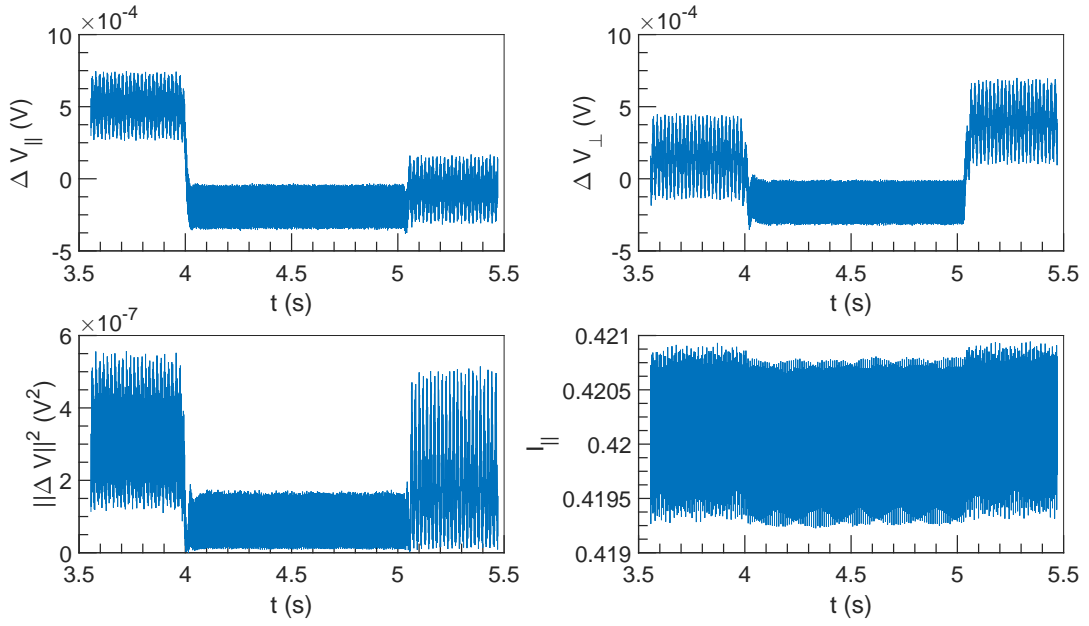


Figure 5.19:  $\Delta V$  and  $I$  vs  $t$  at  $U = 1 \text{ m s}^{-1}$ ,  $\omega = 3142 \text{ rad s}^{-1}$  and  $\alpha = 4.5\%$ .

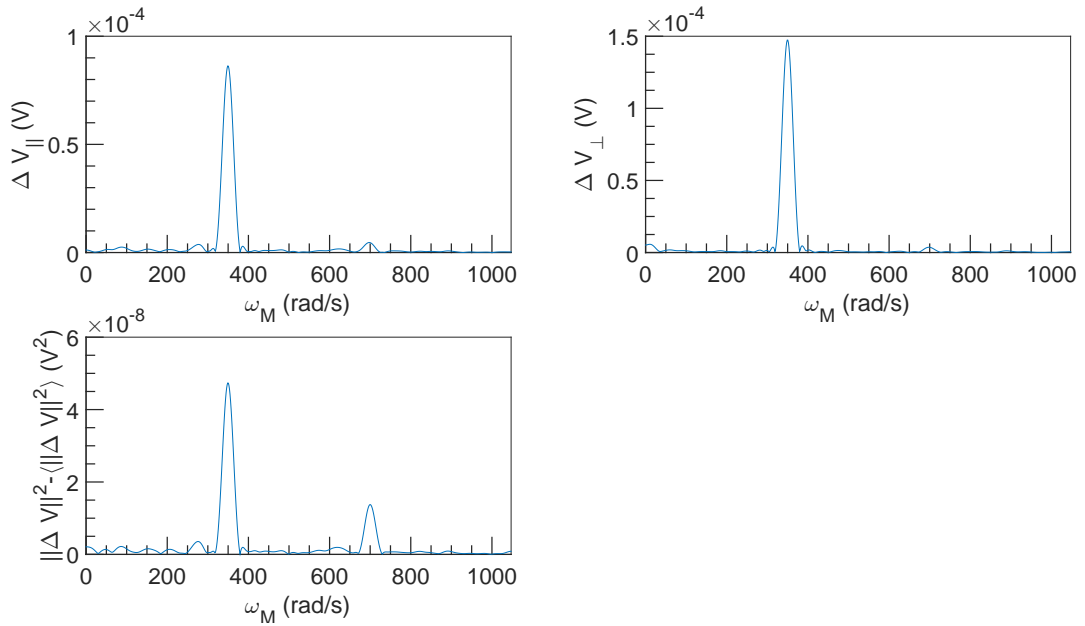


Figure 5.20: FFT spectral density of  $\Delta V$  vs  $\omega_M$  at  $U = 1 \text{ m s}^{-1}$ ,  $\omega = 3142 \text{ rad s}^{-1}$  and  $\alpha = 4.5\%$ .

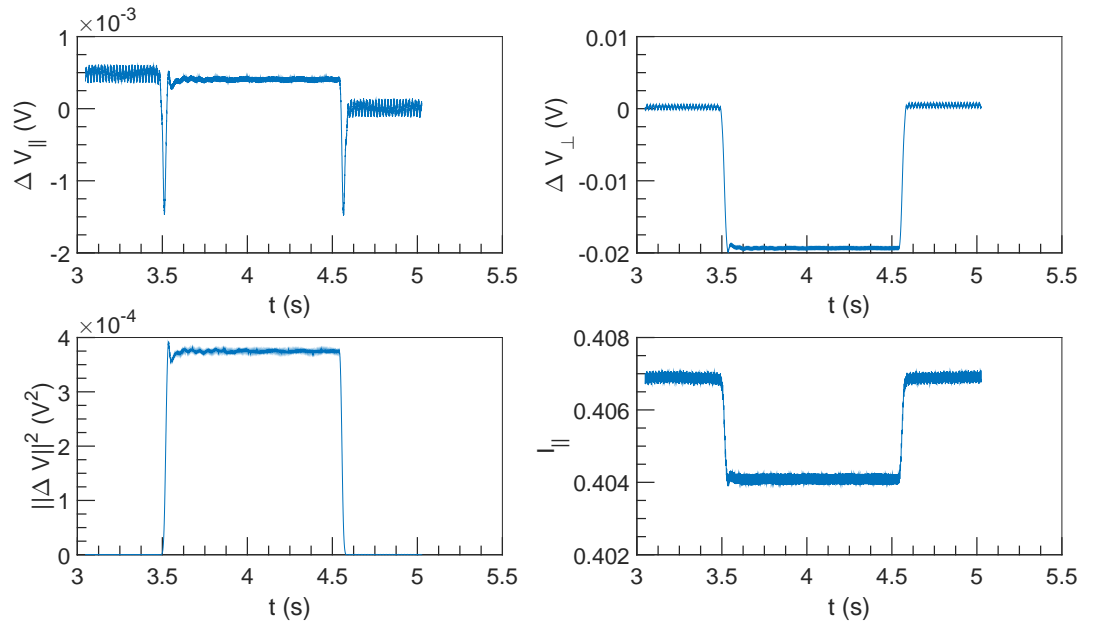


Figure 5.21:  $\Delta V$  and  $I$  vs  $t$  at  $U = 1 \text{ m s}^{-1}$ ,  $\omega = 4712 \text{ rad s}^{-1}$  and  $\alpha = 4.5\%$ .

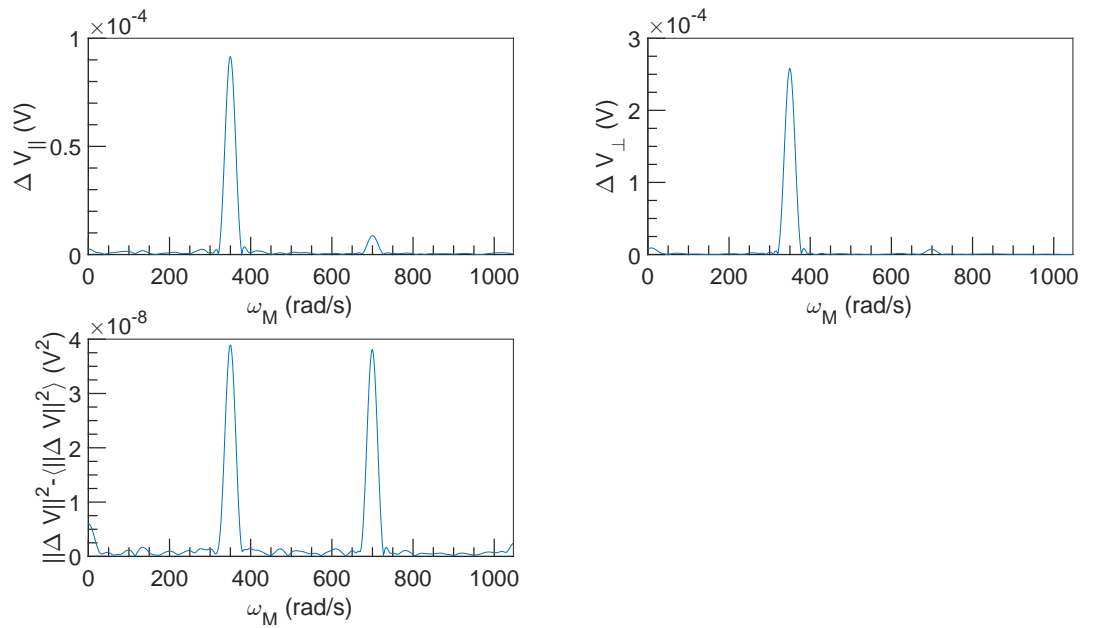


Figure 5.22: FFT spectral density of  $\Delta V$  vs  $\omega_M$  at  $U = 1 \text{ m s}^{-1}$ ,  $\omega = 4712 \text{ rad s}^{-1}$  and  $\alpha = 4.5\%$ .

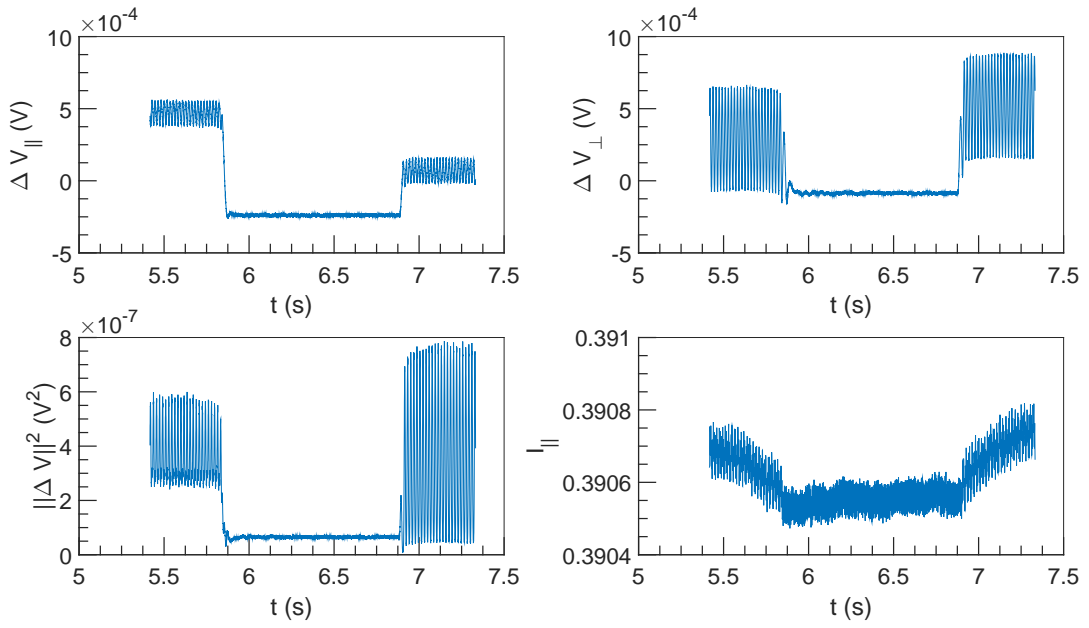


Figure 5.23:  $\Delta V$  and  $I$  vs  $t$  at  $U = 1 \text{ ms}^{-1}$ ,  $\omega = 6283 \text{ rad s}^{-1}$  and  $\alpha = 4.5\%$ .

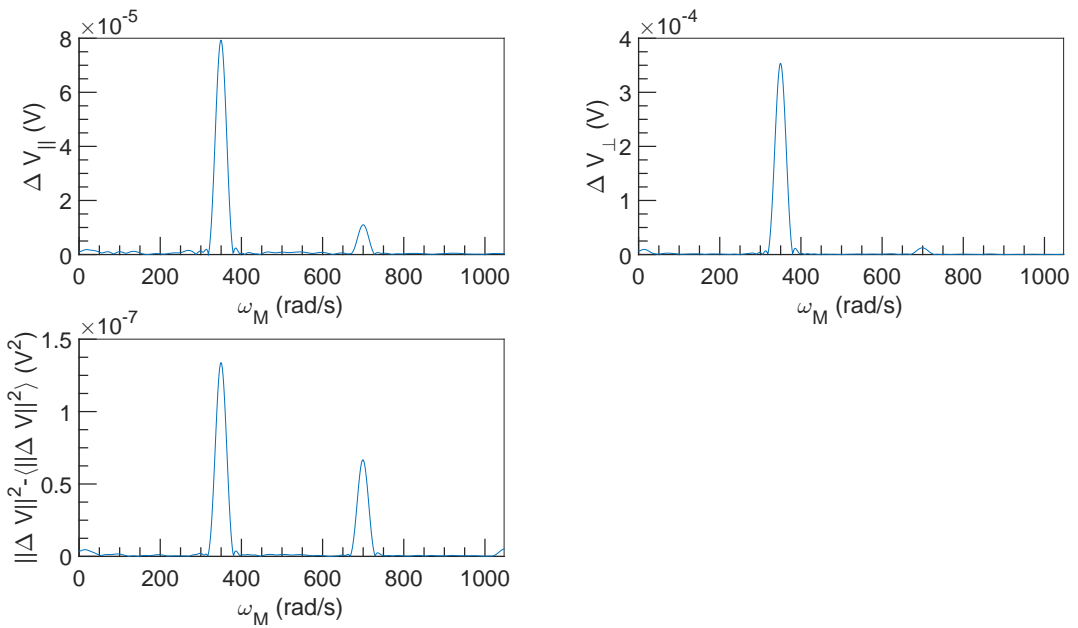


Figure 5.24: FFT spectral density of  $\Delta V$  vs  $\omega_M$  at  $U = 1 \text{ ms}^{-1}$ ,  $\omega = 6283 \text{ rad s}^{-1}$  and  $\alpha = 4.5\%$ .

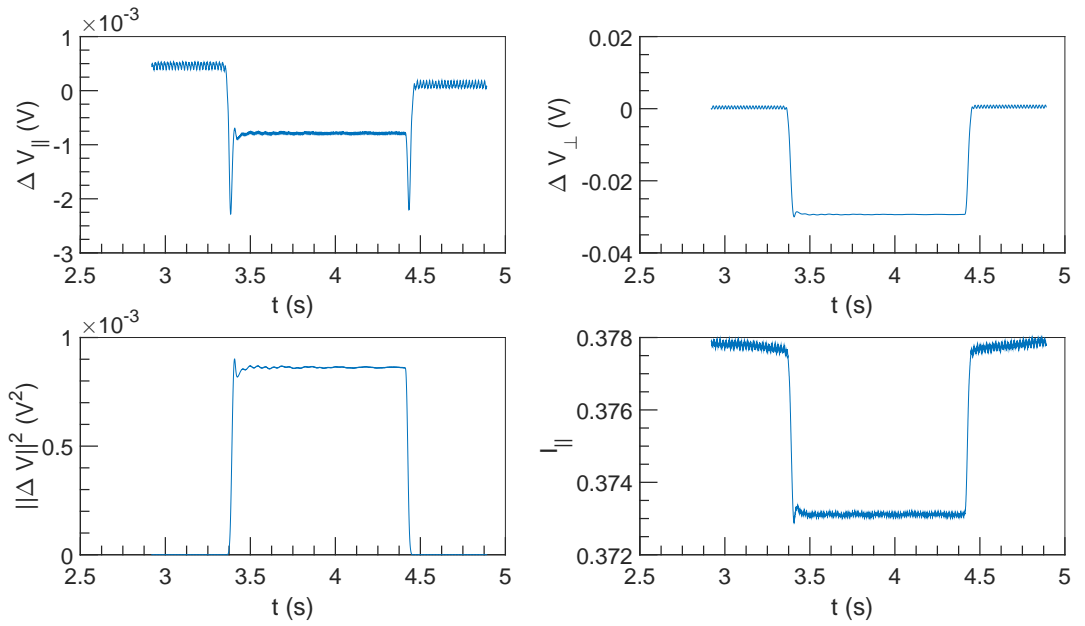


Figure 5.25:  $\Delta V$  and  $I$  vs  $t$  at  $U = 1 \text{ m s}^{-1}$ ,  $\omega = 7854 \text{ rad s}^{-1}$  and  $\alpha = 4.5\%$ .

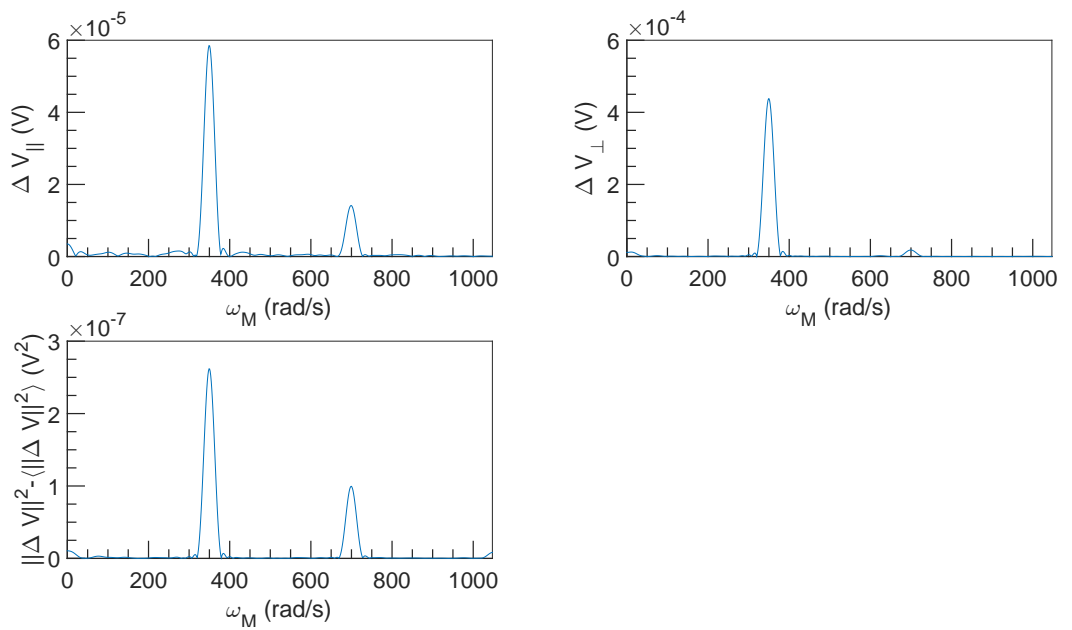


Figure 5.26: FFT spectral density of  $\Delta V$  vs  $\omega_M$  at  $U = 1 \text{ m s}^{-1}$ ,  $\omega = 7854 \text{ rad s}^{-1}$  and  $\alpha = 4.5\%$ .

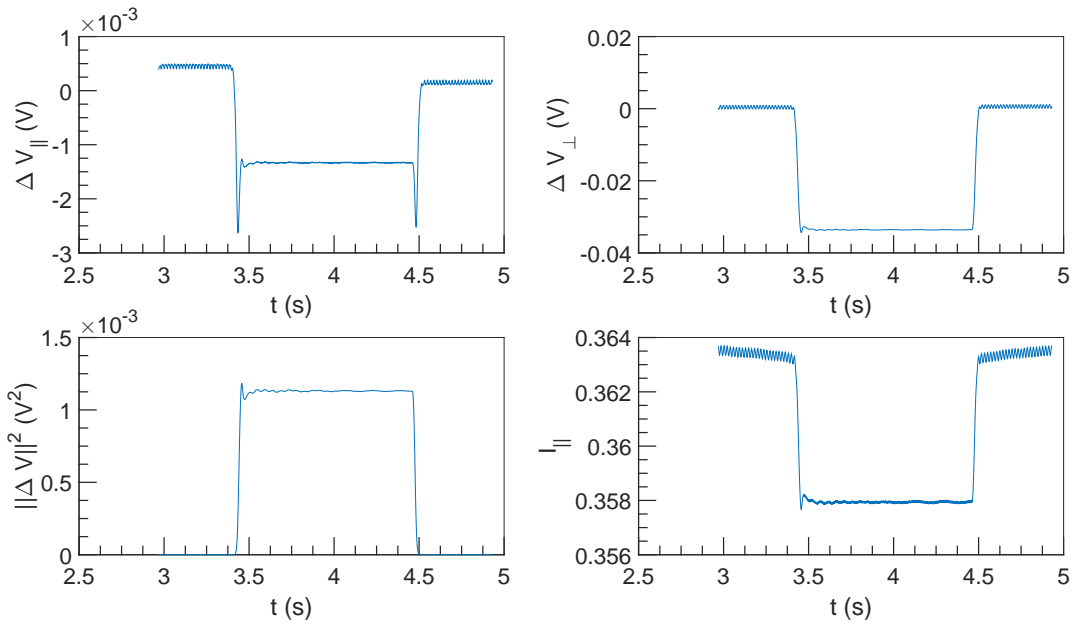


Figure 5.27:  $\Delta V$  and  $I$  vs  $t$  at  $U = 1 \text{ m s}^{-1}$ ,  $\omega = 9425 \text{ rad s}^{-1}$  and  $\alpha = 4.5\%$ .

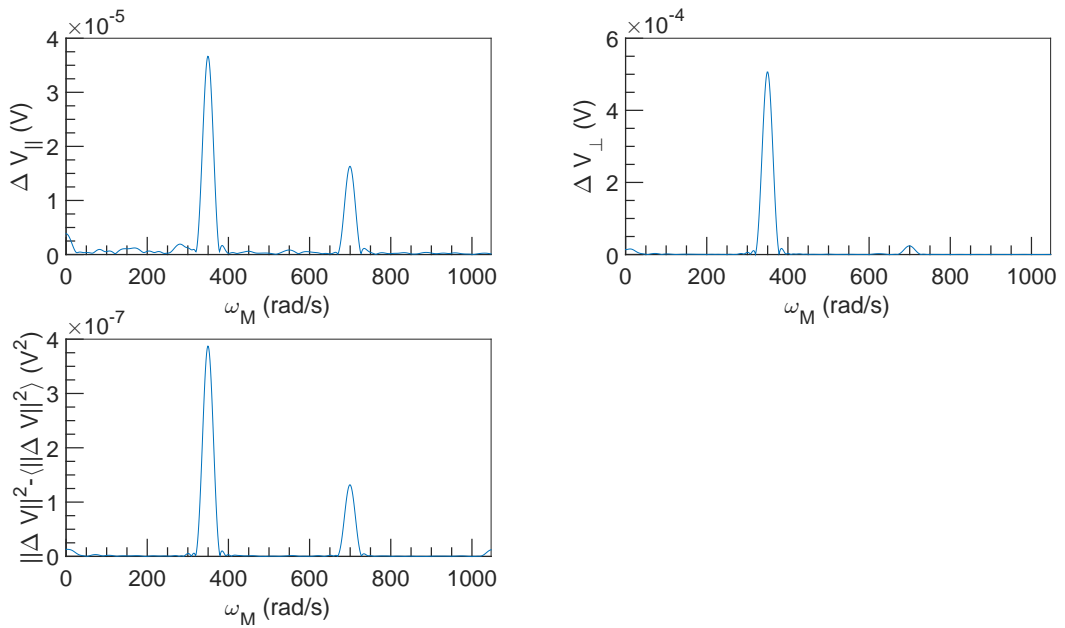


Figure 5.28: FFT spectral density of  $\Delta V$  vs  $\omega_M$  at  $U = 1 \text{ m s}^{-1}$ ,  $\omega = 9425 \text{ rad s}^{-1}$  and  $\alpha = 4.5\%$ .

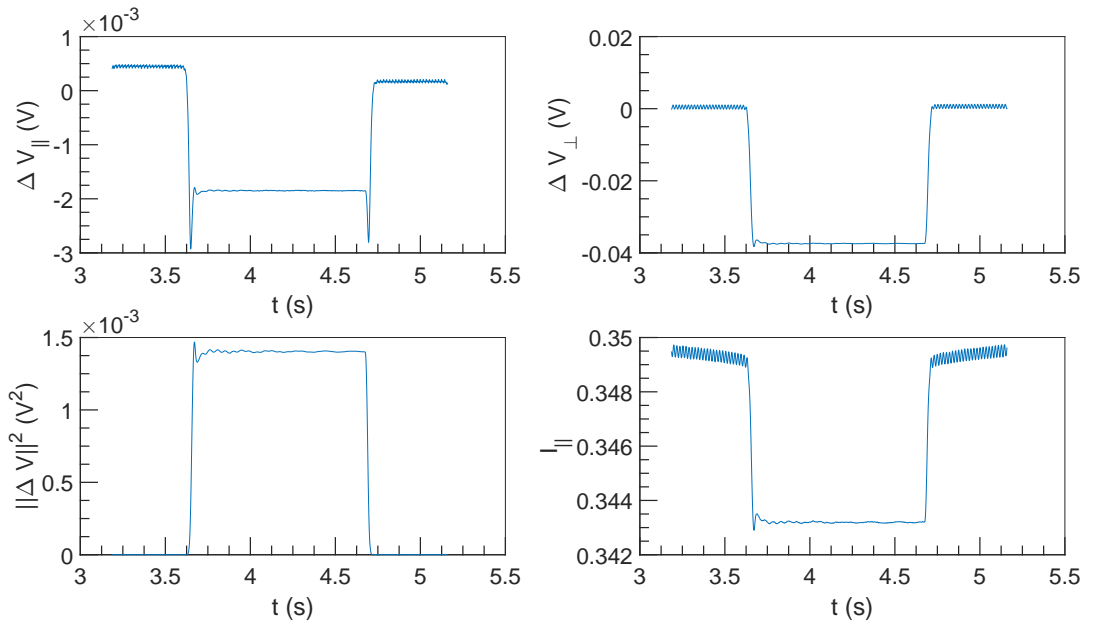


Figure 5.29:  $\Delta V$  and  $I$  vs  $t$  at  $U = 1 \text{ m s}^{-1}$ ,  $\omega = 10\,996 \text{ rad s}^{-1}$  and  $\alpha = 4.5\%$ .

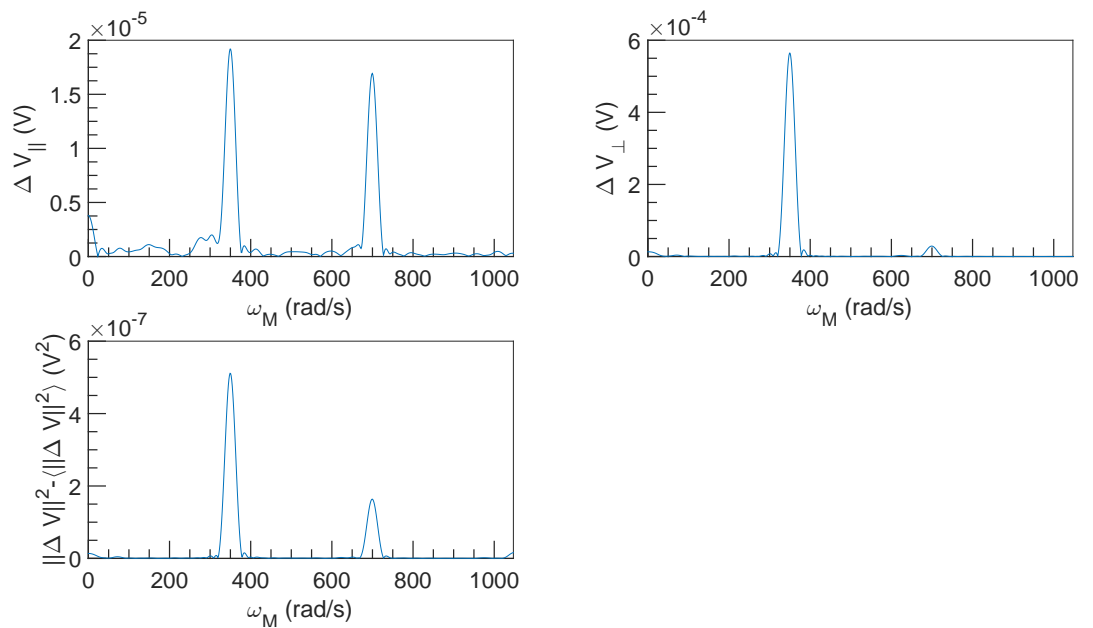


Figure 5.30: FFT spectral density of  $\Delta V$  vs  $\omega_M$  at  $U = 1 \text{ m s}^{-1}$ ,  $\omega = 10\,996 \text{ rad s}^{-1}$  and  $\alpha = 4.5\%$ .

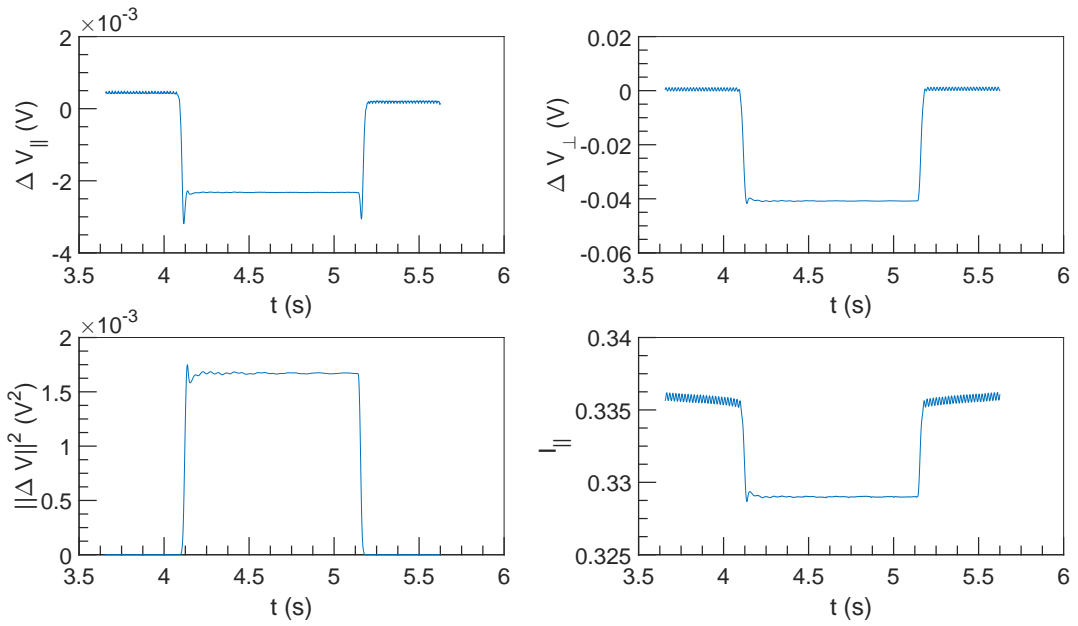


Figure 5.31:  $\Delta V$  and  $I$  vs  $t$  at  $U = 1 \text{ m s}^{-1}$ ,  $\omega = 12\,566 \text{ rad s}^{-1}$  and  $\alpha = 4.5\%$ .

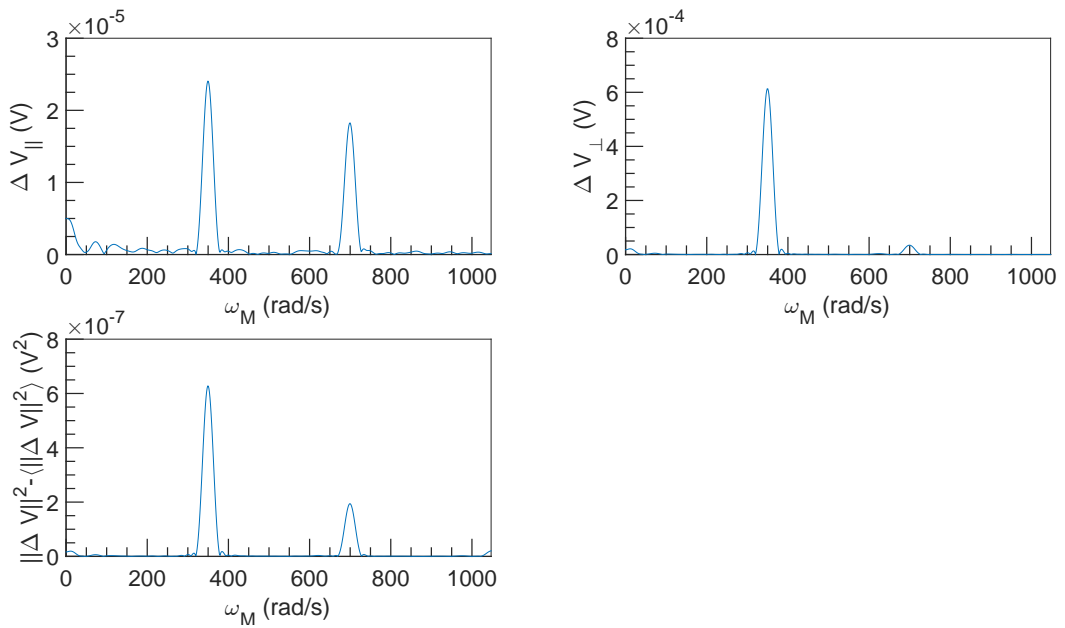


Figure 5.32: FFT spectral density of  $\Delta V$  vs  $\omega_M$  at  $U = 1 \text{ m s}^{-1}$ ,  $\omega = 12\,566 \text{ rad s}^{-1}$  and  $\alpha = 4.5\%$ .

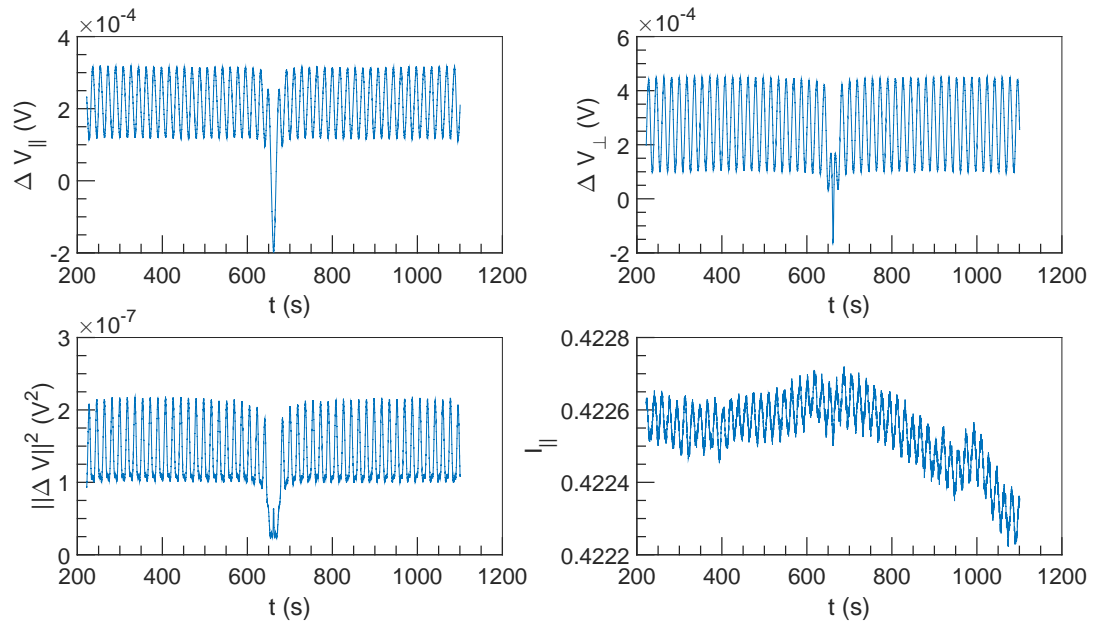


Figure 5.33:  $\Delta V$  and  $I$  vs  $t$  at  $U = 10^{-3} \text{ m s}^{-1}$ ,  $\omega = 3142 \text{ rad s}^{-1}$  and  $\alpha = 4.5\%$ .

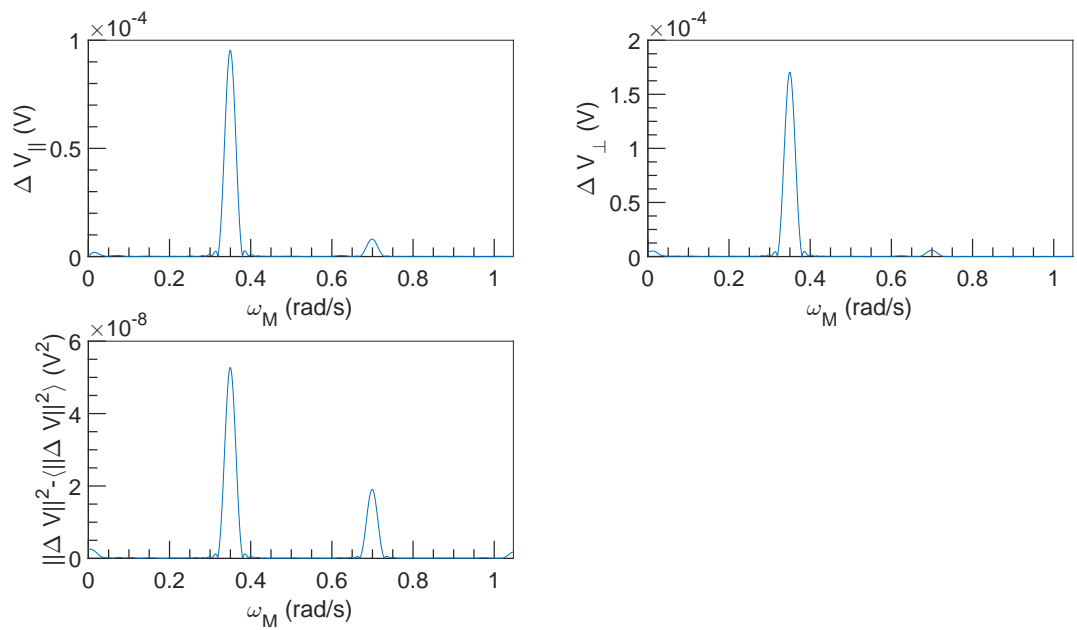


Figure 5.34: FFT spectral density of  $\Delta V$  vs  $\omega_M$  at  $U = 10^{-3} \text{ m s}^{-1}$ ,  $\omega = 3142 \text{ rad s}^{-1}$  and  $\alpha = 4.5\%$ .



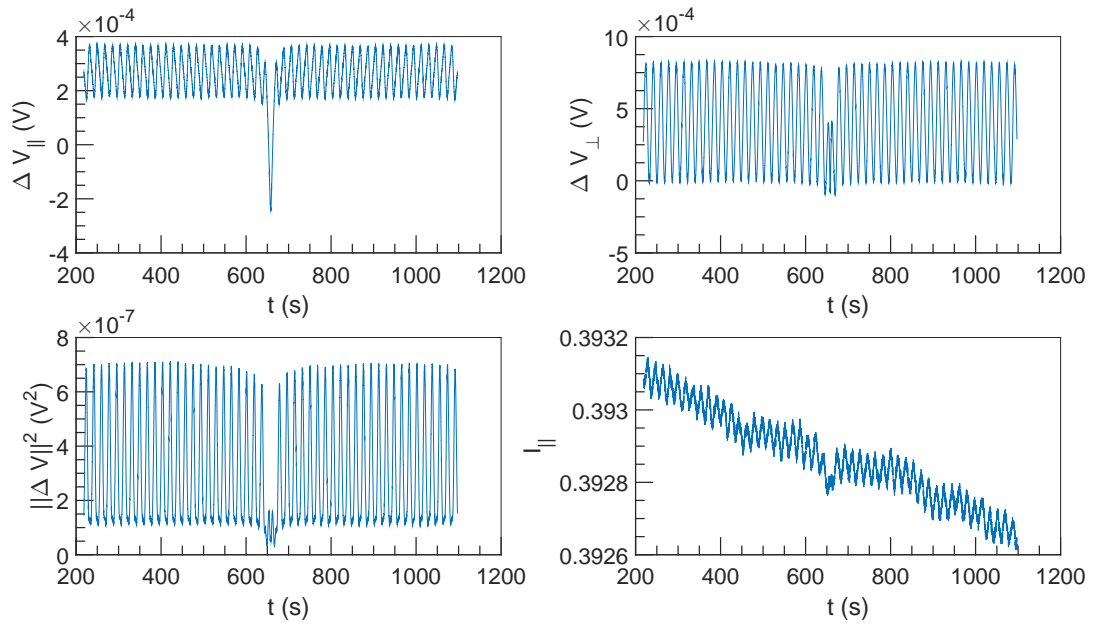


Figure 5.35:  $\Delta V$  and  $I$  vs  $t$  at  $U = 10^{-3} \text{ m s}^{-1}$ ,  $\omega = 6283 \text{ rad s}^{-1}$  and  $\alpha = 4.5\%$ .

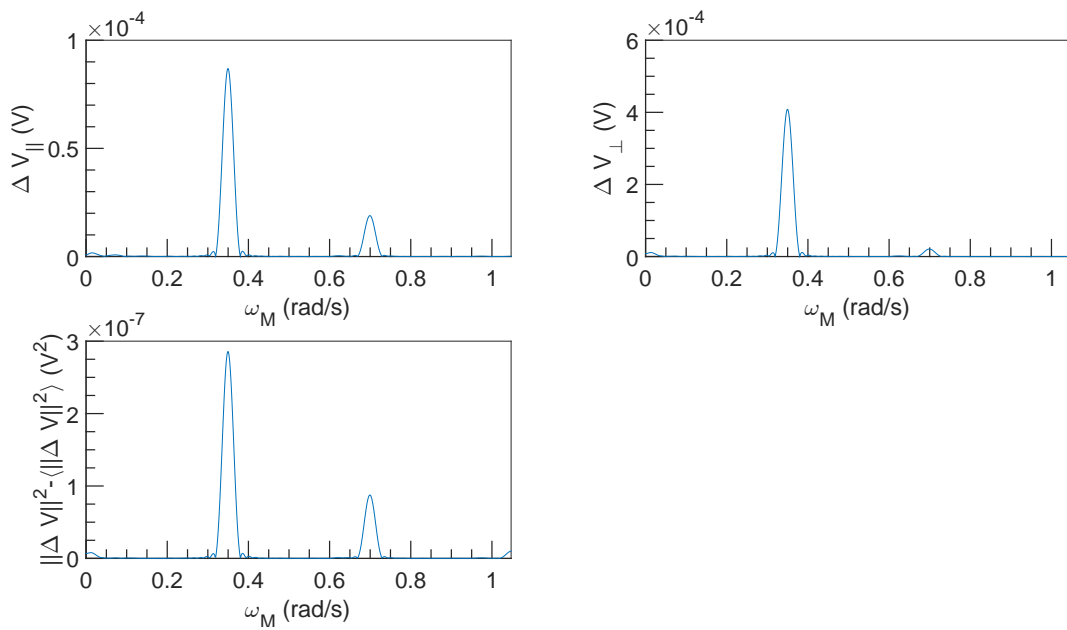


Figure 5.36: FFT spectral density of  $\Delta V$  vs  $\omega_M$  at  $U = 10^{-3} \text{ m s}^{-1}$ ,  $\omega = 6283 \text{ rad s}^{-1}$  and  $\alpha = 4.5\%$ .

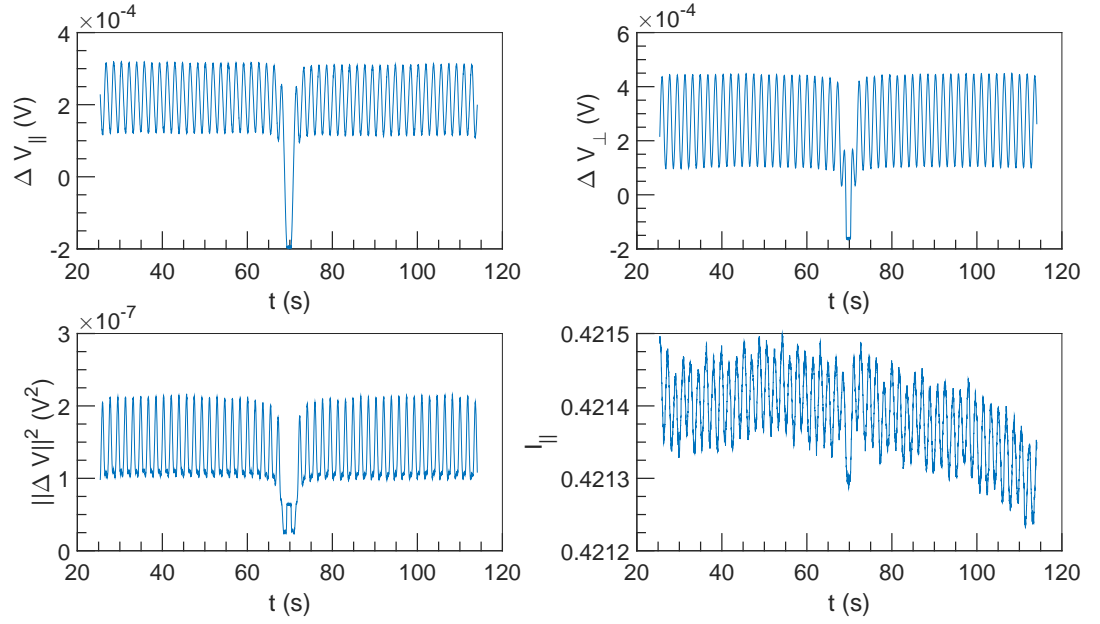


Figure 5.37:  $\Delta V$  and  $I$  vs  $t$  at  $U = 10^{-2} \text{ m s}^{-1}$ ,  $\omega = 3142 \text{ rad s}^{-1}$  and  $\alpha = 4.5\%$ .

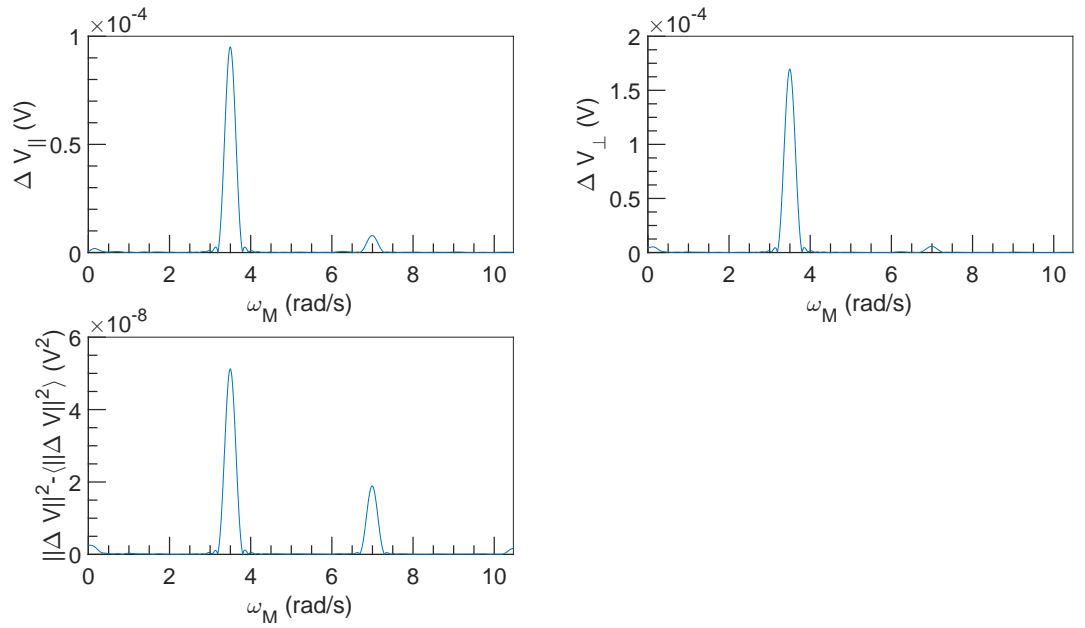


Figure 5.38: FFT spectral density of  $\Delta V$  vs  $\omega_M$  at  $U = 10^{-2} \text{ m s}^{-1}$ ,  $\omega = 3142 \text{ rad s}^{-1}$  and  $\alpha = 4.5\%$ .

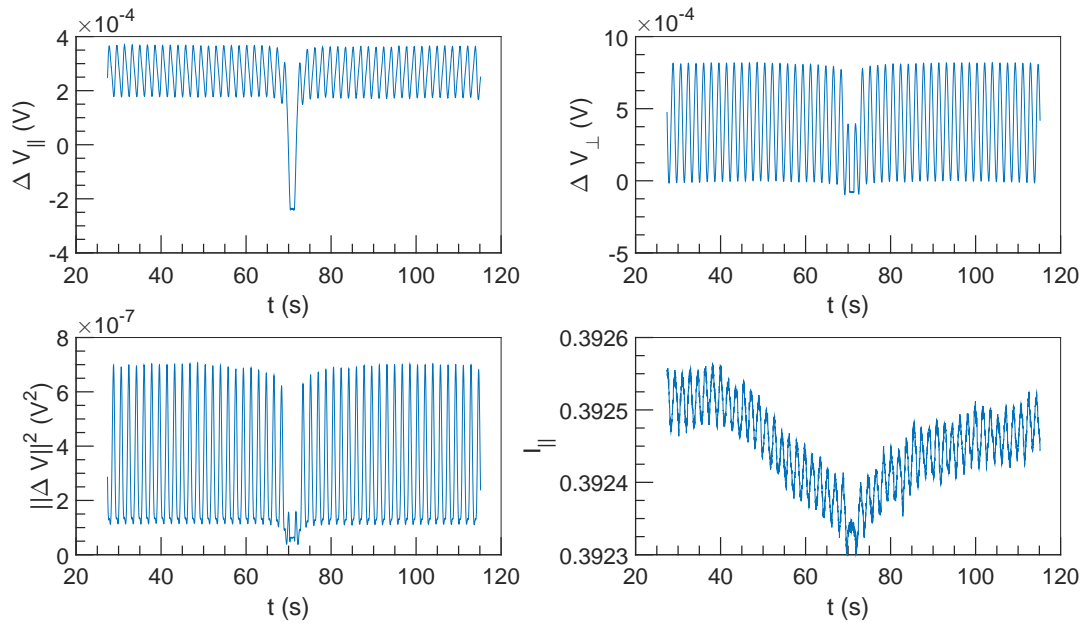


Figure 5.39:  $\Delta V$  and  $I$  vs  $t$  at  $U = 10^{-2} \text{ m s}^{-1}$ ,  $\omega = 6283 \text{ rad s}^{-1}$  and  $\alpha = 4.5\%$ .

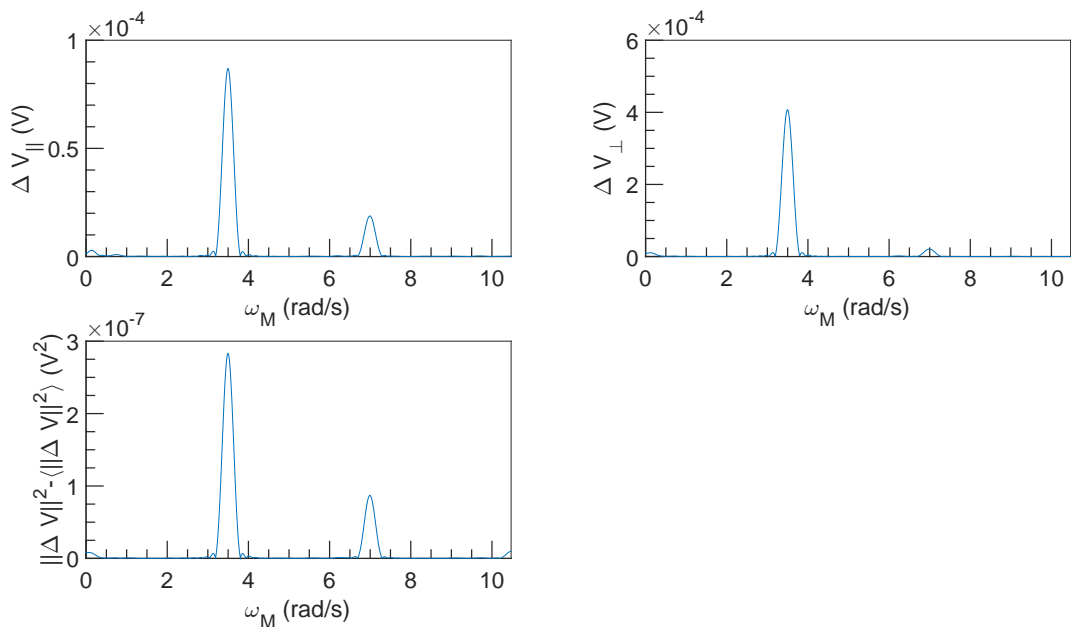


Figure 5.40: FFT spectral density of  $\Delta V$  vs  $\omega_M$  at  $U = 10^{-2} \text{ m s}^{-1}$ ,  $\omega = 6283 \text{ rad s}^{-1}$  and  $\alpha = 4.5\%$ .

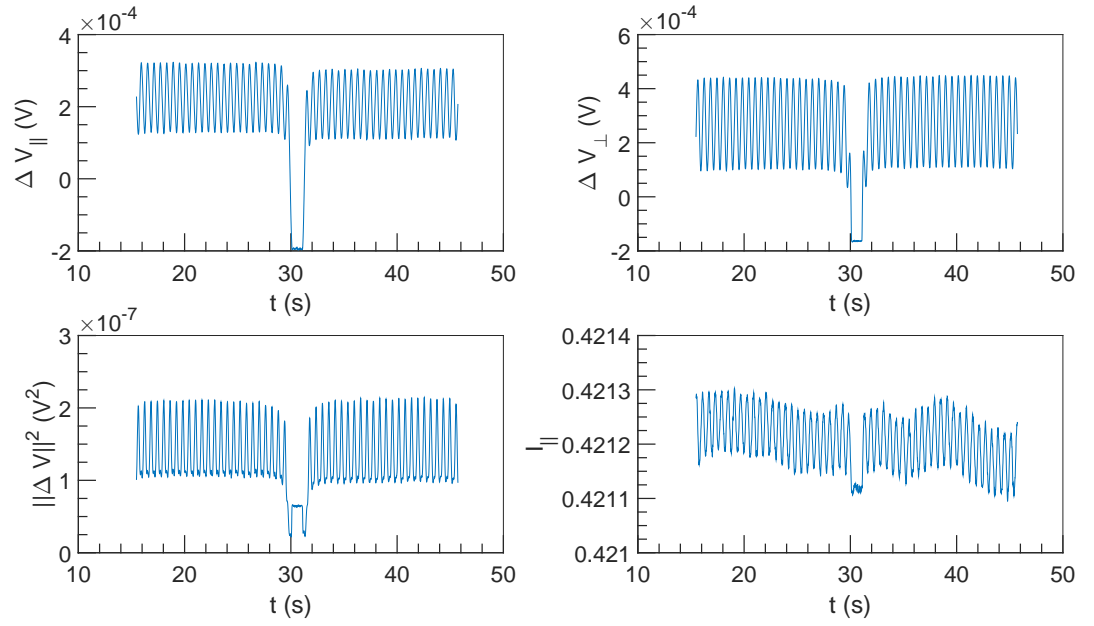


Figure 5.41:  $\Delta V$  and  $I$  vs  $t$  at  $U = 3 \times 10^{-2} \text{ m s}^{-1}$ ,  $\omega = 3142 \text{ rad s}^{-1}$  and  $\alpha = 4.5\%$ .

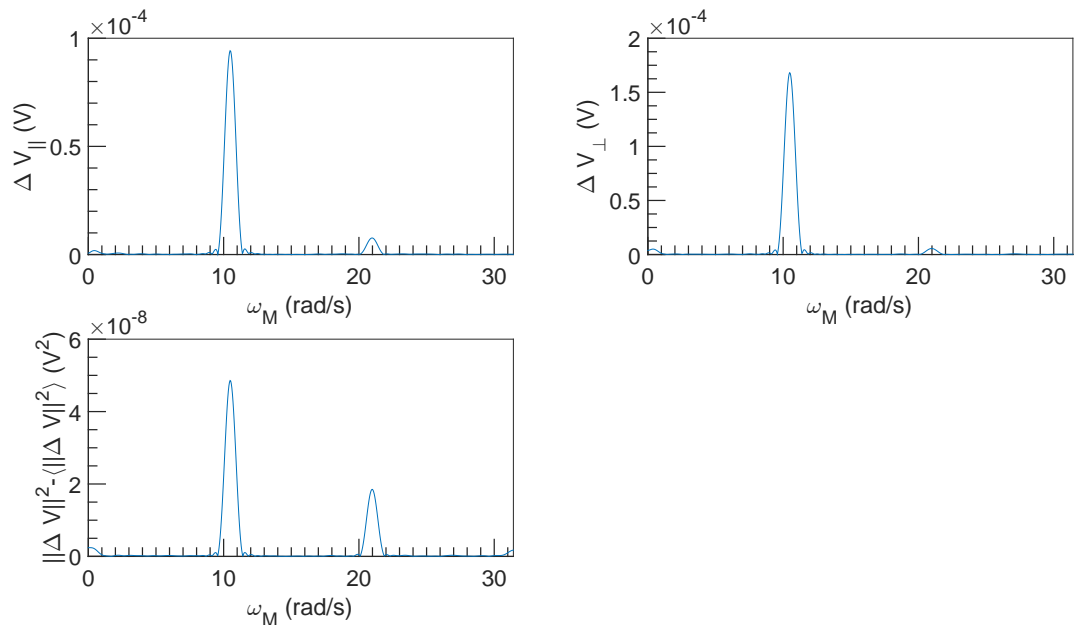


Figure 5.42: FFT spectral density of  $\Delta V$  vs  $\omega_M$  at  $U = 3 \times 10^{-2} \text{ m s}^{-1}$ ,  $\omega = 3142 \text{ rad s}^{-1}$  and  $\alpha = 4.5\%$ .

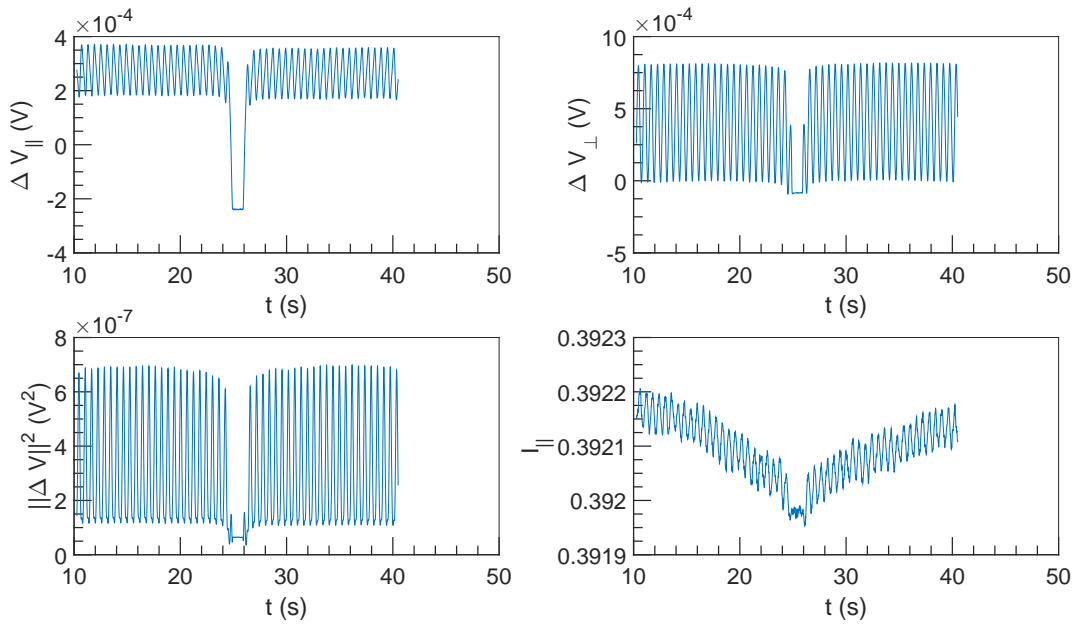


Figure 5.43:  $\Delta V$  and  $I$  vs  $t$  at  $U = 3 \times 10^{-2} \text{ m s}^{-1}$ ,  $\omega = 6283 \text{ rad s}^{-1}$  and  $\alpha = 4.5\%$ .

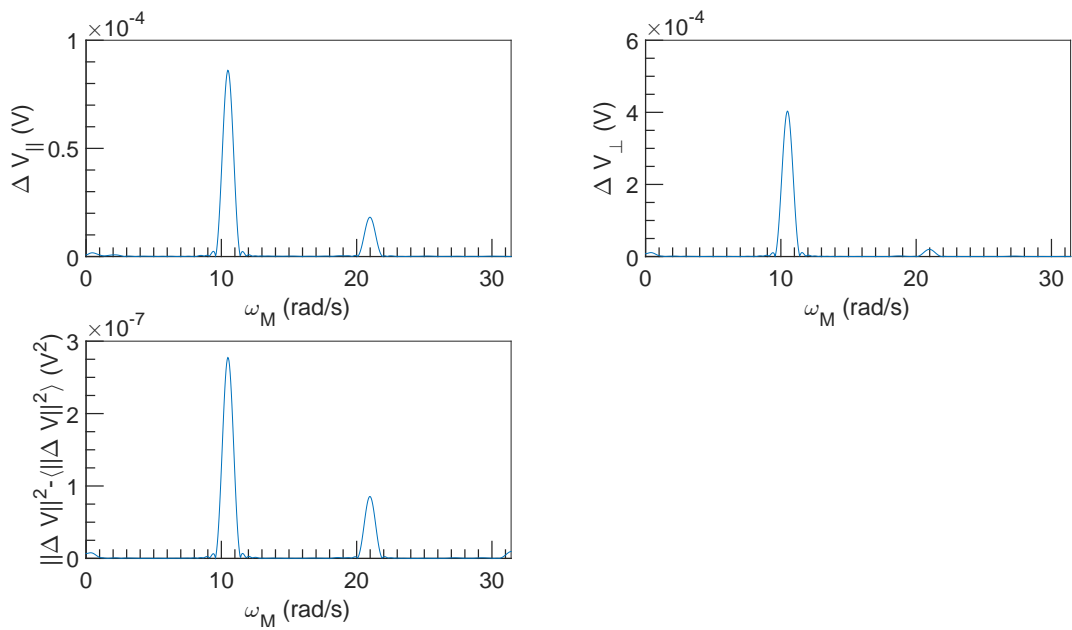


Figure 5.44: FFT spectral density of  $\Delta V$  vs  $\omega_M$  at  $U = 3 \times 10^{-2} \text{ m s}^{-1}$ ,  $\omega = 6283 \text{ rad s}^{-1}$  and  $\alpha = 4.5\%$ .

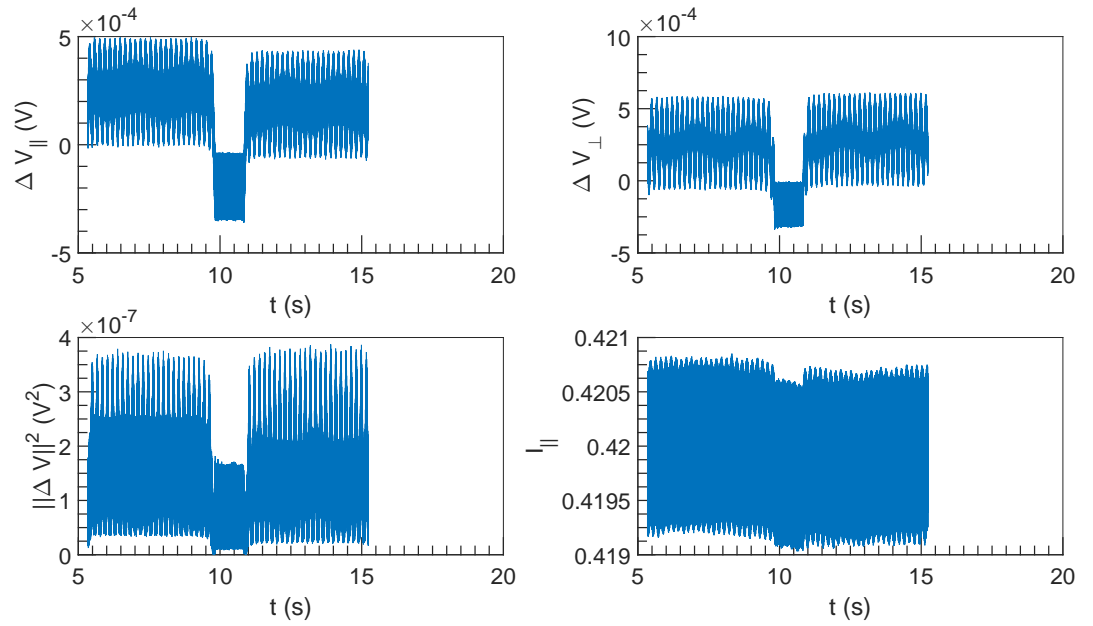


Figure 5.45:  $\Delta V$  and  $I$  vs  $t$  at  $U = 0.1 \text{ m s}^{-1}$ ,  $\omega = 3142 \text{ rad s}^{-1}$  and  $\alpha = 4.5 \%$ .

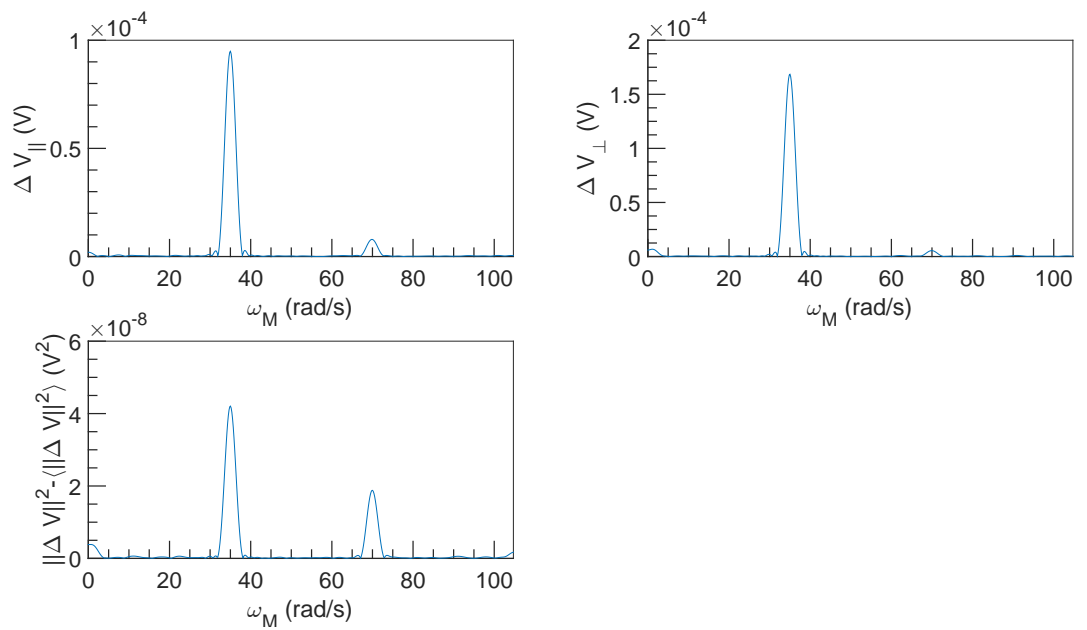


Figure 5.46: FFT spectral density of  $\Delta V$  vs  $\omega_M$  at  $U = 0.1 \text{ m s}^{-1}$ ,  $\omega = 3142 \text{ rad s}^{-1}$  and  $\alpha = 4.5 \%$ .

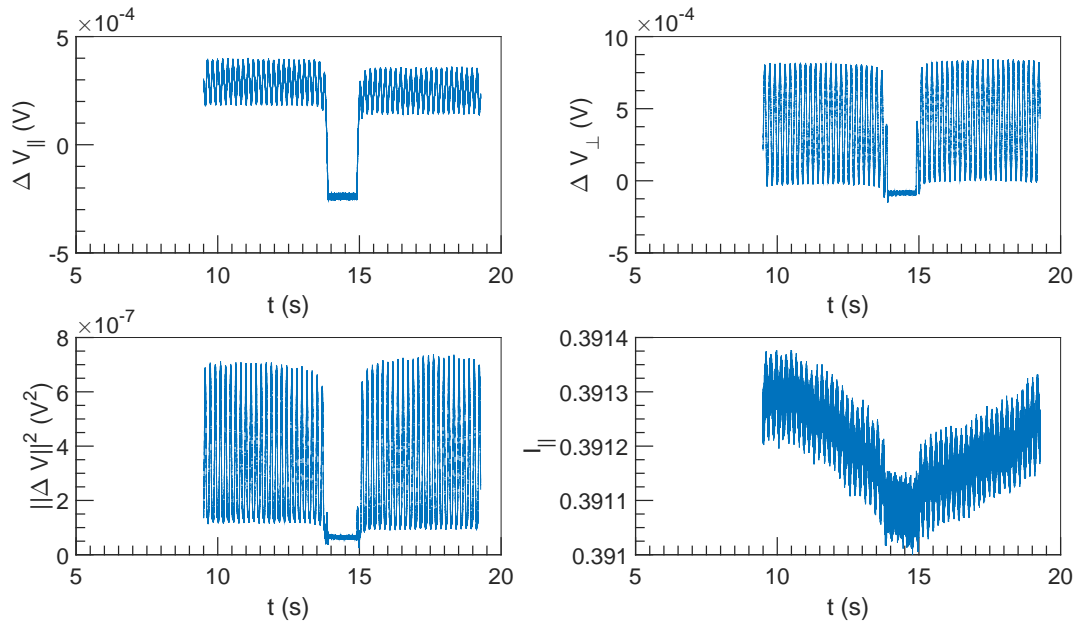


Figure 5.47:  $\Delta V$  and  $I$  vs  $t$  at  $U = 0.1 \text{ m s}^{-1}$ ,  $\omega = 6283 \text{ rad s}^{-1}$  and  $\alpha = 4.5 \%$ .

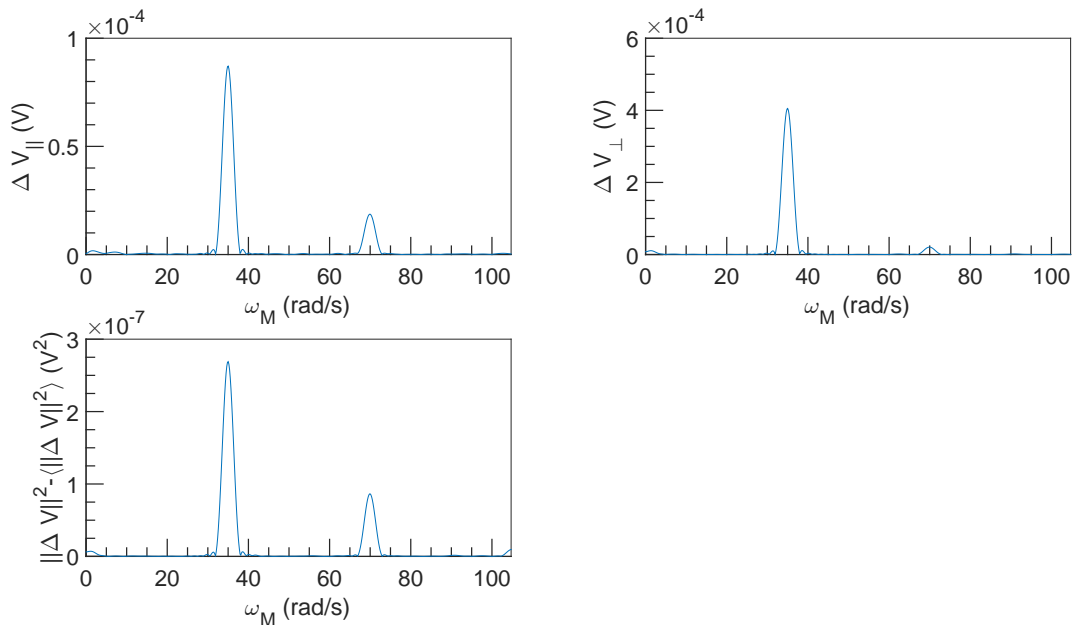


Figure 5.48: FFT spectral density of  $\Delta V$  vs  $\omega_M$  at  $U = 0.1 \text{ m s}^{-1}$ ,  $\omega = 6283 \text{ rad s}^{-1}$  and  $\alpha = 4.5 \%$ .

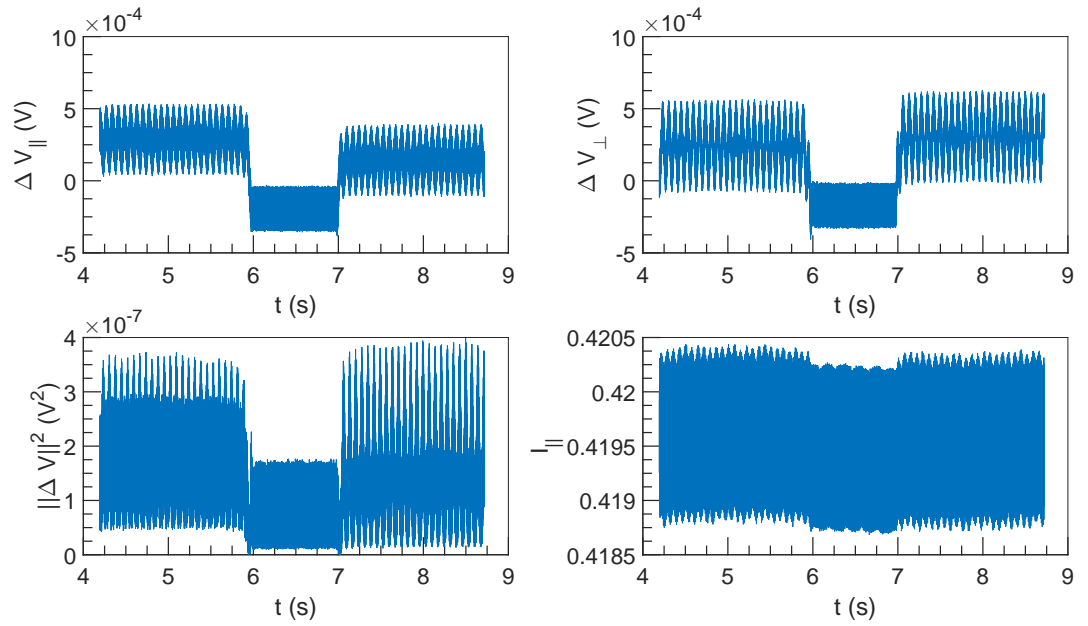


Figure 5.49:  $\Delta V$  and  $I$  vs  $t$  at  $U = 0.25 \text{ ms}^{-1}$ ,  $\omega = 3142 \text{ rad s}^{-1}$  and  $\alpha = 4.5 \%$ .

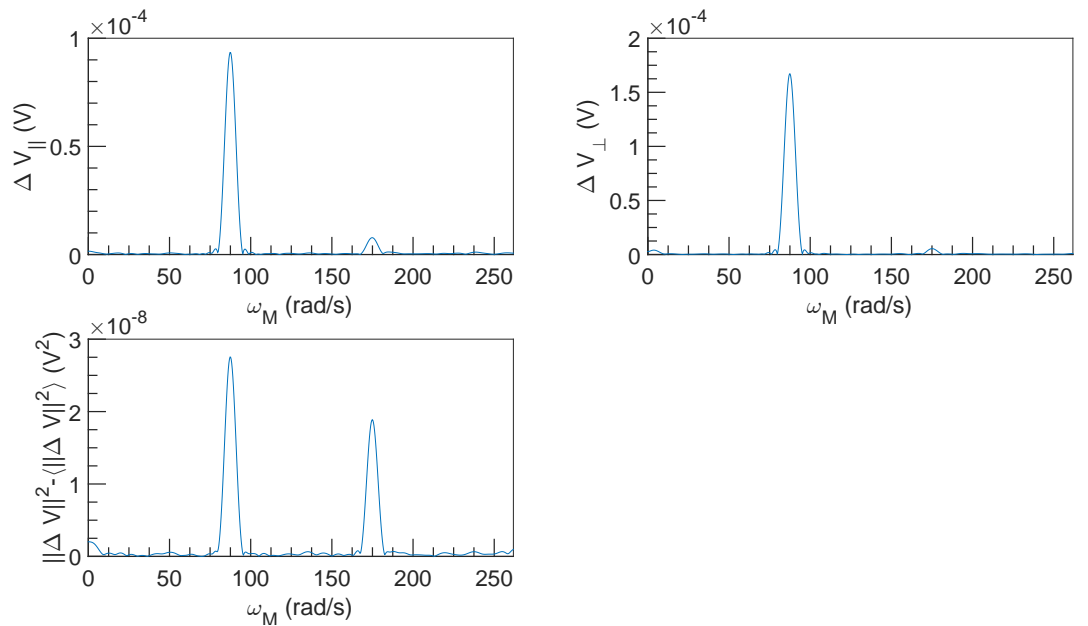


Figure 5.50: FFT spectral density of  $\Delta V$  vs  $\omega_M$  at  $U = 0.25 \text{ ms}^{-1}$ ,  $\omega = 3142 \text{ rad s}^{-1}$  and  $\alpha = 4.5 \%$ .



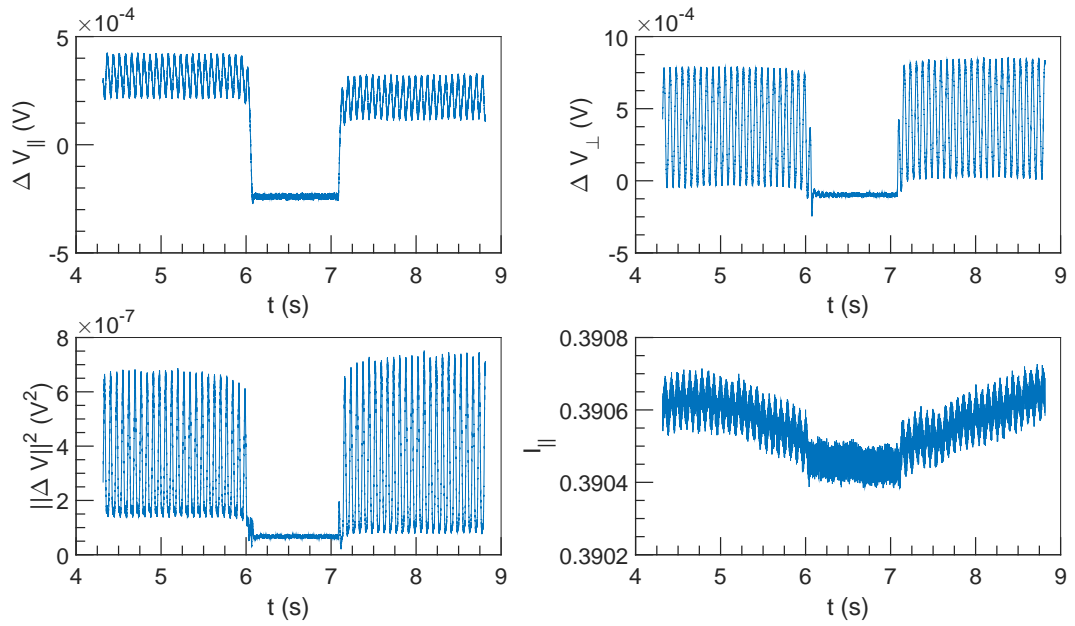


Figure 5.51:  $\Delta V$  and  $I$  vs  $t$  at  $U = 0.25 \text{ m s}^{-1}$ ,  $\omega = 6283 \text{ rad s}^{-1}$  and  $\alpha = 4.5 \%$ .

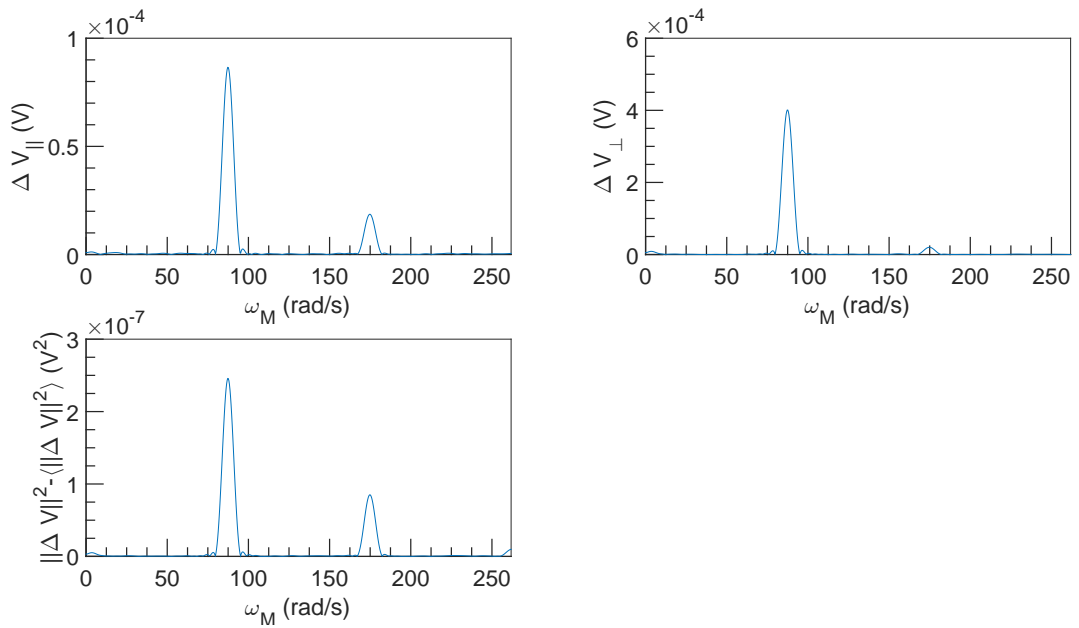


Figure 5.52: FFT spectral density of  $\Delta V$  vs  $\omega_M$  at  $U = 0.25 \text{ m s}^{-1}$ ,  $\omega = 6283 \text{ rad s}^{-1}$  and  $\alpha = 4.5 \%$ .

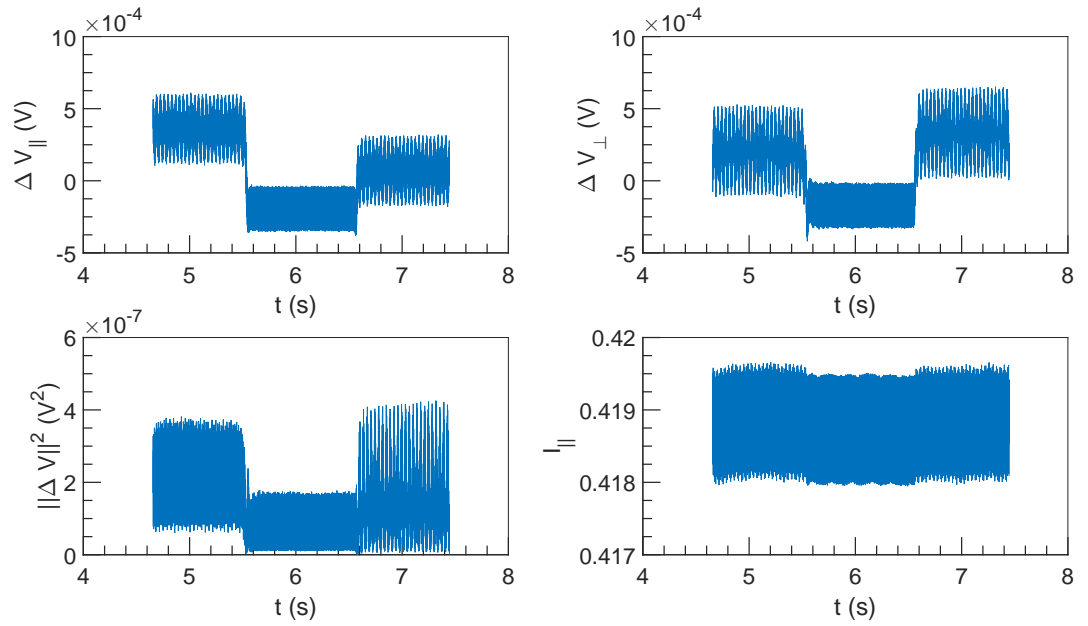


Figure 5.53:  $\Delta V$  and  $I$  vs  $t$  at  $U = 0.5 \text{ m s}^{-1}$ ,  $\omega = 3142 \text{ rad s}^{-1}$  and  $\alpha = 4.5 \%$ .

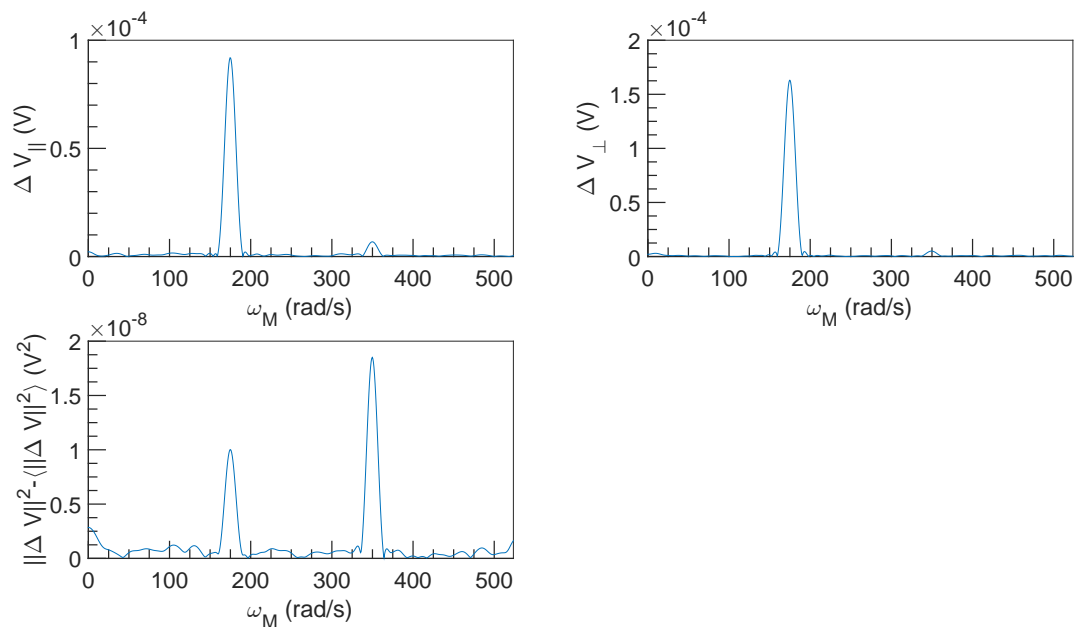


Figure 5.54: FFT spectral density of  $\Delta V$  vs  $\omega_M$  at  $U = 0.5 \text{ m s}^{-1}$ ,  $\omega = 3142 \text{ rad s}^{-1}$  and  $\alpha = 4.5 \%$ .

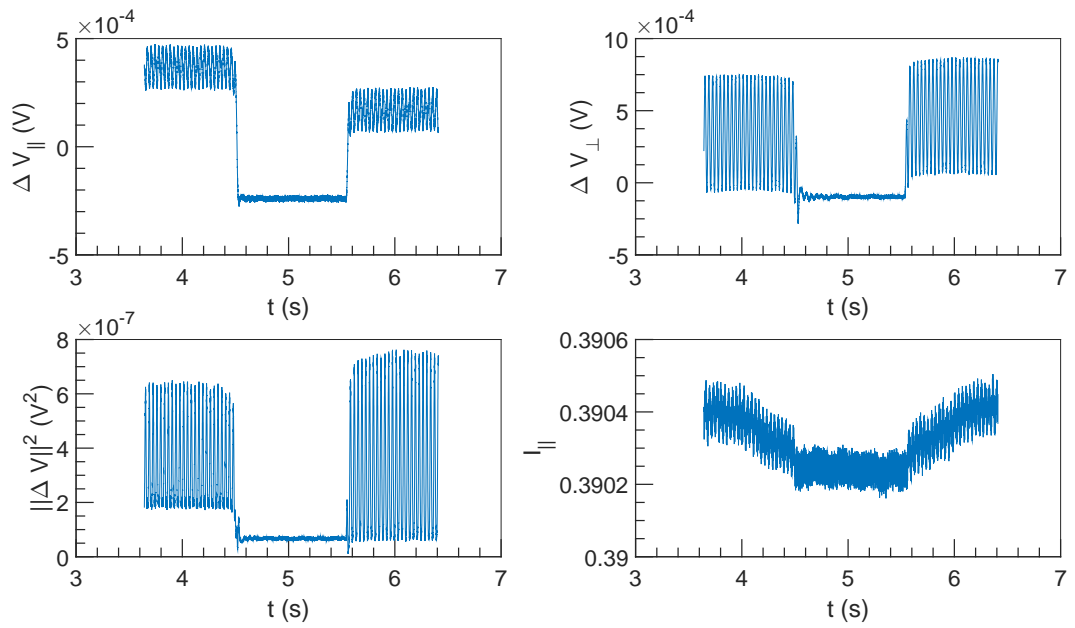


Figure 5.55:  $\Delta V$  and  $I$  vs  $t$  at  $U = 0.5 \text{ m s}^{-1}$ ,  $\omega = 6283 \text{ rad s}^{-1}$  and  $\alpha = 4.5 \%$ .

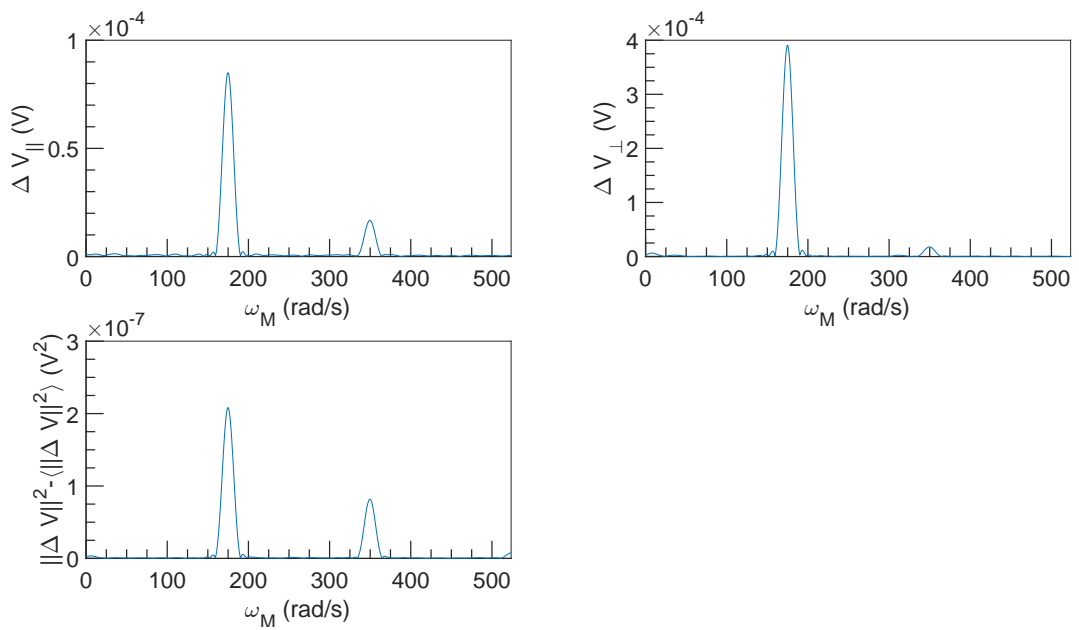


Figure 5.56: FFT spectral density of  $\Delta V$  vs  $\omega_M$  at  $U = 0.5 \text{ m s}^{-1}$ ,  $\omega = 6283 \text{ rad s}^{-1}$  and  $\alpha = 4.5 \%$ .

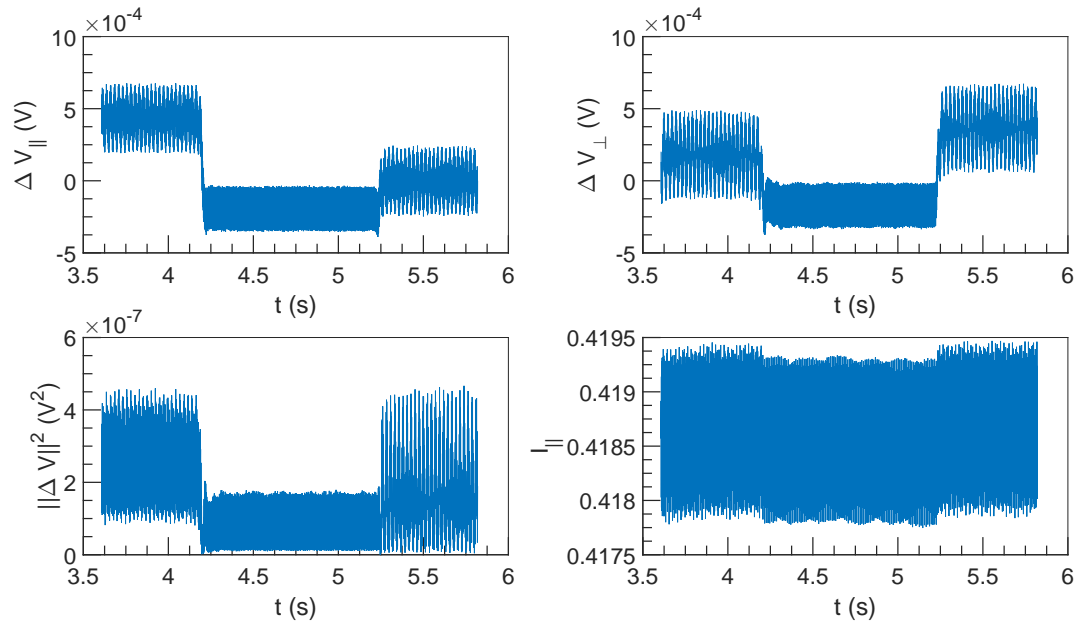


Figure 5.57:  $\Delta V$  and  $I$  vs  $t$  at  $U = 0.75 \text{ ms}^{-1}$ ,  $\omega = 3142 \text{ rad s}^{-1}$  and  $\alpha = 4.5 \%$ .

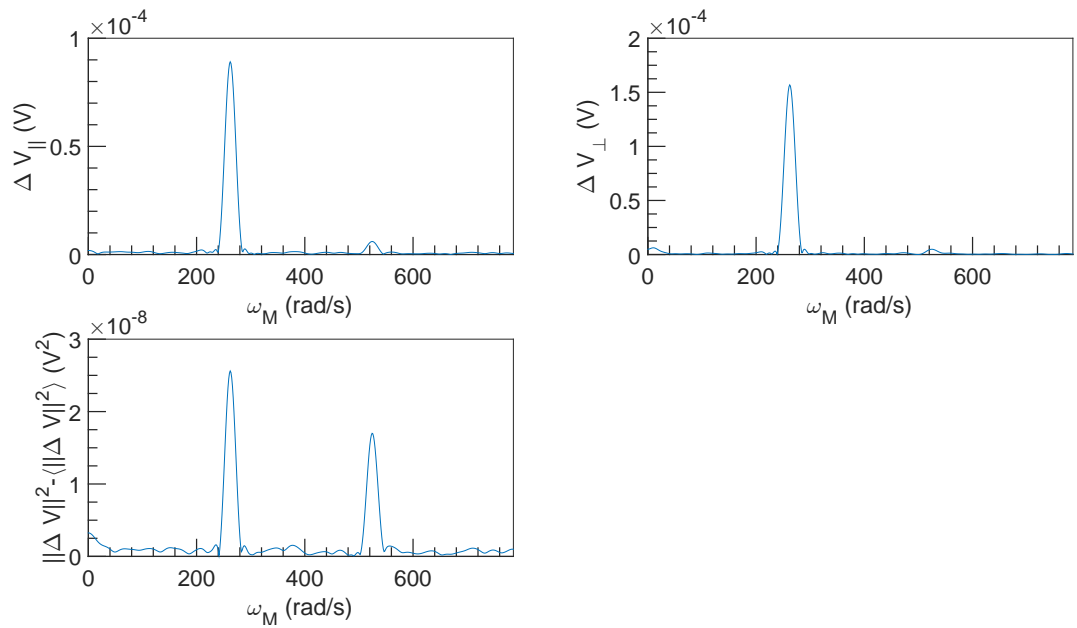


Figure 5.58: FFT spectral density of  $\Delta V$  vs  $\omega_M$  at  $U = 0.75 \text{ ms}^{-1}$ ,  $\omega = 3142 \text{ rad s}^{-1}$  and  $\alpha = 4.5 \%$ .

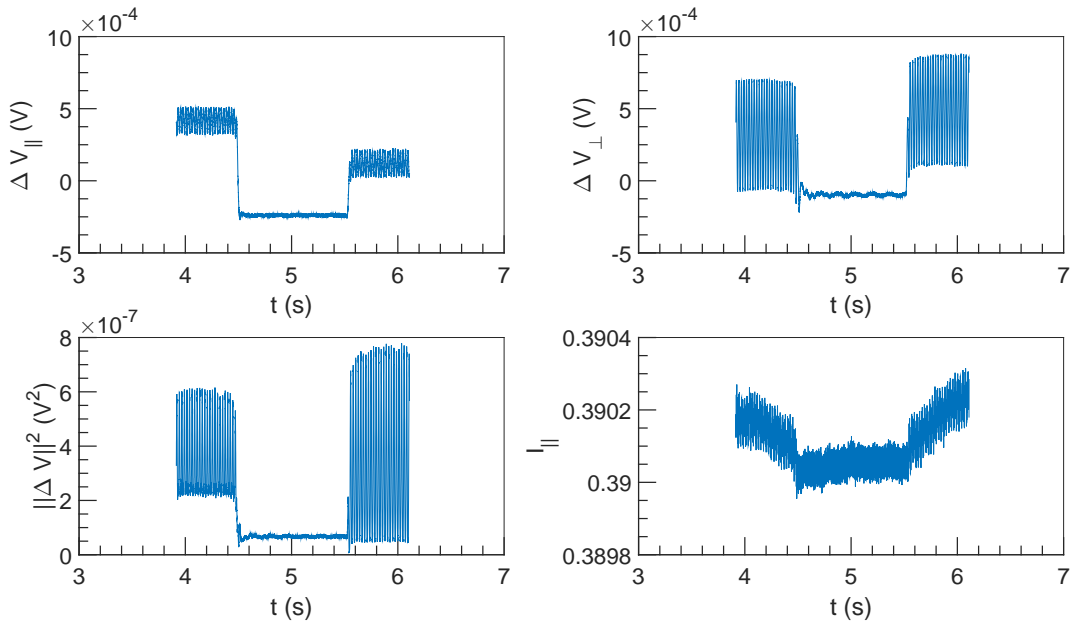


Figure 5.59:  $\Delta V$  and  $I$  vs  $t$  at  $U = 0.75 \text{ m s}^{-1}$ ,  $\omega = 6283 \text{ rad s}^{-1}$  and  $\alpha = 4.5 \%$ .

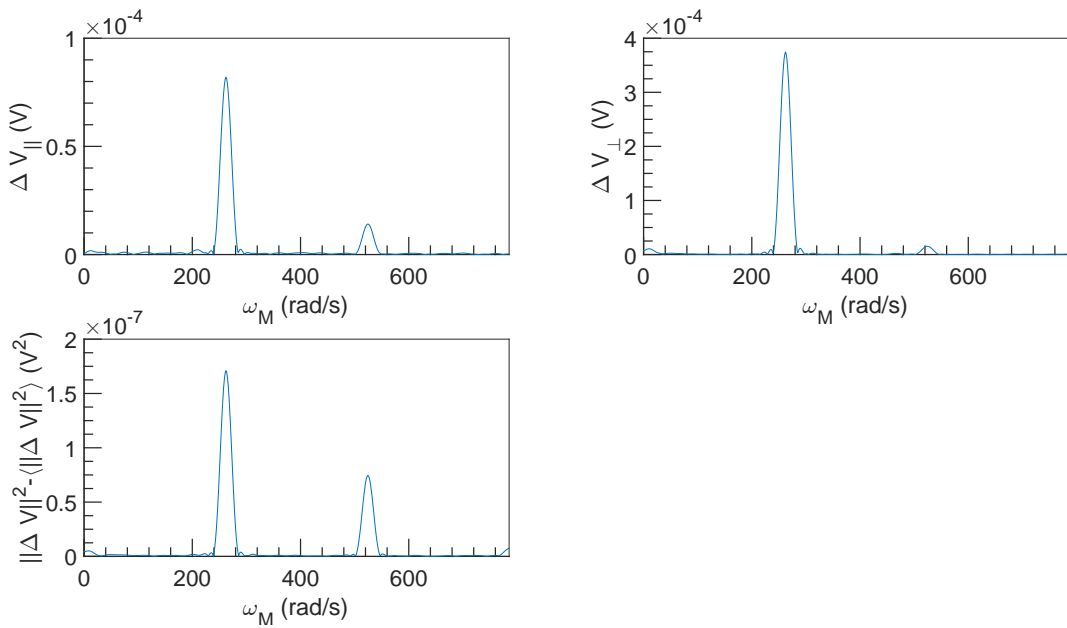


Figure 5.60: FFT spectral density of  $\Delta V$  vs  $\omega_M$  at  $U = 0.75 \text{ m s}^{-1}$ ,  $\omega = 6283 \text{ rad s}^{-1}$  and  $\alpha = 4.5 \%$ .

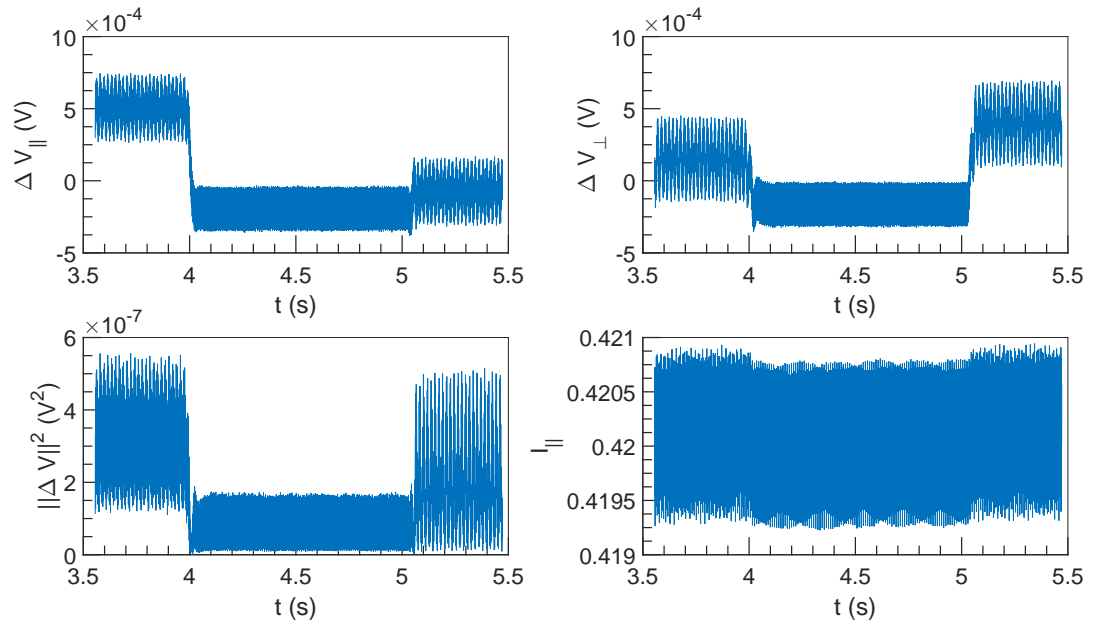


Figure 5.61:  $\Delta V$  and  $I$  vs  $t$  at  $U = 1 \text{ m s}^{-1}$ ,  $\omega = 3142 \text{ rad s}^{-1}$  and  $\alpha = 4.5\%$ .

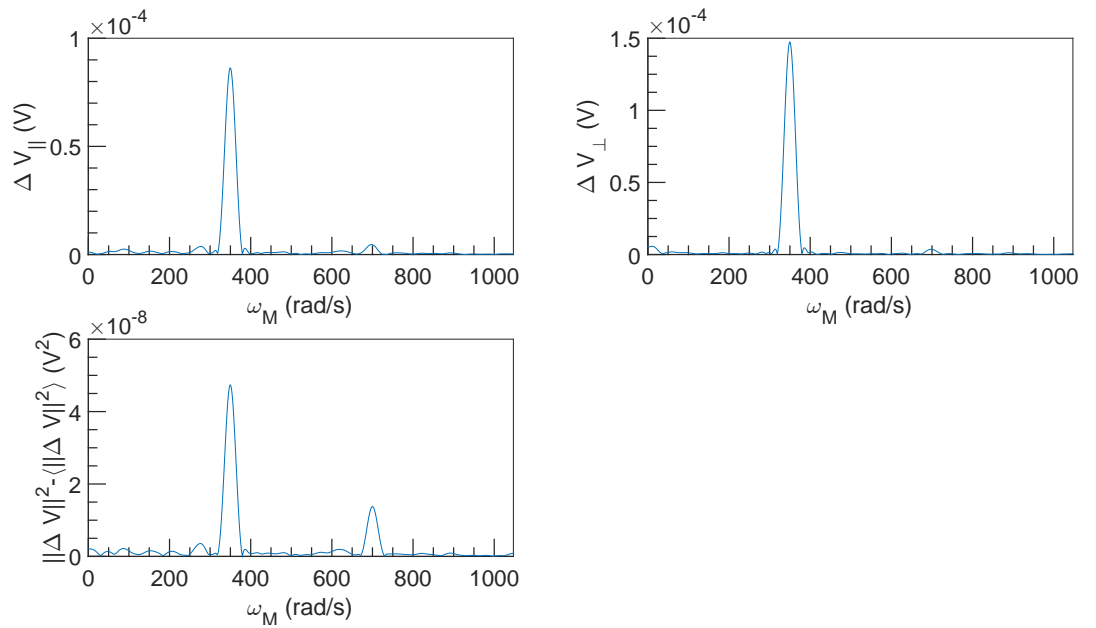


Figure 5.62: FFT spectral density of  $\Delta V$  vs  $\omega_M$  at  $U = 1 \text{ m s}^{-1}$ ,  $\omega = 3142 \text{ rad s}^{-1}$  and  $\alpha = 4.5\%$ .

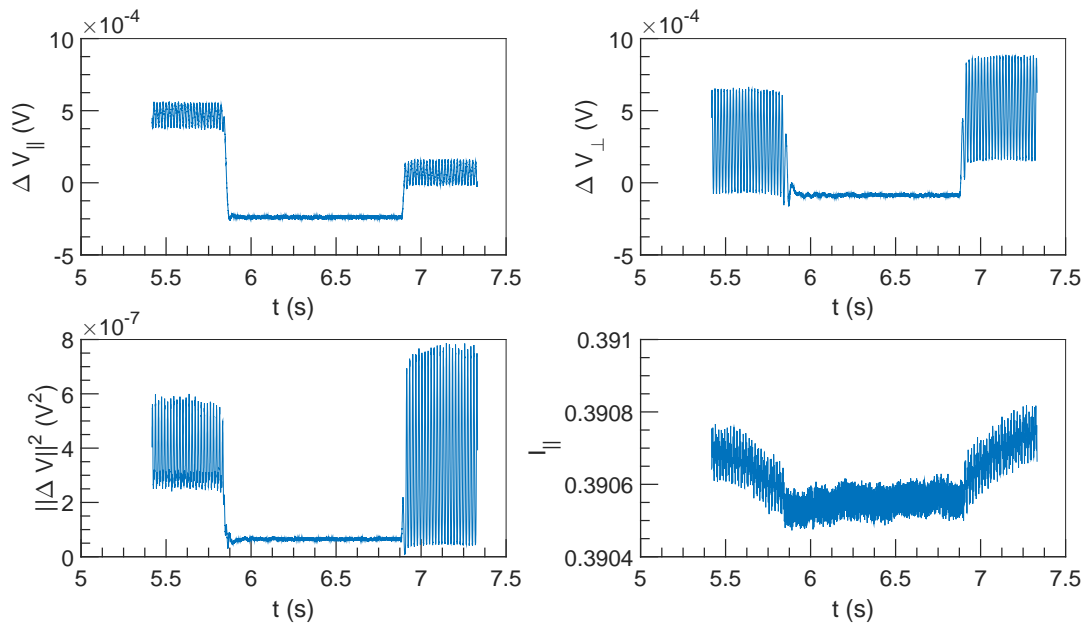


Figure 5.63:  $\Delta V$  and  $I$  vs  $t$  at  $U = 1 \text{ ms}^{-1}$ ,  $\omega = 6283 \text{ rad s}^{-1}$  and  $\alpha = 4.5\%$ .

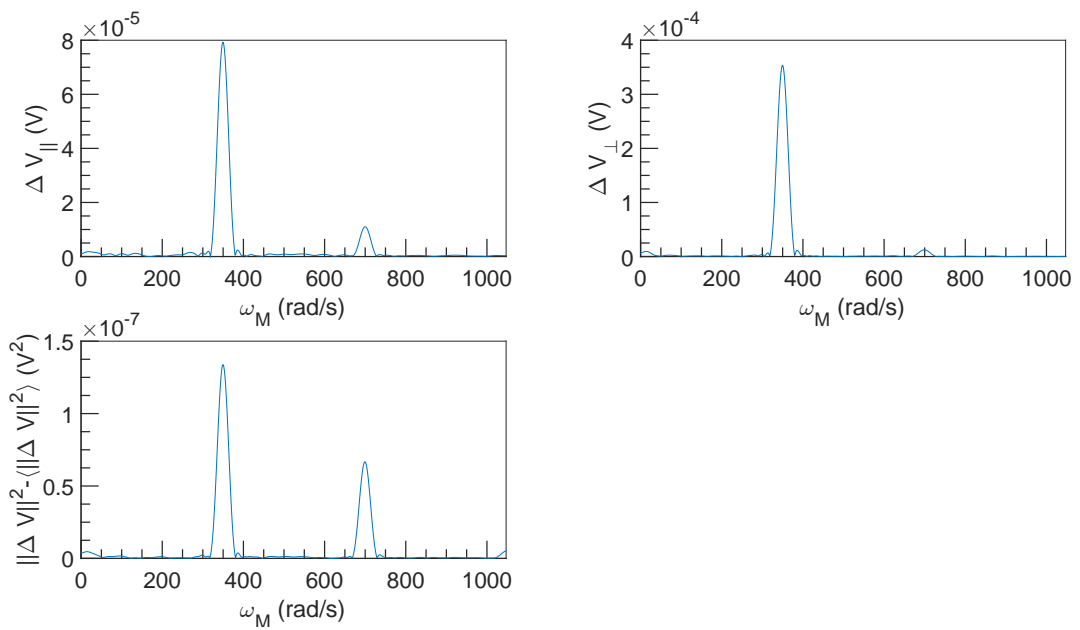


Figure 5.64: FFT spectral density of  $\Delta V$  vs  $\omega_M$  at  $U = 1 \text{ ms}^{-1}$ ,  $\omega = 6283 \text{ rad s}^{-1}$  and  $\alpha = 4.5\%$ .





## Chapter 6

**For**  $\alpha = 0.06\%$

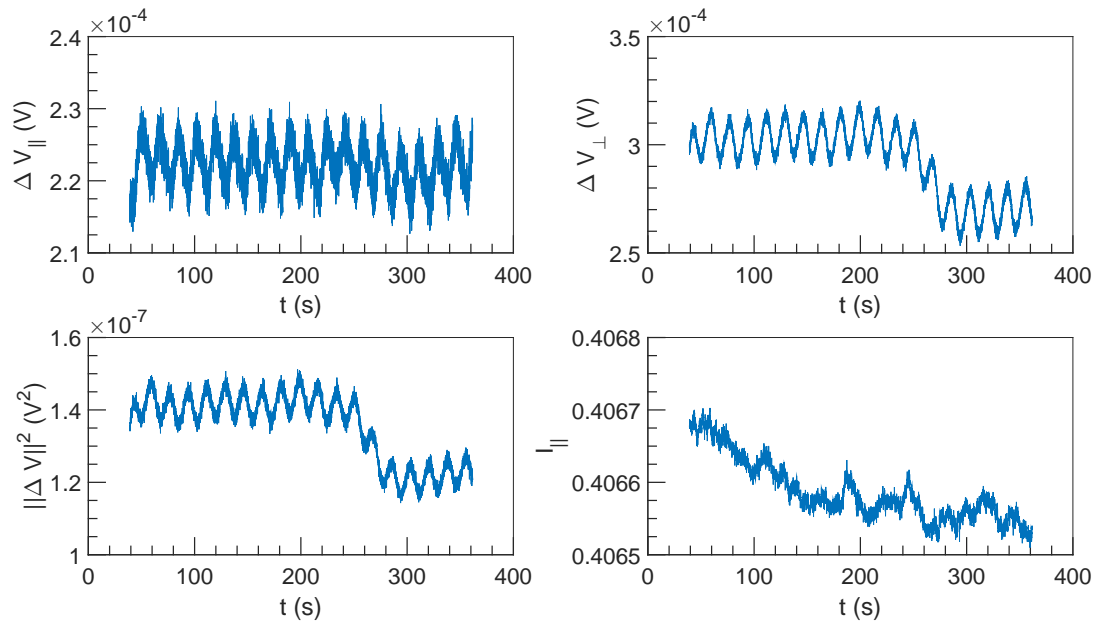


Figure 6.1:  $\Delta V$  and  $I$  vs  $t$  at  $U = 10^{-3} \text{ m s}^{-1}$ ,  $\omega = 4712 \text{ rad s}^{-1}$  and  $\alpha = 0.06 \%$ .

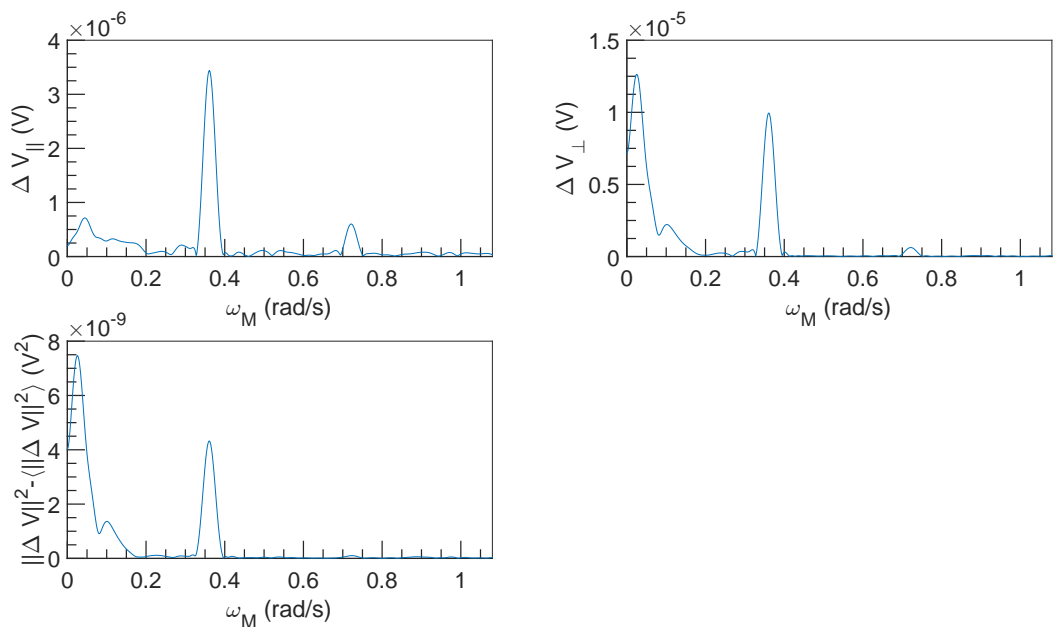


Figure 6.2: FFT spectral density of  $\Delta V$  vs  $\omega_M$  at  $U = 10^{-3} \text{ m s}^{-1}$ ,  $\omega = 4712 \text{ rad s}^{-1}$  and  $\alpha = 0.06 \%$ .

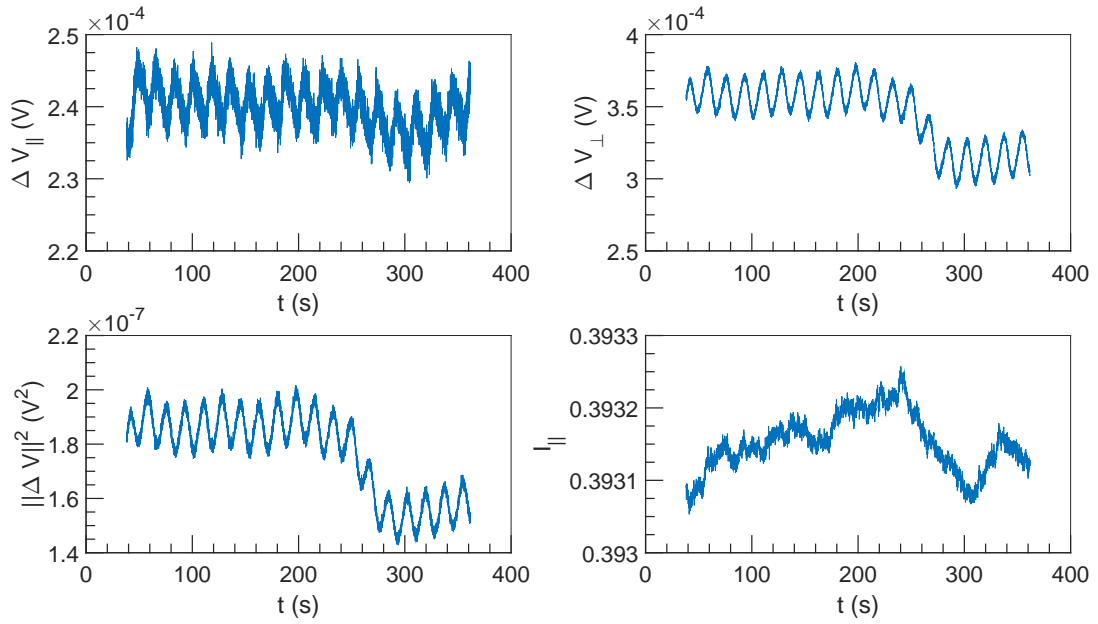


Figure 6.3:  $\Delta V$  and  $I$  vs  $t$  at  $U = 10^{-3} \text{ m s}^{-1}$ ,  $\omega = 6283 \text{ rad s}^{-1}$  and  $\alpha = 0.06 \%$ .

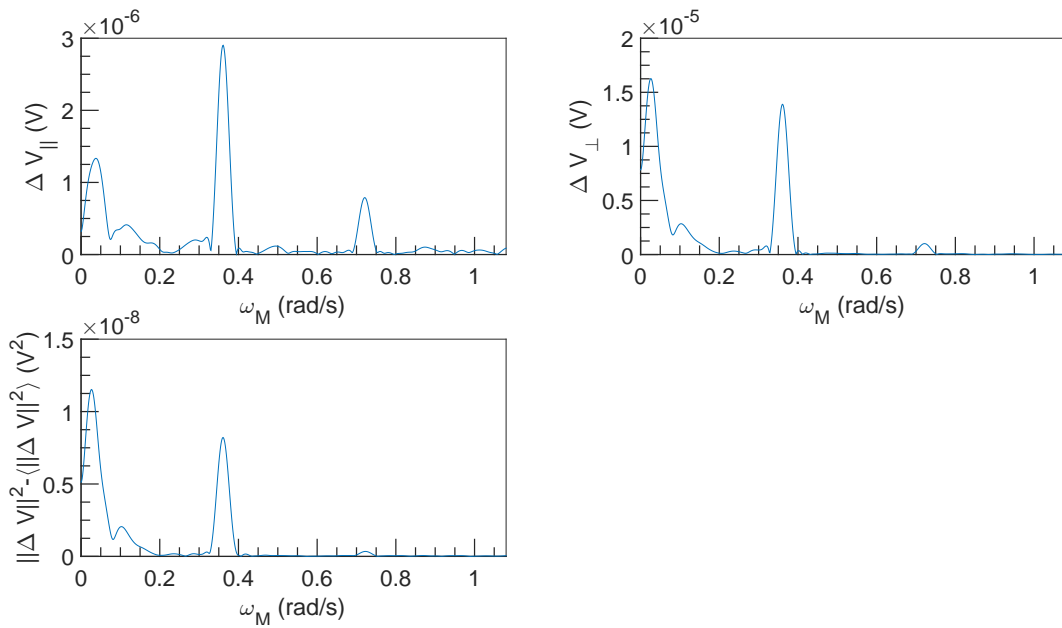


Figure 6.4: FFT spectral density of  $\Delta V$  vs  $\omega_M$  at  $U = 10^{-3} \text{ m s}^{-1}$ ,  $\omega = 6283 \text{ rad s}^{-1}$  and  $\alpha = 0.06 \%$ .

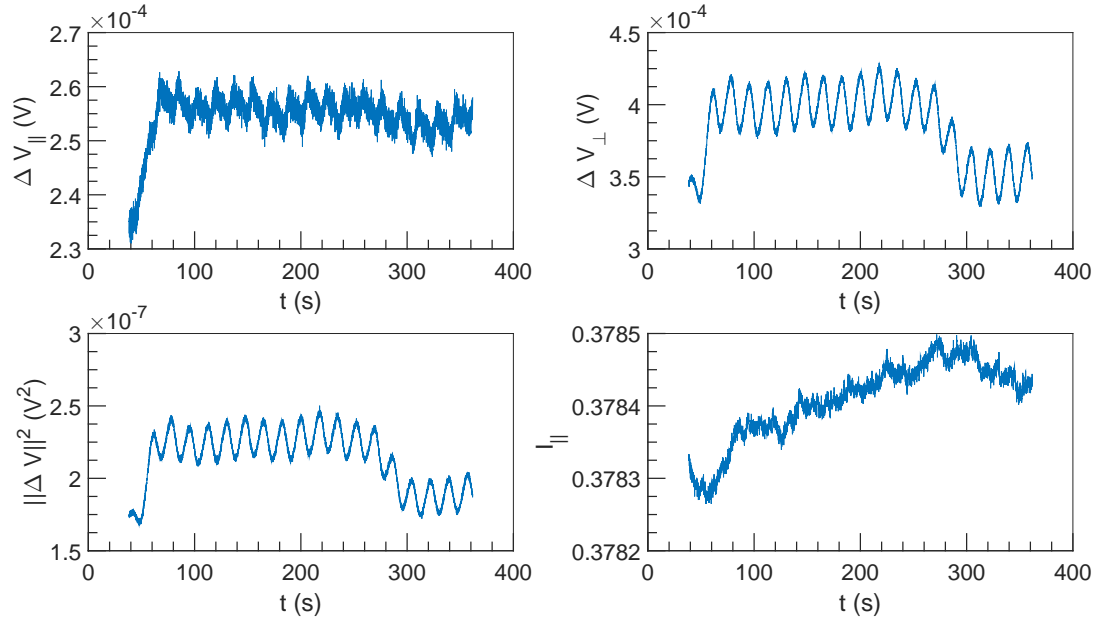


Figure 6.5:  $\Delta V$  and  $I$  vs  $t$  at  $U = 10^{-3} \text{ m s}^{-1}$ ,  $\omega = 7854 \text{ rad s}^{-1}$  and  $\alpha = 0.06 \%$ .

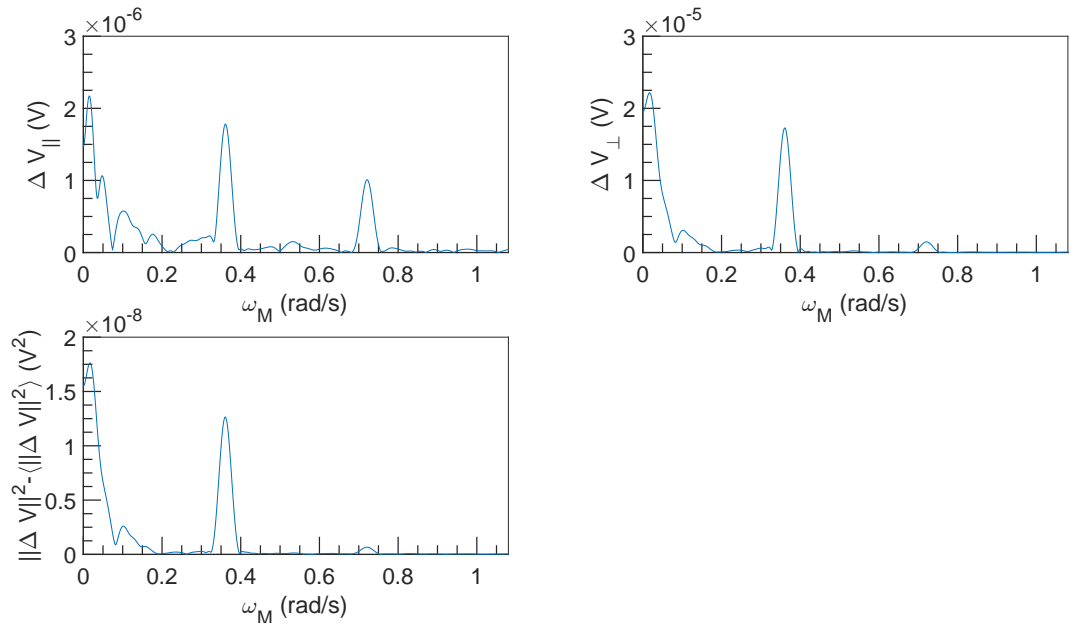


Figure 6.6: FFT spectral density of  $\Delta V$  vs  $\omega_M$  at  $U = 10^{-3} \text{ m s}^{-1}$ ,  $\omega = 7854 \text{ rad s}^{-1}$  and  $\alpha = 0.06 \%$ .

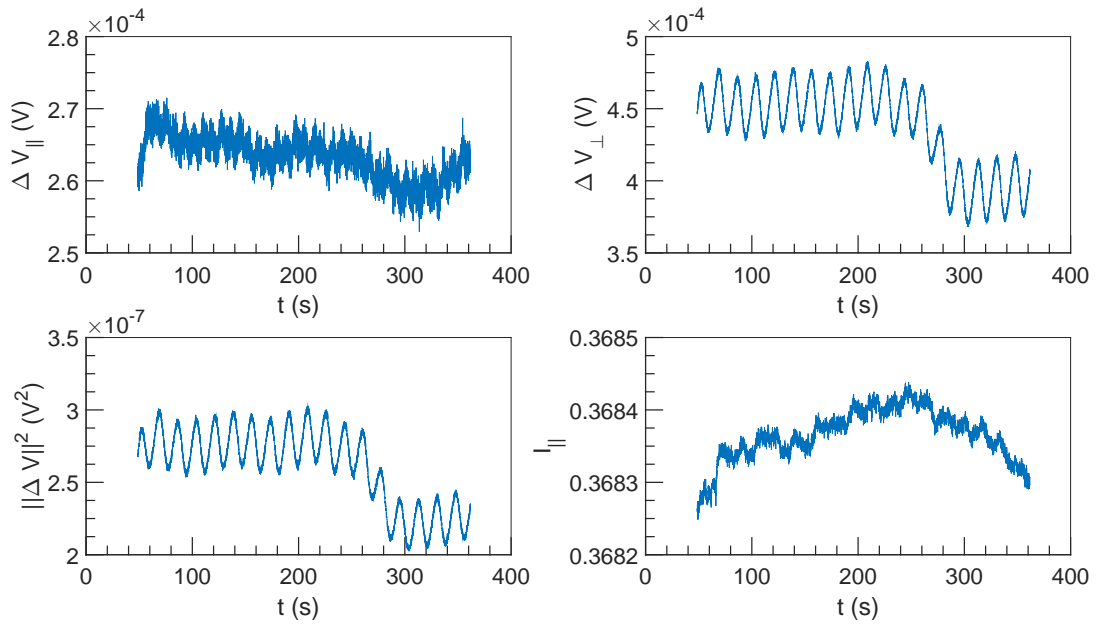


Figure 6.7:  $\Delta V$  and  $I$  vs  $t$  at  $U = 10^{-3} \text{ m s}^{-1}$ ,  $\omega = 9425 \text{ rad s}^{-1}$  and  $\alpha = 0.06 \%$ .

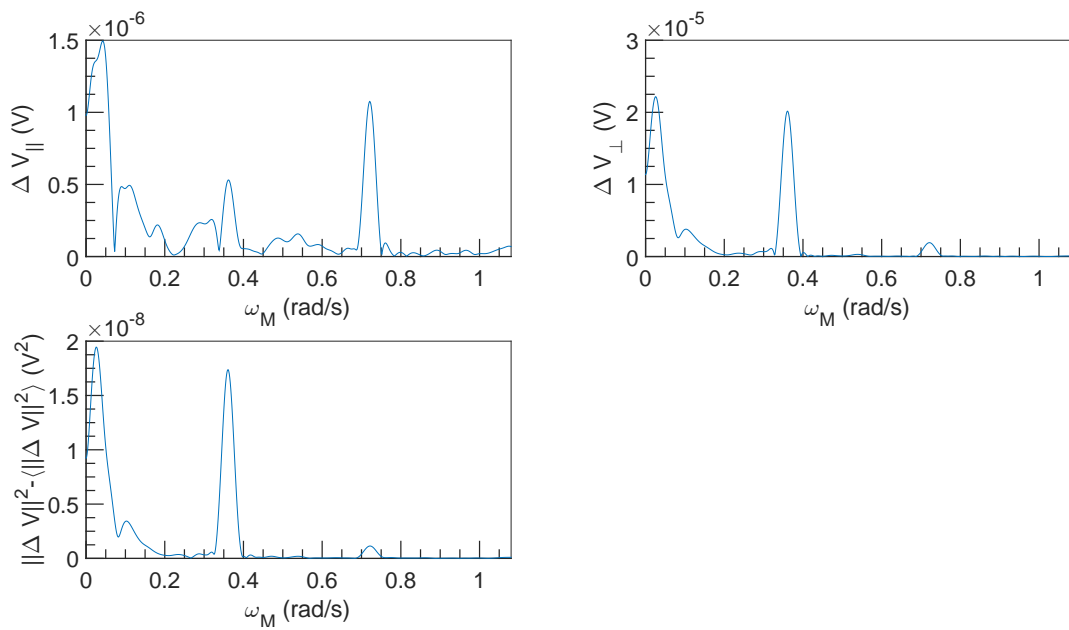


Figure 6.8: FFT spectral density of  $\Delta V$  vs  $\omega_M$  at  $U = 10^{-3} \text{ m s}^{-1}$ ,  $\omega = 9425 \text{ rad s}^{-1}$  and  $\alpha = 0.06 \%$ .

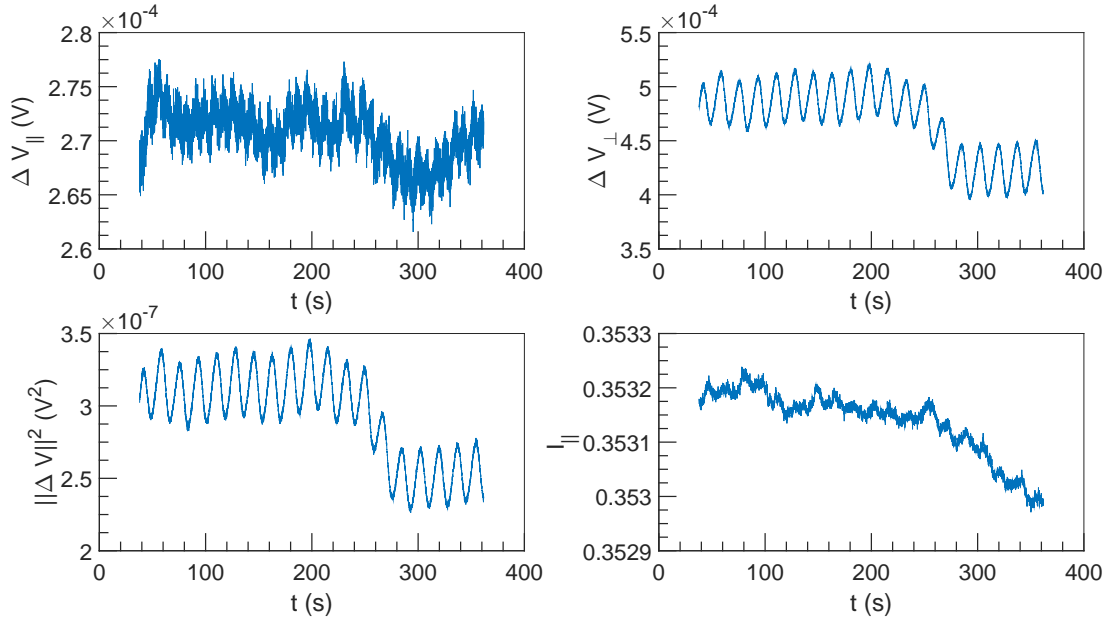


Figure 6.9:  $\Delta V$  and  $I$  vs  $t$  at  $U = 10^{-3} \text{ m s}^{-1}$ ,  $\omega = 10\,996 \text{ rad s}^{-1}$  and  $\alpha = 0.06\%$ .

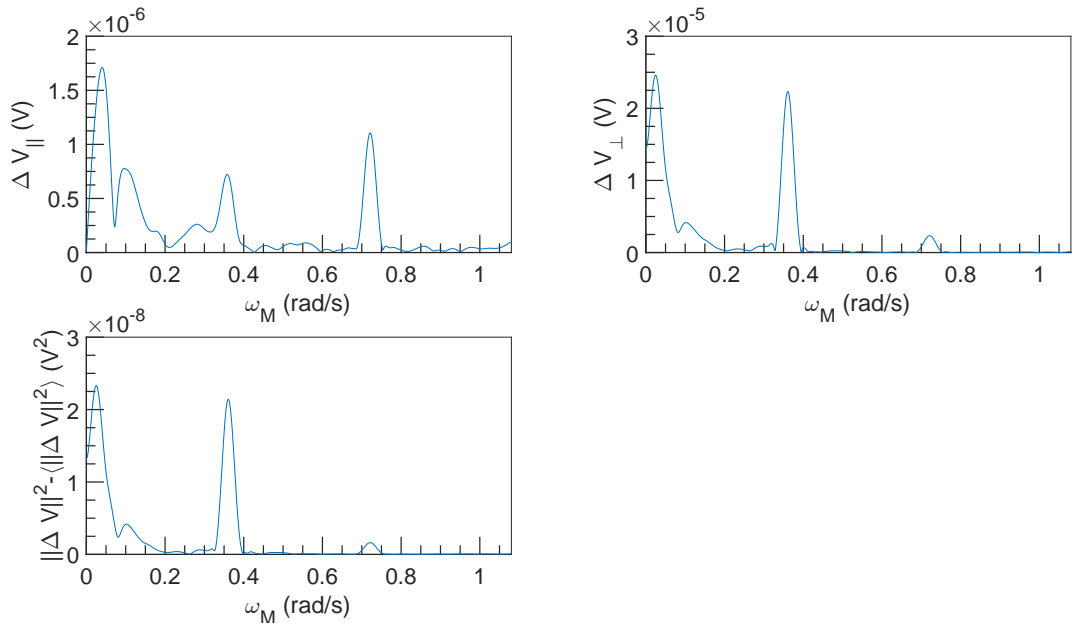


Figure 6.10: FFT spectral density of  $\Delta V$  vs  $\omega_M$  at  $U = 10^{-3} \text{ m s}^{-1}$ ,  $\omega = 10\,996 \text{ rad s}^{-1}$  and  $\alpha = 0.06\%$ .

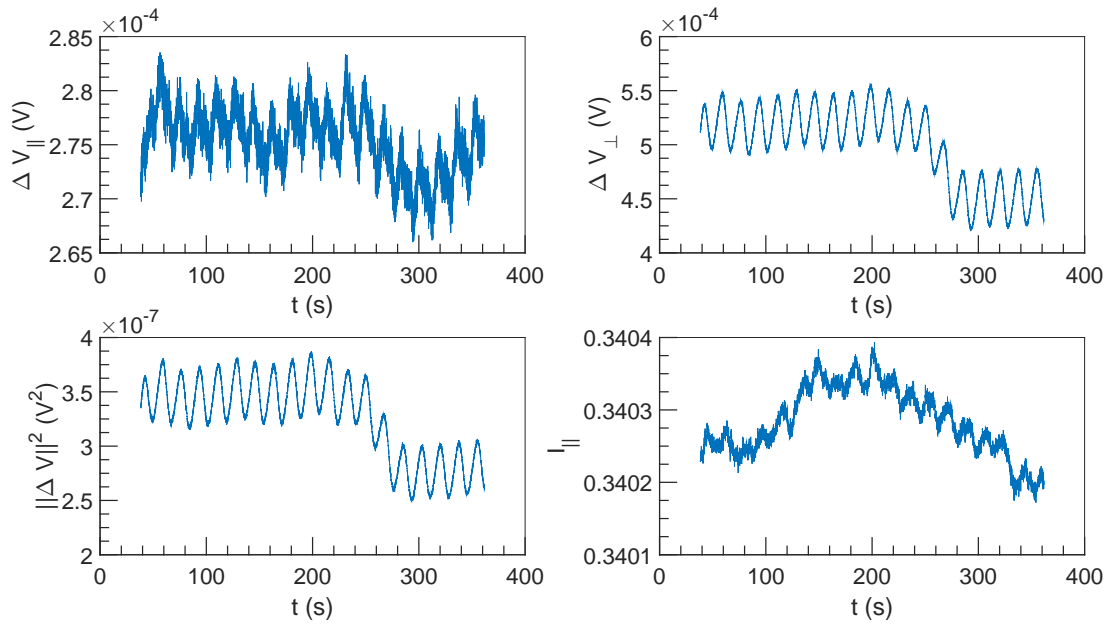


Figure 6.11:  $\Delta V$  and  $I$  vs  $t$  at  $U = 10^{-3} \text{ m s}^{-1}$ ,  $\omega = 12566 \text{ rad s}^{-1}$  and  $\alpha = 0.06\%$ .

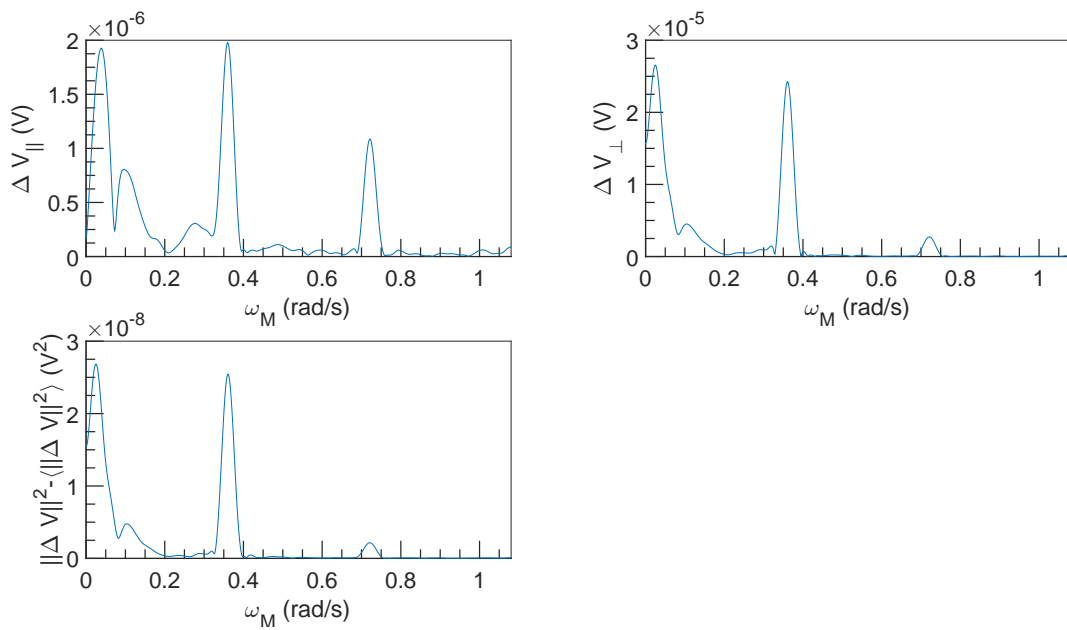


Figure 6.12: FFT spectral density of  $\Delta V$  vs  $\omega_M$  at  $U = 10^{-3} \text{ m s}^{-1}$ ,  $\omega = 12566 \text{ rad s}^{-1}$  and  $\alpha = 0.06\%$ .

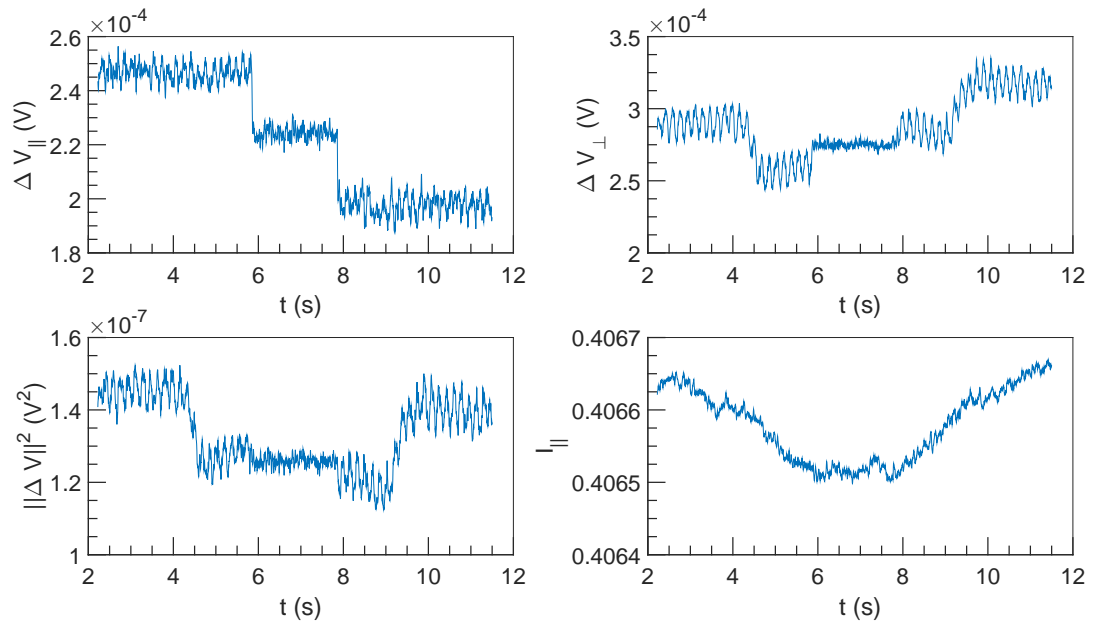


Figure 6.13:  $\Delta V$  and  $I$  vs  $t$  at  $U = 0.1 \text{ m s}^{-1}$ ,  $\omega = 4712 \text{ rad s}^{-1}$  and  $\alpha = 0.06 \%$ .

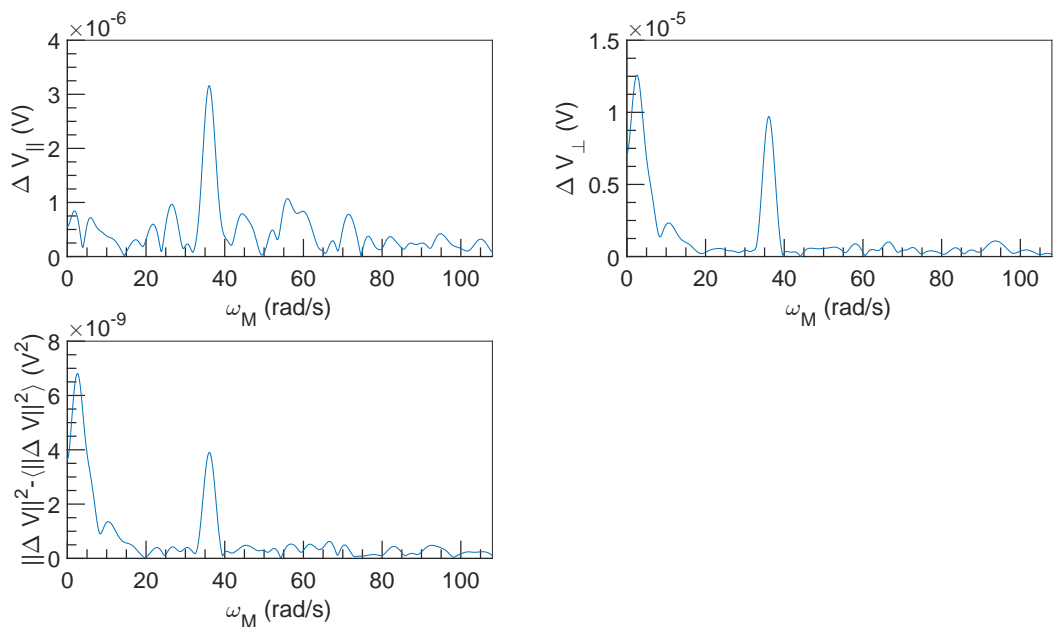


Figure 6.14: FFT spectral density of  $\Delta V$  vs  $\omega_M$  at  $U = 0.1 \text{ m s}^{-1}$ ,  $\omega = 4712 \text{ rad s}^{-1}$  and  $\alpha = 0.06 \%$ .



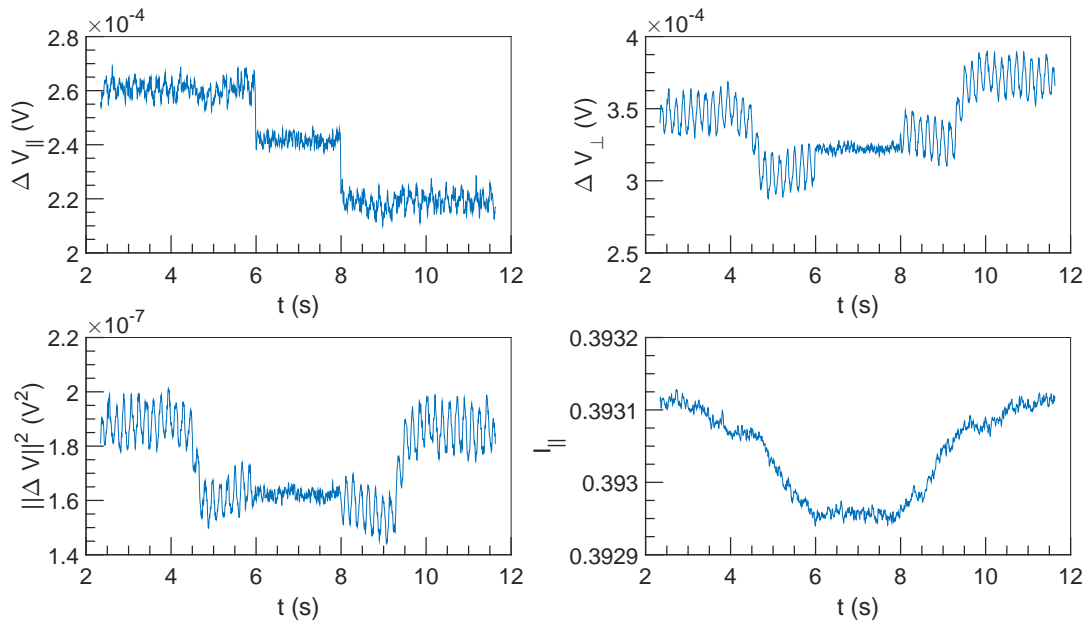


Figure 6.15:  $\Delta V$  and  $I$  vs  $t$  at  $U = 0.1 \text{ m s}^{-1}$ ,  $\omega = 6283 \text{ rad s}^{-1}$  and  $\alpha = 0.06 \%$ .

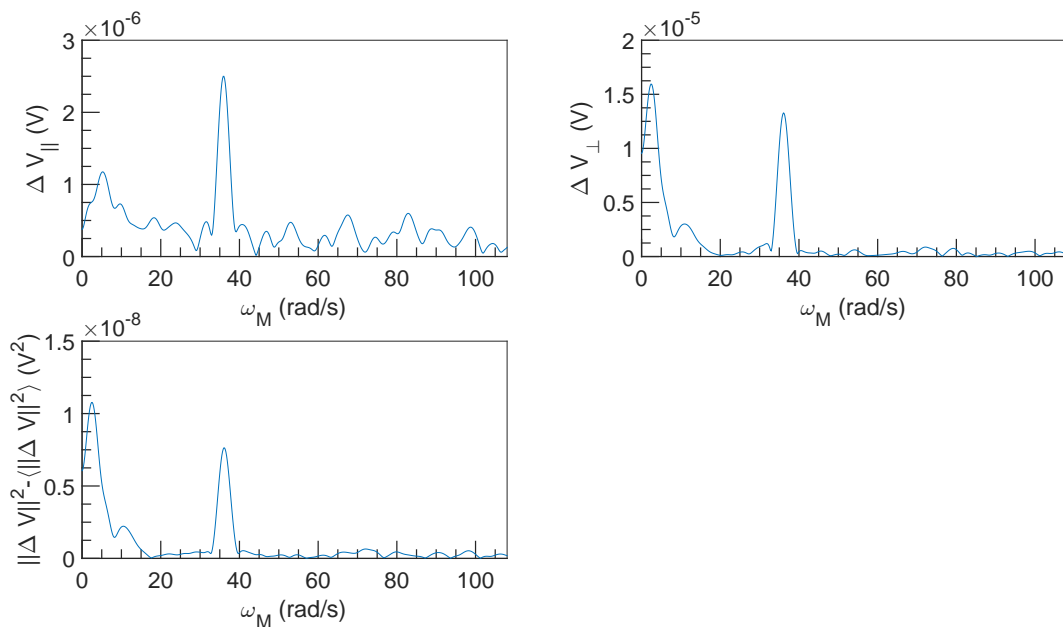


Figure 6.16: FFT spectral density of  $\Delta V$  vs  $\omega_M$  at  $U = 0.1 \text{ m s}^{-1}$ ,  $\omega = 6283 \text{ rad s}^{-1}$  and  $\alpha = 0.06 \%$ .

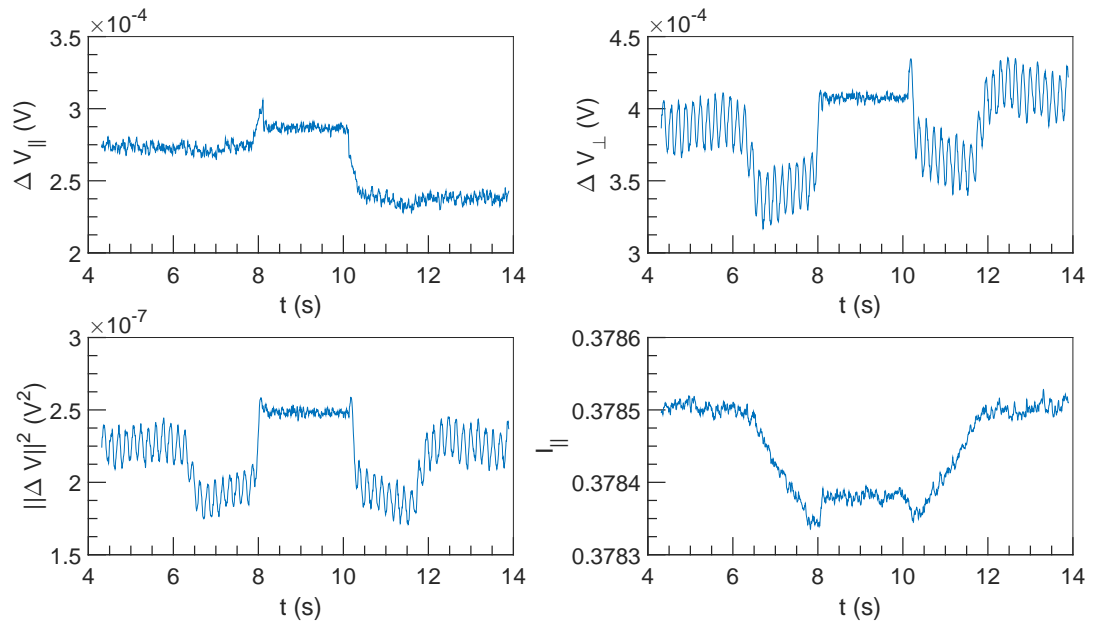


Figure 6.17:  $\Delta V$  and  $I$  vs  $t$  at  $U = 0.1 \text{ m s}^{-1}$ ,  $\omega = 7854 \text{ rad s}^{-1}$  and  $\alpha = 0.06 \%$ .

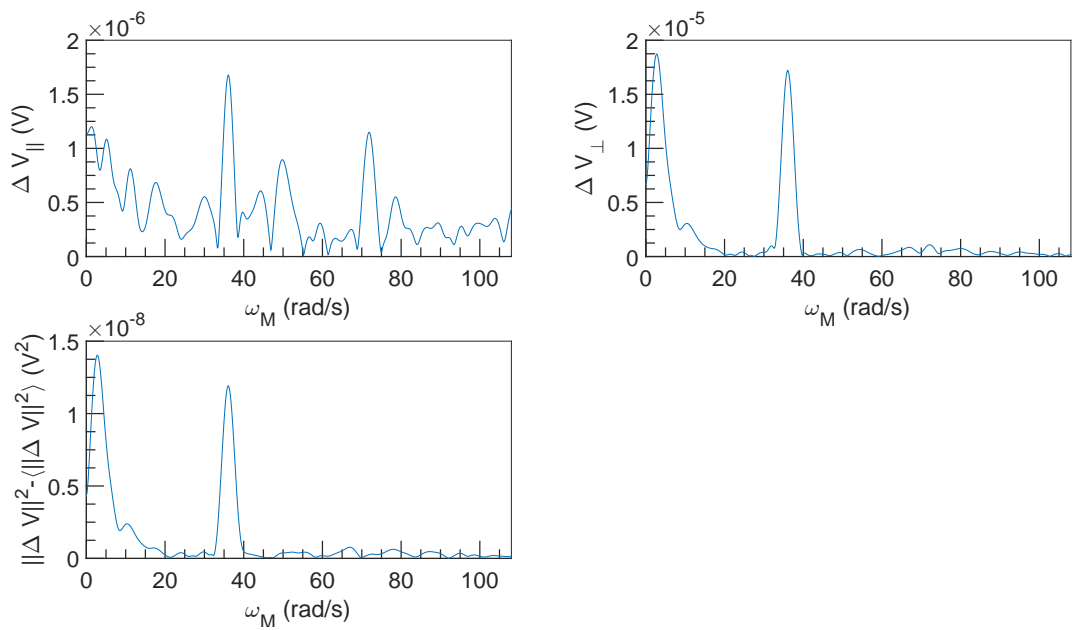


Figure 6.18: FFT spectral density of  $\Delta V$  vs  $\omega_M$  at  $U = 0.1 \text{ m s}^{-1}$ ,  $\omega = 7854 \text{ rad s}^{-1}$  and  $\alpha = 0.06 \%$ .

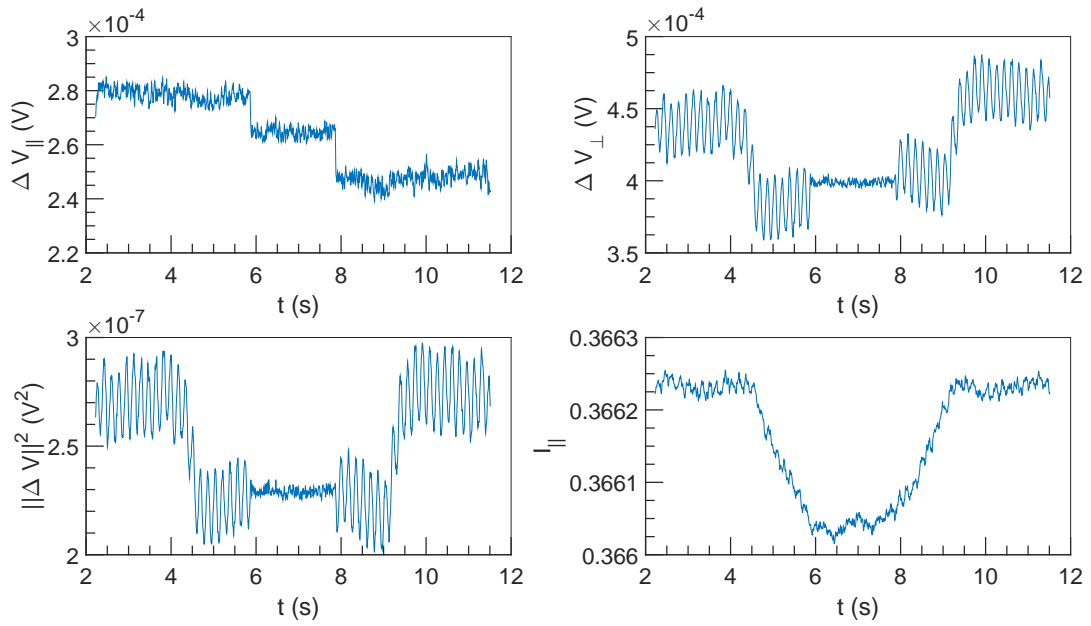


Figure 6.19:  $\Delta V$  and  $I$  vs  $t$  at  $U = 0.1 \text{ m s}^{-1}$ ,  $\omega = 9425 \text{ rad s}^{-1}$  and  $\alpha = 0.06 \%$ .

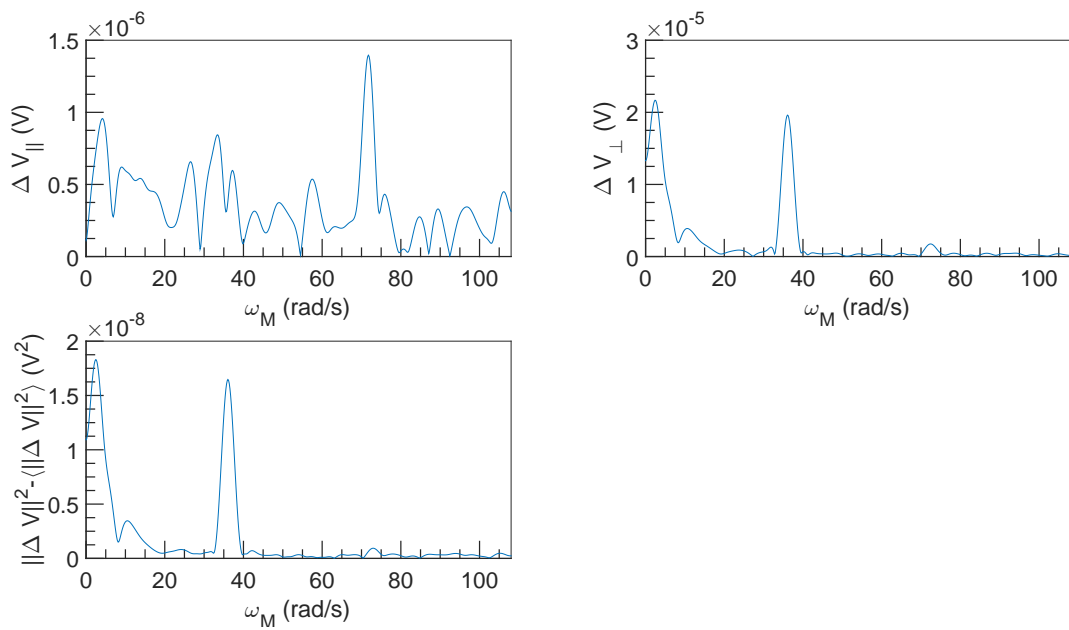


Figure 6.20: FFT spectral density of  $\Delta V$  vs  $\omega_M$  at  $U = 0.1 \text{ m s}^{-1}$ ,  $\omega = 9425 \text{ rad s}^{-1}$  and  $\alpha = 0.06 \%$ .

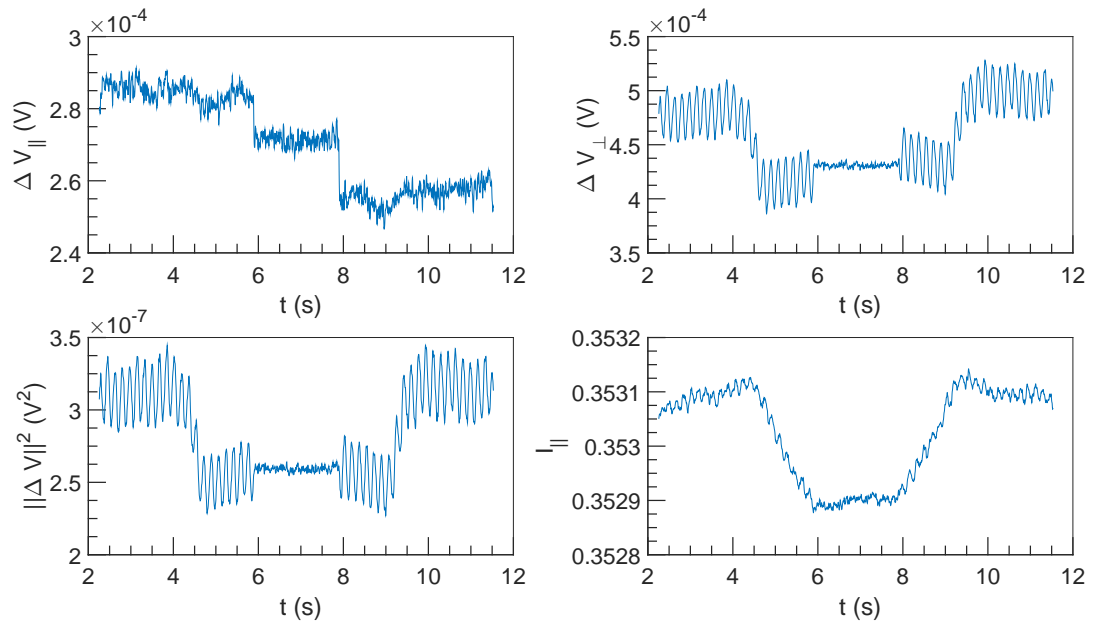


Figure 6.21:  $\Delta V$  and  $I$  vs  $t$  at  $U = 0.1 \text{ m s}^{-1}$ ,  $\omega = 10\,996 \text{ rad s}^{-1}$  and  $\alpha = 0.06 \%$ .

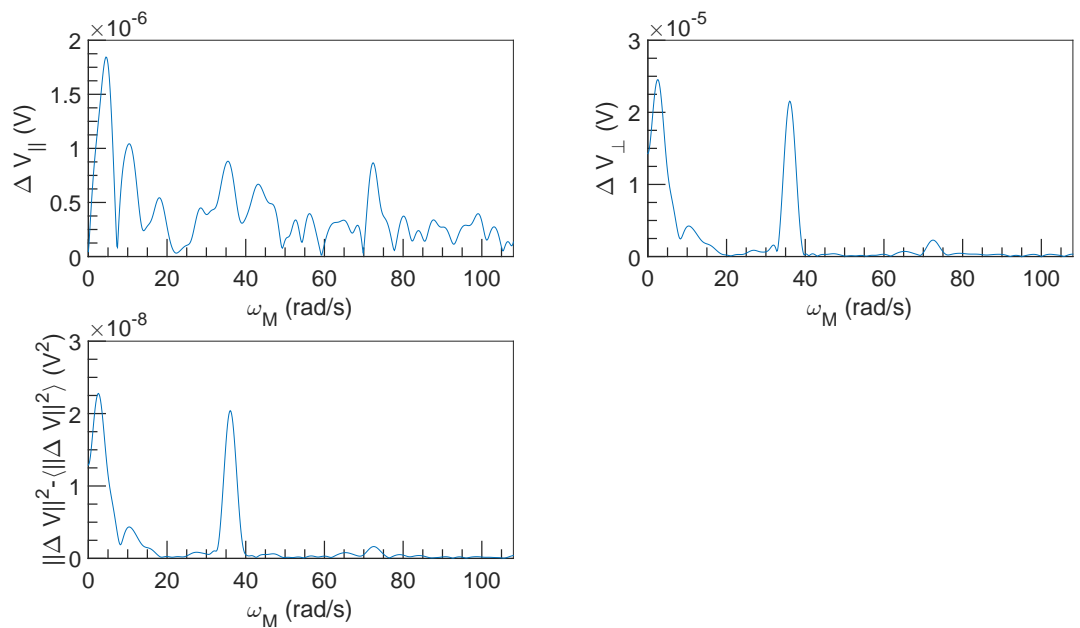


Figure 6.22: FFT spectral density of  $\Delta V$  vs  $\omega_M$  at  $U = 0.1 \text{ m s}^{-1}$ ,  $\omega = 10\,996 \text{ rad s}^{-1}$  and  $\alpha = 0.06 \%$ .

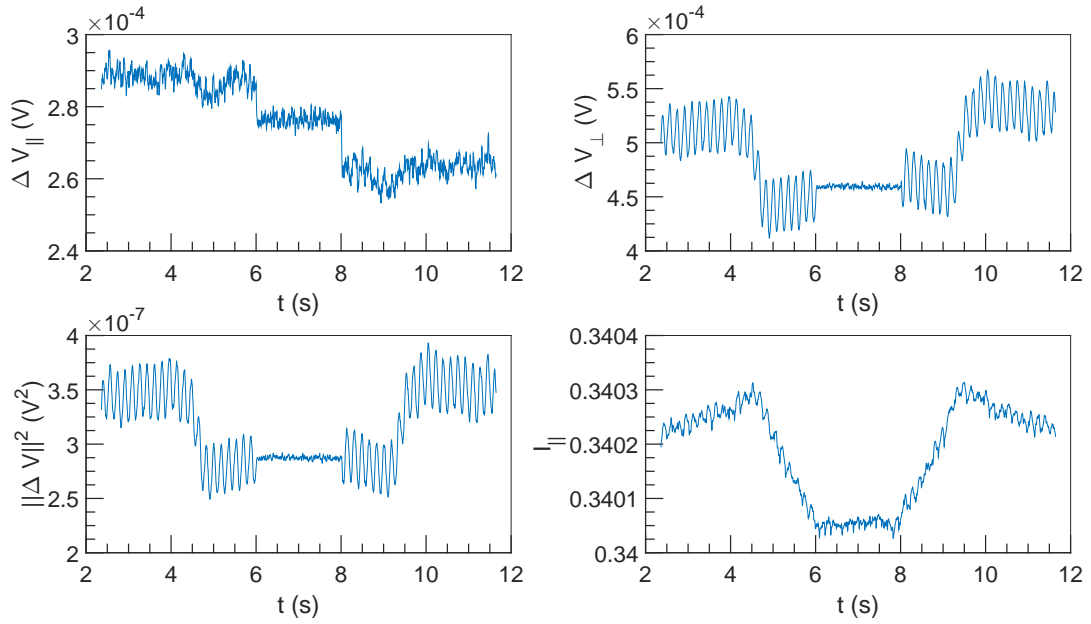


Figure 6.23:  $\Delta V$  and  $I$  vs  $t$  at  $U = 0.1 \text{ m s}^{-1}$ ,  $\omega = 12566 \text{ rad s}^{-1}$  and  $\alpha = 0.06 \%$ .

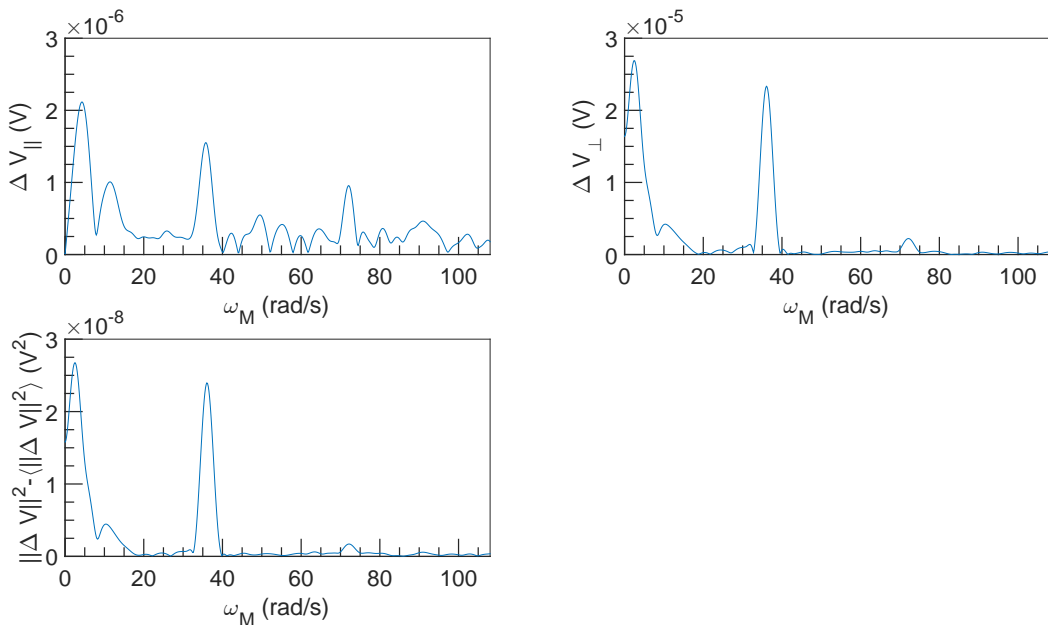


Figure 6.24: FFT spectral density of  $\Delta V$  vs  $\omega_M$  at  $U = 0.1 \text{ m s}^{-1}$ ,  $\omega = 12566 \text{ rad s}^{-1}$  and  $\alpha = 0.06 \%$ .

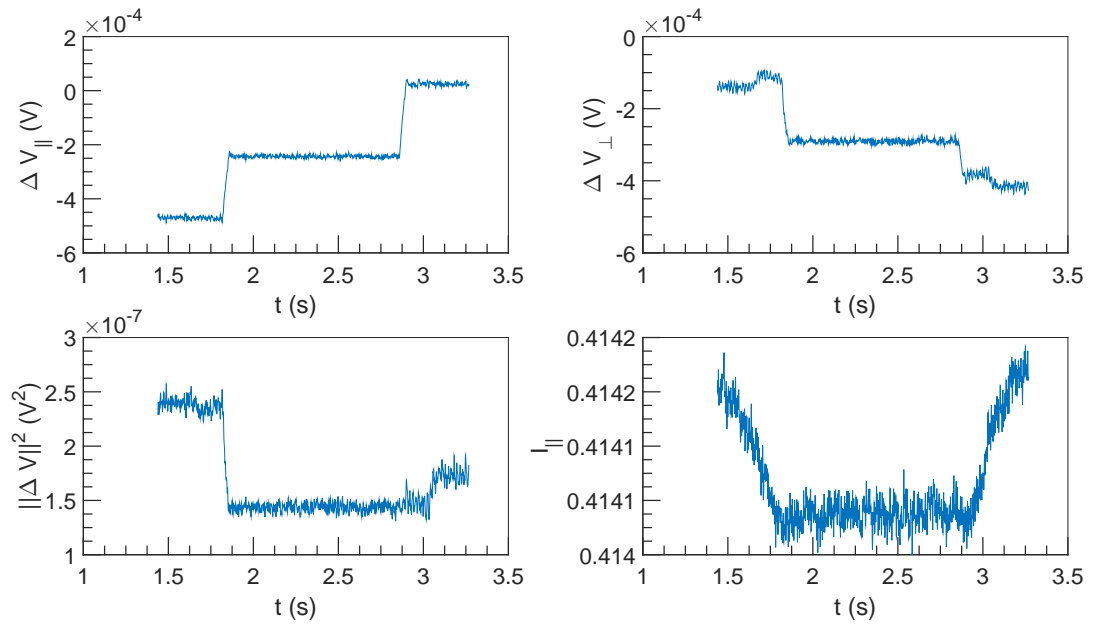


Figure 6.25:  $\Delta V$  and  $I$  vs  $t$  at  $U = 1 \text{ m s}^{-1}$ ,  $\omega = 4712 \text{ rad s}^{-1}$  and  $\alpha = 0.06 \%$ .

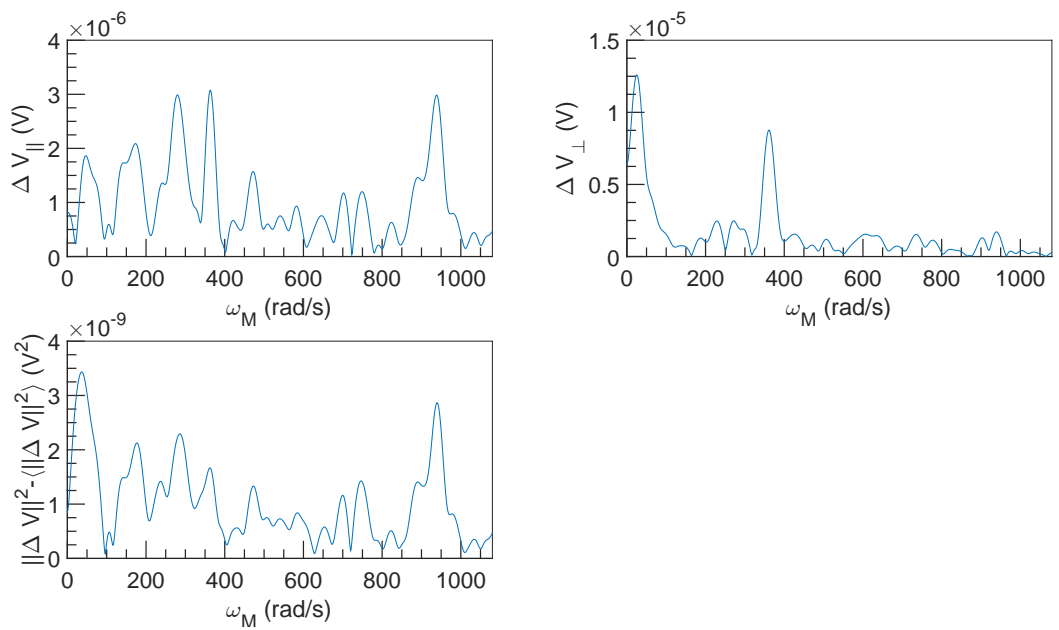


Figure 6.26: FFT spectral density of  $\Delta V$  vs  $\omega_M$  at  $U = 1 \text{ m s}^{-1}$ ,  $\omega = 4712 \text{ rad s}^{-1}$  and  $\alpha = 0.06 \%$ .

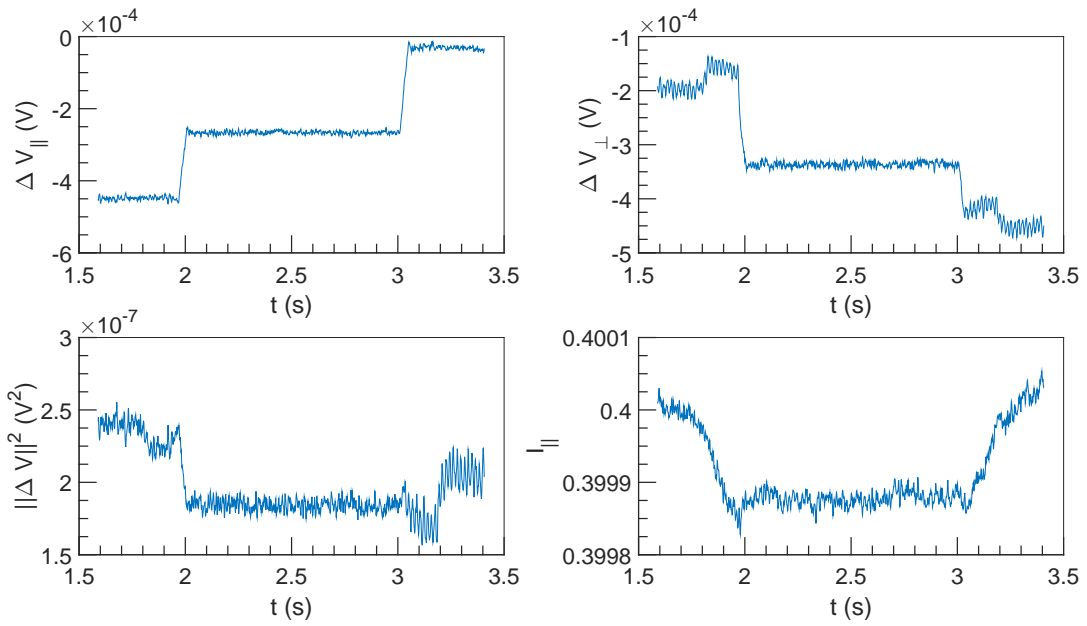


Figure 6.27:  $\Delta V$  and  $I$  vs  $t$  at  $U = 1 \text{ m s}^{-1}$ ,  $\omega = 6283 \text{ rad s}^{-1}$  and  $\alpha = 0.06 \%$ .

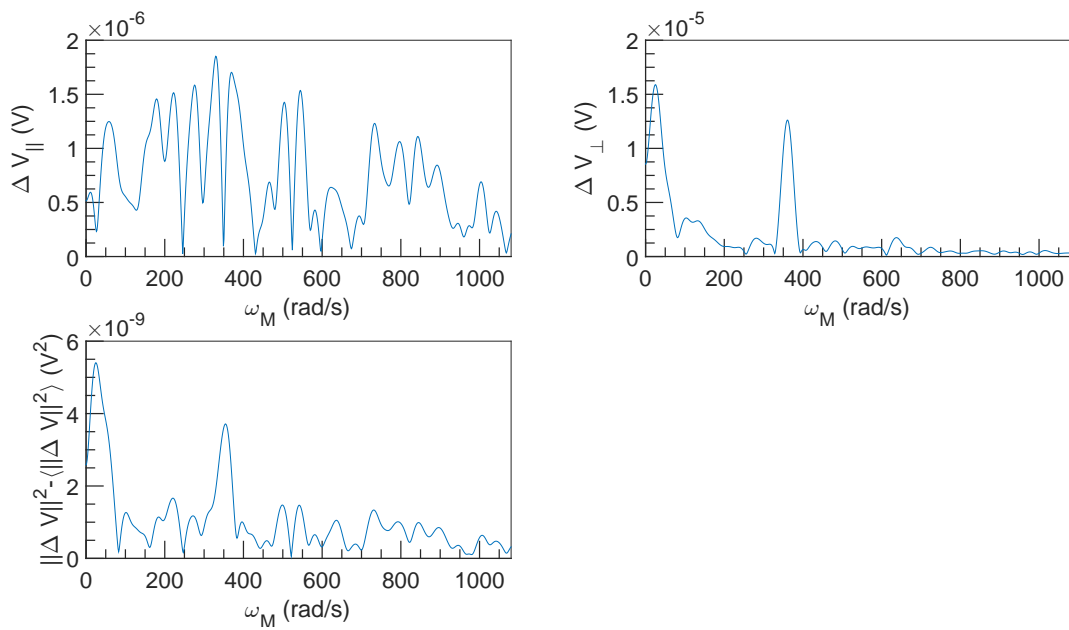


Figure 6.28: FFT spectral density of  $\Delta V$  vs  $\omega_M$  at  $U = 1 \text{ m s}^{-1}$ ,  $\omega = 6283 \text{ rad s}^{-1}$  and  $\alpha = 0.06 \%$ .

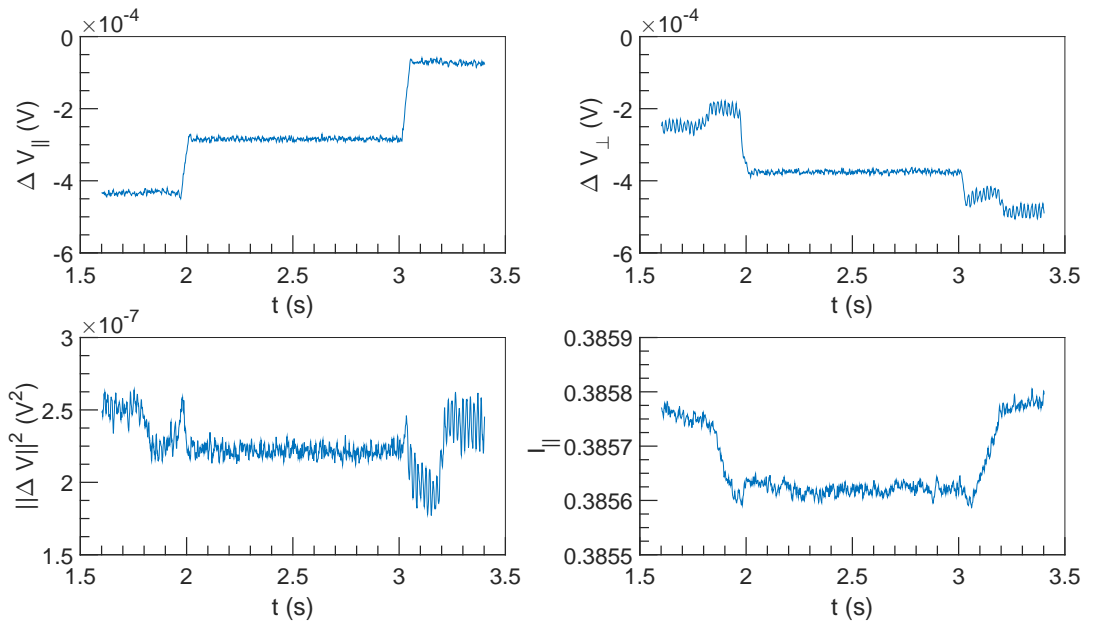


Figure 6.29:  $\Delta V$  and  $I$  vs  $t$  at  $U = 1 \text{ m s}^{-1}$ ,  $\omega = 7854 \text{ rad s}^{-1}$  and  $\alpha = 0.06 \%$ .

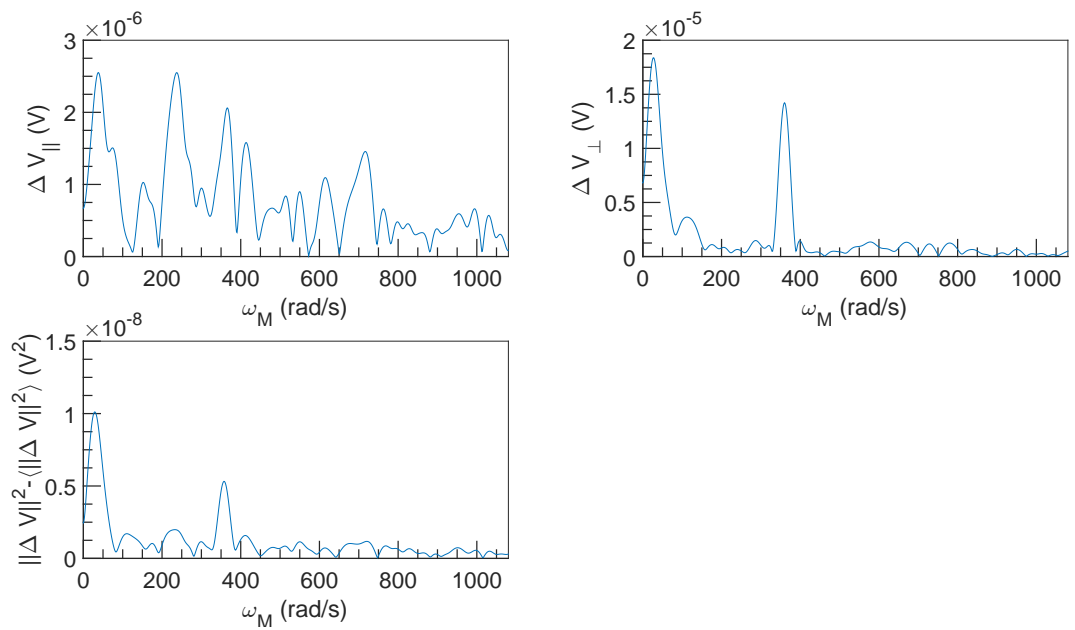


Figure 6.30: FFT spectral density of  $\Delta V$  vs  $\omega_M$  at  $U = 1 \text{ m s}^{-1}$ ,  $\omega = 7854 \text{ rad s}^{-1}$  and  $\alpha = 0.06 \%$ .



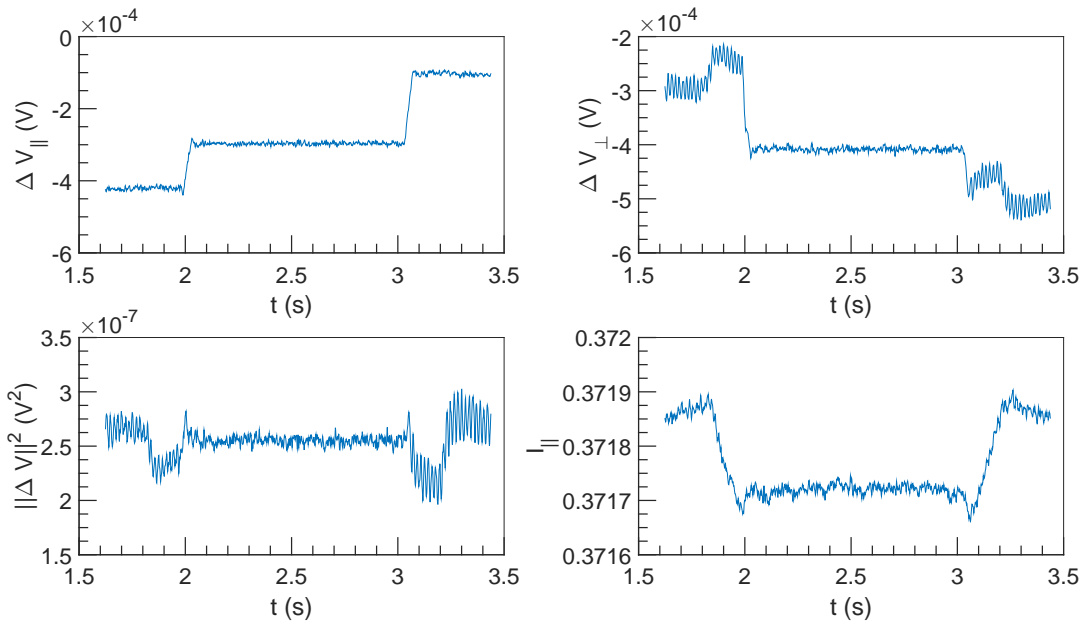


Figure 6.31:  $\Delta V$  and  $I$  vs  $t$  at  $U = 1 \text{ m s}^{-1}$ ,  $\omega = 9425 \text{ rad s}^{-1}$  and  $\alpha = 0.06 \%$ .

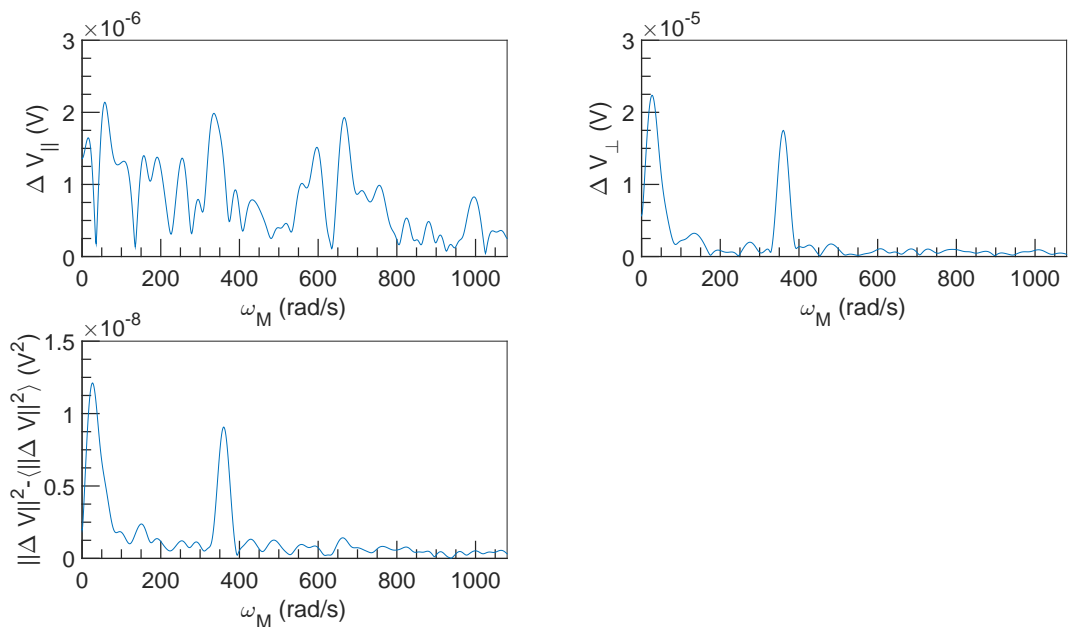


Figure 6.32: FFT spectral density of  $\Delta V$  vs  $\omega_M$  at  $U = 1 \text{ m s}^{-1}$ ,  $\omega = 9425 \text{ rad s}^{-1}$  and  $\alpha = 0.06 \%$ .

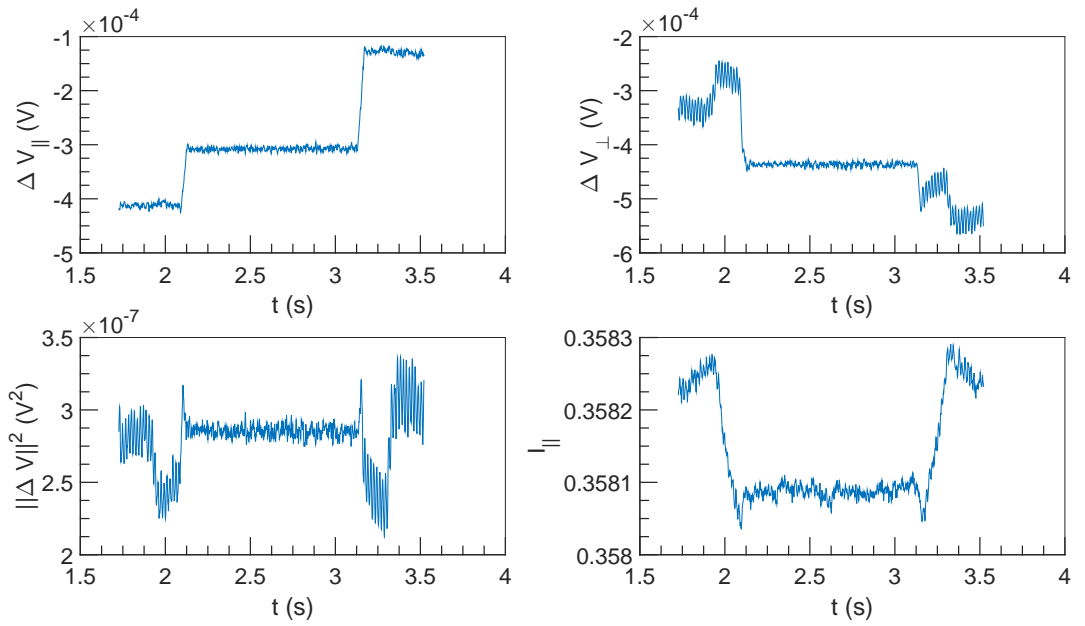


Figure 6.33:  $\Delta V$  and  $I$  vs  $t$  at  $U = 1 \text{ m s}^{-1}$ ,  $\omega = 10996 \text{ rad s}^{-1}$  and  $\alpha = 0.06 \%$ .

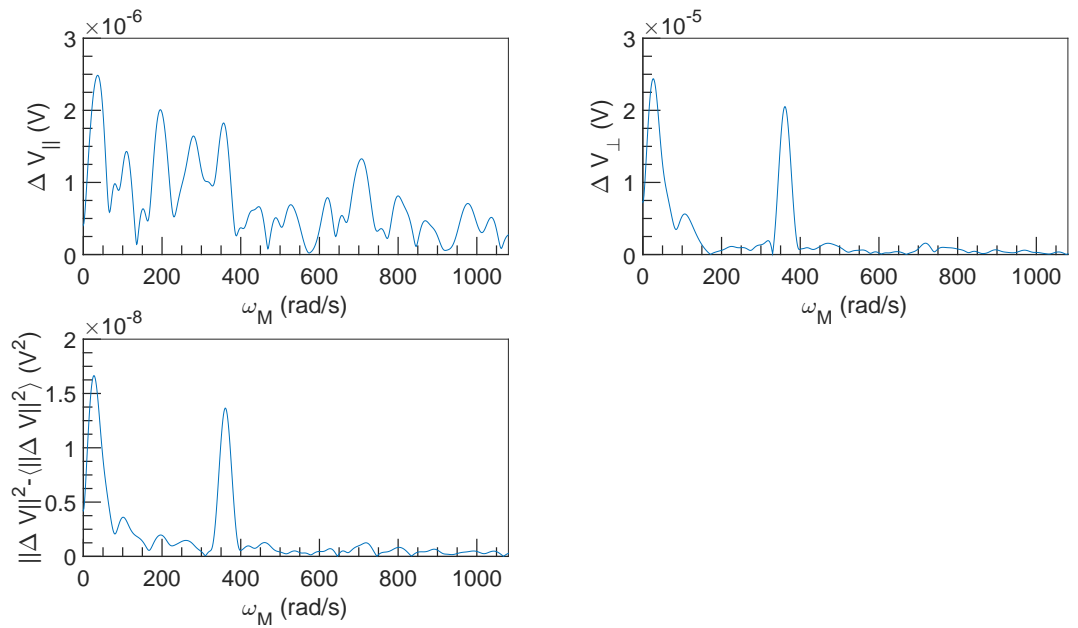


Figure 6.34: FFT spectral density of  $\Delta V$  vs  $\omega_M$  at  $U = 1 \text{ m s}^{-1}$ ,  $\omega = 10996 \text{ rad s}^{-1}$  and  $\alpha = 0.06 \%$ .

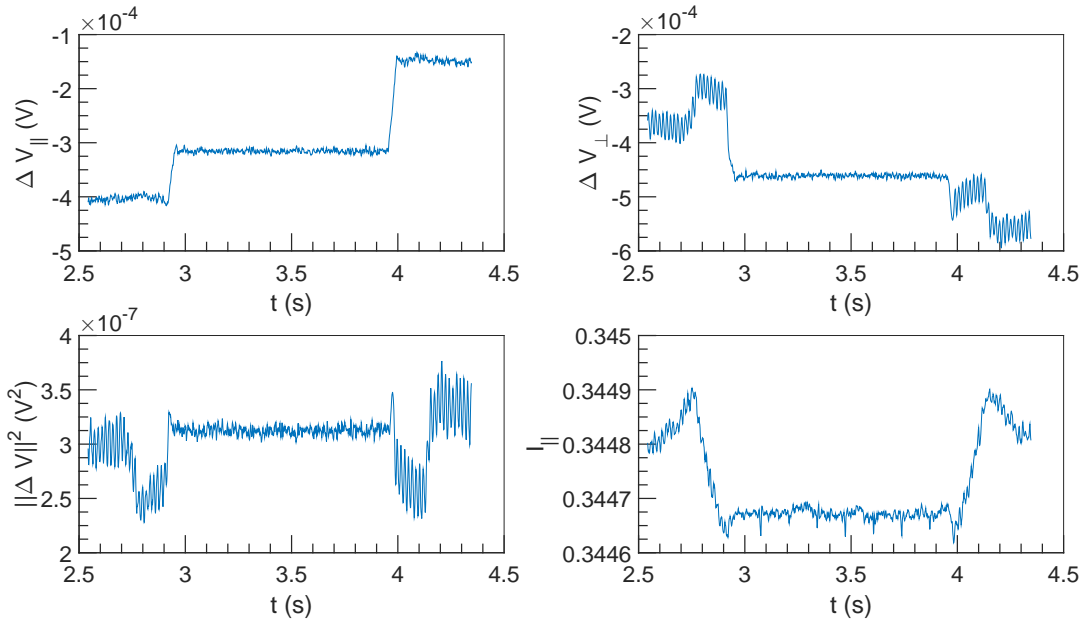


Figure 6.35:  $\Delta V$  and  $I$  vs  $t$  at  $U = 1 \text{ m s}^{-1}$ ,  $\omega = 12566 \text{ rad s}^{-1}$  and  $\alpha = 0.06 \%$ .

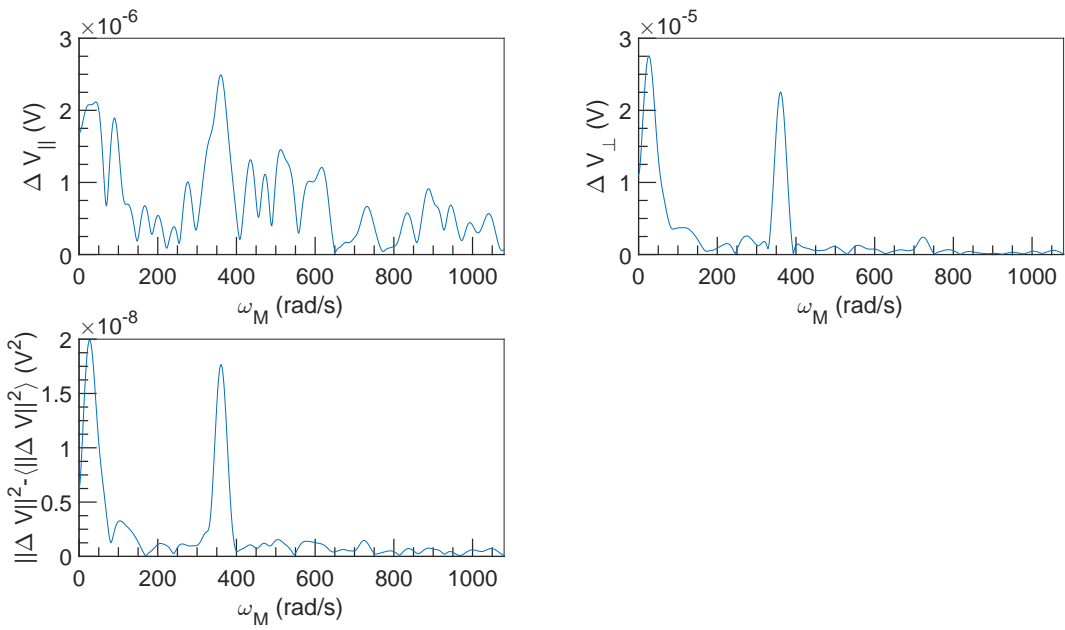


Figure 6.36: FFT spectral density of  $\Delta V$  vs  $\omega_M$  at  $U = 1 \text{ m s}^{-1}$ ,  $\omega = 12566 \text{ rad s}^{-1}$  and  $\alpha = 0.06 \%$ .

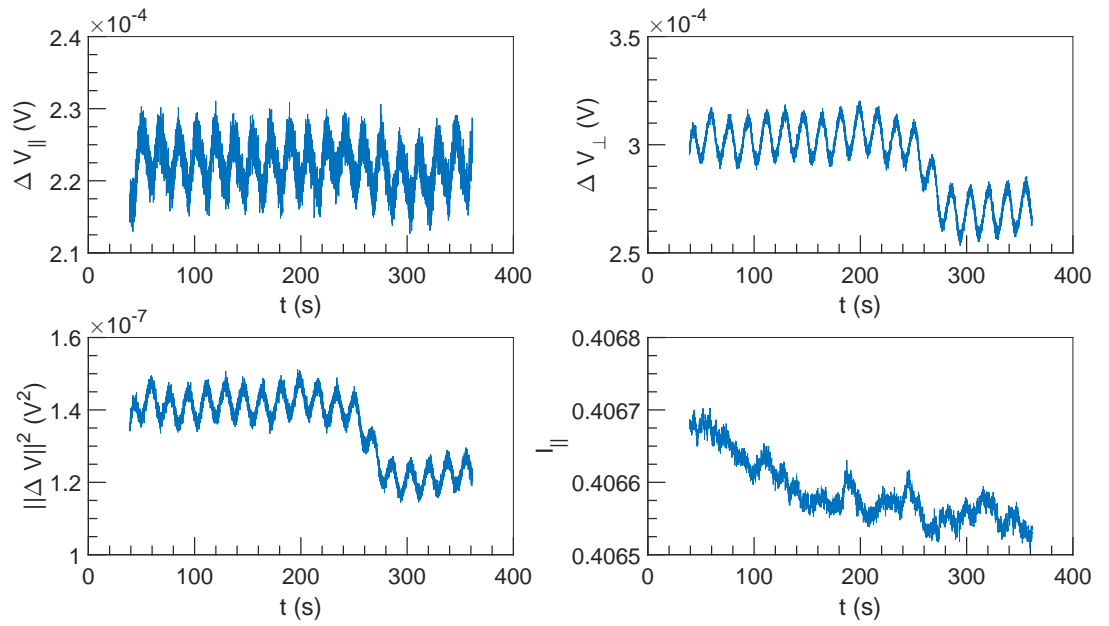


Figure 6.37:  $\Delta V$  and  $I$  vs  $t$  at  $U = 10^{-3} \text{ m s}^{-1}$ ,  $\omega = 4712 \text{ rad s}^{-1}$  and  $\alpha = 0.06 \%$ .

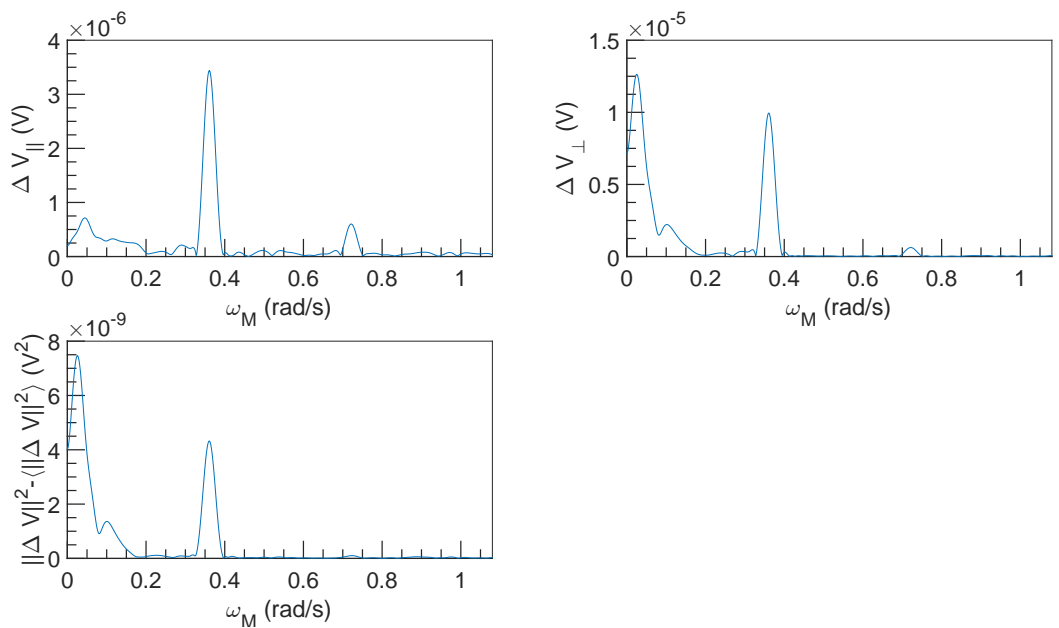


Figure 6.38: FFT spectral density of  $\Delta V$  vs  $\omega_M$  at  $U = 10^{-3} \text{ m s}^{-1}$ ,  $\omega = 4712 \text{ rad s}^{-1}$  and  $\alpha = 0.06 \%$ .

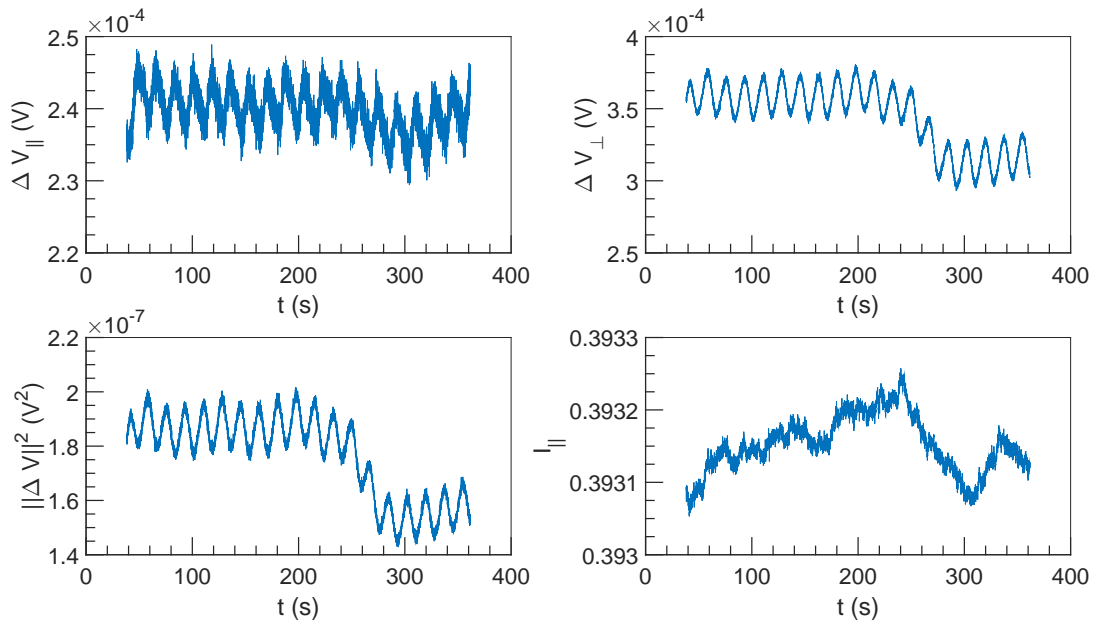


Figure 6.39:  $\Delta V$  and  $I$  vs  $t$  at  $U = 10^{-3} \text{ m s}^{-1}$ ,  $\omega = 6283 \text{ rad s}^{-1}$  and  $\alpha = 0.06 \%$ .

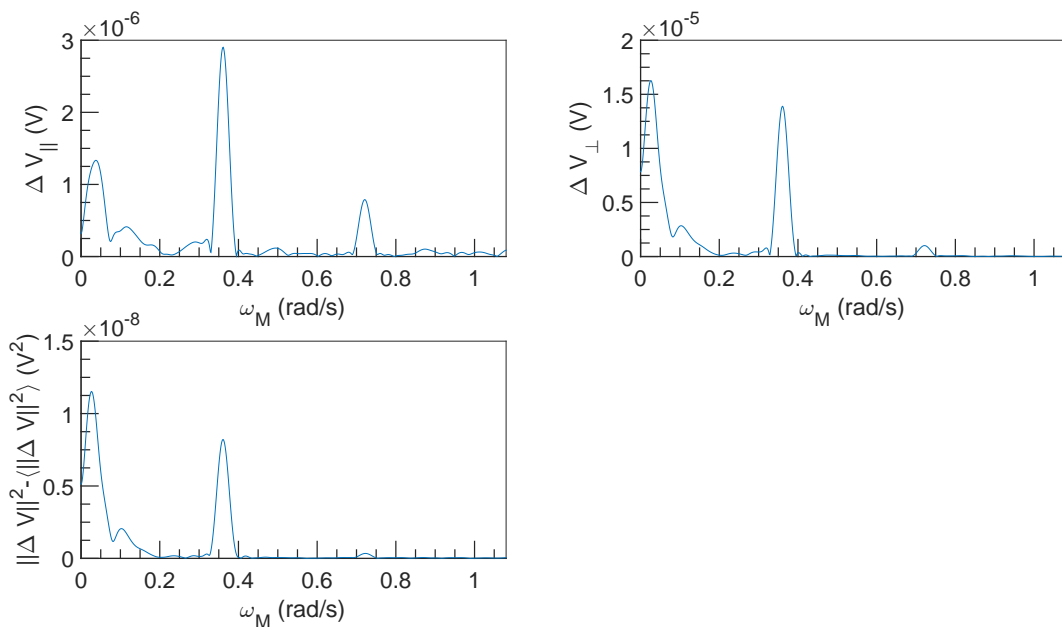


Figure 6.40: FFT spectral density of  $\Delta V$  vs  $\omega_M$  at  $U = 10^{-3} \text{ m s}^{-1}$ ,  $\omega = 6283 \text{ rad s}^{-1}$  and  $\alpha = 0.06 \%$ .

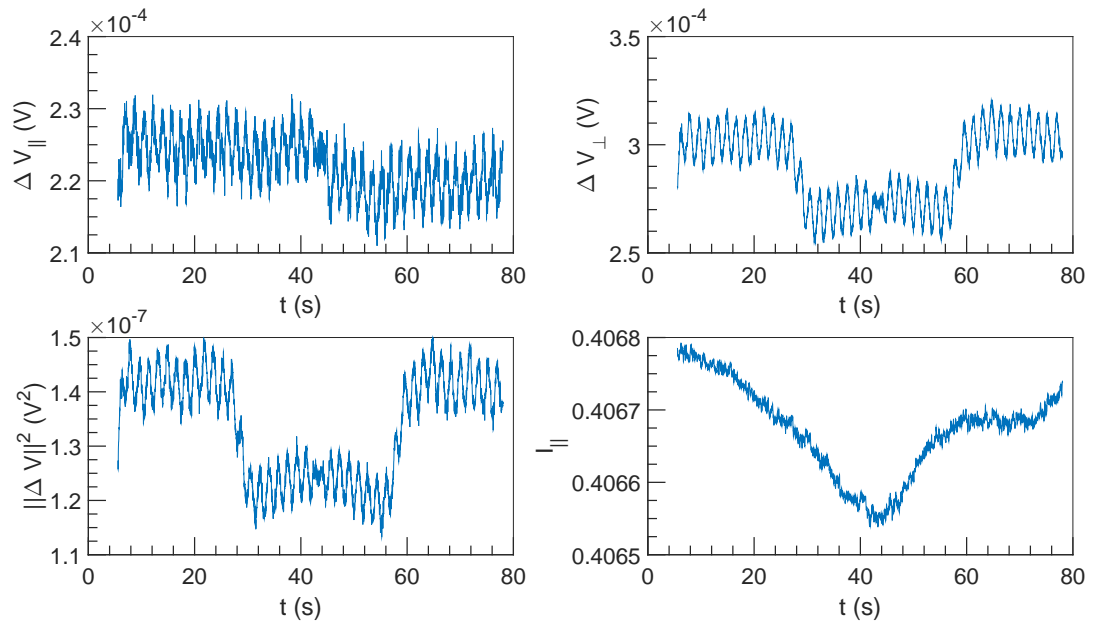


Figure 6.41:  $\Delta V$  and  $I$  vs  $t$  at  $U = 10^{-2} \text{ m s}^{-1}$ ,  $\omega = 4712 \text{ rad s}^{-1}$  and  $\alpha = 0.06 \%$ .

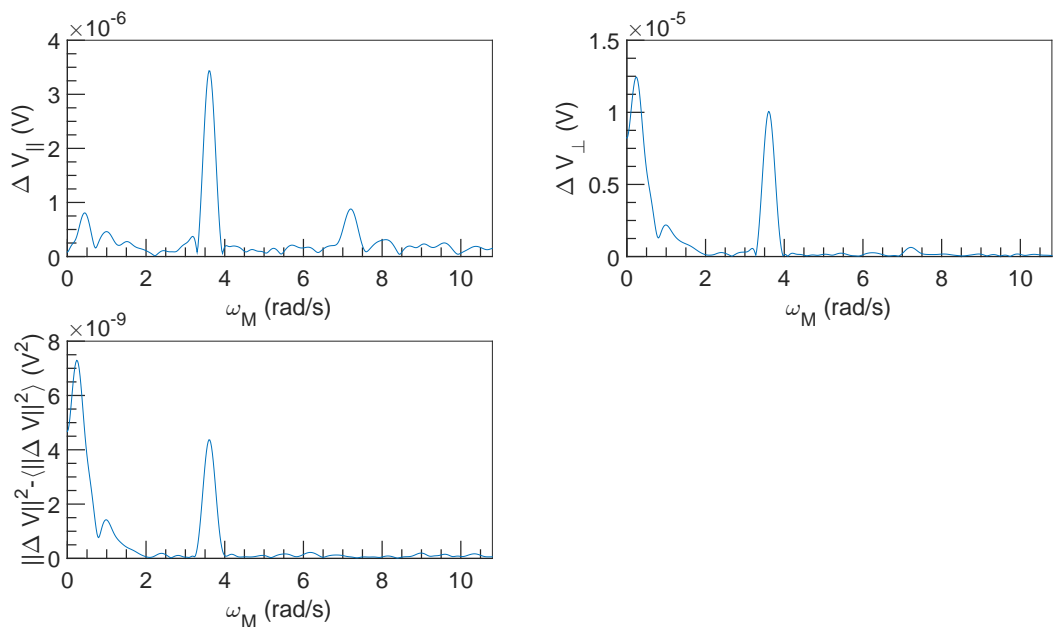


Figure 6.42: FFT spectral density of  $\Delta V$  vs  $\omega_M$  at  $U = 10^{-2} \text{ m s}^{-1}$ ,  $\omega = 4712 \text{ rad s}^{-1}$  and  $\alpha = 0.06 \%$ .

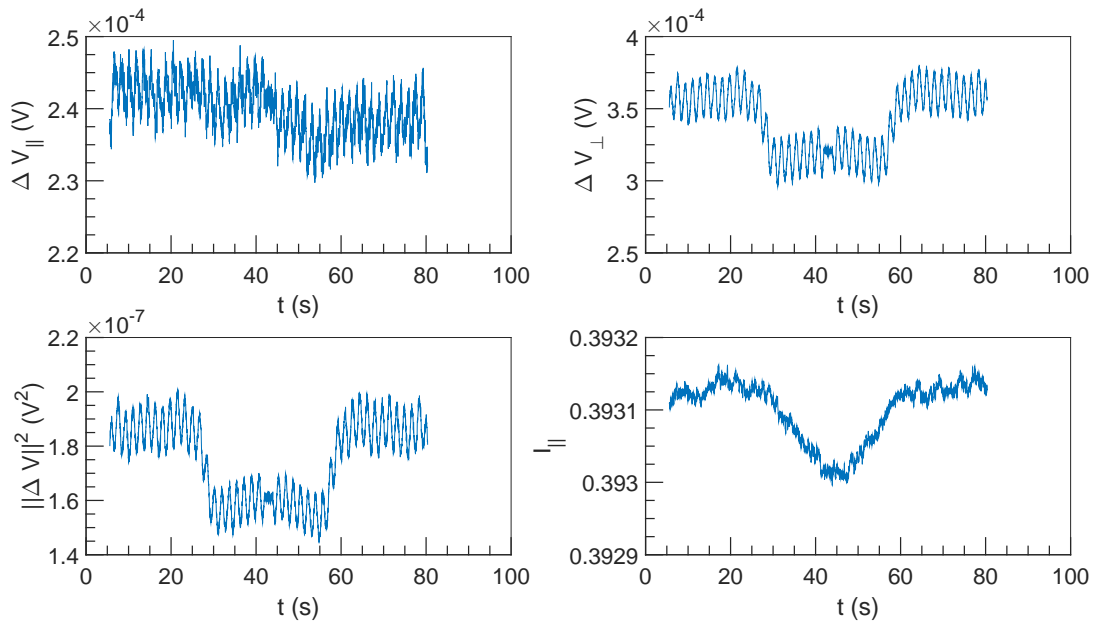


Figure 6.43:  $\Delta V$  and  $I$  vs  $t$  at  $U = 10^{-2} \text{ m s}^{-1}$ ,  $\omega = 6283 \text{ rad s}^{-1}$  and  $\alpha = 0.06 \%$ .

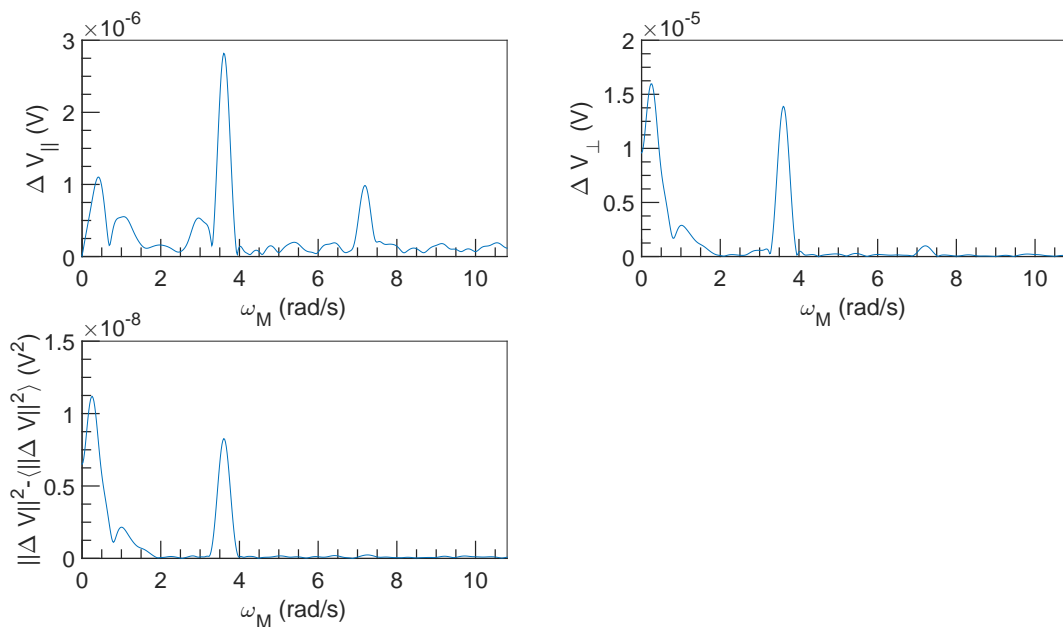


Figure 6.44: FFT spectral density of  $\Delta V$  vs  $\omega_M$  at  $U = 10^{-2} \text{ m s}^{-1}$ ,  $\omega = 6283 \text{ rad s}^{-1}$  and  $\alpha = 0.06 \%$ .

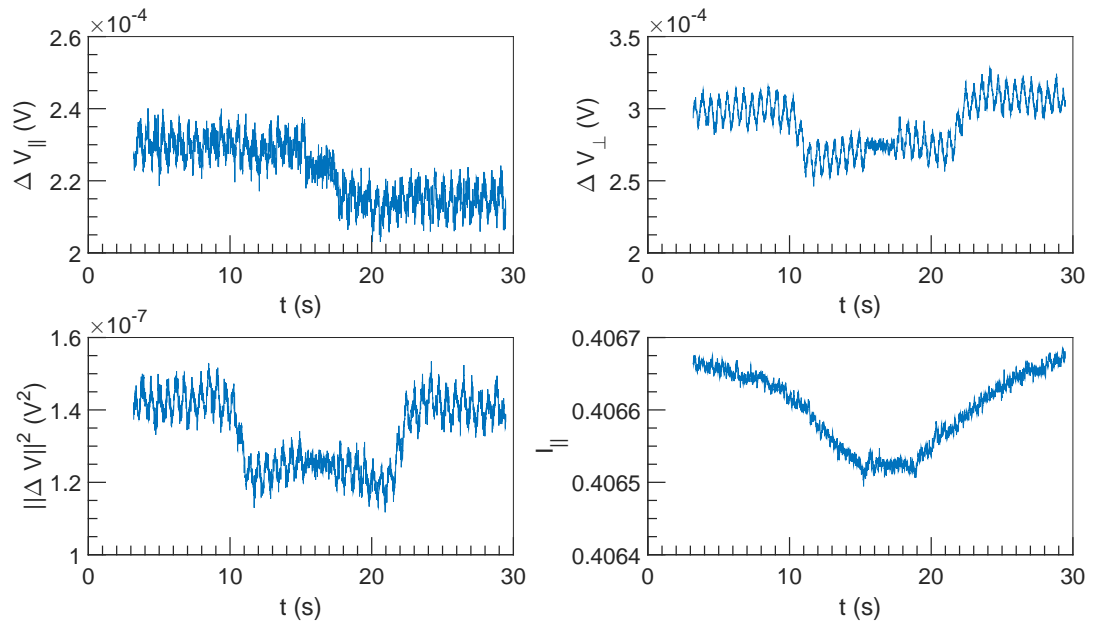


Figure 6.45:  $\Delta V$  and  $I$  vs  $t$  at  $U = 3 \times 10^{-2} \text{ m s}^{-1}$ ,  $\omega = 4712 \text{ rad s}^{-1}$  and  $\alpha = 0.06 \%$ .

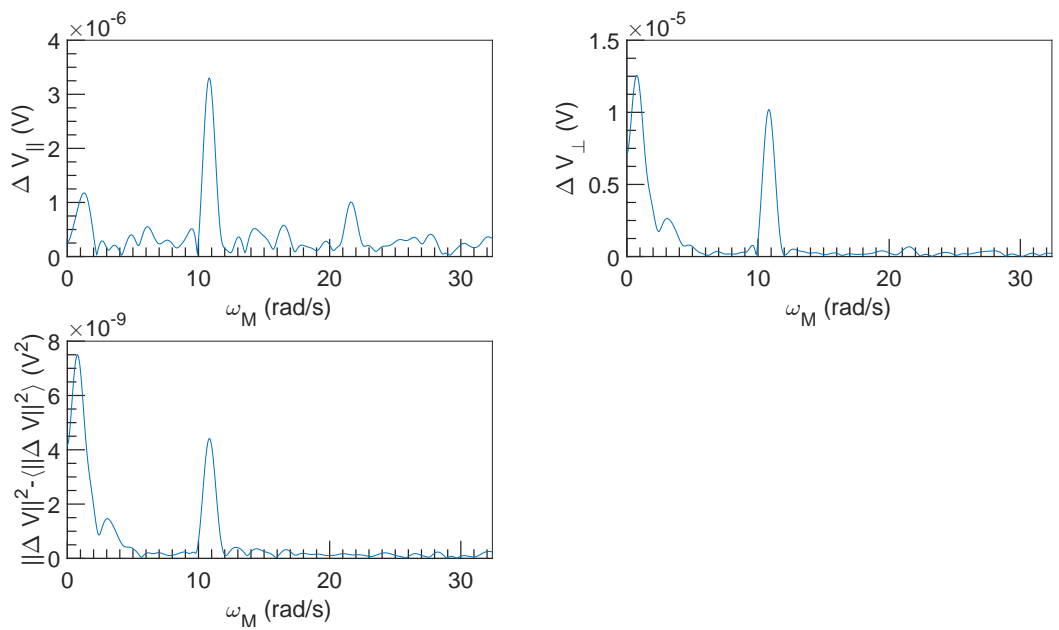


Figure 6.46: FFT spectral density of  $\Delta V$  vs  $\omega_M$  at  $U = 3 \times 10^{-2} \text{ m s}^{-1}$ ,  $\omega = 4712 \text{ rad s}^{-1}$  and  $\alpha = 0.06 \%$ .



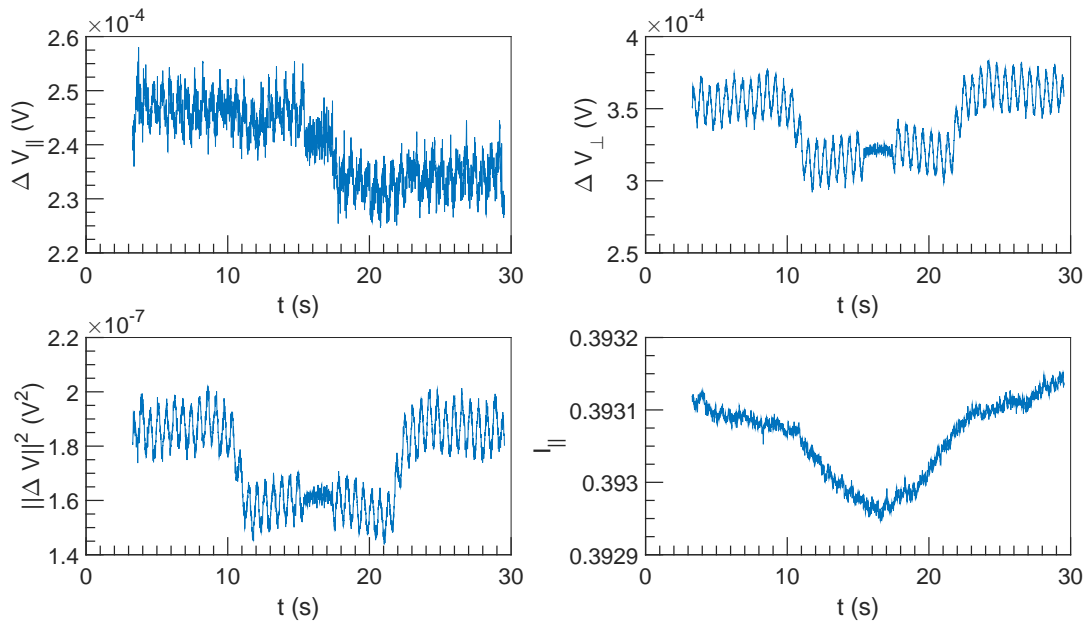


Figure 6.47:  $\Delta V$  and  $I$  vs  $t$  at  $U = 3 \times 10^{-2} \text{ m s}^{-1}$ ,  $\omega = 6283 \text{ rad s}^{-1}$  and  $\alpha = 0.06 \%$ .

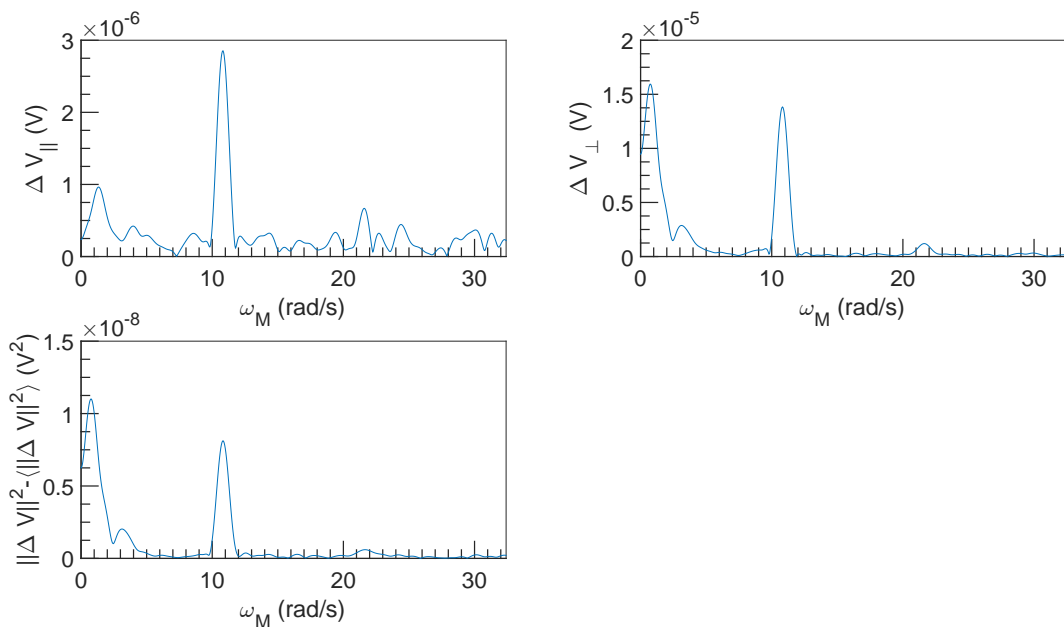


Figure 6.48: FFT spectral density of  $\Delta V$  vs  $\omega_M$  at  $U = 3 \times 10^{-2} \text{ m s}^{-1}$ ,  $\omega = 6283 \text{ rad s}^{-1}$  and  $\alpha = 0.06 \%$ .

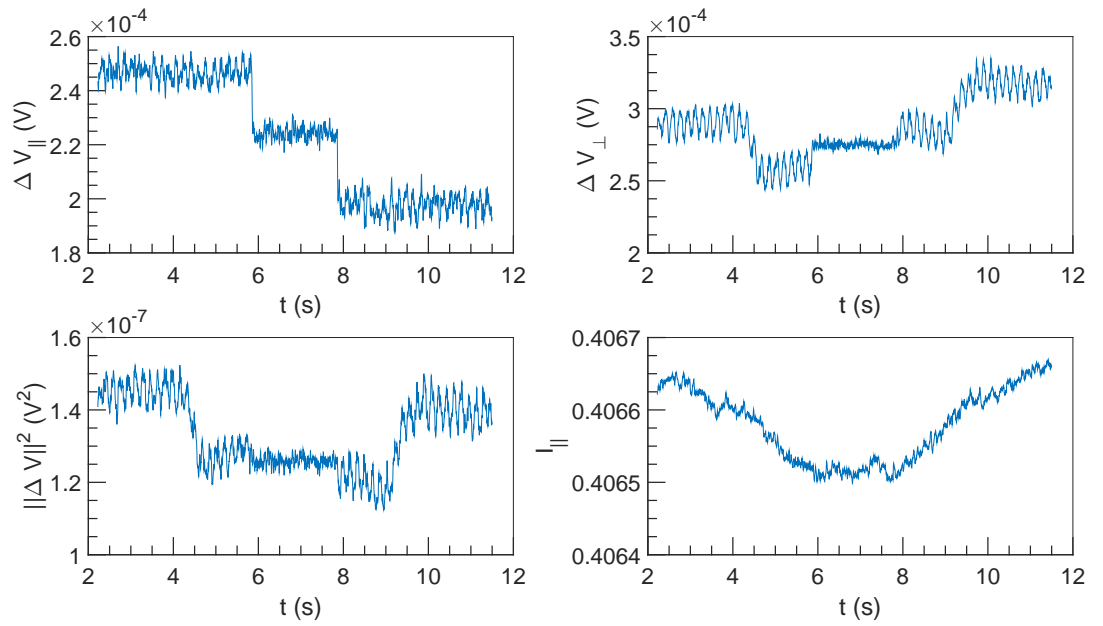


Figure 6.49:  $\Delta V$  and  $I$  vs  $t$  at  $U = 0.1 \text{ m s}^{-1}$ ,  $\omega = 4712 \text{ rad s}^{-1}$  and  $\alpha = 0.06 \%$ .

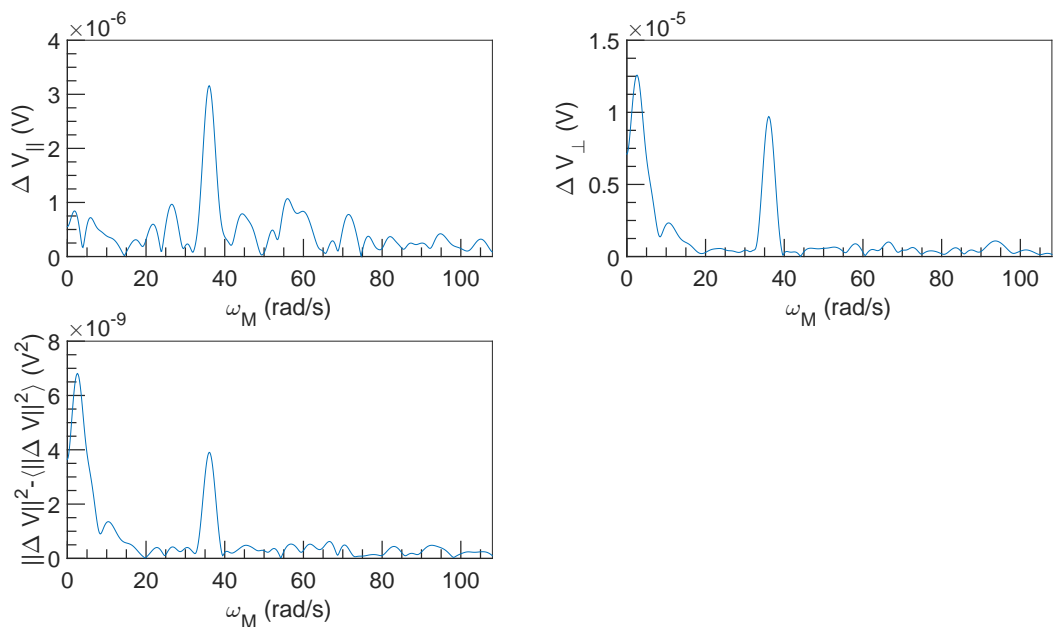


Figure 6.50: FFT spectral density of  $\Delta V$  vs  $\omega_M$  at  $U = 0.1 \text{ m s}^{-1}$ ,  $\omega = 4712 \text{ rad s}^{-1}$  and  $\alpha = 0.06 \%$ .

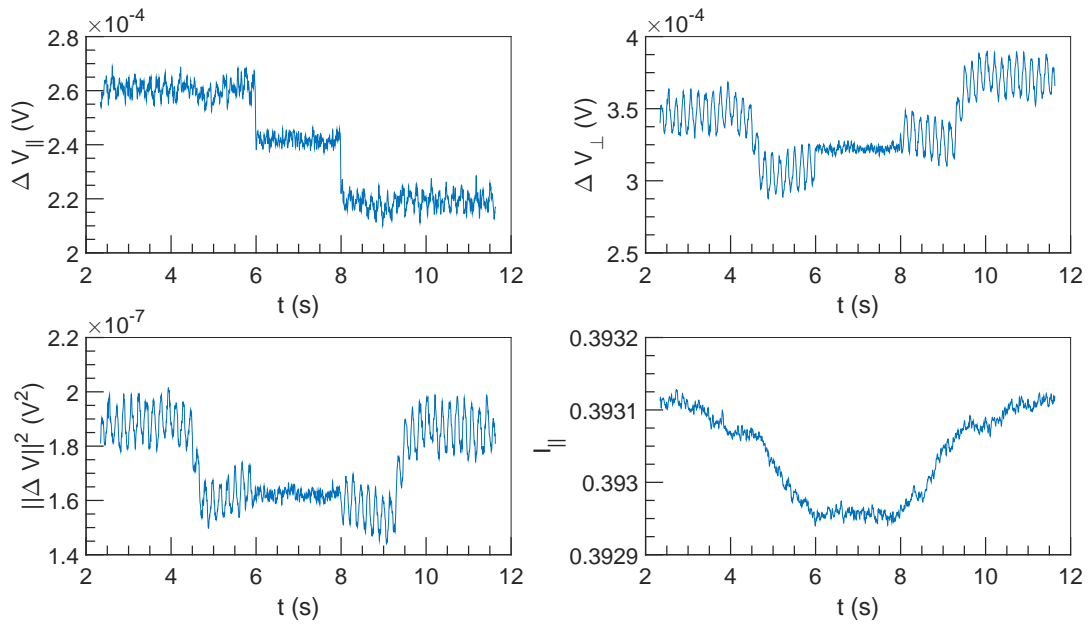


Figure 6.51:  $\Delta V$  and  $I$  vs  $t$  at  $U = 0.1 \text{ m s}^{-1}$ ,  $\omega = 6283 \text{ rad s}^{-1}$  and  $\alpha = 0.06 \%$ .

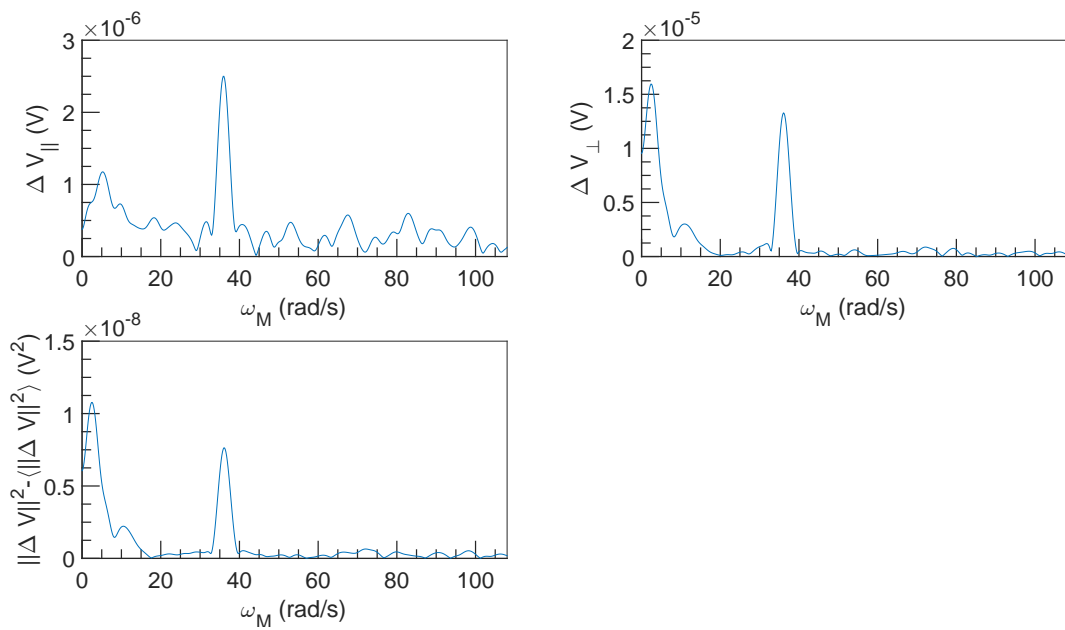


Figure 6.52: FFT spectral density of  $\Delta V$  vs  $\omega_M$  at  $U = 0.1 \text{ m s}^{-1}$ ,  $\omega = 6283 \text{ rad s}^{-1}$  and  $\alpha = 0.06 \%$ .

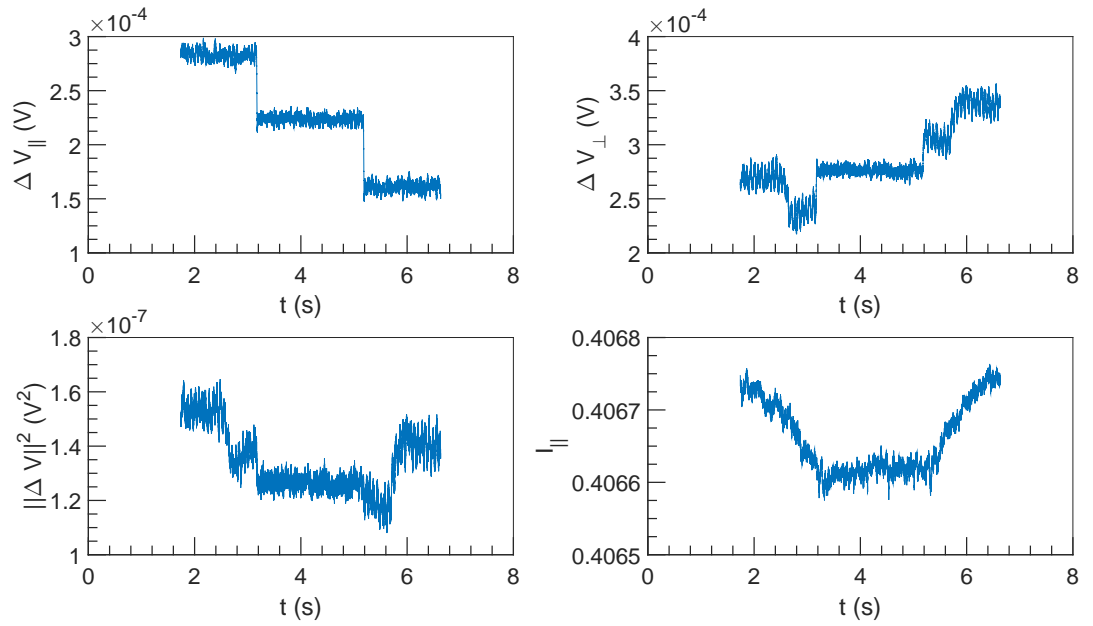


Figure 6.53:  $\Delta V$  and  $I$  vs  $t$  at  $U = 0.25 \text{ m s}^{-1}$ ,  $\omega = 4712 \text{ rad s}^{-1}$  and  $\alpha = 0.06 \%$ .

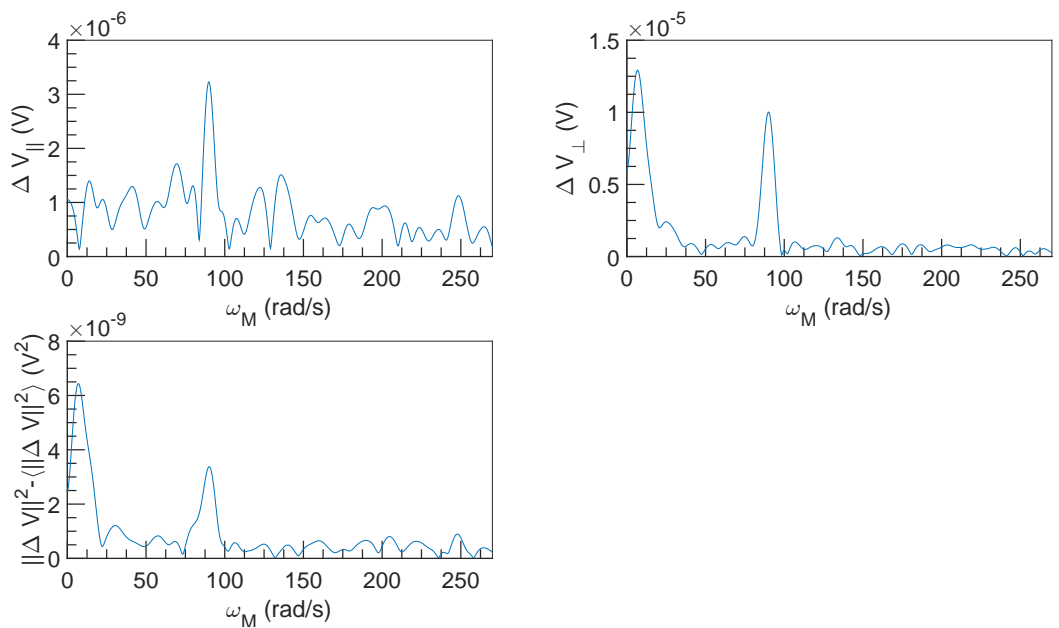


Figure 6.54: FFT spectral density of  $\Delta V$  vs  $\omega_M$  at  $U = 0.25 \text{ m s}^{-1}$ ,  $\omega = 4712 \text{ rad s}^{-1}$  and  $\alpha = 0.06 \%$ .

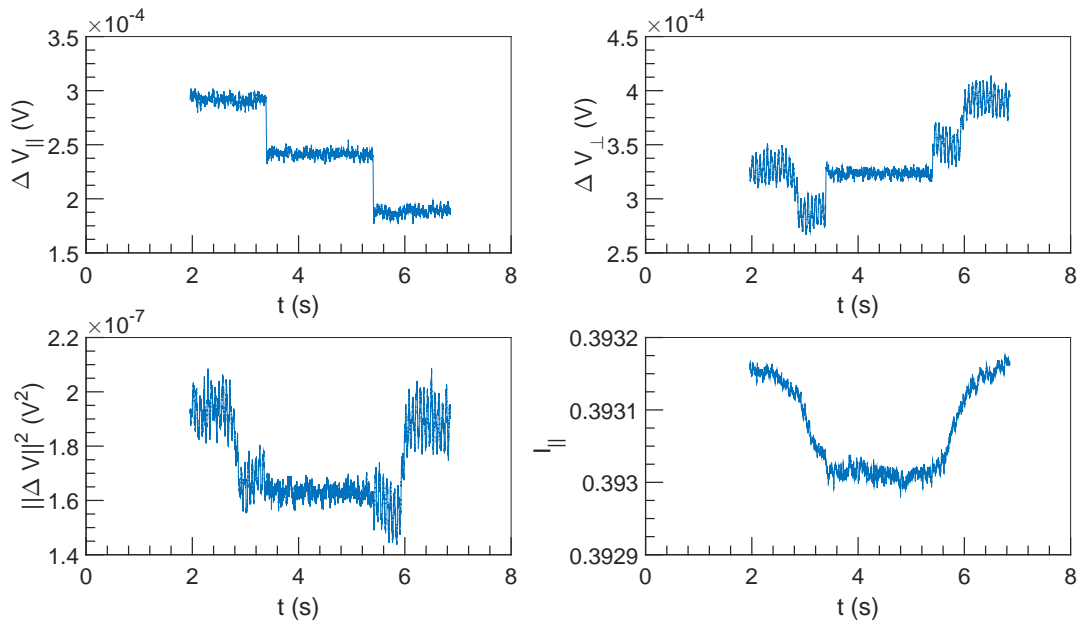


Figure 6.55:  $\Delta V$  and  $I$  vs  $t$  at  $U = 0.25 \text{ m s}^{-1}$ ,  $\omega = 6283 \text{ rad s}^{-1}$  and  $\alpha = 0.06 \%$ .

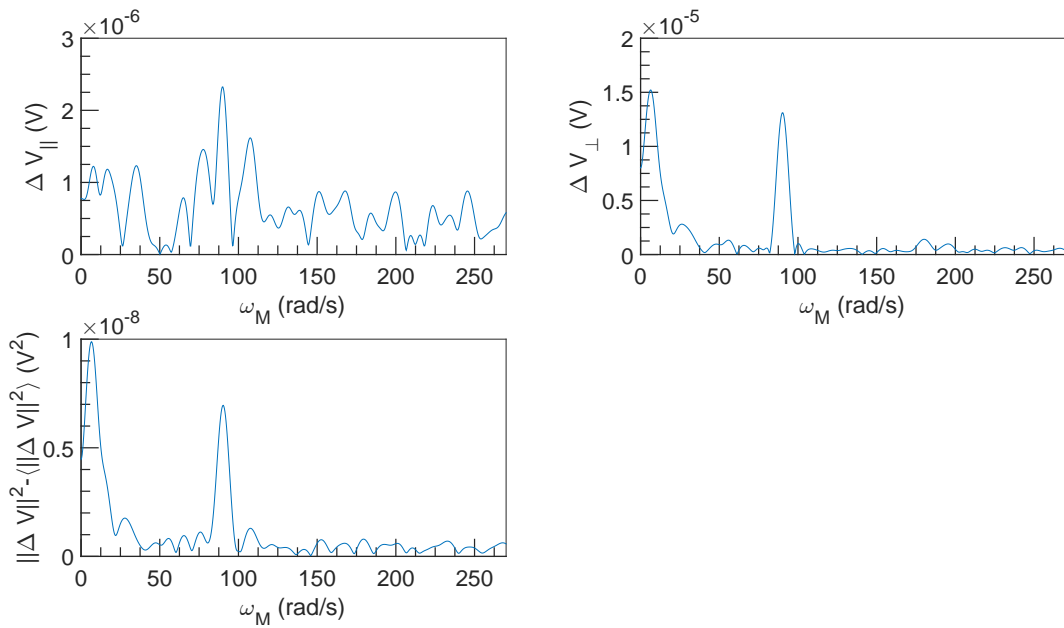


Figure 6.56: FFT spectral density of  $\Delta V$  vs  $\omega_M$  at  $U = 0.25 \text{ m s}^{-1}$ ,  $\omega = 6283 \text{ rad s}^{-1}$  and  $\alpha = 0.06 \%$ .

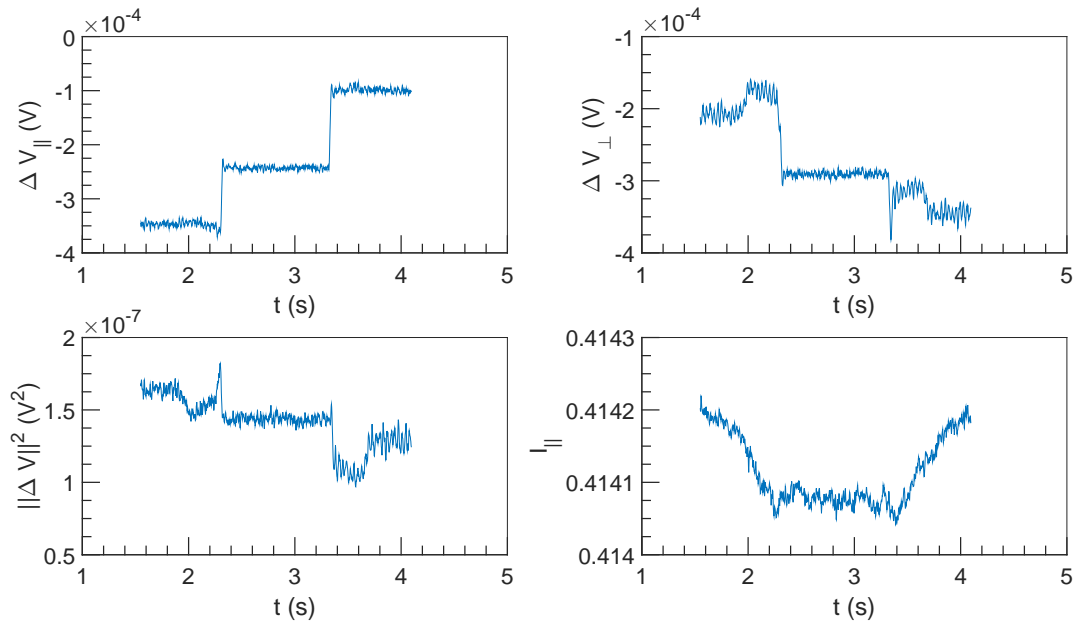


Figure 6.57:  $\Delta V$  and  $I$  vs  $t$  at  $U = 0.5 \text{ m s}^{-1}$ ,  $\omega = 4712 \text{ rad s}^{-1}$  and  $\alpha = 0.06 \%$ .

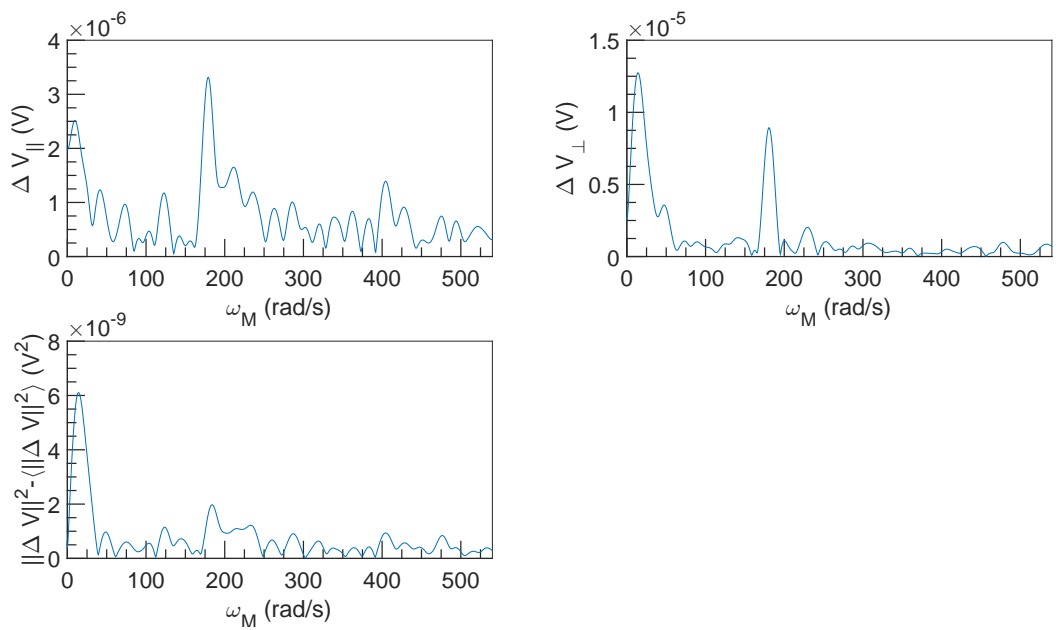


Figure 6.58: FFT spectral density of  $\Delta V$  vs  $\omega_M$  at  $U = 0.5 \text{ m s}^{-1}$ ,  $\omega = 4712 \text{ rad s}^{-1}$  and  $\alpha = 0.06 \%$ .

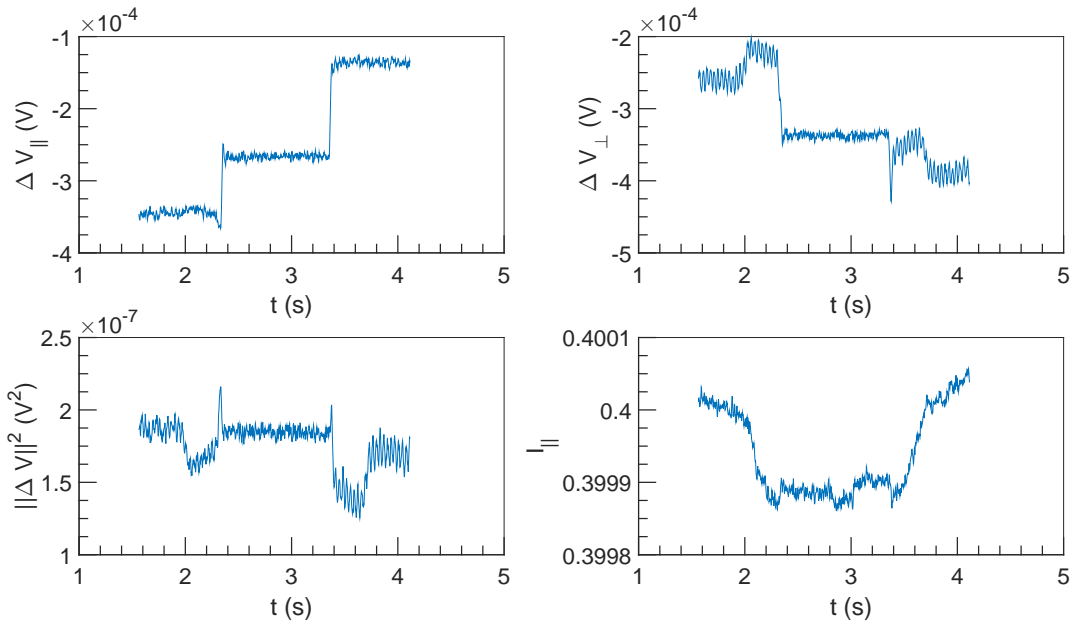


Figure 6.59:  $\Delta V$  and  $I$  vs  $t$  at  $U = 0.5 \text{ m s}^{-1}$ ,  $\omega = 6283 \text{ rad s}^{-1}$  and  $\alpha = 0.06 \%$ .

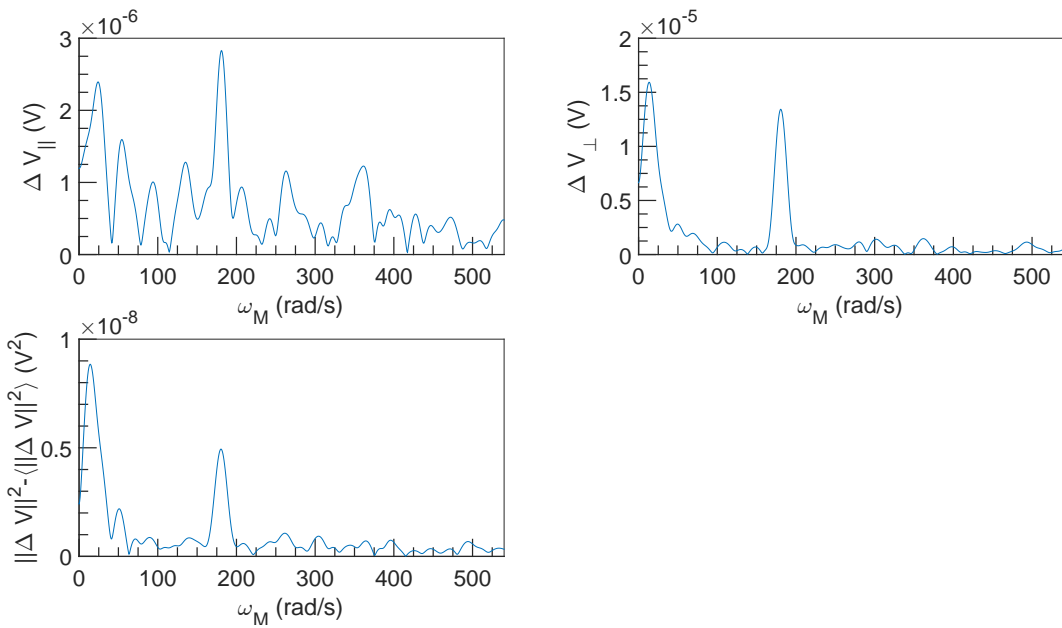


Figure 6.60: FFT spectral density of  $\Delta V$  vs  $\omega_M$  at  $U = 0.5 \text{ m s}^{-1}$ ,  $\omega = 6283 \text{ rad s}^{-1}$  and  $\alpha = 0.06 \%$ .

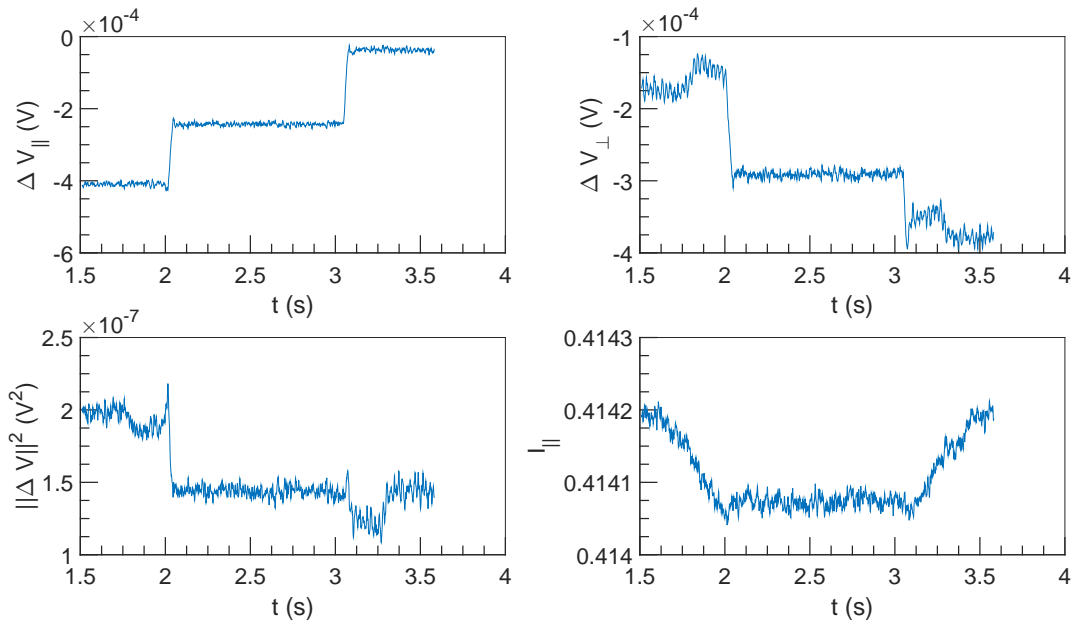


Figure 6.61:  $\Delta V$  and  $I$  vs  $t$  at  $U = 0.75 \text{ m s}^{-1}$ ,  $\omega = 4712 \text{ rad s}^{-1}$  and  $\alpha = 0.06 \%$ .

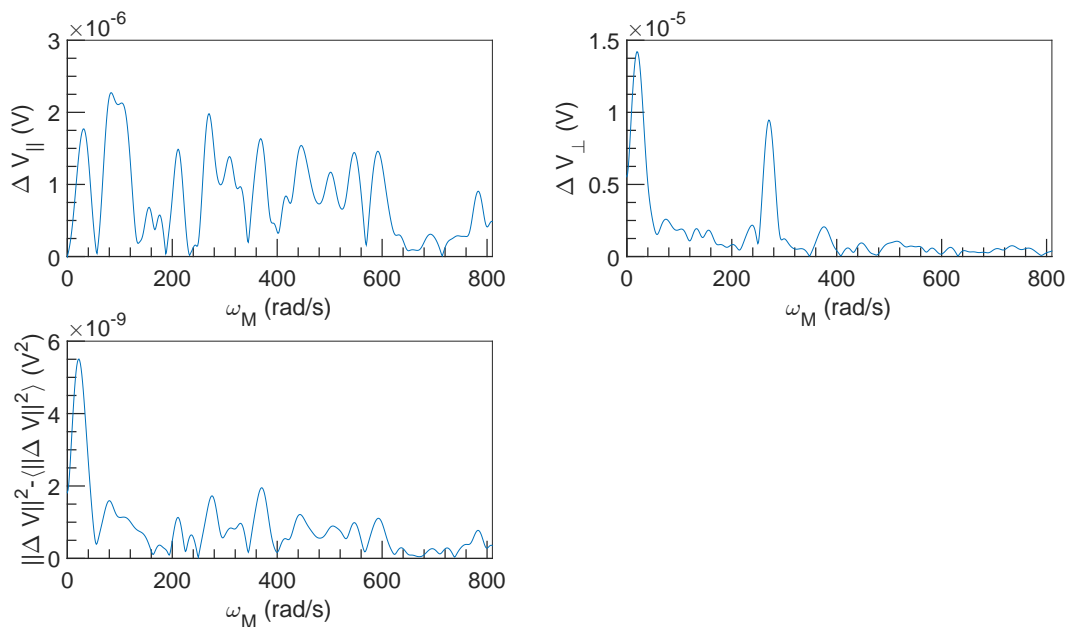


Figure 6.62: FFT spectral density of  $\Delta V$  vs  $\omega_M$  at  $U = 0.75 \text{ m s}^{-1}$ ,  $\omega = 4712 \text{ rad s}^{-1}$  and  $\alpha = 0.06 \%$ .



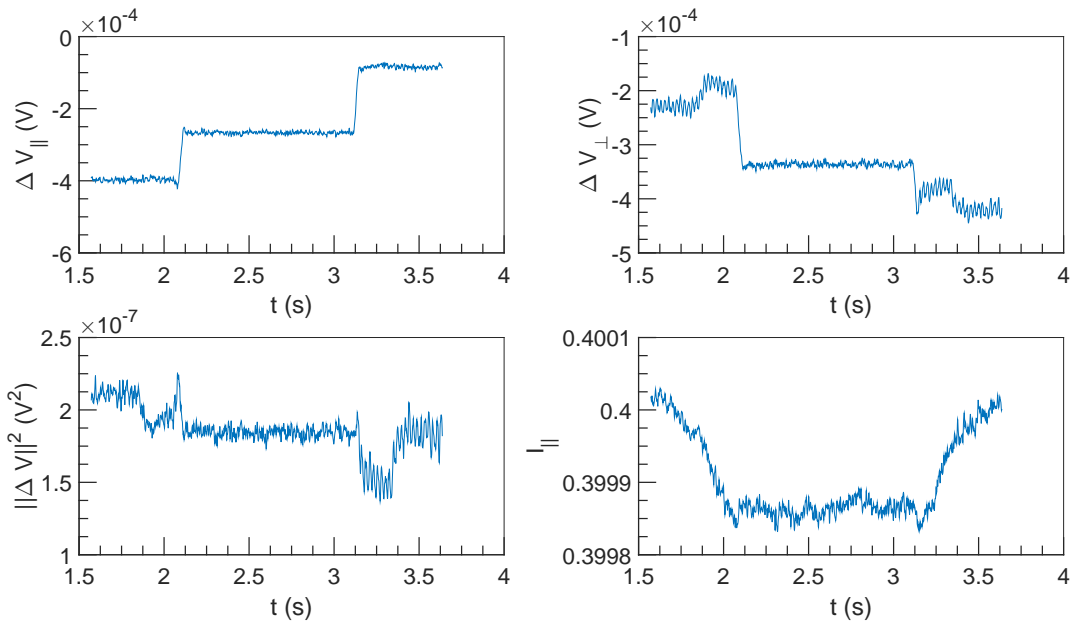


Figure 6.63:  $\Delta V$  and  $I$  vs  $t$  at  $U = 0.75 \text{ m s}^{-1}$ ,  $\omega = 6283 \text{ rad s}^{-1}$  and  $\alpha = 0.06 \%$ .

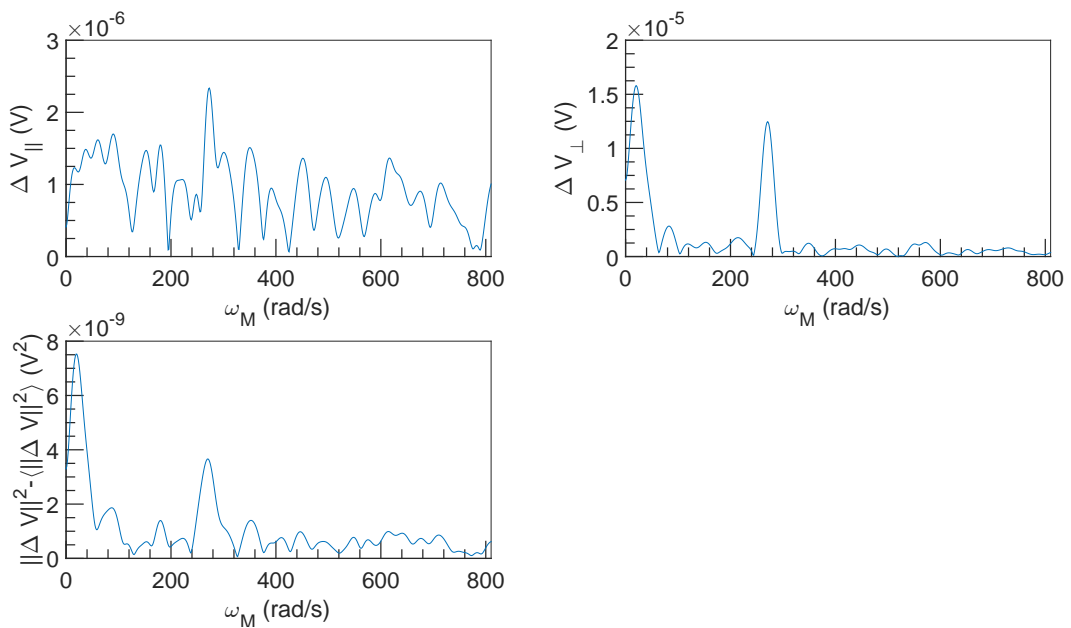


Figure 6.64: FFT spectral density of  $\Delta V$  vs  $\omega_M$  at  $U = 0.75 \text{ m s}^{-1}$ ,  $\omega = 6283 \text{ rad s}^{-1}$  and  $\alpha = 0.06 \%$ .

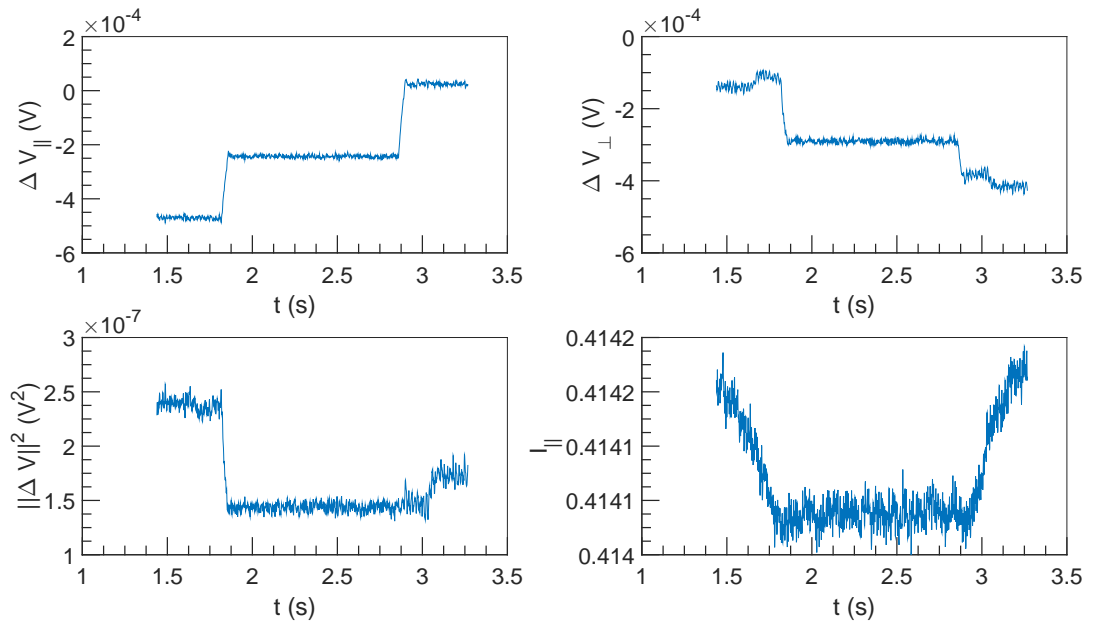


Figure 6.65:  $\Delta V$  and  $I$  vs  $t$  at  $U = 1 \text{ m s}^{-1}$ ,  $\omega = 4712 \text{ rad s}^{-1}$  and  $\alpha = 0.06 \%$ .

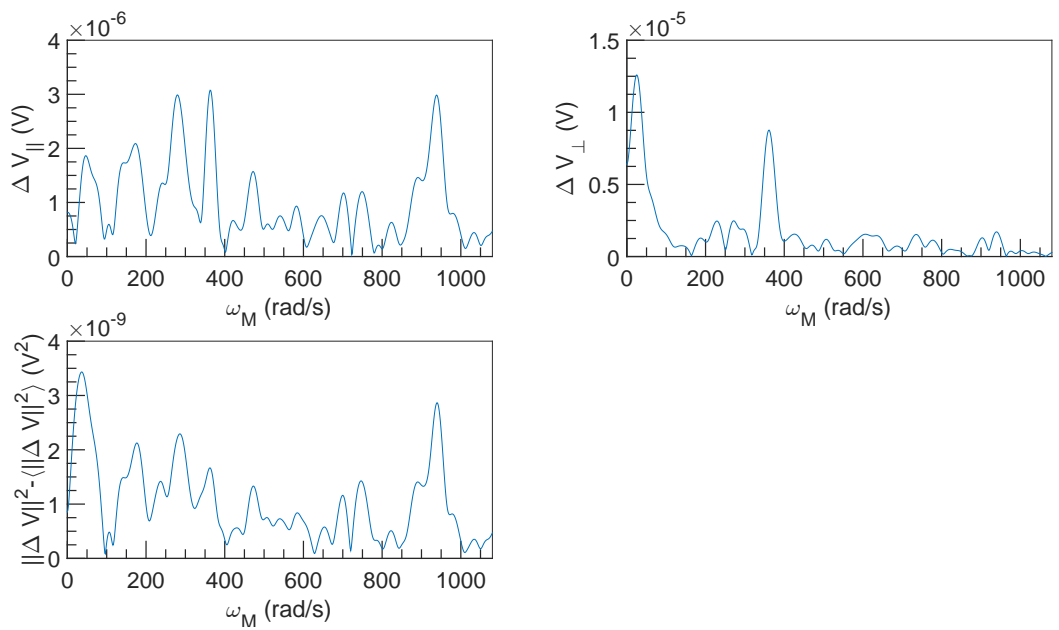


Figure 6.66: FFT spectral density of  $\Delta V$  vs  $\omega_M$  at  $U = 1 \text{ m s}^{-1}$ ,  $\omega = 4712 \text{ rad s}^{-1}$  and  $\alpha = 0.06 \%$ .

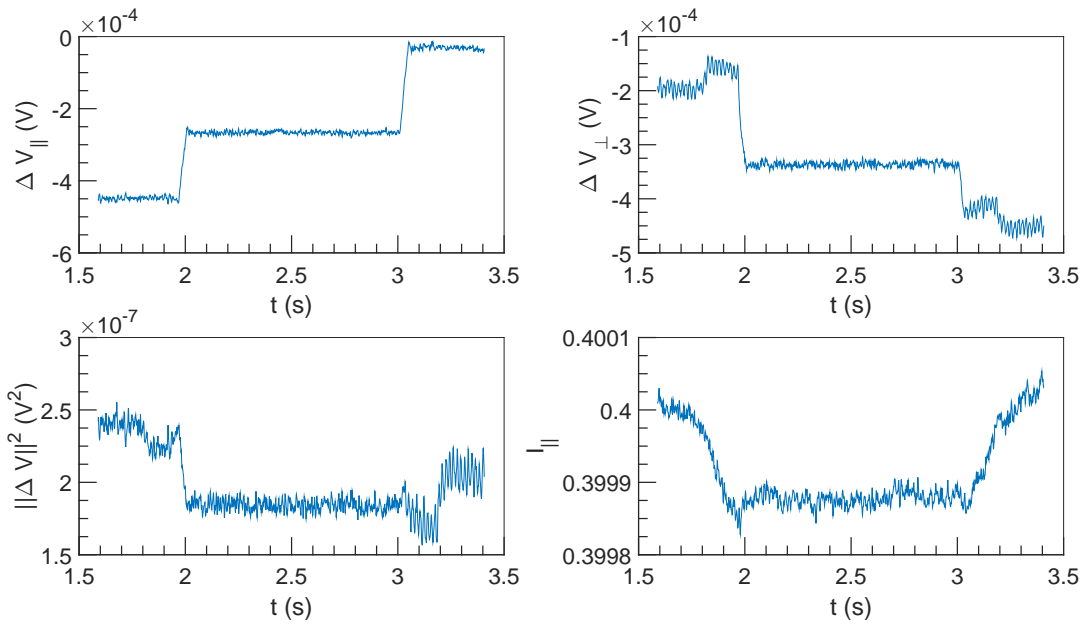


Figure 6.67:  $\Delta V$  and  $I$  vs  $t$  at  $U = 1 \text{ m s}^{-1}$ ,  $\omega = 6283 \text{ rad s}^{-1}$  and  $\alpha = 0.06 \%$ .

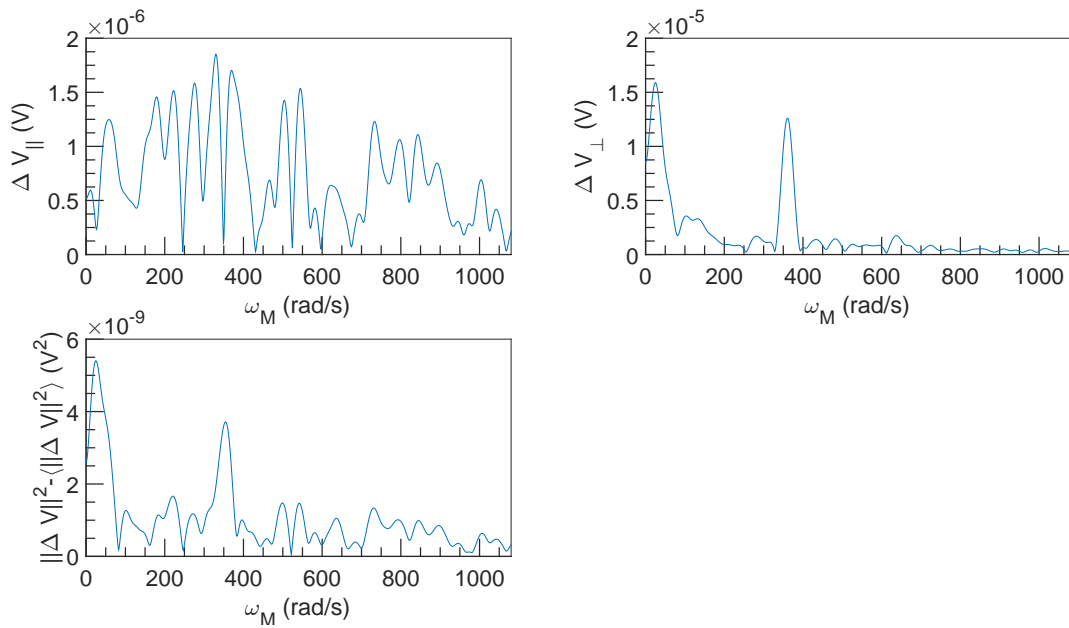


Figure 6.68: FFT spectral density of  $\Delta V$  vs  $\omega_M$  at  $U = 1 \text{ m s}^{-1}$ ,  $\omega = 6283 \text{ rad s}^{-1}$  and  $\alpha = 0.06 \%$ .

## Chapter 7

**For**  $\alpha = 0.22\%$

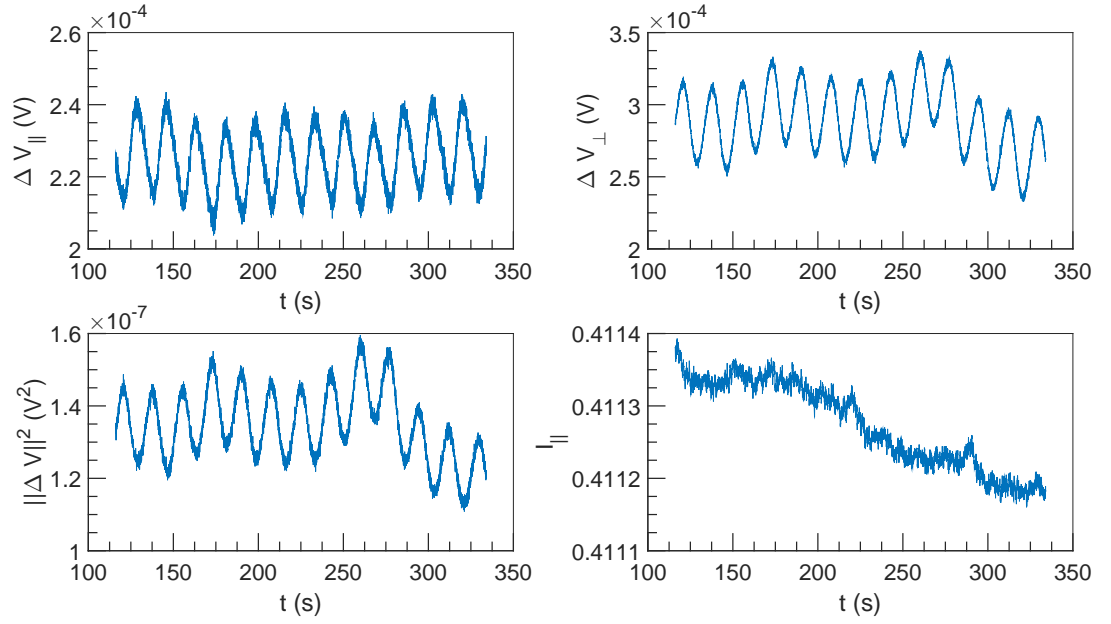


Figure 7.1:  $\Delta V$  and  $I$  vs  $t$  at  $U = 10^{-3} \text{ m s}^{-1}$ ,  $\omega = 4712 \text{ rad s}^{-1}$  and  $\alpha = 0.22 \%$ .

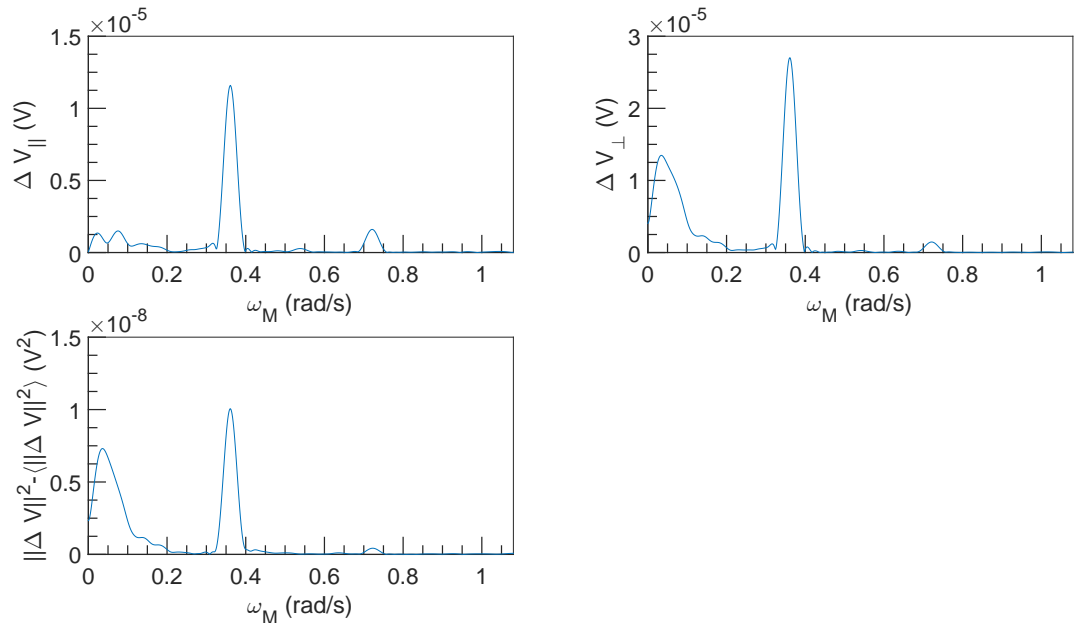


Figure 7.2: FFT spectral density of  $\Delta V$  vs  $\omega_M$  at  $U = 10^{-3} \text{ m s}^{-1}$ ,  $\omega = 4712 \text{ rad s}^{-1}$  and  $\alpha = 0.22 \%$ .

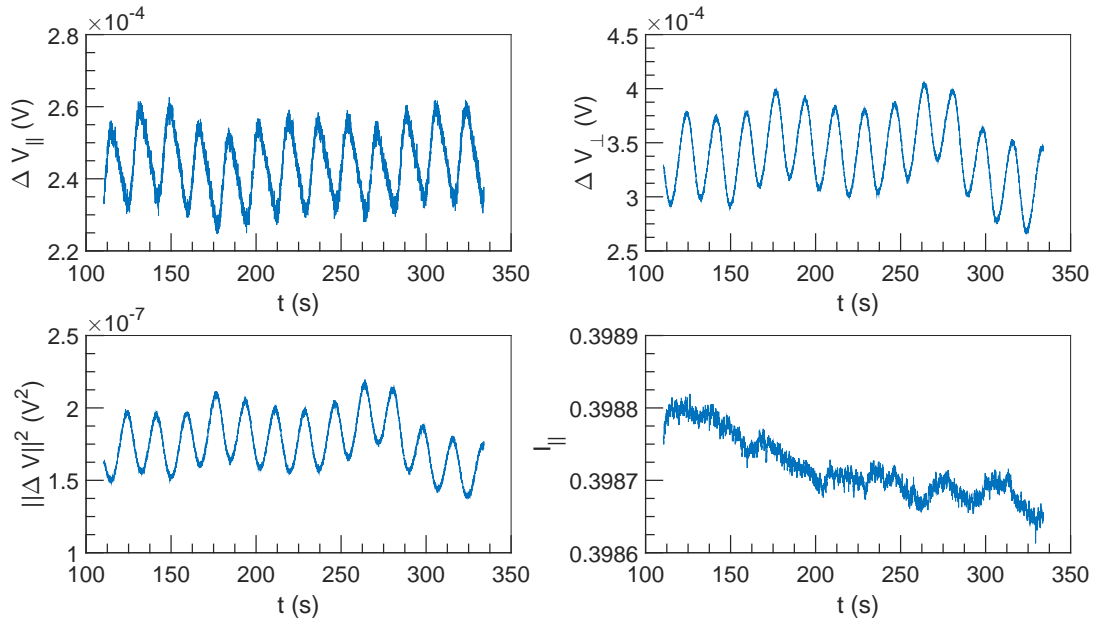


Figure 7.3:  $\Delta V$  and  $I$  vs  $t$  at  $U = 10^{-3} \text{ m s}^{-1}$ ,  $\omega = 6283 \text{ rad s}^{-1}$  and  $\alpha = 0.22 \%$ .

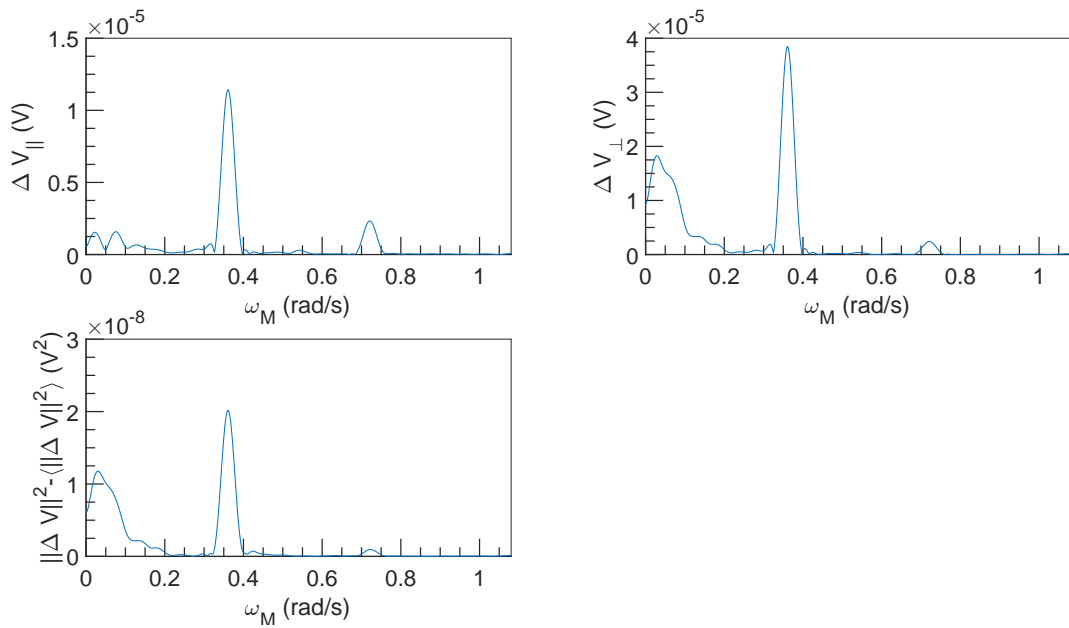


Figure 7.4: FFT spectral density of  $\Delta V$  vs  $\omega_M$  at  $U = 10^{-3} \text{ m s}^{-1}$ ,  $\omega = 6283 \text{ rad s}^{-1}$  and  $\alpha = 0.22 \%$ .

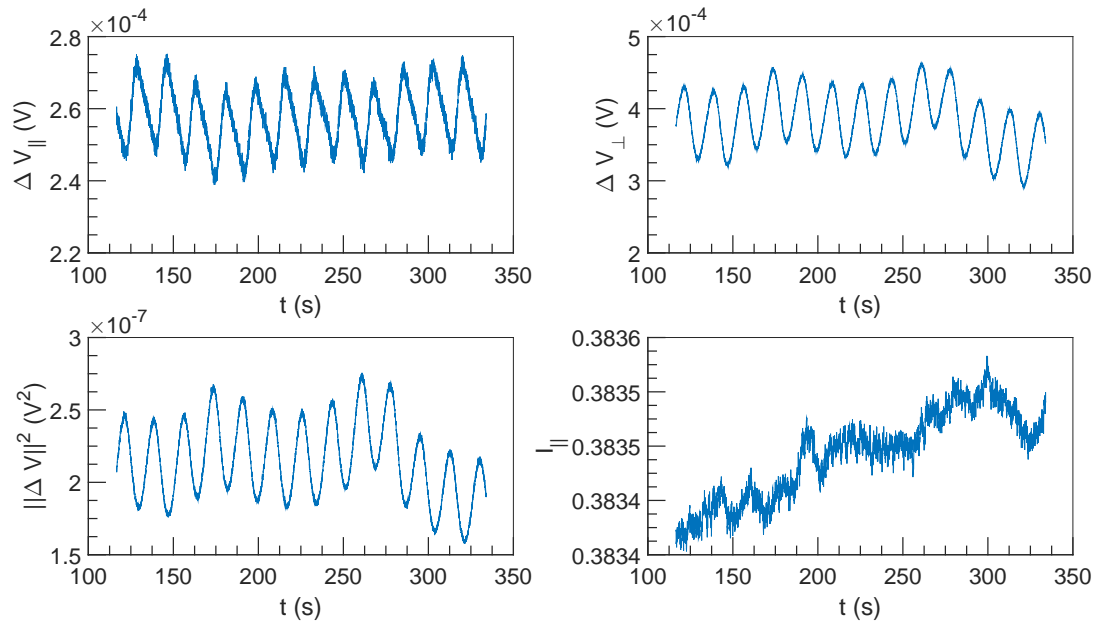


Figure 7.5:  $\Delta V$  and  $I$  vs  $t$  at  $U = 10^{-3} \text{ m s}^{-1}$ ,  $\omega = 7854 \text{ rad s}^{-1}$  and  $\alpha = 0.22 \%$ .

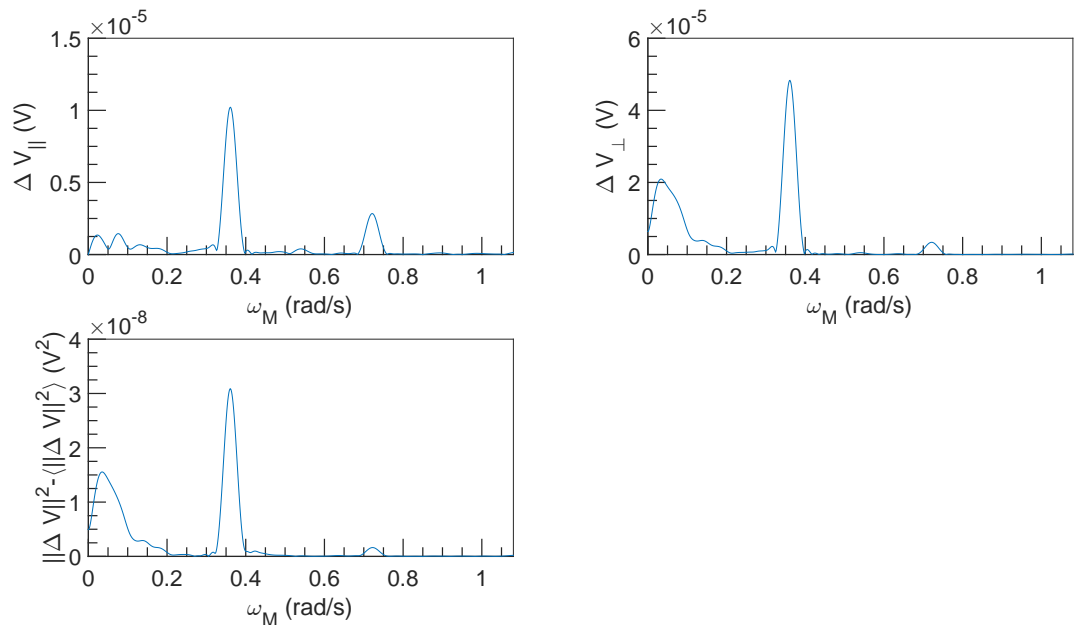


Figure 7.6: FFT spectral density of  $\Delta V$  vs  $\omega_M$  at  $U = 10^{-3} \text{ m s}^{-1}$ ,  $\omega = 7854 \text{ rad s}^{-1}$  and  $\alpha = 0.22 \%$ .

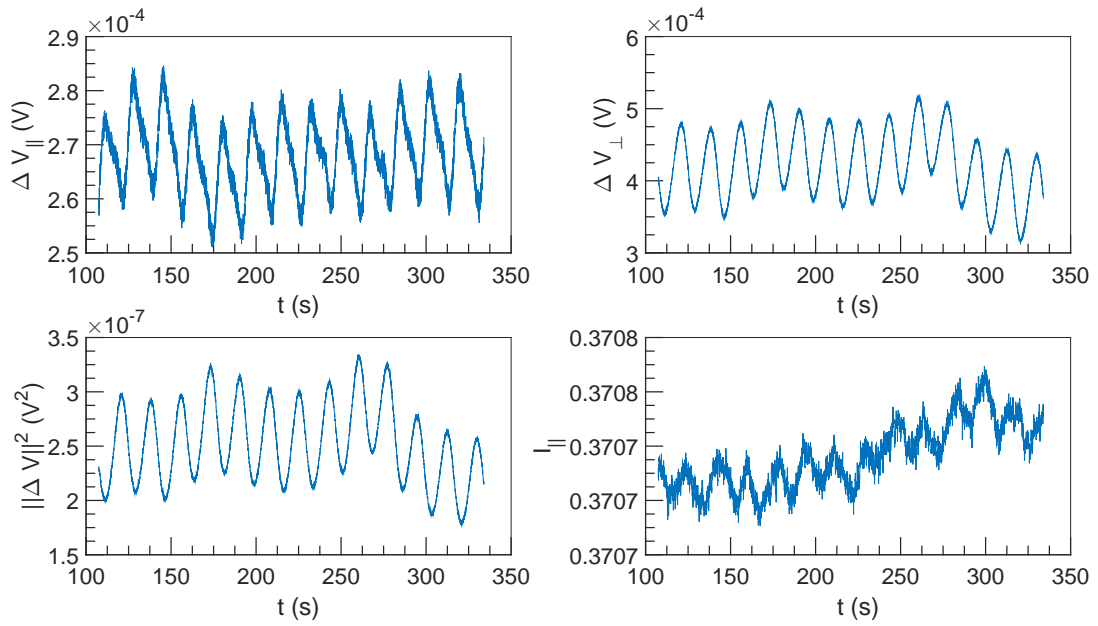


Figure 7.7:  $\Delta V$  and  $I$  vs  $t$  at  $U = 10^{-3} \text{ m s}^{-1}$ ,  $\omega = 9425 \text{ rad s}^{-1}$  and  $\alpha = 0.22 \%$ .

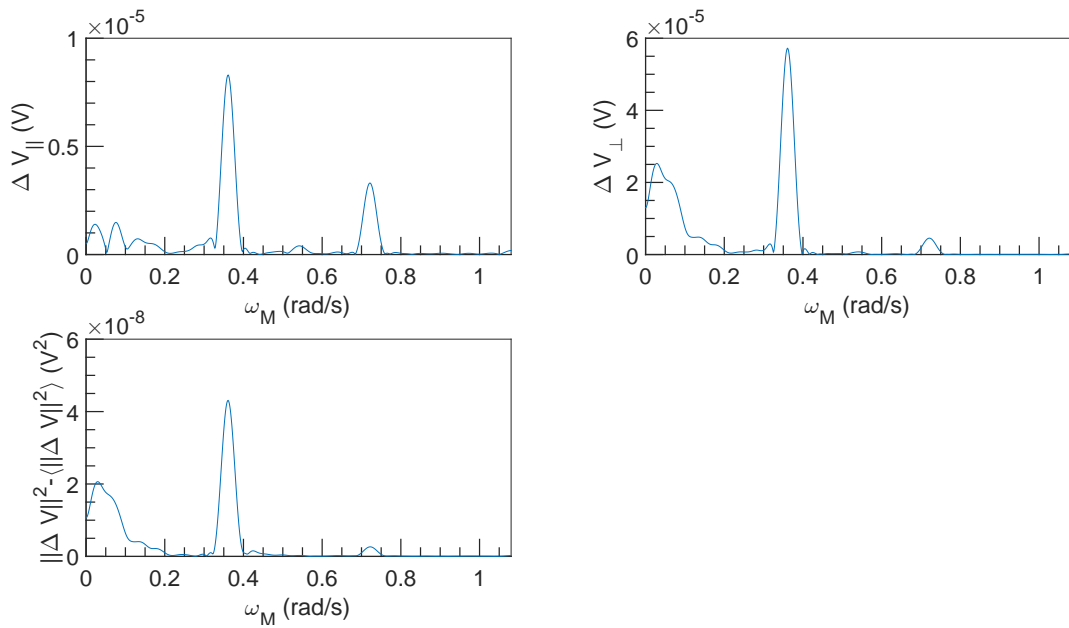


Figure 7.8: FFT spectral density of  $\Delta V$  vs  $\omega_M$  at  $U = 10^{-3} \text{ m s}^{-1}$ ,  $\omega = 9425 \text{ rad s}^{-1}$  and  $\alpha = 0.22 \%$ .



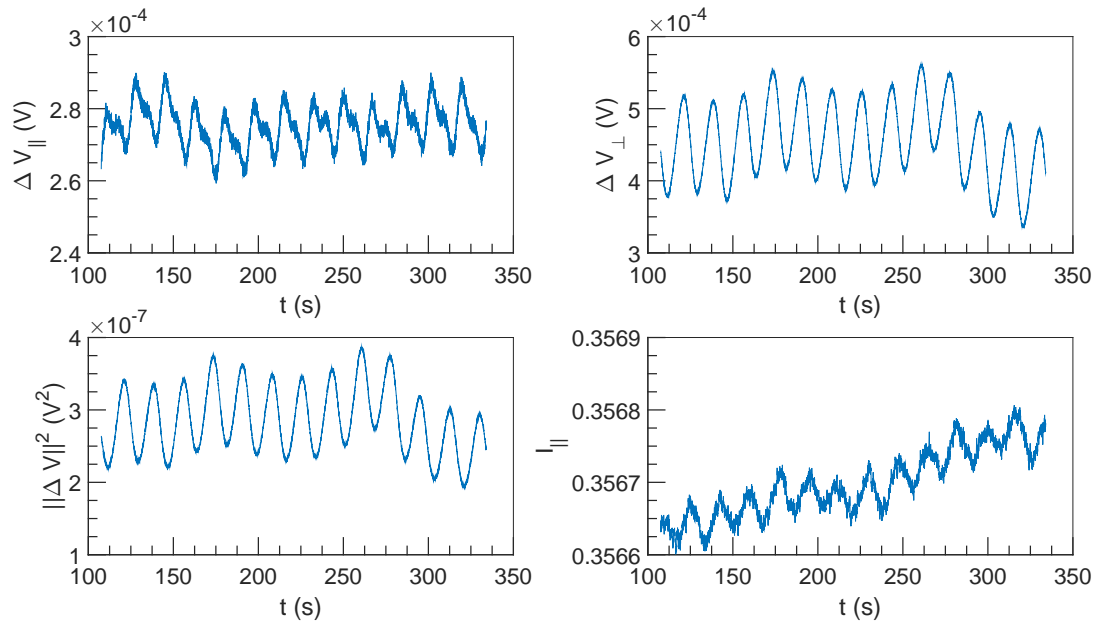


Figure 7.9:  $\Delta V$  and  $I$  vs  $t$  at  $U = 10^{-3} \text{ m s}^{-1}$ ,  $\omega = 10\,996 \text{ rad s}^{-1}$  and  $\alpha = 0.22\%$ .

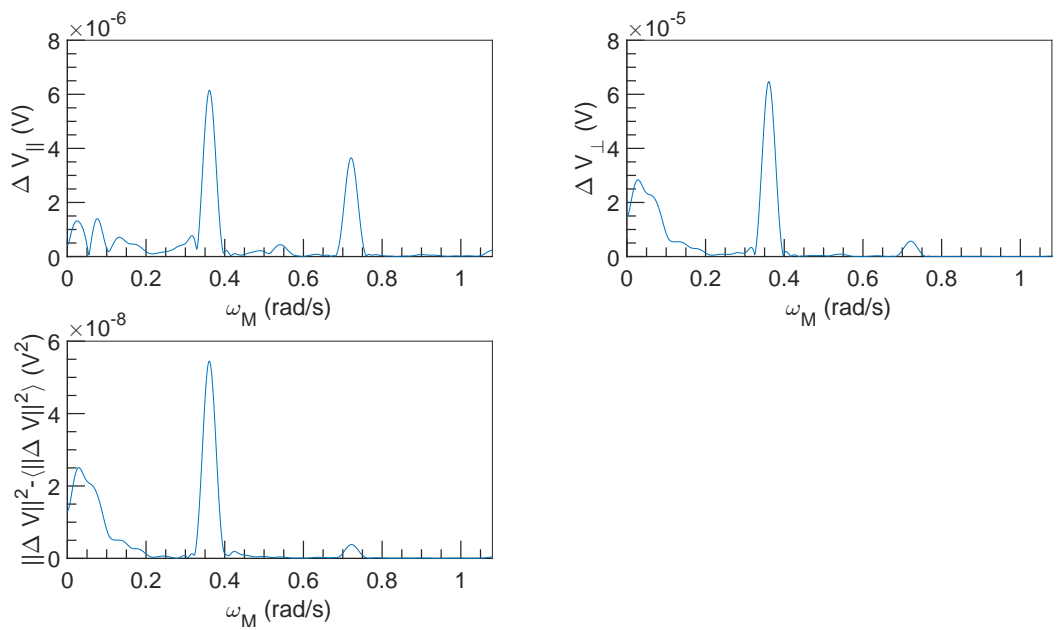


Figure 7.10: FFT spectral density of  $\Delta V$  vs  $\omega_M$  at  $U = 10^{-3} \text{ m s}^{-1}$ ,  $\omega = 10\,996 \text{ rad s}^{-1}$  and  $\alpha = 0.22\%$ .

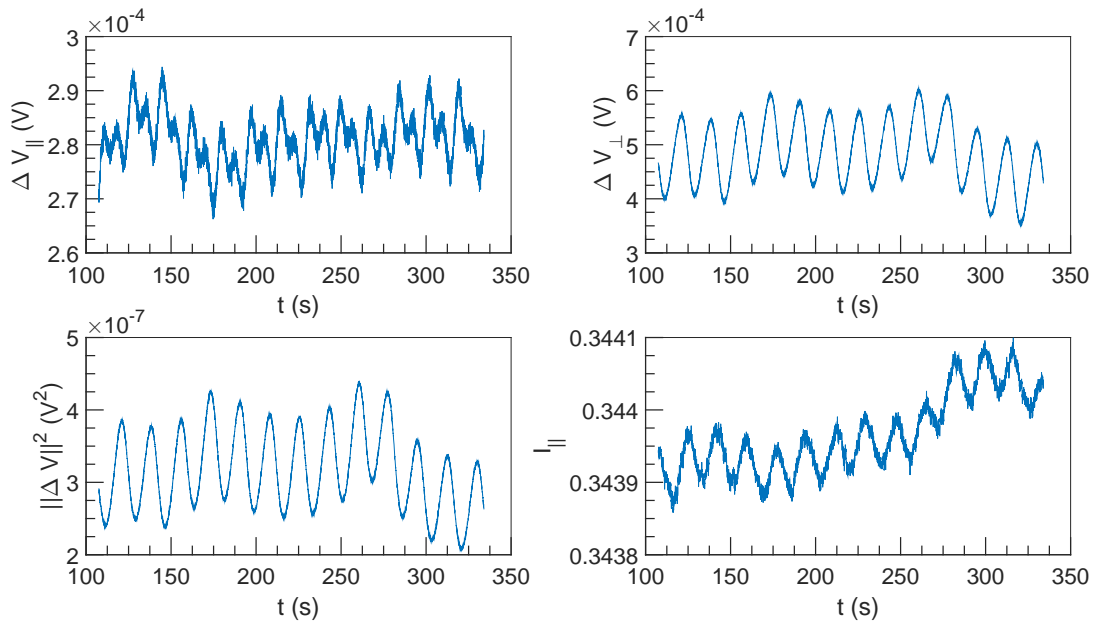


Figure 7.11:  $\Delta V$  and  $I$  vs  $t$  at  $U = 10^{-3} \text{ m s}^{-1}$ ,  $\omega = 12\,566 \text{ rad s}^{-1}$  and  $\alpha = 0.22\%$ .

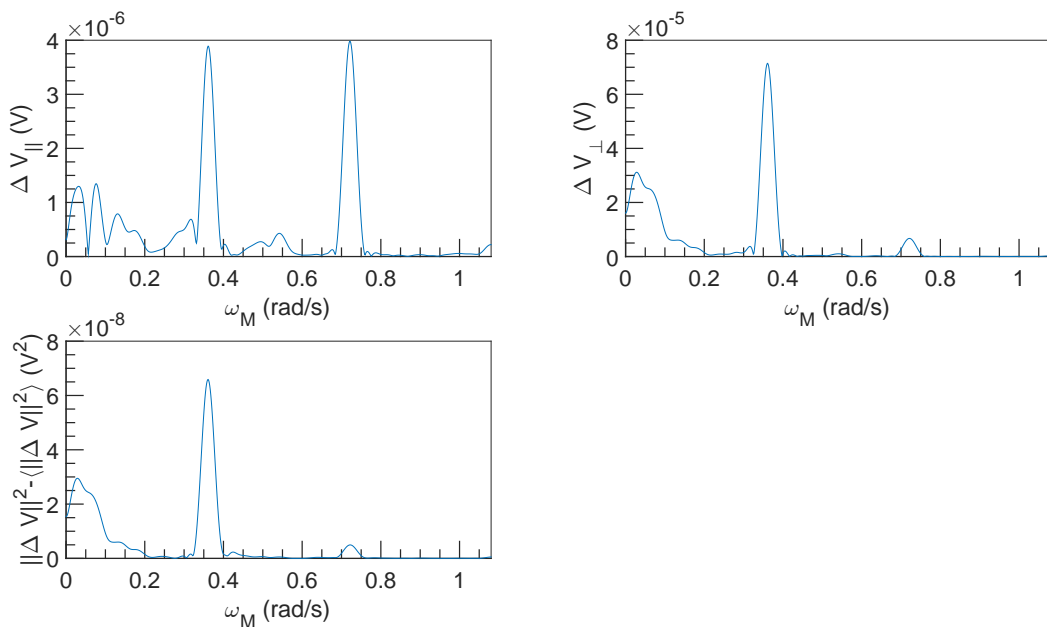


Figure 7.12: FFT spectral density of  $\Delta V$  vs  $\omega_M$  at  $U = 10^{-3} \text{ m s}^{-1}$ ,  $\omega = 12\,566 \text{ rad s}^{-1}$  and  $\alpha = 0.22\%$ .

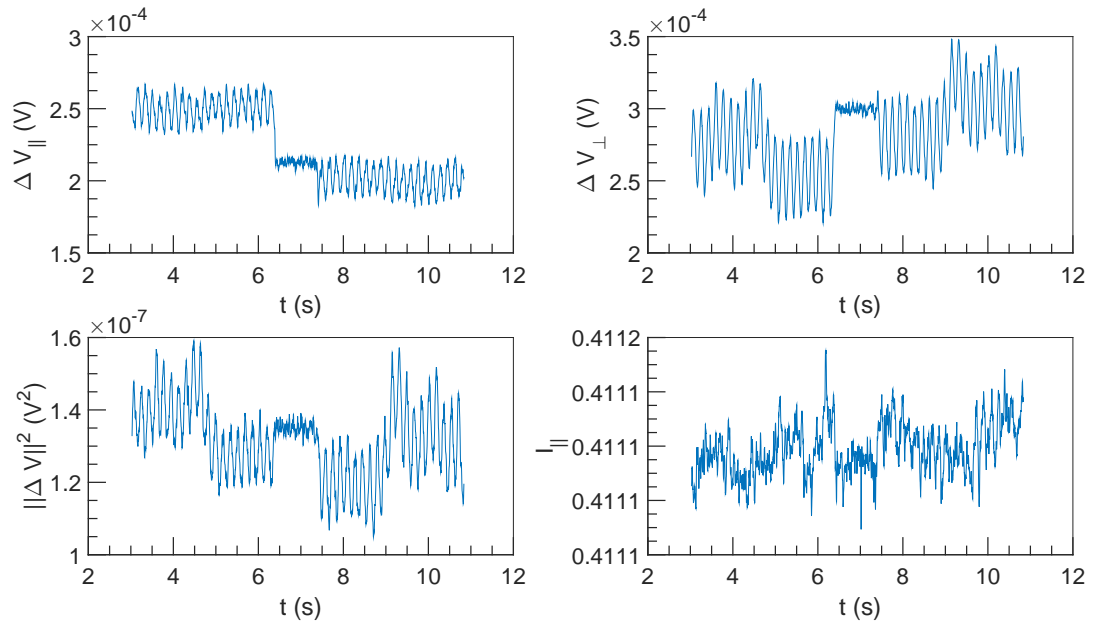


Figure 7.13:  $\Delta V$  and  $I$  vs  $t$  at  $U = 0.1 \text{ m s}^{-1}$ ,  $\omega = 4712 \text{ rad s}^{-1}$  and  $\alpha = 0.22 \%$ .

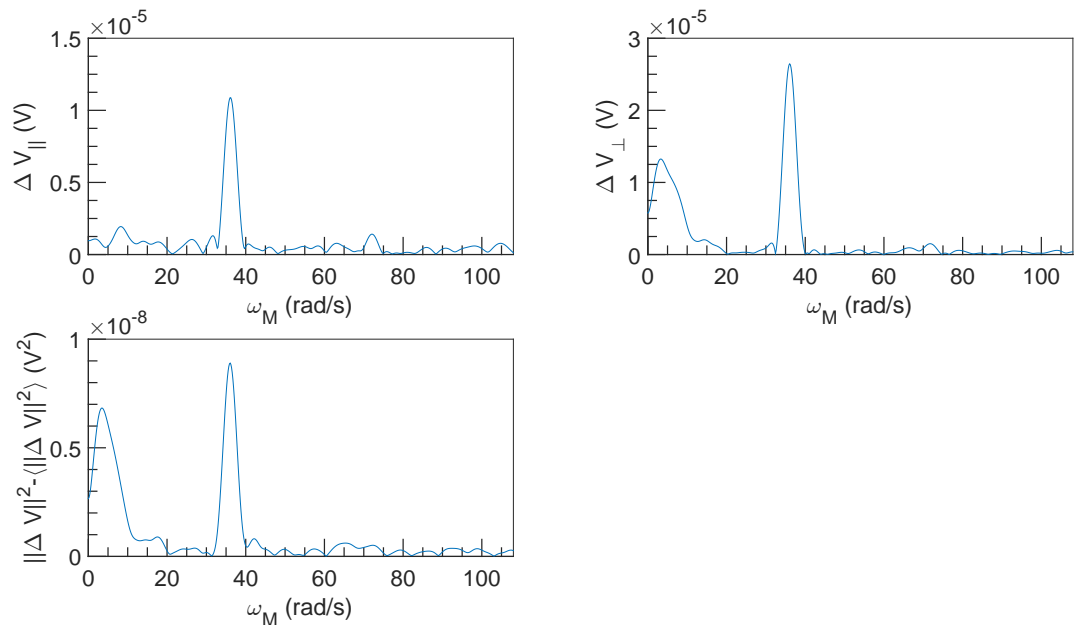


Figure 7.14: FFT spectral density of  $\Delta V$  vs  $\omega_M$  at  $U = 0.1 \text{ m s}^{-1}$ ,  $\omega = 4712 \text{ rad s}^{-1}$  and  $\alpha = 0.22 \%$ .

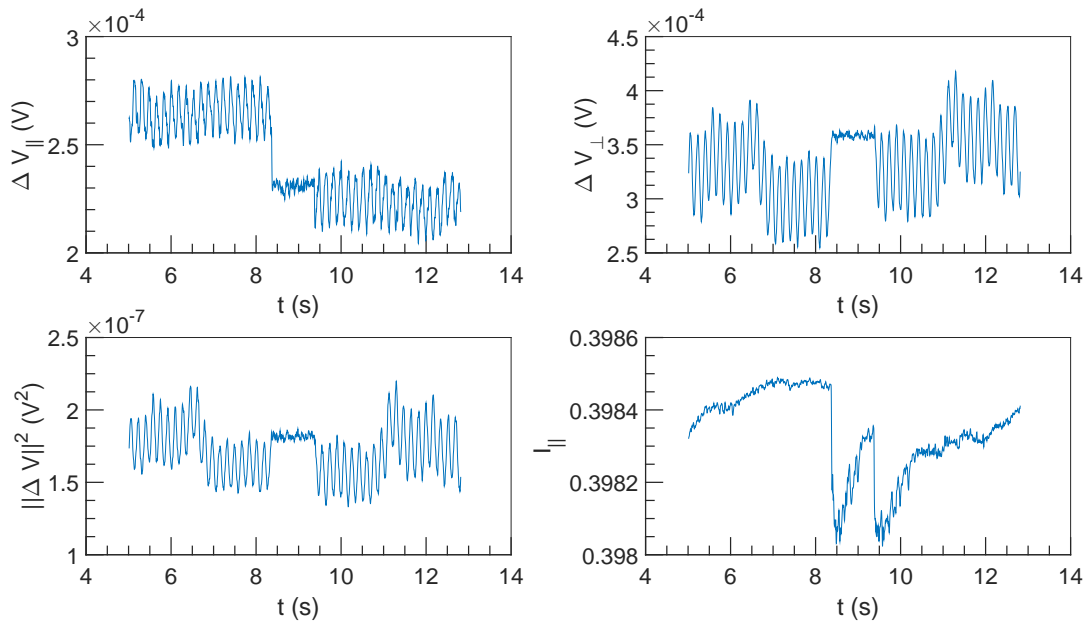


Figure 7.15:  $\Delta V$  and  $I$  vs  $t$  at  $U = 0.1 \text{ m s}^{-1}$ ,  $\omega = 6283 \text{ rad s}^{-1}$  and  $\alpha = 0.22 \%$ .

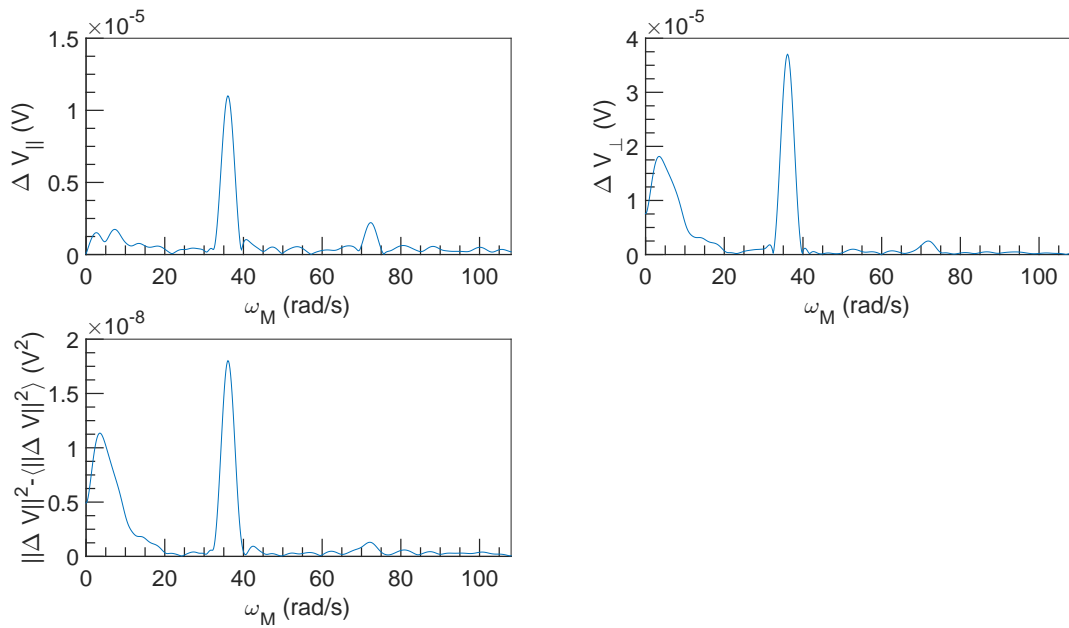


Figure 7.16: FFT spectral density of  $\Delta V$  vs  $\omega_M$  at  $U = 0.1 \text{ m s}^{-1}$ ,  $\omega = 6283 \text{ rad s}^{-1}$  and  $\alpha = 0.22 \%$ .

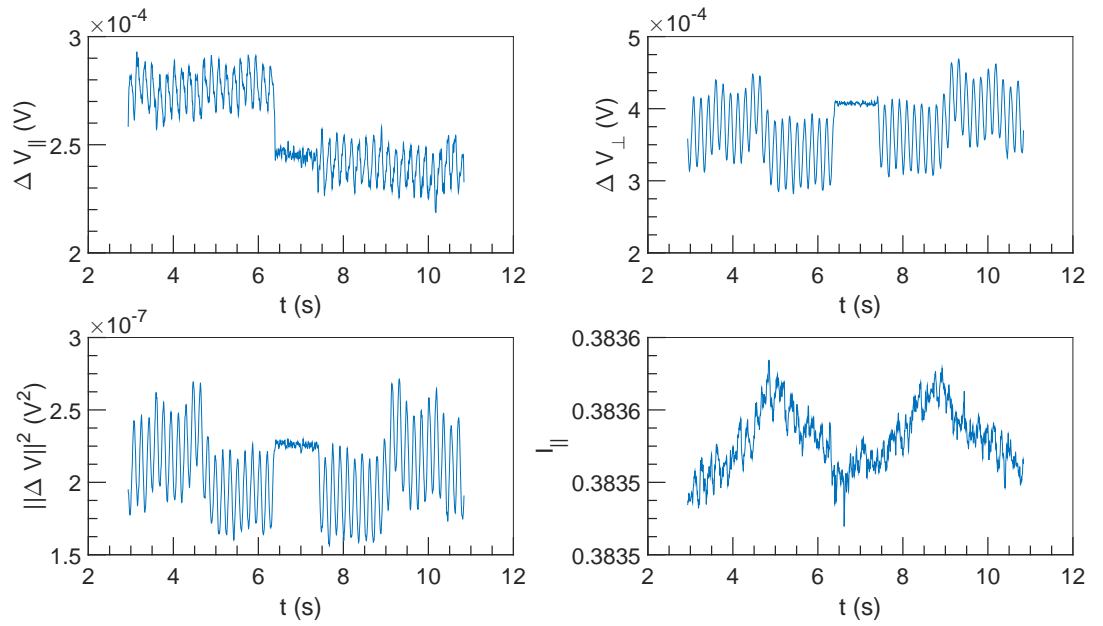


Figure 7.17:  $\Delta V$  and  $I$  vs  $t$  at  $U = 0.1 \text{ m s}^{-1}$ ,  $\omega = 7854 \text{ rad s}^{-1}$  and  $\alpha = 0.22 \%$ .

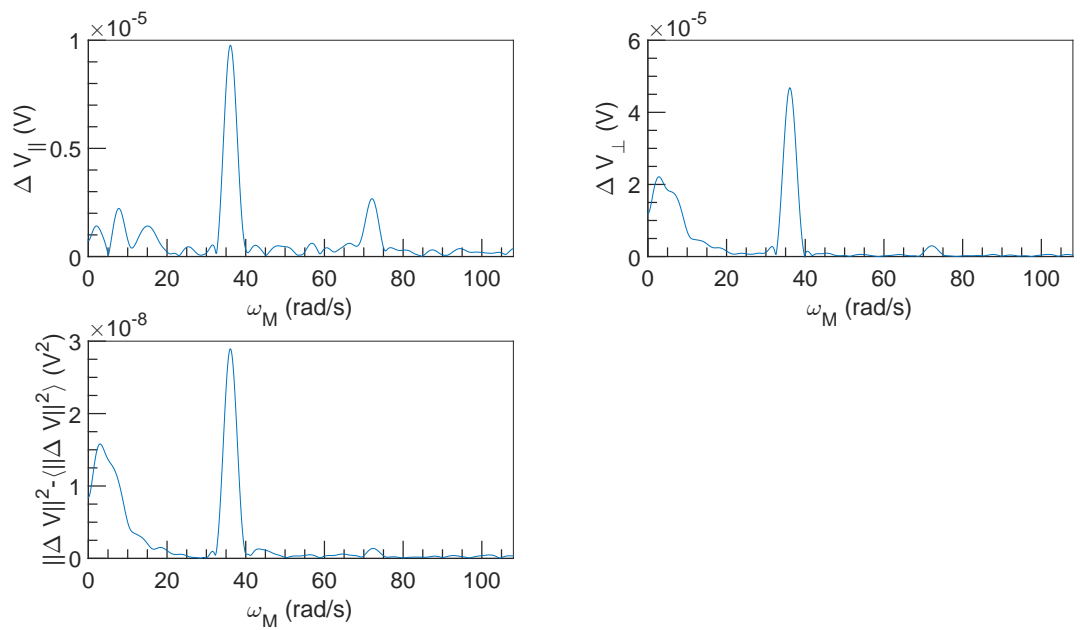


Figure 7.18: FFT spectral density of  $\Delta V$  vs  $\omega_M$  at  $U = 0.1 \text{ m s}^{-1}$ ,  $\omega = 7854 \text{ rad s}^{-1}$  and  $\alpha = 0.22 \%$ .

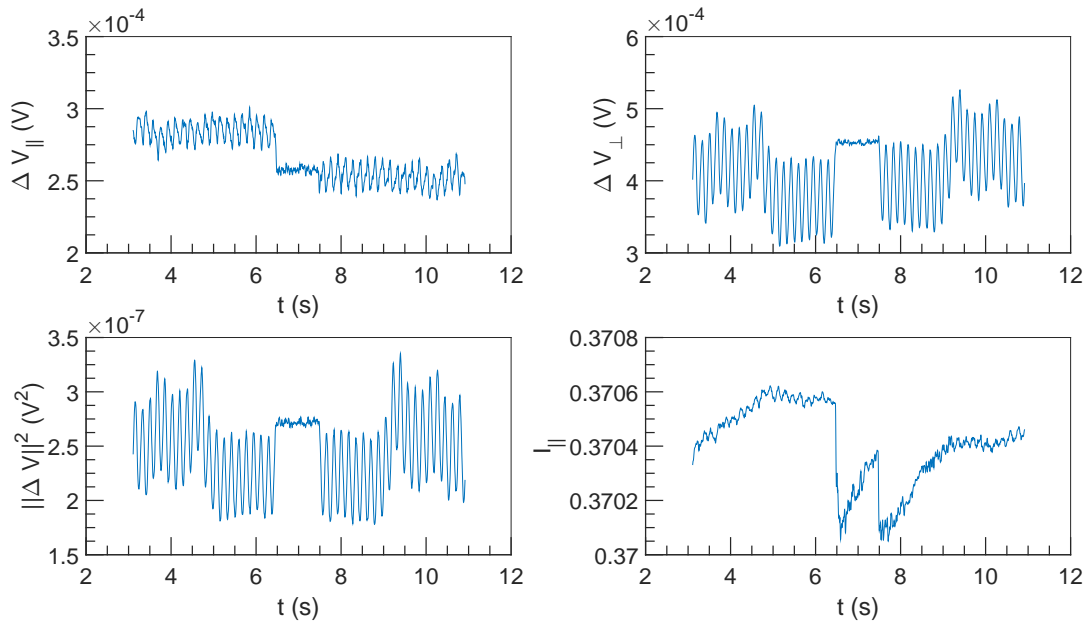


Figure 7.19:  $\Delta V$  and  $I$  vs  $t$  at  $U = 0.1 \text{ m s}^{-1}$ ,  $\omega = 9425 \text{ rad s}^{-1}$  and  $\alpha = 0.22 \%$ .

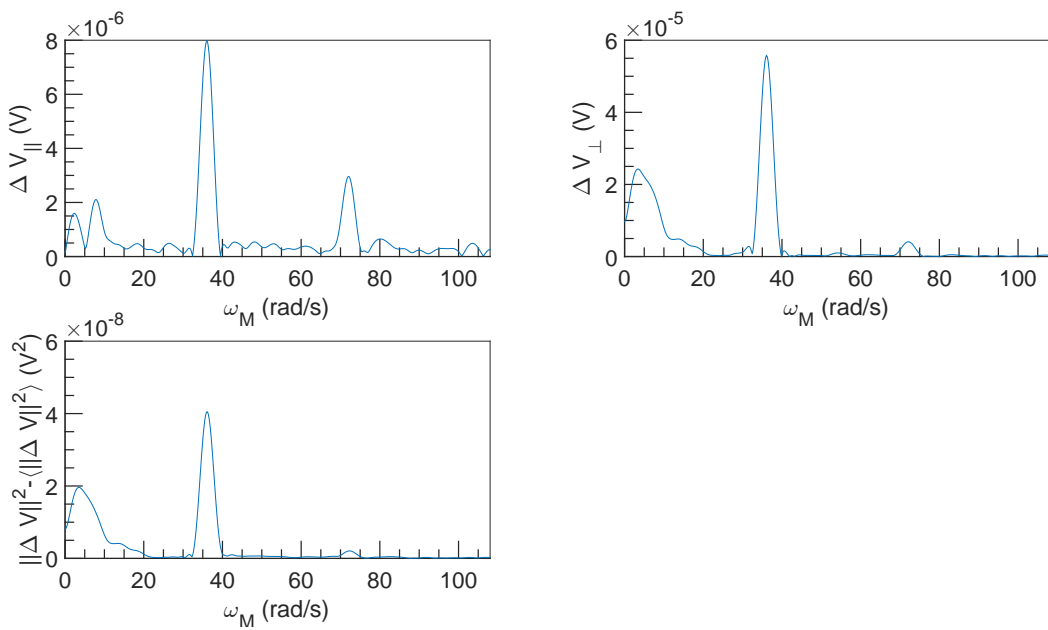


Figure 7.20: FFT spectral density of  $\Delta V$  vs  $\omega_M$  at  $U = 0.1 \text{ m s}^{-1}$ ,  $\omega = 9425 \text{ rad s}^{-1}$  and  $\alpha = 0.22 \%$ .

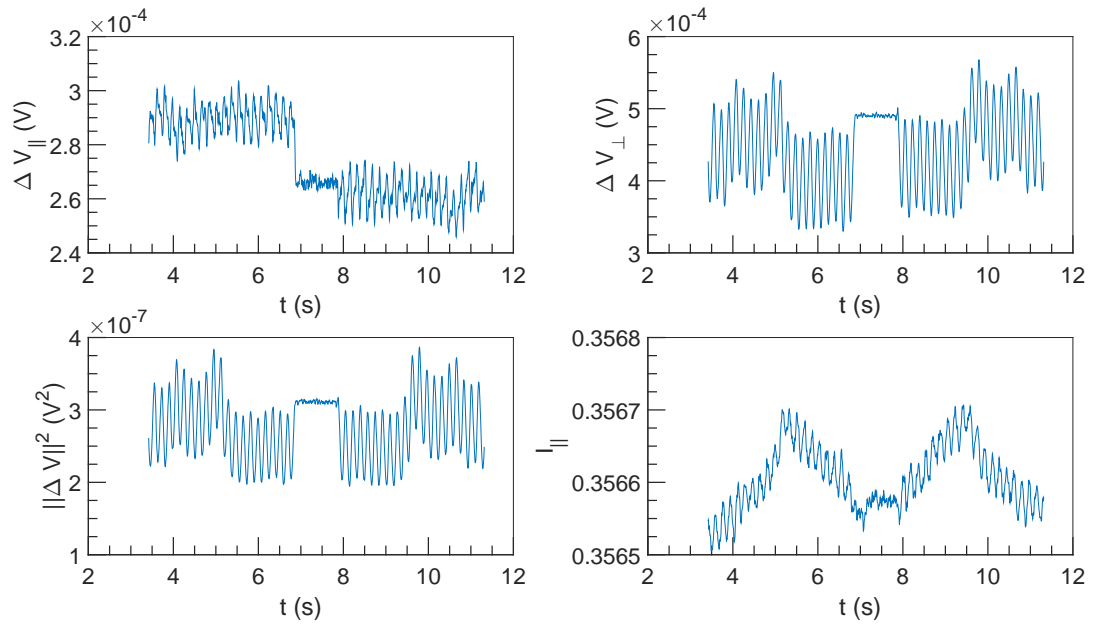


Figure 7.21:  $\Delta V$  and  $I$  vs  $t$  at  $U = 0.1 \text{ m s}^{-1}$ ,  $\omega = 10\,996 \text{ rad s}^{-1}$  and  $\alpha = 0.22\%$ .

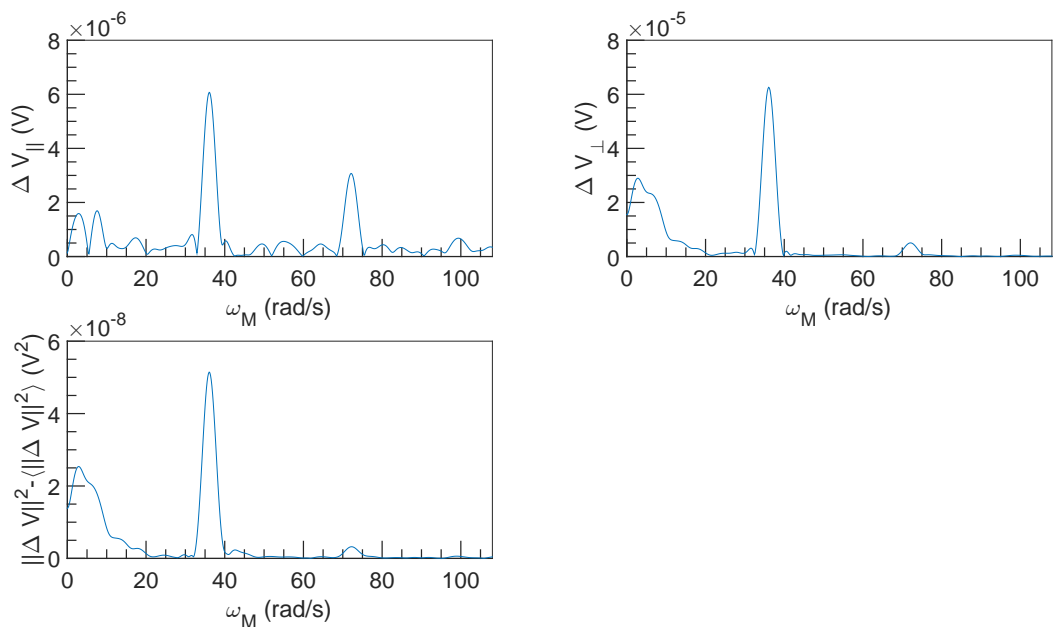


Figure 7.22: FFT spectral density of  $\Delta V$  vs  $\omega_M$  at  $U = 0.1 \text{ m s}^{-1}$ ,  $\omega = 10\,996 \text{ rad s}^{-1}$  and  $\alpha = 0.22\%$ .

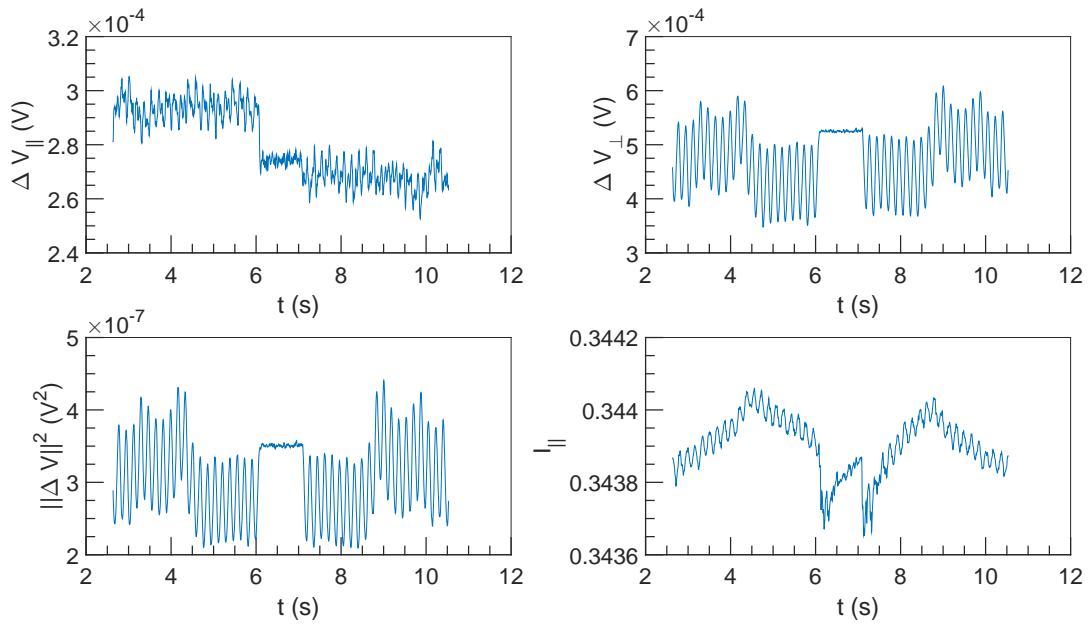


Figure 7.23:  $\Delta V$  and  $I$  vs  $t$  at  $U = 0.1 \text{ m s}^{-1}$ ,  $\omega = 12566 \text{ rad s}^{-1}$  and  $\alpha = 0.22 \%$ .

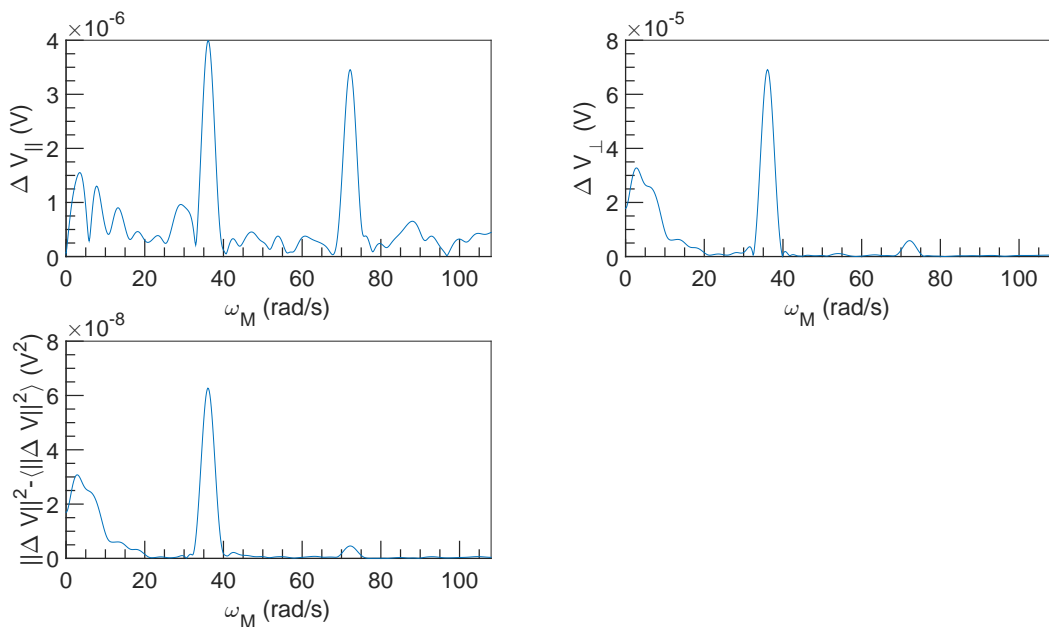


Figure 7.24: FFT spectral density of  $\Delta V$  vs  $\omega_M$  at  $U = 0.1 \text{ m s}^{-1}$ ,  $\omega = 12566 \text{ rad s}^{-1}$  and  $\alpha = 0.22 \%$ .



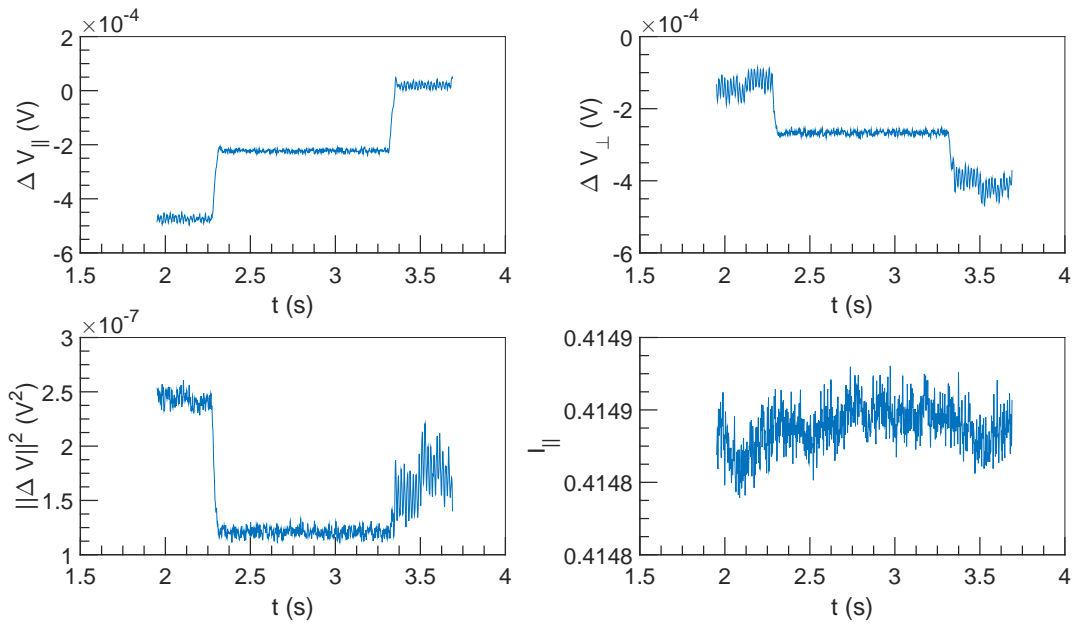


Figure 7.25:  $\Delta V$  and  $I$  vs  $t$  at  $U = 1 \text{ m s}^{-1}$ ,  $\omega = 4712 \text{ rad s}^{-1}$  and  $\alpha = 0.22 \%$ .

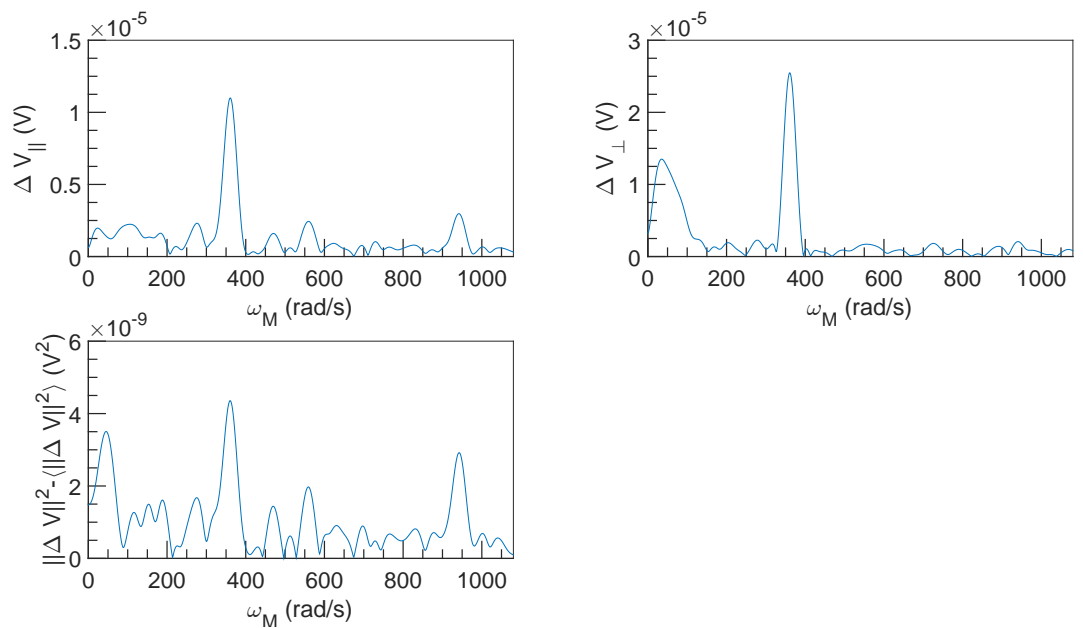


Figure 7.26: FFT spectral density of  $\Delta V$  vs  $\omega_M$  at  $U = 1 \text{ m s}^{-1}$ ,  $\omega = 4712 \text{ rad s}^{-1}$  and  $\alpha = 0.22 \%$ .

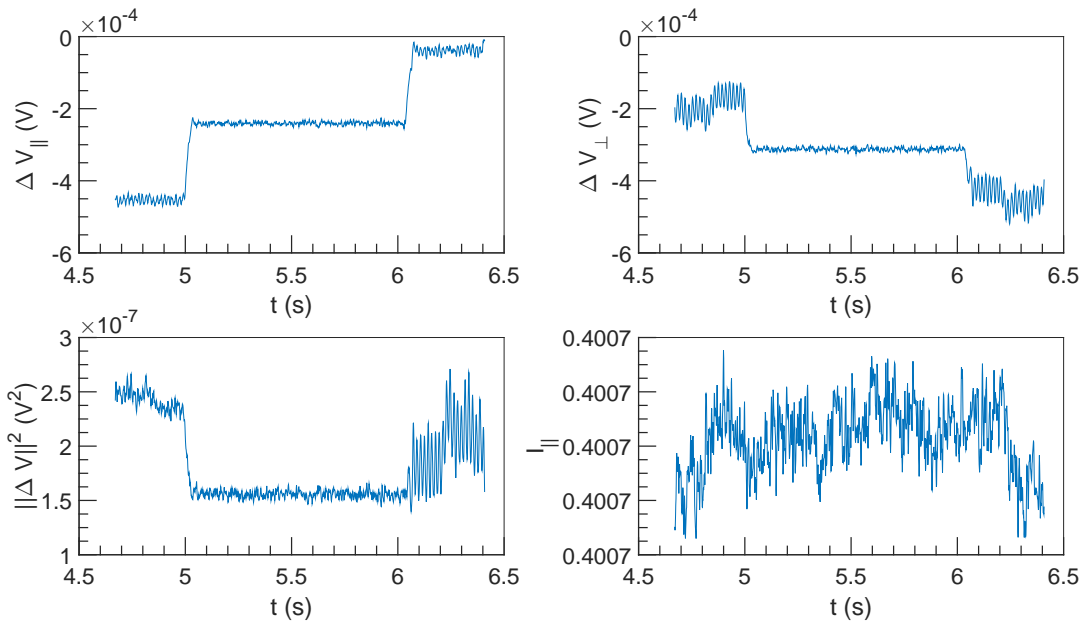


Figure 7.27:  $\Delta V$  and  $I$  vs  $t$  at  $U = 1 \text{ m s}^{-1}$ ,  $\omega = 6283 \text{ rad s}^{-1}$  and  $\alpha = 0.22 \%$ .

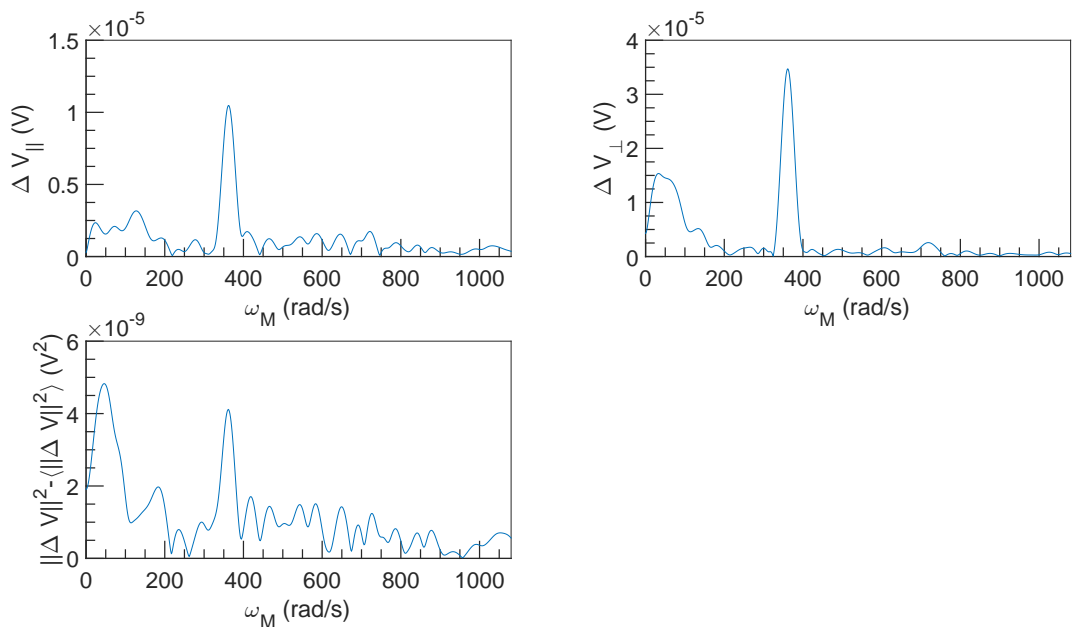


Figure 7.28: FFT spectral density of  $\Delta V$  vs  $\omega_M$  at  $U = 1 \text{ m s}^{-1}$ ,  $\omega = 6283 \text{ rad s}^{-1}$  and  $\alpha = 0.22 \%$ .

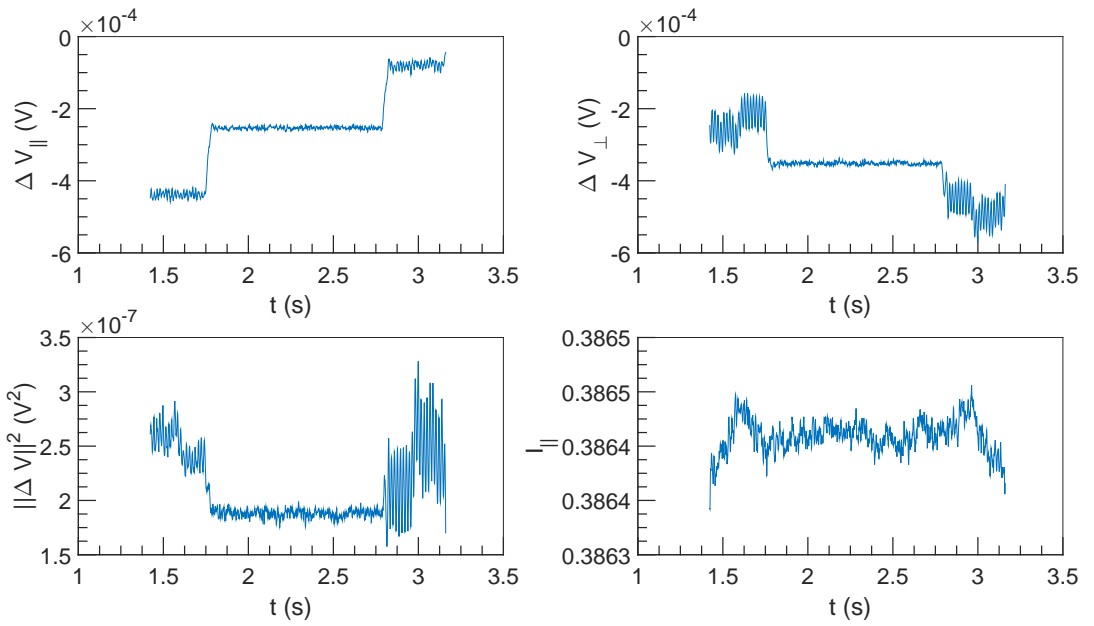


Figure 7.29:  $\Delta V$  and  $I$  vs  $t$  at  $U = 1 \text{ m s}^{-1}$ ,  $\omega = 7854 \text{ rad s}^{-1}$  and  $\alpha = 0.22 \%$ .

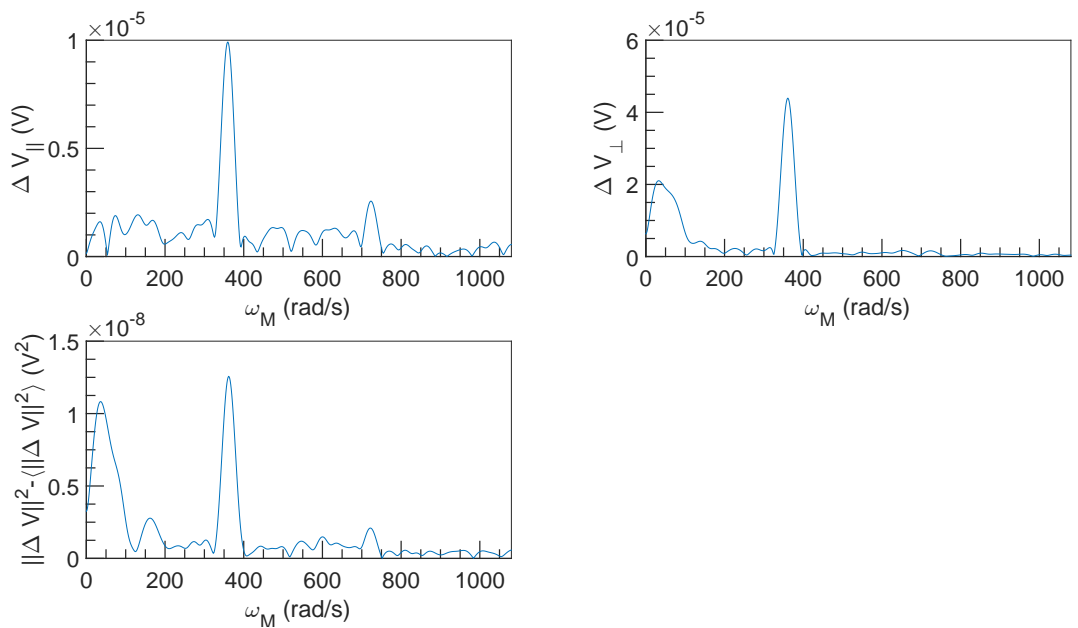


Figure 7.30: FFT spectral density of  $\Delta V$  vs  $\omega_M$  at  $U = 1 \text{ m s}^{-1}$ ,  $\omega = 7854 \text{ rad s}^{-1}$  and  $\alpha = 0.22 \%$ .

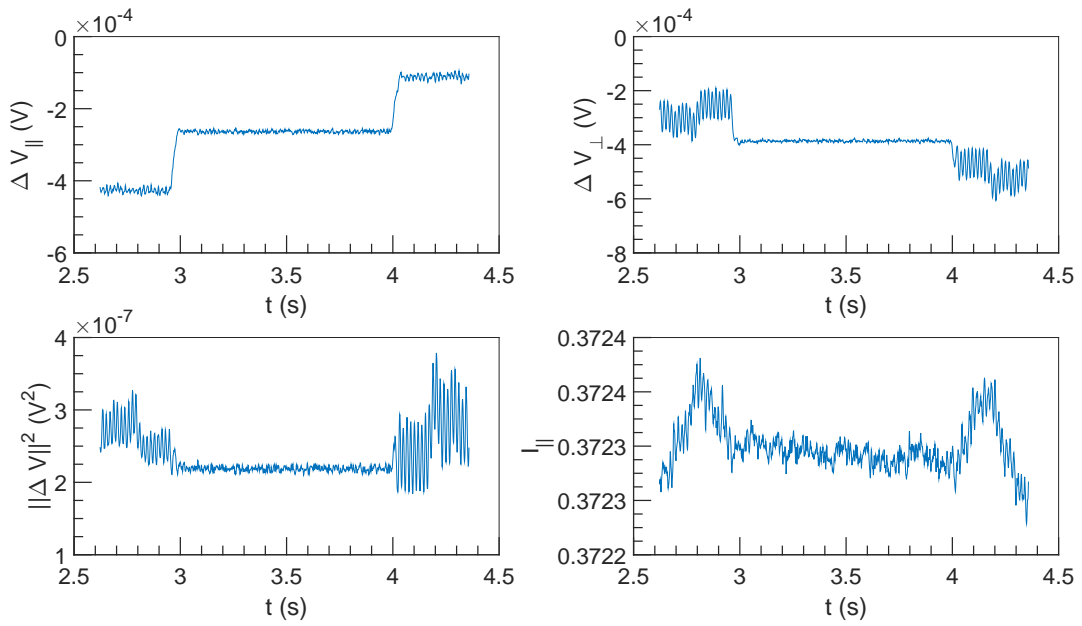


Figure 7.31:  $\Delta V$  and  $I$  vs  $t$  at  $U = 1 \text{ m s}^{-1}$ ,  $\omega = 9425 \text{ rad s}^{-1}$  and  $\alpha = 0.22 \%$ .

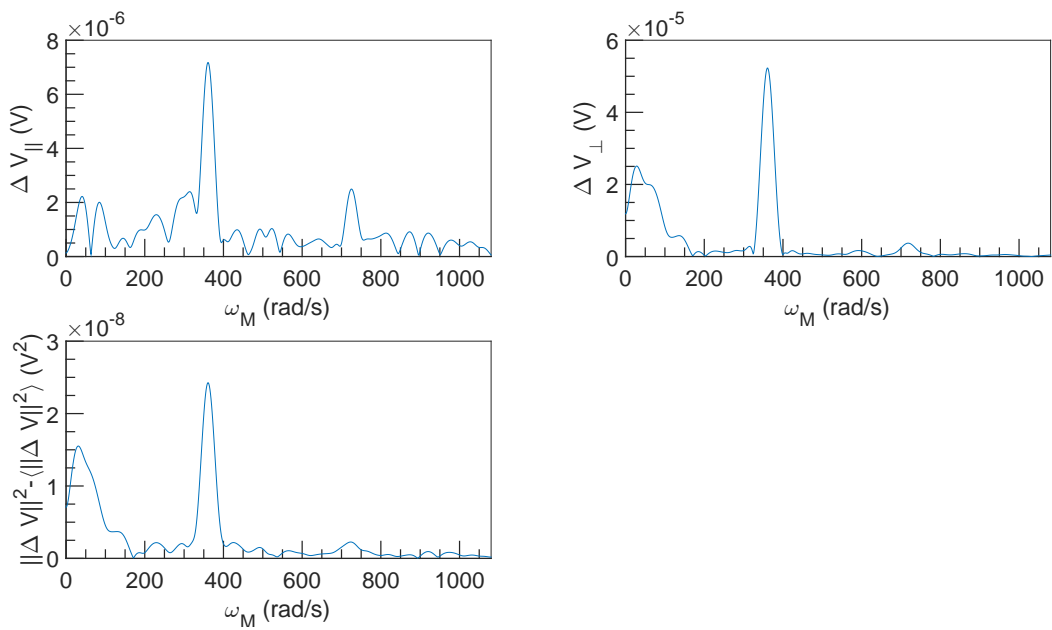


Figure 7.32: FFT spectral density of  $\Delta V$  vs  $\omega_M$  at  $U = 1 \text{ m s}^{-1}$ ,  $\omega = 9425 \text{ rad s}^{-1}$  and  $\alpha = 0.22 \%$ .

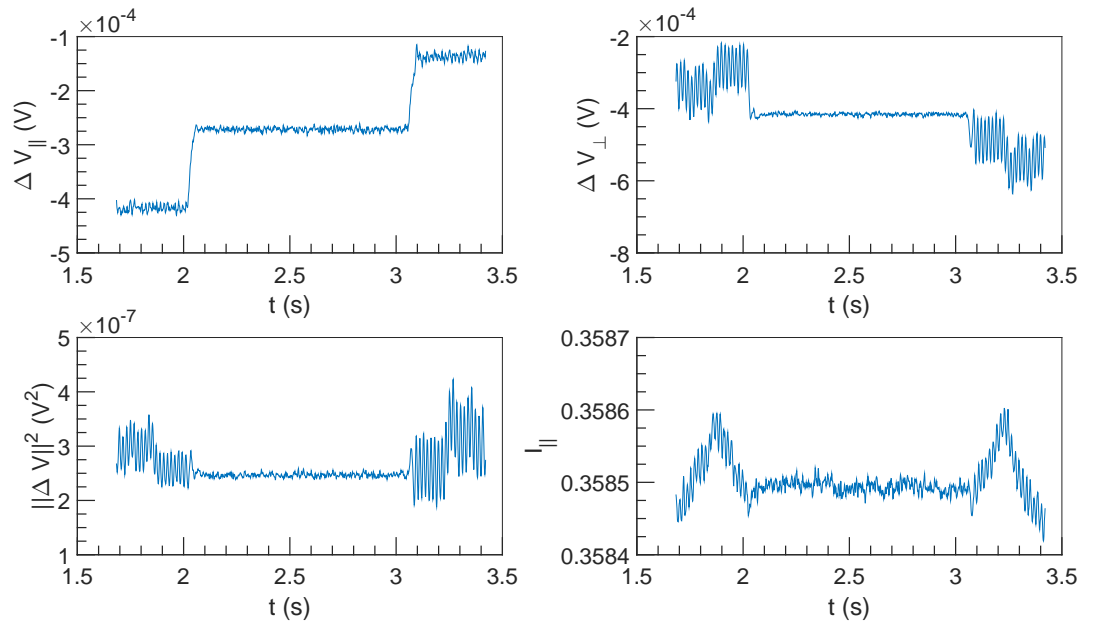


Figure 7.33:  $\Delta V$  and  $I$  vs  $t$  at  $U = 1 \text{ m s}^{-1}$ ,  $\omega = 10996 \text{ rad s}^{-1}$  and  $\alpha = 0.22\%$ .

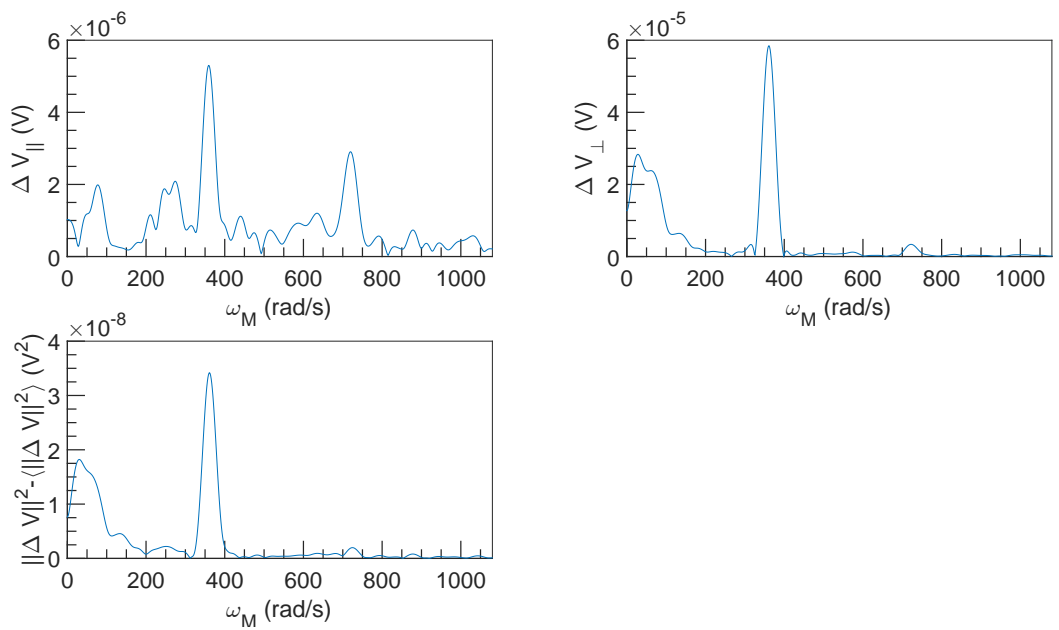


Figure 7.34: FFT spectral density of  $\Delta V$  vs  $\omega_M$  at  $U = 1 \text{ m s}^{-1}$ ,  $\omega = 10996 \text{ rad s}^{-1}$  and  $\alpha = 0.22\%$ .

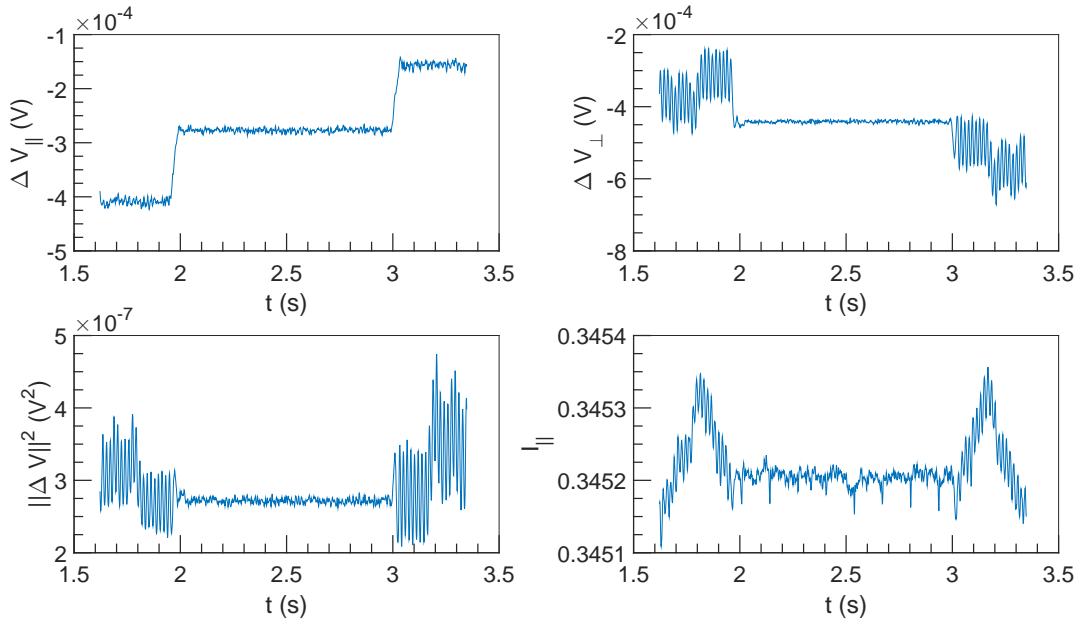


Figure 7.35:  $\Delta V$  and  $I$  vs  $t$  at  $U = 1 \text{ m s}^{-1}$ ,  $\omega = 12566 \text{ rad s}^{-1}$  and  $\alpha = 0.22\%$ .

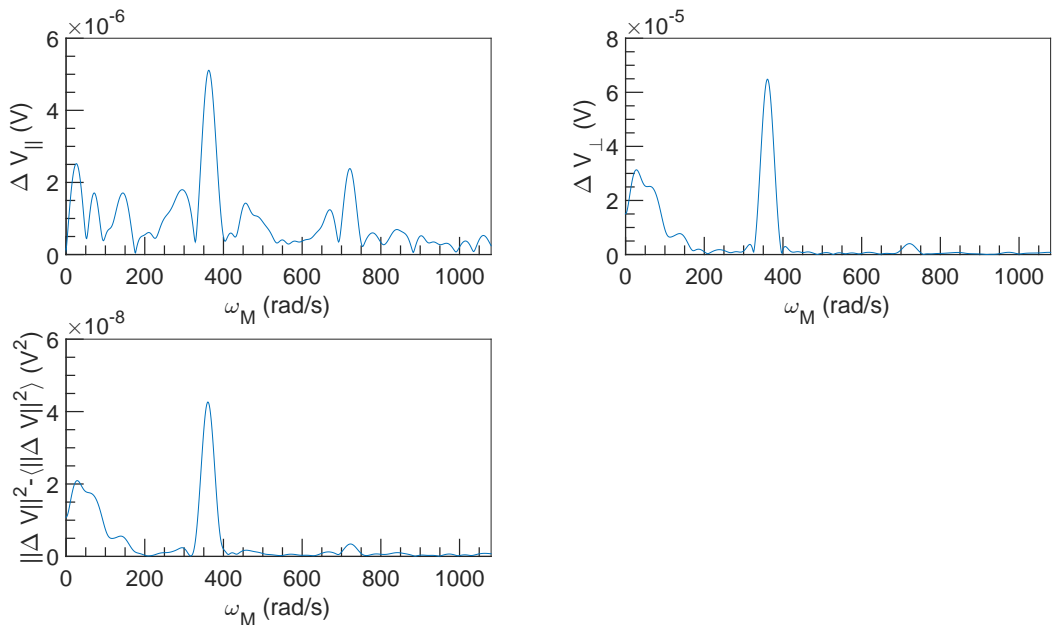


Figure 7.36: FFT spectral density of  $\Delta V$  vs  $\omega_M$  at  $U = 1 \text{ m s}^{-1}$ ,  $\omega = 12566 \text{ rad s}^{-1}$  and  $\alpha = 0.22\%$ .

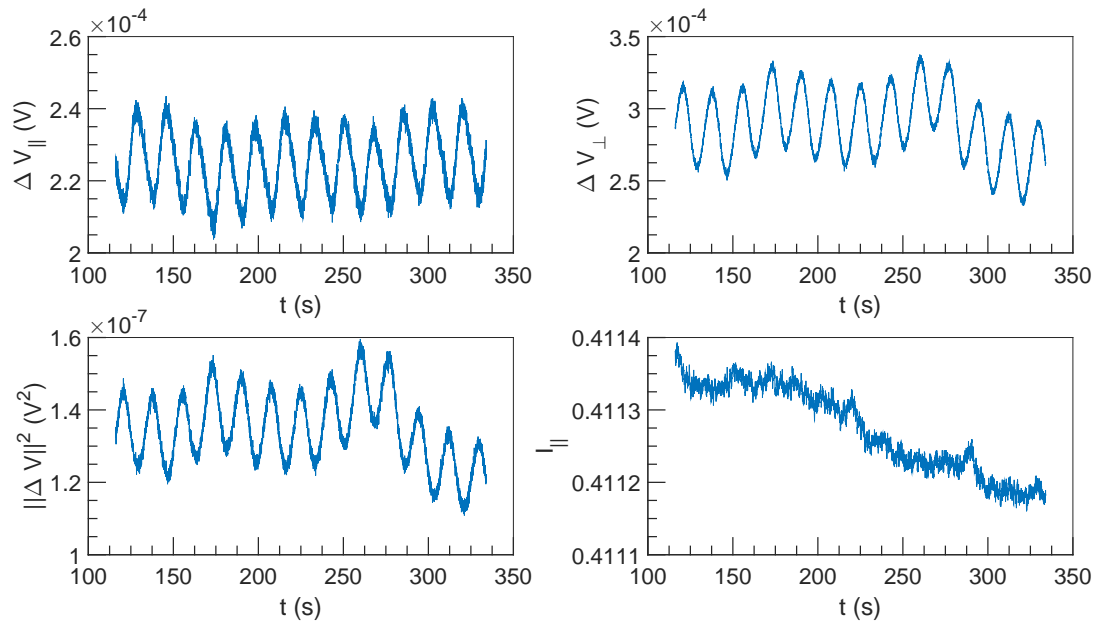


Figure 7.37:  $\Delta V$  and  $I$  vs  $t$  at  $U = 10^{-3} \text{ m s}^{-1}$ ,  $\omega = 4712 \text{ rad s}^{-1}$  and  $\alpha = 0.22 \%$ .

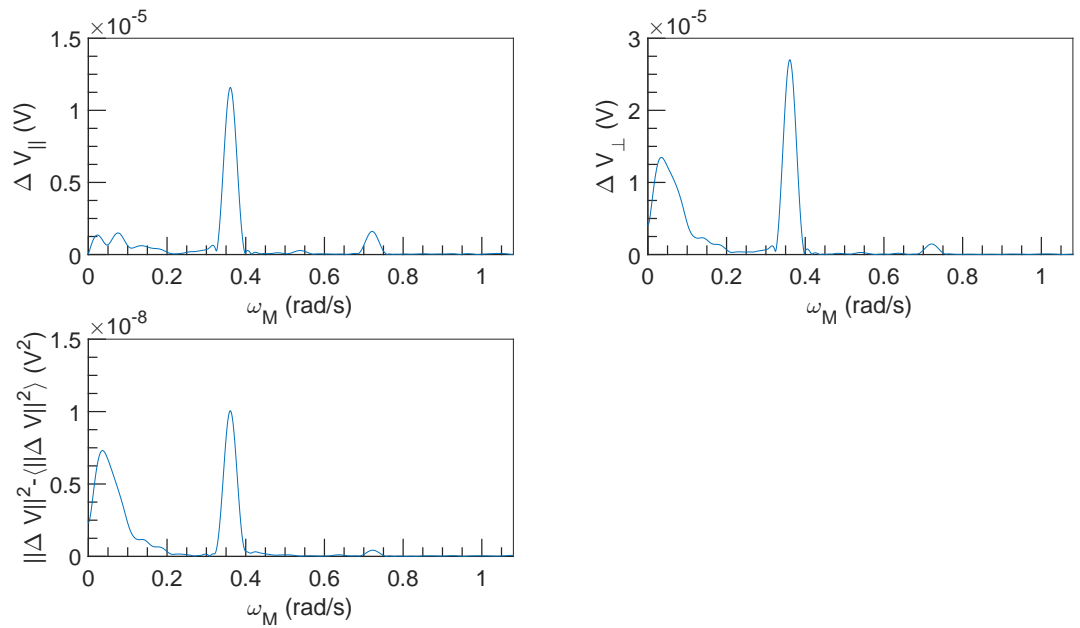


Figure 7.38: FFT spectral density of  $\Delta V$  vs  $\omega_M$  at  $U = 10^{-3} \text{ m s}^{-1}$ ,  $\omega = 4712 \text{ rad s}^{-1}$  and  $\alpha = 0.22 \%$ .

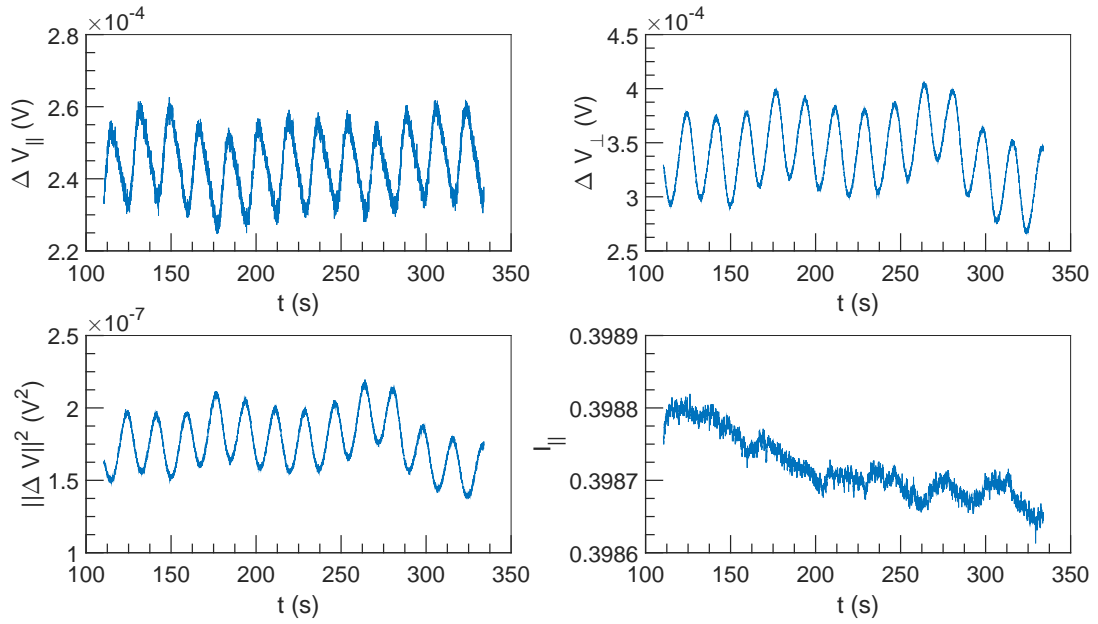


Figure 7.39:  $\Delta V$  and  $I$  vs  $t$  at  $U = 10^{-3} \text{ m s}^{-1}$ ,  $\omega = 6283 \text{ rad s}^{-1}$  and  $\alpha = 0.22\%$ .

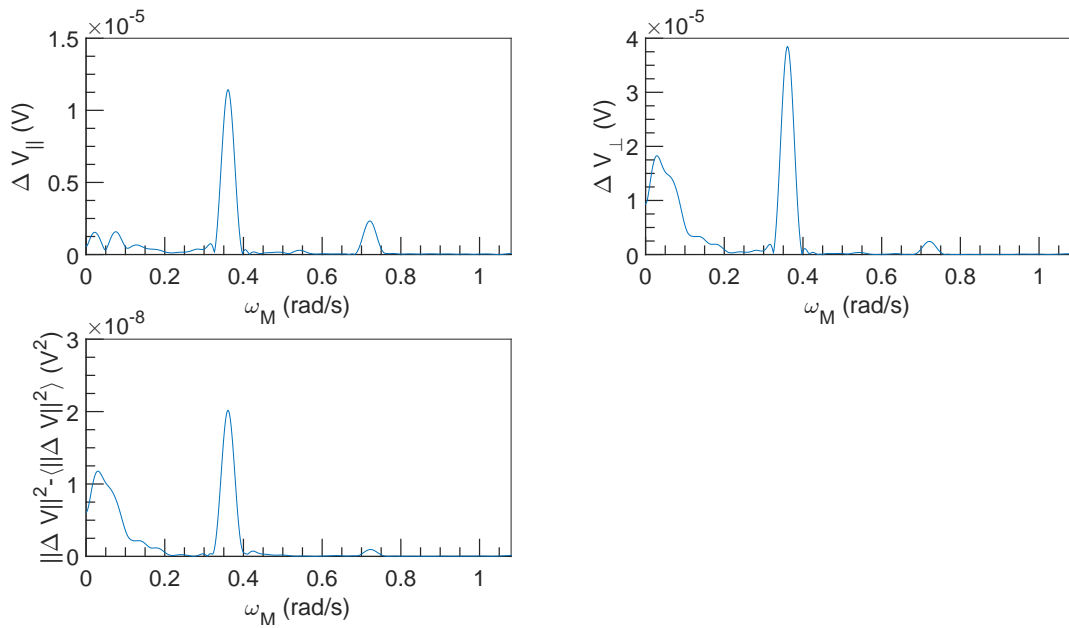


Figure 7.40: FFT spectral density of  $\Delta V$  vs  $\omega_M$  at  $U = 10^{-3} \text{ m s}^{-1}$ ,  $\omega = 6283 \text{ rad s}^{-1}$  and  $\alpha = 0.22\%$ .



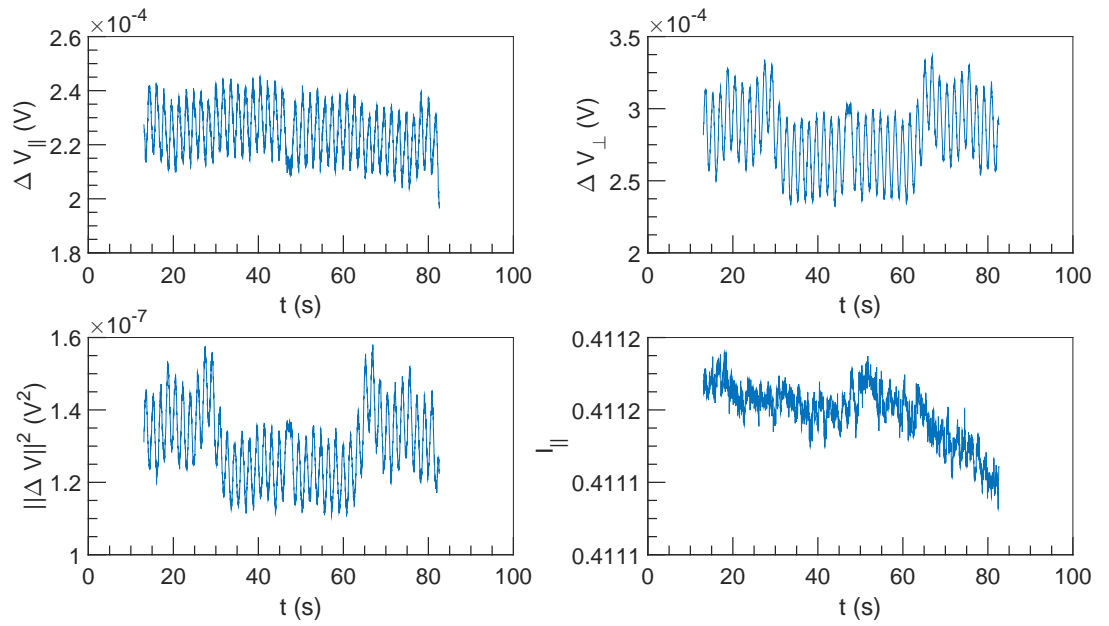


Figure 7.41:  $\Delta V$  and  $I$  vs  $t$  at  $U = 10^{-2} \text{ m s}^{-1}$ ,  $\omega = 4712 \text{ rad s}^{-1}$  and  $\alpha = 0.22 \%$ .

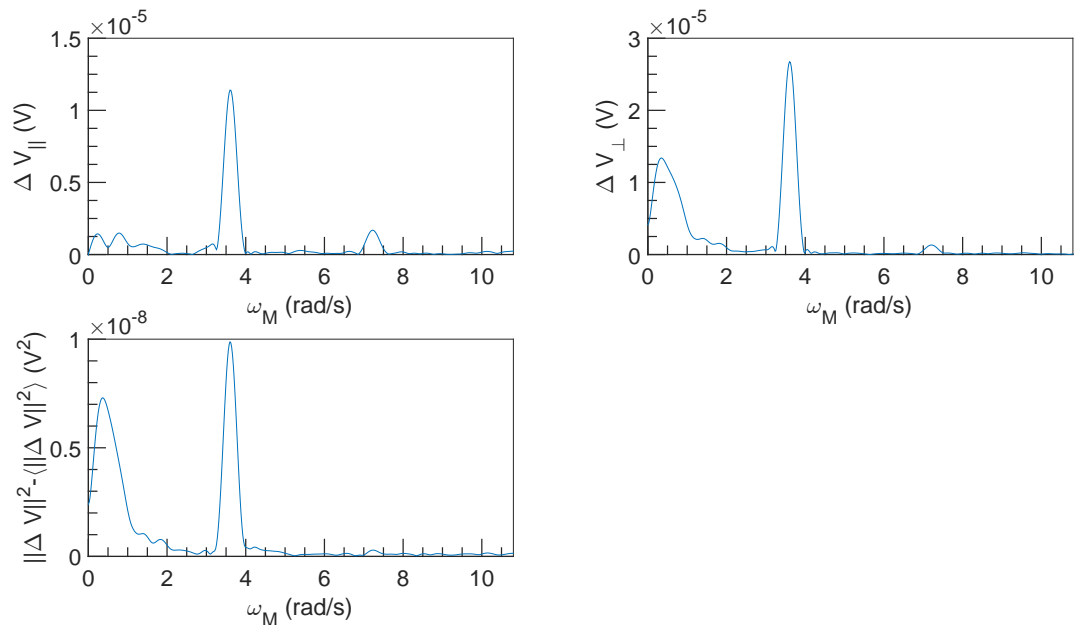


Figure 7.42: FFT spectral density of  $\Delta V$  vs  $\omega_M$  at  $U = 10^{-2} \text{ m s}^{-1}$ ,  $\omega = 4712 \text{ rad s}^{-1}$  and  $\alpha = 0.22 \%$ .

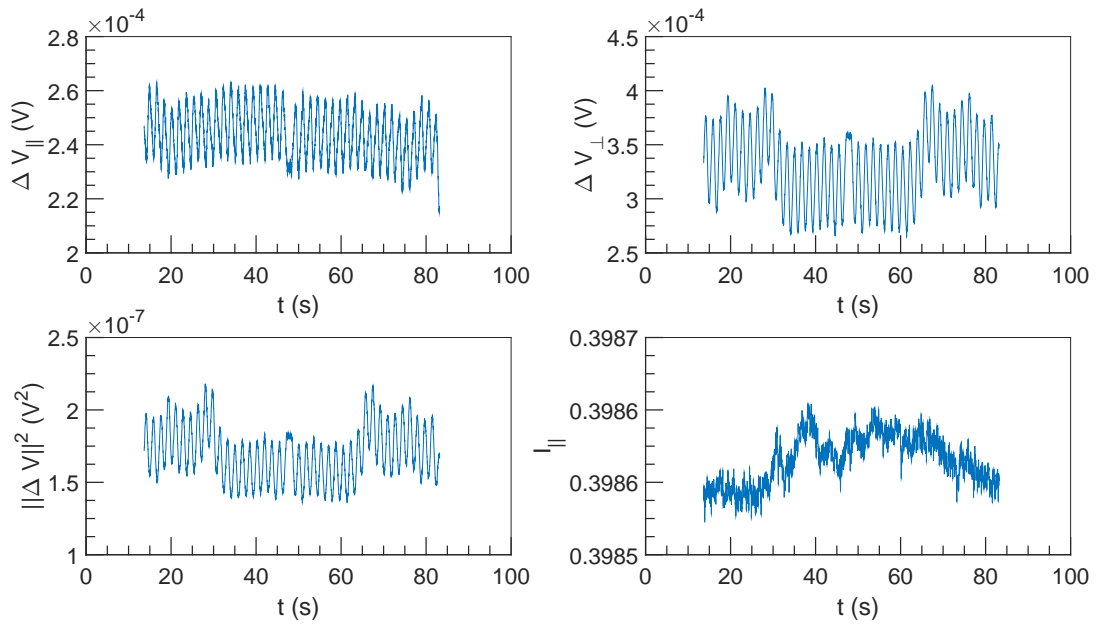


Figure 7.43:  $\Delta V$  and  $I$  vs  $t$  at  $U = 10^{-2} \text{ m s}^{-1}$ ,  $\omega = 6283 \text{ rad s}^{-1}$  and  $\alpha = 0.22\%$ .

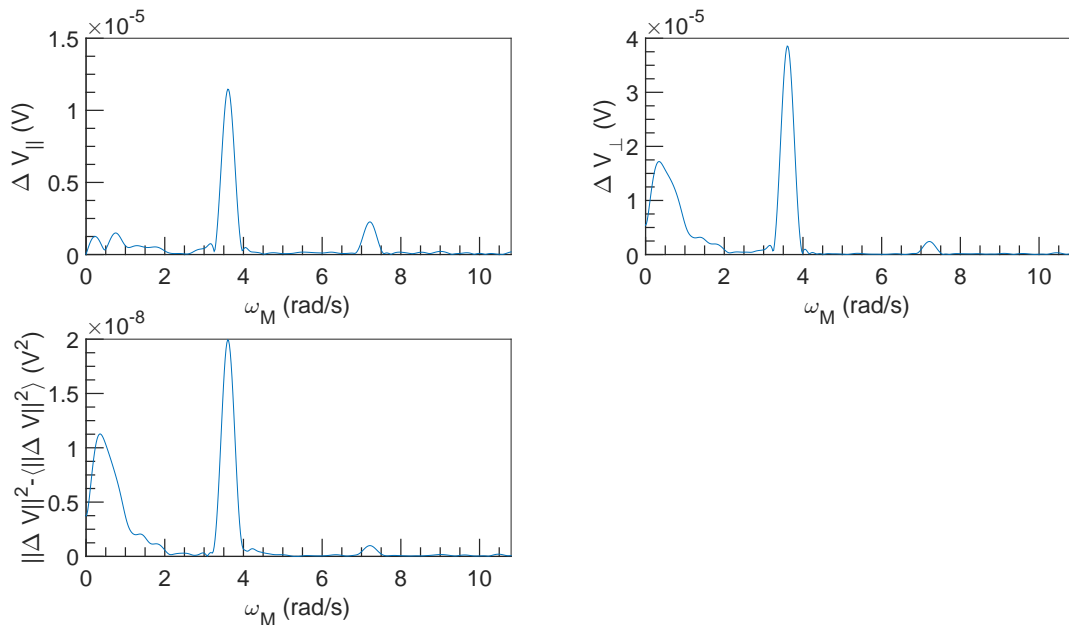


Figure 7.44: FFT spectral density of  $\Delta V$  vs  $\omega_M$  at  $U = 10^{-2} \text{ m s}^{-1}$ ,  $\omega = 6283 \text{ rad s}^{-1}$  and  $\alpha = 0.22\%$ .

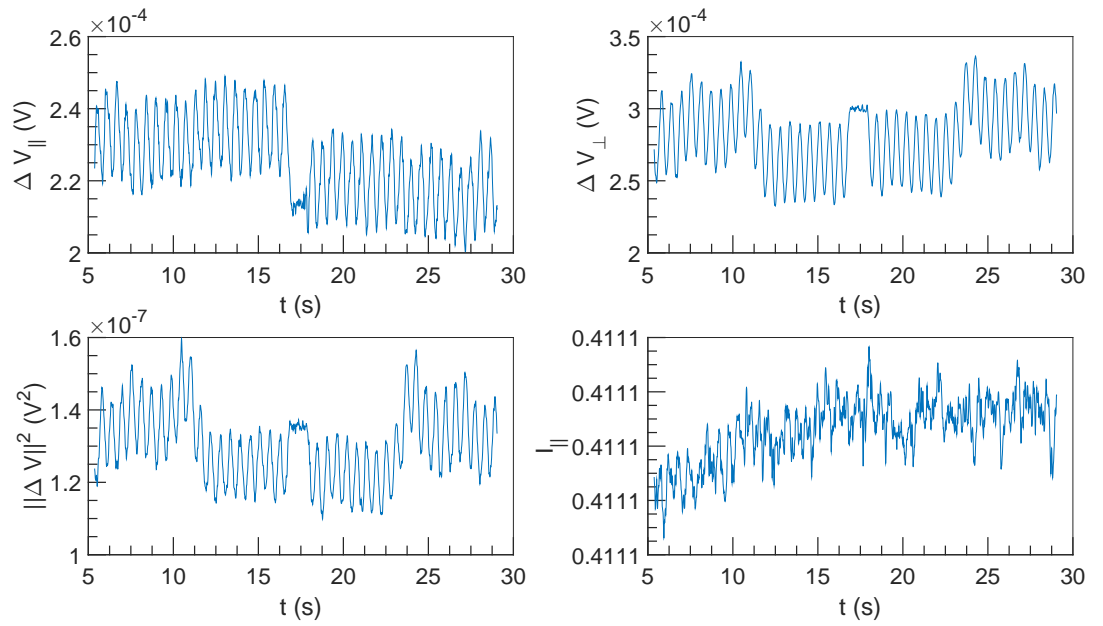


Figure 7.45:  $\Delta V$  and  $I$  vs  $t$  at  $U = 3 \times 10^{-2} \text{ m s}^{-1}$ ,  $\omega = 4712 \text{ rad s}^{-1}$  and  $\alpha = 0.22 \%$ .

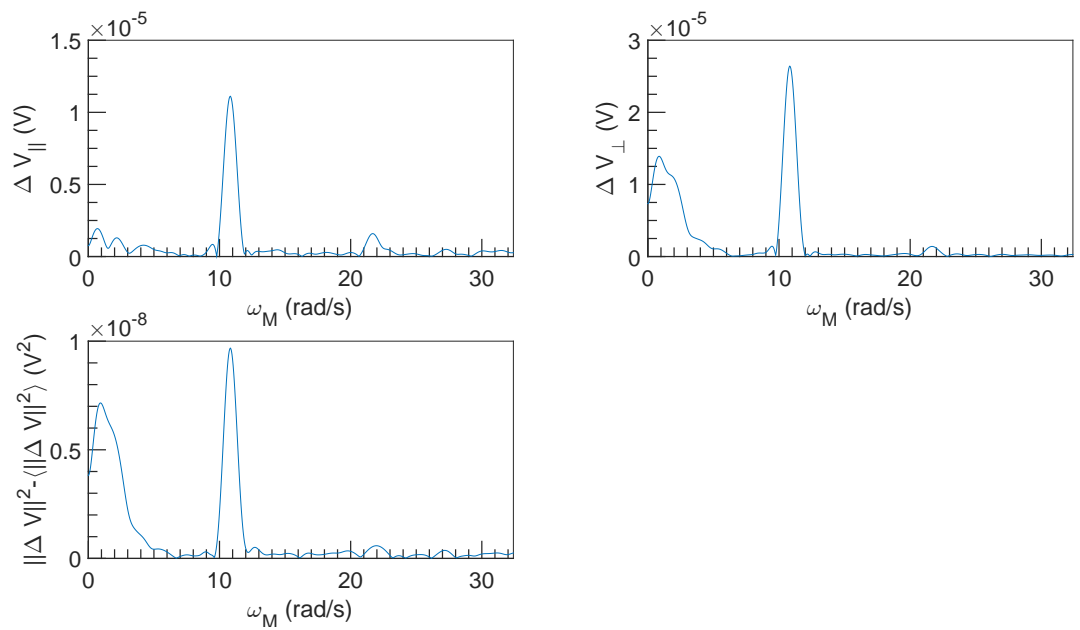


Figure 7.46: FFT spectral density of  $\Delta V$  vs  $\omega_M$  at  $U = 3 \times 10^{-2} \text{ m s}^{-1}$ ,  $\omega = 4712 \text{ rad s}^{-1}$  and  $\alpha = 0.22 \%$ .

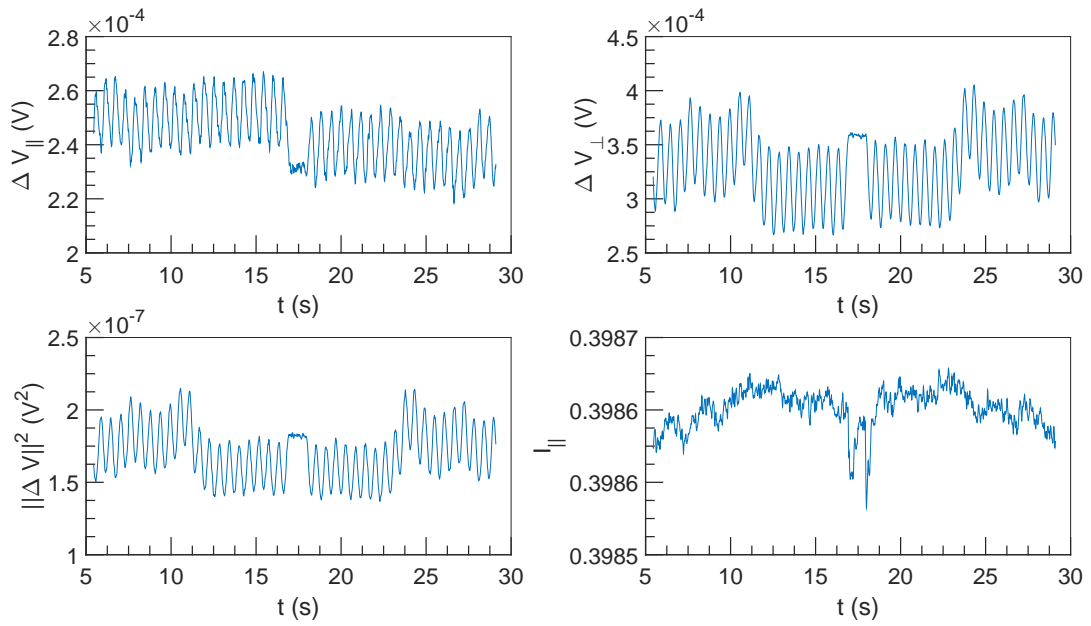


Figure 7.47:  $\Delta V$  and  $I$  vs  $t$  at  $U = 3 \times 10^{-2} \text{ m s}^{-1}$ ,  $\omega = 6283 \text{ rad s}^{-1}$  and  $\alpha = 0.22 \%$ .

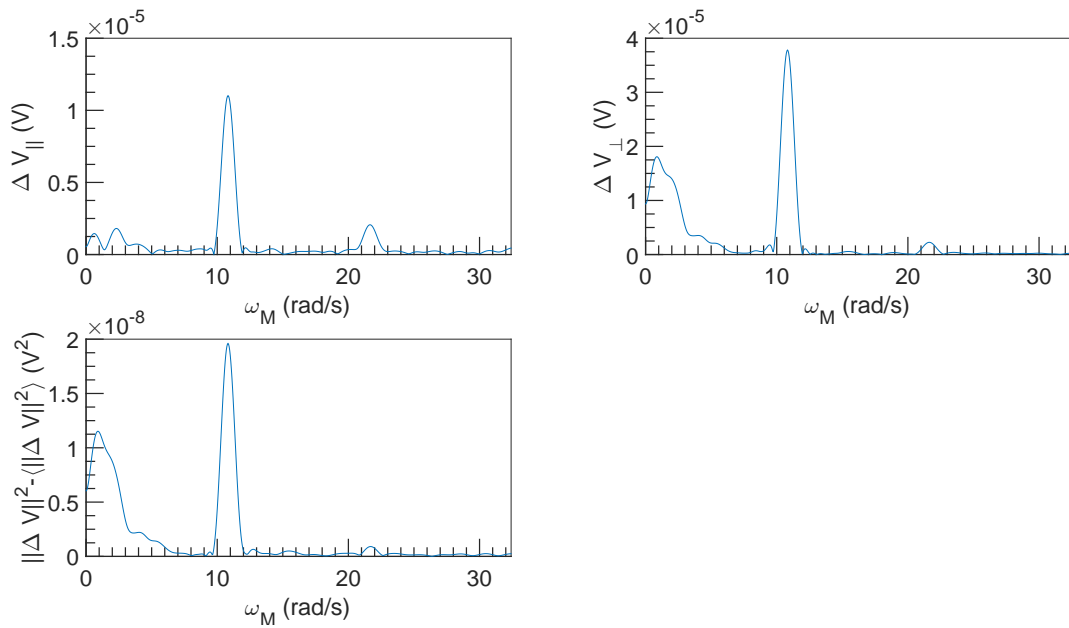


Figure 7.48: FFT spectral density of  $\Delta V$  vs  $\omega_M$  at  $U = 3 \times 10^{-2} \text{ m s}^{-1}$ ,  $\omega = 6283 \text{ rad s}^{-1}$  and  $\alpha = 0.22 \%$ .

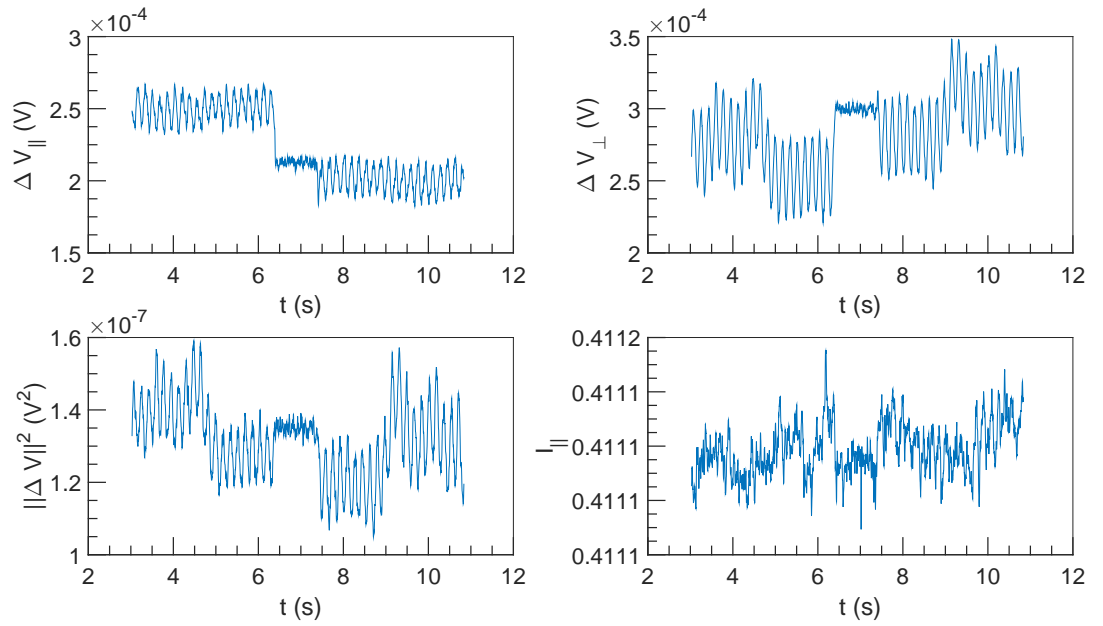


Figure 7.49:  $\Delta V$  and  $I$  vs  $t$  at  $U = 0.1 \text{ m s}^{-1}$ ,  $\omega = 4712 \text{ rad s}^{-1}$  and  $\alpha = 0.22 \%$ .

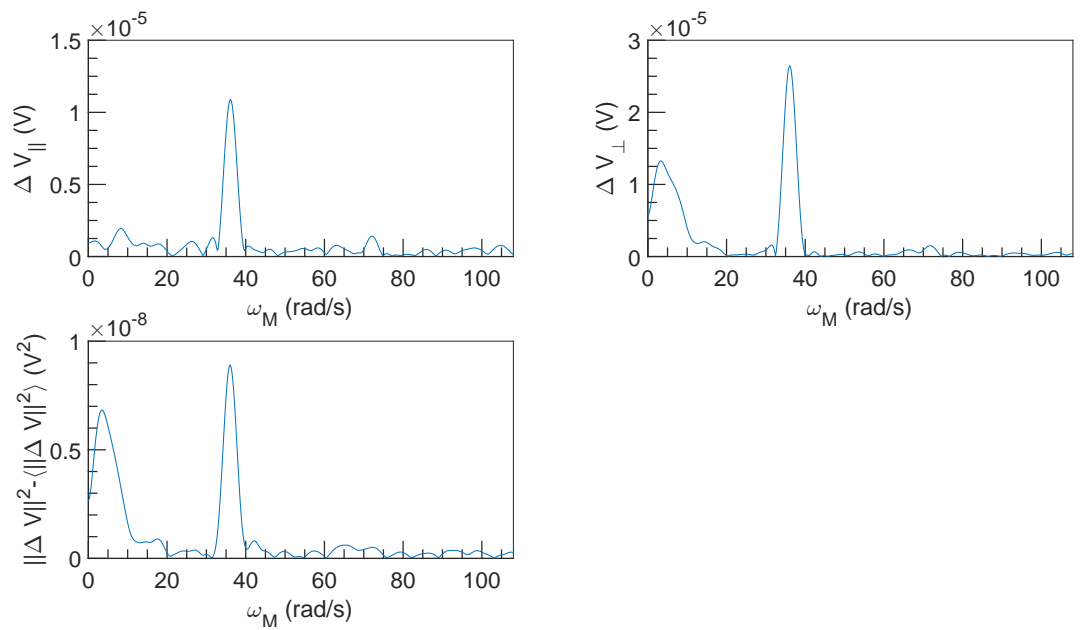


Figure 7.50: FFT spectral density of  $\Delta V$  vs  $\omega_M$  at  $U = 0.1 \text{ m s}^{-1}$ ,  $\omega = 4712 \text{ rad s}^{-1}$  and  $\alpha = 0.22 \%$ .

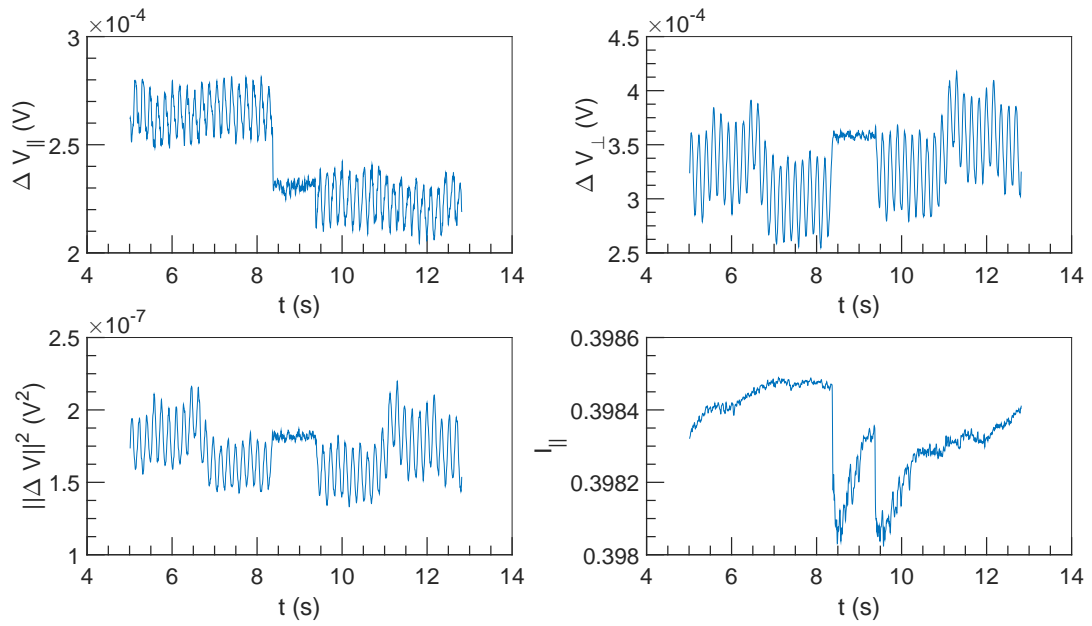


Figure 7.51:  $\Delta V$  and  $I$  vs  $t$  at  $U = 0.1 \text{ m s}^{-1}$ ,  $\omega = 6283 \text{ rad s}^{-1}$  and  $\alpha = 0.22 \%$ .

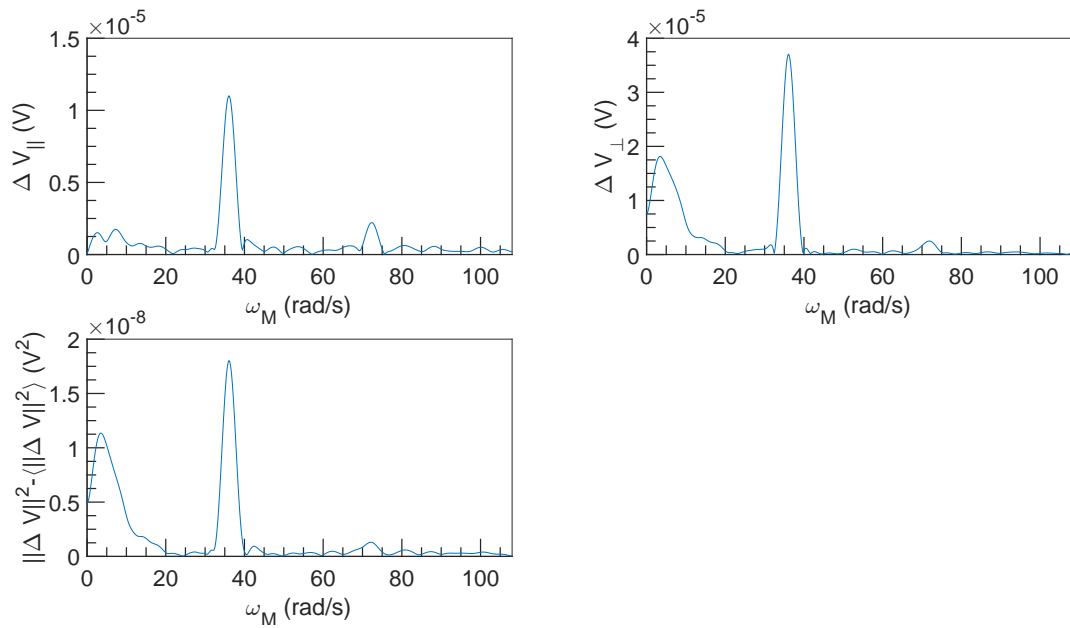


Figure 7.52: FFT spectral density of  $\Delta V$  vs  $\omega_M$  at  $U = 0.1 \text{ m s}^{-1}$ ,  $\omega = 6283 \text{ rad s}^{-1}$  and  $\alpha = 0.22 \%$ .

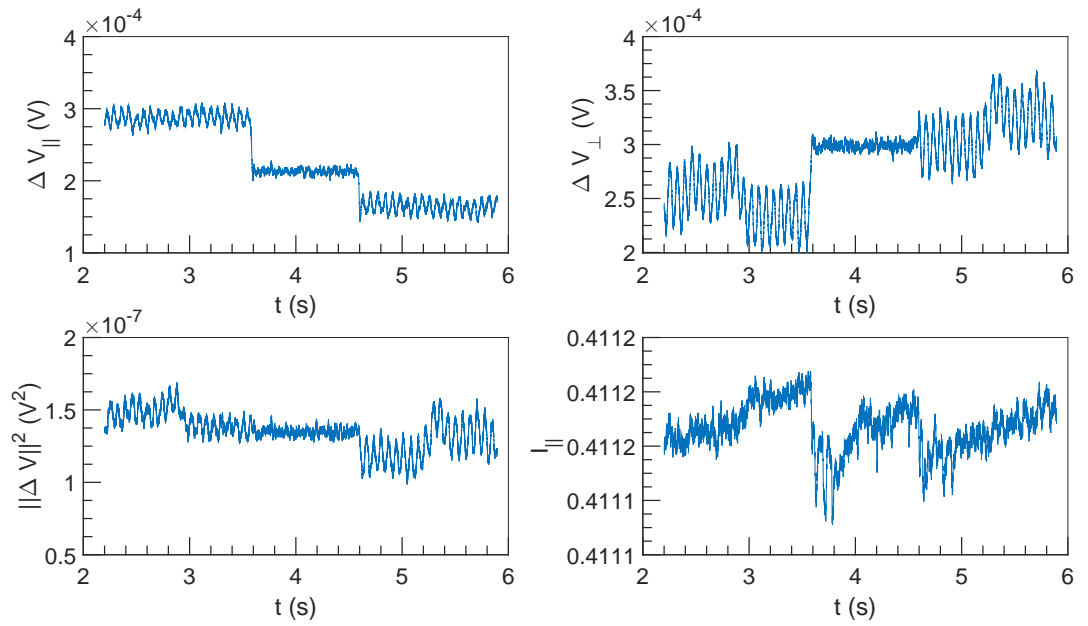


Figure 7.53:  $\Delta V$  and  $I$  vs  $t$  at  $U = 0.25 \text{ m s}^{-1}$ ,  $\omega = 4712 \text{ rad s}^{-1}$  and  $\alpha = 0.22 \%$ .

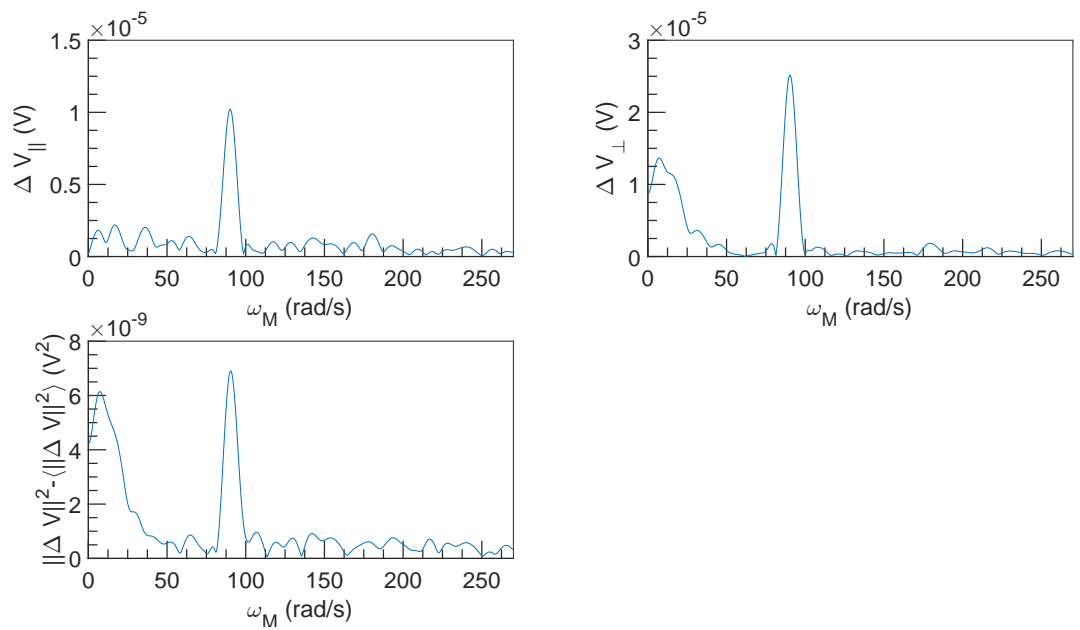


Figure 7.54: FFT spectral density of  $\Delta V$  vs  $\omega_M$  at  $U = 0.25 \text{ m s}^{-1}$ ,  $\omega = 4712 \text{ rad s}^{-1}$  and  $\alpha = 0.22 \%$ .

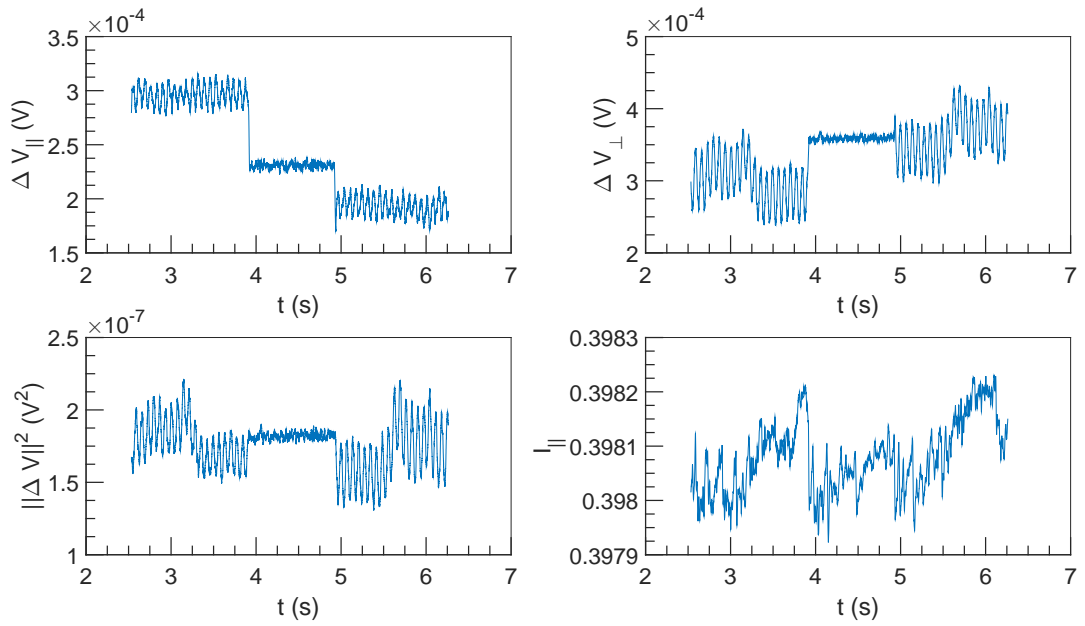


Figure 7.55:  $\Delta V$  and  $I$  vs  $t$  at  $U = 0.25 \text{ m s}^{-1}$ ,  $\omega = 6283 \text{ rad s}^{-1}$  and  $\alpha = 0.22 \%$ .

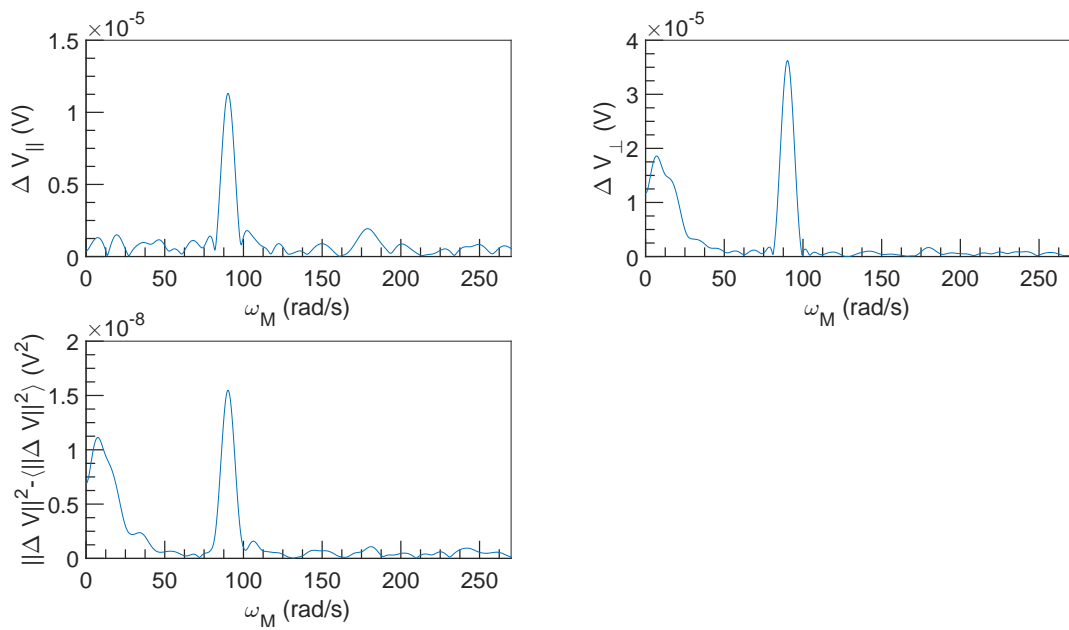


Figure 7.56: FFT spectral density of  $\Delta V$  vs  $\omega_M$  at  $U = 0.25 \text{ m s}^{-1}$ ,  $\omega = 6283 \text{ rad s}^{-1}$  and  $\alpha = 0.22 \%$ .



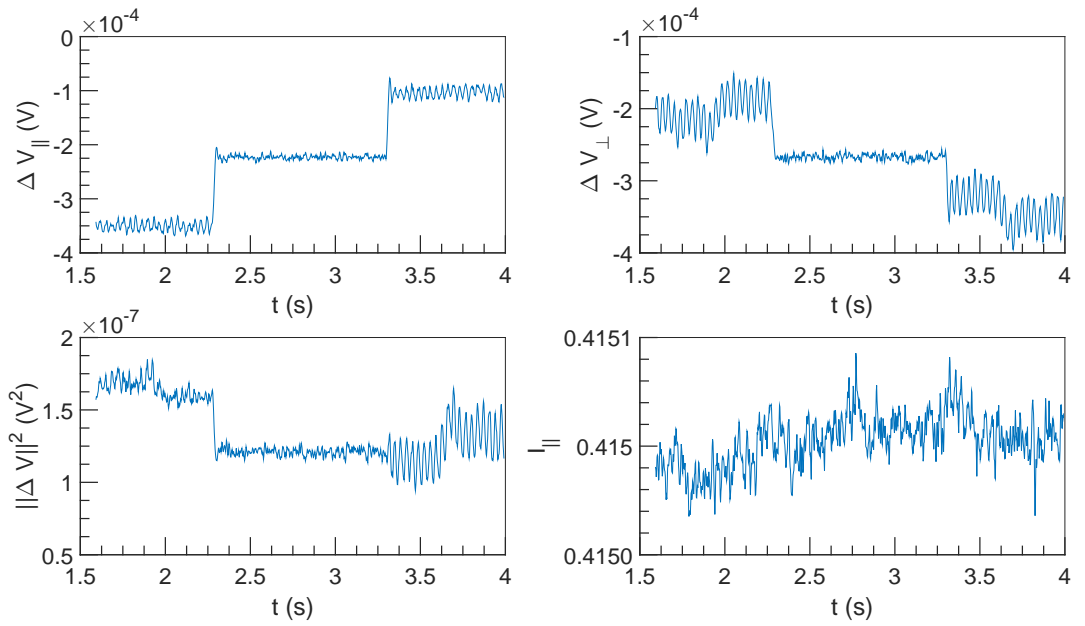


Figure 7.57:  $\Delta V$  and  $I$  vs  $t$  at  $U = 0.5 \text{ m s}^{-1}$ ,  $\omega = 4712 \text{ rad s}^{-1}$  and  $\alpha = 0.22 \%$ .

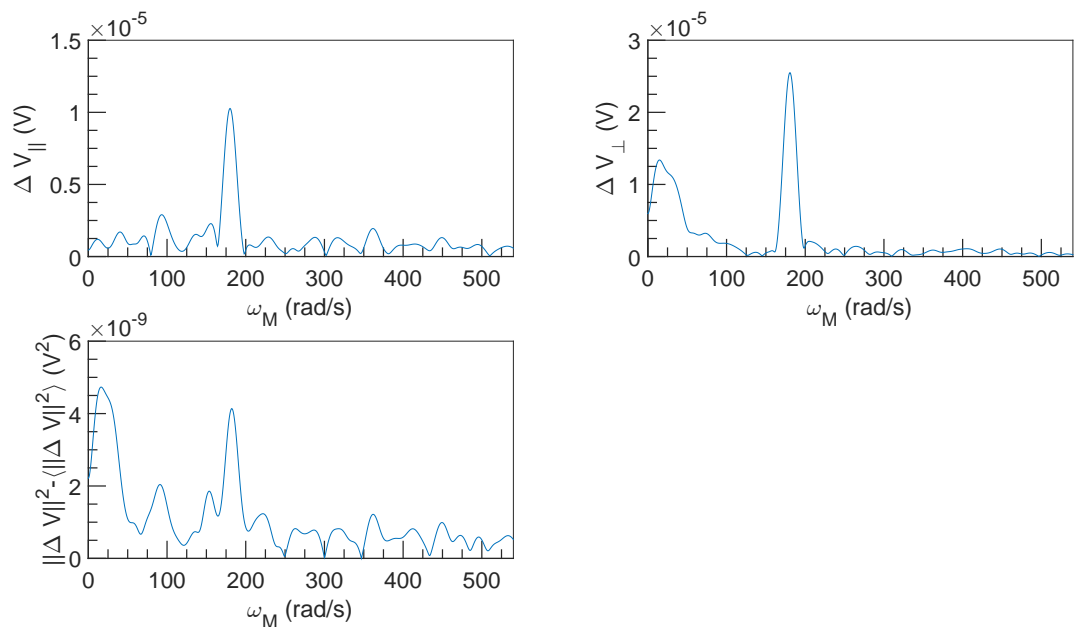


Figure 7.58: FFT spectral density of  $\Delta V$  vs  $\omega_M$  at  $U = 0.5 \text{ m s}^{-1}$ ,  $\omega = 4712 \text{ rad s}^{-1}$  and  $\alpha = 0.22 \%$ .

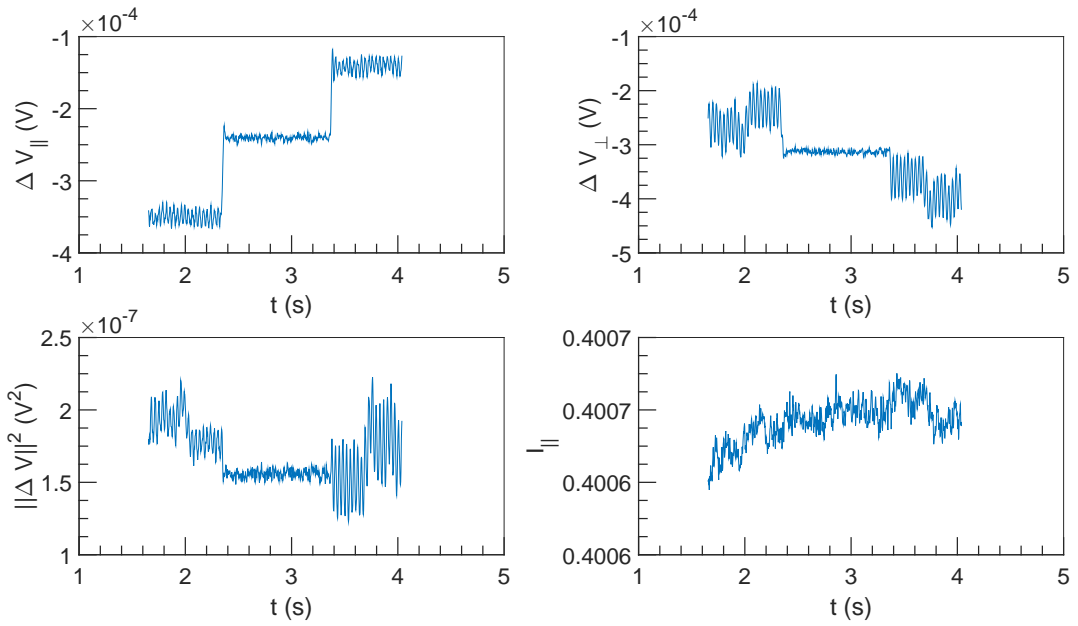


Figure 7.59:  $\Delta V$  and  $I$  vs  $t$  at  $U = 0.5 \text{ m s}^{-1}$ ,  $\omega = 6283 \text{ rad s}^{-1}$  and  $\alpha = 0.22 \%$ .

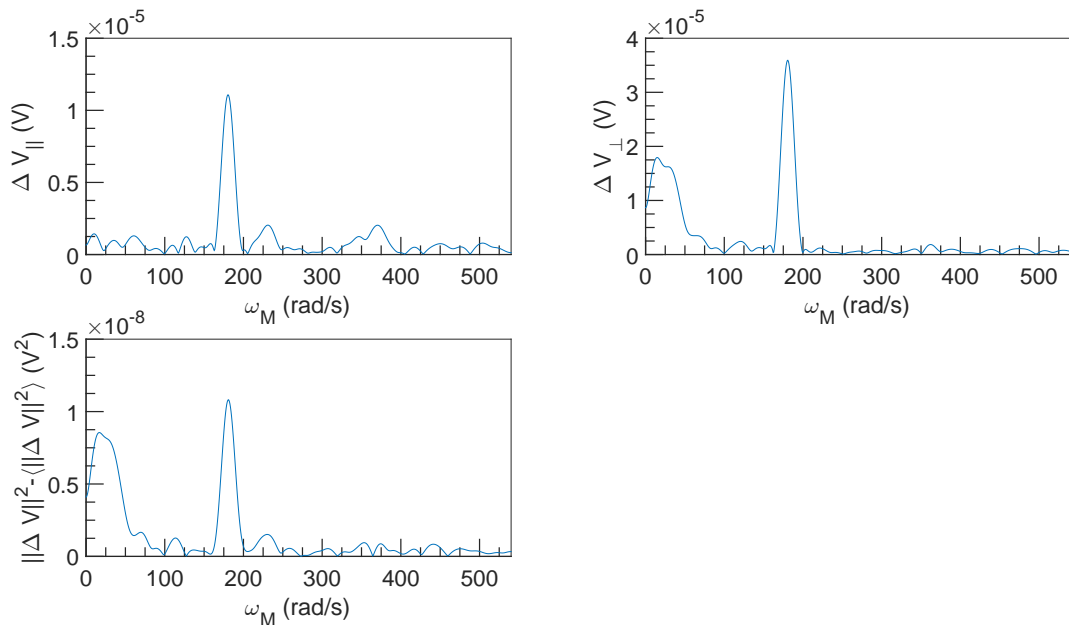


Figure 7.60: FFT spectral density of  $\Delta V$  vs  $\omega_M$  at  $U = 0.5 \text{ m s}^{-1}$ ,  $\omega = 6283 \text{ rad s}^{-1}$  and  $\alpha = 0.22 \%$ .

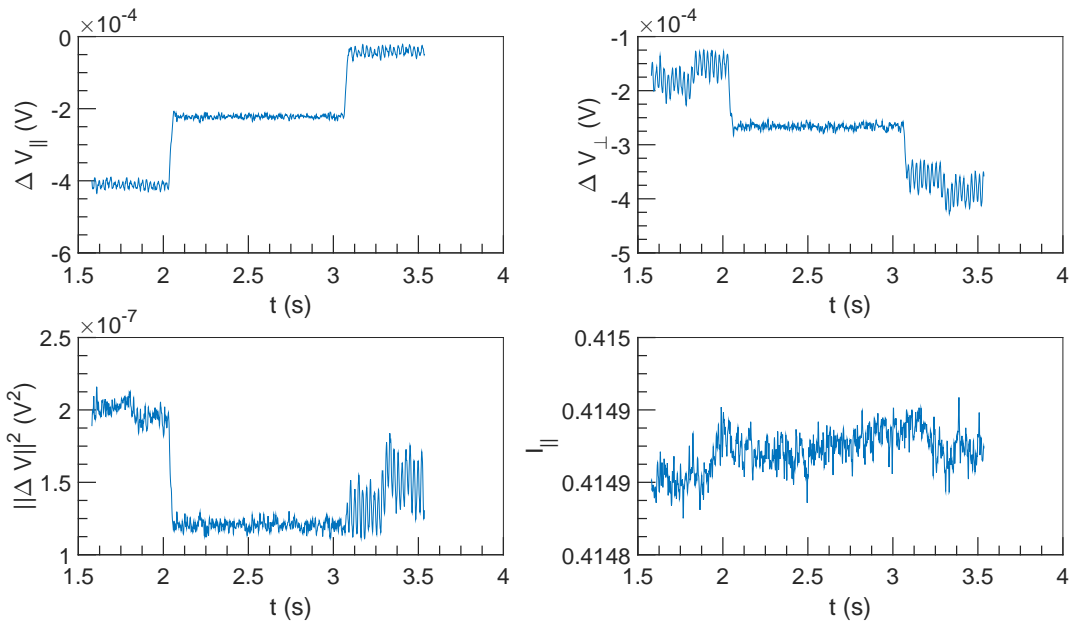


Figure 7.61:  $\Delta V$  and  $I$  vs  $t$  at  $U = 0.75 \text{ m s}^{-1}$ ,  $\omega = 4712 \text{ rad s}^{-1}$  and  $\alpha = 0.22 \%$ .

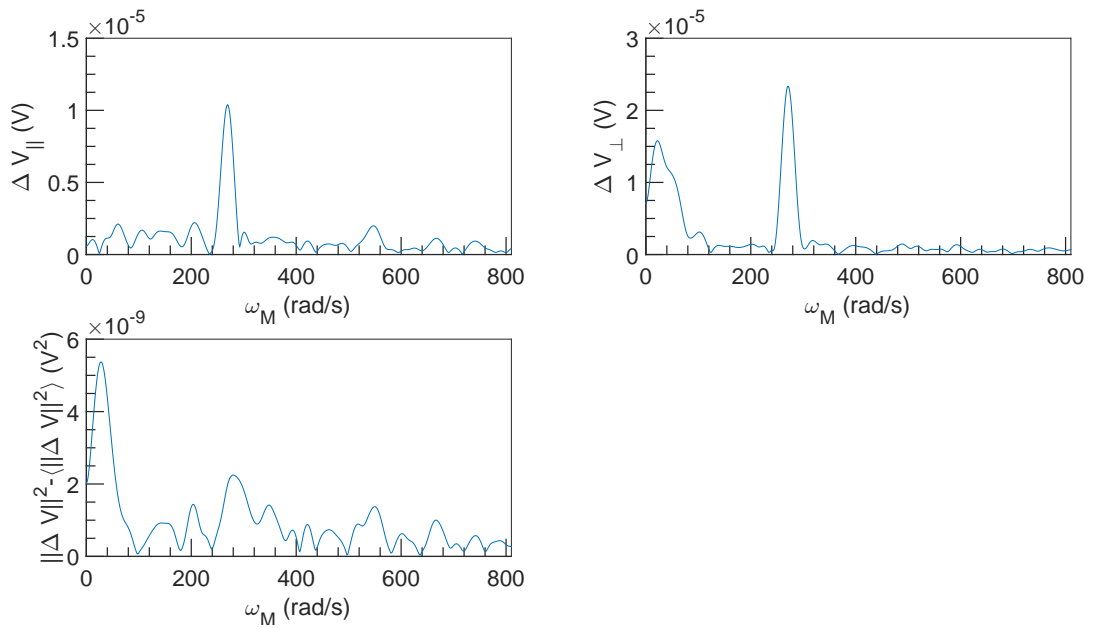


Figure 7.62: FFT spectral density of  $\Delta V$  vs  $\omega_M$  at  $U = 0.75 \text{ m s}^{-1}$ ,  $\omega = 4712 \text{ rad s}^{-1}$  and  $\alpha = 0.22 \%$ .

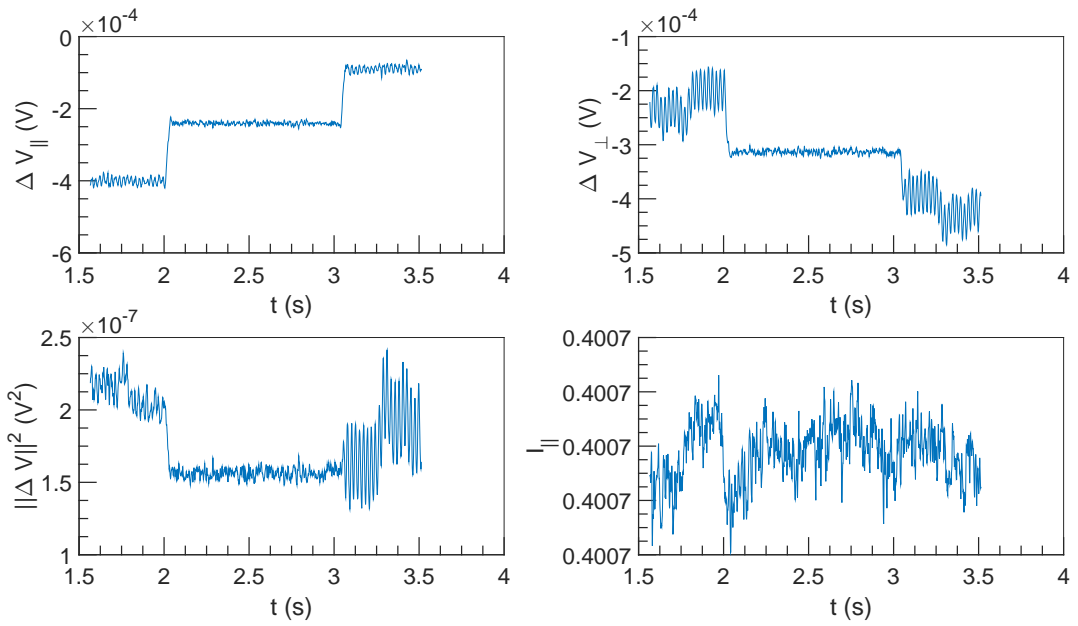


Figure 7.63:  $\Delta V$  and  $I$  vs  $t$  at  $U = 0.75 \text{ m s}^{-1}$ ,  $\omega = 6283 \text{ rad s}^{-1}$  and  $\alpha = 0.22 \%$ .

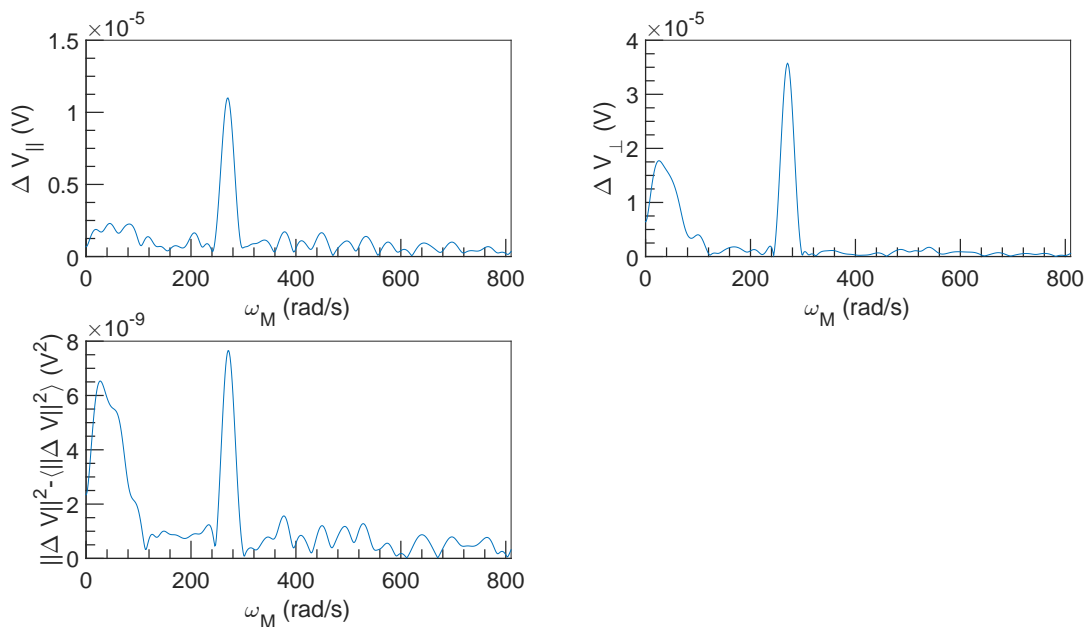


Figure 7.64: FFT spectral density of  $\Delta V$  vs  $\omega_M$  at  $U = 0.75 \text{ m s}^{-1}$ ,  $\omega = 6283 \text{ rad s}^{-1}$  and  $\alpha = 0.22 \%$ .

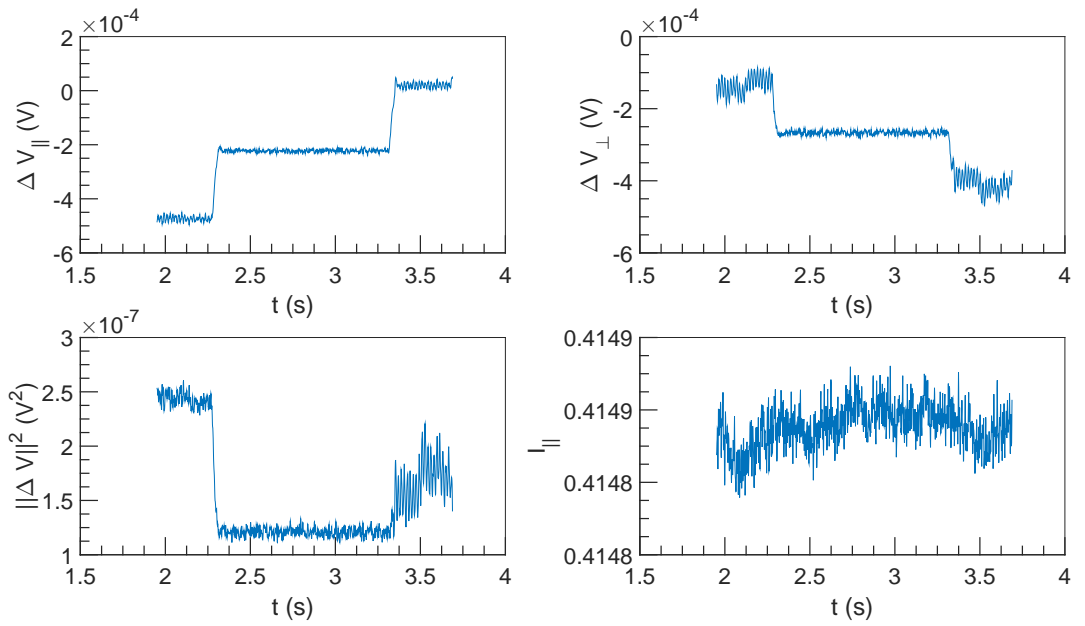


Figure 7.65:  $\Delta V$  and  $I$  vs  $t$  at  $U = 1 \text{ m s}^{-1}$ ,  $\omega = 4712 \text{ rad s}^{-1}$  and  $\alpha = 0.22 \%$ .

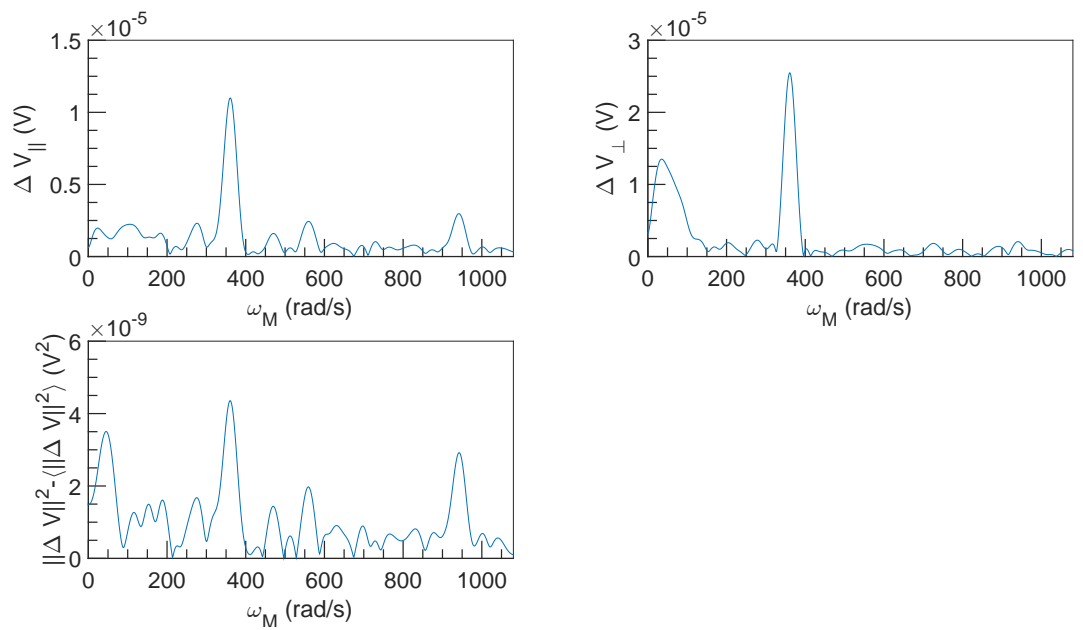


Figure 7.66: FFT spectral density of  $\Delta V$  vs  $\omega_M$  at  $U = 1 \text{ m s}^{-1}$ ,  $\omega = 4712 \text{ rad s}^{-1}$  and  $\alpha = 0.22 \%$ .

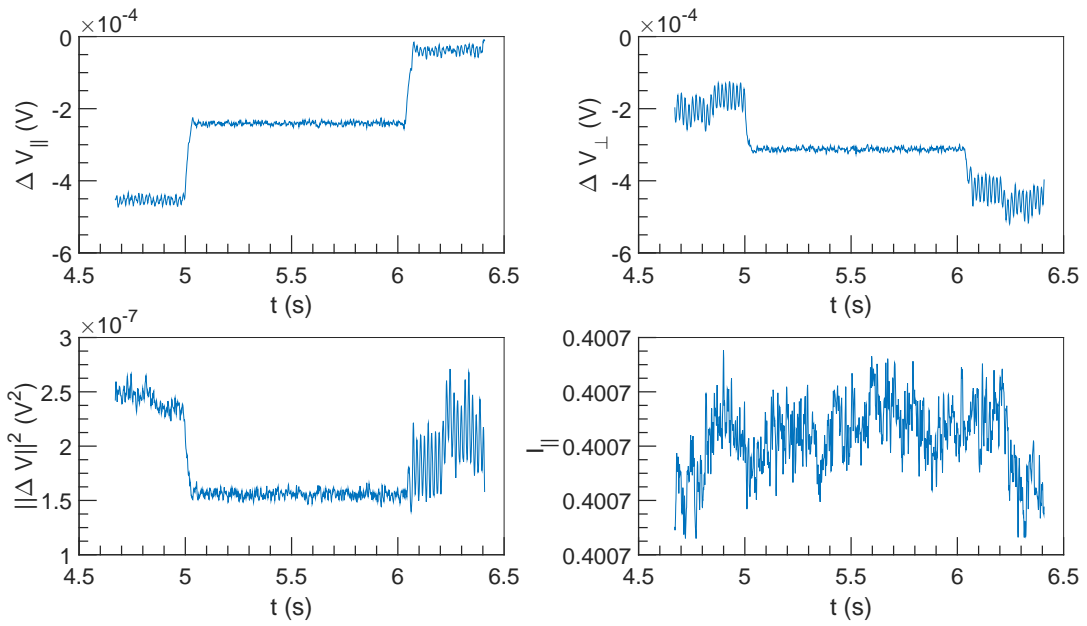


Figure 7.67:  $\Delta V$  and  $I$  vs  $t$  at  $U = 1 \text{ m s}^{-1}$ ,  $\omega = 6283 \text{ rad s}^{-1}$  and  $\alpha = 0.22 \%$ .

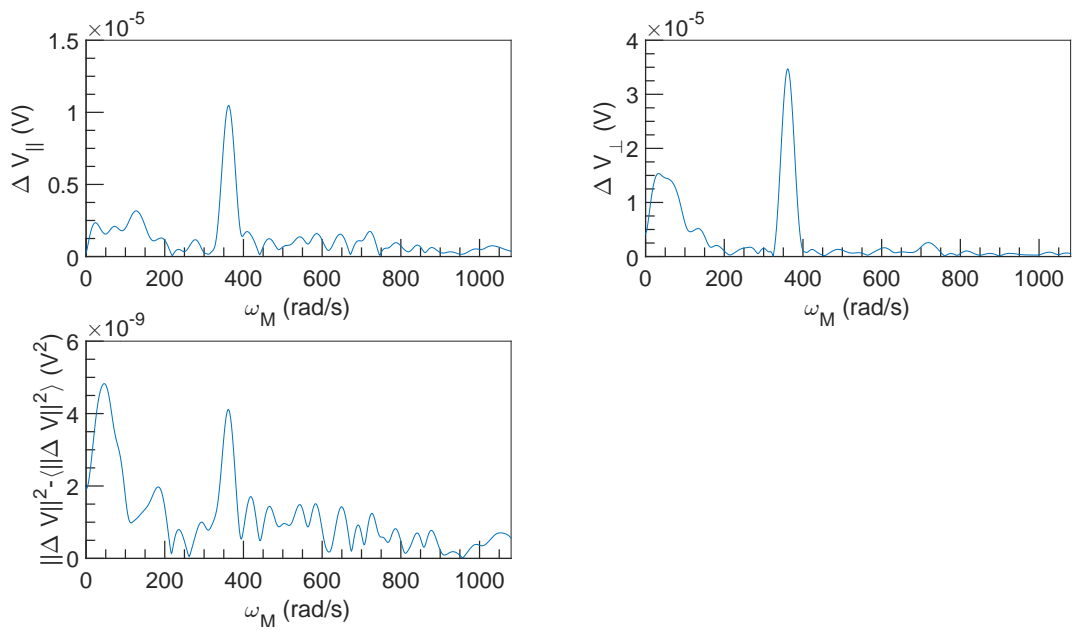


Figure 7.68: FFT spectral density of  $\Delta V$  vs  $\omega_M$  at  $U = 1 \text{ m s}^{-1}$ ,  $\omega = 6283 \text{ rad s}^{-1}$  and  $\alpha = 0.22 \%$ .



## Chapter 8

**For**  $\alpha = 0.54\%$



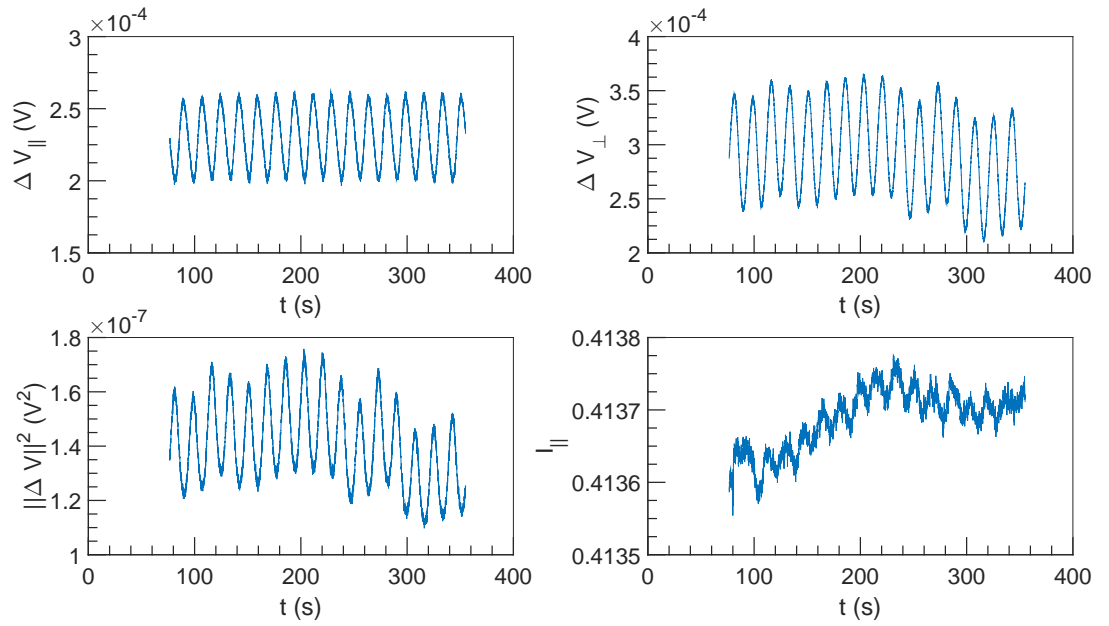


Figure 8.1:  $\Delta V$  and  $I$  vs  $t$  at  $U = 10^{-3} \text{ m s}^{-1}$ ,  $\omega = 4712 \text{ rad s}^{-1}$  and  $\alpha = 0.54 \%$ .

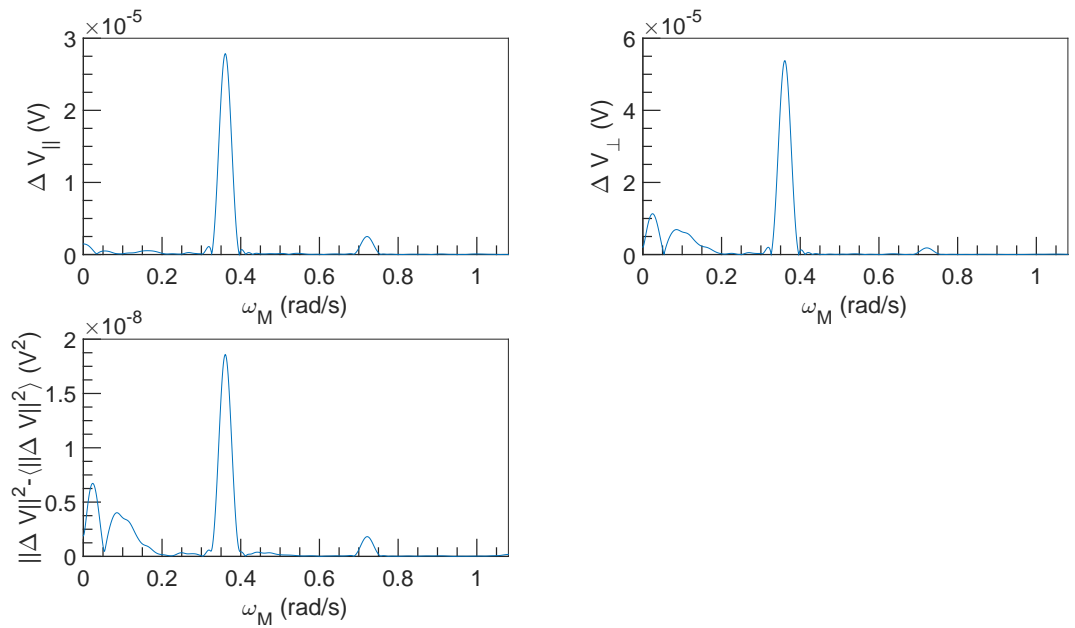


Figure 8.2: FFT spectral density of  $\Delta V$  vs  $\omega_M$  at  $U = 10^{-3} \text{ m s}^{-1}$ ,  $\omega = 4712 \text{ rad s}^{-1}$  and  $\alpha = 0.54 \%$ .

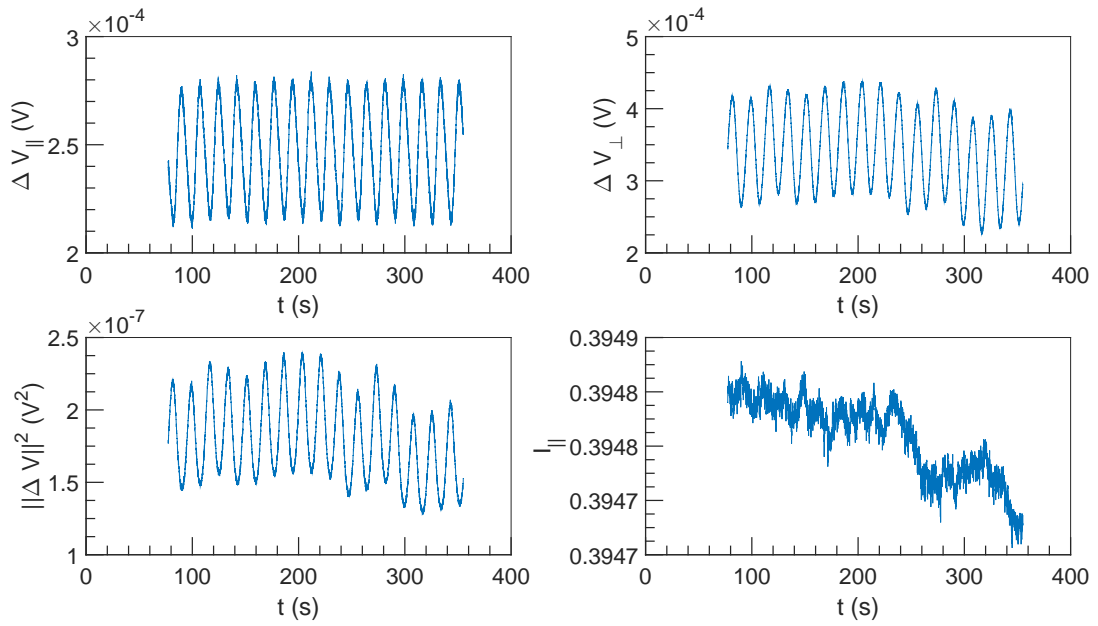


Figure 8.3:  $\Delta V$  and  $I$  vs  $t$  at  $U = 10^{-3} \text{ m s}^{-1}$ ,  $\omega = 6283 \text{ rad s}^{-1}$  and  $\alpha = 0.54 \%$ .

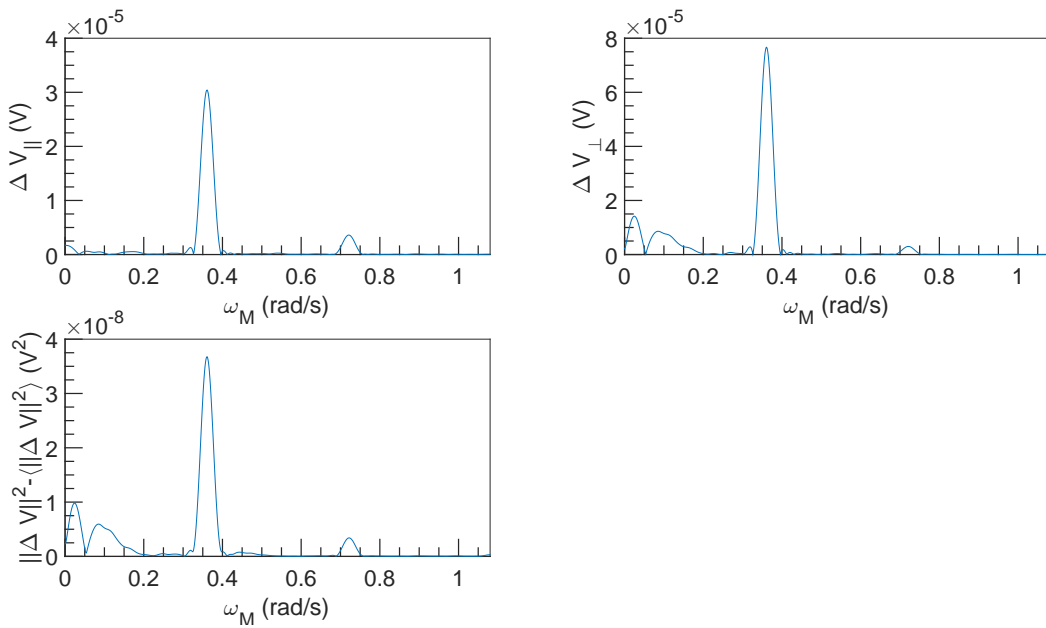


Figure 8.4: FFT spectral density of  $\Delta V$  vs  $\omega_M$  at  $U = 10^{-3} \text{ m s}^{-1}$ ,  $\omega = 6283 \text{ rad s}^{-1}$  and  $\alpha = 0.54 \%$ .

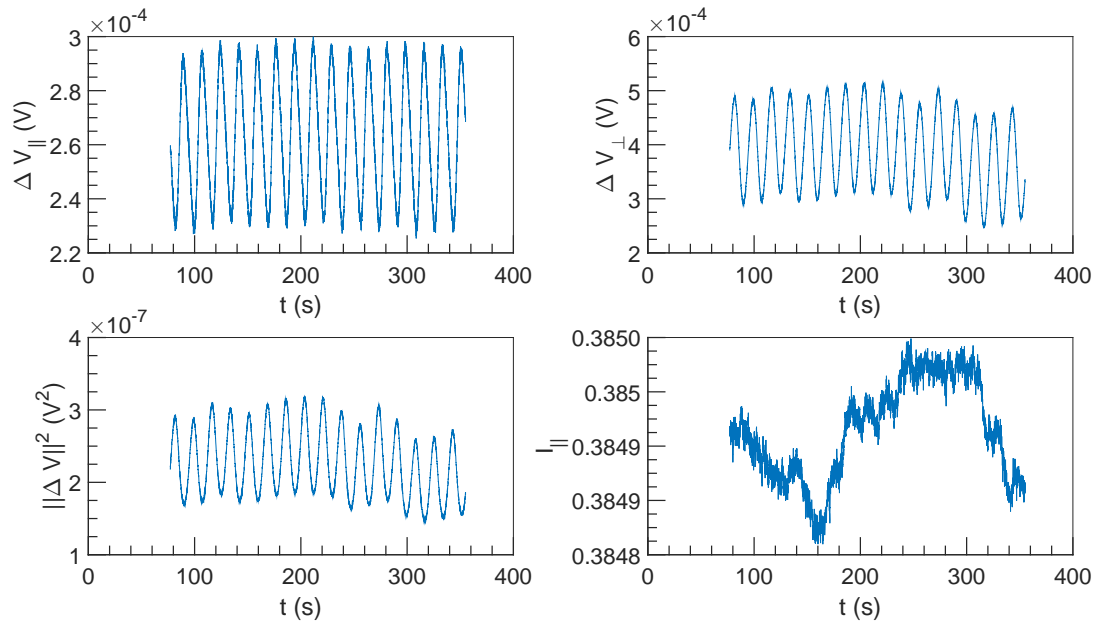


Figure 8.5:  $\Delta V$  and  $I$  vs  $t$  at  $U = 10^{-3} \text{ m s}^{-1}$ ,  $\omega = 7854 \text{ rad s}^{-1}$  and  $\alpha = 0.54 \%$ .

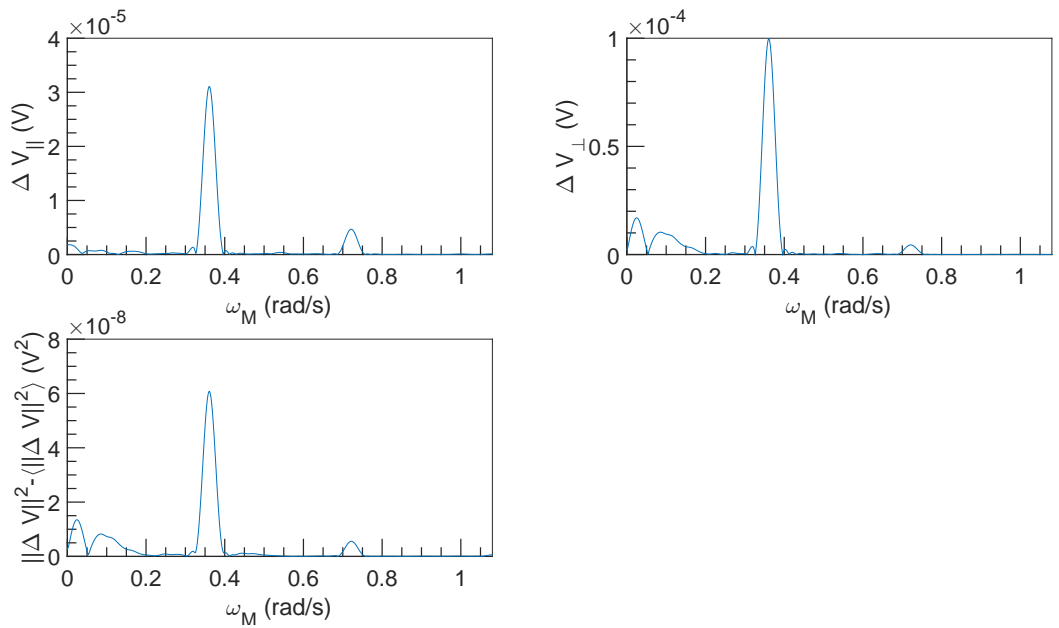


Figure 8.6: FFT spectral density of  $\Delta V$  vs  $\omega_M$  at  $U = 10^{-3} \text{ m s}^{-1}$ ,  $\omega = 7854 \text{ rad s}^{-1}$  and  $\alpha = 0.54 \%$ .

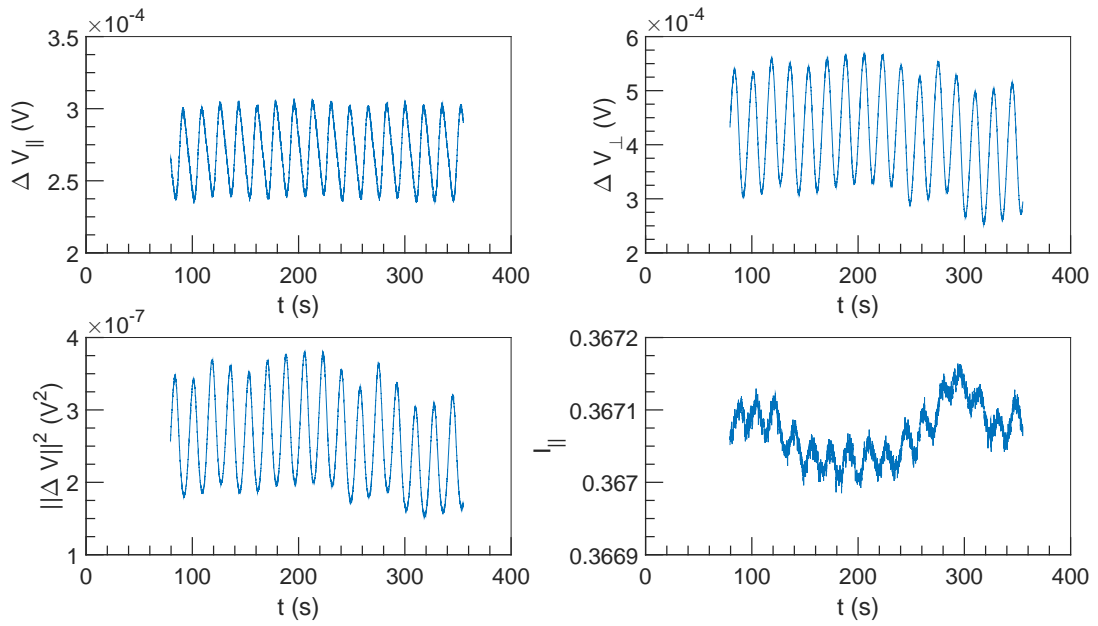


Figure 8.7:  $\Delta V$  and  $I$  vs  $t$  at  $U = 10^{-3} \text{ m s}^{-1}$ ,  $\omega = 9425 \text{ rad s}^{-1}$  and  $\alpha = 0.54 \%$ .

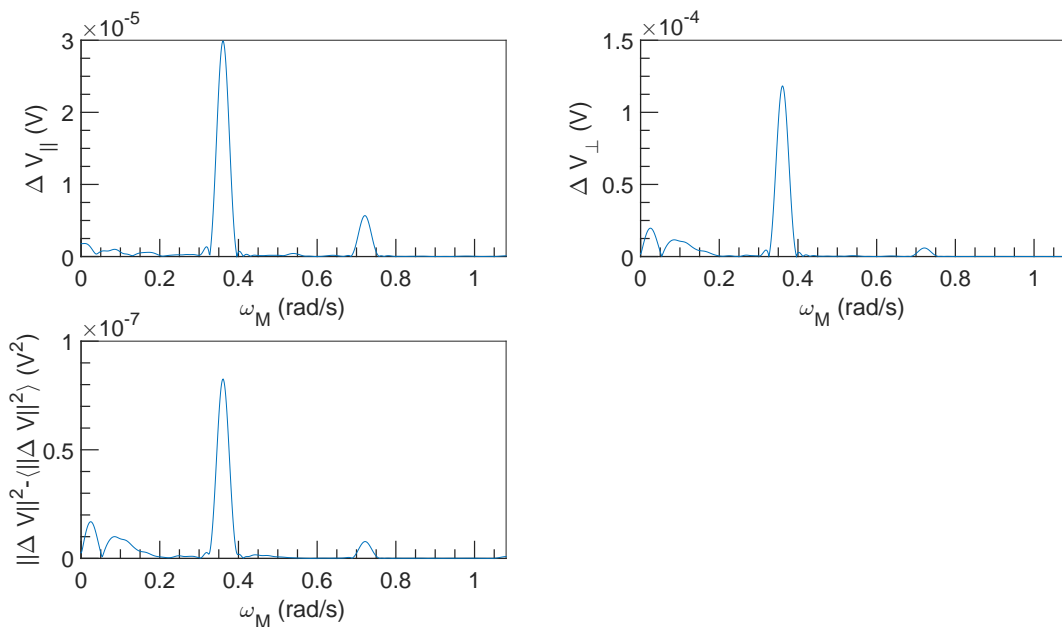


Figure 8.8: FFT spectral density of  $\Delta V$  vs  $\omega_M$  at  $U = 10^{-3} \text{ m s}^{-1}$ ,  $\omega = 9425 \text{ rad s}^{-1}$  and  $\alpha = 0.54 \%$ .

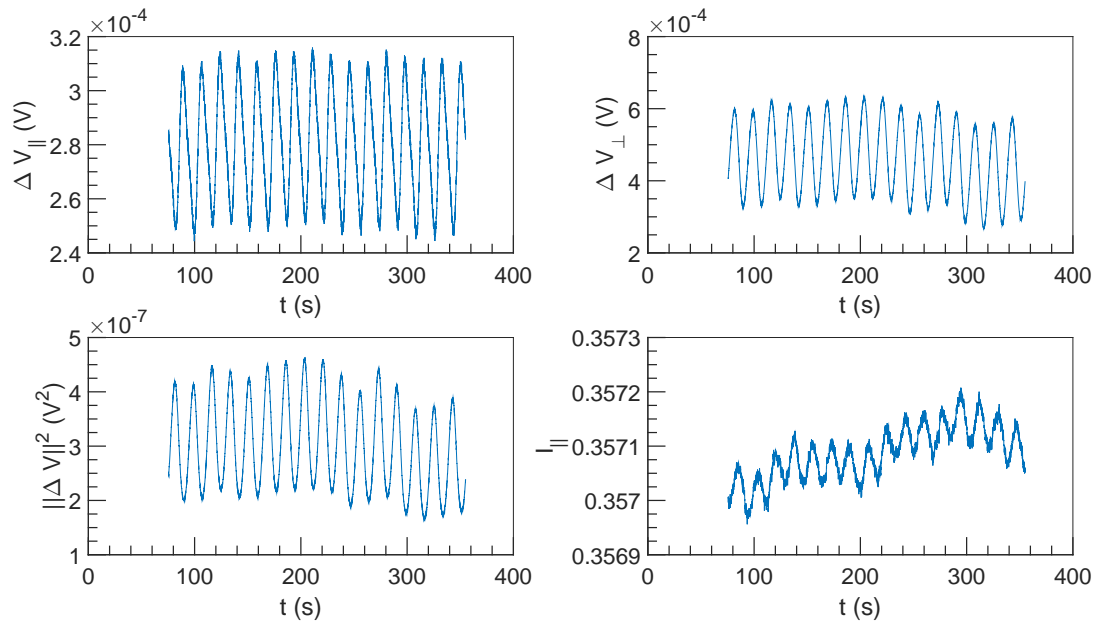


Figure 8.9:  $\Delta V$  and  $I$  vs  $t$  at  $U = 10^{-3} \text{ m s}^{-1}$ ,  $\omega = 10\,996 \text{ rad s}^{-1}$  and  $\alpha = 0.54\%$ .

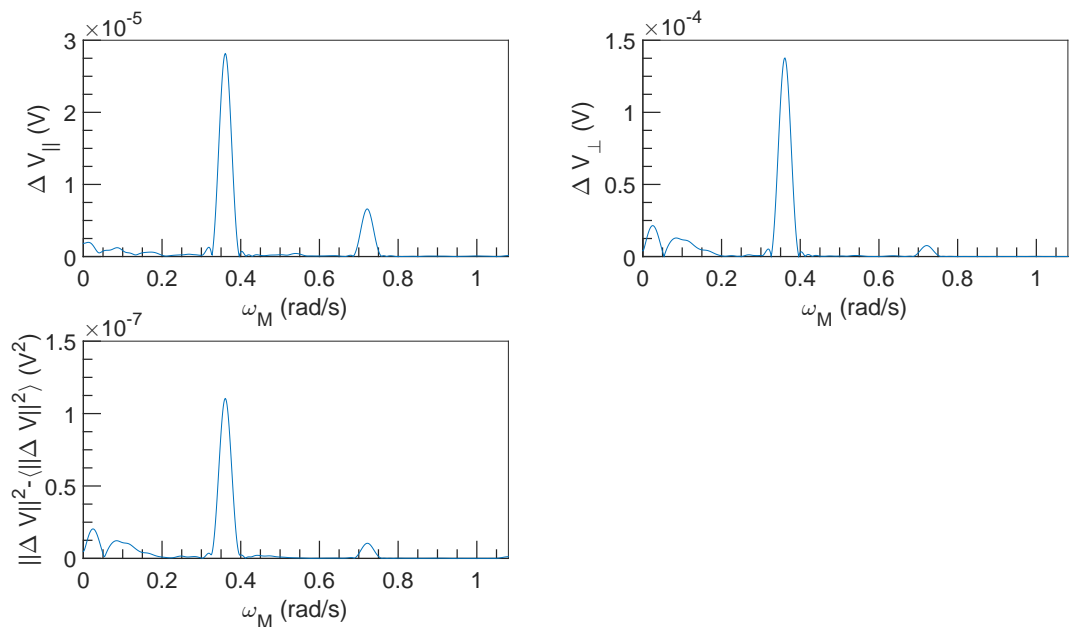


Figure 8.10: FFT spectral density of  $\Delta V$  vs  $\omega_M$  at  $U = 10^{-3} \text{ m s}^{-1}$ ,  $\omega = 10\,996 \text{ rad s}^{-1}$  and  $\alpha = 0.54\%$ .

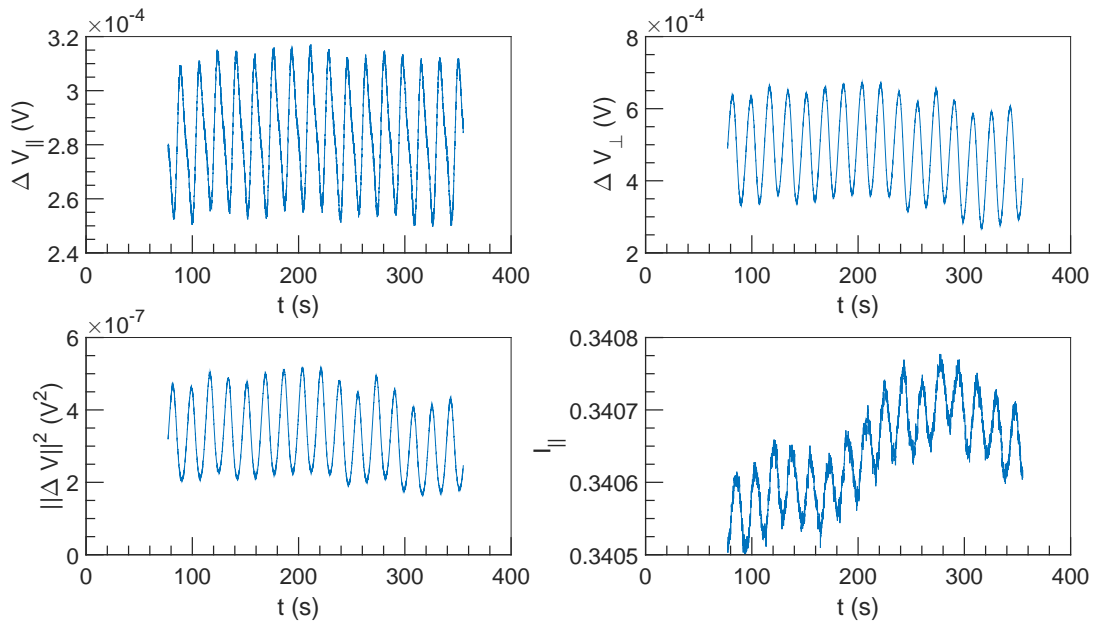


Figure 8.11:  $\Delta V$  and  $I$  vs  $t$  at  $U = 10^{-3} \text{ m s}^{-1}$ ,  $\omega = 12566 \text{ rad s}^{-1}$  and  $\alpha = 0.54\%$ .

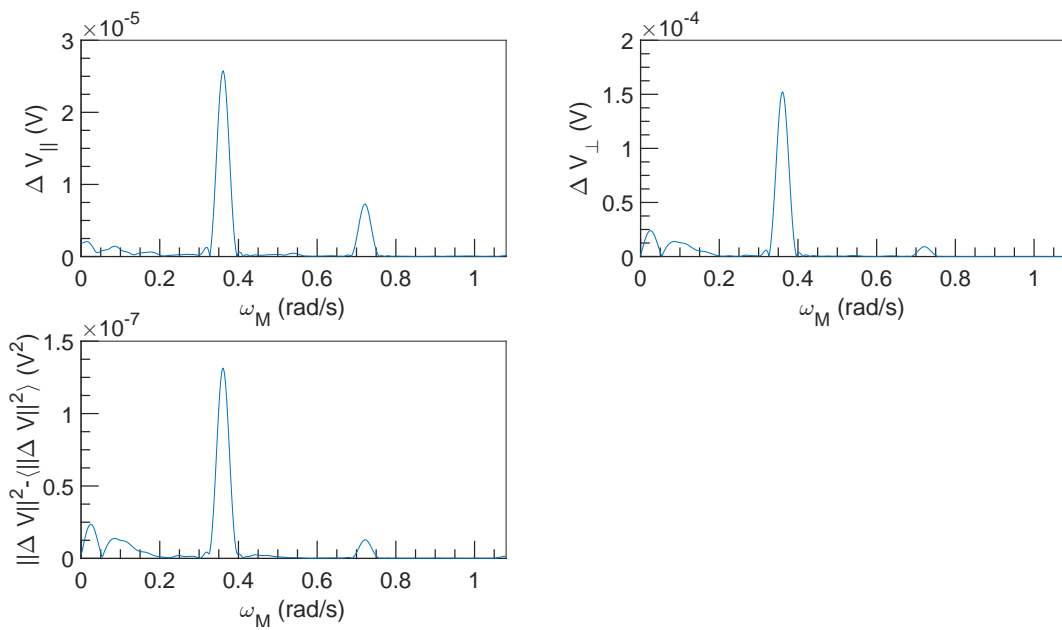


Figure 8.12: FFT spectral density of  $\Delta V$  vs  $\omega_M$  at  $U = 10^{-3} \text{ m s}^{-1}$ ,  $\omega = 12566 \text{ rad s}^{-1}$  and  $\alpha = 0.54\%$ .

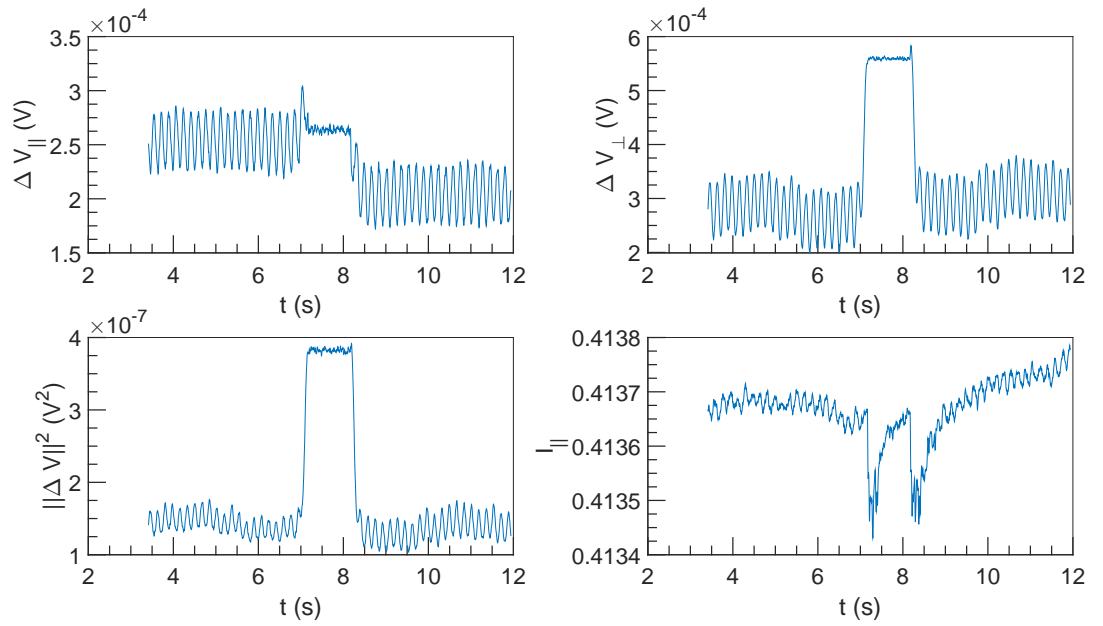


Figure 8.13:  $\Delta V$  and  $I$  vs  $t$  at  $U = 0.1 \text{ m s}^{-1}$ ,  $\omega = 4712 \text{ rad s}^{-1}$  and  $\alpha = 0.54\%$ .

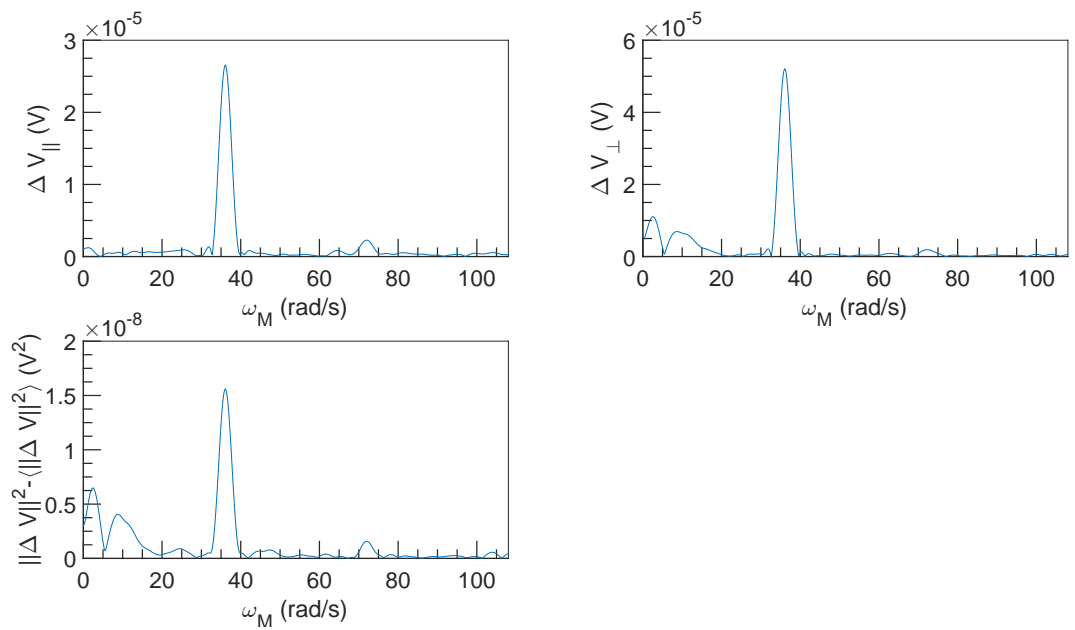


Figure 8.14: FFT spectral density of  $\Delta V$  vs  $\omega_M$  at  $U = 0.1 \text{ m s}^{-1}$ ,  $\omega = 4712 \text{ rad s}^{-1}$  and  $\alpha = 0.54\%$ .

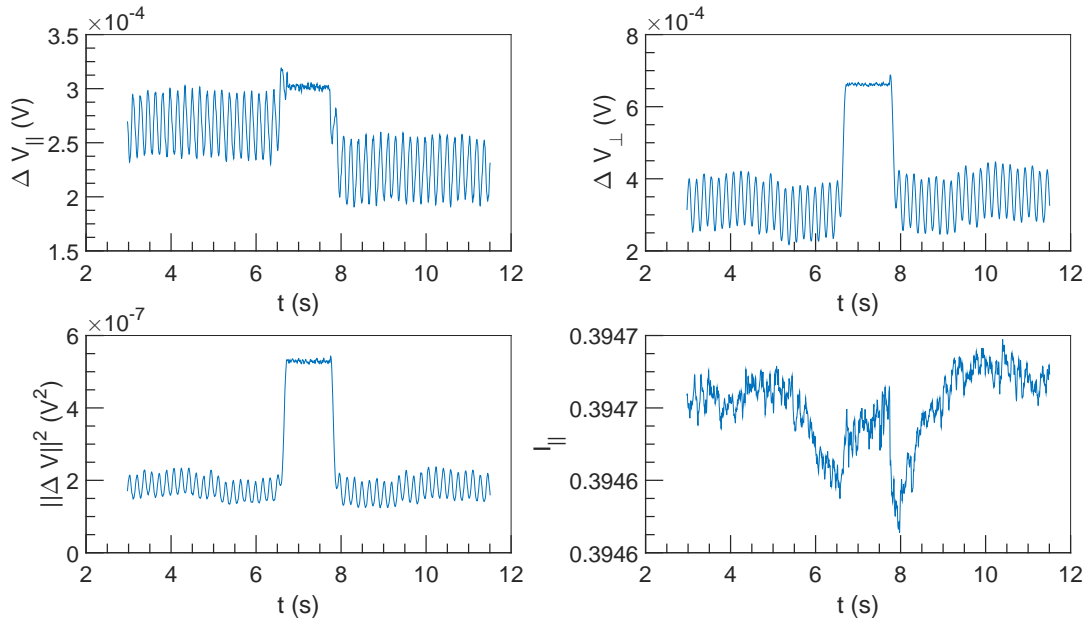


Figure 8.15:  $\Delta V$  and  $I$  vs  $t$  at  $U = 0.1 \text{ m s}^{-1}$ ,  $\omega = 6283 \text{ rad s}^{-1}$  and  $\alpha = 0.54 \%$ .

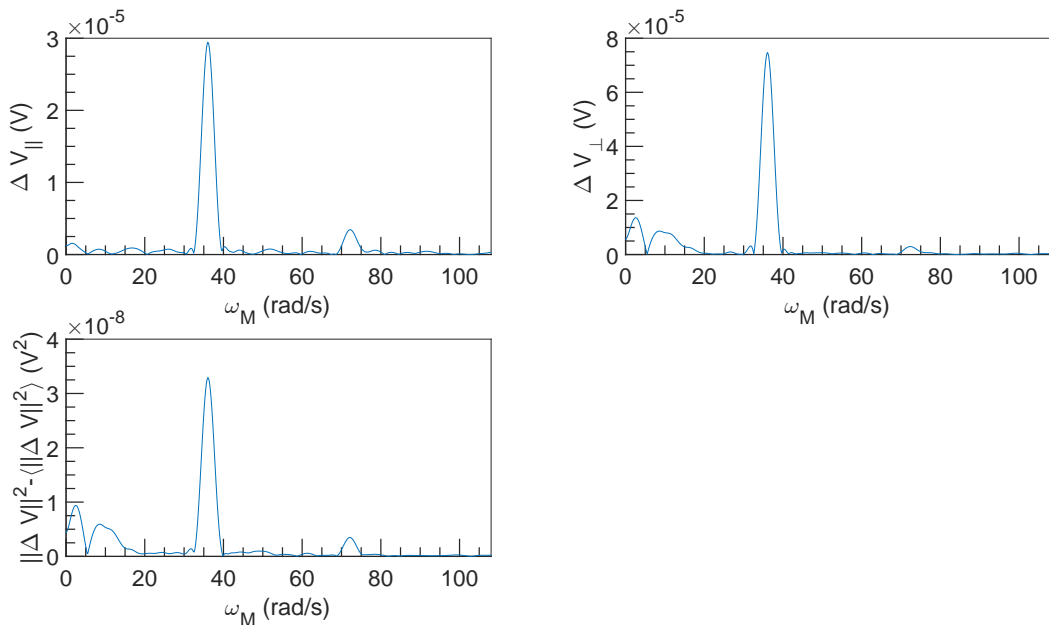


Figure 8.16: FFT spectral density of  $\Delta V$  vs  $\omega_M$  at  $U = 0.1 \text{ m s}^{-1}$ ,  $\omega = 6283 \text{ rad s}^{-1}$  and  $\alpha = 0.54 \%$ .



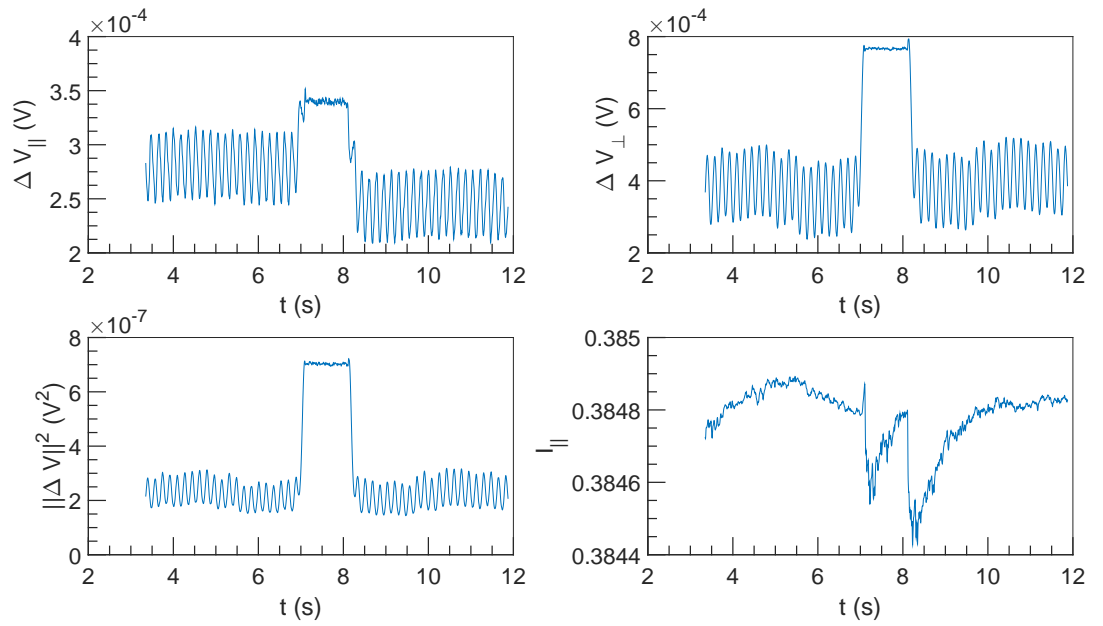


Figure 8.17:  $\Delta V$  and  $I$  vs  $t$  at  $U = 0.1 \text{ m s}^{-1}$ ,  $\omega = 7854 \text{ rad s}^{-1}$  and  $\alpha = 0.54\%$ .

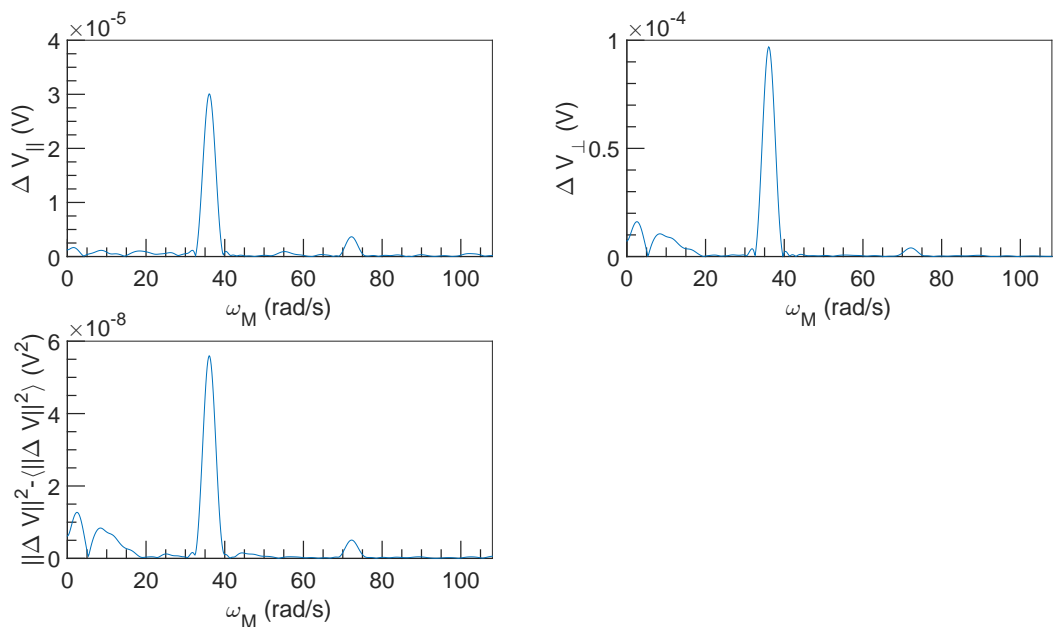


Figure 8.18: FFT spectral density of  $\Delta V$  vs  $\omega_M$  at  $U = 0.1 \text{ m s}^{-1}$ ,  $\omega = 7854 \text{ rad s}^{-1}$  and  $\alpha = 0.54\%$ .

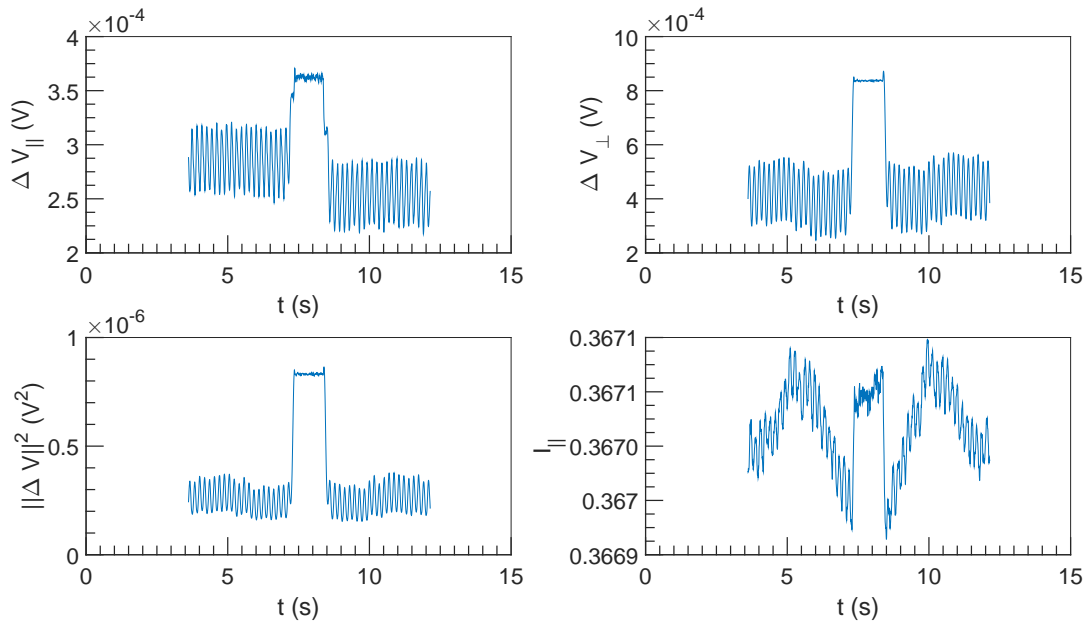


Figure 8.19:  $\Delta V$  and  $I$  vs  $t$  at  $U = 0.1 \text{ m s}^{-1}$ ,  $\omega = 9425 \text{ rad s}^{-1}$  and  $\alpha = 0.54 \%$ .

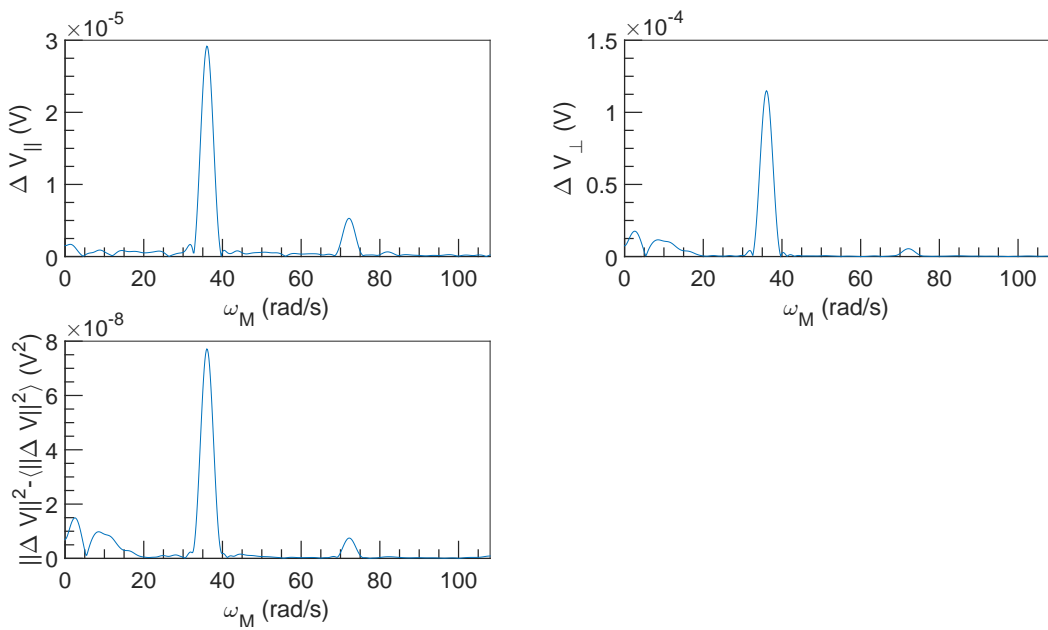


Figure 8.20: FFT spectral density of  $\Delta V$  vs  $\omega_M$  at  $U = 0.1 \text{ m s}^{-1}$ ,  $\omega = 9425 \text{ rad s}^{-1}$  and  $\alpha = 0.54 \%$ .

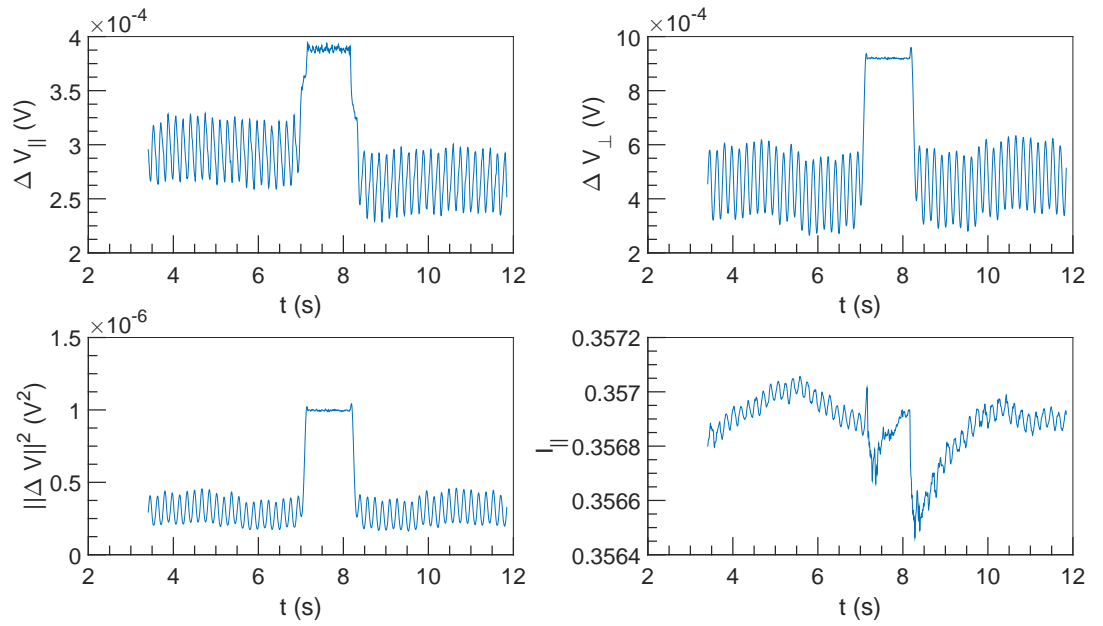


Figure 8.21:  $\Delta V$  and  $I$  vs  $t$  at  $U = 0.1 \text{ m s}^{-1}$ ,  $\omega = 10\,996 \text{ rad s}^{-1}$  and  $\alpha = 0.54\%$ .

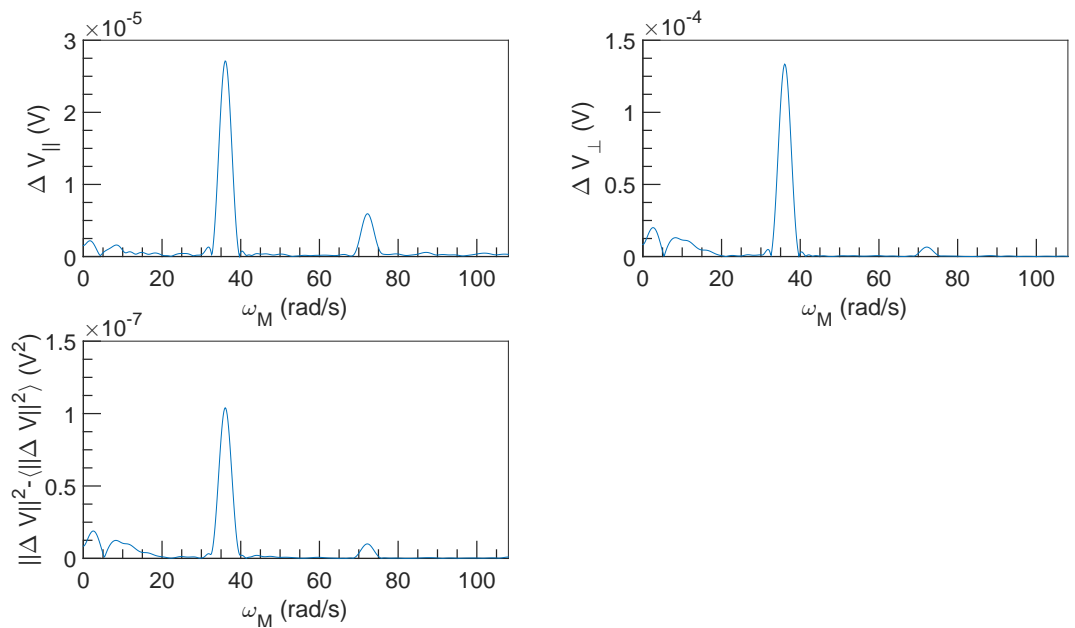


Figure 8.22: FFT spectral density of  $\Delta V$  vs  $\omega_M$  at  $U = 0.1 \text{ m s}^{-1}$ ,  $\omega = 10\,996 \text{ rad s}^{-1}$  and  $\alpha = 0.54\%$ .

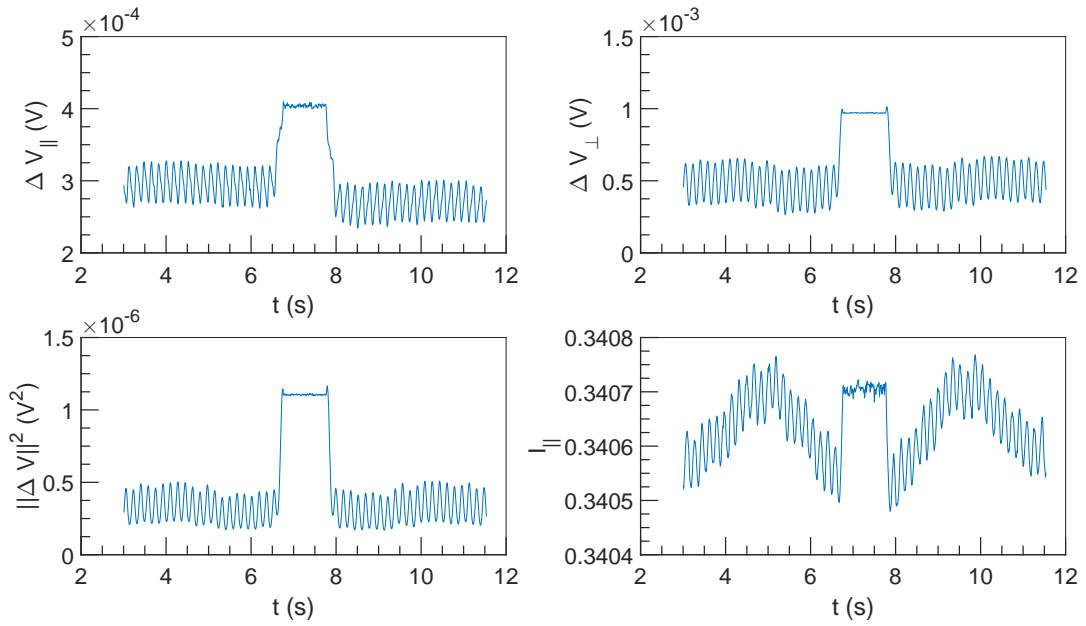


Figure 8.23:  $\Delta V$  and  $I$  vs  $t$  at  $U = 0.1 \text{ m s}^{-1}$ ,  $\omega = 12566 \text{ rad s}^{-1}$  and  $\alpha = 0.54 \%$ .

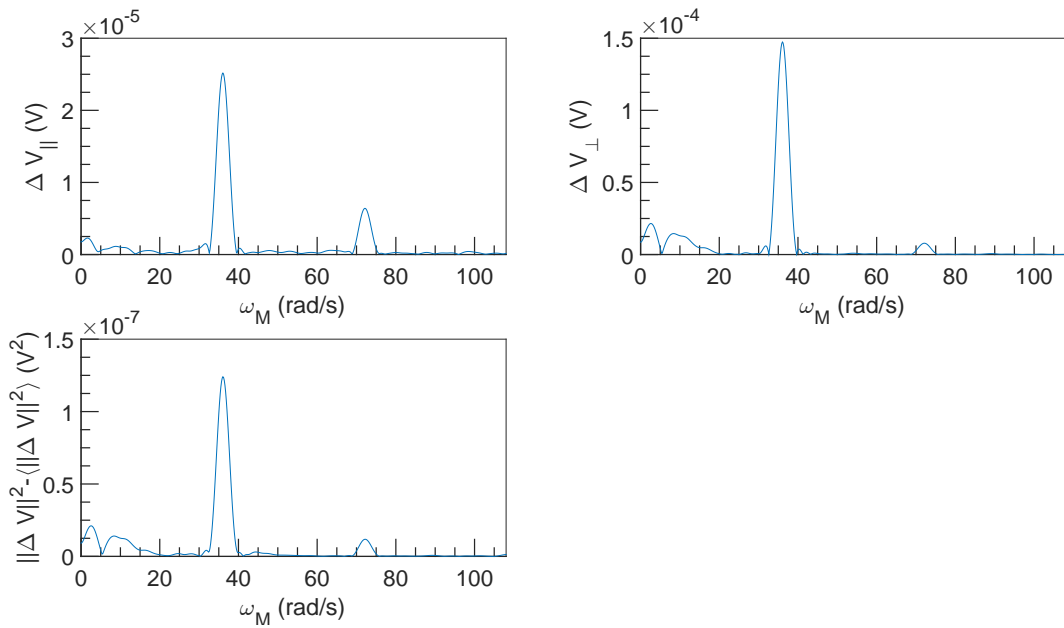


Figure 8.24: FFT spectral density of  $\Delta V$  vs  $\omega_M$  at  $U = 0.1 \text{ m s}^{-1}$ ,  $\omega = 12566 \text{ rad s}^{-1}$  and  $\alpha = 0.54 \%$ .

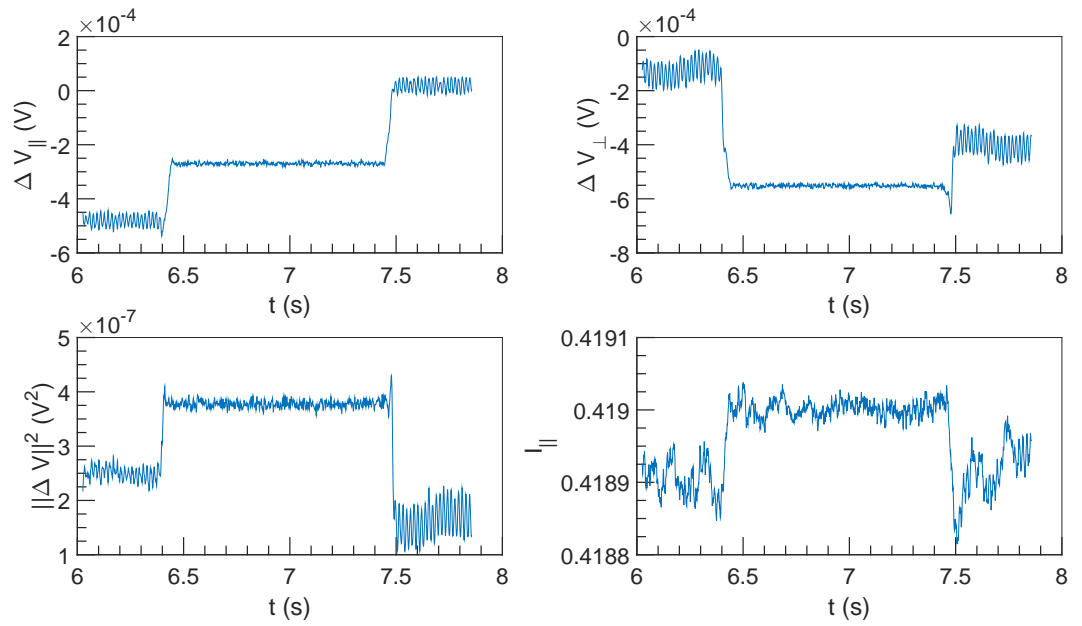


Figure 8.25:  $\Delta V$  and  $I$  vs  $t$  at  $U = 1 \text{ m s}^{-1}$ ,  $\omega = 4712 \text{ rad s}^{-1}$  and  $\alpha = 0.54 \%$ .

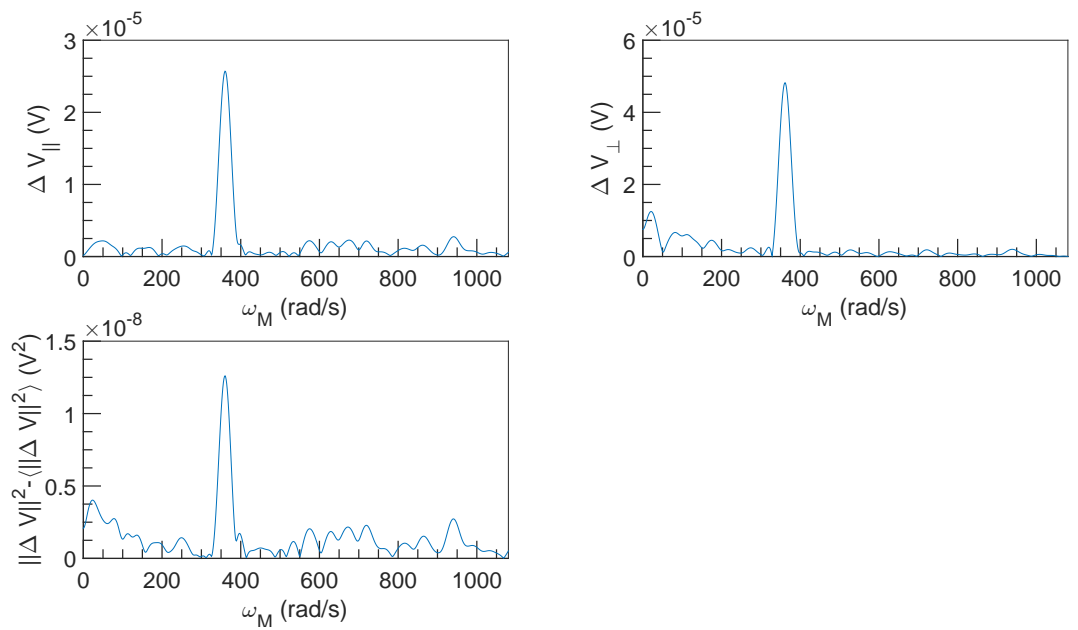


Figure 8.26: FFT spectral density of  $\Delta V$  vs  $\omega_M$  at  $U = 1 \text{ m s}^{-1}$ ,  $\omega = 4712 \text{ rad s}^{-1}$  and  $\alpha = 0.54 \%$ .

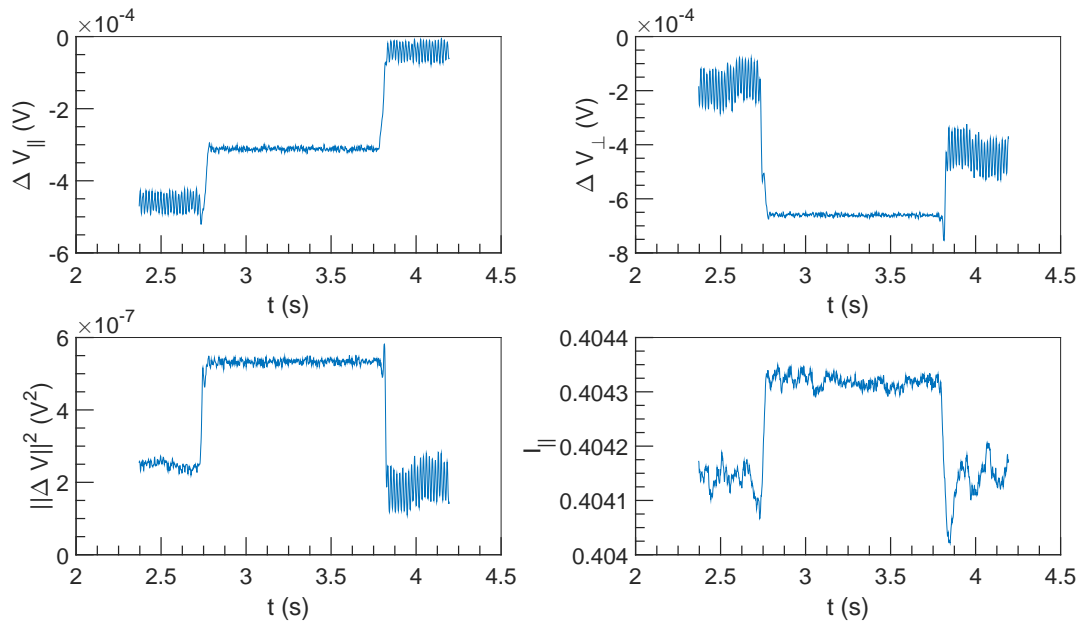


Figure 8.27:  $\Delta V$  and  $I$  vs  $t$  at  $U = 1 \text{ m s}^{-1}$ ,  $\omega = 6283 \text{ rad s}^{-1}$  and  $\alpha = 0.54 \%$ .

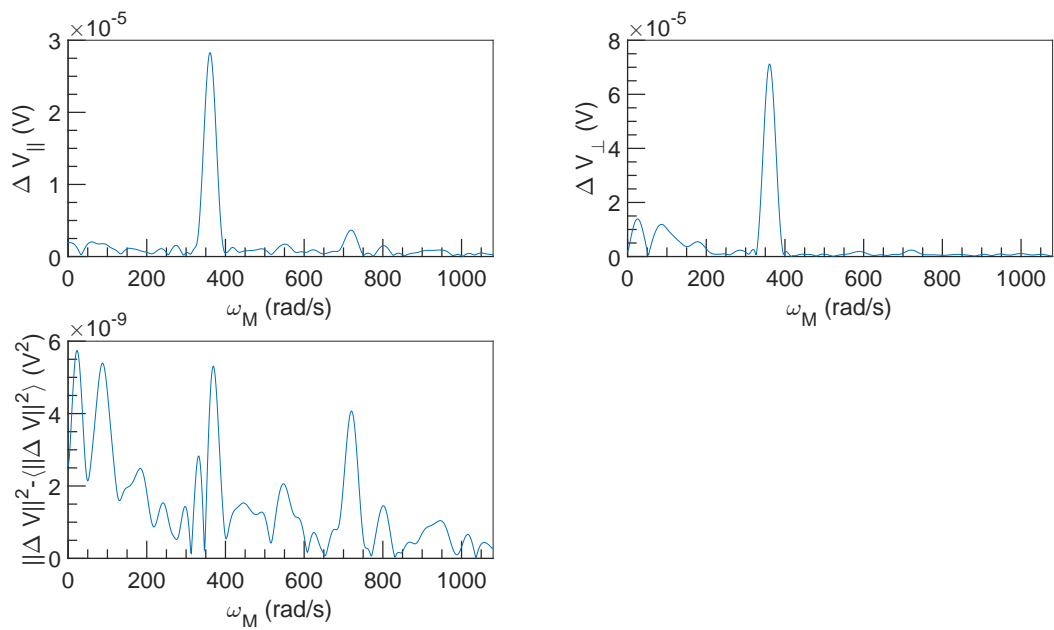


Figure 8.28: FFT spectral density of  $\Delta V$  vs  $\omega_M$  at  $U = 1 \text{ m s}^{-1}$ ,  $\omega = 6283 \text{ rad s}^{-1}$  and  $\alpha = 0.54 \%$ .

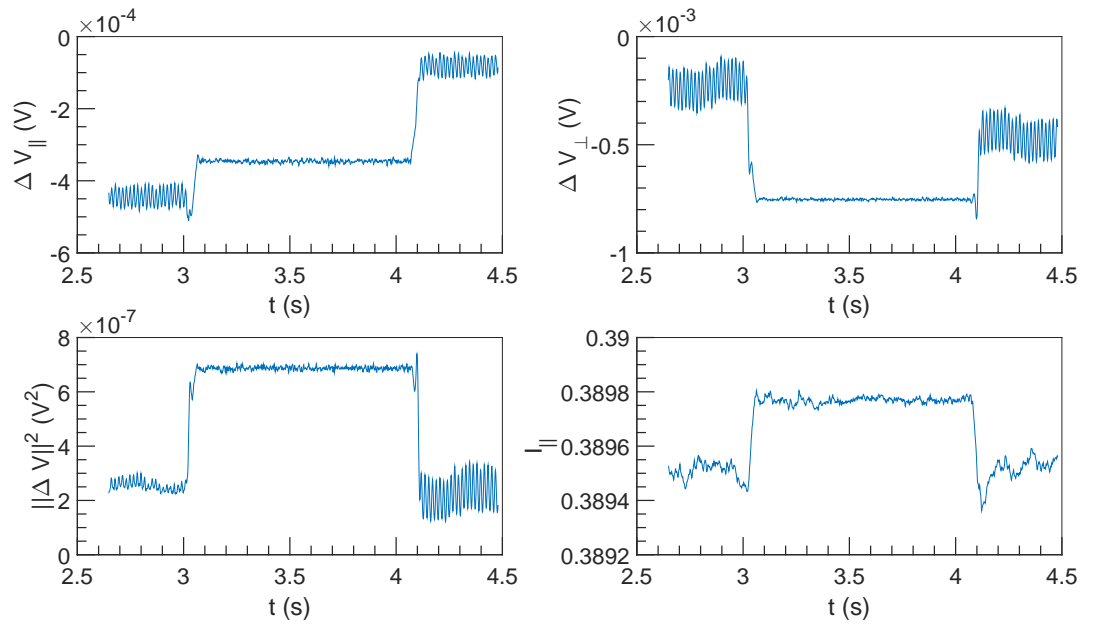


Figure 8.29:  $\Delta V$  and  $I$  vs  $t$  at  $U = 1 \text{ m s}^{-1}$ ,  $\omega = 7854 \text{ rad s}^{-1}$  and  $\alpha = 0.54 \%$ .

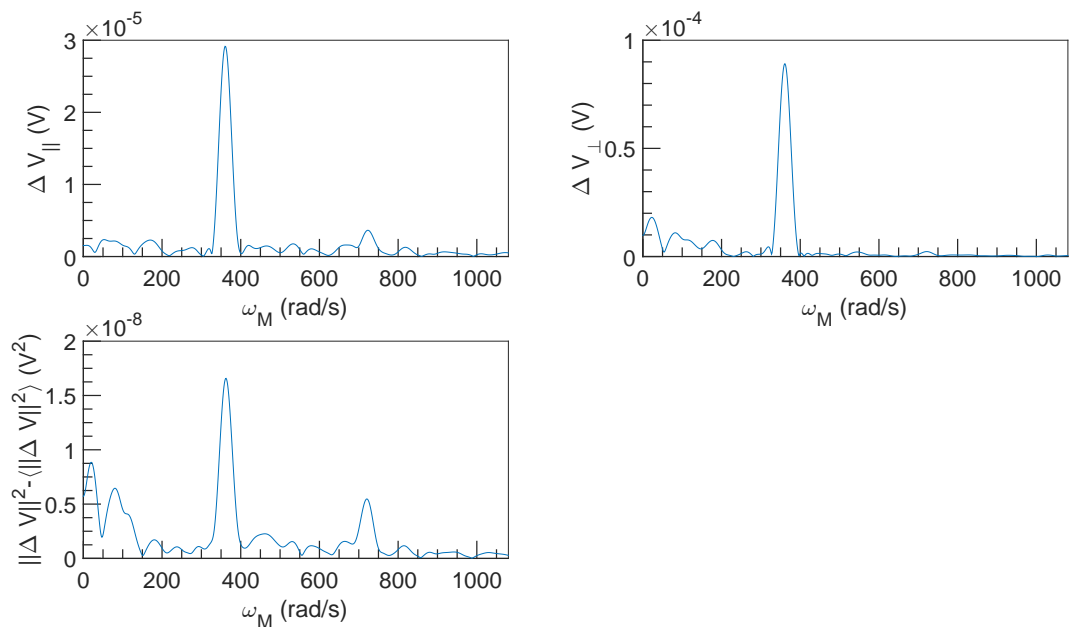


Figure 8.30: FFT spectral density of  $\Delta V$  vs  $\omega_M$  at  $U = 1 \text{ m s}^{-1}$ ,  $\omega = 7854 \text{ rad s}^{-1}$  and  $\alpha = 0.54 \%$ .

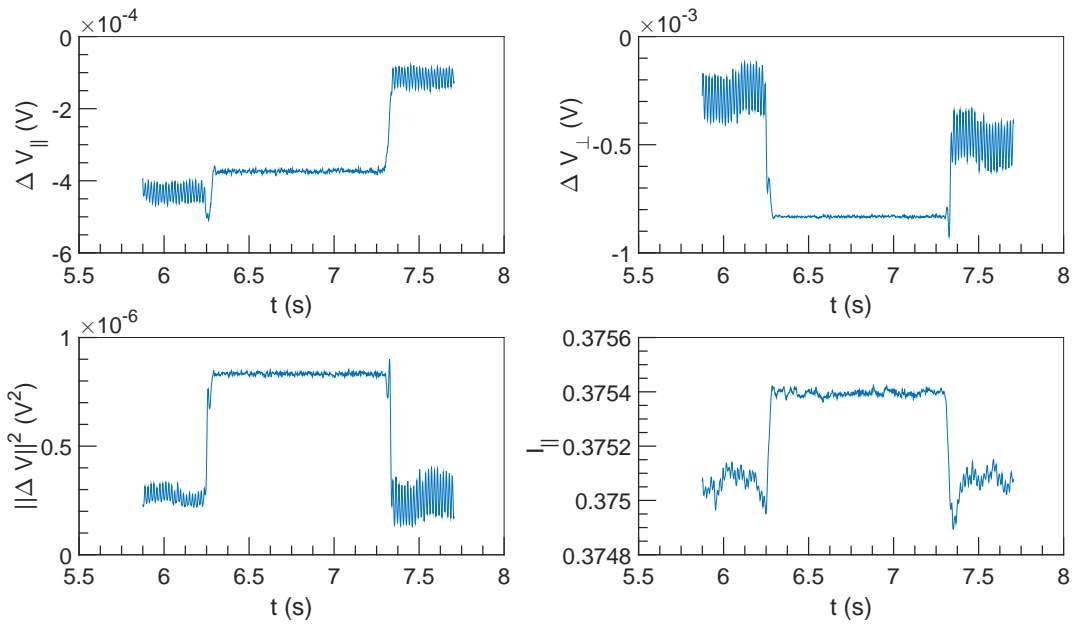


Figure 8.31:  $\Delta V$  and  $I$  vs  $t$  at  $U = 1 \text{ m s}^{-1}$ ,  $\omega = 9425 \text{ rad s}^{-1}$  and  $\alpha = 0.54 \%$ .

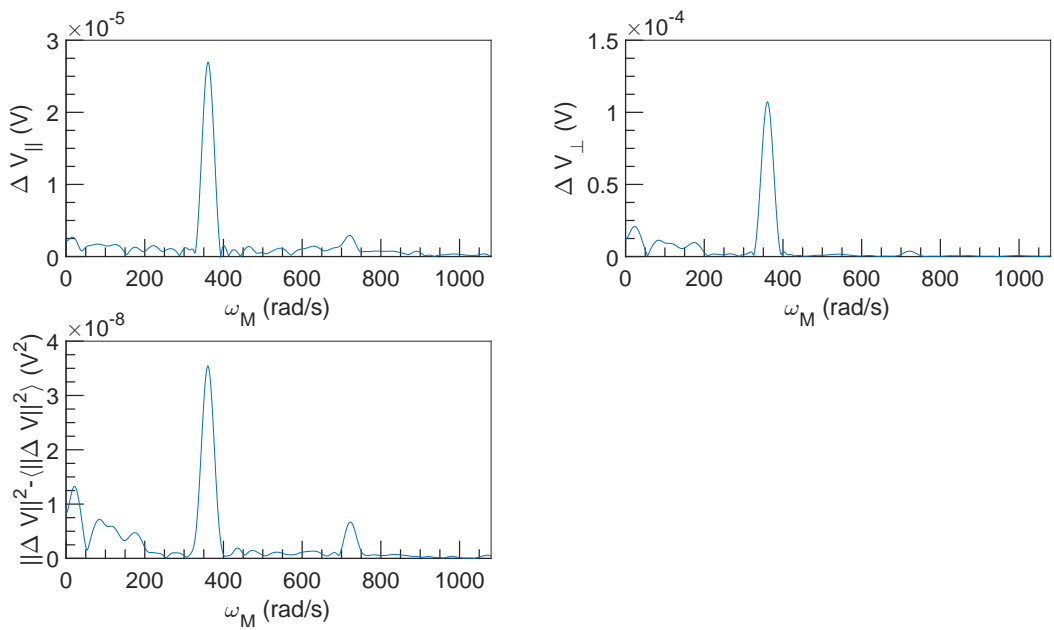


Figure 8.32: FFT spectral density of  $\Delta V$  vs  $\omega_M$  at  $U = 1 \text{ m s}^{-1}$ ,  $\omega = 9425 \text{ rad s}^{-1}$  and  $\alpha = 0.54 \%$ .



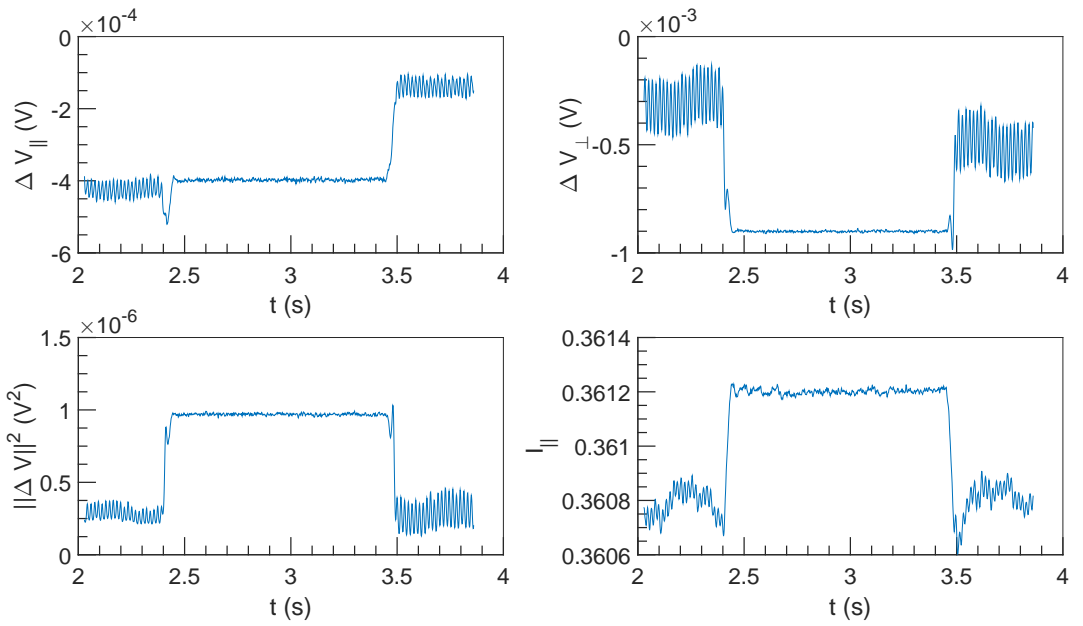


Figure 8.33:  $\Delta V$  and  $I$  vs  $t$  at  $U = 1 \text{ m s}^{-1}$ ,  $\omega = 10996 \text{ rad s}^{-1}$  and  $\alpha = 0.54 \%$ .

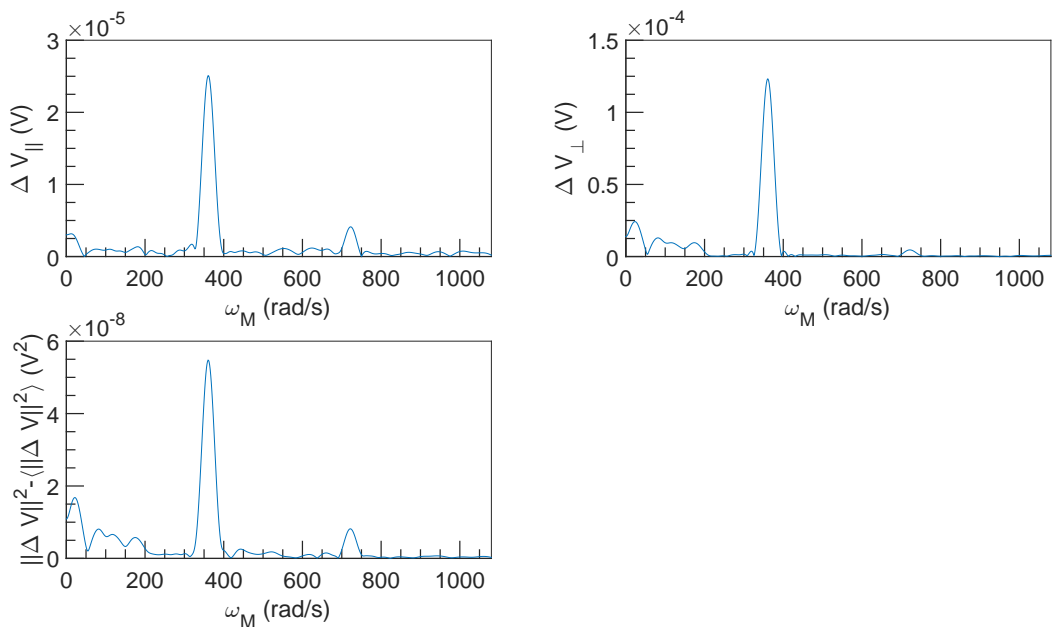


Figure 8.34: FFT spectral density of  $\Delta V$  vs  $\omega_M$  at  $U = 1 \text{ m s}^{-1}$ ,  $\omega = 10996 \text{ rad s}^{-1}$  and  $\alpha = 0.54 \%$ .

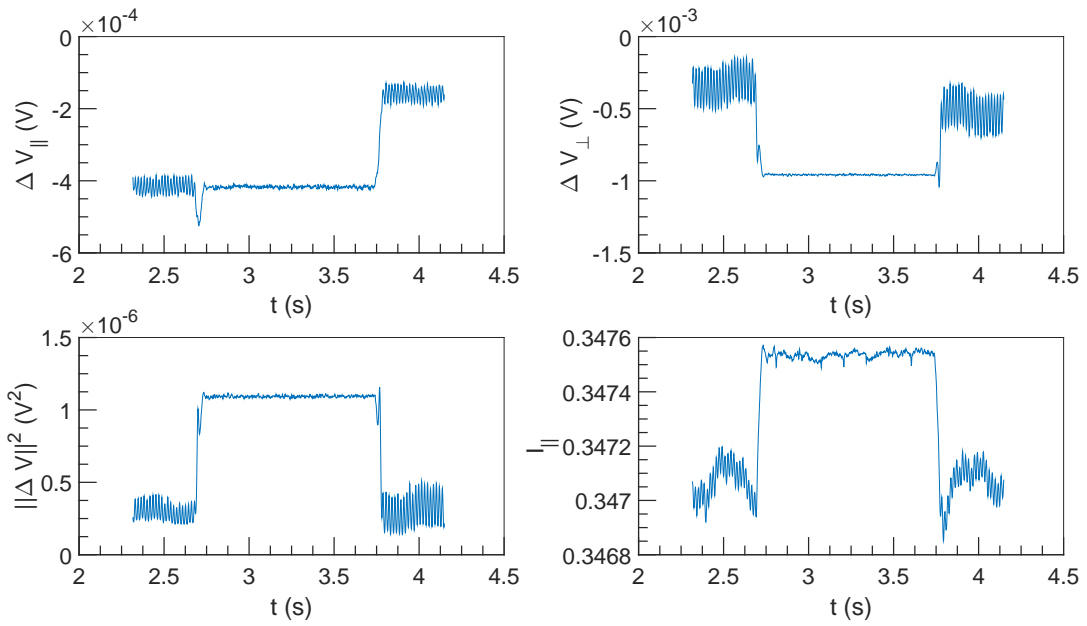


Figure 8.35:  $\Delta V$  and  $I$  vs  $t$  at  $U = 1 \text{ m s}^{-1}$ ,  $\omega = 12566 \text{ rad s}^{-1}$  and  $\alpha = 0.54\%$ .

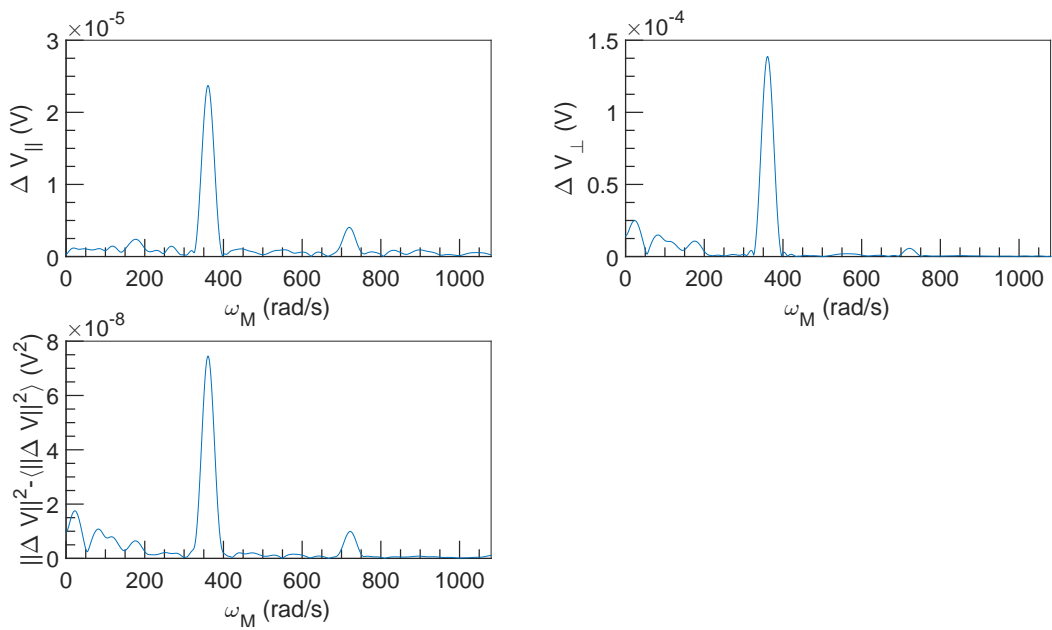


Figure 8.36: FFT spectral density of  $\Delta V$  vs  $\omega_M$  at  $U = 1 \text{ m s}^{-1}$ ,  $\omega = 12566 \text{ rad s}^{-1}$  and  $\alpha = 0.54\%$ .

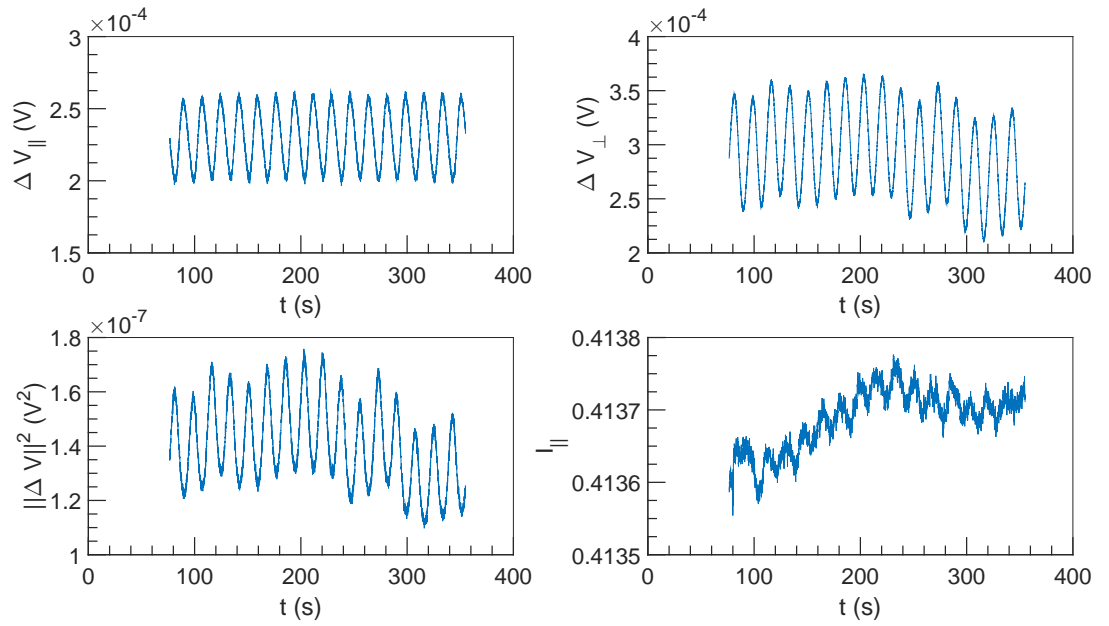


Figure 8.37:  $\Delta V$  and  $I$  vs  $t$  at  $U = 10^{-3} \text{ m s}^{-1}$ ,  $\omega = 4712 \text{ rad s}^{-1}$  and  $\alpha = 0.54\%$ .

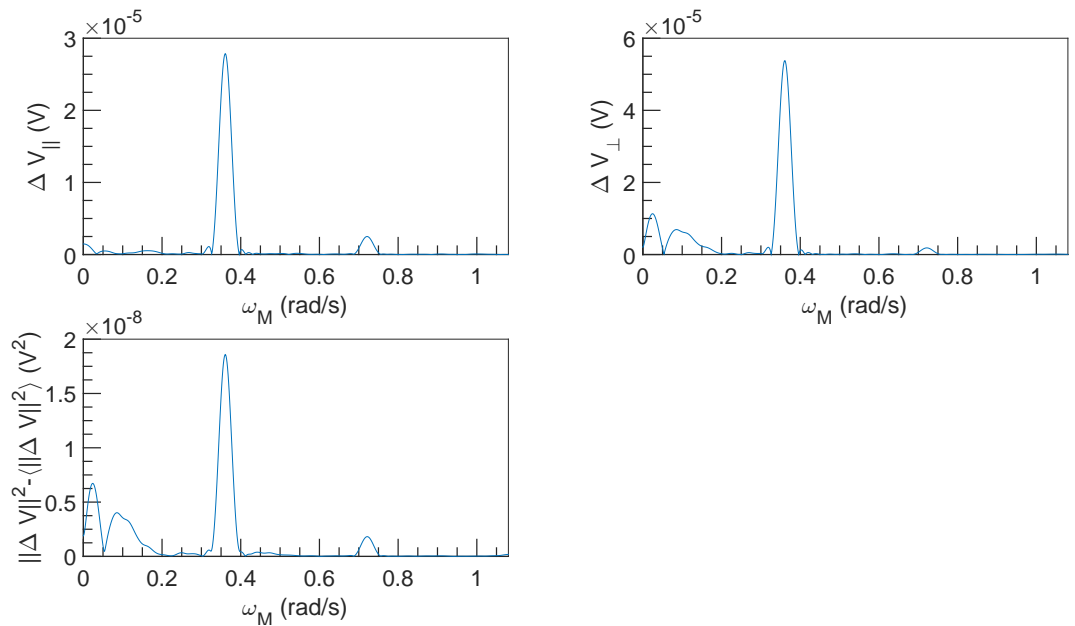


Figure 8.38: FFT spectral density of  $\Delta V$  vs  $\omega_M$  at  $U = 10^{-3} \text{ m s}^{-1}$ ,  $\omega = 4712 \text{ rad s}^{-1}$  and  $\alpha = 0.54\%$ .

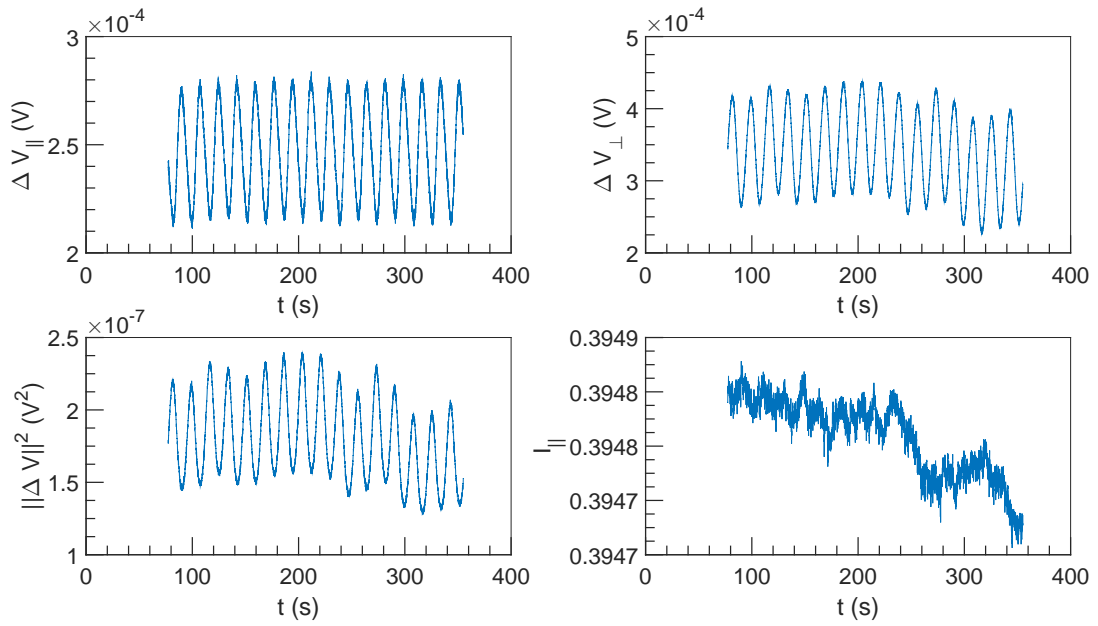


Figure 8.39:  $\Delta V$  and  $I$  vs  $t$  at  $U = 10^{-3} \text{ m s}^{-1}$ ,  $\omega = 6283 \text{ rad s}^{-1}$  and  $\alpha = 0.54\%$ .

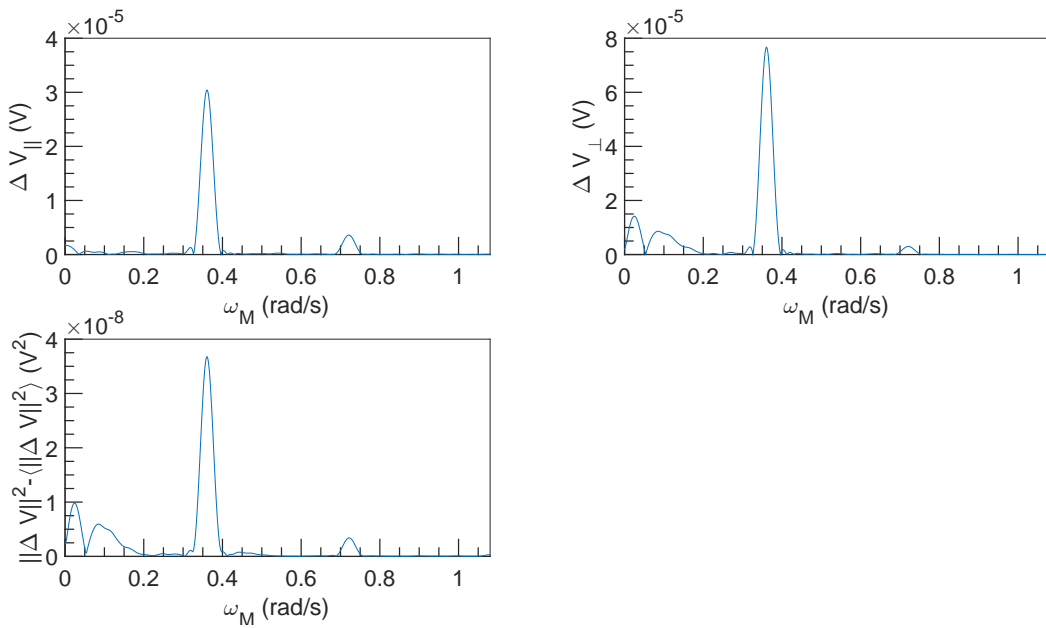


Figure 8.40: FFT spectral density of  $\Delta V$  vs  $\omega_M$  at  $U = 10^{-3} \text{ m s}^{-1}$ ,  $\omega = 6283 \text{ rad s}^{-1}$  and  $\alpha = 0.54\%$ .

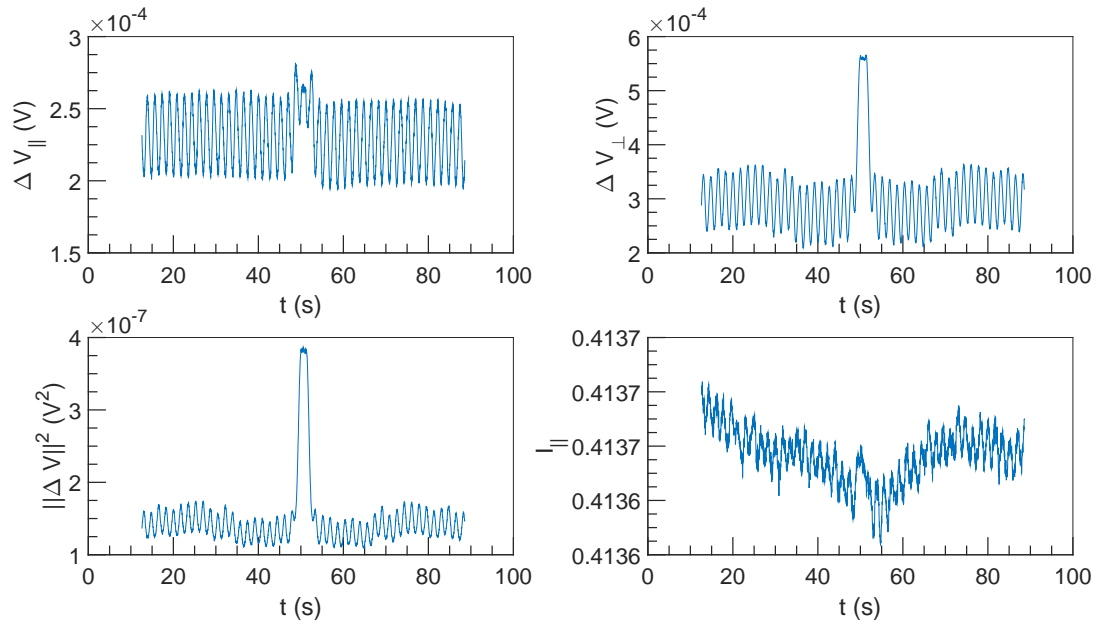


Figure 8.41:  $\Delta V$  and  $I$  vs  $t$  at  $U = 10^{-2} \text{ m s}^{-1}$ ,  $\omega = 4712 \text{ rad s}^{-1}$  and  $\alpha = 0.54\%$ .

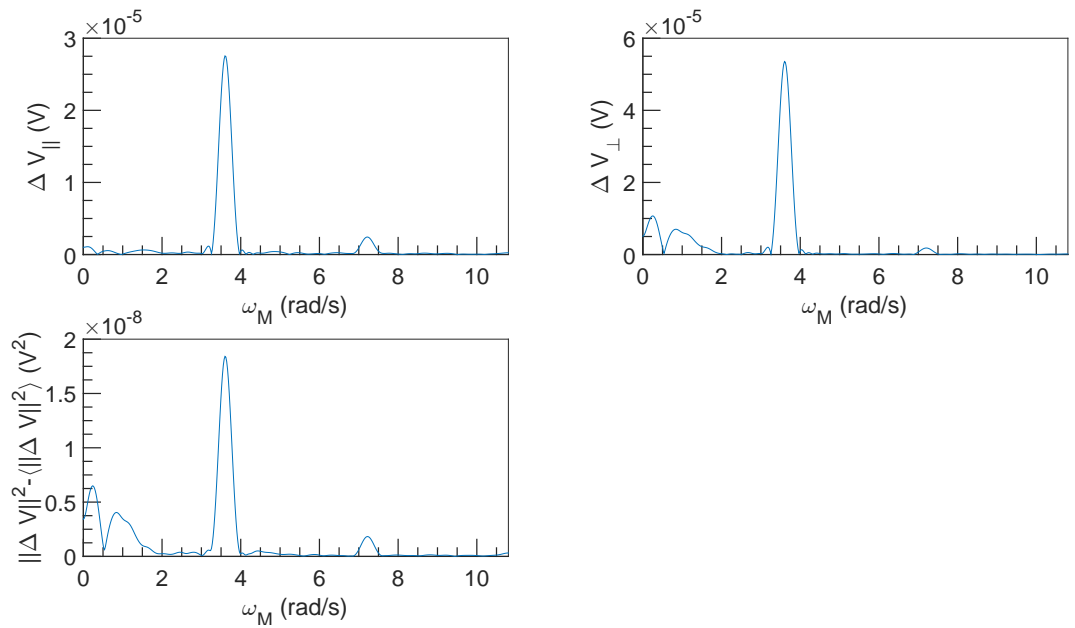


Figure 8.42: FFT spectral density of  $\Delta V$  vs  $\omega_M$  at  $U = 10^{-2} \text{ m s}^{-1}$ ,  $\omega = 4712 \text{ rad s}^{-1}$  and  $\alpha = 0.54\%$ .

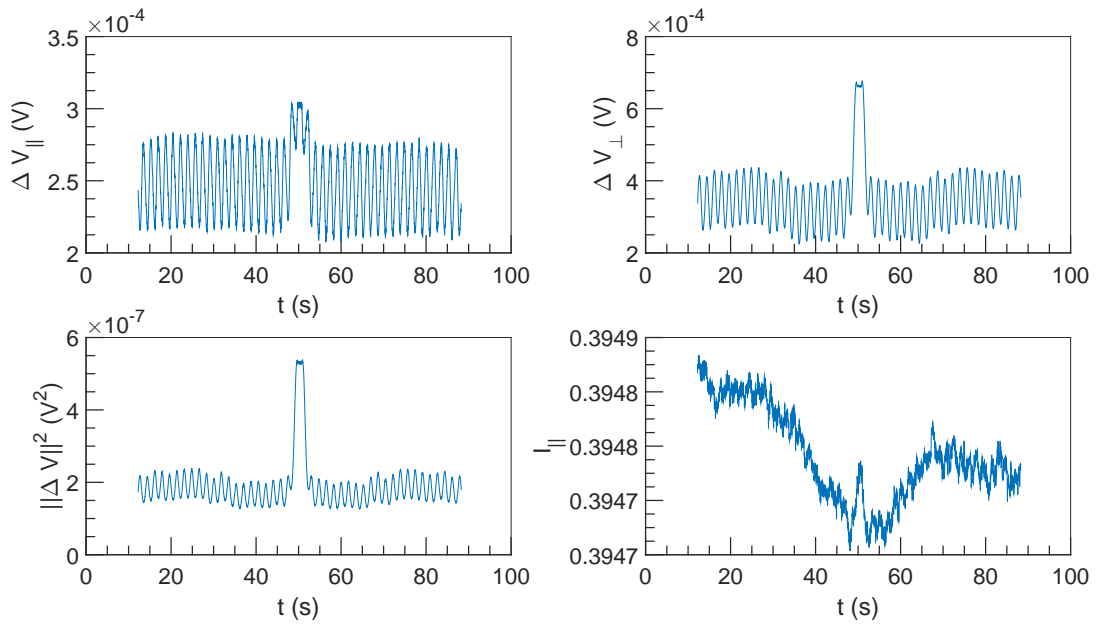


Figure 8.43:  $\Delta V$  and  $I$  vs  $t$  at  $U = 10^{-2} \text{ m s}^{-1}$ ,  $\omega = 6283 \text{ rad s}^{-1}$  and  $\alpha = 0.54\%$ .

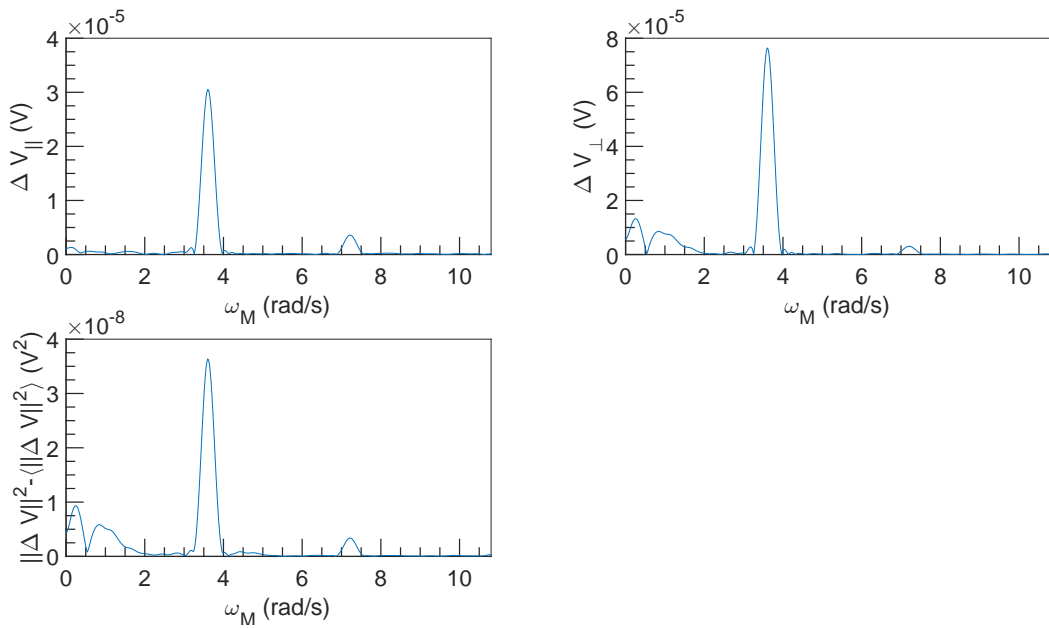


Figure 8.44: FFT spectral density of  $\Delta V$  vs  $\omega_M$  at  $U = 10^{-2} \text{ m s}^{-1}$ ,  $\omega = 6283 \text{ rad s}^{-1}$  and  $\alpha = 0.54\%$ .

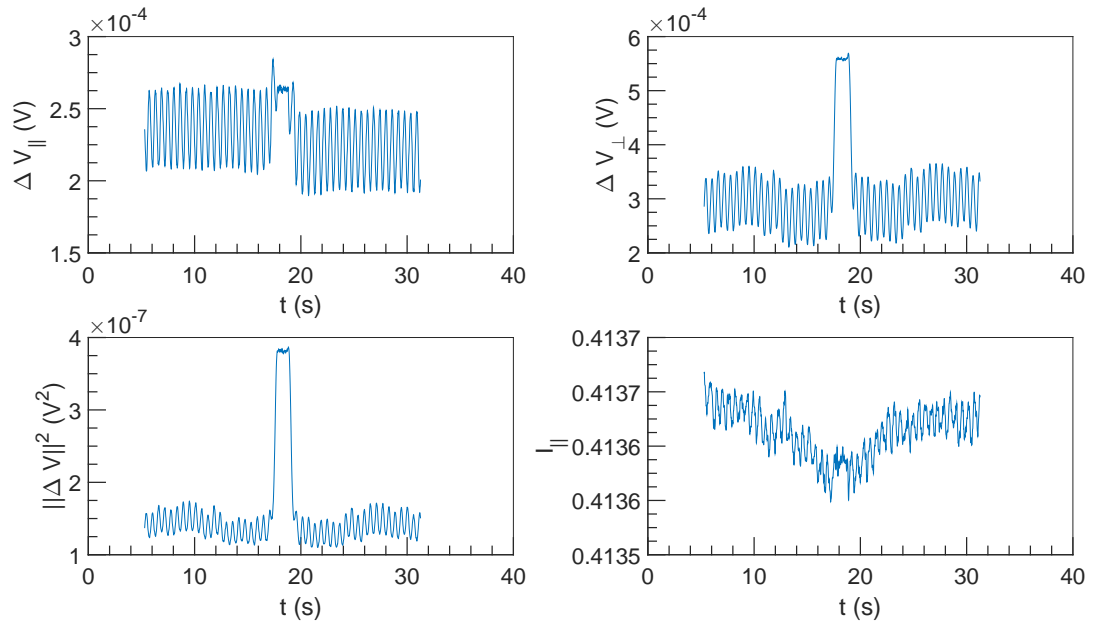


Figure 8.45:  $\Delta V$  and  $I$  vs  $t$  at  $U = 3 \times 10^{-2} \text{ m s}^{-1}$ ,  $\omega = 4712 \text{ rad s}^{-1}$  and  $\alpha = 0.54 \%$ .

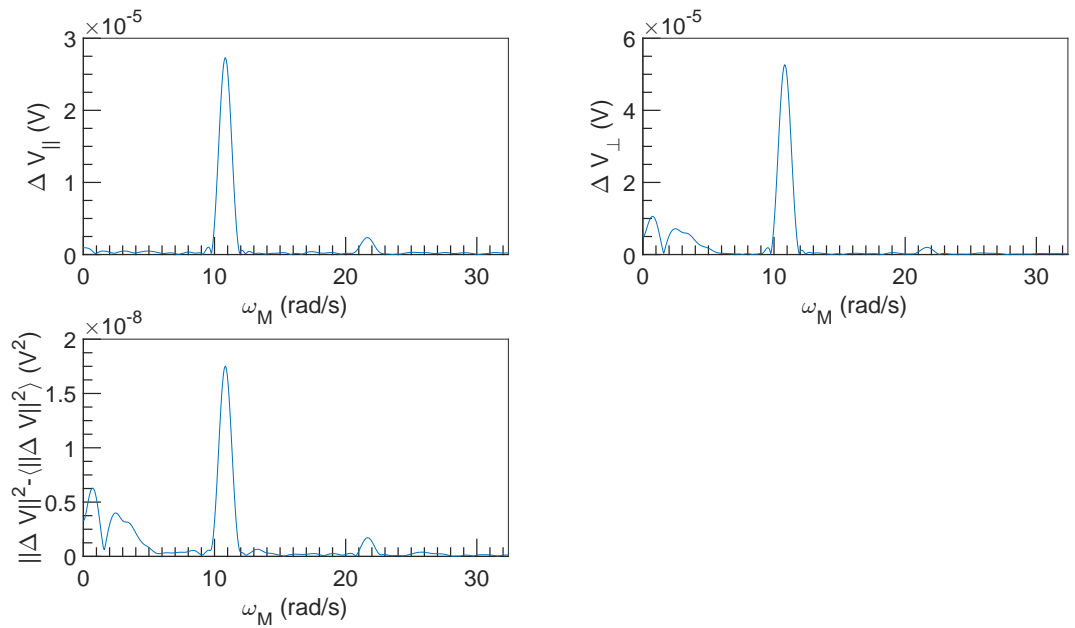


Figure 8.46: FFT spectral density of  $\Delta V$  vs  $\omega_M$  at  $U = 3 \times 10^{-2} \text{ m s}^{-1}$ ,  $\omega = 4712 \text{ rad s}^{-1}$  and  $\alpha = 0.54 \%$ .

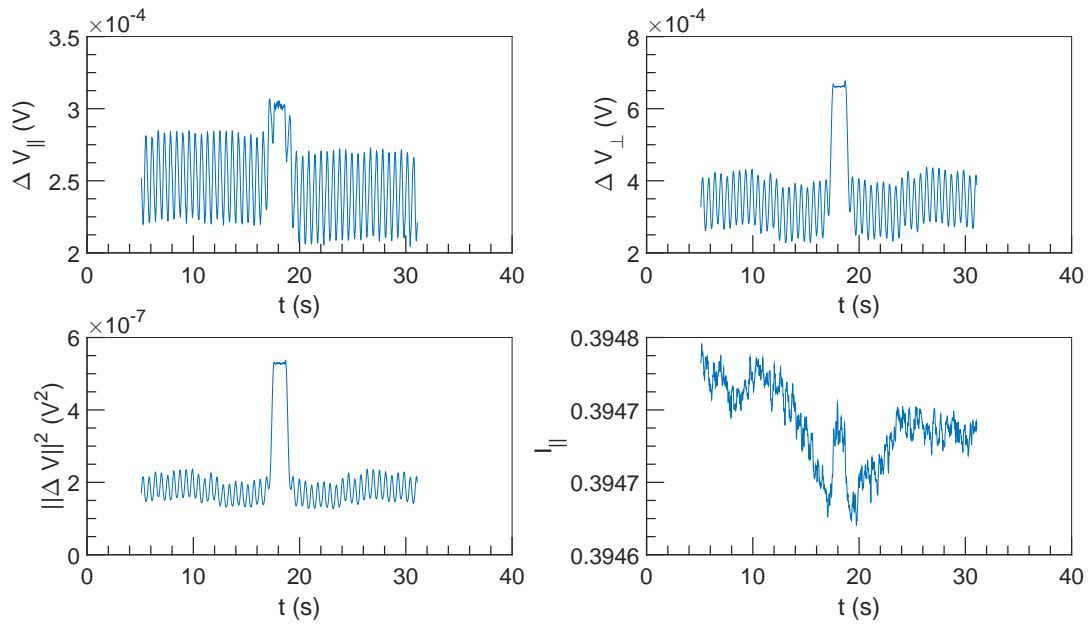


Figure 8.47:  $\Delta V$  and  $I$  vs  $t$  at  $U = 3 \times 10^{-2} \text{ m s}^{-1}$ ,  $\omega = 6283 \text{ rad s}^{-1}$  and  $\alpha = 0.54 \%$ .

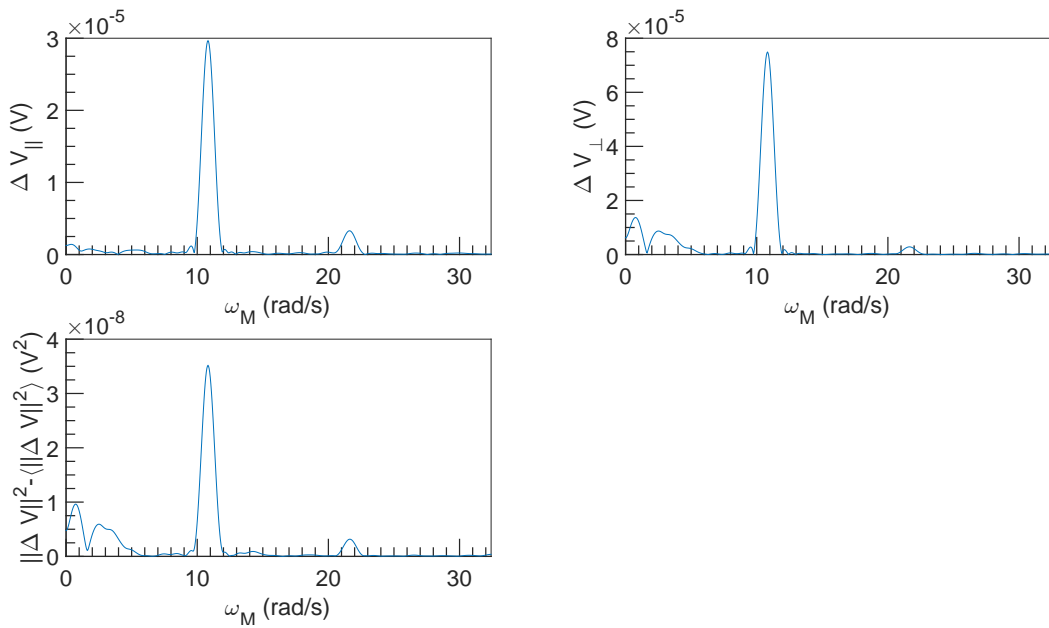


Figure 8.48: FFT spectral density of  $\Delta V$  vs  $\omega_M$  at  $U = 3 \times 10^{-2} \text{ m s}^{-1}$ ,  $\omega = 6283 \text{ rad s}^{-1}$  and  $\alpha = 0.54 \%$ .



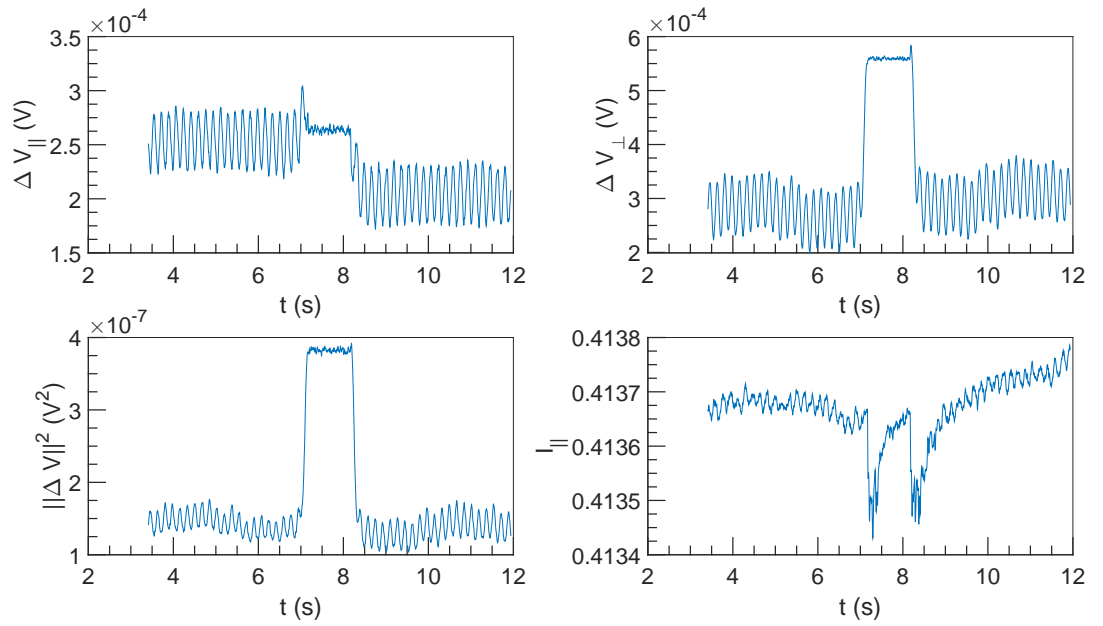


Figure 8.49:  $\Delta V$  and  $I$  vs  $t$  at  $U = 0.1 \text{ m s}^{-1}$ ,  $\omega = 4712 \text{ rad s}^{-1}$  and  $\alpha = 0.54\%$ .

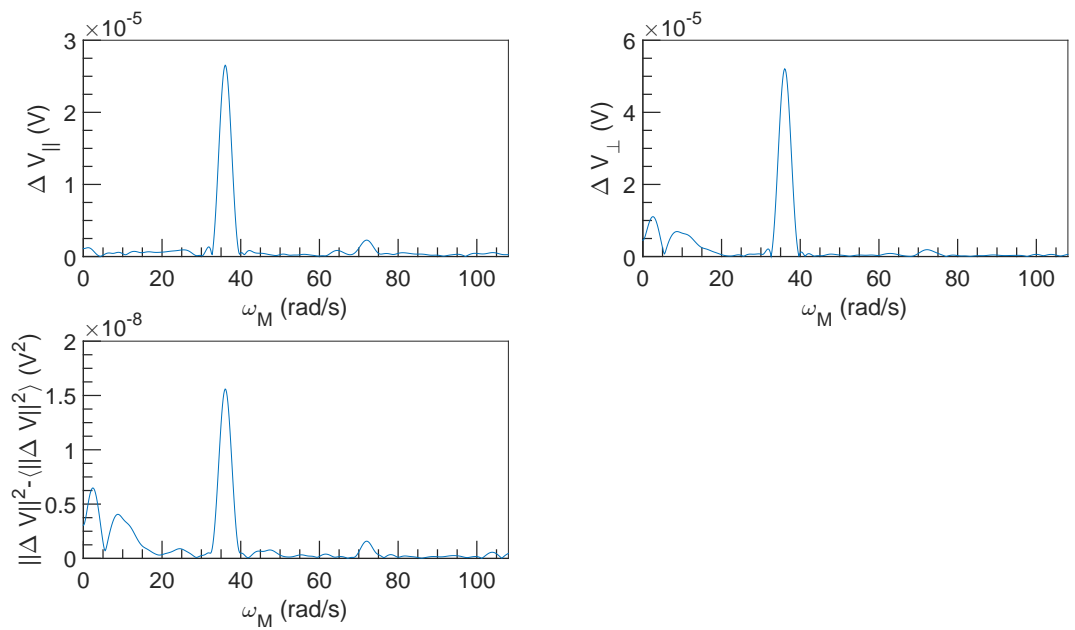


Figure 8.50: FFT spectral density of  $\Delta V$  vs  $\omega_M$  at  $U = 0.1 \text{ m s}^{-1}$ ,  $\omega = 4712 \text{ rad s}^{-1}$  and  $\alpha = 0.54\%$ .

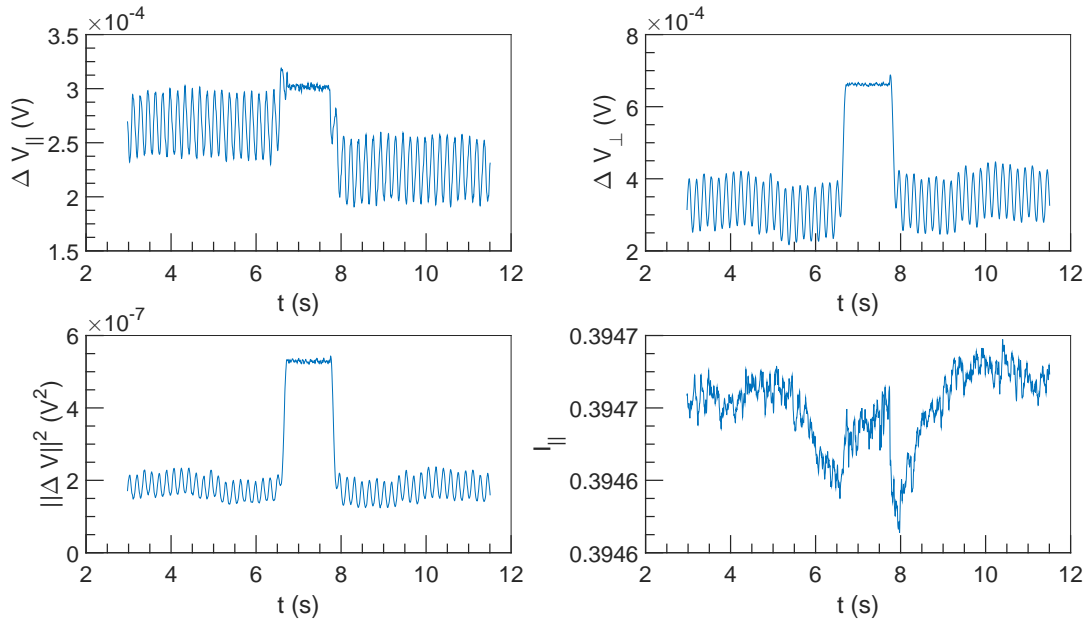


Figure 8.51:  $\Delta V$  and  $I$  vs  $t$  at  $U = 0.1 \text{ m s}^{-1}$ ,  $\omega = 6283 \text{ rad s}^{-1}$  and  $\alpha = 0.54 \%$ .

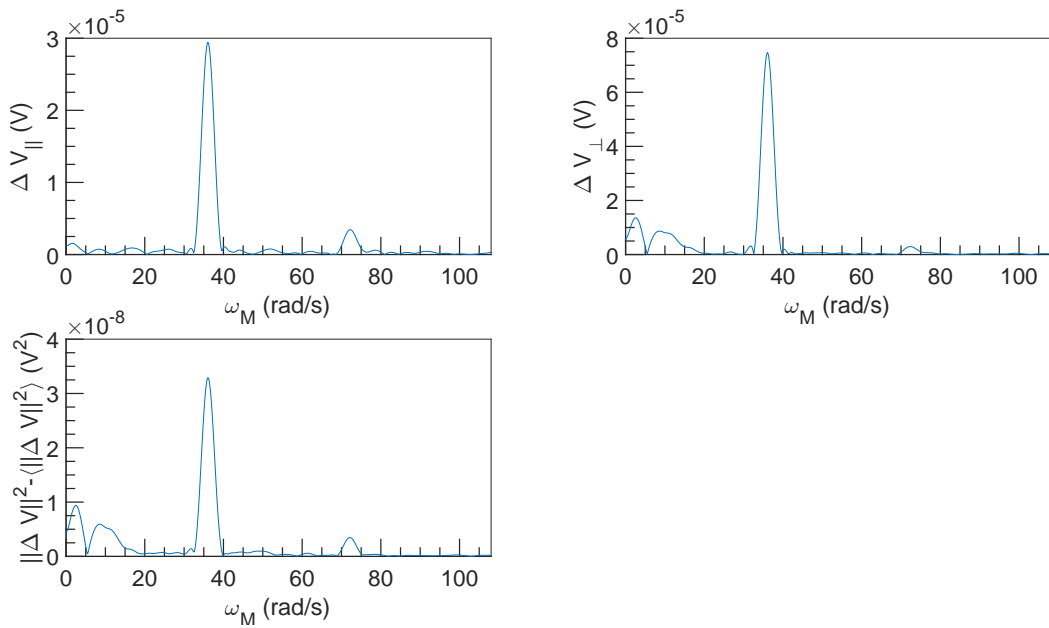


Figure 8.52: FFT spectral density of  $\Delta V$  vs  $\omega_M$  at  $U = 0.1 \text{ m s}^{-1}$ ,  $\omega = 6283 \text{ rad s}^{-1}$  and  $\alpha = 0.54 \%$ .

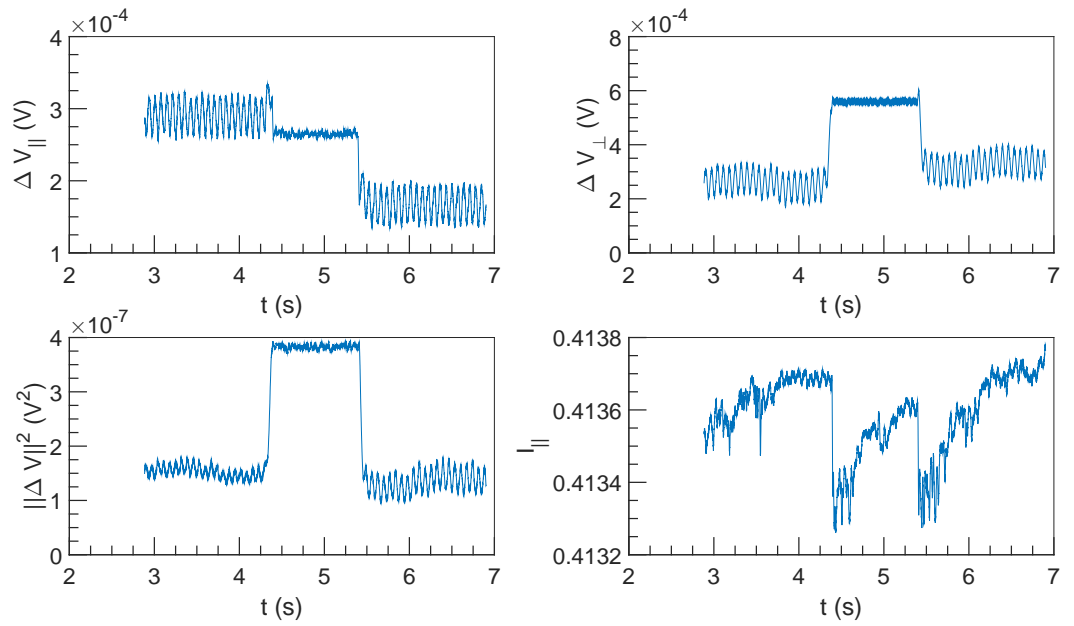


Figure 8.53:  $\Delta V$  and  $I$  vs  $t$  at  $U = 0.25 \text{ m s}^{-1}$ ,  $\omega = 4712 \text{ rad s}^{-1}$  and  $\alpha = 0.54 \%$ .

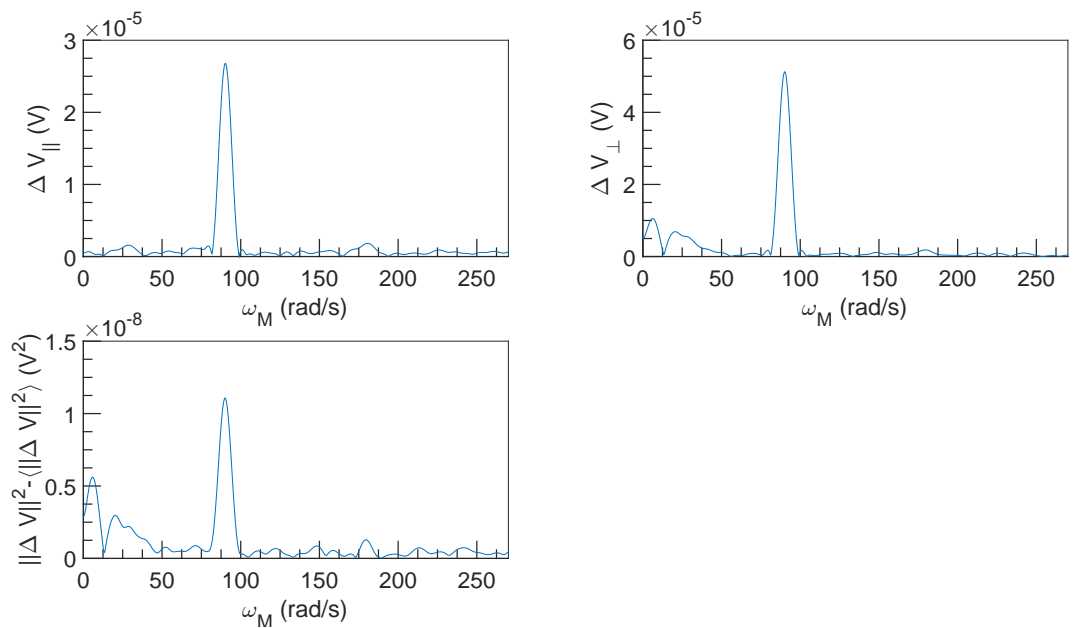


Figure 8.54: FFT spectral density of  $\Delta V$  vs  $\omega_M$  at  $U = 0.25 \text{ m s}^{-1}$ ,  $\omega = 4712 \text{ rad s}^{-1}$  and  $\alpha = 0.54 \%$ .

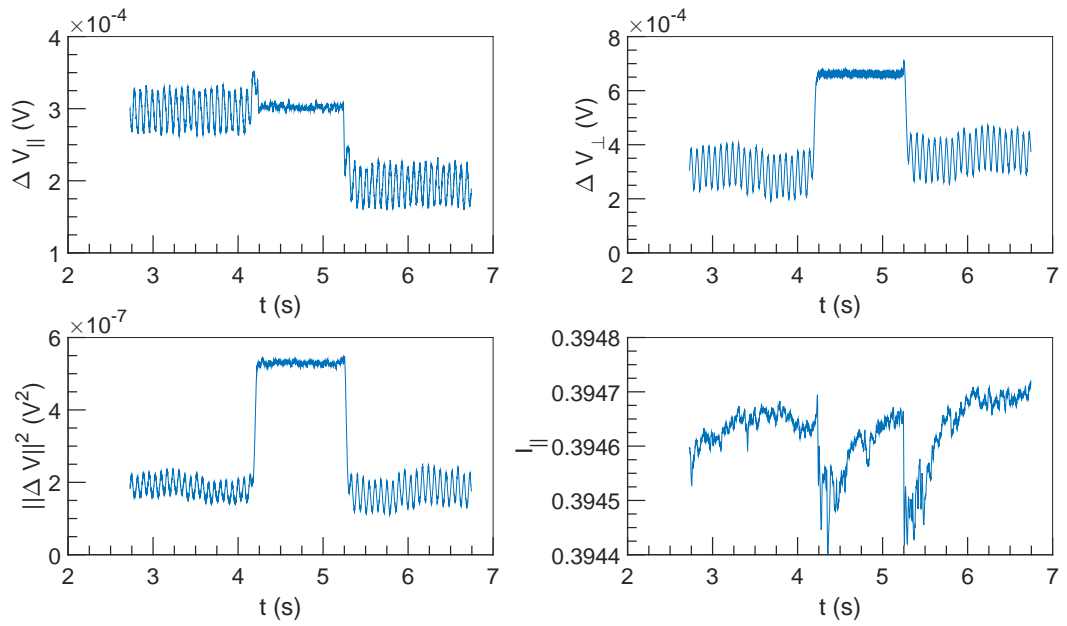


Figure 8.55:  $\Delta V$  and  $I$  vs  $t$  at  $U = 0.25 \text{ m s}^{-1}$ ,  $\omega = 6283 \text{ rad s}^{-1}$  and  $\alpha = 0.54 \%$ .

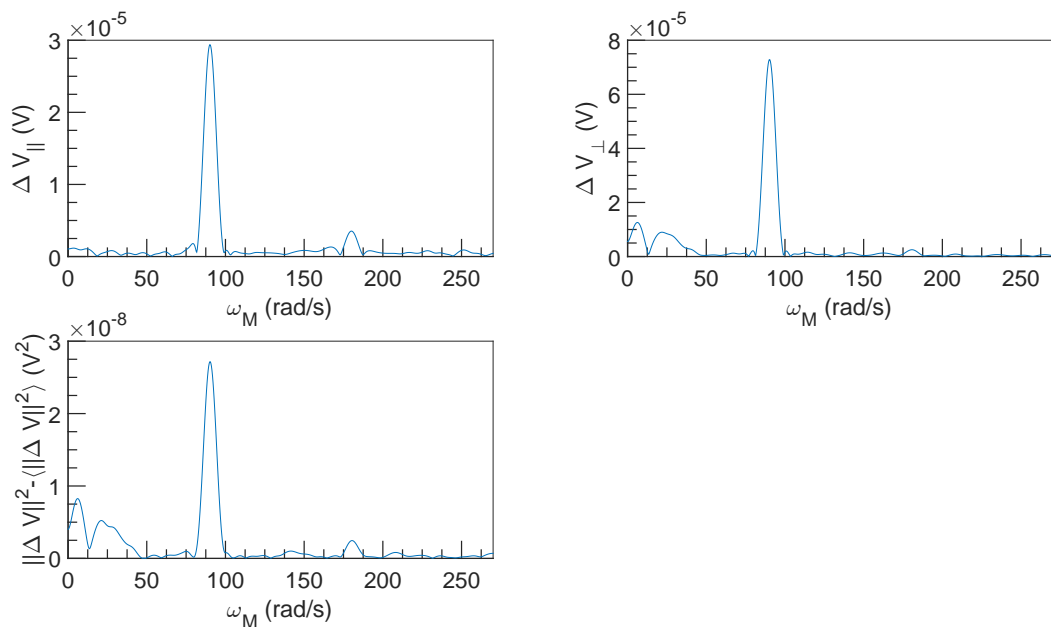


Figure 8.56: FFT spectral density of  $\Delta V$  vs  $\omega_M$  at  $U = 0.25 \text{ m s}^{-1}$ ,  $\omega = 6283 \text{ rad s}^{-1}$  and  $\alpha = 0.54 \%$ .

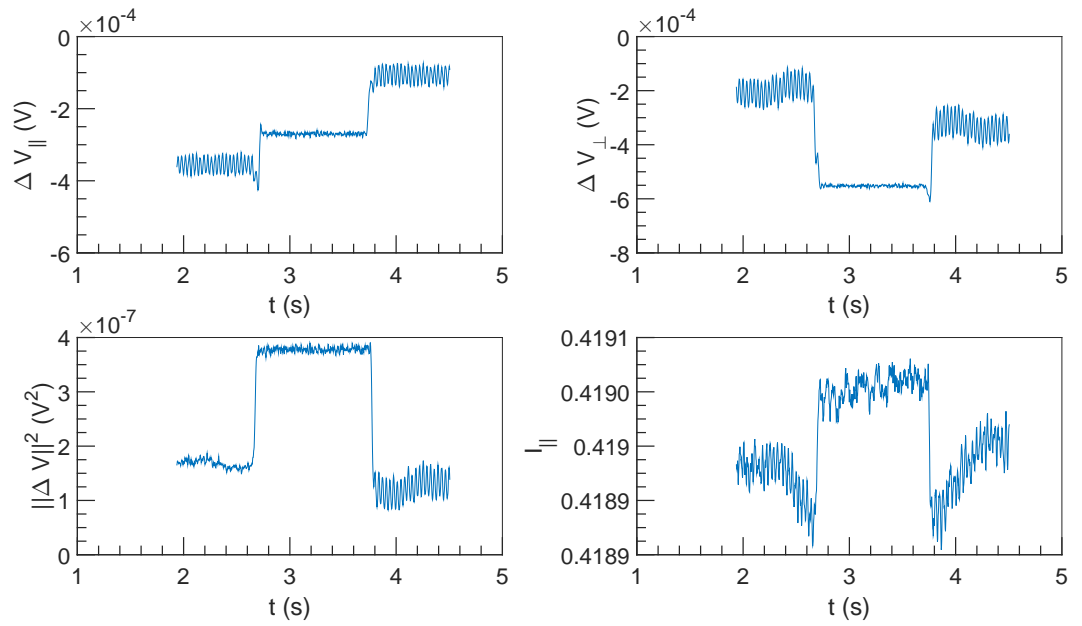


Figure 8.57:  $\Delta V$  and  $I$  vs  $t$  at  $U = 0.5 \text{ m s}^{-1}$ ,  $\omega = 4712 \text{ rad s}^{-1}$  and  $\alpha = 0.54\%$ .

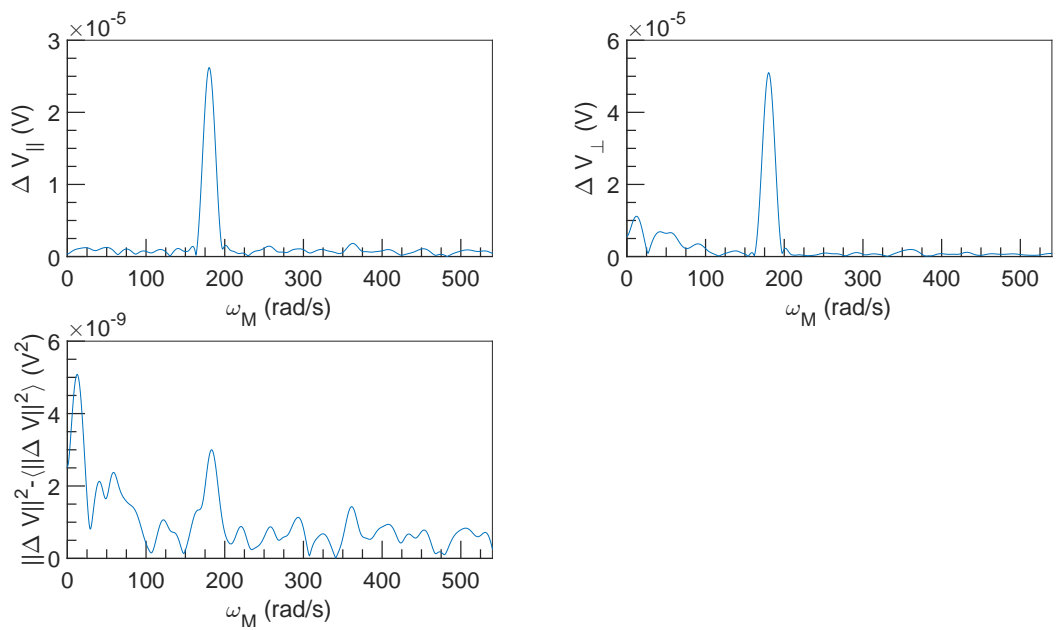


Figure 8.58: FFT spectral density of  $\Delta V$  vs  $\omega_M$  at  $U = 0.5 \text{ m s}^{-1}$ ,  $\omega = 4712 \text{ rad s}^{-1}$  and  $\alpha = 0.54\%$ .

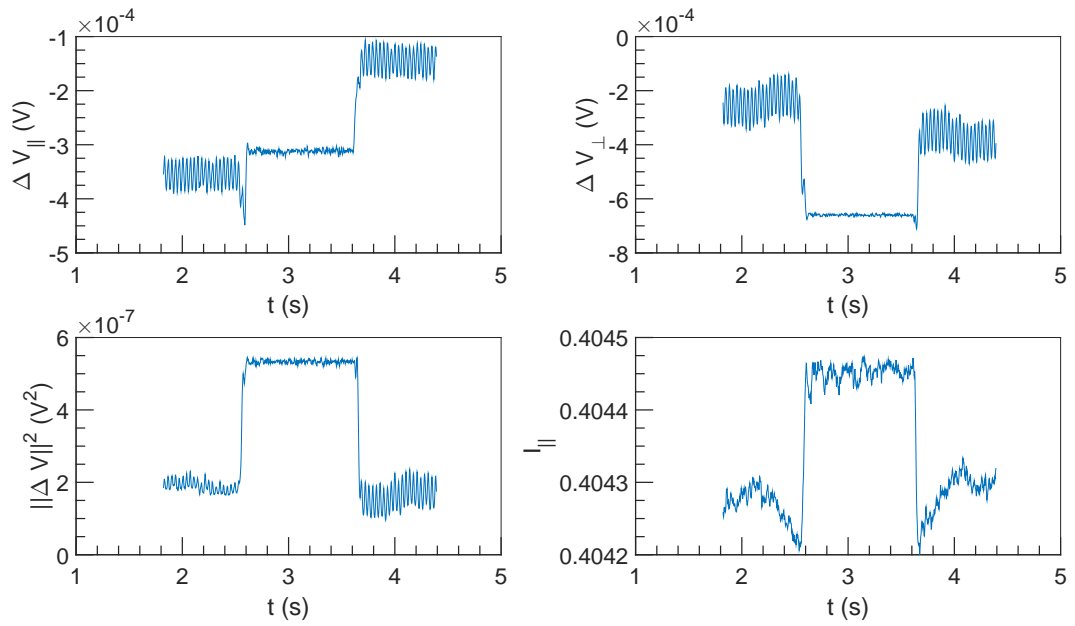


Figure 8.59:  $\Delta V$  and  $I$  vs  $t$  at  $U = 0.5 \text{ m s}^{-1}$ ,  $\omega = 6283 \text{ rad s}^{-1}$  and  $\alpha = 0.54 \%$ .

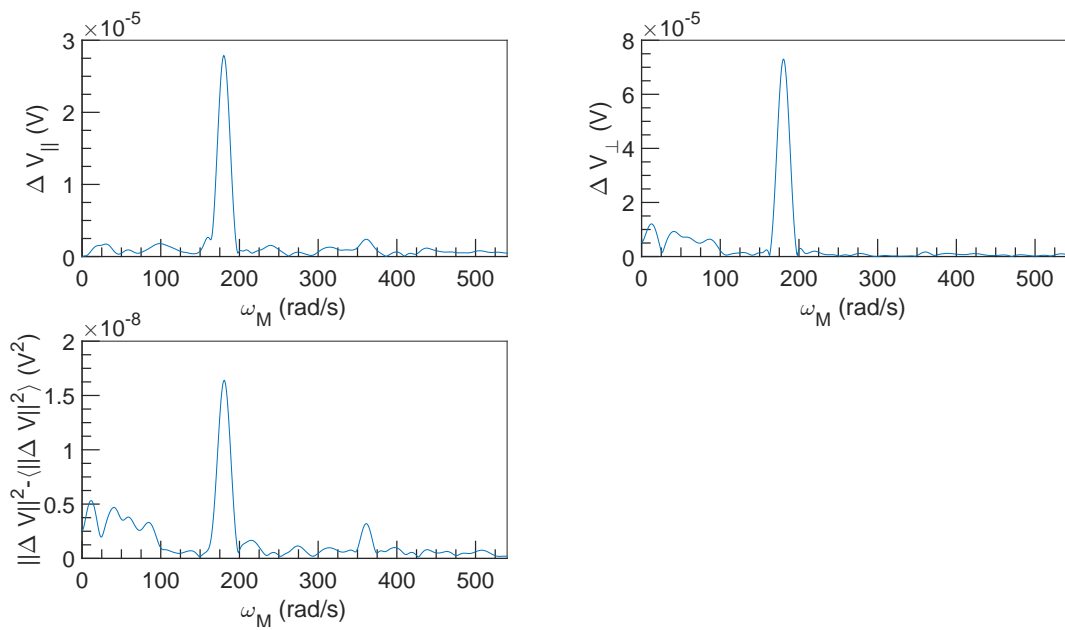


Figure 8.60: FFT spectral density of  $\Delta V$  vs  $\omega_M$  at  $U = 0.5 \text{ m s}^{-1}$ ,  $\omega = 6283 \text{ rad s}^{-1}$  and  $\alpha = 0.54 \%$ .

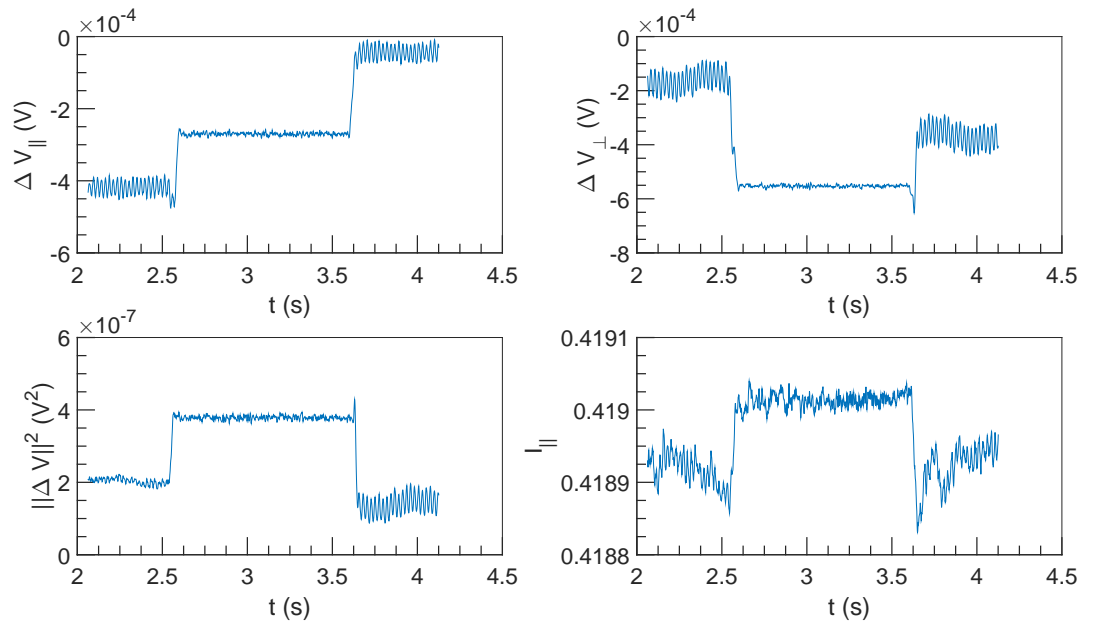


Figure 8.61:  $\Delta V$  and  $I$  vs  $t$  at  $U = 0.75 \text{ m s}^{-1}$ ,  $\omega = 4712 \text{ rad s}^{-1}$  and  $\alpha = 0.54 \%$ .

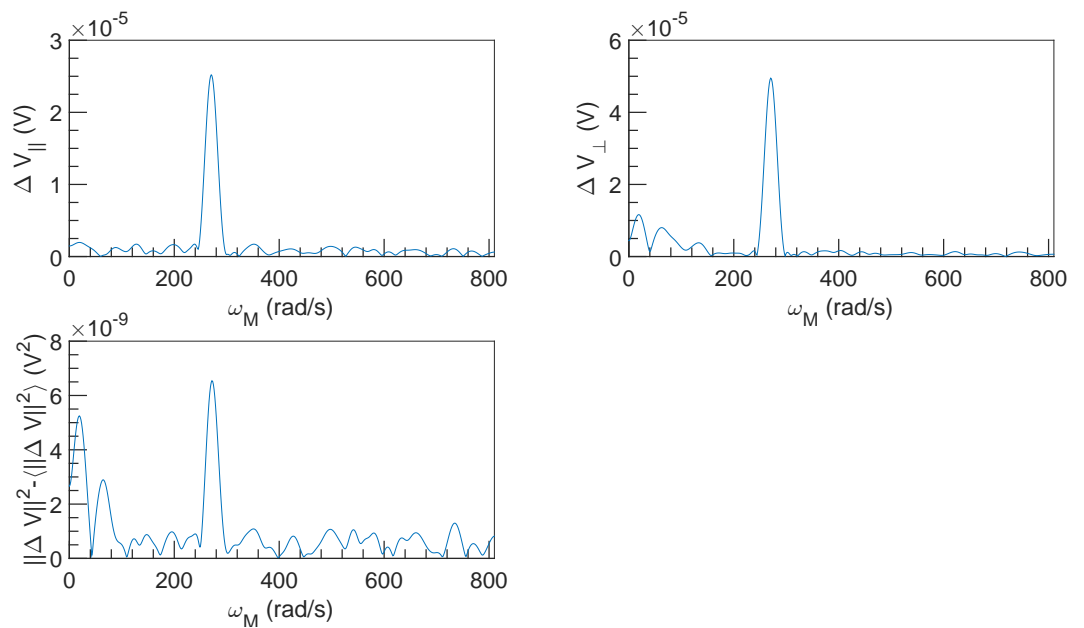


Figure 8.62: FFT spectral density of  $\Delta V$  vs  $\omega_M$  at  $U = 0.75 \text{ m s}^{-1}$ ,  $\omega = 4712 \text{ rad s}^{-1}$  and  $\alpha = 0.54 \%$ .

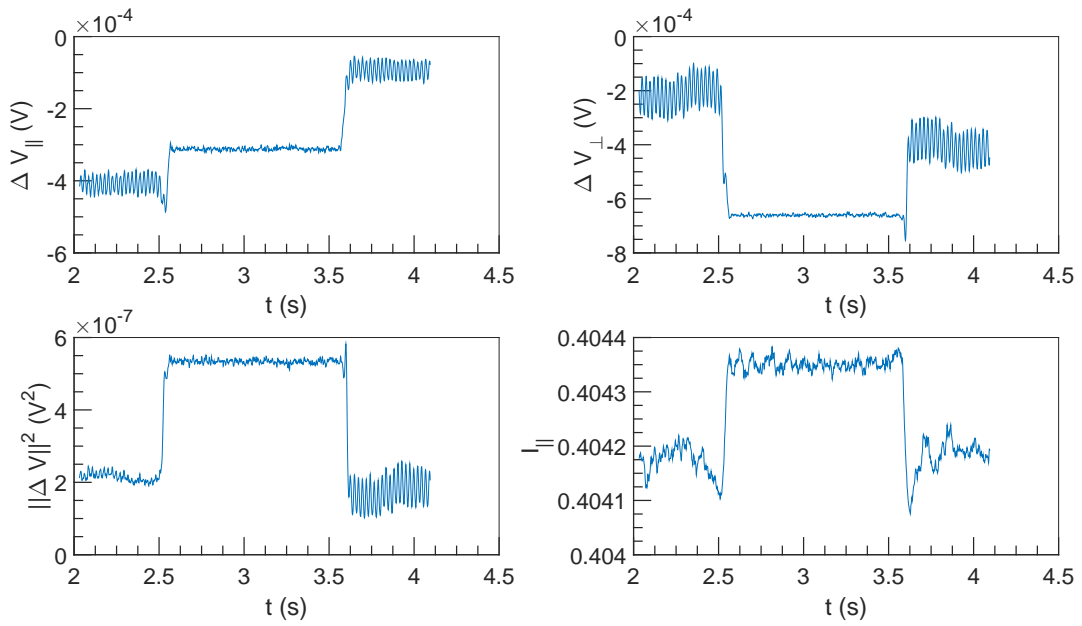


Figure 8.63:  $\Delta V$  and  $I$  vs  $t$  at  $U = 0.75 \text{ m s}^{-1}$ ,  $\omega = 6283 \text{ rad s}^{-1}$  and  $\alpha = 0.54 \%$ .

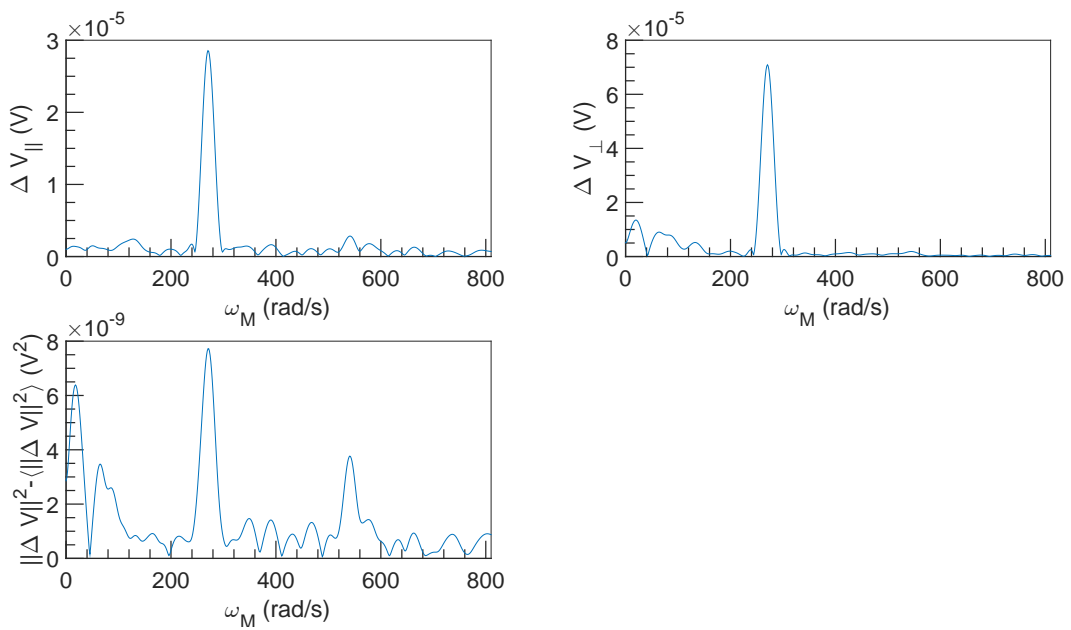


Figure 8.64: FFT spectral density of  $\Delta V$  vs  $\omega_M$  at  $U = 0.75 \text{ m s}^{-1}$ ,  $\omega = 6283 \text{ rad s}^{-1}$  and  $\alpha = 0.54 \%$ .



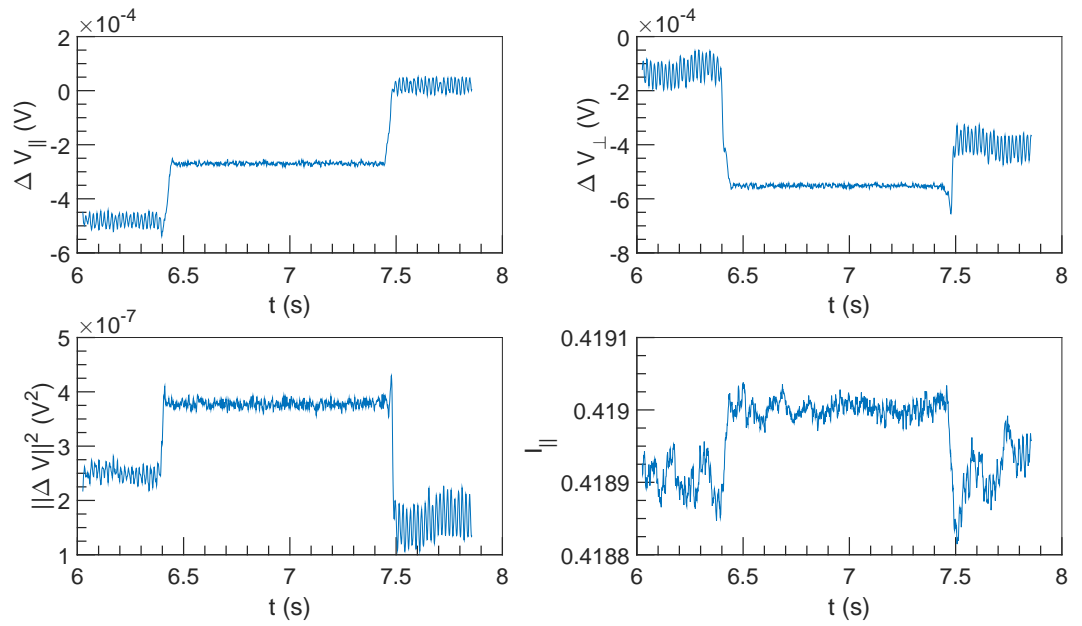


Figure 8.65:  $\Delta V$  and  $I$  vs  $t$  at  $U = 1 \text{ m s}^{-1}$ ,  $\omega = 4712 \text{ rad s}^{-1}$  and  $\alpha = 0.54 \%$ .

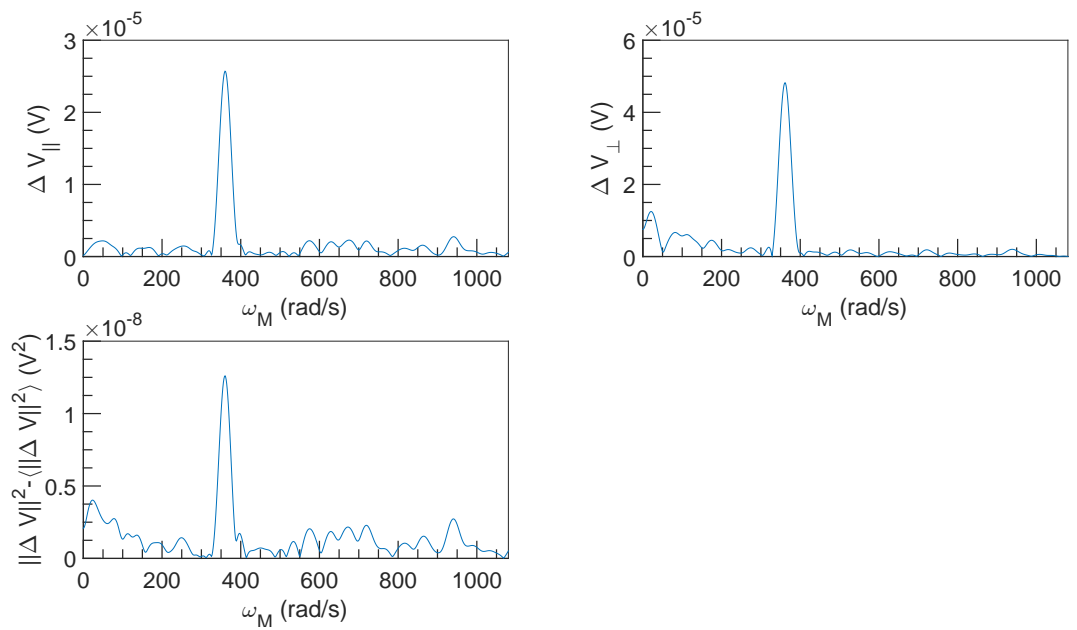


Figure 8.66: FFT spectral density of  $\Delta V$  vs  $\omega_M$  at  $U = 1 \text{ m s}^{-1}$ ,  $\omega = 4712 \text{ rad s}^{-1}$  and  $\alpha = 0.54 \%$ .

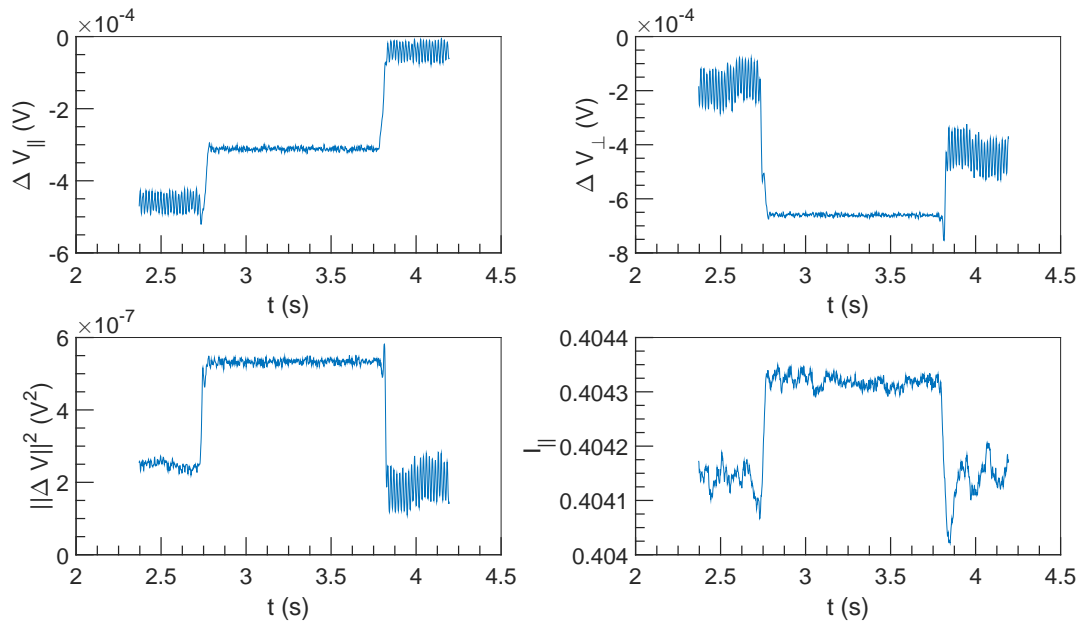


Figure 8.67:  $\Delta V$  and  $I$  vs  $t$  at  $U = 1 \text{ m s}^{-1}$ ,  $\omega = 6283 \text{ rad s}^{-1}$  and  $\alpha = 0.54 \%$ .

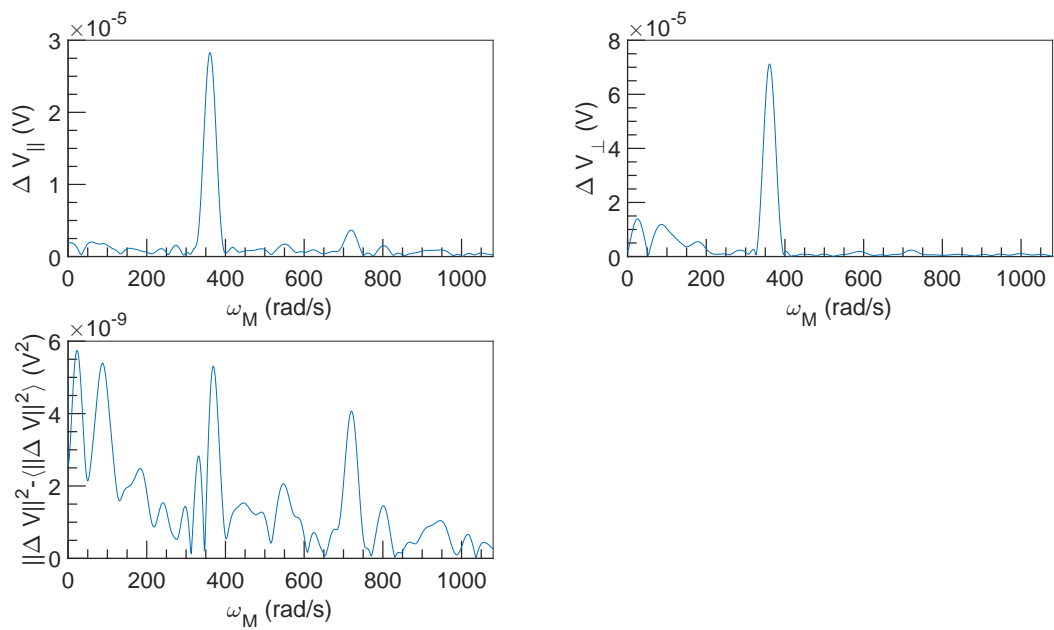


Figure 8.68: FFT spectral density of  $\Delta V$  vs  $\omega_M$  at  $U = 1 \text{ m s}^{-1}$ ,  $\omega = 6283 \text{ rad s}^{-1}$  and  $\alpha = 0.54 \%$ .



## Chapter 9

**For**  $\alpha = 1.62\%$

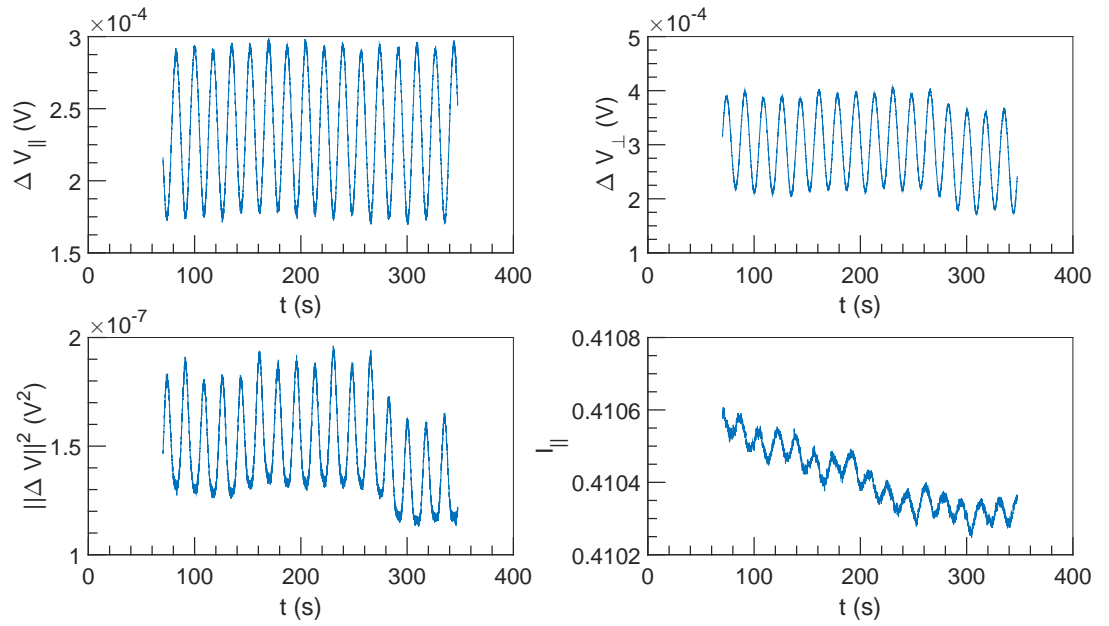


Figure 9.1:  $\Delta V$  and  $I$  vs  $t$  at  $U = 10^{-3} \text{ m s}^{-1}$ ,  $\omega = 4712 \text{ rad s}^{-1}$  and  $\alpha = 1.62 \%$ .

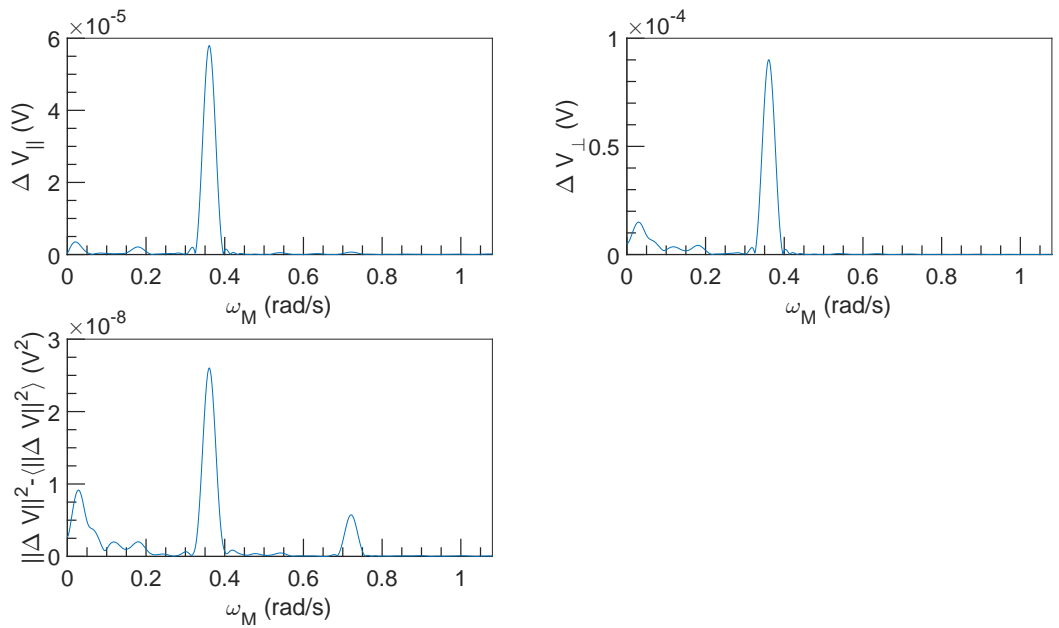


Figure 9.2: FFT spectral density of  $\Delta V$  vs  $\omega_M$  at  $U = 10^{-3} \text{ m s}^{-1}$ ,  $\omega = 4712 \text{ rad s}^{-1}$  and  $\alpha = 1.62 \%$ .

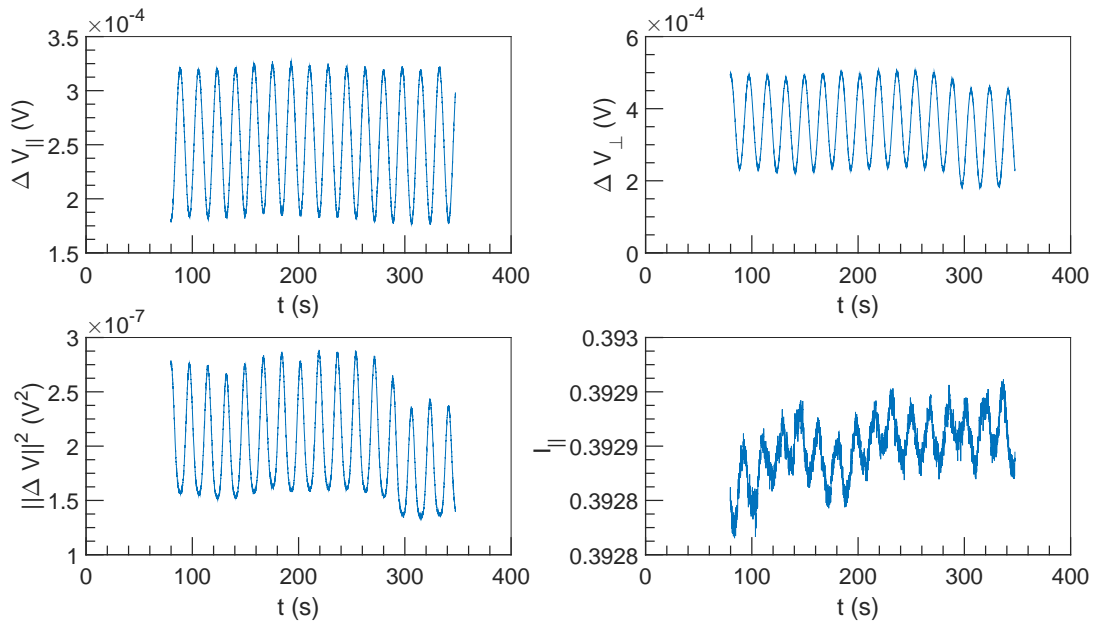


Figure 9.3:  $\Delta V$  and  $I$  vs  $t$  at  $U = 10^{-3} \text{ m s}^{-1}$ ,  $\omega = 6283 \text{ rad s}^{-1}$  and  $\alpha = 1.62 \%$ .

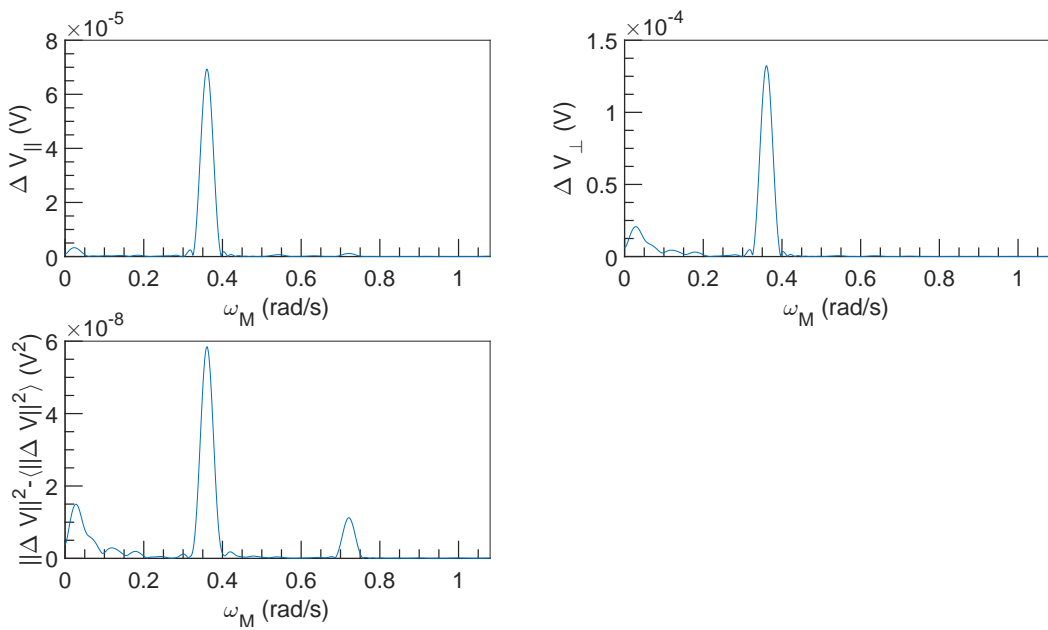


Figure 9.4: FFT spectral density of  $\Delta V$  vs  $\omega_M$  at  $U = 10^{-3} \text{ m s}^{-1}$ ,  $\omega = 6283 \text{ rad s}^{-1}$  and  $\alpha = 1.62 \%$ .

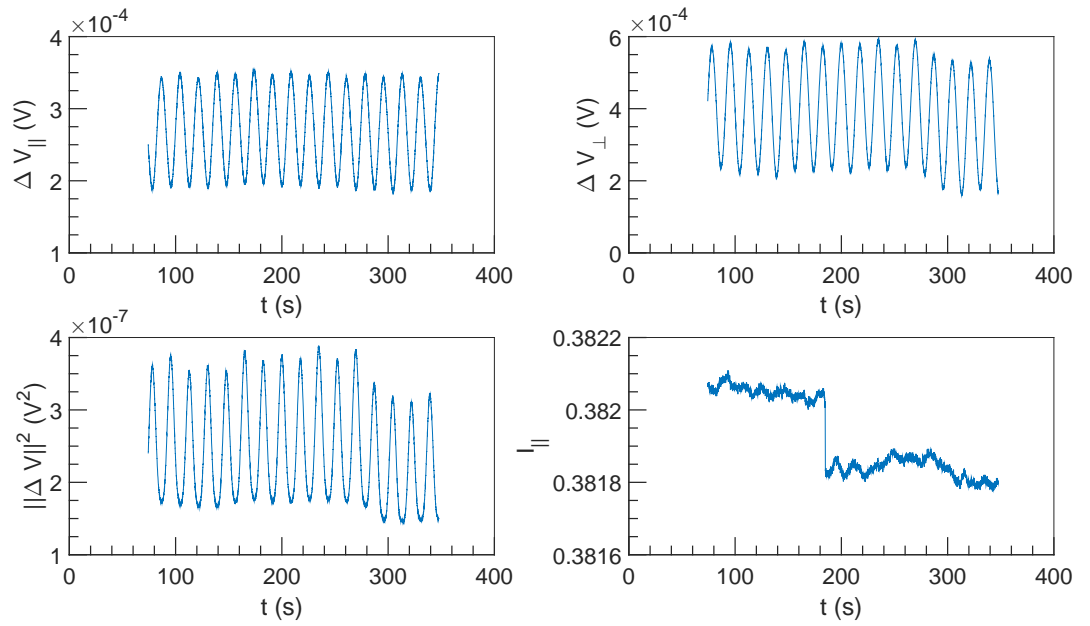


Figure 9.5:  $\Delta V$  and  $I$  vs  $t$  at  $U = 10^{-3} \text{ m s}^{-1}$ ,  $\omega = 7854 \text{ rad s}^{-1}$  and  $\alpha = 1.62 \%$ .

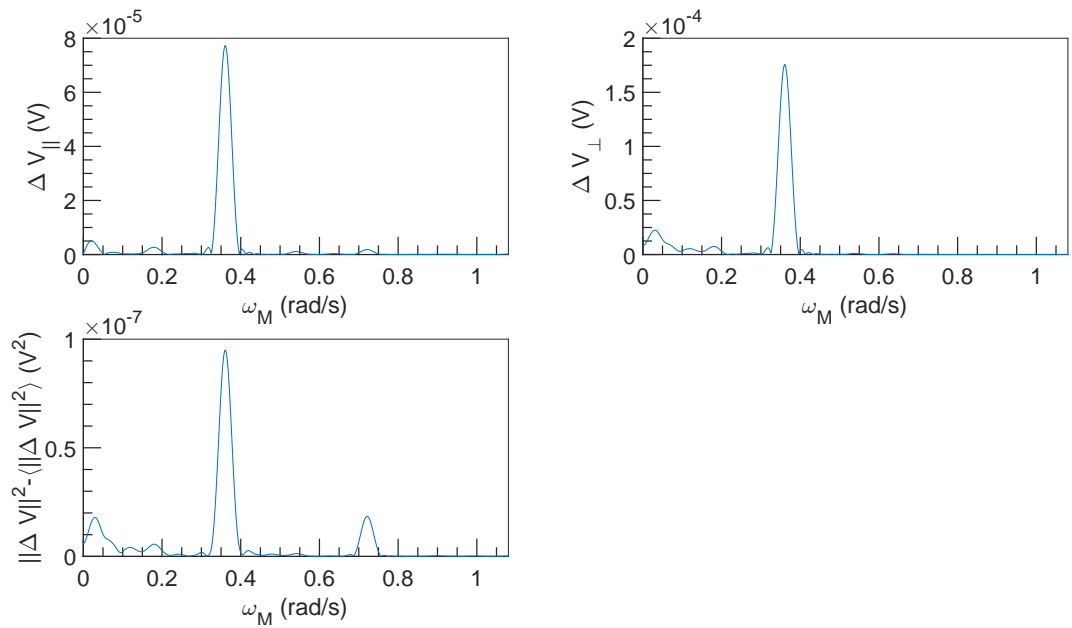


Figure 9.6: FFT spectral density of  $\Delta V$  vs  $\omega_M$  at  $U = 10^{-3} \text{ m s}^{-1}$ ,  $\omega = 7854 \text{ rad s}^{-1}$  and  $\alpha = 1.62 \%$ .

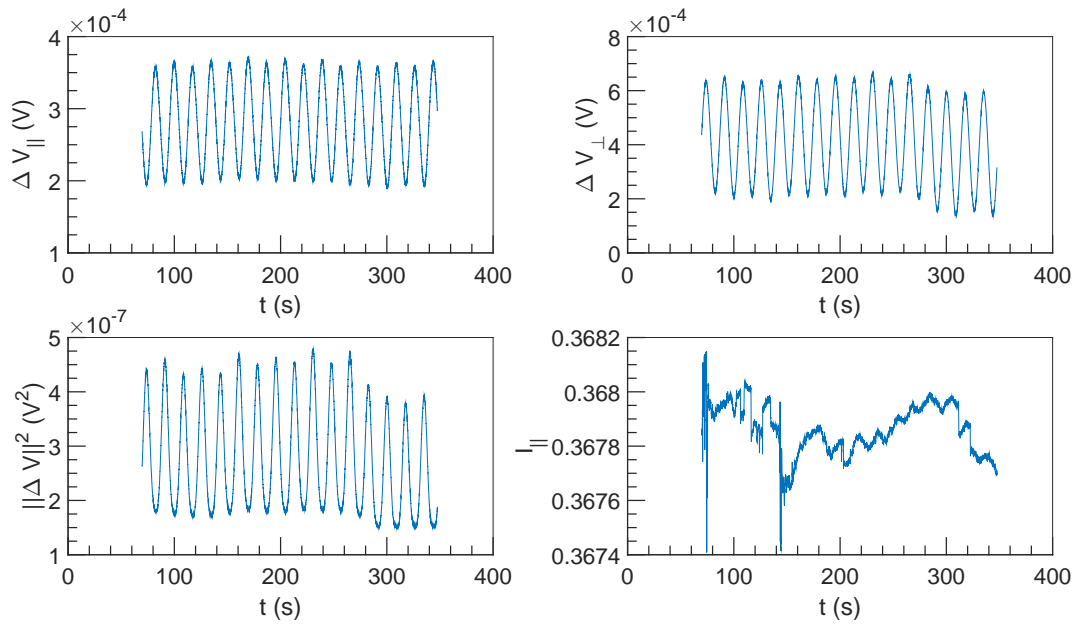


Figure 9.7:  $\Delta V$  and  $I$  vs  $t$  at  $U = 10^{-3} \text{ m s}^{-1}$ ,  $\omega = 9425 \text{ rad s}^{-1}$  and  $\alpha = 1.62 \%$ .

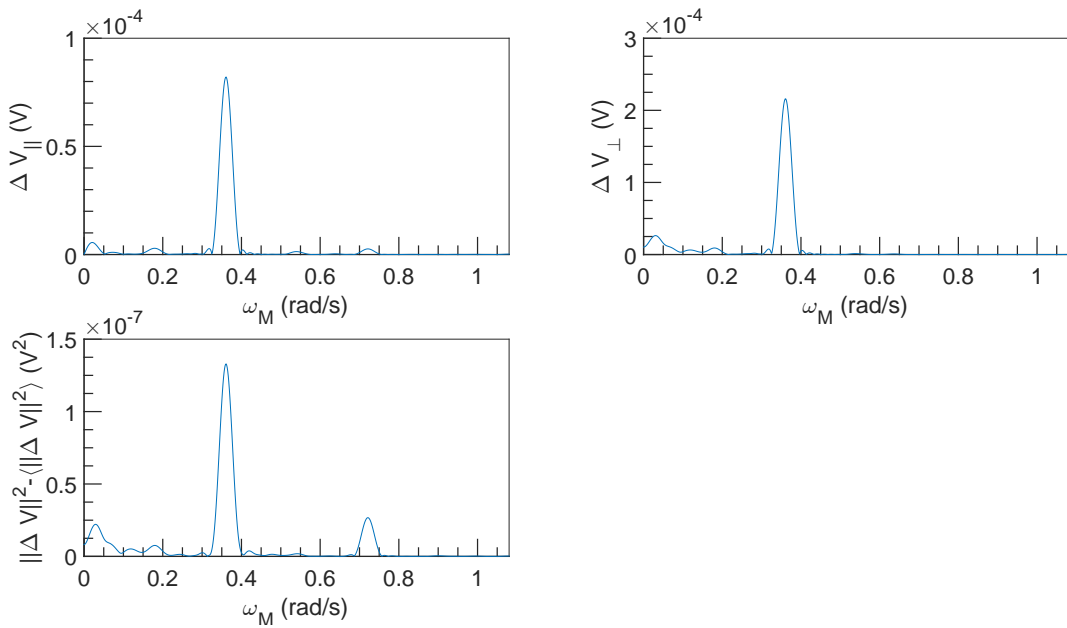


Figure 9.8: FFT spectral density of  $\Delta V$  vs  $\omega_M$  at  $U = 10^{-3} \text{ m s}^{-1}$ ,  $\omega = 9425 \text{ rad s}^{-1}$  and  $\alpha = 1.62 \%$ .



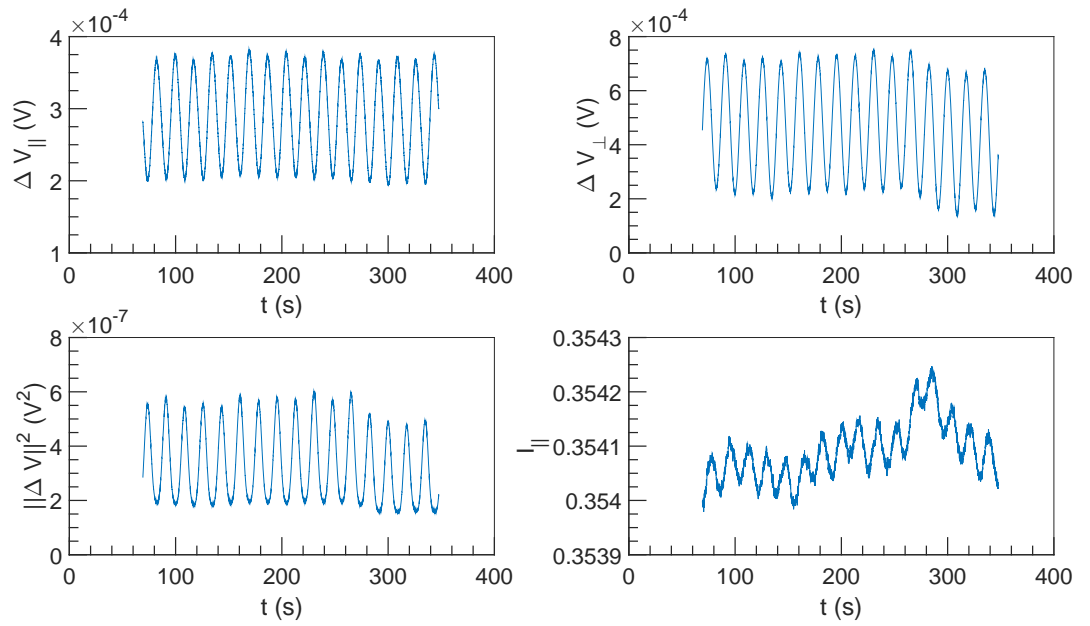


Figure 9.9:  $\Delta V$  and  $I$  vs  $t$  at  $U = 10^{-3} \text{ m s}^{-1}$ ,  $\omega = 10\,996 \text{ rad s}^{-1}$  and  $\alpha = 1.62\%$ .

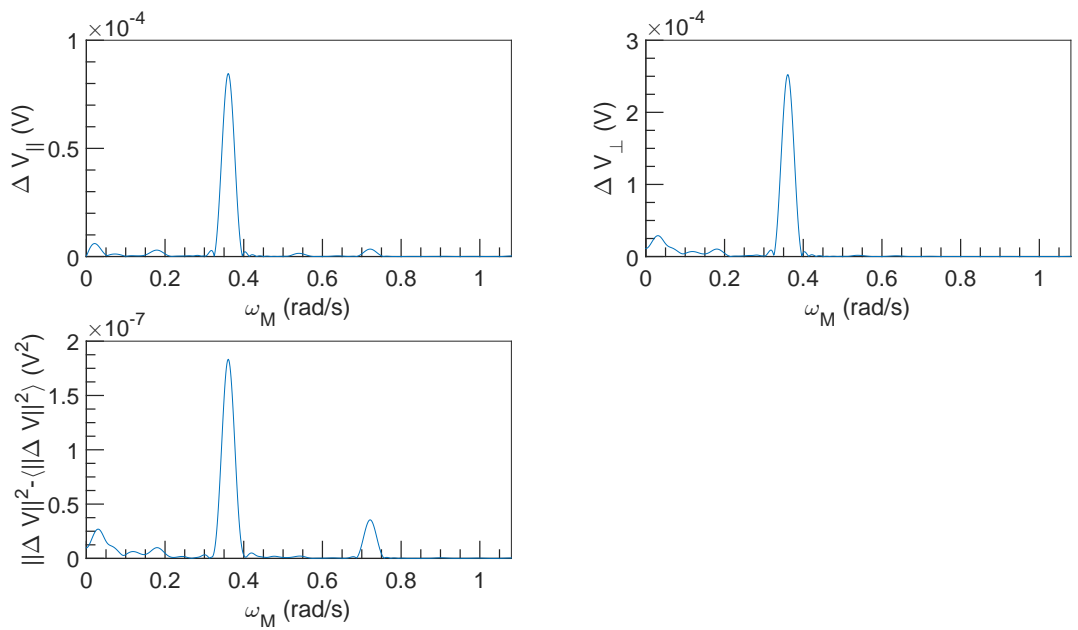


Figure 9.10: FFT spectral density of  $\Delta V$  vs  $\omega_M$  at  $U = 10^{-3} \text{ m s}^{-1}$ ,  $\omega = 10\,996 \text{ rad s}^{-1}$  and  $\alpha = 1.62\%$ .

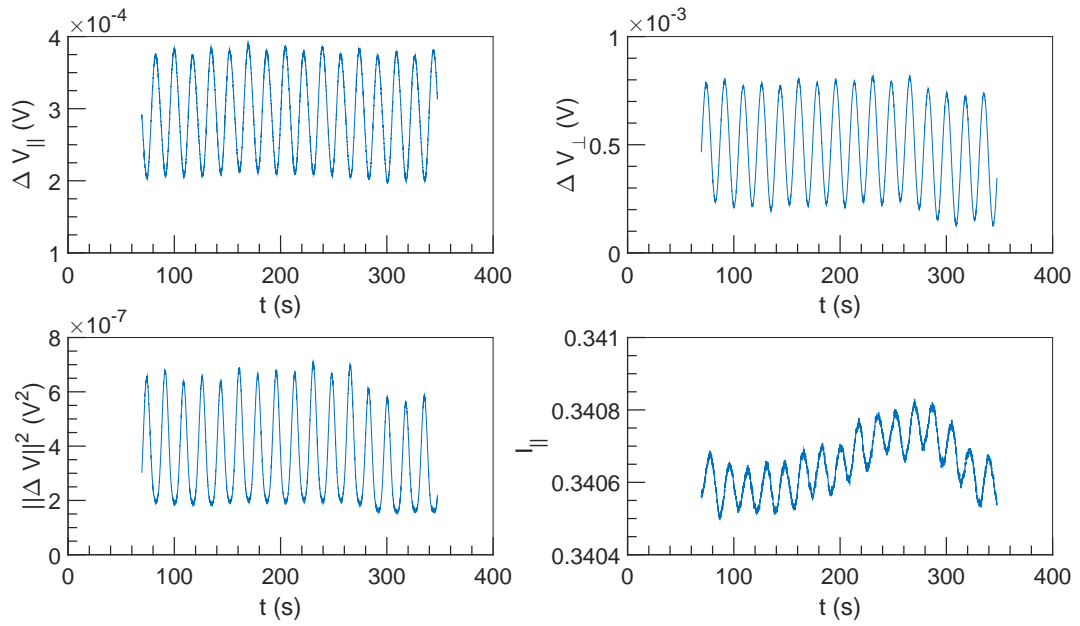


Figure 9.11:  $\Delta V$  and  $I$  vs  $t$  at  $U = 10^{-3} \text{ m s}^{-1}$ ,  $\omega = 12566 \text{ rad s}^{-1}$  and  $\alpha = 1.62\%$ .

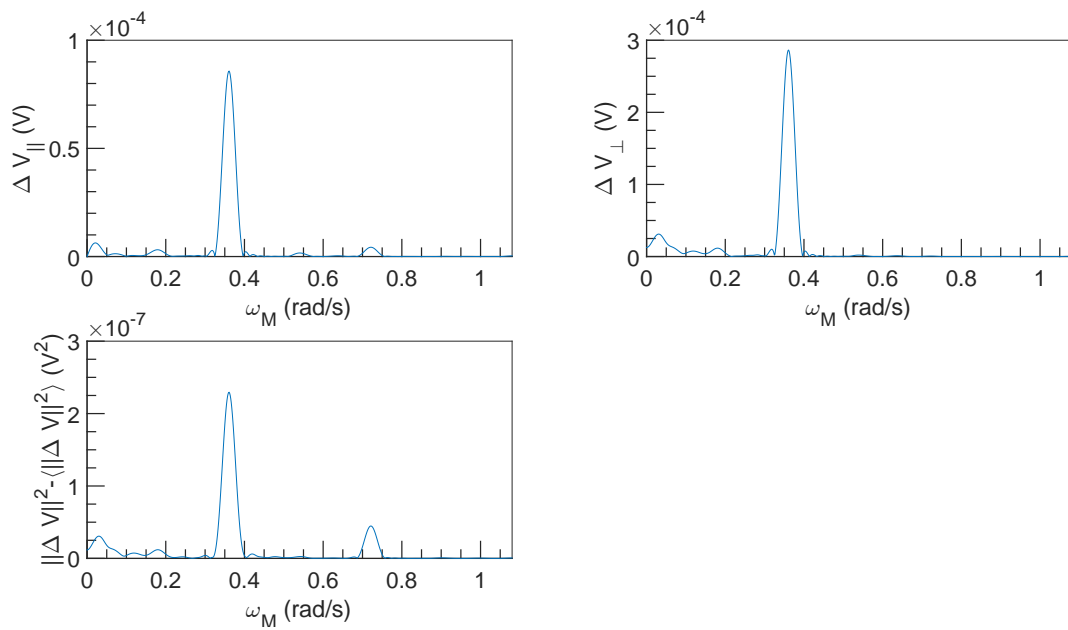


Figure 9.12: FFT spectral density of  $\Delta V$  vs  $\omega_M$  at  $U = 10^{-3} \text{ m s}^{-1}$ ,  $\omega = 12566 \text{ rad s}^{-1}$  and  $\alpha = 1.62\%$ .

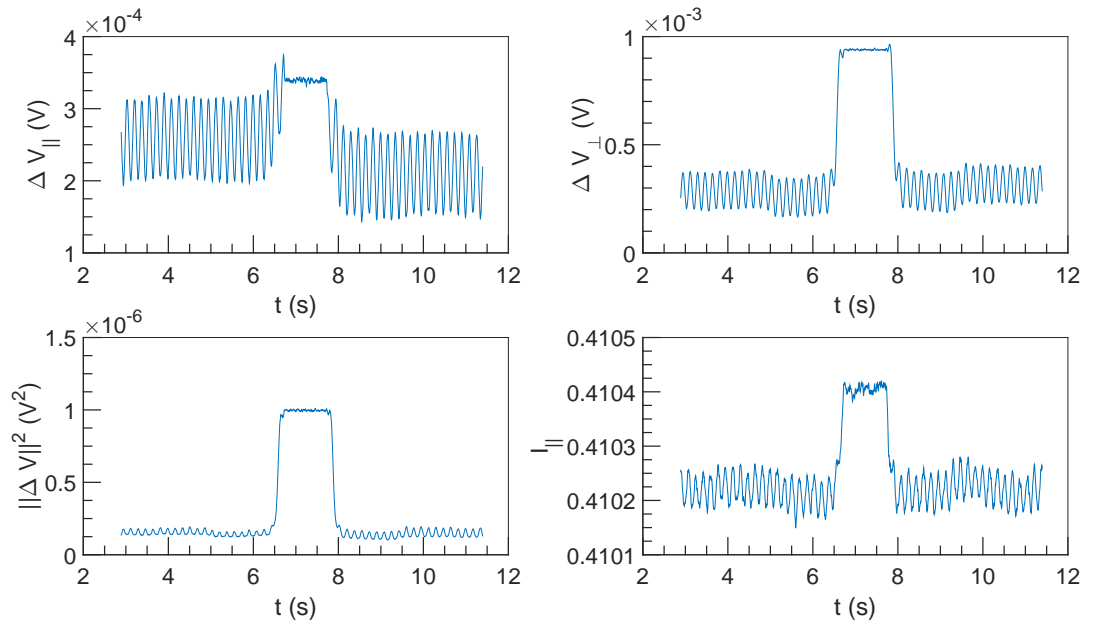


Figure 9.13:  $\Delta V$  and  $I$  vs  $t$  at  $U = 0.1 \text{ m s}^{-1}$ ,  $\omega = 4712 \text{ rad s}^{-1}$  and  $\alpha = 1.62 \%$ .

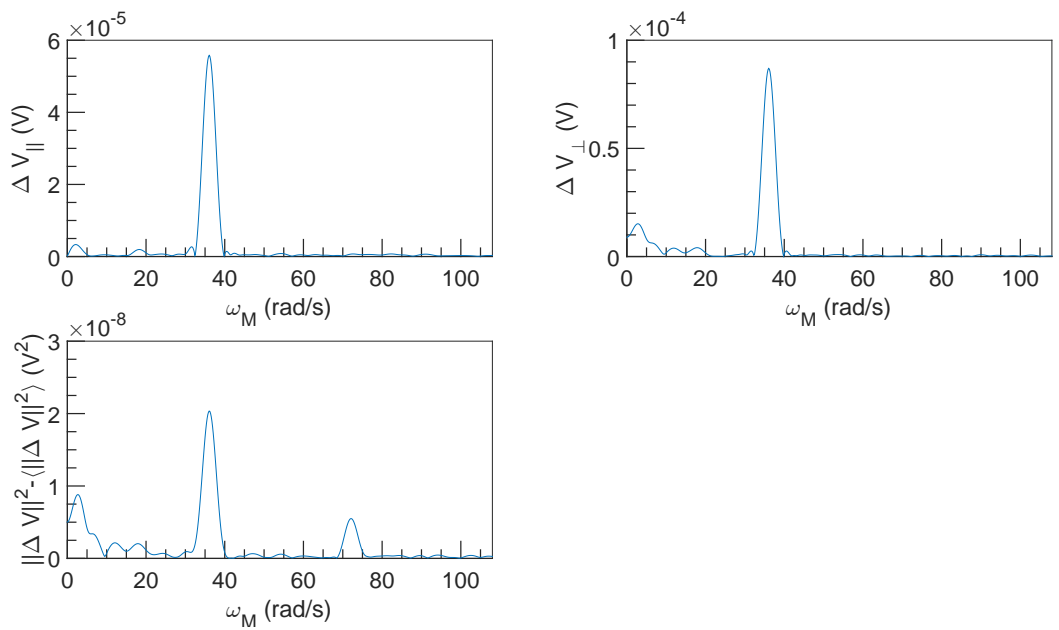


Figure 9.14: FFT spectral density of  $\Delta V$  vs  $\omega_M$  at  $U = 0.1 \text{ m s}^{-1}$ ,  $\omega = 4712 \text{ rad s}^{-1}$  and  $\alpha = 1.62 \%$ .

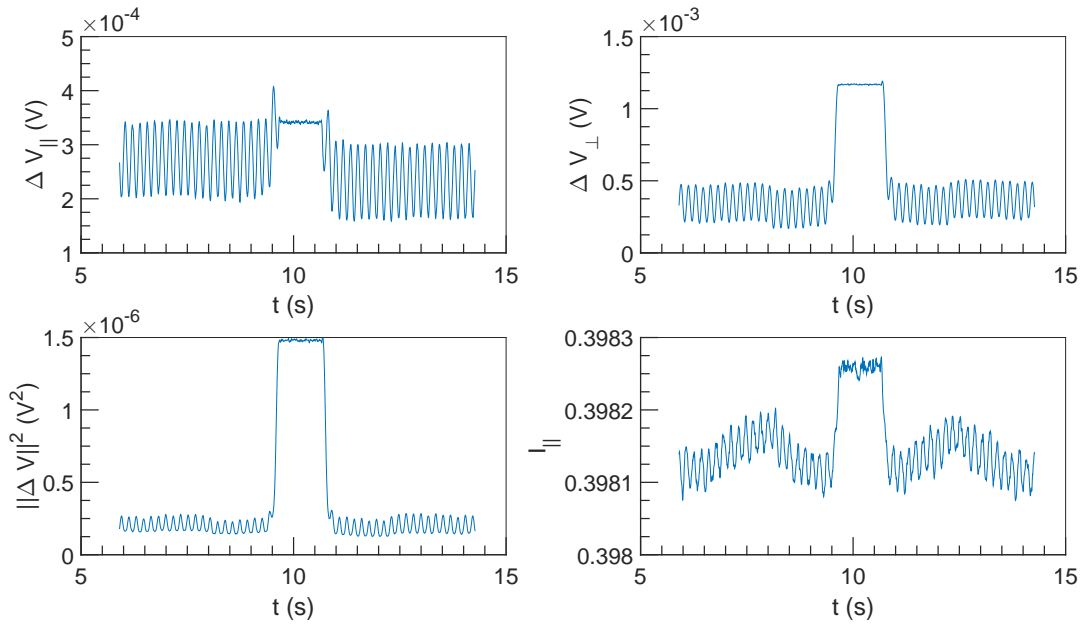


Figure 9.15:  $\Delta V$  and  $I$  vs  $t$  at  $U = 0.1 \text{ m s}^{-1}$ ,  $\omega = 6283 \text{ rad s}^{-1}$  and  $\alpha = 1.62 \%$ .

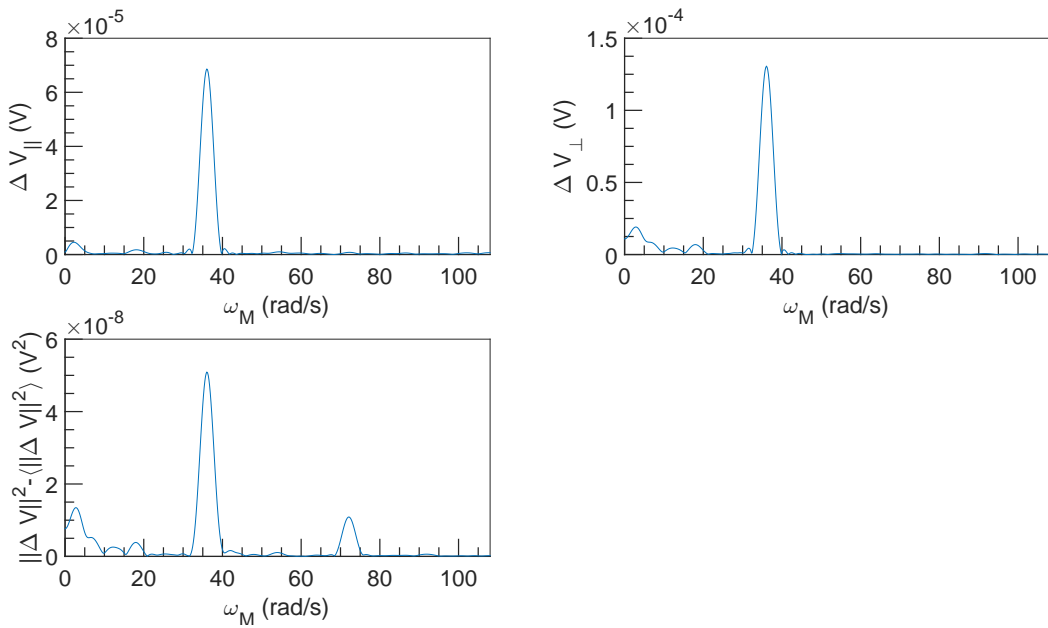


Figure 9.16: FFT spectral density of  $\Delta V$  vs  $\omega_M$  at  $U = 0.1 \text{ m s}^{-1}$ ,  $\omega = 6283 \text{ rad s}^{-1}$  and  $\alpha = 1.62 \%$ .

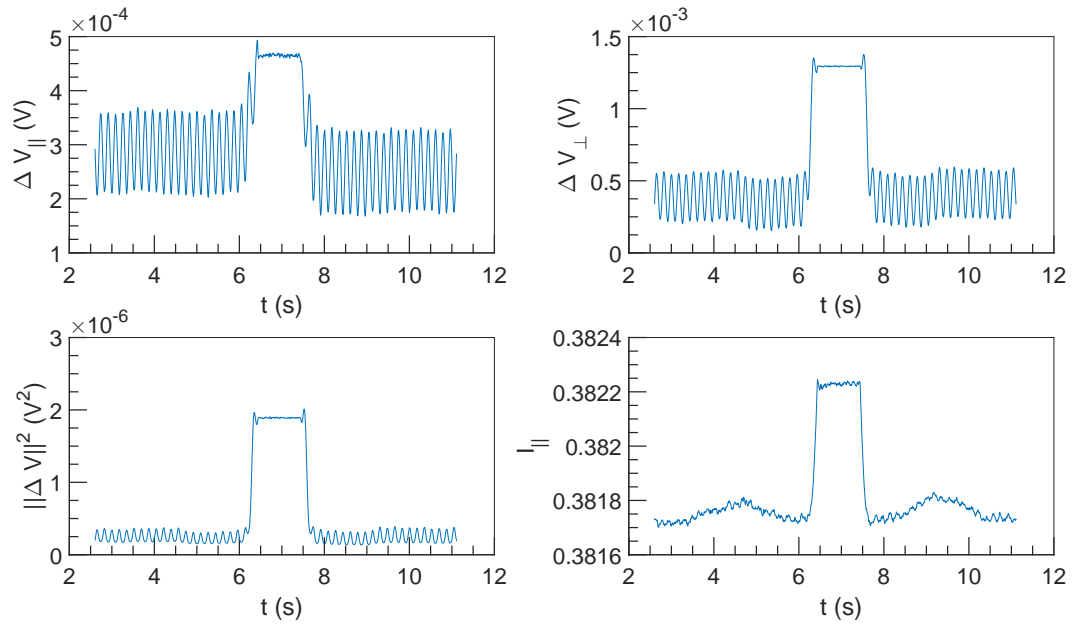


Figure 9.17:  $\Delta V$  and  $I$  vs  $t$  at  $U = 0.1 \text{ m s}^{-1}$ ,  $\omega = 7854 \text{ rad s}^{-1}$  and  $\alpha = 1.62 \%$ .

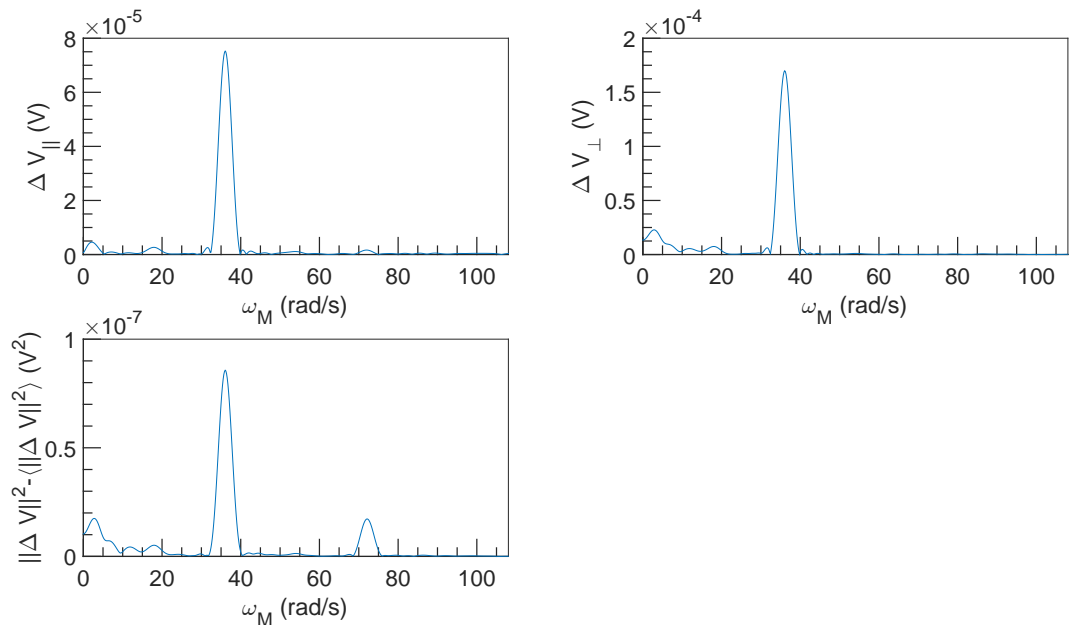


Figure 9.18: FFT spectral density of  $\Delta V$  vs  $\omega_M$  at  $U = 0.1 \text{ m s}^{-1}$ ,  $\omega = 7854 \text{ rad s}^{-1}$  and  $\alpha = 1.62 \%$ .

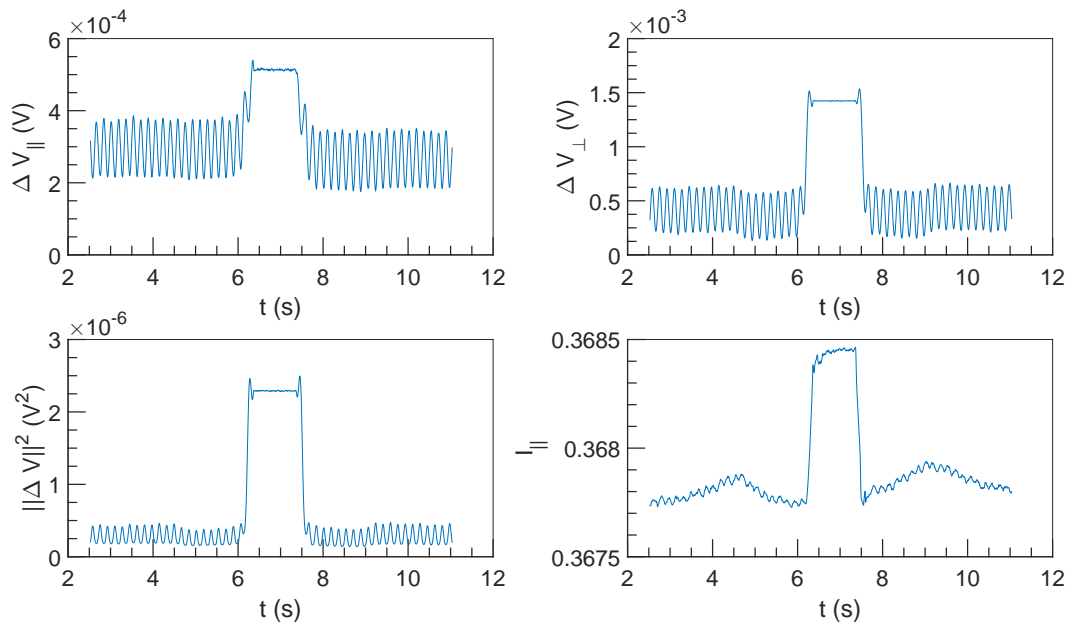


Figure 9.19:  $\Delta V$  and  $I$  vs  $t$  at  $U = 0.1 \text{ m s}^{-1}$ ,  $\omega = 9425 \text{ rad s}^{-1}$  and  $\alpha = 1.62 \%$ .

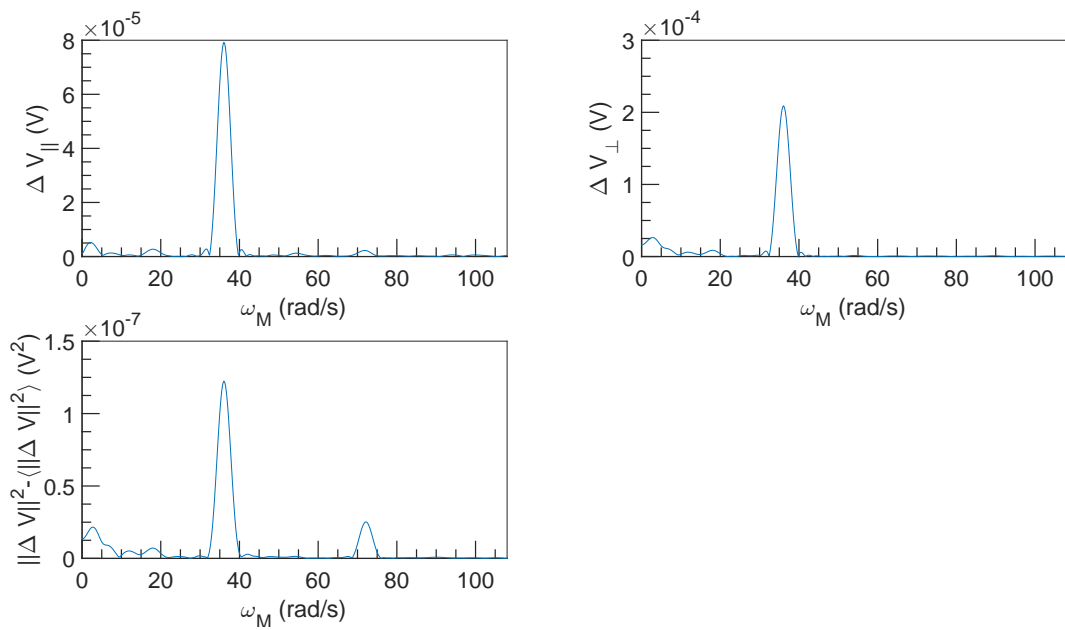


Figure 9.20: FFT spectral density of  $\Delta V$  vs  $\omega_M$  at  $U = 0.1 \text{ m s}^{-1}$ ,  $\omega = 9425 \text{ rad s}^{-1}$  and  $\alpha = 1.62 \%$ .

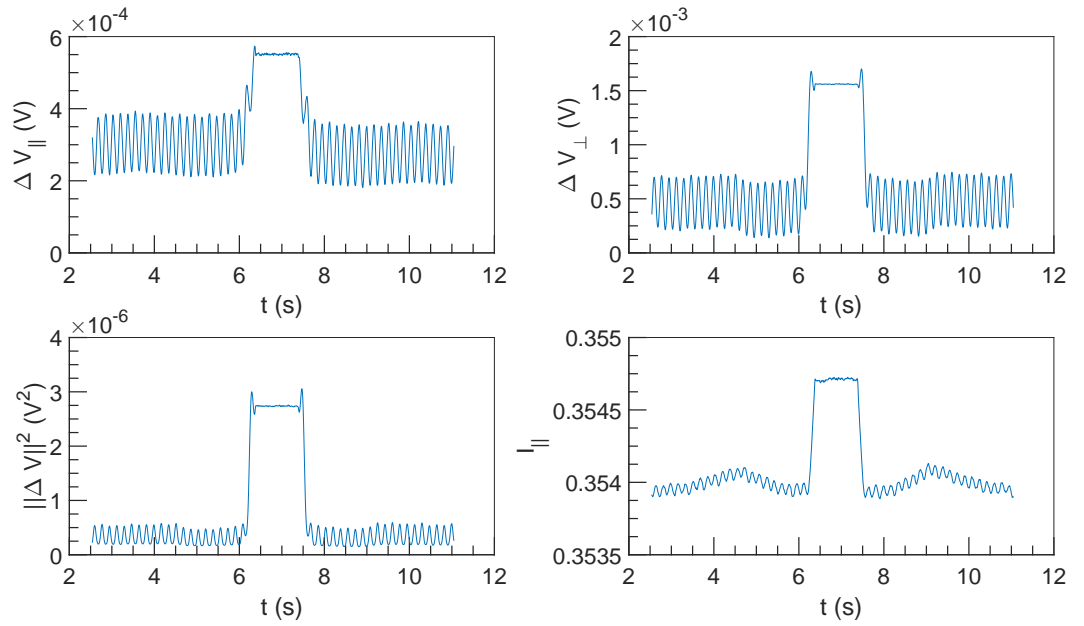


Figure 9.21:  $\Delta V$  and  $I$  vs  $t$  at  $U = 0.1 \text{ m s}^{-1}$ ,  $\omega = 10\,996 \text{ rad s}^{-1}$  and  $\alpha = 1.62\%$ .

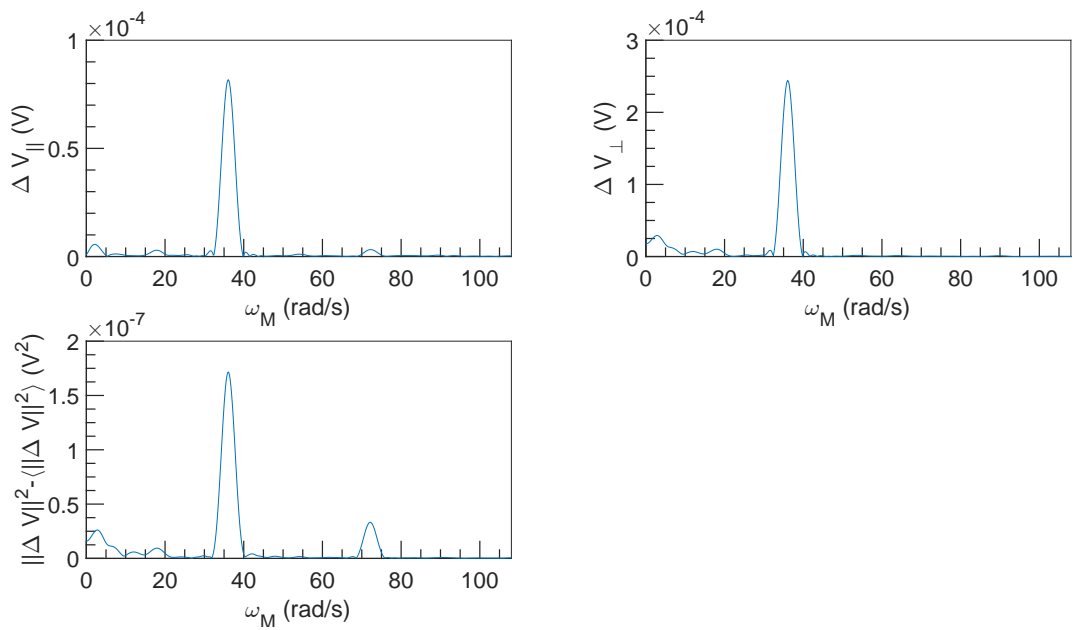


Figure 9.22: FFT spectral density of  $\Delta V$  vs  $\omega_M$  at  $U = 0.1 \text{ m s}^{-1}$ ,  $\omega = 10\,996 \text{ rad s}^{-1}$  and  $\alpha = 1.62\%$ .

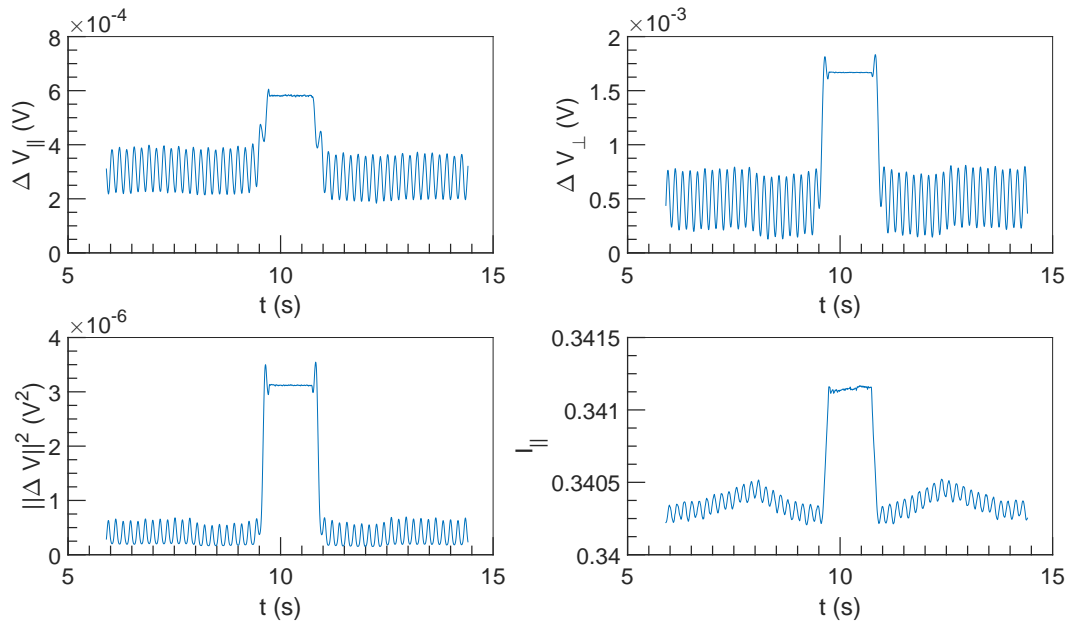


Figure 9.23:  $\Delta V$  and  $I$  vs  $t$  at  $U = 0.1 \text{ m s}^{-1}$ ,  $\omega = 12566 \text{ rad s}^{-1}$  and  $\alpha = 1.62 \%$ .

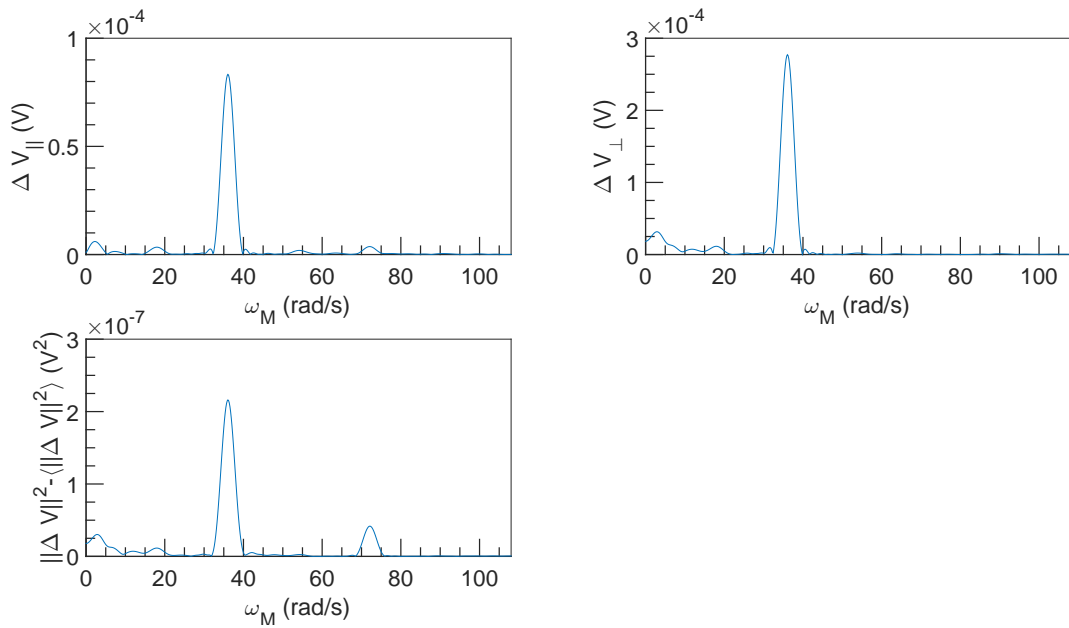


Figure 9.24: FFT spectral density of  $\Delta V$  vs  $\omega_M$  at  $U = 0.1 \text{ m s}^{-1}$ ,  $\omega = 12566 \text{ rad s}^{-1}$  and  $\alpha = 1.62 \%$ .



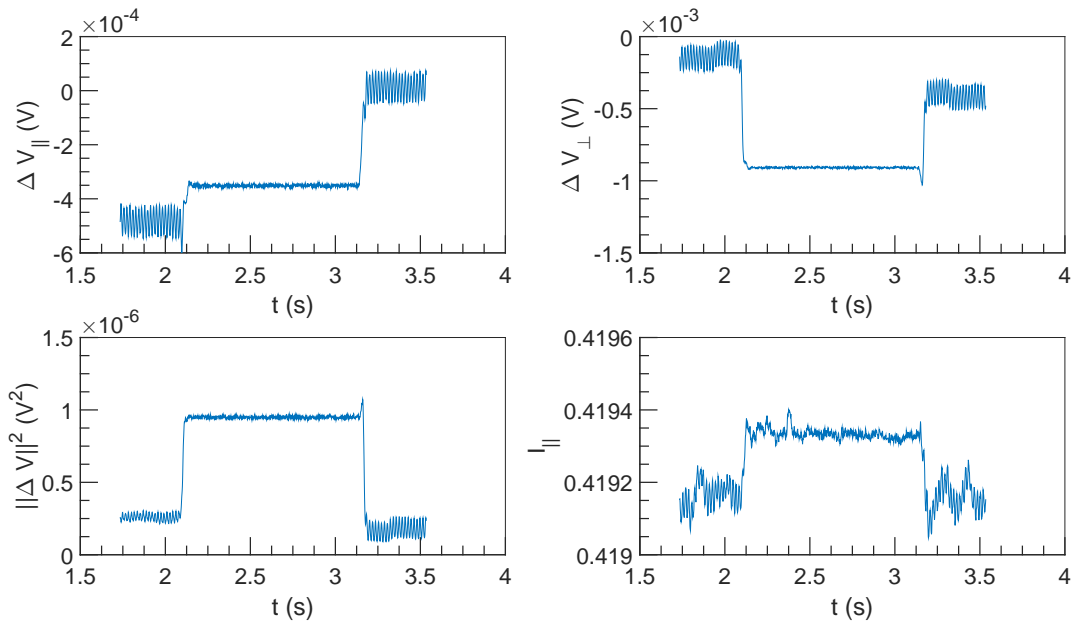


Figure 9.25:  $\Delta V$  and  $I$  vs  $t$  at  $U = 1 \text{ m s}^{-1}$ ,  $\omega = 4712 \text{ rad s}^{-1}$  and  $\alpha = 1.62 \%$ .

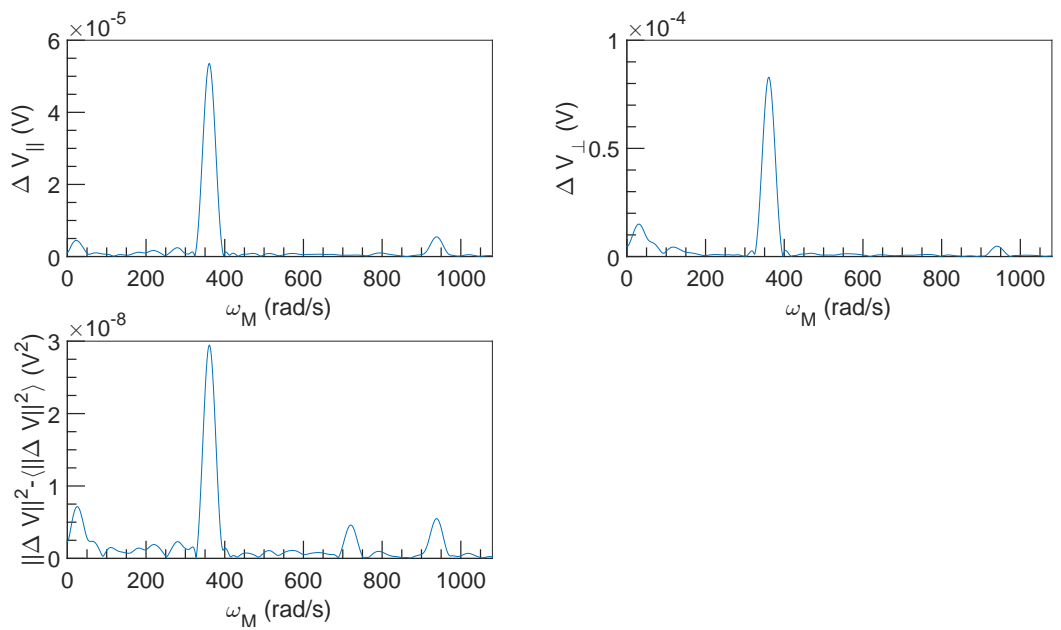


Figure 9.26: FFT spectral density of  $\Delta V$  vs  $\omega_M$  at  $U = 1 \text{ m s}^{-1}$ ,  $\omega = 4712 \text{ rad s}^{-1}$  and  $\alpha = 1.62 \%$ .

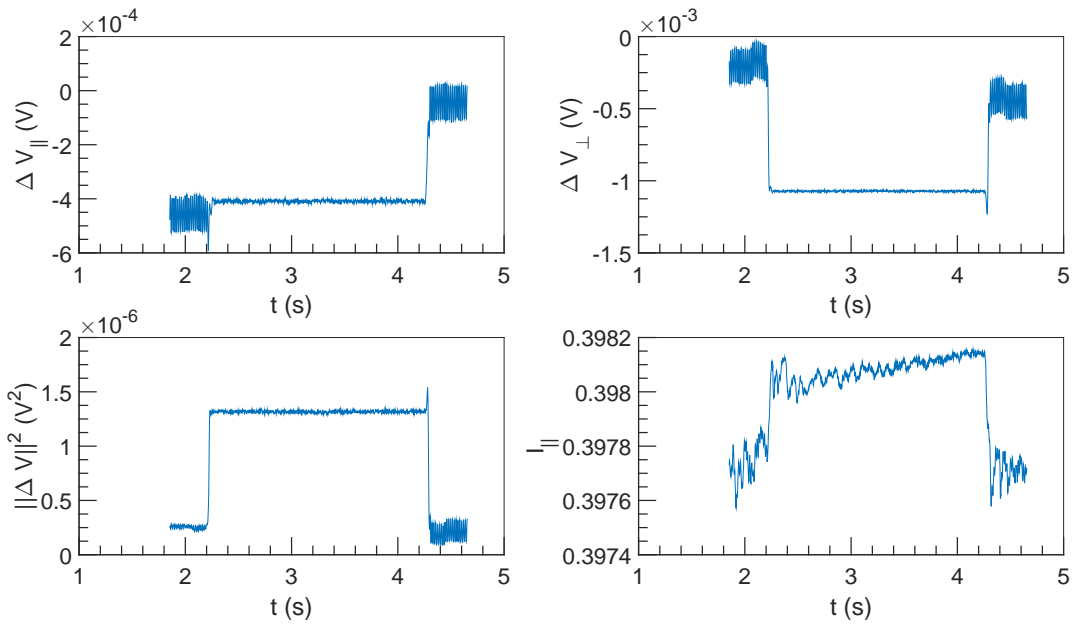


Figure 9.27:  $\Delta V$  and  $I$  vs  $t$  at  $U = 1 \text{ m s}^{-1}$ ,  $\omega = 6283 \text{ rad s}^{-1}$  and  $\alpha = 1.62 \%$ .

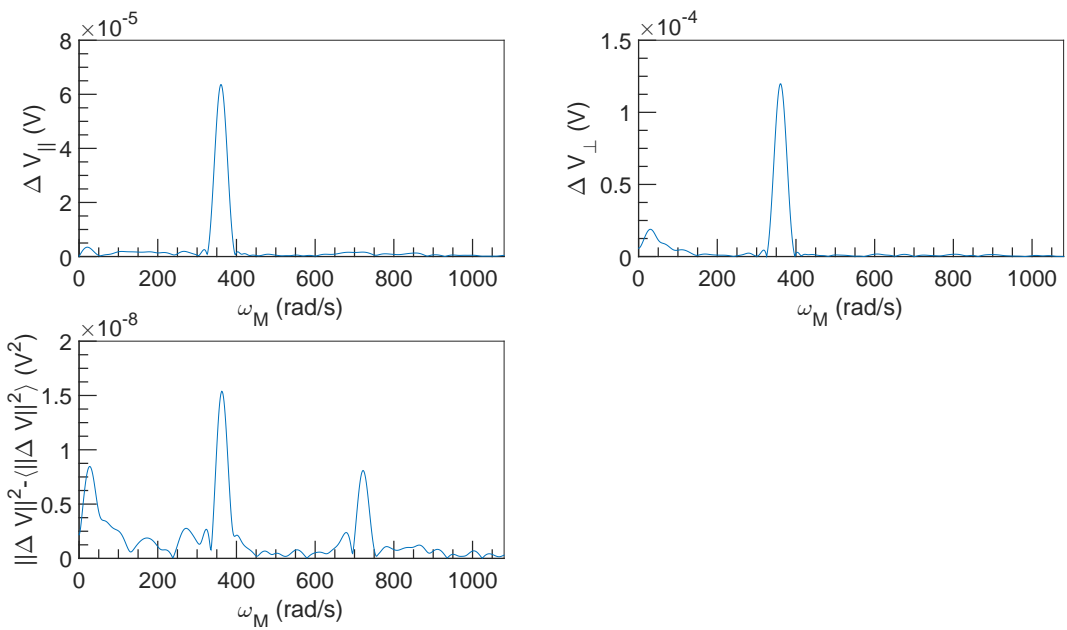


Figure 9.28: FFT spectral density of  $\Delta V$  vs  $\omega_M$  at  $U = 1 \text{ m s}^{-1}$ ,  $\omega = 6283 \text{ rad s}^{-1}$  and  $\alpha = 1.62 \%$ .

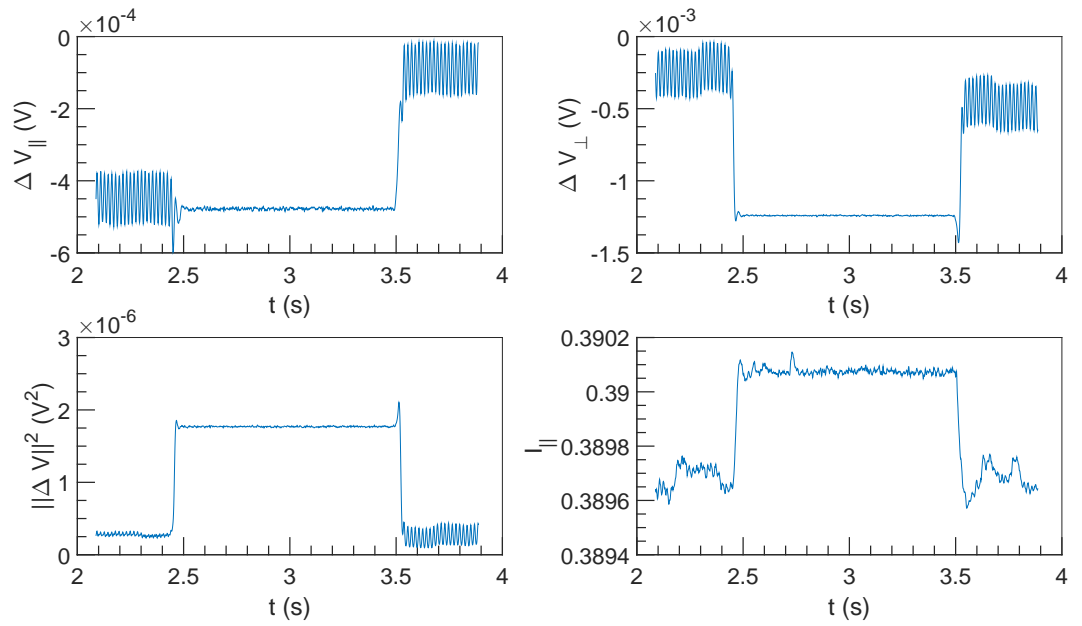


Figure 9.29:  $\Delta V$  and  $I$  vs  $t$  at  $U = 1 \text{ m s}^{-1}$ ,  $\omega = 7854 \text{ rad s}^{-1}$  and  $\alpha = 1.62 \%$ .

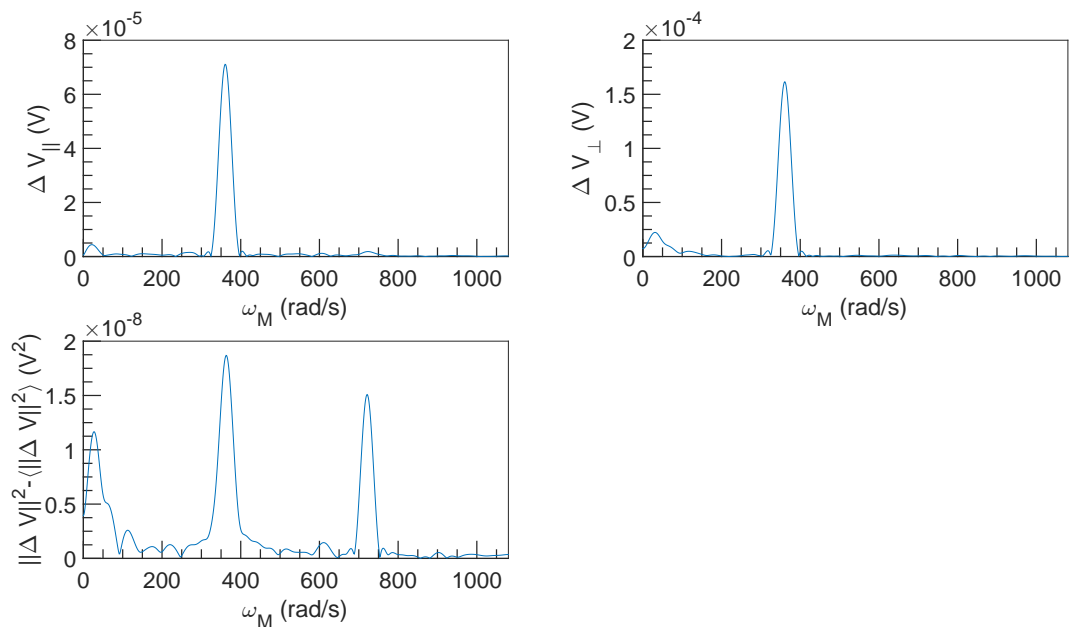


Figure 9.30: FFT spectral density of  $\Delta V$  vs  $\omega_M$  at  $U = 1 \text{ m s}^{-1}$ ,  $\omega = 7854 \text{ rad s}^{-1}$  and  $\alpha = 1.62 \%$ .

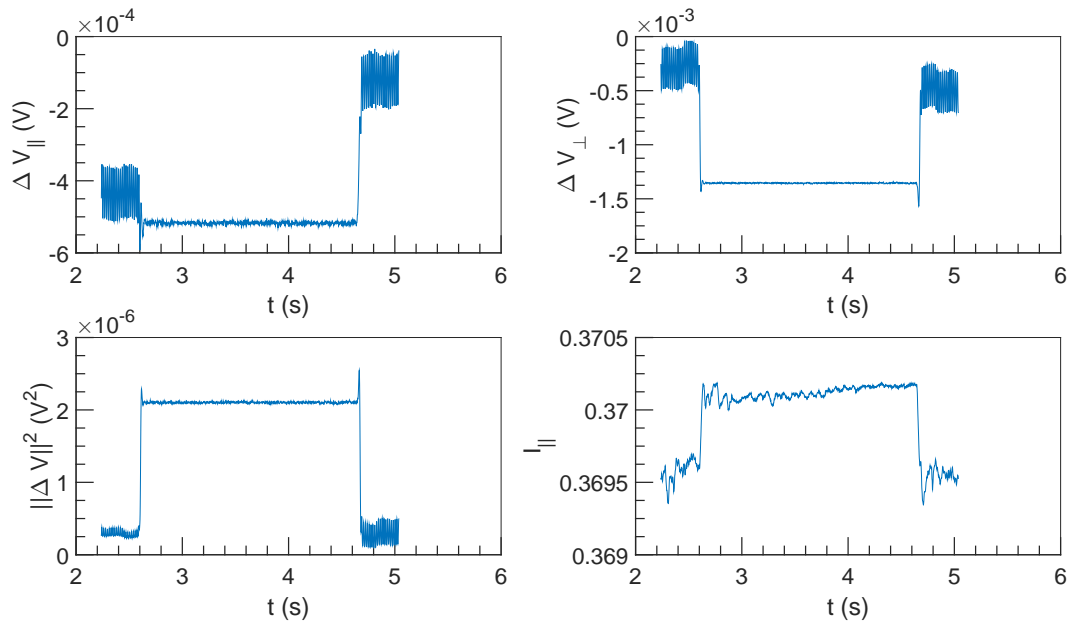


Figure 9.31:  $\Delta V$  and  $I$  vs  $t$  at  $U = 1 \text{ m s}^{-1}$ ,  $\omega = 9425 \text{ rad s}^{-1}$  and  $\alpha = 1.62 \%$ .

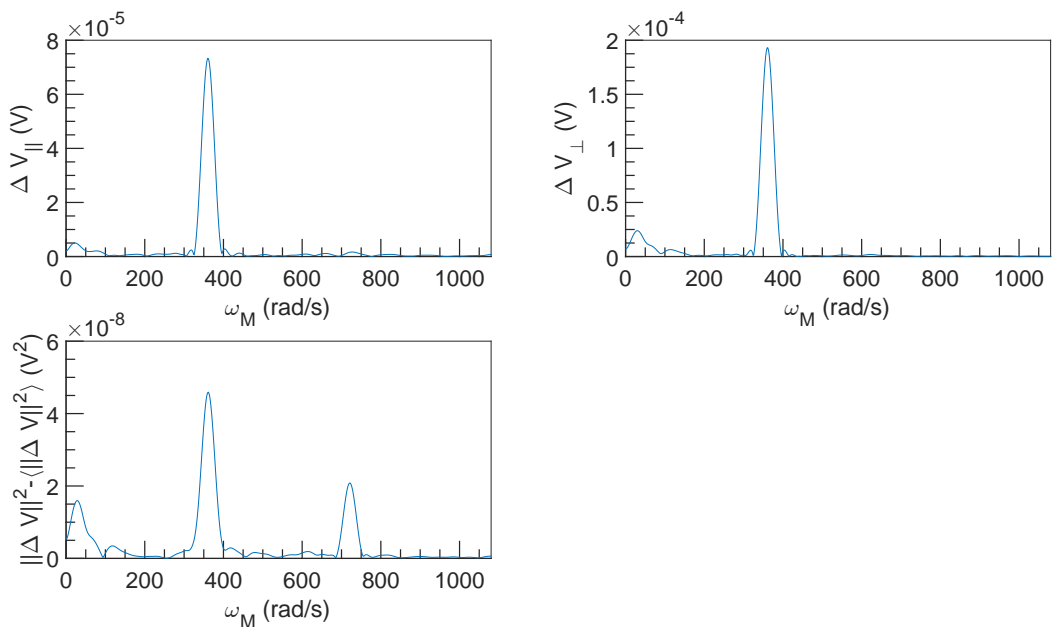


Figure 9.32: FFT spectral density of  $\Delta V$  vs  $\omega_M$  at  $U = 1 \text{ m s}^{-1}$ ,  $\omega = 9425 \text{ rad s}^{-1}$  and  $\alpha = 1.62 \%$ .

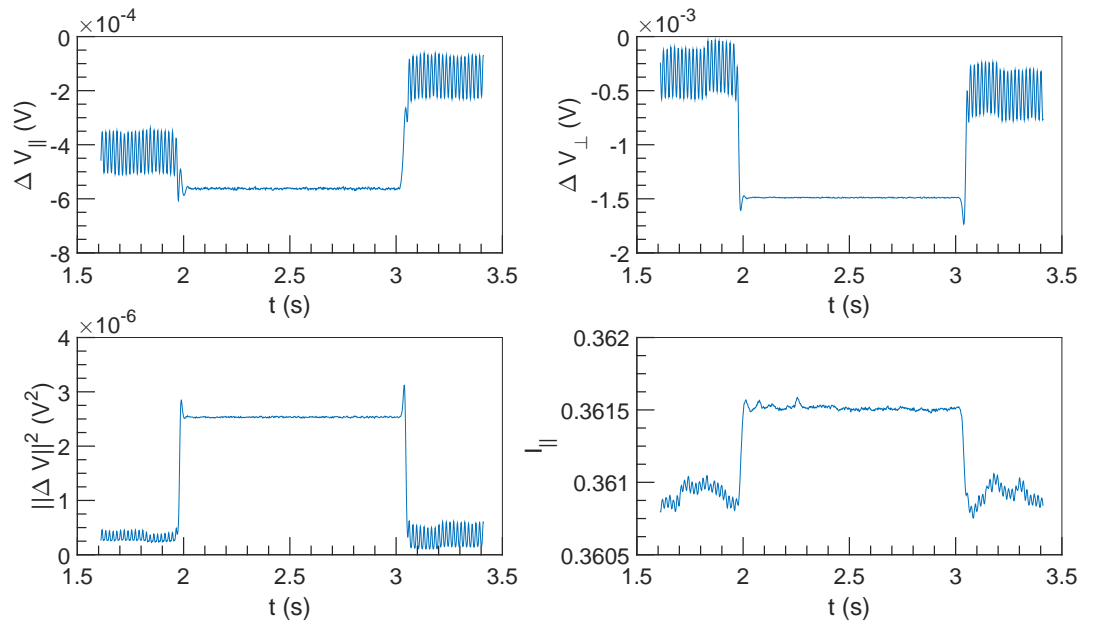


Figure 9.33:  $\Delta V$  and  $I$  vs  $t$  at  $U = 1 \text{ m s}^{-1}$ ,  $\omega = 10996 \text{ rad s}^{-1}$  and  $\alpha = 1.62\%$ .

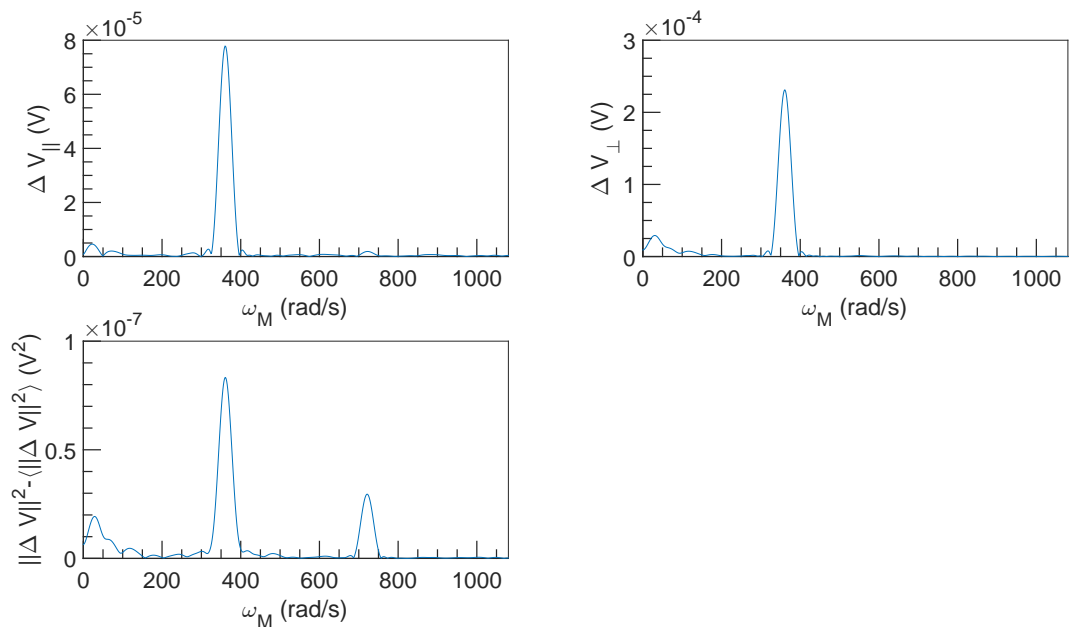


Figure 9.34: FFT spectral density of  $\Delta V$  vs  $\omega_M$  at  $U = 1 \text{ m s}^{-1}$ ,  $\omega = 10996 \text{ rad s}^{-1}$  and  $\alpha = 1.62\%$ .

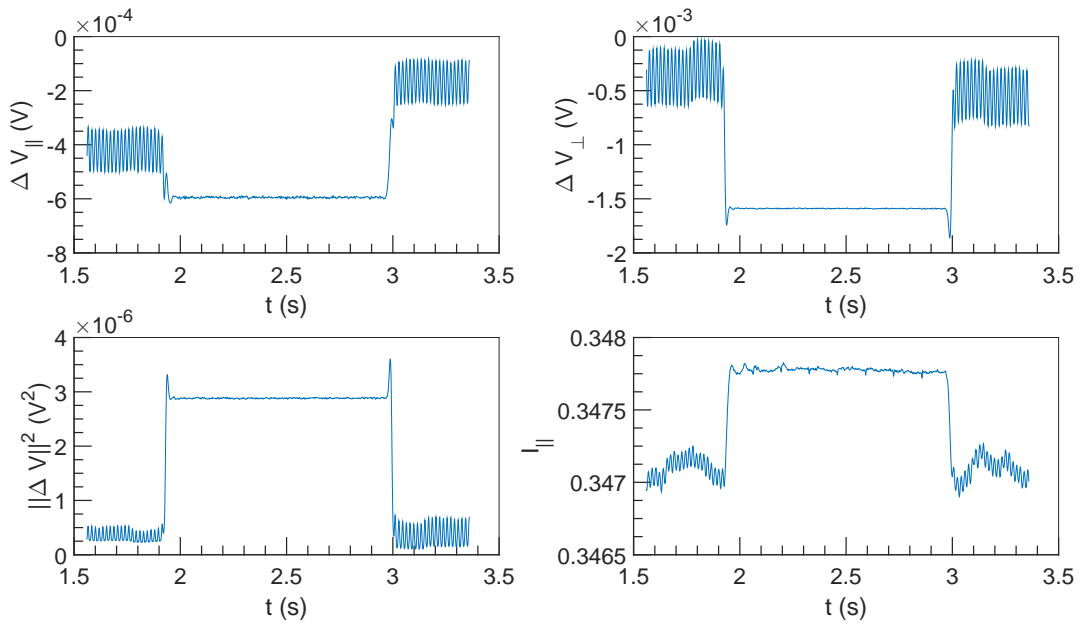


Figure 9.35:  $\Delta V$  and  $I$  vs  $t$  at  $U = 1 \text{ m s}^{-1}$ ,  $\omega = 12566 \text{ rad s}^{-1}$  and  $\alpha = 1.62\%$ .

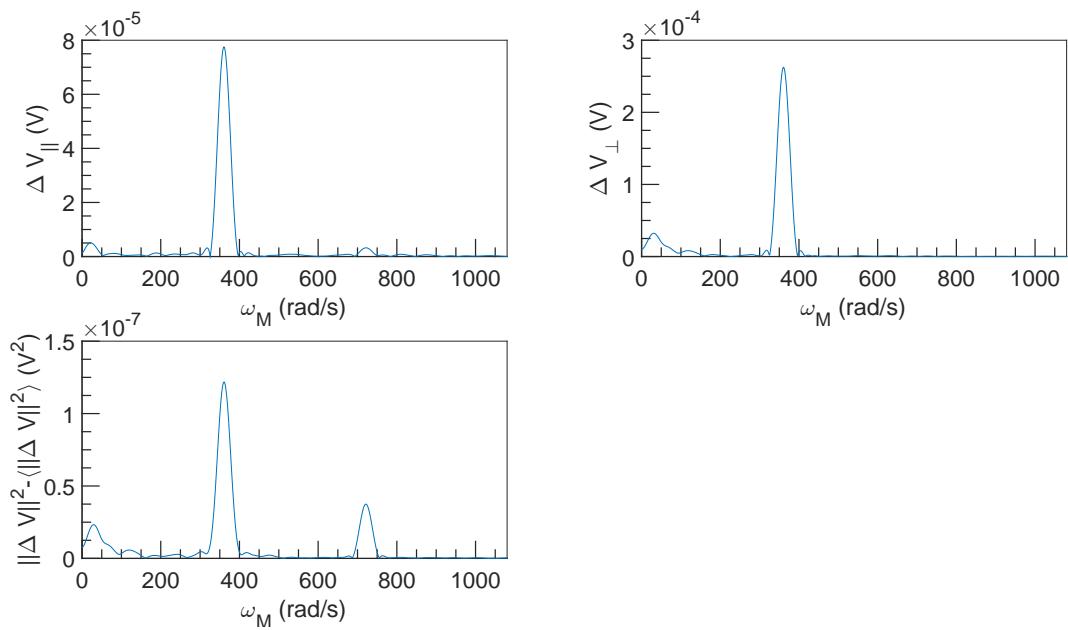


Figure 9.36: FFT spectral density of  $\Delta V$  vs  $\omega_M$  at  $U = 1 \text{ m s}^{-1}$ ,  $\omega = 12566 \text{ rad s}^{-1}$  and  $\alpha = 1.62\%$ .

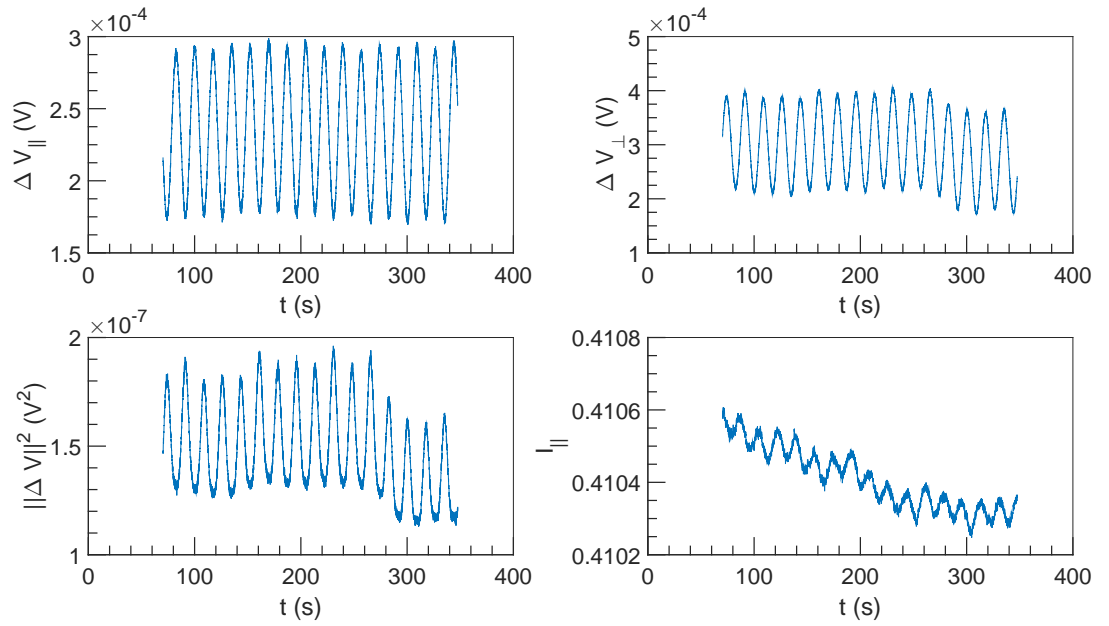


Figure 9.37:  $\Delta V$  and  $I$  vs  $t$  at  $U = 10^{-3} \text{ m s}^{-1}$ ,  $\omega = 4712 \text{ rad s}^{-1}$  and  $\alpha = 1.62\%$ .

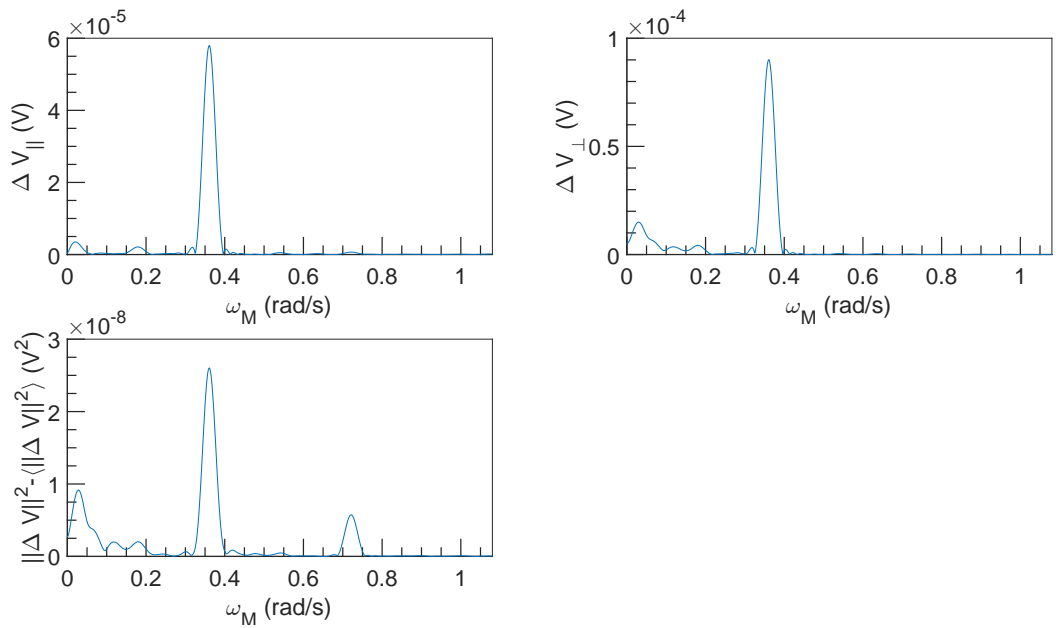


Figure 9.38: FFT spectral density of  $\Delta V$  vs  $\omega_M$  at  $U = 10^{-3} \text{ m s}^{-1}$ ,  $\omega = 4712 \text{ rad s}^{-1}$  and  $\alpha = 1.62\%$ .

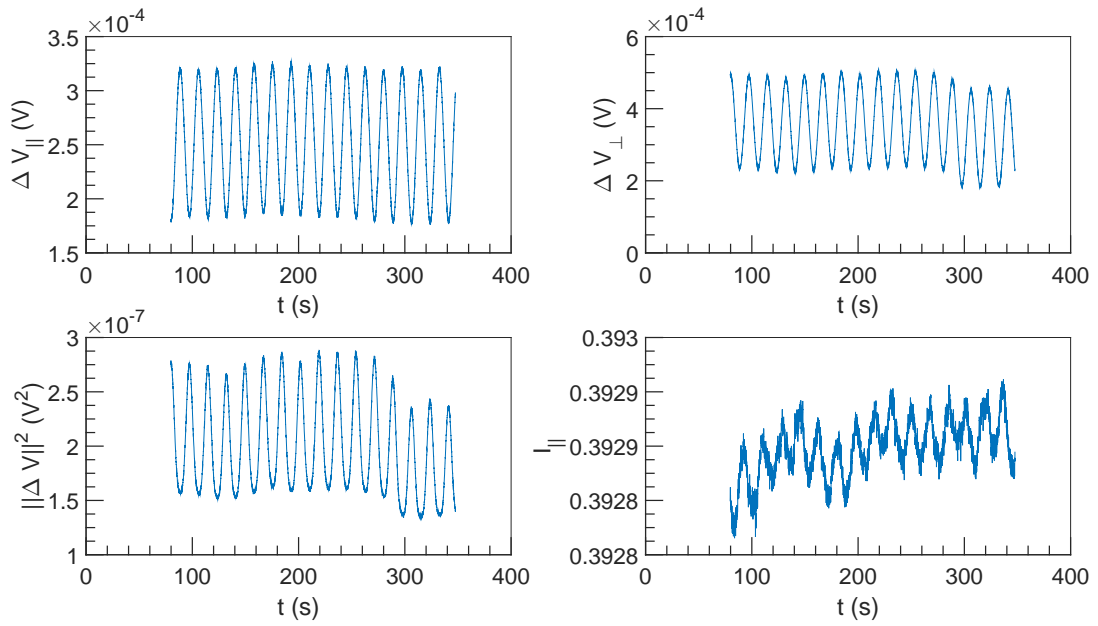


Figure 9.39:  $\Delta V$  and  $I$  vs  $t$  at  $U = 10^{-3} \text{ m s}^{-1}$ ,  $\omega = 6283 \text{ rad s}^{-1}$  and  $\alpha = 1.62\%$ .

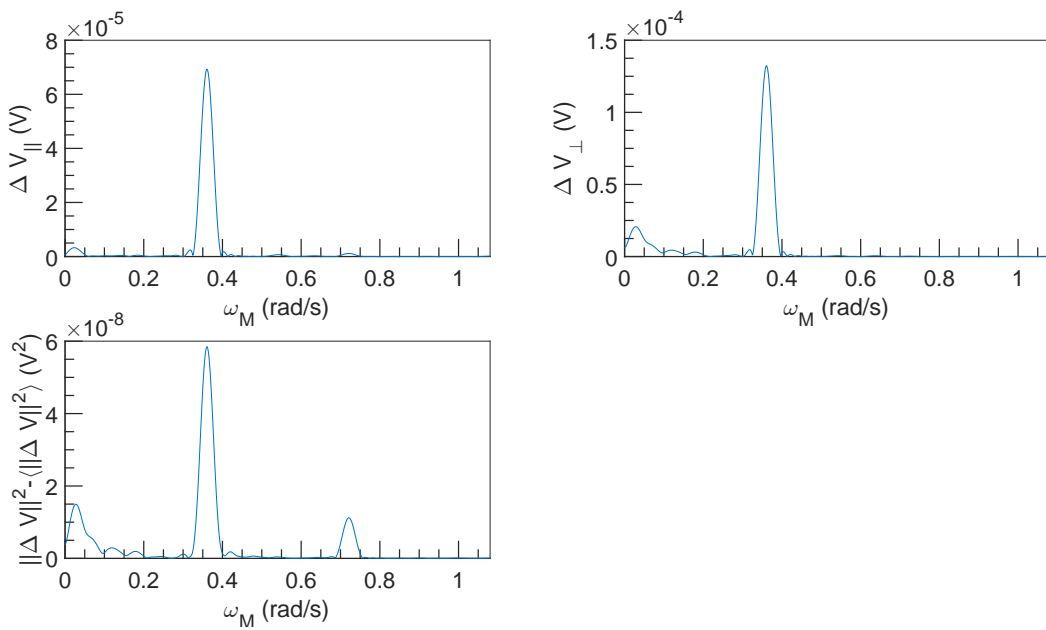


Figure 9.40: FFT spectral density of  $\Delta V$  vs  $\omega_M$  at  $U = 10^{-3} \text{ m s}^{-1}$ ,  $\omega = 6283 \text{ rad s}^{-1}$  and  $\alpha = 1.62\%$ .



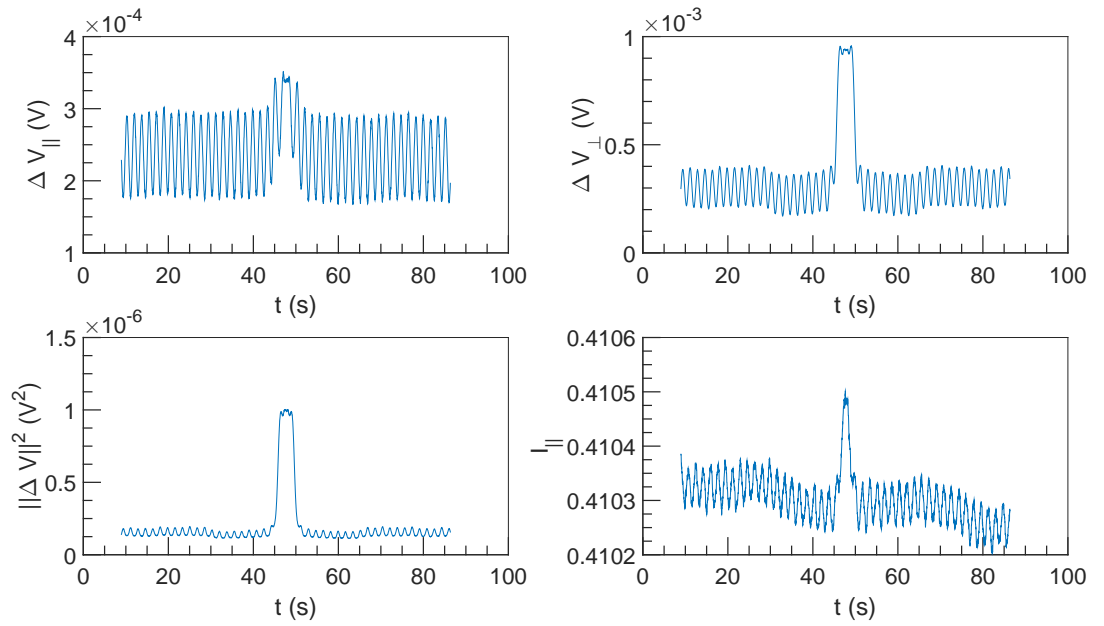


Figure 9.41:  $\Delta V$  and  $I$  vs  $t$  at  $U = 10^{-2} \text{ m s}^{-1}$ ,  $\omega = 4712 \text{ rad s}^{-1}$  and  $\alpha = 1.62\%$ .

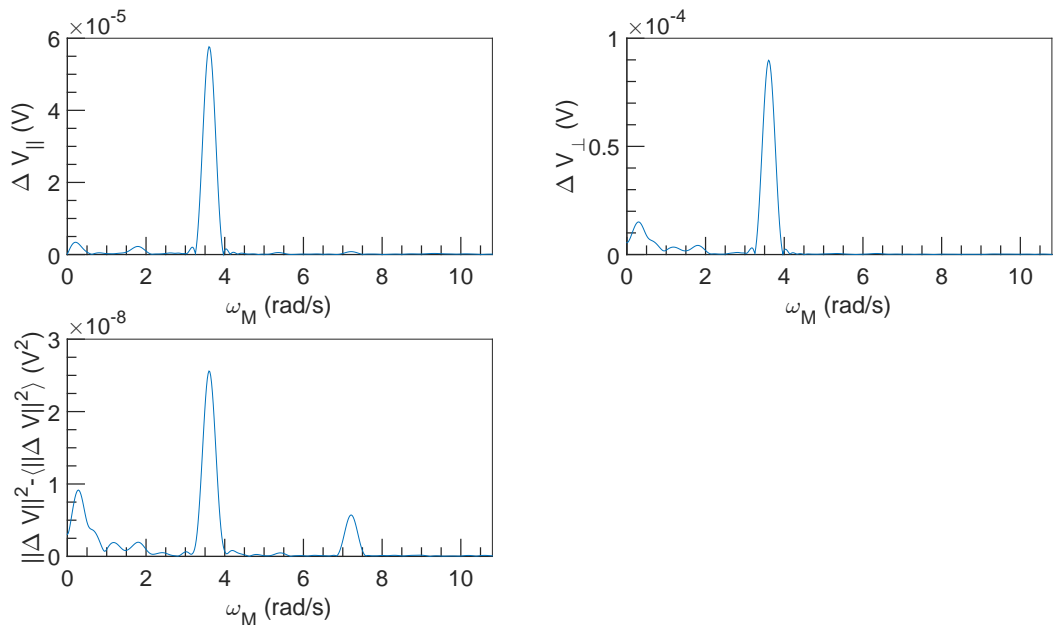


Figure 9.42: FFT spectral density of  $\Delta V$  vs  $\omega_M$  at  $U = 10^{-2} \text{ m s}^{-1}$ ,  $\omega = 4712 \text{ rad s}^{-1}$  and  $\alpha = 1.62\%$ .

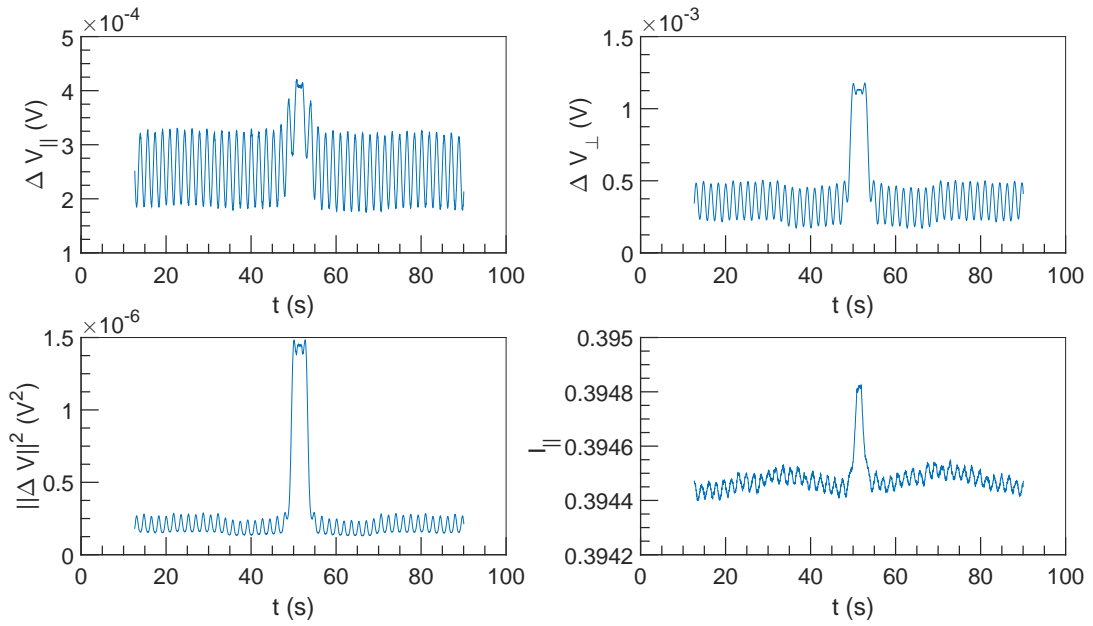


Figure 9.43:  $\Delta V$  and  $I$  vs  $t$  at  $U = 10^{-2} \text{ m s}^{-1}$ ,  $\omega = 6283 \text{ rad s}^{-1}$  and  $\alpha = 1.62 \%$ .

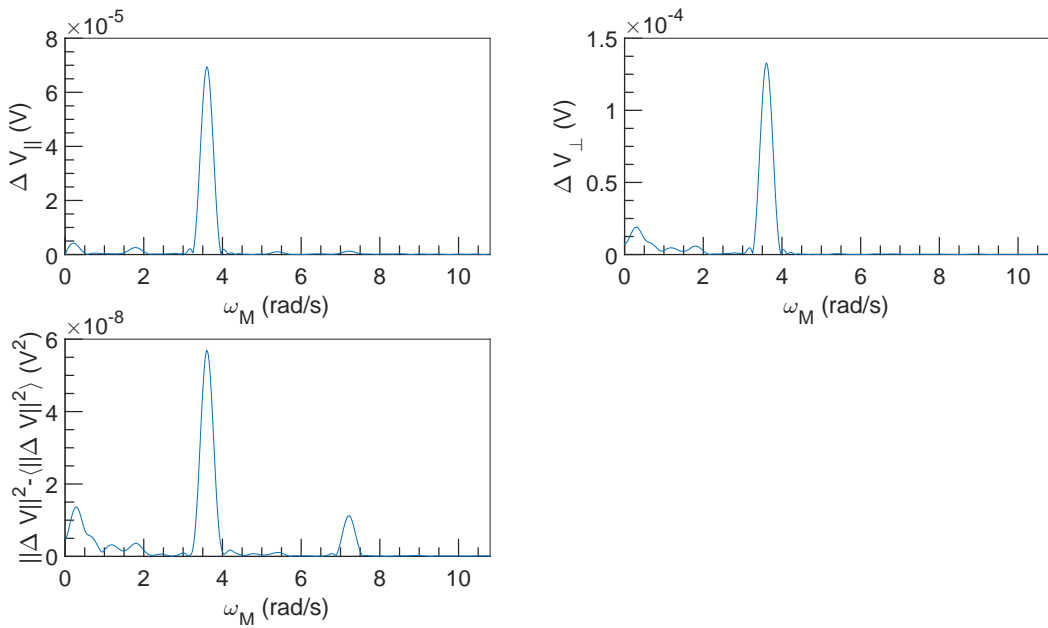


Figure 9.44: FFT spectral density of  $\Delta V$  vs  $\omega_M$  at  $U = 10^{-2} \text{ m s}^{-1}$ ,  $\omega = 6283 \text{ rad s}^{-1}$  and  $\alpha = 1.62 \%$ .

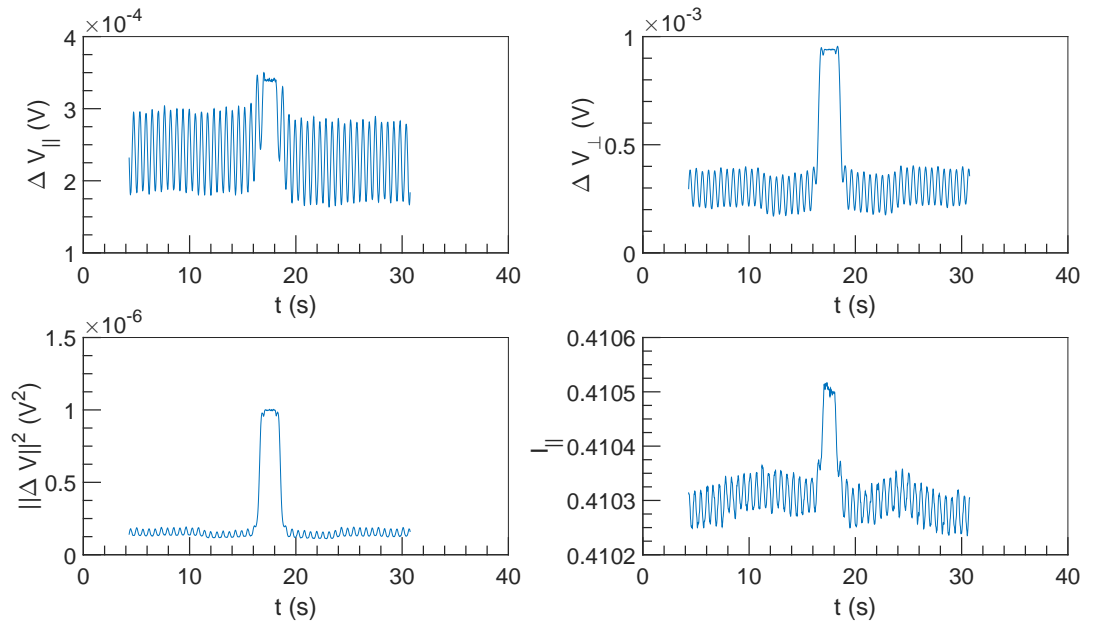


Figure 9.45:  $\Delta V$  and  $I$  vs  $t$  at  $U = 3 \times 10^{-2} \text{ m s}^{-1}$ ,  $\omega = 4712 \text{ rad s}^{-1}$  and  $\alpha = 1.62 \%$ .

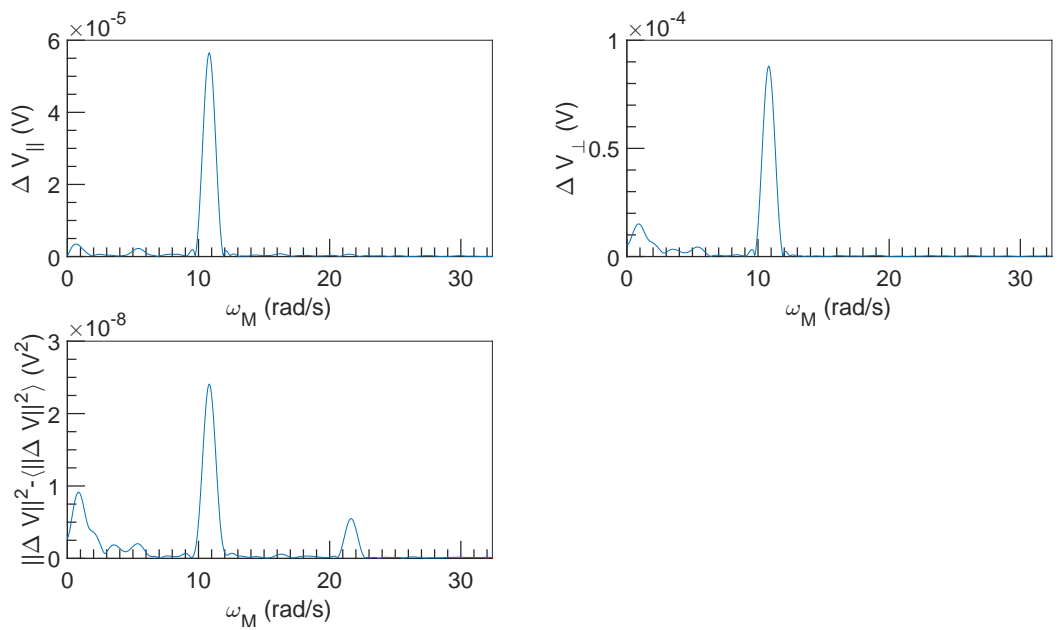


Figure 9.46: FFT spectral density of  $\Delta V$  vs  $\omega_M$  at  $U = 3 \times 10^{-2} \text{ m s}^{-1}$ ,  $\omega = 4712 \text{ rad s}^{-1}$  and  $\alpha = 1.62 \%$ .

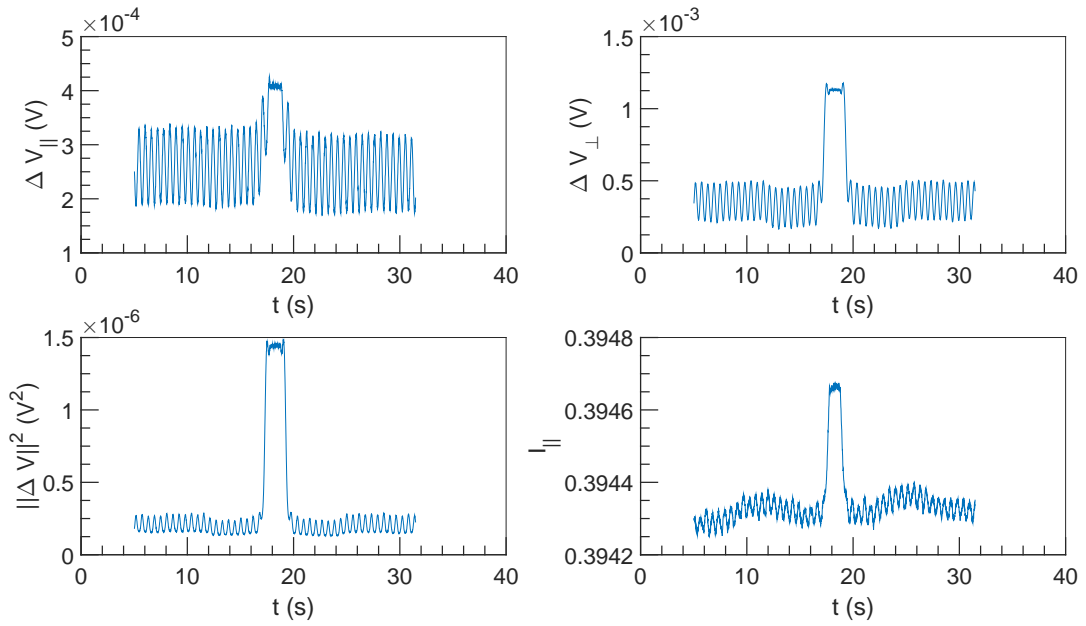


Figure 9.47:  $\Delta V$  and  $I$  vs  $t$  at  $U = 3 \times 10^{-2} \text{ m s}^{-1}$ ,  $\omega = 6283 \text{ rad s}^{-1}$  and  $\alpha = 1.62 \%$ .

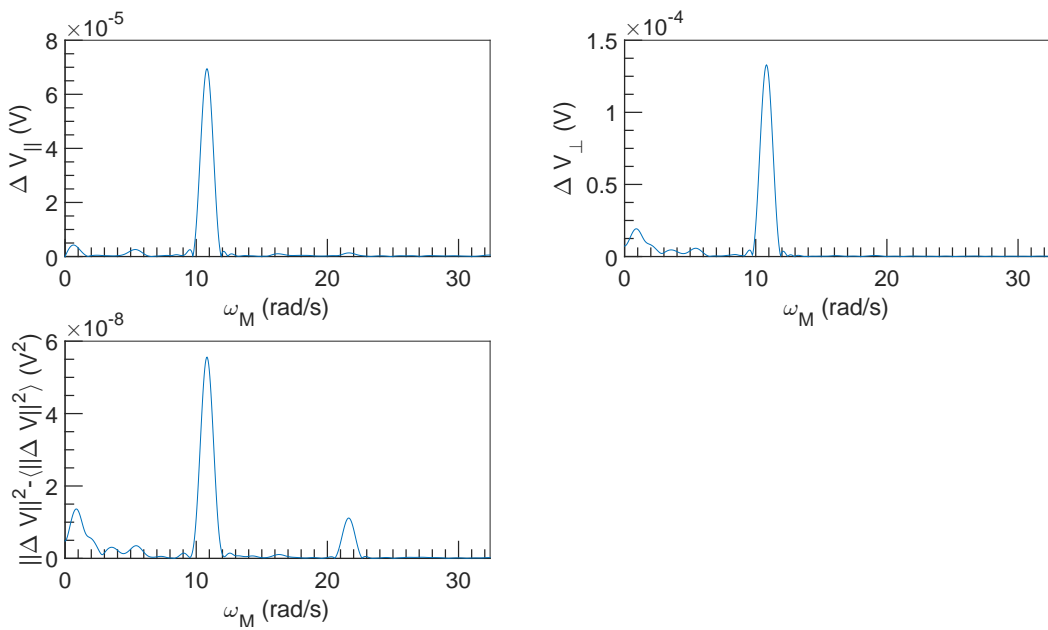


Figure 9.48: FFT spectral density of  $\Delta V$  vs  $\omega_M$  at  $U = 3 \times 10^{-2} \text{ m s}^{-1}$ ,  $\omega = 6283 \text{ rad s}^{-1}$  and  $\alpha = 1.62 \%$ .

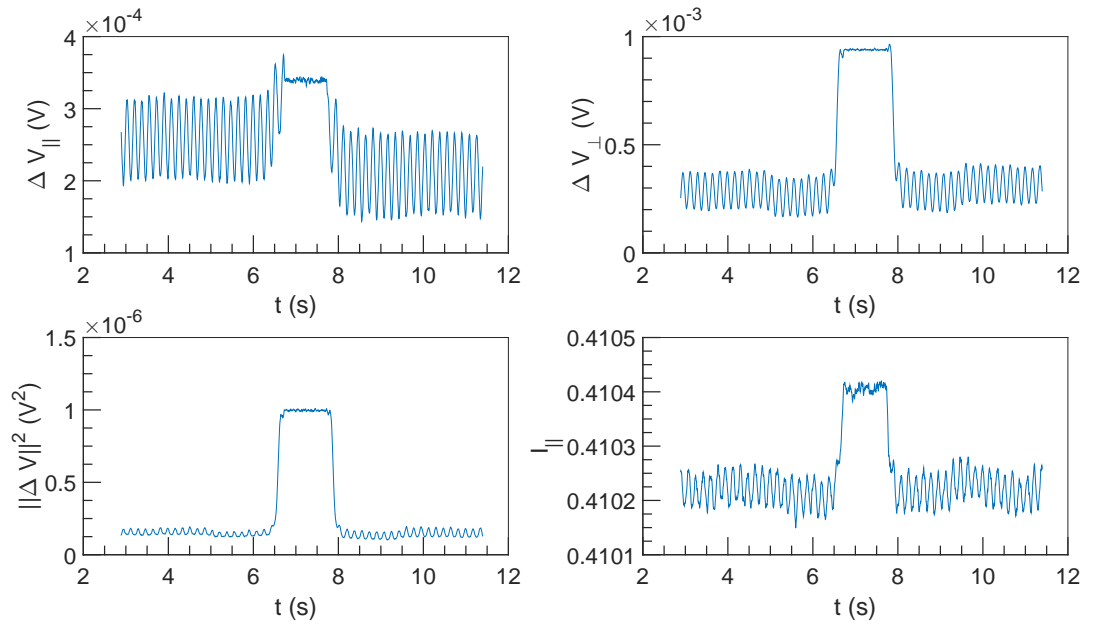


Figure 9.49:  $\Delta V$  and  $I$  vs  $t$  at  $U = 0.1 \text{ m s}^{-1}$ ,  $\omega = 4712 \text{ rad s}^{-1}$  and  $\alpha = 1.62\%$ .

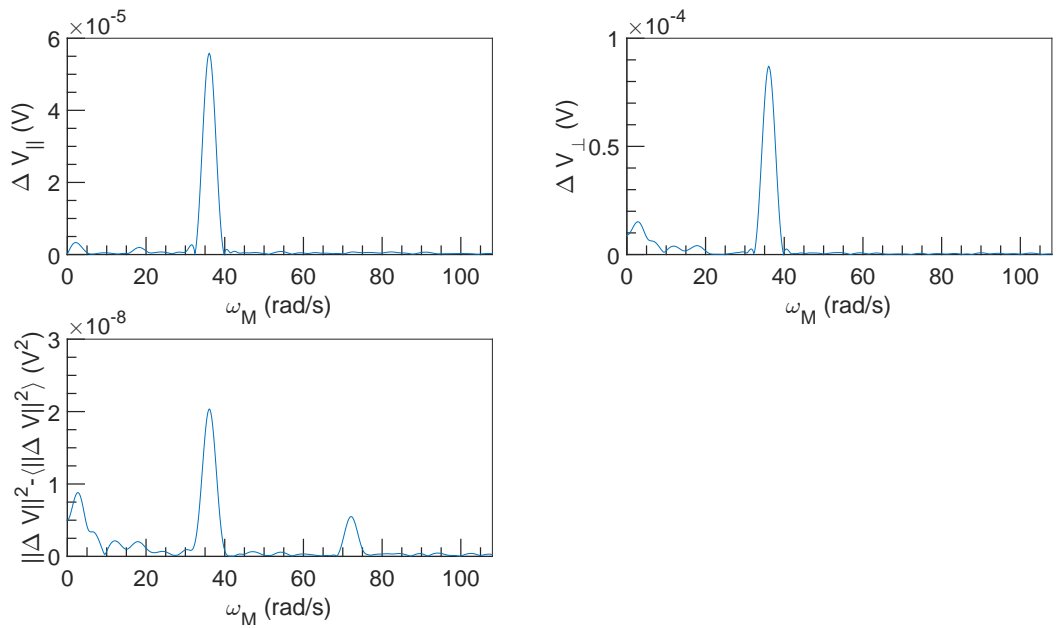


Figure 9.50: FFT spectral density of  $\Delta V$  vs  $\omega_M$  at  $U = 0.1 \text{ m s}^{-1}$ ,  $\omega = 4712 \text{ rad s}^{-1}$  and  $\alpha = 1.62\%$ .

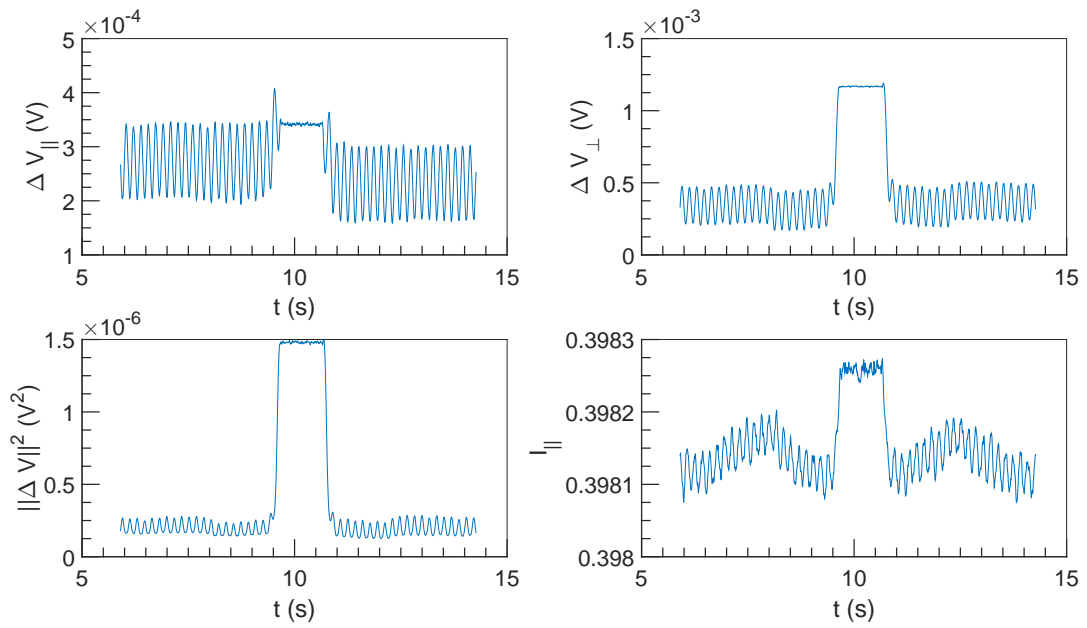


Figure 9.51:  $\Delta V$  and  $I$  vs  $t$  at  $U = 0.1 \text{ m s}^{-1}$ ,  $\omega = 6283 \text{ rad s}^{-1}$  and  $\alpha = 1.62 \%$ .

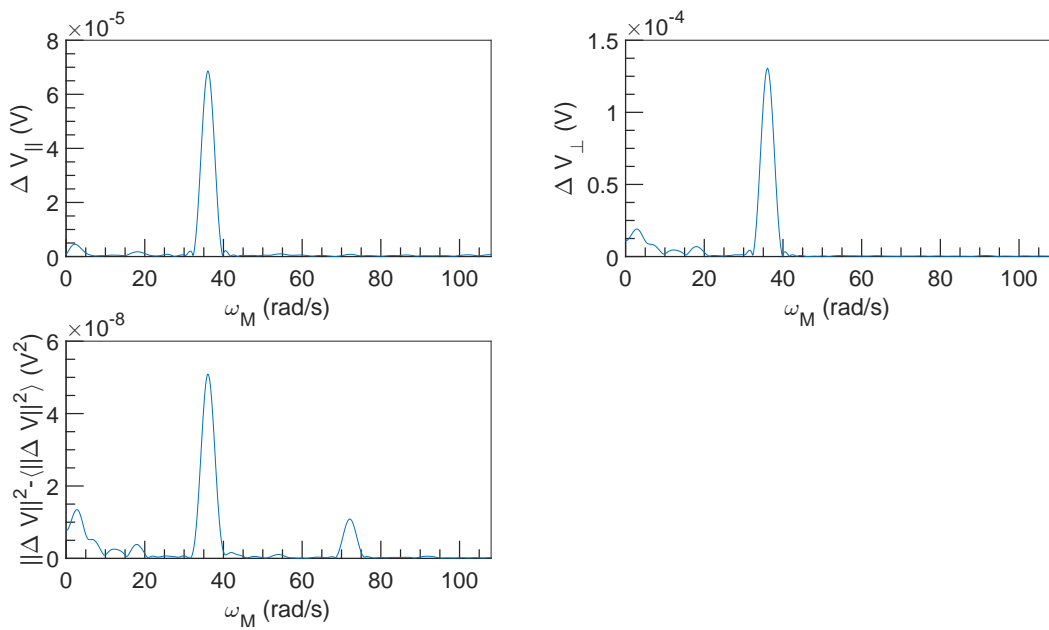


Figure 9.52: FFT spectral density of  $\Delta V$  vs  $\omega_M$  at  $U = 0.1 \text{ m s}^{-1}$ ,  $\omega = 6283 \text{ rad s}^{-1}$  and  $\alpha = 1.62 \%$ .

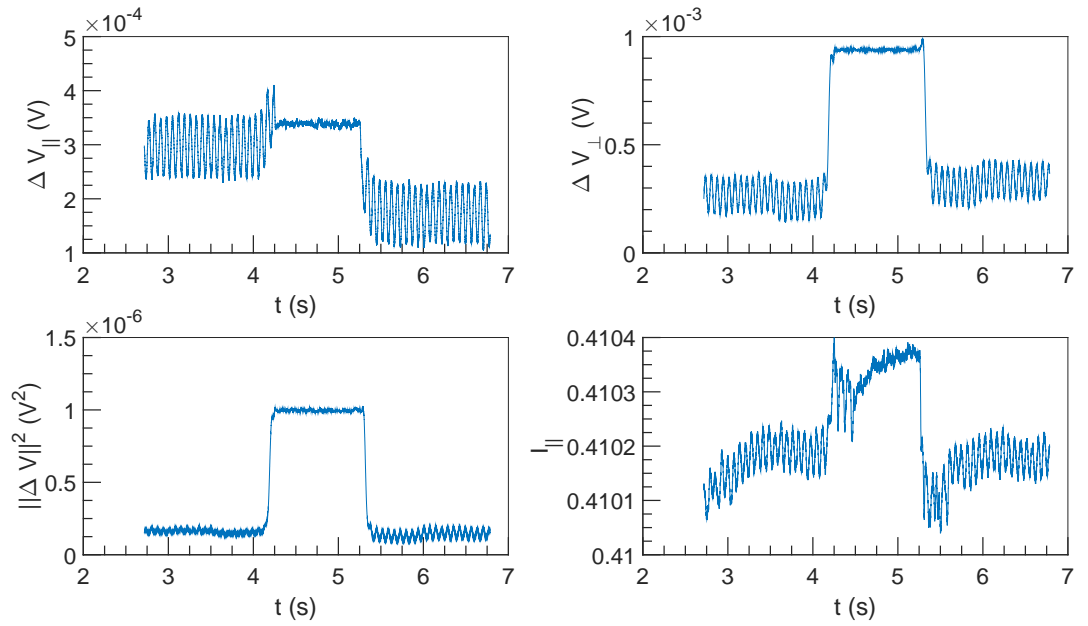


Figure 9.53:  $\Delta V$  and  $I$  vs  $t$  at  $U = 0.25 \text{ m s}^{-1}$ ,  $\omega = 4712 \text{ rad s}^{-1}$  and  $\alpha = 1.62 \%$ .

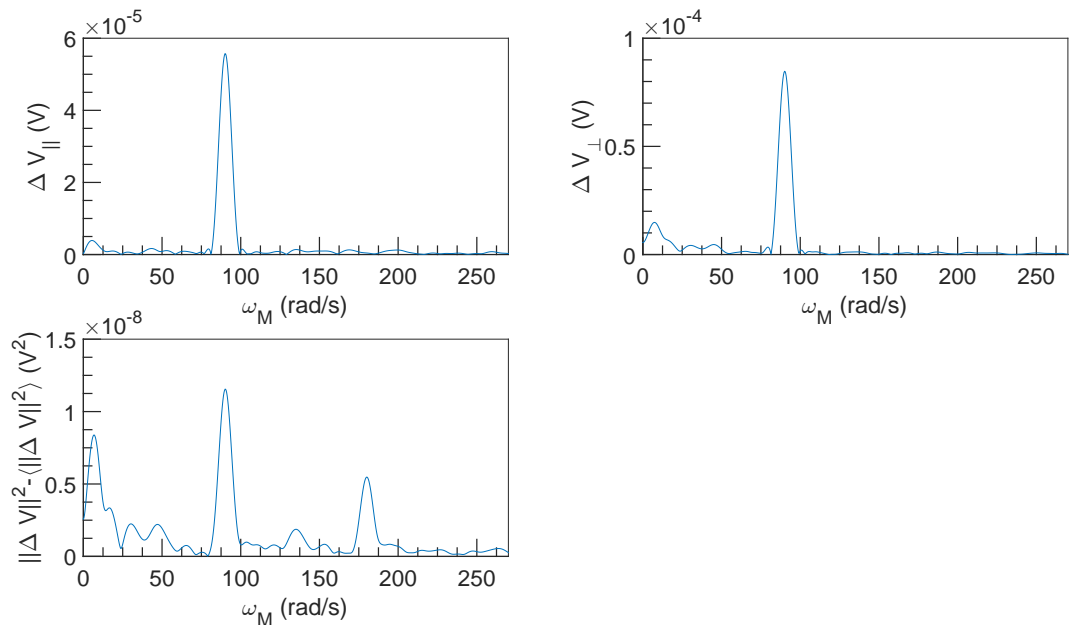


Figure 9.54: FFT spectral density of  $\Delta V$  vs  $\omega_M$  at  $U = 0.25 \text{ m s}^{-1}$ ,  $\omega = 4712 \text{ rad s}^{-1}$  and  $\alpha = 1.62 \%$ .

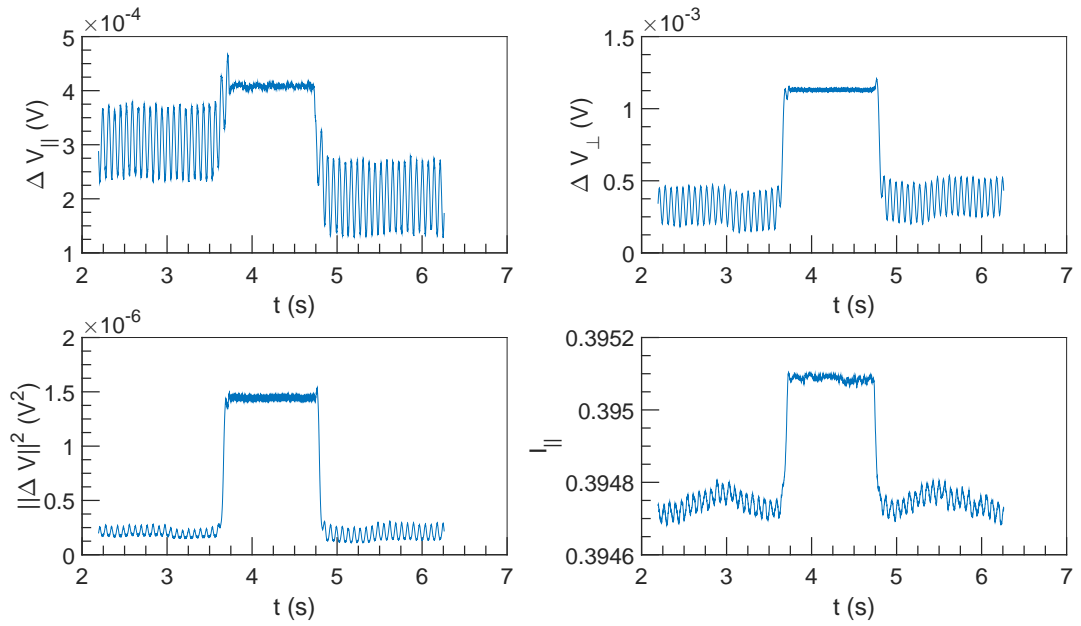


Figure 9.55:  $\Delta V$  and  $I$  vs  $t$  at  $U = 0.25 \text{ m s}^{-1}$ ,  $\omega = 6283 \text{ rad s}^{-1}$  and  $\alpha = 1.62 \%$ .

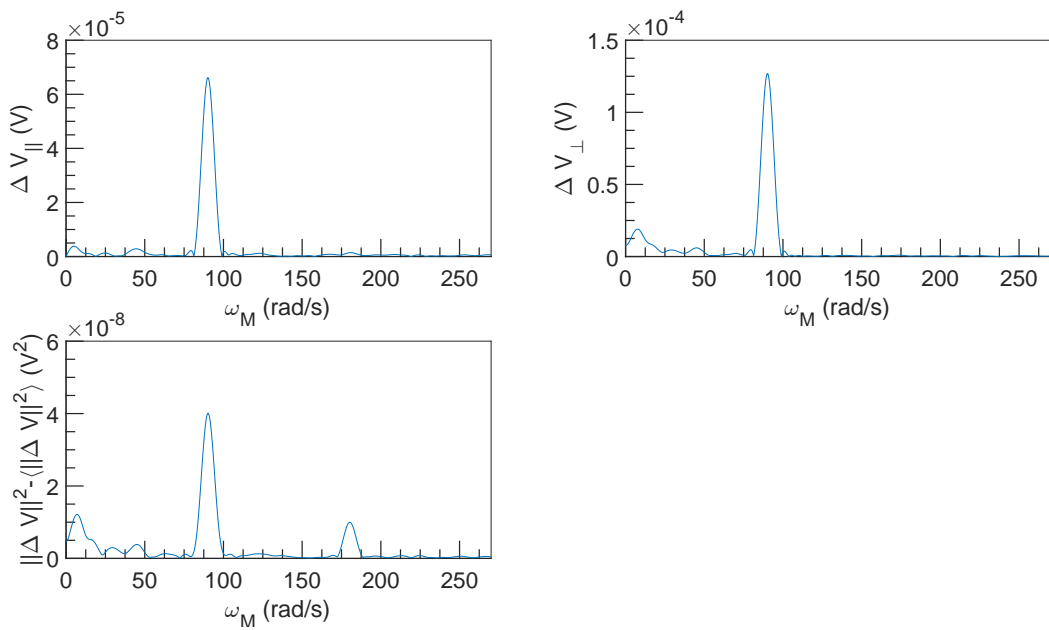


Figure 9.56: FFT spectral density of  $\Delta V$  vs  $\omega_M$  at  $U = 0.25 \text{ m s}^{-1}$ ,  $\omega = 6283 \text{ rad s}^{-1}$  and  $\alpha = 1.62 \%$ .



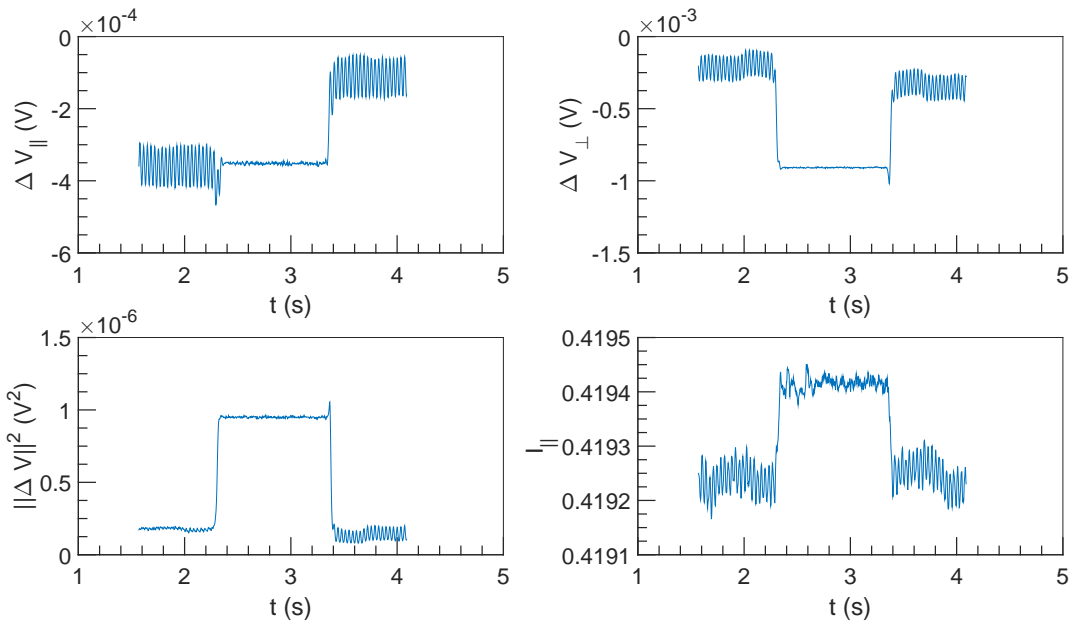


Figure 9.57:  $\Delta V$  and  $I$  vs  $t$  at  $U = 0.5 \text{ m s}^{-1}$ ,  $\omega = 4712 \text{ rad s}^{-1}$  and  $\alpha = 1.62\%$ .

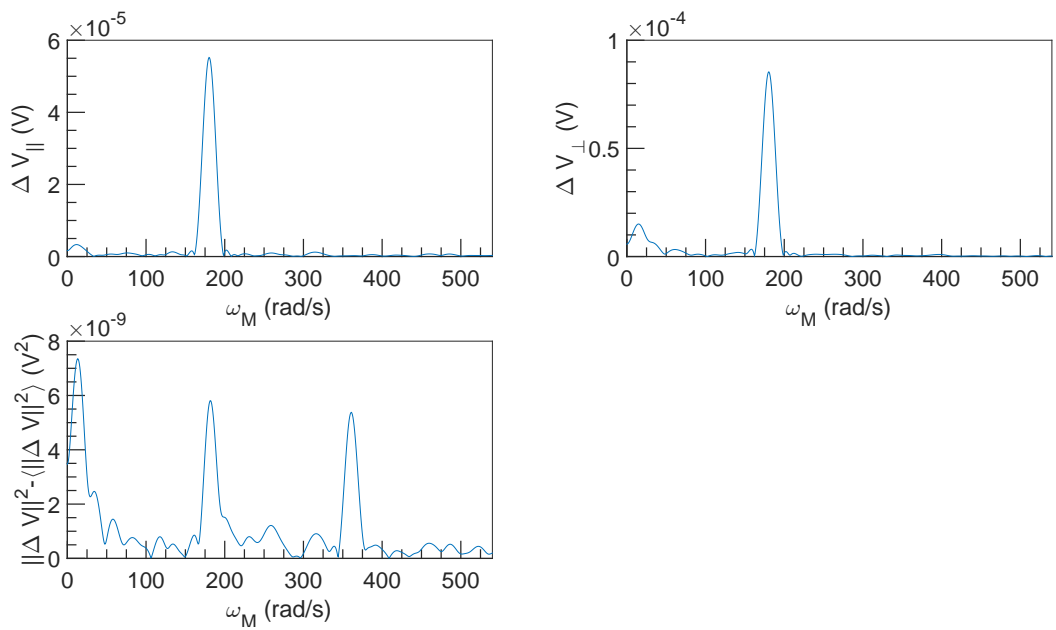


Figure 9.58: FFT spectral density of  $\Delta V$  vs  $\omega_M$  at  $U = 0.5 \text{ m s}^{-1}$ ,  $\omega = 4712 \text{ rad s}^{-1}$  and  $\alpha = 1.62\%$ .

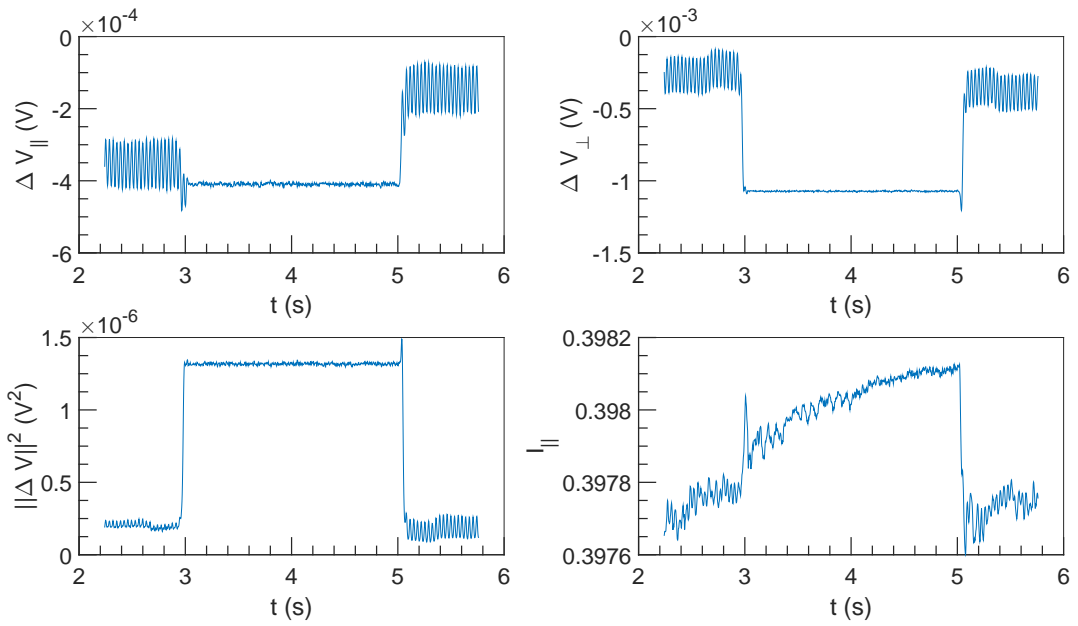


Figure 9.59:  $\Delta V$  and  $I$  vs  $t$  at  $U = 0.5 \text{ m s}^{-1}$ ,  $\omega = 6283 \text{ rad s}^{-1}$  and  $\alpha = 1.62 \%$ .

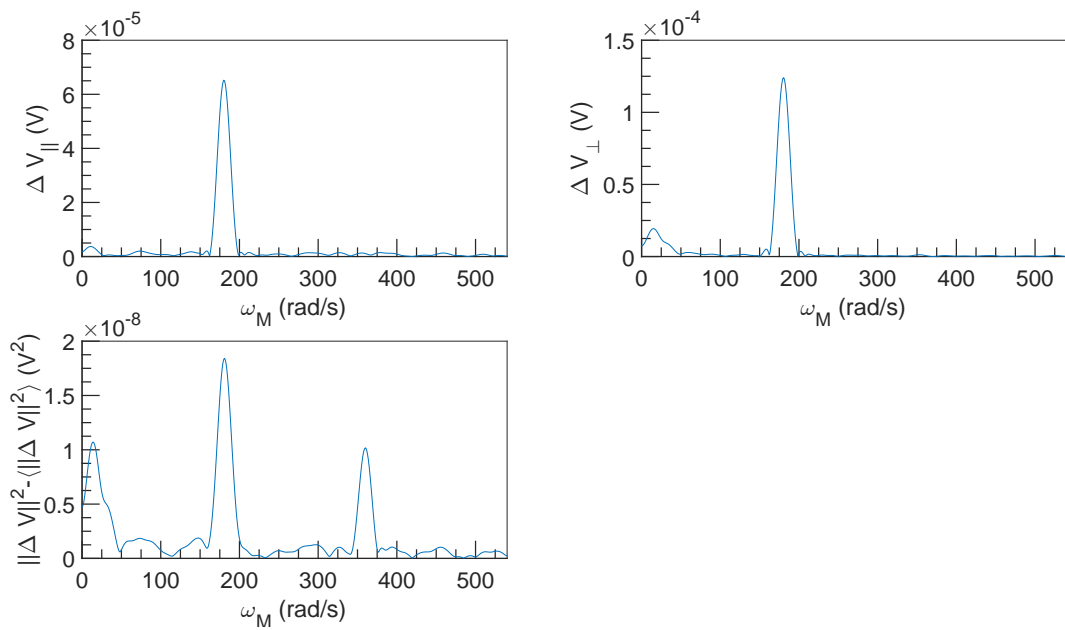


Figure 9.60: FFT spectral density of  $\Delta V$  vs  $\omega_M$  at  $U = 0.5 \text{ m s}^{-1}$ ,  $\omega = 6283 \text{ rad s}^{-1}$  and  $\alpha = 1.62 \%$ .

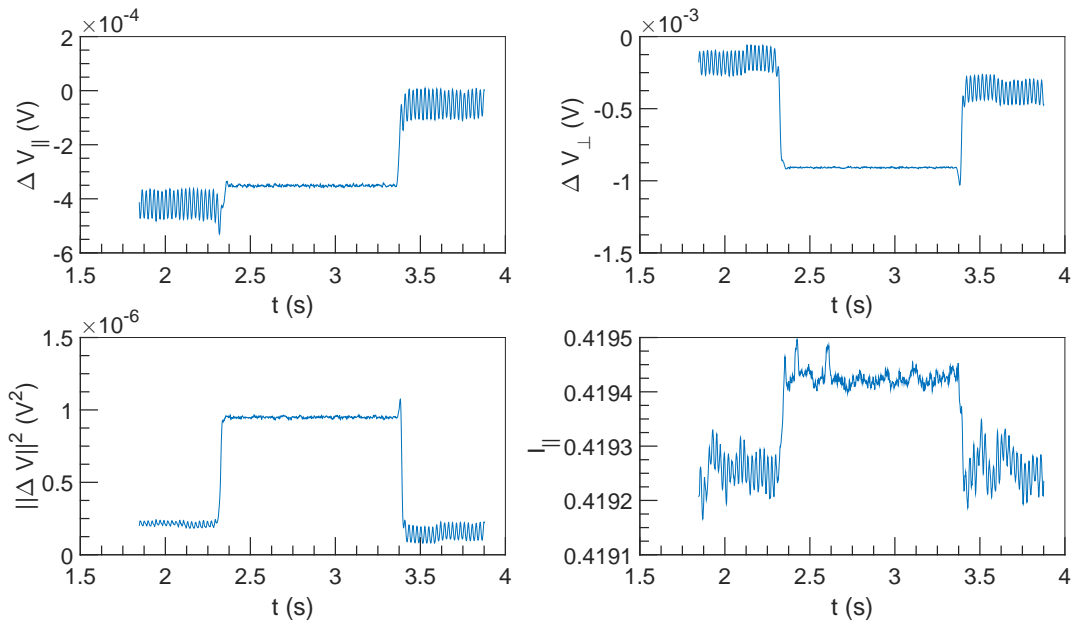


Figure 9.61:  $\Delta V$  and  $I$  vs  $t$  at  $U = 0.75 \text{ m s}^{-1}$ ,  $\omega = 4712 \text{ rad s}^{-1}$  and  $\alpha = 1.62 \%$ .

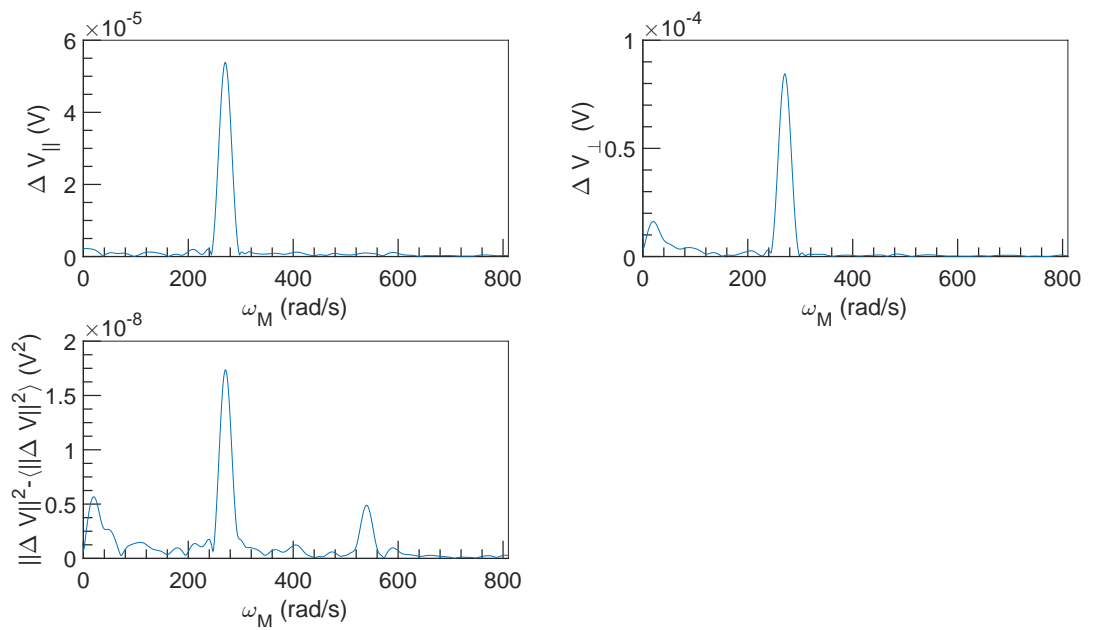


Figure 9.62: FFT spectral density of  $\Delta V$  vs  $\omega_M$  at  $U = 0.75 \text{ m s}^{-1}$ ,  $\omega = 4712 \text{ rad s}^{-1}$  and  $\alpha = 1.62 \%$ .

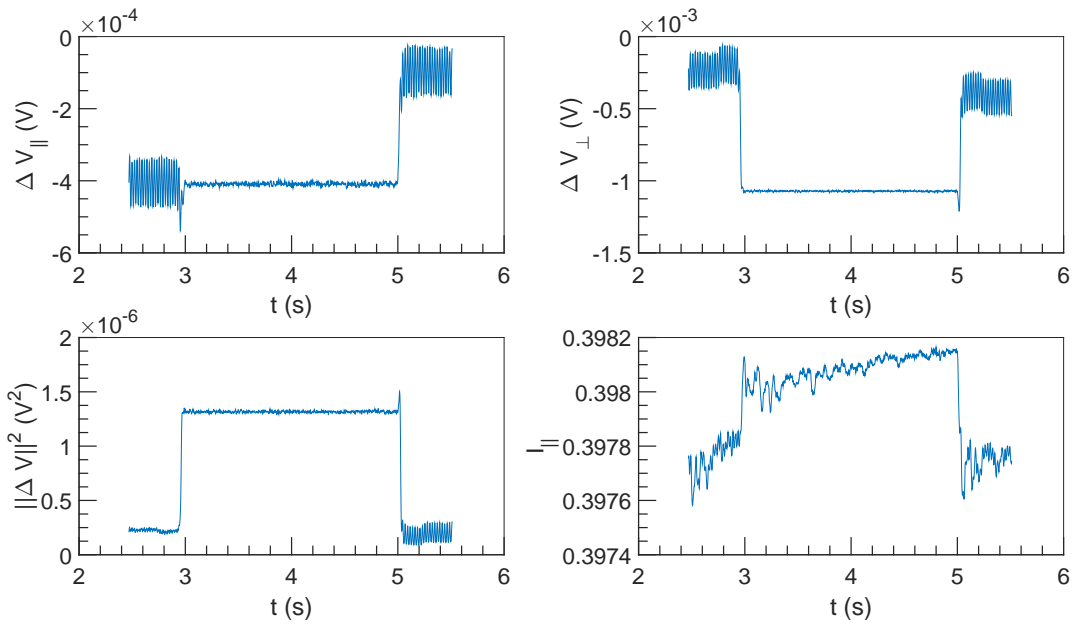


Figure 9.63:  $\Delta V$  and  $I$  vs  $t$  at  $U = 0.75 \text{ m s}^{-1}$ ,  $\omega = 6283 \text{ rad s}^{-1}$  and  $\alpha = 1.62 \%$ .

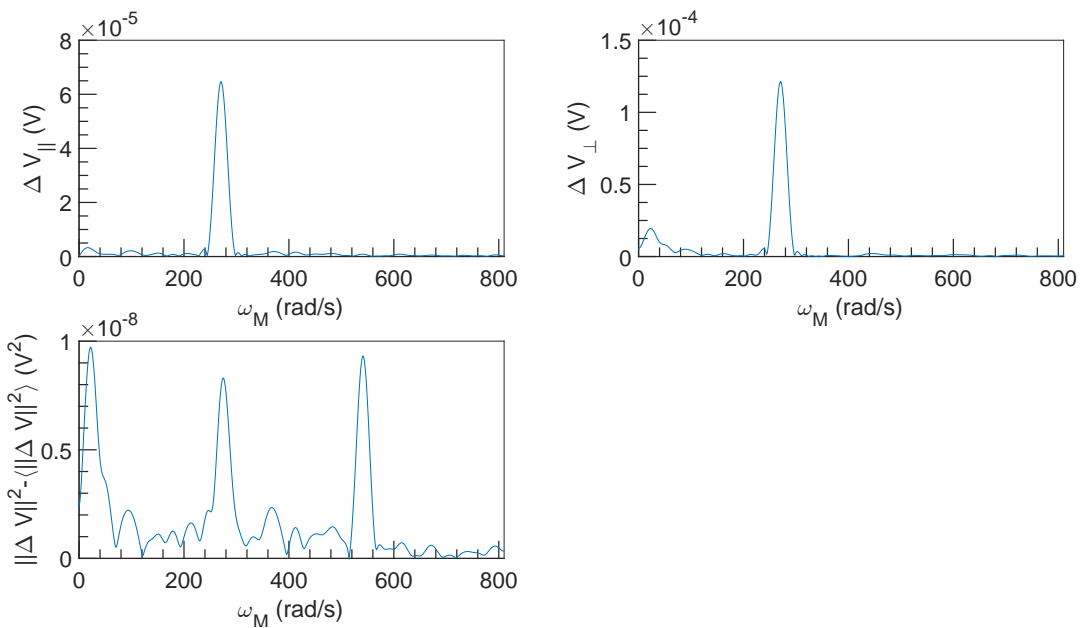


Figure 9.64: FFT spectral density of  $\Delta V$  vs  $\omega_M$  at  $U = 0.75 \text{ m s}^{-1}$ ,  $\omega = 6283 \text{ rad s}^{-1}$  and  $\alpha = 1.62 \%$ .

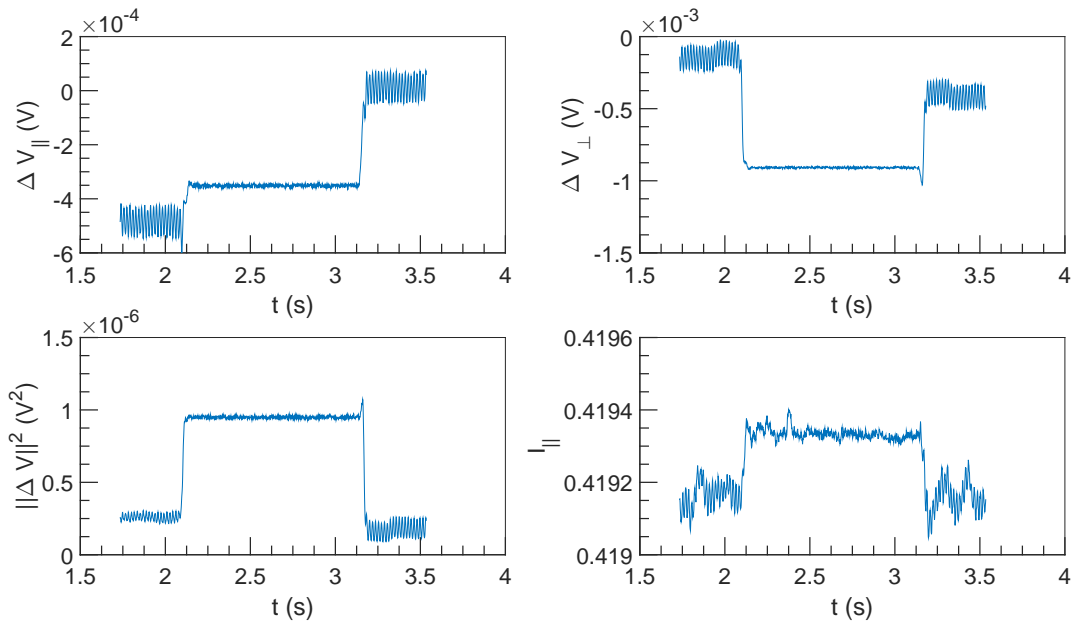


Figure 9.65:  $\Delta V$  and  $I$  vs  $t$  at  $U = 1 \text{ m s}^{-1}$ ,  $\omega = 4712 \text{ rad s}^{-1}$  and  $\alpha = 1.62 \%$ .

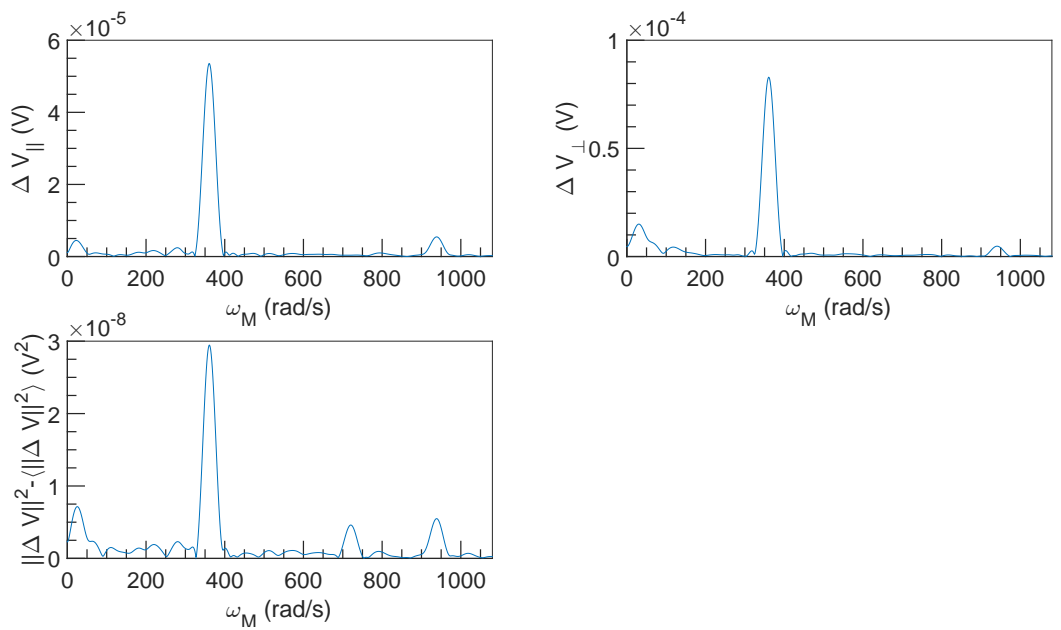


Figure 9.66: FFT spectral density of  $\Delta V$  vs  $\omega_M$  at  $U = 1 \text{ m s}^{-1}$ ,  $\omega = 4712 \text{ rad s}^{-1}$  and  $\alpha = 1.62 \%$ .

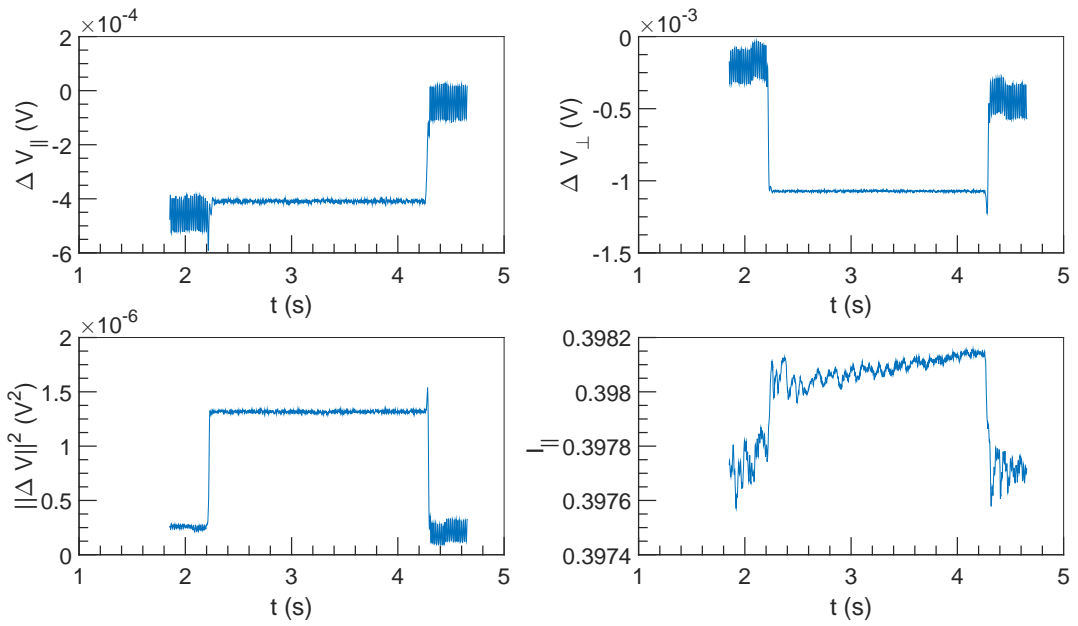


Figure 9.67:  $\Delta V$  and  $I$  vs  $t$  at  $U = 1 \text{ m s}^{-1}$ ,  $\omega = 6283 \text{ rad s}^{-1}$  and  $\alpha = 1.62 \%$ .

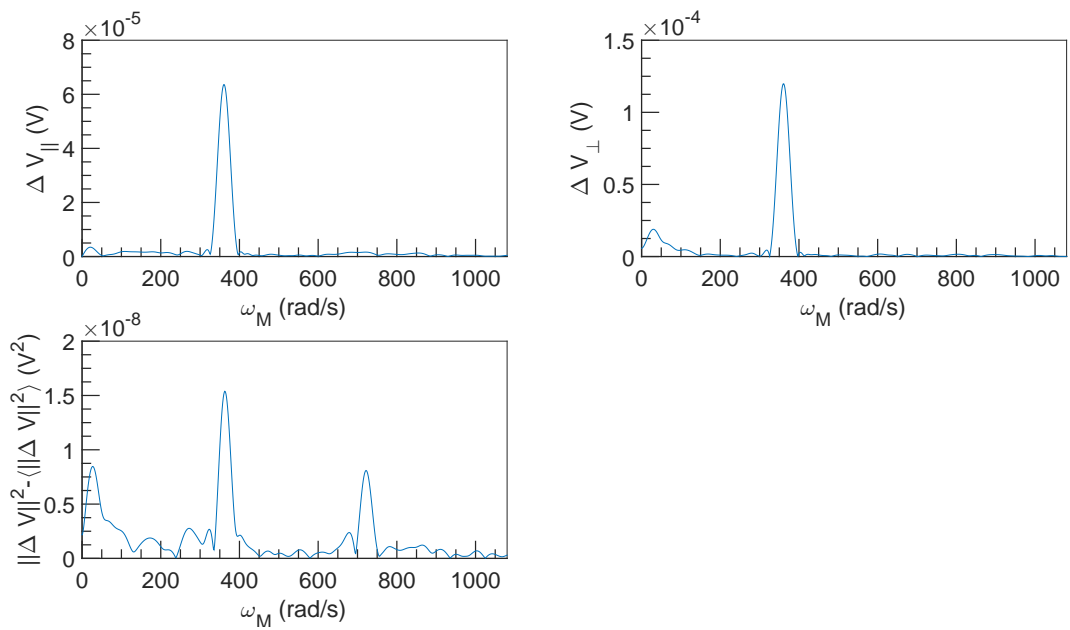


Figure 9.68: FFT spectral density of  $\Delta V$  vs  $\omega_M$  at  $U = 1 \text{ m s}^{-1}$ ,  $\omega = 6283 \text{ rad s}^{-1}$  and  $\alpha = 1.62 \%$ .